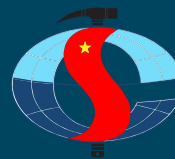




THE STATE COUNCIL FOR PROFESSORSHIP
INTERDISCIPLINARY PROFESSOR COUNCIL
OF THE EARTH AND MINING SCIENCES



IES - VAST

INSTITUTE OF EARTH SCIENCES
VIETNAM ACADEMY OF SCIENCE AND TECHNOLOGY

Advances in the Earth, Mining and Environmental Sciences for Safe and Sustainable Development

Volume 2

Earth, Mine, and Environmental Sciences for
Green, Sustainable, and Prosperous Development
in the Era of a Nation's Rise



PUBLISHING HOUSE FOR SCIENCE AND TECHNOLOGY

PUBLISHING HOUSE FOR SCIENCE AND TECHNOLOGY

A16, 18 Hoang Quoc Viet Road, Nghia Do, Ha Noi

Marketing & Distribution Department: **024.22149040**;

Editorial Department: **024.37917148**

Administration Support Department: **024.22149041**

Fax: **024.37910147**, Email: **nxb@vap.ac.vn**; Website: **www.vap.ac.vn**; **ebook.vap.ac.vn**

**ADVANCES IN THE EARTH, MINING
AND ENVIRONMENTAL SCIENCES FOR SAFE
AND SUSTAINABLE DEVELOPMENT**

Volume 2:

**Earth, Mine, and Environmental Sciences for Green, Sustainable,
and Prosperous Development in the Era of a Nation's Rise**

**Institute of Earth Sciences, Vietnam Academy of Science and Technology
The State Council for Professorship, Interdisciplinary Professor Council
of the Earth and Mining Sciences**

Responsible for Publishing

Director, Editor in Chief

PHAM THI HIEU

Editor:

Le Phi Loan, Nguyen Van Vinh

Computing Technique:

Nguyen Van Vinh

Cover design:

Nguyen Thanh Hung

Corporate publishing: Institute of Earth Sciences

Address: No. 68 Huynh Thuc Khang Street, Lang Ward, Hanoi

ISBN: 978-604-357-453-1

Registered number for Publication: 4637-2025/CXBIPH/01-64/KHTNVCN.

Decision number for Publication: 94/QĐ-KHTNCN was issued on December 02, 2025.

Copyright deposit were completed in 4th quarter, 2025.



THE STATE COUNCIL FOR PROFESSORSHIP
INTERDISCIPLINARY PROFESSOR COUNCIL
OF THE EARTH AND MINING SCIENCES



IES - VAST

INSTITUTE OF EARTH SCIENCES
VIETNAM ACADEMY OF SCIENCE AND TECHNOLOGY

ADVANCES IN THE EARTH, MINING AND ENVIRONMENTAL SCIENCES FOR SAFE AND SUSTAINABLE DEVELOPMENT

Volume 2:

**Earth, Mine, and Environmental Sciences for Green,
Sustainable, and Prosperous Development
in the Era of a Nation's Rise**



PUBLISHING HOUSE FOR SCIENCE AND TECHNOLOGY

SERIES EDITORS

Mai Trong Nhuan
VNU University of Science
Vietnam National University, Vietnam

Tran Thanh Hai
Hanoi University of Mining and Geology
Vietnam

ASSISTANT EDITORS-IN-CHIEF

Vu Thi Minh Nguyet
Institute of Earth Sciences, Vietnam
Academy of Science and Technology

Do Minh Duc
VNU University of Science
Vietnam National University, Vietnam

ADVISORY COMMITTEE

Tran Tuan Anh
Vietnam Academy of Science and
Technology, Vietnam

Tran Hong Thai
Vietnam Academy of Science and
Technology, Vietnam

Hoang Ngoc Ha
Hanoi University of Mining and Geology,
Vietnam

Nguyen Cao Huan
Association of Geography Vietnam

Nguyen Manh Khai
VNU University of Science
Vietnam National University, Vietnam

Nguyen Tai Tue
VNU University of Science
Vietnam National University, Vietnam

Nguyen Tien Giang
VNU University of Science
Vietnam National University, Vietnam

Pham Hoang Hai
Institute of Environment and Sustainable
Development, Vietnam

Phan Van Tan
VNU University of Science
Vietnam National University, Vietnam

Rajinder Bhasin
Norwegian Geotechnical Institute, Norway

Tran Duc Thanh
Institute of Science and Technology for
Energy and Environment, Vietnam Academy
of Science and Technology

Truong Quang Hai
Institute of Vietnamese Studies and
Development Science

Vo Trong Hung
Hanoi University of Mining and Geology
Hanoi, Vietnam

Nguyen Dang Hoi
Joint Vietnam-Russia Tropical Science and
Technology Research Center

EDITORS

Nguyen Xuan Anh
Institute of Earth Sciences, Vietnam
Academy of Science and Technology

Tran Anh Tuan
Institute of Earth Science, Vietnam
Academy of Science and Technology

Phan Thi Thanh Hang
Institute of Earth Sciences, Vietnam
Academy of Science and Technology

Hendy Setiawan
Universitas Gadjah Mada
Indonesia

Lai Hop Phong
Institute of Earth Sciences, Vietnam
Academy of Science and Technology

Nguyen Thanh Hoan
Institute of Earth Sciences, Vietnam
Academy of Science and Technology

Takeshi ITO
National Institute of Technology Akita & D-
Academy Tohoku, Japan

SweePeng Koay
Universiti Sains Malaysia, Penang Malaysia

Pawel Kroh
University of the National Educational
Commission, Institute of Biology and Earth
Sciences, Poland

Dang Quang Khang
VNU University of Science Vietnam
National University, Vietnam

Łukasz Pawlik
University of Silesia, Institute of Earth
Sciences, Poland

Wenbing Shi
Guizhou University
China

Foreword

The publication series “*Advances in the Earth, Mining and Environmental Sciences for Safe and Sustainable Development*” was conceived as a platform to promote scientific innovation, interdisciplinary collaboration, and knowledge exchange in support of safer, greener, and more sustainable development. *Volume 1: Advanced Technologies and Artificial Intelligence in the Earth and Environmental Sciences* established this foundation by highlighting the rapid emergence of digital technologies, artificial intelligence, and computational approaches that are reshaping the way we observe, analyze, and understand the Earth system.

Building upon this momentum, *Volume 2: Earth, Mine, and Environmental Sciences for Green, Sustainable, and Prosperous Development in the Era of a Nation’s Rise* extends the vision of the series into a broader scientific and societal context. While Volume 1 emphasized technological advancement, Volume 2 focuses on how these technologies - along with traditional and emerging scientific approaches - are being integrated to address real-world challenges related to environmental stewardship, sustainable resource management, climate resilience, and green growth.

This volume comprises 79 peer-reviewed articles contributed by authors from 10 countries and regions, reflecting an expanding network of international collaboration and the growing global commitment to advancing Earth, mining, and environmental sciences. The diversity of institutional backgrounds and research approaches represented here underscores the relevance of these topics to the shared pursuit of green, resilient, and inclusive development.

The volume is structured into three thematic parts, each representing a critical axis of sustainability-oriented research:

Part 1 – Earth, Mine and Environmental Sciences towards the Sustainability

This part brings together studies on geohazards, geotechnical engineering, mining science, hydrogeology, and environmental geology. The contributions highlight innovative approaches to landslide and geohazard assessment, advanced geotechnical modeling and underground construction behavior, sustainable mining practices, and environmental monitoring for land, water, and geological systems. These works reinforce the essential principles of ensuring safety, environmental protection, and sustainable resource utilization, forming the foundation for resilient national progress.

Part 2 – Digital Transformation for Prosperous Development

The second part illustrates how AI, machine learning, remote sensing, WebGIS, and geospatial intelligence are revolutionizing data acquisition, environmental monitoring, hazard prediction, and decision-making. The studies presented explore big data and deep learning techniques for landslide modeling, WebGIS-based early warning systems, UAV and hyperspectral imaging applications, groundwater forecasting, air quality assessment, and digital transformation-driven environmental governance. These contributions

demonstrate the transformative role of digital technologies in fostering prosperous, evidence-based, and future-ready development.

Part 3 – Green Development: Perspectives of the Earth, Mine and Environmental Sciences

The final part focuses on the scientific foundations and practical pathways toward green growth, environmental restoration, and sustainable livelihoods. The articles cover marine and coastal ecosystem management, microplastic pollution, wastewater treatment, green materials and circular economy solutions, biodiversity and climate-related studies, greenhouse gas monitoring, and sustainable tourism planning. Collectively, these contributions reflect a holistic, interdisciplinary approach to green development, integrating environmental science, socio-economic considerations, and policy-relevant insights.

As a whole, Volume 2 presents a comprehensive and timely collection of scientific advances that align with national and global priorities for sustainability. It showcases how Earth, mining, and environmental sciences are evolving to meet the challenges of a rapidly changing world, advancing the shared goal of a safer, greener, and more prosperous future.

We extend our sincere appreciation to all authors, reviewers, editors, and supporting institutions for their dedication and contributions. Their collective efforts have made this volume a meaningful addition to the scientific literature and a valuable reference for researchers, practitioners, policymakers, and students.

Editorial Board

TABLE OF CONTENT

Foreword

v

PART 1: EARTH, MINE AND ENVIRONMENTAL SCIENCES TOWARDS THE SUSTAINABILITY

1	GEOTECHNICAL APPROACHES FOR GEOHAZARDS DUE TO CLAY SWELLING BEHAVIOR	3
	Takeshil Ito and Saiichi Sakajo	
2	OPTIMIZING LANDSLIDE SUSCEPTIBILITY MAPPING: INVESTIGATING SAMPLE RATIOS AND VALIDATION METHODS USING RANDOM FOREST IN THE NAM MA WATERSHED, NORTHERN VIETNAM	13
	Van-Trung Chu, Shou-Hao Chiang, and Tang-Huang Lin	
3	PRELIMINARY ANALYSIS OF LANDSLIDE-GENERATED SEISMIC SIGNALS: POTENTIAL FOR REAL-TIME DETECTION AND EARLY WARNING IN VIETNAM	22
	Pham Van Tien, Ha Thi Giang, Nguyen Van Duong, Pham The Truyen, Vu Cao Minh, Dao Minh Duc, Lukasz Pawlik, Pawel Kroh, Bui Phuong Thao	
4	ASSESSING RAINFALL INDUCE LANDSLIDE THRESHOLD IN VAN CHAN – GIA HOI AREA, LAO CAI PROVINCE	30
	Duong Thi Toan	
5	EXPERIMENTAL STUDY ON PHYSICAL SIMULATION OF MINING SLOPE COLLAPSE UNDER THE EFFECT OF RAINFALL	39
	Wenbing Shi, Fengliang, Tongwei Tao, Xingyuan Jiang, Shaozheng Xiong	
6	LANDSLIDE SUSCEPTIBILITY MAPPING ALONG HIGHWAY 40B, VIETNAM, USING LOGISTIC REGRESSION	51
	Giang Nguyen Khac Hoang	
7	MORPHOLOGICAL FACTORS CONTROLLING LANDSLIDE FORMATION IN NORTHERN VIETNAM – REMARKS AFTER THREE YEARS OF OBSERVATIONS	59
	Pawel Kroh, Łukasz Pawlik, Pham Van Tien, Le Hong Luong	
8	STUDY OF REFORESTATION FOR REDUCING SLOPE FAILURE AND GLOBAL WARMING	66
	SweePeng Koay, Kazuho Ito, Satoshi Murakami, Zaharin Yusoff	
9	IMPROVING THE PROCESS OF MINING THE STEEP COAL SEAM. CASE STUDY OF THE SEAM 6(7) IN NAM KHE TAM MINE, QUANG NINH, VIETNAM	74
	Phi Hung Nguyen, Hoang Hiep Do, Manh Tung Bui	
10	INVESTIGATION OF THE INFLUENCE OF THE SOIL'S ELASTIC MODULUS SURROUNDING THE SQUARE TUNNEL ON THE INTERNAL FORCE VALUES IN THE TUNNEL LINING	89
	Manh Tung Bui, Anh Son Do, Chi Thanh Nguyen	

11	IMPROVING POWER QUALITY IN UNDERGROUND MINES' GRID BY UTILIZING SVC SYSTEM	95
	Ho Viet Bun, Le Xuan Thanh	
12	SIMULATION OF CONVEYOR'S MOTOR FOR ANALYZING POWER CONSUMPTION IN VIETNAMESE UNDERGROUND MINES' GRID	104
	Nguyen Dinh Tien, Le Xuan Thanh	
13	RESEARCH OF THE RELATIONSHIP BETWEEN ROCK MASS ELASTIC MODULUS AND THE MAXIMUM SURFACE SUBSIDENCE FOR DEVELOPING A GEOMECHANICAL MODEL OF THE KHE CHAM COAL MINE	113
	Chung Pham Van, Nghia Nguyen Viet, Long Nguyen Quoc, Canh Le Van, Dinh Thanh Tuan	
14	CONSTRUCTION OF A GRAVITY MODEL FOR THE EAST SEA FOR APPLICATION IN WAVE ENERGY POTENTIAL ASSESSMENT	119
	Nguyen Van Sang, Nguyen Thanh Thuy	
15	APPLICATION OF HIGH-FREQUENCY RADAR SYSTEM IN MONITORING THE POTENTIAL OF MARINE ENERGY IN VIETNAM	127
	Kim Cuong Nguyen, Xuan Loc Nguyen, Ngoc Anh Tran, Ba Thuy Nguyen	
16	CHARACTERISTICS OF GRAVITY ANOMALIES IN THE CUU LONG BASIN, VIETNAM	133
	Tran Tuan Duong, Tran Tuan Dung, Nguyen Quang Minh, Tran Trong Lap, Nguyen Thi Nhan	
17	GEOCHEMICAL CHARACTERIZATION OF LITHIUM MINERALIZATION IN THE LA VI AREA (CENTRAL VIETNAM): IMPLICATIONS FOR DEPOSIT-TYPE CLASSIFICATION AND RESOURCE – ENVIRONMENTAL GOVERNANCE	139
	Nguyen Van Niem, Do Duc Nguyen, Pham Nguyen Ha Vu, Nguyen Minh Trung, Bui Huu Viet	
18	GEOCHEMICAL CHARACTERISTICS AND ASSESSMENT OF HEAVY METAL CONTAMINATION IN GROUNDWATER: A CASE STUDY FROM THE MOUNTAINOUS REGION OF HA GIANG, NORTHERN VIETNAM	158
	Do Thi Thu, Pham Thi Dung, Tran Tuan Anh, Pham Thanh Dang, Nguyen Thi Lien, Nguyen Xuan Qua, Nguyen Thi Thu, Le Thi Phuong Dung, Doan Thi Thu Tra, Vu Dinh Hai, Bui Thi Sinh Vuong, Nguyen Trong Tai	
19	ENVIRONMENTAL PROTECTION AND LANDSCAPE RESTORATION SOLUTIONS IN MINERAL EXPLOITATION AT LOC AN MINE CLUSTER, PHUOC HAI COMMUNE, HO CHI MINH CITY	171
	Au Nguyen Hai, Thi Tuyet Nhi Pham, Hong Minh Vy Tat, Khanh Linh Luu	
20	URBAN EXPANSION MONITORING USING SENTINEL-1 AND SENTINEL-2 DATA FUSION ON GOOGLE EARTH ENGINE	180
	Hung Nguyen Manh, Tuan Vu Anh, Toan Dao Duy, Son Le Mai, Giang Nguyen Cong, Hang Le Thi Thu	

21	APPLICATION OF LSTM-ARIMA MODEL IN AIR QUALITY FORECASTING IN BARRIA – VUNG TAU PROVINCE	190
	Ho Minh Dung, Ton Minh Hien	
22	SPATIAL CONVERGENCE AND HOTSPOT CLUSTERING OF PROVINCIAL HUMAN DEVELOPMENT INDEX IN VIET NAM	201
	Truong Van Canh	
23	OPERATIONALIZING SF-MST AND GSTC INDICATORS FOR SUSTAINABLE TOURISM ASSESSMENT: THE CASE OF CON DAO, VIETNAM	210
	Tran Thi Tuyen	
24	METHODS FOR ASSESSING ENVIRONMENTAL CARRYING CAPACITY FOR SUSTAINABLE TOURISM DEVELOPMENT: A CASE STUDY OF SA PA NATIONAL TOURIST AREA	220
	Quyen Ngo Thi, Truc Nguyen Ngoc, Huong Nguyen Thi Quynh	
25	INTRODUCTION OF NOVEL TECHNOLOGIES AND MODELS FOR ON-SITE CONVERSION OF COAL BOTTOM ASH AND COAL FLY ASH INTO HIGH-VALUE MATERIALS	230
	Nguyen Ngoc Truc, Do Xuan Duc, Ngo Thi Quyen, Dinh The Hien	
26	INFLUENCE OF TWIN STACKED TUNNELS EXCAVATION ON PILE BEHAVIOR – A CASE STUDY IN HO CHI MINH CITY	240
	Tien Nguyen Tai, Vi Pham Van, Chuong Phan Hoang	
27	ACCELERATING VIETNAM'S TRANSITION FROM COAL-FIRED POWER TO RENEWABLE ENERGY: CHALLENGES AND STRATEGIC SOLUTIONS	251
	Vu Thi Phuong Thao, Bui Manh Tung, Nguyen Duc Toan	

PART 2: DIGITAL TRANSFORMATION FOR PROSPEROUS DEVELOPMENT

28	BIG DATA, MACHINE AND DEEP LEARNING TECHNIQUES FOR LANDSLIDE MODELING, PREDICTION, AND DETECTION	259
	Łukasz Pawlik, Hieu Trung Tran, Pham Van Tien, Paweł Kroh	
29	DEVELOPMENT AND APPLICATION OF A WEBGIS-BASED EARLY WARNING SYSTEM FOR LANDSLIDES	264
	Duong Thi Toan, Do Minh Duc	
30	INSTALLATION OF COST-EFFECTIVE LANDSLIDE EARLY WARNING SYSTEMS IN SOUTH AND SOUTH-EAST ASIAN COUNTRIES	279
	Rajinder Bhasin, Lloyd Tunbridge, Do Minh Duc, Khang Dang	
31	DEEP LEARNING-ASSISTED DETECTION OF COASTLINE SHIFTS AT CUA DAI, VIETNAM	285
	Kinh Bac Dang, Tuan Linh Giang	

32	WARNING SYSTEM FOR LAND SUBSIDENCE RISK DUE TO DROUGHT AND GROUNDWATER EXTRACTION: A STEP TOWARD SUSTAINABLE DEVELOPMENT	293
	Doan Quang Tri, Pham Tien Duc	
33	FROM PERCEPTION TO IDENTIFICATION AND ACTION: DESIGNING DIGITAL CO-CREATION PLATFORMS TO PROMOTE WILLINGNESS TO PAY FOR DROUGHT RISK MANAGEMENT - A REGIONAL CASE STUDY FROM EAST ASIA	302
	Wen Chin, Hsu, Chi-Wei, Peng	
34	SMART HEALTH MONITORING AND INFORMATION MANAGEMENT FRAMEWORK FOR DROUGHT-AFFECTED COMMUNITIES: A DIGITAL TRANSFORMATION APPROACH TO CLIMATE RESILIENCE	310
	Hsiao-Ting Tseng, Chien-wen Shen	
35	OPTIMIZING UAV-BASED HYPERSPECTRAL VEGETATION INDICES FOR ESTIMATING LEAF CHLOROPHYLL CONTENT IN RICE	321
	Lan Thi Pham, Phu Vinh Nguyen, Canh Van Le, Son Si Tong, Trang Thi Thu Nguyen	
36	FOREST CANOPY HEIGHT MAP IN CUC PHUONG NATIONAL PARK USING FIELD DATA AND AI-EXTRACTED FEATURES ALPHAEARTH FOUNDATIONS (AEF)	334
	Duc Anh Ngo, Anh Tuan Vu, Viet Luong Nguyen, Tien Cong Nguyen, Nhat Kieu Thi Truong, Thanh Binh Nguyen	
37	UAV HYPERSPECTRAL IMAGING AND MACHINE LEARNING FOR FRESH TEA YIELD ESTIMATION	345
	Duc-Duy Nguyen, Si-Son Tong, Hoang-Long Nguyen	
38	AI ₄ BIOCHAR: INTEGRATING AI-DRIVEN FIELD BOUNDARY RECOGNITION FOR SUSTAINABLE BIOCHAR DEVELOPMENT IN VIET NAM	358
	Alessandro Flammini, Mehmet Furkan Celik, Claudia Paris, Francesco Nicola Tubiello	
39	FORECASTING GROUNDWATER LEVEL DECLINE AND SALTWATER INTRUSION IN THE COASTAL AQUIFERS OF THE RED RIVER DELTA BY 2030 AND 2040	363
	Trung Dang Tran, Thu Trinh Hoai, Hung Nguyen Kim, Huong Tran Thi Thuy, Anh Bui Thi Bao, Hang Pham Thi Thu, Tung Nguyen Xuan, Hung Pham Duc, Ngan Phan Kieu	
40	GRAVITY ANOMALY MODELING OVER THE GULF OF THAILAND FROM AIRBORNE GRAVITY DATA	377
	Tham Bui Thi Hong, Thanh Le Duy, Hoai Do Thi, Thu Trinh Thi Hoai	
41	UTILIZING REMOTE SENSING AND STATISTICAL METHODS TO ASSESS THE IMPACT OF LAND USE ON SOIL ORGANIC CARBON	385
	Trong Dieu Hien Le, Pham Phuong Thanh Bui	

42	INTEGRATING GEOSPATIAL DATA FOR RUSLE SOIL EROSION MODELING IN GOOGLE EARTH ENGINE: A CASE STUDY OF THE DAK NONG PLATEAU, VIETNAM	394
	Ngoc Hoang Thi Huyen, Son Nguyen Thai, Ha Nguyen Manh, Dung Bui Quang, Linh Giang Tuan	
43	UNDERSTANDING VEGETATION RECOVERY AFTER DISTURBANCE BY NATURAL HAZARDS USING GEOSPATIAL TECHNOLOGIES	408
	Takashi Oguchi	
44	7-SEAS URBAN-AQ: A REGIONAL INITIATIVE FOR UNDERSTANDING URBAN AIR QUALITY IN SOUTHEAST ASIA	416
	Nguyen Xuan Anh, Pham Xuan Thanh, Nguyen Van Hiep, Nguyen Nhu Vinh, Bui Ngoc Minh, Pham Le Khuong, Do Ngoc Thuy, Markova I. S.	
45	RANDOM FOREST-BASED PM _{2.5} ESTIMATION USING MULTISOURCE REMOTE SENSING DATA: A CASE STUDY OF HO CHI MINH CITY	426
	Dai Long Nguyen, Thu Ha Hoang Thi, Kim Cuc Luong Thi, Van Manh Nguyen, Ngoc Bich Uyen Vo, Thi Hai Yen Ngo	
46	SEGMENTING TRAFFIC ACCIDENT RISK USING REMOTE SENSING AND GIS DATA: A COMPARATIVE ANALYSIS OF RANDOM FOREST AND WEIGHTED OVERLAY METHODS	438
	Ha Le Thi, Thao Vu Thi Phuong, Thao Do Thi Phuong	
47	APPLICATION OF MACHINE LEARNING AND WEBGIS FOR LAND-USE PLANNING INFORMATION UTILIZATION TO SUPPORT DIGITAL TRANSFORMATION OF LAND ADMINISTRATION	447
	Nguyen Xuan Linh, Tran Quoc Binh, Pham Le Tuan, Bui Ngoc Tu	
48	THE NORMAL GEOMAGNETIC FIELD MODEL OVER VIETNAM AND ADJACENT AREAS FROM SWARMSATELLITE	456
	Thanh Le Truong, Mai Nguyen Thi, Minh Le Huy, Dung Nguyen Thanh, Thanh Nguyen Ha, Vinh Nguyen Ba, Nam Vu Dao, Hien Phi Thi Thu, Hai Phan Thanh	
49	ANALYSIS OF DEFORMATION DISPLACEMENT USING GNSS TECHNOLOGY IN THE LOCAL TOPOCENTRIC COORDINATE SYSTEM	467
	Hoang Ngoc Ha, Luu Anh Tuan, Le Ngoc Giang, Ngo Thi Men Thuong	
50	DATA QUALITY ASSESSMENT AND STATION CLASSIFICATION OF THE CORS STATIONS – CASE STUDY OF CORS STATION IN NGHE AN PROVINCE, VIETNAM	473
	Trong Tran Dinh, Huy Nguyen Dinh, Hue Tran Thi	
51	DESIGNING FOR VALUE: LINKING TRANSPARENCY AND INCENTIVES TO ECONOMIC, SOCIAL, AND ENVIRONMENTAL CO-CREATION	483
	Wen Chin Hsu, Chi-Wei Peng	

**PART 3: GREEN DEVELOPMENT: PERSPECTIVES OF
THE EARTH, MINE AND ENVIRONMENTAL SCIENCES**

52	ASSESSMENT OF CUMULATIVE IMPACTS ON COASTAL MARINE ECOSYSTEMS IN HA TINH PROVINCE Nguyen Tai Tue, Luu Viet Dung, Pham Lan Anh, Nguyen Doanh Khoa, Tran Dang Quy, Mai Trong Nhuan	493
53	AN INTEGRATED MULTI-SCALE FRAMEWORK FOR URBAN HEAT RISK MONITORING AND ADAPTATION: EVIDENCE FROM TAIWAN Hsiao-Ting Tseng, Meng-Hua Hsu, Yue-Lin CHEN	502
54	ADJUSTING OF THE BUFFER ZONE BOUNDARIES IN HA LONG BAY WORLD NATURAL HERITAGE: SCIENTIFIC AND PRACTICAL FOUNDATIONS FOR SUSTAINABLE MANAGEMENT ORIENTATION Luu The Anh, Bui Manh Tung, Ngo Thi Hai Yen, Duong Anh Quan, Bui Ngoc Quy	509
55	PRELIMINARY SURVEY OF MICROCLIMATE AND ENVIRONMENTAL CONDITIONS IN SHOW CAVES IN HOA BINH AND PHONG NHA – KE BANG AREAS Vu Thi Minh Nguyet, Nguyen Thuy Duong, Czuppon György, Stieber József , Van Phu Hung, Ha Tung Lam, Bui Van Quynh	522
56	ASSESSING AND MITIGATING URBAN HEAT RISK IN A RAPIDLY URBANIZING SUBTROPICAL CITY: A REVIEW AND APPLICATION FOR CASE STUDY OF TAOYUAN, TAIWAN Cheng-Ling Kuo, Wenqian Chang, Yuei-An Liou	535
57	SHRIMP FARMING WASTEWATER TREATMENT BY AQUATIC PLANTS Nguyen Minh Phuong, Nguyen Huu Hung	546
58	SUSTAINABLE RECOVERY OF STRUVITE FERTILIZER FROM SWINE WASTEWATER BY FLUIDIZED BED HOMOGENEOUS CRYSTALLIZATION Nguyen Gia Cuong, Le Van Giang, Nguyen Thi Thuy, Bui Ngoc Quy, Luu The Anh	554
59	RECOVERY OF ALUMINUM FROM WASTEWATER VIA FLUIDIZED BED HOMOGENEOUS CRYSTALLIZATION Le Van Giang, Nguyen Thi Thuy, Nguyen Thi Thu, Bui Ngoc Quy	562
60	UPCYCLING ELECTRONIC WASTE INTO CATALYTIC MATERIALS FOR SUSTAINABLE WATER TREATMENT VIA CATALYTIC WET PEROXIDE OXIDATION OF METHYLENE BLUE DYE Hai Nguyen Tran and Dong Thanh Nguyen	569
61	DISTRIBUTION CHARACTERISTICS OF TRACE ELEMENTS IN SOIL, BAT XAT AREA, LAO CAI PROVINCE Nguyen Thi Lien, Pham Thi Dung, Tran Tuan Anh, Pham Thanh Dang, Nguyen Xuan Qua, Doan Thi Thu Tra, Do Thi Thu, Cu Sy Thang, Nguyen Thi Thu, Le Thi Phuong Dung	582

62	SOIL GEOMOGRAPHIC CHARACTERISTICS IN THE MOUNTAINOUS REGION OF SA THAY	591
	Nguyen Van Dung	
63	EFFECT OF THE INITIAL CLAY-WATER CONTENT ON THE COMPRESSIVE STRENGTH OF SOIL-CEMENT-RICE STRAW ASH ADMIXTURE	597
	Nguyen Thanh Duong	
64	ASSESSMENT OF MARINE DEBRIS POLLUTION INDEX AT SOME BEACHES IN NGHE AN PROVINCE	604
	Dang Tran Quan, Duong Thi Lim, Nguyen Tran Dinh, Nguyen Thi Hue	
65	ASSESSMENT OF MICROPLASTIC POLLUTION IN COASTAL WATERS OF THE CAI LON – CAI BE ESTUARY, VIETNAM	616
	Nguyen Thi Thu Uyen, Pham Lan Anh, Tran Dang Quy, Nguyen Dinh Thai, Dang Bao Duong, Nguyen Hai Nam, Nguyen Doanh Khoa, Nguyen Thi Huyen Trang, Ha Ngoc Anh, Luu Viet Dung	
66	STATUS OF PLASTIC WASTE GENERATION IN THE CAI LON – CAI BE ESTUARY, AN GIANG PROVINCE, VIETNAM	624
	Pham Lan Anh, Nguyen Tai Tue, Luu Viet Dung, Tran Dang Quy, Mai Trong Nhuan	
67	EVALUATION OF CAFFEINE CONTENT IN OYSTER MUSHROOMS CULTIVATED ON SPENT COFFEE GROUNDS UNDER URBAN AGRICULTURE CONDITIONS	633
	Nguyen Thi Thanh Thao, Tran Thi An	
68	SELECTION OF PHOSPHATE-SOLUBILIZING BACTERIA AND EVALUATION OF THEIR ABILITY TO RESIST PLANT PATHOGENIC FUNGI	642
	Mai Van Dinh, Manh Ha Nguyen	
69	ASSESSING THE INFLUENCE OF GEOGRAPHICAL FACTORS ON THE DISTRIBUTION OF THE GENUS PHALLUS IN THE SREPOK RIVER BASIN, VIETNAM: IMPLICATIONS FOR CONSERVATION AND SUSTAINABLE DEVELOPMENT OF VALUABLE FUNGAL RESOURCES	650
	Nguyen Thi Bich, Nguyen Thanh Long, Phan Thi Thanh Hang, Nguyen Vu Viet, Nguyen Thi Thuy, Nguyen Ngoc Thang, Ngo Thanh Nga	
70	ASSESSMENT OF RAIN CHANGES IN NINH BINH PROVINCE IN THE PERIOD 2000 – 2024	663
	Trinh Nguyen Dieu, Lan Vu Thi Thu, Son Hoang Thanh, Tuan Bui Anh	
71	ASSESSMENT OF PRECIPITATION VARIATION TRENDS IN NGHE AN PROVINCE UNDER THE CONTEXT OF CLIMATE CHANGE	671
	Le Thi Nguyet	
72	MONITORING THE GREEN HOUSE GASES CONCENTRATION IN BINH DUONG PROVINCE USING SENTINEL-5P REMOTE SENSED DATA AND GIS TECHNOLOGY	678
	Le Thanh Khong, Tran Thi An	

73	UNDERSTANDING GEN Z'S ATTITUDES AND BEHAVIORAL INTENTIONS TOWARDS GREEN DESTINATIONS: IMPLICATIONS FOR SUSTAINABLE TOURISM DEVELOPMENT IN VIETNAM	688
	Phan Trinh Thi, Nga Nguyen Thi Phuong	
74	ASSESSING FISH FARMERS' PERCEPTIONS OF ENVIRONMENTAL DRIVERS SHAPING CULTURED FISH COMMUNITIES IN CHAU DOC, VIETNAM	700
	Noor Syafiq Bin Abdul Rashid, Dung Duc Tran, Thien Duc Nguyen, Edward Park	
75	EVALUATION OF THE INFLUENCE OF CRACK GEOMETRY IN HIGH-PERFORMANCE CONCRETE MEMBERS USING NON-DESTRUCTIVE TESTING FOR STRUCTURAL SAFETY MANAGEMENT	709
	Nhan Pham Thi, Phi Dang Van	
76	ASSESSMENT OF INTERFACIAL BONDING OF RECYCLED POLYMER FIBERS FROM WASTE FISHING NETS IN CONCRETE	718
	Dang Van Phi	
77	PROPOSING A SOLUTION TO BUILD PEDESTRIAN TUNNELS COMBINED WITH COMMERCIAL SPACES IN BIG CITIES IN VIET NAM	724
	Dang Van Kien, Trivié Jeremy, Daniel Dias, Do Ngoc Anh, Vo Trong Hung, Tran Tuan Diep, Nguyen Khoa Linh	
78	RESEARCH ON THE EFFECT OF THE THERMODYNAMICS IN THE LPG STORAGE CAVERN OF CAI MEP	734
	Vu Tien Dung, Dang Van Kien, Nicolas Gitzinger, Ngo Minh Hoang, Le Sy Ha	
79	ANTI-SALINITY SOLUTIONS FOR CIVIL STRUCTURES: A BRIEF REVIEW	743
	Trong Van Nguyen, Ngoc Truc Nguyen, Thao Ly Nguyen	

Part 1

EARTH, MINE AND ENVIRONMENTAL SCIENCES TOWARDS THE SUSTAINABILITY

Geotechnical Approaches for Geohazards Due to Clay Swelling Behavior

Takeshi Ito^{1,*} and Saiichi Sakajo²

¹National Institute of Technology Akita & D-Academy Tohoku, Akita City, Japan

²Geo-electronics Co., Ltd. Sakae-machi, Inba-gun, Chiba, Japan

*Email: gyo.ito@gmail.com; msqqm372@ybb.ne.jp

Abstract: Natural disasters are often triggered by extreme weather events, earthquakes, volcanic eruptions, and tsunamis, which can subsequently induce secondary hazards such as river floods, mudflows, and landslides.

Among these, geohazards related to soil swelling (expansive soil phenomena) frequently occur in sedimentary layers. Swelling soils can lead to structural failures of buildings, roads, tunnels, railways, retaining walls, and other infrastructures, and can also induce landslides.

However, the mechanisms of soil swelling are still not fully understood. Such phenomena are typically observed in soils containing clay minerals such as smectite, with montmorillonite being the most expansive. To clarify these mechanisms, laboratory tests were conducted using samples with varying montmorillonite contents. From the experimental results, a practical equation was derived for fitting the swelling behavior of soils.

For the early detection or prediction of such geohazards, various monitoring systems have been developed. This paper also introduces a newly developed geophone-based monitoring system for early detection and prediction of such geohazards.

Keywords: soil swelling test; montmorillonite; geohazard; monitoring system.

INTRODUCTION

In recent years, extreme weather events have been frequently observed worldwide. In addition, large-scale geological hazards have been reported-particularly in Asian countries, where about 65% of such events occur. These disasters often appear as landslides, mudflows,

and river floods, and are frequently accelerated by rapid land development associated with population growth.

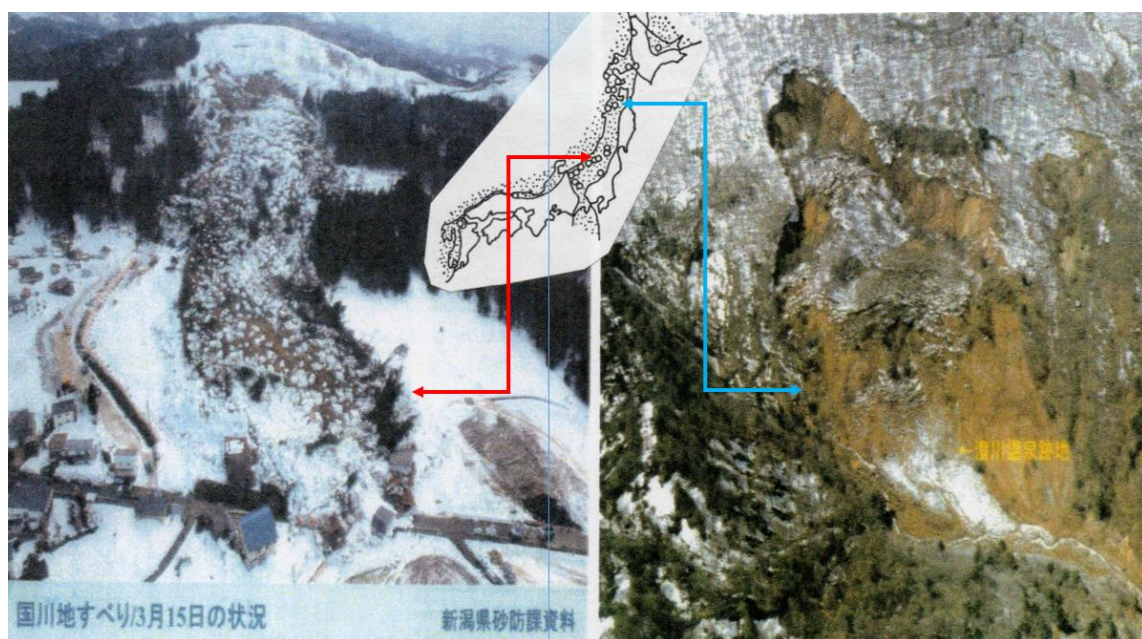
Most affected regions consist of sedimentary and tuffaceous volcanic formations, where weathering and hydrothermal alteration have produced smectite-rich clay layers. These formations are closely related to soil swelling and expansive clay behavior, which often contribute to landslide activity in these areas. [14, 23]

Swelling phenomena in soils are mainly caused by specific clay minerals such as smectite, among which montmorillonite shows the strongest swelling capacity. Many studies have been conducted on these phenomena. [9, 11, 16, 19, 20]

Figure 1 presents two famous examples of landslides that occurred during the snowmelt season in Niigata and Akira Japan. In both cases, the slip surfaces contained smectite.

Both landslides occurred during the snowmelt season within the Green Tuff Belt Zone along the Japan Sea side, where old bentonite mines are also distributed.

Figure 2 shows landslide disaster statistics over the past 83 years (1915-1997) in Akita Prefecture, Japan. Both of the above-mentioned landslides are included in this dataset. The chart indicates that large landslides mostly occur at the end of the snowmelt season in regions characterized by Green Tuff formations of Quaternary and Tertiary origin. These areas are typically near valleys, mountains, or hilly terrain, where many geohazards have been recorded.



(a) The Kokugawa Landslide, occurred in March 2012 in Niigata Prefecture

(b) The Hachimantai Sumikawa Hot Spa Landslide, occurred in May 1997 in Akita Prefecture

Figure 1. Two examples of landslides occurred during the snowmelt season in Japan. In both cases, the slip surfaces contained smectite

(The dotted area indicates the Green Tuff zone, and ○ indicates an old bentonite mine on the map of Japan).

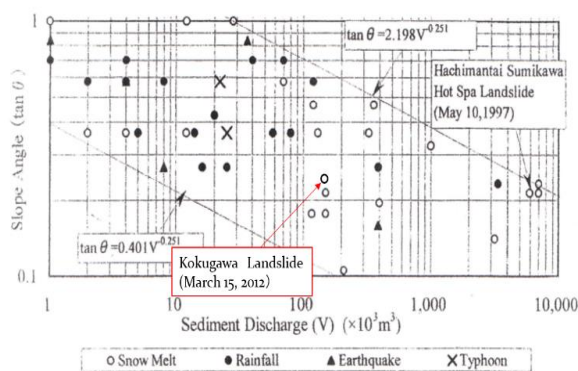


Figure 2 Landslide sediment discharge against slope angle by 40 cases

According to the statistics, approximately 70% of landslides along the Japan Sea side occur during the thawing season. In these regions, most slip surfaces are found within the same geological formation—the Green Tuff areas rich in swelling clay and affected by abundant snowmelt water. Therefore, landslides in these areas are considered to be accelerated by the combined effects of both factors.

Figure 3 shows simple images of landslide slope conditions (a) snow cover season and (b) snow melting time. Figure 4 shows meteorological data corresponding to the landslide in Figure 1(b).

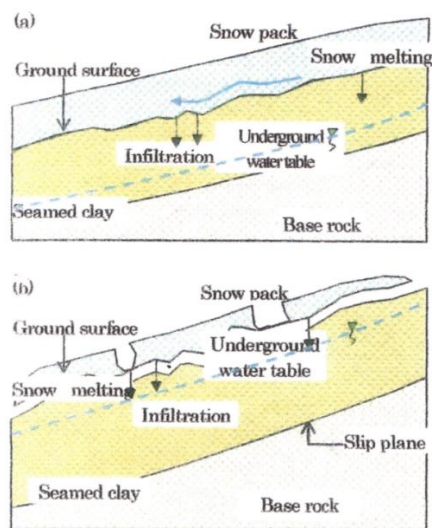


Figure 3. Slope conditions during (a) the snow-covered period and (b) the snowmelt period

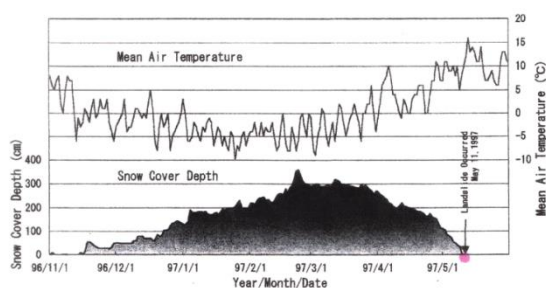


Figure 4 Meteorological Data corresponding to the landslide in Figure 1(b) (Sumikawa Electrical Station data)

It is considered that water table of the underground stays usually at low level in snow season, however at the end of winter season, its level getting high according snow melting together with air temperature become high. Besides, snow melting accelerates and then underground water level naturally rises up to more high level as shown in the figures. At the same time soil temperature is getting high, then covered snow weight become light and then underground water level rising up together. Due to these reasons make frequent landslide events in these Green Tuff areas. [1, 2, 4, 5, 8, 15, 17, 18, 23]

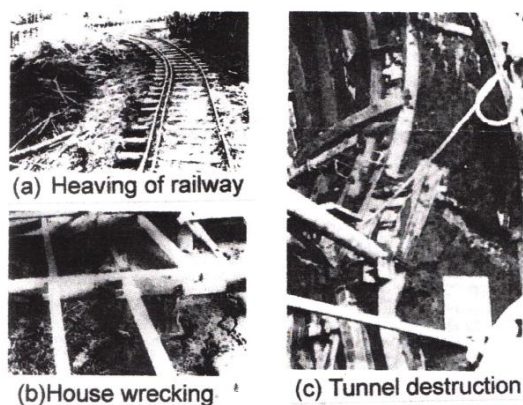


Figure 5 Geohazards by swelling phenomena

Figure 5 shows another geo-hazards due to swelling phenomena of soil. As shown in this figure, the swelling phenomenon of soils is difficult to understand because of its complex mechanisms involving mineral composition, moisture variation, and stress conditions. This unpredictable behavior frequently leads to serious ground deformation, causing damage to

foundations, pavements, and other structures. Consequently, swelling-induced failures have resulted in considerable economic losses in many construction projects worldwide.

UNDERSTANDING SWELLING BEHAVIOR OF CLAYS: LABORATORY EXPERIMENTS AND FIELD APPLICATIONS

To better understand the swelling characteristics of clays that contribute to landslide hazards, several laboratory experiments have been conducted. [1, 2, 4, 8, 18] Based on these experimental results using montmorillonite, a swelling equation was developed. Furthermore, its applicability was tested against field cases of swelling observed during mining and tunneling, where the equation successfully described the observed deformations. [7]

Numerous landslides in sedimentary soil areas have also been linked to swelling clays, together with long-term creeping behavior frequently observed. For early detecting sensor of this kind of geohazards, there are many types of monitoring systems had been developed till today. [3]

In this paper, geophone-based monitoring system is recommended as one of the excellent redefining measurement systems for geohazards.

MECHANISMS OF SOIL SWELLING AND EXPERIMENTAL MATERIALS

Swelling-prone ground often causes various geotechnical troubles in design and construction, which are mainly attributed to the following factors.

Following detail would be the most of reasons of swelling and expansion of soil.

- (1) Mechanical expansion caused by water absorption.
- (2) Including swelling clays.
- (3) Clay structural change caused by water absorption.
- (4) Heat and pressure cause changes in the crystal structure.

- (5) Relaxation of concealed earth pressure.
- (6) Plastic deformation by tectonic movement
- (7) Freezing of pore water increasing.

These are almost relate to the volume change and relate to accelerated many kinds of geohazards [5].

Swelling may occur by the reason mainly following physical and mechanical conditions.

From the above, swelling behavior basically express as following sample conditions. The swelling behavior can be expressed by the following general function:

$$Ps = f(Ck, Mq, Wp, Wc, Sp, Ec, Pc, Wi, T, \dots) \dots \dots (1)$$

where Ck: kind of clay minerals, Mq: content of swelling clay minerals, Wp: kind of pore water, Wc: ionic density of pore water, Sp: structure and arrangement of clay, Ec: compacted hardness of sample, Pc: confining pressure, Wi: initial water content of the sample, and T: temperature. etc.

In this way, there are so many kind of factors existing for measurement against geotechnical swelling behavior by laboratory experiments, therefore, several limited factors were selected for laboratory tests. In which, due to these volume change factors are not yet analyzed well, it has also been still remained several problems to be researched especially the mechanism of swelling.

In this study, available predicting explanations for swelling are proposed through the laboratory tests by using a newly developed apparatus.

The samples used in this study were pure montmorillonite powder (called Kunigel V1: M100, as shown in **Figure 7**) and mixtures of Kunigel V1 with pure kaolinite powder (called CT Kaolinite), prepared under controlled conditions with varying water contents and compaction levels, while maintaining a stable chamber temperature of 15 °C [6].

Figure 6 shows an original rock called Kunigel V1 of original bentonite rock including much of montmorillonite.



Figure 6. shows an original rock of Kunigel V1

Figure 7 shows the X-ray diffraction (XRD) pattern of Kunigel V1. The XRD analysis indicates that Kunigel V1 contains small amounts of feldspar and quartz, but it is known as the highest-purity montmorillonite-bearing rock in Japan. [16, 20]

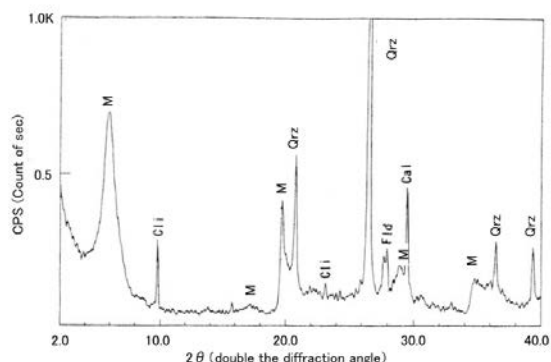


Figure 7. X-ray diffraction spectrum of Kunigel V1 : Kunigel V1 is the original rock of montmorillonite, containing small amounts of quartz, feldspar, and sericite.

Figure 8 shows one of the soil mechanical experiment results between Kunigel V1 (M) and Kaolinite (K) mixing materials. Kaolinite believed as non-swelling material. Therefore, to understand the behavior of these mixing materials, several experimental results obtained.

As one of the results, Figure 8 shows the relationship between sample flow index (If) and liquid limit (WL). From the chart, there is a high linear relationship was found obtained as

shown in the figure. That is, in case of high montmorillonite content shows high flow index If-value as is shown in the equation of the Figure 8.

In this figure, M50-K50 means each sample mixed in %. According to the test results, we can say why the soil mass (landslide) moving on a slope estimate that landslide may accelerate generally by the degree of containing of montmorillonite.

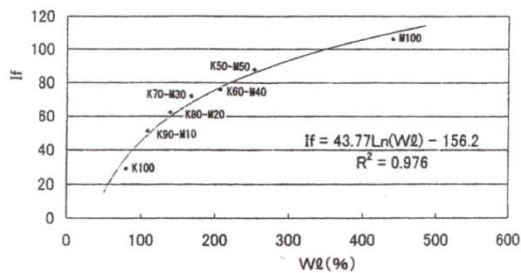


Figure 8. Soil mechanical characteristics of mixed clay powder composed of montmorillonite (M) and kaolinite (K)

Figure 8 shows the soil mechanical characteristics of mixed clay powders composed of montmorillonite (M) and kaolinite (K). As the M mixing ratio of montmorillonite increases, the flow index (If) also increases.

From above soil mechanical experiments, a good relationship was shown with a following linear equation as shown in Figure 8. According to the relation, big If -value was obtained in the area of high montmorillonite content sample. This is a one of the substantial sources that landslide behavior may be accelerated depends on the If-value. Addition to this, almost soil of landslide in green tuff area rich in montmorillonite.

Therefore, If-value is considered as an additional symbol for the possibility of land-sliding. The swelling of montmorillonite-rich layers induces micro-fracturing and small particle movements that generate detectable ground vibrations. In addition, the bulk movement of the mass can produce significant impacts or vibrations. This provides a sound

basis for applying geophone-based monitoring to swelling-induced geohazards.

SWELLING PRESSURE (PS) BY LABORATORY TESTS

Soft foundation including swelling clay minerals such as montmorillonite behaves accompanying with elastic-perfectly plastic deformations. The purpose of this paper is to investigate such the stress strain relationship of montmorillonite-kaolinite mixture materials. First of all, how long does it take to come final swelling phenomena? Next how big the final swelling pressure? These are investigated first using different mixture montmorillonite samples. These are already have been tried by many researchers until today, and had proposed many types of expression about swelling potential. [1, 2, 4, 18]

In this study, Ps was measured by handmade apparatus using montmorillonite mixed sample setting up inside oedometer, then distilled water was supplied to the samples packed in the consolidation oedometer vessel of which volume keeping at any time constant. Then the swelling pressure was measured under the constant temperature at 15 °C.

Figure 9 shows experimental results of swelling pressure Ps against time. Swelling test tried for the different montmorillonite content samples varying 100% (M100) to 20% (M20). In case of M100 sample, swelling phenomena appeared 3 weeks more over till to be finished. From the result of M100 sample swelling, it is estimated that the swelling pressure may yield approximate 200 kPa at the maximum.

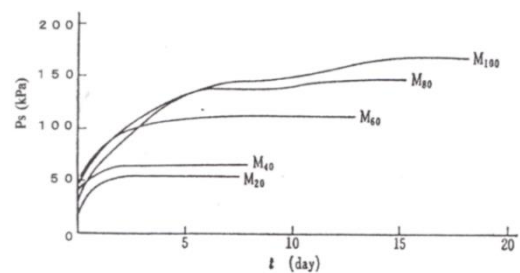


Figure 9. Experimental results of swelling pressure against time

Next, the time scale was converted into a logarithmic scale, as shown in **Figure 10**. This transformation allowed the swelling behavior to be represented by a logistic-type equation as follows:

$$P_s = P_{sf} / [1 + \exp(a - k \cdot t)] \dots (2)$$

where P_{sf} (in kPa) is the final swelling pressure, k is a constant depending on the montmorillonite content, and t is the elapsed time (in minutes).

The use of the logarithmic time scale made it possible to fit the experimental data with a single equation that can also be applied to field observations, such as swelling deformation encountered during coal mine construction as shown in **Figure 11**.

When P_s is converted into deformation (in cm), the same equation can describe other swelling phenomena as well. Therefore, the proposed equation is considered applicable to a wide range of similar geohazards.

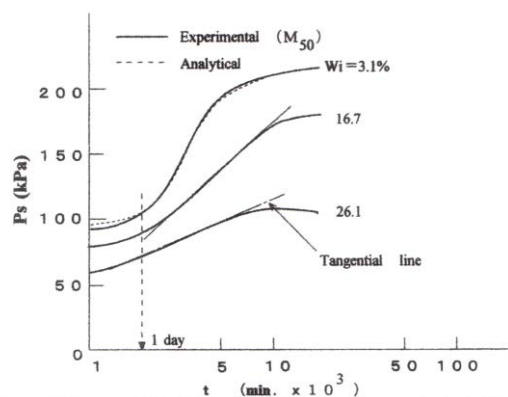


Figure 10. Water content (W_i) different material chart for M50

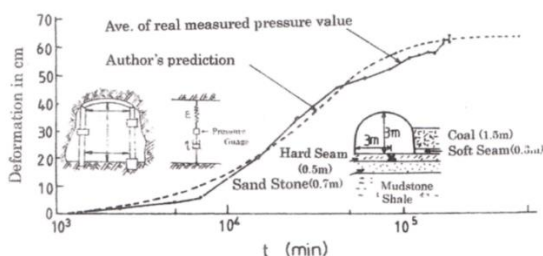


Figure 11. Application of swelling equation for Mining Construction [19].

MONITORING SYSTEM AND NEW DEVELOPED DEVICE FOR GEOPHONE

In recent years, the frequency of record-breaking heavy rainfall events associated with global warming, as well as sediment disasters triggered by earthquakes in mountainous regions, has been increasing worldwide. These phenomena have caused severe damage to infrastructure, residential areas, and transportation networks, highlighting the vulnerability of natural slopes and engineered embankments. Consequently, the development of reliable technologies for continuous and real-time monitoring of sediment movement has become an urgent issue, not only for early warning and disaster prevention but also for improving the understanding of slope failure mechanisms and enhancing the resilience of geotechnical structures.

Even when considering the above-mentioned geotechnical characteristics, it is actually difficult to predict and prevent ground failures in advance. Therefore, various monitoring techniques have been developed to mitigate landslide disasters; however, the current situation is still far from sufficient. The main reason is that the development of methods to directly observe “soil movement,” which serves as a clear precursor phenomenon before slope failure, has not been adequately pursued so far. The following section describes the latest technique that enables continuous monitoring of soil movement.

In recent years, the frequency of record-breaking heavy rainfall associated with global warming, as well as sediment disasters triggered by earthquakes in mountainous regions, has been increasing worldwide. Consequently, the development of technologies for continuous monitoring of sediment movement has become an urgent issue.

Among the available sensing devices, geophones have attracted particular attention because they are capable of continuously monitoring ground vibrations and quantifying the impact energy generated by sediment collisions. [12, 13, 21, 22].

Research Overview

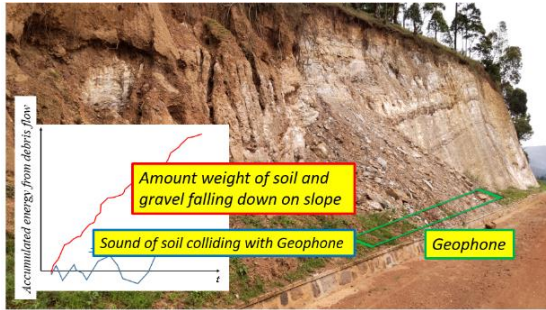


Figure 12. Overview of full time monitoring of slope collapse by geophone

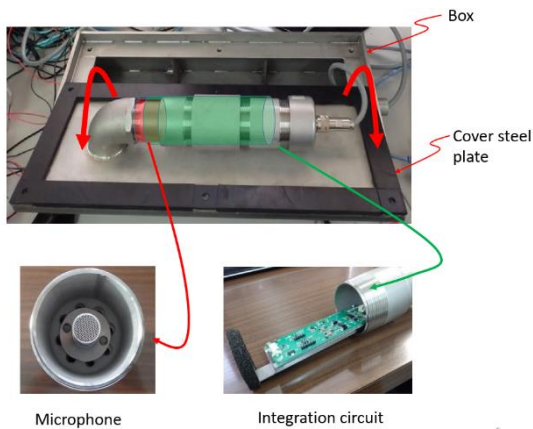
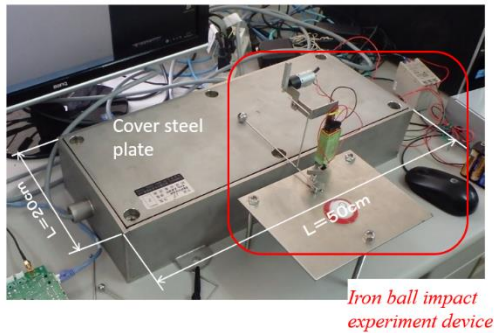


Figure 13. Geophone appearance and configuration

This study proposes a method for the continuous monitoring of slope failures using geophones integrated with IoT-based communication technologies. A geophone detects acoustic or vibrational signals generated by the impacts of soil and gravel particles, while an integrating circuit integrates these signals to calculate the corresponding energy or weight values. This process allows

the system to provide quantitative, real-time evaluations of sediment movement, offering a practical tool for the early detection of slope instability and landslide hazards.

Figure 12 presents an overview of continuous slope-collapse monitoring using geophones. Figure 13 shows the geophone's appearance and its configuration for this monitoring system, while Figure 14 illustrates the integration of sound pressure resulting from soil impacts.

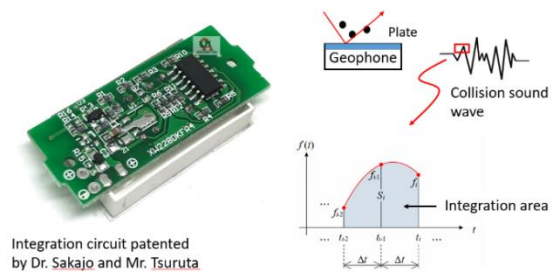


Figure 14. Integration of sound pressure from soil impact

Experiments and Results

Laboratory experiments using iron ball impacts were conducted to simulate soil collisions. The results confirmed a correlation between impact acoustic pressure and soil weight. The relationship can be expressed as a linear equation

$$W = \alpha \cdot P \dots (3)$$

where W represents the soil weight, P is the integrated acoustic pressure, and α means an experimentally derived proportionality constant.

Figure 15 shows the integration of sound pressure into the weight of falling soil.

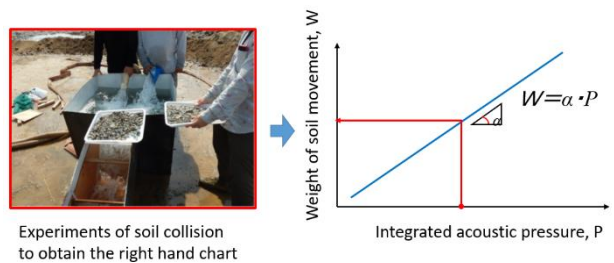


Figure 15. Converting the integral sound pressure into the weight of falling soil

Before measurement, slope-collapse experiments were conducted using soil of known weight. By this, both the soil weight during collapse and the impact acoustic pressure detected by geophones were recorded, allowing the proportionality constant α to be estimated.

System Configuration

The proposed system consists of the following components:

1. Geophone and Integration Circuit – Measurement and conversion of sediment collision energy.
2. IoT Module – Data transmission to a cloud server via PC or mobile devices.
3. Auxiliary Sensors – Water level gauge, cameras, and other sensors for enhanced monitoring.
4. Power Supply – Solar power system enabling autonomous operation in off-grid areas.

Figure 16 and Figure 17 show the concept of IOT system and the concept of continuous monitoring system, respectively.

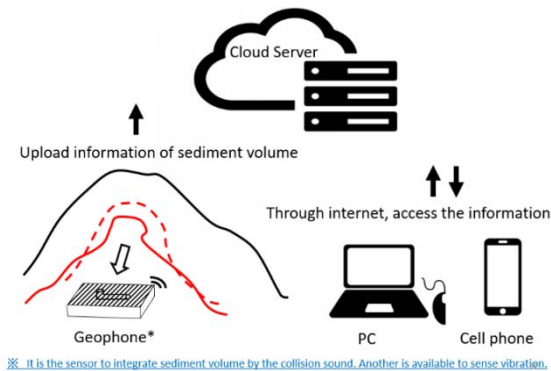


Figure 16. The concept of IOT system

As shown in Figure 16, with the advancement of IoT technologies, field monitoring data from remote sites can now be transmitted in real time and accessed through computers or mobile devices at the office. This capability enables engineers and disaster management authorities to continuously observe slope conditions, detect early warning

signs of potential landslides, and make prompt decisions for the rapid implementation of preventive measures, thereby significantly enhancing the effectiveness of landslide risk management and early warning systems.

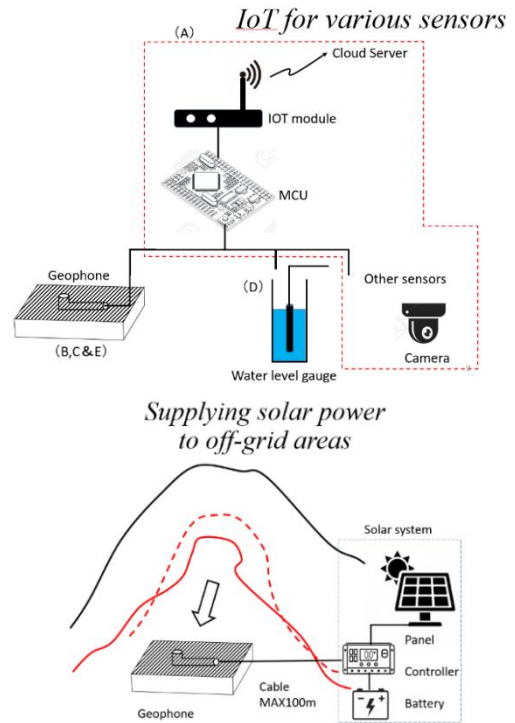


Figure 17. The concept of continuous monitoring system

As shown in Figure 17, this system not only monitors sediment movement using geophones but also captures data on groundwater fluctuations and photographs of surface deformations, enabling a comprehensive observation of landslide dynamics. By utilizing solar panels, the system can operate without an external power supply. In addition, it can run continuously for up to one month using a high-capacity battery.

Application Examples

Applications of geophones can be explained as follows.

- (1) Detection of debris flows in mountain streams.
- (2) Monitoring of slope deformation for early warning of collapse.

- (3) Continuous monitoring of complex disasters such as cliff collapses, landslides, and debris flows triggered by earthquakes and heavy rain.
- (4) A proposal for continuous monitoring of sediment movement using geophones during complex disasters

Figure 18 shows an example of geophone installation in a mountain stream. Figure 19 presents a proposal for installing geophones on a slope.

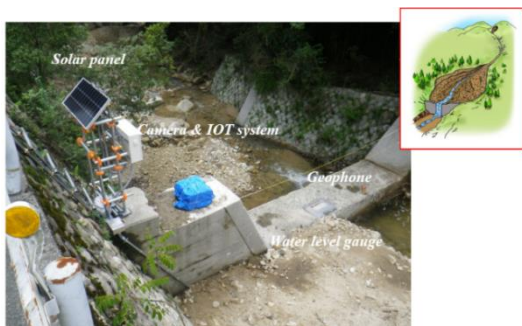


Figure 18. Example of geophone installation in a mountain stream

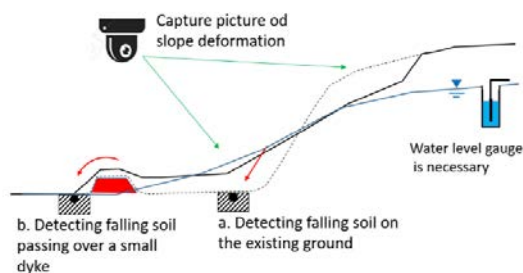


Figure 19. Proposal for installing geophones on a slope

Figure 20 illustrates a proposal for geophone installation to address various types of hazards, indicating that geophones could be applied in multiple scenarios. Figure 21 demonstrates the potential for complex geohazard events.

As shown in Figure 20, sediment movement occurs as a precursor phenomenon in all three types of mass movements: (a) cliff collapse, (b) landslide, and (c) debris flow. In addition, as illustrated in Figure 21, sediment movement caused by river flooding and

geophone measurements in the surrounding mountainous areas can be simultaneously observed. This capability is expected to be useful for early warning of compound disasters triggered by earthquakes or heavy rainfall.

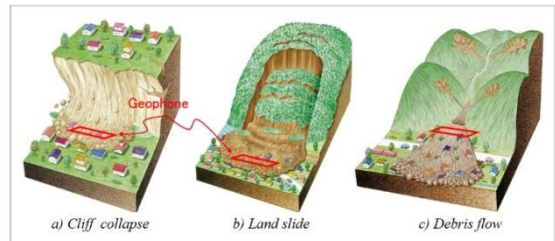


Figure 20. Proposal for installing geophones to deal with various types of geological hazards



Figure 21 Complex Disaster by the Noto Peninsular Earthquake January 1, 2024 and February Heavy rain February 1-5, 2024.

The geophones were calibrated by applying various waveforms under different temperature conditions and verifying their agreement with theoretical values. The reliability of the measurements can be evaluated by analyzing the recorded data, and continuous measurements over a seven-day period allow the observation of daily variations and trends.

CONCLUSION

The following conclusions have been developed.

- (1) Swelling-induced geohazards frequently occur in soils containing montmorillonite, particularly within sedimentary formations such as the Green Tuff zone.
- (2) Laboratory experiments showed that swelling pressure and deformation are

strongly influenced by montmorillonite content and can be effectively described using a logistic-type model.

- (3) The flow index (If) is proposed as a practical indicator for assessing landslide susceptibility in montmorillonite-rich soils.
- (4) The newly developed geophone-based monitoring system offers a viable early-warning tool for detecting ground deformations related to swelling phenomena.
- (5) The continuous geophone monitoring system demonstrates high potential for early detection and prediction of sediment-related disasters. Its integration with IoT and renewable energy technologies enables stable operation even in remote areas, and future deployment across diverse topographies is expected to significantly mitigate disaster risks.

REFERENCES

- [1] Chen, F.H. (1975). *Foundation on Expansive Soils*. Elsevier, 280 pp.
- [2] Gillott, J.E. (1968). *Clay in Engineering Geology*. Elsevier, 296 pp.
- [3] Grim, R. & Guven, N. (1978). *Bentonite*. Essex: Elsevier.
- [4] Haefeli (1965). *Creep and progressive failure in snow, soil, rock and ice*. 6th Int'l Conf. SMFE, Vol. 4, 134–168.
- [5] Holtz, W. & Gibbs, H. (1954). *Engineering properties of expansive clays*. ASCE, 2814, 641–677.
- [6] Ito, T. (1980). *Swelling behavior with respect to geological hazards (in Japanese)*. Tsuchi to Kiso, JSSMFE, 28(2), 31–38.
- [7] Ito, T. (2001). *Strain softening of unsaturated swelling clays*. Proc. Int'l Symp. on Suction, Swelling, Permeability and Structure of Clays (IS-SHIZUOKA), Balkema, 137–142.
- [8] Ito, T. (1999). *Snow-induced landslide in Japan*. Proc. Int'l Symposium on Slope Stability Engineering (IS-SHIKOKU'99), 1223–1226.
- [9] Komamura, F. (1988). *Predicting of surface failure due to rainfall (in Japanese)*. Jr. of Japan Landslide Society, 25(1), 7–12.
- [10] Komornik, A. & David, D. (1969). *Prediction of swelling pressure of clay*. ASCE, SM1, 222–223.
- [11] Mogami, T. (1958). *Soil Mechanics (in Japanese)*. Iwanami Shoten.
- [12] Sakajo, S., Bhandary, N. P., & Kato, T. (2024). *Possibility of geophones in slope failure and landslide monitoring (Poster session)*. International Conference Series of the Nepal Geotechnical Society: Geotechnics for Sustainable Infrastructure.
- [13] Sakajo, S. & Tsuruta, K. (2015). *Practical application of a method for detecting debris flow using hydrophone (in Japanese)*. Tokyo.
- [14] Seed, H.B., Woodward, R.J., & Lundgren, R. (1962). *Prediction of swelling potential for compacted clays*. ASCE, SM3, 54–87.
- [15] Shibasaki, T. & Yamasaki, T. (2010). *Experimental investigation on temperature effect on residual strength characteristics of soil*. Jr. of the Japan Landslide Society, 47(5), 255–264.
- [16] Shirazu, H. (1988). *Nendo Koubutsu Gaku (in Japanese)*. Asakura Shoten, 185 pp.
- [17] Shoery, P.R. & Dunham, R.K. (1978). *An approximate analysis of floor heave occurring in roadways behind advancing longwall face*. Int'l Jr. Rock Mechanics & Mining Science & Geo-mechanical Abstracts, 15, 277–288.
- [18] Sikh, T.E. (1993). *Swelling soils*. ASCE, 119-GT4, 791–792.
- [19] Satake, M. & Ito, T. (1981). *Geotechnical data analysis of swelling phenomena (Bojunsei Jiban no Saigai Kaiseki, in Japanese)*. Shizen Saigai Shiryō Kaiseki, Vol. 8, 111–122.
- [20] Sudo, T. (1961). *Clay Minerals (in Japanese)*. Iwanami Shoten.
- [21] Tsuruta, K. & Sakajo, S. (2014). *Development of a method for detecting debris flow using hydrophone (in Japanese)*. Tokyo Metropolitan Government New Product and Technology Development Subsidy, CORVAC Co., Ltd.
- [22] Tsuruta, K. (2021). *Enhancing geophone landslide warning system using communication technology (in Japanese)*. Tokyo Metropolitan Small and Medium Enterprise Support Center.
- [23] Weaver, C.E. (1989). *Clays, Muds and Shales*. Elsevier, 819 pp.

Optimizing Landslide Susceptibility Mapping: Investigating Sample Ratios and Validation Methods using Random Forest in the Nam Ma Watershed, Northern Vietnam

Van-Trung Chu^{1,3*}, Shou-Hao Chiang^{1,2}, Tang-Huang Lin¹

¹Centre for Space and Remote Sensing Research, National Central University, Taoyuan 32001, Taiwan (China)

²Department of Civil Engineering, National Central University, Taoyuan 32001, Taiwan (China)

³Faculty of Resources Management, Thai Nguyen University of Agriculture and Forestry, Vietnam

*Email: chuvantrung@tuaf.edu.vn

Abstract: Landslides represent one of the most severe environmental hazards in mountainous regions, threatening sustainable development, ecosystem stability, and community safety. This study addresses landslide susceptibility mapping in the Nam Ma watershed, Northern Vietnam, as a contribution to green and climate-resilient development. We employ a Random Forest model integrated with digital geospatial techniques to explore the effects of sample ratios and validation methods on predictive performance. Seventeen predisposing factors related to topography, geology, land use, and hydrology were analyzed. Three validation strategies designed partition (70/30), random cross-validation, and spatial-clustered cross-validation were compared to enhance model robustness. Results indicate that increasing the proportion of landslide-free samples improves specificity but reduces sensitivity, revealing a trade-off that requires optimization. The optimal ratio of 1:1.33 yielded balanced performance, while random cross-validation slightly outperformed other methods. The findings highlight the importance of methodological design in machine learning-based hazard modeling. Beyond methodological insights, this research underlines the potential of Data-driven digital transformation in environmental sciences to support land management, disaster prevention, and sustainable development in landslide-prone areas.

Keywords: landslide susceptibility, random forest, sample ratio, model validation method, Nam Ma watershed.

INTRODUCTION

Landslides are among the most destructive natural hazards in mountainous regions, causing severe damage to infrastructure, property, and human lives. Identifying areas prone to landslides is essential for effective disaster risk management and sustainable land-use planning (Guzzetti, Reichenbach, Ardizzone, Cardinali, & Galli, 2006). In recent decades, various approaches have been applied for landslide susceptibility mapping, ranging from statistical to machine learning (ML) techniques (Lima, Steger, Glade, & Murillo-García, 2022; Reichenbach, Rossi, Malamud, Mihir, & Guzzetti, 2018). Among them, the Random Forest (RF) model has become one of the most widely used due to its strong capability to manage complex, nonlinear data and its robustness against noise (Behnia & Blais-Stevens, 2018; Goetz, Brenning, Petschko, & Leopold, 2015; Hong, Miao, Liu, & Zhu, 2019; Park & Kim, 2019; Trigila, Iadanza, Esposito, & Scarascia-Mugnozza, 2015).

However, landslide datasets often suffer from class imbalance, as recorded landslides occupy only a small portion of the study area. Ensemble methods such as Balanced Random Forest and EasyEnsemble can mitigate this issue, but data imbalance remains a major source of uncertainty in model prediction (Al-Najjar, Pradhan, Sarkar, Beydoun, & Alamri, 2021). The selection of appropriate ratios between landslide and non-landslide samples plays a crucial role in model performance

(Guns & Vanacker, 2012; Heckmann, Gegg, Gegg, & Becht, 2014; Hong et al., 2019; Pourghasemi, Kornejady, Kerle, & Shabani, 2020; Van Den Eeckhaut et al., 2006), while the choice of validation strategy such as design-based split, random k-fold, or spatial cross-validation significantly affects the reliability of susceptibility mapping (Bui, Tuan, Klempe, Pradhan, & Revhaug, 2016a; Merghadi, Abderrahmane, & Bui, 2018).

This study examines the influence of different sample ratios and validation methods on the performance of the Random Forest model for landslide susceptibility mapping in the Nam Ma watershed, Lai Chau Province, Vietnam. The watershed is characterized by steep terrain, high rainfall, and complex geological conditions, making it highly susceptible to landslides. The findings aim to provide insights into selecting optimal sampling and validation strategies to enhance the accuracy and reliability of landslide susceptibility assessment in mountainous regions.

STUDY AREA AND DATA

The Nam Ma watershed, a tributary of the Da River, is located in Sin Ho District, Lai Chau Province, northern Vietnam. The basin covers approximately 732 km², with the main river extending about 55 km. The area is characterized by rugged topography, complex geology, and active tectonics typical of the northwestern mountain ranges of Vietnam. Sixteen lithological units occur within the basin, with dominant formations including Ban Phap, Vien Nam, Yen Chau, and Bac Son. Several fault systems trending northwest-southeast shape the drainage network and geomorphic pattern. The region experiences a tropical monsoon climate, with heavy rainfall concentrated from April to October and peak precipitation in June–July. Land cover is primarily forest, agricultural, and unused land; however, deforestation and shifting cultivation

have significantly reduced forest cover in recent decades. According to the Lai Chau Disaster Prevention Agency, landslides frequently cause severe damage to houses, cropland, and infrastructure. Notably, after intense rainfall on 27 June 2018, a large landslide buried 28 houses in Sang Tung village, Ta Ngao commune, illustrating the high landslide risk in the basin.

Based on the data accessibility and literature review, seventeen predisposing factors were selected for landslide susceptibility modelling, covering topographic, environmental, geological, and hydrological domains (Table 1). These include elevation, slope, aspect, plan and profile curvature, topographic wetness index (TWI), height above the nearest drainage (HAND), Normalized Different Vegetation Index (NDVI), land cover, land use, soil depth, lithology, distance to faults, distance to streams, distance to roads, distance to edge (ridge), and maximum 24-hour rainfall.

Topographic variables derived from a 10 m DEM are vital for representing slope stability conditions. Slope, TWI (Beven & Kirkby, 1979), and HAND (Nobre et al., 2011; Rennó et al., 2008) were key indicators of hydrological accumulation and relative terrain position. Environmental factors such as NDVI and land cover were obtained from a Sentinel-2 image (21 February 2018) using supervised classification, while land use data were extracted from the 2015 Sin Ho district map (1:25,000 scale). Rainfall data were interpolated from 14 rain gauge stations to generate a spatial map of long-term maximum daily precipitation. Geological data, including lithology and fault distribution, were derived from the 1:200,000 national geological map, and soil depth data from the provincial soil map. All spatial data were resampled to 10 m resolution and projected to UTM Zone 48N (WGS84) for consistent analysis in ArcGIS.

Table 1. Data used for landslide predisposing factors in Nam Ma (Viet Nam)

Data	Conditioning factor	Data source	Min	Max
Topographical factors	Elevation	Topographic maps (1:10 000) provided by Viet Nam Department of the Survey, mapping, and Geographic Information	151.6 m	2463.5 m
	Slope (degree)	DEM - derived	0	83.34
	Aspect	DEM - derived	Category	
	Plan curvature	DEM - derived	-5.54905	8.50977
	Profile Curvature	DEM - derived	-16.1187	13.6822
	TWI	DEM - derived	-2.148	20.41
	HAND	DEM - derived	0 m	998.35 m
Environmental factors	NDVI	Sentinel 2 - derived	-0.57	0.994
	Land cover	Sentinel 2 - derived	Category	
	Land use	Land use map 2015 of Sin Ho district (1:25,000) provided by the local government	Category	
	Distance to stream	Stream derived by DEM	0 m	2468.4 m
	Distance to edge	Edge derived by DEM	0 m	970.824 m
	Max daily rainfall	30 years daily rainfall 14 rain gauge stations provided by (National Centre for Hydro-Meteorological Forecasting	205.19 mm/day	399.71 mm/day
	Distance to road	Road network extract from the Lai Chau Road map	0 m	> 5000 m
Geological factor	Lithological formations	Geological map (1:200 000) Provided by the Department of Geology and Minerals Viet Nam	Category	
	Distance to fault	Fault line extracted from the Geological map. Provided by the Department of Geology and Minerals Viet Nam	0 m	5148.98 m

METHODOLOGY

Sample selection strategies

Landslide sample points were derived from a combination of post-event Google Earth imagery (landslides recorded in 2018) and the official landslide inventory map of Lai Chau Province compiled by the Vietnam Institute of Geosciences and Mineral Resources (Hung et al., 2017). A total of 1,242 landslide centroids were extracted, with the largest landslide (about 28 ha include source and damaged area)

located in Sang Tung village, Ta Ngao commune.

To obtain reliable non-landslide samples, areas without known landslide activity were identified using the LandTrendr algorithm (Kennedy, Yang, & Cohen, 2010), which detects long-term surface disturbance from Landsat time series. This approach minimizes misclassification by excluding unstable terrain (Chu, Chiang, & Lin, 2020). For model training and validation, 80% of the landslide samples (1,004 points) were used, while 20% (238

points) were reserved as an independent testing subset. The same number of non-landslide points (238) was selected for testing to ensure a balanced evaluation.

Ten sampling ratios between landslide and non-landslide data were then established for model calibration (Table 2), ranging from 1:0.33 to 1:6. Each ratio was used to generate a separate model (MOD₁–MOD₁₀), allowing the evaluation of model sensitivity to sample proportion.

Table 2. Description of the sample strategies

Model	Ratio Landslide/Non- landslide	Landslide	Non- landslide	Total
MOD ₁	1:0.33	1004	331	1335
MOD ₂	1:0.5	1004	502	1506
MOD ₃	1:1	1004	1004	2008
MOD ₄	1:1.33	1004	1335	2339
MOD ₅	1:1.5	1004	1506	2510
MOD ₆	1:2	1004	2008	3012
MOD ₇	1:3	1004	3012	4016
MOD ₈	1:4	1004	4016	5020
MOD ₉	1:5	1004	5020	6024
MOD ₁₀	1:6	1004	6024	7028

Random forest

RF is a powerful machine-learning technique that uses the Bootstrap sample approach to train many decision trees (DTs) with large depths. The RF ensemble model combines the results of the DTs by taking a majority vote for classification tasks or counting an average for regression tasks. This approach ensures that the model generalizes well and does not overfit the training data (Breiman, 2001). RF is suitable for continuous and categorical predictor variables and can minimize variance while maintaining the ensemble's bias (Maxwell et al., 2020). The unselected samples (out-of-bag) are used to evaluate the uncertainties of the model training. RF is widely used in various fields, including landslide susceptibility research, due to its ability to generalize well (Behnia & Blais-Stevens, 2018; Goetz et al., 2015; Hong et al., 2019; Lai, Chiang, & Tsai, 2019; Trigila et al., 2015). This study used RStudio software with updated packages to develop the RF model.

Model performance

Model performance was evaluated using both validation subsets and independent test data under three validation schemes:

- Design-based split (70/30): random partition of training (70%) and validation (30%) data.
- Random k-fold cross-validation (RandomCV): the dataset divided into $k = 10$ random folds, iteratively trained and validated.
- Spatial cluster k-fold cross-validation (SpatialClusterCV): spatially constrained folds created through hierarchical clustering based on sample coordinates to reduce spatial autocorrelation.

Performance metrics included sensitivity (producer's accuracy), specificity, precision (user's accuracy), overall accuracy, Kappa coefficient, and area under the ROC curve (AUC) (Chung & Fabbri, 2003; Congalton, 1991; Maxwell et al., 2020). These indices quantify different aspects of predictive performance and reliability. Models with $AUC > 0.9$ were considered excellent, and $Kappa > 0.6$ indicated substantial agreement (Van Den Eeckhaut et al., 2006).

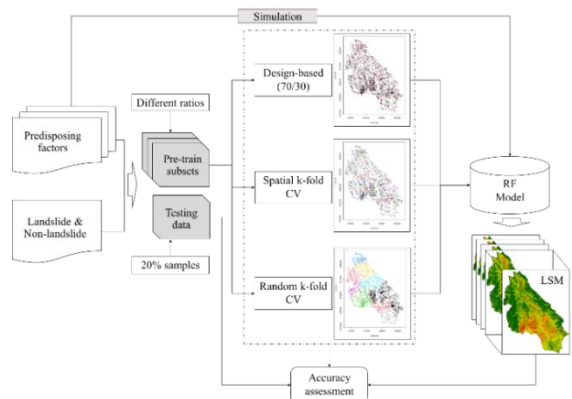


Figure 1. Workflow of this study

By maintaining a constant independent testing subset across all experiments, the study ensured that variations in model performance were attributed solely to changes in sampling ratio and validation strategy rather than differences in test data. The overall

methodological workflow is illustrated in Figure 1.

RESULTS AND DISCUSSION

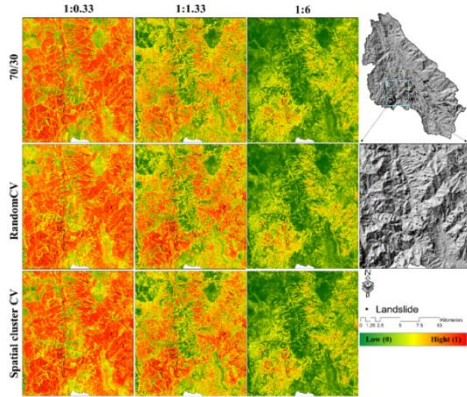


Figure 2. Landslide susceptibility map (enlarged area): over prediction (MOD₁ ratio 1:0.33), The appropriate result (MOD₄ ratio 1:1.33), and under prediction (MOD₁₀ ratio 1:6).

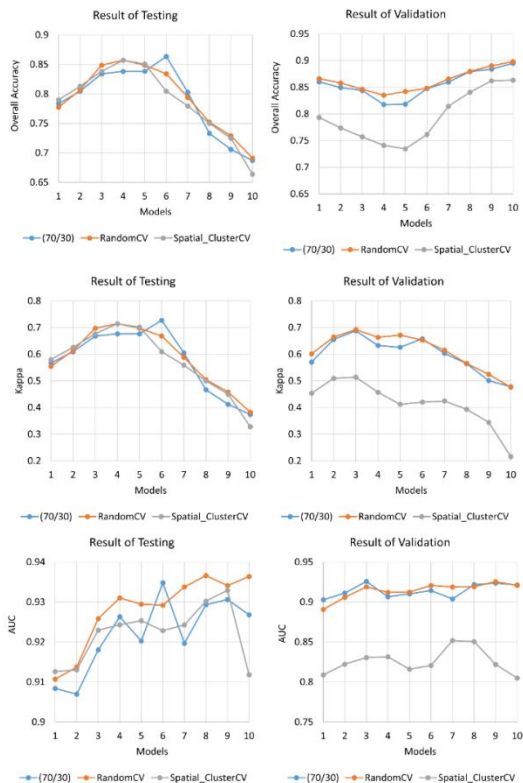


Figure 3. Accuracy assessment of different training cases

Model validation and testing results show in Figure 3. In general, the change in the ratio lead model results in predictability variation. Results show that by increasing the ratio from 1:0.33 (MOD₁) to 1:1.33 (MOD₄), testing results increase gradually in accuracy values (except specificity). The test result also shows that accuracy decreases when the ratio increases above 1:1.33 (except AUC, specificity, and precision keep increasing). However, it is not the same case with validation results. Sensitivity, specificity, kappa, and AUC are quite consistent, but the overall accuracy and precision show the opposite of the test result.

In this study, according to the result of different sample ratios between landslide and non-landslide samples, the precision and recall will be crossed at the point where the ratio at 1.33. So, based on this result, we summarize that the best ratio of landslide and non-landslide should be higher than 1:1 and smaller than 1:1.5.

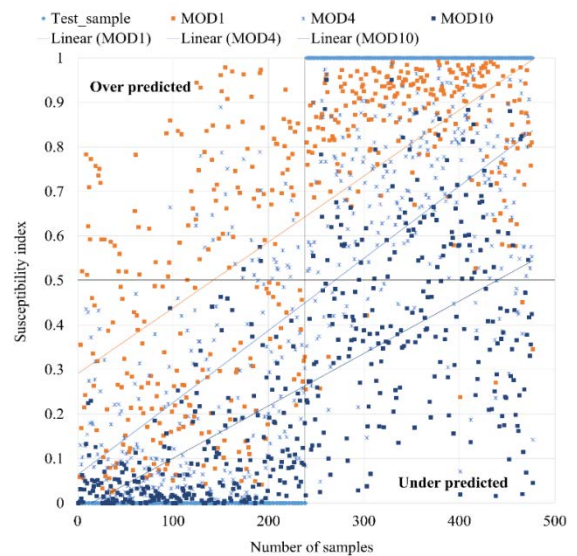


Figure 4. Uncertainty of model prediction: the cases with over prediction (MOD₁ ratio 1:0.33), the appropriate result (MOD₄ ratio 1:1.33), and under prediction (MOD₁₀ ratio 1:6)

The result in Figure 4 shows that the model result will tend to over predicted landslides when the number of non-landslide samples is smaller than the amount of landslide (red point); in contrast, the problem will

obviously occur when increasing the proportion of non-landslides much higher than total landslide sample in training data. In that case (MOD9, ratio: 1:5), more landslide area will be missed classification in the model result (brown point). The better performance is present at the MOD4 with the proportion of 1:1.33 (blue point).

Contribution of selected predisposing factor

The selected predisposing factors were under the multicollinearity test before feeding the model. The result of variance inflation (VIF) and tolerance (TOL) values of each factor. The values of $VIF < 3$ and $TOL > 0.3$ indicate that seventeen factors are no multicollinearity. Results in Figure 5 show the relative importance of predisposing factors with three specific cases MOD1, MOD4 and MOD10. Generally, different training subsets will lead to different ranks of factors contributing to the model. However, we can see that the seven important factors in all the cases are land cover, NDVI, slope, elevation, rainfall (max 24-hour rainfall), distance to road, and distance to fault.

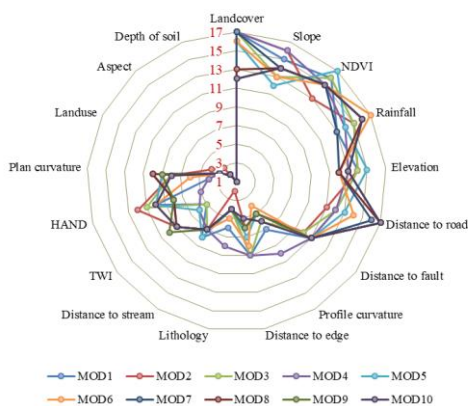


Figure 5. Relative rank of predisposing factor important over the training cases

Discussion

This study developed a semi-automatic approach to examine how varying the ratios between landslide and non-landslide samples influence the performance of landslide susceptibility models using three Random Forest-based validation strategies. The results

demonstrate that the balance between positive and negative samples plays a critical role in model reliability. For the Nam Ma watershed, employing seventeen predisposing factors, the optimal proportion was found between 1:1 and 1:1.5, with the most suitable at 1:1.33. When either class becomes predominant, the model tends to over- or underpredict susceptibility. This aligns with previous studies that emphasize the need for a balanced dataset to ensure stable model behavior (Heckmann et al., 2014; Pourghasemi, Kornejady, Kerle, & Shabani, 2019).

Among the three validation methods, the design-based 70/30 split and the random k-fold cross-validation produced similar and consistent results, with random CV performing slightly better. In contrast, the spatial cluster cross-validation achieved the lowest accuracy and showed underestimation tendencies at higher sample ratios. The simplicity of the design-based 70/30 split explains its popularity in previous research (Bui, Pradhan, Lofman, Revhaug, & Dick, 2012; Chen, Zhang, Li, & Shahabi, 2018; Kadavi, Lee, & Lee, 2018; Pourghasemi et al., 2020; Wang et al., 2016). Nevertheless, this study supports the recommendation of Petschko et al. (2014) that non-spatial random cross-validation provides a more robust framework for landslide susceptibility modelling (H. Petschko, A. Brenning, R. Bell, J. Goetz, & Glade, 2014).

Maintaining a constant independent testing subset for all experiments proved essential for fair comparison between training conditions and validation approaches. The results further suggest that increasing training data generally improves model stability, but excessively large or small samples may reduce performance due to data imbalance or overfitting. The trade-off between sensitivity (producer's accuracy) and precision (user's accuracy) can guide the selection of an appropriate ratio for optimizing predictive performance. Therefore, future studies should carefully consider sampling ratios and validation schemes to ensure accurate, transferable, and reliable landslide susceptibility models.

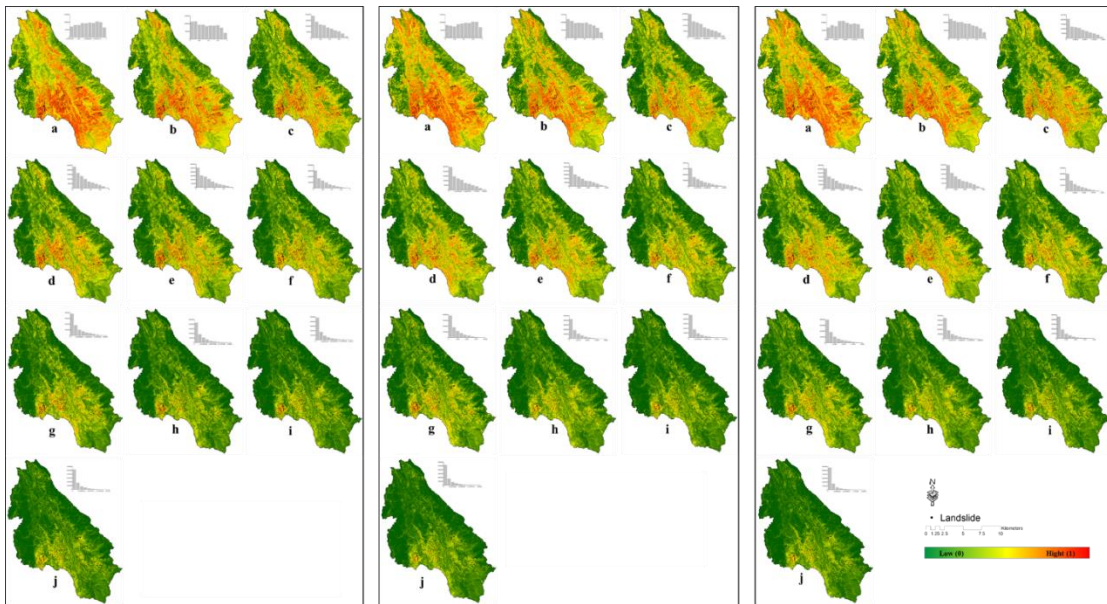


Figure 6. Landslide susceptibility maps based on different training subsets with Design-based (left); RandomCV (center) and Spatial-cluster CV (right) method (a) MOD₁, (b) MOD₂, (c) MOD₃, (d) MOD₄, (e) MOD₅, (f) MOD₆, (g) MOD₇, (h) MOD₈, (i) MOD₉, and (j) MOD₁₀

CONCLUSIONS

This study evaluated the impact of varying ratios between landslide and non-landslide samples on landslide susceptibility modelling using the Random Forest algorithm in the Nam Ma watershed, Lai Chau Province, Vietnam. A total of seventeen conditioning factors representing topographic, geological, hydrological, and land-cover conditions were incorporated into the model. The results confirmed that the ratio between landslide and non-landslide samples plays a crucial role in determining model accuracy and predictive stability. When the number of non-landslide samples was smaller than that of landslides, the model tended to overestimate susceptibility, while an excessively large proportion of non-landslide samples led to underestimation.

Three validation methods: design-based (70/30), random k-fold, and spatial cluster k-fold cross-validation were compared to assess model robustness. The findings indicated that the design-based and random k-fold validations produced consistent and reliable results, whereas spatial cluster cross-validation

yielded slightly lower accuracy due to spatial dependence within the dataset. The top seven contributing factors to landslide occurrence were identified as land cover, NDVI, slope, elevation, maximum 24-hour rainfall, distance to road, and distance to fault, emphasizing their strong influence on slope instability in the region.

Overall, this study highlights the importance of selecting representative and balanced datasets to ensure the reliability of machine learning-based landslide susceptibility models. The outcomes provide valuable insights for optimizing sampling and validation strategies, supporting the application of Random Forest in landslide risk assessment. These results also serve as a scientific basis for local authorities to enhance land-use planning and develop effective landslide mitigation measures in mountainous areas.

REFERENCES

- Al-Najjar, H. A., Pradhan, B., Sarkar, R., Beydoun, G., & Alamri, A. (2021). A new integrated approach for landslide data balancing and spatial prediction based

- on generative adversarial networks (GAN). *Remote Sensing*, 13(19), 4011.
- Behnia, P., & Blais-Stevens, A. (2018). Landslide susceptibility modelling using the quantitative random forest method along the northern portion of the Yukon Alaska Highway Corridor, Canada. *Natural Hazards and Earth System Sciences*, 90(3), 1407-1426.
- Beven, K. J., & Kirkby, M. J. (1979). A physically based, variable contributing area model of basin hydrology/Un modèle à base physique de zone d'appel variable de l'hydrologie du bassin versant. *Hydrological Sciences Journal*, 24(1), 43-69.
- Breiman, L. (2001). Random forests. *Machine learning*, 45(1), 5-32.
- Bui, D. T., Pradhan, B., Lofman, O., Revhaug, I., & Dick, O. B. (2012). Landslide susceptibility mapping at Hoa Binh province (Vietnam) using an adaptive neuro-fuzzy inference system and GIS. *Computers & Geosciences*, 45, 199-211. doi:10.1016/j.cageo.2011.10.031
- Bui, D. T., Tuan, T. A., Klempe, H., Pradhan, B., & Revhaug, I. (2016a). Spatial prediction models for shallow landslide hazards: a comparative assessment of the efficacy of support vector machines, artificial neural networks, kernel logistic regression, and logistic model tree. *Landslides*, 13(2), 361-378. doi:10.1007/s10346-015-0557-6
- Chen, W., Zhang, S., Li, R. W., & Shahabi, H. (2018). Performance evaluation of the GIS-based data mining techniques of best-first decision tree, random forest, and naive Bayes tree for landslide susceptibility modeling. *Science of the Total Environment*, 644, 1006-1018. doi:10.1016/j.scitotenv.2018.06.389
- Chu, V. T., Chiang, S. H., & Lin, T. H. (2020). *Sample Position Affect Landslide Susceptibility Models in Hotspot Area of Nam Ma Basin, Lai Chau, Viet Nam*. Paper presented at the EGU General Assembly Conference.
- Chung, C.-J. F., & Fabbri, A. G. (2003). Validation of spatial prediction models for landslide hazard mapping. *Natural Hazards and Earth System Sciences*, 30(3), 451-472.
- Congalton, R. G. (1991). A review of assessing the accuracy of classifications of remotely sensed data. *Remote Sensing of Environment*, 37(1), 35-46.
- Goetz, J., Brenning, A., Petschko, H., & Leopold, P. (2015). Evaluating machine learning and statistical prediction techniques for landslide susceptibility modeling. *Computers geosciences*, 81, 1-11.
- Guns, M., & Vanacker, V. (2012). Logistic regression applied to natural hazards: rare event logistic regression with replications. *Natural Hazards and Earth System Sciences*, 12(6), 1937-1947.
- Guzzetti, F., Reichenbach, P., Ardizzone, F., Cardinali, M., & Galli, M. (2006). Estimating the quality of landslide susceptibility models. *Geomorphology*, 81(1-2), 166-184. doi:10.1016/j.geomorph.2006.04.007.
- H. Petschko, A. Brenning, R. Bell, J. Goetz, & Glade, T. (2014). Assessing the quality of landslide susceptibility maps – case study Lower Austria. *Natural Hazards and Earth System Sciences*, 14, 95–118. doi:doi:10.5194/nhess-14-95-2014
- Heckmann, T., Gegg, K., Gegg, A., & Becht, M. (2014). Sample size matters: investigating the effect of sample size on a logistic regression susceptibility model for debris flows. *Natural Hazards Earth System Sciences*, 14(2), 259.
- Hong, H., Miao, Y., Liu, J., & Zhu, A.-X. (2019). Exploring the effects of the design and quantity of absence data on the performance of random forest-based landslide susceptibility mapping. *Catena*, 176, 45-64.
- Hung, L. Q., Van, N. T. H., Son, P. V., Ninh, N. H., Tam, N., & Huyen, N. T. (2017). *Landslide inventory mapping in the fourteen Northern provinces of Vietnam: achievements and difficulties*. Paper presented at the Advancing Culture of Living with Landslides: Volume 1 ISDR-ICL Sendai Partnerships 2015-2025.
- Kadavi, P. R., Lee, C. W., & Lee, S. (2018). Application of Ensemble-Based Machine Learning Models to Landslide Susceptibility Mapping. *Remote Sensing*, 10(8).
- Kennedy, R. E., Yang, Z., & Cohen, W. B. (2010). Detecting trends in forest disturbance and recovery using yearly Landsat time series: 1. LandTrendr—Temporal segmentation algorithms. *Remote Sensing of Environment*, 114(12), 2897-2910.
- Lai, J.-S., Chiang, S.-H., & Tsai, F. (2019). Exploring Influence of Sampling Strategies on Event-Based Landslide Susceptibility Modeling. *ISPRS International Journal of Geo-Information*, 8(9), 397.
- Lima, P., Steger, S., Glade, T., & Murillo-García, F. G. (2022). Literature review and bibliometric analysis on data-driven assessment of landslide susceptibility. *Journal of Mountain Science*, 19(6), 1670-1698.

- Maxwell, A. E., Sharma, M., Kite, J. S., Donaldson, K. A., Thompson, J. A., Bell, M. L., & Maynard, S. M. (2020). Slope Failure Prediction Using Random Forest Machine Learning and LiDAR in an Eroded Folded Mountain Belt. *Remote Sensing Letters*, 12(3), 486.
- Merghadi, A., Abderrahmane, B., & Bui, D. T. (2018). Landslide Susceptibility Assessment at Mila Basin (Algeria): A Comparative Assessment of Prediction Capability of Advanced Machine Learning Methods. *Isprs International Journal of Geo-Information*, 7(7).
- Nobre, A. D., Cuartas, L. A., Hodnett, M., Rennó, C. D., Rodrigues, G., Silveira, A., & Saleska, S. (2011). Height Above the Nearest Drainage—a hydrologically relevant new terrain model. *Journal of Hydrology*, 404(1-2), 13-29.
- Park, S., & Kim, J. (2019). Landslide susceptibility mapping based on random Forest and boosted regression tree models, and a comparison of their performance. *Applied Sciences*, 9(5), 942.
- Pourghasemi, H. R., Kornejady, A., Kerle, N., & Shabani, F. (2019). Investigating the effects of different landslide positioning techniques, landslide partitioning approaches, and presence-absence balances on landslide susceptibility mapping. *Catena*, 104364.
- Pourghasemi, H. R., Kornejady, A., Kerle, N., & Shabani, F. (2020). Investigating the effects of different landslide positioning techniques, landslide partitioning approaches, and presence-absence balances on landslide susceptibility mapping. *Catena*, 187, 104364. doi:doi.org/10.1016/j.catena.2019.104364.
- Reichenbach, P., Rossi, M., Malamud, B. D., Mihir, M., & Guzzetti, F. (2018). A review of statistically-based landslide susceptibility models. *Earth-Science Reviews*, 180, 60-91. doi:10.1016/j.earscirev.2018.03.001.
- Rennó, C. D., Nobre, A. D., Cuartas, L. A., Soares, J. V., Hodnett, M. G., & Tomasella, J. (2008). HAND, a new terrain descriptor using SRTM-DEM: Mapping terra-firme rainforest environments in Amazonia. *Remote Sensing of Environment*, 112(9), 3469-3481.
- Trigila, A., Iadanza, C., Esposito, C., & Scarascia-Mugnozza, G. (2015). Comparison of Logistic Regression and Random Forests techniques for shallow landslide susceptibility assessment in Giampilieri (NE Sicily, Italy). *Geomorphology*, 249, 119-136.
- Van Den Eeckhaut, M., Vanwalleghem, T., Poesen, J., Govers, G., Verstraeten, G., & Vandekerckhove, L. (2006). Prediction of landslide susceptibility using rare events logistic regression: a case-study in the Flemish Ardennes (Belgium). *Geomorphology*, 76(3-4), 392-410.
- Wang, Q. Q., Li, W. P., Xing, M. L., Wu, Y. L., Pei, Y. B., Yang, D. D., & Bai, H. Y. (2016). Landslide susceptibility mapping at Gongliu county, China using artificial neural network and weight of evidence models. *Geosciences Journal*, 20(5), 705-718. doi:10.1007/s12303-016-0003-3

Preliminary analysis of landslide-generated seismic signals: potential for real-time detection and early warning in Vietnam

Pham Van Tien^{1,*}, Ha Thi Giang^{1,2}, Nguyen Van Duong¹, Pham The Truyen¹, Vu Cao Minh¹, Dao Minh Duc¹, Lukasz Pawlik³, Pawel Kroh⁴, Bui Phuong Thao¹

¹Institute of Earth Sciences, Vietnam Academy of Science and Technology, Hanoi, Vietnam

²Hanoi University of Mining and Geology, Hanoi, Vietnam

³Institute of Earth Sciences, University of Silesia in Katowice, Sosnowiec, Poland

⁴University of the National Educational Commission, Institute of Biology and Earth Sciences, Krakow, Poland

*Email: Phamtiengtv@gmail.com

Abstract: In September 2024, Typhoon Yagi brought prolonged and intense rainfall, triggering thousands of landslides that caused catastrophic damage and severe casualties in Northern Vietnam. This paper presents a preliminary analysis of landslide-induced seismic wave signals recorded at the broadband seismic monitoring stations. Three seismic events were generated by rainfall-induced deep-seated landslides in Lang Nu, Ba Thau and Khe Bin villages. The data examination indicates that the duration of landslide seismic ranged from tens of seconds to several minutes, indicating phases corresponding to initiation, rapid downslope motion, and deposition. Notably, spectral analysis of landslide signals revealed the same seismograms characterized by elongated waveform patterns with gradual onsets and without defined P- or S-wave phases. The seismic signals of the Lang Nu long-traveling landslide generated the longest ground motion among the recorded events, which lasted for more than two minutes. These distinct signatures are consistent with many studies worldwide and provide valuable spectrogram features for identifying and characterizing landslide-generated seismic events. The findings represent the first documented evidence of landslide-related seismic signals in Vietnam. They highlight the potential for developing real-time seismic monitoring systems for detecting, identifying and issuing early warnings of catastrophic landslides in remote mountainous regions.

Keywords: landslides, rainfall, seismic signals, early warning, Vietnam

INTRODUCTION

Typhoon Yagi struck mainland Vietnam in September 2024, producing torrential rainfall, causing extensive economic and human losses due to widespread of landslides across the Northern provinces (Fig. 1). According to the Vietnam Disaster and Dyke Management Authority (VDMA, 2024), by September 19, 2024, Typhoon Yagi had left 333 people dead or missing and 1,929 injured. The three former provinces with the highest number of casualties were Lao Cai, Cao Bang and Yen Bai with corresponding death and missing tolls of 150, 57, and 54 people, respectively (VDMA, 2024). In which landslides were responsible for 264 of the deaths, accounting for 79% of all fatalities (Tien et al., 2025). The newly established Lao Cai province, which included both Lao Cai and Yen Bai provinces before July 1, 2025, was severely affected by economic losses and fatalities caused by landslides.

Fig. 1 shows rainfall data monitored at rain-gauge stations of Tinh Tuc (Cao Bang province), Pho Rang, Tan Phuong and Luc Yen (Lao Cai province) in the period from 7 to 12 September. According to collected data, landslides mainly occurred on 9 and 10 September when the cumulative rainfall reached approximately 370 after 3 days to 635

mm after 4 days, respectively. Notably, single events of rapid and deep-seated landslides caused catastrophic disasters with a very high number of fatalities, for example: the rapid, long-traveling Lang Nu landslides claimed 67 lives; the Khuoi Ngoa landslide caused 34 deaths; the Nam Tong landslide buried 18 people; and the Lung Sung debris avalanche left 11 people dead. The formation of large-scale landslides not only caused shocking human casualties but also forced many households in residential areas to relocate to new settlements. The details of the study area, locations and photos of several deep landslides are presented in Fig. 2.

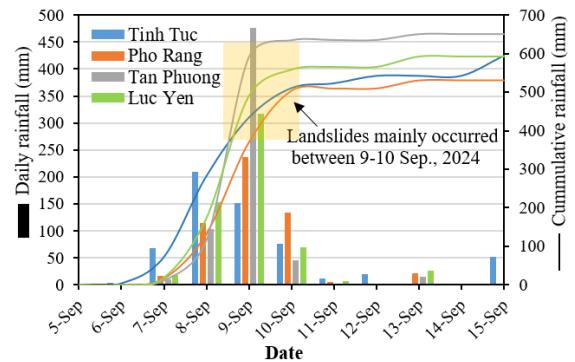
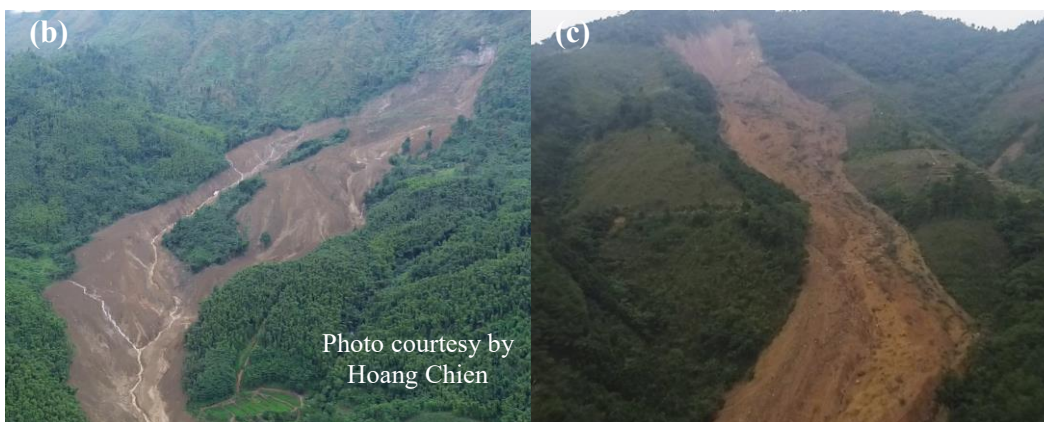
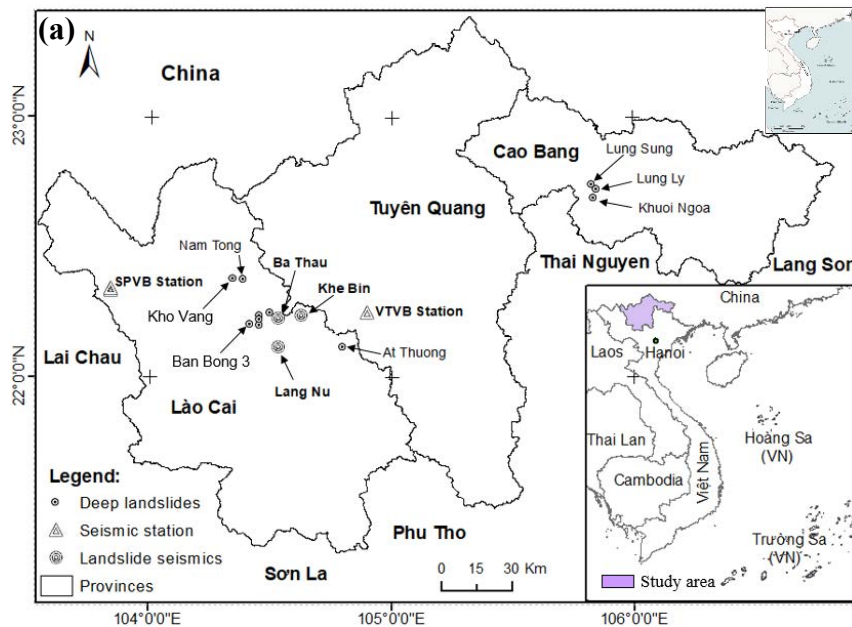


Figure 1. Rainfall associated with Typhoon Yagi between 7 and 13 September, 2024 at Tinh Tuc, Pho Rang, Tan Phuong and Luc Yen rain-gauge stations (source: VDMA 2024)



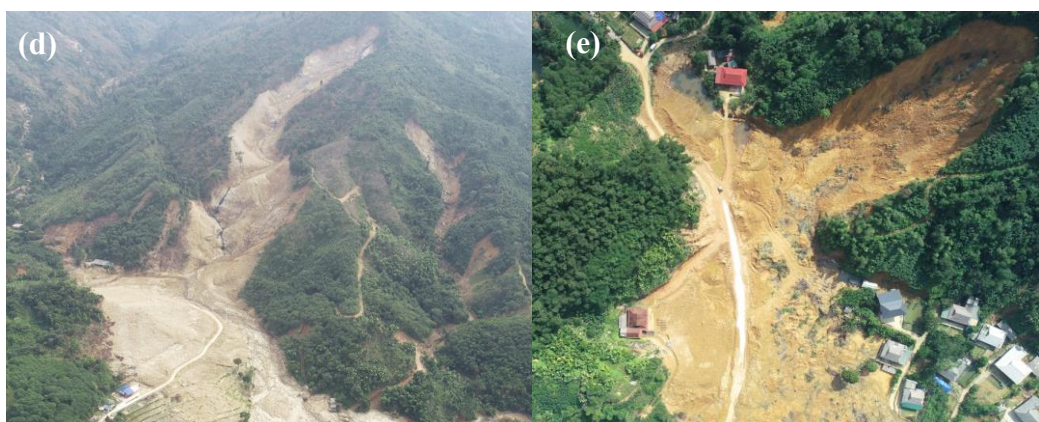


Figure 2. (a) Study area with location of deep-seated landslides and seismic monitoring stations; UAV photos showing deep-seated landslide, including (b) Lang Nu, (c) Ba Thau, (d) Khe Bin and (e) At Thuong

Several deep-seated landslides rapidly moved downslope and produced strong ground motions. The Vinh Tuy and Sa Pa broadband seismic stations in the Northern region recorded clear ground motion signals coinciding with the temporal occurrence of three large landslides in Lang Nu, At Thuong and Ba Thau villages. These broadband seismic stations consisted of VTVB located at Vinh Tuy town, Bac Quang district, Ha Giang province (currently Vinh Tuy commune, Cao Bang province); and SPVO and SPVB in Sa Pa town, Lao Cai province (currently Sa Pa ward, Lao Cai province) (Fig. 2). In which, the VTVB station was closest to the three seismic-generated landslides in At Thuong, Ba Thau and Lang Nu villages with a distance of 28, 38 and 41 km, respectively. Whereas, the two SPVO and SPVB seismic stations are located in close proximity to each other in Sa Pa ward and are about 75 km away from the Lang Nu landslide.

The 2024 Lang Nu rockslide is located in Phuc Khanh commune, Lao Cai province, which was induced by rainfall at about 5:55 AM (local time in GMT+7) on 10 September 2024 (Tien et al., 2025). The large-scale deep landslide, approximately 370 m long, 190 m wide, and 45 m deep, mobilized roughly 1.1 million m³ of material (Fig. 2b). The sliding mass traveled a distance of about 4,220 m at an estimated average velocity of 10 m/s, burying 37

households in Lang Nu village. The Lang Nu has been considered one of the most devastating natural landslides in Vietnam's history, given the large number of casualties and its profound socio-economic consequences (Tien et al., 2025).

The other two deep-seated landslides that generated seismic signals occurred in Khe Bin village (Lam Thuong commune) and Ba Thau village (Bao Yen commune) of Lao Cai province. These events occurred at approximately 12:45 p.m. on 9 September and 6:00 a.m. on 12 September (local time, GMT+7), respectively. The Ba Thau large-scale landslide's source was about 300 m long, 110 m wide, and 50 m deep, mobilized a runout distance of about 820 m (Fig. 2c). Whereas, the At Thuong rockslide with its source body measured up to 160 m in length, 75 m in width and 20 m in deep. This landslide produced a long traveling runout of around 600 and buried two people and many houses. Among three landslide seismic events, the Lang Nu sliding initiation and motion had a longest duration ranging from 3 to 5 minutes (Tien et al., 2025).

Seismic signals generated by landslides, often referred to as "landslide-triggered earthquakes", have been widely investigated in by many scientists in countries such as Japan, Taiwan, China, France, Italia, Switzerland, Canada and the United States (Surinach et al., 2005; Favreau et al., 2010; Lacroix et al., 2012;

Hibert et al., 2014; Yamada et al., 2016; Li et al., 2019; Chao et al., 2017, Kuo et al., 2018). Recording seismic data from deep-seated landslides is crucial for landslide study because it enables the identification of the landslide location and occurrence time, as well as the interpretation of the underlying physical processes. These factors provide valuable information for real-time detection and early warning in remote mountainous areas. Numerous events on deep-seated landslides triggered by rainfall were studied in Vietnam (Luong et al., 2016; Lan et al., 2019; Van Tien et al., 2021a; 2021b; 2023; and 2025). However, Vietnam still lacks comprehensive studies and sufficient seismic observations of landslide-generated signals. Therefore, this study presents the initial results of an investigation into landslide-generated seismic waves, to provide a scientific basis for detecting large-scale landslides in remote mountainous areas of Vietnam.

METHODS

We conducted a total of six site surveys between September and December, 2024 to collect amounts of information on landslides triggered by Typhoon Yagi in Lao Cai (including the former Lao Cai and Yen Bai provinces), Tuyen Quang (including the former Ha Giang and Tuyen Quang provinces), and Cao Bang provinces. Particularly, the detailed information on fourteen deep-seated landslides (such as location and time occurrence) was collected and verified by interviewing witnesses and residents (Fig. 2). Wave signals recorded from broadband seismic stations, namely VTVB, SPVO and SPVB, was examined in detail according to the temporal occurrence of deep-seated landslides.

Identification of seismic signals generated by landslides, local earthquakes, or anthropogenic noise was visually conducted on the spectrogram of seismic waves, which was based on typical signatures regarding the shape, frequency content, amplitude variation and duration of the seismic signals. In which tectonic earthquake waves are dominantly characterized by distinct P- and S-waves and

low-frequency content (Li et al., 2019). In contrast, landslide seismic signals show a longer duration, chaotic and large frequency content than local earthquakes (Chen et al., 2013). According to previous studies (Surinach et al., 2005; Chen et al., 2013; Allstadt, 2013; Lacroix, 2012), the duration of local earthquakes typically ranges from a few seconds to several tens of seconds. In contrast, deep-seated landslides often generate seismic signals that last from several tens of seconds to several minutes. In terms of frequency content, landslide-induced seismic signals may extend up to 10–20 Hz, whereas small earthquakes generally exhibit dominant energy below 5 Hz. Fig. 3 shows key features of seismic signals generated by the Kon Tum earthquake (Magnitude = 3.0), which took place on December 01, 2024. It is clear to identify the P-wave and S-wave from the seismogram band. The duration of the earthquake was about 38 seconds.

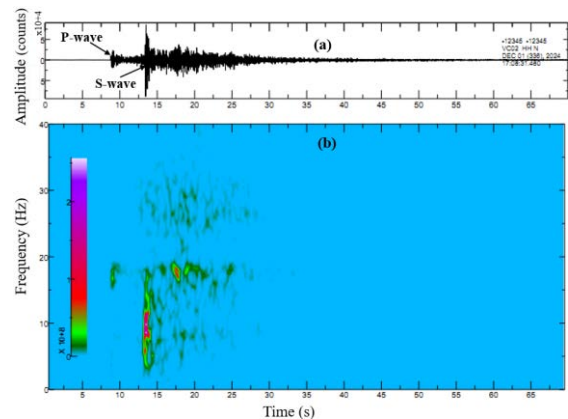


Figure 3. Seismic signal generated by the 3.0M Kon Tum earthquake: (a) N-S component seismogram, and (b) Time-frequency characteristics

Available seismic data recorded at the Vinh Tuy (VT) and Sa Pa (SP) stations (namely VTVB, SPVB and SPVO stations) were manually examined, separated and extracted from the ambient noise. The seismic signal was first processed with a 1–20 Hz band-pass filter to suppress background noise. A Fourier transform was subsequently applied to derive the time–frequency spectrum. The analysis used a 1024-sample window with 80% overlap, providing a balanced trade-off between

temporal and frequency resolution for detecting landslide-related signals. The power spectral density was converted to decibels to improve visual contrast, and only frequency components below 60 Hz were retained to emphasize the dominant seismic energy associated with landslide processes. Fig. 4 shows the spectrograms of ambient background noise and the landslide-induced seismic signal recorded at the Vinh Tuy station. The ambient noise exhibits a stable and uniform frequency distribution with nearly constant energy over time, reflecting typical stationary background conditions. Whereas the landslide-generated seismic signal displays significantly higher energy levels with irregular and chaotic frequency content.

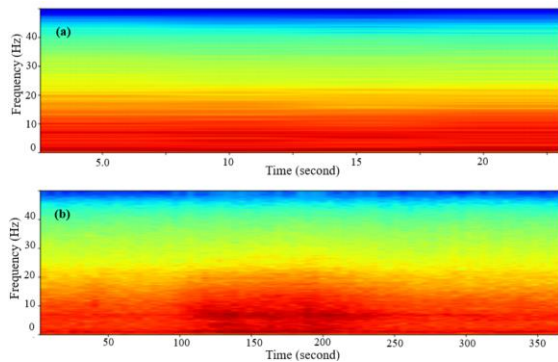


Figure 4. Spectrogram features of Lang Nu seismic signals recorded at the Vinh Tuy station: (a) 30 seconds before, and (b) during the sliding

RESULTS AND DISCUSSION

Seismic signals generated by Lang Nu landslide

The original broadband seismic waveforms of the Lang Nu landslide were recorded at three stations, namely SPVO, SPVB, and VTVB stations (Figs. 5 and 6). Each station displays three seismic components (HHE, HHN, and HHZ). The recorded waveforms reveal an emergent and long-duration signal distinguished from the preceding background noise. In Fig. 6, the dashed rectangle represents the seismic signals identified from the landslide event. In the time-series data, a distinct energy increase is observed beginning around 70 seconds and lasting until approximately 220 seconds,

corresponding to a total duration of about 150 seconds (Fig. 6). This time duration is interpreted as the period of the main slope movement, representing the initiation, acceleration, and deceleration phases of the Lang Nu landslide. The seismic signal revealed that the Lang Nu landslide occurred at 22:57:40 GMT+0 (5:57:40 am at local time in GMT+7).

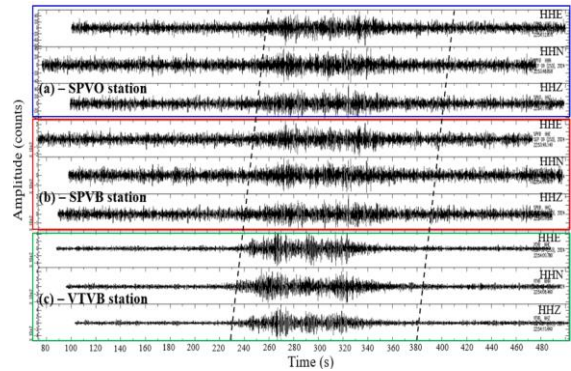


Figure 5. Original seismic waveform of the Lang Nu landslide recorded at (a) the SPVO, (b) the SPVB, and (c) VTVB broadband seismic stations

Based on these original seismic records, spectrogram and seismogram analyses were conducted to characterize further the frequency content, temporal evolution, and dynamic process of the Lang Nu landslide event. The Lang Nu spectrogram is characterized by emergent onset, prolonged strong energy release, and the absence of clear P- and S-wave arrivals (Fig. 6). Significantly, the spectrogram signature of the Lang Nu landslide signal showed a cigar-shaped feature.

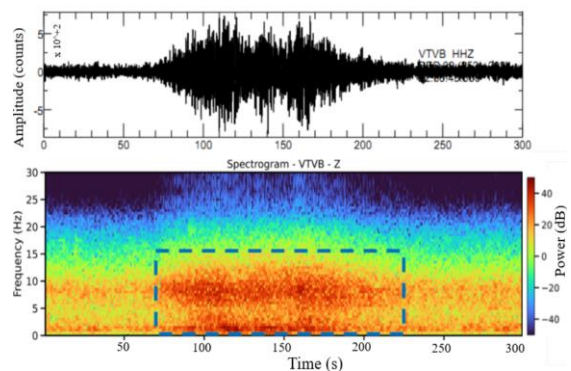


Figure 6. The N-S component seismogram showing spectrogram features of the Lang Nu landslide seismic

Seismic signals generated by Ba Thau landslide

Fig. 7 presents the broadband seismic waveform and its corresponding spectrograms of the Ba Thau landslide, recorded at the VTVB station. According to the time series of wave data, the landslide took place at 6:00 am on September 12, 2025. The waveform exhibits an emergent onset followed by a gradual increase in amplitude. The total duration of the main signal was about 50 s, which indicates the long-period failure process rather than a short impulsive source. The spectrograms (E-W and N-S components) display concentrated energy primarily in the 1–22 Hz frequency band, with a chaotic and irregular distribution.

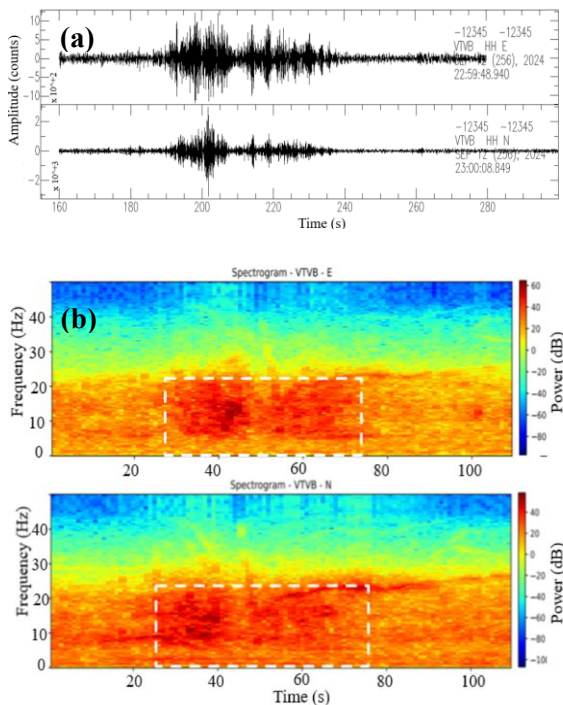


Figure 7. The Ba Thau landslide seismic: (a) original seismic waveform and the N-S component seismogram

Seismic signals generated by Khe Bin landslide

For the Khe Bin landslide seismic, the waveform shows a large high-frequency content for approximately 50 seconds, suggesting a strong energy mass movement process. It also revealed an absence of distinct P- and S-waves during the acceleration of the ground motion. In the spectrogram, the energy

is mainly confined to the high-frequency band ($\sim 10\div 20$ Hz) with limited vertical extension (Fig. 8). Despite being the nearest to the VTVB station among the three landslide seismic sites, the Khe Bin landslide generated a relatively weak seismic signal, most likely because of its smaller scale. Characteristics of landslide-generated seismic signals of three sliding event are denoted in Table 1.

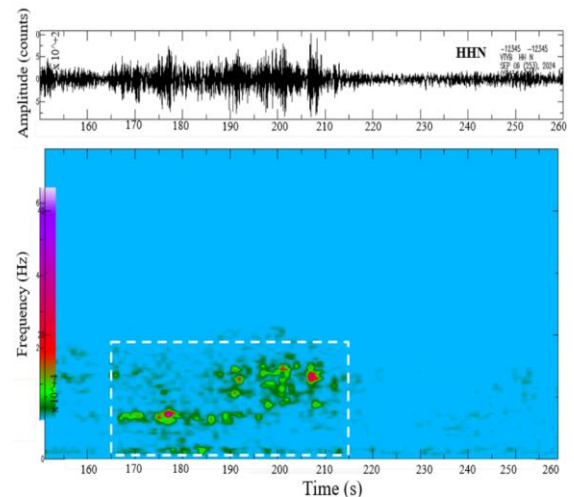


Figure 8. Seismic signal generated by the Khe Bin landslide: (a) N-S component seismogram, and (b) spectrogram features

Based on extensive interviews with local eyewitnesses, the estimated landslide occurrence times are nearly consistent with the onset times of the recorded seismic signals. The observed time difference, which is likely on the order of several tens of seconds, primarily reflects the seismic wave travel time and the distance between the landslide source and the seismic monitoring stations. Accurately determining the timing of landslide occurrence contributes to a better understanding of landslide phenomena and their mechanisms, supporting hazard assessment and the development of appropriate response scenarios. In the case of Lang Nu village, the seismic data indicate that the single landslide occurred at approximately 05:57:40 am on 10 September 2024 and the associated long-runout movement rapidly traveled downslope and burried the village.

Table 1. Summary of landslide-generated seismic signals

Seismic signals	Duration (s)	Frequency (Hz)
Lang Nu	~ 140	1-15
Ba Thau	~ 50	1-22
Khe Bin	~ 50	1-20

The results also provide important insights into their potential application for real-time detection and early warning. The distinct seismic characteristics observed—including long-duration signals, lack of clear P- and S-wave phases, and dominant energy in the 1–20 Hz frequency band—can serve as robust diagnostic indicators for automatic event classification. These parameters could be integrated into real-time detection algorithms, for example through continuous spectrogram monitoring and machine-learning-based classifiers to identify non-earthquake emergent signals. Incorporating these spectral and temporal features into an operational warning framework would enable near-real-time recognition of large, fast-moving landslides, even at night or in remote areas where no human observations are possible.

With a denser broadband-seismic monitoring network, the identification of unidentified deep-seated landslides becomes significantly more reliable by using signals recorded at a minimum of three seismic stations. Although the density of available broadband seismic monitoring stations in the northern Vietnam study area is very sparse, three large landslide seismic generating detectable seismic signals have confirmed the reliability of the observations. It strongly demonstrates the significance and necessity of developing a more comprehensive broadband seismic monitoring network to effectively capture the seismic signatures of large-scale deep-seated landslides. In northern Vietnam, where remote mountainous areas are highly susceptible to landslides, effective detection and warning will depend on a denser, strategically distributed network to enhance the capability to identify landquake events (e.g., landslides and their secondary hazards).

CONCLUSIONS

Three large deep-seated landslides induced seismic signals were recorded in Lang Nu, Ba Thau and Khe Bin villages during Typhoon Yagi in September 2024. The seismogram indicates a long-period, elongated waveforms with emergent onset and no clearly distinct P or S wave arrivals. The seismic signals provide information on the timing of occurrence and the duration of these landslide events. Whereas the analysis of waveform and spectrogram features helps to distinguish landslide signals from tectonic earthquakes. Large high-frequency contents lasted approximately one to three minutes, indicating phases corresponding to initiation, rapid downslope motion, and deposition.

The data analysis strongly demonstrates the significance and necessity of development of broadband seismic monitoring systems in order to capture the seismic signals of large landslides. In northern Vietnam, remote mountainous areas are highly prone to landslides, effective detection and warning will depend on a dense seismic network to significantly enhance the capability to identify landquake events (such as landslides, debris flows). The broadband seismic monitoring systems would not only enhance scientific understanding of landslide dynamics but also contribute significantly to mitigating the impacts of landslides and their consequent secondary hazards in Northern Vietnam.

ACKNOWLEDGMENT

This research was funded by the Vietnam Academy of Science and Technology (VAST) under Project Code KHCBTĐ.02/24-25. This study is partly funded by Quang Ninh Department of Science and Technology under the grant number: NV.CT.H49.2025.08. We acknowledge the project 2023/49/B/ST10/02879 under the support of the Polish National Science Centre for the using of field research data. We sincerely thanks to the Earthquake Monitoring Department, Institute of Earth Sciences,

Vietnam Academy of Science and Technology for providing seismic signal data in this study.

REFERENCES

- Chao, W.A., Wu, Y.M., Zhao, L. *et al.* A first near real-time seismology-based landslide monitoring system. *Sci Rep* **7**, 43510 (2017). <https://doi.org/10.1038/srep43510>.
- Favreau, P., Mangeney, A., Lucas, A., Crosta, G., & Bouchut, F. (2010). Numerical modeling of landquakes. *Geophysical Research Letters*, **37**, L15305. <https://doi.org/10.1029/2010GL043512>.
- Hibert, C., Stark, C. P., & Ekström, G. (2015). *Dynamics of the Oso-Steelhead landslide from broadband seismic analysis*. *Natural Hazards and Earth System Sciences*, **15**, 1265–1273. <https://doi.org/10.5194/nhess-15-1265-2015>.
- Kuo, H.-L., Lin, G.-W., Chen, C.-W., Saito, H., Lin, C.-W., Chen, H., & Chao, W.-A. (2018). Evaluating critical rainfall conditions for large-scale landslides by detecting event times from seismic records. *Natural Hazards and Earth System Sciences*, **18**, 2877–2891. <https://doi.org/10.5194/nhess-18-2877-2018>.
- Lacroix, P., Grasso, J.-R., Roulle, J., Giraud, G., Goetz, D., Morin, S., & Helmstetter, A. (2012). Monitoring of snow avalanches using a seismic array: Location, speed estimation, and relationships to meteorological variables. *Journal of Geophysical Research: Earth Surface*, **117**, F01034. <https://doi.org/10.1029/2011JF002106>.
- Lan C.N, Tien P.V, Do T.N (2019) Deep-seated rainfall-induced landslides on a new expressway: a case study in Vietnam. *Landslides*, **17**(2), 395–407.
- Li, Z., Huang, X., Yu, D., Su, J., & Xu, Q. (2019). Broadband-seismic analysis of a massive landslide in southwestern China: Dynamics and fragmentation implications. *Geomorphology*, **331**, 12–24. <https://doi.org/10.1016/j.geomorph.2019.03.015>.
- Luong L.H, Miyagi T and Tien P.V (2016) Mapping of large scale landslide topographic area by aerial photograph interpretation and possibilities for application to risk assessment for the Ho Chi Minh route – Vietnam. *Transactions, Japanese Geomorphological Union*, pp. 97–118.
- Suriñach, E., Vilajosana, I., Khazaradze, G., Biescas, B., Furdada, G., & Vilaplana, J. M. (2005). Seismic detection and characterization of landslides and other mass movements. *Natural Hazards and Earth System Sciences*, **5**, 791–798. <https://doi.org/10.5194/nhess-5-791-2005>.
- Tien P.V, Luong L.H, Duc D.M, Trinh P.T, Quynh D.T, Lan N.C, Thuy D.T, Phi N.Q, Cuong T.Q, Khang D, Loi D.H (2021) Rainfall-Induced Catastrophic Landslide in Quang Tri Province: the Deadliest Single Landslide Event in Vietnam in 2020. *Landslides* **18**(6), 2323–2327. <https://doi.org/10.1007/s10346-021-01664-y>.
- Tien P.V, Luong L.H, Nhan T.T, Phi N.Q, Trinh P.T, Quynh D.T, Duc D.M, Lan N.C, Cuong N.H (2023) Mechanism and numerical simulation of a rapid deep-seated landslide in Van Hoi reservoir, Vietnam. *Vietnam Journal of Earth Sciences*, **45**(3), 357–373. <https://doi.org/10.15625/2615-9783/18539>.
- Tien P.V, Trinh P.T, Luong L.H, Nhat L.M, Duc D.M, Hieu T.T, Cuong T.Q, Nhan T.T (2021) The October 13, 2020 deadly rapid landslide triggered by heavy rainfall in Phong Dien, Thua Thien Hue, Vietnam. *Landslides* **18** (6), 2329–2333 <https://doi.org/10.1007/s10346-021-01663-z>.
- Tien, P.V., Minh, V.C., Duc, D.M. et al. (2025) Rainfall-induced catastrophic rapid and long-traveling landslide in Lang Nu hamlet: the worst natural landslide disaster in Vietnam. *Landslides* (2025). <https://doi.org/10.1007/s10346-025-02490-2>.
- VDMA (2024) Documents and reports (in Vietnamese), and rainfall data provided by Vietnam Disaster and Dyke Management Authority.
- Yamada, M., Mangeney, A., Matsushi, Y., & Moretti, L. (2016). Estimation of dynamic friction of the Akatani landslide from seismic waveform inversion and numerical simulation. *Geophysical Journal International*, **206**(3), 1479–1486. <https://doi.org/10.1093/gji/ggw216>.

DOI: 10.15625/vap.2025.0180

Assessing Rainfall-Induced Landslide Thresholds in the Van Chan – Gia Hoi Area, Lao Cai Province

Duong Thi Toan*

University of Science, Vietnam National University, Hanoi

Email: duongtoan@hus.edu.vn

Abstract: This study establishes rainfall thresholds for landslides along National Highway No. 32 (NH32) through Van Chan – Gia Hoi, Lao Cai Province, based on 24 major events recorded between 2000 and 2024. Analytical approaches include the rainfall intensity–duration (I–D) relationship and the Bayesian probability model $P(A|I,D)$. Three dominant rainfall types were identified: (i) short-duration, high-intensity rainfall (2–5 days) triggering failures within 1–3 days; (ii) medium-duration rainfall (4–8 days) causing failures after 3–5 days; and (iii) long-duration, low-intensity rainfall (9–10 days) leading to delayed failures with high cumulative totals. Four empirical thresholds (I_{10} , I_{25} , I_{50} , and I_{90}) were derived, and I_{50} represents the baseline warning threshold. Bayesian analysis shows that landslide probability $P(A|I,D) > 0.5$ mainly occurs under short, high-intensity rainfall exceeding 40–60 mm/day for more than 2–3 consecutive days. The integration of I–D and Bayesian models enables the development of dynamic probabilistic thresholds, enhancing the effectiveness of early warning and landslide prevention for mountainous areas of Van Chan – Tu Le regions.

Keywords: Landslide; Bayesian probability; intensity–duration relationship; early warning

INTRODUCTION

In recent years, under the influence of climate change and the increasing frequency of extreme weather events, severe landslides and flash floods have occurred in many countries, including Vietnam. Studies on rainfall-induced landslides typically focus on detailed analyses of rainfall duration, intensity, and cumulative

amount over a given period and area to identify the triggering rainfall thresholds.

Within the context of global climate change, numerous studies have reported increasing trends in both intensity and duration of extreme rainfall—key factors contributing to the rising risk of landslides. Bi et al. (2023) analyzed a 60-year rainfall record (1961–2020) across nine regions in China and documented several long-lasting rainfall events (4–40 days) with total precipitation ranging from 150 to 400 mm that caused typical landslides. Zhou et al. (2019) employed the *Probable Maximum Precipitation* (PMP) index to assess extreme rainfall in Hong Kong and found that 24-hour totals could reach 668–1290 mm, sufficient to trigger debris flows. In Thailand, Chaithong (2023) applied the Generalized Extreme Value (GEV) model to construct I–F–D curves, revealing extreme rainfall events of 90–175 mm/day with an upward recurrence trend. In Taiwan, rainfall exceeding 800 mm/day or intensities over 80 mm/h have frequently led to catastrophic slope failures (Wu, 2019). In Japan, Sato and Shuin (2023) as well as Mori and Ono (2019) reported that cumulative rainfall of 300–600 mm within five days caused hundreds of severe landslides. These findings demonstrate that extreme rainfall has become increasingly common across monsoonal Asia, highlighting the urgent need for more scientific and quantitative determination of rainfall thresholds for landslide initiation.

Building upon this foundation, numerous studies have focused on developing rainfall thresholds using probabilistic, statistical, and machine learning approaches to improve

landslide prediction. Berti et al. (2012) pioneered the application of Bayesian conditional probability to derive probabilistic rainfall thresholds in the Emilia-Romagna region of Italy, using 4,141 landslide events and daily rainfall records from 1939 to 2012. Their results revealed a sharp increase in landslide probability beyond a specific intensity-duration threshold, representing a physical boundary of system response. Do and Yin (2018) extended this approach to the Ha Giang region of Vietnam, utilizing 57 years of rainfall data and 37 recorded landslides to establish a 3-day rainfall threshold, where landslide probability rose sharply from 0.08 to 0.67 when rainfall intensity exceeded 40 mm.

At a broader scale, He et al. (2020) applied quantile regression to determine event-duration (E-D) thresholds for the whole of China based on 771 events (1998–2017), showing that dry-season thresholds are significantly lower than those of the wet season. Ning et al. (2023) developed intensity-duration (I-D) thresholds from downscaled TRMM satellite data (500 m resolution) using machine learning, identifying an optimal threshold of $I_{50} = 21.03 \times D^{-1.004}$ for the Wudu area. More recently, Peng and Wu (2024) employed Multilayer Perceptron (MLP) and 3D Convolutional Neural Network (CNN-3D) models to construct E-D-R frameworks that integrate rainfall thresholds with landslide susceptibility mapping for daily hazard warning in the Three Gorges Reservoir area.

Overall, recent studies reveal a clear shift from analyzing the characteristics of extreme rainfall events toward the development of probabilistic and machine learning-based rainfall thresholds. This modern approach not only captures the inherent uncertainty in the rainfall-landslide relationship but also enhances the applicability of landslide early warning systems at regional and national scales. Determining rainfall thresholds through statistical analysis of historical rainfall-landslide datasets is considered an effective method, particularly when reliable and long-term data are available.

In this study, a dataset covering the period 2005–2024 (nearly 20 years) of rainfall and landslide events was compiled and statistically analyzed to establish rainfall thresholds for landslide initiation in the southwestern part of Lao Cai Province. Furthermore, the Bayesian probability approach was integrated to define probabilistic warning levels, providing a basis for improved prediction and prevention of rainfall-induced landslides in mountainous regions.

STUDY AREA

The study area is located along the section of National Highway No. 32 from Van Chan to Gia Hoi and includes adjacent areas within Lao Cai Province (Figure 1). It lies in the Tu Le depression, at elevations ranging from 200 to 800 m above sea level, and is characterized by a tropical monsoon climate with strong seasonal variability. The mean annual temperature ranges from 18°C to 32°C, and heavy rainfall commonly occurs during the summer months from June to September.

Based on the 1:50,000-scale geological map, the region comprises the Tram Tau, Tu Le, and Sinh Quyen formations, as well as the Nam Kim and Tu Le, Ngoi Thia complexes. The predominant lithologies along NH.32 and at observed landslide sites are rhyolite and trachyte, metamorphosed sedimentary rock containing organic coal with displaying varying structural patterns. Most landslide-prone slopes consist of foliated to thinly foliated and moderately to highly weathered rocks. The rock fabric, bedding orientation, and degree of weathering are key factors controlling slope instability and active landslide zones in the area. Along NH.32, several locations exhibit high landslide susceptibility, notably in Gia Hoi (Nam Bung, Nam Pui, Nam Lanh, Nam Kip), and Nam Muoi-Son Luong communes. These areas were selected for detailed rainfall-landslide correlation analysis and geotechnical investigation in the subsequent sections. A general overview of the geographical and geological settings of the study area is presented in Figure 1.

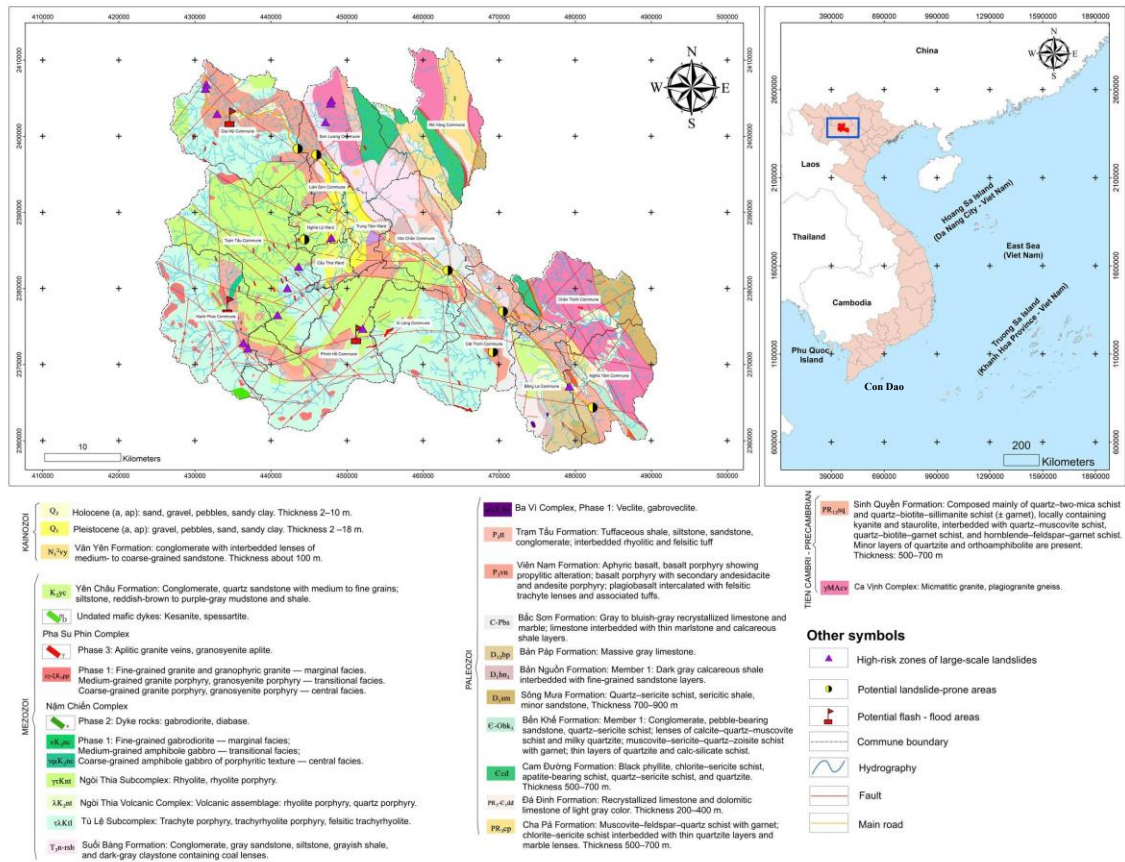


Figure 1 Geological map of the study area and potential landslide locations

DATA AND METHODS

Data collection

The datasets used for analyzing the correlation between rainfall and historical landslide events were compiled from multiple sources, including previous research projects, published studies, and local records (Duong, 2025). The analysis focused on major rainfall and landslide events that occurred between 2000 and 2024. For each event, rainfall parameters such as the number of rainy days, rainfall intensity, and cumulative rainfall were extracted and statistically analyzed. These parameters were then used to estimate rainfall probability, the conditional probability of rainfall-induced landslides, and to define rainfall thresholds for landslide initiation.

Rainfall data were obtained from the Van Chan meteorological station, which is

managed by the National Hydro-Meteorological Service of Vietnam. Landslide event information was cross-checked with field reports and secondary data from local authorities to ensure reliability and temporal accuracy.

Determination of rainfall thresholds

Rainfall thresholds for landslide initiation were determined using the empirical intensity-duration (I–D) relationship. This approach identifies the minimum rainfall conditions capable of triggering slope failures by examining the correlation between mean rainfall intensity (I) and rainfall duration (D) prior to each landslide event. The pairs of values (I, D) were plotted on a log-log scale, and statistical regression was applied to estimate the threshold curve. The results confirm that the minimum rainfall intensity

required to trigger landslides decreases with increasing rainfall duration, following a power-law relationship expressed as: $I = \alpha D^{-\beta}$

Bayesian probability analysis

Bayes' theorem was applied to evaluate the conditional probability of landslide occurrence under different rainfall conditions (Berti et. al., 2012). The dimensional Bayesian model is expressed as:

$$P(A | B) = \frac{P(B|A) \cdot P(A)}{P(B)} \quad (1)$$

where: A represents the occurrence of a landslide event, B represents the rainfall condition;

$P(A|B)$ is the posterior probability, i.e., the probability of a landslide given that rainfall B has occurred;

$P(B|A)$ is the likelihood, i.e., the conditional probability of observing rainfall B given that a landslide has occurred;

$P(A)$ is the prior probability, i.e., the probability of a landslide occurring regardless of rainfall conditions;

$P(B)$ is the marginal probability, i.e., the total probability of observing rainfall B without considering whether a landslide occurred.

The individual probabilities are estimated as follows

$$P(A) = \frac{N_A}{N_R}; P(A) = \frac{N_B}{N_R}; P(B | A) = \frac{N(B|A)}{N_A}$$

where: N_R is the total number of rainfall events during the study period (2000–2024) with a cumulative rainfall of more than 5 mm over two consecutive days, N_A is the total number of rainfall events that triggered landslides, N_B is the total number of rainfall events with rainfall magnitude B, $N(B|A)$ is the number of rainfall events of magnitude B that coincided with landslides. This probabilistic framework allows the estimation of the conditional probability $P(A|B)$, thereby quantifying the likelihood of landslide occurrence under specific rainfall intensities and durations.

RESULTS AND DISCUSSION

Characteristics of Rainfall Patterns Triggering Landslides

Based on the collected data and analysis of rainfall events that triggered landslides, 24 cases were identified between 2000 and 2024 in the Van Chan area (Yen Bai Province). The results, summarized in Table 1, show that these rainfall events exhibit three dominant patterns as described below.

Type I – Short-duration, high-intensity rainfall events

This group includes heavy or extreme rainfall events lasting 2–5 days, with landslides typically occurring very early—within the first 1–3 days of the rainfall sequence. Representative cases include SK03, SK07, SK16, SK18, SK20, SK21, SK22, SK23, and SK24 (Table 1). Figure 2 shows the rainfall intensity and accumulated rainfall as an example for type I. The mean rainfall intensity during these events ranged from 13.3 to 63.5 mm/day, while daily rainfall at the time of failure reached 24–159 mm/day, reflecting the strong impact of short-term concentrated precipitation. The cumulative rainfall prior to failure generally ranged from 24 to 194 mm, which is lower than that of the other two types. These events commonly occur during the main rainy season (July–September), coinciding with widespread heavy rainfall over the Van Chan region.

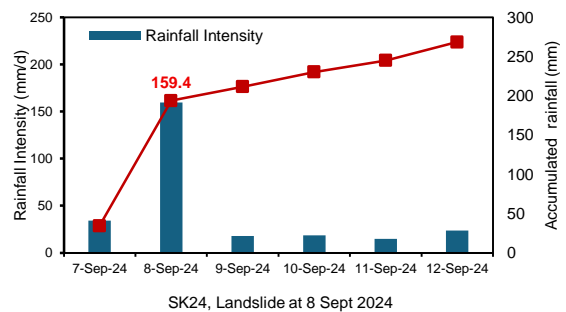


Figure 2. Example of a rainfall event of Type I

Type II – Medium-duration, moderate-intensity rainfall events:

These events last for about 4–8 days, with landslides typically occurring after 3–5 days of rainfall, as an example in Figure 3. Representative cases include SK01, SK02, SK04, SK05, SK09, SK13, SK14, and SK15. The mean rainfall intensity during the events ranged from 15 to 52 mm/day, while daily rainfall on the day of landsliding reached 13–104 mm/day. The cumulative rainfall at the time of failure varied from 47 to 260 mm, suggesting that prolonged infiltration and soil saturation play an important role. These events mainly occur during late summer and early autumn (July–October), when antecedent soil moisture is already high due to previous rainfall.

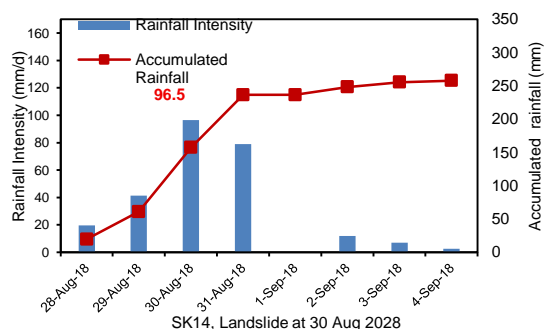


Figure 3. Example of a rainfall event of Type II

Type III – Long-duration, low-intensity rainfall events

This group is characterized by prolonged rainfall lasting 9–10 days, with landslides occurring later in the sequence, typically between the 6th and 10th days, as shown in Figure 4. Representative cases include SK06, SK08, SK10, SK11, SK12, SK17, and SK19. The

mean rainfall intensity throughout the events was relatively low (11–39 mm/day), but cumulative rainfall at failure was very high, ranging from 68 to 383 mm. Daily rainfall on the day of landsliding was quite high (21–155 mm/day), indicating that gradual saturation processes were the dominant triggering mechanism. Such events usually occur during the peak rainy season (June–September), when long-term rainfall accumulation exceeds the slope's hydrological threshold.

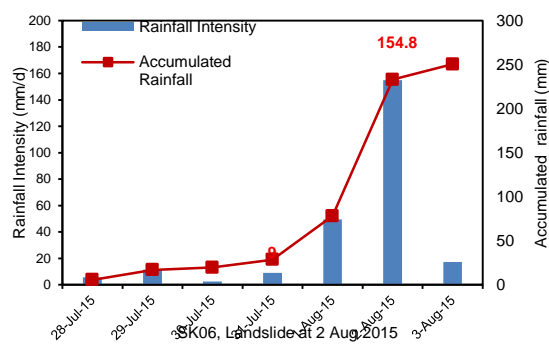


Figure 4. Example of a rainfall event of Type III

Correlation between rainfall intensity and duration (I–D relationship)

From the collected data and the analysis of the above events, a correlation diagram was constructed to examine the relationship between the mean rainfall intensity or the cumulative rainfall up to the time of failure and the total rainfall duration until landslide occurrence (Figure 5). This study demonstrates the rainfall intensity–duration (I–D) relationship for landslide-triggering events as presenting in Figure 5. The empirical I–D threshold curves obtained from the dataset are expressed as follows:

Table 1. Characteristics of rainfall patterns inducing landslide in Van Chan–Tu Le area

No.	Landslide event and date (dd/mm/yyyy)		Entire rainfall event causing landslide			At the time of landslide occurrence			
			Total rainy days	Cumulative rainfall of the entire event (mm)	Mean rainfall intensity (mm/day)	Day of failure since rainfall onset	Rainfall Intensity on the day of failure (mm)	Cumulative rainfall up to failure (mm)	Maximum daily rainfall I _{max} (mm/day)
1	SK03	8/8/2008	5	188,3	37,66	2	123,7	128,1	123,7
2	SK07	19/8/2016	5	189,5	37,9	1	78,9	78,9	78,9
3	SK16	10/9/2019	2	25,9	12,95	1	24,8	24,8	24,8

4	SK18	15/10/2020	3	190,6	63,53	2	96,6	149,1	96,6
5	SK20	4/9/2022	2	43,5	21,75	2	38,6	43,5	38,6
6	SK21	12/9/2022	4	57,8	14,45	2	42	46,6	42
7	SK22	2/10/2022	4	53	13,25	2	46,7	51,6	46,7
8	SK23	25/06/2024	5	144,8	28,96	2	17,3	93,6	76,3
9	SK24	8/9/2024	7	269	38,43	2	159,4	193,7	159,4
10	SK01	28/9/2005	4	195,5	48,88	3	104	194,6	104
11	SK02	7/8/2006	5	84,1	16,82	3	41,2	56,6	41,2
12	SK04	23/1/2010	3	47	15,67	3	13,7	47	23,1
13	SK05	30/7/2013	5	261,6	52,32	4	61,7	259,3	109,4
14	SK09	5/8/2017	5	66,9	13,38	4	51,3	64,8	51,3
15	SK13	25/8/2018	3	42,9	14,3	3	37,9	42,9	37,9
16	SK14	30/8/2018	8	258	36,86	3	96,5	157,5	96,5
17	SK15	30/8/2019	8	196,3	28,04	4	63,5	86,2	63,5
18	SK06	2/8/2015	8	252,1	31,51	6	154,8	233	154,8
19	SK08	12/7/2017	6	68,3	11,38	5	21,4	68	30,8
20	SK11	11/10/2017	6	259,2	51,84	5	125,3	257,6	125,3
21	SK10	16/9/2017	10	169,7	18,86	10	69,5	169,7	69,5
22	SK12	21/7/2018	10	391,3	39,13	8	70,4	382,8	121,8
23	SK17	18/08/2020	9	216,4	24,04	6	38,2	143,3	38,2
24	SK19	10/6/2021	9	258,4	28,71	5	46,8	146,4	46,8

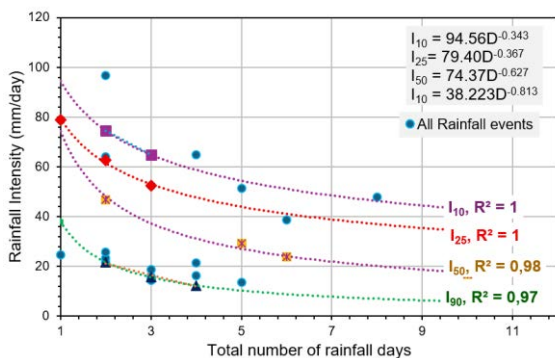


Figure 5. Correlation between rainfall intensity and duration triggering landslides

$I_{10} = 94.56 D^{-0.343}$ represents the extreme rainfall threshold, typically associated with short-duration (1–3 days) and very high-intensity rainfall exceeding 70–100 mm/day. These events often trigger rapid and widespread landslides, corresponding to Type I rainfall conditions.

$I_{25} = 79.40 D^{-0.367}$ reflects strong rainfall events lasting 3–5 days, high-intensity rainfall of 50–65 mm/d, and in which may induce localized landslides once slopes become saturated. This level is generally associated with Type II rainfall patterns.

$I_{50} = 74.37 D^{-0.627}$ represents the median (baseline) threshold, corresponding to the

rainfall exceeding 25 mm/d. It is considered the basic warning threshold for the Van Chan–Tu Le area, applicable to Type II and Type III events where prolonged infiltration weakens slope stability.

$I_{90} = 38.22 D^{-0.813}$ denotes the low-intensity (less than 25 mm/d), long-duration threshold. Landslides under such conditions primarily result from cumulative saturation and progressive slope weakening.

The I–D model not only characterizes the variability of rainfall parameters leading to landslides but also enables a clear ranking of hazard levels according to distinct rainfall patterns, providing a scientific basis for establishing area-specific rainfall–landslide warning thresholds for study area. The statistical correlation between rainfall and landslide occurrences derived here thus serves as the primary basis for defining operational warning thresholds in the study area. However, for large-scale landslides, local conditions vary significantly and some landslide bodies require more detailed site-specific analysis to determine precise, location-specific triggering thresholds. Based on the statistical classification, representative rainfall scenarios were identified; these characteristic patterns are then used to construct rainfall scenarios for

site-level stability analyses of individual landslide masses.

The intensity–duration (I–D) relationship has been widely applied in recent studies and is recognized as an effective empirical tool for establishing rainfall thresholds because it is constructed directly from historical rainfall–landslide records specific to each region (Berti et al., 2012; He et al., 2020; Ning et al., 2023). The common power-law form $I = aD^{-b}$ varies significantly across different study areas, as the coefficients a and b strongly depend on local climatic conditions, terrain steepness, and soil–rock characteristics. In this study, the threshold $I_{50} = 74.37 \cdot D^{-0.627}$ exhibits a relatively high coefficient a and a steeper exponent b compared with many humid mountainous regions in China ($b \approx 0.3$ – 0.5 in He et al., 2020; Ning et al., 2023), indicating that short-duration high-intensity rainfall plays a more dominant role along National Highway 32. Our b value is also higher than the ranges commonly reported in broad international reviews (Guzzetti et al., 2007; Peruccacci et al., 2017), reflecting the steep topography, weakly weathered materials, and clustered extreme rainfall typical of the Northwest Vietnam region. These findings are consistent with Do and Yin (2018), who emphasized that antecedent saturation and extreme rainfall in mountainous Vietnam can steepen the I–D curve compared with temperate regions. Therefore, the threshold proposed in this study is appropriate for the local context but should be calibrated when applied elsewhere.

Results on the Probability of Landslide Occurrence

In the Bayesian model, $P(A|I,D)$ represents the conditional probability of a landslide occurrence given rainfall intensity (I) and duration (D). For practical use in early warning, probability levels were classified by color: $P > 0.5$ (red) – high risk, requiring immediate warning; $0.3 \leq P \leq 0.5$ (orange) – moderate risk, requiring close monitoring; and $P < 0.3$ (yellow–green) – low risk, typically corresponding to short or low-intensity rainfall. This classification facilitates the conversion of

probabilistic results into intuitive visual information, supporting timely decision-making by local authorities.

Based on the statistical dataset of rainfall and landslide events from 2000 to 2024, the Bayesian conditional probability model was applied to evaluate landslide occurrence as a function of rainfall intensity and duration. The results indicate a significant increase in landslide probability when rainfall intensity exceeds 40 mm/day and duration extends beyond 2–3 consecutive days. The red bars in the figure mark the zones with the highest probability ($P > 0.5$), corresponding to short-duration, high-intensity rainfall events (Type I) identified in Table 1.

Conversely, orange and green areas represent medium to low probabilities ($P < 0.3$), mainly associated with long-duration, low-intensity rainfall (Type II and Type III), where landslides occur primarily due to cumulative soil saturation. The Bayesian model highlights the nonlinear relationship between rainfall parameters and landslide likelihood: rainfall intensity acts as a direct triggering factor, while rainfall duration governs the process of water accumulation and progressive slope weakening.

The integration of the I–D and Bayesian models demonstrates a clear complementarity: the I–D model defines the quantitative rainfall thresholds for triggering conditions, whereas the Bayesian model provides the corresponding probability of landslide occurrence for each (I , D) combination. This integration shifts the approach from static threshold-based assessment to dynamic probabilistic early warning, enabling near real-time risk forecasting. The results show that the highest landslide risk occurs when rainfall intensity exceeds 40–60 mm/day for more than 2–3 consecutive days, where the Bayesian probability $P(A|I,D)$ exceeds 0.5 — corresponding to a red warning level. Under such conditions, the early warning system should be activated, and local mitigation measures promptly implemented to reduce landslide risk in the Van Chan – Gia Hoi area.

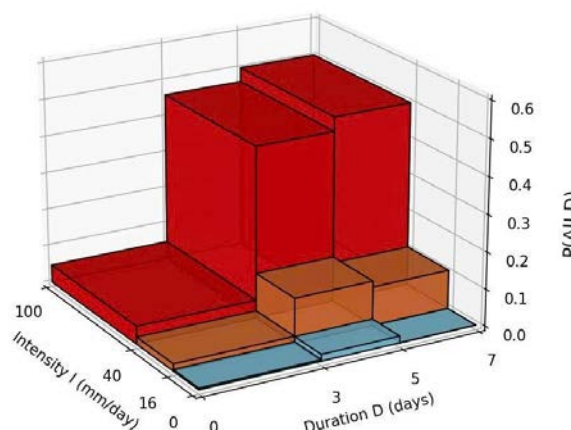


Figure 6. Probability of landslide occurrence based on rainfall intensity and duration

CONCLUSIONS

This study is part of a research project aimed at defining rainfall thresholds for landslide initiation along NH.32 in Lao Cai province (Van Chan-Gia Hoi), based on statistical records of rainfall and landslide events from 2000 to 2024. A total of 24 major landslide events were analyzed using the rainfall intensity-duration (I-D) relationship and the Bayesian conditional probability model $P(A|I,D)$ to establish a scientific foundation for landslide early warning.

(1) The results indicate three primary rainfall types in this area: (i) short-duration, high-intensity rainfall (2–5 days) triggering early failures within the first 1–3 days, with daily rainfall of 42–160 mm/day; (ii) moderate, medium-duration rainfall (4–8 days) causing landslides after 3–5 days, with daily rainfall of 13–104 mm/day; and (iii) long-duration, low-intensity rainfall (9–10 days) resulting in delayed failures (days 6–10) with daily rainfall (21–154 mm/day) but high cumulative totals (68–383 mm).

(2) The I-D analysis established four rainfall thresholds (I_{10} , I_{25} , I_{50} , I_{90}) corresponding to different exceedance probabilities. Among them, I_{50} represents the basic warning threshold, while I_{10} – I_{25} characterize extreme rainfall conditions capable of triggering rapid and widespread

failures. Bayesian analysis further revealed that short, high-intensity rainfall events (Type I) exhibit high probabilities of landslide occurrence ($P(A|I,D) > 0.5$), particularly when rainfall intensity exceeds 40–60 mm/day for more than 2–3 consecutive days.

This study proposes integrating the I-D threshold model with the Bayesian probability model for dynamic landslide early warning. Specifically, when I and D exceed or approach the I_{10} – I_{25} thresholds and $P(A|I,D) > 0.5$, a red alert (very high risk) should be issued.

ACKNOWLEDGMENTS

This paper was supported by the project with the code number of ĐTĐL.CN-37/23, funded by the Program: Basic Scientific Research Program in the fields of Chemistry, Life Sciences, Earth Sciences, and Marine Sciences for the period 2017–2025, under the Earth Sciences sector, managed by the Ministry of Science and Technology of Vietnam. The author gratefully acknowledges this support.

REFERENCES

- Berti, M., Martina, M. L. V., Franceschini, S., Pignone, S., Simoni, A., & Pizzolo, M. (2012). Probabilistic rainfall thresholds for landslide occurrence using a Bayesian approach. *Journal of Geophysical Research: Earth Surface*, 117(F4). <https://doi.org/10.1029/2012JF002367>.
- Bi, X., Fan, Q., He, L., Zhang, C., Diao, Y., & Han, Y. (2023). Analysis and evaluation of extreme rainfall trends and geological hazard risk in the Lower Jinshajiang River. *Applied Sciences* (Switzerland), 13(6). <https://doi.org/10.3390/app13064021>
- Chaithong, T. (2023). Influence of changes in extreme daily rainfall distribution on the stability of residual soil slopes. *Big Earth Data*, 7(1), 111–135. <https://doi.org/10.1080/20964471.2022.2046306>
- Do HM, Yin KL (2018) Rainfall threshold analysis and Bayesian probability method for landslide initiation based on landslides and rainfall events in the past. *Open J Geol* 8(7):674.
- Duong, T. T. (Principal Investigator). Study on the formation mechanism, distribution patterns, and early warning of large-scale landslides in Vietnam using the integration of remote sensing, artificial intelligence, and unsaturated soil mechanics theory

- (Project No. ĐTĐL.CN-37/23) (2023-2025. Hanoi University of Science, Vietnam National University, Hanoi.
- Guzzetti, F., Peruccacci, S., Rossi, M., & Stark, C. P. (2007). Rainfall thresholds for the initiation of landslides in central and southern Europe. *Meteorology and Atmospheric Physics*, 98(3–4), 239–267
- He, S., Wang, J., & Liu, S. (2020). Rainfall event–duration thresholds for landslide occurrences in China. *Water*, 12(2), 494.
- Mori, S., & Ono, K. (2019). Landslide disasters in Ehime Prefecture resulting from the July 2018 heavy rain event in Japan. *Soils and Foundations*, 59(6), 2396–2409. <https://doi.org/10.1016/j.sandf.2019.11.009>
- Ning, S., Ge, Y., Bai, S., Ma, C., & Sun, Y. (2023). I–D Threshold Analysis of Rainfall-Triggered Landslides Based on TRMM Precipitation Data in Wudu, China. *Remote Sensing*, 15(15), 3892.
- Peng, B., & Wu, X. (2024). Optimizing rainfall-triggered landslide thresholds for daily landslide hazard warning in the Three Gorges Reservoir area. *Natural Hazards and Earth System Sciences*, 24(11), 3991–4013.
- Peruccacci, S., Rossi, M., Luciani, S., & Guzzetti, F. (2017). Rainfall thresholds for possible landslide occurrence in Italy. *Geomorphology*, 290, 1–13.
- Sato, T., & Shuin, Y. (2023). Estimation of extreme daily rainfall probabilities: A case study in Kyushu Region, Japan. *Forests*, 14(1), 1–13. <https://doi.org/10.3390/f14010147>
- Wu, C. (2019). Landslide susceptibility based on extreme rainfall-induced landslide inventories and subsequent landslide evolution. *Water (Switzerland)*, 11(12). <https://doi.org/10.3390/w11122609>
- Zhou, S. Y., Gao, L., & Zhang, L. M. (2019). Predicting debris-flow clusters under extreme rainstorms: A case study on Hong Kong Island. *Bulletin of Engineering Geology and the Environment*, 78(8), 5775–5794. <https://doi.org/10.1007/s10064-019-01504-3>.

Experimental study on physical simulation of mining slope collapse under the effect of rainfall

Wenbing Shi^{1,2,3*}, Fengliang^{1,3}, Tongwei Tao^{1,2}, Xingyuan Jiang^{1,2}, Shaozheng Xiong²

¹College of Resources and Environmental Engineering, Guizhou University, Guiyang, China

²Key Laboratory of Karst Georesources and Environment, Ministry of Education, Guizhou University, Guiyang, China

³Mountain Geohazard Prevention R&D Center of Guizhou Province, Guizhou University, Guiyang, China

*Email: wbsi@gzu.edu.cn

Abstract: Accelerated by China's booming economy and rising energy demands, the frequency of mining activities has increased significantly, and the rainfall has intensified the impact of mining activities. In these mining areas, Numerous mining slope destabilization failures have occurred, leading to significant loss of life and property. Therefore, this study to explore the deformation and failure mechanism of collapse can provide prevention and control value for such slopes in southwest China.

The physical model test results revealed that sequential mining and rainfall activities induce progressively increasing stress variations, exhibiting a cyclical pattern of stress concentration, relaxation, and stabilization. Mining initiated the formation of tension and separation fractures, which were exacerbated by rainfall. Through these cracks and infiltration of rock and soil, rainwater causes the moisture content in the upper part of the model to increase faster. Displacement values within the model progressively increased with ongoing coal seam mining, primarily occurring in the mining area's roof and extending to the model's top following rainfall.

Mining operations disrupt the slope's stress equilibrium, generating an extensive fracture network in the overburden and adjacent to the mined-out area. Monitoring data from the physical model reveal that stress redistributes upward over time, resulting in fractures at the slope's trailing edge. These

fractures progressively extend downward to intersect with the mined-out area, creating potential sliding planes within the slope. During rainfall events, rainwater infiltrates the slope through both the geotechnical bodies and existing mining fractures. This leads to increased saturation levels in the slope's geotechnical bodies. As rainwater penetrates deeper, alterations in pore water pressure trigger deformation failure mechanisms within the slope, and also exacerbating the spread of mining-related fractures toward the free face, which greatly affects the stability of the slope. The failure mode of the Pusa slope is characterized by the following sequence: bending-pulling-subsidence-creep-dumping.

The deformation and failure processes can be categorized into four stages: mining-induced disturbances, fractures propagation and extension, creep deformation, instability failure.

Keywords: Geological effects of underground mining, Heavy rainfall, Deformation and failure mechanism, mining slope, Physical model test.

INTRODUCTION

With the rapid development of China's economy and increased energy demand, the intensity of various mining activities has increased, and mining collapses in the southwestern mountainous areas have become increasingly frequent (Zhang et al. 2020; Chen et al. 2021; Liu et al. 2022;). Mining induced collapse s usually have characteristics such as

large scale, strong suddenness, and complex disaster patterns and have received worldwide attention due to the significant risks (Stephen et al. 2006; Yu et al. 2020). Moreover, frequent rainfall and mining activities occur frequently in southwest China, and large-scale collapses often occur under the combined action of these internal and external forces, resulting in serious loss of life and property (Xu et al. 2016; Ma 2017; Tao et al. 2022). In southwest China, there are a large number of mining slopes, which are usually steep at the top and slow at the bottom, hard at the top and soft at the bottom, and have complicated geological conditions (Li et al. 2016; Zheng et al. 2018). Coupled with external factors such as frequent human mining activities and heavy rainfall, it makes favorable condition for the occurrence of collapse hazards (Yang et al. 2022b; Sun et al. 2021). Therefore, it is of great social significance to study the failure mechanism of such slopes.

Frequent underground mining activities are very likely to cause the collapse of the roof of the mined-out area, which causes the rock mass to form "cantilever beam effect" and thus generate mining fractures (Ma et al. 2018; Fernandez et al. 2020). The deformation process of mining slope can be divided into four stages, that is initial deformation stage, slow deformation stage, sharp deformation stage, and stable deformation stage (Shi et al. 2016; Zhao et al. 2016). In 2009, a large rock slide occurred in Jiwei Mountain, Wulong, Chongqing, China, resulting in 74 people killed and 8 injured, and many scholars conducted research on it; Xu et al. (2009) used remote sensing, 3D laser scanning and numerical simulation to analyze the landslide of Jiwei Mountain affected by underground mining; Feng et al. (2016) used physical similar model experiments to simulate the deformation and damage process of the landslide.

The scholars have studied the deformation mechanisms of mining landslides by different method, this paper takes the Pusha collapse in Guizhou as an example, and studies the interlayer stress, fracture progress, moisture content and overburden displacement

characteristics of the slope under the action of mining and rainfall through field geological investigation and physical similar model experiment, revealing its mining stress-fracture-displacement dynamic change characteristics and distribution evolution law; the research result provides a reference basis for future analysis of the failure mechanism of mining collapse.

GENERAL CHARACTERISTICS OF THE PUSA COLLAPSE

Geological characteristics

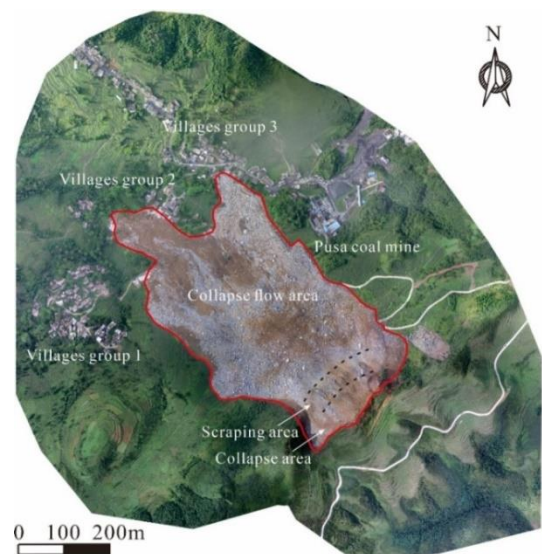


Fig. 1. Aerial photo of Pusa collapse

On August 28, 2017, a large collapse occurred in Pusa Village, Zhangjiawan Town, Nayong County, Guizhou Province, resulting in 26 deaths, 9 missing and 8 injured (Fan et al. 2018; Cui et al. 2022). Pusa collapse topography is "steep at the top and slow at the bottom", reaching 70° at the steep slope and 10° - 25° at the slow slope. The collapse area is divided into collapse source area (I), scraping area (II) and accumulation area (III); the elevation of the trailing edge of the collapse is about 2120 m, the elevation of the foot of the slope is about 1922 m, and the relative elevation difference is about 200 m; the horizontal distance from the collapse source area to the front of the accumulation area is 780 m, the average thickness of the accumulation body is 4m, the

square volume is 860000 m³, and the maximum width of the accumulation area is 480 m. there are three faults (F1, F2, and F3) in the area, and the faults have no direct influence on the coal seam and the collapse zone (Fig. 2) (Xiong et al. 2022).

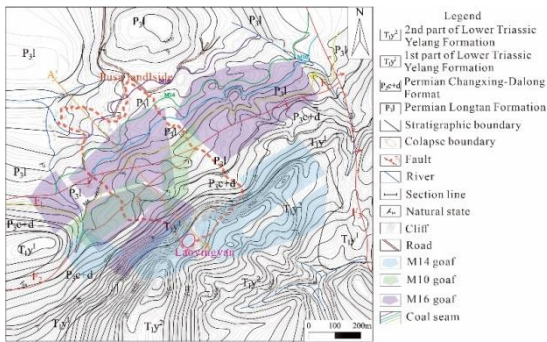


Fig. 2. Plane graph of study area

The attitude of rock is generally $200^{\circ}\angle 9^{\circ}$, there are 3 groups of joints developed in the slope, namely, $N_{10} \sim 15^{\circ}E/SE\angle 80^{\circ} \sim 90^{\circ}$, $N_{81} \sim 84^{\circ}W/NE\angle 80^{\circ} \sim 90^{\circ}$, and $N_{50} \sim 60^{\circ}E/SE\angle 80^{\circ} \sim 90^{\circ}$ and the exposed strata are from top to bottom (Fig. 3): ① Quaternary (Q₄): distributed on the top of the slope and the gentle slope, the thickness is unevenly distributed between 0 and 15 m. ② Lower Triassic Yelang Formation (T_y): distributed in the middle and upper part of the slope, the strata are divided into two sections; the upper section (T_y²) is mainly limestone, gray in color, about 50 m thick; the lower section (T_y¹) is mainly muddy siltstone, purple in color, about 70 m thick. ③ Upper Permian Changxing-Dalong Formation (P₃c+d): distributed in the lower part of the slope, mainly limestone, gray in color, about 18 m thick. ④ Upper Permian Longtan Formation (P₃l): distributed in the lower part of the slope and is a coal strata, mainly mudstone, siltstone and coal; this strata contains a total of 26-44 coal seams, among which there are 6 recoverable coal seams, M6, M10, M14, M16, M18 and M20, the average thickness of the mined M16, M14 and M10 is 1.48 m, 1.23 m and 2.12 m respectively.

Coal seam mining characteristics

The coal seams that have been mined so far are M16, M14 and M10. The sequence of coal

seam mining is M16-M14-M10 from the bottom to the top, all using the long wall coal mining method. Before 2012, M16 was mainly mined, and deep and large fractures occurred on the trailing edge of the slope from September to December 2011; M14 and M10 were mined from 2013 to 2017. During the mining period, the slope surface occasionally collapsed. The mine eventually ceased mining in August 2017, at which point M16, M14 and M10 were essentially mined out (Fig. 2).

Rainfall

Affected by the monsoon climate, the area is mainly concentrated in the summer rainfall, while the winter rainfall is less, and the collapse occurs in August when the rainfall is more concentrated. According to the perennial rainfall monitoring data, it can be seen that the most rainfall is in June every year, and the accumulated rainfall can reach 223 mm, while the least in December, only 22 mm. the accumulated rainfall in Nayong County from January to May, 161.6 mm in June, 228.7 mm in July, and 162.3 mm in August 2017, and the daily rainfall in August is shown in Fig. 4.

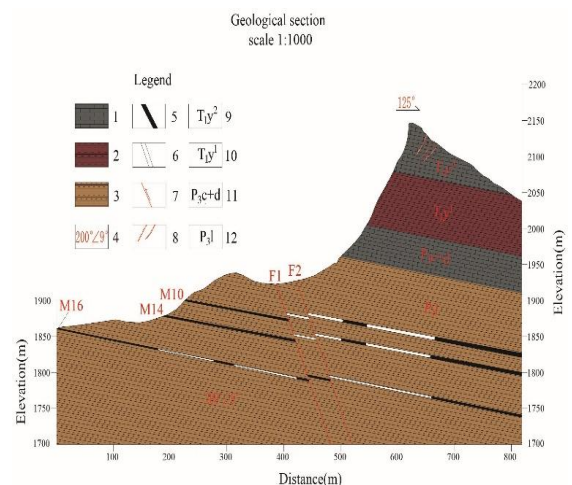


Fig. 3. Profile of the Pusa collapse along principal sliding direction (A-A' in Fig. 2): 1. Limestone; 2. Muddy siltstone; 3. Mudstone; 4. Attitude; 5. Coal seam; 6. Mined-out area; 7. Fault; 8. Karst fissures; 9. Second member of the Yelang Formation of the Lower Triassic; 10. First member of the Yelang Formation of the Lower Triassic; 11. The Changxing-Dalong Formation of the upper Permian; 12. Upper Permian Longtan Formation

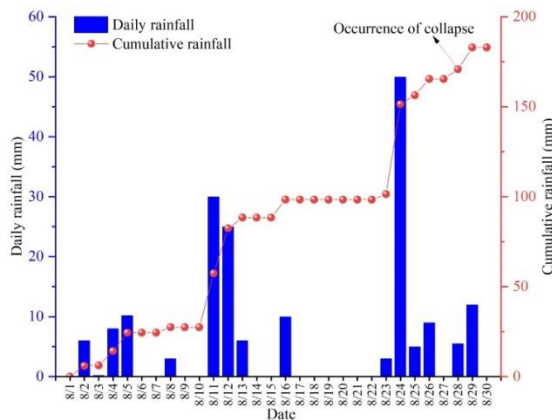


Fig. 4. Diagram describing the rainfall over the entire month preceding the collapse

RESEARCH METHODS AND PRINCIPLES

In order to reveal the deformation and damage mechanism of the slope, a generalized physical model of Pusa collapse engineering was established (Fig. 5). The similarity constants of the model are determined according to the three theories of similarity (geometric similarity, mechanical similarity, and physical similarity); geometric similarity is a similar relationship between the model and the prototype in terms of size and shape, mechanical similarity is a similar relationship in terms of mass size, and the mechanical similarity can also be expressed in terms of unit weight, and physical similarity is a similar relationship in terms of physical properties such as compressive strength, cohesion, angle of internal friction, etc. Firstly, based on the size of the Pusa collapse and experimental conditions, the geometric similarity constant C_L is determined to be 400, then the length, width and height of the model size are designed to be 160 cm, 50 cm and 110 cm respectively (Fig. 5); secondly, the similarity constant of the weight of the rock mass C_γ is determined to be 1; finally, the similarity constant of the physical properties C_σ is determined to be 400. Since it is difficult to keep all the physical and mechanical parameters of the model similar to the prototype (Dong et al. 2020; Wang et al. 2022), and this experiment focuses on the deformation and failure mechanism of the slope, the physical property similarity index is the compressive strength and the mechanical similarity index is the unit weight.

Based on available information, the fault in the study area has no direct influence on this collapse,

so the effect of the fault is not considered in the current experiment (Xiong et al. 2022). As the rock joints have an important role in the deformation and damage of slopes, they are considered in the experiment using mica sheets, and the spacing and trace length are considered as geometric similarity ratio (Fig.6g). Model box, rainfall equipment, data acquisition and monitoring equipment are required for the experiment (Figs. 6b-f).

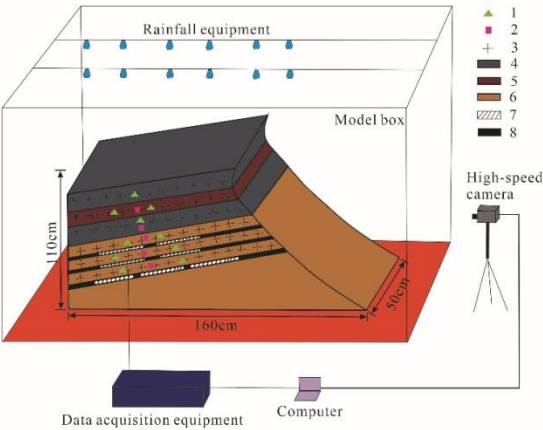


Fig. 5. Generalized model: 1. Stress monitoring point; 2. Moisture content monitoring point; 3. Displacement monitoring point; 4. Limestone; 5. Muddy siltstone; 6. Mudstone; 7. Mined-out area; 8. Coal seam

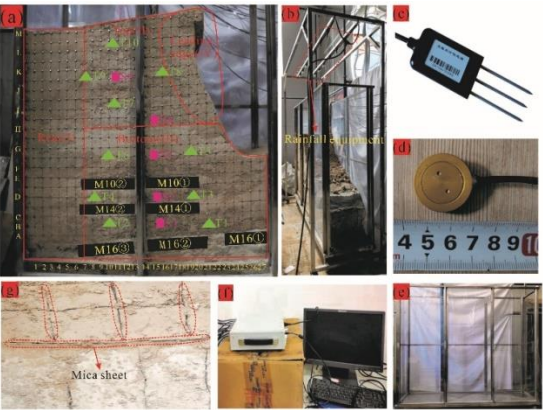


Fig. 6. Distribution of monitoring points and experiment equipments: (a) distribution of monitoring points: T is the stress monitoring point, S is the moisture content monitoring point, the numbers at the bottom and left of the model are those of the displacement grid method; (b) rainfall equipment; (c) moisture sensor; (d) stress sensor; (e) model box; (f) equipment for data collection; (g) joints made of mica sheets

The similar materials of the model are two parts: aggregate and cementing material, quartz sand and barite powder are chosen for aggregate, gypsum and cement are chosen for cementing material, and borax is used as an additive to better restore the actual situation and derive the slope deformation damage law. Material 1 simulates

limestone, material 2 simulates argillaceous siltstone, material 3 simulates mudstone, and material 4 simulates coal seam. The designed coal seam to be excavated is simulated by sand, and the mechanical parameters and the matching of each strata with similar materials are shown in Table 1.

Table 1 Mechanic parameters of lithology and similar materials

Lithology	Density (g/cm ³)	Compressive strength (kPa)	Quartz sand: Cementing material	Gypsum: Cement	Barite powder/Aggregate
Limestone	2.71	83.6×10 ³	/	/	/
Argillaceous siltstone	2.21	47.7×10 ³	/	/	/
Mudstone	1.83	29.8×10 ³	/	/	/
Coal seams	1.62	22.7×10 ³	/	/	/
Material 1	2.69	232	14:1	5:1	50%
Material 2	2.14	173	5:1	1:0	50%
Material 3	1.75	73	3:2	1:0	10%
Material 4	1.57	62	12:1	10:1	10%

THE SCHEME OF MINING AND RAINFALL

Sand is used to simulate coal seam mining by first filling plastic bags with sand to make sand bags, and setting coal pillars between the sand bags. The coal seam mining process from bottom to top is M16, M14 and M10 respectively, where M16 mines 3 mining areas and M14 and M10 mine 2 mining areas separately. The mining sequence is M16①→M16②→M16③→M16 coal pillar→M14①→M14②→M14 coal pillar→M10①→M10②→M10 coal pillar (Fig.6a). The simulated rainfall strength is set to three levels: 30 mm/day, 60 mm/day and 140 mm/day, and the rainfall start time and duration of each level are adjusted according to the deformation and damage of the model until the rainfall is maintained for a period of time even after the slope destabilization and damage.

DATA MONITORING AND COLLECTION

The stress changes, fracture progress, moisture content and overburden displacement in different locations need to be monitored. The grid method is used on the side of the model to monitor the change law of overburden displacement, and the camera is used to take pictures at regular intervals and record the fracture progress at the same time. Stress monitoring points are set up at each strata and coal seam roof location, 10 in total, and the stress change process is continuously

collected using TESTER static signal collector with a 10s interval. The moisture content of each strata is monitored to reflect the influence of rainfall infiltration on slope stability; 5 moisture content monitoring points are arranged, and the moisture content of each strata is collected by the moisture content sensor, and the collection time interval is 10s (Fig.6a).

EXPERIMENTS RESULTS

The law of rock stress variation

A total of 10 stress monitoring points are arranged in the experiment (Fig. 6a). Coal seam mining and rainfall will break the original stress balance of the slope, and thus stress adjustment will occur, so it is necessary to find out its change law through monitoring (Fig. 7). The initial stress values of monitoring points 1~10 were 18.17 kPa, 18.09 kPa, 15.91 kPa, 15.52 kPa, 12.67 kPa, 12.27 kPa, 9.49 kPa, 6.21 kPa, 5.96 kPa, and 1.07 kPa.

When mining M16, the rock mass unloading occurs thus leading to stress relaxation, causing the stresses in the nearby T1, T2 and T4 to drop rapidly at the 5 h, while the upper monitoring points farther away from M16 show a slow rising trend due to the concentration of stress in the rock mass. At 10 h, the upper plate of M16 was separated and collapsed, while rock fractures began to develop, and the stresses in T2 and T4 increased by 6.1 kPa and 5.0 kPa respectively. After the

collapse of roof of M16, a small fluctuation of stress occurred in all monitoring points; after the stress adjustment, the slope is in a balanced state at 30 h–40 h.

When mining M14, the stress in T4 suddenly increased by 7.5 kPa at 58 h, while the stress was transferred upward, causing a small increase in T7, T8 and T9 stresses, and the roof of M14 was separated and collapsed. At 60 h–90 h, small-scale block dropping, delamination and collapse continued to occur on the upper plate of M14, and the stresses in T7, T9 and T10 dropped to 8.8 kPa, 4.2 kPa and -0.8 kPa, respectively, while the stresses at other monitoring points remained stable overall.

When mining M10, the stress in the upper part of T5, T6 and T7 increased by about 3.0 kPa at 105 h, and the roof of M10 fell and collapsed at 115 h, leading to delamination and unloading in the upper part of the rock, and most of the monitoring points experienced a slow increase in stress due to the extrusion. With the continued mining of M10, a widespread collapse occurred at approximately 131 h, and the rock mass was extremely fragmented and the slope was continuously deformed toward the free face, with abrupt changes in stresses at T3, T4, T7, T8, and T9.

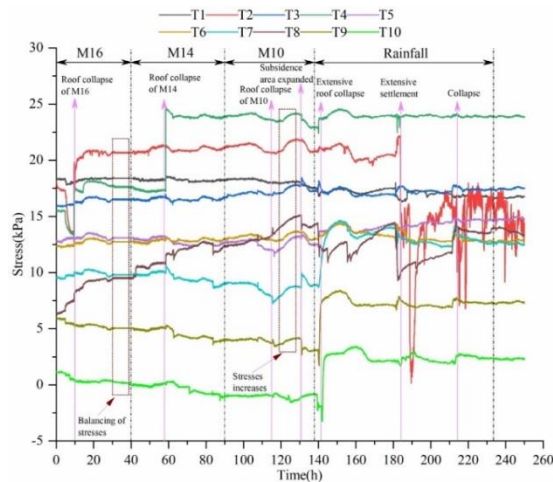


Fig. 7. The law of rock stress variation during mining

After the rainfall, the roof of the mining area collapsed extensively at 142 h, and all monitoring points experienced stress changes. As the rainfall continued, it promoted the further development of fractures resulting in rock fragmentation, and the slope intensified deformation and dumping to the

free face, and a large-scale subsidence displacement occurred at 181 h, and finally the slope collapsed at 213 h.

Fracture Evolution

After the mining of M16, the slope fractures appear firstly in the coal seam roof. Two obvious delaminated fractures D1 and D2 were developed in the roof, of which D1 was 48 cm long and 1 mm wide; D2 was 28 cm long and 1 mm wide. D3 and D4 are developed in the bottom plate of M14 and M10 respectively, D3 is 52 m long and 1 mm wide; D4 is 28 cm long and 0.8 mm wide. The more obvious tension fractures are T1 and T2, T1 is about 28 cm long and 1 mm wide; at the same time, small-scale tension fractures are also developed near M16, which connect with each other and make the upper roof rock fall and collapse (Fig. 8a).

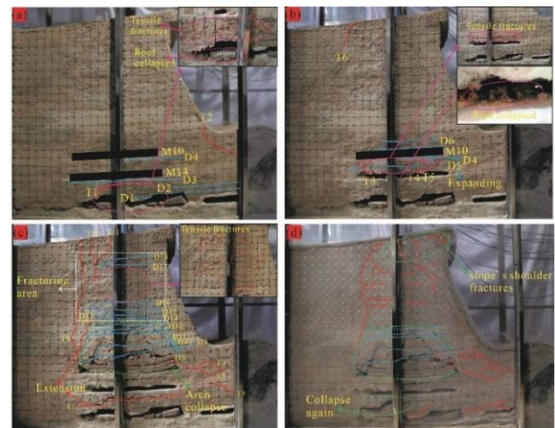


Fig. 8. Fracture evolution under mining and rainfall (D represents the separation fracture, and T represents the tensile fracture): (a) the excavation of the M16; (b) the excavation of the M14; (c) the excavation of the M10; (d) rainfall

After M14 mine-out, the roof had a tendency to collapse downward after losing support over a large area, and several new tension fractures and separation fractures were added. Meanwhile, the width of D4 was expanded from 0.8 mm to 1.5 mm, new tension fractures T3, T4, T5 and separation fractures D5 were added to the M14 roof, and new separation fractures D6 and D7 were added to the M10 roof and extended along the horizontal direction with about 24 cm length. As the slope model has a tendency to deform and dump to the free face, it leads to stress concentration in the upper part of the left side of

M10, forming tension fracture T6 and extending to the top of the slope with 11.2 cm length (Fig. 8b).

After the completion of M10 mining, the overburden bent and settled downward to form an "arch collapse zone". The mining of M10 affects almost the whole model, and the mining fractures are strongly developed, producing multiple parallel separation fractures from bottom to top, and more tension fractures in the middle and upper part of the model, forming a "fracture zone". The width and extension length of M10 roof separation fractures do not differ significantly, with extension lengths ranging from 35 cm to 45 cm and widths ranging from 1 mm to 3 mm. As time progressed, T6 extended downward to connect with the fracture near M10, and T1 at the bottom of M14 extended in a horizontal direction (Fig. 8c).

After the deformation of the model is stabilized under the action of mining, then rainfall is applied and the rainwater penetrates into the interior of the slope along the fractures, and the erosion of the rainwater promotes the development of the fractures of the slope, which gradually extend and connect with each other. The continuous deformation of the middle and lower rock masses in the model has led to the development of fractures in the shoulder of the slope. Although rainfall can promote fracture extension penetration, the fractures are mainly formed under the action of mining.

Rainfall Infiltration

After the model mining deformation stress is stabilized, the rainfall simulation experiment is conducted. The first rainfall is performed between hours 139 and 142, with a strength of 30 mm/day; the second rainfall is performed between hours 82 and 186, with a strength of 60 mm/day; and the third rainfall is performed between hours 210 and 215 with a strength of 140 mm/day. As shown in Fig. 9, the trends of the overall changes of S4 and S5 after rainfall are generally consistent, and the changes of S1, S2 and S3 are also generally the same. When the first rainfall was conducted, S4 and S5 responded rapidly and the moisture content increased more, to 22.2% and 25.3%, respectively, while S1, S2 and S3 increased by less; then the first rainfall stops after 142 h, and the water content of the five monitoring points gradually decreases to the stable value. The response rate of all five monitoring points was faster after the

second rainfall, which was due to the increase of rainfall intensity to 60 mm/day. The third rainfall intensity reaches 140 mm/day, and the peak moisture content of the monitoring points increases compared with the first two times, and the increase of S3 is consistent with S4 and S5, indicating that the downward development of the upper fracture provides a good channel for the infiltration of rainwater at this monitoring point. After three rainfalls, the infiltration of rainwater increases the water pressure inside the slope (Ray et al. 2007; Qiu et al. 2020; Ma et al. 2022), and the rainwater promotes the basic penetration of the slope fractures, and the slope reaches the critical point of instability damage, and finally the slope collapses under the push of water pressure.

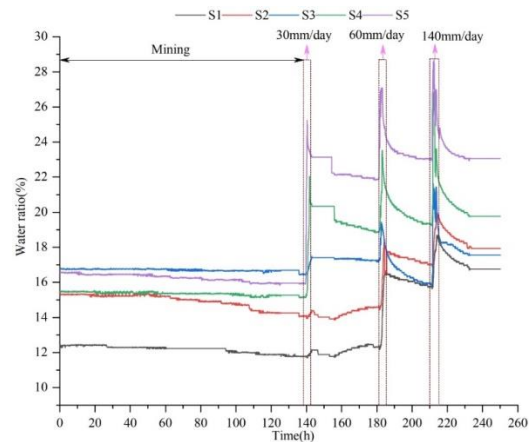


Fig. 9. Change of water ration during rainfall

Overburden Displacement

The model has 13 horizontal measurement lines (A~M) from top to bottom and 27 vertical measurement lines (1~27) from left to right; among them, the location of measurement lines A, B and C is the upper plate of M16, measurement line D is the upper plate of M14, and above measurement line E is the overburden of M10.

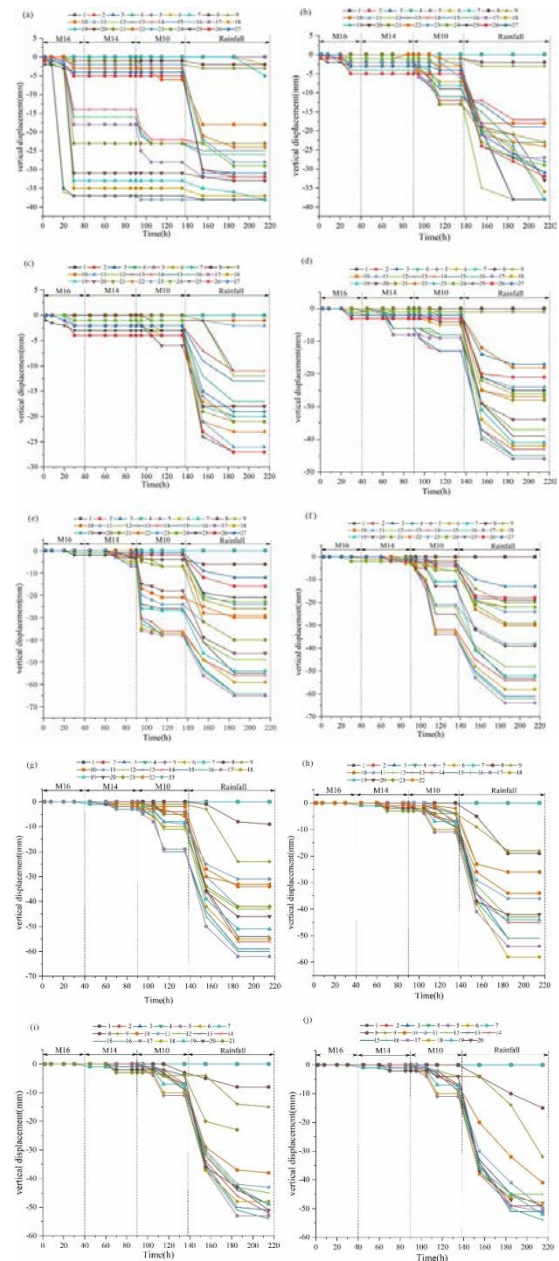
When mining M16, the subsidence of the two measurement points of the A measurement line is less than 5 mm, the subsidence of the B~F measurement lines are less than 5 mm, and the subsidence of the other measurement lines is smaller compared to the A~F measurement lines.

M14 mining makes the upper rock mass occur cracking and separation, which has an impact on D~M measurement line, among which the subsidence of D and E measurement line is larger,

also the roof of this mining area also shows the phenomenon of "big in the middle and small at the end". When mining M10, the fracture expansion penetration caused the overburden deformation to intensify and bending subsidence occurred, especially the E~G measurement line in the upper part of M10 experienced a large amount of subsidence, and the maximum displacement could reach 38 mm. The A~D measurement line was compressed by the upper rock mass of M10, and a smaller amount of subsidence occurred. Subsequent rainfall caused the model to undergo subsidence and deformation on a wide scale. It can be seen that with the mining of coal seams, different degrees of subsidence will occur at different locations, but the overall trend of subsidence is rising, especially the upper plate of the mining area will show a substantial increase with the continuous mining of coal seams; finally, under the action of rainfall subsidence further expands until destabilization damage occurs.

The horizontal displacement mainly occurs in the late mining stage and rainfall stage. It is stipulated that the horizontal displacement is positive to the outside of the slope and negative to the inside of the slope (because it is difficult to collect the horizontal displacement data in the rainfall stage and the model mainly occurs vertical displacement, so this experiment only records the vertical measurement line with relatively large horizontal displacement, as Fig. 10n shows). The horizontal displacement of the rear part of the model (I) is mainly concentrated in the upper part of this area, when M16, M14 and M10 are finished mining and the horizontal displacement only increases about 2 mm after rainfall. The horizontal displacement of the upper part of the model (II) has a decreasing trend from the top of the slope downward; after the mining of M14, fractures appear on the trailing edge; with the mining of M10, the fractures on the trailing edge expand and extend until they penetrate the mining area, and new fractures appear on the crest of the slope; after the rainfall, rainwater prompted the fractures on the trailing edge to open and expand, and the horizontal displacement continues to increase under the pushing and squeezing effect of water pressure, and the maximum horizontal displacement can reach 68 mm. The bottom part of the model (III) moves both outward and inward, but the displacement is relatively small; with the expansion of the mining area, the fractures gradually penetrate, the upper

plate appears to bend and break, and the rock mass moves horizontally outward; The horizontal deformation of the leading edge of the slope (IV) is especially intense. With the continuous mining of the coal seam, the rock mass of the leading edge is pushed by the rock mass of the trailing edge to dip and deform to the free face, and the rainfall effect makes the fractures expand, resulting in the continuous dip of the rock mass of the leading edge to the outside of the slope, and the maximum horizontal displacement is 70 mm.



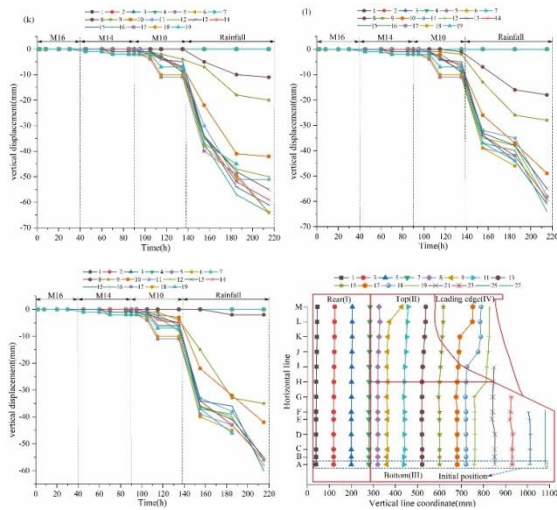


Fig. 10. Overburden displacement during mining and rainfall: (a)~(m) vertical displacement of the monitoring points, 1 to 27 indicates vertical measurement lines; (n) horizontal displacement of the monitoring points

ANALYSIS OF DEFORMATION AND FAILURE MECHANISM

In summary, the deformation and damage process of Pusa collapse can be divided into four stages (Fig. 11):

(1) Mining disturbance

After M16 mining, stress redistribution occurs in the roof of the mining area, the rock mass unloads to the mining area, generating separation fractures and will be accompanied by the phenomenon of falling and collapse, and the stress jump occurs before and after the collapse; with the continuous mining of M16, stress adjustment occurs near the mining area, and several small tension fractures appear.

(2) Fracture propagation and extension

With the mining of M14, multiple separation fractures and tension fractures were developed in the roof, and the rock at the top of the slope began to dip and deform to the free face leading to tension fractures at the trailing edge of the slope. After M10 mining, the deformation and damage of the slope intensified, and the upper part of the mining area formed a bubble area and a fracture development area, and the fracture at the trailing edge extended downward to the mining area.

(3) Creeping and slipping deformation

After rainfall, the rainwater penetrates into the slope along the trailing edge fractures, and the rock mass in the middle and lower part of the slope is infiltrated, resulting in reduced strength and horizontal shear deformation, and reduced slip resistance, and the slope starts to creep and slip deformation to the airside under the action of water pressure; as the rainfall continues, the trailing edge fractures through the mining area gradually widen and gradually fill with water, and the water pressure generated inside the slope body accelerates the creep and slip.

(4) Instability failure

Due to the continuous rainfall and the expansion of the influence of the collapse area, the fractures become wider and longer, and the strength of the rock mass decreases due to fragmentation, the water pressure increases continuously, which makes the "locking section" of the slope body suddenly be sheared off, and the rock mass is broken instantly releasing huge energy, which is quickly converted into mechanical energy of movement, so that the slope is sliding out at high speed in the way of debris flow, and the collapsed body is blocked by the small hill at the foot of the slope to move in two directions and finally accumulates at the foot of the slope in a "fishtail shape".

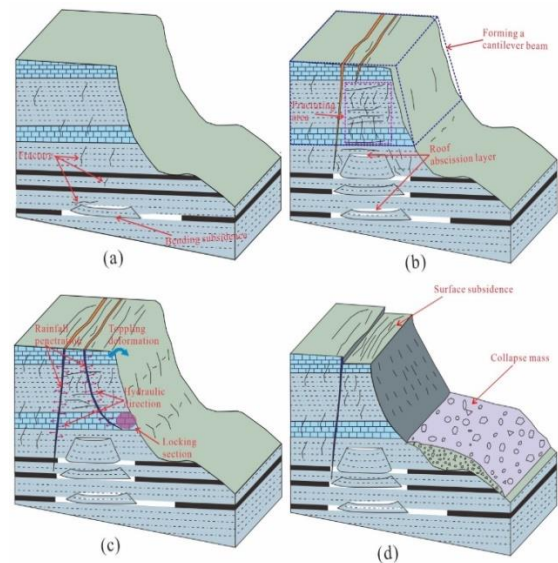


Fig. 11. Slope deformation and failure process: (a) mining disturbance (b) fracture propagation and extension; (c) creep deformation; (d) instability failure

CONCLUSION

In this paper, the interlayer stress, fracture progress, moisture content and overburden displacement characteristics of the slope under the successive effects of mining and rainfall are studied by field investigation and similar model experiments in the context of the Pusa collapse in Guizhou; The following points were obtained:

(1) When mining M16, the stress change in the roof of M16 is obvious, but the stress change in the upper part of the model is small, with a stress lag effect; with the successive mining of M14 and M10, the overall stress change in the model is larger. After the rainfall, the stress response is more obvious, and the phenomenon of "sudden rise and sudden fall" appears; stress concentration appears near the mining area, and a large number of tension fractures are formed, providing boundary conditions for the occurrence of collapse.

(2) When the coal seam is mined, the fractures and tension fractures are developed, and rainfall promote propagation of the fractures; the separation fractures are mainly located in the fall zone above the mining area, while the tension fractures are mainly located near the mining area and in the upper part of the model.

(3) After the rainfall, the rainwater infiltrates downward from the fractures at the trailing edge to the interior of the slope, and the moisture content response of the upper rock mass is more drastic than that of the lower rock mass. As the rainfall continues, the rainwater promotes the propagation of fractures and the softening of the rock, while the water pressure inside the slope rises and pushes the slope towards the airside for creeping and slipping deformation.

(4) Slope deformation damage can be divided into four stages, namely mining disturbance, fracture propagation and extension, creeping deformation, and instability failure. At the beginning of mining, stress adjustment occurs in the overlying rock, and the roof of the mining area collapses and departs from the seam; as the coal seam continues to be mined, the stress redistribution range expands, and a large number of fractures appear near the upper plate and the mining area, the overlying rock seam appears the "cantilever effect". As the rainfall infiltrates, the fractures widen and lengthen; meanwhile, the water pressure rises, the slope is deformed by creeping

and sliding to the free face, and the cantilever beam structure begins to fracture gradually; as the rainfall continues, the "locking section" (Fig. 12c) of the slope is suddenly sheared off, and the cantilever beam structure is completely destroyed, thus releasing great energy and finally the slope was destabilized.

(5) The terrain height and steepness and well-developed joints cannot be artificially controlled, but the mining process can be artificially optimized to minimize the disturbance to the mountain. In future, satellite remote sensing, InSAR technology and UAV remote sensing technology can be used to monitor its surface displacement to achieve early warning of disasters and thus avoid a lot of losses.

ACKNOWLEDGEMENTS

This study is financially supported by the Guizhou Provincial Program on Commercialization of Scientific and Technological Achievements (N0.QKHCG-LH2024-ZD025).

REFERENCES

- Cui FP, Li B, Xiong C, Yang ZP, Peng JQ, Li JS, Li HW (2022) Dynamic triggering mechanism of the Pusa mining-induced landslide in Nayong County, Guizhou Province, China. *Geomat Nat Haz Risk* 13(1):123–147. <https://doi.org/10.1080/19475705.2021.2017020>
- Chen LQ, Zhao CY, Li B, et al (2021) Deformation monitoring and failure mode research of mining-induced Jianshanying landslide in karst mountain area, China with ALOS/PALSAR-2 images[J]. *Landslides* 18:2739–2750. <https://doi.org/10.1007/s10346-021-01678-6>.
- Dai ZY, Tang JX, Jiang J, et al (2016b) Similarity modeling on instability and failure of rock bedding slope with weak interlayer caused by underground mining[J]. *Journal of China Coal Society* 41(11):2714–2720. <https://doi.org/10.13225/j.cnki.jccs.2016.0409>
- Dong ML, Zhang FM., Lv JQ, Hu MJ, Li ZN (2020) Study on deformation and failure law of soft-hard rock interbedding toppling slope base on similar test. *Bull Eng Geol Environ* 79:4625–4637. <https://doi.org/10.1007/s10064-020-01845-4>.
- Fernandez PR, Granda GR, Krzemień A, Cortes SG, Valverde GF (2020) Subsidence versus natural landslides when dealing with property damage liabilities in underground coal mines[J]. *Int J Rock Mech Min* 126:104175. <https://doi.org/10.1016/j.ijrmms.2019.104175>.

- Fan XM, Xu Q, Scaringi G, Zheng G, Huang RQ, Dai LX, Ju YZ (2018) The “long” runout rock avalanche in Pusa, China, on August 28, 2017: a preliminary report. *Landslides*. 16(1):139–154. <https://doi.org/10.1007/s10346-018-1084-z>.
- Feng Z, Li B, Cai QP, et al (2016) Initiation Mechanism of the Jiweishan Landslide in Chongqing, Southwestern China[J]. *Environmental&Engineering Geoscience* 22(4):341-351. <https://doi.org/10.2113/gsegeosci.22.4.341>.
- Liu ZY, Mei G, Sun YJ (2022) Investigating deformation patterns of a mining-induced landslide using multisource remote sensing: The songmugou landslide in Shanxi Province, China[J]. *Bull Eng Geol Environ* 81:226. [https://doi.org/10.1007/s10064-022-02699-813\(6\):1555–1570](https://doi.org/10.1007/s10064-022-02699-813(6):1555–1570). <https://doi.org/10.1007/s10346-016-0717-3>.
- Li B, Feng Z, Wang GZ, et al (2016) Processes and behaviors of block topple avalanches resulting from carbonate slope failures due to underground mining[J]. *Environmental Earth Sciences* 75(8):1435-1441. <https://doi.org/10.1007/s12665-016-5529-1>
- Ma GT, Hu XW, Yin YP, Luo G, Pan YX (2018) Failure mechanisms and development of catastrophic rockslides triggered by precipitation and open-pit mining in Emei, Sichuan, China[J]. *Landslides* 15:1401-1414. <https://doi.org/10.1007/s10346-018-0981-5>.
- Ma YT (2017) Physical Simulation Study on Genetic Mechanism of Mining Landslide Under Rainfall Condition – take Madaling landslide in Guizhou Province as an example[D]. Chengdu University of Technology. (in chinese).
- Ma SY, Qiu HJ, Yang DD, et al (2022) Surface multi-hazard effect of underground coal mining[J]. *Landslides* 2022:1612-5118. <https://doi.org/10.1007/s10346-022-01961-0>
- Qiu HJ, Cui YF, Pei YQ, et al (2020) Temporal patterns of nonseismically triggered landslides in Shaanxi Province[J]. *China Catena* 187:104356. <https://doi.org/10.1016/j.catena.2019.104356>.
- Ray R, Jacobs J (2007) Relationships among remotely sensed soil moisture, precipitation and landslide events[J]. *Nat Hazards* 43(2):211–222. <https://doi.org/10.1007/s11069-006-9095-9>.
- Shi WB, Huang RQ, Zhao JJ, et al (2016) Genetic mechanism of mining cracks of gently inclined slope in mountains[J]. *Journal of Engineering Geology* 24(05):768-774. (in chinese) <https://doi.org/10.13544/j.cnki.jeg.2016.05.006>.
- Stephen FG, Cortland FE, Douglas CP, Alexander R (2006) Coal and the environment. American Geological Institute, Alexandria.
- Sun SW, Pang B, Hu JB, et al (2021) Characteristics and mechanism of a landslide at Anqia-n iron mine, China[J]. *Landslides* 18(7):2593–2607. <https://doi.org/10.1007/s10346-021-01671-z>.
- Tao, T., Shi, W., Liang, F. et al (2022) Failure mechanism and evolution of the Jinhaihu landslide in Bijie City, China, on January 3, 2022. *Landslides*, 2727–2736. <https://doi.org/10.1007/s10346-022-01957-w>.
- Wang YQ, Wang X., Zhang JS, Yang BS, Zhu WJ, Wang ZP (2022) Similar experimental study on retaining waterproof coal pillar in composite strata mining. *Sci Rep* 12:1366. <https://doi.org/10.1038/s41598-022-05369-7>.
- Xiong SZ, Shi WB, Wang Y, et al. (2022) Deformation and Failure Process of Slope Caused by Underground Mining: A Case Study of Pusa Collapse in Nayong County, Guizhou Province, China[J]. *Geofluids* 2022:19. <https://doi.org/10.1155/2022/1592703>.
- Xu Q, Liu H, Ran J, Li W, Sun X (2016) Field monitoring of groundwater responses to heavy rainfalls and the early warning of the Kualiangzi landslide in Sichuan Basin, southwestern China. *Landslides*.
- Xu Q, Huang RQ, Yin YP, et al (2009) The JiWeiShan landslide of June 5, 2009 in WuLong, ChongQing: characteristics and failure mechanism[J]. *Journal of Engineering Geology* 17(04):433-444. (in chinese) [https://doi.org/1004-9665/2009/17\(04\)-0433-12](https://doi.org/1004-9665/2009/17(04)-0433-12).
- Yang CW, Shi WB, Peng XW, et al (2022b) Numerical simulation of layered anti-inclined mining slopes based on different free face characteristics[J]. *Bull Eng Geol Environ* 81:359. <https://doi.org/10.1007/s10064-022-02855-0>.
- Yu XY, Mao XW (2020) A preliminary discrimination model of a deep mining landslide and its application in the Guanwen coal mine[J]. *Bull Eng Geol Environ* 79:485–493. <https://doi.org/10.1007/s10064-019-01565-4>.
- Zhao JJ, Xiao JG, Min LL, et al (2016b) Discrete element modeling of a mining-induced rock slide[J]. *Springerplus* 5(1):1633. <https://doi.org/10.1186/s40064-016-3305-z>.

Zhang C, Li TF, Han XD (2020) Slope failure mechanism affected by mining subsidence: a case study of highway slopes in Yangquan, Shanxi Province, China[J]. IOP Conference Series:Earth and Environmental Science 570:022067. <https://doi.org/10.1088/1755-1315/570/2/022067>.

Zheng G, Xu Q, Ju YZ, et al (2018) The Pusacun rockavalanche on August 28, 2017 in Zhangjiawan Nayongxian, Guizhou: characteristics and failure mechanism[J]. Journal of Engineering Geology 26 (1):223-240. **(in chinese)** <https://doi.org/10.13544/j.cnki.jeg.2018.01.023>.

DOI: 10.15625/vap.2025.0182

Landslide susceptibility mapping along highway 40B, Vietnam, using logistic regression

Giang Nguyen Khac Hoang^{*}

Hanoi University of Natural Resources and Environment

E-mail: nkhgiang@hunre.edu.vn

Abstract: Landslides are one of the most serious natural hazards threatening transportation safety and socio-economic development in mountainous regions of Central Vietnam. National Highway 40B, which traverses steep terrain in Quang Nam Province, is highly vulnerable to frequent landslides, particularly during the rainy season. This study aims to assess and zonate landslide susceptibility along Highway 40B using a logistic regression model combined with extensive field survey data. A landslide inventory was constructed from field observations and historical records, in which a total of 278 landslides were identified across Quang Nam Province, including 137 sites located along National Highway 40B that were used for detailed analysis in this study. Ten conditioning factors were selected based on their geomorphological and geological relevance, including slope, aspect, elevation, lithology, distance to faults, distance to rivers, distance to roads, land use, normalized difference vegetation index (NDVI), and rainfall. Logistic regression was employed to establish the statistical relationship between the presence or absence of landslides and these conditioning variables. The resulting susceptibility map was classified into five categories: very low, low, moderate, high, and very high. Model performance was evaluated using the receiver operating characteristic (ROC) curve, yielding an area under the curve (AUC) value of 0.83, indicating good predictive capability. The results highlight that slope angle, lithology, and distance to roads are the most significant factors influencing landslide occurrence. The susceptibility map provides critical information for local authorities and

transport agencies to prioritize monitoring, maintenance, and mitigation measures along Highway 40B. This study demonstrates the effectiveness of logistic regression in landslide susceptibility assessment and contributes to improving road safety and disaster risk management in mountainous areas of Vietnam.

Keywords: Landslide susceptibility, Logistic regression, Highway 40B, Quang Nam Province, Field survey.

INTRODUCTION

Vietnam's mountainous regions are highly prone to landslides due to steep topography, fragile geological structures, and intense monsoonal rainfall. The central provinces, including Quang Nam, experience frequent slope failures that severely affect roads, settlements, and local livelihoods. National Highway 40B, a vital transportation corridor linking the lowlands of Quang Nam to the Central Highlands, has been repeatedly disrupted by landslides during heavy rainfall events. For example, in the 2023 rainy season, more than 10 major slope failures occurred along the Nam Tra My segment, damaging road surfaces and causing economic losses exceeding 19 billion VND.

Landslide susceptibility mapping (LSM) has become an essential tool for disaster risk reduction and land-use management in mountainous regions. Among various statistical and machine learning methods, logistic regression is widely used due to its simplicity, interpretability, and ability to handle both categorical and continuous variables. When combined with GIS and remote sensing, LR can efficiently model spatial relationships between

landslides and conditioning factors, providing reliable susceptibility zonation maps even in data-scarce regions.

Previous studies in Vietnam have applied logistic regression and machine learning models for regional-scale landslide susceptibility mapping (Pham et al., 2017; Nguyen et al., 2020; Hong et al., 2016). However, few have focused specifically on transportation corridors, where both natural and anthropogenic factors strongly interact. This study addresses that gap by analyzing the spatial susceptibility of landslides along Highway 40B a critical yet highly vulnerable route in Central Vietnam.

The main objectives of this study are: (i) to develop a verified landslide inventory and conditioning factor database for Highway 40B; (ii) to quantify the relative contribution of each factor using logistic regression; and (iii) to produce a validated susceptibility map for practical hazard mitigation and infrastructure planning.

STUDY AREA

The study area covers the mountainous segment of National Highway 40B within Quang Nam Province, central Vietnam. The terrain is characterized by elevations ranging from 100 to over 1,500 m above sea level, dissected by steep slopes exceeding 30°. Geographically, the study area extends from approximately 15°04' to 15°20'N and 108°00' to 108°30'E, covering about 1,200 km² of mountainous terrain along the Nam Tra My and Bac Tra My districts. The region lies on the western flank of the Truong Son Range, dominated by metamorphic and sedimentary rocks of the Paleozoic–Mesozoic age, frequently cut by faults and weathered zones.

According to the geological map (Figure 1), the dominant lithological units include schist, sandstone, shale, and weathered granite belonging to the Paleozoic–Mesozoic formations. Metamorphic rocks such as gneiss and amphibolite are widely distributed in the upper slopes, while intrusive rocks such as biotite granite occur along several road

sections. These formations are highly fractured and weathered, which significantly reduce slope stability, especially where cut slopes intersect fault zones. In addition, colluvial and alluvial deposits occupy the lower valleys and road embankments, contributing to shallow landslides after intense rainfall events. The map of the study area was constructed using the original 1:50,000-scale administrative and geological maps of Quang Nam Province as base maps.

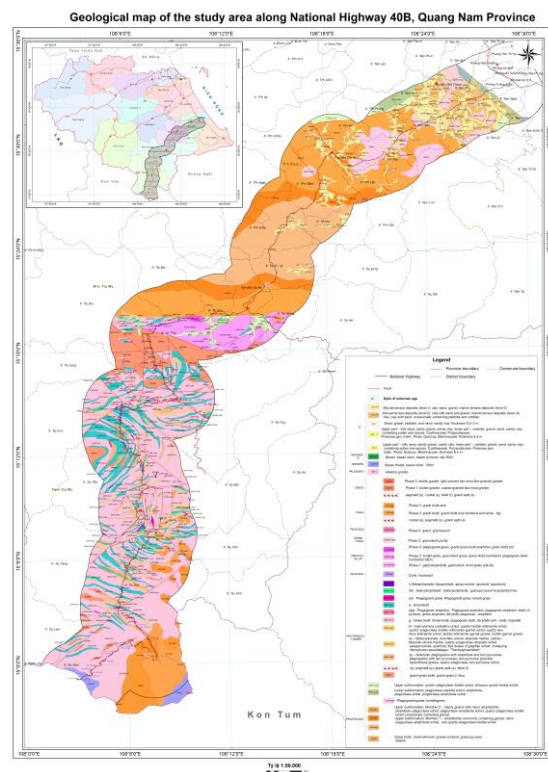


Figure 1. Geological map of the study area along National Highway 40B, Quang Nam Province.

The tropical monsoon climate produces high annual rainfall (2,500–3,000 mm), concentrated between September and December. Intense storms and typhoons are the main triggers of slope failures. Vegetation cover varies from dense natural forest in upper elevations to agricultural and degraded land near roads and settlements. In addition to natural conditions, anthropogenic activities have increasingly contributed to slope instability. Extensive road construction

involving slope cutting, along with hillside cultivation and deforestation, has significantly disturbed the natural slope equilibrium, thereby intensifying landslide occurrences along the highway corridor.

Given the combination of steep topography, complex geology, and heavy rainfall, this section of Highway 40B represents one of the most landslide-prone areas in Central Vietnam, making it suitable for detailed susceptibility analysis using logistic regression.

DATA AND METHODS

Data Sources

Surveys were conducted along National Highway 40B during the 2023 rainy season. A total of 278 landslides were recorded in Quang Nam Province, of which 137 were located along National Highway 40B and used for model construction. Topographic information (slope, aspect, and elevation) was derived from the 30 m-resolution SRTM DEM. Lithology and faults were digitized from the 1:50,000-scale geological map of Quang Nam Province published by the Department of Geology and Minerals of Vietnam and validated through field observations. Distance to roads and rivers was generated using Euclidean distance analysis in ArcGIS 10.4.1, based on updated OpenStreetMap and topographic maps. Land use and NDVI were extracted from Sentinel-2 imagery (2023). Rainfall data (2013–2023) were collected from ten meteorological stations managed by the Quang Nam Hydro-Meteorological Center.

All spatial datasets were standardized to a 30 m grid resolution to ensure consistency across analyses. The data sources, purposes, and formats are summarized in Table 1.

Table 1. Data sources and descriptions

Factor	Description	Source	Format / Resolution
Elevation (m)	Derived from the Digital Elevation Model (DEM)	SRTM DEM (NASA)	Raster, 30 m

Slope (°)	Calculated from DEM	Derived from DEM	Raster, 30 m
Aspect (°)	Calculated from DEM	Derived from DEM	Raster, 30 m
Lithology	Geological formations and rock types	Geological map of Quang Nam Province (1:50,000), Department of Geology and Minerals of Vietnam	Vector (polygon)
Distance to faults (m)	Euclidean distance from mapped fault lines	Derived from geological map (1:50,000)	Raster, 30 m
Distance to rivers (m)	Euclidean distance from main rivers	Derived from topographic map	Raster, 30 m
Distance to roads (m)	Euclidean distance from road network	OpenStreetMap, updated by field survey (2023)	Raster, 30 m
Land use / land cover	Land classification categories	Sentinel-2 imagery (2023)	Raster, 30 m
NDVI	Normalized Difference Vegetation Index	Calculated from Sentinel-2 (2023)	Raster, 30 m
Rainfall (mm)	Mean annual rainfall (2013–2023)	Quang Nam Hydro-Meteorological Center	Raster (interpolated), 30 m
Landslide inventory	278 mapped landslides (137 along Highway 40B)	Google Earth (2021–2023), Field verification (2023)	Point (vector)

Following the compilation and standardization of all datasets (Table 1), the spatial database was integrated into ArcGIS 10.4.1 for analysis. Each thematic layer was resampled to a uniform 30 m resolution to ensure spatial compatibility. The landslide inventory and conditioning factors were then overlaid to extract variable values for both landslide and non-landslide points, forming the input dataset for subsequent modeling using logistic regression.

Landslide Inventory

A detailed landslide inventory was constructed using a combination of Google Earth imagery (2021–2023) and extensive field

investigations conducted during the 2023 rainy season. A total of 278 landslides were identified across Quang Nam Province, among which 137 sites were located along National Highway 40B and used for model development. Landslide boundaries were manually delineated on high-resolution images and verified in the field to ensure spatial accuracy.

The inventory was categorized by landslide type, size, and geomorphological setting. Each site was cross-checked with local government records and previous hazard reports provided by the Quang Nam Department of Transport. Non-landslide points were randomly selected from stable slopes with similar topographic and geological conditions, ensuring a balanced dataset for modeling.

Figure 2 illustrates the spatial distribution of mapped landslides along National Highway 40B. Landslide occurrences are mainly concentrated in steep mountainous areas, particularly within zones underlain by highly weathered granite and fractured metamorphic rocks.

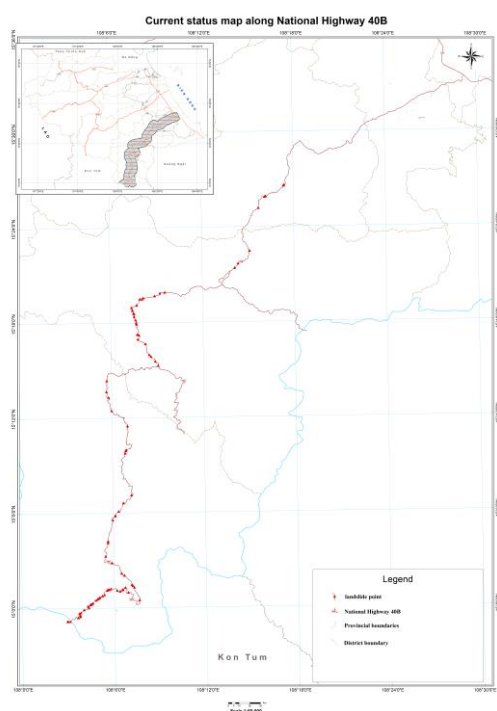


Figure 2. Landslide distribution map along National Highway 40B

Conditioning Factors

Ten conditioning factors were selected based on their geomorphological and geological relevance as well as data availability. These factors include slope angle, aspect, elevation, lithology, distance to faults, distance to rivers, distance to roads, land use, NDVI, and rainfall. The selection was guided by previous regional studies and best practices in landslide susceptibility mapping, and by the characteristics of mountainous terrain in Central Vietnam, where rainfall, slope, and lithology play dominant roles in slope instability.

Topographic parameters (slope, aspect, elevation) were derived from the 30 m SRTM DEM. Lithology and fault systems were digitized from the 1:50,000-scale geological map, while distance-based factors (roads, rivers, and faults) were computed using the Euclidean distance tool in ArcGIS 10.4.1. Land use and NDVI were obtained from Sentinel-2 imagery (2023), reclassified into five major categories: forest, plantation, agriculture, bare land, and built-up area. Mean annual rainfall (2013–2023) was interpolated from ten meteorological stations using the Inverse Distance Weighting (IDW) method.

All conditioning factor layers were standardized to a uniform 30 m spatial resolution and aligned within a common coordinate system (VN-2000, Zone 48N). Multicollinearity among factors was tested using the Variance Inflation Factor (VIF) in SPSS, and only variables with $VIF < 5$ were retained for the logistic regression model.

Statistical testing indicated that seven predictors retained in the final logistic regression equation were significant ($P < 0.05$): slope, aspect, rainfall, weak lithology (lithology class), bare land (land-use class), distance to stream, and distance to road. Three variables—elevation, NDVI, and distance to faults—were not statistically significant, with P-values of 0.33, 0.17, and 0.19, respectively. Therefore, these three non-significant factors were excluded from the final model to improve

model performance and avoid over-parameterization.

Logistic Regression Model

The logistic regression model relates the probability of landslide occurrence (P) to the set of independent variables (Xi) as:

$$P = \frac{1}{1 + e^{-(\beta_0 + \beta_1 X_1 + \beta_2 X_2 + \beta_3 X_3 + \dots + \beta_n X_n)}}$$

where β_0 is the intercept and β_i are regression coefficients. The model was implemented in SPSS 26 using the maximum likelihood estimation method. Significant variables were selected based on the Wald statistic ($p < 0.05$). The resulting coefficients were exported to GIS to generate a spatial probability map.

Model Validation

Model performance was evaluated using the ROC curve and AUC (Area Under the Curve). AUC values between 0.8 and 0.9 indicate good prediction accuracy. Additionally, a confusion matrix was used to calculate accuracy, sensitivity, and specificity.

RESULTS

Statistical Analysis

The logistic regression analysis produced a statistically significant model ($P < 0.05$) that effectively distinguishes between landslide and non-landslide locations. The final model incorporated seven conditioning factors with both positive and negative coefficients reflecting their influence on landslide occurrence.

The regression coefficients indicate that slope angle ($\beta = 0.089$) and weak lithology ($\beta = 0.412$) have the strongest positive influence on landslide probability. Steeper slopes increase shear stress and reduce gravitational stability, while weathered granite and schist lithologies exhibit low cohesion and shear strength. Bare land ($\beta = 0.258$) also increases susceptibility due to the absence of vegetation roots and higher surface runoff during heavy rainfall. Negative coefficients for distance to stream and distance to road indicate that slopes located closer to drainage channels or cut slopes are

more prone to failure because of toe erosion and excavation. These relationships are consistent with physical observations in tropical mountainous terrains of Central Vietnam.

The final regression equation obtained from SPSS analysis is expressed as: $\text{Logit}(P) = -3.274 + 0.089(\text{Slope}) + 0.307(\text{Aspect}) + 0.067(\text{Rainfall}) + 0.412(\text{Weak lithology}) + 0.258(\text{Bare land}) - 0.031(\text{Distance to stream}) + 0.022(\text{Distance to road})$.

This equation was used to compute the probability of landslide occurrence across the study area, which was then transformed into a spatial susceptibility index using ArcGIS 10.4.1.

Landslide Susceptibility Mapping

The calculated landslide susceptibility index (LSI) was classified into five levels using the natural breaks (Jenks) method: very low, low, moderate, high, and very high susceptibility. Figure 3 shows the spatial distribution of susceptibility along National Highway 40B. The results indicate that approximately 31.7% of the study area falls within the high and very high classes, 25.4% within moderate, and the remaining 42.9% within low or very low susceptibility zones. Table 2 presents the distribution of landslide susceptibility levels across 98 segments of Highway 40B. These quantitative results provide the basis for interpreting the spatial pattern of susceptibility in Figure 3.

Table 2. Distribution of landslide susceptibility levels across 98 segments of Highway 40B

Susceptibility Level	Estimated number of segment	Segment proportion (%)
Very Low	25	26
Low	36	37
Moderate	15	15
High	12	12
Very High	10	10
Total	98	100

The predicted “very high” and “high” susceptibility zones correspond closely with actual landslide clusters observed during field

surveys in 2023, particularly between km 75–95 in Nam Tra My District. This spatial agreement between predicted and observed landslides demonstrates the reliability of the logistic regression model for practical road hazard management along Highway 40B. Most of these areas are characterized by steep slopes and weak lithology, where slope cuts for road widening and drainage construction further decrease stability.

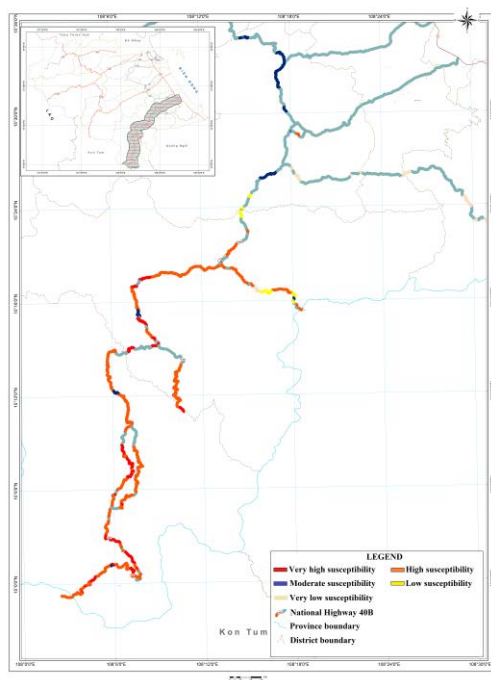


Figure 3. Classified landslide susceptibility zones along National Highway 40B

Model Validation

Model performance was evaluated using the receiver operating characteristic (ROC) curve shown in Figure 4. The ROC curve measures the ability of the logistic regression model to distinguish between landslide and non-landslide locations based on the predicted probability values. The area under the ROC curve (AUC) value of 0.823 indicates good predictive capability, confirming that the model effectively discriminates between stable and unstable slopes along the highway corridor.

The validation results showed that more than 80% of the recorded landslides were

located within the high and very high susceptibility zones predicted by the model. This strong correspondence between predicted and observed landslide locations demonstrates the reliability and robustness of the logistic regression model for practical hazard assessment.

The findings suggest that the logistic regression approach provides a realistic representation of landslide susceptibility along Highway 40B. Nevertheless, certain local discrepancies remain in areas with limited field data or where land-use changes have occurred recently. Incorporating higher-resolution rainfall data, soil geotechnical properties, and dynamic triggering factors in future work could further improve model precision and predictive performance.

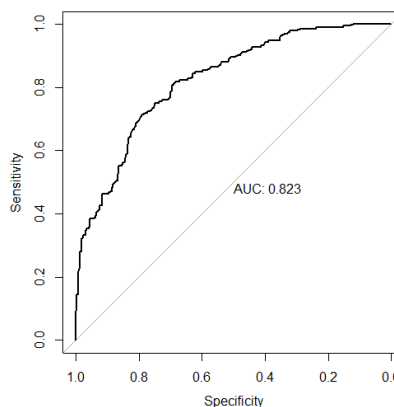


Figure 4. Receiver Operating Characteristic (ROC) curve of the logistic regression model.

DISCUSSION

The spatial pattern of high susceptibility zones aligns well with observed landslide events along Highway 40B. Slope steepness and lithological weakness are the dominant intrinsic factors, while heavy rainfall acts as the primary trigger. Anthropogenic influences—especially road cuts and deforestation—further aggravate slope instability.

Compared to previous studies in northern Vietnam (e.g., Lao Cai, Yen Bai), the AUC value obtained here is slightly higher, reflecting good model reliability despite limited data. Logistic regression remains a valuable and transparent

tool for regional-scale landslide assessment, particularly when combined with GIS. However, some limitations exist: (i) the model assumes linearity between predictors and $\text{logit}(P)$; (ii) rainfall data lack high temporal resolution; and (iii) the inventory may underrepresent small or historical landslides.

Future work should integrate more dynamic parameters (soil moisture, vegetation index), employ higher-resolution DEMs, and explore hybrid models combining logistic regression with machine learning algorithms.

The results highlight the need for integrating landslide susceptibility assessment into road design and maintenance planning in mountainous areas of Quang Nam Province. In particular, the high-susceptibility segments identified along Highway 40B should be prioritized for slope stabilization, drainage improvement, and continuous monitoring. These findings provide scientific support for local authorities to allocate resources efficiently for disaster risk reduction and infrastructure resilience.

CONCLUSIONS

The logistic regression model provided a statistically consistent and interpretable framework for evaluating the spatial probability of landslides along National Highway 40B. The results indicate that slope, lithology, and rainfall are the most influential factors controlling slope instability in the study area. These findings align with previous research in tropical mountainous regions (Pham et al., 2017; Nguyen et al., 2020; Hong et al., 2016), which emphasized the role of steep gradients and weak lithologies under intense monsoonal rainfall conditions.

Compared with earlier regional-scale susceptibility studies in Vietnam (e.g., Nguyen et al., 2020), the present research focuses specifically on the transportation corridor level, which provides more practical insights for infrastructure management. The AUC value of 0.823 obtained in this study is comparable to those reported in other logistic regression-based models in Southeast Asia, demonstrating

the robustness of the approach when applied to limited field data.

The strong correlation between predicted high-susceptibility zones and actual landslide occurrences suggests that the model effectively captures both the geomorphological and anthropogenic factors influencing slope failures. In particular, the concentration of high-risk segments in Nam Tra My District corresponds to areas with active slope cutting, poor drainage, and weathered metamorphic rock formations, confirming that road construction and human modification of slopes significantly accelerate landslide processes.

Despite the model's good performance, certain limitations must be acknowledged. The logistic regression approach assumes linear relationships between conditioning factors and landslide probability, which may oversimplify the complex interactions among rainfall, lithology, and slope structure. Moreover, the rainfall data used were averaged over a ten-year period, which may not capture short-term storm intensity peaks that trigger failures. Future studies should integrate time-dependent rainfall variables, soil moisture data, and higher-resolution DEMs to enhance prediction accuracy.

The findings also have direct implications for local planning and disaster mitigation. Integrating the susceptibility results into transportation management systems would enable the Quang Nam Department of Transport to prioritize slope stabilization and monitoring at critical road segments. In particular, the high-susceptibility zones identified between km 75–95 along Highway 40B should be treated as priority areas for maintenance and drainage reinforcement.

Overall, this study demonstrates that logistic regression remains a cost-effective and reliable tool for landslide susceptibility assessment in data-scarce mountainous areas. When coupled with GIS and field verification, it can support more resilient road network design and proactive hazard management in Central Vietnam.

REFERENCES

- Dai, F.C., Lee, C.F. (2002). *Geomorphology*, 42(3–4), 213–228.
- Guzzetti, F. et al. (2006). *Geomorphology*, 72(1–4), 272–299.
- Hong, H. et al. (2016). *Landslides*, 13(2), 423–440.
- Lee, S., Pradhan, B. (2007). *Landslides*, 4(1), 33–41.
- Nguyen, V.Q. et al. (2020). *Geomatics, Natural Hazards and Risk*, 11(1), 1542–1563.
- Pham, B.T. et al. (2017). *Environmental Modelling & Software*, 95, 245–258.
- Varnes, D.J. (1984). UNESCO, Paris.
- Van Westen, C.J., Castellanos, E., Kuriakose, S.L. (2008). *Engineering Geology*, 102(3–4), 126–147.
- Yilmaz, I. (2009). *Computers & Geosciences*, 35(6), 1125–1138.
- Pradhan, B. (2010). *Environmental Earth Sciences*, 60, 1037–1054.
- Ayalew, L., Yamagishi, H. (2005). *Geomorphology*, 65(1–2), 15–31.
- Lee, S., Min, K. (2001). *Engineering Geology*, 58(3–4), 231–243.

Morphological factors controlling landslide formation in Northern Vietnam – remarks after three years of observations

Pawel Kroh^{1*}, Łukasz Pawlik², Pham Van Tien³, Le Hong Luong⁴

¹University of the National Educational Commission, Institute of Biology and Earth Sciences, Krakow, ul. Podcharazych 2, Poland

²University of Silesia, Institute of Earth Sciences, ul. Będzińska 60, 41-200 Sosnowiec, Poland

³Vietnam Academy of Science and Technology, Institute of Earth Sciences, Hanoi, Viet Nam

⁴Vietnam Ministry of Transport, Institute of Transport Science and Technology, Hanoi, Viet Nam

*Email: pawel.kroh@uken.krakow.pl

Abstract: Monsoon and typhoon regions are simultaneously global hotspots for landslides, including Northern Vietnam. While monsoon/typhoon rainfall is the dominant triggering factor, the response of the environmental system to this trigger differs across areas. A similar amount of rainfall can trigger isolated shallow landslides, clusters of shallow landslides, or deep-seated landslides—all during the same event. Geomorphological observations of various landforms have allowed us to identify several predisposing features responsible for landslide development of a specific type and size. The first factor is the permeability of the sliding surface. When the sliding surface is permeable, differences in soil saturation levels and the increased weight of the top layers become a significant landslide trigger. In the case of an impermeable sliding surface, rainwater does not infiltrate the soil profile, and liquefaction of weathered material and soil just above the sliding surface causes the mass wasting process. The second factor is the type of bedrock. Solid bedrock parallel to the slope direction at shallow depth increases the probability of rock material sliding. Deeply weathered rock material suggests higher friction and should be more stable. The third factor is a slope meso-topography. Convex slopes, with higher slope angle in some sections are more prone for landsliding. Most of the source areas were located above a

steeper section, which suggests important role of this relief element.

Keywords landslides, triggering factors, landforms, geomorphology, meso-topography, North Vietnam.

INTRODUCTION

Vietnam is one of the most landslide-prone countries in the world and a hotspot for various mass movements that occur annually due to steep elevation differences and heavy monsoon and typhoon rainfalls (Tu et al. 2016; Froude and Petley 2018; Van Tien et al. 2021b, a, 2024; Gómez et al. 2023; Fidan et al. 2024). Mountainous areas in this country are also highly populated, meaning that all landslide events directly affect local communities (Van Tien et al. 2021a). The wide range of environmental, geological, and hydrological conditions under the annual and seasonal pressure of extreme rainfall presents major challenges for understanding and analyzing landslide processes. Most research on rainfall-induced landslides focuses on rainfall as the primary trigger—its amount, intensity, and temporal accumulation. In this article, the authors aim to draw the reader's attention to other environmental factors that act as co-triggers influencing the occurrence of landslides in specific locations. As the title indicates, we do not yet have numerical results; instead, we would like to share general field observations as a basis for future discussion.

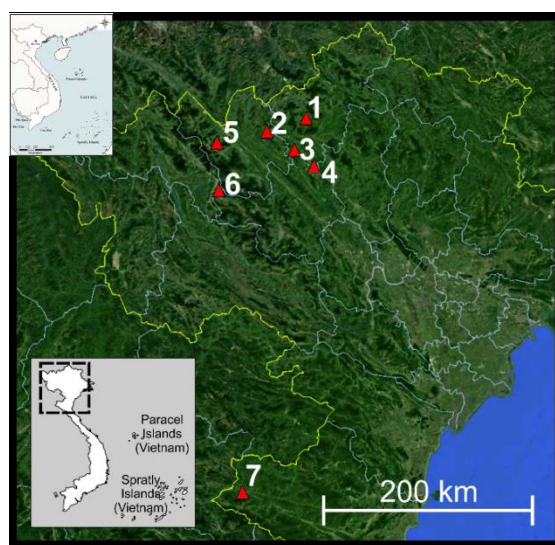


Figure 1. Location of the study sites: 1- Tien Nguyen, Pac Peng, Lang Cang, Nam Chang, 2- Nam Luc, Nam Tong, 3- Tan Phuong, 4- Minh Xuan, 5- Muong Hoa, 6- Ho Bon 1-3, 7- Ky Son. background map by Google Earth.

Table 1. General information of studied landslides. Length of accumulation/transport zone calculated from highest source zone in the catchment till end of accumulation in the valley bottom.

Location	Source zone type by Varnes' classification	Shallow/deep-seated	Flash flood or debris flow	Transport/accumulation zone length*
Ho Bon 1	Translational slide	Shallow	Yes	140 m
Ho Bon 2	Translational slide	Shallow	Yes	90 m
Ho Bon 3	Slump	Shallow	Yes	30 m
Nam Chang (cluster)	Translational slide	Shallow	Yes	1720 m
Nam Luc	Translational slide	Deep-seated	No	249 m
Muong Hoa	Translational slide	Shallow	No	1163 m
Ky Son (sandstone, cluster)	Earth flow	Shallow	Yes	3800 m
Ky Son (garnite, cluster)	Translational slides	Shallow	Yes	3800 m
Lang Cang	Translational slide	Shallow	No	104 m
Pac Peng	Translational slide	Shallow	No	20 m
Nam Tong	Translational slide	Deep-seated	No	752 m
Tan Phuong	Translational slide	Deep-seated	No	671 m
Tien Nguyen	Debris flow	Deep-seated	No	640 m
Minh Xuan	Rotational slide	Deep-seated	No	299 m

Study area

Northern Vietnam, with an elevation range from the highest peak, Phan Xi Păng (3,147 m a.s.l.), down to about 30 m a.s.l. in the Red River valley, is a mountainous region characterized by very high relative relief. As the result, the terrain forms long, steep slopes with high potential energy. The warm and humid climate leads to intensive rock weathering and the development

of thick weathered soil mantles, even on steep slopes (Gian et al. 2017). The area has the tropical monsoon climate with two distinct seasons: rainy and dry season. Mean total annual rainfall varies strongly and is between approx. 1,800 mm in western parts till even 4,600 mm in some parts (Gobin et al. 2016). The very strong rainfall events are connected with tropical typhoons, which are the main cause of significant number of fatal landslide accidents

and damage (Pham-Thanh et al. 2020). The average annual temperature is between 19 and 22°C. The vegetation is mainly mixed forest, in some part cinnamon plantations, croplands, and rice planted on terraces.

The study sites investigated during three post-monsoon field campaigns included observations on few dozens of landforms and detailed mapping on 14 landslides located in villages: Ho Bon, Nam Chang, Nam Luc, Muong Hoa, Ky Son, Lang Cang, Pac Peng, Nam Tong, Tan Phuong, Tien Nguyen, Minh Xuan at four provinces: Lao Cai, Yen Bai, Ha Giang, and Nghe An (Figure 1). Most of the locations were investigated only once, shortly after the monsoon-triggered landslide events. Only the Nam Chang landslide cluster was visited twice to collect additional soil samples.

The study sites represent a variety of landform types. Some of them are shallow landslide clusters (e.g., Ky Son or Nam Chang), while others consist of individual landslides occurring within catchments that are strongly affected by landsliding (each landslide is a separate landform, but at the catchment scale they form a cluster, e.g., Ho Bon). Some sites, such as Ho Bon, were also affected by a flash flood event in the valley bottom, which exhibited very strong morphological energy due to the large amount of rock material delivered to the valleys from landslides (e.g., Ky Son, Nam Chang). Deep-seated landslides occurred in all cases as individual landforms, not connected with other cascading geohazards, but they transported huge volumes of rock material.

Methods

The geomorphological insights presented in this paper are based on a field survey, including relief mapping and measurements of landforms associated with landslides such as the main scarp, slope angles of the sliding surface and transport zone, and other features related to morphogenetic processes. Field campaigns were conducted during three consecutive post-monsoon seasons in 2022, 2023, and 2024. The fieldwork included assessments of

geomorphological conditions across entire catchments or slopes, detailed field documentation, landslide geomorphological mapping, UAV surveys, and soil sampling. Additionally, analysis of local situation and slope location on Google Earth imagery was performed.

RESULTS AND DISCUSSION

Observed landslide landforms were highly diverse. While this may seem obvious, the considerable variation found within a single monsoon region supports the conclusion that rainfall is the dominant triggering factor, but other influences such as geology, topography, and soil depth are very important factors influencing the final mechanism in a much larger scale than is usually assumed. The same initial trigger (monsoon or typhoon rainfall) generates different mechanisms in nearby areas. Neighbouring catchments, with a similar amount of rainfall, manifest mass movement as clusters of shallow slides, isolated single landslides, or deep-seated failures etc. This indicates that although intense rainfall serves as the primary trigger, other environmental factors act as modifiers that determine the specific failure mechanisms, geomorphological processes, and ultimately, the resulting landforms. Their role is still not enough recognised and need to be research much deeper.

Following the widely accepted, updated Varnes landslide classification (Hungr et al. 2014), the most common source zones in the study area can be categorized as translational slides (Figure 2A), while the corresponding accumulation zones are typically earth or debris flows (Figure 2B). Part of landforms have features typical for debris avalanche, but usually the accumulation zone indicates strong hydration of the deposited material (Highland, Bobrovsky 2008). This discrepancy suggests that the most frequently occurring landslide type is “complex,” which is not particularly informative for detailed geomorphological interpretation. Different types of landslides in the source zones ultimately create very similar cone-shaped landforms and share similar

transport and accumulation mechanisms. This is an effect of deep weathering in the warm-humid climate, which results in the lack of compact rock formations above potential sliding surfaces. Strongly weathered, sandy-gravel slope material after the sliding process does not form rock packets, but rather highly saturated earth/gravel masses covering slope below, reaching valley bottom or even transported further to lower parts of channels as cascading geohazard (landslide-debris flow-flush flood). This regularity appears to be, at least in part, independent of the geological substrate, since the same pattern was observed across different lithologies, including granite (Nam Chang), metamorphic rocks (Nam Luc), and sandstone (Ky Son).

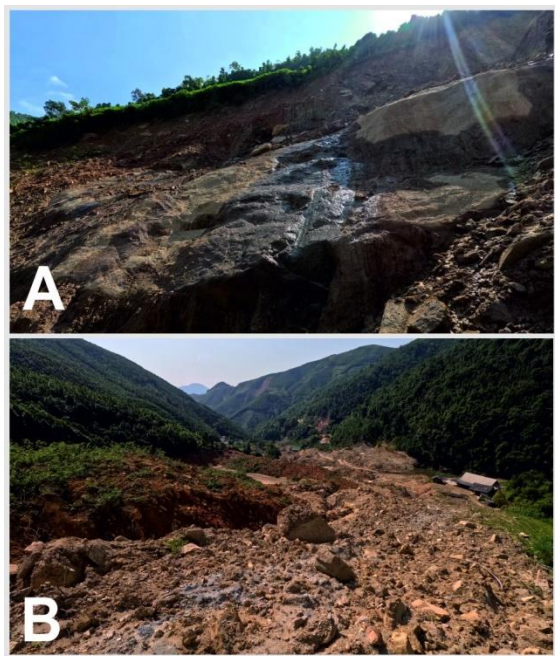


Figure 2. Source zone classified as translational slide (A), accumulation zone as earth flow (B). Nam Tong landslide, 2024. Photos by P. Kroh.

An important factor is the permeability of the sliding surface. When the sliding surface is permeable, differences in soil saturation levels and increased weight of upper layers become the direct trigger of the landslide. In the case of an impermeable sliding surface, rainwater does not infiltrate deeper into the soil profile, and the liquefaction of weathered material just

above the sliding surface initiates the process. The depth of mobilized slope deposits is related to this mechanism and influences the volume of transported material, especially in shallow landslides.

The liquefaction of soil above bedrock is sometimes associated with suffusion, and its more advanced stage — soil piping. The soil-piping process leads to the concentration of subsurface water flow and the accumulation of additional rainwater infiltrating into the soil profile from a larger area, with a delay relative to the typhoon/monsoon event. Evidence of such mechanisms was observed at the Nam Tong study site, where a pipe outlet was visible on the main scarp, with water flowing out of it (Figure 2A). This mechanism is further supported by the timing of the landslide, which occurred two days after the main typhoon rainfall.

In certain landscape settings, landslides occur more often and in greater numbers under the same triggering conditions. A topographical feature observed at most study sites with the bedrock as the sliding surface was a steeper slope section located below the source area (Figure 3). In some locations, it was in the form of a bedrock step, while in others, it appeared as a locally steepened part of the slope. Generally, the meso-scale slope profile was convex, with the landslide niche situated just above the most convex section.

Another geomorphological characteristic that distinguishes Vietnamese landslides from those in the temperate climate zone is much stronger erosional effect within the transport zone. This effect is associated with the deeply weathered slope materials typical of warm, humid climates. Weathered slope deposits are poorly consolidated and are therefore highly susceptible to erosional forces. Even relatively small and shallow landslides can mobilize large volumes of soil from the slopes below the initial area, producing extensive earth or debris flows. The typical textbook scenario—where an accumulation zone lies directly below the landslide niche—was rarely observed in the studied areas. Almost all examined sites

displayed long transport channels with strong erosional effects (Figure 4). Moreover, the accumulation zones were usually much larger than what could be accounted for by the volume of slope deposits from the source zones alone.



Figure 3. Steeper section of the slope manifested as bedrock step below landslide source zone. Muong Hoa landslide, 2024. Photo by P. Kroh.



Figure 4. Example of strong erosional effect below relatively small landslide source zone. Nam Chang landslide cluster, 2022. Photo by P. Kroh.

An important morphological factor influencing the sliding surface in the studied areas is its strong relationship with the dip and strike of the bedrock. In semi-arid and temperate climatic zones, the relationship between landslides and bedrock is traditionally classified as asequent, consequent, or insequent (Varnes, 1978). However, in the studied region of Vietnam, the vast majority of landslides were consequent. The sliding surface followed the bedrock surface, so the dip and

strike of the bedrock corresponded to the azimuth and slope angle of the landslide plane (Figure 5). This is also an effect of the weathering conditions in warm-humid climate and poor consolidation of the slope deposits with the underlying bedrock, as mentioned above.



Figure 5. Sliding surface corresponds with dip and strike of the bedrock. Nam Chang landslide cluster. Photo by P. Kroh.

The complexity of the nature is a truism, yet all scientists must confront this challenge when attempting to understand natural processes. Research on landslide mechanisms in northern Vietnam highlights this problem very clearly. The links between individual environmental components are so intricate that a complete understanding of these mechanisms remains extremely challenging. The role of specific processes, such as the type of sliding surface or the presence of piping or subsurface water flow can often only be evaluated post-factum, once their effects become visible in the landscape.

Meso-scale slope topography and bedrock depth can be identified prior to landslide events, and are increasingly feasible to analyze using remote-sensing big-data approaches with machine-learning tools. However, many important mechanisms, such as mentioned above suffusion or piping, still cannot be reliably assessed at larger spatial scales, for which predictions or forecasts for a village or commune would be required. Even with very advanced algorithms, these environmental

factors currently remain beyond our ability to analyze with sufficient accuracy.

Despite these challenges, geomorphological mapping remains a highly effective method for understanding the mechanisms governing the formation of mountain landscapes.

CONCLUSIONS AND FINAL REMARKS

Seasonal monsoon and typhoon rainfall, combined with described above geomorphological conditions create a significant landslide hazard. Interactions between rainfall, topography, geology, and soil properties are highly complex, and the role of individual components within this system is difficult to evaluate. Geomorphological analyses of rainfall-induced landslides indicate that, although monsoon and typhoon rainfall remains the primary trigger, other environmental factors determine the type, scale, volume, and extent of landslide processes. A good example of this complexity is the set of secondary processes, such as suffusion and soil piping, which are rarely considered by researchers, yet may play a crucial role in controlling the location of landslides.

Long-term weathering has produced slope deposits that are easily saturated and poorly consolidated. This condition promotes intense erosion within the transport zone, as well as flow-type transport and accumulation of rock masses. As a result, the earth/debris flow type dominates in the accumulation zones, even when the source zones can be classified differently.

The strong predominance of translational landslides in the source zones indicates that the dip and strike of the bedrock are key factors, playing a much greater role in this region than in temperate or colder climates, where the proportion between rotational and translational landslides differs.

ACKNOWLEDGMENTS

The research activities financed by the funds granted under the Polish National

Science Centre project no 2023/49/B/ST10/02879.

REFERENCES

- Fidan S, Tanyaş H, Akbaş A, et al (2024) Understanding fatal landslides at global scales: a summary of topographic, climatic, and anthropogenic perspectives. *Natural Hazards* 120:6437–6455. <https://doi.org/10.1007/s11069-024-06487-3>.
- Froude MJ, Petley DN (2018) Global fatal landslide occurrence from 2004 to 2016. *Natural Hazards and Earth System Sciences* 18:2161–2181. <https://doi.org/10.5194/nhess-18-2161-2018>.
- Gian QA, Tran D-T, Nguyen DC, et al (2017) Design and implementation of site-specific rainfall-induced landslide early warning and monitoring system: a case study at Nam Dan landslide (Vietnam). *Geomatics, Natural Hazards and Risk* 8:1978–1996. <https://doi.org/10.1080/19475705.2017.1401561>.
- Gobin A, Nguyen HT, Pham VQ, Pham HTT (2016) Heavy rainfall patterns in Vietnam and their relation with ENSO cycles. *International Journal of Climatology* 36:1686–1699. <https://doi.org/10.1002/joc.4451>.
- Gómez D, García EF, Aristizábal E (2023) Spatial and temporal landslide distributions using global and open landslide databases. *Natural Hazards* 117:25–55. <https://doi.org/10.1007/s11069-023-05848-8>.
- Highland, L. M., & Bobrowsky, P. (2008). The landslide handbook-A guide to understanding landslides (No. 1325). US Geological Survey.
- Hung O, Leroueil S, Picarelli L (2014) The Varnes classification of landslide types, an update. *Landslides* 11:167–194. <https://doi.org/10.1007/s10346-013-0436-y>.
- Pham-Thanh H, Ngo-Duc T, Matsumoto J, et al (2020) Rainfall Trends in Vietnam and Their Associations with Tropical Cyclones during 1979-2019. *SOLA* 16:169–174. <https://doi.org/10.2151/sola.2020-029>.
- Tu TV, Duc DM, Tung NM, Cong VD (2016) Preliminary assessments of debris flow hazard in relation to geological environment changes in mountainous regions, North Vietnam. *Vietnam J Earth Sci* 38:277–286. <https://doi.org/10.15625/0866-7187/38/3/8712>.
- Van Tien P, Luong LH, Duc DM, et al (2021a) Rainfall-induced catastrophic landslide in Quang Tri Province: the deadliest single landslide event in Vietnam in 2020. *Landslides* 18:2323–2327. <https://doi.org/10.1007/s10346-021-01664-y>.

- Van Tien P, Nhan TT, Luong LH, Cuong TQ (2024) Physical Mechanism and Numerical Simulation of Landslide Dam Formation. In: Abolmasov B, Alcántara-Ayala I, Arbanas Ž, et al. (eds) *Progress in Landslide Research and Technology*, Volume 3 Issue 1, 2024. Springer Nature Switzerland, Cham, 399–408.
- Van Tien P, Trinh PT, Luong LH, et al (2021b) The October 13, 2020, deadly rapid landslide triggered by heavy rainfall in Phong Dien, Thua Thien Hue, Vietnam. *Landslides* 18:2329–2333. <https://doi.org/10.1007/s10346-021-01663-z>.
- Varnes, D. J. (1978). Slope movement types and processes. In: Schuster, R. L., & Krizek, R. J. (eds.) *Special Report 176. Landslides: Analysis and Control* Transportation and Road Research Board, National Academy of Sciences, Washington, DC: 11-33.

DOI: 10.15625/vap.2025.0184

Study of Reforestation for Reducing Slope Failure and Global Warming

SweePeng Koay^{1,*}, Kazuho Ito², Satoshi Murakami³, Zaharin Yusoff⁴

¹SPEC Advances Services, Penang, Malaysia

²Yamanashi University, Kofu, Japan

³Fukuoka University, Fukuoka City, Japan

⁴Universiti Sains Malaysia, Penang, Malaysia

*Email: spkoay.09@gmail.com

Abstract: Deforestation without reforestation causes global warming which, undoubtedly, is a risk to human beings. Floods in deserts, glaciers collapsing, lakes and rivers drying up, mountain wild fires, and occurrences of unpredicted weather that damage crops, are various recent phenomena alerting us to protect the nature of the earth. Increment of carbon dioxide in the atmosphere is the main reason causing global warming and abnormal weather, which is a fact pointed out by many natural environmental scientists. Unplanned logging on forest slopes along roadsides causes landslides resulting in casualties every year in this world. It is also one of the causes of increment in carbon dioxide and destruction of the environment. Well planned reforestation with suitable plants can reduce such casualties and prevent environmental damage, as trees play an important role in stabilizing the slopes to prevent the occurrence of landslides as well as reducing carbon dioxide and contributing to environment conservation. Given this situation, in this study we propose the selection of the appropriate trees as a countermeasure to shallow landslides.

Keywords: Reforestation, Slope Failure, Global Warming, Carbon Dioxide, Environment, Sustainability.

INTRODUCTION

Nowadays, there are many natural disasters that are happening and causing billions of dollars in economic loss every year. Undoubtedly, human beings' activities, namely

unplanned loggings, fuel burnings and unnecessary developments, trigger the tremendous climate changes that damage the earth's environment. Incidents such as: i) unpredicted heavy rainfall caused floods in Dubai on 16 April, 2024; ii) the Blatten glacier collapse occurred on 28 May 2025, in Switzerland, resulted in many casualties; iii) the land ice sheets in both the Antarctica (as shown in Figure 1) and Greenland have been losing mass year by year; iv) the occurrence of a linear precipitation band in Kyushu, Japan, has caused many slope failures and floods in Fukuoka, Nagasaki, Kumamoto and Kagoshima in August 2025, which is something that had never happened in their history before. The trend of the rising number of days in a year with temperatures higher than 35°, in Japan (as given in Figure 2) shows a clear sign of global warming. These abnormal phenomena have occurred due to the increment of greenhouse gases, such as carbon dioxide, methane and nitrous oxide, which are released to the atmosphere, thus contributing to global warming, according to the study <https://news.climate.columbia.edu/2021/02/25/carbon-dioxide-cause-global-warming/> by Jason E Smerdon.

Suitable reforestation and replanting activities, and saving energy usage are very much encouraged to prevent the situation becoming worse as well as to bring back the green to our planet, the earth. Reforestation is not only to secure the environment and to stop desertification, it can also prevent slope surface

failures to save human lives and properties. Here, we shall discuss, in particular, about the function of plant roots as a means in the prevention of shallow landslides in the hill slopes and in mitigating global warming by planting trees for reducing carbon dioxide emissions towards environmental conservation.

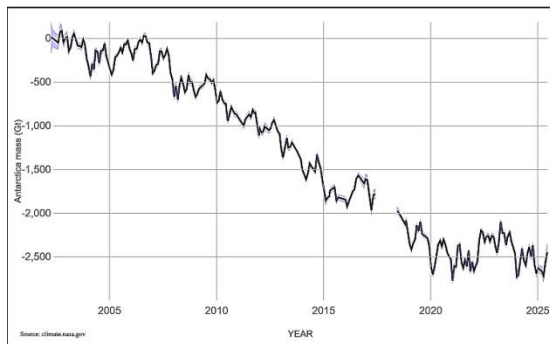


Figure 1. Antarctica Mass Variation since 2002
(Data source: Ice mass measurement by NASA's GRACE satellites, NASA)

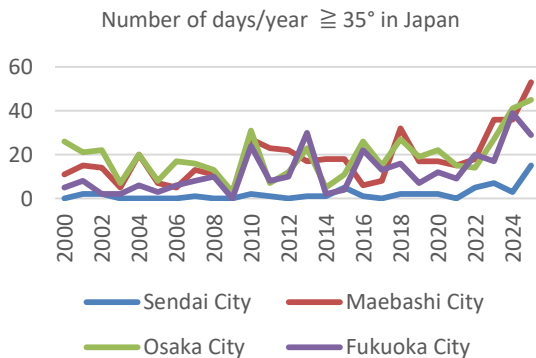


Figure 2. Number of days with temperatures $\geq 35^\circ$ in Japan, from 1 Jan. 2000 until 25 September 2025
(Data source: Japan Meteorological Agency)

THE ADVANTAGES OF PLANTING TREES

Root Functions and Slope Failure Prevention

Recently, unexpected rainfall volume, caused by a linear precipitation band in many places, triggered slope failures in hilly areas, and the number of incidents has increased tremendously, year by year. Reforestation by planting trees on the slope is one of the natural approaches to prevent surface landslides and also to provide: a) water source cultivation function, such as flood mitigation, water

resource retention, and water purification, b) creating a comfortable environment, as the roots absorb water and the evaporation of water from the leaves to cool down the temperature, c) the plants' fine roots which are symbiotic with soil microorganisms, fostering nutrient absorption provides a conservation function of biodiversity, and d) a timber production function, as stated by Hirano Y. (2024).

Most tall trees, such as the *Quercus serrata* (Figure 4) and the Japanese cedar (fir), have two types of roots to stabilize themselves (Makita N., 2024). There are horizontal roots and taproots. Horizontal roots overlap one another with the roots of neighbouring trees to form a network to strengthen retention, thus preventing their displacement. Taproots play an anchor role to grow deep into the soil like stakes, to prevent sloping land movements (Figure 3). As the lengths of the *Quercus serrata* and Japanese cedar taproots are approximately 3 meters, they are very effective to prevent surface landslide, which is less than 3 meters depth.

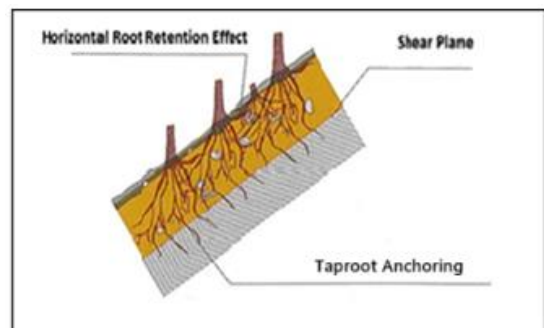


Figure 3. Root Soil Shear Resistance
(Source from "Guideline for Building Disaster-Resilient Forests" by Forestry Division, Nagano Prefectural Government, 2008)

Oil palm trees (Figure 5), also have 2 types of roots, and they are mostly found in Malaysia and Indonesia. They are cultivated not only for producing oil for food, oil for industry, and as biofuel, but they can also prevent slope failures and conserve a green environment. In accordance with Yazid I. I. (2018), the horizontal oil palm roots can be found at a

depth of 15-20 cm and spread along 2 m from the stem. The taproots are found at a depth of 90 cm up to 2 m inside the ground.

Similar to the *Quercus serrata* and the Japanese cedar, the horizontal roots that spread in the surface layer of the soil will grip the soil, and the taproots serve to anchor the soil that structurally support the plant stand so that the trees would not be easily uprooted by the movement of the soil mass.

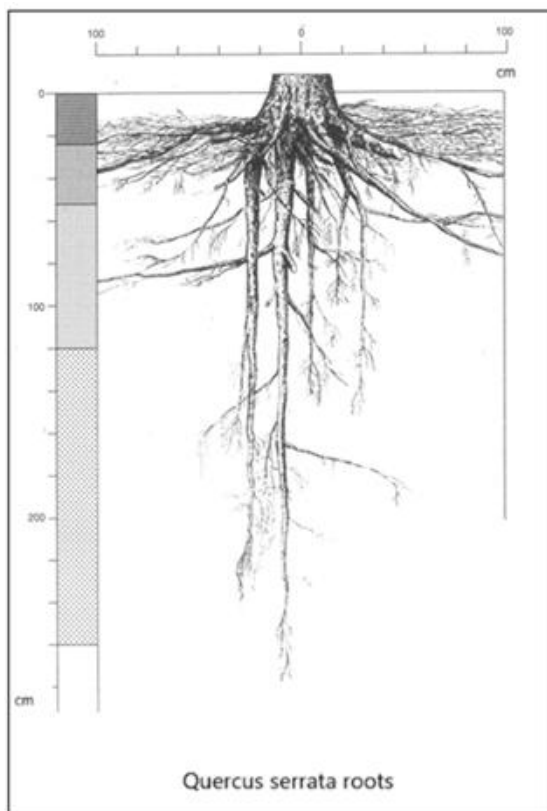


Figure 4 The radius of horizontal *Quercus serrata* roots is about 1 meter and the depth of taproots is more than 2 meters (source from Nine Sketch Co., Ltd, Hamamatsu City, Japan <https://www.gsketch.com/archives/date/2022/01>)

Besides stabilization from land movements, by planting oil palm trees (reforestation), oil palm roots also play an important role in providing a conducive environment for microbial activity and final bacillus decomposition of organic materials in the form of organic acid, where it can improve both physical soil properties in terms of

chemical composition and porosity. These changes are expected to create an environment suitable for the roots to grow and develop optimally.

Oil palm roots can also be seen as a help in maintaining the growing environment balance system by generating a natural water catchment. This can be seen in the dry season, where the grass under the oil palm trees do not dry out very quickly, and with the soil humidity being maintained in quite optimal conditions.

To maintain such an optimal environment, the prevention of nutrient losses through runoff needs to be implemented. In a study reported in Vijiandran J.R. (2017), heavy rainfall causes soil and nutrient loss through surface runoff and erosion in oil palm plantations. Compound fertilisers are recommended for maintaining the health of oil palm trees, as they clearly contribute towards much lower losses for nitrogen, phosphorus and magnesium compared to the use of the straight fertilisers. Potassium losses were reported to be marginally higher for the compound fertilisers compared to the straight fertilisers. Other than the terracing method, Mohsen B. (2014) recommended organic mulches and silt pits to conserve water, soil and nutrients from runoffs by rainfall in sloping lands to contribute towards an optimal environment.



Figure 5 Oil palm trees (Source from: The Oil Palm Tree: Parts, Anatomy, Structure, and Characteristics by Chimeremeze Emeh, Palm Oil Pathway)

It is thus clear that reforestation with suitable plants on the slopes, together with proper biological, chemical and physical

treatment, can prevent surface erosion, which could otherwise lead to slope failure. The proposed steps would conserve the surroundings environment by storing water, purifying water, allowing rainwater to soak into the surface soil for flood prevention, as well as provide fresh air supply, especially oxygen, and lowering temperatures.

Study on Shear Reinforcement Strength by Tree Roots

In Abe K. (1997), the simulation and analysis of slope stabilization using tree roots, on different types of soil, were carried out and the results were reported, as given in Table 1 and Table 2. As a target of comparison, Type A has 80 cm thickness of top soil that is direct contact with the bedrock. The bedrock does not have fractures. Essentially, the top soil is not stable in the steep slope. Type B slope has 80 cm thickness of top soil that is direct contact with the bedrock, but the bedrock has many fractures. Taproots can penetrate these bedrock fractures, and their intrusions made the slope stable. Type C slope also has 80 cm thickness of top soil, but in between the top soil and bedrock, there is transition layer. Tree roots can grow through this transition layer but can be affected by the hardness of the transition layer. After surveying (forest stand and tree root distribution) and running pull-out tests, without considering the pulling angle and root displacement, by applying a practical ΔS (shear reinforcement strength) model and a root distribution model, the increment of values of ΔS occupied as a factor of safety values can be obtained.

However, according to a study by Kaketani R. (2018), after taking into account the pulling angle and root displacements, the deterrence of slope failure in the slope, the ratio of ΔS in Abe K. (1997) study, was considered to be overestimated by 29% to 58%. Figure 6 is the graph showing data on the ratio of ΔS obtained in factor of safety vs forest age, with the pulling angle and root displacement being taken into account.

Table 1. Slope factors (initial condition for slope stability simulation)

Slope Type	A	B	C
Slope Angle (°)	32	32	32
Thickness of top soil (cm)	80	80	80
Soil cohesion (N/cm ²)	0.2	0.2	0.2
Soil internal angle (°)	30	30	30
Cohesion of bed rock (N/cm ²)	20	20	20
Internal angle of bedrock (°)	40	40	40
Depth of subsurface ground water (cm)	0	0	0
Soil density (t/m ³)	1.3	1.3	1.3
Density of bedrock (t/m ³)	2.5	2.5	2.5
Maximum depth of root growth(cm)	80	100	100

Table 2. Tree factors

Tree Age (Japanese Cedar)	10	20	30	40
Diameter at Breast Height(cm)	5.0	13.8	20.0	24.3
Tree Height (m)	5.4	12.1	15.8	18.1
Tree trunk density(ha ⁻¹)	3430	2265	1345	1030
A ₀ (m ²)	2.9	4.4	7.4	9.7

Note: A₀: Area occupied by one tree.

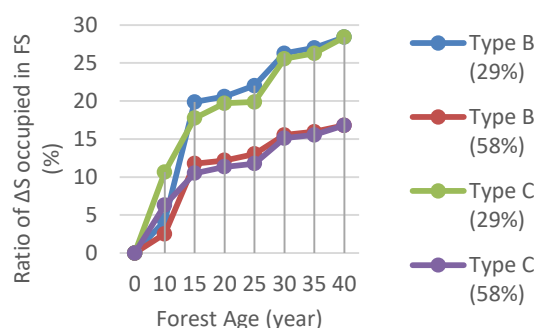


Figure 6. Relationships between forest age and ratio of ΔS occupied in a factor of safety

Factor of Safety Calculation with and without Shear Strength Reinforcement by Tree Roots

The factor of safety value is calculated by using simulation (Koay et al., 2013) on the equation of factor of safety (Hiramatsu et al., 1992) as below:

$$F = \frac{\tau_r}{\tau} = \frac{\frac{c}{\cos \theta} + \{\gamma_s \cdot H - (\gamma_s - \gamma_b) \cdot H_1\} \cdot \cos \theta \cdot \tan \Phi}{\{\gamma_s \cdot H + (\gamma_t - \gamma_s) \cdot H_1\} \cdot \sin \theta}$$

where H is soil height (m), H_1 is ground water table (m), θ is slope angle ($^\circ$), τ_r is resisting force of the slope (N/cm²), τ is sliding force (N/cm²), c = cohesion force (soil sticky force) (N/cm²), Φ = internal friction angle ($^\circ$), γ_s = soil unit weight (g/cm³), γ_t = saturated soil unit weight (g/cm³) and γ_b = soil unit weight in water (g/cm³), the slope angle = 28° , and the soil properties: cohesion = 0.25 N/cm², effective porosity/valid porosity = 0.4, saturated hydraulic conductivity = 0.02 m/h, internal friction angle = 35° and soil unit weight = 1.36 g/cm³, which data are obtained by site surveying and laboratory test. With the consideration of tree roots contribute shear reinforcement strength positively for slope stabilization, the factor of safety becomes

$$F_n = x \cdot F$$

where the value x is depending on the age of forest. We apply the data from Abe K. (1997) and assume 58% overestimated Kaketani R. (2018). The simulation results, by using F calculation (Koay et al., 2013), show that after 4 hours continuous 20mm/h rainfall, factor of safety value is 0.996 as 1st. row in Table 3, which means the slope is in the risk condition. Other rows in Table 3 show F_n result of the simulation, and the effectiveness of shear reinforcement strength by tree roots in slope stability is well proven.

Table 3. Effectiveness of the tree roots by simulation

Forest Age (years)	x (58% overrated)	F_n value < 1
0(without tree)	1.000	after 4th hour
10	1.017	after 5th hour
15	1.069	after 6th hour
20	1.114	after 8th hour
25	1.133	after 8th hour
30	1.147	after 8th hour
35	1.161	after 9th hour
40	1.168	after 9th hour
45	1.181	after 9th hour
50	1.185	after 9th hour

Analysis Data from the Monitoring Site

The rain gauge, in the monitoring site (Figure 7), which is located $05^\circ, 36.042'N$; $101^\circ, 35.546'E$, elevation 906m and the height of the peak is 1065 m, along East-West Highway in Malaysia, recorded the volume of rainfall exceeded 415cm in 3 days, from 00:00 22nd. December, 2014 to 23:59 24th. December, 2014, where the slope angle was 33° . Inclinometers started showing the movement of slope at 05:00, 22/12/2014. And, our simulation result, with the slope angle = 33° (site survey) and the soil properties: cohesion = 0.25 N/cm², effective porosity/valid porosity = 0.4, saturated hydraulic conductivity = 0.02 m/h, internal friction angle = 35° and soil unit weight = 1.36 g/cm³, showed that the F value was also below 1 in the slope, at 05:00, 22/12/2014, as Table 4.



Figure 7. Monitoring site $05^\circ, 36.042'N$; $101^\circ, 35.546'E$ along East-West Highway in Malaysia (taken on 22nd. April 2014)



Figure 8. The site photo (inclinometer case) was taken on 22nd. April, 2014 before the slope failure

Table 4. Simulation result of F values by using rainfall data from rain gauge

Date and Time	Rainfall (cm/h)	F Value
22/12/2014 1:00	7.5	1.0161
22/12/2014 2:00	14	1.012
22/12/2014 3:00	20	1.0078
22/12/2014 4:00	8	1.0054
22/12/2014 5:00	12.5	0.9941
22/12/2014 6:00	15.5	0.9882
22/12/2014 7:00	7.5	0.9853
22/12/2014 8:00	5.5	0.9756
22/12/2014 9:00	6.5	0.9708
22/12/2014 10:00	3.5	0.9704
22/12/2014 11:00	5.5	0.9716
22/12/2014 12:00	5	0.9759
22/12/2014 13:00	1	0.9829
22/12/2014 14:00	0.5	0.9910
22/12/2014 15:00	0.5	0.9994

After the heavy rainfall, the crack occurred surroundings the inclinometer case Figure 9 comparing to Figure 8. From the result of the simulation as in Table 4, F value was below 1 at 05:00, 22nd. December, 2014 and the inclinometer also showed the slope movement at 05:00, 22nd. December, 2014 (Figure 10).



Figure 9. The site photo (inclinometer case) was taken on 16th. February 2015 after the slope failure

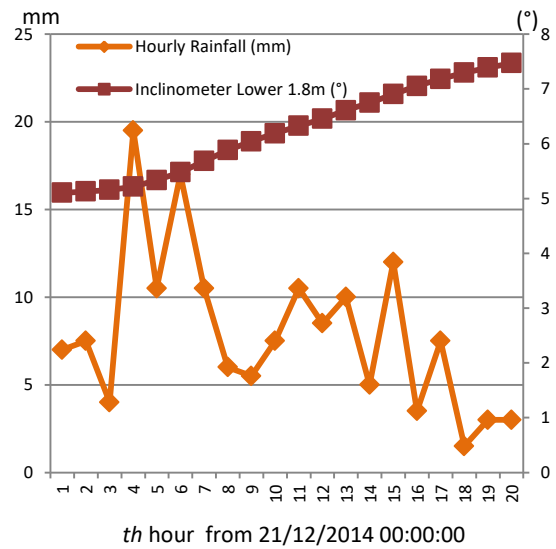


Figure 10. Data from inclinometer and rain gauge in the site



Figure 11 Monitoring site photo which was taken on 26th December 2014 after landslides happened in 05°,36.066'N; 101°,30.483'E

According to the news, landslides happened in 05°,36.066'N; 101°,30.483'E at 8:59 pm, 23rd. December 2014, where is near to monitoring site (<https://api.nst.com.my/news/2015/09/east-west-highway-closed-after-cave>). Figure 11, which was taken on 26th. December 2014., shows that there were still trees in above the head scarp. We can conclude that tree roots raised F_n value to above 1. With the assumption that trees age was 15 years, top soil height was 100 cm, and with the survey results from Abe K. (1997) and Kaketani R. (2018), F_n was equal or larger than 1.0271 ((1 +

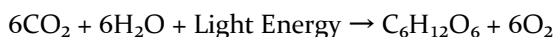
$0.139 \cdot 0.42) \cdot 0.9704$, where 0.9704 is the lowest F value in Table 4). Trees still in above the head scarp, after heavy rainfall during that period, proved that the tree roots had effect to prevent landslide. In the other words, if reforestation, by planting suitable trees, was carried out in the monitoring site, the slope movement might not happen.

GREEN AND HEALTHY ENVIRONMENT

Energy Sustainability and Reducing Carbon Dioxide for Preventing Global Warming

Besides increasing shear reinforcement strength by trees, photosynthesis process by green plants, with chlorophyll, under sunlight produces glucose and oxygen. During photosynthesis, plants take in carbon dioxide from the air and water from the soil. Using sunlight, they transform these carbon dioxide and water into glucose and oxygen. This process is essential for producing food and oxygen, reducing greenhouse gases which cause global warming, and supporting lives on the earth. Planting more trees in the garden and hilly areas is not only to stabilize the slope, it also reduces carbon dioxide and protects the green environment.

By the below photosynthesis equation:



it is clear that trees absorb carbon dioxide and produce oxygen which is needed for breathing. According to the survey by Forestry Agency, Japan in year 2022 (https://www.rinya.maff.go.jp/j/sin_riyou/ondanka/20141113_topics2_2.html) and the calculation, in one year, one fir tree (36 years to 40 years) can absorb approximately 8.8 kg carbon dioxide and it also produces about 6.4 kg O_2 to atmosphere. In one year, one family consumes 30.9 GJ energy and emits 2.74 tonne of carbon dioxide was reported by Ministry of The Environment, Japan in 2023. It needs at least 312 fir trees to absorb one family carbon dioxide emission in Japan. In Kira T. and Tsunahide T. (1967) study, the gross productivity may follow the same trend with increasing stand age. The biomass of woody organs also increases monotonously

with age. The amount of organic matter in the soil which is consumed by the respiration of woody organs might have the same increment ratio. The respiratory consumption by leaves is naturally expected to be proportional to their biomass.

According to The Indonesian Palm Oil Association (GAPKI) report, every hectare of oil palm plantations can absorb around 161 tons of carbon dioxide every year, and produce oxygen at around 18.7 tons (<https://gapki.id/en/news/2020/07/11/ecology-the-hidden-side-of-palm-oil/>). The higher the outcome of production of oil palm plantations will absorb more carbon dioxide from the air, and the more oxygen will be emitted to the air for human beings.

Moreover, the oil palm plantations are also part of the important chain that links the sun light with the energy sources which are needed by human beings, and planted in hill slopes in Indonesia and Malaysia. Through the photosynthesis process, the energy from the sun is captured and stored in the forms of chemical energy sources as biomass.

Trees absorbs carbon dioxide and stores the energy sources by conversion carbon to biomass. The combustion of biomass, for example tree trunks and palm oil, emits carbon dioxide. Carbon dioxide will be absorbed again by trees without increasing the volume of carbon dioxide to become carbon neutral. It helps to prevent the increment of carbon dioxide toward energy and green environment sustainability.

Reforestation Activities

Reforestation, by planting suitable type of trees in the deforestation areas, especially in the hilly areas, can prevent the slope failures, the erosion and the soil runoff. However, as it will cause uncontrolled plants diseases and pollen allergy to the public, monoculture should be avoided, although it is more economical effectiveness in the short term. Multi-species plantation, in reforestation activities, is much recommended for the long term. By the same time, heavy punishment laws on natural forest destruction activities

should be imposed to stop unnecessary deforestation.

The above-mentioned trees, *Quercus serrata*, fir and oil palm tree are just examples for the study. It does not carry out the meaning of encouragement planting such trees for reforestation in everywhere. Right type of trees for right type of environment must be taken in consideration for sustainability to counter global warming to reduce disaster happening.

CONCLUSION

Slope stabilization by reforestation is an approach that is both environment friendly and contributes towards biological sustainability, as well as avoids losses of lives, the occurrence of desertification, and economic losses. Planting more plants in urban areas is very much encouraged for a healthy living environment and also for global warming mitigation. The reforestation actions for bringing back the green on this planet should be taken immediately before it is too late.

ACKNOWLEDGEMENT

We would like to thank the late Prof. Dr. Hiroshi Fukuoka, the late Toshikazu Morohoshi and Teruki Fukuzono for giving us advices and encouragements in the slope stabilization study. We are extremely grateful to Mitsuru Yabe for providing us valuable advices and data collection and special thanks to Kazuko Maeda who gave valuable ideas to save our planet. Financial supports for implementing monitoring sites from Japan International Cooperation Agency (JICA), Japan and Ministry of Higher Education, Malaysia are gratefully acknowledged.

REFERENCES

- Abe K. (1997) A Method for Evaluating the Effect of Tree Roots on Preventing Shallow-Seated Landslides. Bulletin of the Forestry and Forest Products Research Institute, Japan No. 373, 1997 105-181.
- Chapter 2 The Basics of Tree Roots (2024) (in Japan Language) Makita N., Japanese Society for Root Research, Seibundo Shinkosha Publishing Co., Ltd., Japan. (ISBN978-4-416-62309-1). 136-137.
- Chapter 3 The Basics of Tree Roots (2024) (in Japan Language) Hirano Y., Japanese Society for Root Research, Seibundo Shinkosha Publishing Co., Ltd., Japan. (ISBN978-4-416-62309-1). 144-145.
- Hiramatsu S., Mizuyama T., Ogawa S. and Ishikawa Y. (1992) Influence of Rainfall Time Distribution on Shallow Landslides. Japan Society of Erosion Control Engineering Vol.44 No.5, Ser. No.178: 3 -13.
- Kaketani R., Takizawa H., Kosaka I., Sonohara W., Ishigaki I. and Abe K. (2018), Study on Evaluating Method Using Root Pull-Out Resistance for Tree Roots Effect to Prevent Shallow Landslide. Japan Society of Erosion Control Engineering Vol. 71, No. 3, 3-11.
- Kira T. and Tsunahide T. (1967), Primary Production and Turnover of Organic Matter in Different Forest Ecosystems of The Western Pacific. Japanese Journal of Ecology Vol. 17, No.2, 70-87.
- Koay S.P., Habibah L., Sakai N., Morohoshi T. and Fukuzono T. (2012) Landslide Prediction Using Numerical Analysis. Caspian Journal of Applied Sciences Research, 2(AICCE'12 & GIZ' 12) . 336-342.
- Mohsen B., Teh C.B.S., Husni M.H.A. and Zaharah A.R. Soil (2014) Nutrients and Water Conservation Practices in Oil Palm Plantations on Sloping and Steep Lands in Malaysia. International Agriculture Congress 2014, 37 – 40.
- Vijiandran J.R., Husni M.H.A., Teh C.B.S., Zaharah A. R. and Xavier A. (2017) Nutrient Losses Through Runoff from Several Types of Fertilisers Under Mature Oil Palm. Malaysian Journal of Soil Science Vol. 21, 113-121.
- Yazid I. I., Abimanyu D. N., Supanjani, Zulfahrum C. and Riska E. (2018) Oil Palm Roots Architecture in Response to Soil Humidity. International Journal of Oil Palm Vol. 1, No. 1, 79 – 89.

DOI: 10.15625/vap.2025.0185

Improving the process of mining the steep coal seam. Case study of the seam 6(7) in Nam Khe Tam mine, Quang Ninh, Vietnam

Phi Hung Nguyen, Hoang Hiep Do, Manh Tung Bui*

Ha noi University of Mining and Geology

*Email: buimantung@humg.edu.vn

Abstract: Safe and efficient exploitation of steep coal seams is a significant challenge for Vietnamese mining engineers. Traditional extraction techniques—including shortwall methods with wood support, single hydraulic supports, and flexible shield models (such as XDY)—have proven to offer low efficiency and result in high casualty rates. Some mines have attempted longwall technology; however, mechanized coal separation is often unsuccessful due to poor adaptation of equipment to strong impacts from complex geological conditions. Recent experimental trials have successfully demonstrated the diagonal longwall technique using the ZRY support model, providing a foundation for wider application across Vietnamese mines. Nonetheless, this technique revealed drawbacks during the mining preparation phase.

Previously, installation of ZRY flexible supports was performed in an upward sequence from below, causing imbalance at the roadway floor and uneven loading at the roof, which led to support failure and collapse at the longwall face. This paper analyzes mining systems and leverages the technical features of the ZRY support to reorganize the initial installation direction—from the ventilating roadway down to the haulage roadway, progressing stepwise toward the transport entry.

Research results and actual applications have demonstrated that the improved method eliminates the cost of additional installation roadways, shortens the time required for

longwall faces to reach design capacity by 10–15 days (from 85–90 days down to 75 days), achieves a coal recovery rate of 90–95% (25–30% higher than traditional shortwall methods at 70–75%), and attains labor productivity of 6.0–6.5 tons per shift—2–3 times higher than conventional sublevel mining methods.

Keywords: Support model ZRY, ventilating roadway, transportation roadway, installation raise, load, coal seam 6(7).

INTRODUCTION

A coal seam is considered to be dip when the buried angle is more than 45° , mining for these steeply inclined hard coal deposits is very difficult [1]. Compared to the gently inclined coal seams, mining for the LDACSs (large dip angle coal seams) causes a reduction in the normal component and an increase in the tangential component of supporting gravity [2]. The reduction in the normal component leads to a reduced weight that the support can bear, therefore, smaller working of the support will be resisted. The high tangential element increases the sliding power, which impacts the support along the inclination direction of the coalface. As a result, support is likely to tilt and slide [3]. Moreover, the stability of longwalls with steep seams is affected not only by the dip angle but also by the strike angle of the coal seams (i.e. underhand or overhand mining) or passing through faults and other tectonic zones [4]. In particular, the support in the coalface is subjected to the large horizontal stress imposed by the roof, which will significantly reduce stability of the support [5]. Thus,

mining for the large dip coal seams has potential risks because of instability caused by the weak nature of the surrounding rocks and their movement after excavation 253944.

The shortwall techniques such as sublevel, room and pillar, blasting gallery... or the longwall can be used to exploited the steep seams. The sublevel caving system originated from the ore mining, sublevel caving (SLC) is a mass mining method that based on using the gravity flow of the blasted ore and waste rock in cave. This method has been applied for mining the dipping steep coal seams for over sixty years despite only being fully mechanized at the beginning of the 21st century 194851. In recent years, with the saturation of conventional coal mine resources, increasingly, steeply dipping coal seams (SDCS) with a dip angle of 35–55 and complex enrichment conditions are being mined 2952. Many scholars have carried out systematic research on the mining technology of SDCS, for example, top-coal caving mining and staggered roadway layout mining were successfully applied for SDCS 4851.

To extract high-quality coal resources, a completely mechanized variant of the sublevel caving system was designed on the basis of standard machines and equipment applied in coal mining. Exploitation was conducted from top to down at the levels of the particular mining sub-level drilling wells with the roof caving 23. The faces in the extracted coal release areas were protected by a pair of system of specially designed mechanized mining. One of the basic issues that is revealed during the extraction process of subsequent mining panels is the changeability of the rate of resource mining. The mining losses changed in the available resources from 10% to 50% 5051.

The room and pillar method, known as the bord and pillar method, is a shortwall method. This method is developed by pushing the water to drift from the main roadways to the block of coal seam forming the rooms. Pillars are formed by letting the coal be non-adhesive between the rooms. Depending on the characteristics of the coal and the rock above the seam, a part of coal in the pillars will be extracted, the remaining coal pillars will be

used to support the roof and control the movement of the strata. The diagram of the room and pillar method is presented in Figure 2b. This method is widely applied in areas whose surfaces need to be improved, for example, coal seams located under the residential areas, rivers, or roadways. The room and pillar method is also applied in areas where longwall methods face up with difficulties due to poor corrosion of coal at the top and/or in the beneath strata 42527.

Another method, named the blasting gallery (BG) method which is considered a modern room and pillar method, has been used in French and Indian coal mines. Operation of the BG method is roadway development along the door of the coal seam in the room and pillar pattern, following as the final extraction of the seam in the transmission line, creating drill holes from the developed galleries in ring patterns. The coal will be broken by the blasting method then. Blasted coal is removed by load haul dump machines (LHD) 42527. The difference between the two methods is that coal extraction from the pillar in the BG method is undertaken by the drill and blasting method, while in the room and pillar method, roadway development and coal extraction are carried out by the continuous miners. As a result, the BG method can exploit very thick seams by one transmission line, which is usually divided into slices when the continuous miners extract. A diagram of the BG method is presented in Figure 2c and 2d. The shortwall methods achieve high productivity but a low rate of coal recovery, resulting in a lot of labor accidents.

In the 1970s, the Soviet Union developed fully mechanized mining technologies for mining thick, medium-thick, and steeply dipping coal seams 56. In the 1980s and 1990s, the United States, Germany, France, the United Kingdom, India, Spain, and other countries also applied mechanized mining methods and ground control techniques to access steeply dipping coal seams; these methods were also used to handle limited experiments 131424. After nearly two decades of

research and development, China has made significant progress in developing the mining theory, application of essential technology and equipment to exploit steeply dipping coal seams, has succeeded in transforming from non-mechanized mining to fully mechanized longwall mining (fully mechanized caving) in certain conditions, and has solved the basic safety problem in mining steeply dipping seams 2122145. The main technical difficulties in applying fully mechanized mining technology are controlling the surrounding rock and mining equipment stability, skidding prevention, and flying gangue prevention. Based on the analyzed trend, prosperous development directions for steeply inclined coal seam mining are proposed 93347. Hongsheng said that: 1. Controlling the equipment stability of steeply inclined working face needs to be advanced. Gliding and toppling over of equipment are the main problems in steeply inclined working faces during mining. The adaptive capacity of supports to the change in coal seam thickness must be improved; 2. More working faces need to be automated. The difficulty for workers in walking in the steeply inclined working faces restricts the cutting speed since the machines are operated by those workers. Thus, automatic mining machines and self-advancing supports are investigated and developed. 3. Rib spalling control techniques need to be improved. Anytime, the roof fractures and the face guard are not stretched out, the massive rib spalling can happen. This would lead roof falling which block the lower end of the working face. Therefore, the structure and capacity of face guard should be enhanced to change the mechanical characteristics of coal walls and the wall stability.

Thus, almost all mines still use non-mechanized mining methods such as oblique short-wall and longwall, except for some mines that have medium-thick or extra-thick coal seams, which are mined by the fully mechanized methods. Mines in which fully mechanized methods are not applied meet restrictions of production and operation, such as low production efficiency, poor safety

operating environments, and frequent casualty accidents. Fully mechanized mining is very clearly difficult for a steep coal seam with a large inclination angle and a hard roof 262849.

DIFFICULTIES IN MINING THE STEEP SEAMS IN VIETNAM

In Viet Nam, coal is distributed mainly in Quang Ninh, Thai Nguyen, Hoa Binh, Hai Duong.... but the coal basin in Quang Ninh possesses most of the national coal reserves. All mines in Quang Ninh have steep seams such as seam 5, seam 6, seam 7 in Ha Lam coal mine, seam 10, 9V, 9T, 9BT in the South of the projects of shield pillar underground mining in Mao Khe, Uong Bi, Ha Long Moreover, these steep seams have small coal reserves, are divided by faults, strongly changes in thickness, slope angle so it is very difficult to return on investment if fully mechanized mining methods are used there. Total coal reserves at these steep seams are 40% of the reserves in the whole region. The steep seams have been exploited with the support of wood instruments, I-shaped steel bars tied by cables, the single hydraulic support, the flexible shield for a long time. In the longwall, most of the working faces are supported by the wood instruments, therefore the height of the longwall is usually from 2,0 - 2,2 meters, thus workers of average height can access the roof and attach the beams, as well as control the risks that may occur when the roof falls. However, the main problem of mining the thick seams is that coal is left on the roof or at the door of the mining table 13738. With an effort for increasing the coal production and improving the rate of recovery coal, the longwall method with many slices is used to exploit seams whose thickness is more than 4,5 meters. This method was applied at the end of 1980s in some Quang Ninh underground mines such as Vang Danh, Ha Lam, with a view of improving the ability of coal recovery in mining the thick seams. A thick seam of coal is mined by two or more slices taken parallel to the mine in descending order. Slices are sequentially taken in independent sides from top to end, simultaneously or not simultaneously; the

height of each slice is 2.0-2.2m. To separate the underlying slices, an artistic roof is created by leaving a layer of coal seam with a thickness of 0.4 to 1.0m among the slices 353738.

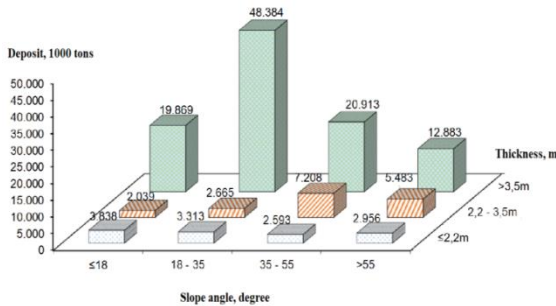


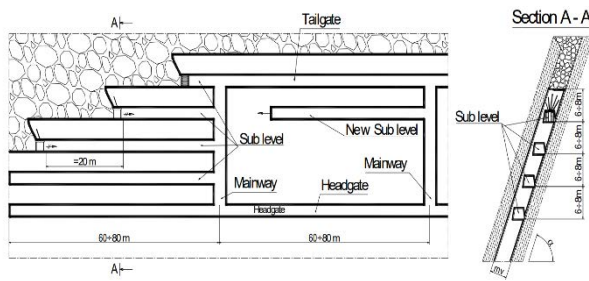
Figure 1. Statistics of reserves with thickness and slope angle of the coal seams in Quang Ninh

Although the multi-slice longwall method improves the rate of coal recovery more than the single-segment longwall, the mining productivity is low due to some peaks. The main issue of extracting the beneath slices is that controls the stability of the roof. The remaining art charcoal layer among the slices is easy to be fractured due to the weight of the rock blocks broken from the goaf of the upper slices. Therefore, if the art coal layer is too thin, it is necessary to do more work to control the potential hazards of the fallen roof on the longwall, especially in which the face of the beneath slices operate under the goaf area of the upper slices. In addition, the instability of the roof can make it unsafe. Leaving a thick layer of art coal among the slices can prevent the potential danger from the broken rock block that falls down, but in this case, loss of coal is greater 63738.

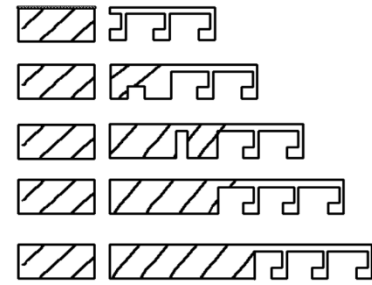
With steep seams, the most common methods used in Vietnam in the past were the blasting gallery method BG as Figure 2c, the Blasting sub-level stopping system in Figure 2a. The supporting material is wood or steel, coal is separated by the dynamite. These two systems have the low investment capital, fast payback time, and easy operation. The other challenge of the application of the room and pillar method in Quang Ninh mines is the road development technology being used there. In the room and pillar method, many gateroads

need to be driven, and coal that was extracted from roadway development accounts for a large proportion of the total coal product. The gateroads should be operated by mechanized mining equipment in order to get a high output from the room and pillar method. However, the disadvantage was seen that almost all gateroads in the underground coal mines in Quangninh have been driven by the drilling and blasting method, coal is loaded on the chain conveyor or locomotive cars by manual means, and the face is supported by steel arches or timber beams 43437. The main reason for the low advance rate is the attrition of time and labor in transporting and erecting support materials, because all the gateroads are supported by arch steels or steel/wooden bars. when the coal seams are so steep that the workers must exploit continuously, driving through the gateroads and transporting support materials by manual method will certainly increase the costs and time of roadway development. Therefore, the low advance rate of the process of roadway development will limit the efficiency and prevent the increase of coal production if the room and pillar method is applied in the Quangninh coal field 43538.

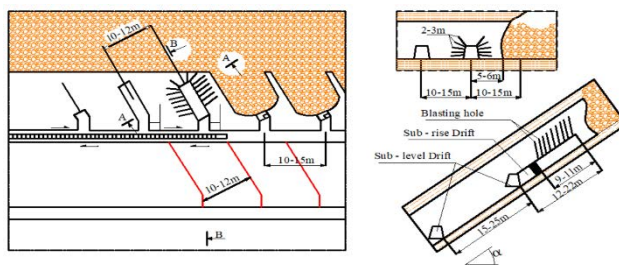
In reality, the production BG method has high productivity per man-shift. However, the ability of coal recovery is low and the proportion of accidents is high, which are disadvantages of the method. Statistics from many coal mines applying the BG method show that coal recovery is less than 60%. The reason is due to the weak or moderately strong roof of seams, so in mining process a large amount of coal is blocked by collapsing rock from the roof, or by drifting props for supporting before blasting, as illustrated in Figure 2d. In some situations, a large volume of coal was still hanging in the goaf area. Workers were easy to break safety management regulations, they entered into the goaf area to drill one or more small blast holes in order to get some of the stuck coal.. In reality, a lot of death has been reported in the Quangninh coal eld because of cases like that 41637.



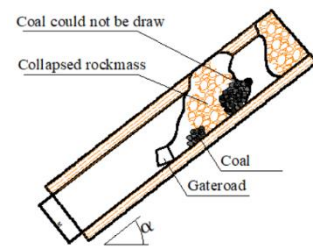
a. Technical diagram of Sublevel mining method



b. System of room and pillar mining



c. The blasting gallery (BG) method



d. coal loss of BG mining system

Figure 2. Mining system of room and pillar method, BG and Sublevel method

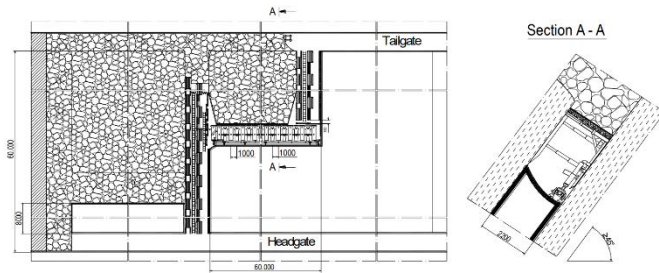
In Viet Nam, exploiting by sublevel method with using the single hydraulic supports, supported by semi-mechanized shields model XDY-iT2 / LY or mining by dynamite are being limited (Shown in fig 2a and 3). This method has the same disadvantages as BG method such as low coal recovery, high proportion of happening accidents, large ratio of roadway development per produced tons of coal, many driven gateroads in steeply flooded conditions 353638. The mechanization technology retreats along with the seam dip, extracting the high steep thin coal seams by coal plough has been applied since 2008 in Mao Khe and Hong Thai coal mine, supported by shield support 2ANSHA. In the period of 2007-2013 (Figure 3a), with mining of steep thick seams, Vang Danh and Ha Long coal mines had trial application of shortwall technology, face was supported by power shield model KDT-1, KDT-2, and top coal caving through blasting drilling in the long hole (Figure 3b) 7811. However, both of the projects fail to achieve the proposed target. Objective reasons are complicated geological conditions, water making coal slurry, too big

mine pressure ... Subjective reasons are that distance between the rigs is large, the manual dynamite charging technology is inefficient and time-consuming due to non mechanized explosion stage, in the bordering area between the longwall and the ventilation roadway, and transportation continuously has to resist cropping ... (for the longwall using the KDT rig); Much work must be done manually, the jacking in the adjacent area between the longwall and the ventilation roadway, transportation takes many stages due to large-scale face sliding, and slipping, toppling of the equipments, so application of fully mechanized mining technology be difficult and limited, the large investment capital is not suitable to the seam with small reserves, the slope angle of the seam makes the support fall ...

Fully mechanized mining is very difficult for a steep coal seam with a large inclination angle and a hard roof [12]. As a simple and easy mining method, a flexible shield method for supporting minerals mining has been widely used in the steep coal seam mining. However, mining under a hard roof by the caving

method, a large area of the roof can be hung, which will lead to a collapse of integrity and

will have a strong impact on the working face 32629.



a. Diagram of mechanized mining in Mao Khe



b. Using the support model KDT

Figure 3. The fully mechanized technique was used in Mao Khe and Ha Long mines

MINING METHOD FOR OVERCOMING THE INFLUENCE OF THE LARGE SLOPE ANGLE

Rationale

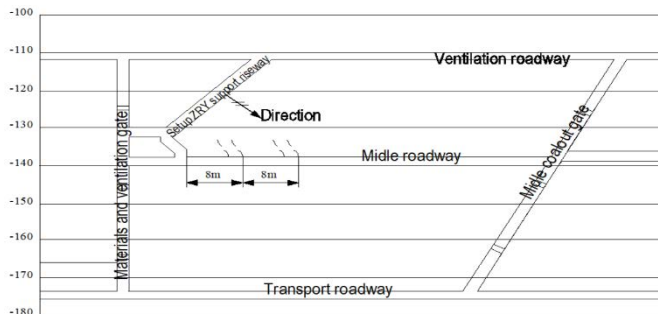
For a long time, underground mining in Vietnam has faced many challenges in exploiting the steep seams; it is essential to increase productivity and safety in these areas. The above analysis shows, shortwall face has high productivity per shift but the amount of preparation roadway is large (sublevel), coal loss is big (room and pillar, BG), or equipment is inappropriate with regional geological conditions (KDT rig or 2ANSH technology) so it is necessary to improve technique to match the specific characteristics of Vietnamese mines 8151832. Besides, the longwall operates more stably than the shortwall. Therefore, the mining direction for the steep seams is the longwall method. In term of geometry, the inclined angle created by the diagonal of the rectangle is always smaller than the right angle. This is an important basis for forming the diagonal longwall system. The diagonal longwall is established by building a raise that is dug diagonally at a steep angle to the direction and slope angle of the seam, then form a diagonal face with a slope angle of 20 to 30 degrees (Figure 4a). The key technical issues for achieving the safe, efficient coal mining and high coal recovery ratio are the surrounding rock control in strong strata behaviors that operate face -to- face, efficient mining technology, and development of equipment in

the complicated mining seam. Thus, the paper studies “hydraulic support and surrounding rock coupling control theory and technology” based on long-term technological research and innovation practice 202941.

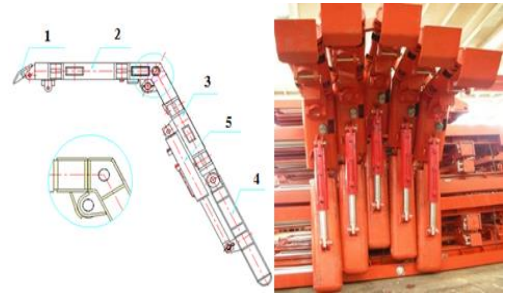
The invent of the support model ZRY (Figure 4b) is the result of specialized research for the slope seams, especially suitable for small-scale seams because the price of the model ZRY is cheaper than the mechanized support [18, 33, 34]. The support ZRY is flexible with all variation conditions in thickness and slope angle of the seam. Each soft support ZRY consists of details: (1) oriented bar: connects to the roof bar by turning pegs, slide on the seamwall when the support moves, (2) roof bar (main bar): connects to the oriented bar (turning pegs) and the rear bar (hard pegs), (3) rear bar: connects to the roof bar (hard pegs) and the tail bar (turning pegs), (4) Tail bar: connects to the rear bar by the turning pegs to control the tail bar straight or folded, (5) Piston for controlling the tail bar: One side is connected to the rear bar, the other is connected to the tail bar, operated by control hand and hydraulic system. – The hydraulic system controls piston of the tail bar: the cyclic hydraulic system, has 3 control hands to operate the tail bars of three supports. With such a structure like that, all the pressure generated by the collapsed rock wall is transferred to enhance the friction force at the top and foot of the support, so, the protection

ability for the longwall space is increased. Because of not having the beneath plate, the hydraulic piston is both a force transfer

element and a flexibility creating part when the thickness and slope angle change.



a. Diagram of digging the mining previous preparation roadway method.



b. The support model ZRY

Figure 4. Diagram of constructing the diagonal longwall using the support model ZRY

Experiment for assessing the production reality

Base on the above analyzed theory, the Vietnam Coal and Minerals Corporation conducted experiments from 2015 to 2018 in 3 different steep seams in some mines such as Hong Thai (2015-2017), Uong Bi (2016-2019), Mong Duong (2017-2020).

Preparation: The mining area is prepared by stratifying according to the ventilation roadway and the transportation roadway. The vertical height of the longwall floor (stratified) is usually chosen $30 \div 50$ m, corresponding to the length of the diagonal longwall of $60 \div 110$ m (the slope angle of the longwall is $25 \div 28^\circ$). At the ventilation level and the transportation level of the floor (or strata), the roadway is dug along the ventilation seam and the transportation seam to the field border. From the longwall along the transportation seam at the border, a coal removing crosscut and the initial travel crosscut are dug, the distance between two crosscuts is $6 \div 8$ m. The length of the crosscut depends on the width of the coal pillar for protecting the transportation roadway, the minimum length of crosscut is 5.0m. At the point where stop digging the crosscut, a roadway that connects two crosscuts is opened, then the diagonal raise is opened up to the ventilation roadway based on the connecting roadway. From the initial raise,

the soft support will be installed to exploit the longwall. During the mining process, digging the coal removing crosscut and ahead ventilating the longwall face is conducted simultaneously, the distance between the crosscut is $6.0 \div 8.0$ m so that, in front of the longwall face, $2 \div 3$ crosscuts are maintained ahead.

The longwall mining: Mining is conducted by drilling and blasting, the sequence of mining is from bottom to top in segment with the length shown according to the mining passport, the mining progress of the face is 0.8m per one cycle. The longwall uses the mechanical soft support, on the top of the support, a steel mesh is covered to prevent and limit rock from entering the longwall and to help the support to be recovered conveniently. At the foot of the longwall, the horizontal longwall is maintained with a length of $15 \div 20$ m, at the head of the longwall, the horizontal longwall is maintained with a length of $10 \div 15$ m. After each mining cycle, the supports themselves move in the direction of the mining face with a distance that is equal to the mining progress through rock pressure broken above the support and the weight of the support. According to the progress of the movement, the horizontal longwall part at the foot is longer and the horizontal longwall part on the ventilation roadway is shorter. Therefore, after a certain number of mining cycles, the supports

at the foot of the longwall need to be recovered and moved to along the ventilation seam to install additionally.

Coal transportation: Coal mined from the longwall face slides down to the coal removal crosscut, then flows to the roadway raking trench along the transportation seam. From the roadway along the transportation seam, coal is transferred outside through the mine's general transportation route

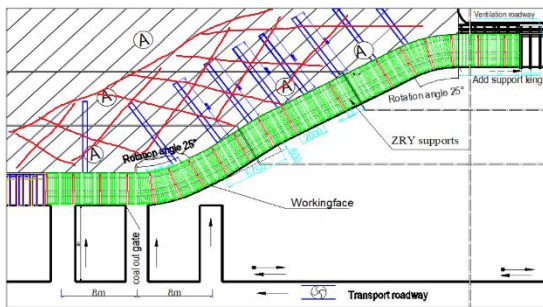
Ventilation: Ventilation for the longwall is conducted through the general pressure reducing line of the entire mine. Clean wind outside enters the open roadway, go up the transportation seam and the coal removing crosscut to ventilate the longwall. The waste wind of the longwall goes through the ventilation seam and is pushed out according to the wind escaping roadway.

Drainage: Water released from the mining area of the longwall flows itself through the drainage ditch system on the roadway designed with an outward slope of 5‰ and drains outside by the drainage system of the mine.

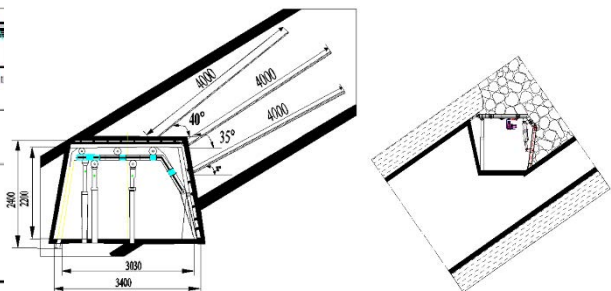
Diagram of preparation and exploitation steps applied for underground mines in Quang Ninh is shown in Figure 3a, 4, 5.

Step 1: Dig the preparation roadway system that includes the transportation raise connecting the ventilation roadway and the main transport roadway, then from the raise excavate the stratified roadway, dig the diagonal raise to install the support model ZRY. Dig other roadways as (Figure 4°, 5a).

Step 2. Install equipment system and the support model ZRY in the diagonal roadway. Drilling and blasting to load for the support (Figure 5b).



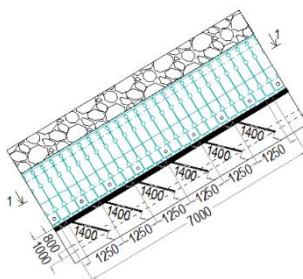
a. Installing the support



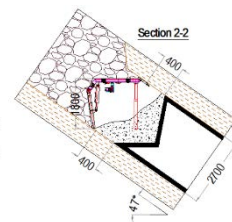
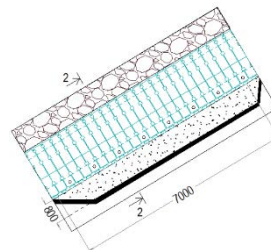
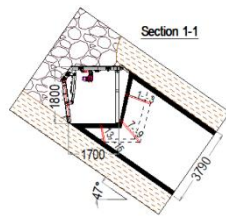
b. Drilling and blasting to load for the support

Figure 5. Install and load for the support

Step 3. Conduct periodic mining (reach design capacity) as Figure 6.



a. Drill the blast holes on the ground



b. Blast to break coal

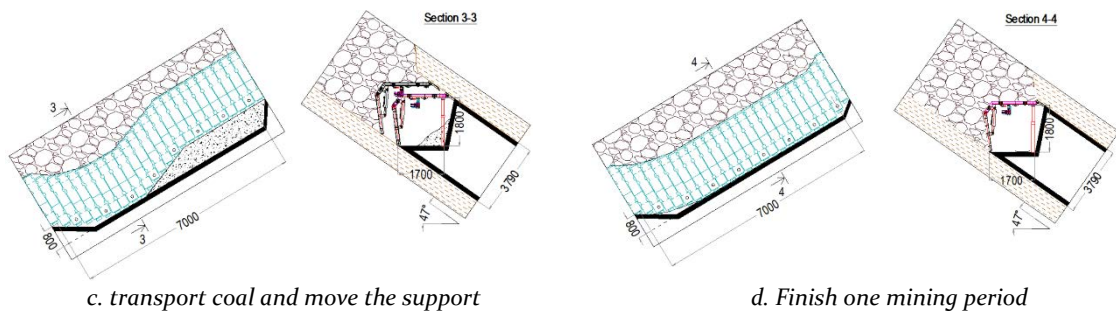


Figure 6. Diagram of the periodic mining

The experiment result in period of 2015-2020

The real experiment was conducted in Hong Thai coal company (2015-2017) at the seam 9B# level + 30 / + 95. The used technology achieved remarkable efficiency: average coal production was 400 tons/a day, the labor productivity reached 5.5-6.0 tons/a day (2-3 times as high as the sublevel method), and the coal loss was only from 12.6-16.3% [1, 18]. This technology has improved safety and has been suitable to working conditions in the steep seams. Moreover, application of the diagonal longwall system with the support ZRY reduced the development speed of roadway per ton of coal production, only 16.7 m/1000 tons (average degree of 30-40 m/1000 tons in sublevel and BG method). The time is 90 days from preparation period of the mining area to mining period with designed capacity achievement, the proportion of residual coal in the goaf area is about 30-35%.

The next tests in Uong Bi (2016-2019) and Mong Duong (2017-2020) had the similar results. Summary of application results of the new method until the end of 2020 shown that this mining technology has many outstanding advantages of technique and safety that are better than the other mining technologies at the same conditions. In terms of economic - technical indicators, the method gains the high labor productivity, coal loss and cost for roadway preparation are low, expense for wood is low. In terms of safety, process of mining is simple and easy to access, the longwall is ventilated by the wind network of mine so the working conditions for workers are improved.

The equipment in the longwall is little, the structure is simple, so the incidents in production are quickly overcome, which helps exploitation stably and continuously. The flexibility of the support model ZRY in geological conditions that strongly changes in thickness, slope angle, ensures a good support for the mining space in the longwall. Average labor productivity of 6.0-6.5 tons/ton (per man-shift) is 2-3 times as high as sublevel mining method. On the other hand, the construction cost for roadway meters/1000 tons of coal of the sublevel mining method is 35-45 m/1000 tons of coal, this of the diagonal longwall method using the support ZRY is 16.7-25 m/1000 tons of coal. This technology has the same productivity and safety level as some longwall faces that operate with lower slope angles and it is very suitable with steep seams, small reserve scale.

IMPROVEMENT OF TECHNIQUE IN THE MINING PREPARATION PHASE. CASE STUDY OF THE LONG WALL AT SEAM 6 (7) LEVEL - 175/-110 IN NAM KHE TAM MINE

Figure 4a shows that the process of load for the support is incapable of recovering fully coal behind the longwall (the red circle lines), the amount of recovery coal is 65-75% of total coal in the letter A area. It takes 85-90 days to complete the preparation steps for the periodic mining phase (gaining the design capacity). However, the rate of recover coal can increase more and the expense of digging the installation roadway is able to be economized on the base of the moving feature of the support ZYR in the diagonal longwall. Therefore, the proposed solution is that

accesses the ventilation roadway and dig down the transportation roadway. To demonstrate the above theory in practice, an experiment is conducted in Nam Khe Tam mine at seam 6(7) level -175/-110.

Natural characteristic of the area

The experimental area is at seam 6, Nam Khe Tam, Cam Pha city, Quang Ninh province, Vietnam. Seam 6(7) has some characteristics as: Average thickness (m_{tb}) is 3.79 m; Average slope angle (α_{tb}) is 48° ; Volumetric weight of coal (γ) is 1.44 T/m^3 ; Side length (L_p) is 260m; Length in slope direction of stratification (L_d) 40; rock in the side of seam: a siltstone layer located directly on the coal seam has the thickness of $8.6 \div 32.2\text{m}$, average of 15.8m, there are layers of claystone, lenticular coal clay. The siltstone layer has compressive strength $\sigma_n = 41.61 \div 3910.00 \text{ G/cm}^2$, average of 425.79 G/cm^2 , average volumetric weight $\gamma = 2.68 \text{ g/cm}^3$. The wall rock layer is a siltstone of moderate stability and collapse. Above the siltstone layer there is a set of sandstone with a thickness of $12.7 \div 34.8\text{m}$, with an average of 22.3m. Compressive strength of sandstone layer $\sigma_n = 117.74 \div 3433.51 \text{ G/cm}^2$, volumetric weight $\gamma = 2.70 \text{ g/cm}^3$. The wall rock layer is sandstone which is stable and difficult to collapse. Pillar

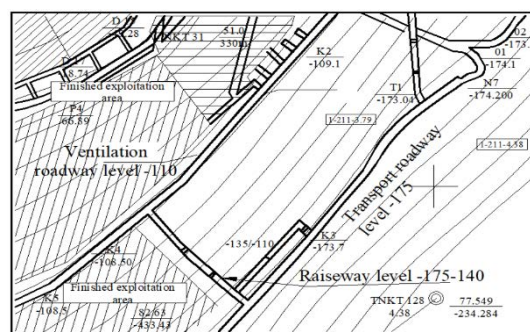
rock: a layer of siltstone whose thickness varies from 2.1 to 3.2m lies under the coal seam.

Designing and experimental construction in the longwall at seam 6(7) level -175/-110 nam khe tam mine

The support was chosen to be ZRY 36/45L model, the distance between central points of the pillars which were used to support the end roof and the roof of the working face is 1.15 m. The guide girder, the top girder, the guard girder and the tail girder were shown as (Figure 3b). Among them, the guide beam (1.000 mm) is connected to the top beam (1.940 mm). The globe-shaped pillar head is used as an auxiliary support. The guard girder (950 mm) is connected to the tail girder (1,200 mm) and a hydraulic jack was installed in the middle of the connection segment to adjust the angle of the tail girder for coal separation and also adjust the chord length of the support with a view to adapting to different changes in thickness of coal. Working range of the model ZRY 36 / 45L is suitable for the thickness of 2.5-6m, the slope angle of the seam from 45° - 81° . Coal was separated by using dynamite. Roadway are dug in coal, level roadway -110 serves ventilation, the one level -175 is used to transport coal. The diagram for establishing the mining system is shown as (Figure 7b).



a. Location of Nam Khe Tam mine

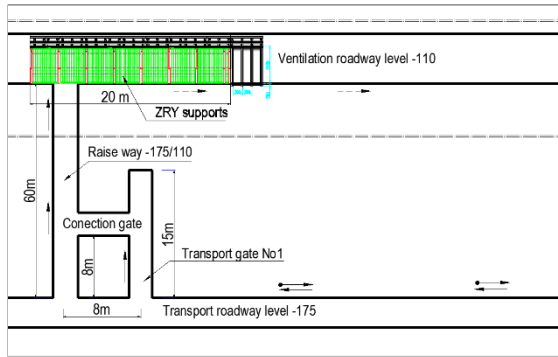


b. Diagram of the design area

Figure 7. Location of the studying area

Step 1. dig the raise level -175/-110, dig other roadways and install the support model ZRY in the ventilation roadway with the length of 20 m as Figure 7b and 8a .

Step 2. Drill blasting and loading on the support in the ventilation roadway (Figure 8b).



a. Step 1 dig the preparation roadway and install the support ZRY in the ventilation roadway

b. Step 2. Drill blasting and load for the support in the ventilation roadway

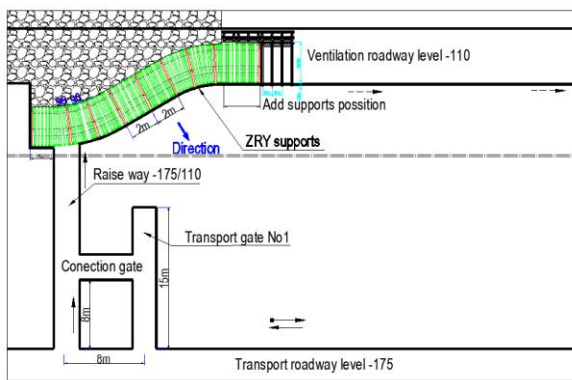
Figure 8. Diagram of construction in step 1 and 2

Step 3. To conduct coal separation, explosives are sequentially loaded into the boreholes to break up the intact coal mass. The procedure progresses in order from the haulage roadway up toward the ventilation roadway.

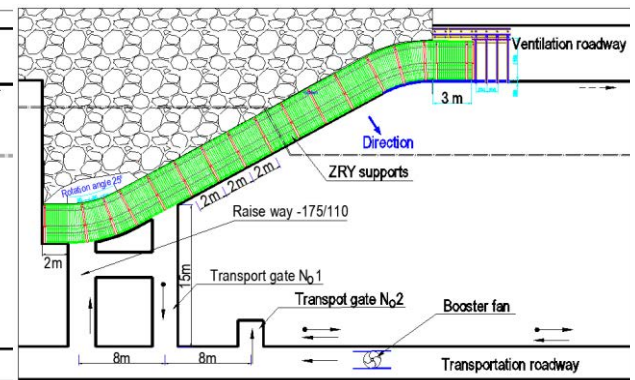
The extension of the longwall resulting from this coal extraction process is supplemented with additional ZRY supports at the ventilation roadway. The footwall points are gradually lowered, step by step bringing the longwall to the designed inclination of 25 to 28 degrees. During the cutting process, the

flexible support at the crown of the longwall becomes shorter; therefore, it is necessary to install auxiliary supports in the ventilation roadway (Figure 9a).

Step 4. Continue to drill and blasting to separate coal - transport - move the support as shown in 9a until the longwall approaches to flute throat 1. At any time, flute throat 1 is the coal loading line, the raise level -170/-110 will be the material transportation roadway (Figure 9b).



a. Step 3. Lower the coal floor

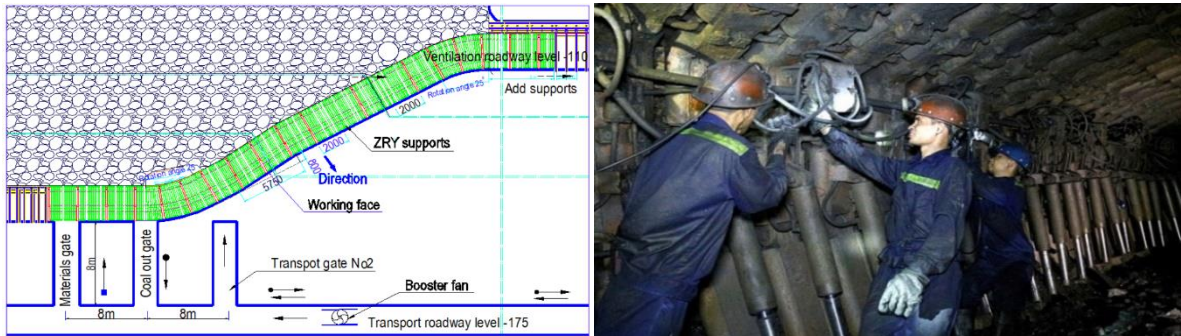


b. Step 4. Lower the coal floor until approaching to the crosscut roadway No.1 (transport gate No.1)

Figure 9. Diagram of implementing in step 3 and 4

Step 5. Continue to align the foot of the furnace to have enough length of 10-15m. At that time, the process of building the diagonal

longwall finishes, the working face transfers to the periodic mining state as shown in Figure 10a.



a. Diagram of building the longwall in the periodic mining phase

b. Image of the longwall using the support model ZRY in the periodic mining phase

Figure 10. Results of building the longwall ZRY in the periodic mining phase

RESULTS AND DISCUSSION

Table 1. Compare obtained results from the old method and the new one

Criteria	The old method (shortwall technique)	The new method (longwall technology)
Construction time for achieving the design capacity	85-90 days	75 days
Rate of coal recovery	70-75%	95%
Expense for production	Must dig the roadway to install equipment	No need to dig the roadway for installing equipment

The new way of mining preparation shortens time of achieving the design capacity with 10 -15 days, hardly spends money and labor digging the installation roadway, the recovered coal production is 9.356 tons (about 95% of total reserves in the area where loads for the support A. The whole *periodic* mining process has gone very smoothly without any significant errors. Thus, the improvement of technique in the initial set-up for the ZRY longwall gives chance to widely apply this technique for many other areas with similar exploitation conditions.

CONCLUSIONS

The diagonal longwall mining technique, utilizing the ZRY support model and dynamite for coal fragmentation, represents an optimal solution for steep, medium-thick, and small-scale coal seams in Quang Ninh. By leveraging the movement characteristics of the ZRY support, installing support within the ventilation roadway, and progressively lowering the floor level according to the

designed slope angle toward the transportation route, the mining preparation phase can be completed efficiently. Preparation for initial installation as the proposal in the article solves shortcomings of the old plan and achieves some advantages such as: (1) - Longwall was exploited earlier; (2) - Reduce the metres coefficient of the preparation roadway: The upper face at the beginning which was dug perpendicular to the seam is shorter than that in semi-inclined excavation, it was unnecessary to dig the roadway system along the stratified seam, so the cost of support wood was saved; (3)- The initial blast and break almost took place on the support in the DVTG roadway, so the work was very convenient.; (4)- The recovery of resources was maximum, there was no loss of the coal pillar behind the working face of the diagonal longwall.; (5) - Safety in construction and installation was good , the longwall was ventilated by the general antihypertensive of the mine, so microclimate factors were guarante.

REFERENCES

1. Annual coal output report of mines from 2000 to 2018, edited by Vietnam National Coal - Mineral Industries Holding Corporation LTD. (Hanoi, 2018).
2. Bodi J (1997) Safety and technological aspects of manless exploitation technology for steep coal seams. In: Proceedings of the 27th International Conference of Safety in Mine Research Institutes, New Delhi, India, February 20–22, 1997, pp. 955–965. New Delhi: Oxford & IBH Publishing Company;
3. D.Y. Zhu, W.L. Gong, Y. Su, Application of High-Strength Lightweight Concrete in Gob-Side Entry Retaining in Inclined Coal Seam. *Advances in Materials Science and Engineering* (2020). doi:10.1155/2020/8167038
4. Dao Hong Quang, The effect of seam dip on the application of the Longwall Top Coal Caving method for inclined thick seams, A thesis submitted in fulfilment of the requirements for the degree of Doctor of Philosophy, School of Mining Engineering The University of New South Wales Sydney, Australia, 2010;
5. Deb D, Choon SW and Jung YB (2017) Pit optimization for steep coal seams at Pasir coal mine, Indonesia. *Journal of the Korean Society of Mineral and Energy Resources Engineers* 46(5): 509–520.
6. Devi Prasad Mishra¹, Mamtesh Sugla, Prasun Singha, Productivity improvement in underground coal mines – a case study, *Journal of Sustainable Mining*, <https://doi.org/10.7424/jsm130306>; P 48-53;
7. Duong Duc Hai, Le Duc Nguyen, Nguyen Duc Trung, Marian Turek, and Aleksandra Koteras, Increasing Productivity and Safety in Mining as a Chance for Sustainable Development of Vietnam's Mining Industry, Conference Paper · October 2020 DOI: 10.1007/978-3-030-60839-2_15, : <https://www.researchgate.net/publication/345203142>; P 283-307;
8. Duong, D.H., Dinh, V.C., Koteras, A., Do, V.H., Vu, B.T.: Development orientation of mechanized technology of underground mining in Quangninh coalfield, Vietnam. In: AIP Conference Proceedings, vol. 2209 (2020). <https://doi.org/10.1063/5.0000005>;
9. H.W. Wang, Y.P. Wu, J.Q. Jiao, Stability Mechanism and Control Technology for Fully Mechanized Caving Mining of Steeply Inclined Extra-Thick Seams with Variable Angles. *Mining, Metall. Explor.* (2020). doi:10.1007/s42461-020-00360-0
10. Habraie B, Ren G, Zhang X, Smith J. 2015 Physical modelling of subsidence from sequential extraction of partially overlapping longwall panels and study of substrata movement characteristics. *Int. J. Coal Geol.* 140, 71–83. (doi:10.1016/j.coal.2015.01.004)
11. Hai Duong Duc, Cuong Dinh Van, Aleksandra Koteras, Hoang Do Van and Tu Vu Ba; Development Orientation Of Mechanized Technology Of Underground Mining In Quangninh Coalfield, Vietnam, AIP Conference Proceedings 2209, 020004 (2020); <https://doi.org/10.1063/5.0000005>, Published Online: 25 March 2020;
12. Hai Wang, Yan Qin, Hanbin Wang, Yu Chen and Xuancheng Liu, Process of overburden failure in steeply inclined multiseam mining: insights from physical modelling, royalsocietypublishing.org/journal/rsos, R. Soc. Open Sci. 8: 210275. <https://doi.org/10.1098/rsos.21027>
13. Hongsheng Tu, Shihao Tu, Yong Yuan, Fangtian Wang & Qingsheng Bai, Present situation of fully mechanized mining technology for steeply inclined coal seams in China, *Arab J Geosci* DOI 10.1007/s12517-014-1546-0;
14. Hongwei Wang, Yongping Wu, Maofu Liu, Jianqiang Jiao & Shenghu Luo (2020) Roof-breaking mechanism and stress-evolution characteristics in partial backfill mining of steeply inclined seams, *Geomatics, Natural Hazards and Risk*, 11:1, 2006-2035, DOI: 10.1080/19475705.2020.1823491 ,
15. In report on evaluation of mining and driving technology application in period of 2016-2018, orientation stage 2019-2023, edited by Vietnam National Coal - Mineral Industries Holding Corporation LTD. (Quangninh, 2018) (Không có trích dẫn)
16. Industry Investment Consulting Company (2005). Long-term Planning of Mining Development in Vietnam from 2006 to 2015, Prospects to the year 2025, Technical report, Mining Investment and Consulting Joint-Stock Company;
17. Klishin, S.V.; Klishin, V.I.; Opruk, G.Y. Modeling Coal Discharge in Mechanized Steep and Thick Coal Mining. *J. Min. Sci.* 2013, 49, 932–940. [CrossRef]
18. Le Duc Nguyen, Tran Tuan Ngan, Tran Minh Tien, Nguyen Ngoc Giang, Evaluation of the results from the development of the diagonal longwall mining technology with using the flexible shield ZRY at Hong Thai Coal Company and the capability of its application to the dip coal seams at underground

- coal mines belonging to Vinacomin, Mining Technology Bulletin, P 8-14, 2016;
19. Le Trung Tuyen, Study on susceptibility to spontaneous combustion of anthracite in vietnamese coal mines, thesis (doctoral) in Hokkaido uiversity, Japan, 10.14943/doctoral.r7062, P 19, Issue Date 2018-09-25;
20. Li Xiaomeng, Wang Zhaohui, Zhang Jinwang, Stability of roof structure and its control in steeply inclined coal seams, International Journal of Mining Science and Technology, Volume 27, Issue 2, March 2017, Pages 359-364, <https://doi.org/10.1016/j.ijmst.2017.01.018>;
21. Li, Y. H., & Zhou, R. (2018). Analysis of mechanical characteristics and instability law of inverse fault under the influence of mining. Earth Sciences Research Journal, 22(2), 139-144
22. Liu Jun1, a, Yue Gao-wei1,b . Research of Rock Mechanical Mechanics in Steeply Dipping Seam Mining, Advanced Materials Research Vol. 619 (2013) pp 342-346, <https://doi.org/10.4028/www.scientific.net/AMR.619.342>;
23. M.L.Jeremic, Strata mechanics of hydraulic sub-level coal mining, International Journal of Rock Mechanics and Mining Sciences & Geomechanics Abstracts, Volume 19, Issue 3, June 1982, Pages 135-142, [https://doi.org/10.1016/0148-9062\(82\)91153-6](https://doi.org/10.1016/0148-9062(82)91153-6)
24. Miao, S. J., Lai, X. P., & Cui, F. (2011). Top coal flows in an excavation disturbed zone of high section top coal caving of an extremely steep and thick seam. Mining Science and Technology (China), 21(1), 99-105.
25. Otsuka, T. Hydraulic Mining at Sunagawa Coal Mine. In Proceedings of the 4th Joint Meeting MMIJ-AIME, Tokyo, Japan, 4 November 1980; pp. 63–75.
35. Mills, L.J. Hydraulic Mining in the U.S.S.R. Min. Eng. 1978, 6, 655–663.
26. R.A. Frumkin, Predicting rock behaviour in steep seam faces (in Russian). International Journal of Rock Mechanics and Mining Sciences & Geomechanics Abstracts 20 (1), A12-A13 (1983). [doi.org/10.1016/0148-9062\(83\)91717-5](https://doi.org/10.1016/0148-9062(83)91717-5)
27. Saha, R., Jian, D. and Misra, B. (1992). Trends of Underground Thick seam Mining Methods with Potential for application in India, International Symposium on Thick Seam Mining, India pp. 549–5;
28. Shenghu Luo, Tong Wang, Yongping Wu, Jingyu Huangfu, Huatao Zhao, Internal Mechanism of Asymmetric Deformation and Failure Characteristics of the Roof for Longwall Mining of a Steeply Dipping Coal Seam, Arch. Min. Sci. 66 (2021), 1, 101-124, DOI 10.24425/ams.2021.136695;
29. Stanisław prusek, Marian turek, Józef dubiński, Izabela jonek-kowalska, Increasing productivity – a way to improve efficiency of operational management in hard coal mine, arch. min. sci. 63 (2018), 3, 567-58, doi 10.24425/123675;
30. T. Zhao, Z. Zhang, Y. Yin, Y. Tan, and X. Liu, Ground control in mining steeply dipping coal seams by backfilling with waste rock, the Southern African Institute of Mining and Metallurgy, 2018. volume 118, P 15-26;
31. Tien Dung LE and Xuan Nam BUI, Status and prospects of underground coal mining technology in Vietnam, Journal of the Polish Mineral Engineering Society, Doi 10.29227/IM-2019-02-63;
32. Trong Cuong Dao, Manh Phong Do, Vu Chi Dang, Que Thanh Nguyen, The study into the construction of applied conditions of methods for exploiting fairly thick and steeply inclined coalbeds, Vietnam Science and Technology (VISTECH), Vol 22, P 60-64, 2017;
33. Tu HS, Tu SB, Yuan Y, et al. (2015) Present situation of fully mechanized mining technology for steeply inclined coal seams in China. Arabian Journal of Geosciences 8(7): 4485–4494.
34. Tuan, N. (2005). Choosing the Most suitable Mining Technology for Fast, Efficient, and Safe Development in Vietnam Underground Coalmines, Regular Meeting of Vietnam Coalgroup, Cualo, Nghe An, Vietnam;
35. Tuan, N. and Thang, D. (2003). Report of results on Experimental Application of Semi-Mechanized shields into No.7 seam, Thanhung, Nammau coal mine, Technical report, Institute of Mining Science and Technology, Hanoi, Vietnam;
36. Tuan, N., Du, T., Tuan, N. and Ngan, T. (2008). Research on Application of Mechanized Equipment for High Single Pass Longwall or Longwall Top Coal Caving methods in Quangninh coalfield, Technical report, Institute of Mining Science and Technology, Hanoi, Vietnam;
37. Vietnam National Coal - Mineral Industries Holding Corporation LTD, History of coal industry development in Vietnam, see <http://www.vinacomin.vn/gioi-thieu-chung/lich-su-hinh-thanh-va-phat-trien201506031201389356.ht>

38. Vietnam's Ministry of Trade and Industry, In Vietnam energy outlook report 2017, edited by Danish Energy Agency (Hanoi, 2017).
39. Wang JC, Zhao BW, Zhao PF, (2017b) Research on the longwall top-coal caving mining technique in extremely inclined and soft thick coal seam. *Journal of China Coal Society* 42(2): 286–292.
40. Wenyu Lv, Kai Guo, Jianhao Yu, Xufeng Du and Kun Feng, Surrounding Rock Movement of Steeply
42. Wu YP, Xie PS and Ren SG (2010) Analysis of asymmetric structure around coal face of steeply dipping seam mining, *Journal of China Coal Society* 35(2): 182–184.
43. Xiaolou Chi, Ke Yang and Qiang Fu, Analysis of regenerated roof and instability support control countermeasures in a steeply dipping working face, *Energy Exploration & Exploitation* 2020, Vol. 38(4) 1082–1098, First Published December 30, 2019, <https://doi.org/10.1177/0144598719897422>;
44. Xie H, Zhao X, Liu J, Zhang R, Xue D. 2012 Influence of different mining layouts on the mechanical properties of coal. *Int. J. Mining Sci. Technol.* 22, 749–755. (doi:10.1016/j.ijmst.2012.12.010)
45. Xie HP, Zhou HW, Liu JF, & Xue DJ, Mining-induced mechanical behavior in coal seams under different mining layouts. *J. China Coal Soc.* 36, 1067–1074. (doi:10.1007/s12583-011-0163-z), 2011
46. Y.P. Wu, B.S. Hu, D Lang, Risk assessment approach for rockfall hazards in steeply dipping coal seams. *Int. J. Rock Mech. Min. Sci.* 138, 104626 (2021). doi: org/10.1016/j.ijrmms.2021.104626
47. Y.P. Wu, D.F Yun, P.S. Xie, Progress, practice and scientific issues in steeply dipping coal seams fullymechanized mining. *J. China Coal Soc.* 45 (01):24-34 (2020) (in Chinese).
- Dipping Coal Seam Using Backfill Mining, *Hindawi Shock and Vibration Volume* 2021, Article ID 5574563, 17 pages <https://doi.org/10.1155/2021/5574563>;
41. Wu YP and Yu DF (1999) The stability control of support at top caving face with steep seam. *Ground Pressure and Strata Control* 16(3): 82–85.
48. Yanwei Hu, Gang Wang, Jianqiang Chen, Zhiyuan Liu, Cheng Fan & Qian Cheng (2020): Prediction of gas emission from floor coalbed of steeply inclined and extremely thick coal seams mined using the horizontal sublevel top-coal caving method, *Energy Sources, Part A: Recovery, Utilization, and Environmental Effects*, DOI: 10.1080/15567036.2020.1733143;
49. Z. Rak, J. Stasica, Z. Burtan, Technical aspects of mining rate improvement in steeply inclined coal seams: A case study. *Resources* 9 (12), 1-16 (2020). doi:10.3390/resources9120138
50. Zbigniew Rak, Jerzy Stasica, Zbigniew Burtan and Dariusz Chlebowski , Technical Aspects of Mining Rate Improvement in Steeply Inclined Coal Seams: A Case Study, *Resources* 2020, 9, 138; doi:10.3390/resources9120138,
51. Zbigniew Rak, Jerzy Stasica, Zbigniew Burtan, Dariusz Chlebowski, Extraction of Coal from Steeply Inclined Coal Seams, Using a Fully Mechanised Sublevel Caving Mining System in the Kazimierz-Juliusz Coal Mine, info@researchsquare.com, p 1- 18.
52. Wu YP and Yu DF (1999) The stability control of support at top caving face with steep seam. *Ground Pressure and Strata Control* 16(3): 82–85.

DOI: 10.15625/vap.2025.0186

Investigation of the influence of the soil's elastic modulus surrounding the square tunnel on the internal force values in the tunnel lining.

Manh Tung Bui¹, Anh Son Do¹, Chi Thanh Nguyen^{1,2,*}

¹Hanoi University of Mining and Geology, 18 Vien Street, Hanoi, Vietnam

²Tunnelling and Underground Space Technology, HUMG, Vietnam

*Email: nguyenchithanh@humg.edu.vn

Abstract: Square tunnels are increasingly important in underground construction due to their advantages, such as simplified construction of the square shape and efficient use of the tunnel's cross-sectional area. In this paper, based on the characteristics of tunnels in the Hanoi metro system, the authors used the Plaxis2D program to model a square cross-section tunnel at a shallow depth of $H = 20$ m. This paper then conducted a series of simulations to investigate the internal forces in the tunnel lining (made of reinforced concrete with a thickness of $t = 0.35$ m), varying the Young's modulus (E) values of the surrounding soil and rock. The research results show that changes in the elastic modulus E of the soil significantly affect the internal forces in the tunnel lining. This highlights the substantial influence of the surrounding soil and rock properties on the tunnel's stability, as reflected in the internal forces within the lining.

Keywords: elastic modulus, tunnel lining, the internal force, the square tunnel, investigation.

INTRODUCTION

Tunnels with square and rectangular cross-sections were among the first types of tunnels developed. These tunnels offer significant advantages, including simplified construction and calculation, the ability to utilize large cross-sectional areas, lower construction costs, and easier control over the tunnel's shape. Consequently, square and rectangular tunnels are receiving considerable attention in research and practical applications within underground construction projects.

Relevant publications and studies on the design and calculation of these tunnels include: Bierbaumer AH (1913), Wang JN (1993); ITA (1998); Penzien J and Wu C (1998); Wood JH (2004, 2005); Penzien Z (2000); Mashimo, H., & Ishimura, T (2005); Moller, S. C., & Vermeer, P. A (2008); Du D.C et al., 2018; Gospodarikov, A.P et al., 2018; Nguyen T.C et al., 2019; Sahoo, J.P.; Kumar, B (2019); Nguyen C.T et al., 2022; Do NA et al., 2020, and others. Based on existing research, the calculation and determination of loads from the surrounding soil/rock on the supporting structures of square and rectangular tunnels have been addressed in considerable detail. However, the variability of soil/rock environments, the location of underground structures, and the specific characteristics of the tunnels themselves (cross-sectional area, depth, support structure properties, etc.) necessitate further in-depth research. Specifically, the influence of the surrounding soil/rock environment on the internal forces within the tunnel lining requires more comprehensive investigation. This paper utilizes the Finite Element Method (FEM) via Plaxis2D software to model a square tunnel within a soil and rock environment with defined properties. This model enables the study of the influence of the soil and rock environment – specifically, Young's modulus (E) – on the internal forces within the reinforced concrete tunnel lining. The results obtained provide insights into the impact of Young's modulus (E) on these internal forces, enabling an assessment of the tunnel's stability during operation.

MODELING SQUARE TUNNELS USING THE FINITE ELEMENT METHOD WITH PLAXIS2D SOFTWARE

Tunnel Characteristics

This study examines a tunnel with a square cross-section. The tunnel's dimensions are 5.5 x 5.5 meters, and it is located 20 meters ($H = 20$ m) below the ground surface (Nguyen C.T et al., 2022).

Table 1. Characteristics of square tunnel

NO	Parameters	Unit	Value
1	Young's modulus of the tunnel lining, E_v	MPa	35000
2	Poisson of the tunnel lining, ν_v	-	0,15
3	Thickness of tunnel lining, t	m	0,35
4	Tunnel depth, H	m	20

Table 2. Parameters of the soil mass surrounding the tunnel

NO	Parameters	Unit	Value
1	Young's modulus, E	MPa	10
2	Poisson, ν	-	0,34
3	Soil density, γ	kN/m ³	18,1
4	Horizontal pressure coefficient, K_0	-	0,5
5	Cohesion, c	kPa	22,5
6	Angle of internal friction, ϕ	Degree	33

The surrounding soil is assumed to be homogeneous, isotropic, and continuous, without distinct layers or interfaces. The Mohr-Coulomb criterion is used to model the mechanical behavior of the soil and rock around the tunnel (given the research conditions, the tunnel is under a static load, with the surrounding soil is homogeneous and isotropic). The tunnel lining is constructed from monolithic reinforced concrete and is expected to behave in an elastic-plastic manner. Detailed characteristics of the tunnel and the surrounding soil and rock are presented in Table 1 and 2.

Establishing the relationship and operation of the square tunnel with the surrounding soil

As introduced in Part 1, this paper utilizes the finite element method (FEM) to develop a model of a square tunnel and the surrounding soil. Plaxis 2D software was chosen for this

research due to its advantageous features, including its ability to accurately simulate key elements such as the tunnel's geometric dimensions, the supporting structure, and the surrounding soil conditions. Furthermore, the software can establish relationships and simulate simultaneous interaction between the soil around the square tunnel and the tunnel lining. To ensure the accuracy of the research results and compatibility with the computer's configuration, the 15-node element type was selected for simulating both the tunnel and the surrounding soil. The tunnel lining is represented as reinforced concrete, modeled using plate elements. The connection between the tunnel lining and the surrounding soil (interface) is also simulated to allow for simultaneous interaction and deformation. In this study, the surrounding soil and the tunnel lining are considered to deform together.

To ensure the independence of the tunnel model study area and the surrounding soil mass, the study area was designed with the following dimensions: 100 m wide and 40 m high, resulting in a model with 35,195 nodes and 41,360 zones. The dimensions of the study area, which include the square tunnel and the surrounding soil, were determined based on the influence of external factors on the tunnel construction process. By using these dimensions, the impact of external boundary forces on the study results has been minimized. Figure 1 illustrates the established model of the tunnel and its surrounding soil environment. Boundary conditions were applied to the study area model, with the top boundary being free and not fixed or limited in displacement. This study does not consider the influence of the groundwater level on the internal force values within the tunnel lining.

The following steps outline the creation of a square tunnel model within a surrounding soil environment. After establishing the model, this paper will vary and analyze its operation under different conditions, specifically changes in the Young's elastic modulus of the surrounding soil and rock. Based on the results, this paper will analyze and conclude how

changes in the Young's modulus of the soil environment affect the internal forces within the tunnel lining:

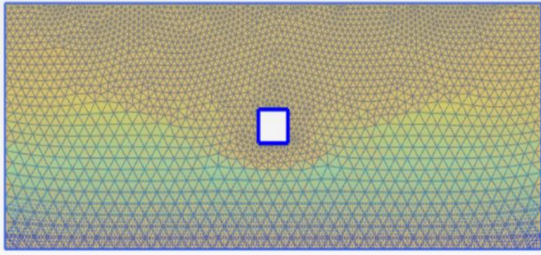


Figure 1. Mesh model of a square tunnel and the surrounding soil.

Step 1: Define the research area, establish boundary conditions and the initial state of the model, and define the properties of the surrounding soil mass;

Step 2: Simulate the construction process of the square tunnel, creating the tunnel outline within the soil mass and installing the initial support structure with defined parameter values;

Step 3: Excavate the tunnel within the area supported by the installed structure;

Step 4: Install the tunnel lining and then modify the Young's modulus of elasticity of the surrounding soil and rock environment according to the chosen lining type and selected parameters;

Step 5: Run the simulation, collect the results, and analyze the internal forces appearing in the tunnel lining under varying Young's modulus values of the surrounding soil mass.

RESEARCH ON THE IMPACT OF THE YOUNG'S MODULUS OF THE SOIL SURROUNDING A SQUARE TUNNEL ON THE INTERNAL FORCES IN THE TUNNEL LINING

A model of the tunnel and surrounding soil was constructed using the working conditions and parameters specified in Tables 1, 2, and 3. The study investigated the influence of the soil's Young's modulus of elasticity on the internal forces within the reinforced concrete tunnel lining, which had a square cross-section. During the research, the Young's modulus (E)

of the surrounding soil was varied across six cases: $E = 10$ MPa; $E = 20$ MPa; $E = 35.5$ MPa; $E = 50$ MPa; $E = 75$ MPa; and $E = 100$ MPa. Based on the research findings, this paper evaluates how the Young's modulus affects the internal forces in the tunnel lining. Consequently, it affirms the impact of the soil's Young's modulus on the stability of the square tunnel during its lifespan and operation. For clarity in research and presentation, the results of the internal force values in the tunnel lining, corresponding to fixed tunnel lining properties and varying Young's modulus values in different soil environments, are displayed along the tunnel's cross-section. The center of the tunnel cross-section serves as the origin of the coordinate system. The internal force values were surveyed at locations on the tunnel lining determined by angles measured from the center of the tunnel cross-section. This representation clearly illustrates how the internal force values change along the tunnel lining's cross-section at each location.

This section of the paper focuses on the internal force values within a square tunnel lining, with a fixed lining thickness of $t = 0.35$ m. The Young's modulus of elasticity for the surrounding soil was varied across six values, as detailed in the paper: $E = 10$ MPa, $E = 20$ MPa, $E = 35.5$ MPa, $E = 50$ MPa, $E = 75$ MPa, and $E = 100$ MPa. A square tunnel model was used, incorporating both the material properties of the lining and the characteristics of the surrounding soil. The resulting internal forces within the tunnel lining are illustrated in Figures 2, 3, and 4.

Based on the results shown in Figures 2-4, this paper can conclude that when the tunnel lining thickness is $t = 0.35$ m, the moment value M in the square tunnel lining tends to concentrate. With the parameters defined, it reaches positive extreme values at angles 0° , 90° , 180° , and 360° as you rotate counterclockwise around the tunnel face's cross-section. Conversely, the negative extreme moment values in the tunnel lining appear at positions 45° , 135° , 225° , and 315° . This can be explained by considering the square tunnel's lining as load-bearing beams. Under the pressure from the

surrounding soil, the corners of the lining, which experience the maximum positive moment, undergo significant bending. Meanwhile, the sections of the tunnel lining experiencing negative moment are subjected to tension.

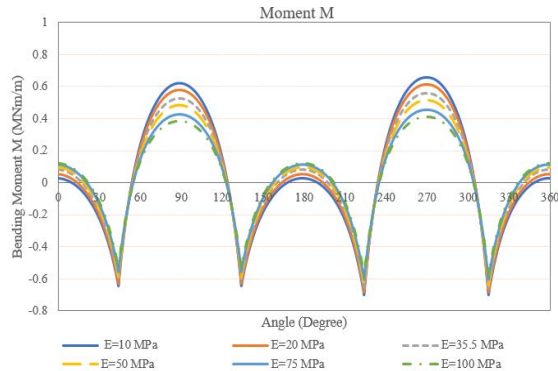


Figure 2. Moments appear in the tunnel lining when the Young's modulus of elasticity of the surrounding soil changes within the expected range.

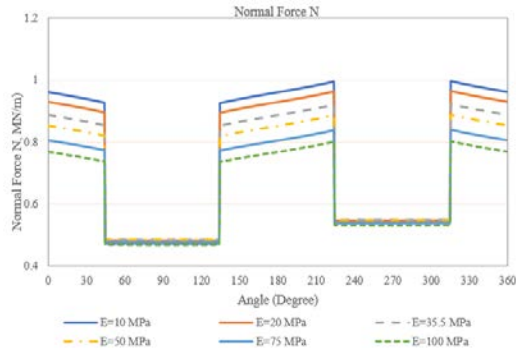


Figure 3. Normal force N appears in the tunnel lining when the Young's modulus of elasticity of the surrounding soil changes within the expected range.

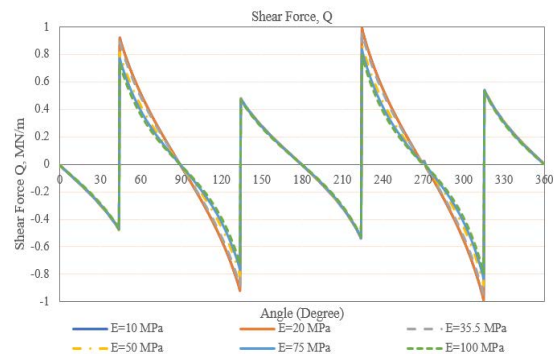


Figure 4. Shear force Q appears in the tunnel lining when the Young's modulus of elasticity of the surrounding soil changes within the expected range.

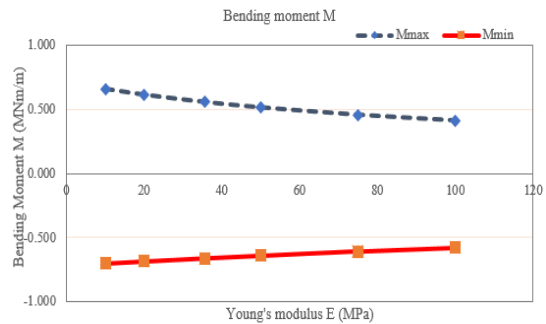


Figure 5. The maximum and minimum bending moment M in the tunnel lining occur when the soil's Young's modulus changes within the considered range of values.

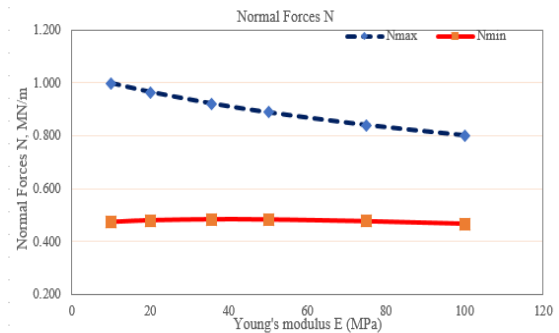


Figure 6. The maximum and minimum normal forces N in the tunnel lining occur when the soil's Young's modulus changes within the considered range of values.

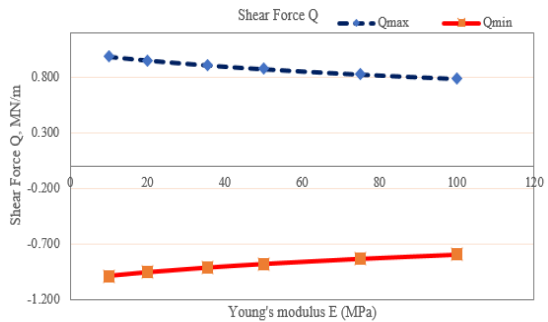


Figure 7. The maximum and minimum shear force Q in the tunnel lining occur when the soil's Young's modulus changes within the considered range of values.

Regarding the longitudinal force, N, in the tunnel lining, the values tend to increase and peak at angles of 45°, 135°, 225°, and 315°. Conversely, between 45° and 135°, and between

225° and 315°, the longitudinal force in the tunnel lining tends to decrease, reaching minimum values. This is likely because the tunnel lining experiences concentrated compressive loads at the points where the longitudinal force is at its maximum.

An investigation of horizontal shear force Q in a square tunnel lining with a thickness of $t = 0.35$ m reveals specific patterns. The maximum shear force values occur at points corresponding to 0°, 45°, 135°, 225°, and 315° around the tunnel lining. Conversely, the minimum absolute shear force values are found at 90°, 180°, 270°, and 360°. This can be attributed to stress concentration at the corners of the tunnel lining, leading to these maximum shear force values.

Based on the maximum and minimum internal forces observed in the square tunnel lining, including the maximum and minimum moment (M), longitudinal force (N), and shear force (Q) (Figures 5, 6, and 7), in relation to changes of the Young's modulus of the surrounding rock mass, the following observations can be made: The absolute values of the moment, longitudinal force, and shear force in the tunnel lining are inversely proportional to the Young's modulus of the surrounding soil mass. In other words, as the Young's modulus of the surrounding soil increases, the internal forces in the tunnel lining decrease, and vice versa. This is logical in practice. When constructing tunnels and underground structures in the soil mass with strong physical and mechanical properties, the soil load on the tunnel lining is generally less than the soil load effect on the tunnel lining when the surrounding soil mass has weaker physical and mechanical properties. This difference arises because weaker soil has less cohesion between its particles, allowing the soil mass around the tunnel to displace into the newly created space. This displacement increases the soil load on the tunnel lining. Furthermore, the area of soil directly contributing to the load on the tunnel lining expands in this case, increasing the weight of the soil sliding into the tunnel face's cross-

section and, consequently, the soil load on the tunnel lining.

CONCLUSION

This paper investigates the impact of variations in the Young's modulus of the soil mass surrounding square tunnels on the internal forces within the tunnel lining. A numerical model, encompassing the tunnel, its lining, and the surrounding soil mass, was developed using Plaxis2D software. Careful consideration was given to the dimensions of the study area, boundary conditions, tunnel construction stages, and lining installation to ensure the accurate assessment of how the Young's modulus (E) of the soil mass affects internal forces in the square tunnel lining. Based on the results, the following conclusions can be drawn:

- When the Young's modulus (E) of the soil surrounding a square tunnel changes, the maximum and minimum internal forces in the tunnel lining are generally inversely proportional to this value. Based on the moment (M) values observed in the tunnel lining as the soil's Young's modulus changes, the moment is more significantly affected than the longitudinal force (N) and shear force (Q);

- The internal forces in the square tunnel lining tend to be inversely proportional to the Young's modulus of elasticity of the surrounding soil. Specifically, the moment (M), longitudinal force (N), and shear force (Q) all tend to increase as the soil's Young's modulus decreases, and vice versa;

- The survey examined the effect of varying Young's modulus for the soil surrounding a square tunnel. Values used were $E = 10$ MPa, $E = 20$ MPa, $E = 35.5$ MPa, $E = 50$ MPa, $E = 75$ MPa, and $E = 100$ MPa. Using Plaxis2D software, the internal forces in the tunnel lining were analyzed. The results show areas of stress concentration in the tunnel lining, particularly at points with extreme positive values. The bending moment (M) in the square tunnel lining tends to concentrate and reach positive extreme values at angles of 90°, 180° (measured counterclockwise around

the tunnel face). Conversely, negative extreme values of the moment appear at 45° , 135° , 225° , and 315° on the tunnel lining. This indicates that the tunnel lining experiences the greatest bending at the locations of positive extreme moment values. The negative extreme moment values appear at the corners of the lining, where stress concentrates and the tunnel lining's bearing behavior changes. Examination of the vertical force (N) and shear force (Q) in the square tunnel lining revealed that the vertical force tends to increase, reaching its maximum at angles of 45° , 135° , 225° , and 315° . Between 45° and 135° , and again between 225° and 315° , the vertical force tends to decrease, reaching its minimum values. The shear force (Q) values, determined by the angle at the tunnel's center with counterclockwise rotation, reach maximum values at 0° , 45° , 135° , 225° , and 315° . The absolute values of the shear force in the tunnel lining reach a minimum at 90° , 180° , 270° , and 360° . This can be attributed to stress concentration at the tunnel corners, where the roof beam and column intersect.

The research and survey results presented in this paper demonstrate how the Young's modulus of elasticity of the soil and rock surrounding a square tunnel lining affects the internal forces within the lining. This finding highlights an important consideration for the design and construction of square tunnels.

REFERENCES

- Bierbaumer AH (1913). Die dimensionierung des tunnel manerwerks. Leipzig, Germany. 1913.
- Wang JN (1993) Seismic Design of Tunnels: A State of the Art Approach". Monograph 7, Parsons Brinkerhoff Quad & Douglas Inc; NewYork, USA.
- ITA (1998) ITA guidelines for the design of tunnels. Tunnelling & Underground SpaceTechnology 3(3): 237–249.
- Penzien J and Wu C (1998) Stresses in Linings of Bored Tunnels. Journal of Earthquake Eng. Structural Dynamics 27: 283–300.
- Penzien Z (2000) Seismically Induced Racking of Tunnel Linings. Int. J. Earthquake Eng. Struct. Dynamic, 29: 683–691.
- Wood JH (2004) Earthquake Design Procedures for Rectangular Underground Structures. Project Report to Earthquake Commission, EQC Project No 01/470, New Zealand.
- Wood JH (2005) Earthquake Design of Rectangular Underground Structures. NZSEE Conference, New Zealand: 39–47.
- Mashimo, H., & Ishimura, T (2005) Numerical modelling of the behavior of shield tunnel lining during assembly of a tunnel ring. In Proceedings of the Fifth International Symposium on geotechnical aspects of underground construction in soft ground. Amsterdam, Netherlands: Taylor & Francis: 587–593.
- Moller, S. C., & Vermeer, P. A (2008) On numerical simulation of tunnel installation. Tunnelling Underground Space Technology 23: 461–475, DOI: 10.1016/j.tust.2007.08.004.
- Du DC, Dias D, Do NA, Oreste PP (2018) Hyperstatic reaction method for the design of U-shaped tunnel supports. International Journal of Geomechanics 18(6), DOI: 10.1061/(ASCE)GM.1943-5622.0001127.
- Gospodarikov, A.P, Nguyen, T.C (2018). Behaviour of Segmental Tunnel Linings under the Impact of Earthquakes: A Case Study from the Tunnel of Hanoi Metro System. Int. J. GEOMATE, 15: 91–98.
- Sahoo, J.P.; Kumar, B (2019) Support pressure for stability of circular tunnels driven in granular soil under water table. Comput. Geotech 109: 58–68, DOI: 10.1016/j.compgeo.2019.01.005.
- Do NA, Daniel D, Zhang Z, Huang X, Nguyen TT, Pham VV, Ouahcène Nait-R (2020) Study on the behavior of squared and sub-rectangular tunnels using the Hyperstatic Reaction Method. Transportation Geotechnics 22, DOI: 10.1016/j.trgeo.2020.100321
- Nguyen TC, Gospodarikov AP (2020) Hyperstatic reaction method for calculations of tunnels with horseshoe shaped cross-section under the impact of earthquakes. Earthquake Engineering and Engineering Vibration 19(1): 179-188, DOI: 10.1007/s11803-020-0555-0.
- Nguyen C.T, Do N.A, Daniel D, Pham V.V, Gospodarikov A. (2022). Behaviour of Square and Rectangular Tunnels Using an Improved Finite Element Method. *Applied Sciences*. 12, 2050.

Improving power quality in underground mines' grid by utilizing SVC system

Ho Viet Bun, Le Xuan Thanh *

HaNoi University of Mining and Geology, HaNoi, Vietnam

*Email: lexuanthanh@humg.edu.vn

Abstract: The operational efficiency of underground mining systems is strongly dependent on the reliability and performance of electrical equipment, particularly electric motors used for ventilation, pumping, conveyor drives, and hoisting mechanisms. As mining operations expand in both scale and depth, the demand for electrical power has significantly increased, leading to a higher concentration of heavy-duty electrical loads. Consequently, the stability and quality of the supplied electrical power have become critical factors determining both the productivity and safety of the mining process. In many underground mines, the power supply is typically characterized by long cable runs, uneven load distribution, and the presence of nonlinear devices. These factors contribute to undesirable power quality issues such as voltage fluctuation, unbalanced load currents, and harmonic distortion. Among these, the most pervasive problem is the degradation of the power factor due to the inductive nature of electric motors and transformers. A poor power factor not only increases the apparent power demand from the grid but also causes excessive losses in cables, transformers, and switchgear, thereby reducing the overall efficiency of the electrical network. To address these challenges, this study investigates the use of a Static Var Compensator (SVC) as an advanced and flexible solution for improving power quality in mining power distribution systems. The SVC is a member of the Flexible AC Transmission Systems (FACTS) family and operates by dynamically controlling the reactive power in the system through thyristor-controlled reactors (TCR) and thyristor-switched capacitors (TSC). By continuously adjusting the

reactive power compensation according to real-time load variations, the SVC can maintain a near-unity power factor and stabilize the bus voltage within acceptable limits. A simulation is implemented in ETAP to prove the use of SVC in term of mitigating voltage dips and flicker, ensuring the smooth operation of sensitive control and protection devices.

Keywords: Power quality, mining, SVC, ETAP simulation.

INTRODUCTION

SVC overview in mining and industrial application

Mathematic basic equation of SVC

The Static Var Compensator (SVC) (a typical presented in figure 1) is a mature shunt-connected reactive-power device belonging to the FACTS family that provides fast, continuous reactive power support to an AC bus. Its principal objective is to control bus voltage and the system balance of reactive power by injecting or absorbing reactive current ($I_{q_}$), such that the voltage magnitude V at the point of connection remains within pre-set limits under dynamic load variations. The simplest steady-state representation of SVC action can be expressed as an equivalent variable susceptance B_{svc} (positive for capacitive action, negative for inductive action) connected to the compensated bus (as presented in equation (1)) [12], [16]:

$$Q_{svc} = V^2 B_{svc} \quad (1)$$

where Q_{svc} is the reactive power provided (positive = capacitive), and V is the bus RMS voltage.

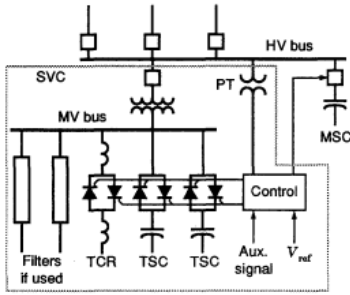


Figure 1: Typical SVC system

Operationally, a conventional SVC comprises combinations of thyristor-controlled reactors (TCR), thyristor-switched capacitors (TSC), and passive harmonic filters. A typical control loop measures bus voltage V and computes a reactive command ΔQ using, for example, a PI (or advanced) regulator; the converter/thyristor stage then modulates current so that the net reactive injection satisfies equation (2):

$$Q_{net}(t) = Q_{TSC}(t) + Q_{TCR}(t) + Q_{filters} \approx Q(t) \quad (2)$$

Fast thyristor phase-angle control of the TCR gives near-continuous inductive adjustment (firing-angle α controls effective reactance), while TSC steps supply capacitive blocks when required. The analytical relation between TCR firing angle α and fundamental reactive current I_1 is well documented in [15], [16]. From a dynamics viewpoint, SVC acts as a voltage-dependent reactive source: around an operating point, the small-signal relation can be linearized as (3).

$$\Delta Q_{svc} \approx K_v \Delta V + \dots \quad (3)$$

where K_v is the static droop or slope parameter implemented in voltage control (negative droop for over-excited behavior). That fast dynamic response (millisecond timescale) is central to advantages reported across field and simulation studies: mitigation of voltage sags, flicker suppression during large transient currents (e.g., arc furnaces, motor starting), improved damping of electromechanical oscillations, and support for weak bus voltage under increased distributed generation penetration [13], [15], [17].

Applications of SVC on Medium Voltage grid and Mining industry

SVCs have been deployed historically at transmission and large industrial points; recent research demonstrates successful MV and distribution-level use for localized power-quality issues (voltage regulation, flicker mitigation, power-factor correction) and for stabilizing grids that host renewables or heavy loads such as furnaces, large conveyors, and variable-speed drives [24], [21], [14]. In mining, site characteristics — long feeders, large asynchronous motor starting currents, and a mix of nonlinear loads — create a compelling use case for SVC: it can reduce voltage dips during hoist or conveyor starting, lower flicker generated by arc furnaces or welding, and improve transformer loading by raising the power factor [12]. Utilizing SVC in mining industry must consider the following sides affection as listed:

Disadvantages & technical risks

Although the Static Var Compensator (SVC) has proven to be an effective solution for dynamic reactive power support, several inherent system and control limitations restrict its performance in demanding industrial and mining environments. One of the most significant weaknesses is that the reactive current output of an SVC decreases proportionally with voltage magnitude, thus its capability to provide compensation diminishes under undervoltage conditions [17]. In addition, the use of thyristor-controlled reactors (TCR) and thyristor-switched capacitors (TSC) produces characteristic harmonics that require complex filter networks to prevent resonance and voltage distortion [13], [15]. The inclusion of large passive filters and reactor banks increases system bulk and installation area, while the response speed of SVCs—typically on the order of tens of milliseconds—is slower than converter-based STATCOMs, reducing their effectiveness in mitigating fast transients [15], [17]. Improper placement or sizing of SVC units can also lead to suboptimal performance

or, in extreme cases, instability due to poor coordination with network impedance and protection systems.

In addition to these inherent control constraints, the operational and environmental conditions of industrial and mining systems impose further challenges. Harsh underground environments characterized by dust, humidity, and vibration require robust protection, enhanced cooling, and corrosion-resistant components, leading to increased maintenance frequency and cost. The complexity of control coordination and the need for skilled technical personnel represent further barriers, as fine-tuning droop slopes, filter resonance, and communication with upstream protection devices are critical to ensure stability [16]. Moreover, in networks with extensive nonlinear loads—such as arc furnaces, large conveyor drives, and high-power motors—SVCs may inadvertently amplify specific harmonics or cause undesirable resonant conditions if network impedance and harmonic spectra are not accurately modeled [13]. These issues perform a careful pre-installation studies and continuous monitoring in mining applications, where load dynamics are highly variable and sensitive to voltage fluctuations. In summarizing 4 keys consideration is listed as:

1. Harmonic generation and filter-design risk. TCR switching introduces characteristic harmonic currents; undersizing or poor filter design can create harmonic amplification or resonances with mine networks — an area of active research and failure modes documented in [15], [23]. Proper network impedance assessment and tuned passive or active filters are mandatory.

2. Initial capital and maintenance: power-electronic valves, control electronics and cooling/protection increase capex and opex compared with conventional switched capacitors; life-cycle economics must factor in energy savings, avoided penalties and maintenance costs [13], [21].

3. Environmental and ruggedization challenges: underground mines impose high dust, humidity, shock/vibration — the SVC enclosures, cooling and filtering must be industrialized for such environments, or the devices must be located on surface substations with suitable HV/MV transformers [1], [7].

4. Control complexity & staff skills: advanced control (e.g., PMU-assisted schemes or fuzzy/PI hybrids) can improve performance but requires trained engineers for commissioning and maintenance [19], [21].

Economic considerations (industrial & mining)

Economic viability is case dependent. The main benefits are reduced energy losses, improved power factor (reducing utility penalties), fewer production interruptions from voltage instability, and deferred network reinforcement. Market reports indicate modest but steady SVC market growth (driven by industrial modernization and renewable integration) — adoption is attractive where high-power motors or furnaces cause frequent voltage events, [21]. A robust cost-benefit analysis should include: (i) capex amortization, (ii) maintenance and replacement of power-electronics, (iii) avoided downtime costs in mining processes, (iv) tariff savings from better power factor, and (v) potential needs for additional harmonic filters or monitoring equipment [22], [15].

SVC in mining industry

In modern underground coal mines, mechanized excavation and extraction systems are increasingly dominated by advanced equipment such as roadheaders, shearers-loaders, and fully mechanized mining complexes integrating multiple high-power electric drives [4]. These machines operate in conjunction with remote control systems, automated protection circuits, and various auxiliary devices designed to enhance safety and operational efficiency. However, the electrical supply feeding such systems is inherently subjected to a wide range of dynamic disturbances, including motor starting

currents, voltage sags caused by heavy-load acceleration, and overvoltage events arising from switching transients or unstable source conditions [4].

As a result, the power supply network within the mining environment experiences continuous fluctuations (as shown in figure 2) that can compromise the stability of voltage and current parameters. Such variations may violate established power quality standards, thereby leading to voltage dips, harmonic distortion, and flicker phenomena [1]. These disturbances exert detrimental impacts on the operational reliability of mining electrical equipment—particularly sensitive electronic controls, relay protection devices, and variable-speed drives—whose performance and lifespan are directly dependent on voltage stability [1]. Consequently, maintaining consistent power quality becomes a critical prerequisite for the reliable and safe operation of high-capacity electrical systems in modern underground coal mining enterprises.

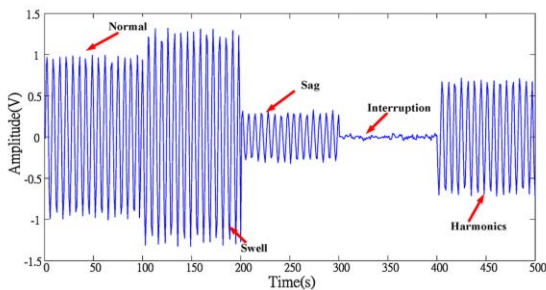


Figure 2. An interruption of power failure in mining grid

As mentioned previously and according to comparative studies and field cases, SVC remains a cost-effective and technically robust solution for many industrial power-quality needs if (and only if) careful pre-deployment studies (impedance/harmonics), filter design, environmental protection and lifecycle economics are addressed [12], [13], [15], [21]. In mining, where reactive transients and voltage dips from large motor starts are frequent, SVC can materially improve production reliability and equipment lifetime. However, the final choice between SVC, STATCOM, or hybrid approaches

must be informed by site-specific dynamic studies, total cost of ownership, and the availability of skilled operational staff [25], [2].

PROPOSE THE USE OF SVC

To enhance power quality in underground coal mining systems, the deployment of Static Var Compensators (SVCs) has proven to be one of the most effective solutions. SVCs are advanced reactive power compensation devices based on power electronic components such as thyristors or triacs equipped with gate control mechanisms, allowing dynamic adjustment of the firing angle in response to voltage variations [6]. The control system, often implemented using microcontrollers such as 8051, PIC16F877, or VAR controllers, provides real-time control of the reactive power exchange between the power source and the load, thereby stabilizing voltage profiles during transient conditions [7].

Structurally, an SVC typically comprises three major functional modules, namely the Thyristor-Controlled Reactor (TCR), Thyristor-Switched Reactor (TSR), and Thyristor-Switched Capacitor (TSC) units [6], [7] (exhibited in figure 3). The TCR allows smooth and continuous regulation of reactive power absorption by adjusting the conduction angle of the thyristor valves, which results in fine-tuned compensation suitable for variable load conditions. The TSR, by contrast, operates in a stepwise switching manner, offering rapid connection and disconnection of reactor banks to respond to sudden changes in reactive demand. Meanwhile, the TSC serves as a dynamic source of capacitive reactive power, delivering fast voltage support during periods of under-voltage, ensuring system voltage remains within acceptable limits [7].

According to [21], SVC systems offer rapid response times in the order of milliseconds, making them particularly beneficial for industrial grids with fluctuating loads such as conveyors, hoists, and ventilation fans in mining environments. Furthermore, [18] demonstrated that the use of coordinated TCR-TSC control significantly mitigates voltage dips

and flicker, which are common issues in mining power systems due to high inrush currents during motor starting. Studies such as [20] also emphasize that SVC-based compensation improves both power factor and harmonic performance, thus extending the operational lifespan of electric drives and reducing the likelihood of protection relay malfunctions.

However, the effectiveness of SVCs is contingent upon appropriate system design, including the tuning of control algorithms, placement within the power distribution network, and harmonic filtering strategies, as excessive reactive power switching may itself introduce distortions if not properly managed [6], [24]. Consequently, SVC implementation in mining applications must consider both electrical performance and operational safety, especially in confined underground environments where voltage stability is directly tied to the reliability of electrically driven excavation and transport systems [7], [25].

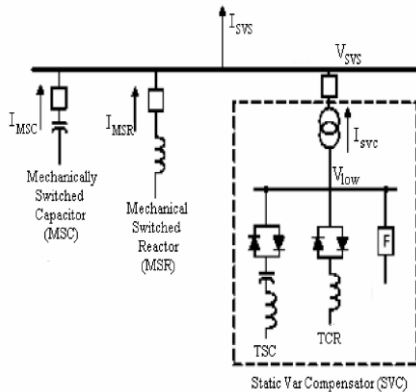


Figure 3. SVC employing TSC and TCR.

Although the SVC system is composed of discrete modules such as TCR, TSC, and TSR, its overall control action exhibits quasi-continuous regulation of reactive power, owing to the combined effect of smooth thyristor firing-angle modulation in the TCR and stepwise compensation through TSC and TSR banks [8], [9], [11]. The integration of these subsystems allows the SVC to maintain a nearly linear voltage-current (U - I) characteristic

within its operating range, as illustrated in Figure 4, thereby providing seamless voltage stabilization under rapidly changing load conditions. Each component of the SVC is connected to the power network through thyristor valve assemblies rather than traditional circuit breakers, ensuring fast, contactless switching and minimizing mechanical wear [8], [9].

This topology enables extremely high control responsiveness—with adjustment times typically below 40 milliseconds—which effectively eliminates transient delays that are often observed in conventional capacitor-reactor switching schemes [11]. According to [22], such rapid dynamic response is essential in industrial and mining networks, where the load fluctuates sharply during conveyor starting, hoist braking, or coal cutting operations. Moreover, [24] reported that the use of thyristor-controlled elements significantly enhances system reliability by reducing switching surges and suppressing voltage flicker during cyclic loading.

The primary operational function of an SVC is to regulate both voltage magnitude and reactive power flow at its point of connection to the grid, as represented in Figure 5. This dual control capability allows the SVC to either absorb or generate reactive power depending on system requirements, maintaining the desired voltage profile and improving the stability margin of the power network [9], [25]. Consequently, SVCs serve not only as voltage stabilizers but also as active dynamic compensators that ensure steady-state and transient voltage support in medium-voltage industrial and mining grids.

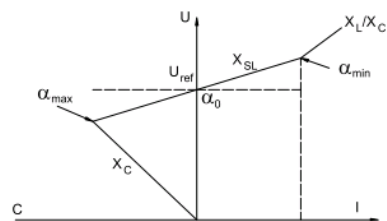


Figure 4. U - I Characteristic of SVC

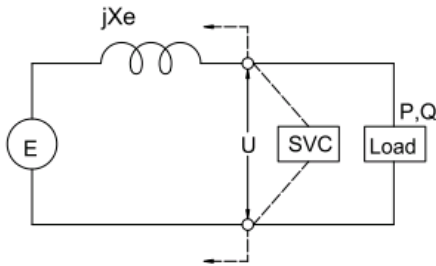


Figure 5. Modifying Voltage profile by SVC

The voltage at the load busbar of an electrical system tends to decrease progressively as the active and reactive components of the load power increase, particularly in the absence of any reactive power compensation devices. This relationship is represented by characteristic curve (a) in Figure 6, which depicts the natural voltage drop behavior of the network caused by the reactive power absorbed by inductive loads. In such conditions, the system operates with a lagging power factor, and voltage stability at the load terminals becomes highly sensitive to load variations [6], [7].

When a Static Var Compensator (SVC) is introduced into the network, the situation improves significantly. The SVC provides dynamic reactive power support within its rated operating range, as shown by characteristic curve (b) in Figure 6. By injecting capacitive reactive power during voltage sags and absorbing reactive power during overvoltage conditions, the SVC maintains a flatter voltage profile and prevents large deviations in bus voltage magnitude under varying load conditions [8], [9], [11]. This stabilizing action not only enhances voltage quality but also reduces power losses along distribution feeders and improves the voltage regulation index of the overall system, as demonstrated in [20] and [22].

However, if the SVC were designed without any upper limitation on its reactive power output, the voltage at the load bus could, in theory, be maintained perfectly constant regardless of load variations, as illustrated by characteristic curve (c) in Figure 6. In practice, such

unlimited control is neither technically feasible nor economically justified because excessive reactive power generation could lead to overcompensation and system resonance issues, especially in weak grids with high harmonic content [7], [24], [25]. Therefore, modern SVC installations incorporate protective constraints and control saturation mechanisms to ensure operational safety and harmonic compliance. These control limits guarantee that voltage regulation remains within acceptable tolerances while preventing device overstress and excessive network distortion.

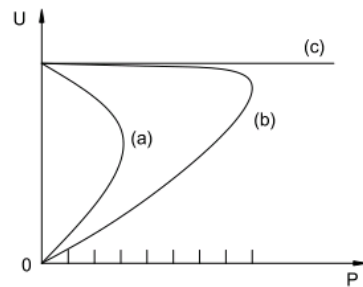


Figure 6. Voltage wave form with and without SVC

SIMULATION AND RESULTS

The ETAP software was employed to simulate the single-line diagram of the power supply system for an underground mining area [3]. The electrical network parameters—including load data, line lengths, and conductor sizes—were input into the model to accurately represent the operating conditions of the mine's distribution system. The electrical schematic was then analyzed using power flow equations to determine the voltage variations occurring along different sections of the network under varying load conditions. Subsequently, the optimal placement of the Static Var Compensator (SVC) was identified based on nodes exhibiting the greatest voltage deviation. Finally, capacitor compensation units were modeled at each bus where voltage drops were detected, enabling a comparative assessment of system performance before and after reactive power compensation.

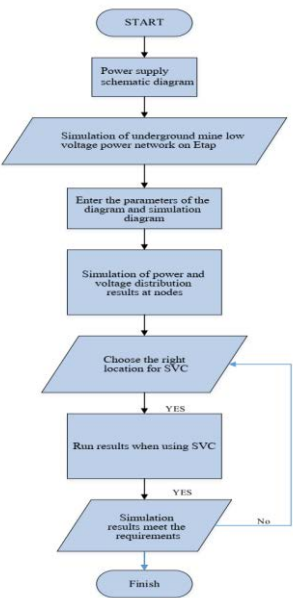


Figure 7. Proposed algorithm of utilizing ETAP for analysing the use of SVC in mining grid

Simulation diagram of the mining grid is performed in figure 8 and 9.

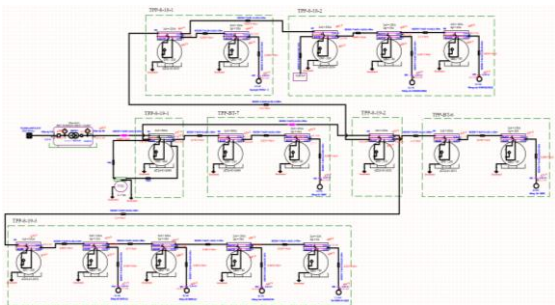


Figure 8. Simulation diagram of mining underground mine without SVC installation

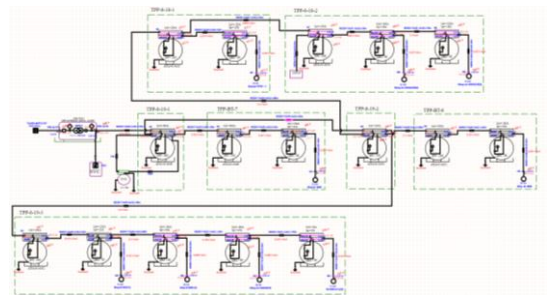


Figure 9. Simulation diagram of mining underground mine with SVC installation

The simulation results obtained from the ETAP software demonstrate a significant improvement in the voltage profile across the distribution network after implementing the Static Var Compensator (SVC). As shown in Figure 10, the voltage magnitude at the load buses increased by approximately 15% compared to the base case without reactive compensation. This enhancement verifies that the SVC effectively maintains a stable voltage level under varying load conditions by dynamically injecting reactive power to counteract voltage drops along the feeder. The smoother slope of the post-compensation curve also indicates a reduction in voltage deviation between buses, contributing to improved system stability and power quality [6], [8], [21].

In contrast, Figure 11 illustrates the variation in active power at different buses before and after SVC installation. While a slight decrease in active power flow is observed following compensation, this reduction is minor and does not adversely affect system efficiency. Instead, it reflects the redistribution of reactive power within the network, which alleviates voltage stress and minimizes reactive losses in transmission lines [7], [20], [22]. The results confirm that SVC integration not only enhances voltage support but also improves the overall power factor and operational reliability of the mining electrical network. Consequently, the use of SVCs in underground mine power systems is validated as a technically and economically feasible approach to maintaining power quality in dynamically varying industrial environments.

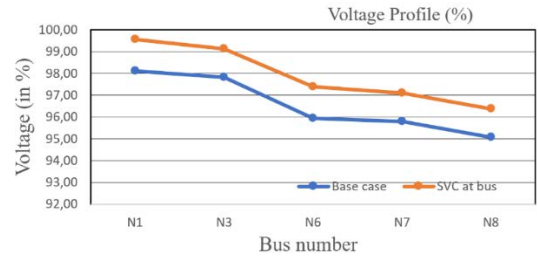


Figure 10. Voltage wave forms before and after SVC installation

Table 1: Power generation before SVC installation

<u>SUMMARY OF TOTAL GENERATION, LOADING & DEMAND</u>				
	MW	Mvar	MVA	% PF
Source (Swing Buses):	0.267	0.132	0.297	89.69 Lagging
Source (Non-Swing Buses):	0.000	0.000	0.000	
Total Demand:	0.267	0.132	0.297	89.69 Lagging
Total Motor Load:	0.260	0.122	0.287	90.51 Lagging

Table 2: Power generation after SVC installation

<u>SUMMARY OF TOTAL GENERATION, LOADING & DEMAND</u>				
	MW	Mvar	MVA	% PF
Source (Swing Buses):	0.275	-0.125	0.302	91.03 Leading
Source (Non-Swing Buses):	0.000	0.000	0.000	
Total Demand:	0.275	-0.125	0.302	91.03 Leading
Total Motor Load:	0.260	0.122	0.287	90.51 Lagging

CONCLUSION

Voltage sag and instability are recognized as major factors affecting power quality, particularly in electrical systems supplying large industrial loads. Such disturbances are especially pronounced in underground mining networks, where multiple high-power electric motors operate simultaneously under variable mechanical stresses. To address this issue, the deployment of a Static Var Compensator (SVC) is proposed as an effective strategy for improving voltage quality and system stability in low-voltage mining grids. The simulation results clearly demonstrate that the integration of SVCs enhances voltage regulation performance, with the busbar voltage level increasing by approximately 15% compared to the uncompensated case, without any significant rise in transmitted power or network losses.

The findings confirm that SVC installation not only strengthens voltage stability margins but also contributes to smoother reactive power flow and improved reliability of the mine's electrical supply. For optimal operation, it is recommended that SVC units be installed at nodes with the greatest voltage sensitivity and configured with adaptive control algorithms capable of responding to rapid load fluctuations. Periodic harmonic monitoring and controller tuning should be conducted to ensure system compatibility and prevent

overcompensation. Moreover, integrating SVC control into a supervisory monitoring platform would allow real-time adjustment of reactive power, thereby maximizing the operational efficiency and safety of underground power distribution systems.

REFERENCES

1. Đỗ Như Ý (2019). Nghiên cứu đề xuất giải pháp giảm dao động điện áp trong mạng điện mỏ. Tạp chí Công nghiệp mỏ, số 5.
2. Hồ Việt Bun (2025). Nghiên cứu ứng dụng phần mềm ETAP trong thiết kế, kiểm tra, quản lý và vận hành mạng cấp điện trong các xí nghiệp mỏ. Tạp chí Công nghiệp mỏ, số 3.
3. Hồ Việt Bun (2025). Nghiên cứu giải pháp nâng cao chất lượng điện áp ở mạng điện hạ áp mỏ hầm lò. Hội thảo quốc tế Thúc đẩy đổi mới và phát triển kết nối các nguyên tắc để tạo ra tác động toàn cầu (Fostering Innovation and Development: Connecting Disciplines to Create Global Impact).
4. Thông tư số 39/2015/TT-BCT ngày 18 tháng 11 năm 2015 của Bộ Công Thương Quy định hệ thống điện phân phối.
5. В. И. Кочкин, Ю. Г. Шакарян, Применение гибких (управляемых) систем электропередачи переменного тока в энергосистемах, 311с-2011.
6. M.Biswas, and K.Das, Voltage Level Improving by Using Static VAR Compensator (SVC), Global Journal of Researches in Engineering,11(5), 2011,13–18.
7. Khandani, S. Soleymani, and B. Mozafari., "Optimal Placement of SVC To Improve Voltage Profile Using Hybrid Genetics Algorithm And Sequential Quadratic Programming", conference on electrical power distribution network (EPDC), 2011.
8. Siddique, A., Xu, Y., Aslaml, W., Albatsh, F.M. : Application of series FACT devices SSSC and TCSC with POD controller in electrical power system network. In Proceedings of the 2018 13th IEEE Conference on Industrial Electronics and Applications (ICIEA), Wuhan, China, pp. 893–899 (31 May 2018–2 June 2018).
9. Mohammed Osman Hassan, "S. J. Cheng, Senior Member, IEEE, Zakaria Anwar Zakaria, Steady-State Modeling of SVC and TCSC for Power Flow Analysis Proceedings of the International Multi Conference of Engineers and Computer Scientists", 2009.

10. V. Ganesh, K. Vasu, K. Venkata Rami Reddy, M. Surendranath Reddy, "Improvement of Transient Stability through SVC", 2012.
11. Mohammed Osman Hassan, "S. J. Cheng, Senior Member, IEEE, Zakaria Anwar Zakaria, Steady-State Modeling of SVC and TCSC for Power Flow Analysis Proceedings of the International Multi Conference of Engineers and Computer Scientists", 2009.
12. J. L. Olabarrieta Rubio, "A Comparative Study of Static VAR Systems for Voltage Support and Power-Quality Improvement," *Icrepq Conference Paper / PDF*, 2023. [Online]. Available: <https://pdfs.semanticscholar.org/4b67/e12ae880be0ca056cccb0aa6293bacab911c.pdf>. Semantic Scholar
13. H. G. Júnior, "General-compensation-purpose Static Var Compensator (SVC)," *Journal / Elsevier*, 2019. [Online]. Available: <https://www.sciencedirect.com/science/article/pii/S2468067218300518>. ScienceDirect
14. M. P. Suresh, "Optimizing smart microgrid performance: Integrating solar generation and static VAR compensator for EV charging impact," *ScienceDirect / Renewable Energy Reports*, 2024. [Online]. Available: <https://www.sciencedirect.com/science/article/pii/S2352484724001252>. ScienceDirect
15. R. M. A. Velásquez, "Harmonic failure in the filter of Static Var Compensator," *Electric Power Systems Research / Elsevier*, 2020. [Online]. Available: <https://www.sciencedirect.com/science/article/abs/pii/S1350630719307381>. ScienceDirect
16. "Static VAR compensator models for power flow and dynamic analysis," *IEEE / Technical report (SVC modeling)*, 2017. [Online]. Available (PDF): https://ptabdata.blob.core.windows.net/files/2017/1PR2017-01135/v8_Exhibit%201005%20-%20IEEE%20SVC.pdf. ptabdata.blob.core.windows.net
17. M. N. Absar, "Power quality improvement of a proposed grid-connected renewable hybrid system by incorporating SVC," *Energy Reports / Elsevier*, 2023. [Online]. Available: <https://www.sciencedirect.com/science/article/pii/S240584402305123X>. ScienceDirect
18. "Design of Static Var Compensator (SVC) for Improving Power Supply of Solar Energy Connected to the Grid," *Conference/ResearchGate*, 2024. [Online]. Available: https://www.researchgate.net/publication/354922798_Design_of_Static_Var_Compensator_SVC_for_Improving_Power_Supply_of_Solar_Energy_Connected_to_the_Grid. ResearchGate
19. F. Alsalem, "Static VAR Compensator Control Using Phasor Measurement Units," *Environmental Systems Engineering / Wiley*, (article), 2024. [Online]. Available: <https://scijournals.onlinelibrary.wiley.com/doi/full/10.1002/ese3.70114>. scijournals.onlinelibrary.wiley.com
20. R. N. Krasnoperov et al., "Performance evaluation of a low-voltage SVC utilizing IoT monitoring and control," *Applied Energy / Elsevier*, 2025 (design/experimental). [Online]. Available: <https://www.sciencedirect.com/science/article/abs/pii/S0378779624010733>. ScienceDirect
21. "Static VAR Compensator for power-factor correction on heavy industry (case studies: arc furnace, traction)," *Applied Case Studies / AIP & Industry Papers*, 2016. [Online]. Available: https://www.researchgate.net/publication/288484863_Application_of_Static_Var_Compensator_of_Ultra-High_Power_Electric_Arc_Furnace_for_Voltage_Drops_Compensation_in_Factory_Power_Supply_System_of_Metallurgical_Enterprise. ResearchGate
22. A. R. Berdugo-Sarmiento, "Improving the Operation of Transmission Systems Based on Centralized and Distributed SVC Strategies," *MDPI Energies / MDPI*, 2025. [Online]. Available: <https://www.mdpi.com/2673-4826/6/3/40>. MDPI
23. "Application of static var compensator with harmonic filters in heavy industry," *ResearchGate / Case study, (2019–2024 surveys)*. [Online]. Available: https://www.researchgate.net/publication/332825538_Application_of_static_var_compensator_with_harmonic_filters_in_the_heavy_industry. ResearchGate
24. "Applying SVCs on Distribution Systems — practitioner white paper / IEEE-related," *Technical Paper / PDF, (open access discussion)*, 2010–2020. [Online]. Available: https://cdn.b12.io/client_media/zaTQ9XtD/7c243e6c-d8b3-11ea-b5bf-0242ac110002-IEEEpaper2.pdf. B12
25. "Comparative assessment: SVC vs STATCOM — power quality & dynamic performance," *Conference/Journal comparative studies*, 2023. (See Olabarrieta Rubio and follow-ons). [Online]. Available: <https://onlinelibrary.wiley.com/doi/10.1155/2023/218048>. Wiley Online Library

DOI: 10.15625/vap.2025.0188

Simulation of Conveyor's motor for analyzing power consumption in Vietnamese underground mines' grid

Nguyen Dinh Tien¹, Le Xuan Thanh^{2,*}

¹HaNoi University of Industry,

²HaNoi University of Mining and Geology,

*Email: lexuanthanh@humg.edu.vn

Abstract: This paper presents a systematic approach for establishing the complete set of mathematical equations describing the electromechanical behavior of synchronous motors used in conveyor drive systems. The formulation is based on the voltage and flux linkage equations expressed in the d-q reference frame, where the inductance matrix **K** plays a central role in representing magnetic coupling between stator and rotor windings. All parameters of the **K matrix** are computed under different operating conditions, taking into account the influence of environmental factors such as ambient temperature, humidity, coal dust concentration, and load torque fluctuations that commonly occur in underground mining conveyors.

The developed equations comprehensively reflect both steady-state and transient processes of the motor under varying load demands. These equations are subsequently implemented in MATLAB/Simulink to construct a detailed simulation model of the asynchronous drive system. The model enables precise analysis of instantaneous voltage, current, electromagnetic torque, and power losses, allowing for accurate estimation of the motor's total energy consumption under real operating conditions.

Furthermore, simulated active energy data will be compared with real-time measurements collected from an operational conveyor system in a coal mine to verify the model's accuracy. The comparison helps to identify discrepancies and propose corrective measures for improving drive efficiency. The

final results serve as a foundation for future study of optimizing drive parameters, selecting appropriate control algorithms, and achieving measurable reductions in the electrical energy consumption of conveyor systems in underground mining operations.

Keywords: K factor, underground mines, power consumption.

INTRODUCTION

In recent years, there have been remarkable institutional and managerial adjustments in Vietnam's energy sector, particularly in the coal mining industry, aimed at improving energy efficiency and power quality. The Ministry of Industry and Trade (MOIT) has issued a series of directives under the revised *Law on Energy Efficiency and Conservation*, requiring coal corporations to implement measurable energy-saving programs and annual audits. These legal and administrative reforms mark a significant shift toward mandatory energy management rather than voluntary compliance. Coal companies are now obliged to monitor and report their energy intensity and implement corrective measures in line with national net-zero commitments by 2050.

Along with these institutional changes, the evaluation and analysis of power consumption in underground coal mines are being rapidly digitalized. Energy auditing—previously conducted manually—is now increasingly supported by intelligent software platforms and automated data acquisition

systems. Advanced analytical tools such as MATLAB/Simulink, DlgSILENT PowerFactory, and ETAP are being widely deployed to simulate electrical networks, assess power losses, and identify sources of power quality in mine grids. These digital methods enable engineers to visualize voltage fluctuations, current harmonics, and transient behaviors caused by heavy equipment such as conveyors and electric excavators.

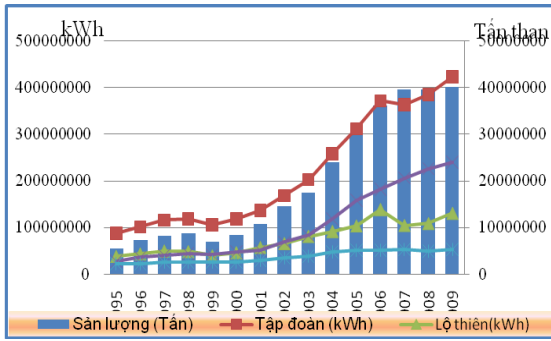


Fig. 1. The relation between Vietnamese domestic coal demand and energy consumption.

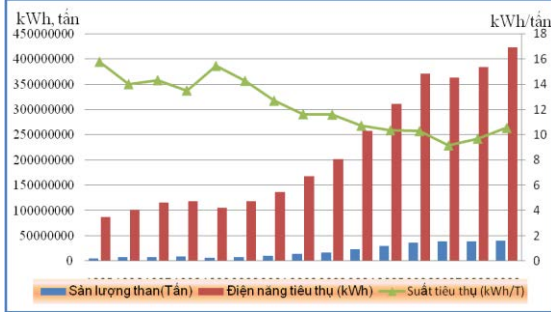


Fig 2: The relation between Coal product (cyan) and Energy consumption (red) of Vietnam coal corporation in 2024.

This digital transformation provides a more accurate and real-time understanding of power consumption issues. By integrating data-driven analysis with simulation models, mining companies can design better control strategies, improve energy efficiency, and ensure compliance with Vietnam's increasingly strict regulatory standards on electrical energy performance and sustainability.

THEORY BASIS OF CALCULATING K FACTORS IN INDUCTANCE MATRIX AND CONVEYOR MOTOR'S CONSUMPTION

General equations

The voltage equation of an electric machine written for each phase can be expressed in the following form [1]:

The outright matrix in this equation expresses fluxes of rotor's and stator's windings. These quantities are also calculated from flux equations as (2). In this equation \underline{L}_x s are 3×3 matrix.

$$\begin{bmatrix} v_{as} \\ v_{bs} \\ v_{cs} \\ v'_{ar} \\ v'_{br} \\ v'_{cr} \end{bmatrix} = \begin{bmatrix} r_s & 0 & 0 & 0 & 0 & 0 \\ 0 & r_s & 0 & 0 & 0 & 0 \\ 0 & 0 & r_s & 0 & 0 & 0 \\ 0 & 0 & 0 & r'_r & 0 & 0 \\ 0 & 0 & 0 & 0 & r'_r & 0 \\ 0 & 0 & 0 & 0 & 0 & r'_r \end{bmatrix} \begin{bmatrix} i_{as} \\ i_{bs} \\ i_{cs} \\ i'_{ar} \\ i'_{br} \\ i'_{cr} \end{bmatrix} + \frac{d}{dt} \begin{bmatrix} \lambda_{as} \\ \lambda_{bs} \\ \lambda_{cs} \\ \lambda'_{ar} \\ \lambda'_{br} \\ \lambda'_{cr} \end{bmatrix} \quad (1)$$

$$\begin{bmatrix} \lambda_{as} \\ \lambda_{bs} \\ \lambda_{cs} \\ \lambda_{ar} \\ \lambda_{br} \\ \lambda_{cr} \end{bmatrix} = \begin{bmatrix} \underline{L}_s & \underline{L}_{sr} \\ \underline{L}_{rs} & \underline{L}_r \end{bmatrix} \begin{bmatrix} i_{as} \\ i_{bs} \\ i_{cs} \\ i_{ar} \\ i_{br} \\ i_{cr} \end{bmatrix} \quad (2)$$

Whereas:

$$\underline{L}_r = \begin{bmatrix} L_{\sigma r} + L_m & -\frac{1}{2}L_m & -\frac{1}{2}L_m \\ -\frac{1}{2}L_m & L_{\sigma r} + L_m & -\frac{1}{2}L_m \\ -\frac{1}{2}L_m & -\frac{1}{2}L_m & L_{\sigma r} + L_m \end{bmatrix}$$

$$\underline{L}_s = \begin{bmatrix} L_{\sigma s} + L_m & -\frac{1}{2}L_m & -\frac{1}{2}L_m \\ -\frac{1}{2}L_m & L_{\sigma s} + L_m & -\frac{1}{2}L_m \\ -\frac{1}{2}L_m & -\frac{1}{2}L_m & L_{\sigma s} + L_m \end{bmatrix}$$

$$L_m \begin{bmatrix} \cos \theta_m & \cos(\theta_m + 120) & \cos(\theta_m - 120) \\ \cos(\theta_m - 120) & \cos \theta_m & \cos(\theta_m + 120) \\ \cos(\theta_m + 120) & \cos(\theta_m - 120) & \cos \theta_m \end{bmatrix}$$

and

$$\underline{L}_{rs} = L_m \begin{bmatrix} \cos \theta_m & \cos(\theta_m - 120^\circ) & \cos(\theta_m + 120^\circ) \\ \cos(\theta_m + 120^\circ) & \cos \theta_m & \cos(\theta_m - 120^\circ) \\ \cos(\theta_m - 120^\circ) & \cos(\theta_m + 120^\circ) & \cos \theta_m \end{bmatrix}$$

Equation (2) obtains a difficulty – that is the stator-rotor and rotor-stator terms, L_{sr} and L_{rs} , are functions of θ_{rotor} . Because θ_{rotor} varies with time, it is clearly that L_{sr} and L_{rs} are functions of time, therefore they need to be differentiated.

$$\theta = \int_0^t \omega(\gamma) d\gamma + \theta(0) \quad (3)$$

K factors in dqo transformation using to simulate synchronous machines

To start calculating K factors, express a, b, c currents in a pair of dq axis, as shown in figure 3. [2]

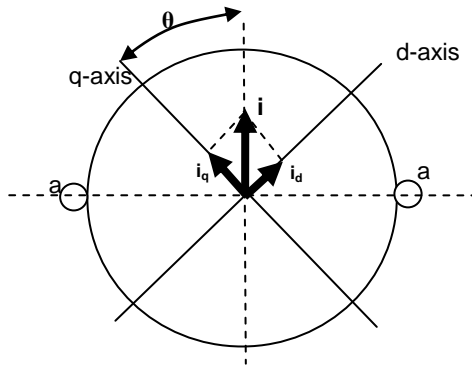


Fig. 3: dq axis expression

Using the above expression, a, b and c currents of synchronous machines are expressed as follow:

$$\begin{aligned} i_q &= k_q (i_a \cos \theta + i_b \cos(\theta - 120^\circ) + i_c \cos(\theta + 120^\circ)) \\ i_d &= k_d (i_a \sin \theta + i_b \sin(\theta - 120^\circ) + i_c \sin(\theta + 120^\circ)) \end{aligned} \quad (4)$$

Identify the zero-sequence current by:

$$i_0 = k_0 (i_a + i_b + i_c) \quad (5)$$

The abc to dqo transformation can be rewritten in the form of matrix as equation (6) [3], [4]:

$$\begin{bmatrix} i_q \\ i_d \\ i_0 \end{bmatrix} = \begin{bmatrix} k_q \cos \theta & k_q \cos(\theta - 120^\circ) & k_q \cos(\theta + 120^\circ) \\ k_d \sin \theta & k_d \sin(\theta - 120^\circ) & k_d \sin(\theta + 120^\circ) \\ k_0 & k_0 & k_0 \end{bmatrix} \begin{bmatrix} i_a \\ i_b \\ i_c \end{bmatrix} \quad (6)$$

Constants k_q , k_d , and k_0 must be calculated suitably to obtain in simulation models.

Determining the factors

Because three phase currents are sinusoidal and symmetry, therefore they can be shown as the following (7):

$$\begin{aligned} i_a &= A \cos \omega t \\ i_b &= A \cos(\omega t - 120^\circ) \\ i_c &= A \cos(\omega t + 120^\circ) \end{aligned} \quad (7)$$

Substitute these quantities into (4):

$$\begin{aligned} i_q &= k_d \left(A \cos \omega t \cos \theta + A \cos(\omega t - 120^\circ) \cos(\theta - 120^\circ) \right. \\ &\quad \left. + A \cos(\omega t + 120^\circ) \cos(\theta + 120^\circ) \right) \\ &= k_d A \left(\cos \omega t \cos \theta + \cos(\omega t - 120^\circ) \cos(\theta - 120^\circ) \right. \\ &\quad \left. + \cos(\omega t + 120^\circ) \cos(\theta + 120^\circ) \right) \end{aligned} \quad (8)$$

Otherwise using maths transfer:

$$\cos(a) \times \cos(b) = (1/2) [\cos(a+b) + \cos(a-b)]$$

i_q can be rewrite as:

$$\begin{aligned} i_q &= \frac{k_d A}{2} \{ \cos(\omega t - \theta) + \cos(\omega t + \theta) + \cos(\omega t - 120^\circ - \theta + 120^\circ) \\ &\quad + \cos(\omega t - 120^\circ + \theta - 120^\circ) \\ &\quad + \cos(\omega t + 120^\circ - \theta - 120^\circ) + \cos(\omega t + 120^\circ + \theta + 120^\circ) \} \\ &= \frac{k_d A}{2} \{ \cos(\omega t - \theta) + \cos(\omega t + \theta) + \cos(\omega t - \theta) \\ &\quad + \cos(\omega t + \theta - 240^\circ) + \cos(\omega t - \theta) + \cos(\omega t + \theta + 240^\circ) \} \\ i_q &= \frac{k_d A}{2} \left\{ 3 \cos(\omega t - \theta) + \left[\cos(\omega t + \theta) + \cos(\omega t + \theta - 240^\circ) \right] \right. \\ &\quad \left. + \cos(\omega t + \theta + 240^\circ) \right\} \end{aligned}$$

Sum in bracket is zero, so finally:

$$i_q = \frac{k_d A}{2} \{3 \cos(\omega t - \theta)\} = \frac{3k_d A}{2} \cos(\omega t - \theta) \quad (9)$$

However from Fig.

$$3i_q = A \cos(\omega t - \theta) \quad (10)$$

Equalize the right sides of (9) and (10):
 $(3k_d A/2) = A$, consequently $k_d = 2/3$.

Carrying out the maths transfer similarly (7), (8), (9) and (10) the k factors are as follow:

$$[k_d \ k_q \ k_o] = [2/3 \ 2/3 \ 1/3] \quad (11)$$

Apply these quantities into general voltage equations of synchronous machines [2], [4], [13] the final model is:

$$\begin{bmatrix} v_{qs} \\ v_{ds} \\ v_{0s} \\ v_{qr} \\ v_{dr} \\ v_{0r} \end{bmatrix} = \begin{bmatrix} r_s & \omega \left(L_{\sigma s} + \frac{3}{2} L_m \right) & 0 & 0 & \frac{3\omega}{2} L_m & 0 \\ -\omega \left(L_{\sigma s} + \frac{3}{2} L_m \right) & r_s & 0 & -\frac{3\omega}{2} L_m & 0 & 0 \\ 0 & 0 & r_s & 0 & 0 & 0 \\ 0 & \frac{3(\omega - \omega_m)}{2} L_m & 0 & r_r & (\omega - \omega_m) \left(L_{\sigma r} + \frac{3}{2} L_m \right) & 0 \\ \frac{-3(\omega - \omega_m)}{2} L_m & 0 & 0 & -(\omega - \omega_m) \left(L_{\sigma r} + \frac{3}{2} L_m \right) & r_r & 0 \\ 0 & 0 & 0 & 0 & 0 & r_r \end{bmatrix} \begin{bmatrix} i_{qs} \\ i_{ds} \\ i_{0s} \\ i_{qr} \\ i_{dr} \\ i_{0r} \end{bmatrix} + \begin{bmatrix} L_{\sigma s} + \frac{3}{2} L_m & 0 & 0 & \frac{3}{2} L_m & 0 & 0 \\ 0 & L_{\sigma s} + \frac{3}{2} L_m & 0 & 0 & \frac{3}{2} L_m & 0 \\ 0 & 0 & L_{\sigma s} & 0 & 0 & 0 \\ \frac{3}{2} L_m & 0 & 0 & L_{\sigma r} + \frac{3}{2} L_m & 0 & 0 \\ 0 & \frac{3}{2} L_m & 0 & 0 & L_{\sigma r} + \frac{3}{2} L_m & 0 \\ 0 & 0 & 0 & 0 & 0 & L_{\sigma r} \end{bmatrix} \begin{bmatrix} i_{qs} \\ i_{ds} \\ i_{0s} \\ i_{qr} \\ i_{dr} \\ i_{0r} \end{bmatrix} \quad (11)$$

Equations of power consumptions in inverters

As presented in [14] the diagram of asynchronous motor is shown in figure 4. Fig 3 shows the main circuit of the frequency converter, including the rectifier, inverter, and intermediate circuit. The turn-on and turn-off of the inverter are controlled by the SVPWM pulse.

There are 3 equations presenting power consumption [15-17]:

- + The on-state loss of the IGBT (Eq. 12).
- + The on-state loss of the fast recovery diode (Eq. 13).
- + The switching loss of the IGBT (Eq. 14).

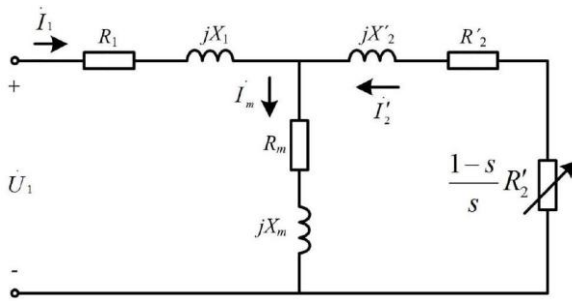


Figure 4. Equivalent circuit diagram of 3phase asynchronous motor in stable operation

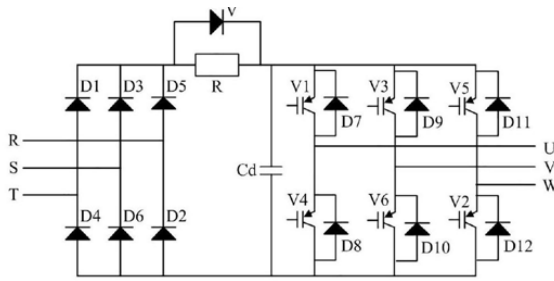


Figure 5. Equivalent circuit diagram of inverter utilized for conveyor motors.

Corresponding to the diagram, the total power consumption of motor containing the inverter is obtain as equation (12)

$$p_{fw/v} = \frac{\alpha^2 p^2 r_{CE} \left(\frac{3}{4} + \frac{2m \cos \phi}{\pi} \right)}{2\pi^2 R^2 (1-s)^2 \left| z_1 + \frac{z_m z_2'}{z_m + z_2'} \right|^2} v^2 + \frac{\sqrt{2} \alpha p V_{CE0} \left(\frac{3}{\pi} + \frac{3m \cos \phi}{4} \right)}{2\pi R (1-s) \left| z_1 + \frac{z_m z_2'}{z_m + z_2'} \right|} v \quad (12)$$

$$p_{fw/D} = \frac{\alpha^2 p^2 r_F \left(\frac{3}{4} - \frac{2m \cos \phi}{\pi} \right)}{2\pi^2 R^2 (1-s)^2 \left| z_1 + \frac{z_m z_2'}{z_m + z_2'} \right|^2} v^2 + \frac{\sqrt{2} \alpha p V_{FO} \left(\frac{3}{\pi} - \frac{3m \cos \phi}{4} \right)}{2\pi R (1-s) \left| z_1 + \frac{z_m z_2'}{z_m + z_2'} \right|} v \quad (13)$$

$$p_{SW} = \frac{6\sqrt{2} \alpha p f_{SW} V_{dc} (E_{SW(on)} + E_{SW(off)})}{2\pi^2 I_{CN} V_{CEN} R (1-s) \left| z_1 + \frac{z_m z_2'}{z_m + z_2'} \right|} v \quad (14)$$

Equations (11) to (14) perform a generous expression of conveyor motor's power consumption, this quantity rely strongly on velocity of the belt.

SIMULATION AND RESULTS APPLYING FOR ENERGY CONSUMPTION ANALYSIS

Matlab models

Matlab models will be built upon on the following equations: (11), (12), (13), (14).

Base on eq. (11), (12), (13), (14) a matlab model of a synchronous machine has been built and is shown in Fig. 6.

Utilizing this model, a connection diagram between a 6kV asynchronous motor with invertter is performed as in Fig. 7.

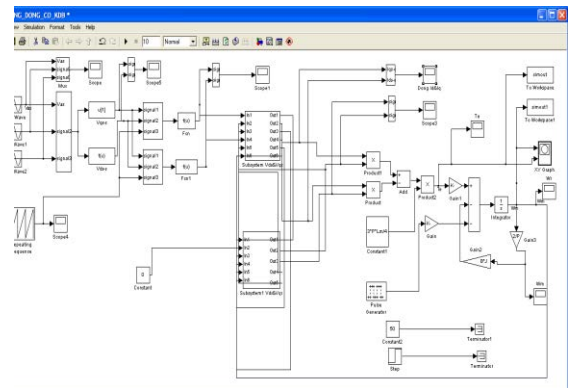


Figure 6. Matlab model of a synchronous machines.

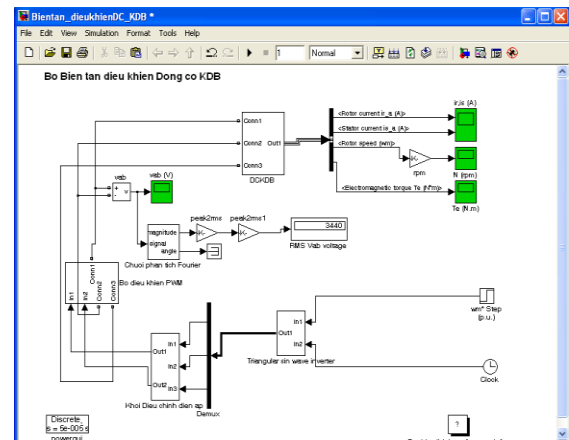


Figure 7. Connection diagram of asynchronous motor and an invertter.

Simulation Results and the application for analyzing Power quality

The K factors are put into simulation diagram on fig.6, the simulation results in Matlab of voltage quality (power harmonic) is compared to the real times measurement.

All are shown in figure 8 to 11. Though the figures the simulation results are matched with real time measurements as well as lab model results [11] and theory voltage waveform [12].

Utilizing the model and making the simulation in MATLab, the outcomes of power consumption of Motor is exhibited in table 1, the values are compared with on-site measurement values shown in Table 2.

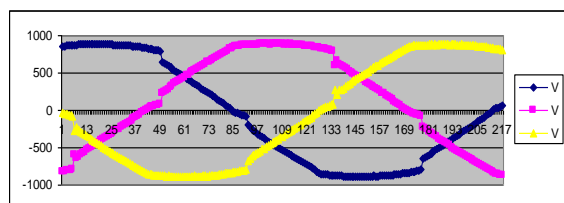


Figure 8 Voltage waveform measured at a PCC node that ECM is connected.

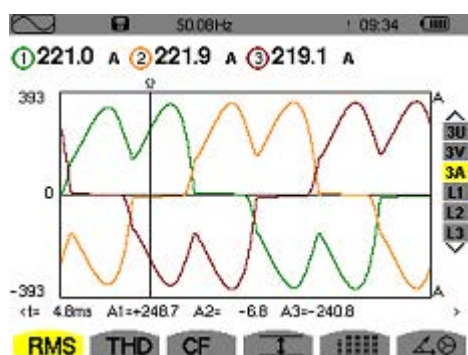


Figure 9: Voltage waveform measured in front of the inverter

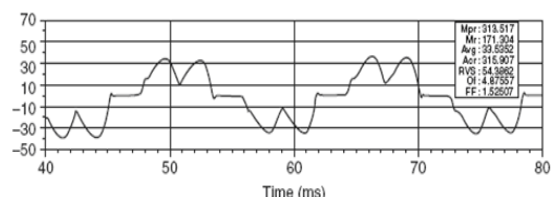


Figure 10: Theory voltage waveform [12]

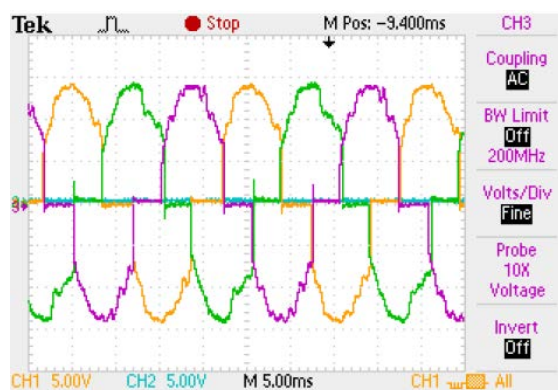


Figure 11. Voltage Lab model waveforms [11]

Table 1. Results deducted from Simulation (W)

Number	Pa	Pb	Pc	P 3phase
1	7074,5	7010,4	7015,4	21100,4
2	7326,8	7420,9	7425,9	22173,6
3	7339,8	7371,3	7376,3	22087,5
4	7441,7	7466,7	7468,7	22377,1
5	7168,4	7179,2	7180,2	21527,7
6	7191,2	7284,1	7286,1	21761,4
7	6750,6	6814,8	6813,8	20379,2
8	7420,4	7441,9	7442,9	22305,3
9	7582,3	7577,6	7582,6	22742,6
10	6817,2	6830,2	6832,2	20479,6
11	7170,4	7224,5	7222,5	21617,3
12	7123,4	7173,9	7177,9	21475,2
13	7019,6	7099,5	7102,5	21221,6
14	6892,9	6935,3	6934,3	20762,5
15	7058,4	7118,2	7121,2	21297,9
16	7414,3	7436,0	7436,0	22286,3
17	7209,7	7275,3	7276,3	21761,2
18	7016,9	7055,1	7058,1	21130,0
19	6962,4	7018,7	7019,7	21000,7
20	6724,6	6795,6	6795,6	20315,7
21	7600,1	7589,7	7591,7	22781,5
22	7502,6	7464,9	7466,9	22434,4
23	7289,7	7363,7	7364,7	22018,1
24	7088,4	7141,7	7141,7	21371,8
25	7113,1	7163,2	7165,2	21441,5
26	7167,3	7221,1	7226,1	21614,6
27	7377,9	7452,7	7457,7	22288,4
28	7343,6	7393,6	7392,6	22129,9
29	7115,0	7179,8	7182,8	21477,6
30	7519,7	7558,1	7562,1	22639,9
31	7193,2	7235,9	7239,9	21669,0
32	7188,9	7232,7	7234,7	21656,3
33	6909,0	6991,4	6989,4	20889,7

34	7038,3	7127,0	7133,0	21298,3
35	7187,2	7276,4	7280,4	21744,0
36	7001,5	7064,6	7067,6	21133,7
37	6973,3	7019,9	7022,9	21016,1
38	6842,9	6941,5	6940,5	20725,0
39	6930,5	7035,8	7035,8	21002,1
40	7107,0	7177,6	7180,6	21465,1
41	7007,6	7080,1	7083,1	21170,8
42	6897,1	6940,0	6942,0	20779,0
43	7254,6	7308,5	7306,5	21869,7
44	7094,9	7136,1	7140,1	21371,1
45	7153,9	7289,6	7288,6	21732,2
46	7253,1	7380,6	7383,6	22017,3
47	7387,5	7513,5	7512,5	22413,4
48	7508,9	7639,9	7645,9	22794,7
49	7634,9	7721,8	7726,8	23083,4
50	7276,0	7352,3	7357,3	21985,6

51	7301,0	7333,4	7337,4	21971,8
52	7451,0	7509,0	7515,0	22475,0
53	7436,7	7448,6	7449,6	22334,8
54	7503,2	7512,1	7516,1	22531,3
55	7601,9	7579,0	7581,0	22761,9
56	7653,8	7612,9	7612,9	22879,6
57	6873,3	6928,1	6934,1	20735,5
58	7396,5	7413,7	7417,7	22228,0
59	7319,7	7363,9	7366,9	22050,6
60	7221,0	7303,7	7301,7	21826,4
61	7432,5	7479,3	7481,3	22393,1
62	7707,8	7817,1	7820,1	23345,1
63	7599,4	7720,8	7719,8	23040,0
64	7866,0	7990,4	7992,4	23848,8
65	7921,6	7984,7	7985,7	23892,0
66	7645,1	7737,4	7738,4	23120,8

Table 2: On-Site measurement results (W)

V1	A1	W1	V2	A2	W2	V3	A3	W3	W3phase
403,2	20,16	7077,5	400,8	20,08	7007,4	405,4	20,12	7102,0	21.186,9
405,7	19,84	7331,8	402,3	20,24	7416,9	406,4	20,04	7418,5	22.167,2
405,8	20,72	7342,8	402,6	20,96	7369,3	407,0	20,84	7407,2	22.119,4
405,2	21,28	7444,7	401,7	21,52	7463,7	406,0	21,40	7501,5	22.409,9
402,6	20,64	7171,4	399,6	20,80	7173,2	404,0	20,72	7224,3	21.568,8
404,3	20,16	7195,2	401,0	20,56	7278,1	405,3	20,36	7284,6	21.757,8
394,1	19,52	6755,6	390,8	19,84	6808,8	395,1	19,68	6828,2	20.392,6
404,5	22,24	7424,4	400,8	22,48	7435,9	405,4	22,36	7481,1	22.341,5
408,0	21,76	7587,3	404,4	21,92	7575,6	408,8	21,84	7630,1	22.793,1
390,3	22,08	6819,2	388,0	22,24	6828,2	391,5	22,16	6865,0	20.512,4
402,0	21,68	7173,4	398,7	22,00	7219,5	403,1	21,84	7246,1	21.638,9
401,3	21,76	7127,4	397,9	22,08	7170,9	402,3	21,92	7197,7	21.496,0
395,1	25,60	7021,6	391,8	26,08	7093,5	396,2	25,84	7107,2	21.222,3
396,4	23,52	6893,9	393,2	23,84	6931,3	397,5	23,68	6960,1	20.785,3
399,7	20,88	7062,4	396,5	21,20	7113,2	400,8	21,04	7136,1	21.311,7
406,1	21,20	7417,3	402,3	21,44	7431,0	406,5	21,32	7466,6	22.314,9
402,3	22,88	7213,7	398,6	23,28	7272,3	403,0	23,08	7289,4	21.775,4
399,9	20,48	7021,9	396,8	20,72	7049,1	400,9	20,60	7080,7	21.151,6
394,9	20,72	6963,4	391,7	21,04	7013,7	395,9	20,88	7035,0	21.012,0
392,8	22,80	6725,6	389,7	23,20	6789,6	393,6	23,00	6798,4	20.313,5
407,3	22,56	7603,1	403,4	22,72	7583,7	408,1	22,64	7645,0	22.831,8
407,7	21,12	7504,6	403,8	21,20	7460,9	408,4	21,16	7531,7	22.497,2
403,9	20,24	7292,7	399,6	20,64	7357,7	403,6	20,44	7359,3	22.009,7
401,6	20,80	7090,4	398,1	21,12	7136,7	401,9	20,96	7150,2	21.377,3
402,6	21,92	7118,1	399,1	22,24	7159,2	403,0	22,08	7177,2	21.454,4
400,6	25,04	7168,3	397,1	25,44	7219,1	401,1	25,24	7234,5	21.622,0
401,1	26,00	7379,9	397,5	26,48	7448,7	401,5	26,24	7455,5	22.284,2
401,1	26,72	7344,6	397,5	27,12	7387,6	401,6	26,92	7408,8	22.141,0
401,6	23,36	7118,0	398,1	23,76	7176,8	402,1	23,56	7187,9	21.482,7
406,9	23,04	7522,7	403,0	23,36	7554,1	407,0	23,20	7576,8	22.653,6
403,3	21,84	7196,2	399,5	22,16	7232,9	403,3	22,00	7249,0	21.678,1
401,1	21,84	7190,9	397,5	22,16	7230,7	401,4	22,00	7249,0	21.670,5
398,7	21,04	6914,0	395,3	21,44	6985,4	399,1	21,24	6986,7	20.886,1
398,2	23,04	7043,3	394,6	23,52	7125,0	398,5	23,28	7122,0	21.290,3
401,9	23,04	7190,2	398,2	23,52	7272,4	402,1	23,28	7268,7	21.731,3
399,2	22,80	7005,5	395,4	23,20	7060,6	399,4	23,00	7070,5	21.136,7
398,6	21,36	6974,3	395,0	21,68	7014,9	399,1	21,52	7035,4	21.024,6

Values in table 1 and 2 show very tiny bias that show the precise of the simulation.

CONCLUSION

This paper successfully developed a comprehensive mathematical and simulation model for analyzing the electrical energy consumption of conveyor drive motors in underground mining operations. The system of voltage and flux linkage equations, formulated using the inductance matrix with accurately determined **K factors**, provides a reliable representation of the motor's electromagnetic and mechanical characteristics under variable operating conditions. Through MATLAB/Simulink simulation, the proposed model was capable of reproducing transient and steady-state behaviors that closely align with real industrial conditions.

Comparative analysis between simulation outcomes and experimental measurements demonstrated a high degree of consistency, validating the precision of the model. Key quantities such as current, voltage, electromagnetic torque, and active energy exhibited deviations within acceptable limits, confirming that the mathematical formulation accurately reflects real energy consumption dynamics. These results not only validate the correctness of the theoretical approach but also establish confidence in its predictive capability.

Moreover, the structure of the developed model—with parameter sets generalized from field data—ensures its **scalability and adaptability**. It can be readily applied to evaluate and optimize energy consumption in other electromechanical subsystems of underground coal mines, including ventilation fans, pumping stations, and hoisting systems. Therefore, the research provides a robust foundation for digital energy management and contributes to enhancing energy efficiency across Vietnam's mining industry in accordance with national sustainability goals.

REFERENCES

- [1] P. Krause, 1995 *Analysis of Electric Machinery*, IEEE Press, pp. 167-168.
- [2] M.Riaz, *Simulation of electric machines and drive system*, Technical report. University of Minnesota.
- [3] R. Park, 1929 *Two reaction theory of synchronous machines* Transactions of the AIEE, v. 48, p. 716-730.
- [4] J. MacCalley, *Electric machines simulation*, Technical report Iowa university.
- [5] Rashid M.H, 1993 *Power Electronics circuits Devices and Applications* Second Edition, Prentice-Hall Inc, Englewood Cliff, Newjersey,
- [6] G.A. Leonov, N.V. Kondrat'Eva, 2009 *Electromechanical and Mathematical models of synchronous electrical machines*, PHYSCON 2009, Catania, Italy, September,
- [7] R.Kisnani, 2001 *Electric motor drive modeling, Analysis and Control*, Prentice Hall, NewJersey,.
- [8] Kamwa, I., et al., 1995, *Experience with Computer-Aided Graphical Analysis of Large Synchronous Machines*, IEEE Transactions on Energy Conversion, Vol. 10, No. 3
- [9] *Reports for power system accounting in open-pitch mines, VIMSAT VietNam 2012.*
- [10] Nguyen Anh Tuan, Nhu Viet Tuan, and Dao Hong Quang *The trend of mechanization development for underground mining in the Quangninh coal field*, - VIMSAT, The 2nd international conference on advances in mining and tunneling, Hanoi, VietNam 2012.
- [11] Ahmed Riyaz, Atif Iqbal, Shaikh Moinoddin, SK. MoinAhmed, Haitham Abu-Rub, 2009, *Comparative performance analysis Thyristors and IGBT based induction motors soft starters*, International Journal of Engineering, Science and Technology, Vol 1. No 1.
- [12] Alexander Kusko, Sc.D., P.E; Marc T.Thompson, PhD. *Power quality in Electrical Systems*, Mc Graw Hill 2007,
- [13] Le Xuan Thanh, Research for solutions to improve power quality in QuangNinh coal mines's grid, PhD Thesis, 2015

- [14] He Daijie, Pang Yusong, Lodewijks Gabriel. Speed control of belt conveyors during transient operation. *Powder Technology*. 2016; 301:622–631.
- [15] Hiltermann J., Lodewijks G., Schott D. L., Rijsenbrij J. C., Dekkers J. A. J. M., Pang Y. A Methodology to Predict Power Savings of Troughed Belt Conveyors by Speed Control. *Particulate Science and Technology*. 2011; 29: 14–27.
- [16] Zhang Shirong, Xia Xiaohua. A New Energy Calculation Model of Belt Conveyor. *IEEE AFRICON*. 2009; 2009:1–6.
- [17] Mathaba Tebello, Xia Xiaohua. A Parametric Energy Model for Energy Management of Long Belt Conveyors. *Energies*. 2015; 8: 13590–13608.

DOI: 10.15625/vap.2025.0189

Research of the relationship between rock mass elastic modulus and the maximum surface subsidence for developing a geomechanical model of the Khe Cham coal mine

Chung Pham Van^{1,*}, Nghia Nguyen Viet¹, Long Nguyen Quoc¹, Canh Le Van¹, Dinh Thanh Tuan²

¹Hanoi University of Mining and Geology, Faculty Of Geomatics and Land Administration, Hanoi, Vietnam

²Dong Hai Measurement Company Limited, My Tho, Dong Thap, Vietnam

*Email: phamvanchung@humg.edu.vn

Abstract: The model allows the study of engineering problems in both heterogeneous and homogeneous environments, as well as in isotropic and anisotropic rock masses. The laws governing rock and soil displacement and deformation determine the distribution of stress, strain, the development of failure zones, and the height of the fractured zone. Their intensity depends on structural characteristics, the stratigraphic sequence of rock layers, and the cross-sectional geometry of mine workings.

This paper determines the elastic modulus of the rock mass using the RocData software. Based on this, the relationship between the elastic modulus and the maximum surface subsidence in the geomechanical model is established. A correlation function is constructed, and the coefficient $K_C = E_C/E_R = 1.24$ is determined for application to the Quang Ninh region.

Keywords: elastic modulus, subsidence, Khe Cham coal mine.

INTRODUCTION

For the calculation and construction of geomechanical models, and for the design of underground structures and underground mining operations, it is essential to obtain the mechanical-physical properties of the rock mass. In practice, there are many methods for determining these properties. Common approaches used in different regions include the Rock Mass Rating (RMR) classification, the Russian method that applies a structural

strength reduction coefficient for rock masses, and the empirical approach proposed by Hoek and Brown, which is based on the Hoek–Brown failure criterion for intact rock and rock mass, and considers the geological strength index (GSI) and the disturbance factor (D) due to blasting damage [Nguyen, T. S., & Pham, V. C. (2009); Nguyen, V. T. (2014)]

Currently, numerous empirical expressions are available to estimate mechanical parameters such as elastic modulus (Young's modulus), compressive strength, tensile strength, as well as internal friction angle and cohesion, in correlation with the indices RMR, GSI, and D.

The development of these methods reflects major scientific achievements in rock mechanics and geotechnical engineering worldwide, while also highlighting the complex mechanical behavior of rock masses governed by both geological conditions and mining technology.

Since these methods rely on different criteria, it is necessary to analyze and compare them to select the most appropriate (fit-for-purpose) approach and to further develop methods suited to Vietnamese conditions.

DETERMINING THE ROCK MASS ELASTIC MODULUS (E) FOR THE KHE CHAM COAL MINE

Overview of the geology in the study area

The Khe Cham coal mine is currently extracting longwall panels 13.1-8V and 12.7 in

the seams 12 and 13 using the full-caving longwall method, from level -225 m up to -100 m. The average depth from the ground surface to the active longwall faces is 220÷250 m. The geological conditions of the seams 12 and 13 are presented in Table 2.1, and a geological cross-section along line XII is shown in Figure 2.1 [Final Report of the Research Project].

Table 2.1. Geological conditions of the seams 12 and 13 [Khe Cham geological report.].

No.	Longwall parameter	Unit	Seam 12 & 13
1	Mining level	m	-225 ÷ -100
2	Seam thickness	m	1.9 ÷ 2.1
3	Seam dip angle	deg	10 ÷ 22
4	Overburden thickness	m	5
5	Longwall length along the dip direction	m	110 ÷ 105
6	Longwall length along the strike direction	m	90 ÷ 236
7	Average depth of the longwall	m	254 ÷ 222

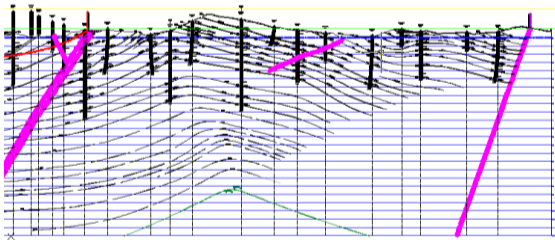


Figure 2.1. Geological cross-section along line XIIIB [Khe Cham geological report.]

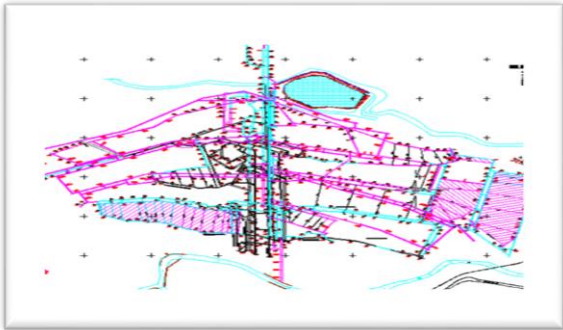


Figure 2.2. Layout of mine roadways (entries and drifts).

It is shown that the geological conditions for underground coal extraction at Khe Chàm are complex, notably due to folds and faults. These structures strongly affect deformation concentration zones and alter the geometry of subsidence troughs (displacement basins). Uniaxial compressive strength (UCS) test results for representative rock samples at Khe Cham are listed in Table 2.2 [Pham, D. H. (2011–2013)].

Table 2.2. Uniaxial compressive strength test results

No.	Rock type	UCS, σ (MPa)
1	Sandstone	114
2	Siltstone	42
3	Argillite	31
4	Coal	17.1

The elastic modulus (E) determined using Rocdata

To determine the elastic modulus E using RocData, it required inputs include uniaxial compressive strength (σ), Geological Strength Index (GSI), and the Disturbance factor (D) for the Quang Ninh coal basin. The GSI and D indices were selected following the expert judgment of Ngo Van Sy. The input data are shown in Table 2.3, and resulting elastic modulus is summarized in Table 2.4.

Table 2.3. Input data for Rocdata

No.	Rock type	σ (MPa)	GSI	Disturbance factor, (D)	Hoek–Brown constant, (m_i)
1	Sandstone	114	45	0.8	17
2	Siltstone	42	37	0.8	7
3	Argillite	31	11	0.8	4
4	Coal	17.1	8	0.8	4

Figures 2.3÷2.6 illustrate the Rocdata determination of E for sandstone, siltstone, argillite, and coal, respectively.

- Case 1: E values from Rocdata—sandstone 2110 MPa, siltstone 690 MPa, argillite 242 MPa; constant ν .

- Case 2: E reduced to 70% of Rocdata—sandstone 1477 MPa, siltstone 483 MPa, argillite 169.4 MPa; constant ν .

- Case 3: E reduced to 50% of Rocdata—sandstone 1055 MPa, siltstone 345 MPa, argillite 121 MPa; constant ν .

- Case 4: E increased to 125% of Rocdata—sandstone 2637.5 MPa, siltstone 862.5 MPa, argillite 302.5 MPa; constant ν .

- Case 5: E reduced to 30% of Rocdata—sandstone 633 MPa, siltstone 207 MPa, argillite 72.6 MPa; constant ν .

- Case 6: E reduced to 10% of Rocdata—sandstone 211 MPa, siltstone 69 MPa, argillite 24.2 MPa; constant ν .

Results for the section oriented along the dip direction of the longwall

Figures 3.1÷3.6 show a clear trend: the larger the elastic modulus, the smaller the maximum subsidence, indicating a strong inverse correlation. The maximum subsidence (η) and the corresponding E values used in each case are summarized in Table 3.1.

Table 3.1. Maximum subsidence and elastic modulus

No	Rock type / Metric	Case 1	Case 2	Case 3	Case 4	Case 5	Case 6
1	Sandstone E (MPa)	2110	1477	1055	2637.5	633	211
2	Siltstone E (MPa)	690	483	345	862.5	207	69
3	Argillite E (MPa)	242	169.4	121	302.5	72.6	24.2
4	Coal E (MPa)	93.01	93.01	93.01	93.01	93.01	93.01
5	Maximum subsidence, η (m)	1.890	1.489	1.918	0.940	2.558	5.065

Figures 3.1÷3.6. Ground-surface subsidence profiles for Cases 1÷6.

For natural rocks, Poisson's ratio typically ranges from 0.1 to 0.3. In addition to the six scenarios above, two more models were run with $\nu = 0.1$ and $\nu = 0.3$, while keeping the elastic modulus values equal to those from

Rocdata. The results changes in maximum subsidence were insignificant compared to the base case with $\nu = 0.2$.

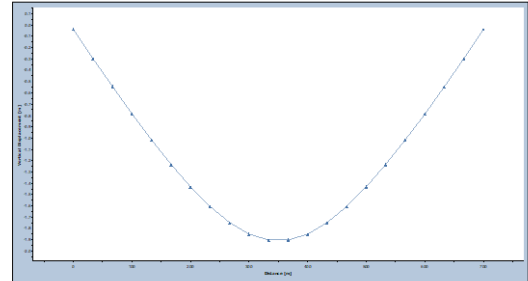


Figure 3.1. Ground surface subsidence in case 1

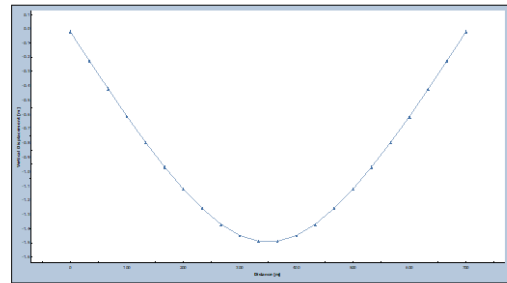


Figure 3.2. Ground surface subsidence in case 2

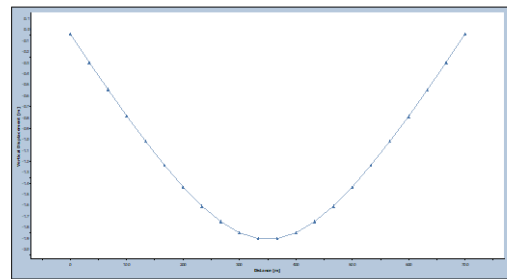


Figure 3.3. Ground surface subsidence in case 3

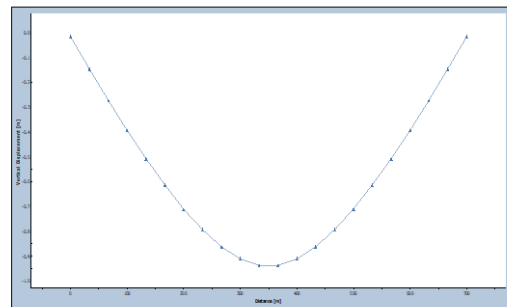


Figure 3.4. Ground surface subsidence in case 4

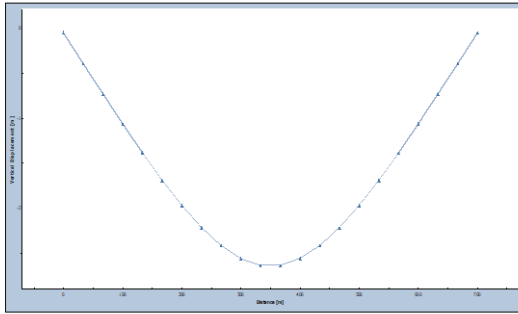


Figure 3.5. Ground surface subsidence in case 5

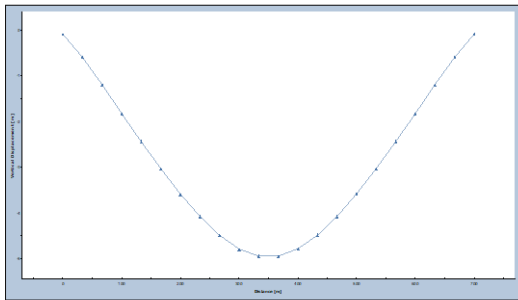


Figure 3.6. Ground surface subsidence in case 6

Relationship between the maximum subsidence and elastic modulus

Statistical analysis plays a key role in converting data obtained from experiments or natural observations into actionable knowledge. The statistical computing environment R (developed by Ross Ihaka and Robert Gentleman) was used to construct correlation plots and derive regression equations relating maximum subsidence (η) to elastic modulus (E) based on the data in Table 3.1 [Nguyen, V. T. (2014)].

To evaluate the significance of the interrelated influencing variables, statistical analysis and graphical language (using the R software) were applied to determine the correlation charts and the equations of the independent variables.

The database was obtained from Table 3.1, and the analysis results are as follows:

For sandstone, siltstone, and argillite, the correlation diagrams are shown in Figures 3.7÷3.9.

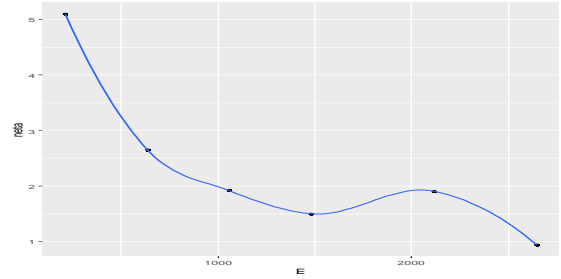


Figure 3.7. Correlation diagram between subsidence and elastic modulus of sandstone

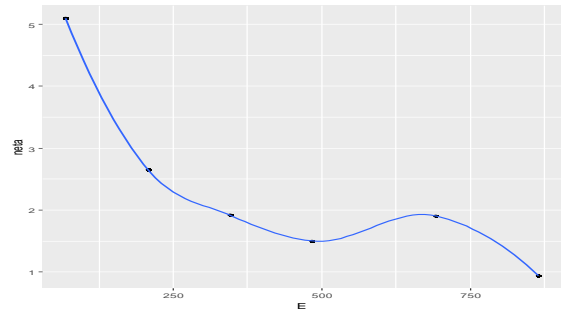


Figure 3.8. Correlation diagram between subsidence and elastic modulus of siltstone

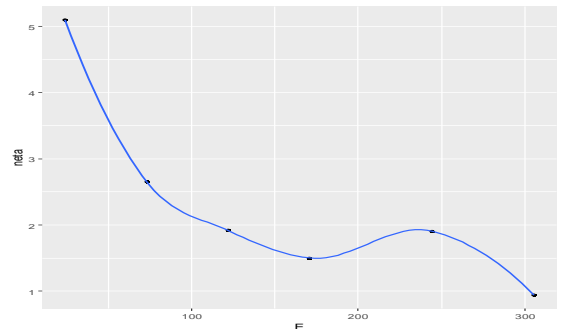


Figure 3.9. Correlation diagram between subsidence and elastic modulus of argillite.

The equation representing the correlation between the maximum subsidence and the elastic modulus of the rock types [Pham V. C. (2018)]:

$$\eta = a + EX + EX^2 + EX^3$$

For sandstone, with its elastic modulus, equation (3.1) is determined.

$$\eta = 7.01 - 1.04 \cdot 10^{-2} \cdot E + 6.50 \cdot 10^{-6} \cdot (E)^2 - 1.30 \cdot 10^{-9} \cdot (E)^3 \quad (3.1)$$

For siltstone, equation (3.2) is determined.

$$\begin{aligned} \eta = & 7.01 - 3.17 \cdot 10^{-2} \cdot E + 6.08 \cdot 10^{-5} \cdot (E)^2 \\ & - 3.72 \cdot 10^{-8} \cdot (E)^3 \end{aligned} \quad (3.2)$$

For argillite, equation (3.3) is determined.

$$\begin{aligned} \eta = & 7.01 - 8.99 \cdot 10^{-2} \cdot E + 4.88 \cdot 10^{-4} \cdot (E)^2 \\ & - 8.46 \cdot 10^{-7} \cdot (E)^3 \end{aligned} \quad (3.3)$$

Thus, by solving equations (3.1), (3.2), and (3.3), the elastic modulus E_C was determined, and the results are presented in Table 3.2.

Table 3.2. Results of calculating the elastic modulus of rock types [Pham V. C. (2018)].

No.	Parameter	Sandstone	Siltstone	Argillite
1	ER (MPa)	2115	691.36	244.03
2	EC (MPa)	2628.788	860.368	303.637

From the results presented in Table 3.2, it can be observed that if the elastic modulus calculated using the Rocdata software (E_R) is applied to the geomechanical model for any region, it becomes possible to predict surface displacement and deformation, as well as to determine the displacement parameters. This provides a basis for developing safe and effective mining solutions.

However, during data processing, when applying the geomechanical model to the Quang Ninh coal basin, the author identified a strength reduction coefficient determined according to equation (3.4) [Pham V. C. (2018)].

$$K_C = E_C / E_R = 1,2 \quad (3.4)$$

CONCLUSIONS

Around the world, numerous geomechanical models have been developed to analyze and predict ground surface movement and deformation, taking various forms. A comprehensive review and analysis indicate that these models all exhibit certain limitations and are generally of local applicability, being closely related to the specific geological conditions of each region or country. Geomechanical models that employ numerical methods possess a high degree of quantitiveness. The accuracy of such models depends on multiple factors, among which the

uniaxial compressive strength test is particularly important.

In practical studies on ground surface movement and deformation caused by underground mining, this dissertation employed a geomechanical model using input data from the Quang Ninh coal basin. The elastic modulus for the model was determined based on field-observed maximum subsidence values, which were used as boundary conditions to calibrate the geomechanical model for greater accuracy and realism.

REFERENCES

- Final Report of the Research Project: "Study on the Assessment of Ground Subsidence Causes and Proposal of Countermeasures for Ground Subsidence at the Khe Cham Coal Preparation Plant" (in Vietnamese). Khe Cham geological report. [in Vietnamese].
- Hoek, E., Marinos, P., & Benissi, M. (1998). Applicability of the Geological Strength Index (GSI) classification for very weak and sheared rock masses: The case of the Athens Schist Formation. *Bulletin of Engineering Geology and the Environment*, 57(2), 151–160.
- Nguyen, V. T. (2014). Data analysis with R. [in Vietnamese]. Ho Chi Minh City General Publishing House. ISBN 978-604-58-2831-1
- Nguyen, T. S., & Pham, V. C. (2009). Investigation and assessment of surface displacement potential of coal seams 15 and 16 at Khe Cham mine to support investment project development and basic design of the coal recovery and screening system in the Northern Khe Cham Area – Cua Suot port Joint Stock Company – TKV. [Project report]. Institute of Mining Science and Technology. [In Vietnamese].
- Pham V. C. (2018). Research on developing a geomechanical variability model for mechanized longwall extraction in thick seams at selected underground coal mines in Quang Ninh [Doctoral dissertation]. [in Vietnamese].
- Pham, D. H. (2011–2013). Development of a geomechanical mine database to support mechanization and modernization of coal mining in Vietnam [Key ministerial project]. Ministry of Industry and Trade. [in Vietnamese].
- VNIMI. (1981). Regulations for protecting structures and natural objects from harmful impacts during underground coal mining. Saint Petersburg: VNIMI. [In Russian].

Construction of a gravity model for the East Sea for application in wave energy potential assessment

Nguyen Van Sang^{1,*}, Nguyen Thanh Thuy²

¹Hanoi University of Mining and Geology, No.18 Vien Street, Dong Ngac, Hanoi, Vietnam

²Institute of Spatial Data, No. 15, Lane 77, Bang Liet Street, Hoang Liet, Hanoi, Vietnam

*Email: nguyenvansang@humg.edu.vn

Abstract: In wave energy potential assessment, an approximate gravity value is often used, however, to achieve accurate results, it is necessary to determine the gravity value at each location with recorded significant wave height. The objective of this paper is to develop a gravity model for the East Sea to support the assessment of wave energy potential. To achieve the stated objective, modern global Earth Gravitational Models and ship-derived gravity in the East Sea were collected. The methods for deriving gravity anomalies/gravity values from global Earth Gravitational Models were examined. By comparing with ship-derived gravity, the most suitable global Earth Gravitational Model for the East Sea was identified. The gravity model for the East Sea, serving the assessment of wave energy potential, was developed based on the integration of the global EGM model with ship-derived gravity. The gravity values at locations requiring wave energy potential estimation were computed by interpolating from the gravity model using the inverse distance weighting method. Experimental results indicate that the SGG-UGM-2 model is the most suitable for the East Sea. The accuracy of the gravity model for the East Sea reaches ± 3.17 mGal.

Keywords: wave energy potential, gravity, East Sea, Earth Gravitational Model.

INTRODUCTION

In the context of increasing energy demand and the depletion of fossil fuel resources, the development of renewable energy has become an urgent requirement. Among marine renewable energy sources, wave

energy is considered to have great potential due to its stability, environmental friendliness, and large-scale exploitation capability. For the East Sea, several domestic and international studies have focused on assessing wave energy potential based on oceanographic observations, ECMWF reanalysis wind data, or numerical models such as SWAN and WAVEWATCH III (Ministry of Natural Resources and Environment, 2022; Curto et al., 2020; Miao et al., 2012; Do et al., 2022; Burhanudin et al., 2019; Le et al., 2017). However, these studies still face limitations such as low resolution, lack of analysis of long-term wave energy stability indices, and especially, the absence of direct utilization of satellite altimetry data.

Meanwhile, worldwide, numerous studies have applied satellite altimetry data to determine wave height and wave energy potential, achieving high accuracy when compared with buoy measurements (Jayaram et al., 2015; Hector et al., 2015; Uti et al., 2018; Kudryavtseva & Soomere, 2016; Queffelec & Bentamy, 2007; Su et al., 2017; Wan et al., 2015). These results confirm that satellite altimetry is an advanced, effective, and suitable method for developing wave energy potential maps.

Thus, it can be seen that although many successful studies worldwide have used satellite data to determine wave energy potential, in Vietnam and the East Sea, no research has deeply explored this application. Notably, no study has yet considered the factor of precise gravity in the problem of determining wave energy potential—a factor that significantly affects the calculation and mapping of wave energy resources.

In the East Sea, direct marine gravity surveys have been conducted since the 1990s with the participation of Vietnam and international partners. However, the collected data remain sparse, of uneven accuracy, and mainly served oil and gas exploration purposes (Bui, 2008). In contrast, satellite altimetry has demonstrated its ability to determine marine gravity anomalies with increasingly high coverage and accuracy, around $\pm 3\text{--}7$ mGal in many regions (Hwang & Parsons, 1995; Sandwell & Smith, 1997; Andersen, 2010). In Vietnam, some initial studies have applied satellite data such as ENVISAT, Saral/AltiKa and CryoSat-2 to compute gravity anomalies in the East Sea, but the results are still limited in scale, with errors usually ranging from ± 2.6 to 8.5 mGal (Nguyen, 2012; Nguyen et al., 2020). To date, there is still no accurate gravity model for the East Sea. Therefore, it is necessary to develop a gravity model for the East Sea by integrating direct measurements and satellite data to improve accuracy and effectively support the assessment of marine wave energy potential.

STUDY AREA AND DATA

Study Area

The study area is in the East Sea, bounded by latitudes $[5.5^\circ\text{N} - 25^\circ\text{N}]$ and longitudes $[104.5^\circ\text{E} - 117.5^\circ\text{E}]$ (Fig. 1). This sea region exhibits complex oceanographic conditions with various tidal regimes: the northern part is mainly diurnal, the central part is irregular diurnal, while the southern part varies from semidiurnal to diurnal tides with large amplitudes (Ha, 2015). The surface currents show distinct seasonal characteristics, forming large-scale cyclonic eddies and convection under the influence of monsoons and the Intertropical Convergence Zone (Rong, 1994; Xu et al., 1980). Wave heights in this area vary significantly, from less than 3 m in the Gulf of Thailand to over 12 m in the northeastern East Sea due to typhoons and the northeast monsoon (Le, 2005).

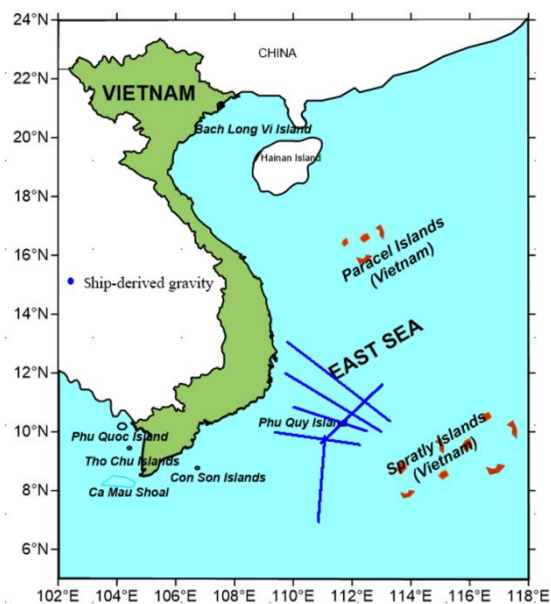


Figure 1. Study area and ship-derived gravity measurements

Research Data

a) Global Gravity Field Model Data

Global gravity field models have been developed by various organizations from 1966 to the present, amounting to 178 models. These data are provided by ICGEM (Ince et al., 2019). The accuracy of these models has been evaluated by comparing them with GNSS/leveling data at 24,014 points, and the standard deviations were computed. Specifically: Australia – 7,224 points, Brazil – 1,154 points, Canada – 2,702 points, Europe – 1,047 points, Japan – 816 points, Mexico – 4,898 points, and the USA – 6,169 points. Fig. 2 illustrates the accuracy of these models (Ince et al., 2019).

From this comparison, six recent models (EGM2008, EIGEN-6C4, GECO, SGG-UGM-1, XGM2019E, and SGG-UGM-2) were selected as the best fit with GNSS/leveling data for evaluation in the East Sea.

b) Shipborne Gravity Data

The gravity anomaly dataset (CSLo7) was measured onboard the vessel Professor Polshkov in 2007 and 2008. The data were

processed by ARK Geophysics Ltd. in Ho Chi Minh City. The coordinates are given in the WGS-84 reference frame. The dataset includes bathymetry, gravity, Free-air and Bouguer anomalies, and magnetic data. Detailed information about this dataset is presented in (Institute of Marine Geology and Geophysics, 2007). In total, 86,162 measurement points were collected. The distribution of ship-derived gravity measurement points is shown in Fig. 1.

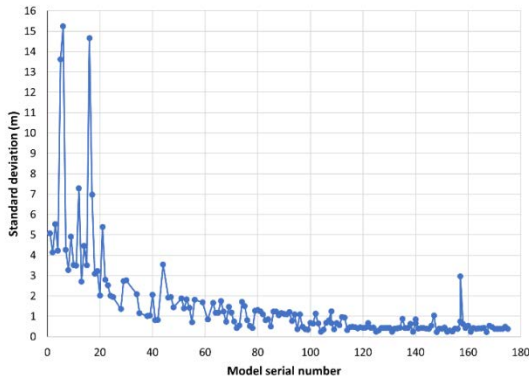


Figure 2. Standard deviations of global gravity field models compared with GNSS/leveling data (Ince et al., 2019).

RESEARCH METHODS

Overview of the Problem of Determining Marine Wave Energy

Wave power density is the most important parameter for evaluating wave energy resources. This parameter has often been calculated in recent studies by integrating spectral models based on numerical wave models. In this case, the wave power density (P_w) per unit crest length is calculated as follows (Iglesias et al., 2009):

$$P_w = \rho g \int_0^{2\pi} \int_0^\infty C_g(f, d) S(f, \theta) df d\theta \quad (1)$$

where ρ is the density of seawater (kg/m^3); g is the gravitational acceleration (m/s^2); C_g is the group velocity of wave energy propagation (m/s); $S(f, \theta)$ is the wave spectrum, f is the wave frequency (Hz), and θ is the wave propagation direction ($^\circ$); and d is the water depth (m) (Iglesias et al., 2009).

Wang & Lu (2009) pointed out that P_w is equivalent to the hydrodynamic pressure (p) on a vertical plane perpendicular to the propagation direction multiplied by the particle velocity (u) crossing the vertical plane, which can be expressed as follows:

$$P_w = \frac{1}{T} \int_0^T \int_{-d}^0 (p + \rho g z) u dt dz \quad (2)$$

where t is time (s); T is the wave period (s); and z is the water depth (m). The above equation can be integrated over the wave period and water depth. Therefore, P_w can be calculated using the following formula (Wang & Lu, 2009):

$$P_w = \bar{E} C_g = \bar{E} \left(\frac{g T_e}{2\pi} \tanh kd \right) P_* \quad (3)$$

where $\bar{E} = (1/16) \cdot \rho g H_s^2$ is the wave energy density (J/m^2); $k = 2\pi/\lambda$ is the wave number (m^{-1}), λ is the wavelength (m); and

$$P_* = \frac{1}{2} \left(1 + \frac{2kd}{\sinh 2kd} \right) \quad (4)$$

Thus, in order to calculate P_w , it is necessary to know the gravitational acceleration g at each point where wave height is measured. In previous studies, g was often assumed to be 9.81 m/s^2 (Deng et al. 2013; Sorek et al. 2023). Some other documents choose $g = 9.80665 \text{ m/s}^2$ (PyGNOME documentation; Seabird Scientific). However, this is only an approximate value and can affect the accuracy of the P_w calculation results.

Evaluation and Selection of EGM Models in the East Sea

The general formula for calculating gravity anomalies from the EGM model is as follows (Barthelmes, 2013; Sneeuw, 2006; NIMA, 2000):

$$\Delta g_{EGM} = \frac{GM}{r^2} \left[\sum_{n=2}^{N_{\max}} \left(\frac{a}{r} \right)^n (n-1) \sum_{m=0}^n (\bar{C}_{n,m} \cos(m\lambda) + \bar{S}_{n,m} \sin(m\lambda)) \bar{P}_{n,m}(\sin \varphi) \right] \quad (5)$$

where: GM – geocentric gravitational constant; r – geocentric radius of the considered point; γ – normal gravity on the reference ellipsoid; a –

semi-major axis of the ellipsoid; φ , λ – geocentric latitude and longitude of the considered point; $\bar{C}_{n,m}$, $\bar{S}_{n,m}$ – fully normalized spherical harmonic coefficients of degree n and order m ; $\bar{P}_{n,m}(\sin \varphi)$ – fully normalized associated Legendre functions; N_{max} – maximum degree of the model.

To evaluate the accuracy of the global gravity field models in the East Sea, we compared the gravity anomalies computed from the EGM models with those derived from shipborne gravity measurements. At ship-derived measurement points, both the observed gravity anomaly (Δg^{ship}) and the EGM-derived gravity anomaly (Δg^{EGM}) are available. The gravity anomaly deviation is calculated as follows:

$$\delta g_i = \Delta g_i^{EGM} - \Delta g_i^{ship}, i = 1, 2, \dots, n, \quad (6)$$

where: n is the number of measurement points.

The mean deviation is calculated as:

$$\delta g_{mean} = \frac{1}{n} \sum_{i=1}^n \delta g_i \quad (7)$$

If the mean deviation is approximately zero, it indicates that the difference between the ship-derived gravity anomalies and those determined from the EGM model has no systematic bias but is purely random. In this case, the root mean square error (RMSE) is calculated using the following formula (Hoang & Truong, 2003):

$$RMS_{\Delta g} = \sqrt{\frac{\sum_{i=1}^n (\delta g_i)^2}{n}} \quad (8)$$

If the mean deviation is not equal to zero, it indicates that the difference between the ship-derived gravity anomalies and those determined from the EGM model is systematic. In this case, the standard deviation is calculated using the following formula (Hoang & Truong, 2003):

$$STD_{\Delta g} = \sqrt{\frac{\sum_{i=1}^n (\delta g_i - \delta g_{mean})^2}{n - 1}} \quad (9)$$

Gravity anomalies computed from the EGM model can also be evaluated using the correlation coefficient R with respect to the ship-derived gravity anomalies. The correlation coefficient R is a measure of the relationship between two datasets. R can range from -1 to $+1$. If $R = 1$, the two datasets are perfectly linearly correlated. If $R = -1$, the two datasets are perfectly negatively correlated. If $R = 0$, the two datasets have no linear correlation. Thus, if the EGM model fits well with the ship-derived measurements, their correlation coefficient will be approximately 1. The correlation coefficient R is calculated as follows (McKean & Sheather, 2003):

$$R = \frac{\sum_{i=1}^n (\Delta g_i^{ship} - \Delta g_{TB}^{ship}) \cdot (\Delta g_i^{EGM} - \Delta g_{TB}^{EGM})}{\sqrt{\sum_{i=1}^n (\Delta g_i^{ship} - \Delta g_{TB}^{ship})^2 \cdot \sum_{i=1}^n (\Delta g_i^{EGM} - \Delta g_{TB}^{EGM})^2}} \quad (10)$$

Determination of Gravity at Points for Wave Energy Calculation

The gravity values at the points where wave energy is to be calculated are determined using the inverse distance weighting (IDW) interpolation method (Shepard, 1968). According to this method, within a circle of radius R around the target point (e.g., $R = 0.1^\circ$), gravity data points are selected. A minimum of four points should be used. If the number of points within the circle is fewer than four, R is increased by a factor of 1.5. This process can be automated in computational programming.

The weights are calculated using the inverse distance weighting formula (Shepard, 1968):

$$P_i = 1/D_i \quad (11)$$

where D_i is the distance from the target point to the i -th point with known gravity.

The gravity value at the target point for wave energy calculation is interpolated using the following formula (Shepard, 1968):

$$g_{inter} = \sum_{i=1}^n g_i P_i / \sum_{i=1}^n P_i \quad (12)$$

This method has the advantage of being applicable both when gravity data are provided as a grid and when they are available as discrete measurement points. The computational load is not too large, and it is suitable for regions with either strong or weak gravity variations. Therefore, in the problem of determining gravity values at satellite altimetry points for wave energy potential calculations, we propose using this method.

RESULTS AND DISCUSSION

Evaluation Results and Selection of EGM Models

Based on the above theoretical framework, we evaluated six EGM models: EGM2008, EIGEN-6C4, GECO, SGG-UGM-1, XGM2019E, and SGG-UGM-2 by comparing them with 86,162 ship-derived gravity measurement points. The evaluation results are summarized in Table 1.

Table 1. Evaluation results of the accuracy of six EGM models compared with ship-derived gravity data.

Model	δg_{max} (mGal)	δg_{min} (mGal)	δg_{mean} (mGal)	RMS (mGal)	STD (mGal)	R
EGM2008	22.05	-33.11	-0.45	3.70	3.68	0.968
EIGEN6-C4	23.69	-27.30	-0.50	4.06	4.03	0.963
GECO	21.83	-33.24	-0.61	3.75	3.70	0.975
SGG-UGM-1	21.72	-33.83	-0.63	3.70	3.65	0.975
XGM2019E	19.45	-27.44	-0.67	3.33	3.26	0.980
SGG-UGM-2	21.22	-23.40	-0.74	3.25	3.17	0.976

From the results in Table 1, it can be seen that all evaluated models show small mean deviations compared with the ship-derived gravity data, ranging from -0.45 mGal to -0.74 mGal. The standard deviations of the models vary from ± 3.17 mGal to ± 4.03 mGal. The smallest deviation is obtained with the SGG-UGM-2 model. Its accuracy reaches 3.17 mGal, with a very small mean deviation (-0.74 mGal), and the correlation between the SGG-UGM-2

model and the ship-derived data is very high (0.976).

The frequency distribution of the deviations of the SGG-UGM-2 model is shown in Fig. 3. From this figure, it can be observed that deviations with large values occur infrequently, while those with small values occur more frequently. This indicates that the frequency distribution of the deviations follows the normal distribution law of random errors. The number of deviations exceeding three times the root mean square error is small.

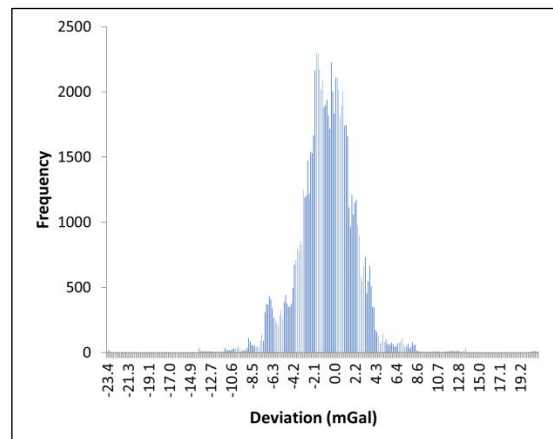


Figure 3. Frequency distribution of deviations for the SGG-UGM-2 model.

Thus, the comparison results indicate that the SGG-UGM-2 model is the most accurate in the East Sea. This is consistent with the fact that SGG-UGM-2 was the most recently developed among the six models evaluated and incorporated a wide range of available datasets. Furthermore, compared with the other models, SGG-UGM-2 utilized shipborne gravity measurements collected in Chinese seas adjacent to the Vietnamese East Sea, making it more suitable for this region.

Construction of the Gravity Model in the East Sea

Based on the SGG-UGM-2 model data combined with shipborne gravity measurements, we constructed a gravity model for the East Sea. The results are presented in Fig. 4. The maximum gravity value is 978,911.6 mGal, the minimum is 977,103.5 mGal, and the mean value is 978,389.4 mGal.

From Fig. 4, it can be seen that the gravity distribution over the East Sea exhibits spatial variation: higher gravity values are generally concentrated in the northern part of the basin, while lower values appear in the southern waters. This distribution reflects the general pattern of the gravity field and highlights the necessity of using an accurate gravity model to support the assessment of wave energy potential.

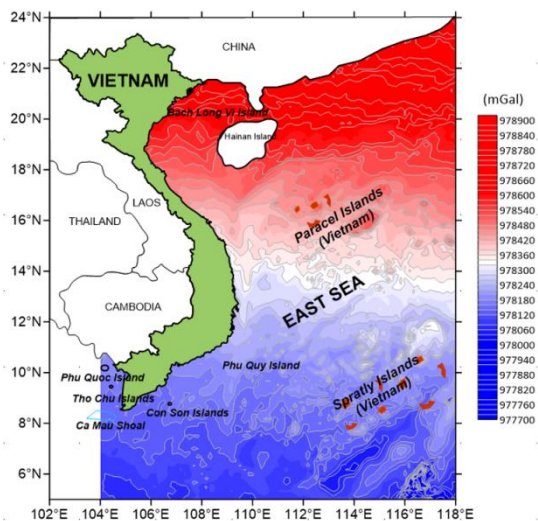


Figure 4. Gravity model over the East Sea for assessing wave energy potential.

CONCLUSION

This study evaluated six modern global Earth gravity models (EGMs) against ship-derived gravity data and identified SGG-UGM-2 as the most accurate for the East Sea. The model shows random deviations with a negligible mean bias (-0.74 mGal), the lowest standard deviation (± 3.17 mGal), and a strong correlation with shipborne observations ($R = 0.976$).

Using SGG-UGM-2 in combination with ship-derived measurements, a regional gravity model of the East Sea was developed to support wave energy assessments. The model yields gravity values ranging from $977,103.5$ to $978,911.6$ mGal, with an average of $978,389.4$ mGal. Its application is expected to enhance the accuracy of wave energy potential estimation based on satellite altimetry.

ACKNOWLEDGMENTS

The authors would like to sincerely thank the research project TNMT.ĐL.2025.06.01 funded by the Ministry of Agriculture and Environment for supporting this study.

REFERENCES

- AVISO. (2025). Satellite altimetry missions. <https://www.aviso.altimetry.fr/en/missions.html>
- Barthelmes, F. (2013). Definition of functionals of the geopotential and their calculation from spherical harmonic models. GFZ German Research Centre for Geosciences.
- Bui, C. Q., et al. (2008). Establishing a unified gravity anomaly map in Vietnamese seas and adjacent areas. *Journal of Marine Science and Technology*, 2, 29–41.
- Burhanudin, J., Ishak, A. M., Abu Hasim, A. S., Burhanudin, J., Dardin, S. M. F. B. S. M., & Ibrahim, T. (2019). A review of wave energy converters in the Southeast Asia region.
- Curto, D., Doan, V. B., Franzitta, V., & Riva Sanseverino, E. (2020). Wave and wind energy systems integration in Vietnam: Analysis of energy potential and economic feasibility. 2020 IEEE International Conference on Environment and Electrical Engineering and 2020 IEEE Industrial and Commercial Power Systems Europe (EEIC/I&CPS Europe).
- Deng, Z., et al. (2013). Wave power extraction by an axisymmetric oscillating-water-column converter. *Ocean Engineering*
- Do, H. T., Nguyen, T. B., & Ly, T. M. (2022). Tidal energy potential in coastal Vietnam. *Vietnam Journal of Science, Technology and Engineering*, 64(1), 85–89. [https://doi.org/10.31276/VJSTE.64\(1\).85-89](https://doi.org/10.31276/VJSTE.64(1).85-89)
- Ha, M. H. (2015). Research on evaluating sea level datums (zero depth, mean, and highest levels) using geodetic, hydrographic, and tectonic methods for coastal construction and planning in Vietnam under climate change. Final research report of project KC.09.19/11-15.
- Hector, H. S., Pierre, Q., & Fabrice, A. (2015). Assessment of SARAL/AltiKa wave height measurements relative to buoy, Jason-2, and Cryosat-2 data. *Marine Geodesy*, 38(Suppl. 1), 449–465. <https://doi.org/10.1080/01490419.2014.1000470>.
- Hoang, N. H., & Truong, Q. H. (2003). Mathematical foundations of geodetic data processing. Transport Publishing House.

- Iglesias, G., López, M., Carballo, R., et al. (2009). Wave energy potential in Galicia (NW Spain). *Renewable Energy*, 34(11), 2323–2333.
- Ince, E. S., Barthelmes, F., Reißland, S., Elger, K., Förste, C., Flechtner, F., & Schuh, H. (2019). ICGEM—15 years of successful collection and distribution of global gravitational models, associated services, and future plans. *Earth System Science Data*, 11(2), 647–674. <https://doi.org/10.5194/essd-11-647-2019>
- Institute of Marine Geology and Geophysics. (2007). Gravity, magnetic and seismic data of RV Professor Polshkov (Russian), 2007–2008.
- Jayaram, C., Bansal, S., Krishnaveni, A. S., Chacko, N., Chowdary, V. M., Dutta, D., Rao, K. H., Dutt, C. B. S., Sharma, J. R., & Dadhwal, V. K. (2015). Evaluation of SARAL/AltiKa measured significant wave height and wind speed in the Indian Ocean region. *Journal of the Indian Society of Remote Sensing*. <https://doi.org/10.1007/s12524-015-0488-7>.
- Korobkin, M., & D'Sa, E. (2007). Significant wave height in the Gulf of Mexico: Validation of Jason-1 measurement against buoy data. Louisiana State University, Coastal Science Institute, Department of Oceanography and Coastal Sciences.
- Kudryavtseva, N. A., & Soomere, T. (2016). Validation of the multi-mission altimeter wave height data for the Baltic Sea region. *Estonian Journal of Earth Sciences*, 65(3), 161–175. <https://doi.org/10.3176/earth.2016.13>.
- Le, D. D., Du, V. T., Nguyen, C. V., & Do, T. H. (2017). Ocean wave energy in the world and research development proposals for Vietnamese seas. *Journal of Climate Change Science*, 105–111.
- Le, D. T. (2005). Marine management. Hanoi National University of Vietnam.
- McKean, J. W., & Sheather, S. J. (2003). Statistics, nonparametric. In R. A. Meyers (Ed.), *Encyclopedia of physical science and technology* (3rd ed., pp. 891–914). Academic Press.
- Miao, H., Ren, H., Zhou, X., Wang, G., & Zhang, J. (2012). Study on altimeter-based inversion model of mean wave period. *Journal of Applied Remote Sensing*, 6(1), 063591. <https://doi.org/10.1117/1.JRS.6.063591>.
- Ministry of Natural Resources and Environment. (2022). Report on offshore wind and wave energy potential in Vietnamese seas.
- National Imagery and Mapping Agency (NIMA). (2000). Department of Defense World Geodetic System 1984. NIMA.
- Nguyen, V. S. (2012). Determination of gravity anomalies for the Vietnamese seas using satellite altimetry data [Doctoral dissertation, Moscow State University of Geodesy and Cartography]. Russian Federation. (In Russian).
- Nguyen, V. S., Pham, V. T., Nguyen, V. L., Andersen, O. B., Forsberg, R., & Bui, T. D. (2020). Marine gravity anomaly mapping for the Gulf of Tonkin area (Vietnam) using CryoSat-2 and SARAL/AltiKa satellite altimetry data. *Advances in Space Research*, 66(3), 706–723. <https://doi.org/10.1016/j.asr.2020.04.051>.
- PyGNOME documentation (NOAA/GNOME) (no date). [gnome.environment.waves module documentation](https://github.com/NOAA-GOES/PyGNOME).
- Queffelec, P., & Bentamy, A. (2007). Analysis of wave height variability using altimeter measurements: Application to the Mediterranean Sea. *Journal of Atmospheric and Oceanic Technology*, 24(6), 2078–2092.
- Rong, Z. M. (1994). Analysis on the surface current features in the East Sea in winter. *Marine Forecasts*, B11(5).
- Sandwell D. T. and Smith W. H. F. (1997), "Marine gravity anomaly from Geosat and ERS 1 satellite altimetry", *Journal of Geophysical Research: Solid Earth*. 102(B5), tr. 10039-10054.
- Seabird Scientific (training manual). (no date). Module 13 — Wave and tide theory and setup (training manual/notes).
- Shepard, D. (1968). A two-dimensional interpolation function for irregularly-spaced data. In *Proceedings of the 1968 ACM National Conference* (pp. 517–524). <https://doi.org/10.1145/800186.810616>.
- Sneeuw, N. (2006). Physical geodesy. Institute of Geodesy, University of Stuttgart.
- Sorek, S., et al. (2023). A serpent-type wave energy converter. *Scientific Reports*, 13, 39337.
- Su, H., Wei, C., Jiang, S., et al. (2017). Revisiting the seasonal wave height variability in the East Sea with merged satellite altimetry observations. *Acta Oceanologica Sinica*, 36(6), 38–50. <https://doi.org/10.1007/s13131-017-1073-4>.
- Uti, M. N., Md Din, A. H., & Yaakob, O. (2018). Significant wave height assessment using multi-mission satellite altimeter over Malaysian seas. *IOP Conference Series: Earth and Environmental Science*,

169(1), 012025. <https://doi.org/10.1088/1755-1315/169/1/012025>.

Wan, Y., Zhang, J., Meng, J., & Wang, J. (2015). A wave energy resource assessment in China's seas based on multi-satellite merged radar altimeter data. *Acta Oceanologica Sinica*, 34(3), 115–124. <https://doi.org/10.1007/s13131-015-0627-6>.

Wang, C., & Lu, W. (2009). Analysis methods and reserves evaluation of ocean energy resources. Beijing: China Ocean Press.

Xu, X. Z., Qiu, Z., & Chen, H. C. (1980). The general descriptions of the horizontal circulation in the East Sea. In *Proceedings of the Symposium on Hydrometeorology of the Chinese Society of Oceanology and Limnology* (pp. 137–145). Science Press.

Application of High-Frequency Radar System in Monitoring the Potential of Marine Energy in Vietnam

Kim Cuong Nguyen^{1,*}, Xuan Loc Nguyen¹, Ngoc Anh Tran¹, Ba Thuy Nguyen²

¹University of Science, Vietnam National University, Hanoi, Vietnam

²National Center for Hydro-Meteorological Forecasting, Hanoi, Vietnam

*Email: cuongnk@hus.edu.vn

Abstract: This paper presents an estimation of wind, wave, and surface current energy in the south-central waters of Vietnam using a High-Frequency Radar (HFR) system. Two HFR stations were deployed in Lam Dong Province for over a year. A dataset of wind, wave, and surface current was collected, providing wide spatial coverage with high temporal and spatial resolution. Based on these observations, wind and current energy potentials were estimated at a representative synthetic station located in the middle of Phan Thiet Bay, Vietnam. This is the first study to assess renewable energy from sea surface observations in Vietnam. The results are compared with other model-based estimations and further analyzed. The results have confirmed that the Lam Dong offshore area has very high potential for wind and wave energy, with the values of 2 kW/m² and 5 kW/m, respectively. The surface current energy was not as high as with waves and wind. The findings confirm that land-based HFR stations can be highly effective for estimating marine energy resources.

Keywords: HF Radar, Wind energy, wave energy.

INTRODUCTION

The significance of wind and wave energy in Vietnam lies in the country's extensive coastal and shelf regions, where strong monsoonal winds and complex nearshore dynamics generate a consistent oceanic energy field. The interaction between the southwest and northeast monsoon systems produces seasonal variations in wave height, period, and direction,

creating favourable conditions for both offshore and nearshore energy extraction. Along the central and southern coasts, the continental shelf gradient and local bathymetry enhance wave transformation and energy flux toward the shore. Understanding the spatial and temporal variability of wind stress, wave energy flux, and spectral wave characteristics is therefore essential for assessing renewable energy potential and integrating marine energy into sustainable coastal management in Vietnam.

In recent years, the development of renewable energy in Vietnam has become a major focus for the government, researchers, and investors, particularly offshore wind energy (Decision 888/QĐ-TTg; Viet SE 2019, 2020). In 2025, the National Centre for Hydro-Meteorological Forecasting (NCHMF), with support from UNDP and the Royal Norwegian Embassy in Vietnam, published a report assessing the technical potential of offshore wind energy in Vietnam. The report was based on in-situ measurements and reanalysis data to describe the spatial and temporal variability of offshore wind energy resources. Currently, numerous projects have been initiated to develop and harness offshore wind potential. However, wave and current energy resources have not yet received significant attention and are still not regarded as promising marine energy sources for the near future.

Many studies have estimated the potential of marine energy from wind and tides in offshore areas (Thuc et al. 2012; World Bank 2021; VNMHA 2022) using reanalysis datasets

and land-based observations. The most recent NCHMF report confirmed that the coastal zone from Ninh Thuan (now Khanh Hoa) to Binh Thuan (now Lam Dong) has high wind energy potential. This area also has high waves and strong currents, which may generate energy potential. This study raises the question of estimating the energy potential of wind, waves, and surface currents from land-based High Frequency Radar (HFR) measurements in Lam Dong Province (Fig. 1). HFR provides wide coverage and real-time observations. It can measure even during extreme events such as storms or strong monsoons. The HFR system was set up on the coast of Lam Dong province from November 2022 to November 2023 (Cuong et al. 2025). The HFR system provided wind speed and direction at 10 m above the sea, surface wave height and direction, and surface currents. For wind energy, the most common height for wind turbines is about 200 m. In this study, wind speeds at 200 m were estimated from 10 m wind data using various theoretical formulas. Then the energy potentials of wind, wave, and current were computed.

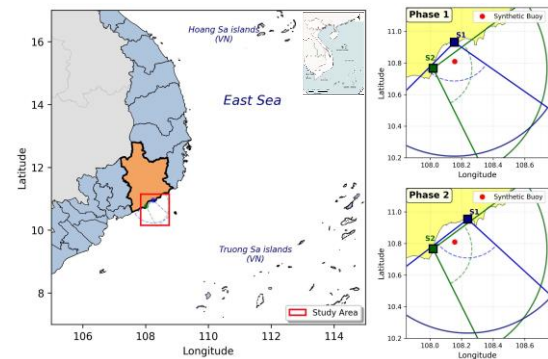


Figure 1. Study area

DATA AND METHODOLOGY

HF Radar dataset

The HFR dataset was archived using a system of two Wera radars installed on the coast of Lam Dong province. The details of installing the HFR system and validating the dataset were described in Cuong et al. (2025). Two sites (S1 and S2 in Fig. 1) were selected for system setup. The distance between these sites was about 30 km. At each site, the system

included four transmitter antennas and 12 receiver antennas (Fig. 2). However, due to the landowner's requirement, in March 2023, the S1 was changed to another Northward site. The system operated continuously from May 2023 to November 2023 and provided data every 30 minutes at a spatial resolution of 1.5 m (Fig. 1). The measurement area extended up to 50 km offshore. However, in this study, the energy potentials were computed at a representative point (called a synthetic buoy) where the temporal coverage is maximum - the coordinate of the synthetic buoy: 10.8098 °N - 108.156 °E (Fig. 1).



Figure 2. The HFR transmitter (upper) and receiver (lower) antennas.

WERA HF radar infers 10-m wind data by measuring the direction and intensity of sea surface waves (Bragg scattering) that are directly driven by the local wind field. By analyzing shifts in the radar-returned wave spectra, the system retrieves wind speed and direction representative of the standard 10-m height over the sea (Helzel et al., 2010).

Marine Energy computation

(1) To compute wind energy at 200 m above the sea surface, the power law, logarithmic law, and Deaves-Harris model were used for measured wind data at 10 m.

a. Power Law

This is the simple and widely used method (Şen et al., 2012; Fernández và Parnás, 2017):

$$U(z) = U_{ref} \cdot \left(\frac{z}{z_{ref}} \right)^\alpha \quad (1)$$

$$V(z) = V_{ref} \cdot \left(\frac{z}{z_{ref}} \right)^\alpha \quad (2)$$

In which: z : the height needs to be computed (200 m)

z_{ref} : the reference height (10 m)

α : the exponent of the power law ($\alpha = 0.1$ (Khalfa et al. 2014)).

b. Logarithmic Law

This is based on the method proposed by Monin-Obukhov for the atmospheric boundary layer (Walshaw, 1994; Khalfa et al., 2014; Wang et al., 2024):

$$U(z) = \frac{u^*}{\kappa} \ln \left(\frac{z}{z_0} \right) \quad (3)$$

In which: z_0 is surface roughness; κ is the von Karman constant (0.4); u^* is the friction speed.

c. Deaves-Harris model

The Deaves-Harries model is optimized according to the logarithmic law and can be effectively applied throughout the entire boundary layer. The expression is:

$$\frac{U(z)}{u^*} = \left(\frac{1}{\kappa} \right) \left\{ \ln \left(\frac{z}{z_0} \right) + 5.75 \left(\frac{z}{z_g} \right) - 1.88 \left(\frac{z}{z_g} \right)^2 - 1.33 \left(\frac{z}{z_g} \right)^3 + 0.25 \left(\frac{z}{z_g} \right)^4 \right\} \quad (4)$$

Where: z_g is boundary layer height and can be computed by the equation:

$$z_g = \frac{u^*}{B'f} \quad (5)$$

In which: B' is the empirical parameter, and f is the Coriolis parameter.

(2) Wind energy can be computed with the formula (Shoaib et al., 2019):

$$P_A = \frac{1}{2} \rho_A v^3 \quad (6)$$

Where P_A (W/m^2) is the actual wind power, and ρ_A is the air density, which is 1.225 kg/m^3 , v is the wind speed (m/s).

(3) Wave energy can be estimated with the formula:

$$P = 0.49 H_{m0}^2 T_E \quad (7)$$

P : Wave energy (kW/m)

H_{m0} : Wave height (m)

T_E : Wave period (s)

$T_E = \alpha T_{02}$, T_{02} : Zero-cross period and could be estimated by: Pierson-Moskowitz: $T_{02} = 0.710 T_p$ or JONSWAP: $T_{02} = 0.781 T_p$

$\alpha = 1.18$ (JONSWAP spectrum)

$\alpha = 1.2$ (Bretschneider spectrum)

(4) The current energy formulation is the same as wind energy (Şen, 2012):

$$P_C = \frac{1}{2} \rho_w v^3 \quad (8)$$

Where P_C (W/m^2) is the actual current energy, ρ_w is the water density, which is 1025 kg/m^3 , and v is the current speed (m/s).

Results

Wind Energy

Fig. 3 depicts the variations in wind speeds at 10 m and 200 m estimated using three methods: power law, logarithmic law, and

Deaves-Harris method. The grey dots show the wind speed at 10 m measured by the HFR system at a synthetic buoy. Across the three methods, the wind speed values are quite similar. At 10 m, the wind speeds were quite strong throughout the whole year. Most of the time, wind speeds were around 10 m/s, but they sometimes exceeded 20 m/s. The wind speed in the NE monsoon is slightly higher than that in the SW monsoon. It has been confirmed that the offshore area of Lam Dong province has very high wind energy potential. In the most recent report, NCHMF (2025) found that in the study area, wind energy reaches its highest levels from November to February, with maximum values exceeding 1.7 kW/m^2 . In this study, the wind energy was computed and shown in Fig. 4. The average wind energy is 2.4, 2.03, and 2.42 kW/m^2 for power, logarithmic, and Deaves-Harris methods, respectively. Across the three methods, wind speed and energy were not significantly different. These values are higher than those reported in the NCHMF. Due to wind speed instability, wind energy varied greatly over the period from November 2022 to November 2023. The periods from January to March and September to October had higher energy than the other measured periods (Fig. 4). Various methods confirmed that, in this area, the average wind energy is over 2 kW/m^2 . This is a new and reliable conclusion that supports the development of offshore wind farms.

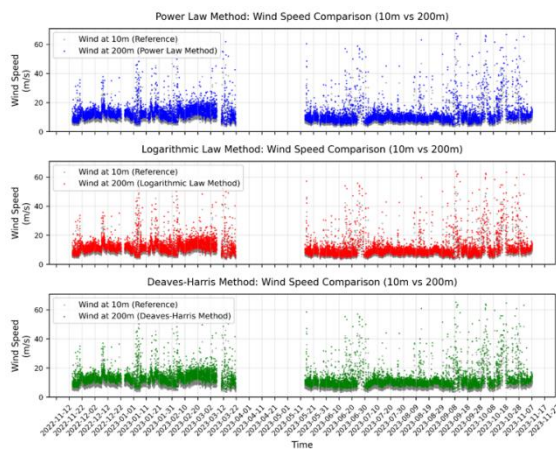


Figure 3. Variations of wind speed at 10 m and 200 m using different computed methods

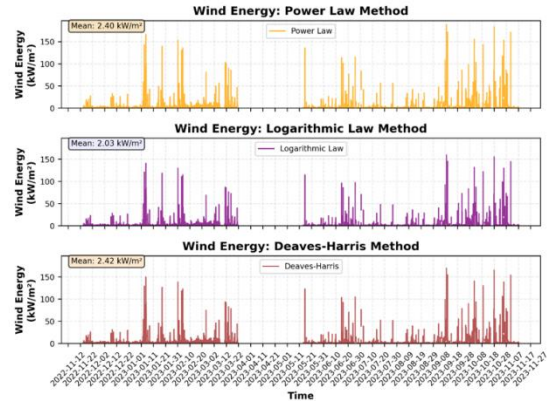


Figure 4. Computed wind energy at 200 m using different methods

Wave and surface current energy

In Phan Thiet Bay, the bathymetry is deep and open to the open ocean, so the significant wave height is quite high (Fig. 5). Throughout the year, the significant wave height is over 1 m, with peak wave periods of over 6 seconds. The mean significant wave height was 1.24 m, and the maximum value was 4.77 m. In the summer, the sea surface was less rough than in the winter, but it was still bumpy and suitable for wave energy development.

Figs. 6-7 shows the wave and current energy at the synthetic buoy. This location is not too far from the shore, so the current energy is quite limited. The mean current energy is only 13.69 W/m^2 . This area is highly dynamic, with strong seasonal currents, but its energy is much lower than that of wind and waves.

In contrast, wave energy in this area was very high, with mean values exceeding 5 kW/m across the four methods (Fig. 6). MONRE (2022) also reported that this area has the highest wave energy in Vietnam. Using different approaches, wave energy was quite consistent, with higher values in winter and lower in summer due to the fetch of wind during different monsoons. With modern techniques, wave energy seems more productive for exploitation than current energy sources.

It should be noted that these estimations were based on a representative point in the middle of Phan Thiet Bay. A high-resolution spatial map should be developed and used to support the search for optimal locations within the study area. From that, robust marine spatial planning for Vietnam can be established. In addition, phased pilot projects could be launched to support environmentally responsible development of large-scale marine renewable energy systems.

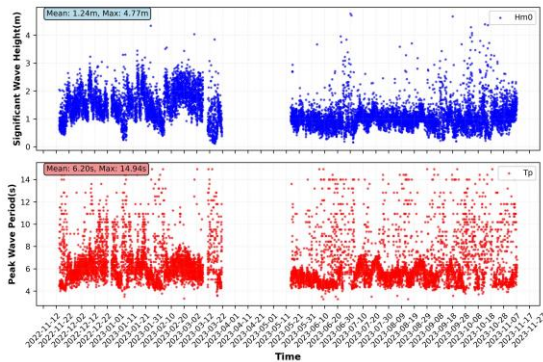


Figure 5. Variations of significant wave height and peak wave period

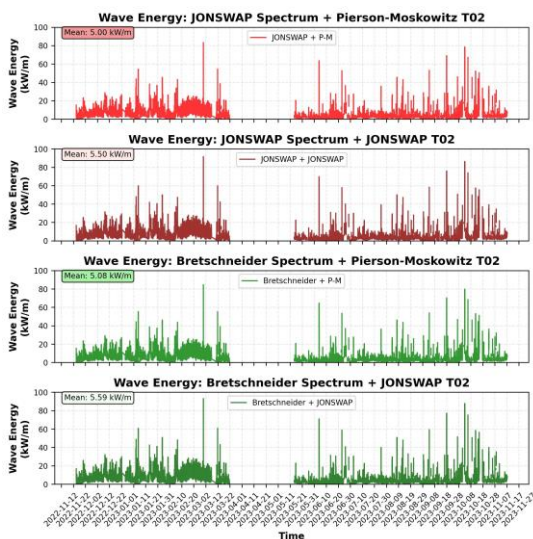


Figure 6. Wave energy in different estimation methods

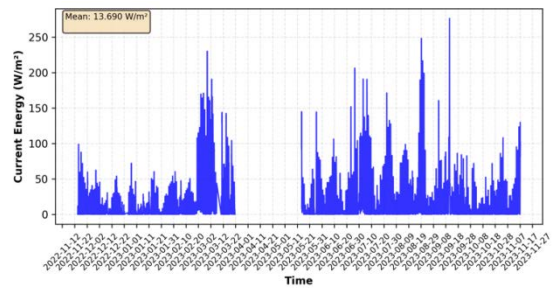


Figure 7. Current energy at the synthetic buoy

CONCLUSION

This paper presents estimates of the potential energy of wind, waves, and currents. The Lam Dong offshore area has very high potential for wind and wave energy, with the values of 2 kW/m² and 5 kW/m, respectively. With HFR observations, it is very productive to have wind, wave, and current fields even in different weather conditions. In the study area, the surface current energy is much smaller than that of wind and waves. In the new era of development in Vietnam, it should pay close attention to planning wind and wave energy farms to increase renewable electricity generation for economic activities and to support net-zero goals.

REFERENCES

- Cuong N.K., Anh T.N., Loc N.X., Binh P.D.H., Dang V.H. (2025). Advanced High-Resolution Measurements of Surface Waves and Currents Using Two Land-Based HF Radars for Offshore Operations. In: Huynh, D.V.K., Doan, H., Cao, T.M., Watson, P. (eds) Proceedings of the 3rd Vietnam Symposium on Advances in Offshore Engineering (VSOE 2024), Lecture Notes in Civil Engineering, vol 590. Springer, Singapore. https://doi.org/10.1007/978-981-96-3912-0_5
- Decision of the Prime Minister No. 888/QĐ-TTg dated 25 July 2022 approving the Project on tasks and solutions to implement the results of the 26th Conference of the Parties to the United Nations Framework Convention on Climate Change.
- Fernández, I., & Parnás, V. E. (2017). Elements for numerical simulation of wind time series. *Revista ingeniería de construcción*, 32(2), 85-92.
- Helzel, T., Kniephoff, M., Petersen, L. (2010). Oceanography radar system WERA: features,

- accuracy, reliability, and limitations. *Turkish Journal of Electrical Engineering and Computer Sciences* 18 (3): 389-398.
- Khalifa, D., Benretem, A., Herous, L. & Meghaoui, I. (2014). Evaluation of the adequacy of the wind speed extrapolation laws for two different roughness meteorological sites. *American Journal of Applied Sciences*, 11(4), 570-583.
- MONRE (2022). Report on the potential of offshore wind and wave power in Vietnam.
- NCHMF (2025). Assessment of the technical potential of offshore wind energy in Vietnam.
- Sen Z., Altunkaynak A., Erdik, T. (2012). Wind velocity vertical extrapolation by extended power law. *Advances in Meteorology*, 2012(1), 178623.
- Şen, Z. (2012). Energy generation possibility from ocean currents: Bosphorus, Istanbul. *Ocean engineering*, 50, 31-37.
- Shoaib, M., Siddiqui, I., Rehman, S., Khan, S., & Alhems, L. M. (2019). Assessment of wind energy potential using wind energy conversion system. *Journal of cleaner production*, 216, 346-360.
- Thuc T., Da T. V., Thang N. V. (2012). Wind energy in Vietnam: Potential and Exploitation capabilities. Science and Technics Publishing House.
- VIET SE (2019). Scenarios for wind energy development in Vietnam by 2030, Vietnam Energy Transition Initiative, Hanoi.
- VIET SE (2020). Policy recommendations for offshore wind energy development in Vietnam. Vietnam Energy Transition Initiative, Hanoi.
- VNMHA (2022). Report on offshore wind and wave energy potential in Vietnam's maritime zones.
- Walshaw, D. (1994). Getting the most from your extreme wind data: a step-by-step guide. *Journal of Research of the National Institute of Standards and Technology*, 99(4), 399.
- Wang, X., Yao, Z., Guo, Y., Li, Y. (2024). Analysis of the near-ground wind field characteristics during typhoon Soulik. *Applied Sciences*, 14(10), 4001.
- World Bank Group (2021). Final report: Offshore Wind Roadmap for Vietnam.

Characteristics of gravity anomalies in the Cuu Long basin, Vietnam

Tran Tuan Duong^{1,2,*}, Tran Tuan Dung¹, Nguyen Quang Minh¹, Tran Trong Lap¹, Nguyen Thi Nhan¹

¹Institute of Earth Sciences, Vietnam Academy of Science and Technology, Hanoi, Vietnam

²Hanoi University of Mining and Geology, Hanoi, Vietnam

*Email: ttduong.hung@gmail.com

Abstract: The gravity anomalies in the Cuu Long Basin (CLB) are characterized by blocky development in the Northeast-Southwest (NE-SW) and North-South (N-S) direction. According to the changes in amplitudes, the regional gravity anomalies can be classified into four distinct zones. Analysis of gravity data in the CLB indicates that: three main sets of faults are developed in the region, namely, the NE-SW, N-S and NW-ES trending faults. NE-SW trending faults are distributed in a wide range, and they are main faults in the region. They are followed by N-S trending faults, while there are a small number of nearly NW-ES trending faults. Large-scale faults are mainly margin controlling faults for the boundary of the basin and uplifts.

Through analysis of gravity anomaly characteristics, combined with location of oil/gas fields, the distribution of petroleum resources was assessed. The results show that petroliferous structures in the CLB are mainly located within zones of negative residual gravity anomalies.

Keyword: SDUST2021GRA, TAHG, oil/gas, Cuu Long basin.

INTRODUCTION

The CLB is a prolific oil/gas basin situated offshore from the southeastern coast of Vietnam (Figure 1). Positioned between the Vietnamese mainland and the Nam Con Son Basin at the southwestern margin of the East Vietnam Sea, the CLB covers an area of approximately 40,000 km². It stands as one of Vietnam's most important petroleum basins

Structurally, the CLB lies offshore southern Vietnam near the Mekong Delta and extends northeastward, parallel to the coastline and the tectonic trends of the Dalat volcano plutonic zone to the northwest. Its southeastern boundary is defined by the Con Son uplift (Tran Tuan Dung et al., 2024).

The basin formed due to extensional tectonics associated with the opening of the East Viet Nam Sea, influenced by the collision of the Indian and Eurasian plates (Tapponnier et al., 1982). Initial rifting in the CLB began in the Eocene-early Oligocene, followed by the uplift and rotation of the crustal blocks at the onset of drifting in the SW East Viet Nam Sea. The initial rifting phase is characterized by rapid subsidence and infilling; various alluvial/fluvial/ lacustrine processes were involved in the synrift sedimentation. The erosion of the uplifted blocks in the late Oligocene marked the transition from rifting to regional subsidence in the CLB. The postrift unit in the CLB is characterized by a deepeningupward succession, grading upward from nonmarine to paralic or shelf sediments (Lee et al., 2001).

The gravity method was the first geophysical technique to be used in oil/gas exploration. Despite being eclipsed by seismology, it has continued to be an important and sometimes crucial constraint in a number of exploration areas. In the CLB, gravity techniques have been instrumental in delineating the basin architecture and identifying fault systems key factors in assessing oil/gas potential.



Figure 1. Location of study area (Cuu Long basin, image courtesy of PetroVietnam)

GRAVITY DATA

Global gravity models derived from satellite altimetry missions have significantly enhanced our understanding of oceanic regions. In this study, the global marine gravity anomaly model SDUST2021GRA was utilized, featuring a grid resolution of $1' \times 1'$ (<https://zenodo.org/records/6668159>).

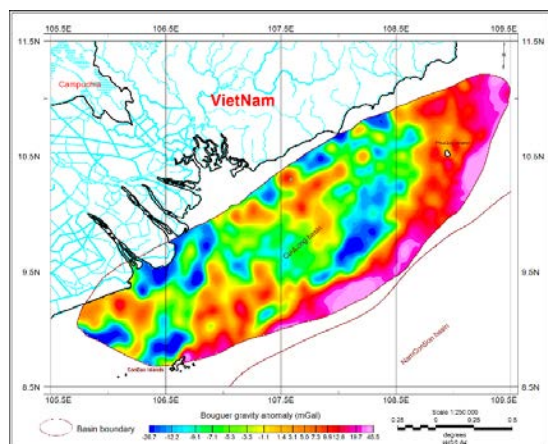


Figure 2. Map of bouguer gravity anomalies

Gravity anomaly characteristics: the bouguer map of the CLB exhibits similarities to its corresponding topographic map, with values ranging from -26.7mGal to 45.5mGal (Figure

2). Areas underlain by denser materials reflect more positive anomalies, while lower density zones generate more negative signatures (Lowrie W, Fichtner A., 2019). In the CLB, negative anomalies zones are generally associated with thick sediment accumulations. Conversely, positive anomaly zone, typically coincide with areas of shallower basement or uplifted blocks. The positive low anomaly zone (central area, value anomaly 0 to 5mGal) that sandwiched the negative gravity zone represent the elevated higher-density mantle rocks and thinning of sedimentary deposits.

METHODOLOGY

Separation of gravity anomalies:

Upward continuation is a widely used technique for isolating regional gravity anomalies caused by deep sources from the original anomaly data. In order to identify the deep and shallow gravity anomalies and structural characteristics of the study area, the author used the upward continuation method to separate anomalies (Gupta, V. & Ramani, N., 1980; Jacobsen, B., 1987). In order to select an appropriate upward extension height, the author extended the gravity anomalies upward at different heights such as 5 km, 10 km, 15 km and 20km (Figure 3). Since deep and large bodies produced long-wavelength and broad anomaly, upward continuation was applied to smooth out near-surface effects.

The comparison between the 15 km upward continued gravity anomaly (Figure 3c) and the bouguer gravity anomaly (Figure 2) shows that the small local anomalies are largely eliminated, and the anomaly becomes smoother, emphasizing deep gravity features. Beyond 15 km, further upward continuation causes minimal change in the overall anomaly patterns. Therefore, the anomalies upward continued to 15 km were selected to represent the regional gravity fields in the study area.

After determining the regional gravity anomalies, the residual gravity anomaly (Figure 4) was obtained by subtracting the regional gravity anomaly (Figure 3c) from the bouguer gravity anomaly (Figure 2).

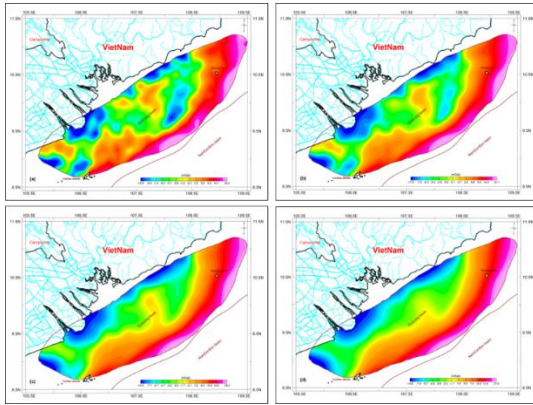


Figure 3. The anomaly maps of bouguer gravity anomaly after upward continuation at different heights: (a) 5km, (b) 10km, (c) 15km, (d) 20km

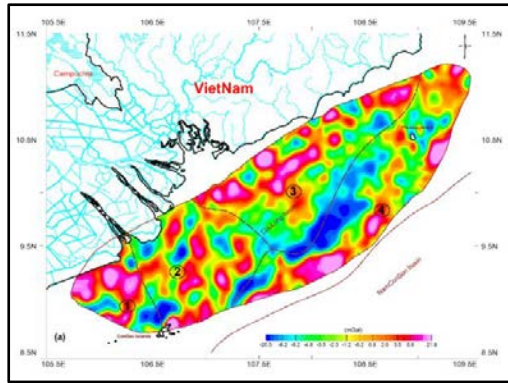


Figure 4. Map of residual gravity anomalies

In Figure 4, illustrates the residual gravity anomaly maps of the study area. The maps show that the residual anomalies are characterized by complex, alternating high and low anomaly patterns, with evident zonality across the region. Based on the characteristics of residual gravity anomalies, the research region can be partitioned into four anomaly zones: (1): residual gravity anomalies that are more pronounced, trending mostly E-W; (2): residual gravity anomalies that are generally N-S trending; (3): the anomalous values of the residual gravity in the zone (3) is an obvious high-value belt in the north and west, and the interior is arranged alternately with local low-value in the NE-SW direction (area bordering zone (4)); (4): residual gravity anomalies exhibit an NE-SW orientation.

Identification of fault systems using gravity data:

The tilt angle of the horizontal gradient method (TAHG) is an edge detection method based on total horizontal derivative (THDR) enhancement of gravity anomalies. The main attributes of this method are to provide maximal amplitudes on the source edges and equalize signals from shallow and deep sources (Blakely et al., 1986). The TAHG is obtained by taking the arctangent of the vertical derivative (VDR) of the THDR, divided by the modulus of the THDR (Ferreira et al., 2013; Tran Tuan Dung et al., 2021; Tran Tuan Duong et al., 2020):

$$TAHG = \tan^{-1} \frac{\frac{\partial THDR}{\partial z}}{\sqrt{\left(\frac{\partial THDR}{\partial x}\right)^2 + \left(\frac{\partial THDR}{\partial y}\right)^2}}$$

where:

- $\Delta g(x, y)$ is the gravity anomalies;

- $VDR = \frac{\partial \Delta g(x, y)}{\partial z}$;

- THDR is the total horizontal derivative is a prevalent edge-detection filter, as given by (Cooper G, Cowan D, 2008);

$$THDR = \sqrt{\left(\frac{\partial \Delta g(x, y)}{\partial x}\right)^2 + \left(\frac{\partial \Delta g(x, y)}{\partial y}\right)^2}$$

$\frac{\partial \Delta g(x, y)}{\partial x}$, $\frac{\partial \Delta g(x, y)}{\partial y}$ are first order derivatives of gravity anomaly field in the x, y directions. Due to the characteristics of the arctangent, the TAHG transform range is from $-\frac{\pi}{2}$ to $+\frac{\pi}{2}$.

In Figure 5, map showing the tilt angle of the horizontal gradient gravity anomaly. By analyzing and connecting the locations and magnitudes of the TAHG points in a suitable approach, the spatial distribution of the faults system is determined and shown in the Figure 6. As can be seen in the Figure 6, three main sets of faults are developed in the region, namely: the NE-SW trend, N-S trend and NW-ES trend faults. NE-SW trending faults are distributed in a wide range, and they are main faults in the region. They are followed by N-S trending faults, while there are a small number

of nearly NW-ES trending faults. Large-scale faults are mainly margin controlling faults for the boundary of the basin and uplifts.

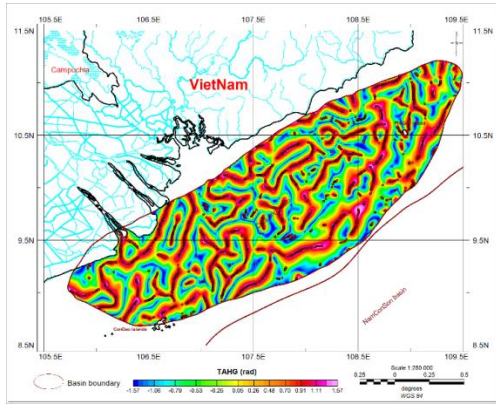


Figure 5. Tilt angle of the horizontal gradient gravity anomaly

As shown in Figure 6, the oil- and gas-bearing structures are located in the center of the CLB, situated between two NE-SW oriented fault zones and at fault intersections, particularly between NE-SW and N-S faults as well as between NE-SW and NW-SE faults.

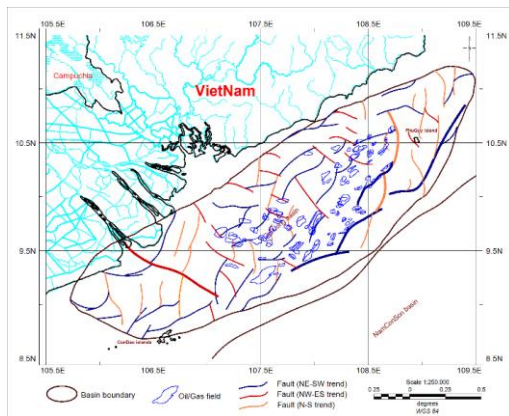


Figure 6. Map of fault distribution

Prediction of potential oil/gas areas:

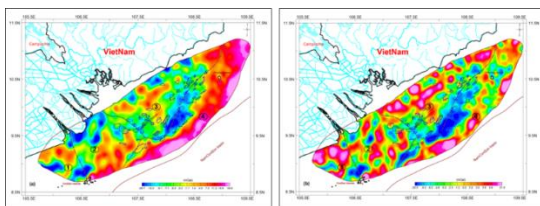


Figure 7. a) gravity anomalies;
b) residual gravity anomalies

In the Figure 7a, the oil/gas fields are primarily located in areas characterized by negative gravity anomalies. Negative bouguer gravity anomalies typically indicate regions with substantial sediment thickness or fracture zones filled with sedimentary material. In the CLB, since the late Oligocene, the transition from the post-rift phase to a period of slow and stable subsidence (Lee *et al.*, 2001), with minimal tectonic disturbance, has favored the preservation of deeper traps, allowing them to retain hydrocarbons without significant remigration or leakage.

Similarly, in Figure 7b, the major oil/gas fields are situated in areas with negative residual gravity anomalies. Such anomalies often correspond to local zones where the sediment layer is thicker and less density than the surrounding rocks, providing favorable conditions for hydrocarbon accumulation.

The integrated interpretation of bouguer and residual gravity anomaly maps (Figure 7), combined with the distribution of identified fault systems (Figure 6), enables the delineation of promising oil/gas fields in the CLB. The analysis indicates that most potential oil/gas fields are located in areas where:

1. The residual gravity anomalies exhibit negative values.
2. Structures are located within zones of negative gravity anomalies.
3. Situated in proximity to NE-SW trending faults.

CONCLUSIONS

Interpretation of gravity data reveals that the Cuu Long Basin (CLB) is structurally governed by three dominant fault trends: NE-SW, N-S, and NW-SE. Among these, the NE-SW trending faults are the most prominent and play a key role in controlling the basin's structural framework.

Negative Bouguer and residual gravity anomalies correspond to areas with thicker, lower-density sedimentary sequences, which

provide favorable conditions for hydrocarbon generation and accumulation. Most of the known oil/gas fields in the CLB occur within these negative anomaly zones and are commonly situated along or near NE–SW fault systems.

These findings confirm that gravity data interpretation, when combined with advanced filtering and edge-detection techniques such as upward continuation and TAHG method, offers a valuable and efficient approach for delineating basin architecture and identifying potential oil/gas bearing structures in offshore regions like the Cuu Long Basin.

REFERENCES

- Blakely, R. J. and Simpson, R.W., 1986. *Approximating edges of source bodies from magnetic or gravity anomalies*. Geophysics, 51, 1494-1498.
- Cooper G, Cowan D, 2008. *Edge enhancement of potential-field data using normalized statistics*. Geophysics 73:H1–H4.
- Eze OE, Okiwelu AA, Ekwok SE, Abdelrahman K, Alzahrani H, Ben UC, Ibrahim A, Akpa C, Andr    P, Ugar SI and Eldosouky AM (2024). *Delineation of deep-seated crustal structures from magnetic data in the southeastern part of the Niger Delta basin, Nigeria*. Front. Earth Sci. 12:1439199. doi: 10.3389/feart.2024.1439199.
- Frifita, Nesrine & Arfaoui, Mohamed & Zargouni, Fouad. (2016). *Relationship between surface and subsurface structures of the northern Atlas foreland of Tunisia deduced from regional gravity analysis*. Journal of Geophysics and Engineering. 13. 634-645. 10.1088/1742-2132/13/4/634.
- Fyhn, M.B.W., Pedersen, S.A.S., Boldreel, L.O., Nielsen, L.H., Green, P.F., Dien, P.T., ... Frei, D., 2010. *Paleocene-early Eocene inversion of the Phuquoc-Kampot Som Basin: SE Asian deformation associated with the suturing of Luconia*. J. Geol. Soc. 167 (2), 281–295. <https://doi.org/10.1144/0016-76492009-039>.
- Gupta, V. & Ramani, N., 1980. *Some aspects of regional-residual separation of gravity anomalies in a Precambrian*, Geophysics, 45, 1412-1426.
- Jacobsen, B., 1987. *A case for upward continuation as a standard separation filter for potential-field 16 maps*, Geophysics, 52, 1138-1148.
- Lee, G. H., Lee, K., and Watkins, J. S., 2001, *Geologic evolution of the Cuu Long and Nam Con Son basins, offshore southern Vietnam, East Sea: American Association of Petroleum Geologists Bulletin*, v. 85, p. 1055-1082.
- Lowrie W, Fichtner A (2019) *Fundamentals of Geophysics*. Cambridge University Press.
- Shellnutt, J.G., Lan, C.-Y., Van Long, T., Usuki, T., Yang, H.-J., Mertzman, S.A., ... Hsu, W.-Y., 2013. *Formation of Cretaceous Cordilleran and post-orogenic granites and their microgranular enclaves from the Dalat zone, southern Vietnam: tectonic implications for the evolution of Southeast Asia*. Lithos 182–183, 229–241. <https://doi.org/10.1016/j.lithos.2013.09.016>.
- Tapponnier, P., Peltzer, G., Le Dain, A.Y., Armijo, R., 1982. *Propagating extrusion tectonics in Asia: new insights from simple experiments with plasticine*. Geology 10, 611–616.
- Tran Tuan Dung, R. G. Kulinich, Nguyen Quang Minh, Nguyen Van Sang, Tran Tuan Duong et al., 2021. *A Study on the Possibility of the Reactivation of the Fault System in the Western Part of the Bien Dong as a Source of Geological Hazards*. ISSN 1819-7140, Russian Journal of Pacific Geology, 15, 6, 555–569.
- Tran Tuan Dung, R. G. Kulinich, Tran Tuan Duong, Nguyen Van Sang, Nguyen Quang Minh, Tran Trong Lap, and Nguyen Ba Dai, 2024. *Analysis of the correlation between the strike direction of oil-gas accumulations and fault systems in the western East Sea*. Russian Journal of Pacific Geology, 2024, Vol. 18, No. 6, pp. 732–744. ISSN 1819-7140. DOI: 10.1134/S1819714024700428.
- Tran Tuan Duong, Nguyen Quang Minh, Tran Trong Lap, 2024. *Evaluation of global marine gravity models using shipborne gravity data in the Southeast Vietnam sea*. Proceeding: ERSD 2024, pp 141-149. ISBN: 978-604-76-3040-0.
- Tran Tuan Duong, Tran Tuan Dung, Nguyen Ba Dai, Tran Trong Lap, Nguyen Kim Dung, Tran Xuan Loi, Bui Ngoc Quang, Tran Hoang Tam, 2020. *Evaluating the effectiveness of total horizontal derivative method and tilt angle of the horizontal gradient method in determining fault structure on the continental shelf and in deep water in the East Sea of Vietnam*. Vietnam Journal of Marine Science and Technology; Vol. 20, No. 4B; 2020: 205–214. DOI: <https://doi.org/10.15625/1859-3097/15832>.

Tran Tuan Duong, Tran Tuan Dung, Nguyen Quang Minh, Tran Trong Lap, 2023. *Forecast of submarine landslides related to the reactive probability of the fault system in the southeast vietnam continental shelf and adjacent areas*. Proceedings: Geospatial Integrated Technologies for Natural Hazards and Environmental Problems, International Conference GIS-IDEAS 2023, pp 20-28. ISBN: 978-604-357-207-0.

William J. Schmidt, Bui Huy Hoang, James W. Handschy, Vu Trong Hai, Trinh Xuan Cuong, Nguyen Thanh Tung, 2019. *Tectonic evolution and regional setting*

of the Cuu Long Basin, Vietnam. Tectonophysics 757 (2019) 36–57. <https://doi.org/10.1016/j.tecto.2019.03.001>

Zhu, C. et al., 2022. *SDUST2021GRA: Global marine gravity anomaly model recovered from Ka-band and Ku-band satellite altimeter data*, <https://doi.org/10.5281/zenodo.6668159>.

DOI: 10.15625/vap.2025.0193

Geochemical Characteristics of Lithium Mineralization in the La Vi Area (Central Vietnam): Implications for Deposit-Type Classification and Resource – Environmental Governance

Nguyen Van Niem^{1,*}, Do Duc Nguyen¹, Pham Nguyen Ha Vu³, Nguyen Minh Trung², Bui Huu Viet¹

¹Department of Geochemistry and Environment, Vietnam Institute of Geosciences and Mineral Resources. No 67, Chien Thang Road, Ha Dong, Noi Town, Vietnam

²Institute of Strategy and Policy on Agriculture and Environment. No 16, Thuy Khue, Tay Ho, Ha Noi Town, Vietnam

³Faculty of Geology, University of Science - Vietnam National University, Hanoi. No 334, Nguyen Trai Road, Thanh Xuan district, Ha Noi Town, Vietnam

*Email: Niemnv78@gmail.com

Abstract: This study investigates the geochemical characteristics of lithium mineralization processes in the La Vi area (formerly Quang Ngai Province, Vietnam) and reveals that the ore bodies are largely concordant with the metamorphic rocks of the Kan Nack Complex. The deposit is classified as a hybrid lithium deposit type (partially melted pegmatite) based on its complex elemental zoning (Li, Be, Mo, Sn, Nb, Cs, Rb, Ta) both vertically (0–180 m) and laterally, its rare earth element (REE) patterns, stable isotope signatures (O, H), U–Pb isotopes in zircon, and indicator minerals. As a newly recognized deposit type, it provides a scientific foundation for guiding future exploration strategies (Selection of mining methods and technologies, recovery product orientation, extended prospecting methods follows the deposit-type) and improving resource–environmental governance in Vietnam (More clearly quantify the material composition by mine type to reasonably approach the minerals to be recovered based on current and future technological capabilities; provide a basis for forecasting the components that are likely to impact the environment from natural mines and mining activities, if any, for many subjects including: government, community, social, business/company,...). The geochemical dataset

also serves as a background for river-basin and coastal-zone governance in lithium-bearing regions under various socio-economic development scenarios, contributing to the transition toward a green economy.

Keywords: Lithium, resource governance, hybrid pegmatite, geochemical characterization, La Vi deposit.

INTRODUCTION

There are many studies on La Vi lithium deposit, providing a lot of data on geological structure, ore distribution characteristics, altered rocks, mineral composition, elemental assemblages, isotopes, formation temperature, preliminary assessment of the origin of mineralization from different aspects (Duong Van Cau and et al., 2004; Đào Duy Anh and et al., 2013; Tuan Anh Nguyen and et al., 2024; Nguyen Dac Dong and et al., 2024; Duong Ngoc Tinh and et al., 2017; Pham Van Thong et al., 2009, 2010). The La Vi lithium deposit was previously classified as a pegmatite-type deposit derived from the Sa Huynh granitic magmatic complex and was considered to share certain characteristics with the Li–Cs–Ta (LCT) type; geochemical dataset is very limited and lacking integration and synchronization. This paper, by integrating geochemical data with structural, geological, and petro-mineralogical

evidence, our study indicates that the La Vi deposit exhibits key features of partially melted pegmatites (type of hybrid pegmatites). These pegmatites are related to deformation processes during the Permian–Triassic (P–T) tectonic regime and represent a transitional source between magmatic and metamorphic processes. For this reason, the La Vi lithium deposit is herein classified as a hybrid-type lithium deposit. According to this genetic model, exploration potential may be extended southward and southwestward along the Kan Nack and Ngoc Linh structural fault zones.

The geochemical parameters investigated reveal both vertical and lateral zoning, as well as diagnostic elemental assemblages, across multiple geological media (host rocks, ores, various pegmatite types, soils, and waters). This provides not only a clearer understanding of the deposit's genesis but also a framework for expanding exploration and adapting prospecting methods. Conventional approaches used for magmatic LCT pegmatites cannot be directly applied here. Furthermore, the data clarify the geochemical behavior of lithium and associated elements in natural environments, which can induce contamination or at least cause significant compositional changes. These insights serve as a foundation for resource and river-basin environmental governance in areas associated with the La Vi lithium deposit. Identifying ore-bearing components and redefining exploration strategies can help managers obtain robust, quantitative datasets for estimating resource potential and predicting environmental impacts, rather than relying solely on regulatory standards and conventional assessments.

The global surge in lithium demand is driven by the green energy transition, including the rise of electric vehicles and the shift toward renewable energy. This creates increasing environmental and social pressures. Worldwide studies now address the environmental, social, and governance (ESG) challenges associated with sustainable lithium extraction, involving diverse stakeholders such as governments, industries, and local

communities. These studies emphasize building transparent institutional frameworks, data infrastructures, and biodiversity integration into mining operations, while strengthening social participation and monitoring (E. Petavratzi et al., 2022). Investigations into lithium levels in coastal ecosystems and sediments have provided background data for monitoring (Wan Hee Cheng et al., 2015) and risk assessment for ecosystem conservation (Chee Kong Yap & Khalid Awadh Al-Mutairi, 2025). The concept of “greening extractivism” has been proposed to evaluate environmentally friendly and climate-mitigating lithium mining, while critically reflecting on its ecological and social challenges (Daniel Macmillen Voskoboynik & Diego Andreucci, 2021; E. Petavratzi et al., 2022).

At the same time, exploration and mining technologies continue to advance, aiming to increase reserves to meet energy transition demands while controlling lithium enrichment across different geological environments, both terrestrial and aquatic. Geochemical methods are essential not only for determining deposit type and origin but also for reconstructing geological histories related to weathering, hydrodynamics, and coastal processes. For example, lithium geochemistry has been applied to trace past mineralization and evaluate the impact of modern mining on the environment (V. Balaram et al., 2024).

These global perspectives highlight that Vietnam is now in a favorable position to adopt integrated resource–environment governance approaches at the earliest stages of lithium exploration and development. The La Vi deposit represents an initial case study to demonstrate how deposit-type recognition, geochemical indicators, and environmental background data can guide sustainable resource management in line with the green energy transition and international integration.

MATERIALS AND METHODS

This study utilized a comprehensive dataset including 857 drill-hole geochemical

samples in the La Vi deposit. These are selected to represent the depth, spatial relationship between the ore and the surrounding altered rocks, distance relationship with granite, wall rocks; orientation of sampling for additional analysis: samples of ore, rock, soil, water; study many related components to further assess the value of deposit and elements that can impact the natural environment. And 25 geochemical samples from altered host rocks surrounding the ore (representative samples for the interpretation of elemental behavior indicating the mineralization process and origin). In addition, 10 deep-profile geochemical samples, 15 samples of granitic rocks, 5 petrographic samples representing both ore and host rocks, 6 artificial heavy-mineral concentrate samples, 3 isotopic samples (O, H), 5 mineral paragenesis samples, and 5 fluid inclusion samples were analyzed (representative samples for the study of origin and deposit type). Furthermore, 10 water samples were collected to represent rivers and streams associated with the mineralized area (both to identify search signatures and to serve as a basis for environmental impact research).

Complementary data on tectonic structures, magmatic evolution, U-Pb zircon geochronology, and stable isotopes (O, H) were also compiled from previously published studies to provide additional geological context.

Lithium and associated elements were analyzed using Inductively Coupled Plasma Mass Spectrometry (ICP-MS), a highly sensitive method for detecting trace and ultra-trace elements, complemented by Atomic Absorption Spectroscopy (AAS).

Mineralogical characterization of lithium-bearing phases was conducted through petrographic analysis and X-ray diffraction (XRD) to support the interpretation of geochemical data for determining ore genesis and classifying the La Vi lithium deposit type.

Geochemical indices and parameters were calculated to identify indicator and associated

elements, aiming to reconstruct the genetic model of the deposit, guide exploration strategies, and predict possible environmental impacts.

Several geochemical parameters were normalized against the regional primary geochemical background of Quang Ngai-Binh Dinh (Vietnam), as reported by Nguyen Van Niem et al. (2024), with average concentrations (ppm) of: Li – 29.47; Be – 0.69; Ta – 19.0; Cs – 4.60 (n = 180).

RESULTS

Structural, Geological, Ore and Geochemical Characteristics of the La Vi Deposit

a. Geological Structure

The Quang Ngai-Binh Dinh area (old) and the La Vi lithium deposit belong to the Sa Huynh-Ba To structural zone, which forms part of the Kon Tum Massif—a Precambrian continental block located on the eastern margin of Indochina. This massif consists primarily of Precambrian folded and recrystallized basement rocks that were uplifted and eroded during the Early to Middle Paleozoic. Tectono-magmatic activity in the region was intense from the Late Paleozoic to the Early-Middle Mesozoic. During the Cenozoic, strike-slip faulting, extensional tectonics, and dome uplift associated with mantle plumes or tectonic upthrust were accompanied by basaltic volcanism.

b. Quartz–Feldspar–Two-Mica Schist

The La Vi deposit area is dominated by quartz–feldspar–two-mica schists of the Kan Nack Formation, which have undergone secondary alteration and weathering. These rocks exhibit a foliated, schistose texture with granoblastic to lepidoblastic fabrics. The main mineral constituents include quartz (~52%), muscovite (23–25%), feldspar (7–8%), biotite (5–7%), with minor epidote and iron hydroxides (8–10%), and a small proportion of ore minerals (1–2%).

c. Granitic Rocks

Granitic rocks belonging to the Sa Huynh magmatic complex crop out mainly near the deposit and include porphyritic granite with large feldspar phenocrysts and granitic pegmatites (Figure 1). Petrographic composition consists of plagioclase (25–28%), K-feldspar (38–48%), quartz (~25%), biotite (7–8%), and muscovite (~2%). Accessory minerals include zircon, epidote, apatite, and minor ore minerals (samples TH.1106/1, TH.1124). Lepidolite appears as small, irregular flakes filling grain boundaries and fractures within the host granite.

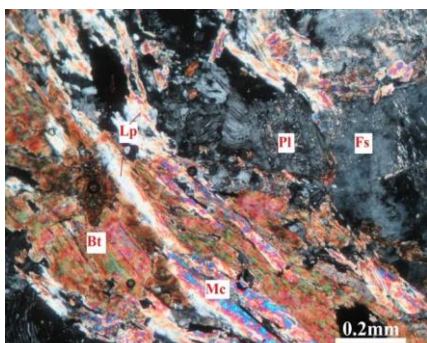


Figure 1. Two-mica granite showing micromite texture with late-stage lepidolite infilling fractures and grain boundaries between primary minerals.

Fk – K-feldspar; Pl – plagioclase; Bt – biotite; Mc – muscovite; Lp – lepidolite (TH.1106/1), Nicol (+).



Figure 2. Lepidolite in granitic pegmatite and porphyritic granite of the Sa Huynh complex (sample TS1106).

Artificial heavy mineral concentrates also contain lepidolite (Figures 2, 3), garnet, tourmaline, sphene, leucoxene, and abundant

ilmenite; ore minerals such as cassiterite, pyrite, and anatase are rare (samples TS1106/2; TS1104/3). Petrographic observations show pyrite and late-stage chalcopyrite but no cassiterite (sample KT.1106/2 – granitic pegmatite; Figure 4), indicating late hydrothermal overprinting.

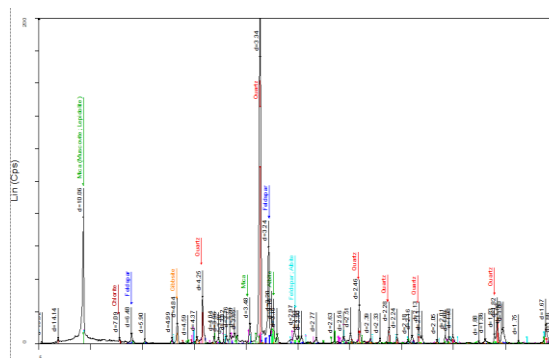


Figure 3. X-ray diffraction pattern identifying lepidolite and other minerals in the porphyritic granite of the Sa Huynh complex adjacent to the La Vi lithium deposit (DH1104/7).

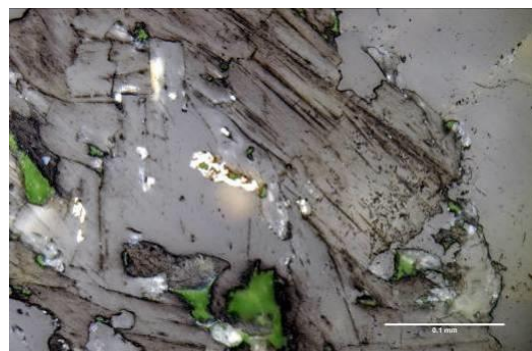


Figure 4. Chalcopyrite within granitic pegmatite of the Sa Huynh complex (KT.1106/2).

d. Ore Characteristics

Fine-grained albite-rich pegmatite veins containing lithium are interbedded within the Kan Nack metamorphic sequence and are unevenly distributed (Figure 5). No boreholes have intersected granitic rocks directly associated with Li-bearing pegmatite veins.

Lithium ore minerals are mainly lepidolite and very fine-grained lithian muscovite (Figure 6). These minerals are much finer than those typically found in pegmatites at the margins of the Sa Huynh granite complex. Cassiterite is

rare; tourmaline occurs sparsely, reflecting boron enrichment (Nguyen Van Niem et al., 2025; sample R1101). Other studies have reported topaz, beryl, and montebrasite associated with fluorine enrichment but no tourmaline (Tuan Anh Nguyen et al., 2024).

The ore zone extends to a depth of 0–180 m but is discontinuous and restricted to Li-bearing pegmatite veins. Average Li_2O content is 0.333 wt% with a high coefficient of variation ($V = 138.62\%$); BeO averages 0.032 wt% ($V = 80.29\%$); Sn content is low but highly variable ($V = 457.61\%$) ($n = 857$). Nb_2O_5 and Ta_2O_5 contents are low and occur as accessory elements (Nguyen Van Niem et al., 2025).

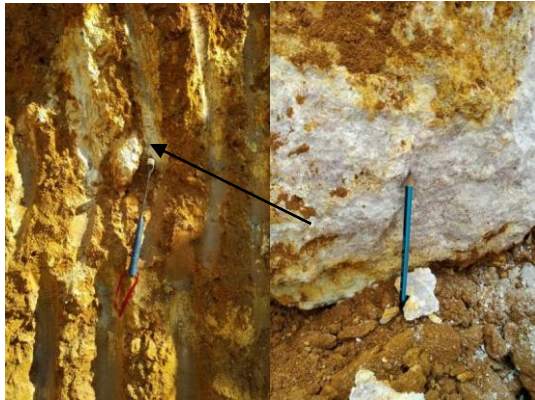


Figure 5. Li-bearing pegmatite vein at ~5 m depth in the La Vi lithium deposit, Quang Ngai (QN1101).

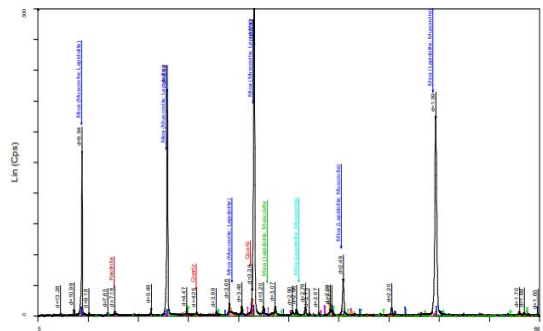


Figure 6. X-ray diffraction pattern identifying lepidolite in a Li-bearing pegmatite vein at ~5 m depth in the La Vi deposit (R1101).

Altered metamorphic rocks adjacent to the veins are also lithium- and beryllium-rich (average $\text{Li}_2\text{O} = 0.092$ wt%, $\text{BeO} = 0.024$ wt%, $n = 25$). Spatially, Li concentrations in schists

above the pegmatite (e.g., 634.11 ppm at ~4 m depth, DH1101) are significantly higher than below (~147.69 ppm at 72 m, DH1401). Boron shows a similar trend, with very high B concentrations in the overlying schists (4305.91 ppm, DH1101) but absent below. Away from the veins, schists still contain moderately high Li (70.82 ppm, DH1102), approaching the minimum geochemical anomaly threshold (75.65 ppm), and $B = 81.83$ ppm. Within the veins themselves, B contents are highly variable - high to very high in some intervals (e.g., DH1401 at 42 m and 65–67 m, DH1101) but low or undetectable in others (DH1401 at 36 m, DH1509 at 30 m, DH1120 near DH1101).

e. Geochemical Characteristics of the La Vi Deposit

ei. Vertical Geochemical Zoning and Spatial Relationship with the Sa Huynh Granite Complex

Vertical geochemical zoning within the central ore zone (Zone M) of the La Vi deposit was determined by calculating element zonation indices (Tables 1 and 2; Figure 7). The general zoning pattern from surface to depth in Zone M is: Li–Be–Mo–Sn–Cs–Rb–Ta. However, at a specific drill hole (K1401), the absolute vertical zoning between 36–67 m depth differs: Be–Sn–Nb–Rb–Cs–Ta–Li.

Table 1. Element zonation indices by depth in the central ore zone (M), La Vi lithium deposit.

Zone	I	II	III	IV	V
Element	0-10m	30m	36m	42m	65-67m
Be	0,0064	0,0059	0,0097	0,0055	0,006
Li	0,6523	0,6525	0,3681	0,2056	0,628
Nb	0,0081	0,0093	0,0426	0,0704	0,019
Rb	0,3063	0,3059	0,4945	0,5922	0,293
Cs	0,0169	0,0160	0,0431	0,0559	0,030
Mo	0,0012	0,0004	0,0142	0,0247	0,015
Sn	0,0052	0,0064	0,0250	0,0412	0,006
Ta	0,0037	0,0036	0,0028	0,0044	0,003

In the near-granite zone (VLK1), the vertical zoning pattern is: Li–Sn–Ta–Nb–Be.

Table 2. Element zonation indices by depth in drill hole K1401 (Zone M), La Vi lithium deposit.

Zone Element	III 36 m	IV 42 m	V 65-67 m
Be	0,0099	0,0057	0,006
Li	0,3734	0,2108	0,638
Nb	0,0432	0,0722	0,019
Rb	0,5017	0,6072	0,297
Cs	0,0437	0,0573	0,030
Sn	0,0253	0,0423	0,006
Ta	0,0028	0,0045	0,003

In the far-granite zone (VLK2 – Figure 7), the pattern is: Li-Ta-Nb-Be-Sn.

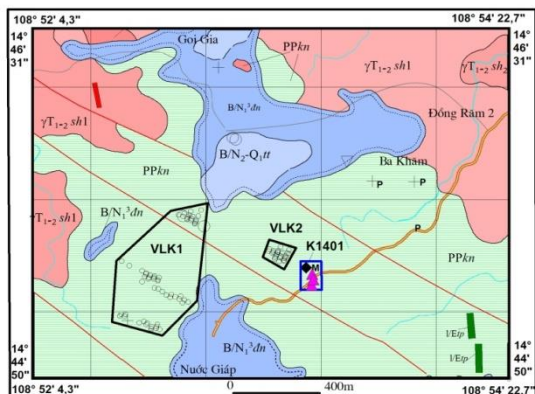


Figure 7. Distribution map of drill holes and geochemical zoning near and far from the Sa Huynh granite complex (VLK1 – near-granite zone; VLK2 – far-granite zone; M – central ore zone; “+” granite outcrops; P – pegmatite with medium to very coarse muscovite flakes; ▲ drill holes with vertical zoning data; ● Li-bearing pegmatite outcrops; □ drill holes near major granite body).

e2. Elemental Associations

Table 3. Correlation coefficients among elements in the La Vi lithium ore zone (0–180 m; 540 samples; drilling data source: Nguyen Dac Dong et al., 2024).

	BeO	Li ₂ O	Nb ₂ O ₅	Sn	SnO ₂	Ta ₂ O ₅
BeO	1					
Li ₂ O	0,15	1				
Nb ₂ O ₅	0,14	0,01	1			
Sn	0,02	0,04	0,21	1		
SnO ₂	0,02	0,04	0,21	1	1	
Ta ₂ O ₅	0,12	0,07	0,80	0,17	0,17	1

Lithium in the La Vi ore bodies (0–180 m) shows weak or no correlation with most other elements. Specifically, Li has a weak positive correlation with Be and a negative correlation with Sn and Ta (Table 3). Only Nb is strongly correlated with Ta; both elements show weak correlations with Sn and Be.

In Sa Huynh granitoids, lithium forms a distinct elemental association Li–Be–Cs–Rb, while Sn is associated with Cs–Be–Ta–Nb (Table 4).

Table 4. Correlation coefficients among elements in Sa Huynh granitoids near the La Vi lithium deposit (10 ICP-MS samples).

	Li	Be	Rb	Nb	Sn	Cs	Ba	Ta
Li	1							
Be	0,62	1						
Rb	0,66	0,86	1					
Nb	0,40	0,87	0,59	1				
Sn	0,38	0,72	0,50	0,77	1			
Cs	0,72	0,95	0,97	0,70	0,62	1		
Ba	0,00	-0,40	-0,30	-0,52	0,01	-0,28	1	
Ta	0,21	0,64	0,34	0,92	0,70	0,43	-0,48	1

In altered metamorphic rocks surrounding Li-bearing pegmatite veins, Li shows moderate correlation with Nb and weak-to-moderate correlation with Be (Table 5).

Table 5. Correlation coefficients among elements in altered host schists around Li-bearing pegmatite veins (25 samples).

	BeO	Li ₂ O	Nb ₂ O ₅	Sn	SnO ₂	Ta ₂ O ₅
BeO	1					
Li ₂ O	0,30	1				
Nb ₂ O ₅	0,68	0,44	1			
Sn	0,02	0,27	-0,04	1		
SnO ₂	0,02	0,27	-0,04	1,0	1	
Ta ₂ O ₅	0,59	0,15	0,57	0,15	0,15	1

e3. Soil Geochemistry

Four main soil types were studied, representing different geological substrates: i) Soils developed on metamorphic rocks; ii) Soils developed on granite and granitic pegmatites; iii) Soils developed on pegmatoid formations

and iv) Soils developed within mineralized or altered zones.

These soil profiles represent a gradient from the ore body outward to surrounding host rocks, approaching the Sa Huynh granite/pegmatite complex and increasing in relative depth. All samples were collected from soils developed on quartz-mica schists of the Kan Nack Formation.

Geochemical patterns show a decrease in Li, Ta, Nb, Be, Cs, and Mo contents with increasing distance and depth from the mineralized zones toward the granite body, whereas Sn, Bi, Rb, Pb, Fe, and As tend to increase outward (Figure 8).

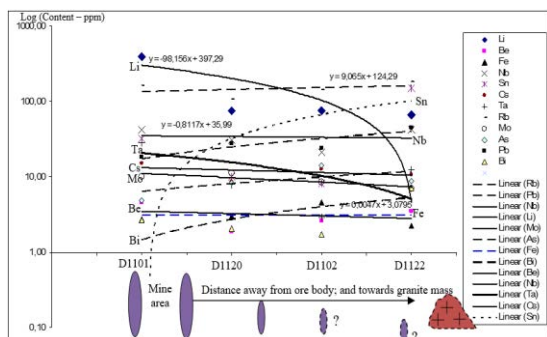


Figure 8. Elemental concentration trends in soils developed on quartz-mica schists around Li ore bodies, plotted against distance and relative depth. Solid lines represent decreasing trends; dashed lines represent increasing trends.

e4. Water Geochemistry

Water samples were collected from springs, streams, and small ponds during the late dry season, when discharge is low and water is clear. Most samples represent high-elevation springs and streams directly associated with the Li mineralized area or nearby predicted pegmatitic zones. The study evaluated the potential mobility and impact of Li and associated elements on the local river-stream network.

Li, Mo, and Cs show significantly elevated concentrations in waters within and near the ore bodies (similar to soil patterns). Boron (B) also increases but with lower differentiation, while Fe shows an opposite trend. Other

elements show minimal change with increasing distance from the ore zone (Figures 9).

Comparative analysis of water chemistry:

i) Spring water at the deposit center (N1121) contains Li 4.53×, Mo 7.83×, Cs 4.31×, B 1.37×, Rb 1.27×, Ta 1.16×, and Nb 1.17× higher than downstream water (N1123), ~1.7 km away.

ii) Compared to regional background water (N1417) from the NW (An Tay commune, ~5.2 km away, draining the Sa Huynh batholith with no Li mineralization), central deposit water (N1121) contains Li 15.5×, B 1.7×, Mo 6.7×, Cs 14×, and Ta-Nb 1.16×..

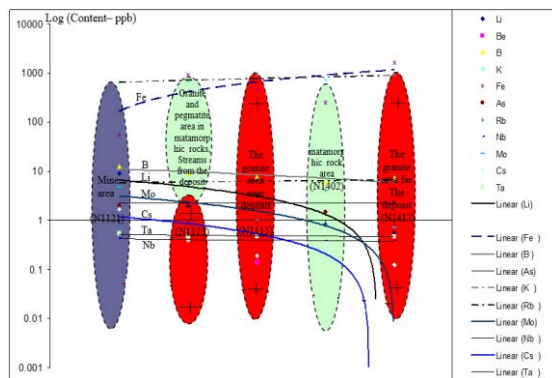


Figure 9. Spatial distribution of Li, Mo, Cs, B, and other elements in waters from the ore center outward; solid lines indicate decreasing trends, dashed lines indicate increasing trends.

In summary, water samples were collected representatively from springs and high-elevation streams within the lithium deposit and extending outward toward its margins. A clear geochemical differentiation is observed: Li, Mo, and Cs show significantly elevated concentrations in the deposit area and near the lithium ore bodies (similar to the patterns found in soils), while B exhibits a comparable but less pronounced trend. In contrast, Fe displays the opposite behavior. Other elements show very limited differentiation, generally decreasing in concentration with increasing distance from the ore bodies (Figure 10). In addition, the concentrations of Li, Mo, and Cs in water tend to increase with higher pH and under reducing conditions ($Eh < 0$) (Figure 11). Springs emerging from the deposit are

characterized by elevated pH (~ 7.5) and strongly reducing redox potential ($E_h = -38.66$ mV).

f. Temperature related to Ore-Forming Processes

Formation temperatures were determined from fluid inclusion analyses in samples representing three spatially distinct pegmatite types within the La Vi lithium deposit: pegmatites outside the vicinity of the granite body, pegmatites adjacent to the granite, and tourmaline-rich pegmatites occurring as independent bodies. These are classified as follows:

Type I – Li pegmatite (lithium ore or Li–B rich), characterized by very fine-grained minerals, including tiny mica flakes, albite, and fine quartz, locally containing tourmaline. These pegmatites occur both near the surface and at greater depths in the central part of the deposit.

Type II – Pegmatite with medium- to coarse-grained mica flakes (commonly 0.1–0.5 mm, white in color), distributed relatively close to the main granite body and moderately enriched in lithium.

Type III – Pegmatite with large muscovite flakes (0.5 cm to several centimeters, white), cutting through and associated with the main granite mass and its surrounding host rocks; relatively Li-rich but B-poor (e.g., drill holes DH119, DH1106/1, DH1118).

Type IV – Tourmaline-rich pegmatite bodies occurring independently, containing abundant black tourmaline, relatively Li-rich (75.79 ppm) and B-rich (131.78 ppm).

All pegmatite types contain two principal types of fluid inclusions: liquid–vapor and vapor–liquid. The measured formation temperature ranges are as follows:

Type I pegmatites: 200–275 °C; 315–405 °C; and possibly above 405 °C.

Type II pegmatites: 215–290 °C; 325–410 °C; and possibly above 410 °C.

Type IV pegmatites: 222–290 °C and 320–415 °C.

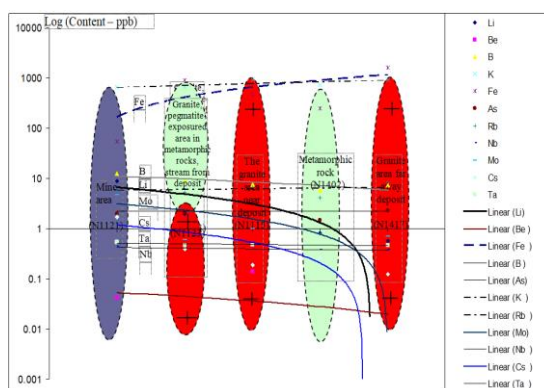


Figure 10. Element concentration patterns in water surrounding the lithium ore bodies and extending outward in different directions (lateral distribution in relation to geological setting). Solid lines indicate decreasing concentrations with increasing distance from the ore bodies; dashed lines represent the opposite trend.

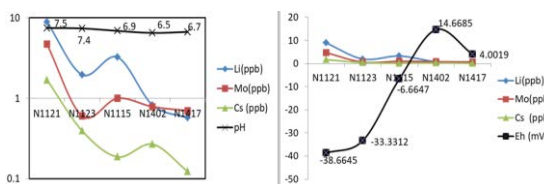


Figure 11. Geochemical environmental characteristics (pH, E_h) and the distribution of Li–Mo–Cs in waters of the La Vi lithium deposit and surrounding areas.

DISCUSSIONS

Origin and Deposit Type of the La Vi Lithium Mineralization

The geochemical zoning of Li mineralization and associated elements in the La Vi deposit is highly complex and differs markedly from the vertical zoning patterns typically observed in pegmatite-type lithium deposits directly related to granitic magmatism worldwide (see History of Research section).

If the deposit is examined in terms of formation processes evolving from the Sa Huynh granitic magma body outward into Li-bearing pegmatite veins along vertical migration, the overall geochemical zoning from top to bottom (integrating multiple drill holes) can be summarized as follows:

- Near the Sa Huynh granite body: Li–Sn–Ta–Nb–Be;

- Farther from the granite body: Li-Ta-Nb-Be-Sn.

In the central part of the deposit (distal from the granite), the vertical zoning from top to bottom is: Li-Be-Mo-Sn-Cs-Rb-Ta.

When considering the absolute depth profile of a single drill hole (36–67 m) at the deposit center, the zoning sequence from top downward is: Be-Sn-Nb-Rb-Cs-Ta-Li.

These results are notably different from previous studies and deviate significantly from the vertical geochemical differentiation model of lithium pegmatites directly fractionated from a single granitic magma source. Consequently, the ore-forming processes at La Vi are likely associated with distinct pegmatite-forming conditions and mixed magmatic-metamorphic to hydrothermal evolution, rather than a simple magmatic fractionation system.

When compared with the geochemical-mineralogical zoning model proposed by Tuan Anh Nguyen et al. (2024), notable differences are observed. In their model, Be is concentrated mainly in the second zone (counting upward from the underlying granite body), just above the muscovite-albite pegmatite zone; Sn is concentrated near the uppermost zone (muscovite-cassiterite), and Li occupies the topmost zone (lepidolite-topaz-albite). This zoning model was established from a limited number of samples and localized areas, focusing only on F-rich pegmatites that lack tourmaline and are poor in, or devoid of boron.

By contrast, the present study evaluates the entire spatial extent of the La Vi deposit, both laterally and vertically (including absolute depth profiles from single drill holes as well as integrated depth trends from multiple drill holes), and directly relates these zonations to the position of the Sa Huynh granitic magma body. As a result, the zoning pattern presented here is considered highly representative, incorporating detailed and spatially explicit sample locations. These findings provide a robust foundation for further investigation into the geochemical behavior of key elements in the subsequent discussion of the genetic model of the deposit.

Considering the overall vertical zoning from the surface to 180 m depth in the La Vi deposit, Li occupies the uppermost part of the sequence. However, the Li-to-underlying-element concentration ratio is highest at 51–60 m depth (laterally close to the Sa Huynh granite) and at 21–30 m depth (laterally distal from the granite) (Tables 6 and 7). In the central ore zone (Zone M), this ratio also peaks at 65–67 m depth (Table 8).

By contrast, when examining the absolute depth profile of a single drill hole (36–67 m), Li shifts to the lower part of the sequence, while Be occupies the upper part, and the normalized (Be/Li)_{cn} ratio reaches its lowest value at 65–67 m depth (Table 9). Moreover, the distribution between these depth intervals (zones) does not follow a linear or continuous trend as would be expected in classical zoning sequences.

Table 6. Ratio of upper- to lower-zone elements in the lithium ore bodies of the La Vi deposit near the Sa Huynh granitoid complex (VLK₁ zone) [Nguyen Van Niem et al., 2025]

Zone Element	I (15 samples) 0-10m	II (43 samples) 10-20m	III (25 samples) 21-30m	IV (25 samples) 31-40m	V (8 samples) 41-50m	VI (39 samples) 51-60m	VII (9 samples) 61-70m	VIII (4 samples) 71-80m
Li/Be	6,495	3,995	2,778	2,229	3,573	16,723	1,587	2,608
LiSn/NbBe	0,00558	0,00391	0,00764	0,00216	0,00165	0,02577	0,00288	0,00408
Be/Li	0,15	0,25	0,36	0,45	0,28	0,06	0,63	0,38
Nb/Li	0,0299	0,0481	0,0582	0,1023	0,0585	0,0109	0,1364	0,0633
Sn/Be	0,3634	0,2172	0,3860	0,2562	0,2501	0,2772	0,4224	0,1639
Ta/Li	0,0300	0,0350	0,0498	0,0884	0,0330	0,0111	0,1422	0,1035

Table 7. Ratio of upper- to lower-zone elements in the lithium ore bodies of the La Vi deposit distal from the Sa Huynh granitoid complex (VLK2 zone) [Nguyen Van Niem et al., 2025]

Zone Elements	I (7 samples) 0-10m	II (14 samples) 10-20m	III (36 samples) 21-30m	IV (18 samples) 31-40m	V (11 samples) 41-50m	VI (4 samples) 51-60m	VII (4 samples) 61-70m	VIII (9 samples) 71-80m	IX (4 samples) 130-140m	X (5 samples) 150-160m
Sn/Li	0,024	0,040	0,01	0,02	0,017	8,70	3,82	7,21	4,24	5,43
BeSn/TaNb	0,00092	0,00064	0,00066	0,00053	0,00028	0,00039	0,00070	0,00037	0,00042	0,00044
Be/Li	0,09	0,06	0,06	0,10	0,12	0,28	0,07	0,06	0,56	0,12

Table 8. Ratio of upper- to lower-zone elements in the central ore bodies of the La Vi deposit (Zone M)

Zone Element	I 0-10m	II 30m	III 36m	IV 42m	V 65-67m
(Li/Ta)cn	16,401	16,666	12,310	4,316	19,193

Table 9. Ratio of upper- to lower-zone elements by absolute depth in drill hole K1401 within the central ore zone of the La Vi deposit (Zone M)

Zone Element	III 36m	IV 42m	V 65-67m
(Be/Li)cn	0,31	0,32	0,12

The vertical geochemical zoning therefore does not exhibit a clear pattern of increasing Be concentration in the deepest portions of the ore body, as typically observed in LCT-type pegmatites or pegmatites derived directly from residual granitic melts. In terms of depth, Li concentrations can locally increase to their highest values (2.16 wt% Li₂O; mean 0.84 wt%) at 155–158.8 m, compared with only 0.52 wt% on average at shallower levels (71–73.2 m) (Nguyen Van Niem et al., 2025).

Additionally, boron enrichment within the pegmatite veins and associated schist horizons shows highly irregular variations - ranging from extremely enriched to below detection limits - from the top downward. This irregularity may reflect the influence of metamorphic layering and material redistribution during the formation of concordant Li-bearing pegmatites within the host schists.

In addition, the highly heterogeneous distribution of Li and B, as noted above, may be directly related to the pegmatite-forming processes and to the redistribution of material from older metamorphic rocks (Kan Nack schists). However, boron itself is also very

unevenly distributed within these metamorphic sequences and across the different magmatic stages that have affected the area.

For the ore bodies, Li shows only a weak correlation with Be and tends to correlate negatively with Sn and Ta. In general, the contents of Sn and Ta in the ore are low. Moreover, these relationships do not exhibit a strictly linear trend (either increasing or decreasing) in response to the geochemical behavior of elements and minerals under varying redox conditions, as described by Tuan Anh Nguyen et al. (2024). According to their study, Fe content in mica within pegmatites decreases upward, and Sn behaves similarly (decreasing with distance from the granite), yet Sn minerals (cassiterite) show the opposite pattern - becoming more abundant farther from the magmatic source. This suggests that in the deep, reducing environment (mica enriched in Fe²⁺ - FeO), Sn may migrate upward and, upon encountering oxidizing conditions, precipitate as cassiterite - a process that would normally be expected.

However, an anomaly is observed at the uppermost zone, where Li is enriched (lepidolite-dominant): here, the Sn and Fe contents in mica decrease, while Mn increases (from the lower to upper zones, causing lepidolite to shift from pink to lavender in color, indicating higher Mn³⁺ relative to Mn²⁺ and thus a more oxidizing environment; Tuan Anh Nguyen et al., 2024). Yet this uppermost zone is not characterized by significant cassiterite accumulation.

This implies that additional geological processes - beyond simple magmatic fractionation and pegmatite differentiation -

may have influenced the genesis of lithium pegmatites at the La Vi deposit, suggesting a more complex evolutionary history than a straightforward residual melt crystallization model from the Sa Huynh granite.

Within the lithium ore veins, Li shows virtually no significant correlation with other elements. In the metamorphic rocks surrounding the veins, as shown above, Li exhibits only a moderate correlation with Nb and a weak-to-moderate correlation with Be. In contrast, within the Sa Huynh granitoid complex in the La Vi deposit area, Li is strongly correlated and forms a distinct elemental association of Li-Be-Cs-Rb. Meanwhile, Sn is associated with Cs-Be-Ta-Nb.

This pattern is markedly different from that of the lithium ore bodies themselves, indicating a lack of geochemical continuity or direct transition from the granitic source into the Li-bearing pegmatites.

Although the granite in this area shows a high degree of specialization in Li, strong boron-related mineralization potential, relatively high specialization in Sn, and notable enrichment in Cs, Be, and Rb, many of these geochemical features do not directly relate to the lithium-bearing pegmatites of the La Vi deposit. However, they may still reflect a common magmatic source. This relationship is clarified further as follows:

The above characteristics reflect the material exchange processes and lithium mineralization that occur along pegmatite veins hosted within the older metamorphic sequences, and they are not typical of the classical LCT-type pegmatites. Nevertheless, the ore-forming role of the granite and its marginal pegmatite veins in this area is highly significant: the granite exhibits high specialization (strong Li anomalies) and serves as both a potential primary source of mineralization and a heat source driving the remobilization and redistribution of elements.

The parent magma could have generated other deposit types that have not yet been identified - possibly because they have been

eroded or exposed (lepidolite is encountered but greisenization is very limited) - and/or may have contributed to epigenetic processes, element migration, and secondary accumulation within Quaternary fluvial-marine sedimentary sequences (e.g., Thanh Lâm, An Tây areas) during periods with favorable geochemical conditions (alkaline and reducing environments). Such secondary lithium deposits hosted in clay-rich strata of foreland or piedmont deltaic basins should be considered in future exploration and resource assessments.

According to the study by Nguyen Van Niem et al. (2025) on the rare earth element (REE) characteristics of four rock/ore types - porphyritic granite (near the deposit), fine-grained light-colored granite (farther from the deposit), Li ore (Type I pegmatite) at different depths of the deposit, and tourmaline-bearing pegmatite (Type IV) - the REE distribution patterns show significant variations.

The deep-seated Li ores (Type I pegmatite) display a positive Eu anomaly and a negative Ce anomaly, clearly distinguishing them from the porphyritic granite and tourmaline-bearing pegmatite; this pattern suggests that the deep Type I pegmatites are influenced by metamorphic and alteration processes. By contrast, the shallow Type I pegmatites exhibit an REE distribution broadly similar to that of the porphyritic granite, although their total REE content is lower (262.93 ppm vs. 628.48 ppm), and both show a positive Eu anomaly, indicating an absence of feldspar fractionation during crystallization. The total REE content of these Type I pegmatites remains significantly enriched relative to chondrite, differing markedly from Li-bearing pegmatites associated with rare-metal granites elsewhere.

The fine-grained light-colored granite shows depletion in total REE (190.69 ppm) and light rare earth elements (LREEs), but relative enrichment in heavy rare earth elements (HREEs) compared with the porphyritic granite. Normalized REE ratios further highlight key differences:

The intra-group ratios - light REE/light REE (La/Ce) and heavy REE/heavy REE (Yb/Lu) - are broadly similar among the Li ores and the examined rock types.

However, the LREE/HREE ratio of porphyritic granite (La/Lu = 30.04) is markedly different from that of deep Type I pegmatite (La/Lu = 4.55), Type IV pegmatite (La/Lu = 7.17), and fine-grained light-colored granite (La/Lu = 6.31), as well as from the shallow Type I pegmatite (La/Lu = 26.16).

These results indicate that while the pegmatites and the granitic magmas (particularly Type III Li-rich pegmatites with medium to very large muscovite flakes along the margins of the magma body) share a co-magmatic origin, their genetic evolution diverges significantly from that of the Li-bearing Type I pegmatites, which are instead linked to tectono-metamorphic processes under distinct P-T conditions.

For the $\delta^{18}\text{O}$ and δD isotopic compositions of fluid inclusions in quartz (at $\sim 400^\circ\text{C}$) from the Li-bearing pegmatite ore bodies, the data indicate that the ore-forming fluids were derived from an intermediate water source, with only one sample plotting within the magmatic water field (Duong Ngoc Tinh, 2019).

Isotopic analyses of O and H in single-mineral separates - lepidolite from the lithium ore bodies and mica from marginal pegmatites to lepidolite-bearing granitic pegmatites of the Sa Huynh complex (which contain small crosscutting pegmatitic veins) - show that:

i) The water forming muscovite in the marginal pegmatites of the Sa Huynh granite was metamorphic in origin;

ii) Lepidolite within the Li ore bodies and lepidolite in the granitic pegmatites are related to secondary alteration processes rather than primary magmatic crystallization.

The lithium ore bodies (characterized by fine- to very fine-grained mica) exhibit $\delta^{18}\text{O}$ values (30.14‰) significantly higher than those of muscovite-bearing pegmatites at the

granite margins (23.572‰) and also higher than those of internal granitic pegmatites within the Sa Huynh complex (28.044‰). In contrast, the δD values of lepidolite from the Li ore bodies are much more negative than those of muscovite in the marginal pegmatites and lepidolite from the internal granitic pegmatites (-54.17‰ vs. -44.74‰ and -43.13‰) (Nguyen Van Niem et al., 2025). These values correspond to the upper range of Li-mica δD (-63 to -53‰), typically associated with late-stage fluid release, rather than magmatic differentiation (Karin Siegel et al., 2016).

Furthermore, even lepidolite formed in true magmatic environments is generally considered a secondary alteration product. In the internal Sa Huynh granite complex, lepidolite occurs with pegmatitic pockets and veins that exhibit significantly higher oxygen isotope ratios compared with true magmatic granites, supporting the interpretation of a late-stage, fluid-related alteration origin rather than primary magmatic fractionation (Nguyen Van Niem and et al., 2025). The temperature conditions for the pegmatites containing lithium ore here are mainly in the intermediate temperature stage as mentioned above (200 - 290°C) and are not typical of true magma source pegmatites.

Isotopic ages. The Li ore bodies yield an age of 264 ± 3.6 Ma (Rb-Sr whole-rock), whereas the Sa Huynh granitoid complex has been dated at 259 ± 7.9 Ma to 251 ± 3 Ma based on U-Pb zircon ages (Duong Ngoc Tinh, 2019). In addition, U-Pb dating of accessory minerals gives ages of 254.7 ± 2.8 Ma for monazite from the muscovite-albite pegmatite zone and 255 ± 5.7 Ma for coltan from the lepidolite-topaz-albite pegmatite zone (Tuan Anh Nguyen et al., 2024). These data indicate that the pegmatites and ore bodies formed during the P-T tectono-metamorphic stage in the region and likely share a co-magmatic origin.

Thus, the initial ore-forming fluids of the Li-bearing pegmatite bodies were probably derived from the same parental magma as the marginal pegmatites and internal granitic pegmatites, yet they are not simply the residual

melt products of the Sa Huynh granite. Instead, they show strong evidence of material exchange with the surrounding host rocks as well as with metamorphic and shallow hydrothermal fluids. This is reflected in the $\delta^{18}\text{O}$ values of lepidolite from the Li ore bodies and of lepidolite and muscovite from associated pegmatites and granitic pegmatites, which are much higher than those reported for micas in magmatic-fractionated LCT-type pegmatites (e.g., Varuträsk, Skellefte district, northern Sweden: 10.3–11.3‰; Karin Siegel et al., 2016).

Such elevated $\delta^{18}\text{O}$ values (exceeding 23‰ and reaching up to 30.14‰ in the La Vi area; Nguyen Van Niem et al., 2025) likely reflect intense metasomatic interaction with carbonate-bearing metamorphic sequences of the Kan Nack Complex, which hosts the lithium ore bodies at depth. This metasomatism provides a robust explanation for the unusually high $\delta^{18}\text{O}$ signatures observed in the La Vi Li-pegmatites.

Based on the geochemical and geological characteristics described above, the La Vi lithium deposit is indicative of a partially melted (hybrid) pegmatite type, formed under transitional P–T conditions between S-type granitic magmatism and metamorphic processes. This interpretation is consistent with the ore-forming evolution at La Vi.

Most of the Li-bearing ore samples (Type I pegmatites - lithium-bearing pegmatites located both laterally and vertically distal from the granite body) plot within the field of partially melted transitional pegmatites between metamorphic and magmatic sources - the so-called “hybrid pegmatites” (DPA₁ field). In contrast, the tourmaline-bearing pegmatites (Type IV) and the marginal pegmatites (Type III) - characterized by large muscovite flakes, Li enrichment, and a direct genetic link to the Sa Huynh granitic residual melt - plot outside the hybrid pegmatite field (DPA₁) (Figure 12).

Based on the above geochemical and geological characteristics, the La Vi lithium deposit can be classified as a hybrid pegmatite-

type deposit, formed by partial melting under transitional P–T conditions between magmatic and metamorphic environments, and directly associated with Permian–Triassic tectonic activity. In terms of composition, it is best described as a pegmatite–albite (sodium-rich)–Li (lepidolite) type. The ore composition and ore body distribution are heterogeneous yet widespread, and the bodies occur in relatively concordant relationships with the older metamorphic sequences.

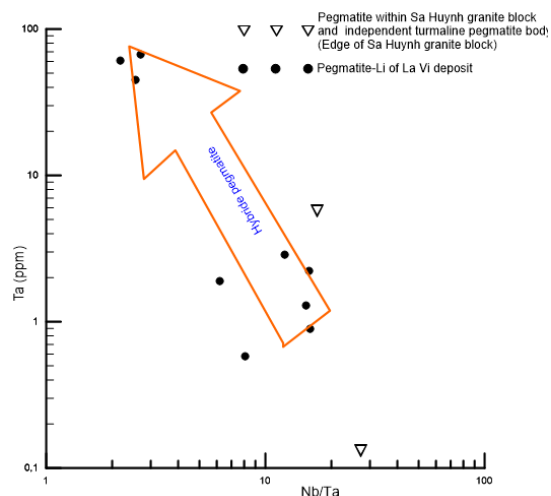


Figure 12. Ta vs. Nb/Ta correlation diagram indicating the transitional pegmatite field between metamorphic and magmatic processes in the La Vi deposit area (after Michelle McKeough et al., 2013).

Key prospecting indicators for exploration include:

Fine-grained pegmatites hosted within the metamorphic sequences of the Kan Nack Formation;

Deep-seated fault zones and tectonic shear zones that define major structural corridors, such as the Ba Tơ–Kon Tum and Ba Tơ–Gia Vực fault systems, and the subterranean boundaries of the Kan Nack (III.1) and Ngọc Linh (III.2) blocks (Figure 13);

Zones of metasomatic alteration within metamorphic rocks, although their surface expression may be subtle or poorly defined.

Exploration indicators

Primary geochemical anomalies: Li and Be show threshold anomaly values of $\text{Li} \geq 50.90$ ppm and $\text{Be} \geq 1.07$ ppm (Nguyen Van Niem et al., 2024), although there is no single, well-defined pathfinder element assemblage for this deposit type.

Secondary geochemical anomalies: enrichment of Li, Ta, Nb, Be, Cs, and Mo in soils; and hydrogeochemical anomalies of Li–Mo–Cs–B in surface and groundwater.

Accessory mineralization: the presence of Sn-, Be-, Nb-, and Ta-bearing minerals is also characteristic of this deposit style and should be regarded as important exploration clues for lithium.

Advanced geochemical tools: where appropriate, isotopic analyses and mineral geochemistry may be applied to refine exploration targeting, depending on the specific geological context of the study area.

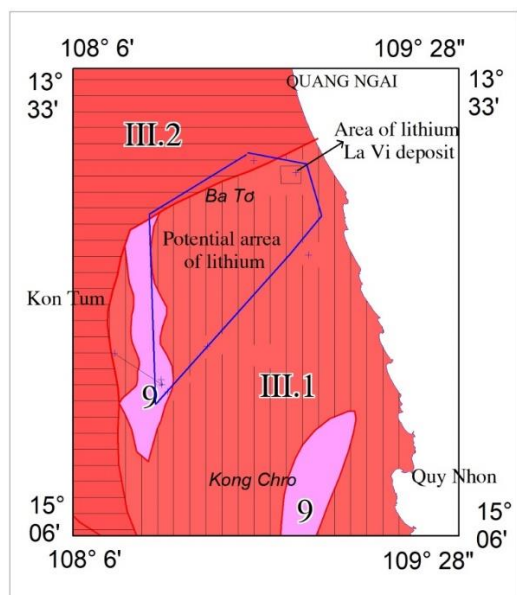


Figure 13. Predictive diagram of potential lithium mineralization zones associated with the hybrid pegmatite-type La Vi deposit (Nguyen Van Niem et al., 2025).

In addition, pegmatites directly associated with magmatic differentiation and enriched in Li may have originally formed LCT-type

deposits but have since been eroded (as indicated by the observable flakes of mica in streams and lakes surrounding the deposit and the granite body). This erosion process could also have supplied lithium to secondary deposits hosted in alkaline and reducing fluvio-marine sedimentary environments within foreland or piedmont basins, potentially giving rise to secondary lithium accumulations in these sedimentary settings.

Resource and Environmental Governance Orientation

To effectively manage resources and the environment associated with this deposit type, it is essential first to clearly understand the concept of a deposit type. A deposit type refers to a group of deposits that share similar indicative material composition, genetic origin, and formation conditions. Classifying deposits by type provides a flexible framework for exploration and exploitation, which can be adapted as new technologies emerge for detecting diagnostic mineralogical–geochemical features and recovering valuable components (Nguyen Van Niem et al., 2021, 2022).

When defining a deposit type, the focus is on both the genetic processes and the material composition, including the recoverable products and associated elements. This classification establishes the foundation for effective prospecting, mining, processing, utilization, and long-term resource planning. All mines, especially metallic deposits, exert certain environmental impacts - particularly on watersheds and river–stream systems. Therefore, managing deposits by type enables comprehensive mineral resource governance, from discovery through exploration, mining, processing, utilization, or strategic stockpiling, guided by the following core principles:

- i) Integrated approach - balance economic, social, and environmental objectives to ensure long-term sustainable development.
- ii) Transparency and accountability - enable effective monitoring of mining, processing, and trade, control illegal activities,

and increase state revenues while ensuring a secure and traceable supply chain.

iii) Multi-stakeholder participation - encourage the active involvement of government, industry (enterprises), and local communities to support informed and equitable decision-making.

iv) Regulatory framework - develop a clear system of laws, standards, and technical regulations to govern the extraction and processing of mineral resources.

v) Benefit sharing - ensure equitable distribution of economic and social benefits from mining between local communities, the state, and enterprises, strengthening local development and social acceptance.

vi) Circular economy principles - promote reuse, recycling, and reprocessing of materials, encourage the development of resource-efficient products, and reduce pressure on primary raw materials, ultimately driving technological innovation and sustainable investment.

Mining, processing, and utilization of mineral resources are inherently linked to river and stream catchments. Therefore, the above-mentioned governance principles should also be integrated with watershed environmental management, guided by the following key principles:

1. Integrated management - establish a holistic connection between river systems, surrounding ecosystems, local communities, and mineral resources, which is essential for sustainable management.

2. Adaptive and integrated governance - incorporate the role of mineral resources within an adaptive management framework that responds to the specific hydrological and ecological characteristics of each watershed, while aligning with local, regional, and global management scales.

3. Resource flow analysis - address the data gaps in mineral extraction and use by tracing material flows; this is a critical first step

toward developing effective regulatory and management mechanisms.

From the characteristics of the hybrid pegmatite-type lithium deposits described above, several key issues should be integrated into watershed environmental governance:

(i) Deposit classification and environmental implications - classify deposits by genetic origin to reveal the intrinsic nature of the mineralization and to identify potential environmental challenges associated with mining activities.

(ii) Critical raw materials research - identify and protect strategic deposits essential for environmental improvement and socioeconomic development.

(iii) Resource depletion and low-grade ores - as large, high-grade deposits become increasingly scarce, focus on the sustainable exploitation of lower-grade deposits, innovate technologies to improve recovery efficiency, and control the dispersion of associated potentially polluting elements, requiring creative environmental management approaches.

(iv) Mining impacts on ecosystems - both natural and anthropogenic mining activities can alter the natural environmental composition and affect entire ecosystems (including human communities). Therefore, deposit-type data and exploration results should serve as a background for environmental monitoring and surveillance, support integrated policy-making, and help identify and trace pollution sources for effective environmental governance.

In the context of green economic development, the demand for lithium is rising sharply due to the rapid expansion of renewable energy and electric vehicles (EVs). For Vietnam, the exploration and expansion of lithium resources and the increase of national reserves are of critical importance. At present, no lithium deposits are under active exploitation in the country.

Beyond mining, Vietnam's emerging

electric vehicle industry and the use of lithium-based batteries are and will continue to exert significant environmental impacts, particularly in the context of the electrification transition. This represents a unique opportunity for Vietnam to establish a comprehensive and sustainable environmental governance framework from the outset - managing the impacts of lithium on the environment in general and on river and watershed ecosystems in particular.

For the La Vi hybrid pegmatite-type deposit, the following resource management directions are proposed:

Mining strategy for explored areas: This deposit type differs significantly from previous models; its composition and distribution patterns are highly heterogeneous, requiring a reassessment and standardization of resource reserve calculations to better reflect the geological conditions and ore-forming processes described above. Mining methods should be adjusted accordingly - for example, Sn was previously considered an important component, but this study demonstrates that Sn content in the La Vi deposit is low and highly irregular. In addition to Li, the deposit also contains beryllium (Be) of potential economic value.

Exploration potential under the new deposit model: This revised genetic model indicates significant potential for further resource expansion (Figure 13), but exploration will require the integration of multiple advanced geochemical approaches for optimal effectiveness, including: Hydrogeochemistry (currently very limited in Vietnam), Soil geochemistry, primary litho-geochemistry, mineral geochemistry, and isotope geochemistry.

Hydrogeochemical methods are particularly effective for detecting concealed ore bodies and are widely applied in countries such as the United States, Russia, and China.

Integration with other geological methods: Future exploration should also combine these geochemical techniques with

structural geology and tectonics, geophysics, petrology, and other supporting disciplines to build a robust, multi-method exploration framework tailored to the La Vi deposit type.

For the La Vi hybrid pegmatite-type deposit, the following resource governance orientations are proposed:

Mining strategy for the explored area: This deposit type is significantly different from previously published models; its composition and distribution patterns are highly heterogeneous, meaning that resource reserve estimations must be recalculated and standardized to better align with the actual geological and ore-forming conditions described above. Mining methods should also be adjusted accordingly - for example, Sn was previously considered an important target element, but the present study shows that Sn content in the La Vi deposit is low and highly irregular. In addition to lithium (Li), the deposit also contains beryllium (Be), which may hold economic potential.

Under this new hybrid pegmatite deposit model, there is significant potential for further exploration (Figure 13). However, successful resource expansion will require the integration of multiple advanced geochemical methods, including: hydrogeochemistry (currently very limited in Vietnam), soil geochemistry, primary litho-geochemistry, mineral geochemistry, and isotope geochemistry.

Among these, hydrogeochemistry is particularly effective for detecting concealed ore bodies and is already widely applied in countries such as the United States, Russia, and China.

These geochemical approaches should be combined with other geological methods, such as structural geology and tectonic analysis, geophysics, and petrology, to build a comprehensive, multi-disciplinary exploration strategy tailored to the La Vi hybrid pegmatite deposit type.

The indicator elements for exploration identified above - in bedrock and ore (Li, Be),

water (Li, Mo, B, Cs), and soil (Li, Ta, Nb, Be, Cs, Mo) - are also potentially dispersible into river and stream catchments and should be monitored and managed from the earliest stages, before mining begins. It is essential to clarify their natural background origin, assess their mobility and transport pathways into watershed systems, and evaluate the natural carrying capacity of rivers, streams, and associated lakes in the La Vi mining area.

For example, An Thọ Lake receives direct inflow from streams draining the deposit, with the La Vi Stream as the main channel. The larger Trà Cầu River basin (Quảng Ngãi) is affected by small tributaries that transport elements from the deposit area. Lithium and associated elements from the La Vi deposit should be considered not only as potential pollutants but also as key geochemical indicators for:

- Assessing the natural carrying capacity of the watershed;
- Differentiating natural vs. anthropogenic contamination sources in future environmental studies, projects, and monitoring programs.

A starting point is the regional geochemical background for lithium already established and used to normalize geochemical parameters in this study: 29.47 ppm (Nguyen Van Niem et al., 2024), along with the minimum anomaly thresholds reported above (considered as the natural anomaly). These values should serve as a reference framework for environmental monitoring of changes over time.

In addition, background geochemical datasets for river and stream catchments in the Đức Phổ-Bà Tơ area are needed to support comprehensive environmental management - covering the deposit characteristics, spatial distribution, temporal variability, potential technical and technological impacts of future mining, and material flux dynamics across the watershed.

CONCLUSION

The La Vi lithium deposit belongs to the hybrid pegmatite type, formed under mixed

genetic conditions with transitional P-T environments between granitic magmatism and metamorphism, driven by regional tectonic activity. This setting produced partially melted (hybrid) pegmatites hosting lithium mineralization. The Li-bearing pegmatites are broadly concordant with the older metamorphic sequences, yet display heterogeneous spatial distribution and highly variable concentrations of Li, Be, Ta, and Nb, though their overall distribution is wide-ranging.

The governance of lithium mineral resources needs to closely align with the specific characteristics of the above-mentioned deposit type (Origin, indicator composition, formation conditions), there are changes different from the previous results determining that the Li pegmatite here is related to the pure magma source of the Sa Huỳnh granite block.

Accordingly, future exploration and mining strategies should:

- Reassess and adapt prospecting, exploitation, and processing plans, recognizing that Li is associated with Be and that elemental distribution is highly irregular.
- Expand exploration by integrating advanced geochemical methods - primary lithogeochemistry, hydrogeochemistry, soil geochemistry - with other geological approaches such as structural geology, petrology, mineral geochemistry, and isotopic analysis.
- Prioritize hidden ore targeting along structural boundaries between the Kan Nack and Ngoc Linh subterranean (to the south and southwest of the La Vi deposit), where hybrid pegmatite formation and mineralization are most likely.

This integrated, deposit-type-based approach will support sustainable resource development, efficient exploration, and environmentally responsible management of Vietnam's emerging lithium resources.).

The geochemical signatures of the La Vi lithium deposit and its exploration indicators -

including bedrock, soil, and water geochemistry - also reflect the natural geological background of an unmined environment. They capture both the absolute concentrations and the spatial variation trends of key elements (Li, Be, Ta, Nb, Cs) as well as their potential impact on the watersheds draining toward the Trà Cầu River.

Integrating these geochemical background content with spatial distribution patterns provides a foundation for sustainable and effective watershed management in the future. This is particularly relevant given the increasing demand for lithium batteries driven by the growth of electric vehicles and the electrification transition, where distinguishing between natural geochemical inputs and anthropogenic (technical) impacts becomes critical.

Such data form the basis for calculating the environmental carrying capacity of river catchments and coastal zones influenced by both natural processes and characteristic natural anomalies associated with the La Vi lithium deposit. The elements Li, Mo, B, Cs, Ta, Nb, and Be serve a dual role:

- Exploration indicators for detecting and evaluating secondary processes affecting watersheds;

- Environmental tracers for implementing regulations, standards, and policies with greater accuracy and site-specific relevance.

This geochemical background dataset and data of this deposit type also provides a critical framework for long-term environmental monitoring in the context of green economic development and sustainable resource use. First of all, the levels of lithium and related elements in natural soil, rock, ore and water in relation to unexploited lithium deposit area as well as the green economy - transition period for the research area and Vietnam (Temporarily considered as background environmental levels for Li).

This result serves as a basis for orientation for many approaching subjects: Government,

society, businesses, non-governmental agencies, researchers, multi-purpose.

Acknowledgements

This paper was completed based on the results of the Ministry-level Science and Technology Project: “Study on the Origin, Formation Conditions, and Distribution Rules of Lithium Resources in Vietnam” (Project Code: TNMT.2023.562.11). It also draws upon findings from numerous other thematic studies and detailed geological investigations (see cited references) to support the interpretation of lithium mineralization in Vietnam.

References

- Đào Duy Anh, Hoàng Thị Minh Thảo, Nguyễn Thị Minh Thuyết, 2013. Đặc điểm thành phần vật chất pegmatit chứa Liti vùng La Vi, tỉnh Quảng Ngãi. *Journal of Sciences of the Earth, Vietnam Academy of Science and Technology*, 35(3), 241-248.
- V. Balaram, M. Santosh, M. Satyanarayanan, N. Srinivas, Harish Gupta (2024). Lithium: A review of applications, occurrence, exploration, extraction, recycling, analysis, and environmental impact. *Geoscience Frontiers* 15 (2024) 101868
- Duong Van Cau (editor-in-chief) and et al., (2004). *Geology and minerals at scale 1:50,000 of Ba To sheet group; Bđ.280*. Center for Information and Archives of Geology. General Department of Geology and Minerals of Vietnam. Ha Noi.
- Wan Hee Cheng, Chee Kong Yap, Mohamad Pauzi Zakaria, Ahmad Zaharin Aris and Tan Soon Guan (2015). Lithium Levels in Peninsular Malaysian Coastal Areas: An Assessment Based on Mangrove Snail *Nerita lineata* and Surface Sediments. *Pertanika J. Trop. Agric. Sci.* 38 (1): 93 - 101 (2015)
- Nguyen Dac Dong (Project leader) and et al., (2024). Report "Exploration of tin ore - rare metal in Dong Ram - La Vi area, Ba Kham commune and Ba Trang commune, Ba To district, Quang Ngai province". Center for Information and Archives of Geology. General Department of Geology and Minerals of Vietnam. Ha Noi.
- Tuan Anh Nguyen, Xiaoyong Yang, Tuan Anh Tran, My Dung Tran, Thi Hien Vu Zhuang Zhao (2024). Mineralogy and geochronology of pegmatites in the Kontum Massif, Central Vietnam: Implications for evolution of rare-metal mineralization. *LITHOS* 484-485 (2024) 107747.

- Nguyen Van Niem (Project leader) and et al., (2021). Research on the geochemical characteristics of copper-deposit types as a scientific basis for explored orientation for hidden minerals (Related to some copper ore types in the central region of Vietnam). Code: VĐCKS.2021.03.06. Mistry of Resources and Environment (older). Ha Noi.
- Nguyen Van Niem (Project leader) and et al., (2022). Research on the geochemical characteristics of tungsten-deposit types as a scientific basis for explored orientation for hidden minerals, contact Vietnam. Code: NVTX.2022.03.04. Ministry of Resources and Environment (Older). Ha Noi.
- Nguyen Van Niem, Do Duc Nguyen, Mai Trong Tu, Nguyen Van Nam, Pham Hung Thanh, Duong Cong Hieu, Bui Huu Viet, Pham Nguyen Ha Vu, Nguyen Thi Hong, Do Van Linh, and Vu Trong Tan (2024). Geochemical Characterization and Potential Sources of Lithium Mineralization in Various Areas of Vietnam. Part of the book series: EAI/Springer Innovations in Communication and Computing (EASICC). eISSN: 2522-8609; pISSN: 2522-8595. EAI/Springer Innovations in Communication and Computing, p. 789-808, 2024
- Nguyen Van Niem (Project leader) et al., (2025). Study on the origin, formation conditions and distribution rules of lithium resources in Vietnam" , Code: TNMT.2023.562.11. National Agency for Science and Technology Information and Statistics. Ministry of Science and Technology. Ha Noi.
- E. Petavratzi, D. Sanchez-Lopez, A. Hughes, J. Stacey, J. Ford, A. Butcher (2022). The impacts of environmental, social and governance (ESG) issues in achieving sustainable lithium supply in the Lithium Triangle. *Mineral Economics* (2022) 35:673–699.
- Pham Van Thong (editor-in-chief) and et al., (2009). Report on Assessment of prospect of tin and rare metal ore (Ta, Li, Be) in La Vi area, Quang Ngai province; Tc.85. Center for Information and Archives of Geology. General Department of Geology and Minerals of Vietnam. Ha Noi.
- Pham Van Thong (Project leader) et al., (2017). "Geological structure of rare metal ore zone in La Vi region and initial assessments of rare metal potential in Kon Tum region". Collection of reports of the 65th anniversary scientific conference of Vietnam geology - Geological Journal series A No. 320, 9-10/2010, pp. 414-422.
- Duong Ngoc Tinh (Project leader) et al., (2017). Research on the distribution rules of lithium rare metal- ore in Kon Tum zone, orientation for investigation and discovery of rare metal ore. National Agency for Science and Technology Information and Statistics. Ministry of Science and Technology. Ha Noi.
- Daniel Macmillen Voskoboynik, Diego Andreucci (2021) Greening extractivism: Environmental discourses and resource governance in the 'Lithium Triangle'. *Environment and Planning E Nature and Space* 0(0) 1–23
- Chee Kong Yap, Khalid Awadh Al-Mutairi (2025). Evaluating Marine Mussels' Lithium, Strontium, and Vanadium Detoxification for Coastal Ecosystem Conservation. *Pol. J. Environ. Stud.* Vol. XX, No. X (XXXX), 1-11
- Book_or_book_chapter__author_surname A A, Author_surname B B, Author C, (2009) Title of book. EditorSurname A (eds). Publisher and location. (ISBN _number_). 450p.
- Journal_paper_author_surname N P, Anotherone K, Thelastone P O (2009) Title of paper. *Canadian Journal of Remote Sensing.* 35(2): 244-253.
- Report_author_surname A A, Author_surname B B, Author C, (2009). Title of report. Publisher and location. (ISBN _number_). 50p.
- Web_site_author_name_surname A A, Author_surname B B, Author C, (2009). Title of Page. URL: <https://maps.app.goo.gl/fNt3FnyZoLXdCvW9> [Last accessed: full date].

Geochemical characteristics and assessment of heavy metal contamination in groundwater: A case study from the mountainous region of Tuyen Quang, Northern Vietnam

Do Thi Thu^{1*}, Pham Thi Dung¹, Tran Tuan Anh¹, Pham Thanh Dang¹, Nguyen Thi Lien¹, Nguyen Xuan Qua¹, Nguyen Thi Thu¹, Le Thi Phuong Dung¹, Doan Thi Thu Tra¹, Vu Dinh Hai¹, Bui Thi Sinh Vuong², Nguyen Trong Tai¹

¹Institute of Earth Sciences, Vietnam Academy of Science and Technology

²Hokkaido University, Japan

*Email: thudothi12@gmail.com

Abstract: Heavy metal contamination in the environment has always been a matter of concern, particularly in areas with active mining operations. Owing to its abundant polymetallic mineral resources, Ha Giang Province (pre-amalgamation) currently hosts several operating mining enterprises that exert significant environmental pressure. In this study, 21 groundwater samples were collected from Quang Binh and Bac Quang districts, Ha Giang Province (at present Tuyen Quang Province) and analyzed for major chemical components and selected heavy metals (Fe, Mn, As, Cd, Cr, Cu, Co, Pb, Zn) to investigate the geochemical characteristics of groundwater and assess the levels of heavy metal contamination and the ecological risks posed by certain metals. Results indicate that groundwater exhibits pH ranging from acidic to slightly alkaline, with total dissolved solids (TDS) varying between 10 and 280 mg/L. This chemical composition pattern predominantly produces Ca-Mg-HCO₃ water type, followed by Na-K-Cl-SO₄ and Na-K-HCO₃ types. The distribution of these water types clearly reflects their association with underlying geological conditions. Assessment of heavy metal concentrations shows that only Fe (2/21 samples) and Mn (3/21 samples) exceed drinking water limits (compared to QCVN and WHO) [1], [2], accounting for 10% of the total samples.

Evaluation using Heavy Metal Pollution Index (HPI), contamination degree (Cd), and Ecological Risk Index (ERI) indicates low

pollution levels, minimal heavy metal contamination risk, and safe conditions for the environment and ecosystems. This study provides a relatively comprehensive insight into groundwater geochemistry and current heavy metal contamination, while emphasizing ecological and environmental risk implications.

Keywords: Geochemistry, Heavy Metals (HMs), HPI, Cd, ERI, Ha Giang, Tuyen Quang.

INTRODUCTION

Groundwater serves as the primary source of domestic water supply in most developing countries, especially in areas lacking centralized water distribution systems. It is commonly extracted from shallow wells, offering several advantages, including low cost, ease of access, and limited need for pretreatment. However, the accelerating processes of urbanization, industrial development, and agricultural intensification have increasingly threatened groundwater quality. Among these threats, heavy metal contamination has emerged as a major environmental concern [3], [4], [5].

Comprehensive studies on water resources, encompassing both quantity and quality, not only assess the current status and condition of water sources but also forecast their potential to meet future demands. Within this context, water geochemistry plays a crucial role. Understanding the geochemical nature and formation processes of natural waters

provides a baseline for evaluating the impacts of natural and anthropogenic factors, while also serving as a foundation for developing effective water resource management policies [6] [7] [8]. Groundwater risk assessment based on monitoring data is crucial for the protection and sustainable management of this essential resource. Indices such as the Heavy Metal Pollution Index (HPI), Contamination Degree (Cd), and Ecological Risk Index (ERI) serve as robust and reliable tools for quantifying the cumulative impact of heavy metal contamination, evaluating overall groundwater quality, and determining its suitability for domestic consumption [9], [10], [11], [12].

Heavy metal pollution in the environment has always been a matter of concern, particularly in regions with active mining operations. Tuyen Quang Province is endowed with abundant mineral resources, including both metallic and non-metallic minerals. According to reports by the Ministry of Natural Resources and Environment, more than 215 mines, ore deposits, and mineral occurrences belonging to 28 different types of minerals have been identified across the province. Among these, four key mineral resources—iron, and lead–zinc—are considered of significant industrial value, with Tuyen Quang hosting the majority of Vietnam’s lead–zinc deposits [13]. Mining activities, however, pose potential risks of environmental contamination, especially affecting soil, surface water, and groundwater systems.

The main objectives of this study are twofold:

- To elucidate the geochemical characteristics of groundwater in the southern region of Tuyen Quang Province;
- To determine the concentrations of selected heavy metals (Fe, Mn, As, Pb, Co, Cd, and Zn) and total dissolved solids (TDS) in groundwater, and to evaluate the degree of contamination using geochemical indices such as the Heavy Metal Pollution Index (HPI), Contamination Degree (Cd), and Ecological Risk Index (ERI).

The findings of this study are expected to provide a reliable scientific basis for environmental management agencies, support the assessment of groundwater quality, and propose effective strategies for safe drinking water management and treatment for local communities in Tuyen Quang Province.

MATERIAL AND METHODS

Study area

The study area covers two districts, Bac Quang and Quang Binh, located in the southern part of Ha Giang Province (*pre-amalgamation*), a mountainous border region in northern Vietnam. It currently includes the communes of Bac Quang, Vinh Tuy, Bang Hanh, Dong Tam, Dong Yen, Lien Hiep, Hung An, Tan Quang, Quang Binh, Yen Thanh, Bang Lang, Tien Yen, Xuan Giang, Tan Trinh, Tien Nguyen, and part of Thong Nguyen Commune in Tuyen Quang Province. It lies between latitudes $22^{\circ}09'39''$ and $22^{\circ}37'37''$ N and longitudes $104^{\circ}26'52''$ and $105^{\circ}07'12''$ E, encompassing an area of approximately 1,614 km². The topography is highly diverse, consisting of valleys, low hills, and high mountains, with mountainous terrain being predominant. Tuyen Quang experiences two distinct seasons: a rainy season from May to October, and a dry (winter) season from November to April of the following year [13].

The area is traversed by the Lo River, Con River, and several smaller tributaries, all characterized by meandering flow patterns influenced by topography, channel width, and gradient. The Lo River originates in China and flows in a north–south direction, serving as the principal river in the study area. River discharge varies according to topographic conditions and is largely controlled by meteorological and hydrological factors [13].

Tuyen Quang Province is covered by four sheets of the Geological and Mineral Resources Map of Vietnam at a scale of 1:200 000, including Bac Kan, Bao Lac, Bac Quang, and Ma Quan [14], [15], [16], [17]. Accordingly, a simplified geological map of the study area is presented in

Figure 1. Based on the compiled geological data, all sampling locations in this study are distributed across four main lithological units: Quaternary sediments; granitic rocks of the Song Chay complex; limestone, sandstone, and shale of the Mia Le Formation; and marble, crystalline limestone, and schist of the Ha Giang Formation. Groundwater in the region is primarily extracted from drilled and dug wells, as well as from natural springs associated with fractured and karstic aquifers corresponding to the four main geological groups: Quaternary sediments, granites, limestone–sandstone–shale formations, and metamorphic rocks such as marble and crystalline limestone. These groundwater sources are widely used for domestic consumption, agriculture, and livestock farming. However, the area is also affected by anthropogenic pollution sources, including agricultural runoff, domestic and industrial wastewater discharge, and unmanaged waste disposal sites. Additionally, mining activities within the region pose potential risks of heavy metal contamination to groundwater resources.

Sampling and analysis

In this study, a total of 21 groundwater samples were collected and preserved during the dry season between 2021 and 2022 (Figure 1). The groundwater samples were obtained from drilled wells, dug wells, and natural springs associated with four major lithological groundwater sources: Quaternary sediments; granitic rocks of the Song Chay Complex; limestone, sandstone, and shale of the Mia Le Formation; and marble, crystalline limestone, and schist of the Ha Giang Formation. Sampling procedures were conducted in accordance with national and international standards, including TCVN 6663-11:2011 (ISO 5667-11:2009) [18].

Field parameters such as pH and total dissolved solids (TDS) were measured in situ using a HANA HI9829-01042 multiparameter device. The collected water samples were filtered through 0.45 µm Millipore membrane filters.

Each sample was acidified to $\text{pH} < 2$ by adding a drop of 16 M HNO_3 and subsequently stored under refrigeration until elemental analysis. Major elements and selected heavy metals were determined using inductively coupled plasma mass spectrometry (ICP-MS, Model 7900, Agilent, USA) [19]. This advanced analytical technique enables precise quantification of heavy metals, thereby enhancing the accuracy and reliability of the analytical results.

The Pollution Assessment Indices

Heavy metal pollution index (HPI)

The contamination status of the water samples was evaluated using the Heavy Metal Pollution Index (HPI). This index quantifies the combined influence of individual heavy metals on the overall water quality [10] and serves as a tool to assess the suitability of water for human consumption [11]. The HPI reflects the overall quality of water with respect to heavy metals, calculated by assigning a weighting factor (W_i) to each parameter, ranging from 0 to 1, to represent its relative significance in water quality assessment. In this study, the WHO and Vietnamese standard QCVN permissible limits for drinking water were employed as reference values [1], [2]. The Heavy Metal Pollution Index (HPI) serves as an effective tool for regulatory authorities and the public sector, facilitating strategic planning and informed decision-making in resource management and pollution control [20].

Degree of contamination (C_d)

The C_d was used to determine the level of pollution at an articular zone [21]. It was determined by summing the contamination factors of all the HMs as shown in (Table. 1), where n is the number of analyzed HMs.

Ecological risk index (ERI)

The ERI evaluates the ecological risk degrees for toxins and heavy metals in soils [21]. The detailed values of the Ecological Risk Index (ERI) are presented in (Table 1).

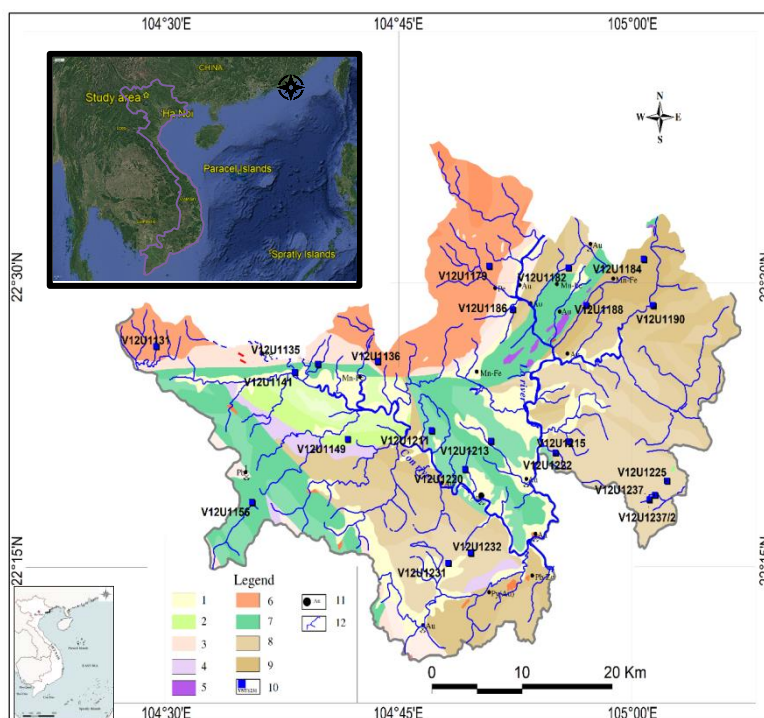


Figure 1. Distribution map of lithological units, water sampling sites in study area. 1 – Quaternary sediment; 2 – Cretaceous conglomerate, sandstone and siltstone of Ban Hang Formation; 3 – Late Precambrian, quartz-mica schist, gneiss, amphibolite, marble, and quartzite of Thac Ba and An Phu formations; 4 – Triassic Conglomerate, sandstone, siltstone of Yen Binh formation; 5 – Proterozoic dunit and harzburgite of Nam But complex; 6 – Devonian biotite granite of Song Chay Complex; 7 – Cambrian marble, limestone and schist of Ha Giang Formation; 8 – Devonian limestone and schist of Mia Le Formation; 9 – Devonian Clay shale of Pia Phuong Formation; 10 – Sampling site; 11 – Metal deposit/ exploitation site; 12 – Stream and river.

RESULTS AND DISCUSSION

Parameters of Groundwater Quality

The Geochemical characteristics of groundwater can be influenced by various factors such as lithology, mineral composition, residence time within the aquifer matrix, water properties, flow pathways through rocks and soils, and the initial recharge conditions of

groundwater [22]. The ionic composition of groundwater reflects its fundamental hydrochemical nature. The results of the physicochemical analysis of groundwater samples collected from the study area are summarized in Table 2. Guidelines for potable water quality were adopted from both Vietnamese and international standards [1], [2].

Table 1. Quality indices and their classification systems

No.	Definition	Contamination categories
1	Heavy metal pollution index (HPI) [23], [24], [12], [25]	
	$HPI = \frac{\sum_{i=1}^n (Q_i \times W_i)}{\sum_{i=1}^n W_i}$ <p>where Q_i is the subindex of the ith parameter, W_i is the unit weight of the ith parameter and n is the number of parameters considered; the</p>	<p>HPI < 15 : Low water pollution</p> <p>15 < HPI < 30: Medium water pollution</p> <p>HPI > 30: High water pollution</p>

	<p>subindex (Q_i) of the parameter is</p> $Q_i = \sum_{i=1}^n \frac{M_i - I_i}{S_i - I_i} \times 100$ <p>where “M_i” represents the monitored value of the heavy metal, “I_i” is the ideal value, and “S_i” is the standard permissible value set by WHO.</p> $W_i = \frac{k}{S_i}$ <p>Where: W_i = unit weight of the i-th parameter S_i = the standard permissible value k = proportionality constant</p> $\sum_{i=1}^n W_i = 1$ <p>Therefore:</p> $k = \frac{1}{\sum_{i=1}^n \frac{1}{S_i}}$	
2	Degree of contamination (C_d) [21]	
	$C_d = \sum_{i=1}^n CF_i$ $CF = \frac{C_n}{C_{Mac}} - 1$ <p>where C_n was the metal concentration in the water sample at the polluted site and C_{Mac} is the maximum permissible concentration of ith component, with reference to the MAC</p>	<p>$C_d < 1$, low contamination; C_d values ranging from 1 to 3 indicate mild contamination; $C_d > 3$, high pollution</p>
3	Ecological risk index (ERI) [21], [5], [26], [27]	
	$ERI = \sum_{i=1}^n RI = \sum T_i \times PI$ $PI = \frac{C_s}{C_b}$ <p>where, RI is the potential ecological risk factor of each heavy metal; T_i is the toxic-response factor of heavy metal; PI is the pollution index;</p>	<p>RI: $RI < 40$ (low potential ecological risk), $40 \leq RI < 80$ (moderate potential ecological risk), $80 \leq RI < 160$ (considerable potential ecological risk), $160 \leq RI < 320$ (high potential ecological risk), and ≥ 320 (very high potential ecological risk)</p>

	<p>Cs is the concentration of heavy metals in the sample; and Cb is the corresponding background values. The toxic-response factor of heavy metals is given as: Cd = 30; As = 10; Co, Cu, Ni and Pb = 5; Fe, Cr, Zn and Mn =1</p>	<p>risk) ERI: ERI < 150 (low ecological risk), 150 ≤ ERI < 300 (moderate ecological risk), 300 ≤ ERI < 600 (considerable ecological risk), and ≥ 600 (very high ecological risk)</p>
--	---	---

The physical and chemical characteristics of groundwater, including pH, total dissolved solids (TDS), major cations (Ca²⁺, Mg²⁺, Na⁺, K⁺), anions (HCO₃⁻, Cl⁻, F⁻, SO₄²⁻, NO₃⁻), and heavy metals (Fe, Mn, As, Cd, Cr, Cu, Co, Pb, and Zn), were compared against permissible limits set by the World Health Organization [2] and Vietnamese National Technical Regulations [1]. Statistical descriptors such as minimum, maximum, mean, standard

deviation (SD), and skewness were also calculated and presented in (Table 2). The low variation between mean and SD values for heavy metal concentrations indicates that the dataset is tightly clustered around the mean. Skewness values ranging from -1.2 to 4 further confirm that most parameters are symmetrically distributed with relatively high data concentration around the central value.

Table 2. Statistical parameters of pH, TDS, major cation, anion and HMs concentrations (mg/ L)

Parameter	N	LOD	Minimum	Maximum	Mean	Std. Deviation	Skewness	QCVN 01-1:2024 /BYT	WHO, 2022
pH	21	-	5.4	7.7	6.900	0.578	-1.232	6.0-8.0	6.5-8.5
TDS	21	-	10	280	79.05	81.98	1.011	1000	1000
HCO ₃ ⁻	21	-	4.88	280.600	96.46	102.38	0.705	-	400
Cl ⁻	21	-	2.807	11.540	4.188	2.037	2.850	-	250
SO ₄ ²⁻	21	-	2.630	6.110	3.402	0.890	1.919	250	250
NO ₃ ⁻	21	-	0.661	24.396	4.607	4.950	3.437	50	50
F ⁻	21	0.05	0.028	0.890	0.119	0.187	3.879	1.5	1.5
Ca ²⁺	21	-	2.004	84.168	26.004	26.655	0.688	-	200
Mg ²⁺	21	-	0.608	20.976	5.310	6.043	1.614	-	150
Na ⁺	21	-	1.659	33.559	6.965	6.809	3.236	200	200
K ⁺	21	-	0.997	16.153	5.620	3.823	1.071	-	30
Fe	21	0.005	0.110	1.486	0.231	0.293	4.320	0.3	0.3
Mn	21	0.005	0.0078	1.300	0.088	0.281	4.397	0.1	0.1
As	21	0.0005	-	0.0024	0.0008	0.0005	1.570	0.01	0.01
Cd	21	0.0005	-	-	-	-	-	0.003	0.003
Cr	21	0.005	-	0.0039	0.0014	0.0011	1.379	0.05	0.05
Cu	21	0.005	0.005	0.0342	0.0113	0.0068	2.393	1	2
Co	21	0.005	-	0.0217	0.0015	0.0048	4.243	-	-
Pb	21	0.005	-	-	-	-	-	0.01	0.01
Zn	21	0.005	0.02	0.111	0.039	0.023	2.083	2	-

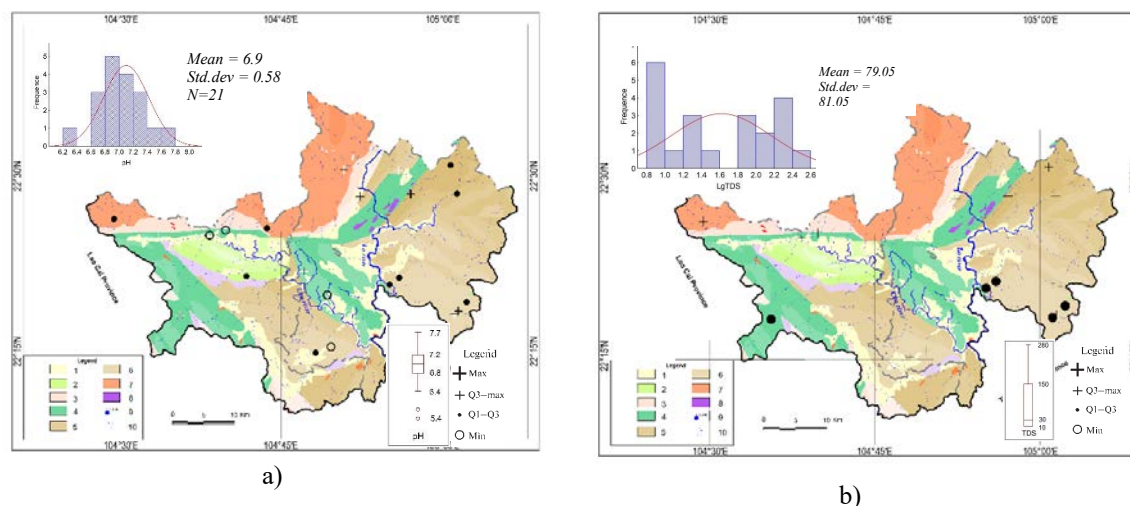


Figure 2. Distribution of pH (a) and TDS (b) in groundwater in study area

The pH of groundwater varied from 5.4 to 7.7, with an average of 6.9, which lies within the safe range (6.5–8.5), indicating that most samples are neutral to slightly acidic. However, 4 out of 21 samples had pH values below 6.5, falling below the recommended threshold. The total dissolved solids (TDS) ranged from 10 to 280 mg/L, with an average of 79.05 mg/L. All samples exhibited very low TDS concentrations, well within the recommended limits of 1,000 mg/L [1], [2], suggesting that groundwater in the study area is safe for domestic use. For major ions (Ca^{2+} , Mg^{2+} , Na^+ , K^+ , HCO_3^- , Cl^- , SO_4^{2-}), all concentrations were found within the permissible limits for drinking water according to both Vietnamese and WHO standards.

The heavy metals analyzed (Fe, Mn, As, Cd, Cr, Cu, Co, Pb, Zn) showed very low concentrations, in most cases below Limit of Detection (LOD) (Table 2). Iron (Fe) and manganese (Mn) are naturally occurring elements in soils, rocks, and minerals; Mn commonly coexists with Fe in the Earth's crust. In this study, Fe concentrations ranged from 0.110 to 1.486 mg/L, with a mean of 0.231 mg/L—within the permissible limit for drinking water [1]. Nineteen out of 21 samples (90%) met the standard, while two samples (10%) exceeded it.

Manganese (Mn^{2+}) concentrations ranged from 0.008 to 1.300 mg/L, with an average of 0.088 mg/L, and were generally within the safe range. Eighteen samples (86%) met the standard, while three (14%) exceeded it. Zinc (Zn) concentrations varied between 0.019 and 0.11 mg/L, averaging 0.039 mg/L, also within the safe limits [1]. Other metals—including As, Cd, Cr, Cu, Co, and Pb—had concentrations either very low or below the limit of detection (Table 2), indicating that groundwater in the study area is safe for drinking and domestic use [1].

Among the heavy metals, Fe and Mn exhibited higher concentrations relative to the others. The mean concentration followed the descending order: $\text{Fe} > \text{Mn} > \text{Zn} > \text{Cu} > \text{Co} > \text{Pb} > \text{Cr} > \text{As} > \text{Cd}$. Overall, groundwater quality analysis showed that only Fe (2 out of 21 samples) and Mn (3 out of 21 samples) exceeded the permissible limits for drinking water [1], [2], while all other parameters remained within safe levels.

Geochemical Characteristics of Groundwater

The chemical composition of groundwater and the processes influencing its chemistry are illustrated in the Piper diagram (Figure 3). This diagram enables the differentiation of various water sources as well as the identification of the chemical composition and migration

processes of dissolved constituents [28]. The lower left and right triangles of the Piper diagram represent the proportions of cations and anions, respectively, while the central diamond depicts the hydrochemical facies of the water samples (Figure 3). The groundwater samples from the study area, plotted on the Piper diagram (Figure 3), are categorized into four groups: groundwater in granite complex; Quaternary sediments; metamorphic formations including marble, limestone, and schist; and clastic sedimentary formations (limestone, sandstone, and schist). The groundwater samples in the study area exhibit noticeable variations depending on the geological formations. Combined with the spatial distribution maps of pH and TDS (Figures 2a, 2b, and 3), it can be observed that

groundwater in the region has pH values ranging from 5.4 to 7.7 and TDS values varying between 10 and 280 mg/L. Groundwater within the Song Chay complex granite generally shows relatively low pH values, reflecting weakly acidic characteristics. The water type varies from Na-K-HCO₃ to Na-K-Cl-SO₄, characterized by the dominance of Na⁺ and K⁺ cations. Groundwater from metamorphic rocks, including marble, limestone, and schist, also exhibits relatively low pH values, indicating weak acidity. These samples display higher TDS values and are typically of the Ca-HCO₃ type, with Ca²⁺ and HCO₃⁻ as the dominant ions. This composition reflects a carbonate origin, typical of limestone and carbonate-bearing metamorphic rock areas.

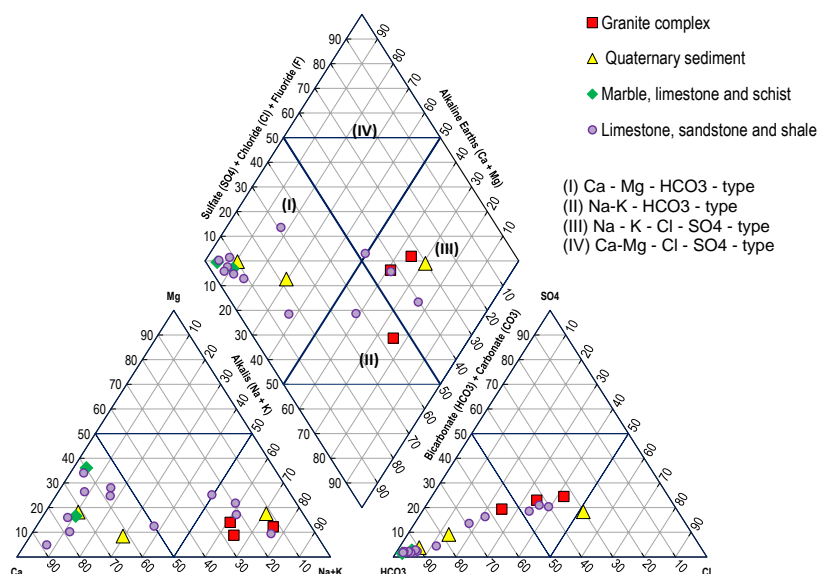


Figure 3. Piper diagram representing the main geochemical facies and groundwater types

The remaining groundwater samples from Quaternary sediments and clastic sedimentary formations (limestone, sandstone, and schist) exhibit mixed water types ranging from Na-K-Cl-SO₄ to Na-K-HCO₃, with the majority falling within the Ca-HCO₃ type. This indicates the predominance of Ca²⁺, Na⁺, and K⁺ among the cations, and HCO₃⁻ and Cl⁻ among the anions. Such hydrochemical characteristics suggest the dissolution of a mixture of various

lithologies, including limestone, sandstone, and schist, resulting in the observed compositional variability of groundwater in these formations, which indicates a clear correlation between lithological composition and the hydrogeochemical characteristics of groundwater.

Pollution Assessment Using HMs Pollution Indices

Heavy metal pollution index (HPI)

The HPI values in the study area range from 3.08 to 34.78, with an average of 7.52. Only one sample (V12U1237) exhibits an HPI value greater than 30, indicating that groundwater at this location is considerably contaminated by heavy metals. In contrast, the majority of groundwater samples (95%) show low levels of heavy metal pollution, suggesting that the groundwater in these areas is generally safe for drinking purposes.

Degree of contamination (C_d)

The C_d values range from -7.35 to 10.34, with an average of -6.04. $C_d < 1$ indicates low contamination, C_d values between 1 and 3 indicate moderate contamination, and $C_d > 3$ represents high contamination [21]. The C_d values also reveal that only one sample (V12U1237) exhibits $C_d > 3$, corresponding to a high contamination level, while the majority of samples (95%) fall within the low contamination category.

At sample V12U1237, elevated concentrations of Fe and Mn led to high values of the heavy metal pollution indices (Cd and HPI). These anomalies are likely associated with dissolution of surrounding rocks and soils or the influence of nearby metal mining activities. Consequently, the utilization of this groundwater source for drinking purposes should be limited, and continued monitoring is strongly recommended.

Ecological risk index (ERI)

The ERI values in the study area range from 3.49 to 41.93, with an average of 7.18. All groundwater samples (100%) exhibit ERI values below 150, indicating a low ecological risk throughout the region. Although toxic heavy metals such as Cd, Pb, and Cr are present in the groundwater, their concentrations remain below the threshold levels that could pose significant ecological impacts.

Table 3. Water quality classifications according to HPI, C_d , and ERI values.

Samples	HPI Value	Class	Cd Value	Class	ERI Value	Class
V12U1220	7.16	Low water pollution	-6.89	Low	5.52	Low ecological risk
V12U1215	4.68	Low water pollution	-7.15	Low	3.93	Low ecological risk
V12U1182	4.68	Low water pollution	-7.24	Low	3.99	Low ecological risk
V12U1222	4.08	Low water pollution	-7.35	Low	3.49	Low ecological risk
V12U1237/2	4.44	Low water pollution	-7.18	Low	4.01	Low ecological risk
V12U1184	5.23	Low water pollution	-6.83	Low	5.77	Low ecological risk
V12U1225	4.07	Low water pollution	-7.25	Low	3.94	Low ecological risk
V12U1190	9.86	Low water pollution	-7.00	Low	7.51	Low ecological risk
V12U1188	4.66	Low water pollution	-6.83	Low	4.26	Low ecological risk
V12U1231	6.38	Low water pollution	-7.04	Low	5.18	Low ecological risk
V12U1237	34.78	High water pollution	10.34	High	41.93	Low ecological risk
V12U1211	3.08	Low water pollution	-7.19	Low	3.82	Low ecological risk
V12U1186	11.69	Low water pollution	-4.39	Low	10.90	Low ecological risk
V12U1179	5.04	Low water pollution	-6.74	Low	6.22	Low ecological risk
V12U1136	5.19	Low water pollution	-6.91	Low	5.44	Low ecological risk
V12U1156	5.61	Low water pollution	-7.20	Low	4.48	Low ecological risk
V12U1149	9.64	Low water pollution	-7.01	Low	6.33	Low ecological risk
V12U1141	5.40	Low water pollution	-7.09	Low	5.17	Low ecological risk
V12U1131	6.61	Low water pollution	-6.84	Low	5.99	Low ecological risk
V12U1135	8.73	Low water pollution	-6.07	Low	7.38	Low ecological risk
V12U1232	7.00	Low water pollution	-6.99	Low	5.46	Low ecological risk

CONCLUSIONS

The study provided insights into the geochemical characteristics of groundwater and assessed the level of heavy metal (HM) contamination using geochemical indices such as HPI, Cd, and ERI in a mountainous region of Ha Giang Province, characterized by complex geological formations and steep terrain. A total of 21 groundwater samples were collected from four major geological formations during the dry season and subsequently analyzed. The results showed that groundwater pH values ranged from slightly acidic to mildly alkaline, with the mean value indicating weak acidity. Total dissolved solids (TDS) ranged from 10 to 280 mg/L, with an average of 79.05 ± 81.05 mg/L. The spatial distribution of TDS exhibited substantial variation, with notably low concentrations in granite-dominated areas and higher concentrations across other lithological units.

Three principal groundwater types were identified in the study area: Ca-Mg-HCO₃ as the dominant type, followed by Na-K-Cl-SO₄ and Na-K-HCO₃, corresponding to different geological formations and clearly reflecting the influence of geological conditions.

The heavy metal pollution indices indicated low contamination levels and suggested that the groundwater is generally safe for drinking purposes. HPI values ranged from 3.08 to 34.78, with an average of 7.52, and approximately 95% of the samples fell into the low pollution category. Cd values ranged from -7.35 to 10.34, with a mean of -6.04, corresponding to low contamination in 95% of the samples. Similarly, ERI values indicated low ecological risk throughout the study area.

This study provides a comprehensive overview of groundwater geochemistry and an

in-depth assessment of current heavy metal contamination levels, while emphasizing the associated ecological and environmental risks. The findings offer valuable reference information for policymakers and stakeholders in developing effective groundwater resource management strategies and implementing monitoring measures related to mining activities in the region. Future research should focus on long-term groundwater quality monitoring, seasonal observation, and expanding the assessment to include additional contaminants.

ACKNOWLEDGEMENTS

This study was funded by the key science and technology projects of VAST under the project code TĐĐHQG.02/21-23, TĐĐHQG.01/21-23. We are grateful to Dr. Duong Thi Lim for help with trace element analysis.

REFERENCES

- [1] “QCVN01-1:2024/BYT. National Technical Regulation on Domestic Water Quality”.
- [2] WHO, “Guidelines for Drinking Water Quality, third ed. World Health Organization, Geneva,” 2022.
- [3] Kale SS, Kadam AK, Kumar S, Pawar NJ , “Evaluating pollution potential of leachate from landfill site, from the Pune metropolitan city and its impact on shallow basaltic aquifers,” Environmental Monitoring and Assessment, vol. 162, p. 327–346, 2010.
- [4] Mohammad Bhuiyan M.A. Islam, S. B. Dampare, Mohammad Bhuiyan, M.A. Islam, S. B. Dampare, Lutfar Parvez, Shigeyuki Suzuki, “Evaluation of hazardous metal pollution in irrigation and drinking water systems in the vicinity of a coal mine area of northwestern

- Bangladesh," *Journal of Hazardous Materials*, Vols. 179(1-3), pp. 1065-77, 2010.
- [5] Rakesh Bhutiani, Dipali Kulkarni, D.R. Khanna, Ashutosh Gautam, "Geochemical distribution and environmental risk assessment of heavy metals in groundwater of an industrial area and its surroundings, Haridwar, India," *Energy Ecology and Environment*, vol. Volume 2, pp. 155-167, 2017.
- [6] David Banks, Ola Magne Sæther, Per Ryghaug, Clemens Reimann, "Hydrochemical distribution patterns in stream waters, Trøndelag, central Norway," *Science of The Total Environment*, Vols. Volume 267, I, no. issues 1-3,, pp. Pages 1-21, 2001.
- [7] Sharma, A., Singh, A.K., and Kumar, K., "Environmental geochemistry and quality assessment of surface and subsurface water of Mahi River basin, western India, *Environm., Environmental Earth Sciences*, vol. 65, no. 4, p. 1231-1250, 2011.
- [8] Nathalie Gassama, Florence Curie, Pierre Vanhooydonck, Nathalie Gassama, Florence Curie, Pierre Vanhooydonck, Xavier Bourrain, David Widory, David Widory, "Determining the Regional Geochemical Background for Dissolved Trace Metals and Metalloids in Stream Waters: Protocol, Results and Limitations—The Upper Loire River Basin (France)," *Water*, vol. 13(13), p. 1845, 2021.
- [9] Tomlinson, D. L., Wilson, J. G., Harris, C. R., & Jeffrey, D. W., "Problems in the Assessment of Heavy-Metal Levels in Estuaries and the Formation of a Pollution Index," *Helgoländer Meeresuntersuchungen*, vol. 33, pp. 566-575, 1980.
- [10] R. Reza, Gurdeep Singh, "Assessment of Ground Water Quality Status by Using Water Quality Index Method in Orissa, India," *India World Appl Sci J*, vol. 9(12), p. 1392-1397, 2010.
- [11] Rizwan Reza, Gurdeep Singh, Manish Jain, "Application of Heavy Metal Pollution Index for Ground Water Quality Assessment in Angul District of Orissa, India," *India Int J Res Chem Environ*, vol. 1(2), p. 118-122, 2011.
- [12] Wagh, V.M.; Panaskar, D.B.; Mukate, S.V.; Gaikwad, S.K.; Muley, A.A.; Varade, A.M., "Health Risk Assessment of Heavy Metal Contamination in Groundwater of Kadava River Basin, Nashik, India," *Modeling Earth Systems and Environment*, vol. 4, no. 3, pp. 969-980, 2018.
- [13] Ministry of Natural Resources and Environment, General Department of Geology and Minerals of Vietnam,, "Report on Mineral Investigation and Assessment in Ha Giang Province (2015-2020).".
- [14] NAWAPI, "Report on Investigation and Assessment of Groundwater Sources in the Midland and Mountainous Areas of Northern Vietnam, Ha Giang Province, Nat. Center Water," 2009.
- [15] N. (. e. a. Quoc, "Geological and Mineral Resources Map of Vietnam on 1 : 200000, Bac Kan: Dept. Geol. Miner. Vietn., Hanoi, 2000.".
- [16] Tinh, H.X. (Ed.) et al., "Geological and Mineral Resources Map of Vietnam on 1 : 200000, Bao Lac: Dept. Geol. Miner. Vietnam, Hanoi, 2000.," 2000.
- [17] Xuyen, T. (Ed.) et al., " Geological and Mineral Resources Map of Vietnam on 1 : 200000, Ma Quan, Dept. Geol. Miner. Vietnam, Hanoi, 2000b.".
- [18] Xuyen, T. (Ed.) et al., "Geological and Mineral resources map of Vietnam on 1 : 200000, Bac

- Quang: Dept. Geol. Miner. Vietnam, Hanoi, 2000a.”.
- [19] TCVN 6663-11:2011 (ISO 5667-11:2009), “Water quality - Sampling - Part 11: Guidance on sampling of groundwaters”.
- [20] Duong Thi Lim, Thi Lan Huong Nguyen, Thi Hue Nguyen, Quan Dang, Thi Huong Thuy Nguyen, Thu Thuy Tran, Ngoc Nhiem Dao, Quang-Bac Nguyen, Van Tien Mai,, “Preliminary assessment of marine debris pollution and coastal water quality on some beaches in Thanh Hoa province, Vietnam,” Vietnam Journal of Marine Science and Technology, vol. 21(3), pp. 329-340, 2021.
- [21] Shankar, B. S, “A critical assay of heavy metal pollution index for the groundwaters of Peenya Industrial Area, Bangalore, India,” Env Monitoring and Assessment, vol. Vol. 5 No. 1 , p. 289, 2019.
- [22] L. Hakanson, “An ecological risk index for aquatic pollution control.a sedimentological approach,” Water Research, vol. 14, no. 8, pp. 975-1001, 1980.
- [23] József Tóth , “Groundwater as a geologic agent: An overview of the causes, processes, and manifestations,” Hydrogeology Journal, vol. 7, p. 1–14, 1999.
- [24] S Venkata MohanP. NithilaS. Jayarama Reddy, “Estimation of heavy metals in drinking water and development of heavy metal pollution index,” Journal of Environmental Science and Health, Vols. A-31, pp. 283-289., 1996.
- [25] Jelena Milivojević, Dragana Krstić , Biljana Šmit , Vera Djekić, “Assessment of Heavy Metal Contamination and Calculation of Its Pollution Index for Uglješnica River, Serbia,” Bull Environ Contam Toxicol, vol. 97, no. 5, pp. 737-742..
- [26] Chuthamat Chiamsathit, Supunnika Auttamana , Surasak Thammarakcharoen, “Heavy metal pollution index for assessment of seasonal groundwater supply quality in hillside area, Kalasin, Thailand,” Applied Water Science, p. 10(142):8, 2020.
- [27] Adimalla, N., Wang, H., “Distribution, contamination, and health risk assessment of heavy metals in surface soils from northern Telangana, India,” Arabian Journal of Geosciences, p. 11(21), 2018.
- [28] Taiwo, A.M., Michael, J.O., Gbadebo, A.M., Oladoyinbo, F.O., “Spatial distribution, pollution index, receptor modelling and health risk assessment of metals in road dust from Lagos metropolis, Southwestern Nigeria,” Environmental Advances, 2019.
- [29] Freeze, R.A. and Cherry, J.A, Groundwater, 2. Edition, Ed., Cliff, NJ: Prentice Hall, Eaglewood, 1979, p. 604 pp.
- [30] Joanne M. Deely, Jack E. Fergusson, “Heavy metal and organic matter concentrations and distributions in dated sediments of a small estuary adjacent to a small urban area,” Science of The Total Environment, vol. 153, no. 1–2, pp. 97-111, 1994.
- [31] Edet, A.E. and Offiong, O.E., “Evaluation of Water Quality Pollution Indices for Heavy Metal Contamination Monitoring. A Study Case from Akpabuyo-Odukpani Area, Lower Cross River Basin (Southeastern Nigeria).,” Geomicrobiology Journal, vol. 57, pp. 295-304, 2002.
- [32] Sanjay S. Kale, Ajay K. Kadam, Suyash Kumar & N. J. Pawar, “Evaluating pollution potential of leachate from landfill site, from the Pune metropolitan city and its impact on shallow basaltic aquifers,” Environmental Monitoring

and Assessment, vol. 162, no. 1-4, p. 327–346, 2010.

[33] G Müller, G. MÜLLER, MÜLLER, Muller, G Müller, G. Putz, “Index of geoaccumulation in sediments of the Rhine River,” *Geojournal.*, vol. 2, pp. 108-118., 1969.

[34] Nguyễn Anh Tuấn, “Geological structure and potentiality of Pb-Zn pseudostratified ores in East Bắc Bộ,” *Journal of geology*, p. 320, 2010.

[35] Adebisi Adebayo, “Application of geochemical and geophysical approach to environmental impact assessment: a case study

of Emirin active open dumpsite, Ado-Ekiti Southwestern Nigeria,” *Modeling Earth Systems and Environment*, vol. 3 (2), pp. 615-633, 2017.

[36] Piper, A.M., “A graphic procedure in the geochemical interpretation of water-analyses,” *Eos, Transactions American Geophysical Union*, vol. 25, no. 6, pp. 914-928, 1944.

[37] Jelena Milivojević, Dragana Krstić , Biljana Šmit , Vera Djekić, “Assessment of Heavy Metal Contamination and Calculation of Its Pollution Index for Uglješnica River, Serbia,” *Bull Environ Contam Toxicol*, vol. 97, no. 5, pp. 737-742., 2016.

DOI: 10.15625/vap.2025.0195

Environmental protection and landscape restoration solutions in mineral exploitation at Loc An mine cluster, Phuoc Hai commune, Ho Chi Minh City

Au Nguyen Hai*, Thi Tuyet Nhi Pham, Hong Minh Vy Tat, Khanh Linh Luu

The Institute for Environment and Resources, 142 To Hien Thanh Street, Dien Hong District, Ho Chi Minh City, Vietnam

*Email: haiau@hcmier.edu.vn

Abstract: Mining activities, especially open-pit mining, have significant impacts on the landscape and environment, deforming topography and degrading ecosystems. The long-term mining of landfill materials in the Loc An mine cluster in Dat Do district, Ba Ria - Vung Tau province (old), now in Phuoc Hai commune, Ho Chi Minh City, has resulted in several environmental issues and an urgent need for rehabilitation and restoration. This study applies multivariate statistics and Multi-Criteria Analysis (MCA) to select the suitable landscape and environmental restoration and rehabilitation solutions for landfill material exploitation areas. At the same time, calculate the benefits and costs for each implementation option using the Cost-Benefit Analysis (CBA) method to select the optimal solution to conduct landscape restoration at the mining area. Three solutions are proposed: (i) developing aquaculture, (ii) constructing an ecotourism resort, and (iii) forming a recreational fishing area. The results show that ecotourism has the highest socio-economic and environmental efficiency while contributing to the improvement of people's lives, the effective use of land, and the aiming for circular economy goals. This research highlights the importance of incorporating scientific methods in assisting the government and stakeholders in prioritizing sustainable land use following extraction.

Keywords mineral exploitation, landfill material, environmental restoration plans, Multi Criteria Analysis (MCA), Cost-Benefit Analysis (CBA).

INTRODUCTION

Mineral exploitation operations in Vietnam are one of the industries that have been playing an important role in socio-economic development, contributing significantly to the national GDP. However, open-pit mining has a number of severe environmental effects, such as terrain deformation, loss of vegetation, groundwater depletion, air pollution, and long-term landscape changes (Bradshaw, 1997). Therefore, in recent years, environmental remediation, restoration, and post-exploitation mine closure have become legal duties through the environmental restoration deposit system. This is seen as an important part of the sustainable development of the mining industry. However, the proposed solutions are still local, lack overall planning, and have not been fully evaluated in terms of costs and benefits.

Mine rehabilitation has taken different approaches across the world, from ecological restoration to landscape reconstruction. Typical examples include re-establishing vegetation to reduce erosion, restore ecological function, and minimize environmental impacts, such as in the United States (Zipper et al., 2011), Australia (Cooke et al., 2002), and Canada (Young, 2000; Audet et al., 2015). Furthermore, several nations, like Germany (Tischew et al., 2007) and the Iberian Peninsula (Sánchez Donoso et al., 2024), recreate artificial landscapes following the closure of open-pit mining, turning mine pits into reservoirs, ecotourism areas, or conservation areas. This

approach not only restores the environment but also creates new socio-economic value for the local community. In Vietnam, several mines after exploitation have been renovated into ecotourism areas or reservoirs, such as the Buu Long tourist area (Thuc et al., 2021). However, the selection of the optimal solution is often not based on comprehensive quantitative analysis. The combination of multivariate statistics, multi-criteria analysis (MCA), and cost-benefit analysis (CBA) can provide a scientific decision-making framework that balances all three aspects: environment, economy, and society, increasing the reliability and comprehensiveness of the assessment (Dong et al., 2024). Studies around the world show that the CBA method has been widely used in the field of post-exploitation environmental restoration as an effective tool to support decision-making and evaluate the socio-economic efficiency of restoration options, such as in the United States (Mishra et al., 2012) and Germany (Von Döhren et al., 2023).

The Loc An mine cluster in Dat Do district, Ba Ria - Vung Tau province (old), now in Phuoc Hai commune, Ho Chi Minh City, is a typical example of exploiting landfill materials (soil, sand) for construction. Mining activities have provided jobs and contributed significantly to the economic growth of the region. However, mining activities have a negative impact on the ecosystem, pollute the soil, water, and air, affect the health of communities near mines and along transportation routes, and especially change land use value if the environment is not rehabilitated and restored after mining. Mineral exploitation is a form of temporary land use. When the mine cluster approaches the end stage, selecting an appropriate plan for post-mining land use and landscape restoration becomes critical to ensure maximum mineral recovery, taking socio-economic efficiency and

environmental protection as basic standards towards sustainable development.

This study aims to apply multivariate statistics and cost-benefit analysis to analyze and select the most suitable landscape improvement and restoration option for the Loc An mining cluster. Contribute a scientific and practical basis in management, and support local governments in planning land use after extraction for sustainability.

STUDY AREA

The Loc An mine cluster is located in Dat Do district, Ba Ria - Vung Tau province (old), now in Phuoc Hai commune, Ho Chi Minh City. The mine is located about 11 km southwest of Ba Ria and about 30 km south of Vung Tau. The mine area is 53.2 hectares including 09 adjacent mines that have finished exploitation (Fig. 1). The local's Melaleuca plantation area is bordered on the east and west; the north borders the Loc An-Lang Dai intercommunity route; and the south borders the commune's shrimp farming planning area.

The mining area has a coastal plain terrain, quite flat, with elevation varying from cote +1 m to cote +5 m. After the end of mining, the mine has a negative terrain relative to the surrounding topography; the bottom of the mine stops at cote -3.5 m. The mine has been renovated to level the mine bottom relatively flat, pit slope stabilization, and planting trees around mine pits. The terrain has formed water reservoirs ranging in depths from 1.5 to 5.5 m. Most mines have one to two floors with a slope of 28 - 34°. After exploitation, the mine cluster has deformed the terrain and landscape of the area, leaving deep holes and areas at risk of landslides, occupying a large portion of cultivated and green areas to open the mine and dump waste rock and soil, polluting water sources and land around the mine, and changing the cultural and social environment.

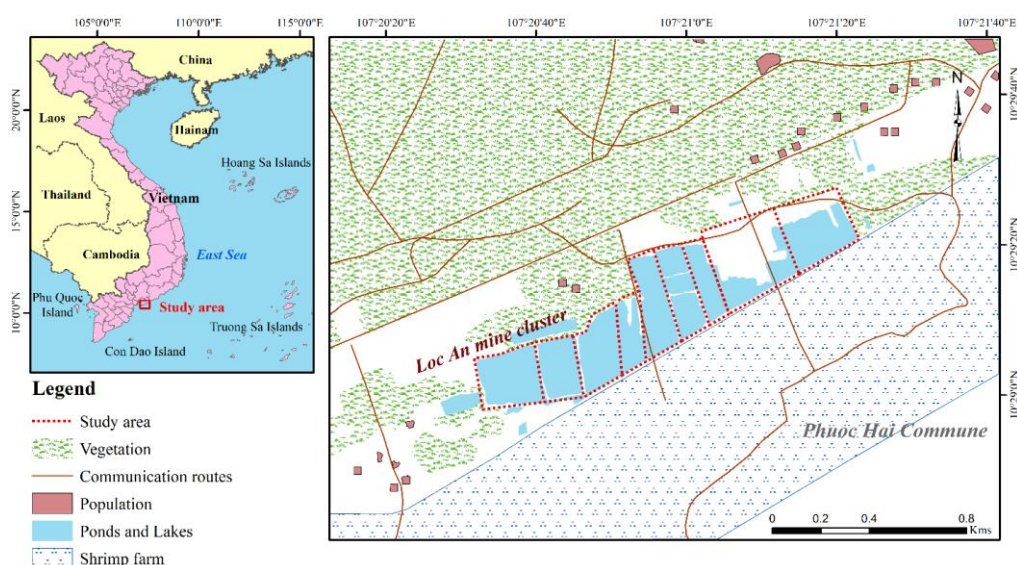


Figure 1. Location of the study area in Ho Chi Minh City

METHODS

Multi Criteria Analysis – MCA

Multi-criteria analysis is a technique of combining different criteria to produce a final result, providing the decision maker with different levels of importance of different criteria, also known as the weights of the relevant criteria.

In a multi-criteria decision-making problem, the first important step is to determine the collection of options as well as the criteria for evaluating them. Then, quantify the criteria by determining the relative importance of the options corresponding to each criterion.

The MCA method uses a system of weights and scores on a scale of 1–5 for each criterion; then calculates a weighted composite score (Weighted Score = Weight × Score) to determine the priority level of each option.

Cost-Benefit Analysis – CBA

According to Campbell (Campbell & Brown, 2005), the processes to develop CBA include:

- Identify the problem;
- Identify options;

- Identify the benefits and costs of the project;

- Quantify the costs and benefits of the project;

- Calculate the net present value (NPV) and other indicators of the project;

- Analyze risks, analyze the sensitivity of the project, and test assumptions;

- Make recommendations.

Evaluation criteria in CBA

Net present value – NPV

$$NPV = \sum_{t=1}^n \frac{B_t}{(1+r)^t} - \left[C_0 + \sum_{i=1}^n \frac{C_t}{(1+r)^t} \right] \quad (1)$$

where, B_t : Project benefits in year t ; C_t : Costs incurred in year t ; r : Discount rate; n : Number of years to implement the project;

If $NPV < 0$, the project is ineffective and should not be funded;

If $NPV = 0$, the project can be funded; based on the unique scenario and requirement of the project, the company can decide whether to cancel or accept it;

If the net present value $NPV > 0$, the investment project is effective.

Internal Rate of Return – IRR

This is the discount rate at which the net present value of the project is 0. This indicator represents the maximum discount rate (interest rate) that the project can choose to still be able to cover all costs.

$$NPV = \sum_{t=0}^n \frac{B_t - C_t}{(1 + IRR)^t} \quad (2)$$

In practice, IRR is calculated through interpolation, which is the method of determining an approximate value between two selected values.

$$IRR = r_1 + \frac{NPV_1}{NPV_1 - NPV_2} (r_2 - r_1) \quad (3)$$

Where, r_1 : Smaller discount rate (r_1 makes $NPV_1 > 0$); r_2 : Lower discount rate (r_2 làm cho $NPV_2 < 0$); NPV_1 : Net present value is positive but close to 0, calculated by r_1 ; NPV_2 : Net present value is negative but close to 0, calculated by r_2 .

Benefit Cost Ratio – BCR

It is the ratio of the total present value of benefits to the total present value of costs. This ratio compares discounted benefits and costs and can be understood as how many benefits are obtained for each dollar of cost.

The present value of the benefit stream > The present value of the cost stream, so this BCR ratio > 1; those are beneficial projects and worth doing. The option with the highest BCR is the most worth choosing.

Principles and criteria for selecting environmental restoration options for the Loc An mine cluster

After surveying the study area and the surrounding landscape, aspects such as natural conditions, population, economy, society, topography, geology, hydrometeorology, and regional ecosystem were used as a basis for developing applicable environmental restoration plans. The Loc An mine cluster's environmental rehabilitation aims to minimize

negative impacts on the environment and optimize the use of post-exploitation areas after the end of exploitation. This creates favorable conditions for ecosystem reorganization and restoration. The rational land use plan for post-exploitation areas is a model that highlights the tight link between the land use form and the characteristics of the mining area, environmental issues, and the highest economic efficiency that the land use form provides. The land use form will provide benefits to the community by ensuring environmental safety, sustainable development, and low maintenance costs, as well as being appropriate for current and future use. Therefore, a reasonable environmental restoration plan is suitable for the requirements of land use at the post-mining site when it meets the following principles: (1) Suitable for the natural characteristics of the mined area; (2) Suitable for the socio-economic characteristics of the region; (3) Ensuring environmental safety; (4) Highest economic efficiency for the community, investors, and localities. The principles include 22 characteristics that reflect decisiveness and mutual assistance to ensure the aim of the environmental restoration solution.

RESULTS

Analyze and select options

According to the specific conditions of the Loc An mine cluster, the following environmental restoration options can be proposed:

- Option 1: Improve and restore the environment of the mine area for aquaculture purposes. This option takes advantage of the terrain and natural conditions after mining; the bottom of the mine is sand and clay, suitable for shrimp farming with the ability to store and retain water in the lake. Open the adjacent mines to form a pond system including settling ponds, waste treatment ponds, and major ponds; construct canals to transport water from the Ray River (saltwater) and the upper Ba Dap River (freshwater), as well as dikes and trees to prevent erosion and leaking. The option aims

for a sustainable shrimp farming model, suitable for local conditions, reducing risks and improving the efficiency of post-mining land exploitation.

- Option 2: Renovating and rehabilitating the environment of the mine area for the purpose of becoming an eco-tourism resort with entertainment complexes and artificial swimming pools. This plan connects adjacent mines; most of the area is reserved for infrastructure with four functional areas, thoroughly renovating the lake, and trees are also recreated around the shore. The plan aims to create a diverse ecological-entertainment-resort space, promoting the effective use of land after mining in a sustainable direction.

- Option 3: Renovating and restoring the mining area environment into a recreational fishing area with a system of 3 fish ponds combined with a floating restaurant area. This plan connects adjacent mines, the pit slopes are reinforced into lake shores, and builds traffic lanes around the lake. The landscape of the area is enhanced with trees, cliffs, and small islands in the middle of the lake, creating a harmonious, attractive, and sustainable recreational-ecological tourism space.

To be able to choose a suitable environmental restoration plan for the mine cluster, it is necessary to analyze and evaluate the correlation between the criteria and the proposed plans to choose the most reasonable plan.

Costs and benefits of implementation

The treatment and restoration of the landscape at the Loc An landfill cluster is expected to begin in 2026, assuming a 10-year implementation period and a constant discount rate. The discount rate takes into account the inflation rate, with the formula $r = [(i-m)/(i+m)] \times 100\%$. Where, i : Discount rate; m : Inflation rate. Currently, the discount rate is calculated using the lending interest rate of the State Bank of Vietnam at 6%. According to the report from the General Statistics Office, Vietnam's core inflation rate in January 2023 increased by 5.21% over the same period last

year (higher than the consumer price index increase of 4.89%), which is the highest increase in the past 10 years. Therefore, the discount rate is $r = 0.75$.

Capital expenditure include earthworks, slope stabilization, infrastructure, and landscape restoration, estimated based on the 2024 regional construction price index for Ba Ria-Vung Tau province. Operational expenses include annual maintenance, personnel, electricity, and water supply for each restoration option. Revenues are estimated from aquaculture productivity (Option 1) and expected visitor numbers and service fees for ecotourism and recreational fishing (Options 2 and 3), using socioeconomic data and similar projects in Phuoc Hai commune. Demand projections are based on provincial tourist and aquaculture statistics for 2023-2024, with an average annual growth rate of 3-5%. These inputs form the basis for calculating the Net Present Value (NPV), Internal Rate of Return (IRR), and Benefit-Cost Ratio (BCR) of each option are evaluated as follows:

Internal Rate of Return (IRR)

Option 1: The total implementation cost is 80,814,001,758 VND (excluding tax), and estimated implementation time is 4 years. The NPV of the project after being calculated gives a positive value of 91,699,250,704 VND > 0. The IRR of the option is 3.597%, meaning that when NPV is 0, this option brings a profit rate of at least 3.597%.

Option 2: The total implementation cost is 78,647,091,869 VND (excluding tax), and the estimated implementation time is 3 years. The NPV of the project after being calculated gives a positive value of 98,106,290,241 VND > 0. The IRR of the option is 5.63%, which means that when the NPV is 0, this option can still bring a profit rate of at least 5.63%.

Option 3: The total implementation cost is 78,601,090,521 VND (excluding tax), and the estimated implementation time is 2 years. The NPV of the project after being calculated gives a positive value of 94,949,323,767 VND > 0. The IRR of the option is 5.35%, which means that

when the NPV is 0, this option can still bring a profit rate of at least 5.35%.

The results show that the IRR of all 3 options is greater than $r = 0.75\%$, showing that these options are all feasible (Table 2). However, with the net present value (NPV) of option 2 > option 3 > option 1, and the IRR of option 2 being the highest (5.63%). It shows that option 2, “Renovating and rehabilitating the environment of the mining area for the purpose of becoming an eco-tourism resort” is the most optimal approach.

Benefit-Cost Ratio (BCR)

The benefit-cost ratio (BCR) values for the three solutions are 1.1346, 1.247, and 1.208, respectively (Table 2). All are greater than 1 and provide benefits when implemented. After calculating each NPV, BCR, and IRR index for each option, the results show that option 2 is the most optimal to implement in terms of benefit-cost ratio value.

Sensitivity analysis was conducted to examine variations in the cost (+10%) and benefit (-10%) scenarios. The Internal Rate of Return (IRR) of Option 2 decreased from 5.63% to 4.8% in the worst-case scenario, but it remains greater than the discount rate, confirming the robustness of the project. Key risks include uncertainty in ecotourism demand and cost escalation during site preparation.

Multi Criteria Analysis (MCA) results

Multi-criteria analysis (MCA) was used to analyze three restoration options: (i) aquaculture, (ii) ecotourism, and (iii) recreational fishing area, not only based on economic efficiency through cost-benefit analysis (CBA) but also comprehensively considering environmental, social, and technical aspects. The MCA results allow the integration of quantitative and qualitative factors, providing a scientific basis for selecting the optimal restoration option, ensuring economic, ecological, and social sustainability.

Table 1. MCA results

Evaluation criteria	Weight (W_i)	Rating (S_i)			Conversion points ($W_i \times S_i$)		
		Option 1	Option 2	Option 3	Option 1	Option 2	Option 3
Socio-economic efficiency	0.30	3	5	4	0.90	1.50	1.20
Environmental efficiency	0.25	4	5	4	1.00	1.25	1.00
Technical feasibility	0.20	5	4	4	1.00	0.80	0.80
Job creation and community engagement	0.15	3	5	4	0.45	0.75	0.60
Landscape & aesthetic impact	0.10	3	5	4	0.30	0.50	0.40
Total	1.00				3.65	4.80	4.00

The results of the multi-criteria analysis (Table 1) show that Option 2 achieved the highest score (4.80/5), demonstrating the balance between socio-economic efficiency, environmental sustainability, and technical implementation capability. Therefore, this option is chosen as the optimal option for landscape and environmental restoration of Loc An mining area.

Orientation for renovation and restoration of mining cluster

Through analysis and evaluation of criteria showing the characteristics of the mine cluster,

resource characteristics, regional socio-economics, and costs and benefits, the solution to restore the environment of the Loc A mine cluster is to renovate the post-mining site into an ecotourism area (Fig. 2).

Description:

Connecting the adjacent mines while retaining the Southeast mine, reinforcing pit margins and leveling the bottom of the mine, constructing a traffic path for the entire mine cluster, and planting additional trees along the margins. Then the mine cluster is divided into

four regions (from the Southwest to the Northeast).

- Zone 1

The entrance will be built in the southwest, near the Lang Dai traffic road. On the planned land for the project, there is an empty land area with few trees, so the surface will be leveled and a tourist reception area combined with a restaurant area will be developed, and around the empty land will be planted Japanese velvet grass. Build ancillary facilities (parking lot, ticket office, etc.).

On the lakeside, build a circular bridge combined with boat docks to moor boats for tourists who want to participate in kayaking sports.

The newly cleared land forms a small island in the center of the lake, which is used to build traditional games and resting cottages. Design the space to suit the type of water entertainment games.

- Zone 2

Divide the terrain into 2 parts; the North will create a swimming pool, and the South will be a lake for tourists to row boats. Separating the 2 parts will create a walkway to the entertainment area (area 3); along the path, several small cabins will be built on the lake.

- Zone 3

The Southeast mine area is currently vacant land; level the ground and build a children's playground (water games, traditional and modern games: water slides, mini golf course, sand sliding...).

Build a dining and resort area in the area.

Plant trees and flowers along the road going to the aforementioned location.

- Zone 4

Building floating tents on buoys to form an arc; the distance between tents is arranged by rafts to move from one tent to another.

Design the area suitable for water recreation games.

CONCLUSION

The study applied multivariate statistics and cost-benefit analysis to select suitable landscape and environmental remediation and restoration options for the Loc An landfill mining cluster in Phuoc Hai commune, Ho Chi Minh City, to ensure consistency, rational exploitation of natural resources, and effective use of post-mining land. From there, the optimal solution was determined to be to renovate and restore the landscape at the mine into an ecotourism area, reducing environmental pollution, improving the ecosystem and environment, and contributing to the creation of jobs for locals in order to promote sustainable socio-economic development.

This result is consistent with the objectives of Decree No. 08/2022/ND-CP (Ministry of Natural Resources and Environment, 2022) and the National Strategy on Circular Economy (Decision No. 687/QD-TTg, 2022 (Prime Minister of Vietnam, 2022)), which emphasize sustainable land reuse, post-mining recovery, and integrating ecological restoration into local development planning.

Table 2. Cost-benefit analysis of options

Years	Option 1			Option 2			Option 3		
	PV(C)	PV(B)	NPV= PV(B) – PV(C)	PV(C)	PV(B)	NPV= PV(B) – PV(C)	PV(C)	PV(B)	NPV= PV(B) – PV(C)
2026	28,534,871,356	10,455,432,761	-18,079,438,595	57,288,082,271	21,031,717,293	-36,256,364,978	57,288,082,270	21,031,717,292	-36,256,364,978
2027	30,368,561,171	10,628,996,410	-19,739,564,761	16,390,864,209	4,917,259,263	-11,473,604,947	21,313,008,251	6,393,902,475	-14,919,105,776
2028	16,850,421,150	5,055,126,345	-11,795,294,805	4,968,145,388	1,738,850,886	6,706,996,274		8,440,463,000	8,440,463,000
2029	5,060,148,081	1,771,051,828	-3,289,096,252		10,059,780,400	10,059,780,400		8,440,463,000	8,440,463,000
2030		10,631,440,560	10,631,440,560		10,059,780,400	10,059,780,400		8,440,463,000	8,440,463,000
2031		10,631,440,560	10,631,440,560		10,059,780,400	10,059,780,400		8,440,463,000	8,440,463,000

2032		10,631,440,560	10,631,440,560		10,059,780,400	10,059,780,400		8,440,463,000	8,440,463,000
2033		10,631,440,560	10,631,440,560		10,059,780,400	10,059,780,400		8,440,463,000	8,440,463,000
2034		10,631,440,560	10,631,440,560		10,059,780,400	10,059,780,400		8,440,463,000	8,440,463,000
2035		10,631,440,560	10,631,440,560		10,059,780,400	10,059,780,400		8,440,463,000	8,440,463,000
Total	80,814,001,758	91,699,250,704	10,885,248,946	78,647,091,869	98,106,290,241	29,395,489,149	78,601,090,521	94,949,323,767	16,348,233,246
IRR			3.597%			5.63%			5.35%
BCR			1.1346			1.247			1.208

PV(C): Present value of costs
PV(B): Present value of revenues
NPV: Net Present Value
IRR: Internal Rate of Return
BCR: Benefit-Cost Ratio

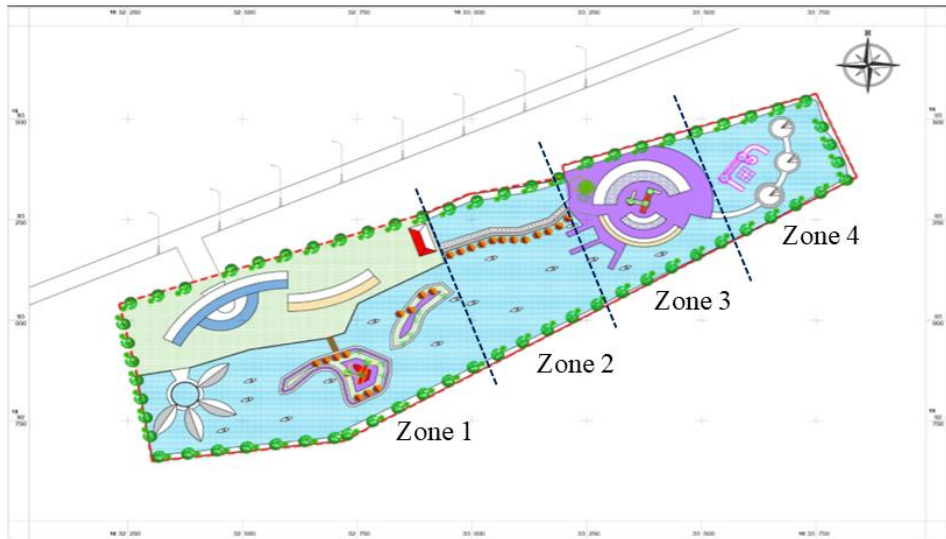


Figure 2. The project to transform into an ecotourism area

ACKNOWLEDGMENTS

This research is also funded by Vietnam National University Ho Chi Minh City (VNU-HCM) under grant number TX2025-24-01.

In addition to the authors listed above, the research team also includes the following contributing authors: Thien Nguyen Duc, Khai Vo Nguyen Quang, and Kien Nguyen Minh from The Institute for Environment and Resources.

REFERENCES

Audet, P., Pinno, B. D., & Thiffault, E. (2015). Reclamation of boreal forest after oil sands mining: anticipating novel challenges in novel environments. Canadian Journal of Forest Research. 45(3): 364-371.

Bradshaw, A. (1997). Restoration of mined lands—using natural processes. Ecological engineering. 8(4): 255-269.

Campbell, H. F., & Brown, R. P. (2005). A multiple account framework for cost–benefit analysis. Evaluation and Program Planning. 28(1): 23-32.

Cooke, J. A., & Johnson, M. S. (2002). Ecological restoration of land with particular reference to the mining of metals and industrial minerals: A review of theory and practice. Environmental Reviews. 10(1): 41-71.

Dong, Z., Bian, Z., Jin, W., Guo, X., Zhang, Y., Liu, X., ... & Guan, D. (2024). An integrated approach to prioritizing ecological restoration of abandoned mine lands based on cost-benefit analysis. Science of The Total Environment. 924: 171579.

- Ministry of Natural Resources and Environment (2022). Decree No. 08/2022/NĐ-CP guiding the Law on Environmental Protection.
- Mishra, S. K., Hitzhusen, F. J., Sohngen, B. L., & Guldmann, J. M. (2012). Costs of abandoned coal mine reclamation and associated recreation benefits in Ohio. *Journal of environmental management*. 100: 52-58.
- Prime Minister of Vietnam (2022). Decision No. 687/QĐ-TTg approving the National Strategy for Circular Economy.
- Sánchez Donoso, R., Martins, M., Tejedor Palomino, M., Esbrí Víctor, J. M., Lillo Ramos, F. J., Pereira, A. M., ... & Martín Duque, J. F. (2024). Geomorphic-based mine rehabilitation coupled with AMD chemical stabilisation in sulphide-rich ore deposits and soils: insights from a pioneering intervention at the Lousal mine, Iberian pyrite Belt. *International Journal of Mining, Reclamation and Environment*. 38(1): 79-97.
- Thuc, T. L. V., Thanh, T. D. V., & Tung, T. L. T. (2021). Environmental rehabilitation and restoration, mine closure after completion of mining in open-pit mines in the world and in Vietnam. *Mining Technology Bulletin*. 5: 13-21.
- Tischew, S., & Kirmer, A. (2007). Implementation of basic studies in the ecological restoration of surface-mined land. *Restoration Ecology*. 15(2): 321-325.
- Von Döhren, P., & Haase, D. (2023). Ecosystem services for planning post-mining landscapes using the DPSIR framework. *Land*. 12(5): 1077.
- Zipper, C. E., Burger, J. A., Skousen, J. G., Angel, P. N., Barton, C. D., Davis, V., & Franklin, J. A. (2011). Restoring forests and associated ecosystem services on Appalachian coal surface mines. *Environmental management*. 47(5): 751-765.
- Young, T. P. (2000). Restoration ecology and conservation biology. *Biological conservation*. 92(1): 73-83.

Urban Expansion Monitoring Using Sentinel-1 and Sentinel-2 Data Fusion on Google Earth Engine

Hung Nguyen Manh^{1,2,*}, Tuan Vu Anh¹, Toan Dao Duy³, Son Le Mai¹,
Giang Nguyen Cong¹, Hang Le Thi Thu¹

¹Vietnam National Space Center, Vietnam Academy of Science and Technology, Hanoi, Vietnam

²Graduate University of Science and Technology, Vietnam Academy of Science and Technology, Hanoi, Vietnam

³Faculty of Bridge and Road, Hanoi University of Civil Engineering, Hanoi, Vietnam

*Email: nmhung@vnsc.org.vn

Abstract: Monitoring urban expansion is crucial for urban planning, resource management, and environmental impact assessment, especially under rapid population growth and urbanization. Mapping land use in heterogeneous environments still faces numerous challenges, including limitations in collecting and maintaining diverse, reliable training data for machine learning and deep learning methods, which hinders the widespread application for large-scale built-up area mapping. This study introduces a framework for monitoring urban expansion by fusing Sentinel-1 and Sentinel-2 data on the Google Earth Engine (GEE) platform, leveraging its capabilities for large-scale geospatial data processing and analysis. By combining the cloud-penetrating ability of Sentinel-1 with the high optical resolution of Sentinel-2, the method provides an effective approach for Earth surface classification, including urban areas, and tracking their dynamics in time. GEE is used to process large datasets, generate classification maps, and analyze urban expansion trends with high accuracy, improving overall accuracy from 88% (Sentinel-2 only) to 92% (combined sources). The results can support urban planners and resource managers in making more sustainable decisions, and highlight GEE as a powerful cloud-based tool for satellite data processing.

Keywords Urban expansion, Fusion, Sentinel imagery, GEE.

INTRODUCTION

Effective urban planning and management rely on accurate land use/land cover (LULC) mapping (Zhang et al., 2020). The integration of remote sensing data with machine learning algorithms has become a critical approach to achieve this goal. Accurate LULC data serves as a valuable tool for numerous applications, including urban planning and environmental monitoring.

Multi-spectral Instrument (MSI) data from the Sentinel-2 satellite has been widely applied across various scientific domains. In particular, Sentinel-2 MSI data has demonstrated significant value in urban land cover mapping. However, a major challenge arises when classifying dark impervious surfaces and water bodies, as their visual distinctions are often ambiguous (Clerici et al., 2017; Bui et al., 2020). Consequently, accurate classification relying solely on Sentinel-2 MSI data becomes difficult, as dark impervious surfaces may be misidentified as water, leading to confusion in the resulting urban LULC map.

In Vietnam, several studies have been conducted on urban land-use change and monitoring using remote sensing and GIS (Saksena, Fox et al. 2014, Phuong and Quang 2021). These studies mainly utilized Landsat or Sentinel-2 imagery to assess urban expansion and its environmental implications. However, most existing research has focused solely on optical data, which is often constrained by cloud contamination and atmospheric effects

in tropical regions like Hanoi. In recent years, some studies have begun to examine the combined use of radar and optical imagery for land cover classification and monitoring over Vietnamese territories, including urban and peri-urban areas (Bui et al., 2020; Hoang et al., 2020; JAXA, 2021; Bao et al., 2022; Bui and Mucsi, 2022; Thanh et al., 2025). Nevertheless, many of these efforts concentrate on forest ecosystems, regional or national-scale mapping, or a single reference year, and comprehensive multi-temporal urban LULC mapping in major cities such as Hanoi using Sentinel-1 and Sentinel-2 data fusion remains limited and requires further development.

Synthetic Aperture Radar (SAR) imagery from Sentinel-1 has been extensively used in multiple applications, including land cover mapping. Notably, Sentinel-1 SAR data serves as a reliable alternative when Sentinel-2 MSI image quality is compromised by cloud cover or fog, owing to its all-weather, day-and-night imaging capability (Clerici et al., 2017). Generating timely land cover maps using Sentinel-1 SAR imagery is particularly valuable for effective urban management. Nevertheless, producing accurate land cover classifications from Sentinel-1 SAR data remains challenging due to the complex material distribution in urban areas.

To address these challenges and improve classification outcomes, researchers have explored combining Sentinel-2 MSI and Sentinel-1 SAR data. Numerous studies have shown that integrating SAR with optical data can significantly enhance land cover classification performance. This combined approach has proven effective in classifying vegetation types, estimating mangrove biomass, and mapping burned areas, and improving urban land cover mapping in different regions, including Vietnam (Hoang et al., 2020; Bao et al., 2022; Bui and Mucsi, 2022; Thanh et al., 2025). By leveraging the complementary strengths of both sensor types, the fusion of Sentinel-2 MSI and Sentinel-1 SAR data yields deeper insights and more robust results (Steinhausen et al., 2018).

In recent years, Google Earth Engine (GEE) has emerged as a powerful platform offering image processing, data fusion, classification, and interactive visualization capabilities for Sentinel-2 MSI and Sentinel-1 SAR data (Gorelick et al., 2017). GEE's cloud-based architecture simplifies access to and processing of large datasets, making it an essential resource for the remote sensing community and enabling efficient implementation of multi-temporal, multi-sensor LULC mapping workflows.

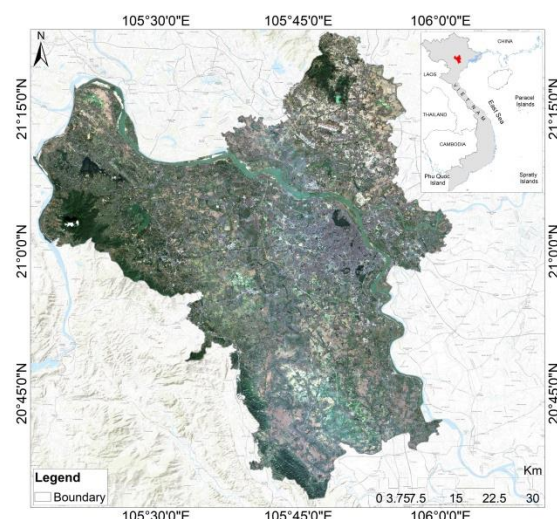


Figure 1. Location of the study area

This study aims to explore and demonstrate the potential benefits of integrating Sentinel-1 SAR and Sentinel-2 MSI imagery for accurate urban land cover classification in the specific context of Hanoi. The research focuses on mapping the urban LULC of Hanoi from 2019 – 2025 to evaluate the effectiveness of this data fusion approach in improving local-scale land cover classification compared with optical-only methods. The results provide valuable insights into the capabilities of combining SAR and optical imagery through machine learning models, thereby overcoming the limitations of traditional optical-based classification methods. Moreover, the findings lay a foundation for future work on multi-temporal monitoring of urban expansion, which can

support sustainable urban planning and management in Hanoi and other cities.

STUDY AREA AND METHODOLOGY

Study area

Hanoi is the national political, economic, and cultural center, and one of Vietnam, and has been among the fastest-urbanizing cities in the country over the past two decades (see Figure 1) (WorldBank, 2020). Administratively, Hanoi covers an area of about 3,360 km² in the Red River Delta region, ranking among the largest capital cities in Southeast Asia by land area. According to the 2024 Midterm Population and Housing Census, the city has a population of roughly 8.7 million residents, making it the second most populous city in Vietnam after Ho Chi Minh City (<https://danso.info/en/dan-so-ha-noi/>). The urban area of Hanoi has continuously expanded into peripheral districts such as Ha Dong, Hoang Mai, Long Bien, Gia Lam, Dong Anh, and Soc Son, accompanied by the rapid development of industrial zones, new urban areas, and transportation infrastructure (Mauro, 2020). This expansion process has significantly altered land-use structures and natural landscapes, while exerting substantial pressure on land and water resources as well as on the urban living environment (Phuong and Quang, 2021). Therefore, evaluating, monitoring, and quantifying Hanoi's urban expansion using remote sensing is essential to support sustainable development planning and effective resource management (Saksena et al., 2014).

Satellite data

This study utilized data from two advanced satellites of the Copernicus Programme to perform land cover classification (Corban et al., 2019). Specifically, Multi-spectral Instrument (MSI) optical data from Sentinel-2 and Synthetic Aperture Radar (SAR) data from Sentinel-1A were acquired for the same study year (Table 1). For the Sentinel-2 MSI data, spectral bands with 10 m spatial resolution covering the visible and near-infrared wavelengths were selected for classification. These optical data were pre-

processed on the GEE platform, including radiometric calibration and atmospheric correction (Gorelick et al., 2017).

Regarding Sentinel-1A SAR radar data, the study employed the Interferometric Wide Swath (IW) acquisition mode, which provides a ground-range resolution of approximately 5 m in range and 20 m in azimuth. This C-band SAR data, capable of acquiring imagery under all weather conditions (day and night), was pre-processed in GEE through radiometric calibration, backscatter normalization, and terrain correction (Filipponi, 2019). The entire workflow from data processing and classification to accuracy assessment and the fusion of complementary information from Sentinel-2 MSI and Sentinel-1A SAR can be implemented on the cloud-based GEE platform (Dagne et al., 2023). This multi-source data integration strategy forms the core of the study's approach to optimizing information extraction and enhancing the accuracy of urban land cover classification. Additionally, PlanetScope imagery acquired in the same year with a 3 m spatial resolution was incorporated as a high-resolution reference dataset (Houborg and McCabe, 2016); full data specifications are detailed in Table 1.

Table 1. Description of usage data

No	Sensor	Date of acquisition	Characteristics			
			Spatial resolution (m)	Band	Polarization	Orbit
1	Sentinel-1	18/5/2019 22/01/2025	5x20	C	VV/HH	Descending
2	Sentinel-2	19/05/2019 12/01/2025	10			
3	PlanetScope	12/01/2025 28/06/2019	3			

Method of data analysis

Sentinel-2 MSI and sentinel-1 SAR image processing in GEE platform

The processing workflow for Sentinel-2 MSI and Sentinel-1 SAR imagery on the GEE platform (Figure 2) consists of several key steps (Gorelick et al., 2017). First, satellite images covering the study area are retrieved from the GEE data catalog. Sentinel-2 images then undergo atmospheric correction and cloud

masking (cloud coverage < 10%), while Sentinel-1 images are pre-processed with radiometric calibration, backscatter normalization, and terrain correction (Zhao et al., 2021). All images are subsequently reprojected to a common coordinate system, and spectral bands from Sentinel-2 together with backscatter metrics from Sentinel-1 are combined to form a unified feature set for land cover classification and change analysis (Mahdianpari et al., 2021).

In this study, the Random Forest (RF) classifier was selected due to its robustness, high accuracy, and ability to handle non-linear, multi-dimensional data from both optical and radar sources (Breiman, 2001). Compared with algorithms such as Support Vector Machine or Neural Networks, RF requires fewer parameter settings, is less prone to overfitting, and performs reliably over heterogeneous urban land cover types. Its ensemble-based structure ensures stable performance even in areas with highly heterogeneous urban land cover. Moreover, RF is natively implemented and optimized in Google Earth Engine through the `ee.Classifier.randomForest()` function, which builds an ensemble of decision trees and applies the trained model to image collections via the `classify(.)` method (Zhao et al., 2021). Based on the native implementation and GEE's cloud-based computation, RF-based workflows can be scaled and reproduced efficiently for large-area environmental and urban monitoring applications (Clerici et al., 2017).

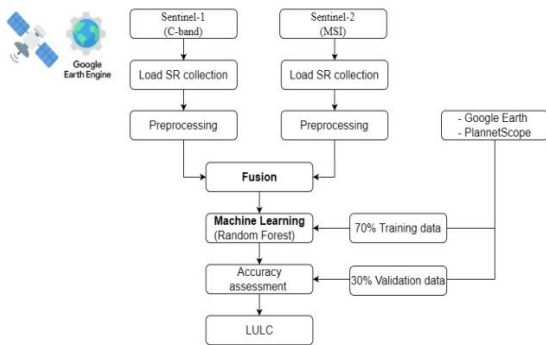


Figure 2. Methodological flowchart

Classification algorithms

The Random Forest algorithm operates based on the principle of ensemble learning by combining multiple decision trees to enhance the model's accuracy and generalization capability (Breiman, 2001; Hastie et al., 2009). The process consists of three main stages.

First, RF constructs a collection of independent decision trees using the bootstrapping technique, which involves random sampling with replacement from the original training dataset to generate multiple bootstrapped subsets. Each tree in the forest is then trained individually on its corresponding subset.

Second, to minimize overfitting and increase diversity among the trees, at each splitting node of every tree, the algorithm considers only a random subset of features rather than the entire input feature set. This approach reduces correlation between trees while improving the stability and generalizability of the model.

Finally, RF aggregates the predictions from all trees to produce the final output: for classification tasks, the result is determined by majority voting; for regression tasks, it is computed as the average of the predicted values from the individual trees.

The original training dataset S consists of N samples, represented as:

$$S = \{(x_k, y_k)\}_{k=1}^N \quad (1)$$

Where:

x_k is the feature vector of the k^{th} sample, and y_k is the corresponding class label (or regression value).

The bootstrapping process creates a bootstrap dataset D for each decision tree, where D is a random subset of S (typically of size N , allowing duplicate samples). The bootstrap dataset D is described as:

$$D = \{(x_i, y_i)\}_{i=1}^n \quad (2)$$

Where:

D : the bootstrapped dataset sampled with replacement.

n : the number of samples in D (usually equal to N , the size of the original dataset).

x_i : the feature vector with M feature values for the i^{th} sample, $x_i \in R^M$.

y_i : the corresponding class label (for classification) or output value (for regression) for the i^{th} sample.

This process is repeated T times (where T is the number of trees in the forest) to generate the ensemble of decision trees $\{h_1(x), h_2(x), \dots, h_T(x)\}$, thereby forming the RF ensemble model. The computational workflow of the Random Forest algorithm can be referred to in the schematic diagrams provided by Horning (Horning, 2010).

Accuracy assessments

The accuracy assessment of the classification results should be evaluated by comparing the classified land cover map with ground truth data (Congalton & Green, 2019). In this work, the training and validation dataset comprised 300 points and 58 ground control regions (GCPs) collected using high-resolution PlanetScope imagery and referenced in Google Earth pro to support classification and validation. The GCPs were evenly distributed across five LULC classes: Built-up (BU), Forest (F), Bare soil (BS), Water body (W), and Agriculture (A). Among these samples, 70% (210 points and 40 regions) were used for training and 30% (90 points and 18 regions) for validation to reduce bias in the accuracy assessment (Figure 2) (Congalton and Green, 2019). On the GEE platform, validation points were imported and their reference labels were compared with the modelled land cover classes at the corresponding locations (Gorelick et al., 2017).

To quantify classification quality, three primary metrics were employed: Overall Accuracy (OA), Kappa Coefficient (K), and F1-score (Talukdar et al., 2020).

OA is the percentage of correctly classified samples:

$$OA = \frac{TP+TN}{TP+TN+FP+FN} \times 100 \quad (3)$$

Where:

TP (True Positive) = correct affirmative, TN (True Negative) = correct negative, FP (False Positive) = incorrect affirmative, FN (False Negative) = incorrect negative.

Kappa Coefficient (K), also known as Cohen's Kappa, measures the agreement between the classification and reference data after accounting for chance:

$$K = \frac{P_o - P_e}{1 - P_e} \quad (4)$$

Where:

P_o and P_e are the observed agreement proportion and the expected chance agreement, respectively.

F1-score is the harmonic mean of Precision and Recall, reflecting the balance between predictive accuracy and completeness.

$$F_1 = 2 \times \frac{\text{Precision} \times \text{Recall}}{\text{Precision} + \text{Recall}} \quad (5)$$

where Precision is the ratio of correct positive predictions to total positive predictions, and Recall is the ratio of correct positive predictions to total actual positives.

In addition, two supplementary metrics are commonly used: Producer's Accuracy (PA) – measures the proportion of pixels in each class correctly classified relative to ground truth, while User's Accuracy (UA) – reflects the reliability of each class in the classification map. Overall, this workflow and these metrics enable an objective, comprehensive, and quantitative evaluation of the remote sensing classification model's accuracy, ensuring high-reliability results suitable for research and practical applications.

RESULTS AND DISCUSSION

Spectral and Backscattering Characteristics of Land Cover Classes:

The analysis of the spectral reflectance characteristics derived from Sentinel-2 MSI data and the backscattering properties from Sentinel-1 SAR data reveals distinct differences among the various land cover (LC) classes

(Figure 3-5). In the Sentinel-2 MSI multispectral images, the Forest class exhibits high reflectance values in the near-infrared (NIR, range 800–900 nm), reflecting dense canopy cover and strong photosynthetic activity. Built-up areas and Bare soil show increased reflectance in both the Visible bands (range 450–650 nm) and the NIR bands (range 800–900 nm), due to the strong reflective properties of artificial materials and dry exposed soil. The Water body class maintains consistently low reflectance across the entire spectrum, attributed to water's high absorption capacity. Agriculture areas display intermediate reflectance values in these ranges, reflecting the influence of vegetation growth stage and crop coverage density.

The LULC map derived from Sentinel-1 SAR and the RF classifier (Figure 3) shows that Forest (green) and Agriculture (light green) dominate most of the province, while Built-up areas (red) are concentrated around the central urban core and along major rivers and transport corridors. Water bodies (blue) clearly delineate the river network and reservoirs, and Bare soil (grey) appears only in small, scattered patches, likely linked to construction or recently cultivated fields. These spatial patterns align with the backscattering coefficients (σ^0): Built-up and Bare soil exhibit high σ^0 , Water has the lowest values, and Forest and Agriculture show intermediate levels. Overall, the distinct spatial and backscattering signatures demonstrate that RF classification using Sentinel-1 SAR effectively separates major land cover types and underscores the complementary value of combining radar and optical data for LULC mapping.

Figure 4 shows the LULC map derived from Sentinel-2. It can be seen that Agriculture (light yellow) is the dominant class, covering most of the central and southern parts of the area. Built-up land (red) is highly concentrated around the main urban core and extends along the river corridor, highlighting a strong urbanization pattern. Forest (green) is mainly distributed in the western and northern upland zones, corresponding to hilly or mountainous

terrain. Water bodies (blue) clearly trace the main river and associated lakes or reservoirs. Bare soil (grey) occurs as small, scattered patches within agricultural and built-up areas, likely representing construction sites or recently ploughed fields.

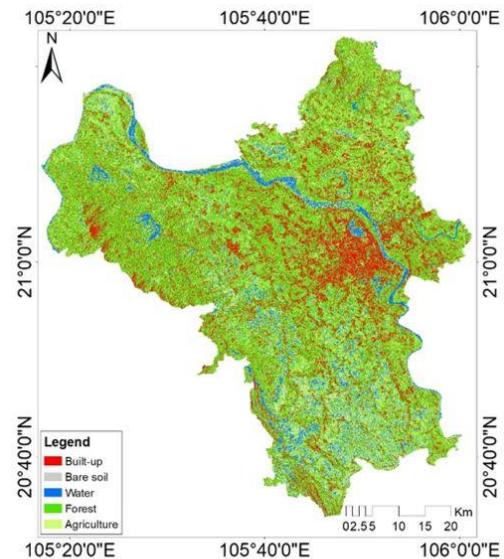


Figure 3. LULC classification from Sentinel-1 SAR using RF algorithm

Figure 3. LULC classification from Sentinel-1 SAR using RF algorithm

Performance of the RF Algorithm on Individual Datasets:

The RF algorithm was applied independently to the Sentinel-2 MSI and Sentinel-1 SAR datasets to evaluate the classification capability of each individual source. For the Sentinel-2 MSI data, the RF algorithm achieved an OA of 0.88 and a Kappa coefficient of 0.87, with consistently high F1-scores across all classes (0.78–0.92), confirming the suitability of optical data for LULC classification (Table 2). In contrast, when applied to the Sentinel-1 SAR data, performance decreased significantly, with OA = 0.58 and Kappa = 0.47; the F1-scores reveal particularly poor discrimination for Bare soil (0.30) and moderate accuracy for Forest and Agriculture, although Water remains relatively well classified ($F_1 = 0.77$) (Table 2). This pattern suggests that speckle noise and similar

backscatter responses among several land cover types reduce the separability of classes in the SAR-only case. These outcomes are consistent with prior studies (Clerici et al., 2017; Dagne et al., 2023), in which optical imagery generally provides superior classification accuracy due to its richer spectral information on vegetation and surface materials.

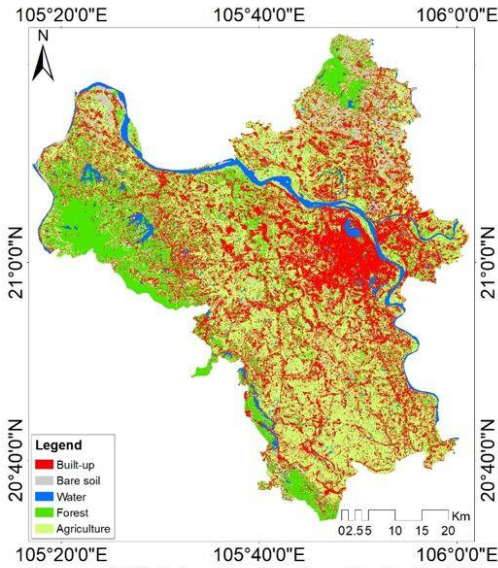


Figure 4. LULC classification from Sentinel 2 MSI using RF algorithm

Figure 4. LULC classification from Sentinel 2 MSI using RF algorithm

Table 1. Performance evaluation of RF in classifying Sentinel 1A SAR and Sentinel 2B MSI data

LULC type	Sentinel-1 SAR			Sentinel-2 MSI		
	PA	UA	F-score	PA	UA	F-score
BU	0.65	0.68	0.70	0.88	0.86	0.86
BS	0.23	0.46	0.30	0.86	0.84	0.78
W	0.81	0.74	0.77	0.95	0.94	0.92
F	0.53	0.51	0.52	0.84	0.86	0.86
A	0.53	0.47	0.48	0.82	0.81	0.78
	OA: 0.58	Kappa: 0.47		OA: 0.88	Kappa: 0.87	

Effectiveness of the RF Model on the Combined Sentinel-1 and Sentinel-2 Dataset:

The integrated Sentinel-1 and Sentinel-2 LULC map for 2025 (Figure 5b) presents a more coherent and realistic spatial pattern than the single-sensor classifications. Built-up areas

form a continuous, densely connected urban core along the main river and transport corridors, capturing both compact city blocks and smaller rural settlements. Forest and agricultural zones are more clearly separated in the western and northern uplands, while water bodies are sharply delineated with minimal confusion with dark impervious surfaces. Overall, fusing Sentinel-1 backscatter with Sentinel-2 spectral information reduces noise and class confusion-especially between Built-up, Bare soil, and Water-resulting in a more detailed and reliable representation of urban-rural land cover.

Table 2. Confusion matrix for the combined datasets

LULC type	BU	BS	W	F	A	Row total	UA
BU	1630	5	0	1	7	1643	0.95
BS	1	600	0	0	4	605	0.87
W	0	0	1377	0	0	137	1
F	3	1	0	1910	2	1916	0.90
A	8	10	0	4	1535	1557	0.89
Column total	1642	616	1377	1915	1548		
PA	0.98	0.87	1	0.90	0.86		

Upon integrating the two data sources, Sentinel-2 MSI and Sentinel-1 SAR, the classification performance demonstrated a significant improvement. The RF algorithm achieved an OA = 0.92 and a Kappa = 0.90, which is noticeably higher than the performance achieved using either source individually. This investigate indicates that combining optical information (spectral reflectance) with radar backscattering enhances the classifier's ability to discriminate between classes that are difficult to separate with a single data type. The resulting Confusion Matrix (Table 3) for the combined dataset further reflects the high per-class performance: the Water body class achieved perfect accuracy with PA = 1.00 and UA = 1.00, while the Built-up class also showed very high accuracies (PA = 0.98, UA = 0.95). The Bare soil and Agriculture classes demonstrated slightly lower performance, with UA = 0.87 and PA = 0.86, respectively, but still benefited from the data fusion compared with the single-sensor classifications.

The results definitively underscore the potential of integrating multi-source data (optical – radar) for robust land cover classification. The combination of Sentinel-1 and Sentinel-2 effectively mitigated the impact

of cloud cover and improved the discrimination capability for classes exhibiting similar reflectance or backscattering characteristics in single-source data.

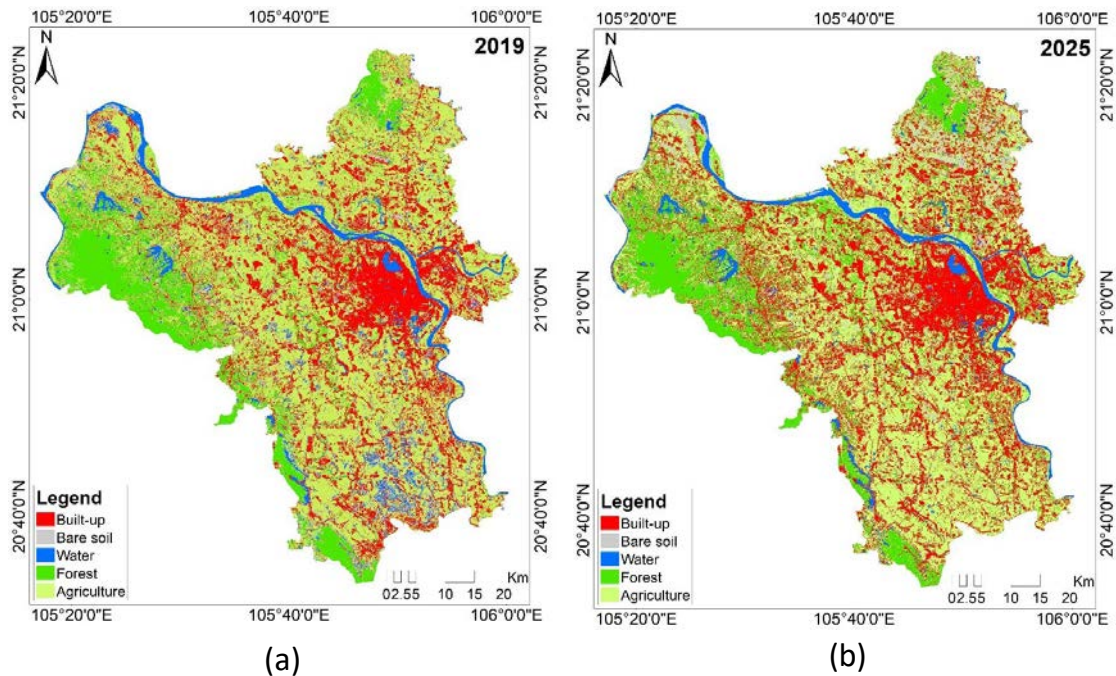


Figure 4. LULC classification of the study area in 2019 (a) and 2025 (b) from fusion Sentinel-1 SAR and Sentinel-2 MSI using RF algorithm

Expansion of Hanoi's urban during the period of 2019-2025:

Based on the fused Sentinel-1 and Sentinel-2 datasets, urban LULC maps for Hanoi were produced for the years 2019 and 2025, as shown in Figure 5. Between 2019 and 2025, the fused S1-S2 maps reveal a clear intensification and outward expansion of built-up land across the metropolitan area. The red built-up patches around the existing urban core become denser and more continuous, forming an almost uninterrupted urban belt along the main river corridor and major transport axes, with new development fronts spreading into the surrounding agricultural zones, particularly in the southern and eastern districts. Agricultural land (yellow) at the city fringe is progressively fragmented and converted to urban uses, while forested areas in the western uplands and water bodies along

the river system remain comparatively stable, although local encroachment appears along some forest-agriculture interfaces. However, some issues still require further clarification and improvement. In particular, the forest class may include mixed pixels of plantations, shrubland, and late-stage crops, making subtle forest loss or degradation difficult to detect at the current resolution. Small-scale clearing and fragmentation along the forest edge may therefore be underestimated, and additional analysis using multi-date time series, higher-resolution imagery, and field surveys is needed to better quantify forest dynamics and validate the observed changes.

Table 4 summarizes the area and proportion of each LULC class in the study area for 2019 and 2025. The results show a marked increase in built-up land, from about 76,970 ha (22.9%) in 2019 to 98,766 ha (29.4%) in 2025,

while agricultural land decreases by roughly 21,500 ha, from 49.7% to 43.3% of the total area, indicating strong conversion of farmland to urban uses. Forest area increases by about 9,000 ha (from 15.0% to 17.6%), which may reflect afforestation, plantation expansion, or reclassification of previously degraded land. In contrast, bare soil and water bodies both shrink in extent, suggesting that open land and aquatic surfaces are being gradually occupied or transformed as urban and agricultural activities intensify.

Table 4. Area of land use classes in the study area

LU/LC cover	Area (ha)		Area (%)	
	2019	2025	2019	2025
Built-up	76,969.7	98,765.5	22.90	29.38
Bare soil	18,930.1	15,835.7	5.63	4.71
Water body	23,065.0	16,771.6	6.86	4.99
Forest	50,254.3	59,302.6	14.95	17.64
Agriculture	166,905.1	145,447.2	49.66	43.27

Building on these findings, it can be seen that the Random Forest algorithm exhibits good generalization capability, attributed to its ensemble mechanism and its proficiency in handling non-linear data. Nevertheless, the classification performance for classes such as Bare soil and Agriculture remains somewhat constrained, possibly due to the inherent similarity in their spectral and backscattering signatures during specific cultivation periods. Overall, the study confirms that the fusion of Sentinel-1 SAR and Sentinel-2 MSI provides superior effectiveness in land cover classification, offering a promising framework for monitoring land-use change and supporting sustainable resource management. These results provide a solid basis for the concluding remarks and suggest several directions for future work, including the integration of higher-resolution data, multi-year time series, and advanced machine learning techniques to further refine urban LULC mapping in Hanoi.

Bao, T. Q., N. Van Thi, D. Le Sy, P. Van Duan, K. La Nguyen, N. T. Cuong, B. T. Hieu, D. T. T. Mai and D. Van Tuyen (2022). "The method of forest change detection using Sentinel-2 optical satellite imagery and Sentinel-1 radar imagery: A case study in Dak

CONCLUSION

The research findings demonstrate that fusing Sentinel-1 SAR and Sentinel-2 MSI data yielded superior classification performance compared to using each data source individually. The Random Forest algorithm achieved an overall accuracy of 0.92 and a Kappa coefficient of 0.90, indicating a stable model with strong generalization capability. Integrating optical reflectance and radar backscatter information not only enhanced the separability land cover classes but also reduced the influence of atmospheric effects and cloud cover. These results highlight the substantial potential of this multi-source data fusion combined with machine learning for robust land cover monitoring, land use change analysis, and assessing the impacts of urban expansion on the urban landscape and environment.

FUNDING

This research was conducted with the support of project code NVCC39.01/25-25. The authors sincerely thank the Vietnam National Space Center (VNSC), Vietnam Academy of Science and Technology (VAST) for providing favorable conditions and support during the execution of this study.

DATA AVAILABILITY

Data are available upon request.

DECLARATIONS

The authors have no competing interests to declare that are relevant to the content of this article.

ETHICS APPROVAL AND CONSENT TO PARTICIPATE

Not applicable.

REFERENCES

- Nong Province, Vietnam." *Biodiversitas Journal of Biological Diversity* 23(9).
- Breiman, L. (2001). "Random forests." *Machine learning* 45(1): 5-32.

- Bui, D. H. and L. Mucsi (2022). "Comparison of layer-stacking and Dempster-Shafer theory-based methods using Sentinel-1 and Sentinel-2 data fusion in urban land cover mapping." *Geo-spatial information science* 25(3): 425-438.
- Bui, N., A. Phan and T. Nguyen (2020). Land-cover Mapping from Sentinel Time-Series Imagery on the Google Earth Engine: A Case Study for Hanoi. 2020 7th NAFOSTED Conference on Information and Computer Science (NICS).
- Clerici, N., C. A. Valbuena Calderón and J. M. Posada (2017). "Fusion of Sentinel-1A and Sentinel-2A data for land cover mapping: a case study in the lower Magdalena region, Colombia." *Journal of Maps* 13(2): 718-726.
- Congalton, R. G. and K. Green (2019). *Assessing the accuracy of remotely sensed data: principles and practices*, CRC press.
- Corban, C., P. Politis and L. Maffneni (2019). "MASADA Sentinel 1 & 2 User Guide."
- Dagne, S. S., H. H. Hirpha, A. T. Tekoye, Y. B. Dessie and A. A. Endeshaw (2023). "Fusion of sentinel-1 SAR and sentinel-2 MSI data for accurate urban land use-land cover classification in Gondar City, Ethiopia." *Environmental Systems Research* 12(1): 40.
- Filipponi, F. (2019). Sentinel-1 GRD preprocessing workflow. *Proceedings, MDPI*.
- Gorelick, N., M. Hancher, M. Dixon, S. Ilyushchenko, D. Thau and R. Moore (2017). "Google Earth Engine: Planetary-scale geospatial analysis for everyone." *Remote sensing of Environment* 202: 18-27.
- Hastie, T., R. Tibshirani and J. Friedman (2009). *The elements of statistical learning*, Springer series in statistics New-York.
- Hoang, T. T., V. T. Truong, M. Hayashi, T. Tadono and K. N. Nasahara (2020). "New JAXA high-resolution land use/land cover map for Vietnam aiming for natural forest and plantation forest monitoring." *Remote sensing* 12(17): 2707.
- Horning, N. (2010). Random Forests: An algorithm for image classification and generation of continuous fields data sets. *Proceedings of the International Conference on Geoinformatics for Spatial Infrastructure Development in Earth and Allied Sciences*, Osaka, Japan.
- Houborg, R. and M. F. McCabe (2016). "High-Resolution NDVI from planet's constellation of earth observing nano-satellites: A new data source for precision agriculture." *Remote Sensing* 8(9): 768.
- JAXA (2021). *Annual Land-Use and Land-Cover Maps across Mainland Vietnam from 1990 to 2020*.
- Mauro, G. (2020). "Rural–urban transition of Hanoi (Vietnam): Using Landsat imagery to map its recent peri-urbanization." *ISPRS International Journal of Geo-Information* 9(11): 669.
- Phuong, L. and N. Quang (2021). "Research on Urban Land Use Change in Ha Noi, Viet Nam Using Remote Sensing and GIS for Planning Oriented Work." *International Journal of Sustainable Construction Engineering Technology* 12(3): 24-34.
- Saksena, S., J. Fox, J. Spencer, M. Castrence, M. DiGregorio, M. Epprecht, N. Sultana, M. Finucane, L. Nguyen and T. Vien (2014). "Classifying and mapping the urban transition in Vietnam." *Applied Geography* 50: 80-89.
- Steinhausen, M. J., P. D. Wagner, B. Narasimhan and B. Waske (2018). "Combining Sentinel-1 and Sentinel-2 data for improved land use and land cover mapping of monsoon regions." *International journal of applied earth observation geoinformation* 73: 595-604.
- Talukdar, S., P. Singha, S. Mahato, S. Pal, Y.-A. Liou and A. Rahman (2020). "Land-use land-cover classification by machine learning classifiers for satellite observations—A review." *Remote sensing* 12(7): 1135.
- Thanh, D. K., D. L. Ngoc, H. D. Dieu and V. A. Tran (2025). "Comparison of random forest and extreme gradient boosting algorithms in land cover classification in van yen district, Yen Bai Province, Vietnam." *Hydro-Environ Res* 23: 50-59.
- WorldBank (2020). *Vietnam urbanization review: Technical assistance report*.
- Zhang, X., L. Liu, X. Chen, Y. Gao, S. Xie and J. Mi (2020). "GLC_FCS30: Global land-cover product with fine classification system at 30 m using time-series Landsat imagery." *Earth System Science Data Discussions* 2020: 1-31.
- Zhao, Q., L. Yu, X. Li, D. Peng, Y. Zhang and P. Gong (2021). "Progress and trends in the application of Google Earth and Google Earth Engine." *Remote Sensing* 13(18): 3778.

DOI: 10.15625/vap.2025.0197

Application of LSTM-ARIMA model in air quality forecasting in Ba Ria – Vung Tau province

Ho Minh Dung¹, Ton Minh Hien^{1,2,*}

¹Institute for Environment and Resources, VNU-HCM, Vietnam

²HCMC Science of Occupational Safety and Health Institute, Vietnam

*Email: H_minhdung@yahoo.com

Abstract: Air pollution is one of the main causes of serious health problems such as lung and cardiovascular diseases and increases the risk of other diseases. Therefore, early forecasting of air quality plays an important role in warning the community and helping people proactively take health protection measures. In this study, the Long Short-Term Memory (LSTM) model was selected due to its ability to identify nonlinear relationships in data, suitable for both short-term and long-term forecasting. In order to improve efficiency, the LSTM model was combined with AutoRegressive Integrated Moving Average (ARIMA) to form a hybrid LSTM-ARIMA model, which gave positive forecasting results. The concentration of CO, NO₂, SO₂ and PM₁₀ (from 2020 to 2024) at the Gieng Nuoc intersection station (in Vung Tau city, Ba Ria – Vung Tau province) were always below the allowable of QCVN 05:2023/BTNMT. The PM_{2.5} concentration was mostly at lower of allowable level, only at one time it almost reached the limit. However, the 8-hour average ozone concentration exceeded the standard at 866 recorded (1.1–1.8 times), and the 1-hour ozone exceeded the standard at 74 recorded (1.1–1.6 times). The air quality is mainly in the “Good” and “Moderate” levels according to the AQI, but tends to decline in 2021, 2022 and 2024. The LSTM-ARIMA model gives 1-day forecast results with high accuracy (RMSE = 14.57; MAE = 7.81; MAPE = 16.3%) and maintains stable performance when forecasting is extended to 7 and 14 days, showing potential application in air quality monitoring and warning.

Keywords: Air quality, LSTM-ARIMA, Gieng Nuoc intersection station.

INTRODUCTION

Air quality forecasting models are divided into two main groups: Deterministic models and Statistical models (Xiang Li, 2017). Although analytical models provide high accuracy, they require detailed emission data and long computation times (Liao Qi, 2020). Statistical models, such as ARMA, ARIMA, GWR, MLR, and SVR (Dewen Seng, 2021; Vivien Mallet, 2008), mainly analyze relationships between meteorological factors and pollution concentrations while neglecting physical and chemical mechanisms (Pablo E. Saide, 2011). Examples include ARMA, ARIMA models for forecasting O₃, NO, NO₂, CO (Ujjwal Kumar, 2009), or MLR for NO_x forecasting in Athens and Helsinki (Aishah Al Yammahi, 2023). However, these models struggle to integrate multi-source heterogeneous data like traffic, meteorological, and landuse. (Yu Jiao, 2019) and perform poorly with complex, large datasets due to high computational demands (Pak Unjin, 2018).

Recent studies have focused on applying deep learning models, especially LSTM and hybrid models, to improve the accuracy of air quality forecasting. LSTM has shown better AQI prediction than ARIMA and linear regression (Klaus Greff, 2018; Yu Jiao, 2019). Several hybrid models have been proposed, such as LSTM-RNN with wireless sensor networks (Sagar V Belavadi, 2020), CNN-LSTM combined with spatiotemporal clustering (Yan

Rui, 2021) and multivariate LSTM (Yue-Shan Chang, 2020). Other studies confirm the superiority of hybrid models are LSTM and NAR-NN outperform statistical ones (Aishah Al Yammahi, 2023; Alex Graves, 2005); RNN-LSTM shows high effectiveness when combined (Navares & Aznarte, 2020); CNN-LSTM improves PM_{2.5} forecasting (Congcong Wen, 2018); and ARIMA-CNN-LSTM-DBO reduces RMSE and increases R² (Gulia Sunil, 2017). In Vietnam, deep learning is mainly applied in water resources such as salinity (Thanh & Giang, 2022), temperature-rainfall (Ha & Nghe, 2022) or river water level (Hien & Hung, 2018). For air quality, initial studies achieved positive results with models like LSTM-MA (Dung & Khang, 2024); LSTM-ANN-RNN (Cao & Pham, 2024); CNN-LSTM (Hung et al., 2021) and LSTM-NA (Phuc & Trieu, 2022); identified SGDRegressor as the most efficient in HoChiMinh City (Rajnish Rakholia, 2022). Overall, deep learning and hybrid modeling are emerging as key approaches for improving accuracy and efficiency in air quality forecasting. Besides, deep learning models have also been applied in several other fields. For example, the LSTM-BILSTM-DRNN, LSTM-CNN models has been used to predict flood events (Muhammad Hafizi Mohd Ali, 2022; Vijendra Kumar 2023); CNN, LSTM, ABi-LSTM and related models have been commonly used to predict wildfire risk (Cesilia Mambile, 2024; Yichao Cao, 2019), etc.

Studies have shown that hybrid models provide more accurate and stable forecasting results than single models. In this study, the ARIMA-LSTM model is used to forecast air quality by taking advantage of both methods. ARIMA is a traditional statistical model, suitable for linear time series, with stable trends and clear relationships between past and present values, but limited in handling nonlinear data and complex fluctuations. In contrast, LSTM is a recurrent neural network capable of learning nonlinear relationships, long-term dependencies, helping to forecast effectively with highly fluctuating data, but requires long training time and is prone to overfitting when data is limited. Combining

these two models helps to compensate for the weaknesses of each model: ARIMA takes care of the linear part and long-term trends, while LSTM handles the nonlinear part and complex dependencies. As a result, the ARIMA-LSTM hybrid model takes advantage of both, improving accuracy, reducing errors and increasing stability for air quality forecasting in both the short and long term.

RESEARCH CONTENT AND METHODOLOGY

Research content

To meet the set objectives, the study will carry out the following contents: (i) Assess air quality through data collected on ambient air quality monitoring in Ba Ria - Vung Tau province: Collect data on air quality monitoring at Gieng Nuoc intersection automatic and continuous monitoring station; Assess the current state of air quality based on collected data; (ii) Pre-process data and build an air quality forecasting model: Pre-process input data; Calculate the air quality index AQI; Standardize data; Build an air quality forecasting model; Conduct LSTM and LSTM-ARIMA model training; (iii) Forecasting air quality changes from the optimal model for Ba Ria - Vung Tau province: Using the optimal model from the process of assessing and forecasting air quality changes for Ba Ria - Vung Tau province; Comparing the results from the forecasting model with the actual collected results.

Research data

The air quality monitoring dataset used in this study is the hourly average concentration of air quality parameters measured at the Gieng Nuoc crossroads air quality monitoring station located in Ward 7, Vung Tau city, with coordinates X: 426939; Y: 146298. The dataset covers 4 years from January 18, 2020 to December 31, 2024. The dataset includes 15 parameters, including 6 meteorological parameters (wind speed, wind direction, temperature, humidity, pressure, solar radiation) and 9 air pollutants (NO, NO₂, NO_x, SO₂, CO, O₃, PM₁₀, PM_{2.5}, TSP).

Research methods

Data preprocessing

Air quality forecasting based on deep learning models requires a large amount of data sets to train the models. Input data is an important part leading to accurate results. However, the collected data sets are unevenly distributed and may be missing due to equipment failures. Therefore, the data sets need to be filled with missing data or interpolated so that deep learning models can be trained better.

- Remove outliers: Outliers are data values that deviate significantly from the rest of the dataset. The process of training a machine learning model is highly dependent on the range and distribution of data points. Outliers can negatively impact the training process, making the training process take longer and reducing the accuracy of the model. Therefore, removing outliers is very important to improve the performance of the model.

A popular method for identifying outliers is to use Z-scores. The Z-score of a sample is a measure of how many standard deviations the sample value differs from the mean value of the data set. The formula for calculating the Z-score of a sample x is defined as follows:

$$Z_i = \frac{(x_i - \mu)}{\sigma} \quad (1)$$

where, Z_i is the Z-score of the i -th data point, x_i is the i -th data point, μ is the mean, and σ is the standard deviation of the data. If the absolute value of the Z-score of any sample is greater than 3, then that sample is considered an outlier and is removed from the data set.

- Filling in missing data: During the process of collecting data from monitoring stations, missing data may occur due to technical problems such as sensor failures, power outages or network failures, leading to interruptions in the transmission of information. These missing values can affect the continuity of the data set and reduce the effectiveness of model training. To solve this problem, missing values will be replaced by

values measured at the same time in the previous week, because these values usually follow the same distribution over time. This data filling process will be handled through SPSS and MS Excel tool.

- Data normalization: To improve computational efficiency and optimize the model training process, data normalization is an important step to help turn noisy data sets into fully structured data. Data features often have differences in scale and distribution, which directly affects the classification efficiency of the model and the convergence ability of optimization algorithms, such as gradient descent. When the features have too different units, the gradient may not converge to the global extreme, resulting in the model not achieving optimal results. Moreover, the difference in units also causes errors in assessing the impact of each feature on the prediction results. To overcome this situation and improve the convergence speed of the model, the data will be normalized to the range [0,1] through the Min-Max normalization method:

$$x' = \frac{x - \min(x)}{\max(x) - \min(x)} \quad (2)$$

where, x' is the transformed data value (0 - 1), x is the original value.

The goal of the method is to bring the values closer to the average value of the variables without changing the shape of the data distribution. This method brings the values to a special range, usually [0,1] or [-1,1].

Method of calculating air quality index (AQI)

The technique for calculating and publishing the Vietnam Air Quality Index (VN_AQI) is regulated based on monitoring data from automatic air monitoring stations, according to Decision No. 1459/QĐ-TCMT dated November 12, 2019. The VN_AQI index is expressed through a scale to provide warning information about air quality and the level of impact on human health.

Deep learning method

The main structure of the LSTM network (Fig. 1) is that the state cell component is a conveyor belt that runs straight through the entire chain with only a few small linear interactions that help information to be transmitted along the stable neural network graph, and the gate is where the information passing through it is filtered, they are combined by a sigmoid network layer. First, the information will be decided to be removed or retained in the state cell through the forget gate layer.

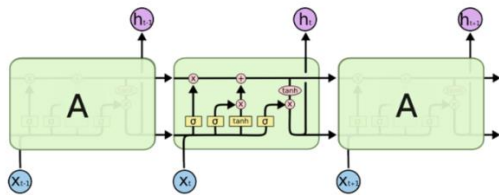


Fig. 1. LSTM network model

The "forget gate layer" receives input h_{t-1} (output value at time $t-1$) and x_t (current input data) and outputs a number in the range $[0,1]$. If the output is 0, all information is removed. If it is 1, all information is passed through. The advantage of the LSTM model is the ability to detect nonlinear relationships in data, so it is suitable for both short-term and long-term forecasting. However, this model has high requirements for the dataset used for training, if the dataset has outlier values, it will take a long time to train the model and the accuracy of the forecast from the model will be reduced. Therefore, the research topic uses the Autoregressive Integrated Moving Average (ARIMA) to filter the data in the past as well as to identify future changing trends of the time series. The dataset is divided into training, evaluation and validation sets. Using Root Mean Squared Error (RMSE), Mean Absolute Error (MAE) and Mean Absolute Percentage Error (MAPE) are used to evaluate the effectiveness of the model.

Method to built LSTM-ARIMA model

The data collected are processed using statistical methods, analyzed and evaluated.

Statistical methods can use Excel which is commonly used and easy to use for basic statistical analysis, Python is powerful programming languages for data analysis and visualization.

Experiment 1: Determining feasible parameters for the ARIMA model

In the first experiment, the main objective was to determine the optimal set of parameters for the ARIMA model to ensure the ability to accurately simulate the dynamic characteristics of the time series. The ARIMA model is characterized by three basic parameters: the autoregressive order (AR - p), the difference order (I - d) and the moving average order (MA - q). The correct choice of these parameters plays a decisive role in the forecasting performance, because they directly reflect the time-dependent relationship and the stability of the series.

The parameter determination process includes:

Testing the stationarity of the series: Use the Augmented Dickey-Fuller test (ADF test) to evaluate the stationarity property. If the series is not stationarized, the difference operation is applied repeatedly until the data reaches stability, thereby determining the value of the parameter d . If the time series is stationary at order 0, we denote it I ($d=0$), if the first difference of the series is stationary, we denote it I ($d=1$), etc. Determining the stationarity of the model is to eliminate variance and stabilize the trend. Stationary series have the characteristic of not changing over time. If the stationarity of the data series is not determined, the series has an unstable trend over time, leading to unstable analysis and forecasting, errors and unreliable results.

Determining the order of AR (autoregressive) and MA (moving average): After testing for stationarity, determine the order of the AR and MA processes through analyzing the graphs of the autocorrelation function (ACF) and partial autocorrelation function (PACF). Identifying the ARIMA(p,d,q) model is to find the appropriate values of p , d ,

q , where d is the order of the difference of the time series under investigation, p is the order of autoregressiveness and q is the order of moving average. Determining p and q will depend on the graphs $PACF = f(t)$ and $ACF = f(t)$.

In addition, many ARIMA models with different combinations of parameters are estimated and then compared based on statistical criteria such as Akaike Information Criterion (AIC) and Bayesian Information Criterion (BIC) to balance the model fit to the data and the complexity of the model. A model with a lower AIC value is better than a higher AIC score. In addition, BIC is another criterion for selecting a good model, limiting the complexity more than AIC. Models with low BIC values are often selected.

Experiment 2 (determining the optimal learning rate): In this experiment, the time delay will be kept the same as the results determined in experiment 1. The study conducts LSTM network training with the initial learning rate varying in the range of 0.001 - 0.009. Other parameters in the hidden neuron number model are 100, the maximum number of iterations is 100, the gradient threshold is 1, the adaptive moment estimation algorithm (Adam). The MSE error is chosen as the loss function to determine the optimal model.

Experiment 3 (determine the predictive ability of the model): After determining the optimal parameters for the LSTM-ARIMA hybrid model, the study proceeded to determine the ability to forecast air quality for the monitoring location. The forecast time (step) of the model was further investigated to evaluate the model's forecasting ability. The study investigated the forecast steps $k = 1$, $k = 7$, $k = 14$ respectively.

RESULTS AND DISCUSSION

Assessment of current air quality at Gieng Nuoc intersection station

The dataset from the Gieng Nuoc intersection station includes 43,250 samples collected from January 2020 to December 2024, with a high data completeness rate of 93–100% for all six pollutants. CO shows the largest fluctuation (standard deviation $582.3 \mu\text{g}/\text{m}^3$) due to traffic and fossil fuel combustion activities, while NO_2 and SO_2 remain stable with average concentrations of 15.7 and $33.6 \mu\text{g}/\text{m}^3$. $\text{PM}_{2.5}$ and PM_{10} average 13.73 and $22.69 \mu\text{g}/\text{m}^3$. During monitoring period, the conc. of CO, NO_2 , and SO_2 stayed within allowable limits, whereas O_3 occasionally exceeded standards 1-hour averages surpassed the limit from 1.1–1.6 times and 8-hour averages from 1.1–1.8 times, mostly during midday and afternoon due to strong sunlight. $\text{PM}_{2.5}$ and PM_{10} levels were generally acceptable but tended to rise during peak traffic hours showing that traffic activities strongly influenced pollutant fluctuations.

Handling outliers and filling in missing data

Data quality is the first and most important prerequisite for visualization and creating effective forecasting models. Preprocessing steps help reduce noise in the data, thereby increasing processing speed and generalization ability for algorithms. The data set will be preprocessed with the Box Whisker method to remove outliers. In which, data points with values greater than $Q_3 + 1.5 \cdot \text{IQR}$ and less than $Q_1 - 1.5 \cdot \text{IQR}$ (in which, Q_1 and Q_3 are the 25% percentile and 75% percentile, respectively, $\text{IQR} = Q_3 - Q_1$) are temporarily suspected as outliers (Table 1).

Table 1. Box-Whisker statistics for raw data sets

Pollutants	Percentile 25% - Q_1	Median	Percentile 75% - Q_3	IQR ($Q_3 - Q_1$)	$Q_3 + 1.5 \cdot \text{IQR}$
CO	239.9	510.19	917.23	677.33	1933.25
NO_2	2.93	10.6	22.4	19.47	51.60
O_3	25.2	43.34	63.82	38.615	121.74
SO_2	2.56	16.2	58.4	55.84	142.16
$\text{PM}_{2.5}$	7.06	10.7	15.8	8.74	28.91
PM_{10}	12.4	18.5	27.2	14.8	49.4

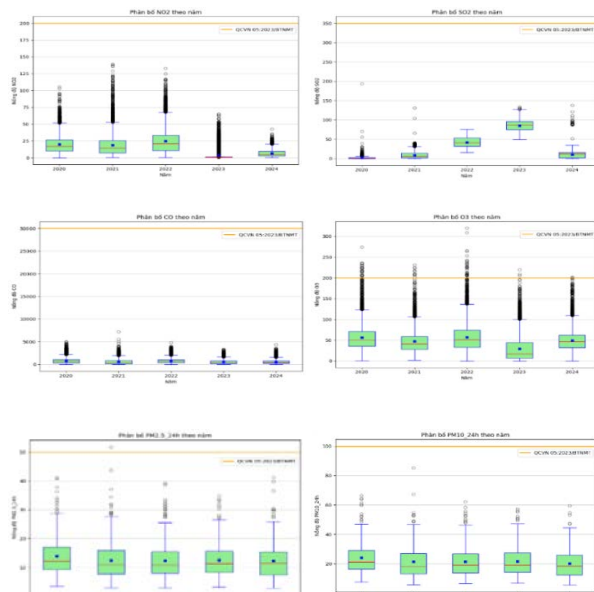


Figure 2. Distribution of concentrations of air pollutants over the years at the Gieng Nuoc intersection station

The statistical results (Fig.2) indicate that outliers are minimal, and comparison with QCVN 05:2023/BTNMT shows that NO_2 , SO_2 , CO , and PM_{10} concentrations remain within allowable limits. Only $\text{PM}_{2.5}$ exceeded the limit once, accounting for a very small proportion of the total dataset. As the data collection rate for all parameters exceeds 93%, removing these few outliers could reduce the objectivity and representativeness of the monitoring data. Therefore, the dataset will be retained in its entirety, with only missing values supplemented.

Calculation and assessment of air quality at Gieng Nuoc intersection station

After data processing, the AQI index will be calculated. The analysis results and evaluation of developments by year and month of AQI will be shown:

Assessment of air quality changes by year

From 2020 to 2024, the daily AQI at the Gieng Nuoc intersection station ranged from 14 to 196, showing clear year-to-year variation. In 2020, air quality was mostly “Good” (80.1%),

with 9.2% “Moderate” and 3.56% “Poor” days. The air quality improved in 2021, with 84.1% “Good” days and a notable AQI drop from June to November due to Covid-19 social distancing. However, air pollution increased in 2022, as “Good” days fell to 73.6% and “Poor” days rose to 14.0%. Air quality improved in 2023 (86.02% “Good” days, AQI 28–132), but declined again in 2024, with only 69.23% of days rated “Good” and 26.1% “Moderate” (AQI = 17–141), reflecting a gradual deterioration in overall air quality (Fig. 3). In general, the air quality at the Gieng Nuoc intersection station area is relatively good with the air quality classification being in the “Good” and “Moderate” groups when classifying AQI.

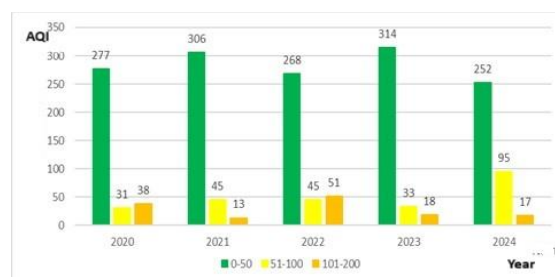


Figure 3. Air quality classification (by AQI) at Gieng Nuoc intersection station by year

Monthly assessment of air quality changes

The average AQI value is 45.3, the AQI index tends to be higher at the beginning and end of the year (from October to April of the following year), and lower in the middle of the year (May to September). In which, July is the time when the AQI index is lowest (15–41) and December is the time when the AQI index is highest. This is because in summer, high solar radiation causes a sharp increase in surface temperature and heats the air near the surface. This leads to increased convection, which is beneficial for the diffusion and deposition of air pollutants. (Yan, 2021). In general, most pollution parameters are within the allowable limits according to QCVN 05:2023/BTNMT and Ozone is the main parameter affecting the daily AQI value in the area.

Calculate the correlation between AQI_d and component AQI

The results indicate that the daily AQI

(AQI_d) has a strong positive correlation with AQI_d of O₃ 8-hour average ($R = 0.91$) and AQI_d of O₃ 1-hour average ($R = 0.84$), consistent with their frequent exceedance of permissible limits. AQI_d of PM₁₀ and PM_{2.5} also show moderate to high correlations with AQI_d, at 0.66 and 0.69 respectively, while AQI_d of NO₂, CO, and SO₂ have weaker correlations of 0.32, 0.19, and 0.12 (Fig. 4). AQI_d of all pollutants exhibit positive correlations with AQI_d, indicating that increases in pollutant concentrations lead to higher AQI_d values and thus poorer air quality.

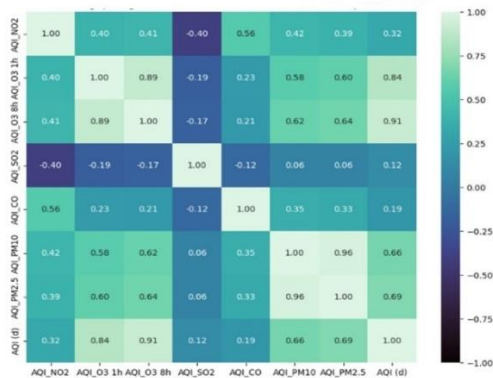


Figure 4. Correlation between daily AQI and component AQI

Evaluation of training results of air quality forecasting model

Choosing the optimal ARIMA model

The original time series analysis shows the time series of the AQI by day. It can be seen that the fluctuations do not revolve around a fixed average value line and the amplitude of the fluctuations is also irregular. The chart has many sharp peaks, indicating sudden and strong fluctuations, in contrast to the stationary series.

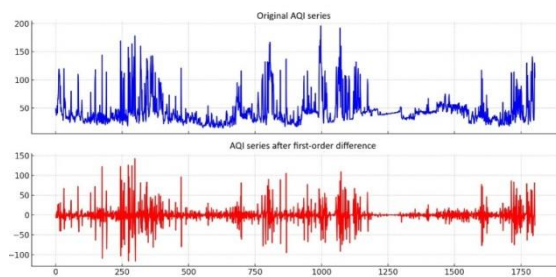


Figure 5. Data series with first difference

Fig. 5 illustrates the difference step in transforming the non-stationary data series into a stationary series with $d=1$. This is a necessary step to prepare the data for building and calibrating forecasting models. It can be seen that the values fluctuate around a stable mean (approximately zero). The amplitude of the series has been smoothed out, there are no longer clusters of too large fluctuations. This stabilizes the trend and reduces variance, thereby improving the reliability of the model.

To ensure that the selected ARIMA model will be a feasible model to implement the hybrid model, we determine the p and q values of the ARIMA model based on the ACF and PACF graphs, showing that the ACF has a decreasing value, no clear cut, the PACF has a strong spike at lag 1, then gradually decreases so choose p as 1 and q as 1. We see that the AC result at lag 1 is 0.66 and the other lags gradually decrease, showing that the series is dependent over time, PAC lag 1 is 0.66 then decreases sharply, this is a characteristic of AR, the p -value at all lags is very small, close to 0, the ARIMA (1,1,1) model is the appropriate model to conduct the study. In addition, we continue to consider the model according to the criteria of lower AIC and BIC values, which will be the preferred model. The ARIMA model is selected with parameters p, d, q respectively (1,1,1) shows that the correlation coefficient (ACF) of the residuals are all within the confidence interval of nearly 0.005, no lag exceeds the significant threshold. Therefore, the residuals are no longer autocorrelated. Similar to ACF, the PACF values of the residuals are all within the confidence interval of nearly 0.005, there is no abnormality at a specific level. The other lags (2-5) fluctuate around the value of 0, the small value is ± 0.005 so the values in this range are within the noise threshold. The model with feasible parameters. To increase the reliability of the model, the study calculated the MAPE of the model and achieved 23.88%, this value is at an acceptable level. So that, the ARIMA model predicts the overall trend and large fluctuations in data over time quite well, however the model is not strong in predicting short-term fluctuations, so

combining it with LSTM can increase the ability to predict smaller, more unusual fluctuations.

LSTM model

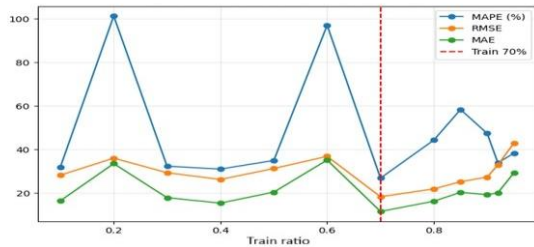


Figure 6. RMSE, MAE and %MAPE errors according to learning rate on training dataset

The learning rate is one of the most important parameters of a model. The size of the learning rate will directly affect the speed at which the model changes its weights to match the algorithm and the model's results. A large learning rate can help the neural network train 10 times faster but can also reduce the accuracy (Yu Jiao, 2019).

The results of Fig. 6 shows that there are many different training ratios and good results such as 40%, 70%. The training ratio of 70% will give stable and better results than other ratios through the lowest RMSE, MAE and MAPE values of 18.30; 11.56 and 26.86% respectively. After calculating and evaluating the current status of daily air quality, take 70% of the calculated data for training and 30% of the verified data.

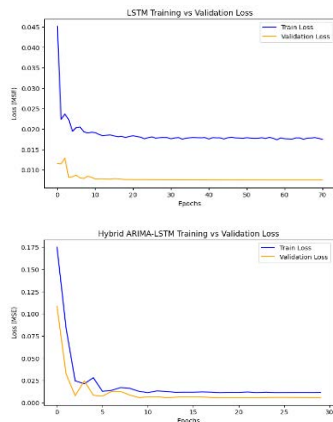


Figure 7. 70% training loss over training epochs for LSTM and LSTM-ARIMA models

During the training process, the accuracy of the model will gradually increase with each epoch, corresponding to a decrease in error. Fig. 7 depicts the change in loss over epochs during the model training process. For the LSTM model, underfitting occurred when the loss from the validation process had a clear gap with the training process. This means that the model cannot capture the complex values in the data as analyzed above and requires the process of removing noise from the dataset. Fig. 7 shows that the loss from the training process for LSTM-ARIMA is significantly improved compared to the original LSTM. The training line and validation line of the LSTM-ARIMA model are very low, ranging from 0.01 to 0.025 and are close to each other.

Air quality forecast for the Gieng Nuoc intersection area

The study assessed the forecasting performance of the LSTM-ARIMA hybrid model for air quality prediction. For 1-day forecasts, the model achieved the highest precision, with RMSE = 14.57, MAE = 7.81, and MAPE = 16.3%. For 1-week and 2-week forecasts (Fig. 8), the accuracy remained acceptable, with MAPE values of 19.23% and 20.39%, respectively, suggesting that although errors increased over time, the model effectively captured AQI trends. Comparisons with the standalone LSTM model showed that LSTM-ARIMA predictions more closely aligned with actual AQI values, especially in capturing short-term fluctuations, though its ability to track extreme peaks and troughs diminished over longer forecast periods. Overall, the hybrid LSTM-ARIMA model demonstrated strong capability in learning historical AQI patterns and maintaining reliable forecasting performance over short to medium timeframes.

The ARIMA model produces the most stable results with low errors (RMSE 14.37–16.41; MAE 7.63–9.25), while the LSTM model performs less accurately (RMSE 24.60–30.17; MAE 18.26–24.24) due to AQI variability. The hybrid LSTM-ARIMA model combines ARIMA's linear processing and LSTM's nonlinear learning, achieving better accuracy (MAPE 16.3–20.39%), notably lower than LSTM (36.9–51.32%)

and comparable to ARIMA. Overall, it offers improved stability, adaptability, and accuracy in air quality forecasting.

It can be seen that the accuracy of the model gradually decreases when forecasting for a long time due to many reasons. First, the cumulative error over each forecasting step increases the total error, reducing the reliability of the results. Although the ARIMA-LSTM hybrid model combines the advantages of ARIMA in handling linear trends and LSTM in learning nonlinear, long-term dependencies, it is still greatly affected by this cumulative error. Second, the ability to capture long-term patterns is limited, because as the forecasting time is extended, the initial information gradually becomes "diluted", making it difficult for LSTM to maintain the dependency relationship, while ARIMA loses the ability to accurately model new nonlinear or cyclical fluctuations. Third, the characteristics of the time series may change over time, such as the appearance of new trends, unusual fluctuations, or sudden environmental factors, making the model trained from past data unable to adapt in time. Finally, combining ARIMA and LSTM often creates a smoothing effect, which helps reduce noise and avoid overfitting but at the same time reduces the model's sensitivity to strong fluctuations, leading to less accurate long-term forecasts, especially during periods of large fluctuations or spikes.

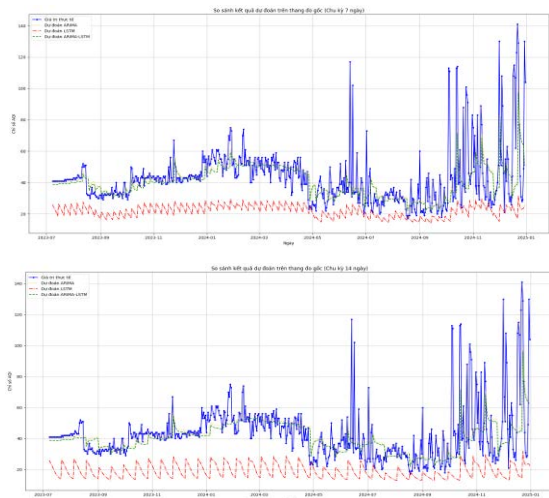


Figure 8. 7-day and 14-day air quality forecast simulation results

Comparing the performance correlation between the LSTM-ARIMA model in this study and some other applied hybrid models (Dung & Khang, 2024; Jiahui Duan, 2023; Yan Rui, 2021) shows that the LSTM-ARIMA model still achieves lower RMSE and MAE indexes than other hybrid models, so it can be applied in forecasting in cycles.

CONCLUSIONS

Based on the calculations and experiments conducted, the study achieved the following results: The current status of air quality at the Gieng Nuoc intersection station in Vung Tau city for the period 2020-2024 was assessed, with the collected dataset achieving a completeness rate of over 93%. According to comparisons with QCVN 05:2023/ BTNMT standards, the air quality in the study area is relatively good when the concentration of CO, NO₂, SO₂, PM₁₀ are all below the allowable threshold during the study period. The monitored PM_{2.5} concentration was recorded at times below the allowable threshold, with only 1 time reaching approximately the standard level. The average 8-hour ozone concentration had 866 recorded times exceeding the allowable standard from 1.1 to 1.8 times. The average 1-hour ozone value has 74 recorded exceeds the allowable standard from 1.1 to 1.6 times; The LSTM-ARIMA hybrid model has been successfully developed with the ability to forecast with high accuracy for the next 1-day period with RMSE of 14.57; MAE of 7.81 and MAPE of 16.3%. When forecasting for a longer period corresponding to 7 days in the future, the model still gives feasible results with evaluation indexes RMSE, MAE and MAPE of 16.7; 8.97; 19.23% respectively. Depending on specific studies, it can be applied to different cycles to make accurate predictions. The above research is a premise to expand the research to data at other monitoring stations in the BRVT area to have a general picture of air quality forecasting around the BRVT area.

ACKNOWLEDGEMENT

This research is funded by Vietnam National University HoChiMinh City (VNU-HCM) under grant number DS.C2025-02.

REFERENCES

- Aishah Al Yammahi, Z. A. (2023). Forecasting the concentration of NO₂ using statistical and machine learning methods: A case study in the UAE. *Heliyon*, 9(2), e12584.
- Alex Graves, J. S. (2005). Framewise phoneme classification with bidirectional LSTM and other neural network architectures. *Neural Networks*, 18(5-6), 602-610.
- Cao, M. Q., & Pham, H. H. (2024). Predicting air pollution from monitoring data using artificial intelligence models. *Transport and Communications Science Journal*, 75(03), 1404 -1412.
- Cesilia Mambile, S. K., and Judith Leo. (2024). Application of Deep Learning in Forest Fire Prediction: A Systematic Review. *IEEE Access*, 12, 190554-190581.
- Congcong Wen, S. L., Xiaojing Yao, Ling Peng, Xiang Li, Yuan Hu, Tianhe Chi (2018). A novel spatiotemporal convolutional long short-term neural network for air pollution prediction. *The Science of The Total Environment*, 654(1).
- Dewen Seng, Q. Z., Xuefeng Zhang, Guangsen Chen, Xiyuan Chen. (2021). Spatiotemporal prediction of air quality based on LSTM neural network. *Alexandria Engineering Journal*, 60, 2021–2032.
- Dung, H. M., & Khang, K. D. A. (2024). Forecasting air quality by the LSTM-MA model, using data at the Gieng Nuoc intersection automatic monitoring station, Ba Ria - Vung Tau province. *Journal of Hydro-meteorology*, 9(765), 75-89.
- Gulia Sunil, N. S. M. S., etc (2017). Extreme Events of Reactive Ambient Air Pollutants and their Distribution Pattern at Urban Hotspots. *Aerosol and Air Quality Research*, 17(2), 394-405.
- Ha, D. T., & Nghe, N. T. (2022). Application of long short-term memory multivariate model in temperature and rainfall forecasting. 58(4A), 8-16.
- Hien, L. X., & Hung, H. V. (2018). Using Long Short-Term Memory Neural Network to Forecast Water level at The Quang Phuc and the Cua Cam stations in Hai Phong, Vietnam. *Journal of Water resources & Environmental engineering*, 62.
- Hung, N. V., Nam, V. H., Anh, V. D., Hiep, T. Q., & Long, L. T. (2021). Air quality index prediction using convolutional neural network and long short-term memory. *Journal of Science and Technology on Information and Communications*, 4, 129-136.
- Jiahui Duan, Y. G., Jun Luo, etc (2023). Air-quality prediction based on the ARIMA-CNN-LSTM combination model optimized by dung beetle optimizer. *Scientific Reports*, 13(1), 12127.
- Klaus Greff, R. K. S., Jan Koutník, Bas R. Steunebrink, Jurgen Schmidhuber. (2018). LSTM: A Search Space Odyssey. *Transactions on Neural Networks and Learning Systems*.
- Liao Qi, Z. M., Wu Lin, etc (2020). Deep Learning for Air Quality Forecasts: a Review. *Current Pollution Reports*, 6(4), 399-409.
- Muhammad Hafizi Mohd Ali, S. A. A., Z. Zainal Abidin, Zuraida Abal Abas, Nurul A. Emran. (2022). Flood Prediction using Deep Learning Models. *International Journal of Advanced Computer Science and Applications*, 13(9).
- Navares, R., & Aznarte, J. L. (2020). Predicting air quality with deep learning LSTM: Towards comprehensive models. *Ecological Informatics*, 55.
- Pablo E. Saide, G. R. C., Scott N. Spak, Laura Gallardo, Axel E. Osses, Marcelo A. Mena-Carrasco, Mariusz Pagowski (2011). Forecasting urban PM₁₀ and PM_{2.5} pollution episodes in very stable nocturnal conditions and complex terrain using WRF–Chem CO tracer model. *Atmospheric Environment*, 45(16), 2769-2780.
- Pak Unjin, K. C., Ryu Unsok, Sok Kyongjin, Pak Sunnam. (2018). A hybrid model based on convolutional neural networks and long short-term memory for ozone concentration prediction. *Air Quality, Atmosphere & Health*, 11(8), 883-895.
- Phuc, L. B., & Trieu, D. V. (2022). Study on the artificial intelligence model of LSTM - NA in the air quality forecast for deep open pit coal mines. *Mining Science and Technology Information*, 3.
- Rajnish Rakholia, Q. L., Khue Vu, Bang Quoc Ho, Ricardo Simon Carbajo. (2022). AI-based air quality PM_{2.5} forecasting models for developing countries: A case study of Ho Chi Minh City, Vietnam. *Urban Climate*, 46, 101315.
- Sagar V Belavadi, S. R., Ranjani R, Rajasekar Mohan. (2020). Air Quality Forecasting using LSTM RNN and Wireless Sensor Networks. *Procedia Computer Science*, 170, 241–248.
- Thanh, N. C., etc (2022). Building LSTM (Long Short-Term Memory) machine learning model for water salinity forecasting in Dai Ngai. *Vietnam Journal of Hydrometeorology*, 8(740(1)), 98-104.
- Ujjwal Kumar, V. K. J. (2009). ARIMA forecasting of

- ambient air pollutants (O₃, NO, NO₂ and CO). 24(5), 751-760.
- Vijendra Kumar , H. M. A., Kul Vaibhav Sharma, etc (2023). The State of the Art in Deep Learning Applications, Challenges, and Future Prospects: A Comprehensive Review of Flood Forecasting and Management. *sustainability*, 15, 10543.
- Vivien Mallet, B. S. (2008). Air quality modeling: From deterministic to stochastic approaches. *Computers and Mathematics with Applications*, 55, 2329–2337.
- Xiang Li, L. P., Xiaojing Yao, Shaolong Cui, Yuan Hu, Chengzeng You, Tianhe Chi. (2017). Long short-term memory neural network for air pollutant concentration predictions: Method development and evaluation. *Environ Pollut*, 231, 997-1004.
- Yan, R. (2021). Multi-hour and multi-site air quality index forecasting in Beijing using CNN, LSTM, CNN-LSTM, and spatiotemporal clustering. *Expert Systems With Applications* 169.
- Yan Rui, L. J., Yang Jie, Sun Wei, Nong Mingyue, Li Feipeng. (2021). Multi-hour and multi-site air quality index forecasting in Beijing using CNN, LSTM, CNN-LSTM, and spatiotemporal clustering. *Expert Systems with Applications*, 169.
- Yichao Cao, F. Y., Qingfei Tang, and Xiaobo Lu. (2019). An Attention Enhanced Bidirectional LSTM for Early Forest Fire Smoke Recognition. *IEEE Access*, 7, 154732-154742.
- Yu Jiao, Z. W., Yang Zhang. (2019). Prediction of Air Quality Index Based on LSTM 2019 IEEE 8th Joint International Information Technology and Artificial Intelligence Conference (ITAIC 2019),
- Yue-Shan Chang, H.-T. C., Satheesh Abimannan, etc (2020). An LSTM-based aggregated model for air pollution forecasting. *Atmospheric Pollution Research*, 11, 1451–1463.

DOI: 10.15625/vap.2025.0198

Spatial Convergence and Hotspot Clustering of Provincial Human Development Index in Viet Nam

Truong Van Canh

The University of Danang – University of Science and Education, Da Nang, Viet Nam

Email: tvcanh@ued.udn.vn

Abstract: Understanding how human development evolves across space and time is central to evaluate progress toward inclusive and sustainable growth. This study examines the spatial convergence and hotspot clustering of the provincial human development index in Viet Nam during the period 2016–2024. Using the Human Development Index (HDI) as a multidimensional measure of socioeconomic well-being, the research integrates classical convergence models with spatial statistical techniques to uncover both temporal and geographical patterns. The sigma (σ) convergence analysis, based on the coefficient of variation of HDI across provinces, shows a modest but fluctuating downward trend, implying a slow reduction in overall regional disparities and incomplete equalization of human development outcomes. The results also reveal a statistically significant absolute beta (β) convergence ($\beta = -0.020$, $p < 0.001$), indicating that provinces with lower initial HDI levels experienced faster improvements over time. However, the estimated convergence speed ($\lambda \approx 2.18\%$ per year) and half-life of 34.3 years suggest a relatively slow catch-up process. The Global Moran's I values, ranging from 0.296 to 0.519, confirm a persistent and significant positive spatial autocorrelation ($p < 0.001$), implying that provinces with similar development levels are geographically clustered rather than randomly distributed. The Getis-Ord General G statistic further validates the existence of distinct hotspot regions in the Red River Delta and the Southeastern provinces, while coldspots prevail in the Northern Midland and Mountainous Region. These findings highlight the coexistence of temporal convergence and spatial polarization in

Vietnam's human development landscape. The study underscores the need for spatially differentiated policy interventions to strengthen social infrastructure, education, and healthcare in lagging regions while sustaining inclusive growth in advanced provinces.

Keywords: Human Development Index (HDI); Spatial Convergence; σ -Convergence; β -Convergence; Moran's I; Getis-Ord G_i^* ; Spatial Inequality; Viet Nam

INTRODUCTION

The Human Development Index, introduced by the United Nations Development Programme (UNDP) in 1990, remains one of the most widely recognized composite measures of welfare, combining three essential dimensions: health, education, and standard of living. (UNDP, 2024). Unlike purely economic indicators such as GDP per capita, HDI captures the multidimensional nature of human well-being, making it a valuable lens for assessing spatial inequalities in quality of life. For policymakers, HDI serves both as a benchmark for progress and a diagnostic tool for identifying lagging regions, particularly in the context of decentralization and regional development planning. (UNDP, 2020). Over the past three decades, Vietnam has achieved remarkable improvements in human development. Its national HDI reached 0.766 in 2023, placing the country within the “high human development” category. (UNDP, 2025). However, beneath this national progress lies a persistent spatial divide: the Red River Delta and Southeastern regions consistently outperform other areas, whereas the Northern Midland and Mountainous, the Central Highlands, and Mekong Delta regions

lag in key social and human development outcomes. (GSO, 2021).

The theoretical foundation of convergence in human development is rooted in the neoclassical Solow–Swan growth model (Solow, 1956; Swan, 1956), which postulates that economies sharing similar structural characteristics, such as savings rates, population growth, and technological progress, will gradually converge toward a steady-state equilibrium of per capita income and welfare. Building upon this framework, the notion of regional convergence has been extensively applied to assess whether less-developed regions are catching up with more advanced ones over time, thereby reducing spatial disparities in economic and social outcomes (Barro & Sala-i-Martin, 1992; Monfort, 2008). Two forms of convergence are commonly discussed: sigma (σ) convergence, which reflects a reduction in dispersion across regions, and beta (β) convergence, which indicates faster growth in areas with lower initial levels of development. While σ and β -convergence have been commonly studied in the context of income and GDP (Rey & Janikas, 2005), their application to multidimensional indices such as the HDI remains limited, particularly in developing economies. Given that HDI incorporates structural factors – health, education, and income – its convergence dynamics reveal more profound insights into long-term equity and sustainable growth patterns. Traditional convergence models, however, often assume spatial independence, implying that regions evolve in isolation. In practice, provinces are interconnected through migration, infrastructure networks, investment spillovers, and policy diffusion, leading to spatial dependence and spatial spillover effects (Getis, 2007; Anselin, 2010). Ignoring spatial dependence can bias convergence estimates and obscure the existence of spatial clusters (Le Gallo & Ertur, 2003). Spatial econometric and statistical techniques, such as Global Moran's I and Getis-Ord G_i^* , enable researchers to test for global and local spatial autocorrelation, thereby revealing patterns of “hotspots” and “coldspots” in regional development (Getis & Ord, 1992).

In Vietnam, numerous studies have addressed the issues of growing income disparities and convergence among its provinces (Nguyen, 2024). Far fewer studies have integrated both temporal and spatial perspectives of human development using subnational HDI data. Given Vietnam's diverse geography, economic heterogeneity, and varying access to infrastructure and social services, examining the spatial convergence and hotspot clustering of HDI can provide new insights into regional equity and policy design. This study contributes to the literature by integrating σ and β -convergence models with spatial statistical analysis to examine the evolution and spatial clustering of provincial HDI across Vietnam during 2016–2024. Specifically, it seeks to answer three research questions: Has σ -convergence occurred, indicating a reduction in cross-provincial disparities in HDI? Does absolute β -convergence exist in provincial HDI across Vietnam? What are the spatial clustering patterns of HDI, and where are the persistent hotspots and coldspots located? By combining convergence analysis and spatial autocorrelation methods, this paper provides a comprehensive view of the spatial polarization and temporal convergence of human development in Vietnam. The findings are expected to inform regionally differentiated policy interventions that promote social inclusion, human capital formation, and balanced development across provinces.

METHODOLOGY

Data and study scope

This study examines the spatial convergence and hotspot clustering of the HDI across 63 provinces and centrally governed cities of Vietnam during the period 2016–2024. Provincial HDI data were compiled from the General Statistics Office (GSO, 2021, 2025), which provides annual updates on the components of HDI following the global UNDP methodology. All data were transformed into a panel format, enabling both cross-sectional and temporal analysis. The study's spatial units correspond to the official administrative boundaries the adjustment of provincial-level

administrative units. Spatial relationships among provinces were defined using a queen-contiguity spatial weight matrix (W), in which each province is linked to its neighboring provinces that share either a boundary or a vertex. All spatial analyses were conducted using ArcGIS 10.8 software, ensuring the reproducibility of results.

Sigma (σ) convergence

To assess whether disparities in HDI decreased over time, the study applied the σ -convergence test, which evaluates the temporal evolution of cross-sectional dispersion. Following standard practice (Sala-I-Martin, 1996), dispersion was measured as the coefficient of variation (CV):

$$\sigma_t = \frac{\sqrt{\frac{1}{N} \sum_{i=1}^N (HDI_{i,t} - \overline{HDI}_t)^2}}{\overline{HDI}_t} \quad (1)$$

where $HDI_{i,t}$ is the human development index of province i in year t , and \overline{HDI}_t is the national mean in that year. A downward trend in σ -values over time indicates convergence (i.e., narrowing disparities), while an upward trend suggests divergence. To visualize temporal dynamics, σ -values were plotted as a trend line from 2016 to 2024, enabling interpretation of whether Vietnam's human development disparities are diminishing.

Beta (β) convergence

While the σ -convergence results describe the declining dispersion in HDI across provinces, the β -convergence analysis tests whether less-developed provinces are improving faster than their more developed counterparts. The absolute β -convergence model evaluates the inverse relationship between the initial level of HDI and the subsequent growth rate over the study period. The model of absolute β -convergence was estimated using an ordinary least squares (OLS) regression, following the Barro-Sala-i-Martin (1992) framework:

$$\frac{1}{T} \ln \left(\frac{HDI_{i,t_2}}{HDI_{i,t_1}} \right) = \alpha + \beta \ln(HDI_{i,t_1}) + \varepsilon_i \quad (2)$$

where HDI_{i,t_1} and HDI_{i,t_2} denote HDI in the initial and terminal years (2016 and 2024, respectively), and T is the interval length (eight years). A negative β coefficient indicates convergence: provinces with lower initial HDI experience higher subsequent growth. All regressions were implemented in SPSS 20.0. The annual convergence rate (r) can be derived as $r = -\frac{1}{T} \ln(1 + \beta T)$. The half-life ($t_{1/2}$) of convergence is the number of years required for the initial disparity between provinces to be reduced by half, assuming the current pace of convergence remains constant. It is calculated as: $t_{1/2} = -\ln(2)/\ln(1 + \beta)$.

Global Moran's I

The Global Moran's I (Moran, 1950) statistic measures the degree of overall spatial autocorrelation in provincial HDI, capturing whether similar HDI values cluster geographically. The statistic is computed as:

$$I = \frac{N}{\sum_i \sum_j w_{ij}} \cdot \frac{\sum_i \sum_j w_{ij} (x_i - \bar{x})(x_j - \bar{x})}{\sum_i (x_i - \bar{x})^2} \quad (3)$$

where N is the number of space units, x_i and x_j represent HDI values of provinces i and j , \bar{x} is the average value of the variable x , and w_{ij} denotes the elements of the spatial weight matrix W . A positive and statistically significant Moran's I implies positive spatial clustering (high-HDI provinces near high-HDI provinces, and vice versa), while negative values suggest spatial dispersion. Significance was assessed using permutation tests, yielding z -scores and p -values for each year.

Getis-Ord G_i^* analysis

The Getis-Ord G_i^* statistic measures the degree of local spatial clustering of high or low values around each observation (Getis & Ord, 1992). Unlike the global Moran's I, which evaluates overall spatial dependence across the entire study area, the G_i^* index ($G_i^* \text{Score}$) identifies localized "hotspots" and "coldspots", specific areas where values are significantly higher or lower than the global mean. Mathematically, the statistic is expressed as:

$$G_i^* = \frac{\sum_j w_{ij} x_j - \bar{X} \sum_j w_{ij}}{s \sqrt{\frac{n \sum_j w_{ij}^2 - (\sum_j w_{ij})^2}{n-1}}} \quad (4)$$

where x_j is the HDI value of province j , \bar{X} the mean HDI, n is the number of space units, and S its standard deviation. A high positive G_i^* ($z \geq 1.96$, $p < 0.05$) identifies hotspots, provinces surrounded by others with similarly high HDI values. Conversely, a low negative G_i^* ($z \leq -1.96$, $p < 0.05$) marks coldspots, indicating spatial concentrations of low human development. Visualization in ArcGIS of G_i^* z-scores for provincial HDI values of 2024 enables identification of persistent spatial clusters.

RESULTS AND DISCUSSION

Dispersion of provincial Human Development Index

The analysis of σ -convergence provides an overview of the temporal evolution of disparities in human development among Vietnam's provinces from 2016 to 2024. Figure 1 illustrates the trend of the coefficient of variation (CV) of the provincial HDI values, reflecting the degree of inequality in human development across the country. Over the period 2016–2024, Vietnam's CV of provincial HDI declined from 0.0760 to 0.0651, corresponding to a relative reduction of approximately 14.5%. This downward trend indicates that human development disparities across provinces have gradually narrowed, consistent with σ -convergence. The pattern suggests that provinces with lower HDI levels in earlier years are catching up to more developed counterparts, thereby reducing national multidimensional welfare inequality.

The trajectory of σ -convergence, however, is non-linear. After a period of relative stability from 2016 to 2019, the dispersion of HDI values declined sharply between 2020 and 2023, corresponding to the years of the COVID-19 pandemic. This temporary acceleration of convergence was primarily driven by the pandemic's widespread socioeconomic disruptions. Yet, following 2023, the convergence momentum slowed and slightly

reversed, as evidenced by the rise in CV from 0.0639 in 2023 to 0.0651 in 2024. This uptick suggests that post-pandemic economic recovery has not been spatially uniform. Provinces with greater industrial and service-sector capacity rebounded more rapidly, while lagging areas recovered more slowly due to weaker fiscal and infrastructural foundations. As a result, the HDI gap between dynamic and peripheral regions began to widen again.

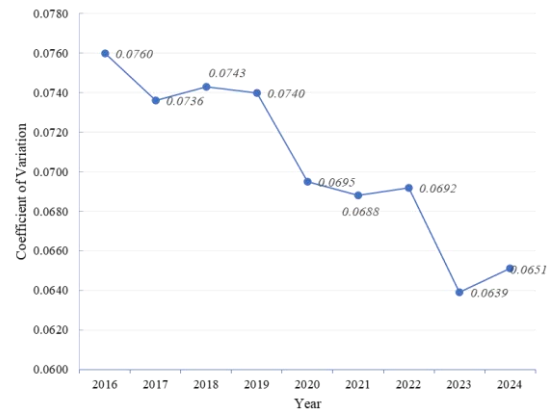


Figure 1. Coefficient of Variation (CV) of Provincial HDI in Vietnam (2016–2024)

Beta (β) convergence of provincial Human Development Index

To complement the σ -convergence findings, the β -convergence model was employed to test whether provinces with lower initial HDI levels in 2016 achieved higher growth in human development during 2016–2024. The regression results presented in Table 1 indicate a statistically significant and negative relationship between the logarithm of initial HDI and subsequent HDI growth.

The estimated coefficient of $\beta = -0.020$ ($p < 0.001$) confirms the existence of absolute β -convergence among Vietnam's provinces. This negative sign implies that provinces starting with lower HDI in 2016 experienced faster improvements in human development than more advanced ones, reflecting a measurable catch-up effect. The standardized coefficient ($\beta_{std} = -0.650$) further underscores a strong inverse association between initial HDI and growth, highlighting the robustness of the convergence process. Using the conventional

transformation $r = -\frac{1}{T}\ln(1 + \beta T)$ with $T = 8$ years, the annual rate of convergence is approximately 2.18 % per year, corresponding to a half-life of about 34.3 years - that is, the time

required for interprovincial disparities in HDI to be reduced by half if the current rate of convergence is maintained.

Table 1. Regression results for β -convergence of provincial HDI in Vietnam, 2016–2024

Model	Unstandardized Coefficients B	Std. Error	Standardized Coefficients Beta	t	Sig.
(Constant)	0.002	0.001		1.907	0.061
Log (HDI_2016)	-0.020	0.003	-0.650	-6.684	0.000

Note. Dependent Variable: annual growth of HDI 2016–2024.

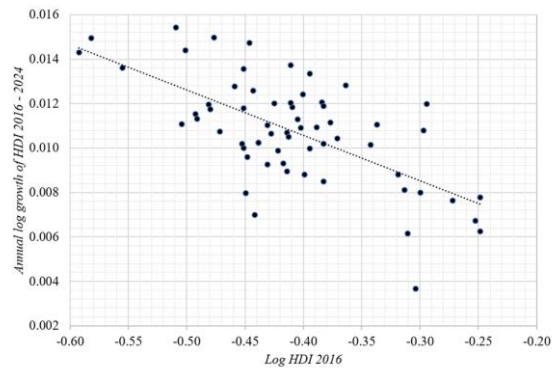


Figure 2. Scatter plot of absolute β -convergence in HDI (2016–2024)

Figure 2 illustrates a significant negative relationship between the initial level of human development ($\log(\text{HDI}_{2016})$) and the subsequent growth rate of HDI from 2016 to 2024. This shows provinces with lower initial HDI values in 2016 tend to exhibit higher growth rates during the following period, while those starting with higher HDI levels show slower improvement.

Spatial autocorrelation of provincial Human Development Index

To examine the spatial dependence and clustering tendencies of human development across Vietnam’s provinces, the study employed the Global Moran’s I statistic for each year from 2016 to 2024. This measure identifies whether provinces with similar HDI values are spatially clustered or randomly distributed across the national territory. The results are summarized in Table 2.

Table 2. Global Moran’s I of provincial HDI in Vietnam (2016–2024)

Year	Moran’s I	Z-score	p-value	Interpretation
2016	0.499	5.986	0.000	Strong positive spatial autocorrelation
2017	0.487	5.857	0.000	Strong positive spatial autocorrelation
2018	0.486	5.836	0.000	Strong positive spatial autocorrelation
2019	0.497	5.963	0.000	Strong positive spatial autocorrelation
2020	0.515	6.165	0.000	Strong positive spatial autocorrelation
2021	0.296	3.626	0.0003	Moderate spatial autocorrelation (temporary weakening)
2022	0.298	3.654	0.0003	Moderate spatial autocorrelation (recovering)
2023	0.519	6.206	0.000	Strong positive spatial autocorrelation
2024	0.505	6.051	0.000	Strong positive spatial autocorrelation

The results reveal that Vietnam’s provincial HDI exhibits persistent and statistically significant positive spatial autocorrelation throughout the 2016–2024 period. Moran’s I values consistently range between 0.296 and 0.519 ($p < 0.001$), indicating a high degree of spatial clustering, provinces

with high-HDI values tend to be located near one another, while low-HDI provinces also form geographically contiguous groups. The temporal trajectory shows relative stability in the degree of spatial dependence, with only a temporary weakening during 2021–2022 (Moran's $I = 0.296 - 0.298$). This short-term fluctuation likely reflects the asymmetric regional impact of the COVID-19 pandemic, during which major urban centers experienced slower HDI growth due to economic contraction, while some rural provinces maintained social welfare gains through targeted support programs. The recovery of Moran's I values in 2023–2024 suggests a re-emergence of spatial clustering, consistent with the resumption of economic activities and regional policy continuity. In 2024, the Global Moran's I value (0.505) with a z-score of 6.051 ($p < 0.000$) indicates a statistically significant positive spatial autocorrelation (Fig.3).

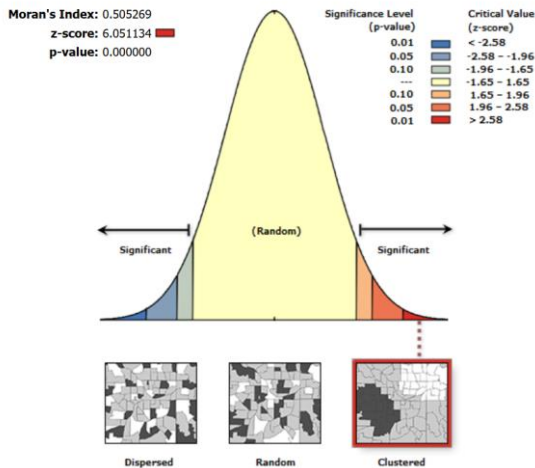


Figure 3. Global Moran's I Results for Provincial HDI in Vietnam, 2024.

The persistence of spatial autocorrelation even under national convergence (as demonstrated in Sections 4.1–4.2) underscores a critical insight: temporal convergence does not automatically translate into spatial equalization. Rather, Vietnam's human development process remains regionally embedded, with spatial dependence reflecting both cumulative advantage (in developed urban cores) and structural constraints (in peripheral

provinces). The Global Moran's I analysis provides empirical justification for subsequent local spatial analysis (Getis–Ord G_i^*) to identify specific hotspot and coldspot provinces.

Local spatial patterns of provincial Human Development Index

While Global Moran's I confirmed the existence of strong positive spatial dependence in Vietnam's HDI distribution, the Getis–Ord G_i^* analysis reveals a distinctly polarized spatial structure of human development across Vietnam's provinces in 2024 (Fig.4). The G_i^* Score results demonstrate a statistically significant clustering of both hotspots (high–high clusters) and coldspots (low–low clusters), underscoring the spatially uneven progress of human development in the country.

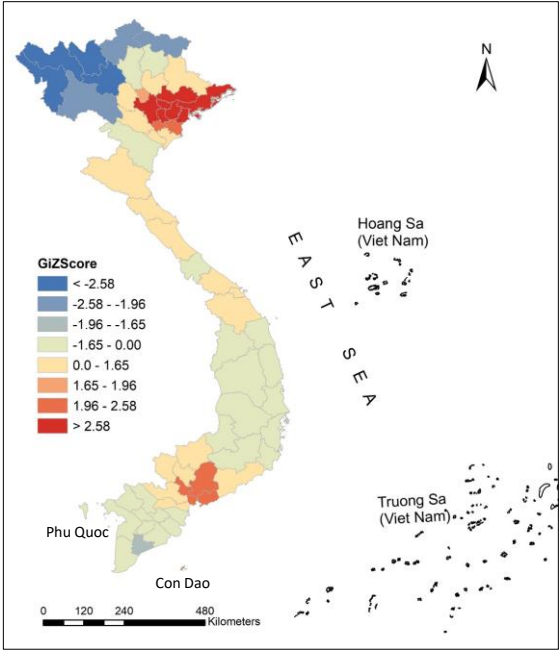


Figure 4. Local Hotspot and Coldspot Patterns of Provincial HDI in Vietnam, 2024 (Getis–Ord G_i^* Results), reduced from a map at a scale of 1: 12 000 000 (*The study's spatial units correspond to the official administrative boundaries prior to the adjustment of provincial-level administrative units*)

At the lower end of the spatial distribution, strong and moderate coldspots ($z \leq -1.96$, $p < 0.05$) are concentrated in the

Northern Midland and Mountainous Region, including Dien Bien, Lai Chau, Lao Cai, Yen Bai, Son La, Ha Giang, and Cao Bang. These provinces are characterized by limited accessibility, rugged terrain, and underdeveloped infrastructure, which constrain economic diversification and social service delivery. The persistent low HDI scores in these areas stem from geographical isolation, low education attainment, and insufficient healthcare coverage, all of which reflect the structural disadvantages of upland economies. A weaker coldspot ($-1.96 < z \leq -1.65$, $p < 0.10$) appears in Bac Lieu Province in the Mekong Delta, where environmental vulnerability and salinization pressures exacerbate livelihood insecurity and slow improvements in human well-being.

In contrast, strong hotspots ($z > 2.58$, $p < 0.01$) are clustered within the Red River Delta region, encompassing Ha Noi, Bac Giang, Bac Ninh, Hai Duong, Hung Yen, Hai Phong, and Quang Ninh. These provinces exhibit the highest levels of human development in the country, supported by intensive industrialization, high educational attainment, and comprehensive healthcare access. The spatial proximity to the national capital fosters policy diffusion, labor mobility, and technological spillovers, consolidating this region as Vietnam's most dynamic and inclusive development pole. A secondary group of moderate hotspots ($1.96 \leq z \leq 2.58$, $p < 0.05$) appears in Ha Nam and Thai Binh (within the Red River Delta) and in Ho Chi Minh City, Dong Nai, and Ba Ria-Vung Tau (the Southeast Region). The provinces in the Southeast Region benefit from industrial clustering, export-oriented economies, and strong connectivity to national and global value chains. Their sustained human development progress can be attributed to robust fiscal capacity, private-sector dynamism, and inclusive urban governance, which collectively reinforce spatial agglomeration advantages. A weak hotspot ($1.65 \leq z < 1.96$) in Vinh Phuc Province further reflects the gradual northward expansion of development from Hanoi's urban core.

Together, these spatial patterns illustrate Vietnam's bipolar development structure, anchored by two major growth poles — the Red River Delta in the North and the Southeast Region in the South — separated by a wide central corridor exhibiting statistically insignificant clustering. The formation of hotspots in the Red River and Southeast regions reflects the concentration of industrial production, urbanization, and policy-driven investment, while the persistence of coldspots in mountainous and deltaic peripheries underscores the enduring influence of topographic barriers, environmental constraints, and institutional disparities.

Conclusion and policy implications

This study examined the spatial convergence and hotspot clustering of human development across Vietnam's 63 provinces during 2016–2024, employing an integrated framework of σ -convergence, σ -convergence and β -convergence analysis, complemented by spatial econometric methods (Global Moran's I and Getis-Ord G_i^*).

The findings offer robust empirical evidence of moderate but significant convergence in human development, accompanied by persistent spatial clustering and regional polarization. The σ -convergence results reveal a gradual decline in the dispersion of provincial HDI values, suggesting a slow but steady narrowing of disparities in education, health, and income dimensions. The β -convergence model further supports this trend, with a significant negative coefficient ($\beta = -0.020$, $p < 0.001$), indicating that provinces with lower initial HDI levels have grown faster over time. The implied annual convergence rate of approximately 2.18% underscores a tangible, though modest, process of equalization in multidimensional well-being. The Global Moran's I statistics demonstrate strong and consistent positive spatial autocorrelation ($I \approx 0.296$ – 0.519 , $p < 0.001$), confirming that provinces with similar HDI values are geographically clustered. However, local analysis using Getis-Ord G_i^* reveals clear spatial heterogeneity: high-HDI hotspots are concentrated in the Red River Delta and the

- Singapore. <https://doi.org/10.1007/s41685-024-00334-w>.
- Rey, S. J., & Janikas, M. V. (2005). Regional convergence, inequality, and space. *Journal of Economic Geography*, 5(2), 155–176. <https://doi.org/10.1093/jnlecg/lbh044>.
- Sala-I-Martin, X. X. (1996). Regional cohesion: Evidence and theories of regional growth and convergence. *European Economic Review*, 40, 1325–1352.
- Solow, R. M. (1956). A Contribution to the Theory of Economic Growth Author (s): Robert M . Solow Source. *The Quartely Journal of Economics*, 70(1), 65–94. <http://www.jstor.org/stable/1884513>.
- Swan, T. W. (1956). Economic growth and capital accumulation. *Economic Record*, 32(2), 334–361. <https://doi.org/10.1111/j.1475-4932.1957.tb01279.x>.
- UNDP. (2020). *Human Development Report 2020: The Next Frontier Human Development and the Anthropocene*. The United Nations Development Programme.
- UNDP. (2024). *Human Development Report 2023/24: Breaking the gridlock*. The United Nations Development Programme.
- UNDP. (2025). *Human Development Report 2025: A matter of choice: People and possibilities in the age of AI*. The United Nations Development Programme.

DOI: 10.15625/vap.2025.0199

Operationalizing SF-MST and GSTC indicators for sustainable tourism assessment: The case of Con Dao, Vietnam

Tran Thi Tuyen

Sai Gon University, Ho Chi Minh City

Email: tttuyen1982@sgu.edu

Abstract: This study assesses the sustainability of tourism development in Con Dao, Vietnam, using the UNWTO's Statistical Framework for Measuring the Sustainability of Tourism (SF-MST) in combination with the GSTC destination criteria. Key quantitative indicators including energy and water consumption, solid waste generation, and CO₂ emissions per visitor-night that were benchmarked against international thresholds. Results show that although Con Dao possesses strong ecological and cultural assets, its performance falls short across major GSTC pillars, such as destination management lacks systematic monitoring, socio-economic benefits are unevenly distributed, cultural heritage faces increasing risks of commercialization, and environmental management remains weak in waste, water, and renewable energy systems. Comparative insights from international island destinations highlight effective practices in monitoring, circular waste management, renewable energy adoption, and community engagement. The study provides empirical evidence to guide sustainable tourism policy in Vietnam and demonstrates the practical utility of SF-MST and GSTC frameworks for island destination management.

Keywords: Con Dao, sustainable tourism, SF-MST, GSTC, Ecotourism management.

INTRODUCTION

Over the past two decades, sustainable tourism has emerged as a global strategic priority aimed at mitigating environmental impacts and improving socio-economic outcomes for local communities. Rigorous evaluation of sustainability performance now

increasingly draws on standardized international frameworks. The Statistical Framework for Measuring the Sustainability of Tourism (SF-MST), developed by the United Nations Statistics Division in collaboration with UNWTO, offers an integrated accounting system that links the environmental, economic, and social dimensions of tourism within the broader SEEA framework (UNWTO, 2021). Complementing this, the Global Sustainable Tourism Criteria (GSTC) provide globally recognized principles for destination management, socio-economic benefit sharing, cultural heritage conservation, and environmental stewardship (GSTC, 2019). Together, the SF-MST and GSTC frameworks establish a robust and complementary foundation for measuring, monitoring, and guiding tourism development toward sustainability.

Con Dao, an offshore archipelago of Vietnam, is internationally recognized as a UNESCO Biosphere Reserve and is distinguished by its extensive marine biodiversity and significant cultural-historical assets. However, rapid tourism expansion, particularly in the post-COVID-19 period has heightened pressures on its fragile ecosystems and overstretched local management capacities. Existing scholarship on Con Dao has primarily focused on marine conservation, protected-area governance, and visitor dynamics (Khuu, Jones, & Ekins, 2021; Tkachenko et al., 2022; Pham, 2024). Governance analyses employing the Marine Protected Area Governance (MPAG) framework describe a “state-led yet increasingly decentralized” model that depends

heavily on international and NGO financing, while also revealing persistent tensions between economic growth objectives and conservation mandates (Khuu et al., 2021). Ecological assessments document high coral cover, notable species richness, and relative resilience to thermal anomalies, reaffirming the ecological significance of Con Dao National Park (Tkachenko et al., 2022). Visitor studies indicate strong nature-based motivations particularly related to sea turtles, coral reefs, and forest ecosystems but highlight that service quality and communication strongly shape visitor behavior (Pham, 2024). More recently, Tuyen (2025) advanced a circular-economy approach to regenerative tourism, emphasizing enabling policy environments and community participation in ecosystem stewardship. Collectively, this body of research demonstrates that Con Dao's biodiversity, seagrass meadows, turtle populations, and cultural-historical heritage constitute a robust foundation for ecotourism, while simultaneously underscoring the mounting sustainability challenges associated with accelerating visitor growth.

Despite this evidence, few studies in Vietnam have applied global sustainability assessment frameworks such as the UNWTO's *Statistical Framework for Measuring the Sustainability of Tourism (SF-MST)* (UNWTO, 2018) or the *Global Sustainable Tourism Criteria* (GSTC, 2021). This study addresses that gap by quantitatively measuring sustainability indicators in Con Dao, benchmarking them against international thresholds, and identifying strategies for more resilient destination governance. Specifically, it evaluates resource efficiency, environmental impacts, socio-economic benefits, and governance, providing policy recommendations for advancing sustainable ecotourism in Vietnam and other sensitive island ecosystems.

METHODOLOGY

Data Used

Fieldwork and Sociological Surveys

Fieldwork was carried out in Con Dao National Park (CDNP) to observe and evaluate landscapes and environmental conditions through direct site visits. In addition, sociological surveys were conducted targeting two groups of respondents: (i) tourists visiting CDNP and (ii) staff members of the National Park and the Con Dao District People's Committee. Data collection methods included structured questionnaires for tourists and face-to-face interviews with officials. Semi-structured interviews were also conducted with local residents and visitors, complemented by expert consultations with CDNP staff.

Table 1. Descriptive Profile of Survey Respondents

Characteristic	Category	Percentage (%)
Gender	Male	48
	Female	52
Age Group	18–30	34
	31–45	41
	46–60	19
	>60	6
Education Level	High school or below	22
	College/University	63
	Postgraduate	15
Income Range (monthly, USD)	<700	28
	700–1500	47
	>1500	25
Nationality	Vietnamese	88
	International	12

The selection of 120 tourist questionnaires was based on Cochran's (1977) sample size calculation for social surveys. Using a 95% confidence level, $p = 0.5$, and a 10% margin of error, the minimum required sample size was 96. To ensure sufficient valid responses and accommodate potential non-responses, the target sample was increased to 120. This sample size aligns with common practice in small-island tourism studies, where surveys typically range between 100 and 150 respondents. Ultimately, 103 valid responses were collected, meeting the threshold for reliable descriptive analysis and internal consistency testing (Cronbach's $\alpha = 0.82$). The survey sample ($n = 103$) was dominated by domestic tourists, with balanced gender representation, most respondents aged 18–45, and the majority

holding university-level education. Income levels were concentrated in the USD 700–1,500 range, indicating a predominantly middle-income visitor segment (Table 1).

Qualitative data were collected through semi-structured interviews with key stakeholder groups directly involved in or affected by tourism activities in Con Dao. A total of 29 interviews were conducted, including 15 local residents (representing fisher households, small business operators, and community organizations), 8 staff members from Con Dao National Park, and 6 district government officials from the tourism, environment, and infrastructure departments. Participants were selected using purposive sampling to ensure representation of diverse perspectives and practical experience with tourism development, resource use, and governance. Interviews followed a flexible protocol that allowed respondents to elaborate on issues related to sustainability, community engagement, and destination management.

All interviews were audio-recorded with participant consent, transcribed verbatim, and analyzed using a thematic analysis approach. Coding followed both deductive categories derived from the research questions and inductive themes emerging from the data. The analysis identified five dominant thematic clusters (i) Tourism-derived household income and livelihood dependence; (ii) Benefit-sharing mechanisms and levels of community participation; (iii) Visitor behavior and perceived environmental pressures; (iv) Cultural and heritage preservation practices and associated challenges; (v) Governance gaps, institutional coordination, and enforcement capacity. Coding was performed manually and cross-validated among researchers to minimize interpretative bias and enhance reliability.

Data Collection Processing and Analysis

The study employed a quantitative approach based on the Statistical Framework for Measuring the Sustainability of Tourism (SF-MST) developed by UNWTO and the

Global Sustainable Tourism Council (GSTC) criteria. The objective was to measure and benchmark resource use and environmental impacts of tourism in Con Dao against international standards. Four core indicators were selected: (1) Electricity consumption (kWh per visitor-night) were obtained from monthly utility records and on-site meters at accommodation facilities; (2) Water consumption (m³ per visitor-night) was measured through invoices and meters provided by the local supply company and desalination plants; net freshwater use accounted for reuse systems (e.g., greywater, rainwater); (3) Solid waste generation (kg per visitor-night) were collected from waste management units and accommodation providers, including direct weighing and seven-day waste audits in selected facilities to estimate generation rates and composition; (4) Greenhouse gas (GHG) emissions (tCO₂ per visitor-night) were calculated using electricity, fuel, and waste data, following the IPCC (2006, 2019) and GHG Protocol methodologies, with emission factors sourced from national inventories (MONRE, 2020) or IPCC defaults. These indicators follow recommendations from UNWTO, GSTC, and the World Travel & Tourism Council (WTTC) through the Hotel Carbon Measurement Initiative (HCMi) and the Hotel Water Measurement Initiative (HwMI).

Data Processing and Normalization

All selected data were standardized to a per visitor-night basis to allow comparability across facilities and against international benchmarks. Visitor-night statistics were obtained from the Ba Ria-Vung Tau Department of Tourism and hotel Property Management Systems (PMS) for 2024. Day visitors were converted into “equivalent visitor-nights” using a factor of 0.3–0.5, following UNWTO (2018). The normalization procedure for each indicator was as follows:

Electricity consumption: Total electricity use (from utility bills, on-site meters, and diesel generator logs) was divided by the number of visitor-nights in each facility. For

diesel generators, electricity output was estimated from fuel consumption and generator efficiency before normalization.

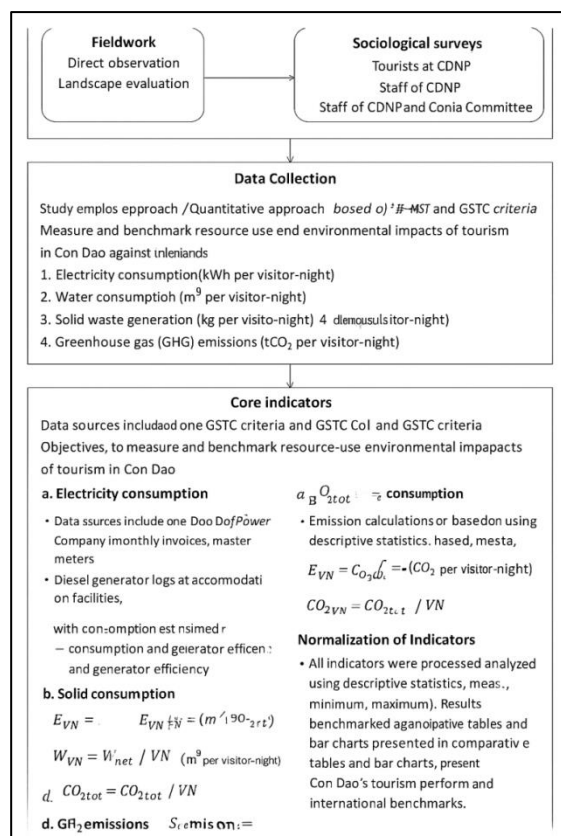


Figure 1. Flowchart of Research Design

Water consumption: Water use (from supply company invoices, desalination plants, and facility meters) was divided by visitor-nights. In cases with water reuse systems (greywater recycling or rainwater harvesting), reused volumes were deducted to calculate net freshwater consumption per visitor-night.

Solid Waste Generation: Total solid waste (measured at collection points and verified with transport records) was divided by visitor-nights. In selected facilities, seven-day waste audits were conducted to establish waste generation coefficients and composition, which were then scaled to the visitor-night unit.

CO₂ Emissions: GHG emissions were calculated using electricity, diesel, LPG, and waste data, applying IPCC (2006; updated 2019)

and GHG Protocol methodologies. Emission factors were sourced from national inventories (MONRE, 2020). The resulting emissions were normalized by visitor-nights to derive tCO₂ per visitor-night.

Total emissions:

$$CO_{2,tot} = Emissions_{elec} + Emissions_{fuel} + Emissions_{waste}$$

Normalize per visitor-night (convert tCO₂ to desired unit; note EF units):

$$CO_{2,VN} = x = \frac{CO_{2,tot}}{VN} \text{ (tCO}_2 \text{ per visitor-night)}$$

Normalized indicators were summarized and benchmarked against UNWTO and GSTC reference values. Results were presented in comparative tables and bar charts to illustrate deviations between Con Dao's tourism performance and international sustainability standards.

RESULTS AND DISCUSSIONS

Potential for Green Tourism Development in Con Dao

Con Dao is a small offshore archipelago in southern Vietnam with strategic accessibility by air and sea. Covering 76 km² across 16 islands, it retains relatively pristine natural environments, including tropical forests, wetlands, coral reefs, and seagrass beds. The biodiversity is exceptionally high, with more than 1,000 plant species (44 endemics), 160 wildlife species, and coral reefs exhibiting 62–95% live cover with 168 hard coral species (Hieu et al., 2023). Such ecosystems offer strong potential for ecotourism, environmental education, and climate-adaptive green tourism initiatives. The combination of ecological uniqueness and cultural-historical depth provides Con Dao with a dual advantage for developing sustainable tourism. However, realizing this potential requires balancing visitor growth with resource conservation, embedding community participation, and aligning destination management with global sustainability frameworks such as SF-MST and GSTC.



Figure 2. Natural and historical landscapes for tourism in Con Dao

Figure 2 provides an integrated overview of Con Dao's key tourism landscapes, revealing a spatial mosaic of natural, cultural, and historical attractions that collectively shape the archipelago's heritage-nature tourism identity. The natural landscape is characterized by pristine beaches such as Dam Trau, rugged mountainous terrain, and extensive coral reef systems that support high marine biodiversity. These ecological assets form the foundation for nature-based tourism activities including snorkeling, wildlife observation, and coastal recreation. Complementing the natural environment is a dense system of cultural and historical heritage sites. Figure 2 highlights emblematic locations such as Con Dao Prison and associated relics, which document the island's layered history of struggle and remembrance. Hang Duong Cemetery and An Son Temple represent significant spiritual landmarks, serving as focal points for commemorative practices, pilgrimages, and intangible cultural traditions. Annual rituals, memorial ceremonies, and community-led festivals attract both domestic and international visitors, reinforcing Con Dao's role as a destination where cultural identity, remembrance, and spiritual values are interwoven with ecological significance. Together, these natural and heritage elements illustrate a diversified tourism landscape in which ecological conservation, historical education, and cultural spirituality coexist. This combination not only enhances the island's attractiveness but also positions Con Dao as a

distinctive model of integrated heritage-nature tourism in Vietnam.

Assessing the Sustainability of Tourism in Con Dao

Tourism sustainability in Con Dao is evaluated through internationally recognized frameworks that emphasize balanced development and long-term resilience. In this study, four key criteria are applied, resource efficiency (energy and water use), environmental integrity (waste generation and emissions), socio-economic benefits, and governance quality, providing a comprehensive basis for assessment.

Destination Governance and Management

Con Dao has developed a master plan for ecotourism in association with the National Park, providing a foundation for sustainable destination management. However, quantitative monitoring and reporting tools remain limited, particularly as no specific indicator system has been established under the UNWTO Statistical Framework for Measuring the Sustainability of Tourism (SF-MST). At present, key metrics such as energy and water consumption, solid waste generation, and greenhouse gas emissions per visitor-night are not systematically measured. Moreover, coordination across management levels is fragmented, resulting in inconsistent implementation of green tourism policies. Independent oversight by local communities and NGOs remains weak, leaving little scope for social accountability. As noted by Khuu, Jones, and Ekins (2021), governance of Con Dao National Park still faces significant challenges, including limited enforcement capacity, weak community engagement, and poor institutional coordination, despite substantial international donor support. Against GSTC standards, Con Dao's destination governance falls short, underscoring the urgent need for data-driven management systems and transparent reporting to enhance effectiveness.

Both quantitative and qualitative results point to a clear gap between planning and implementation. While most surveyed

residents (68%) recognize that tourism development plans exist, only a small proportion (27%) perceive regular monitoring or follow-up evaluation. Interviews with officials and park staff confirm that coordination among agencies remains fragmented and reporting is irregular. Many residents (54%) also feel inadequately informed about tourism policies. Planning frameworks exist, but weak monitoring, fragmented coordination, and limited public communication result in an underperforming destination management system.

Socio-Economic Benefits and Community Participation

According to GSTC criteria, sustainable tourism requires creating employment, reducing inequality, and ensuring meaningful local participation. The household survey (n = 103) shows that tourism contributes substantially to local livelihoods, with 62% of respondents reporting that tourism provides at least one-third of their household income. Among tourism-engaged households, the average monthly income from homestays, informal guiding, small restaurants, and transport services ranges from USD 320–560, confirming tourism's economic relevance.

However, benefits are unevenly distributed. Only 21% of low-income households reported improved income from tourism, compared with 47% of middle-income households. Interview data indicate that limited start-up capital, lack of professional skills, and competition from outside businesses restrict broader community participation. Concrete evidence from local programs illustrates this imbalance. The “Green Offering Basket” program implemented by the district Women's Union, currently involves 37 small enterprises and households (equivalent to roughly 9% of local microbusinesses). Although it has reduced the use of plastic bags by an estimated 15,000 units per month during peak season (Con Dao Report, 2024), its economic benefits remain modest, contributing less than 5% of monthly income for participating households. Similarly, plastic-free campaigns

led by the National Park have engaged 18 tourism businesses (hotels, cafes, and boat operators), yet interviews reveal that only 6 of these businesses have maintained consistent compliance. Besides, pilot circular-economy initiatives, such as composting organic waste and upcycling abandoned fishing nets are small-scale, involving 12–15 households in An Hai and Co Ong wards. While promising, these initiatives have not yet become integrated components of the tourism value chain. Overall, relative to GSTC socio-economic criteria, Con Dao demonstrates progress in livelihood contribution but insufficient depth in community participation, benefit-sharing, and scaling of local entrepreneurship models. Stronger institutional support is required to expand homestays, improve skills training, and integrate local products into formal tourism supply chains.

Cultural Heritage and Historical Tourism

One of Con Dao's core strengths lies in its rich cultural-historical heritage, including the prison complex, Hang Duong Cemetery, and numerous temples, all of which have been relatively well preserved through sustained government investment. Survey results further indicate that both local authorities and residents increasingly recognize the importance of safeguarding this heritage landscape, particularly sites associated with wartime history and memorial tourism. Among 29 interviewed officials, 72% reported concerns about visitor etiquette at spiritual-memorial sites and noted that existing communication efforts remain insufficient to guide tourists toward respectful behavior. Meanwhile, 61% of the 103 surveyed households stated that they rarely observe structured heritage interpretation activities beyond basic signage, suggesting that educational content has not yet effectively reached the broader community.

Community awareness related to “thanatourism” also reveals notable gaps. More than half of surveyed residents (54%) acknowledge the emotional and ethical specificity of dark heritage tourism and agree that visitors should receive clearer orientation

on appropriate conduct and cultural meaning. However, only 38% reported any participation in public education or community workshops on heritage preservation. Furthermore, 46% of households stated that they feel insufficiently equipped to explain Con Dao's wartime history to visitors, especially younger generations. Interviews with community leaders add that many residents still regard heritage tourism primarily as an economic activity rather than a form of remembrance or moral education, which reduces incentives for deeper participatory engagement. Without targeted educational programs, they warn that local understanding of Con Dao's traumatic past may gradually erode, undermining the authenticity and long-term sustainability of "thanatourism" initiatives.

These findings align with concerns raised by Hayward and Tran (2014), who argue that heritage tourism in Con Dao shows early signs of commercialization. Activities linked to dark heritage, such as prison and cemetery visits are increasingly bundled with nature-based tours but often lack substantive cultural interpretation. This trend risks diminishing the symbolic value of memorial sites while underutilizing their educational and identity-building potential.

Relative to GSTC cultural criteria, Con Dao performs strongly in the conservation of tangible heritage but remains weak in interpretive depth, visitor management, and community involvement. Strengthening heritage communication through guided thematic tours (history, memory, spirituality, ecology), community-based interpretation programs, and culturally grounded educational materials would help shift tourism from a "visiting-consuming" model toward an "experiencing-learning-respecting" approach, thereby enhancing both visitor understanding and local cultural continuity.

Sustainable Development and Future Strategy

Insights from the 29 semi-structured interviews provide a deeper understanding of

how local authorities, community members, and conservation staff perceive the future trajectory of tourism development in Con Dao. Across stakeholder groups, there was strong consensus that sustainable tourism must become the core orientation for the island's long-term development. Officials noted that the district's development plan for 2025 targets a 4.4% annual increase in tourist arrivals and a 13.2% rise in accommodation revenue, accompanied by a strategic shift toward ecotourism, wellness tourism, and green tourism models. Interviewees emphasized that such growth must be carefully managed to avoid surpassing ecological thresholds, particularly in marine protected areas.

Looking toward 2050, stakeholders articulated a shared vision of transforming Con Dao into a smart, circular, and green island destination. This vision includes large-scale adoption of renewable energy, improved waste reduction and segregation systems, expansion of wastewater treatment facilities, and investment in sustainable public infrastructure. Local residents highlighted the need for transparent benefit-sharing mechanisms to ensure that the economic gains from tourism contribute to community well-being, while National Park staff stressed the importance of strengthening enforcement capacity and implementing visitor-management tools such as zoning, carrying-capacity limits, and digital monitoring systems. Overall, the qualitative findings reinforce the alignment between community expectations, conservation priorities, and official development objectives, while also underscoring the need for integrated governance and long-term environmental safeguards to achieve the island's sustainability vision.

Environment and Natural Resources

The GSTC criteria emphasize (i) efficient management of energy, water, and waste; (ii) reduction of greenhouse gas emissions; and (iii) conservation of biodiversity and landscapes. Current sustainability indicators reveal significant performance gaps in Con Dao when benchmarked against international

standards (Figure 3 and Table 2). Electricity consumption reached 28.0 kWh per visitor-night in 2024, nearly 40% above the recommended benchmark of 20 kWh, largely due to dependence on inefficient diesel generators while renewable energy adoption remains minimal. Water consumption averaged 0.32 m³ per visitor-night (\approx 320 liters), exceeding the global threshold of 0.25 m³, reflecting limited implementation of water-saving and recycling technologies and a reliance on energy-intensive desalination. Solid waste generation was measured at 2.1 kg per visitor-night, approximately 1.4 times higher than the benchmark of 1.5 kg, with single-use plastics from hospitality services and religious offerings comprising the largest share; although waste is transported to the mainland, local recycling and treatment capacity remains weak. Greenhouse gas emissions averaged 0.012 tCO₂ per visitor-night (12 kg), 50% above the recommended threshold (<0.008 tCO₂), primarily driven by diesel-based electricity production and non-sustainable transport modes. Collectively, these findings underscore the urgent need for systemic interventions in energy, water, and waste management, alongside structural shifts toward low-carbon infrastructure and circular economy practices.

Table 2: Sustainability Indicators

Indicator	Con Dao Value	International Benchmark	Deviation (%)
Electricity (kWh/visitor-night)	28.0	20	+40%
Water (m ³ /visitor-night)	0.32	0.25	+28%
Solid Waste (kg/visitor-night)	2.1	1.5	+40%
CO ₂ (t/visitor-night)	0.012	<0.008	+50%

Source: Results of observation, statistics, comparison with UNWTO, 2024

The two weakest performance areas are energy and waste, underscoring structural deficiencies in renewable energy deployment and waste management capacity. While the absolute gaps may appear moderate, the cumulative impacts across hundreds of

thousands of visitor-nights annually are substantial. Therefore, phasing out diesel-based power, scaling up renewable energy adoption, and investing in integrated waste and water management systems are critical steps toward sustainable destination governance.

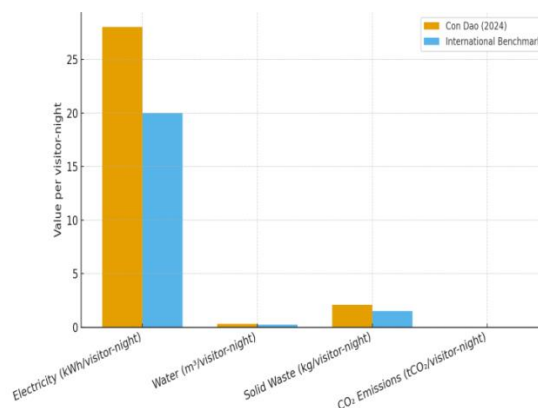


Figure 3. Comparison of Tourism Sustainability Indicators in Con Dao and International Benchmarks (GSTC Criteria)

Con Dao holds strong natural and cultural-historical assets for ecotourism, but benchmarking against the four GSTC pillars reveals persistent gaps: governance lacks quantitative monitoring and transparency; socio-economic benefits are unevenly distributed with limited community participation; cultural heritage use remains commercialized; and environmental management is weak, particularly in waste treatment and renewable energy adoption. While the island performs relatively well in biodiversity conservation and heritage protection, overall it only partially meets GSTC standards, with resource use intensity exceeding international benchmarks. These results, consistent with previous findings on limited transparency and weak cross-sector coordination in CDPN governance (Khuu et al., 2021), underscore the need for systemic reforms. Drawing on lessons from the Galápagos (visitor quotas and fees), Palau (“high value–low volume” strategy), and the Maldives (transition to renewables), three priorities are critical for Con Dao: establishing a quantitative monitoring system (SF-

MST/GSTC), investing in renewable energy and waste management, and strengthening community engagement while orienting tourism toward a “high-quality, moderate-volume” model.

Table 3. Assessment of Con Dao Tourism against GSTC Criteria

GSTC Criteria	Current Status in Con Dao	Compliance Level
Destination Management	Planning exists but lacks monitoring and periodic reporting	Not met
Socio-economic Benefits	Job creation but benefits unevenly distributed; limited community participation	Partially met
Cultural Heritage	Heritage well preserved but risk of commercialization	Partially met
Environment	Unique ecosystems but weak waste, water and renewable energy management	Not met

These findings underscore the ecological pressures and governance challenges facing Con Dao, highlighting the need for structural reforms in energy, waste, and community-based management, issues that will be explored further in the discussion of policy implications and strategic pathways for sustainable island tourism. The evaluation of Con Dao against international sustainability indicators reveals both its comparative advantages and persistent shortcomings. Despite its strong natural and cultural capital, the island’s rapid tourism growth has exposed structural weaknesses in governance, socio-economic benefit sharing, cultural heritage management, and environmental performance.

(1) Governance: Con Dao’s destination governance remains largely top-down, with limited quantitative monitoring or transparent reporting systems. The absence of a comprehensive SF-MST-based framework restricts evidence-based policymaking. Greater integration of multi-level actors and independent oversight is needed to ensure accountability and adaptive management. (2) Socio-economic benefits: Tourism has generated jobs and income, yet economic gains

are concentrated in external enterprises, while local community participation remains modest. Expanding community-based tourism models, homestays, and local supply chains could help distribute benefits more equitably, consistent with GSTC principles. (3) Cultural heritage: The island’s historical sites and spiritual landmarks are well preserved, but their use tends toward commodification rather than educational and community-oriented experiences. Reframing heritage tourism toward cultural interpretation and environmental education could enhance both authenticity and visitor learning. (4) Environmental management: Energy and waste indicators show the weakest performance, with high dependence on diesel power, limited renewable adoption, and inadequate recycling capacity. Transitioning toward renewable energy, strengthening water reuse technologies, and implementing circular waste systems are urgent priorities to reduce ecological pressures.

Overall, Con Dao demonstrates partial alignment with GSTC standards, performing strongly in biodiversity and heritage conservation but lagging in governance, benefit-sharing, and environmental systems. Lessons from the Galápagos, Palau, and the Maldives highlight the importance of carrying-capacity controls, high-value/low-volume strategies, and renewable energy transitions. For Con Dao, building a robust monitoring system (SF-MST/GSTC), investing in green infrastructure, and empowering community participation represent critical pathways to achieve sustainable island tourism.

CONCLUSIONS

Con Dao possesses substantial natural and cultural assets for ecotourism, yet it currently falls short of meeting global sustainability benchmarks. Core indicators related to electricity consumption, water use, solid waste, and CO₂ emissions all exceed recommended thresholds, highlighting the urgent need for integrated resource and environmental management. The combined application of the SF-MST and GSTC frameworks provides a

robust basis for evidence-based governance, improved resource efficiency, and more inclusive community development. To transition toward a sustainable island model, Con Dao should: (i) institutionalize systematic monitoring and reporting under SF-MST; (ii) invest in renewable energy systems and circular waste-management infrastructure; (iii) establish equitable benefit-sharing mechanisms for local communities; and (iv) adopt international best practices in visitor management.

This study advances the literature on island ecotourism by being among the first to operationalize the UNWTO's SF-MST framework and GSTC criteria in the Vietnamese context. While previous research on Con Dao has examined marine ecology, protected-area governance, and visitor behavior (Khuu et al., 2021; Tkachenko et al., 2022; Pham, 2024; Tuyen, 2025), no study has systematically benchmarked the island's tourism performance against international sustainability indicators. By integrating quantitative measurements of resource efficiency, environmental impacts, socio-economic benefits, and governance quality, this research provides empirical evidence that can inform policy design. The findings contribute theoretically by extending the application of global sustainability-assessment tools to small-island ecosystems and practically by offering actionable insights for sustainable tourism governance in Vietnam.

This study also faces several limitations, including the small survey sample size, the absence of longitudinal monitoring data, and restricted access to private-sector resource-use information. Future research should implement periodic SF-MST accounting, expand socio-economic impact analyses, and incorporate geospatial tools to monitor environmental pressures over time.

ACKNOWLEDGEMENTS

The authors gratefully acknowledge the support of local households engaged in tourism, hotels in Bai Sau, Vung Tau City, and

the local authorities. Their valuable contributions were essential to the completion of this study.

REFERENCES

- Con Dao National Park Management Board. (2021). *Ecotourism, resort, and recreation development plan for Con Dao to 2030* [in Vietnamese]. Con Dao National Park Management Board.
- Global Sustainable Tourism Council. (2024). *GSTC standards*. <https://www.gstc.org/gstc-criteria/>.
- Gössling, S. (2020). Tourism, resource use and environmental sustainability: A review. *Journal of Sustainable Tourism*. <https://doi.org/10.1080/09669582.2019.1667929>.
- Hayward, P., & Tran, G. T. H. (2014). At the edge: Heritage and tourism development in Vietnam's Con Dao archipelago. *Journal of Marine and Island Cultures*, 3(2), 113–124. <https://doi.org/10.1016/j.imic.2014.10.002>.
- Hieu, T. N., Huong, L. Q., & Do, A. D. (2023). Coral oasis on Con Dao Islands: A potential refuge of healthy coral ecosystems in Vietnam. *Biodiversity*, 15(1), 4. <https://doi.org/10.3390/biodiversity15010004>.
- Khuu, D. T., Jones, P. J. S., & Ekins, P. (2021). A governance analysis of Con Dao National Park, Vietnam. *Marine Policy*, 127, 103986. <https://doi.org/10.1016/j.marpol.2020.103986>.
- Pham, T. D. (2024). Assessment of factors influencing eco-tourism choice in Con Dao, Vietnam. *IOP Conference Series: Earth and Environmental Science*, 1349, 012035. <https://doi.org/10.1088/1755-1315/1349/1/012035>.
- Tkachenko, K. S., Dung, V. V., & Ha, V. T. (2023). Coral resilience in Con Dao Islands: Potential refuge in offshore Vietnam. *Diversity*, 15(1), 4. <https://doi.org/10.3390/d15010004>.
- Tuyen, T. (2025). Applying Circular Economy to Regenerative Tourism on Island: Insights from Con Dao, Vietnam. *International Journal of Qualitative Research*, 4(3), 274–284. <https://doi.org/10.47540/ijqr.v4i3.1771>.
- UNWTO. (2024). *Statistical framework for measuring the sustainability of tourism (SF-MST)*. United Nations World Tourism Organization.
- World Bank. (2021). *Vietnam: Plastic pollution diagnostics*. World Bank Group.

Methods for assessing environmental carrying capacity in tourism: A case study of Sa Pa National Tourist area

Quyen Ngo Thi¹, Truc Nguyen Ngoc^{1,*}, Huong Nguyen Thi Quynh²

¹VNU-School of Interdisciplinary Sciences and Arts, Vietnam National University, Hanoi

²Thuongmai University

*Email: trucnn@vnu.edu.vn

Abstract: Tourism growth has increasingly raised concerns about environmental overload, posing significant challenges to sustainable development. Environmental carrying capacity (ECC) provides a scientific framework for evaluating the threshold of ecosystems, infrastructure, and local communities under tourism pressures. This study reviews and synthesizes four widely applied approaches: Physical Carrying Capacity (PCC), Pollution Load Inventory, Limits of Acceptable Change (LAC), and Environmental Carrying Capacity assessment. Their conceptual foundations, advantages, limitations, and applicability to different destination types are systematically analyzed. Building on this framework, the research applies two selected methods, Pollution Load Inventory and ECC assessment, to the case of the Sa Pa National Tourism Center, Vietnam. Using field-based environmental data, carrying capacity indices (Lc, Lctb) were quantified for soil, surface water, and ambient air. The results indicate critical stress factors and spatial hotspots of environmental pressure, providing an evidence-based basis for management priorities. The findings underscore both the theoretical value and practical utility of carrying capacity assessment, contributing to the advancement of sustainable tourism planning and destination management in developing country contexts.

Keywords Environmental carrying capacity, Tourism carrying capacity, Sustainable tourism, Pollution load, Sa Pa tourism.

INTRODUCTION

In the context of rapid global tourism growth, environmental overloading has become a major barrier to achieving sustainable development goals. The surge in tourist arrivals, especially in ecologically and culturally sensitive areas, has intensified pressure on natural resources, ecosystems, and infrastructure (UNEP, 2003). In developing countries such as Vietnam, this challenge is more critical due to limited environmental management capacity within the tourism sector. Consequently, assessing environmental carrying capacity has become an essential tool for identifying the maximum level of ecosystem, infrastructure, and community tolerance to tourism impacts without degrading environmental quality or destination value (Coccossis & Mexa, 2004). Such assessments are not only academically important but also serve as a practical basis for aligning economic growth with resource conservation.

Globally, several approaches have been developed to quantify environmental carrying capacity, including Physical Carrying Capacity (PCC), pollution load inventories, Limits of Acceptable Change (LAC), and Environmental Carrying Capacity (ECC). Each offers unique strengths and limitations, collectively forming a scientific foundation for sustainable tourism management.

In Vietnam, despite tourism being a key economic driver, quantitative studies on environmental carrying capacity remain scarce, with most focusing on socio-economic or cultural aspects. Sa Pa, a major tourism hub

known for its mountain landscapes, temperate climate, and cultural diversity, faces growing challenges of infrastructure strain, pollution, congestion, and landscape degradation. Yet, as the core of a National Tourism Center, Sa Pa still lacks a comprehensive quantitative assessment of its environmental capacity. This highlights the urgent need for data-driven methods to identify environmental “hotspots” and develop effective management strategies for sustainable tourism.

Building on this context, the present study synthesizes and compares four key methods for assessing environmental carrying capacity and applies an integrated approach in the Sa Pa National Tourism Area. By combining pollution load inventory analysis with Environmental Carrying Capacity (ECC) assessment, the study quantifies ecosystem tolerance levels and demonstrates the practical applicability of these methods as a scientific basis for sustainable tourism management.

METHODS FOR ASSESSING ENVIRONMENTAL CARRYING CAPACITY

Physical carrying capacity (PCC) assessment method

One of the classical and most widely used quantitative approaches for evaluating the environmental carrying capacity of tourism destinations is the Physical Carrying Capacity (PCC) method. The standard formula, introduced and widely disseminated by UNWTO (1991), Cifuentes (1992), and UNEP & WTO (2005), is expressed as follows:

$$PCC = \frac{Aa}{a_a} \times Rf \times Mf$$

where: Aa is the total area actually available for tourism use (m^2). a_a is the average area occupied by one tourist at a given time ($m^2/person$). Rf is the rotation factor - the number of tourist turnovers possible per day. Mf is the modification factor - an environmental adjustment coefficient.

The Physical Carrying Capacity (PCC) method is a straightforward and easily applicable approach when quantitative data on

spatial area and tourism activity duration are available. It provides an estimate of the maximum number of visitors a destination can accommodate in a single day without causing spatial-use conflicts. However, PCC only reflects the general physical capacity for visitor reception and does not account for more subtle or long-term ecological impacts such as soil erosion or changes in vegetation cover. It also overlooks social and managerial dimensions, including visitor satisfaction, community acceptance, and management capacity. Therefore, PCC serves primarily as an initial reference and should be integrated with other assessment methods to achieve a more comprehensive evaluation of environmental carrying capacity.

Pollution load inventory method

Emission Factor-Based Pollution Load Inventory

This method enables the estimation of the total amount of pollutants generated from various socio-economic activities, such as tourism, residential areas, industry, transportation, and agriculture, and compares these emissions with the assimilative capacity of the receiving environment. The approach is based on standardized emission factors (WHO, 1993; UNEP, 1994) and has been adapted to national conditions through technical guidelines issued by the Ministry of Natural Resources and Environment (Decision No. 1074/QĐ-BTNMT, 2022).

The total pollutant load Q_i is calculated using the general equation:

$$Q_i = \sum_{j=1}^n (H_j \times EF_{ij})$$

where: Q_i is the total load of pollutant i (kg/year or tons/year); H_j is the activity level of source j (e.g., population, production volume, wastewater discharge, etc.); EF_{ij} is the emission factor of pollutant i from source j (kg per unit of activity); n is the total number of emission sources.

Emission sources are generally categorized into three groups: point sources (e.g., hotels,

processing facilities, industrial zones, hospitals), area sources (e.g., agricultural cultivation, small-scale livestock farming, dispersed residential areas, community-based tourism), and mobile sources (e.g., transportation and tourism vehicles).

The emission factor-based pollution load inventory method offers several advantages: it is simple, cost-effective, and time-efficient, making it suitable for conditions with limited monitoring data or when rapid estimation of pollutant loads over large areas is required. However, the accuracy of this method depends heavily on the reliability of the emission factors, which often represent average values and may not capture temporal variability or local characteristics. Furthermore, it does not allow for detailed analysis of pollutant composition, thereby limiting its overall precision and applicability in complex environmental assessments.

Direct measurement-based pollution load inventory method

The direct inventory method relies on field monitoring data to determine pollutant loads from individual emission sources with high accuracy. The general principle is to calculate pollutant loads based on measured discharge volumes and pollutant concentrations in air, water, or solid waste samples.

Point sources (e.g., centralized wastewater systems, production facilities, hotels, and tourism complexes). The pollutant load of substance i from source j is calculated as:

$$Q_{ij} = V_j \times C_{ij}$$

where: Q_{ij} is the load of pollutant i from source j (kg/year or tons/year); V_j is the total wastewater volume generated by source j (m³/year); C_{ij} is the concentration of pollutant i in wastewater (mg/L), determined through laboratory analysis.

Air emission sources (e.g., transport vehicles, combustion equipment, service facilities):

The pollutant load is estimated using the following formula:

$$Q_{ij} = G_j \times C_{ij}$$

where: G_j is the total exhaust gas volume (Nm³/year); C_{ij} is the concentration of pollutant i in the exhaust gas (mg/Nm³).

Solid waste sources. The total quantity of solid waste is determined through direct weighing, recording of transport frequency, or statistical estimation of daily, weekly, or monthly waste generation. Pollutant loads for key components (e.g., heavy metals, organic compounds) are identified through representative sample analyses. The measured pollutant loads are then compared with relevant national standards and technical regulations, including QCVN 08:2023/BTNMT for surface water, QCVN 05:2023/BTNMT for ambient air, and QCVN 07:2009/BTNMT for solid waste, to determine whether the receiving environment is within capacity, approaching its limit, or overloaded.

This method provides high accuracy and a realistic representation of actual emissions, making it particularly suitable for detailed studies in areas with concentrated tourism activities. However, it requires significant monitoring costs, laboratory infrastructure, and continuous data collection, which makes it difficult to apply to small or dispersed sources.

Limits of Acceptable Change (LAC) Method

The Limits of Acceptable Change (LAC) framework, developed by McCool and Stankey (1984), was designed to address the limitations of traditional carrying capacity approaches. Rather than determining a fixed maximum number of visitors, LAC focuses on managing the degree of environmental and social change that can be deemed acceptable at a destination. This method involves developing a set of indicators that reflect ecological, landscape, and socio-cultural conditions, followed by establishing acceptable thresholds of change for each indicator. When these thresholds are exceeded, corresponding management or restoration measures must be implemented.

The main strength of the LAC approach lies in its flexibility, making it particularly suitable for protected areas and national parks where maintaining a balance between conservation and tourism utilization is essential. However, its application is often complex and time-consuming, requiring the participation of multiple stakeholders and potentially being influenced by subjective judgments in determining what constitutes an “acceptable” level of change.

Limits of Acceptable Change (LAC) framework comprises nine iterative steps that balance conservation and tourism management in sensitive destinations. The process includes: defining management zones; setting objectives and desired ecological-social conditions; selecting monitoring indicators; establishing acceptable change thresholds; assessing current conditions; developing and implementing management strategies; and continuously monitoring, evaluating, and revising actions. This adaptive framework enables ongoing adjustment of policies based on observed changes, ensuring sustainable tourism and ecosystem integrity.

Ecological–environmental carrying capacity (ECC) method

This method was proposed by Professor Trần Nghi (Nguyễn Văn Nam, 2025), in which the carrying capacity is represented by a dimensionless index reflecting the relationship between the actual negative load and the maximum assimilative limit of the ecosystem.

The formula for calculating the carrying capacity index of a specific environmental component is defined as follows:

$$Lc = 1 - \frac{A}{B}$$

where: Lc is the carrying capacity index of a specific environmental component; A is the actual negative load (e.g., pollution, exploitation, erosion); B is the maximum carrying threshold that the component can assimilate without degradation.

The formula for determining the overall ecological–environmental carrying capacity index is expressed as follows:

$$Lctb = \frac{1}{n} \sum_{i=1}^n Lc_i$$

where: Lctb is the mean value of all individual Lc indices, representing the overall carrying capacity of the ecosystem; Lci is the carrying capacity index of each environmental component; n is the total number of components considered.

Since both A and B share the same dimension, the ratio A/B is dimensionless. When interpreting the Lc values, a positive Lc (> 0) indicates that the ecosystem is still capable of absorbing additional pressure without experiencing degradation, whereas Lc = 0 signifies that the ecosystem has reached its maximum absorption threshold. Conversely, a negative Lc (< 0) means that the negative load has surpassed the system’s carrying capacity. Based on the mean Lctb value, the overall carrying capacity level of the ecosystem can be classified into four categories: high (0.75–1.00), moderate (0.50–0.74), low (0.10–0.49), and overloaded (< 0.10).

This method is based on the integrated calculation of ecological, environmental, and social indicators to comprehensively assess the carrying capacity. Such an approach is particularly suitable for urban contexts, integrated tourism zones, or destinations where multiple influencing factors overlap. The strength of the ECC method lies in its ability to capture the interrelationships among the natural environment, technical infrastructure, and social perceptions, thereby providing a balanced and interdisciplinary assessment. However, its main limitation is the complexity of the indicator system, which requires extensive datasets and advanced analytical methods.

APPLICATION OF ENVIRONMENTAL CARRYING CAPACITY ASSESSMENT IN SAPA NATIONAL TOURISM AREA

Study area and scope

Sa Pa is one of Vietnam's key tourist destinations, renowned for its mountainous landscapes, temperate climate, and rich cultural diversity, attracting millions of visitors each year. However, the rapid expansion of tourism has exerted considerable pressure on local infrastructure and the environment, as evidenced by traffic congestion, solid waste accumulation, air pollution, and the potential degradation of natural landscapes. Therefore, this study focuses on assessing the environmental carrying capacity of the Sa Pa National Tourism Center based on field measurement data. The assessment covers the entire planned administrative boundary and considers three key environmental components: surface water (rivers, streams, lakes), soil (urban-service zones and open-air tourist sites), and air (residential-service areas, public squares, and transport corridors). In addition, several representative sub-basins and tourist sites are selected for detailed analysis.

Data Basis

Sampling

Sampling was conducted in 2024 within the central area of the Sa Pa National Tourism Center, covering approximately 6,090 hectares. This includes the existing core urban-tourism zone of Sa Pa (about 5,525 ha) and an expanded research area (around 565 ha). The sampling framework was designed to reflect the region's multidisciplinary development characteristics, where urban, service, tourism, construction, agricultural, and handicraft activities coexist. Sampling sites were distributed across five major functional subzones, focusing on three key environmental components: surface water, soil, and ambient air. A total of 45 samples were collected, including 15 surface water samples, 15 soil samples, and 15 air samples. Sampling campaigns were conducted during two representative periods (the high and low tourist seasons), coinciding with the peak

tourism and construction activities in Sa Pa. Procedures for sample collection, preservation, and transportation strictly followed laboratory QA/QC requirements to ensure data reliability and consistency.

Data Analysis and Processing

Environmental samples were analyzed in the laboratory using standardized parameter sets for each environmental component. For surface water, indicators included organic-nutrient parameters (BOD₅, COD, NH₄⁺, total N, total P, TSS, oil and grease, NO₂⁻), heavy metals (Cd, Fe, Ni, Hg, Pb, As, Mn, Cu, Cr, Zn), microbiological indicators (Coliform), and priority toxic substances (CN⁻, Phenol, Cr(VI)). Soil samples were analyzed for heavy metals (Pb, Cd, As, Hg, Cu, Zn, Cr, Ni), organochlorine compounds (DDT, Dieldrin, Endrin, Aldrin, Heptachlor), and PCBs. Air samples were tested for TSP, PM₁₀, PM_{2.5}, NO₂, and SO₂. For each environmental parameter, the analytical results from the 15 surface water samples, 15 soil samples, and 15 air samples were averaged. The resulting mean concentration was used as the representative value for the entire study area in subsequent calculations of the environmental carrying capacity indices. Post-analysis, all data were standardized by units, treated for values below detection limits, outliers were removed, and time-series consistency was verified. Results were compiled into a unified dataset covering all three environmental components, structured as follows: measured value (A) – regulatory threshold (B, following QCVN standards) – load capacity index (Lc) – evaluation classification. This served as the basis for calculating the environmental carrying capacity.

Method Selection

The environmental carrying capacity assessment for the Sa Pa National Tourism Area was conducted through a combination of two complementary approaches: pollution load inventory and environmental carrying capacity (ECC) computation. The pollution load inventory was implemented based on direct field measurements of environmental

parameters, supported by laboratory analyses to determine pollutant concentrations. The obtained results were spatially referenced to sub-basins or functional zones to ensure coherence with the specific receiving environments. The environmental carrying capacity was quantified using the index formula $L_c = 1 - A/B$, where A represents the observed pollutant concentration and B denotes the corresponding regulatory threshold according to the Vietnamese Environmental Quality Standards (QCVN 2023/BTNMT). For individual environmental components, $L_c > 0$ indicates remaining assimilative capacity, $L_c = 0$ marks the threshold limit, and $L_c < 0$ reflects an overloaded state. The L_{ctb} values were categorized into four levels: $L_{ctb} = 0.75-1.00$ indicates high carrying capacity; $L_{ctb} = 0.50-0.74$ reflects moderate carrying capacity; $L_{ctb} = 0.10-0.49$ denotes low carrying capacity; and $L_{ctb} < 0.10$ indicates an overloaded condition. L_c values for each pollutant parameter were aggregated to generate component-level indices (for water, soil, and air) using median or mean statistics. These component indices were subsequently integrated to calculate the composite ECC index (L_{ctb}), which characterizes the overall level of environmental load utilization across the entire study area.

The combined approach was chosen because the emission-inventory (pollution load) method provides a quantitative estimate of pollutant sources and loads (useful for targeting management actions), while the ECC index (L_c , L_{ctb}) translates those loads into the receiving environment's assimilative capacity and vulnerability. The inventory gives source-oriented diagnostics (where emissions come from and approximate magnitude), and ECC provides receptor-based interpretation (whether the environment can absorb those loads without degradation). Together they enable spatially-explicit prioritization (sub-catchment level), seasonal comparison, and actionable recommendations for wastewater treatment, solid waste control, and dust/traffic management in a data-limited, rapidly-developing tourism context such as Sa Pa.

Results of environmental carrying capacity assessment in the Sa Pa National Tourism Area

Carrying capacity of soil environment

For the soil environment, the negative load consists of harmful substances such as organochlorine compounds (total DDT, Dieldrin, Endrin, Aldrin, and Heptachlor) and heavy metals that contribute to soil pollution (Pb, Cd, As, Hg, Cu, Zn, Cr, Ni) (Table 1).

Table 1. Soil Carrying Capacity (L_c) for Toxic Elements Affecting Soil Quality in the Sa Pa National Tourism Area

No.	Pollutant Component	Unit	Measured Value (A)	Standard Threshold (B)	L_c
1	Pb	mg/kg	<1.3	200	0.994
2	Cd	mg/kg	<0.5	4	0.875
3	As	mg/kg	3.21	25	0.872
4	Hg	mg/kg	< 0.01	12	0.999
5	Cu	mg/kg	8.5	150	0.943
6	Zn	mg/kg	5.7	300	0.981
7	Cr	mg/kg	<3.2	150	0.979
8	Ni	mg/kg	1.2	100	0.988
9	DDT	mg/kg	0.0005	1.1	1.000
10	Dieldrin	mg/kg	0.0001	0.08	0.999
11	Endrin	mg/kg	0.0001	0.11	0.999
12	Aldrin	mg/kg	0.0001	0.04	0.997
13	Heptachol	mg/kg	0.0002	0.08	0.998
14	PCBs	mg/kg	0.005	1	0.995
Average load capacity of soil environment (L_{ctbs}): 0.973					

Based on the component-wise carrying capacity index (L_c), all 14 soil pollutants exhibit positive L_c values, indicating that none of the parameters exceed their regulatory thresholds. The lowest L_c values are observed in As ($L_c = 0.872$) and Cd ($L_c = 0.875$), yet both remain far above the critical limit of $L_c = 0$. Heavy metals such as Cu ($L_c = 0.943$), Zn (0.981), Cr (0.979), Ni (0.988), and Pb (0.994) also retain substantial assimilative margins relative to their thresholds. Organic pollutants including DDT ($L_c = 0.999$), Dieldrin (0.999), Endrin (0.999), Aldrin (0.998), Heptachlor (0.998), and PCBs (0.995) show very high carrying capacity, reflecting extremely low measured concentrations compared to permissible limits. When aggregated, the soil environment yields an overall carrying capacity index of $L_{ctbs} =$

0.973, corresponding to the “high carrying capacity” category (0.75–1.00). These results indicate that the soil environment remains well within its assimilative potential under current conditions.

Carrying capacity of surface water environment

The carrying capacity assessment of surface water in the central area of the Sa Pa National Tourism Site shows a pronounced imbalance among pollutant groups. Organic indicators exhibit the most critical exceedances: BOD₅ and COD yield negative carrying-capacity values ($L_c = -1.550$ and -0.560), confirming that the system has surpassed its assimilation limits for biodegradable organic matter. Nutrient parameters also reflect stress, with total P overloaded ($L_c = -0.200$), NH₄⁺ and Fe at their thresholds ($L_c = 0.000$), while total N retains

only moderate capacity ($L_c = 0.417$) and TSS shows a similar moderate condition ($L_c = 0.360$). In contrast, most heavy metals and hazardous substances remain well below regulatory limits, reflected in high or moderate L_c values such as Zn (0.964), Cd (0.900), Cr(total) (0.840), Cu (0.600), Mn (0.500), As (0.400), Pb (0.350), Hg (0.300), Ni (0.020), Cr(VI) (0.200), as well as oil and grease (0.802), CN- (0.800), phenol (0.800), and coliform (0.700). Despite this, the overall average carrying capacity of the surface water environment ($L_{ctbsw} = 0.345$) falls into the “low carrying-capacity” level, indicating that although most inorganic pollutants remain within acceptable limits, the system is significantly constrained by overload in key organic and nutrient parameters, which disproportionately depress the environmental resilience of the entire water body.

Table 2. Carrying capacity (L_c) of dissolved hazardous elements in surface water within the central area

No.	Pollutant Component	Unit	Measured Value (A)	Standard Threshold (B)	L_c
1	BOD ₅	mg/L	10.2	4	-1.550
2	COD	mg/L	15.6	10	-0.560
3	NH ₄ ⁺	mg/L	0.3	0.3	0.000
4	Total P	mg/L	0.12	0.1	-0.200
5	Total N	mg/L	0.35	0.6	0.417
6	Total oil & grease	mg/L	0.99	5	0.802
7	TSS	mg/L	16	25	0.360
8	NO ₂ ⁻	mg/L	0.003	0.05	0.940
9	Cd	mg/L	0.0005	0.005	0.900
10	Fe	mg/L	0.5	0.5	0.000
11	Ni	mg/L	0.098	0.1	0.020
12	Hg	mg/L	0.0007	0.001	0.300
13	Pb	mg/L	0.013	0.02	0.350
14	As	mg/L	0.006	0.01	0.400
15	Mn	mg/L	0.05	0.1	0.500
16	Cu	mg/L	0.04	0.1	0.600
17	Cr (total)	mg/L	0.008	0.05	0.840
18	Zn	mg/L	0.018	0.5	0.964
19	Coliform	MPN/ 100mL	300	1000	0.700
20	CN ⁻	mg/L	0.002	0.01	0.800
21	Phenol	mg/L	0.001	0.005	0.800
22	Cr(VI)	mg/L	0.008	0.01	0.200
Average load capacity of surface water environment (L_{ctbsw}): 0.345					

Carrying capacity of ambient air environment

The ambient air carrying capacity in the central area of the Sa Pa National Tourism Site remains generally moderate, with noticeable

differences among pollutants (Table 3). Particulate matter shows the strongest pressure: TSP ($L_c = 0.750$), PM₁₀ (0.670), and especially PM_{2.5} (0.636) indicate only moderate

resilience. In contrast, gaseous pollutants maintain higher capacity, with NO_2 (0.800) and SO_2 (0.760) reflecting relatively low emission pressure. The overall carrying capacity ($\text{Lctba} = 0.723$) is moderate, suggesting that while the air environment is not overloaded, fine particulate matter (particularly $\text{PM}_{2.5}$) remains the key limiting factor requiring attention.

Table 3. Load capacity (Lc) of selected hazardous substances in the ambient air of Sa Pa National Tourism Area

No.	Pollutant Component	Unit	Measured Value (A)	Standard Threshold (B)	Lc
1	TSP	mg/m^3	0.05	0.2	0.750
2	PM_{10}	mg/m^3	0.033	0.1	0.670
3	$\text{PM}_{2.5}$	mg/m^3	0.0164	0.045	0.636
4	NO_2	mg/m^3	0.02	0.1	0.800
5	SO_2	mg/m^3	0.03	0.125	0.760
Average load capacity of ambient air environment (Lctba): 0.723					

Overall Environmental Carrying Capacity of Sapa National Tourism Area

Table 4 presents the results of the overall environmental carrying capacity (ECC) assessment for the Sa Pa National Tourism Area. The overall environmental carrying capacity is 0.680, corresponding to a moderate level and revealing clear disparities among environmental components.

Table 4. Results of the overall environmental carrying capacity of SaPa National Tourism Area

Carrying capacity	Soil environment (Lcs)	Surface water environment (Lcsw)	Air environment (Lca)
Lci	0.973	0.345	0.723
Lctbsp	0.680		

The soil environment maintains a very high carrying capacity ($\text{Lctbs} = 0.973$) and therefore contributes almost no pressure to the system, while the ambient air shows a moderate capacity ($\text{Lctba} = 0.723$), mainly constrained by fine particulate matter ($\text{PM}_{2.5}$, PM_{10} , TSP). In contrast, surface water ($\text{Lctbsw} = 0.345$) is the dominant limiting factor, heavily influenced by severe overloads in key organic and nutrient indicators such as BOD_5 , COD,

and total phosphorus. To illustrate the relative contribution of each component to the overall environmental pressure, the carrying-capacity values were converted into assimilative-capacity deficits using the expression $(1 - \text{Lc})$. The results show that surface water accounts for 68.3% of the total environmental pressure, ambient air contributes 28.9%, and soil only 2.8%, indicating that most environmental stress in Sa Pa arises from the degradation of surface water quality rather than from soil or air. Consequently, the moderate overall carrying capacity of the area is chiefly governed by the constraints of the surface water environment.

The soil environment maintains very high carrying capacity and currently poses no constraint, though routine monitoring remains necessary to prevent risks associated with land-use change and tourism expansion. Surface water is the most critical limiting factor, with severe overloads in BOD_5 , COD, and total phosphorus indicating significant organic and nutrient pollution; priority actions should therefore focus on strengthening wastewater collection and treatment systems, improving drainage infrastructure, and reducing diffuse nutrient inputs. Ambient air shows moderate carrying capacity but is constrained by elevated particulate matter, suggesting the need for improved traffic regulation, better control of construction-related dust, and enhanced urban sanitation practices. Overall, environmental management efforts should concentrate on restoring water quality while gradually improving air conditions and maintaining the stable status of soil, thereby enhancing the area's overall environmental resilience and supporting sustainable tourism development.

CONCLUSION

This study reviews four major approaches to assessing environmental carrying capacity in tourism, Physical Carrying Capacity (PCC), Pollution Load Inventory, Limits of Acceptable Change (LAC), and the Environmental Carrying Capacity (ECC) framework based on Lc and Lctb indices. Each method contributes a different dimension to capacity assessment,

from quantifying spatial limits and pollutant loads to incorporating management thresholds and community-based standards. When integrated, these approaches form a complementary framework that enhances the precision and applicability of carrying-capacity evaluations. Applying the combined Pollution Load Inventory-ECC approach to the Sa Pa National Tourism Area using 2024 monitoring data, the results show an overall carrying capacity of $L_{ctbsp} = 0.680$, corresponding to a moderate condition with remaining room for development. However, the system is strongly constrained by the surface water environment ($L_{csw} = 0.345$), mainly due to overload of organic and nutrient indicators and several related toxic substances. Air quality maintains a moderate level ($L_{ca} = 0.723$), with fine particulate matter being the key limiting factor, while soil quality exhibits high carrying capacity ($L_{cs} = 0.973$), aside from slight accumulation of As and Cd.

These findings underscore the need to prioritize upgrades to wastewater treatment and urban drainage, enhance particulate-matter control in densely visited areas, and continue periodic soil monitoring to detect emerging risks. The integrated use of load inventories and ECC analysis demonstrates strong capacity to identify environmental pressures and spatial hotspots, providing a reliable scientific foundation for adaptive management. This combined framework offers substantial potential for application in other rapidly developing tourism destinations seeking to balance growth with environmental sustainability.

ACKNOWLEDGEMENTS

This research was funded by the scientific project following the Contract No. 02/2024/HDKHCN signed on July 30, 2024 between the Department of Science and Technology of Lao Cai province and the VNU-School of Interdisciplinary Sciences and Arts, Vietnam National University, Hanoi.

References

- Cifuentes M. (1992). Determinación de capacidad de carga turística en áreas protegidas (No. 194). Bib. Orton IICA/CATIE, Costa Rica.
- Coccossis H., Mexa A. (2004). The challenge of tourism carrying capacity assessment: Theory and practice. Ashgate Publishing Ltd., UK.
- McCool S. F., Stankey G. H. (1984). Limits of acceptable change: A new framework for managing the impacts of recreation. USDA Forest Service, General Technical Report INT-176.
- Ministry of Natural Resources and Environment. (2023). QCVN 03:2023/BTNMT – National Technical Regulation on Soil Quality. Natural Resources – Environment and Vietnam Map Publishing House, Hanoi.
- Ministry of Natural Resources and Environment. (2023). QCVN 08:2023/BTNMT – National Technical Regulation on Surface Water Quality. Natural Resources – Environment and Vietnam Map Publishing House, Hanoi.
- Ministry of Natural Resources and Environment. (2023). QCVN 05:2023/BTNMT – National Technical Regulation on Ambient Air Quality. Natural Resources – Environment and Vietnam Map Publishing House, Hanoi.
- Ministry of Natural Resources and Environment. (2022). Decision No. 1074/QĐ-BTNMT on the issuance of Guidelines for identifying and inventorying pollution-causing emission sources. Ministry of Natural Resources and Environment, Hanoi.
- Ministry of Natural Resources and Environment. (2017). Circular No. 76/2017/TT-BTNMT promulgating the procedure for assessing the load capacity and wastewater receiving capacity of surface water bodies. Ministry of Natural Resources and Environment, Hanoi.
- Nguyen Van Nam. (2025). Assessment of the Environmental Carrying Capacity of Phong Nha – Ke Bang Tourism. Doctoral Dissertation, VNU University of Science, Vietnam National University, Hanoi.
- Stankey G. H., Cole D. N., Lucas R. C., Petersen M. E., Frissell S. S. (1985). The limits of acceptable change (LAC) system for wilderness planning. USDA Forest Service, General Technical Report INT-176.
- United Nations Environment Programme. (1994). Pollution control and waste minimization in small- and medium-scale industries. UNEP, Nairobi.

United Nations Environment Programme. (2003). Tourism and Local Agenda 21: The role of local authorities in sustainable tourism. UNEP, Nairobi.

UNEP & WTO. (2005). Making tourism more sustainable: A guide for policy makers. United Nations Environment Programme and World Tourism Organization.

UNWTO. (1991). Guidelines: Development of national parks and protected areas for tourism. United Nations World Tourism Organization, Madrid.

World Health Organization. (1993). Environmental health criteria 143: Principles for evaluating health risks from chemicals during infancy and early childhood. WHO, Geneva.

Introduction of Novel technologies and models for on-site conversion of coal bottom ash and coal fly ash into high-value materials

Nguyen Ngoc Truc^{1*}, Do Xuan Duc¹, Ngo Thi Quyen¹, Dinh The Hien²

¹VNU-School of Interdisciplinary Sciences and Arts, Vietnam National University, Hanoi

²Hanoi University of Civil Engineering

*Email: trucnn@vnu.edu.vn

Abstract: This paper presents the results of research and development of novel technologies and models for on-site treatment of thermal power plant coal bottom ash (CBA) and coal fly ash (CFA) to produce high-value-added materials, thereby promoting a circular economy and reducing environmental pollution. Through surveys, experiments, and practical studies conducted on CBA and CFA sources from thermal power plants in Thai Nguyen, Quang Ninh, Ninh Binh, Ha Tinh, Vinh Tan, and Duyen Hai, the authors propose three specific application models: (1) production of artificial sand from CBA using selective fractionation and deactivation technologies, yielding products that meet the Vietnamese standard TCVN 7570:2006; (2) Recovery of residual coal, iron compounds, and silica minerals from CFA using a processing system with a capacity of 40 m³/hour, increasing the added value of CFA by 5.5 times; (3) Utilization of recovered silica minerals from CFA for the production of ceramic tiles, porcelain, dry mortar, and tile adhesives, achieving high product quality while reducing raw material costs and CO₂ emissions. The research confirms the technical, economic, and environmental feasibility of the proposed models, opening new pathways for industrial waste management and sustainable development in Vietnam's construction materials sector.

Keywords: Coal fly ash; Coal bottom ash; Artificial sand; Silica mineral; Residual coal.

INTRODUCTION

Coal bottom ash (CBA) from coal-fired power plants is a byproduct discharged from the furnace bottom during coal combustion and typically accounts for 15-50% of total coal combustion by-products. It consists of coarse and angular particles with a specific gravity of 1.8-2.5 g/cm³. In countries with developed thermal power industries such as China, the United States, India, and those in Europe, CBA has been widely studied and applied in construction, transportation, and environmental remediation. Japan reuses 100% of its coal combustion by-products, while South Korea and Taiwan achieve utilization rates of approximately 97% (Nguyen Van Nam, 2019).

CBA can replace natural sand, serve as sub-base and base course materials in road construction, and function as landfill cover or structural layers. When used as sand replacement, the workability and density of concrete vary depending on CBA characteristics (Kumar, Hemalatha, and Anadinni, 2015). Kumari and Thandavamoorthy (2017) demonstrated that CBA can be used in both conventional and high-performance concretes, achieving 28-day compressive strengths exceeding 70 MPa, tensile strengths over 5.56 MPa, and flexural strengths above 6.64 MPa with 25-75% sand replacement.

In Vietnam, approximately 33 coal-fired power plants generate more than 25 million tons of coal combustion by-products annually, with CBA contributing a significant fraction.

National standards such as TCVN 12249:2018, TCVN 12660:2019, and TCVN 8825:2011 emphasize the reuse of coal ash in filling materials, road subgrades, and roller-compacted concrete. Several studies have explored CBA's applicability: Vu Ba Thao et al. (2019) confirmed that CBA-based concrete meets technical requirements for rural pavement; CESTI (2019) reported technological trends for coal ash utilization in non-fired bricks, landfill materials, and concrete additives; and Dinh Quoc Dan et al. (2019) assessed geotechnical properties of coal combustion residues and proposed engineering solutions to enhance their reuse. Expanding CBA utilization supports environmental protection and circular economy development in Vietnam.

Coal fly ash (CFA), which typically represents 50-85% of total coal combustion residues, is collected from electrostatic precipitators during flue gas cleaning. CFA consists of fine spherical particles (0.5-300 μm). Major coal-based electricity producers such as China, the United States, and India generate large quantities of CFA (Heidrich et al., 2013). China has a CFA utilization rate of 67.96%, compared with 46.74% in the United States and 55.79% in India. Global CFA production is around 750 million tons annually and is expected to rise (Yao et al., 2015). Worldwide, about 50-60% of CFA is reused, with applications in concrete, geopolymers, adsorbents, zeolites, ceramics, and fertilizers (Yadav and Pandita, 2019). Recent research focuses on recovering silica, alumina, iron, and unburned carbon from CFA. Depending on coal type and combustion technology, CFA typically contains 5-15% iron, 5-40% unburned carbon, 40-60% silica, 20-40% alumina, and 0.5-15% calcium (Yadav et al., 2022). Carbon can be recovered via screening, gravity separation, electrostatic separation, flotation (Zhang et al., 2013), and oil agglomeration (Hower et al., 2017). Iron recovery is commonly performed using magnetic separation, and its characteristics have been documented using TEM, SEM-EDX, ESEM, Raman spectroscopy, XRD, and FTIR (Fulekar and Yadav, 2017). Xue

and Lu (2008) examined CFA iron particles via SEM-EDS and proposed magnetic separation methods. Silica recovery through alkaline dissolution (NaOH/KOH) has also been widely investigated, including in Vietnam (Vu Dinh Hieu & Bui Hoang Bac, 2019).

According to Vietnam's national power development plan (Decision No. 428/QD-TTg), by 2030 the country may operate about 70 coal-fired power plants with a total capacity of 75,000 MW, consuming 170 million tons of coal and generating about 38 million tons of coal combustion residues annually. The accumulated CFA and CBA is expected to reach 422 million tons. Currently, 50-60% of CFA is reused, mainly in cement production (41%), brick and tile manufacturing (26%), and concrete (19%), with the remainder used in road construction, embankments, agriculture, and the recovery of valuable minerals (Cao Van Thanh, 2021).

Although coal combustion by-products (CFA and CBA) have substantial utilization potential, Vietnam faces challenges in recognizing them as valuable resources and developing high-value reuse technologies. This study presents on-site treatment technologies and models for producing value-added materials, including: (1) using CBA to produce artificial sand; (2) recovering residual carbon, iron, and silica from CFA; and (3) applying recovered silica in dry mortar and tile adhesive production.

METHODOLOGY

To conduct this study, the author carried out field surveys and collected CFA and CBA samples from coal-fired power plants located in Thai Nguyen, Quang Ninh, Ninh Binh, Ha Tinh, Vinh Tan, and Duyen Hai. Approximately 20 kg of ash samples were collected from each plant for laboratory experiments. The evaluation of the potential utilization of CFA and CBA was performed through (1) analysis of their composition and physical characteristics, and (2) assessment and comparison of the products derived from ash utilization with equivalent natural materials.

In the study on artificial sand development, the author established a novel technological process for producing high-quality artificial sand, consisting of three main stages with seven technical steps, and has filed a patent application for this invention. The artificial sand was evaluated indirectly through concrete mixtures and hardened concrete samples incorporating the produced sand. The analysis was conducted using a series of tests, including alkali-silica reactivity, workability, compressive strength, and flexural strength of the concrete specimens.

In the study on utilizing CFA for the separation and recovery of residual carbon, iron, and silica minerals, the author developed a new technological process comprising six stages and thirteen technical steps, for which a patent application has been submitted. In this process, CFA samples were collected and analyzed in the laboratory to determine their mineralogical, chemical, and physical characteristics. Subsequently, residual carbon, iron, and silica minerals were separated and recovered using advanced materials and mineral processing techniques. Finally, the recovered products were analyzed for their mineralogical and chemical compositions to assess their potential applicability as raw materials for various industrial sectors.

Silica minerals are among the recovered products obtained from CFA. They are used as an essential fine aggregate component in the production of dry mortar and tile adhesive, helping to reduce the amount of cement and fine sand required while enhancing the workability and overall quality of the final products. This approach effectively lowers production costs without compromising, and in some cases even improving, product performance.

NEW TECHNOLOGY FOR CFA AND CBA TREATMENT TO PRODUCE HIGH-VALUE MATERIALS

Technology for CBA processing to manufacture artificial sand

In previous studies, researchers have identified several limitations of CBA that make

its direct use as a construction material impractical, representing the main difference between CBA particles and natural sand. CBA particles exhibit low mechanical strength, high swelling and reactivity, and significant heterogeneity, with angular shapes and elongated, flattened forms. Based on these observations, the authors proposed solutions to mitigate these drawbacks and enhance the applicability of CBA in the construction materials sector.

CBA shares many characteristics with natural sand. Figure 1 illustrates the particle size distribution curves of these materials. Compared with CBA, natural sand tends to be finer, as indicated by its higher cumulative passing percentage in the particle-size range below 1 mm and the steeper curve in the 0.1-1 mm interval. This suggests that CBA is more heterogeneous, containing a larger proportion of coarse and gravel-sized particles, whereas natural sand has a more uniform and finer particle structure.

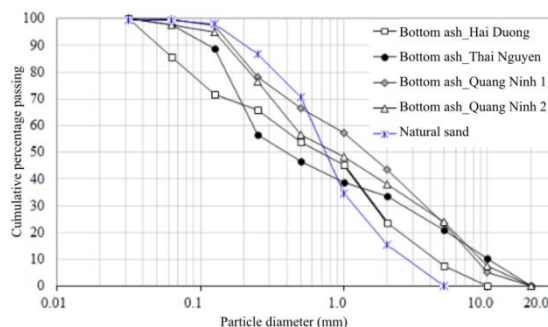


Figure 1. Particle size distribution curves of CBA and natural sand

The chemical composition analysis of CBA, presented in Table 1, shows considerable variability due to the use of different coal sources and types by thermal power plants. The oxides SiO_2 and Al_2O_3 constitute the largest fractions of CBA and play a key role in enhancing its quality when used as a construction material or in ceramic and tile production. Although CaO and MgO are present in lower proportions, they significantly increase the pH of the ash, sometimes up to 13. On one hand, these alkaline and alkaline-earth oxides can cause agglomeration, posing

challenges for artificial sand production as well as concrete and mortar manufacturing; on the other hand, they contribute to improved bonding in concrete and mortar. However, in reinforced concrete applications, free CaO represents a considerable risk and must be properly treated.

Table 1. Chemical composition of CBA

Component	Content (%)	Component	Content (%)
SiO ₂	34.40 - 62.30	CaO	1.00 - 19.67
Al ₂ O ₃	11.93 - 24.93	MgO	1.00 - 3.71
Fe ₂ O ₃	2.30 - 6.70	K ₂ O	0.25 - 3.18
TiO ₂	0.30 - 0.64	Na ₂ O	0.05 - 0.30
SO ₃	0.77 - 8.76	C	2.36 - 6.80

Based on the research, the author developed a “selective fractionation and deactivation” technology to address the inherent limitations of CBA, rendering its properties closer to those of natural sand. Treated CBA can thus be utilized to produce artificial sand as a substitute for natural sand. The produced artificial sand exhibits a particle size modulus ranging from 0.7 to 2.0 or from 2.0 to 3.3, suitable for use in concrete, masonry mortar, weak soil stabilization, or embankment filling. The proposed technology comprises three main stages encompassing seven technical steps.

In the first step, CBA particles are selected to match the grain size ranges permitted by current construction standards of TCVN 7570:2006, i.e. larger than 0.14 mm. The procedures in this step focus on removing oversized particles using a vibrating screen with a mesh size of 5.0 mm when producing artificial sand with a particle size modulus of 2.0-3.3, or a mesh size of 2.5 mm for a modulus of 0.7-2.0. Fine particles with diameters ≤ 0.14 mm are removed using a continuous centrifugal screening system. After selecting CBA in the particle size ranges of 0.14-5.0 mm or 0.14-2.5 mm, the material is transferred to the treatment tank in Step 2.

The second step is carried out in a treatment tank to reduce the reactivity and swelling potential of CBA. CBA contains significant amounts of alkali and alkaline-earth oxides, particularly free CaO and MgO, which generate a strongly alkaline environment upon contact with water, with leachate pH exceeding 10. Free CaO in CBA can be detrimental to construction materials, causing volumetric expansion, cracking, and structural damage in concrete and masonry due to the formation of Ca(OH)₂, which increases the alkalinity of concrete and can lead to steel reinforcement corrosion if the protective layer is compromised (TCVN 10302:2014). Concrete containing CBA with high free CaO content generally exhibits lower durability and is more susceptible to environmental degradation, including acid rain, seawater, or industrial chemicals. Free CaO also affects workability by altering the setting rate of concrete, reducing fluidity, or causing uneven hardening. The proposed solution is to convert free CaO into CaCO₃ instead of Ca(OH)₂. This is achieved by using a weak acid treatment, such as CO₂ gas sparging, to precipitate stable CaCO₃, thereby reducing alkalinity and the risk of volumetric expansion. Moist curing can be applied using NaHCO₃ (sodium bicarbonate) or CH₃COOH (acetic acid). All treatment processes are conducted in specially designed tanks. The treatment solution is injected directly into the interior of the CBA mass rather than sprayed on the surface, minimizing weak acid decomposition and enhancing the efficiency of the conversion reactions.

In the third step, after CBA has been treated, it is thoroughly mixed with natural sand (yellow or black sand) or crushed sand according to weight ratios calculated for specific applications, such as masonry mortar, finishing mortar, concrete, or embankment filling. Homogeneous mixing allows spherical sand particles to interpose between or fill the concave angles of CBA particles, enhancing the mechanical strength of the sand-ash composite, minimizing volumetric changes, and reducing particle elongation. The resulting artificial sand achieves a particle size modulus in the range of 0.7-2.0 or 2.0-3.3.

Technology for the recovery and production of residual carbon, iron, and silica minerals from CFA

CFA often contains a significant amount of unburned coal (residual carbon), iron and aluminum compounds, and silica minerals derived from clay and amorphous phases. When present in sufficient quantities, these components can be separated and recovered individually for use as fuel or high-value raw materials. This study presents a technology for the separation and recovery of valuable components from CFA to produce industrial raw materials and fuel within a closed-loop, zero-waste model. The recovered products using this technology include residual carbon, iron compounds, white silica (low iron), and gray silica (high iron). The proposed technology consists of six stages encompassing thirteen technical steps.

The recovery process of valuable components from CFA is carried out through six integrated steps. First, CFA is conditioned in a mixing tank with water and a collector agent (e.g., xanthate-based, dithiophosphate-based compounds, or oils) to optimize separation efficiency. Second, residual carbon is recovered via a four-stage flotation process, including rough, cleaning, scavenger flotation, and dewatering to produce purified carbon. Third, magnetic compounds are separated through high- and low-intensity magnetic separation to obtain the final iron product. Fourth, clean silica (low-iron) is recovered from the tailings of the high-intensity magnetic separator by settling, dewatering to $\leq 20\%$ moisture, and low-temperature drying. Fifth, iron-rich silica is obtained similarly from the tailings of the low-intensity magnetic separator through settling, dewatering, and drying. Finally, water from all process stages, including residual carbon and silica recovery, is collected and recycled, creating a closed-loop, zero-waste system.

PROPOSED NEW MODELS FOR HIGH-VALUE MATERIAL PRODUCTION FROM COAL THERMAL POWER PLANT CFA AND CBA AT SOURCE

Artificial sand in-situ production model

Several companies producing and trading concrete or construction materials have

attempted to use CBA directly as a substitute for natural sand; however, most of these attempts have been unsuccessful. Using the three-step process described above, we successfully produced artificial sand that meets the requirements of TCVN 7570:2006.

After producing the artificial sand, its performance was evaluated indirectly using concrete mixtures and hardened concrete specimens with artificial sand as fine aggregate (Figure 2). In this study, a concrete mix incorporating artificial sand with a particle size modulus of 2.5 was prepared. The mix composition consisted of 350 kg of PC40 cement, 1079 kg of 20 mm crushed stone, 787 kg of artificial sand mixed with 50% natural sand by weight, and 216 liters of mixing water. Tests were conducted on the fresh concrete, while the remaining mix was cast into hardened concrete specimens measuring $150 \times 150 \times 150$ mm for compressive strength testing and $150 \times 150 \times 600$ mm for flexural strength testing. The experimental results are presented in Table 2.

The measured properties of the fresh concrete meet the practical construction requirements for most general structures. The unit weight of concrete using artificial sand is only 2348 kg/m^3 , which is lighter than conventional concrete. The mix exhibits relatively high bleeding, while the slump after 30 minutes is low. These issues can be mitigated through the use of appropriate admixtures.

Table 2. Experimental results of fresh and hardened concrete using artificial sand as fine aggregate

Parameter		Unit	Value
Bulk density of concrete mix		(kg/m^3)	2348
Bleeding		%	0.41
Initial slump		cm	11.9
Slump after 30 min		cm	6.3
Alkali-silica reactivity	R_c	mmol/L	370
	S_c	mmol/L	31.8
	3 days		2.104
	7 days		3.104
Compressive strength	14 days	MPa	3.574
	28 days		3.997

Flexural strength	3 days	MPa	1.43
	7 days		1.56
	14 days		1.74
	28 days		1.85

The alkali-silica reaction tests on fresh concrete indicated that the artificial sand falls within the innocuous aggregate range, showing no potential for causing deleterious reactions. The flexural and compressive strengths of the hardened concrete specimens, cured for 14-28 days, were high and fully complied with the requirements of current construction standards.

The study results indicate that artificial sand produced from CBA using the above three-step process fully meets the technical requirements of current construction standards and can be applied in construction, transportation, and hydraulic engineering. The artificial sand is approximately 10% lighter than natural sand, and its cost is about 25% lower. The development of a full-scale artificial sand production model is entirely feasible from technical, economic, and environmental perspectives (Nguyen Ngoc Truc & Nguyen Van Vu, 2018).



Figure 2. Artificial sand and concrete specimens after compressive strength testing

Recovery and production of residual carbon, iron, and silica minerals from CFA model

In Vietnam, CFA is mostly used as a cement or concrete additive and for brick

production, yielding relatively low added value. Developing a model to recover residual carbon, iron, iron-rich silica, and clean silica from coal-fired power plant CFA not only diversifies the raw material supply for various industrial sectors but also significantly increases the added value of CFA. Therefore, this model holds substantial practical significance in the current Vietnamese context.

As mentioned above, the technology for recovering residual carbon, iron, and silica from CFA consists of six steps and 13 stages. We developed a practical model by designing and testing a pilot-scale processing system with a capacity of 40 m³ of CFA per hour to achieve optimal and thorough recovery of residual carbon, iron, and silica. Survey results indicate that CFA from most coal-fired power plants is compatible with this technology, particularly CFA from the provinces and city of Quang Ninh, Hai Phong, Ha Tinh, Binh Thuan, and Tra Vinh. In this study, CFA from a circulating fluidized bed coal-fired power plant in Quang Ninh was used as a case example.

The CFA has a bulk density of 0.8 t/m³. The processing system has a capacity of 40 m³/h (32 t/h) and operates 8 hours per day, equivalent to 256 t/day. The required water supply is 64 t/h (CFA to water ratio of 1:2), totaling 512 t/day. The collector used is fuel oil (FO), and the frother is pine oil. Both the collector and frother are emulsified prior to use.

The recovery of residual carbon is carried out through the primary, secondary, and scavenger flotation stages. The amount of clean coal recovered is 9.5%, corresponding to 3.04 t/h, or 24.32 t per 8-hour shift, with a moisture content of approximately 12% in the final product.

The recovery of iron-bearing compounds is performed using three optimally designed magnetic separators with magnetic intensities ranging from 1,000 to 12,000 Gauss to minimize silica losses. The recovered iron product is a fine powder or oxide, accounting for approximately 4.5% of the total CFA weight, corresponding to 1.44 t/h or 11.52 t per 8-hour

shift, with a moisture content of 8% and an iron content exceeding 35%.

The recovery of clean silica (iron-poor silica) is conducted downstream of the magnetic separator operating at 9,000-12,000 Gauss. The material is transferred to a settling tank, where environmental-balancing additives are added, excess water is removed, and clean silica is separated. Clean silica accounts for 73% of the total CFA weight, corresponding to 23.36 t/h or 186.88 t per 8-hour shift, with a moisture content of 12%. The residual iron content in the iron-poor silica ranges from 1.0 to 1.8%.

The recovery of iron-rich silica is carried out downstream of the magnetic separator operating at 1,000-1,500 Gauss. The material is transferred to a settling tank, where environmental-balancing additives are added, excess water is removed, and the iron-rich silica is separated. Iron-rich silica accounts for 13% of the total CFA weight, corresponding to 4.16 t/h or 33.28 t per 8-hour shift, with a moisture content of 12%. The residual iron content in the iron-rich silica can reach up to 4.5%.

The water recycling unit in the CFA treatment system operates continuously, collecting all water separated from the products as well as process wastewater, accounting for 35% of the total, corresponding to 179.2 t/day. This water is treated and purified on-site before being returned to the production cycle.

The products obtained from the model for processing, separating, and recovering residual coal, iron compounds, and silica minerals from 256 t/day of CFA according to the aforementioned process are summarized in Table 3. Images of the products are shown in Figure 3.

Table 3. Recovered products from 256 tons of CFA per day

Product	Proportion (%)	Weight (t)
Residual coal	9.5	24.32
Iron compounds	4.5	11.52
Clean silica	73.0	186.88
Iron-rich silica	13.0	33.28

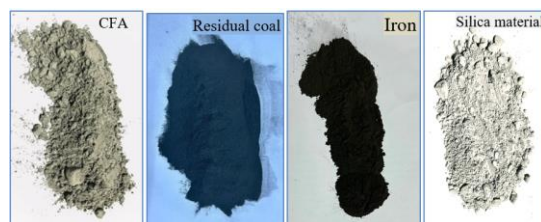


Figure 3. Images of recovered products from CFA

The recovered iron product is magnetic, with its main component being magnetite (Fe_3O_4). In contrast, the iron-rich silica contains iron primarily in the form of goethite ($\text{FeO}(\text{OH})$), siderite (FeCO_3), and a minor fraction of magnetite (Fe_3O_4). The characteristics of the residual coal and silica minerals are provided in Tables 4, 5, and 6.

Parameters such as ash content (dry basis), volatile matter (dry basis), total sulfur (dry basis), and calorific value are essential for assessing the quality and potential applications of the recovered products. As shown in Table 4, the calorific value is the most critical parameter for evaluating fuel potential. The experimental result of 5509 cal/g falls within the standard range of 4000-6500 kcal/kg. The recovered coal is classified as 6b middling coal.

Table 4. Analysis results of residual coal recovered from CFA

Average Content of Analytical Parameters in Coal Samples (%)				
Q_{pt} (cal/g) - Gross calorific value	A_{pt} - Ash content (dry basis)	V_{pt} - Volatile matter (dry basis)	S_{k} - Total sulfur (dry basis)	P_{pt} - Phosphorus content
5509	28.0	0.89	0.33	0.002

Table 5. Chemical composition analysis of silica recovered from CFA

Analytical Parameter	Parameter	Clean Silica	Iron-rich Silica
Content (%)	SiO_2	61.01	56.71
	Al_2O_3	26.73	25.06
	TiO_2	0.98	0.99
	Fe_2O_3	1.62	4.40

FeO	0.64	1.10
CaO	1.46	2.12
MgO	1.14	1.76
K ₂ O	4.62	4.20
Na ₂ O	0.25	0.20
MnO	0.04	0.09
P ₂ O ₅	0.33	0.40
SO ₃	0.15	0.11
MKN	0.50	1.27

Table 6. Mineralogical composition analysis of silica recovered from CFA

- Sample type: Clean silica mineral	Mineral composition	Approximate content (%)
	Quartz, SiO ₂	20 - 22
	Mullite, Al ₆ Si ₂ O ₁₃	17 - 19
	Illite, KAl ₂ [AlSi ₃ O ₁₀](OH) ₂	≤ 1
- Equipment: D8 Advance	Kaolinite and Chlorite	1 - 3
- Method error: ±2%	Amorphous phase	58 - 62

Based on the Rietveld analysis of the recovered silica, there is no significant difference in mineral composition between the iron-poor silica and the iron-rich silica. The main distinction lies in the content of iron-containing compounds.

The average yields of products obtained from the above model are presented in Table 7. It can be observed that the separation and recovery model for residual coal, iron, and silica minerals increases the added value of CFA by approximately 5.5 times (assuming an average CFA price of 100,000 VND/ton).

Table 7. Average yields and value of products separated and recovered from 256 tons of CFA per day

Recovered Product	Weight (t)	Unit Price (VND/t)	Total Value (VND)
Residual coal	24.32	1,400,000	32,648,000
Iron powder ore	11.52	600,000	6,912,000
Clean silica	186.88	500,000	93,440,000
Iron-rich silica	33.28	200,000	6,656,000
Total	256.0		141,056,000

The above analysis demonstrates that the development of a model for recovering unburned coal, iron compounds, iron-rich silica, and high-purity silica from CFA of coal-

fired power plants is scientifically, technically, and technologically feasible, while also being economically and investment-wise viable.

Models for utilizing silica minerals to produce construction materials, ceramic tiles, and porcelain

Use of recovered silica minerals from CFA for ceramic tile and porcelain production

Silica minerals recovered from CFA possess high SiO₂ content (over 60%), high purity, and fine, stable particle structures, making them highly suitable as the primary raw material for ceramic tile and porcelain production.

The application model is implemented through the following steps:

Classification and refinement of silica: Silica is separated from CFA using magnetic separation and chemical treatment, followed by drying to achieve a stable particle size below 75 μm.

Batch preparation: The refined silica is mixed with other raw materials such as kaolin, feldspar, and clay in appropriate proportions to form a homogeneous mixture for ceramic tile or porcelain production.

Shaping and forming: The mixture is shaped by semi-dry pressing or extrusion, then dried and fired at temperatures ranging from 1000-1250°C, depending on the product type.

Quality evaluation: Fired products exhibit high whiteness, good mechanical strength, water resistance, and thermal durability, meeting TCVN standards for ceramic tiles and porcelain (TCVN 13113:2020).

The recovered silica is bright white, has low iron content, high alumina and alkali levels, and uniform fine particles, making it particularly suitable for the proposed model. Using CFA-derived silica for ceramic and porcelain production offers multiple advantages, including reduced raw material costs, utilization of readily available CFA at thermal power plants, decreased CO₂ emissions, and promotion of a circular economy.



Figure 4. Images of recovered silica and ceramic products produced using the material

Utilization of silica minerals for the production of dry mortar and tile adhesives

Silica recovered from CFA can partially replace fine sand and cement in the production of dry mortar and tile adhesives due to its pozzolanic activity and high fineness.

The application model involves several steps. First, raw material preparation: the recovered silica is blended with cement, fine sand, polymer additives, and bonding enhancers in optimized proportions. Second, dry mixing and packaging: the mixture is thoroughly mixed using industrial mixers and then packaged as a dry powder. The final product can be applied directly on construction sites, requiring only the addition of water to form the mortar or tile adhesive.

The resulting dry mortar exhibits a bonding strength of ≥ 0.8 MPa and a setting time compatible with practical construction requirements. The tile adhesive achieves a slip of < 0.5 mm and a tensile strength after water immersion of ≥ 1.0 MPa. The inclusion of silica allows a reduction of cement usage by up to 15%, lowering the product cost by 10-20%.

This model for utilizing silica recovered from CFA in the production of dry mortar and tile adhesives offers significant benefits. Beyond technical advantages, environmental benefits include reduced extraction of natural sand, lower particulate and greenhouse gas emissions, and improved efficiency in using CFA as a resource. Both

application models demonstrate the high potential of enhancing the value of silica recovered from CFA while promoting sustainable development in the construction materials sector in Vietnam.

CONCLUSIONS

Based on both scientific and practical investigations, this study demonstrates the feasibility and effectiveness of developing new technologies and in-situ models for processing coal-fired power plant CFA and CBA to produce higher-value materials. Three specific application models were successfully developed:

First, the artificial sand production model from CBA uses the “segmented selection and deactivation reduction” technology to produce artificial sand meeting TCVN 7570:2006 standards, with appropriate particle size distribution, lower bulk density compared to natural sand, approximately 25% lower cost, and excellent compressive and flexural strength in concrete, fully complying with current standards. Second, the recovery model for residual coal, iron compounds, and silica minerals from CFA was established with a system comprising 20 modules and a processing capacity of 40 m³/h (32 t/h). The results show that the proposed technology and equipment system can effectively recover useful components from CFA, including residual coal, iron compounds, clean silica, and iron-rich silica, increasing the added value of CFA by approximately 5.5 times. Third, silica minerals recovered from CFA can be effectively applied in the production of ceramic tiles, porcelain, dry mortars, and tile adhesives. The resulting products demonstrate high quality, reduced raw material costs, improved resource utilization, and environmental emission reduction. This research not only provides a new approach for industrial waste management but also contributes to promoting a circular economy and sustainable development in Vietnam’s construction materials sector.

ACKNOWLEDGEMENTS

This research was funded by Vietnam National University, Hanoi, under grant number QG.24.62, "Perfecting technology for separating and recovering coal, iron, and silica minerals from fly ash of coal-fired thermal power plants in Vietnam towards large-scale raw material production".

REFERENCES

- Cao Van Thanh. (2021). Study on the production of high-strength concrete using a large amount of fly ash. Master's thesis, Hanoi University of Civil Engineering, Faculty of Materials Engineering.
- Center for Science and Technology Information and Statistics (CESTI) (2019). Trend Analysis Report: Application Trends of Coal Fly Ash and Bottom Ash in the Production of Construction Materials. Ho Chi Minh City Department of Science and Technology, Ho Chi Minh City, Vietnam. March 2019.
- Dinh Quoc Dan, Doan The Tuong, Do Ngoc Son. (2019). Using thermal power plant ash as backfilling material. *Journal of Construction Science & Technology - Geotechnics*, IBST, 1(2019), 35-44.
- Fulekar M. H., Yadav V. K. (2017). Method for separation of ferrous, alumina and silica from fly ash. Patent No. 201721035720.
- Heidrich C., Feuerborn H. J., Weir A. (2013). Coal combustion products: A global perspective. In *World of Coal Ash (WOCA) Conference*, April 22-25, 2013, Lexington.
- Hower J. C., et al. (2017). Coal-derived unburned carbons in fly ash: A review. *International Journal of Coal Geology*, 179, 11-27.
- Kumar K. N. V., Hemalatha B. R., Anadinni S. B. (2015). Study on strength of concrete using fly ash and bottom ash as a partial replacement for cement and sand. *International Journal of Informative & Futuristic Research (IJIFR)*, 2(7), 2344-2335.
- Kumari S. L., Thandavamoorthy S. (2017). Development of high performance concrete using bottom ash as fine aggregate. *International Journal of Civil Engineering and Technology (IJCIET)*, 8(12), 354-361.
- Nguyen Van Nam. (2021). Treatment of fly ash and bottom ash from coal-fired power plants: Issues raised in environmental protection work. URL: <https://nnmt.net.vn/xu-ly-tro-xi-cua-cac-nha-may-nhiet-dien-than-nhung-van-de-dat-ra-trong-cong-tac-bao-ve-moi-truong> [Last accessed: 14 November 2025].
- Nguyen Ngoc Truc, Nguyen Van Vu. (2018). Partial replacement of natural sand by granulated blast furnace slag (GBFS) in fine aggregate for concrete: Practical application in Vietnam. *SGEM 2018*, 18(1.2), 523-530. DOI: 10.5593/sgem2018/1.2/S02.066.
- Vietnam Ministry of Science and Technology (2014). TCVN 10302:2014 - Fly ash for use as an active mineral admixture in concrete, mortar, and cement. Ministry of Science and Technology, Vietnam.
- Vietnam Ministry of Science and Technology (2020). TCVN 13113:2020 (ISO 13006:2018) - Ceramic tiles: Definitions, classification, characteristics and marking. Ministry of Science and Technology, Vietnam.
- Vu Ba Thao, et al. (2019). Study on the use of bottom ash from the Nhan Co Dak Nong alumina thermal power plant for cement concrete pavement. *Journal of Hydraulic Science and Technology*, 57, 2019.
- Vu Dinh Hieu., Bui Hoang Bac. (2019). *Journal of Mining and Geology Engineering*, 60(1), 26-33.
- Xue Q. F., Lu S. G. (2008). Microstructure of ferrospheres in fly ashes: SEM, EDX and ESEM analysis. *Journal of Zhejiang University Science A: Applied Physics & Engineering*, 9, 1595-1600.
- Yadav V. K., et al. (2022). Status of coal-based thermal power plants, coal fly ash production, utilization in India and emerging applications. *Minerals*, 12(12), 1503.
- Yadav V. K., Pandita P. R. (2019). Fly ash properties and their applications as a soil ameliorant. In: Rathoure A. K. (ed.), *Amelioration Technology for Soil Sustainability*. IGI Global, Hershey, PA, USA, pp. 59-89.
- Yao Z. T., et al. (2015). A comprehensive review on the applications of coal fly ash. *Earth-Science Reviews*, 141, 105-121. DOI: 10.1016/j.earscirev.2014.11.016.
- Zhang H., et al. (2013). Cyclonic-static micro-bubble flotation column. *Minerals Engineering*, 45, 1-3.

DOI: 10.15625/vap.2025.0202

Influence of twin stacked tunnels excavation on pile behavior – A case study in Ho Chi Minh City

Tien Nguyen Tai^{1,2,*}, Vi Pham Van³, Chuong Phan Hoang⁴

¹Hanoi University of Mining and Geology, Hanoi, Vietnam

²Tunneling and Underground Space Technology Research Team, Hanoi University of Mining and Geology, Vietnam

³Electric Power University, Hanoi, Vietnam

⁴Construction Appraisal and Consulting Co., Ltd. No. 9, Ho Chi Minh, Vietnam

*E-mail: nguyentaitien@humg.edu.vn

Abstract: The expansion of the economy has generated a growing demand for transportation infrastructure, particularly in large metropolitan areas. The development of metro tunnel systems has emerged as an inevitable solution in such contexts, where surface space is constrained. However, constructing metro tunnels beneath areas where surface structures are already in place poses significant engineering challenges. Tunnel excavation alters the stress state within the soil mass and induces ground displacements surrounding the tunnel. These displacements subsequently propagate upward to the ground surface, resulting in surface settlement that can adversely affect the stability of superstructures as well as the performance of their foundation systems. In this study, the influence of tunnel excavation on pile foundations of surface buildings is investigated under the geotechnical conditions of the Ben Thanh–Suoi Tien metro line in Ho Chi Minh City. A numerical model representing twin stacked tunnels and a building with pile foundations was first established. The settlement results obtained from the numerical simulation were validated against field monitoring data. Subsequently, the effects of tunnel excavation on different piles of the building were examined. In addition, the influence of the relative distance between the tunnel alignment and the pile foundations was analyzed. The results indicate that, at the same relative distance between the tunnel and the pile group

(1D), the farther a pile is from the tunnel, the smaller the influence on its behavior. The greater the distance between the tunnel and the pile group, the smaller the impact. When the tunnel is more than 3D away from the pile group, the influence becomes negligible. The outcomes provide valuable insights into soil–structure interaction during urban tunneling, thereby contributing to safer and more sustainable underground infrastructure development.

Keywords: Pile behavior, twin stacked tunnels, Ho Chi Minh.

INTRODUCTION

According to the Hanoi Transport Master Plan (Decision No. 519/QĐ-TTg, 2016), the urban railway network is planned to comprise 10 lines with a total length of up to 417.8 km by 2030, with a vision toward 2050. Similarly, under the Ho Chi Minh City Master Plan for the period 2021–2030 with a vision to 2050 (Decision No. 1711/QĐ-TTg, 2024), the urban railway network is designed to consist of 12 lines, with a cumulative length reaching approximately 510 km. A substantial portion of these urban railway lines is planned to run underground, particularly in densely built-up areas. The construction of these tunnels inevitably induces ground surface settlement, which in turn may adversely affect surface structures and their foundation.

Tunnel construction in proximity to pile foundations of existing buildings can significantly influence pile performance. This issue has been investigated using various approaches, including numerical modeling (Maji & Sundar, 2021; Lee, 2012; Surjadinata et al., 2006), analytical methods (Li et al., 2023; Abd-Elhamed, 2021; Marshall & Haji, 2015; Huang et al., 2009), and experimental studies (Lim et al., 2023; Ng et al., 2012; Selemetas, 2005; Poulos et al., 2000). The pile–tunnel interaction is primarily governed by factors such as ground displacements, soil properties, pile geometry, the relative position between the tunnel and the pile and tunneling methods. Understanding these factors is critical for ensuring both tunneling stability and the integrity of overlying structures.

The relative position of the tunnel with respect to the pile is a key determinant of pile–tunnel interaction. Studies by Jongpradist et al. (2013) and Soomro et al., (2017) demonstrated that pile lateral displacement and bending moment increase considerably when tunneling occurs within a distance of $1.5\text{--}2D$ (where D is the tunnel diameter). Conversely, Al-Omari et al. (2019) reported that when the tunnel–pile clearance exceeds $2.5D$, tunneling-induced effects on piles diminish significantly. Based on these findings, Su et al. (2025) recommend a minimum tunnel–pile clearance of $2D$ to $2.5D$ to ensure structural safety.

Soil conditions also play a crucial role in tunnel–pile interaction mechanisms. In sandy soils, piles tend to undergo pronounced lateral displacement as the tunnel face approaches, due to rapid drainage and stress redistribution leading to immediate settlement (Jacobsz et al., 2004). In contrast, tunneling in clayey soils initially causes short-term heave, followed by long-term consolidation settlement that progressively drags piles downward (Chen et al., 1999).

It is evident that tunneling under varying geological conditions results in distinct ground responses, which in turn induce different

structural behaviors in the pile foundations of existing buildings. The Ben Thanh–Suoi Tien metro line, the first urban railway constructed and operated in Ho Chi Minh City, includes a 2.6 km underground section. Existing studies (Do et al., 2021; Hieu et al., 2019; Nguyen, et al., 2023) have primarily focused on tunneling-induced ground settlement along this metro line. Lam et al. (2022) compared surface settlement predictions derived from Hardening Soil and Mohr–Coulomb soil models.

Overall, no prior research has comprehensively assessed the effects of tunneling on pile foundations of surface structures under the ground conditions of the Ben Thanh–Suoi Tien line in Ho Chi Minh City. The present study aims to evaluate tunneling-induced impacts on piles in a representative building and to examine how tunnel–pile spacing influences pile structural behavior.

NUMERICAL MODELING AND VERIFICATION

The Metro Line No. 1 (Ben Thanh – Suoi Tien) has a total length of 19.7 km with 2.6 km underground. The line was completed and put into operation in 2024. The tunnel section was excavated using the Earth Pressure Balance (EPB) shield machine, with a cutterhead diameter of 6.82 m and an outer shield diameter of 6.79 m. This section, extending 780 m from Km 0+805 to Km 1+586, comprises twin tunnels initiated at Ba Son Station (Km 1+586) at the same elevation, which gradually shift into a stacked configuration and terminate at the Opera House Station (Km 0+805). The tunnels were constructed at maximum and minimum depths of 25 m and 12 m, respectively (measured from the tunnel centerline). The geotechnical parameters of the soil layers are presented in Table 1. The outer and inner diameters of the tunnel lining are 6.65 m and 6.35 m, respectively, with a segmental ring width of 1.2 m. The mechanical properties of the tunnel lining are summarized in Table 3 (Shimizu – Maeda., 2016).

Table 1. Geotechnical properties

Parameter	BackFill	Alluvial Clay (AC)	Alluvial Sand (ASi)	Diluvial Sand (AS2)	Diluvial Clay (DC)
Unit weight, γ_{unsat} kN/m ³	19.00	16.50	20.50	20.50	21.00
Young Modulus E, kPa	10×10^3	-	-	-	85×10^3
E_{50}^{ref} , kPa	-	5,600	15×10^3	27.3×10^3	-
$E_{\text{oed}}^{\text{ref}}$, kPa	-	4,049	15×10^3	27.3×10^3	-
$E_{\text{ur}}^{\text{ref}}$, kPa	-	11.25×10^3	45×10^3	81.9×10^3	-
Cohesion, c_{ref} kPa	10.00	11.4	1	1	1
Friction angle, ϕ (degree)	25.00	17.1	31	34	35
Dilatancy angle, ψ (degree)	0	0	1	4	5

Table 2. Input parameters of pile (embedded beam rows)

Parameter	Symbol	Unit	Value
Young Modulus	Ep	MPa	46×10^6
Unit weight	γ	kN/m ³	25
Diameter	D	m	0.3
Base resistance	Fmax	kN	309
Axial skin resistance at the pile bottom	-	kN/m	145

Table 3. Input parameters of plate element

Parameter	Unit	Lining	Pile cap	Building Frame	Floor slab
Flexural stiffness, EI	kN/m	78.75×10^3	312.5×10^3	107.2×10^3	54.88×10^3
Axial stiffness, EA	kN.m ² /m	10.5×10^6	15×10^6	10.50×10^6	8.4×10^6
Thickness, d	m	0.3	0.5	0.35	0.28
Unit weight, w	kN/ m ³	7.5	12.50	8.750	7.0
Poisson, ν		0.15	0.15	0.15	0.15
Parameters	Unit	Lining	Pile cap	Building Frame	Floor slab

In this study, the construction conditions at chainage Km 1+023 were selected as the reference case. The groundwater level at the site is -2.0 m from the ground surface. The numerical model was developed using Plaxis 2D, a finite element method (FEM)-based program. The model domain dimensions were set to 200 m in width (X-direction) and 45 m in height (Y-direction). For the boundary conditions, the bottom model was fixed in both vertical and horizontal directions, the lateral boundaries were fixed in the horizontal direction, while the top boundary was free in both vertical and horizontal directions (Plaxis - Bentley Systems, 2020).

The simulation stages are as follows:

Initial: Establishment of initial parameters and definition of boundary conditions;

Phase 1: Excavation and lining installation of the lower tunnel;

Phase 2: Application of the volume loss (VL) for the lower tunnel;

Phase 3: Excavation and lining installation of the upper tunnel;

Phase 4: Application of the volume loss (VL) for the upper tunnel.

In this study, a volume loss of VL = 0.88% was adopted, corresponding to the volumetric discrepancy between the outer diameter of the cutter head (6.82 m) and the outer diameter of the shield (6.79 m) (Plaxis 2D, Manual). The model was assumed under greenfield conditions. Figure 1 illustrates the results obtained from the numerical model compared with field measurement data. The findings indicate that the maximum settlement

predicted by the numerical model is only marginally higher than the field measurements, by approximately 6.6%, corresponding to 23.78 mm and 22.30 mm, respectively. Therefore, the numerical model can be considered a reliable tool for further parametric studies and predictive analyses.

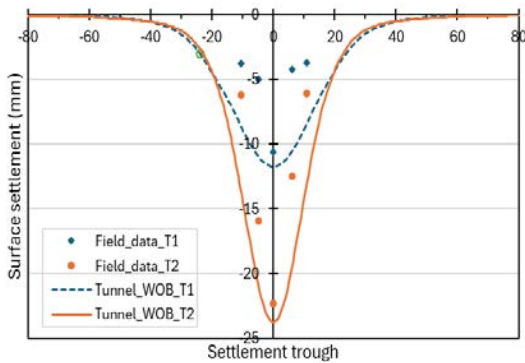


Figure 1. Comparison of settlement obtained from numerical model and field measurements

INVESTIGATION OF PILE FOUNDATION RESPONSE

As previously discussed, tunneling in densely built-up urban areas inevitably influences the performance of surface structures and their foundation. In this study, the reinforced concrete pile foundations are considered. The piles, with a diameter of 0.30 m and a length of 21.3 m, are modeled using the embedded beam element approach, and their properties are summarized in Table 2.

The superstructure is represented by a 9-story building with an overall height of 31.5 m and a single basement level extending to a depth of 3.0 m (Figure 2). The building frame, floor slabs, and pile cap are modeled as plate elements, with the corresponding input parameters listed in Table 2.

The simulation stages follow the same procedure as the reference case. However, in this scenario, the building and its pile foundation are constructed prior to the subsequent tunnel excavation. At the stage corresponding to the underground tunnel excavation, the displacements induced by the earlier construction of the building and piles

are removed (i.e., they are not carried forward into the tunneling stage).

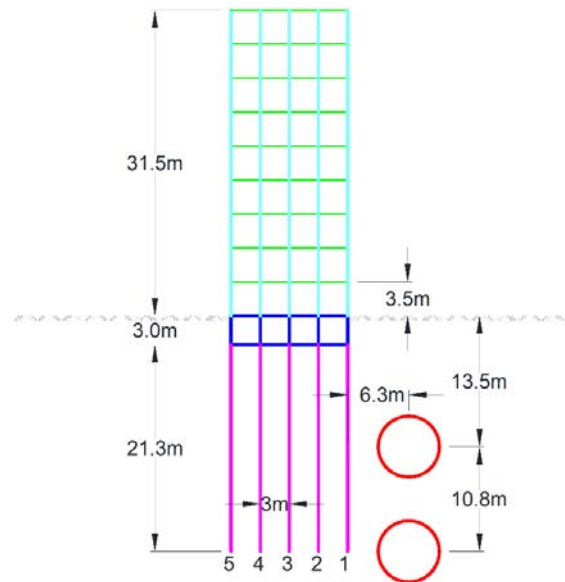


Figure 2. A case study of twin stacked tunnels, a building, and its foundation

Pile behavior under tunnel construction

In this scenario, the horizontal distance between the tunnel centerline and the building is set to 1D ($D = 6.3$ m). The response of piles 1 through 5 was analyzed in order to assess the potential impacts of tunnel excavation on pile foundations within a representative building. All other input parameters were kept consistent with those in the reference case to ensure comparability. The numerical results, in terms of the maximum and minimum bending moments and normal forces are summarized in Table 4 and illustrated in Figure 3, 4.

Prior to tunnel excavation (i.e., after pile installation), the results indicate that the bending moment in the central pile (Pile 3) was the smallest, whereas the two outer piles experienced the largest moments, exhibiting a symmetric distribution.

For Pile 1, the maximum bending moment (M_{max}) decreased from 25.47 kN after pile installation to 22.83 kN with the lower tunnel excavation and further to 15.34 kN with the upper tunnel. This trend suggests that tunnel construction leads to a reduction in peak

bending moments due to load redistribution, as the surrounding soil tends to move toward the tunnel. In Pile 2, M_{max} also dropped sharply from 12.26 kN to 2.796 kN during the upper tunnel excavation. By contrast, changes in Piles 3–5 were minor, indicating that the tunnel–pile interaction effect diminishes with increasing distance from the tunnel.

Regarding the minimum bending moment (M_{min}), Pile 1 exhibited a transition from a negative value (−6.561 kN) after pile installation to positive values (8.442 kN and 5.456 kN) during the lower and upper tunnel excavations, respectively. This reversal of moment direction

can be attributed to lateral soil movement toward the tunnel. For Piles 2–5, M_{min} remained negative, with larger magnitudes observed for piles located farther from the tunnel (e.g., Pile 5: from −25.89 kN to −30.84 kN during lower tunnel excavation, then reduced to −21.13 kN during upper tunnel excavation). These results suggest that piles farther from the tunnel are more susceptible to negative bending moments during lower tunnel excavation, while the subsequent upper tunnel excavation slightly mitigates these adverse effects.

Table 4. Internal forces and displacements of piles at a tunnel–building distance of 1D

		M_{max} (kN)	M_{min} (kN)	N_{max} (kN/m)	N_{min} (kN/m)	$U_{x,max}$ (mm)	$U_{y,max}$ (mm)
Pile 1	Building	25.47	−6.561	513.4	99.01	2.33	−24.69
	Lower tunnel	22.83	8.442	437.5	135.2	5.4	−11.59
	Upper tunnel	15.34	5.456	543.3	146.7	9.83	−11.66
Pile 2	Building	12.26	−2.702	319.295	88.74	9.93	−25.21
	Lower tunnel	4.017	−2.882	362.2	137.1	5.4	−9.01
	Upper tunnel	2.796	−1.469	393.7	150.5	9.84	−9.07
Pile 3	Building	0.1341	−0.1884	286.2	87.66	2.74	−25.43
	Lower tunnel	1.735	−8.86	343.2	119.5	5.41	−6.92
	Upper tunnel	0.9611	−5.517	356.4	126.3	9.84	−6.76
Pile 4	Building	2.763	−12.66	319.6	91.73	1.6	−25.13
	Lower tunnel	2.989	−19.83	348.8	109.6	5.41	−5.07
	Upper tunnel	2.059	−13.33	353.5	111.3	9.84	−4.42
Pile 5	Building	6.625	−25.89	514.3	106.1	2.963	−24.53
	Lower tunnel	6.08	−30.84	469	111.2	5.416	−3.45
	Upper tunnel	4.167	−21.13	458.5	109.4	9.841	−2.97

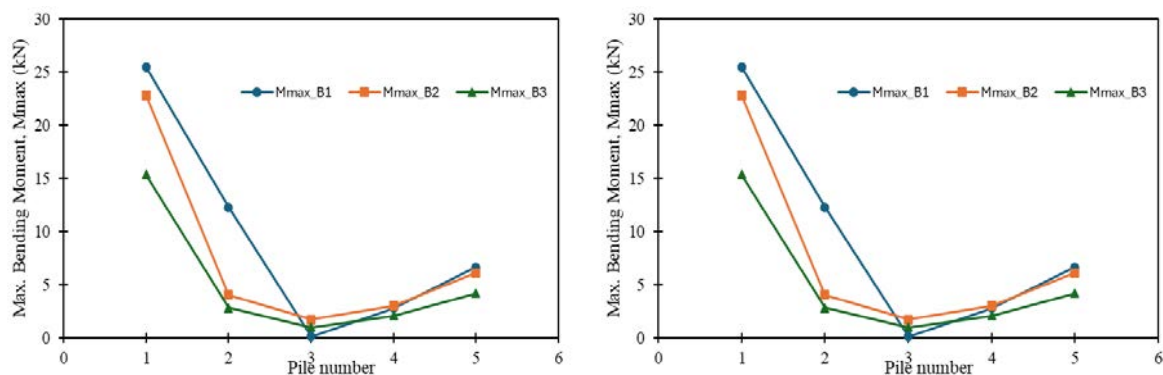


Figure 3. Max. and Min. bending moment in piles

For Pile 1, the maximum axial force (N_{max}) showed a pronounced reduction following the excavation of the lower tunnel (Fig. 4). This can be explained by the pile toe being located directly along the axis of the lower tunnel, which induced lateral displacement and load redistribution. Consequently, the axial force increased near the pile toe but decreased at the pile head. During the upper tunnel excavation, further displacement occurred along the mid-section

of Pile 1, resulting in a localized increase in axial force. For Piles 2 through 5, a similar trend was observed, yet the magnitude of change in N_{max} was substantially smaller.

After the construction of the building and its foundation, the maximum horizontal displacement ($U_{x,max}$) of Piles 1–2 was found to be symmetric with that of Piles 4–5 with respect to the central pile (Pile 3). Among all piles, the central pile exhibited the smallest lateral displacement (Fig.5).

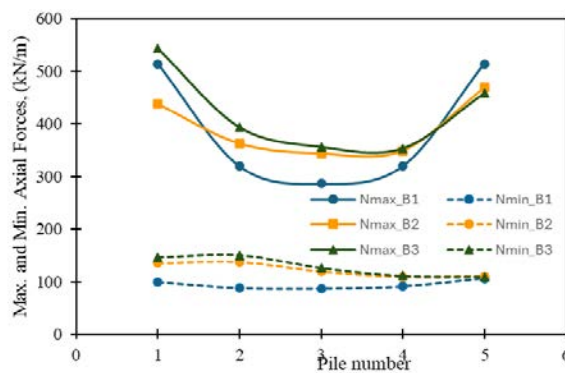


Figure 4. Max. and min. normal forces in piles

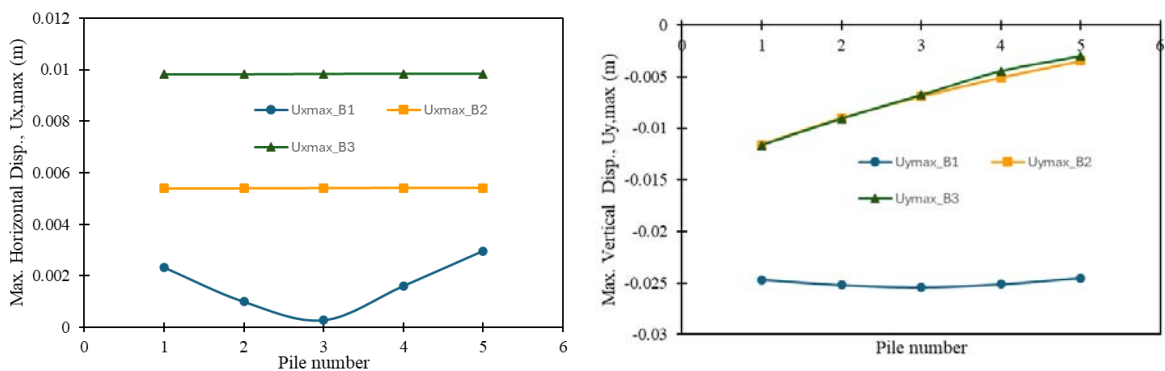


Figure 5. Maximum horizontal and vertical displacement of piles ($U_{x,max}$ and $U_{y,max}$)

Following the excavation of the lower tunnel, ground movements induced by tunneling caused all piles to displace toward the tunnel side. The $U_{x,max}$ was observed at the pile head, and the pattern was consistent across all piles (Piles 1 to 5). Subsequent excavation of the upper tunnel further amplified soil movement, resulting in additional pile displacements and an increase in $U_{x,max}$. These results emphasize the

progressive nature of pile–soil–tunnel interaction, where sequential tunneling activities significantly influence pile performance, particularly in terms of lateral stability.

The $U_{y,max}$ of the piles prior to tunnel excavation was relatively large, primarily due to the effect of structure loading. During tunnel excavation, ground settlement occurred both

around the tunnel and at the ground surface. The magnitude of pile settlement was strongly dependent on the pile's location relative to the settlement trough: Pile 5, positioned farther from the trough, exhibited smaller vertical displacements

compared with Pile 1, which was closer to the trough. In the case of the upper tunnel excavation, the influence on vertical displacements was considerably less significant, as the tunnel alignment intersected approximately at the mid-depth of the piles rather than at their toes. These results confirm that lower tunnel excavation imposes greater

effects on pile settlement, whereas the upper tunnel contributes only marginal additional displacement.

Pile behavior in relation to pile–tunnel distance

To investigate the influence of tunnel–pile spacing on pile performance, a parametric study was conducted. The horizontal distance between the tunnel centerline and the nearest pile (on the tunnel side) was varied from 1D, 1.5D, 2D, 3D, 4D, 5D, to 6D, where D denotes the tunnel diameter (6.3 m). The corresponding results regarding pile internal forces and displacements are summarized in Table 5 and 6.

Table 5. Internal forces and displacements of pile 1 after construction of the lower tunnel

Distance (xD)	Lower tunnel						
	1	1.5	2	3	4	5	6
Mmax (kN)	22.83	21.32	20.71	21.69	23.74	24.96	25.37
Mmin (kN)	-8.442	-6.917	-5.771	-4.932	-5.442	-6.061	-6.348
Nmax (kN/m)	437.5	464.5	489.1	509.1	512.3	511.9	511.6
Nmin (kN/m)	135.2	133.9	132.7	115.5	107.5	105.2	105.3
Ux,max (mm)	5.40	5.08	4.55	3.18	1.98	1.15	0.640
Uy,max (mm)	-11.59	-8.14	-5.75	-3.04	-1.81	-1.22	-1.01

Table 6. Internal forces and displacements of pile 1 after construction of the upper tunnel

Distance (xD)	Upper tunnel						
	1	1.5	2	3	4	5	6
Mmax (kN)	15.34	15.17	17.3	21.76	24.91	25.81	25.81
Mmin (kN)	-5.456	-3.517	-3.433	-4.29	-5.572	-6.283	-6.512
Nmax (kN/m)	543.3	515.1	510.5	513.2	515	513.2	512.1
Nmin (kN/m)	146.7	149.8	144	116.8	107	104.2	105
Ux,max (mm)	9.83	8.55	7.04	4.10	2.11	1.11	0.679
Uy,max (mm)	-11.66	-8.42	-6.10	-2.98	-1.72	-1.26	-1.16

During the excavation of the lower tunnel, at a pile–tunnel spacing of 1D (6.3 m), the maximum bending moment (Mmax) decreased to 22.83 kN· compared with 25.47 kN prior to tunneling. As the spacing increased, Mmax further decreased to 20.71 kN·at 2D, before gradually increasing and reaching 25.37 kN at 6D, which is nearly identical to the initial value. This indicates that lower tunnel excavation reduces Mmax for piles located close to the tunnel (1D–2D), owing to soil movements toward the tunnel that relieve loading on the piles. Beyond 3D, the influence

of tunneling becomes negligible, with Mmax returning to values comparable to the initial condition (Fig. 6).

For the upper tunnel excavation, Mmax at 1D dropped more significantly to 15.34 kN, compared with 22.83 kN during the lower tunnel excavation and 25.47 kN before tunneling. With increasing spacing, Mmax progressively increased and reached 25.81 kN·at 5D and 6D, essentially equivalent to the pre-tunneling condition. These results confirm that the upper tunnel further amplifies soil displacement around the piles, leading to

additional reductions in M_{max} for piles located close to the tunnel (1D–2D). However, at larger spacings ($\geq 4D$), the effect of the upper tunnel diminishes rapidly, with M_{max} approaching its initial value.

Overall, the sequential excavation of the lower and upper tunnels produces two distinct phases of stress redistribution within the soil mass. The lower tunnel induces the first reduction in M_{max} , while the subsequent excavation of the upper tunnel imposes additional stress and displacement changes, further reducing M_{max} at piles in close proximity to the tunnel. Nonetheless, the influence decays rapidly with distance, highlighting that piles beyond approximately 3–4D are largely unaffected (Fig. 6).

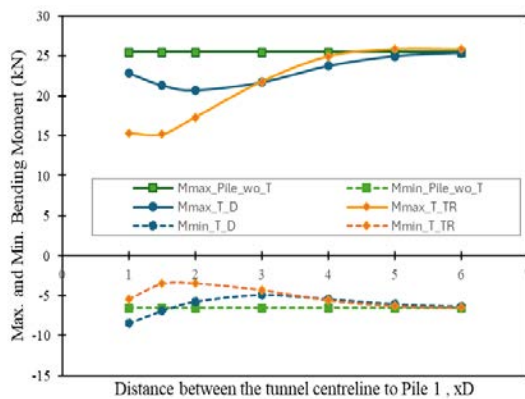


Figure 6. Max. and min. bending moments in pile 1

During the excavation of the lower tunnel, at a pile–tunnel spacing of 1D, the maximum axial force (N_{max}) decreased significantly to 437.5 kN/m compared with 513.4 kN/m prior to tunneling. As the spacing increased, N_{max} gradually recovered, reaching 511.6 kN/m at 6D, which is nearly identical to the initial value. This indicates that lower tunnel excavation reduces N_{max} in piles located close to the tunnel (particularly Pile 1), whereas at greater distances the influence becomes negligible and N_{max} returns to its pre-tunneling level.

In contrast, during the excavation of the upper tunnel, N_{max} at 1D increased to 543.3 kN/m, exceeding both the initial value (513.4 kN/m) and the value after lower tunnel excavation (437.5 kN/m). With increasing

spacing, N_{max} slightly decreased and stabilized within the range of 510–515 kN/m, which is essentially equivalent to the pre-tunneling condition. These results suggest that the lower tunnel, located near the pile toe, tends to induce downward drag on the pile, thereby reducing N_{max} , whereas the upper tunnel, positioned around the mid-depth of the pile, promotes additional lateral displacement and bending of the pile shaft, leading to an increase in N_{max} . The influence of the upper tunnel, however, diminishes rapidly when the tunnel–pile spacing exceeds approximately 2D.

Regarding the minimum axial force (N_{min}), both the lower and upper tunnel excavations caused an increase in N_{min} , particularly for piles located close to the tunnel. This effect also attenuated with greater pile–tunnel distances (Fig. 7).

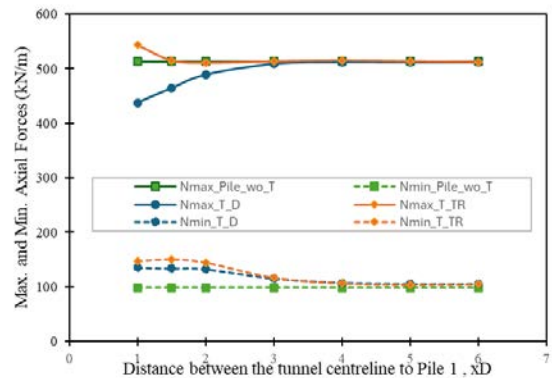


Figure 7. Max. and min. axial forces in pile 1

After the excavation of the lower tunnel, the maximum lateral displacement of pile 1 occurred at 1D (6.3 mm), reaching $U_{x,max} = 5.40$ mm, the highest recorded value. This reflects notable lateral movement when the tunnel is close to the pile, primarily due to soil shifting toward the tunnel (the ground loss-induced displacement effect). With increasing distance, $U_{x,max}$ progressively decreased from 5.08 mm at 1.5D to 0.640 mm at 6D, representing an 88% reduction. This indicates that the influence of the lower tunnel on pile lateral displacement diminishes rapidly with distance, consistent with the attenuation of soil disturbance.

Following the excavation of the upper tunnel, the maximum lateral displacement at 1D increased to $U_{x,max} = 9.83$ mm, representing an 82% increase compared to the lower tunnel (5.40 mm). With increasing distance, displacements reduced from 8.55 mm at 1.5D to 0.679 mm at 6D, corresponding to an approximate 93% reduction. At all distances, lateral displacement induced by the upper tunnel exceeded that of the lower tunnel, especially at piles close to the tunnel (1D–2D), reflecting stronger soil disturbance due to its shallower depth and alignment with the pile. At larger offsets ($\geq 4D$), displacements became negligible, indicating minimal tunneling influence. The tunneling sequence (lower followed by upper) was also found to have an insignificant effect on $U_{x,max}$ of pile (Fig. 8).

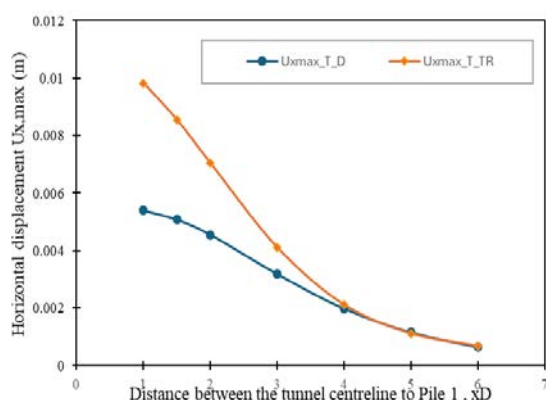


Figure 8. Max. horizontal displacement ($U_{x,max}$) of pile 1

After the construction of the lower tunnel, at 1D, the maximum vertical displacement (settlement) was, $U_{y,max} = -11.59$ mm, the largest among all distances. With increasing distance, $U_{y,max}$ decreased markedly: -8.14 mm (1.5D), -5.75 mm (2D), -3.04 mm (3D), -1.81 mm (4D), -1.22 mm (5D), and -1.01 mm (6D), representing a 91% reduction from 1D to 6D. For the upper tunnel, at 1D, the maximum settlement was $U_{y,max} = -11.66$ mm, nearly identical to that of the lower tunnel (a marginal increase of 0.6%). As the distance increased, settlement decreased from: -8.42 mm (1.5D), -6.10 mm (2D), -2.98 mm (3D), -1.72 mm (4D), -1.26 mm (5D), and -1.16 mm (6D), a 90% reduction (Fig. 9).

The largest vertical displacement occurred at the pile closest to the tunnels (1D–2D) and diminished rapidly with distance, confirming that tunneling effects on pile settlement are distance-dependent. The difference in $U_{y,max}$ between the two tunneling stages was negligible. The subsequent construction of the upper tunnel did not cause additional significant settlement but maintained the decreasing trend with distance. This suggests that soil disturbance from the upper tunnel primarily contributed to lateral displacement, while vertical settlement was governed by the lower tunnel excavation, as the soil beneath the pile toe had already stabilized after the first excavation.

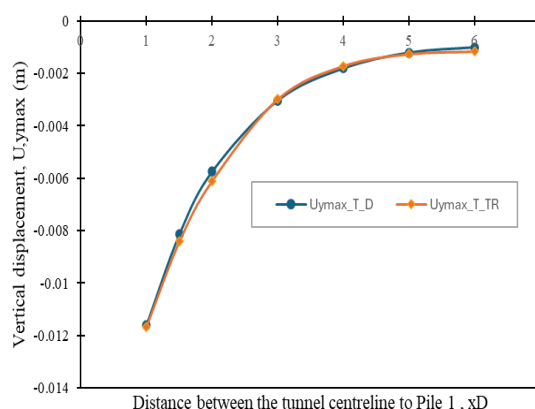


Figure 9. Max. vertical displacement ($U_{y,max}$) of pile 1

CONCLUSIONS

From the above results, it is evident that tunnel construction has a clear impact on the behavior of pile foundations. The degree of this influence depends on multiple factors. In this study, the author focused on analyzing the effect of the distance between the tunnel and the pile group. The main conclusions can be summarized as follows:

Before tunnel construction, the piles located at the outer boundaries exhibit the largest internal forces and displacements. Moving toward the center of the structure, both internal forces and displacements gradually decrease, with the central piles experiencing the smallest values.

At the same relative distance between the tunnel and the pile group (1D), the farther a pile is from the tunnel, the smaller the influence on its behavior.

Regarding the effect of tunnel position, the greater the distance between the tunnel and the pile group, the smaller the impact. When the tunnel is more than 3D away from the pile group (measured to the nearest pile on the tunnel side), the influence becomes negligible.

It should be noted that the present study was carried out using a two-dimensional (2D) numerical model, which does not fully capture the effects of the construction process (e.g., tunneling machine operation parameters, interactions between adjacent pile groups). Therefore, future work will focus on developing a three-dimensional (3D) numerical model to provide a more comprehensive simulation of the tunneling process and its impact on pile foundations.

ACKNOWLEDGEMENT

This research was funded by the Ministry of Education and Training under grant B2025-MDA-02. This funding is greatly appreciated.

REFERENCES

- Abd-Elhamed, A. (2021). Analytical Solution of Laterally Loaded Free-Head Long Piles in Elasto-Plastic Cohesive Soils. *Mathematics*, 9. <https://doi.org/https://doi.org/10.3390/math9161961>.
- Al-Omari, R. R., Al-Sou, M. S., & Al-Zuhairi, O. I. (2019). Effect of Tunnel Progress on the Settlement of Existing Piled Foundation. *Studia Geotechnica et Mechanica*, 41(2), 102-113. <https://doi.org/10.2478/sgem-2019-0008>.
- Chen, L. T., Poulos, H. G., & Loganathan, N. (1999). Pile Responses Caused by Tunneling. *Journal of Geotechnical and Geoenvironmental Engineering*, 125(3). [https://doi.org/https://doi.org/10.1061/\(ASCE\)1090-0241\(1999\)125:3\(207\)](https://doi.org/https://doi.org/10.1061/(ASCE)1090-0241(1999)125:3(207)).
- Decision No. 1711/QĐ-TTg. (2024). *Ho Chi Minh City Planning for the period 2021–2030, with a vision to 2050*. Hanoi.
- Decision No. 519/QĐ-TTg. (2016). *Approving the transport master plan for Hanoi capital through 2030, with a vision toward 2050 (in Vietnamese)*. Hanoi: The Prime Minister.
- Do, N. A., Dias, D., & Dang, T. T. (2021). A numerical investigation of the impact of shield machine's operation parameters on the settlements above twin stacked tunnels - A case study of Ho Chi Minh urban railway Line 1. *Vietnam Journal of Earth Sciences*, 43(4), 409–423. <https://doi.org/10.15625/2615-9783/16442>.
- Hieu, N. T., Giao, P. H., & Phien-wej, N. (2019). Tunneling induced ground settlements in the first metro line of Ho Chi Minh City, Vietnam. *Geotechnics for Sustainable Infrastructure Development. Lecture Notes in Civil Engineering*. 62, pp. 297–304. Hanoi: Springer, Singapore. https://doi.org/10.1007/978-981-15-2184-3_37.
- Huang, M., Zhang, C., & Li, Z. (2009). A simplified analysis method for the influence of tunneling on grouped piles. *Tunnelling and Underground Space Technology*, 24(4), 410-422. <https://doi.org/10.1016/j.tust.2008.11.005>.
- Jacobsz, S., Standing, J., Mair, R., Hagiwara, T., & Sugiyama, T. (2004). Centrifuge Modelling of Tunnelling Near Driven Piles. *Soils and Foundations*, 44(1), 49-56. <https://doi.org/10.3208/sandf.44.49>.
- Jongpradist, P., Kaewsri, T., Sawatparnich, A., Suwansawat, S., Youwai, S., Kongkitkul, W., & Sunitsakul, J. (2013). Development of tunneling influence zones for adjacent pile foundations by numerical analyses. *Tunnelling and Underground Space Technology*, 34, 96-109. <https://doi.org/https://doi.org/10.1016/j.tust.2012.11.005>.
- Lam, D. H., Chi, D. T., & Dong, N. B. (2022). A practical approach for modeling twin-tunnel excavation in Ho chi minh city. *The Transport and Communications Science Journal*, 73(7), 724-734. <https://doi.org/10.47869/tcsj.73.7.6>.
- Lee, C. (2012). Numerical analysis of the interface shear transference mechanism of a single pile to tunneling in weathered residual soil. *Computers and Geotechnics*, 42, 193-203. <https://doi.org/https://doi.org/10.1016/j.compgeo.2012.01.009>.
- Li, T., Yang, M., & Chen, X. (2023). A Simplified Analytical Method for the Deformation of Pile Foundations Induced by Adjacent Excavation in Soft Clay. *Buildings*, 13. <https://doi.org/https://doi.org/10.3390/buildings13081919>.

- Lim, C. B., Jusoh, S. N., Lim, C. X., Hasbollah, D. Z., & Sohaei, H. (2023). Tunnel – Pile interaction sequence: Parametric studies. *Physics and Chemistry of the Earth, Parts A/B/C*, 129. <https://doi.org/https://doi.org/10.1016/j.pce.2022.103312>.
- Maji, V. B., & Sundar, P. S. (2021). A numerical study on the influence of tunnel excavation on pile foundation. *International Journal of Mining and Geo-Engineering*, 57(1), 27-33. [10.22059/ijmge.2022.333489.594939](https://doi.org/10.22059/ijmge.2022.333489.594939).
- Marshall, A., & Haji, T. (2015). An analytical study of tunnel-pile interaction. *Tunn. Undergr. Space Technol.*, 45, 43-51. <https://doi.org/10.1016/j.tust.2014.09.001>.
- Ng, C., Lu, H., & Peng, S. (2012). Three-dimensional centrifuge modelling of the effects of twin tunnelling on an existing pile. *Tunn. Undergr. Space Technol.*, 35, 189-199. <https://doi.org/10.1016/j.tust.2012.07.008>.
- Nguyen, H. V., Nguyen, D. D., Nguyen, T. T., & Le, D. T. (2023). A 3D Finite Element Analysis and Field Monitoring of the Residual Displacement of the Existing TBM Tunnel After Underground Culvert Construction: A Case Study in Ho Chi Minh City. In P. D. Long, & N. T. Dung (Ed.), *Proceedings of the 5th International Conference on Geotechnics for Sustainable Infrastructure Development* (pp. 23-632). Hanoi: Springer. https://doi.org/10.1007/978-981-99-9722-0_41.
- Plaxis - Bentley Systems. (2020). *PLAXIS 2D Reference Manual 2020*. Delft, Netherlands.
- Poulos, H. G., Stewart, D. P., & Loganathan, N. (2000). Centrifuge model testing of tunneling induced ground and pile deformations. *Geotechnique*, 50(3), 283-294. <https://doi.org/10.1680/geot.2000.50.3.283>.
- Shimizu – Maeda. (2016). *Ho Chi Minh City Urban Railway Construction Project (HUP), Ben Thanh - Suoi Tien Section (Line 1). Contract Package-1b: Civil (Underground Section KM 0+615 to KM 2+360): Bored tunnel - Segmental lining - Technical design report*. Shimizu-Maeda joint operation.
- Selemetas, D. (2005). *The response of full-scale piles and piled structures to tunnelling*. Cambridge University.
- Soomro, M., Keerio, M., & Bangwar, D. (2017). 3D Centrifuge Modeling of the Effect of Twin Tunneling to an Existing Pile Group. *Engineering, Technology & Applied Science Research*, 7(5), 2030-2040. <https://doi.org/10.1016/j.tust.2020.103486>.
- Su, J., Pan, Y., Niu, X., & Zhang, C. (2025). Effect of shield tunneling on adjacent pile foundations in water-rich strata. *Transportation Geotechnics*, 52. <https://doi.org/10.1016/j.trgeo.2025.101557>.
- Surjadinata, J., Hull, T. S., Carter, J. P., & Poulos, H. G. (2006). Combined Finite- and Boundary-Element Analysis of the Effects of Tunneling on Single Piles. *International Journal of Geomechanics*, 6(5). [https://doi.org/10.1061/\(ASCE\)1532-3641\(2006\)6:5\(374\)](https://doi.org/10.1061/(ASCE)1532-3641(2006)6:5(374)).

DOI: 10.15625/vap.2025.0203

Accelerating Vietnam's Transition from Coal-Fired Power to Renewable Energy: Challenges and Strategic Solutions

Vu Thi Phuong Thao^{1,*}, Bui Manh Tung¹, Nguyen Duc Toan²

¹Hanoi University of Mining and Geology, 18 Vien street, Dong Ngac commune, Hanoi, Vietnam

²Vietnam Agency of Seas and Islands, Ministry of Agriculture and Environment, 10 Ton That Thuyet, Hanoi

*Email: vuthiphuongthao@humg.edu.vn

Abstract: Vietnam's commitment to achieve net-zero greenhouse gas emissions by 2050 presents both an environmental necessity and a development opportunity. Yet, the country's transition from coal-fired power to renewable energy remains constrained by financing bottlenecks, infrastructure deficits, regulatory ambiguity, and socio-economic adjustment costs. This paper provides a comprehensive assessment of Vietnam's energy transition through policy, technical, and socio-economic lenses. Drawing upon national datasets, international frameworks, and sectoral studies, the analysis identifies five systemic barriers: (1) financial barriers, (2) Grid and infrastructure limitations, (3) Regulatory complexity, (4) Technological and operational issues, and (5) labour dislocation in the fossil fuel sector. An integrated, sequenced transition framework combining innovative financing, accelerated grid digitalisation, regulatory streamlining, localisation of renewable manufacturing, and workforce reskilling under a just-transition model were proposed. The study concludes that Vietnam can achieve a secure and equitable energy transition if institutional coordination, investment de-risking, and social inclusion are strengthened in parallel.

Keywords: Energy transition, coal-fired power, renewable energy.

INTRODUCTION

Coal-fired power has served as a foundation of Vietnam's industrialisation and electrification since the late nineteenth

century. The first coal plant, Nha Den Vuon Hoa, was built in Hai Phong in 1894 under French colonial administration. By May 2023, the nation operated 29 coal-fired power plants with a total installed capacity of 26,087 MW, representing 32.3% of national generation capacity. Coal accounted for 104.9 TWh, or 39.1% of total electricity output in 2022 (Chuong Phuong, 2024).

While coal ensured energy reliability during decades of rapid economic growth, its externalities—air pollution, carbon emissions, and ecosystem degradation—are increasingly unsustainable. The United Nations Development Programme warns that current and planned global coal capacities exceed the trajectory consistent with limiting global warming to 1.5 °C (Cuong, T.T. et al, 2021).

Vietnam, as a signatory to the Paris Agreement and COP26 commitments, has pledged to phase down coal use, with the Politburo's Resolution No. 55-NQ/TW (2020) establishing a national energy development strategy to 2030 and vision to 2045 (Ministry of Industry and Trade, 2018). This shift demands balancing energy security, economic competitiveness, and social justice - an exceptionally complex optimisation problem for a developing, export-oriented economy.

In National policy evolution, over the past decade, Vietnam has enacted an extensive policy framework to support renewable energy. Key milestones include in Table 1.

Table 1. Key milestones of policy framework to support renewable energy.

No.	Year	Policy / Regulation	Strategic Objective
1	2007	Decision No. 1855/QĐ-TTg	National Energy Development Strategy 2020–2050
2	2015	Decision No. 2068/QĐ-TTg	Renewable Energy Development Strategy 2030–2050
3	2017	Decision No. 11/2017/QĐ-TTg	Feed-in Tariff (FiT) for Solar Power
4	2020	Resolution No. 55-NQ/TW	Energy restructuring; 15–20% renewables by 2030
5	2023	Power Development Plan VIII	Full coal phase-out by 2050; 67–71% renewables share

Sources: Prime Minister (2015); Ministry of Industry and Trade (2018; 2019; 2021).

These instruments collectively envision renewables providing 32% of electricity by 2030 and 43% by 2050. PDP VIII further specifies that solar and wind will contribute ~65% of total generation by mid-century, while coal's share will decline from 33% (2022) to zero by 2050.

At COP26 in Glasgow 2021, Vietnam pledged to reach net-zero emissions by 2050 (Politburo, 2020). The Just Energy Transition Partnership (JETP), launched at COP28 2023, mobilises US \$15.5 billion in concessional and private finance to accelerate decarbonisation while ensuring fairness for workers and communities (Prime Minister, 2007). Vietnam's success in operationalising the JETP will determine its credibility in global climate governance and its ability to attract green capital.

METHODOLOGY

This study integrates policy document analysis, energy data synthesis, and comparative benchmarking with regional peers

(Indonesia, Philippines, Thailand). Data sources include Ministry of Industry and Trade (MOIT)'s annual reports, Electricity of Vietnam (EVN) statistics (2015–2025), UNDP JETP assessments, International labor organization (ILO) and academic literature. The research employs a multi-criteria evaluation framework (MCEF) encompassing four dimensions (Jessica V. L. et al. 2025) as in table 2.

Table 2. Four dimensions used for multi-criteria evaluation framework in this study

No	Dimension	Evaluation Metrics	Data Sources
1	Financial	Levelized Cost of Electricity trends, Capital Expenditure/MW, FiT stability	MOIT
2	Technical	Grid loss rates, storage penetration, curtailment ratio	EVN, UNDP
3	Institutional	Permitting duration, policy clarity, inter-agency coordination	MOIT,
4	Social	Employment shifts, regional equity, energy access	ILO

A qualitative comparative analysis (QCA) approach is applied to identify barrier interdependencies and formulate a sequenced solution roadmap.

RESULTS AND DISCUSSION

Renewable Energy Resource Potential

Vietnam's tropical monsoon climate, diverse topography, and extensive coastline yield substantial renewable resources.

Solar energy: Annual solar radiation ranges from 897–2,108 kWh/m²/year, with the highest levels in the Central Highlands and southern provinces as Dak Lak, Gia Lai, Khanh Hoa, Tay Ninh. Average insolation exceeds 5 kWh/m²/day in southern Vietnam, compared to 4 kWh/m²/day in the north (Prime Minister (a), 2017); Prime Minister (b), 2017). The

technical potential is estimated at 386 GW, positioning Vietnam as ASEAN's solar leader.

Wind energy: With 3,260 km of coastline and mean wind speeds of 6 m/s at 65 m hub height, Vietnam possesses roughly 311 GW of onshore and 475 GW of offshore wind potential. About 31,000 km² of land are suitable for wind generation, including 865 km² with generation cost < USD 0.06/kWh (Priyanka Sharma, 2024).

Biomass energy: Agricultural residues and municipal waste can support up to 5,000 MW of generation capacity (P. T. S. Thuong, N.T.Truong, 2024; Phan Trang, 2023). Rice straw alone can yield 2,565 MW, with Kiên Giang and An Giang provinces showing highest density.

Hydropower: Vietnam's 2,360 rivers and annual rainfall of 1,600–2,000 mm generate an exploitable hydropower potential of 120 billion kWh/year (UNDP, 2016). While large-scale hydropower is nearing saturation, small and pumped-storage hydropower remains promising for balancing renewables.

Key Challenges of developing Renewable Energy Resource

a) Financial barriers

Renewables demand high upfront capital: onshore wind USD 1.7 million/MW, offshore USD 3.5 million/MW, compared to coal's USD 1.3 million/MW. Limited domestic capital markets and unclear power purchase agreements discourage long-term investors (UNDP, 2024).

Vietnam's previous high solar prices created a solar boom but also overloaded the grid, and recent moves to retroactively revise FiT contracts have put more than US\$13 billion of solar and wind investment at risk and damaged investor confidence (Mark Barnes, 2023).

b) Grid and infrastructure limitations

Transmission congestion, especially in Khanh Hoa and Lam Dong causes curtailment losses of 10–20% for solar and wind projects

(Vietnam Energy Association, 2017). In 2020, the rapid deployment of solar and wind power, about 25% of installed capacity, has outpaced the capacity of Vietnam's grid and storage infrastructure, leading to congestion and frequent renewable energy curtailments, (Case for Southeast Asia, 2021).

c) Regulatory complexity

Permitting for renewable projects often exceeds 18 months, with inconsistent environmental and technical standards. Absence of unified grid codes and land-use zoning slows project rollout (Vietnam Energy Association, 2020).

Moreover, at present, there is no integrated planning platform that connects the scenarios from the National Power Development Plan (PDP8) with JETP commitments, grid constraints, and climate risk models. Additionally, there is no access to non-sensitive data. Coordination among ministries, the EVN, and local authorities within the Energy Transition Council is weak, and there is a lack of coherence in policies.

d) Technological and operational issues

High renewable penetration increases variability and grid imbalance. Curtailment and line losses (averaging 6.7%) cost EVN about 200 million USD annually (Vietnam Electricity Group, 2023).

e) Labour dislocation in the fossil fuel sector

Over 100,000 coal miners and 10,000 plant workers face displacement (ILO, 2022). Reskilling programs remain fragmented and underfunded. The social cost of a poorly managed transition could erode public support for decarbonisation.

Comparative regional analysis

Vietnam's renewable adoption rate surpasses regional peers, but integration readiness particularly grid flexibility and storage is comparatively weaker. Table 3 present comparative regional analysis of renewable energy

Table 3. Comparative regional analysis of renewable energy

STT	Country	Renewable Share (2022)	JETP/Equivalent	Coal Phase-Out Target	Feed-in Tariff Scheme
1	Vietnam	26.4%	JETP (2023)	2050	Solar (USD 0.0935/kWh); Wind (USD 0.085/kWh)
2	Indonesia	14.5%	JETP (2022)	2050	Mixed auction + FiT
3	Philippines	24%	Clean Energy Transition	2040	Competitive auction
4	Thailand	20%	None (policy alignment)	2050	Reverse auction

Proposed Solutions to Overcome Transition Challenges

a) Strategic priorities

A central priority is upgrading the transmission system: early PDP8 investments should focus on 220-kV-and-above trunk lines, North-Central - South interconnections, and grid digitalization. Clear rules for storage - pumped hydro, batteries, and flexible biomass or gas - are needed so these assets function as real balancing resources.

Regulatory predictability is essential. Vietnam should avoid retroactive PPA changes (Prime Minister, 2023), resolve FiT disputes transparently, and improve Decree 57's capped-tariff system by publishing auction schedules, grid-connection rules, and standardized PPAs (Prime Minister, 2025).

PDP8 must align with feasible financing. Meeting the 183 - 236 GW target by 2030 - including scaling solar, wind, and reintroducing nuclear- requires USD 8 - 10 billion annually for renewables and storage. The country should use the JETP's USD 15.5-billion package to derisk grid and storage projects and build standardized, pre-permitted pipelines to attract global capital.

Power-market reform is essential. Expanding direct PPAs would allow industrial users to contract directly with renewable generators, reduce pressure on EVN's balance sheet, and create more stable cash flows.

A just transition requires early identification of job losses in coal, oil, and gas through a national employment inventory

linked to PDP8's retirement schedule. Support should include temporary income assistance, early-retirement options, and continued health and pension benefits. Reskilling must target real labour demand grid expansion, renewables, transmission and storage, industrial efficiency, and environmental remediation delivered through short certified courses in local vocational colleges, with public funding tied to job-placement outcomes.

b) Policy implications

Institutional coordination is critical. Inter-agency overlaps among Ministry of Industry and Trade, Ministry of Agriculture and Environment, and provincial authorities causes delays of more than 18 months per project. Investment derisking via long-term power purchase agreements (PPAs), stable tariffs, and transparent auctions could attract USD 20–25 billion annually. Social acceptance hinges on equitable benefit-sharing. Community ownership models (2–5% equity stake) have succeeded in Thailand and Denmark and could be piloted in Vietnam's Mekong Delta.

CONCLUSION

Vietnam's pathway from coal to renewable energy represents one of the most ambitious transitions in Southeast Asia. The technical potential is vast, policy commitment is evident, yet institutional inertia and financing constraints remain decisive bottlenecks. A coordinated "Finance - Infrastructure - Policy - Society" approach offers a pragmatic framework for balancing decarbonisation with economic growth. By

leveraging JETP financing, localising supply chains, and ensuring just transition measures, Vietnam can achieve a resilient, low carbon energy system by mid-century and emerge as a model for equitable transition in the Global South.

REFERENCES

- Chuong Phuong (2024). *Hundreds of billions of USD are needed to convert coal-fired thermal power plants. Where will the money come from?* Vietnam Economic Times. <https://vneconomy.vn/can-hang-tram-ty-usd-de-chuyen-doi-cac-nha-may-nhiet-dien-than-huy-dong-tien-tu-dau.htm>.
- Case for Southeast Asia (2021). The energy transition in Viet Nam is happening at an unprecedented speed and scale. https://caseforsea.org/vietnam/?utm_source=chatgpt.com.
- Cuong, T.T.; Le, H.A.; Khai, N.M.; Hung, P.A.; Linh, L.T.; Thanh, N.V.; Tri, N.D.; Huan, N.X. *Renewable energy from biomass surplus resource: Potential of power generation from rice straw in Vietnam*. Sci. Rep. 2021, 11, 792. Sci Rep. 2021; 11: 792. doi: 10.1038/s41598-020-80678-3.
- International labour organization (2022). A just energy transition in Southeast Asia: The impact of coal phase-out on jobs. <https://www.ilo.org/publications/just-energy-transition-southeast-asia-impact-coal-phase-out-jobs>.
- Jessica V. L. et al. (2025). *Evaluation of Technological Alternatives for the Energy Transition of Coal-Fired Power Plants, with a Multi-Criteria Approach*. Energies.
- Mark Barnes, (2023). *Explained: Vietnam's FiT Rates for Solar and Wind Power Projects*. Vietnam Briefing. [7]. MOIT (2018). *Report "Potential for renewable energy development"*. <http://nangluongvietnam.vn/news/en/nucle-renewable/> kỳ vọng về năng lượng tái tạo phát triển.html.
- MOIT(2019). *Overview of coal-fired thermal power development in Vietnam*. <https://www.evn.com.vn/d6/news/Tong-quan-ve-phat-trien-nhiet-dien-than-o-Viet-Nam-6-12-24125.aspx>.
- MOIT(2021). *Expectations from the COP26 climate conference*. <https://moit.gov.vn/phat-trien-ben-vung/nhung-ky-vong-tu-hoi-nghi-khi-hau-cop26.html>.
- Ministry of Natural Resources and Environment (2023). *Just Energy Transition Partnership and Vietnam JETP Declaration*. <https://monre.gov.vn/Pages/quan-he-doi-tac-chuyen-doi-nang-luong-cong-bang-va-tuyen-bo-jetp-cua-viet-nam.aspx>.
- Nguyen, K.Q. (2020). *Wind energy in Vietnam: Resource assessment, development status and future implications*. Energy Policy, 138, 1405–1413. <https://sites.uni.edu/apetrov/wind/Boolean/Nguyen2007.pdf>.
- Politburo (2020). *Resolution No. 55-NQ/TW dated February 11, 2020 of the Politburo on the orientation of Vietnam's national energy development strategy to 2030, with a vision to 2045*. <https://tulieuvankien.dangcongsan.vn/he-thong-van-ban/van-ban-cua-dang/ngghi-quyet-so-55-nqtw-ngay-11022020-cua-bo-chinh-tri-ve-dinh-huong-chien-luoc-phat-trien-nang-luong-quoc-gia-cua-viet-nam-den-6096>.
- Prime Minister (2007). *Decision No. 1855/QĐ-TTg of the Prime Minister approving Vietnam's National Energy Development Strategy to 2020, with a vision to 2050*. <https://vbpl.vn/bolao dong/Pages/vbpqtoanvan.aspx?ItemID=12973306608.aspx>.
- Prime Minister (2015). *Decision 2068/QĐ-TTg of the Prime Minister, Approving the Strategy for Renewable Energy Development of Vietnam to 2030, with a vision to 2050*. <https://vanban.chinhphu.vn/default.aspx?pageid=27160&doid=182255>.
- Prime Minister (2017). *Decision No. 11/2017/QĐ-TTg of the Prime Minister dated April 11, 2017, on the mechanism to encourage the development of solar power projects in Vietnam*. <https://vanban.chinhphu.vn/default.aspx?pageid=27160&doid=189336>.
- Prime Minister (2017). *Adjusted Power Plan VII*. <https://thuvienphapluat.vn/van-ban/Thuong-mai/Quy-dinh-428-QĐ-TTg-de-an-dieu-chinh-quy-hoach-phat-trien-dien-luc-quoc-gia-2011-2020-2030-2016->.
- Prime Minister (2023). *Decision No. 500/QĐ-TTg. Approving the National Power Development Plan VIII for the 2021-2030 period, with a vision to 2050*. <https://xaydungchinh sach.chinhphu.vn/toan-van-quy-hoach-phat-trien-dien-luc-quoc-gia-11923051616315244.htm>.
- Prime Minister (2025). *Decision No. 768/ QĐ-TTg. Approving the adjustment of National Power Development Plan VIII for the 2021-2030 period, with a vision to 2050*. <https://baochinhphu.vn/thu-tuong-chinh-phu-phe-duyet-dieu-chinh-quy-hoach-dien-viii-102250416180716025.htm>.
- Prime Minister (2025). *Decree No. 57/2025/ND-CP: Regulations on the mechanism for direct electricity*

trading between renewable energy generators and large electricity users.

Priyanka Sharma (2024). *Energy Autonomy: Local Solutions for Global Resource Challenges*. Journal of Sustainable Solutions. https://www.researchgate.net/publication/383802807_Energy_Autonomy_Local_Solutions_for_Global_Resource_Challenges.

Phan Thi Song Thuong, Nguyen Tat Truong (2024). *Some issues on renewable energy development in Vietnam today: Current situation, potential and solution implications*. Communist Magazine. <https://www.tapchicongsan.org.vn/web/guest/nghien-cu/-/2018/906102/mot-so-van-de-ve-phat-trien-nang-luong-tai-ao-viet-nam-hien-nay--thuc-trang-2C-tiem-nang-va-ham-y-giai-phap.aspx>

UNDP (2016). *Pursuing the 1,5°C Limit - Benefits and Opportunities*. https://www.undp.org/sites/g/files/zskgke326/files/publications/Pursuing_1-5C-Limit.pdf.

UNDP (2024). *Transition pathways for Vietnam's major coal-thermal power plants*. <https://www.undp.org/vietnam/press-releases/transition-pathways-vietnams-major-coal-thermal-power-plants>.

Vietnam Energy Association (2017). *Exploitation and use of Vietnam's hydropower resources*. <https://nangluongvietnam.vn/khai-thac-su-dung-nguon-thuy-dien-viet-nam-19933.html>.

Vietnam Energy Association (2020). *Update on survey data on solar radiation intensity in Vietnam*. <https://nangluongvietnam.vn/cap-nhat-so-lieu-khao-sat-cuong-do-buc-xa-mat-troi-o-viet-nam-24728.html>.

Vietnam Electricity Group (2023). *Some general figures on national electricity sources in 2023*. <https://www.evn.com.vn/d6/news/Mot-so-so-lieu-tong-quan-ve-nguon-dien-toan-quoc-nam-2023-66-142-124707.aspx>.

Part 2

DIGITAL TRANSFORMATION FOR PROSPEROUS DEVELOPMENT

Big data, machine and deep learning techniques for landslide modeling, prediction, and detection

Łukasz Pawlik^{1,*}, Hieu Trung Tran^{1,2,3}, Pham Van Tien³, Paweł Kroh⁴

¹University of Silesia, Institute of Earth Sciences, ul. Będzińska 60, 41-200 Sosnowiec, Poland

²International Environmental Doctoral School, University of Silesia, ul. Będzińska 60, 41-200 Sosnowiec, Poland

³Vietnam Academy of Science and Technology, Institute of Earth Sciences, Hanoi, Viet Nam

⁴University of the National Education Commission, Institute of Biology and Earth Sciences, ul. Podchorążych 2, 30-084 Kraków, Poland

*Email: lukasz.pawlik@us.edu.pl

Abstract: Landslides occur under specific conditions, which can be a subject of in-depth evaluation and summary. When this type of geohazard forms in large quantities, the most convenient way to assess it is using remote sensing datasets collected during multiple satellite missions. In this paper, we summarize the results of several machine learning and deep learning techniques applied to construct landslide susceptibility maps for selected regions in Vietnam. The techniques used included random forest (RF), support vector machine (SVM), extreme gradient boosting (XGB), convolutional neural networks (CNN), and deep neural networks (DNN). In our models, the response variable consisted of a binary variable with two categories: landslide and non-landslide observations. Landslide observations were the result of manual interpretation of PlanetScope satellite images. The best model was built using XGB (AUC=0.915) with rainfall, elevation and aspect as the most important predictors. Hybrid CNN-DNN model had even higher precision (AUC=0.965) but different features with the highest importance, i.e., distance to roads and faults, and elevation. Landslide susceptibility maps are a key product in spatial management planning and strategies that mitigate the adverse outcomes of landslides and related geohazards. The maps should be regularly updated to provide the most accurate information for environmental management and risk evaluation.

Keywords geohazard, landslide, machine learning, deep learning, landslide susceptibility map, spatial prediction.

INTRODUCTION

In landslide studies, the volume and range of the data at hand are significant but never complete because the subject of modeling is part of the natural geosystem, which has infinite complexity. In this paper, we review some typical approaches used for landslide susceptibility mapping and detection, utilizing machine learning and deep learning methods, as well as the range of commonly applied predictors. Recently, deep learning models have gathered significant attention over conventional machine learning models in LSM due to their ability to fully discover representative features of the data and handle large amounts of data (Merghadi et al., 2020; Azarafza et al., 2021). However, these methods also have several disadvantages, such as large data requirements, complex data preprocessing, high computational costs, and the risk of overfitting. The aim of this paper is to show capabilities of machine and deep learning techniques to build highly accurate models used for landslide susceptibility mapping. To reach the aim a set of manually detect landslides from selected regions in Vietnam were used.

MODELLING APPROACHES

Landslide data – response variable

When modeling landslides, a frequent question we look for is where these geohazards are likely to form. For the task, we need a response variable of binary character, i.e.,

consisting of two classes: landslide and non-landslide points. We focused on solving a classification problem. In the examples presented here, landslides were identified manually from high-resolution satellite imagery via the Planet Basemap (4.7 m/px) (<https://www.planet.com/basemaps/>) and Google Earth software. Non-landslide points were randomly generated at a minimum distance of 400 m from the landslide polygons (Guo et al. 2024). It is a common approach, but its validity must be tested in the regional context of each study plot. In our case, the response variable dataset was balanced. It means the number of observations was equal between landslide and nonlandslide points.

The examples of modelling presented in this paper are based on study areas in Than Uyen, Muong La, and Mu Cang Chai districts in northern Vietnam (Figs. 1 and 2).

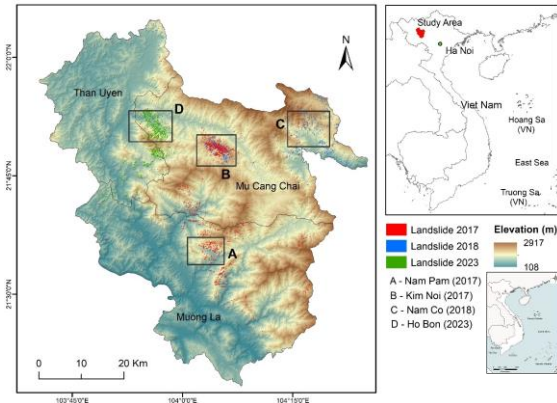


Figure 1. Study area and landslide inventory map across Than Uyen, Muong La, and Mu Cang Chai districts (Tran et al., 2025a).

Potential predictors

Potential predictors can vary in character and type, and their selection should be based on common historical knowledge and previous experience. For instance, when dealing with rainfall-induced landslides, rainfall data should be the most obvious input information, although it is frequently not available at high spatiotemporal resolution. In the examples shown here, we selected 12 predictors to construct landslide susceptibility models. Among these factors, elevation, slope angle,

aspect, profile curvature, topographic wetness index (TWI), river density, distance to roads, distance to faults, and lithology served as static landslide conditioning factors. The average annual rainfall, land cover, and normalized difference vegetation index (NDVI) were considered key factors in dynamic landslide assessment.

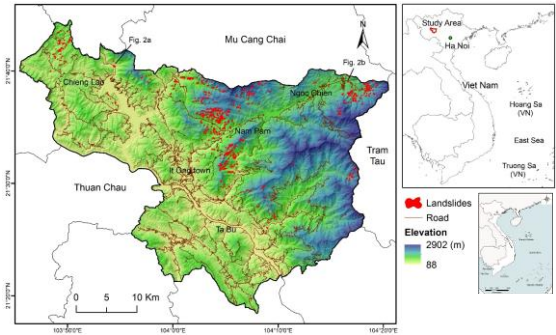


Figure 2. Study area and landslide inventory map across Muong La district in Son La Province, Northwest Vietnam (Tran et al., 2025b).

A 30-metre digital elevation model (DEM) (JPL, 2020) was used to generate topographic variables, such as curvature, aspect, and slope angle. The TWI quantified the terrain-driven variation in soil moisture. The TWI integrated the water supply from the upslope catchment area and downslope water drainage for each cell in a DEM. The lithology provides information on the rock's characteristics, including composition, texture, and strength. The average annual rainfall was calculated from both daily rainfall data from the Climate Hazards Group InfraRed Precipitation with Station data (CHIRPS) (Funk et al., 2015). Land cover maps were derived from the Regional Land Cover Monitoring System (<https://www.landcovermapping.org/en/landcover/>), which uses satellite technology to facilitate high-quality regional land cover maps at a 30-m resolution from Landsat and MODIS images. The NDVI describes the density and health conditions of vegetation on the ground and is used as an effective predictor of vegetation cover changes due to landslides (Ha et al., 2024). NDVI indicates water or clouds ($NDVI < 0$); very little vegetation, bare soil, or early stages of cultivation ($NDVI$ close to 0); and vigorous vegetation cover ($NDVI$ close to 1).

Modelling algorithms

In our recent approach, we used three machine learning techniques (random forest, support vector machine, and extreme gradient boosting), and two deep learning techniques (deep and convolutional neural networks). Random Forest (RF) is an algorithm that is a supervised learning technique, which combines several decision trees for enhanced performance (Breiman, 2001). The support vector machine (SVM) aims to find the optimal hyperplane for separating data points into distinct classes (Vapnik, 1995). Extreme Gradient Boosting (XGB) generates a prediction model in the form of a boosting ensemble of weak classification trees by optimizing the loss function using gradient descent, along with several enhancements and regularization techniques. Deep neural networks (DNNs) utilize multilayer feedforward artificial neural networks characterized by their depth and trained using the backpropagation algorithm (Alqadhi et al., 2023). Convolutional neural networks (CNNs) are a type of artificial neural network used to analyse visual imagery. The CNN-DNN model was designed to leverage the advantages of both the CNN and the DNN. Based on its ability to learn local features, the CNN processes input data to identify the primary features associated with landslide susceptibility. These features are then flattened for use as input data for the DNN. This hybrid model can handle landslide classification tasks (Azarafza et al., 2021).

RESULTS AND DISCUSSION

Landslide susceptibility mapping is typically based on historical information, which is used to train the model and calculate probabilities. In the examples of studies presented here, three landslide susceptibility models were developed by applying the extreme gradient boosting method to 12 predictors and multitemporal landslide inventories collected in 2017, 2018, and 2023. We assessed the spatiotemporal changes in landslide susceptibility maps using successive landslide inventories and dynamic predictors

(annual average rainfall, land cover, and NDVI) to retain susceptibility information from previous events (Tran et al., 2025a). The results indicate significant changes in landslide susceptibility across the first study area over time. The post-2017 susceptibility map reveals that the central and northeastern parts of the study area are highly susceptible, whereas the susceptibility levels are low in the northwestern and southern parts. The model classifies 61.27% of the study area as having very low or low landslide susceptibility, whereas 11.6% and 13.2% of the area are highly and very highly prone to landslides, respectively (Tran et al., 2025a). However, some landslides could have occurred in areas with low to very low susceptibility, highlighting the uncertainties of maps and the stochastic nature of rainfall events. The uncertainty in landslide susceptibility can be attributed to the quality of input data, data preprocessing, and model selection. Compared with the post-2017 map, approximately 12.8% of the study area experiences a considerable increase in landslide susceptibility values, from very low and low classes to high and very high classes (Fig. 3). In contrast, 7.35% of the area experiences a significant decline from the high and very high classes to the low and very low classes (Fig. 3). Our results suggested that scenarios built upon average annual rainfall are necessary for landslide susceptibility mapping in the future. Rainfall is a significant factor triggering landslides because it affects soil saturation. Intense and prolonged rainfall can increase the soil pore water pressure, reducing the strength and cohesion of the soil and bedrock and facilitating landslide initiation. According to the RCP4.5 climate change scenario, the annual rainfall in the Lai Chau, Yen Bai, and Son La Provinces will increase by 8.8–9.9% in the mid-21st century (2046–2065) and by 7.5–12.9% at the end of the 21st century (2080–2099) (Thang et al. 2020). This scenario indicates that the impact of rainfall on landslides may increase in the future. However, the quality of rainfall data must be considered, as the limitations of data availability and spatiotemporal resolution have adverse effects on modeling and prediction.

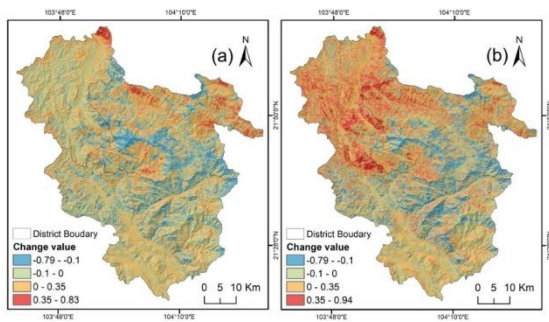


Figure 3 The change in landslide susceptibility probability values (a) 2017- 2018 (b) 2017-2023 (Tran et al., 2025a).

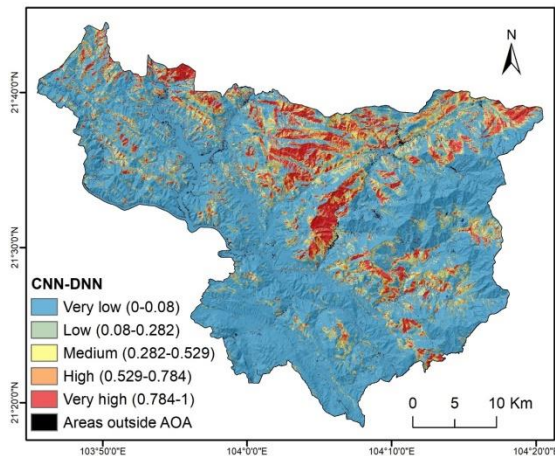


Figure 4. Landslide susceptibility map using the CNN-DNN model (Tran et al., 2025b).

The CNN-DNN model was used to construct an LSM for the Muong La district. Using the natural break approach, the LSM was divided into five classes: very low, low, moderate, high, and very high. These classes covered 74%, 8.36%, 5.54%, 5.16 %, and 6.94%, respectively (Fig. 4). We found that most of the testing data landslides fall into the very high and high classes (>94%). This finding demonstrates the high accuracy of the LSM (Tran et al., 2025b). The performance of the models was evaluated by various criteria, revealing that the CNN-DNN model had the best performance, with an AUC of 0.971. We found an increasing landslide probability with increasing slope, annual average rainfall, curvature, elevation reaching 1,500 m, aspect (0–100°), and river density reaching 2 km/km². This study represents an advancement of the CNN-DNN model, making it applicable to

various geographic locations and environmental situations.

CONCLUSIONS

The results revealed high and very high landslide susceptibility changes in the northwestern and northeastern regions and moderate reductions in the central areas during the study period. Annual average rainfall, elevation, and aspect were identified as the three most significant predictors of landslides in our first study site; however, rainfall was not found to be a significant predictor at the second study site. Although rainfall data were the most difficult to collect in large quantities for vast areas, we showed that this problem could be partially overcome through data interpolation and model updates. Future advancements will be necessary to develop predictive models that can operate under various conditions of a constantly evolving and changing Vietnamese landscape.

ACKNOWLEDGMENTS

The research activities financed by the funds granted under the Polish National Science Centre project no 2023/49/B/ST10/02879.

REFERENCES

- Azarafza M, Azarafza M, Akgün H, Atkinson PM, Derakhshani R (2021) Deep learning-based landslide susceptibility mapping. *Sci Rep* 11:24112. <https://doi.org/10.1038/s41598-021-03585-1>.
- Alqadhi S, Mallick J, Alkahtani M (2023) Integrated deep learning with explainable artificial intelligence for enhanced landslide management. *Nat Hazards* 120. <https://doi.org/10.1007/s11069-023-06260-y>.
- Breiman L (2001) Random Forests. *Mach Learn* 45:5–32. <https://doi.org/10.1023/A:1010933404324>.
- Guo H, (2017) Big Earth data: A new frontier in Earth and information sciences. *Big Earth Data* 1, 1-2, 4-20, 10.1080/20964471.2017.1403062.
- Guo Z, Tian B, Zhu Y, et al (2024) How do the landslide and non-landslide sampling strategies impact landslide susceptibility assessment? — A catchment-scale case study from China. *J Rock Mech Geotech Eng* 16:877–894. <https://doi.org/10.1016/j.jrmge.2023.07.026>.

- Funk C, Peterson P, Landsfeld M, et al (2015) The climate hazards infrared precipitation with stations—a new environmental record for monitoring extremes. *Sci Data* 2:150066. <https://doi.org/10.1038/sdata.2015.66>.
- JPL N (2020) NASADEM Merged DEM Global 1 arc second V001.
- Merghadi A, Yunus AP, Dou J, Whiteley J, Thaipham B, Bui T, Avtar R, Boumezbeur A, Pham B (2020) Machine learning methods for landslide susceptibility studies: A comparative overview of algorithm performance. *Earth-Sci Rev.* <https://doi.org/10.1016/j.earscirev.2020.103225>.
- Pawlik Ł, (2025) *R Applications in Earth Sciences*. Springer, 174. <https://doi.org/10.1007/978-3-031-89673-6>.
- Tran H T, Pawlik Ł, Pham V T, Nguyen C Q, (2025a). Evaluating spatiotemporal variations in landslide susceptibility in northwest Vietnam. *Bulletin of Engineering Geology and the Environment* (under review).
- Tran H T, Pawlik Ł, Pham V T. (2025b). High-resolution landslide susceptibility mapping via deep learning models: a case study in Son La Province, Vietnam. *Environmental Science and Pollution Research* (under review).
- Vapnik V (1995) *The Nature of Statistical Learning Theory*. Springer-Verlag, NewYork.

DOI: 10.15625/vap.2025.0205

Development and Application of a WebGIS-Based Early Warning System for Landslides

Duong Thi Toan*, Do Minh Duc

University of Science, Vietnam National University, Hanoi, Vietnam

*Email: duongtoan@hus.edu.vn

Abstract This paper presents a landslide early warning model and evaluates the effectiveness of its WebGIS-based communication system, which was developed to support disaster prevention in the mountainous areas of Lao Cai Province (formerly the Lao Cai-Yen Bai region). The model integrates multi-source data, including observed rainfall, meteorological forecasts, topographic and geological characteristics, and landslide susceptibility maps, allowing real-time determination and visualization of warning levels. The WebGIS platform was developed using open-source technologies to ensure flexible access via the Internet and mobile devices. The system was tested along National Highway 32 and in several mountainous communes of Lao Cai Province. Results demonstrate that the model effectively detected and warned of landslide risks during Storms No. 5, 10, and 11 in 2025, providing 6–48 hours of lead time that enabled local authorities to take proactive measures and minimize losses of life and property.

Keywords Landslide; Early Warning System; WebGIS

INTRODUCTION

Landslides, particularly large-scale slope failures, are among the most severe natural hazards, causing significant losses to human lives, property, and transportation infrastructure. In recent years, both the frequency and magnitude of landslides have tended to increase, notably in Lao Cai, Tuyen Quang, and several central provinces. Large-scale landslides in Vietnam are often associated with prolonged or extreme rainfall events,

combined with the impacts of socio-economic development activities. Among various risk reduction measures, early warning systems are regarded as an effective and sustainable approach to enhance community preparedness and response capacity to geohazards (Kong et al., 2020)

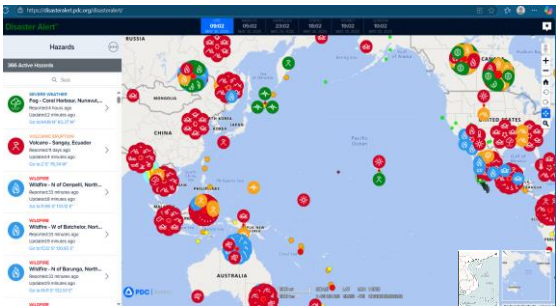


Figure 1. Early Warning System of the Pacific Disaster Center

Globally, many countries have made significant investments in intelligent early warning systems capable of integrating rainfall data, geotechnical sensors, satellite imagery, and real-time forecasting models (Li et al., 2025; Haque, 2025). The early warning system developed by the Pacific Disaster Center (PDC), managed by the University of Hawaii, is widely recognized worldwide. DisasterAware is a customizable platform that can be expanded with various data types and visualization tools to provide global risk information, early warnings, and one of the largest collections of scientifically verified geospatial datasets for disaster risk and impact assessment (Figure 1). The Japan Meteorological Agency (JMA) has developed a real-time landslide warning website, that provides hazard information with a spatial

resolution of 5×5 km and five hazard levels (Hidayat et. al., 2024) (Figure 2).

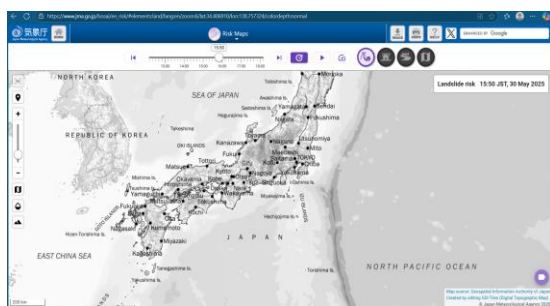


Figure 2. Landslide Warning Website of the Japan (JMA)

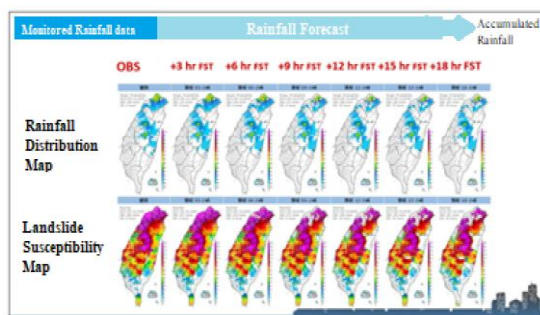


Figure 3. Estimation of Landslide Occurrence Probability Based on Rainfall Data (Taiwan)

Similarly, the National Science and Technology Center for Disaster Reduction (NCDR) in Taiwan operates a real-time early warning system based on hazard maps and observation data, which uses real-time rainfall forecasting to estimate landslide probability 1–2 days in advance (Figure 3).

In Vietnam, several early warning systems have been developed, notably the real-time flash flood and landslide early warning system established by the National Center for Hydro-Meteorological Forecasting (NCHMF), which provides detailed warnings down to the commune level (Figure 4). In addition, the Institute of Geo-Environmental Technology has developed an online landslide warning system accessible at <https://truotlo.com/trang-chu>, displaying maps of potential landslide areas represented by color-coded hazard levels. These systems enable monitoring, updating, and sharing of landslide hazard information across various regions of the country, thereby

contributing effectively to disaster prevention and risk management efforts (Figure 5).

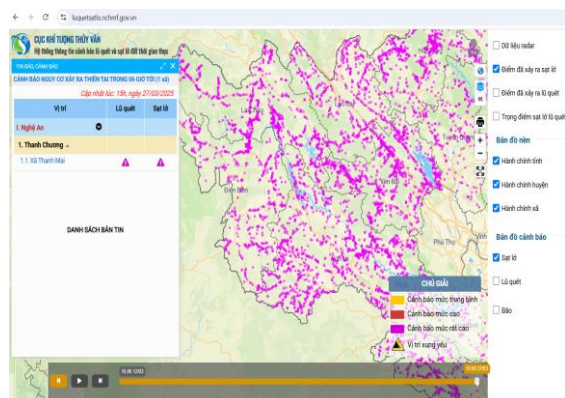


Figure 4. Regional Display of Landslide Information (NCHMF)

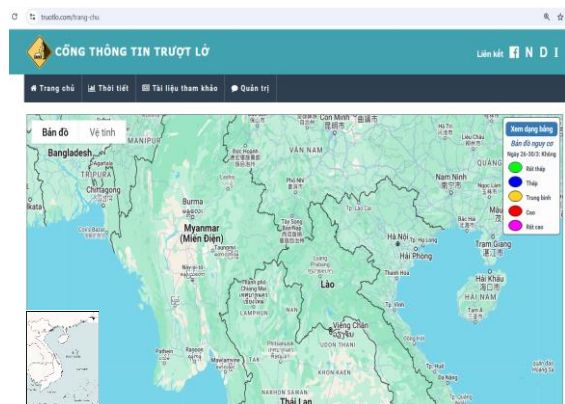


Figure 5. Display of Landslide Occurrences Nationwide (IGET)

Based on the practical need for early warning and the initial results of existing systems, the National Project “Study on the formation mechanisms, distribution patterns, and early warning of large-scale landslides in Vietnam by integrating remote sensing technology, artificial intelligence, and unsaturated soil mechanics theory” (Duong, 2025) has developed an early warning model for landslide hazards adapted to the topographical, climatic, and data conditions of Vietnam, with a pilot implementation along National Highway 32 in Lao Cai Province (formerly part of Yen Bai Province).

The model was designed on the principle of multi-component integration and

interconnection, making optimal use of available datasets such as observed rainfall, meteorological forecasts, rainfall thresholds for landslide initiation, terrain characteristics, and current hazard conditions. The system consists of two major components: a technical-analytical module (early detection, rainfall threshold estimation, data acquisition and processing) and a communication module (displaying warning information via mobile application and Web/WebGIS platform).

The objective of this paper is to present this early warning model, with a focus on its system architecture, operational principles, and visualization features on the WebGIS platform.

This paper introduces an early warning model, with the main objective of presenting the WebGIS-Based Warning Information System, including its system architecture and visualization features. In addition, the paper describes the system's operation, mechanisms for communicating information to the public, and the effectiveness of its implementation during the 2025 rainy and storm season in Lao Cai Province.

INFORMATION ON METHODS TO BUILD THE EARLY WARNING MODEL AND THE WEBGIS-BASED WARNING INFORMATION SYSTEM

Building the Early Warning Model

The landslide early warning model is designed to detect early changes in conditions that may trigger slope failures. It functions as an integrated, multi-source system that enables the assessment and forecasting of landslide hazards in mountainous areas based on hydro-geodynamic factors such as rainfall, soil moisture, topography, and geological structure (Figure 1). A typical Landslide Early Warning System (LEWS) consists of three main components: (1) monitoring and data acquisition (rain gauges, sensors, radar, remote sensing, etc.); (2) hazard assessment and modeling (hydrological-infiltration models, slope stability models, rainfall-duration thresholds); and (3) dissemination and

visualization (software, maps, and user interfaces). This landslide early warning model was built upon the state-funded project conducted by (Duong, 2025).

The proposed model is developed on the principles of integration and automation, combining Earth science analysis, GIS-remote sensing technologies, artificial intelligence, and multi-platform communication. The database is established from field surveys, remote sensing images, UAV data, and geotechnical-geomorphological information, and processed using statistical analysis and unsaturated soil mechanics models (GeoSlope, LS-Rapid) to delineate potential landslide zones (TQML).

The warning system is built upon hazard zonation maps that integrate topographic, geological, hydrological, and meteorological factors with slope stability analysis and rainfall threshold calculations. It classifies warning levels from H₀ (safe) to H₄ (very high risk). The results are displayed on a WebGIS platform, providing real-time information on location, hazard level, and representative imagery. The integration of observed and forecasted rainfall data enhances proactive decision-making for local authorities and communities, supporting disaster risk management, spatial planning, and mitigation efforts.

Building the WebGIS-Based Warning Information System

The WebGIS-Based Warning Information System was developed as a web-based application utilizing open-source technologies to ensure flexibility, scalability, and accessibility.

This system was programmed in PHP 8.x using the Laravel framework, with HTML, CSS, JavaScript, and AJAX applied for interactive front-end development. Visual Studio Code served as the development environment, and the web server was deployed on Nginx running under Ubuntu Server 22.04 LTS.

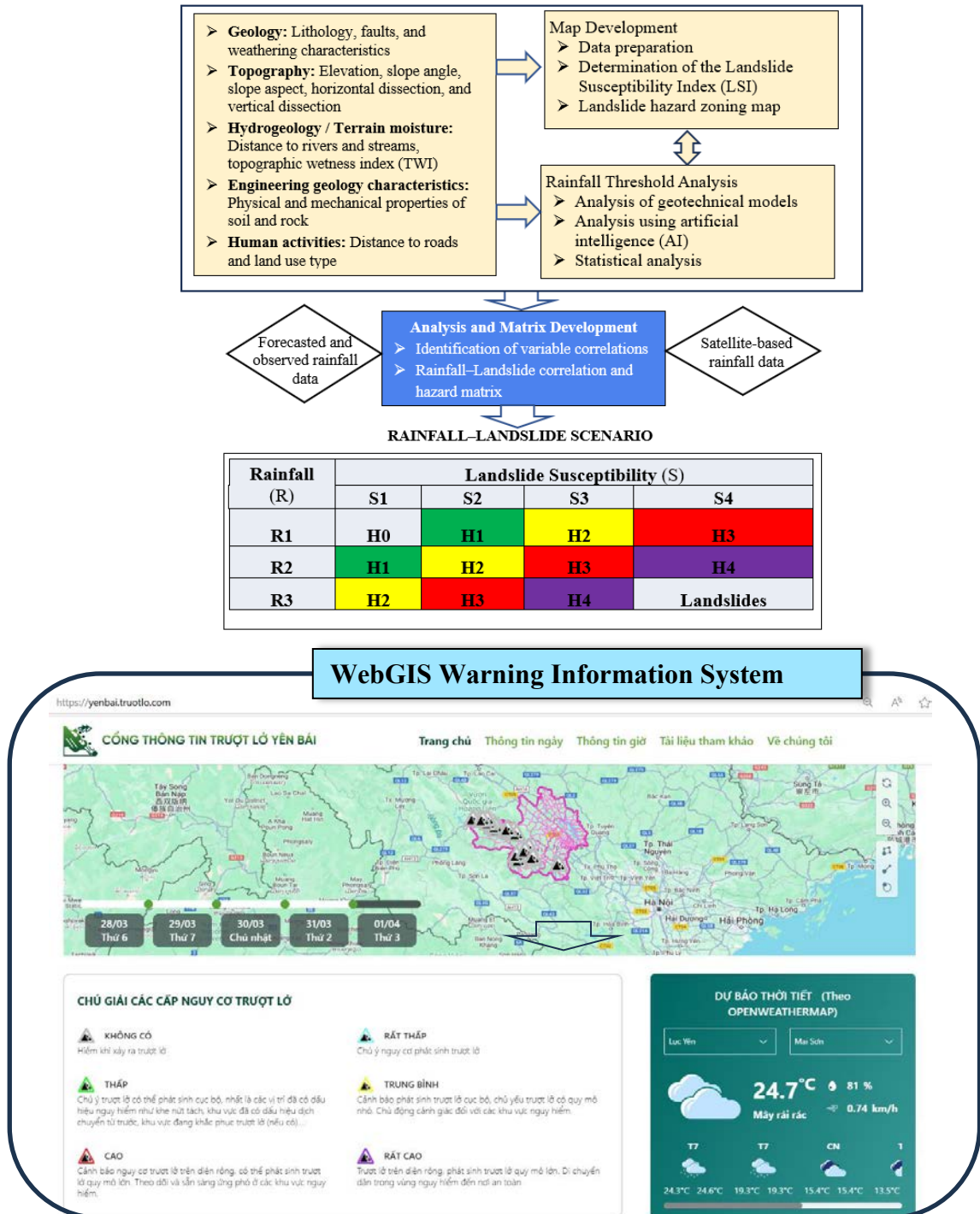


Figure 6. Structure and linkage of the Early Warning Model and WebGIS Warning Information System

The spatial database was managed with PostgreSQL 17.1 integrated with the PostGIS extension to enable efficient geospatial data

storage and analysis. WebGIS functionalities were implemented through the OpenLayers platform, providing real-time visualization of

rainfall and landslide-prone areas. JasperReports was employed for generating automated analytical and statistical reports. The system operates seamlessly within LAN, WAN, and Internet environments and is compatible with both Linux and Windows operating systems. Users can access the platform via standard web browsers such as Chrome, Firefox, and Microsoft Edge, ensuring broad accessibility and user convenience.

The rainfall data used for the warning model include both forecasted and observed data, as shown in Figure 6: (i) Forecasted data are obtained from AccuWeather and WorldWeatherOnline. AccuWeather is a private U.S. media company that provides commercial hourly weather forecasts worldwide. WorldWeatherOnline, headquartered in State College, Pennsylvania, also provides global weather forecast services and utilizes data from geostationary and polar-orbit satellites to monitor weather conditions worldwide. For this study, due to the limited number of API calls required, the free API service provided via email was used. (ii) Observed hourly rainfall data were collected from the Vrain station network within the study area. These data were used to validate and adjust the forecast data for the warning system.

To provide warning information, forecasted rainfall data are compared with the landslide-triggering rainfall thresholds of each watershed and landslide mass in the study area. These rainfall thresholds are analyzed based on the natural characteristics of the region (including topography, engineering geology, hydrogeology, and degree of weathering) as well as the local rainfall patterns. The analysis and determination of rainfall thresholds is a key aspect of the study (Duong, 2025) utilized in this paper. The method combines statistical analysis and geotechnical program analysis, and the results are presented using correlation diagrams between rainfall intensity and rainfall duration that trigger landslides ($I = aD - b$).

WEBGIS SYSTEM DEVELOPMENT AND TESTING RESULTS

WebGIS Display Information

Landslides are a common geological hazard occurring along National Highway No. 32, causing significant damage to lives, property, and transportation infrastructure in recent years. This study integrates information technology and landslide susceptibility modeling results to develop the website <https://yenbai.truotlo.com/>. The website provides key contents including daily and hourly warning bulletins, hazard maps, regional weather forecasts, and updated landslide information for Yen Bai Province. Utilizing this platform enables local authorities and residents to proactively prevent and mitigate landslide-related damages. The website consists of five main sections: Home, Daily Information, Hourly Information, References, and About Us (Figures 7 and 8).

On the homepage, the system displays a map showing potential large-scale landslide locations along National Highway No. 32, from Van Chan to Mu Cang Chai (former district), including daily and hourly hazard levels, a legend explaining risk categories (Table 1), and a weather forecast panel (Figure 8a). The “Daily Information” and “Hourly Information” pages provide detailed content as described in Figure 7, with corresponding warning displays (Figures 8b and 8c).

Users can select to view hazard levels by day or hour using the toolbar on the left side of the screen. Landslide-prone points are displayed on the base map with basic descriptive data. When clicking on each triangular icon, an information window appears showing: site name, coordinates, commune, location, current condition, landslide history, geological and topographic features, weathered layer thickness, and a photograph of the landslide area (Figure 9).

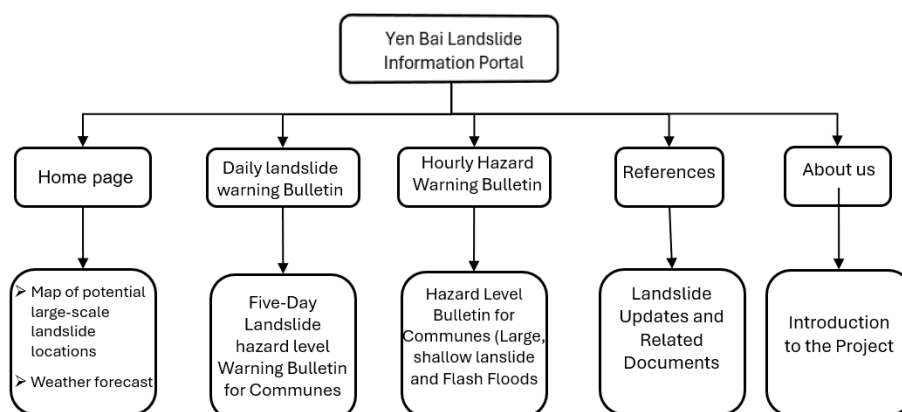


Figure 7. Structure and linkage of the Early Warning Model and WebGIS Warning Information System

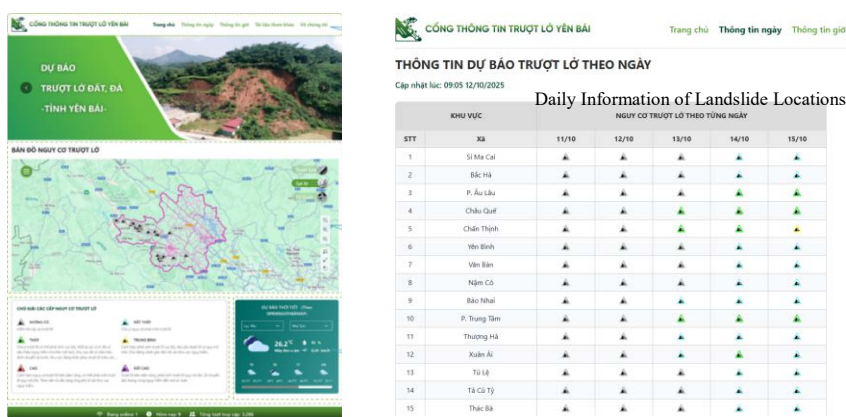


Figure 8a. Main interface of the homepage and daily information

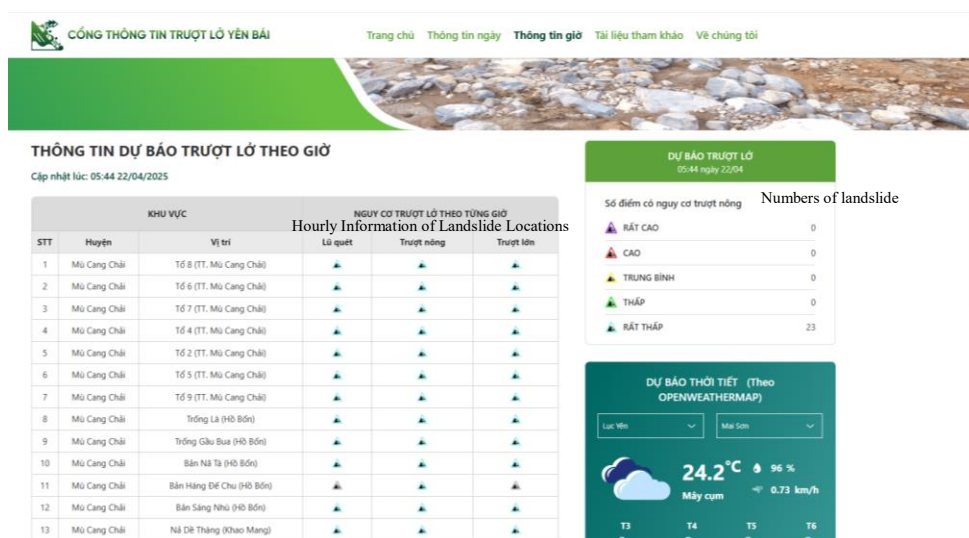


Figure 8b. Hourly information on landslide locations

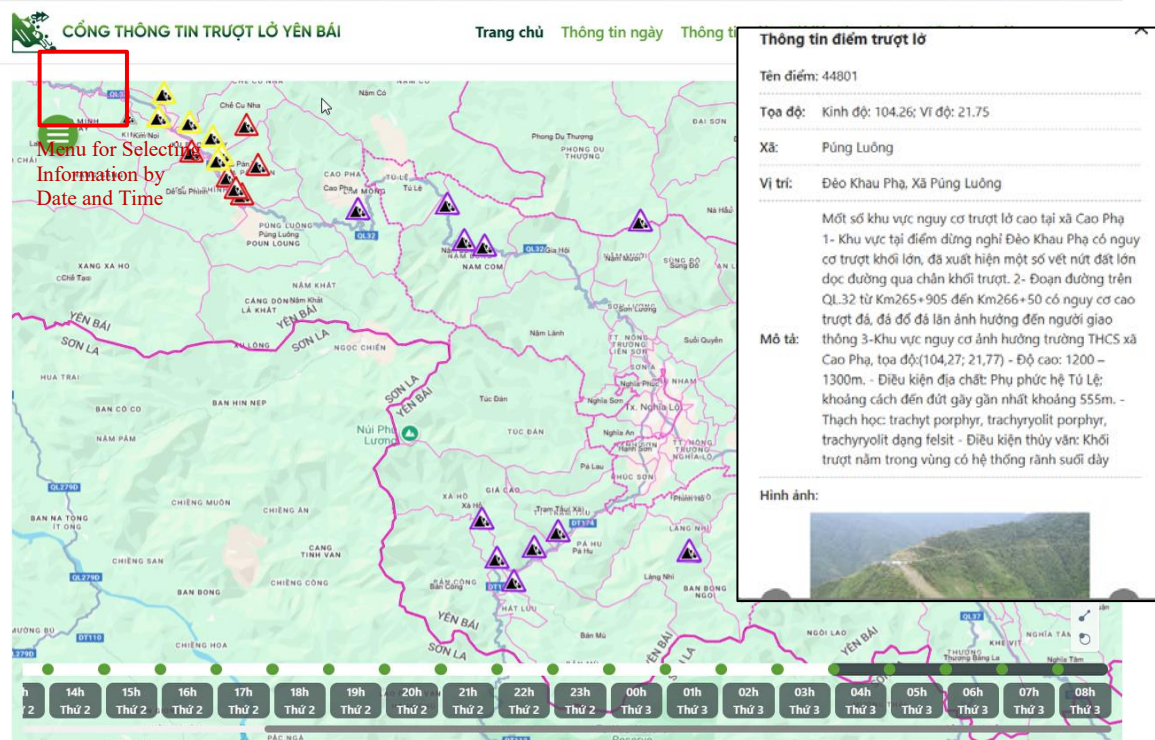


Figure 9. Information on large-scale landslide hazard points

In particular, the system now provides simultaneous early warnings for three types of hazards — large-scale landslides, small-scale slope failures, and flash floods. Among these, large-scale landslide warnings have not been addressed in previous research or implemented in other WebGIS-based warning systems in Vietnam, representing a clear difference and a significant added value of the proposed system.

This update highlights that the system not only integrates multiple hazard types in a single interface but also introduces large-scale landslide warnings, a feature that distinguishes it from previously developed early warning platforms in Vietnam.

Procedure for introducing the WebGIS system to the community

After the model was developed, its operation focused on testing the application of the early warning system for rainfall-induced landslides during the rainy season, while

updating input data, collecting user feedback, and calibrating the model. The warning model was introduced and tested with local authorities and communities to enhance functionality, improve reliability, and prepare for technology transfer to support local disaster risk reduction efforts. The pilot implementation emphasized user training and interpretation of information displayed on the WebGIS platform: <https://yenbai.truotlo.com/>.

The operational procedure of the early warning system follows three main phases: before, during, and after the rainy season, corresponding to the Prepare-Respond-Recover cycle in the UNDRR (2019, 2020) disaster risk management framework.

(i) Before the rainy season, the focus is on preparedness and community capacity building through training workshops and technical seminars for local officers and residents on landslide risk identification, use of the WebGIS and mobile warning applications, and

strengthening the local “four-on-the-spot” disaster response network. Information is disseminated through training sessions, official letters, emails, and Zalo messages, using documents, posters, and visual materials. (Figure 10 a, b, c).

(ii) During the rainy season, the system operates in real-time warning mode, continuously updating information via WebGIS, mobile apps, and communication channels to enable timely response and evacuation, while also collecting on-site feedback. Warning messages are shared through email, Zalo, and social media

(Facebook) in the form of bulletins, images, and posters (Figure 11, 12).

(iii) After the rainy season, the process includes system evaluation, calibration, and recovery, as well as compiling local damage reports and feedback to update hazard maps, refine rainfall thresholds, and improve system accuracy for subsequent operational cycles

Table 1. Legend of hazard levels







Symbol	Hazard level		Brief description
0		No hazard	Landslides are unlikely to occur.
1		Very low	Stay alert for possible initial signs of slope movement.
2		Low	Localized landslides may occur, especially in areas showing cracks, ground separation, past movement, or ongoing slope repair.
3		Moderate	Small or localized landslides may occur. Increased vigilance is advised, and close monitoring of warning information with readiness for
4		High	Potential for large-scale or widespread landslides. Closely monitor warning information and prepare appropriate response measures.
5		Very high	Widespread and large-scale landslides are likely. Immediate evacuation from hazardous areas is required.



Figure 10 a. Organizing community-based seminars and training programs



Figure 10 b. Providing training and guidance for local officers and residents to access and use the WebGIS-based landslide warning system

T

Dương Toàn <duongtoan@hus.edu.vn>
đến trangocluan, hamanhcuong, nguyenthabinh, vnhah, ccthuylaiyb, sang67yb, hungkhanhduc, anhvanminh, anh1011, lien.tta, quynh.trng, huonggt981, hieyb1981, hoanggiang.hung82, hieuccbmtyb, thurongngh

14:38 CN, 20 thg 7

Kính gửi Sở Nông nghiệp và Môi trường Lào Cai

Kính gửi các đơn vị địa phương tỉnh Lào Cai

Dự báo từ tối ngày 20 đến 23/7 nguy cơ **sạt lở, lũ quét** RẤT CAO, CAO ở khu vực miền núi phía Bắc, các tỉnh Thanh Hóa, Nghệ An, Hà Tĩnh. Một số khu vực còn tiếp tục ngày 24-25/7 (theo dõi bản tin sau).

Đặc biệt lưu ý KHU VỰC MIỀN NÚI PHÍA TÂY CÁC TỈNH THANH HÓA VÀ NGHỆ AN, các tỉnh Sơn La và Lào Cai.

Từ thực tiễn bão Yagi năm 2024, Trà Leng (2020), Mù Cang Chải (2017)... một số kinh nghiệm quan trọng nghiên cứu **ứng phó sạt lở, lũ quét** quy mô lớn bao gồm:

(1) Thường xuyên rà soát phát hiện dấu hiệu phát sinh khối trượt lở như khe nứt kéo dài trên mái dốc. Một số khe nứt sẽ không dẫn ngay đến **sạt lở**, nhưng một khi đã xuất hiện khe nứt thì nguy cơ **sạt lở** luôn tiềm ẩn. Đối với các khu vực đã có các dấu hiệu trượt **lở** lớn (vị trí trên <https://yenbai.truotlo.com/>) cần chú ý nhắc nhở người dân theo dõi thông tin cảnh để **ứng phó** kịp thời

Thông tin cảnh báo gồm danh sách vị trí các điểm có nguy cơ xem trong mục Thông tin ngày tại website: <https://yenbai.truotlo.com/thong-tin-ngay>

(2) Khi mưa lớn phải luôn cảnh giác đối với khu vực dân cư, đoạn đường giao cắt với suối có hướng từ phía trên sườn dốc xuống, kể cả khi suối không có dòng chảy thường xuyên.

(3) Thường xuyên rà soát dọc các suối nhánh, dòng chảy xem có hiện tượng **sạt lở** hay cây gãy đổ gây nghẽn dòng chảy không, nếu có cần khai thông dòng chảy hoặc di chuyển người dân ở nơi trũng thấp vùng hạ lưu đến nơi an toàn. Lưu ý, trên một dòng chảy có thể có một hay nhiều điểm nghẽn. Chú ý các dòng suối có nước có nước lạnh.

(4) Theo dõi lượng mưa lớn trên ứng dụng **Sat Lở** Việt Nam (nếu đã cài đặt) với bán kính 3.000-5.000 mét (3-5 km). Khi mưa lớn cần thường xuyên kiểm tra các dòng chảy có khu dân cư ở lân cận, khoảng 30-60 phút/lần. Nếu mưa lớn tiếp diễn mạnh mà mực nước không tăng, thậm chí giảm thì cần cảnh báo ngay và di chuyển đến địa hình cao hơn dòng chảy ít nhất 5-6 mét.

Thông tin chi tiết hơn và cài đặt app di động "**Sat Lở** Việt Nam 2.2" tại:
<https://drive.google.com/.../1Q6NzOpRSVaCC1RGqE9fX0eHnYV9...>

(5) Các đợt mưa lớn gây thiệt hại nghiêm trọng nhất thường kéo dài nhiều ngày và có 2-3 khoảng thời gian khác nhau lượng mưa vượt ngưỡng nguy hiểm (một cách vắn tắt 150-180mm/ngày, 60mm/h, 90-100mm/3h, 110-120mm/6h).

(6) Khối trượt lở và **lũ quét** do nghẽn dòng có thể xảy ra ngay cả khi mưa giảm hẳn. Do vậy, chỉ quay trở lại khi không còn cảnh báo nguy cơ thiên tai.

Lưu ý: Thông tin được dựa trên các tài liệu và kết quả của nhóm nghiên cứu, không thay thế các bản tin chính thức về cảnh báo thiên tai. Thông tin liên quan xin liên hệ: email, điện thoại: duongtoan@hus.edu.vn (Ms. Toan, 0934543261); ducgeo@gmail.com (Mr. Đức), di động: 0365834875 (Ms. Quỳnh). Website: truotlo.com

Trân trọng !

CNDT, Dương Thị Toàn, Trường ĐH Khoa học Tự nhiên - ĐH Quốc gia Hà Nội

HƯỚNG DẪN CÀI ĐẶT TIỆN ÍCH "Trượt lở" TRÊN ỨNG DỤNG ZALO và Đăng ký nhận e-mail

Di chuyển camera để quét

Đăng ký e-mail để nhận bản tin dự báo, cảnh báo trượt lở theo ngày và thời gian thực (theo giờ) theo mẫu sau:

Họ và tên:
Cơ quan công tác:
E-mail đăng ký:
Gửi tới: truotlovn@gmail.com

Trượt lở

14:15 ngày 30-09-2025: Chủ ý nguy cơ THẤP trượt lở, lũ quét tại xã Mù Cang Chải.

15:15 ngày 30-09-2025: Chủ ý nguy cơ THẤP trượt lở, lũ quét tại xã Mù Cang Chải.

16:05/30/09/2025

NGUY CƠ SẠT LỞ, LŨ QUÉT ĐO BẢO SỐ 11

Chỉ tiết tại đây.

Figure 10 c. Sending warning information and guidance using WebGIS system via Email and Zalo

Effectiveness of the Warning System during Typhoon No. 5

Typhoon No. 5 (Kajiki, 2025) formed from a tropical depression and affected Vietnam from 22–26 August 2025. Making landfall between Thanh Hoa and northern Quang Tri on 25 August, it brought intense and widespread rainfall across the North Central and Northern regions, especially in mountainous provinces such as Thanh Hoa, Nghe An, Ha Tinh, and Quang Tri, triggering flash floods, local inundation, and landslides.

As the affected area expanded toward the Northwest, the early warning system issued

alerts on the night of 25 August and the morning of 26 August to communes along National Highway 32 (Figure 11). By early afternoon, heavy rainfall induced several landslides in Gia Hoi (former Nam Bung and Gia Hoi communes), Tu Le, and Pung Luong. The system successfully forecasted these events approximately 18 hours in advance, about 5–6 hours earlier than the actual occurrence of landslides and flash floods. Although there were significant property damages, no casualties were reported, demonstrating the system's effective early warning capability (Figure 12).

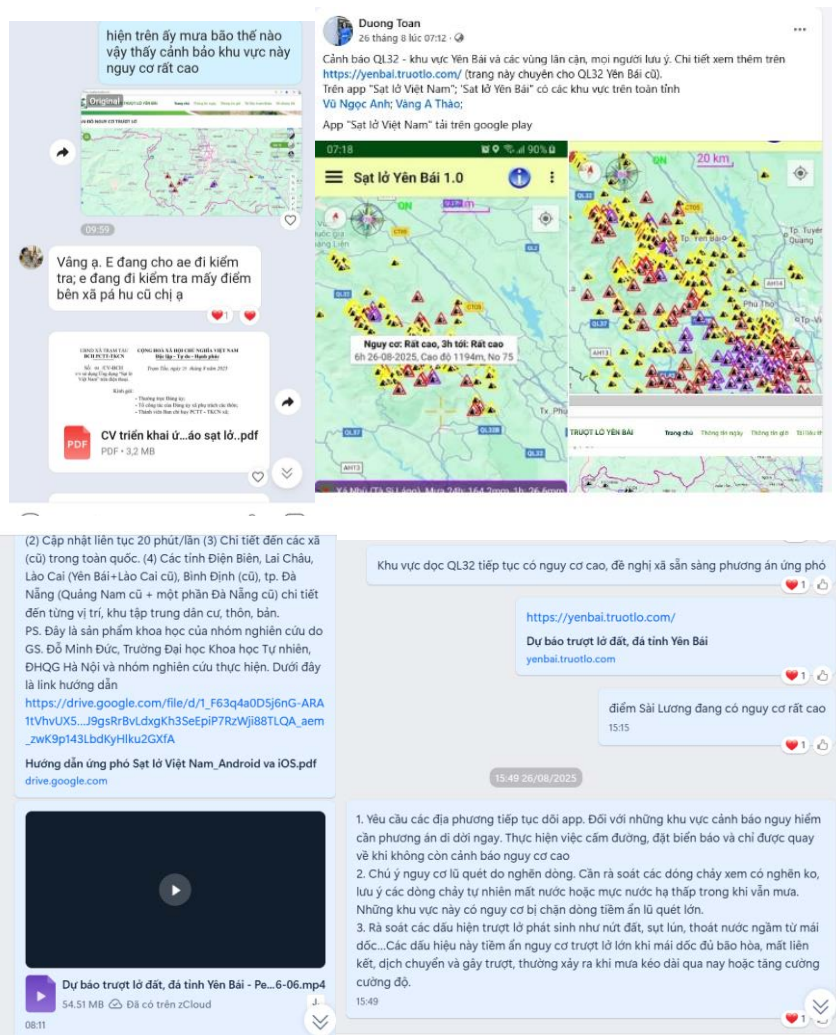


Figure 11. Warning information issued 18 hours, 6 hours before the landslide event, on the morning of 26/8/2025.

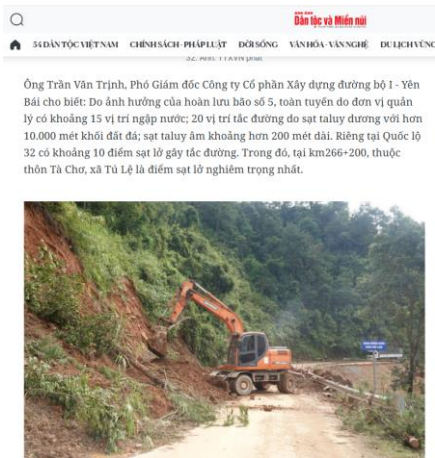


Figure 12. Landslide events occurred within the previously warned areas (TTXVN, 2025)

Effectiveness of the Warning System in Typhoon No. 10

Typhoon No. 10 (Bualoi, 2025) made landfall in Vietnam, causing severe damage across several provinces, particularly in the North Central region. The storm resulted in significant human and property losses, with mountainous districts in Thanh Hoa, Nghe An, and Ha Tinh being the most affected by widespread landslides and flooding, while transportation infrastructure suffered extensive damage.

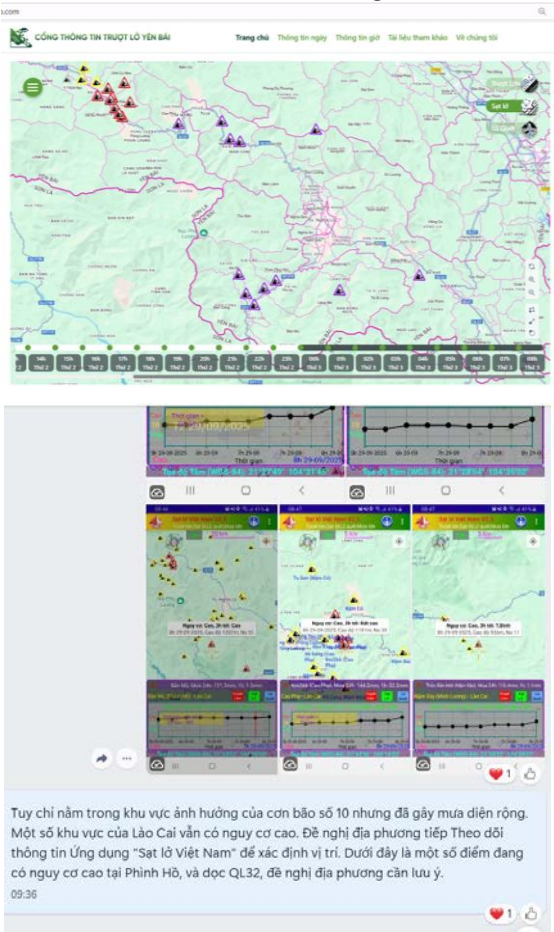


Figure 13. Warning information issued 29/9/2025.

For this event, the project issued early warning messages between September 28–29, one to two days before the occurrence of landslides and flash floods on the morning of

October 1, 2025, at Km 269 + 750 m on National Highway 32 (Figure 13). At this location, a 30-meter section of road collapsed due to a landslide, causing traffic disruption for 2–3 days

and interrupting travel and tourism to Mu Cang Chai. Several smaller landslides were also recorded along National Highway 32 and in other parts of Lao Cai Province (Figure 14).

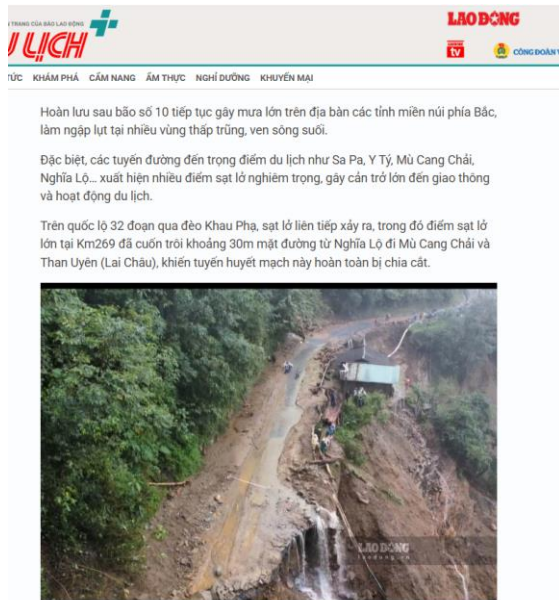


Figure 14. Landslide events occurred within the previously warned areas in QL32 (Duc, 2025)

Effectiveness of the Warning System in Typhoon No. 11

Typhoon No. 11 (Matmo, 2025) was a strong storm that made landfall in the North Central region and expanded northward, affecting the Viet Bac area. It caused extremely heavy rainfall in Thai Nguyen, Cao Bang, Ha Giang, and parts of Lao Cai, resulting in severe flooding and landslides, with the most serious damage reported in Thai Nguyen, Cao Bang, and Lang Son provinces.

The research team issued early warnings via messages and the mobile application to the Provincial Steering Committees for Natural Disaster Prevention and Control (PCTT&TKCN) starting on October 5, and simultaneously disseminated alerts to communes in Lao Cai Province, advising local authorities to review high-risk areas and evacuate residents (Figure 15). On October 7, a major landslide occurred in Phong Hai Commune, destroying three houses; however, timely warnings and evacuations prevented any loss of life (Figure 16).

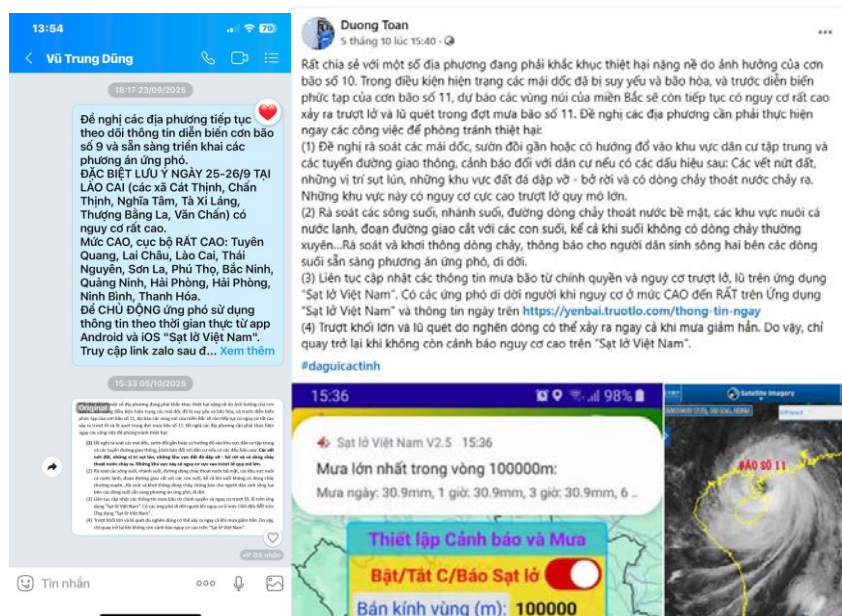


Figure 15. Warning information issued 5/10/2025

Ông Vũ Trung Dũng, Chủ tịch UBND xã Phong Hải cho biết, khoảng 9h sáng nay (7/10), tại Km9, QL 70 thuộc bản Cắm xảy ra vụ sạt lở đất. Đất đá từ taluy dương sạt xuống khiến một ngôi nhà hai tầng kiên cố cùng hai căn nhà lợp tôn bị đổ, sập. Rất may, không có thiệt hại về người.

"Nhận được tin cảnh báo hoàn lưu bão số 11, chính quyền đã vận động người dân di dời từ trước nên hạn chế được thiệt hại", ông Dũng nói.



THÔNG TIN DỰ BÁO TRƯỢT LỞ THEO NGÀY

Cập nhật lúc: 13:34 07/10/2025

KHU VỰC		NGUY CƠ TRƯỢT LỞ THEO TỪNG NGÀY				
STT	Xã	07/10	08/10	09/10	10/10	11/10
54	Phong Hải					
55	Pha Long					
56	Đường Cường					
57	Thác Bà					
58	Gia Phú					
59	Cốc Lầu					
60	P. Cầu Thia					
61	Nậm Chảy					
62	Mỏ Vàng					
63	Lào Chải					
64	Dương Quý					
65	Tả Phìn					
90	Si Ma Cai					



Figure 16. Large landslides occurred in Phong Hai, Si Ma Cai, and several other communes in LAo Cai in 7/10

CONCLUSION

This study presents a WebGIS-based early warning system for landslides and flash floods, piloted in Lao Cai Province (formerly Yen Bai – Lao Cai area), particularly along National Highway 32. The system has been completed and introduced to local authorities and communities through training sessions,

seminars, and communication channels such as email, Zalo, text messages, and social media.

Operational results during major typhoon events in 2025 demonstrate that the system functioned reliably, providing timely warnings consistent with actual landslide occurrences, thereby confirming its high reliability and applicability for disaster risk reduction. The

WebGIS platform has proven to be a practical support tool for local management, although its effectiveness depends largely on community awareness and local coordination.

A key distinction of this system is its ability to provide simultaneous early warnings for multiple hazard types — large-scale landslides, small-scale slope failures, and flash floods. Notably, large-scale landslide warnings have not been addressed in previous research or implemented in other WebGIS-based warning systems in Vietnam, representing a unique and valuable feature of the proposed system.

Moving forward, the system should be expanded and regularly applied across Lao Cai. Local authorities are recommended to: (i) Conduct regular inspections and early warnings for slopes, hillsides, residential areas, and transportation routes prone to instability, especially where cracks or concentrated runoff are observed; (ii) Review and clear river channels, drainage paths, and aquaculture zones, and prepare relocation plans when necessary; (iii) Continuously update rainfall and landslide information on the Website and be prepared to evacuate when the High or Very High warning levels are reached. Since large-scale landslide early warning systems are still limited in Vietnam, this system continues to be researched and developed for other high-risk areas across the country.

ACKNOWLEDGMENTS

This paper was supported by the project with the code number of ĐTĐL.CN-37/23, funded by the Program: Basic Scientific Research Program in the fields of Chemistry, Life Sciences, Earth Sciences, and Marine Sciences for the period 2017–2025, under the Earth Sciences sector, managed by the Ministry of Science and Technology of Vietnam. The authors gratefully acknowledges this support.

REFERENCES

Duc, V. (2025). Severe landslides on Khau Pha Pass cut off National Highway 32. [https://laodong.vn/xa-](https://laodong.vn/xa-hoi/sat-lo-nghiem-trong-tren-deo-khau-pha-chia-cat-quoc-lo-32-1584492.ido)

[hoi/sat-lo-nghiem-trong-tren-deo-khau-pha-chia-cat-quoc-lo-32-1584492.ido](https://laodong.vn/xa-hoi/sat-lo-nghiem-trong-tren-deo-khau-pha-chia-cat-quoc-lo-32-1584492.ido)

Duong, T. T. (Principal Investigator). (2023–2025). Study on the formation mechanism, distribution patterns, and early warning of large-scale landslides in Vietnam using the integration of remote sensing, artificial intelligence, and unsaturated soil mechanics theory (Project No. ĐTĐL.CN-37/23). Hanoi University of Science, Vietnam National University, Hanoi.

Haque, A. (2025). Building resilient ocean communities: Early warning systems and knowledge management for Pacific Islands countries. Available at SSRN 5530218.

Hidayat, M. N., Hazarika, H., Murai, M., & Kanaya, H. (2024, April). Application of early warning system for monitoring landslide vulnerability of slope. In *International Conference Series on Geotechnics, Civil Engineering and Structures* (pp. 772–780). Singapore: Springer Nature Singapore.

Institute of Geo-Environmental Technology (IGET). (n.d.). *Display of landslide occurrences nationwide*. <https://truotlo.com/>

Japan Meteorological Agency (JMA). (n.d.). *Landslide Warning Website of the Japan Meteorological Agency (JMA)*. <https://jma.go.jp/en/doshamesh/>

Kong, V. W. W., Kwan, J. S. H., & Pun, W. K. (2020). Hong Kong's landslip warning system—40 years of progress. *Landslides*, 17(6), 1453–1463. <https://doi.org/10.1007/s10346-019-01326-z>

Li, Z., Shi, G., Wu, S., Li, T., Lu, Z., & Ding, X. (2025). Mapping and early warning of hidden landslides under forests: A case in Lantau, Hong Kong. *Remote Sensing of Environment*, 331, 115039. <https://doi.org/10.1016/j.rse.2024.115039>

National Center for Hydro-Meteorological Forecasting (NCHMF). (n.d.). *Regional display of landslide information*. <https://luquetsatlo.nchmf.gov.vn/>

National Science and Technology Center for Disaster Reduction (NCDR). (n.d.). Community-based disaster risk management (CBDRM). Retrieved October 12, 2025, from <https://www.ncdr.nat.gov.tw/>

Pacific Disaster Center (PDC). (n.d.). *Early Warning System of the Pacific Disaster Center (PDC)*. <https://disasteralert.pdc.org/disasteralert/>

TTXVN/Vietnam. (2025). Lao Cai has basically recovered from the damage caused by the remnants of Storm No. 5.

<https://www.vietnamplus.vn/lao-cai-co-ban-khac-phuc-xong-thiet-hai-do-hoan-luu-con-bao-so-5-post1058697.vnp>

UNDRR. (2019). Words into action guidelines: National disaster risk assessment – Governance system, methodologies, and use of results. United Nations

Office for Disaster Risk Reduction, Geneva, Switzerland.

UNDRR. (2020). Words into action: Multi-hazard early warning systems – A checklist. United Nations Office for Disaster Risk Reduction, Geneva, Switzerland.

DOI: 10.15625/vap.2025.0206

Installation of cost-effective landslide early warning systems in South and South-East Asian Countries

Rajinder Bhasin^{1,*}, Lloyd Tunbridge¹, Do Minh Duc², Khang Dang²

¹Norwegian Geotechnical Institute (NGI), Oslo, Norway (RKB@NGI.NO)

²Vietnam National University, Hanoi (VNU), Vietnam

*Email: Rajinder.Kumar.Bhasin@ngi.no

Abstract: A review of available literature on landslides in South and South-East Asian countries emphasises the role of precipitation as an important factor for triggering landslides. Due to ongoing climate change, the frequency and intensity of landslides in Asia have increased significantly over the past years causing extensive damages to life and property in the affected regions. Extreme precipitation events have been a key triggering factor for many of the landslides. Landslides are often triggered by weather events that are in excess of some thresholds. Therefore, it is necessary to investigate the possibility of interpreting landslide events in terms of the rainfall patterns immediately preceding the slide event. Rainfall threshold values vary from region to region due to differences in existing soil characteristics and climatological patterns in different areas. Therefore, a complete study of the rainfall patterns in landslide prone areas and their records of landslides are warranted. This will help predict reasonable threshold values of rainfall and use them as a tool for landslide forecasting.

The Norwegian Geotechnical Institute (NGI), in cooperation with various mandated national institutions in India, Bangladesh, Bhutan, Vietnam and Sri Lanka has installed cost effective instrumentation for landslide early warning systems (EWS) in order to monitor triggering conditions of rainfall-induced landslides. Although the appropriate implementation and operation of a landslide EWS is a complex task, the operation of the installed instruments has proved to be highly effective in limiting the damages to lives and

properties especially in the densely populated areas of Bangladesh where scores of lives have been saved (The Daily Star, 2015 & Prothom Alo, 2015).

This paper describes the cost-effective method for early warning of rainfall-induced landslides in the above countries where instrumentation is performed for monitoring triggering conditions of rainfall-induced landslides. Both the tipping bucket mechanisms and the optical rainfall gauges have been installed for monitoring rainfall.

Keywords: Landslides, Early warning, optical rain gauge, rainfall thresholds.

TRIGGERING FACTORS

The most common natural landslide triggers for landslides include intense rainfall, rapid snowmelt, water-level change, volcanic eruption and earthquake shaking. Some examples with geological conditions that lead to susceptibility to landsliding caused by these triggers have been described by Turner and Schuster (1996).

In addition to rainfall as the main triggering factor, increase in the occurrence of landslides has been associated with a combination of factors and several attributes such as geological, topographic, morphometric, climatic and anthropogenesis nature that directly or indirectly contribute to the phenomena of slope instability.

Landslides are often triggered in areas with past landslide history and monitoring of the landslides using community-based

approaches are proven to be highly effective. In most areas, development activities seem to be responsible for reactivation of dormant landslides. Hence, communities living in areas with landslide history should be warned in due time through constant monitoring and early warning of potential reactivation. In addition, slow moving slides on hill slopes need constant monitoring as many of developing countries in Asia cannot afford to undertake mitigation measures or to resettle people to safer areas after identification of the potential threat.

Several major studies have revealed a close relationship between rainfall intensity and activation of landslides. The rapid infiltration of rainfall, causing soil saturation and a temporary rise in pore-water pressure is generally believed to be the mechanism by which most shallow landslides are generated during intense rainfall e.g. during storms. With the advent of improved instrumentation and electronic monitoring devices, transient elevated pore pressures have been measured in hillside soils and shallow bedrock during rainstorms associated with abundant shallow landsliding. Loose or weak soils are especially prone to landslides triggered by intense rainfall.

DESIGN AND IMPLEMENTATION OF COST EFFECTIVE EARLY WARNING SYSTEMS

Hundreds of people are killed each year by landslides and debris flows in the Asian Region. These recurring events are therefore a serious threat to life, welfare and local economy of the communities residing in the hilly regions, which are prone to landslides.

The appropriate implementation and operation of a landslide EWS is a complex task and only few examples can be found worldwide. Probably the earliest landslide EWS was developed in the San Francisco Bay region (USA) in the mid-1980s and consisted of a real-time network of rain gauges, precipitation forecasts, and relations between rainfall and landslide initiation to define the alert level (Keefer et al., 1987). The relation between rainfall and landslide occurrence, or in more

general terms, the understanding when, why, and how large landslides occur is an important basis for an early warning system (EWS). A EWS comprises of four main activities: monitoring, analysis of data and forecasting, warning and response. A block diagram of a typical EWS is shown in Fig. 1.

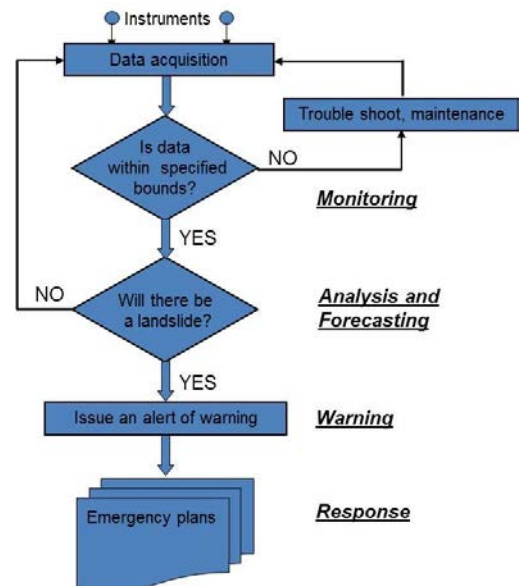


Fig. 1. Block diagram of a typical EWS (Di Biaggio and Kjekstad, 2007)

Empirical relations between rainfall duration or intensity and landslide initiation are typically applied for EWS. These relations need to be established by a record of landslide-triggering rainfall events. Several relations have been presented for different regions worldwide (Guzzetti et al., 2007). Due to the strong variability of rainfall and soil conditions, it is indispensable to develop a rainfall-landslide relation adapted to the region where the EWS is to be implemented.

Regional and global precipitation thresholds

Depending on the available classes of meteorological events, thresholds can be estimated as follows, (see Fig. 2) according to Cepeda and Devoli (2008):

- Only occurrences of landslides: the threshold is a lower bound to the

meteorological events. See Figure 2a. Examples: Caine (1980), Crosta (1998) and Guzzetti et al. (2007).

- Only non-occurrences of landslides: the threshold is an upper bound to the meteorological events. See Figure 2b. Examples: Cannon and Ellen (1988).

- Both, occurrence and non-occurrences of landslides: in this case, the threshold is a boundary separating the two classes. See Figure 2c. Examples: Wieczorek and Sarmiento (1988) and Jakob and Lambert, (2009). Some authors have estimated thresholds by fitting curves to the occurrence class (Rodolfo and Arguden 1991; Van Westen and Daag 2005).

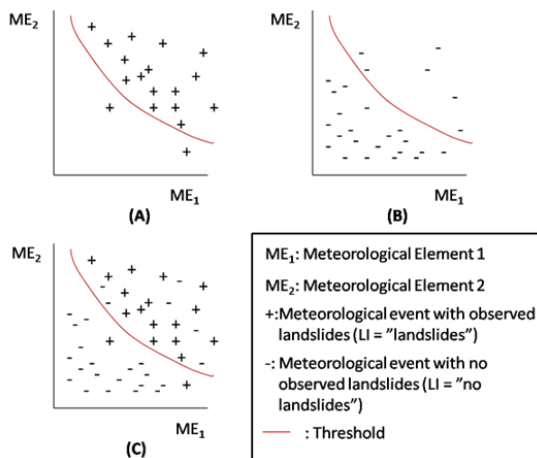


Fig. 2. Types of thresholds based on the available classes of meteorological events Adapted from Cepeda and Devoli (2008). For simplicity, a threshold based only on two meteorological elements (ME) is shown. The proportion of “landslide” events in relation to “no landslides” events is usually very small and does not correspond to the proportion shown in (c), which is presented for illustration purposes only.

From Figure 2, it can be noted that a threshold may not classify correctly all the meteorological events. Events with observed landslides (“+” in Figure 2) and located below the threshold are missed events, while events with no landslides (“-” in Figure 2) and above the threshold are false alarms. One of the main

challenges in the estimation of thresholds is to achieve an optimum performance such that both missed events and false alarms are minimized as much as practical operational conditions allow (i.e., in the framework of an early-warning system).

Installed instrumentation for early warning systems in Asia

The instruments for early warning of rainfall-induced landslides comprises of the following components (Bhasin and Singh, 2015):

- A tipping bucket rain gauge or an optical rain gauge;
- An instrument enclosure with solar panel comprising:
 - + GSM logging and alarm unit;
 - + Solar charge controller;
 - + Battery.

Figures 3A-D show the various components of the installed **tipping bucket rain gauge system** for landslide early warnings in Bangladesh. Recently NGI has installed the new optical rain gauge system for the Rohingya refugee camps in Cox’s Bazar, see Figures 4A-D. Ten such optical rain gauge systems have been installed in Cox’s Bazar. The various components of both the tipping bucket and the optical system cost around USD 1500. Fortunately, there have been no false alarms in the system so far and the rainfall thresholds for initiating landslides are being updated based on landslide observations in areas where the system is not yet installed. The local communities are being made aware of the rainfall thresholds and capacity building programs for the local disaster management agencies have been performed. The landslide early warning system is being sustained in the long run as there is a sense of ownership of the equipment by the community being affected by landslides.

Difference between a tipping bucket and optical rain gauge system

NGI has tested and installed the Hydreon optical rain gauge (rainsensors.com) in Cox’

Bazar Bangladesh. As per their website description, the optical rain gauge sensing technology overcomes many of the shortcomings of conventional tipping bucket rain gauges. The sensor can work in mobile environments and there is no collecting funnel to clog with leaves, and the round shape of the optical rain gauge makes it essentially self-cleaning, see Fig. 4. So far NGI does not have any adverse experience to what has been stated above. The mechanical tipping bucket works by gathering water into a large funnel and filling a mechanical bucket that tips when the weight of the water reaches a threshold. This approach is simple, accurate, fragile, and requires regular maintenance which NGI has also experienced in tropical countries. Debris can clog the collection funnel and requires to be cleaned periodically. The tipping bucket system does not start to register until enough rain has gathered on the funnel and filled the bucket which may be typically several hundredths of an inch. In contrast, the optical rain gauge counts individual droplets and are considered hundred times more sensitive than a typical tipping bucket. Further, this type of solid-state rain gauge is self-cleaning as the sensing surface is convex (rainsensors.com), see Fig. 4b.

The new EWS instrument (optical) which have recently been installed has the capacity to send alarm messages (via SMS) to unlimited mobiles whose numbers have been programmed in the system. If the rainfall threshold values, (previously set up in the system) are exceeded, then early warnings are sent automatically from the cloud-based server to the various mobile users. In addition, the users can also request status messages, change users and change all other programmable options such as threshold values. Details concerning the system are described in an NGI report (NGI, 2024). In Bangladesh, the fatalities due to landslides in Cox's Bazar, Chittagong and Teknaf area have been significantly reduced after the installation of automatic rain gauges at the sites (Ali and Khan 2014).



Fig. 3 A Rainfall warning system



Fig. 3 B Instrument enclosure



Fig. 3 C Logging and alarm unit



Fig. 3 D. FWS set-up Chittagong Bangladesh



Fig. 4 A Optical rain gauge system

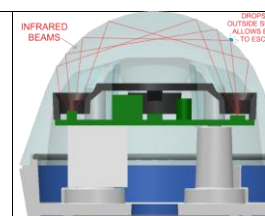


Fig. 4 B Optical Instrument enclosure (rainsensors.com)

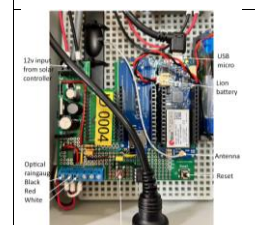


Fig. 4C details of connections



Fig. D Installation in Cox's Bazar, Bangladesh

Rainfall thresholds

Cepeda (2018) has carried out a preliminary assessment of rainfall thresholds in the Badulla district of Sri Lanka. According to the results, the following generalized threshold has been calibrated for this district:

$$\text{Rain}_{24h} = 138.5 - 0.2357 A_{20d}$$

Where:

A_{20d} is the antecedent and cumulative 20-day rainfall in mm.

Rain_{24h} is the triggering 24-hour rainfall, in mm.

This threshold can be used as a component of an early-warning system as follows:

1. Calculate 20-day precipitation before today using observations from a station.
2. Estimate threshold value using equation $\rightarrow \text{Rain}_{24\text{h threshold}}$
3. Estimate forecast for the next 24 h, $\text{Rain}_{24\text{h}}$ and compare with $R_{24\text{h threshold}}$
4. If $R_{24\text{h}} < R_{24\text{h threshold}}$, no warning is issued.
5. If $R_{24\text{h}} < R_{24\text{h threshold}}$, issue of a warning level depending on how far the forecasted value is from the threshold value.
6. If $R_{24\text{h}} \geq R_{24\text{h threshold}}$, a warning level must be issued, but the acute level of the response depends on how far the forecast is from the threshold value.
7. The number and position of the warning levels, both below and above the threshold can be set based on a back-analysis of historical landslides in the region.

CONCLUSION

One of the key triggering factor for many of the landslides in Asian countries is the precipitation events that occur over a period of time. Precipitation plays an important role on the initiation of slope failures and provides evidence that landslides are often triggered by meteo-climatic events that are in excess of some thresholds. Rainfall threshold values vary from region to region due to the differences in existing soil characteristics and climatological patterns in different areas. In collaboration with its regional cooperating partners in Asia including Vietnam, NGI has set-up cost-effective instrumentation for early warning of critical landslide prone areas to predict rainfall induced landslides. Both the tipping bucket mechanisms and the optical rainfall gauges have been installed for monitoring rainfall. It has been found that the optical raingauge is more sensitive and requires less maintenance than the tipping bucket system.

REFERENCES

- Ali, R.M.E. and Khan, S.R. (2014): Parameters influencing landslides and landslides early warning in Bangladesh. *Regional meeting under the Asian Program for Regional Capacity Enhancement for Landslide Impact mitigation*, 28-29 April 2014, Kathmandu.
- Bhasin, R. and Singh, B., (2015). Cost effective method for early warning of rainfall induced landslides in Asian countries. *Journal of Engineering Geology/Proceedings of EGNM 2015*, 27-29 Oct. New Delhi, India.
- Cannon, S. H., and Ellen, S. D., (1988) Rainfall that resulted in abundant debris-flow activity during the storm, in Ellen, S. D., and Wieczorek, G. F., eds., *Landslides, floods, and marine effects of the storm of January 3-5, 1982, in the San Francisco Bay region, California: U. S. Geological Survey Professional Paper no. 1434*, p. 27-34.
- Cepeda, J., and Devoli, G. (2008). "Rainfall thresholds for landslide triggering following volcanic ash eruptions and earthquakes." *European Geosciences Union General Assembly 2008*, Vienna, Austria. www.cosis.net/abstracts/EGU2008/03879/EGU2008-A-03879.pdf.
- Cepeda, J. (2018) Third World Bank workshop on landslide risk reduction. Colombo, Sri Lanka.
- Crosta, G. (1998): Rainfall threshold regionalization: an aid for landslide susceptibility zonation. *Environmental Geology*, 35, (2/3), 131– 145, 1998
- Di Biagio, E., & Kjekstad, O. (2007). Early Warning. *Instrumentation and Monitoring Landslides. 2nd Regional Training Course, RECLAIM II*, 29th January-3rd February.
- Guzzetti, F., Peruccacci, S., Rossi, M. & Stark, C.P. (2007). Rainfall thresholds for the initiation of landslides in central and southern Europe. *Meteorology and Atmospheric Physics* 98: 239-267.
- Jakob, M. & Lambert, S. (2009). Climate change effects on landslides along the southwest coast of British Columbia. *Geomorphology* 107: 275–284
- Keefer, D.K., Wilson, E.C., Mark, R.K., Brown, W.M., Ellen, S.D., Harp, E.L., Wieczorek, G.F., Alger, C.S. and Zarkin, R.S. (1987): Real-Time landslide monitoring warning during heavy rainfall, *Science* 13 November 1987: Vol. 238 no. 4829 pp. 921-925 DOI: 10.1126/science.238.4829.921.

- NGI (2024), Automatic Optical rain gauge for landslide early warning; draft report, prepared by Lloyd Tunbridge, *NGI report*, July 2024.
- Prothom Alo Bangladesh (2015): Landslide forecasts sent to mobile phones <http://en.prothomalo.com/bangladesh/news/77481/Landslide-forecasts-sent-to-mobile-phones>, August 30 2015.
- Rodolfo, K. S., and Arguden, A. T, (1991). Rain-lahar generation and sediment delivery systems at Mayon Volcano, Philippines. In Fisher, R. J. and Smith, G. A. (Eds.), *Sedimentation in Volcanic Settings. Spec. Publ.-Soc. Econ. Paleontol. Mineral*, 45:71-87.
- The Daily Star Bangladesh (2015): Forecast saves scores of Bangladeshis this rainy season <https://www.thedailystar.net/backpage/alert-saves-scores-rainy-season-151078>, October 3, 2015.
- Turner and Schuster (1996). Landslides, Investigation and Mitigation, *Special report 247 Transportation Research Board*, National Research Council, National Academy Press, Washington D.C. 1996.
- Van Westen, C.J. and Daag, A.S. (2005). Analyzing the relation between rainfall characteristics and lahar activity at Mount Pinatubo, Philippines. In: *Earth surface processes and landforms*, 30 (2005)13 pp. 1663-1674.
- Wieczorek, G.F., and Sarmiento, J. (1988). Rainfall, piezometric levels and debris flows near La Honda, California in the January 3–5, 1982, and other storms between 1975 and 1983, in Ellen, S.D., and Wieczorek, G.F., eds., *Landslides, floods, and marine effects of the January 3–5, 1982, storm in the San Francisco Bay region, California: U.S. Geological Survey Professional Paper 1434*, p. 43–62.

DOI: 10.15625/vap.2025.0207

Deep Learning-Assisted Detection of Coastline Shifts at Cua Dai, Vietnam

Kinh Bac Dang¹, Tuan Linh Giang^{1,2,*}

¹VNU University of Science, 334 Nguyen Trai, Thanh Xuan, Hanoi, Vietnam

²VNU Institute of Vietnamese Studies & Development Science, 336 Nguyen Trai, Thanh Xuan, Hanoi, Vietnam

*Email: linhgt@vnu.edu.vn

Abstract: This study focuses on assessing coastline changes in the Cua Dai area (Danang city) during the period 2004–2024 by using remote sensing, the deep learning model U-Net 256, and the DSAS model. High-resolution satellite and UAV imagery were used for interpretation, coastline extraction, and analysis of erosion–accretion trends over time. The results indicate that coastal erosion dominates the Cua Dai area, with more than 75% of transects showing an average erosion rate of 1–2 m/year. Accretion areas are limited and temporary in nature. The main causes are identified as the combined impacts of sea-level rise, extreme storm waves, and human activities such as seawall construction, land reclamation, sand mining, and coastal tourism development. The findings provide an important scientific basis for coastal monitoring, early warning, and integrated coastal zone management, contributing to sustainable protection and restoration of the Cua Dai coastline.

Keywords: Cua Dai, erosion, accretion, deep learning, DSAS, GIS, Coastline Shifts.

INTRODUCTION

Cua Dai is one of the coastal areas most strongly affected by climate change and economic–tourism development activities in Central Vietnam (Dang, Ngo, et al., 2022; Tin et al., 2021). Over the past two decades, this area has experienced significant coastline changes resulting from the combined influences of natural and human factors (Veettil et al., 2020). The average sea-level rise of 2.6 mm/year, together with frequent extreme storm waves,

has caused severe coastal erosion, threatening coastal infrastructure, residential areas, and beachfront resorts (Ngo et al., 2020). In addition, the construction of hard seawalls and the expansion of tourism complexes have an influence on the coastal dynamic equilibrium, leading to increasingly complex coastline morphology changes.

In this context, assessing coastline dynamics in the Cua Dai area is not only of scientific significance but also of high practical value for coastal planning and integrated management. Traditional methods are based on satellite imagery and manual analysis, which often lack accuracy and are difficult to update over time. The development of artificial intelligence, particularly deep learning models such as U-Net, offers a new approach for interpretation, identification, and extraction of coastlines in high-resolution data with greater accuracy (Dang, Dang, et al., 2022; Giang et al., 2023). When combined with the DSAS model, it has the ability to efficiently determine erosion–accretion intensity, classify vulnerable coastline segments, and quantify change rates over time (Abdul Maulud et al., 2022; Santos et al., 2021; Sowmya et al., 2019).

Therefore, the analysis of coastline dynamics in the Cua Dai area for the period 2004–2024, supported by machine learning technologies, not only aims to quantify morphological changes but also provides a scientific database for forecasting, protection, and sustainable development of the coastal zone. This is an urgent requirement in the face of challenges of climate change, sea-level rise,

and increasing pressure from economic and tourism development.

STUDY AREA AND METHODOLOGY

Study area

The study area is the Cua Dai coastal zone, located within Hoi An City and Duy Xuyen District, Quang Nam Province (Danang now) (Figure 1). It is one of the major estuaries of the Thu Bon-Vu Gia River system, playing an important role in hydrological regulation, transportation, and marine economic development in the central coastal region of Vietnam. Cua Dai is located in the heart of the Central Vietnam economic corridor, with convenient transportation links and connections to key economic zones such as Chu Lai-Dung Quat in the south and Chan May-Lang Co in the north.

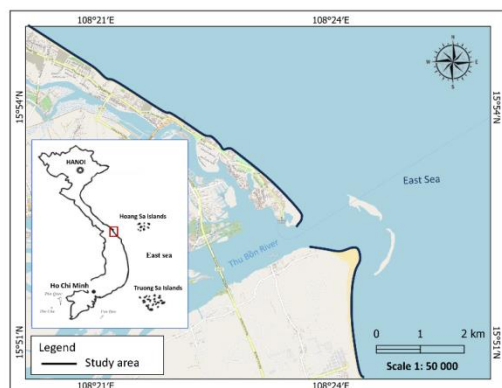


Figure 1. Study area

The topography of the area is characterized by fine sandy coastlines stretching in a north-south direction, interspersed with sand spits, dunes, and tidal flats. Inland areas include coastal residential zones, resorts, and protective *Casuarina* forests. The estuarine section is highly dynamic, frequently influenced by river discharge, tides, and wave action, particularly during the storm season. The interaction of these natural processes results in continuous coastline changes—with some areas experiencing severe erosion while others undergo temporary accretion. This is forming a complex and dynamic coastal geomorphology.

Over the past two decades, Cua Dai has become a hotspot of coastal erosion in Central Vietnam. Since 2009, especially after Typhoon Ketsana, the coastline in Cua Dai Ward and Duy Hai Commune has been increasingly eroded. In this season, many sections of the coast lost tens of meters. Human activities such as the construction of dikes and seawalls, coastal resort development, sand mining, and channel dredging have intensified morphological changes. These factors make Cua Dai a case study for assessing coastline dynamics and erosion-accretion trends and for analyzing the natural and anthropogenic drivers governing these processes.

Methods and Research Process

The shoreline consists of hydrodynamic phenomena, including tidal, wave, and river events, which encompass fluctuations in sea levels (Dang, Dang, et al., 2022; Phan et al., 2019). Coastlines offer a more solid border than shorelines and are not affected by short-term tidal fluctuations, leading to the concentration of human activities, such as aquaculture and infrastructure development (Nguyen & Takewaka, 2020; Tsai, 2022), along these areas, where the primary focus of study is on long-term trends and resilience. The evaluation of coastal alterations due to major weather phenomena, like hurricanes and typhoons, alongside the effects of both natural and human-made structures such as seawalls, depends on the examination of long-term trends. Consequently, in this study, the authors selected coastline to monitor coastal change.

The study was conducted by integrating remote sensing technology, deep learning models, and Geographic Information Systems (GIS) to identify, interpret, and assess coastline changes in the Cua Dai area during the period 2004–2024. The research workflow consists of four main steps (Figure 2):

Step 1: Data collection and preprocessing. High-resolution remote sensing imagery and UAV images were collected in 2004, 2010, 2015, 2020, and 2024. For the 2004–2010 period, QuickBird and IKONOS images with 1–2.5 m

resolution were extracted from Google Earth Pro, while for 2011–2024, GEP images with 0.7–1 m resolution were used, primarily derived from commercial satellites including GeoEye-1, WorldView-2, and WorldView-3. And UAV data was collected at the following times: July 2022, June 2023, and March 2025 and coastline positions were verified using GPS-referenced ground observations. The data were geometrically corrected, clipped to the study area, and standardized to the same coordinate system (VN2000). Geometric and radiometric errors were corrected to ensure consistency and compatibility among datasets.

Step 2: Coastline interpretation and extraction using the U-Net 256 deep learning model. U-Net 256 is a convolutional neural network architecture designed for high-precision image segmentation (Ronneberger et al., 2015). U-Net 256 is a convolutional neural network architecture capable of highly accurate object segmentation from imagery (Dang et al., 2020; Dang, Dang, et al., 2022). It follows an encoder–decoder structure with skip connections that preserve spatial information and improve boundary detection accuracy. The training dataset was created from manually labelled samples of beaches and other areas. The input data include images and the training dataset, while the output is a binary segmentation mask distinguishing beach and other areas. The model was trained using 80% of the dataset and validated with the remaining 20%. Accuracy assessment employed the Intersection over Union (IoU), F1-score, and overall accuracy, confirming strong model performance. After training, the best model was applied to classify the entire Cua Dai area, and the results are coastline layers for each study year.

Step 3: Integration of data into the DSAS (Digital Shoreline Analysis System) model by using ArcGIS. The DSAS model was used to calculate indicators of coastline change, including End Point Rate (EPR), Linear Regression Rate (LRR), and Weighted Linear Regression (WLR). There were 868 transects, spaced 20 meters apart and oriented

perpendicular to the baseline to ensure detailed and statistically robust analysis.

Step 4: Result analysis and change mapping. The coastline segments were classified according to the degree of erosion or accretion—from very strong to weak—to identify high-risk areas. The results were compared with field data and UAV imagery to verify their accuracy. Field verification focused on identifying erosion and accretion areas along representative coastline segments. This comparison between the field-observed conditions and modelled coastline positions provides a qualitative validation of the accuracy and reliability of the erosion–accretion mapping in this study.

The combination of machine learning and spatial analysis tools provided an understanding of the coastline change patterns and rates at Cua Dai over the past two decades. This workflow not only supports early warning and monitoring but also provides a scientific basis for marine spatial planning, coastal protection design, and sustainable coastal tourism management.

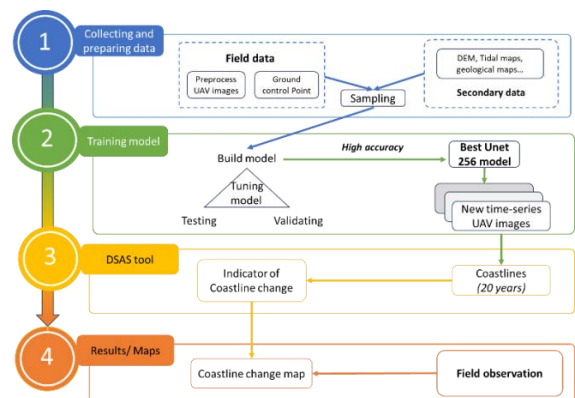


Figure 2 Flowchart of data processing

RESULTS AND DISCUSSION

Image Interpretation Results Using Machine Learning Model

The Cua Dai area is part of the coastal urban chain along Vietnam's Central Coast. Its favourable geographical location, developed transportation network, and interregional connectivity enable strong links with major

economic zones, including Chan May–Lang Co Economic Zone (Thua Thien Hue) to the north and the Chu Lai Open Economic Zone and Dung Quat Industrial Zone to the south. These factors provide an important foundation for establishing and expanding economic linkages among districts, provinces, and cities within the region.

However, the area is highly exposed to storm waves and sea-level rise. According to the Ministry of Natural Resources and Environment (2021), the sea-level change trend in the Quang Nam–Da Nang region during 1978–2018 (based on observed data from the Son Tra hydrological station) shows an increase of 2.6 mm/year. Meanwhile, the observed change in mean wave height at the same station during 1982–2018 indicates a decreasing trend of −3.8 mm/year.

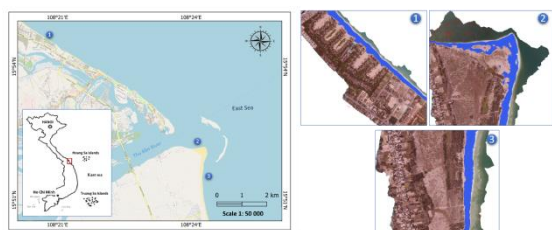


Figure 3. Selected interpretation results (coastline (blue) and land (red)) in several areas of Cua Dai: 1) coastal area with developed resorts; 2) estuarine area; 3) sandy coastline area

Some interpretation results from the U-Net 256 model (Figure 3) demonstrate its effective capability in distinguishing land areas (in red) and marine areas (in blue) across different coastal segments of the Cua Dai region. In areas with tourism development (1), the coastline is clearly delineated, showing no confusion with inner sandy zones within resort areas. The model performs well in identifying the boundary between land and sea in zones with built infrastructure. In estuarine areas (2), however, the coastline boundary appears more dispersed and complex. The sparse and uneven vegetation cover around the river mouth introduces challenges for the model in processing transitional zones, thus requiring post-processing corrections after model interpretation. In sandy beach areas (3), the

model produces a continuous coastline closely matching the actual topography, demonstrating high classification accuracy in relatively homogeneous natural environments.

To determine the current coastline status of the area, the study utilized high-resolution remote sensing images and UAV imagery from 2004 to 2024 (with a resolution of 0.7 m) and applied the U-Net 256 deep learning model to interpret the coastline. The extracted results were then integrated into the DSAS model by using ArcGIS to assess the coastline dynamics of the Cua Dai area (Figure 4).

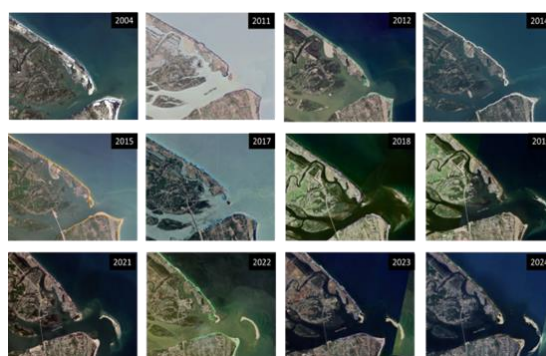


Figure 4. Coastlines in the Cua Dai area, Danang, extracted from 2004 to 2024 for input into the DSAS model

Accuracy Assessment of Coastline Change

To calculate the coastline change rate using the methods mentioned above, 868 transects were established perpendicular to the coastlines and baseline in the Cua Dai area, with a distance of 20 meters between each transect. The results show that the range of coastline change (between the furthest and closest lines) in this area reached a maximum value of 409.3m and a minimum of 0m. Based on the regression analysis methods, the Weighted Linear Regression (WLR) approach generally provides the most reliable results; therefore, it was selected for detailed analysis and evaluation of coastline change in each sub-area.

The calculations indicate that the median value of coastline displacement between 2004 and 2024 is 36.82 meters. The results from all three methods—End Point Rate (EPR), Linear Regression Rate (LRR), and Weighted Linear

Regression (WLR)—are generally consistent. According to the WLR results, the maximum erosion rate in the study area reached approximately -41.66 m/year, while the highest accretion rate was about 33.21 m/year. Statistical analysis shows that 651 out of 868 transects (75%) exhibit an erosional trend (erosion rate < -0.2 m/year), while 146 transects (16.82%) display an accretion trend (accretion rate > 0.5 m/year) across the study area (Table 1).

Table 1. Summary of parameters calculated using different methods for the period 2004–2024

Parameters	Period 2004 - 2024			
	SCE (m)	EPR	LRR	WLR
Max	409,3	10,92	10,1	33,2
Min	0	-41,42	-44,2	-41,7
Median	36,82	-0,84	-0,9	-1,2
Mean	71,53	-1,95	-1,8	-1,25
% of eroding transects (erosion rate < -0.2 m/year)	-	72,93	75,8	75
% of accreting transects (accretion rate > 0.5 m/year)	-	15,55	12,7	16,8
% of stable transects (rate between -0.2 and 0.5 m/year)	-	11,52	11,5	8,2

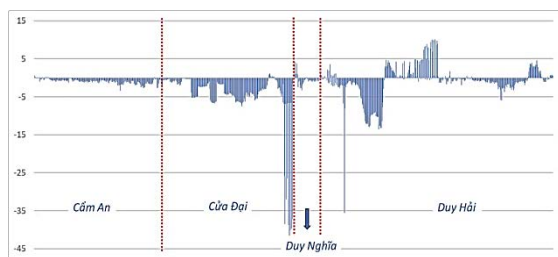


Figure 5. Coastline change trends in the Cua Dai area from 2004 to 2024 using the LRR method (unit: m/year)

Using the Linear Regression Rate (LRR) method, the results show significant coastline variation (Figure 5). The major erosion areas include the Cua Dai estuary, with erosion exceeding 35 meters, and some coastal areas in Duy Hai, where erosion reaches nearly 15 meters. Areas experiencing accretion are also mainly located along the Duy Hai coastal zone, with accretion rates ranging from 5–7 meters.

The highest error levels are observed in the Cua Dai and Duy Hai areas (Figure 6).

The Weighted Linear Regression (WLR) method, which applies weighting factors in regression analysis, also reveals strong coastline dynamics (Figure 7). The erosion and accretion patterns obtained using this method are generally consistent with those derived from the LRR method. Significant erosion is recorded along the Cua Dai coastline (over 35 meters), especially in the southern part of Cua Dai. Several beaches in Cam An and Duy Hai also show severe erosion, exceeding 5 m/year.

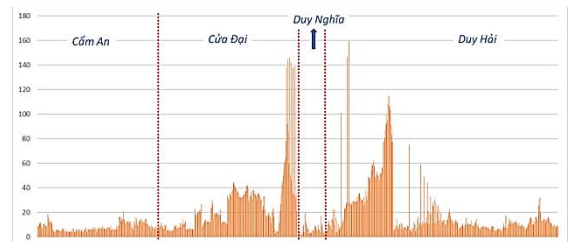


Figure 6. Distribution of calculation errors using the LRR method (error represented as LSE) for the period 2004–2024 (unit: m²)

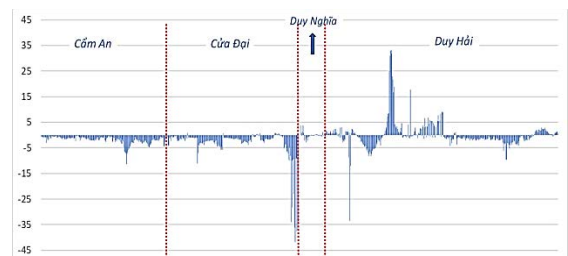


Figure 7. Coastline change trends in the Cua Dai area from 2004 to 2024 using the WLR methods (unit: m/year).

According to Table 1, there are substantial differences between the erosion values obtained from the WLR method and those from the other two methods. This discrepancy can be explained by the fact that, when all coastline generations are combined for computation, the accuracy of coastline extraction varies across time periods, leading to differing levels of reliability. The EPR method only considers two coastlines (2004 and 2024), so its results do not fully capture the recent rapid coastline changes occurring at Cua Dai.

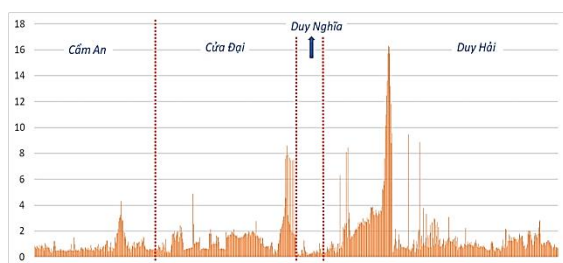


Figure 8. Distribution of calculation errors using the WLR method (error represented as WSE) for the period 2004–2024 (unit: m^2)

For the LRR method, because it assigns equal weights to all coastline data, regardless of accuracy differences, its results may not adequately reflect the actual coastline dynamics. In contrast, the WLR method gives higher priority to more accurate datasets when constructing the regression equation, gradually reducing the influence of less accurate data. Consequently, the error of the WLR method is significantly lower than that of the standard LRR method (Figures 6 and 8). The spatial resolution of satellite images from GE has improved considerably in recent years, resulting in more precise coastline delineation. Therefore, recent coastlines have the highest reliability and receive greater weighting in the WLR calculation, and the results show the highest accuracy.

Assessment of the Current Status of Coastline Change

Based on the calculated results of coastline changes from 2004 to 2024, the study divided the Cua Dai coastal area into segments according to erosion and accretion characteristics. Accordingly, the coastline was classified into eight risk groups, ranging from very strong, strong, moderate, and weak accretion to weak, moderate, strong, and very strong (potentially disastrous) erosion (Figure 9). Among these, the moderately eroding segments are dominant, accounting for 28%, followed by strongly eroding segments at 23%, and weakly eroding segments at approximately 20%. Segments with very strong erosion account for about 7% of the total coastal length, while very strong accretion segments make up only about 3%. In the study area, 5% of the coast

shows moderate accretion and 9% shows weak accretion. Overall, the coastal area tends to experience stronger erosion than accretion.

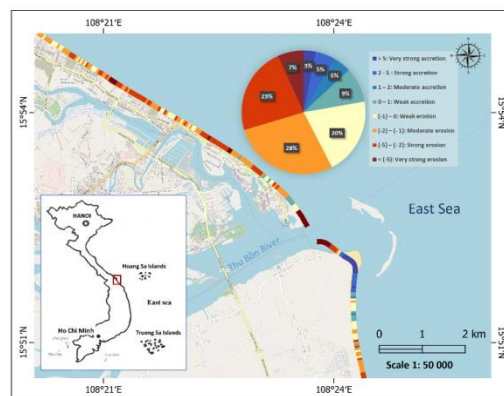


Figure 9. Coastline change map of the Cua Dai area from 2004 to 2024

The coastline dynamics at Cua Dai are closely linked to temporal changes in both natural and socio-economic conditions. Between 2002 and 2012, this period saw intensified impacts from economic development activities and extreme weather events affecting the coast and beaches. Notably, toward the end of this period (2007–2009), the region was severely impacted by major storms. In particular, Typhoon Ketsana (Storm No. 9, 2009) — considered the strongest storm in 40 years (since 1969) — made direct landfall in the study area. At the same time, the construction of coastal resort complexes encroaching upon the beach areas disrupted the natural balance of the coastal system. As a result, erosion during this phase was especially intense along several coastline segments, such as in Cua Dai Ward, Hoi An.

From 2012 to the present, the months from September to December mark the storm season, during which coastal erosion becomes extremely severe, with waves directly impacting residential areas inland. Besides natural factors, this period has also witnessed the strongest impacts of human economic development activities on the coastline. The large-scale construction of beachfront resorts has significantly disturbed the natural equilibrium of the coastal area (Figure 10).

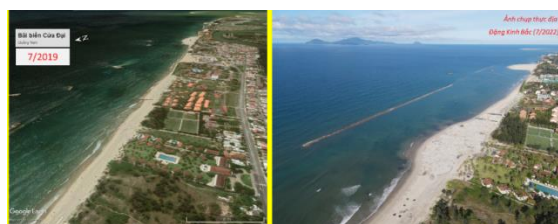


Figure 10. Changes in Cua Dai Beach from 2019 to 2022 after the construction of parallel coastal revetments and beach nourishment (Photo by Đặng Kinh Bắc, 2022)

Consequently, many coastline segments have required the construction of concrete seawalls; however, severe erosion still occurs in many areas, particularly along the northern coast of Cua Dai. According to field surveys in 2025, the An Bang–Cam An coast exhibits steep erosional scarps, where waves have progressively removed beach material, uprooting *Casuarina* trees and causing severe ecological degradation. The most eroded section lies only 19.7 meters from a tourist complex and about 36 meters from the road network (Figure 11).

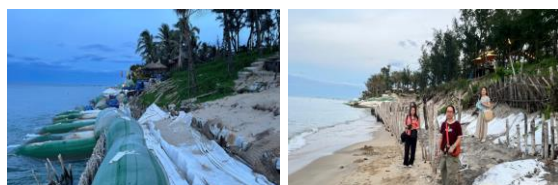


Figure 11. Current erosion situation along the Cam An coastline (Photo by Giang Tuấn Linh, 2025)

CONCLUSION

The research results indicate that the Cua Dai area has experienced intense and complex coastline changes over the past two decades. Coastline interpretation using the U-Net 256 deep learning model combined with DSAS analysis clearly reveals a dominant erosion trend along most of the coastline. Between 2004 and 2024, more than 75% of the transects show erosion, with an average rate of 1–2 m/year, and several segments reaching extreme values exceeding 40 m/year — particularly in Cua Dai Ward and Cam An Commune. Accretional zones account for a smaller proportion, generally localized and temporary, mainly around the Duy Hải estuary.

The study confirms the effectiveness of applying artificial intelligence in coastline monitoring, enhancing both data accuracy and temporal update capability. The findings are not only valuable for assessing current conditions but also provide scientific guidance for technical and management solutions aimed at protecting and restoring the Cua Dai coast to adapt to climate change and develop sustainably.

ACKNOWLEDGMENTS

This research was funded by the research project QG.24.56 of Vietnam National University, Hanoi.

REFERENCES

- Abdul Maulud, K. N., Selamat, S. N., Mohd, F. A., Md Noor, N., Wan Mohd Jaafar, W. S., Kamarudin, M. K. A., Ariffin, E. H., Adnan, N. A., & Ahmad, A. (2022). Assessment of Shoreline Changes for the Selangor Coast, Malaysia, Using the Digital Shoreline Analysis System Technique. *Urban Science*, 6(4), 1–14. <https://doi.org/10.3390/urbansci6040071>.
- Dang, K. B., Dang, V. B., Ngo, V. L., Vu, K. C., Nguyen, H., Nguyen, D. A., Nguyen, T. D. L., Pham, T. P. N., Giang, T. L., Nguyen, H. D., & Hieu Do, T. (2022). Application of deep learning models to detect coastlines and shorelines. *Journal of Environmental Management*, 320(March), 115732. <https://doi.org/10.1016/j.jenvman.2022.115732>.
- Dang, K. B., Ngo, C. C., Ngo, V. L., & Dang, V. B. (2022). Coastal Vulnerability Assessment in Son Tra – Cua Dai region. *VNU Journal of Science: Earth and Environmental Sciences*, 38(3), 55–65. <https://doi.org/10.25073/2588-1094/vnuees.4842>.
- Dang, K. B., Nguyen, M. H., Nguyen, D. A., Phan, T. T. H., Giang, T. L., Pham, H. H., Nguyen, T. N., Van Tran, T. T., & Bui, D. T. (2020). Coastal wetland classification with deep u-net convolutional networks and sentinel-2 imagery: A case study at the tien yen estuary of vietnam. *Remote Sensing*, 12(19), 1–26. <https://doi.org/10.3390/rs12193270>.
- Giang, T. L., Dang, K. B., & Bui, Q. T. (2023). Coastline and shoreline change assessment in sandy coasts based on machine learning models and high-resolution satellite images. *Vietnam Journal of Earth Sciences*, 45(2), 251–270.
- Ngo, V. L., Dang, V. B., Dang, K. B., Ngo, C. C., Pham, T. P. N., Benjamin, B., & Giap, T. K. C. (2020). Assessment

- of shoreline changes for setback zone establishment from Son Tra (Da Nang city) to Cua Dai (Hoi An city), Vietnam. *Science of the Earth*, 42(2), 363–383. <https://doi.org/https://doi.org/10.15625/0866-7187/42/4/15410>.
- Nguyen, Q. H., & Takewaka, S. (2020). Land subsidence and its effects on coastal erosion in the Nam Dinh Coast (Vietnam). *Continental Shelf Research*, 207(August), 104227. <https://doi.org/10.1016/j.csr.2020.104227>.
- Phan, H. M., Ye, Q., Reniers, A. J. H. M., & Stive, M. J. F. (2019). Tidal wave propagation along The Mekong deltaic coast. *Estuarine, Coastal and Shelf Science*, 220(February), 73–98. <https://doi.org/10.1016/j.ecss.2019.01.026>.
- Ronneberger, O., Fischer, P., & Brox, T. (2015). U-Net: Convolutional Networks for Biomedical Image Segmentation. In *Lecture Notes in Computer Science* (including subseries *Lecture Notes in Artificial Intelligence* and *Lecture Notes in Bioinformatics*) (Vol. 9351, pp. 234–241). https://doi.org/10.1007/978-3-319-24574-4_28.
- Santos, C. A. G., Nascimento, T. V. M. do, Mishra, M., & Silva, R. M. da. (2021). Analysis of long- and short-term shoreline change dynamics: A study case of João Pessoa city in Brazil. *Science of The Total Environment*, 769, 144889. <https://doi.org/10.1016/J.SCITOTENV.2020.144889>.
- Sowmya, K., Sri, M. D., Bhaskar, A. S., & Jayappa, K. S. (2019). Long-term coastal erosion assessment along the coast of Karnataka, west coast of India. *International Journal of Sediment Research*, 34(4), 335–344. <https://doi.org/10.1016/j.ijsrc.2018.12.007>.
- Tin, H. C., Phung, B. T., & Hieu, D. V. (2021). Species biodiversity and distribution of seagrass beds in several coastal areas of central Vietnam. *Regional Studies in Marine Science*, 41, 101531. <https://doi.org/10.1016/j.rsma.2020.101531>.
- Tsai, Y. L. S. (2022). Monitoring 23-year of shoreline changes of the Zengwun Estuary in Southern Taiwan using time-series Landsat data and edge detection techniques. *Science of the Total Environment*, 839(March), 156310. <https://doi.org/10.1016/j.scitotenv.2022.156310>.
- Veettil, B. K., Costi, J., Marques, W. C., Tran, X. L., Quang, N. X., Van, D. D., & Hoai, P. N. (2020). Coastal environmental changes in Southeast Asia: A study from Quang Nam Province, Central Vietnam. *Regional Studies in Marine Science*, 39, 101420. <https://doi.org/10.1016/j.rsma.2020.101420>.

DOI: 10.15625/vap.2025.0208

Warning System for Land Subsidence Risk due to Drought and Groundwater Extraction: A Step Toward Sustainable Development

Doan Quang Tri*, Pham Tien Duc

Hydrometeorological Information and Data Center, Vietnam Meteorological and Hydrological Administration, Hanoi, Vietnam

*Email: doanquangtrikttv@gmail.com

Abstract: Land subsidence is a major hazard in the Ca Mau Peninsula, threatening ecosystems, infrastructure, and livelihoods. This study develops a digital warning system for subsidence risk driven by drought and groundwater extraction, with the goal of supporting sustainable development and climate resilience. Key influencing factors were identified using the Delphi method and KAMET rule-based table, and their relative weights were determined through the Analytic Hierarchy Process (AHP). These factors were integrated into a Geographic Information System (GIS) to generate a risk zoning map. Validation with observed events during the 2024 dry season showed strong agreement with field survey data, achieving an overall accuracy of 88.9% and a Kappa coefficient of 0.82, confirming the model's reliability. The findings demonstrate the potential of combining expert knowledge, multi-criteria analysis, and GIS for hazard mapping. The proposed system marks an important step toward digital transformation in disaster risk management, offering practical tools for local authorities in planning and resource management.

Keywords: Land subsidence, drought, groundwater exploitation, land subsidence risk warning system, Ca Mau Peninsula.

INTRODUCTION

Land subsidence has become an increasingly severe hazard in the Ca Mau Peninsula, where prolonged drought and excessive groundwater extraction have accelerated ground instability.

This process threatens ecosystems, infrastructure, and livelihoods, posing long-term risks to socio-economic development. Unlike floods and droughts, where monitoring and early warning systems are already in place, no dedicated framework exists in Vietnam to detect and predict subsidence, despite its growing severity. This gap highlights both the urgency and the novelty of establishing a digital-based warning system for subsidence risk.

Globally, advances in GIS, remote sensing, IoT, and InSAR techniques have enabled diverse approaches to subsidence monitoring, from UAV mapping in France to integrated multi-source systems in China and radar interferometry in Nanjing (Ghosha et al., 2010; Hemmelder et al., 2018; Mallick & Parvin, 2019; Ning et al., 2023; Chen et al., 2024). These efforts underscore a global trend toward digital transformation in disaster risk management. In Vietnam, progress has been made with AHP-GIS models for landslide (Thanh et al., 2020; Tuyen et al., 2021; Tuan & Tuyet, 2021), flash flood (Tran & Hoang, 2022), and arsenic risk mapping (Trung et al., 2020), as well as radar-based monitoring of land deformation in Can Tho (PSInSAR). However, these studies remain fragmented and largely exclude subsidence-specific frameworks in the southernmost provinces.

Developing a digital warning system for land subsidence in the Ca Mau Peninsula therefore represents both a scientific innovation and a practical necessity. By integrating expert-based methods such as

Delphi, AHP, and KAMET with GIS, the system will produce risk zoning maps validated against observed events. More importantly, it pioneers the application of digital technologies to a neglected hazard, aligning with Vietnam's broader trajectory toward technology-driven resilience. The proposed system will provide timely, actionable information for local authorities, enhancing socio-economic planning, optimizing land and water use, and contributing to climate change adaptation. As such, it marks a crucial step in advancing digital transformation for sustainable development in one of Vietnam's most vulnerable regions.

Unlike previous studies such as Tri et al. (2024), which focused primarily on risk zoning using the AHP-GIS approach, the present study advances the field by developing a digital early warning system for land subsidence that combines expert-based evaluation (Delphi and KAMET methods), multi-criteria weighting (AHP), and real-time processing and visualization through Python and Dart programming. This integration provides a dynamic, user-oriented tool for assessing and communicating subsidence risk due to drought and groundwater exploitation.

The objectives of this study are to: (1) identify and prioritize the key factors influencing land subsidence in the Ca Mau Peninsula using the Delphi-KAMET and AHP methods; (2) develop a GIS-based model to generate land subsidence risk zoning maps; and (3) design and validate a digital early warning system capable of updating, analyzing, and visualizing subsidence risk in near real time.

MATERIALS AND METHODS

Data collection

The data used in the article include:

- Meteorological data of stations in the study area (Source: Information and Data Center, Vietnam Meteorological and Hydrological Administration).
- Data on groundwater exploitation flow (Source: National Center for Water Resources Planning and Investigation).

- Information on factors: 1) geology, 2) soil, 3) evaporation, 4) dry season flow, 5) land use and 6) groundwater exploitation (Source: Department of Survey, Mapping and Geographic Information Viet Nam).

Methodology

- Subsidence in the study area can result from multiple factors; however, only those with reliable and measurable data were considered. Key indicators were identified using the Delphi method combined with the KAMET rule. The Delphi method synthesizes expert judgment through iterative rounds until consensus is reached, while the KAMET rule defines the threshold for stopping the process.

- To evaluate the consistency and reliability of expert opinions within the Delphi-KAMET framework, three statistical indicators were employed: M_{qi} , Q_{qi} , and V_{qi} (%). Specifically, M_{qi} represents the mean score of expert evaluations for each indicator, reflecting the overall level of importance assigned by the experts. Q_{qi} denotes the interquartile range, used to measure the dispersion of expert ratings and identify the degree of consensus. V_{qi} (%) indicates the coefficient of variation, which expresses the relative variability of expert judgments in percentage form. According to the KAMET rule, when the variation coefficient V_{qi} (%) falls below the predetermined threshold, the factor is considered stable and can be retained for the next Delphi round or for inclusion in the AHP analysis. These indicators ensure that the final set of influencing factors is derived from a statistically consistent and consensus-based expert assessment.

- The combination of the Delphi-KAMET-AHP framework was selected over data-driven weighting techniques such as entropy or principal component analysis (PCA) for three main reasons. First, the Delphi-KAMET process captures expert consensus and ensures factor selection stability through iterative validation, which is particularly valuable when field data are limited or heterogeneous. Second, the AHP method provides a structured way to quantify expert

judgments and evaluate the consistency ratio (CR), enabling transparent comparison among factors. Third, compared with entropy or PCA, which rely primarily on statistical variance, the Delphi-KAMET-AHP approach integrates both expert knowledge and quantitative logic, ensuring that socio-environmental relevance is not lost during data reduction. This integration has been widely applied in multi-criteria environmental assessments under data-scarce conditions.

- Application of AHP method (Cheng et al., 2002; Saaty, 2008) to determine factor weights: The factors affecting subsidence due to drought and groundwater exploitation in the study area were selected are: 1) geological structure; 2) Groundwater flow exploitation; 3) Water flow in the dry season; 4) Current land use status; 5) Evaporation in the dry season. This article used AHP to calculate the weights of factors affecting subsidence in the study area (Fig. 1).

- All spatial datasets were converted to a uniform coordinate system (VN-2000, UTM Zone 48N) and resampled to a spatial resolution of 30×30 m to ensure comparability. Each thematic layer geology, soil, land use, groundwater extraction, dry-season flow, and evaporation was normalized using the min-max normalization method, scaling all factor values to a range of 0–1. Temporal data series, including meteorological and groundwater extraction records, covered the 2013–2023 period, representing a full decade of hydrometeorological variability. All raster and vector layers were processed in ArcGIS 10.8 before overlay analysis. These normalization and resampling steps ensured consistent spatial-temporal comparability among datasets used to generate the subsidence risk zoning maps.

- Applying Python and Dart programming languages to build a warning system: 1) Python programming language is used to calculate and process results to build a warning system for the risk of subsidence due to drought and groundwater exploitation in

the study area; 2) Dart programming language is used to build the user interface and display results of drought subsidence warning systems and groundwater exploitation for the study area.

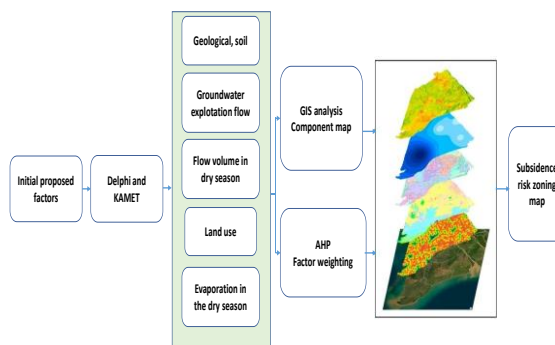


Figure 1. A flowchart of the structure of this study.

RESULTS AND DISCUSSION

Results of expert opinions on the index set according to the Delphi and KAMET rule methods

Based on documents on subsidence in the study area, the long-term cause is mainly due to the process of underground water exploitation, in addition to influencing factors such as flow speed to the study area, the ability to evaporate, geological and soil characteristics of the study area, and characteristics of groundwater exploitation and use in the study area. Table 1 shows the selected criteria used to evaluate the risk of land subsidence. The collected data is based on the results of the Delphi and KAMET rule methods to select the main influencing factors on subsidence in the study area.

Table 1 summarizes the results of the experts' evaluation as prescribed. A total of 24 experts participated in the evaluation process, representing hydrology, geology, and remote sensing disciplines, including a group of local officials (12 experts from representative offices for 6 provinces in the Ca Mau peninsula region, 1 local leader - a person with comprehensive knowledge about the current subsidence situation in the study area and 1 main expert in charge of natural disasters in the area) and 10 independent experts on subsidence research in Vietnam.

Table 1. Results of asking for expert opinions on the index set

Consultation Round	Index	M_{qi}	Q_{qi}	V_{qi} (%)
Round 1	Geological characteristics	4.1		
Round 2		3.6	0	15.2
Round 3		3.5	0	12.5
Round 1	Soil characteristics	4.5	0.5	
Round 2		4.2	0.38	25
Round 3		3.7	0.5	6.3
Round 1	Land use characteristics	4.3		
Round 2		4.1	0.5	1.52
Round 3		4	0.5	12.5
Round 1	Annual flow characteristics (*)	3.7		
Round 2		3.5	0.88	37.5
Round 3		3.1	0.38	18.8
Round 1	Dry-season flow characteristics	3.9		
Round 2		3.8	0.5	18.8
Round 3		3.6	0.5	12.5
Round 1	Evaporation throughout the year (*)	3.7		
Round 2		3.6	1	43.8
Round 3		3.2	1	31.3
Round 1	Characteristics of evaporation in the dry season	3.8		
Round 2		3.6	0.5	18.8
Round 3		3.5	0.5	12.5
Round 1	Characteristics of underground water exploitation	4.4		
Round 2		4.1	0.5	18.8
Round 3		3.8	0.5	12.5
Round 1	Topographic characteristics (*)	3.7		
Round 2		3.5	1.38	43.8
Round 3		3.3	1.38	37.5
Round 1	Characteristics of construction (*)	3.6		
Round 2		3.5	1	37.5
Round 3		3.4	0.5	56.3

Note: (*) Factors are not selected because they don't meet the KAMET rules.

The main factors affecting subsidence after being refined by KAMET rules in the study area are presented in Table 2.

Table 2. Factors affecting the study area.

No.	Factor	Symbol
1	Geological characteristics	Geo
2	Soil characteristics	Soil
3	Characteristics of underground water exploitation	Gw
4	Dry-season flow characteristics	Flow
5	Land use characteristics	Land
6	Characteristics of evaporation in the dry season	Eva

Results of AHP Application to Calculate Factor Weight

After results from section 3.1, the study selects 6 main factors affecting subsidence in the study area to evaluate the influence of weight. The selected factors are presented in Table 3.

Table 3. Selected criteria for assessing the risk of land subsidence

No.	Selection criteria	Data sources used
1	Geological structure	Geological map of the study area (scale 1:10,000)
2	Soil documents	National Center for Water Resources Planning and Investigation
3	Groundwater flow exploitation	National Center for Water Resources Planning and Investigation
4	Water flow in the dry season	Calculated according to SCS (Curve Number Method, 1964, 1972)
5	Current land use status	Land use map of the study area (scale 1:10,000)
6	Evaporation in the dry season	Calculated according to Penman-Monteith formula (Allen et al., 1998; FAO, 2000)

This study used the AHP analytical hierarchy method to establish a calculation matrix. The matrix table comparing the evaluation criteria is shown in Table 4.

Table 4. Matrix for comparing evaluation criteria.

Rate	Land	Q _{dry}	Geological	Land use	ET _{dry}	Q _{exploit}
Land	1	1/3	1/3	1/7	1/7	1/9
Q _{dry}	3	1	3	3	3	3
Geological	3	1/3	1	1/9	1/5	1/9
Land use	7	1/3	9	1	1/7	1/3
ET _{dry}	7	1/3	5	3	1	1/7
Q _{exploit}	9	1/3	9	3	7	1

The weight calculation was carried out by dividing each value in each column of the matrix by the total number of values in that column. The result was a weight between 0 and 1, as shown in Table 5.

Table 5. Weight matrix of evaluation factors.

Element	Land	Q _{dry}	Geological	Land use	ET _{dry}	Q _{exploit}
Land	0.033	0.125	0.012	0.014	0.012	0.024
Q _{dry}	0.100	0.375	0.110	0.293	0.261	0.639
Geological	0.100	0.125	0.037	0.011	0.017	0.024
Land use	0.233	0.125	0.329	0.098	0.012	0.071
ET _{dry}	0.233	0.125	0.183	0.293	0.087	0.030
Q _{exploit}	0.300	0.125	0.329	0.293	0.609	0.213
Land	0.033	0.125	0.012	0.014	0.012	0.024
Q _{dry}	0.100	0.375	0.110	0.293	0.261	0.639
Geological	0.100	0.125	0.037	0.011	0.017	0.024

The result shows that CI = 0.101 and CR = 8.1%. As the CR value is less than 10%, the weight can be used.

The subsidence risk index of the study area is calculated according to the following formula:

$$\text{Risk of subsidence (C)} = (\text{Land} \times 0.036) + (\text{Q}_{\text{dry}} \times 0.296) + (\text{Geological} \times 0.052) + (\text{Land use} \times 0.145) + (\text{ET}_{\text{dry}} \times 0.159) + (\text{Groundwater exploitation} \times 0.312) \quad (1)$$

Formula (1), weighted with the influencing factors (land, Q_{dry}, geological, land use, ET_{dry}, groundwater exploitation), was applied to build a land subsidence risk zoning map, as shown in Fig. 2. The study results are shown in a subsidence risk zoning map that provides an intuitive and general overview of the areas with high subsidence risk and can be

a document to help managers consult in the work of building a socio-economic development plan for the Ca Mau Peninsula region.

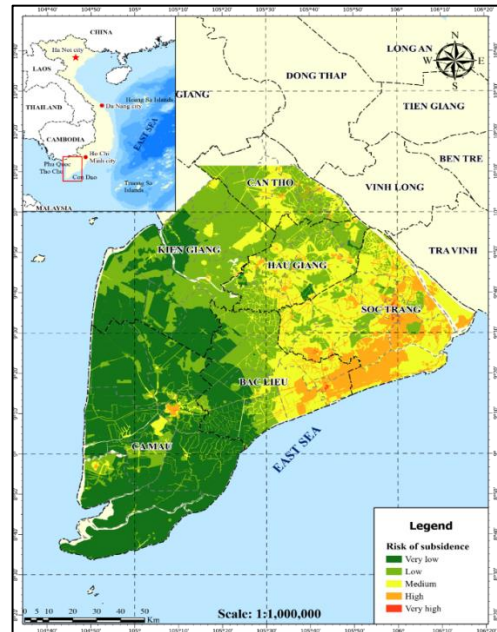


Figure 2 Subsidence risk zoning map in the Ca Mau Peninsula area (Tri et al., 2024).

Early Warning System for Subsidence Risk Due to Drought and Groundwater Exploitation

The main modules and their functional relationships within the subsidence risk warning system are illustrated in Figs. 3 and 4. Each module ranging from data input, hydrological computation, and factor weighting to GIS-based mapping and result visualization is explicitly labeled to show the system's integrated workflow.

- Water inflow update module allows users to update total inflow data that vary over time, as well as forecasted inflows (calculated based on long-term hydrological forecasts with a one-month period).

- Evapotranspiration calculation module enables users to calculate forecasted evapotranspiration according to the selected formula.

- Water allocation module manages the spatial and temporal distribution of water

exploitation and use, allowing updates of recharge values as well as the total exploited and used water volume within the study area.

- Influencing factor update module allows users to update changes in factors affecting landslides and subsidence in the area.

- Data classification module supports the updating and reclassification of influencing factor groups.

- Weight update module enables users to adjust the weights corresponding to different influencing factors.

- Map overlay module allows users to compile composite maps by overlaying factor layers within the study area.

- Result display module provides visualization of areas at risk of landslides and subsidence under different groundwater exploitation scenarios and drought conditions.

- Warning publication module enables the generation of warning bulletins in Word format, following a predefined template, for dissemination to relevant stakeholders.

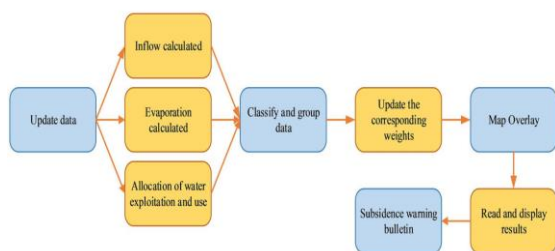


Figure 3. Structure of the subsidence risk warning system.



Figure 4. Subsidence Risk Warning System for the Ca Mau Peninsula.

The subsidence risk warning system caused by drought and groundwater exploitation was tested using data from the 2024 drought period. The results of the system testing are presented below.

The map has been tested for the dry season in 2024. The subsidence risk map results were compared with the subsidence location of the research area that was surveyed. Table 6 is the actual surveyed subsidence location in the dry season in 2024.

Table 6 Subsidence locations in the study area.

No.	Subsidence locations	Characteristic
1	Rach Ruong Canal, Khanh Loc Commune, Tran Van Thoi District	Subsidence of about 500 m (new canal and road built in 2023, about 1 km long) Subsidence just occurred in 2024, never occurred before
2	Canal No. 2, Khanh Loc Commune, Tran Van Thoi District	A section of road subsided about 30 m The subsidence just occurred in 2024, never happened before
3	Rach Ruong C, Khanh Loc Commune, Tran Van Thoi District	Subsidence of about 50 m road Subsidence occurred in 2024, never happened before
4	Hao Sai Canal, Khanh Loc Commune, Tran Van Thoi District	A road section of about 200 m has subsided. The subsidence just occurred in 2024, never happened before
5	Nha May Canal, Khanh Hung Commune, Tran Van Thoi District	Subsidence of about 70 m road Subsidence just occurred in 2024, never happened before
6	Khanh Hung Commune, Tran Van Thoi District	A road section of about 100 m subsided The subsidence just occurred in 2024, never happened before
7	Cong Nghiep B Canal, Hung Commune, Tran Van Thoi District	A road section subsided about 60 m New subsidence occurred in 2024, never happened before
8	Ngang Canal, Trum Thuat B Hamlet, Khanh Hai Commune, Tran Van Thoi District	A road section subsided about 50 m New subsidence

		occurred in 2024, never happened before
9	Khanh Hung A Canal, Khanh Hung A Hamlet, Khanh Hai Commune, Tran Van Thoi District	A road section subsided about 30 m New subsidence occurred in 2024, never happened before

The comparison results are shown below in Figure 5. It is evident that the computation results when compared to real survey data collected in the research area, are reasonably accurate in terms of the sites of subsidence that happened during the dry season of 2024 at certain points. The map of subsidence risk, which is the outcome of a warning system for the risk of subsidence due to drought and groundwater exploitation that has been tested, shows that the 10 points in the study area where subsidence actually occurred during the dry season of 2024 all correspond with areas with high risk of subsidence (orange). As a result, a warning system for the possibility of landslides and subsidence in the Ca Mau peninsula region has been constructed using calculating software.



Figure 5 The subsidence risk map in Ca Mau Peninsula have been surveyed in the field for dry season in 2024 (Tri et al., 2024).

Quantitative validation of the subsidence risk map was performed by comparing predicted high-risk zones with the nine field-surveyed subsidence locations recorded during the 2024 dry season. The results show that 8 out of 9 observed points (88.9%) fall within areas classified as high or very high risk on the model output, indicating a strong predictive correspondence between the simulation results and real-world events. This level of agreement demonstrates the robustness of the Delphi-KAMET-AHP-GIS framework in capturing the dominant drivers of land subsidence.

Spatial analysis further reveals that high-risk zones are concentrated along Tran Van Thoi, Khanh Loc, and Khanh Hung communes, where groundwater extraction intensity is highest and Holocene clay thickness exceeds 20 meters. These areas also experience reduced surface flow during the dry season, resulting in limited recharge and increased vertical compaction. Conversely, lower-risk areas are mainly located in regions with shallow groundwater tables and mixed land-use patterns, where the interaction between recharge and extraction remains balanced.

Among the influencing factors, groundwater exploitation (weight = 0.312) and dry-season flow (weight = 0.296) were found to have the largest impact, underscoring the hydrological control on land stability. The geological and evaporation factors, while still significant, contributed secondary effects by modulating soil compressibility and evapotranspiration-driven water loss. These findings align with the field-observed deformation patterns and provide valuable insights for prioritizing water resource management and urban development in the Ca Mau Peninsula.

The warning system, after being successfully transferred and pilot-applied at the National Center for Hydro-Meteorological Forecasting, the Southern Regional Hydro-Meteorological Station, and the Ca Mau Hydro-Meteorological Station, has been filed for patent acceptance and copyright registration

with the Copyright Office under the Ministry of Science and Technology (Fig. 6).



Figure 6. Decision on acceptance of patent application and copyright certificate.

CONCLUSION

This study has developed and validated a digital early warning system for land subsidence risks caused by drought and groundwater exploitation in the Ca Mau Peninsula. By integrating expert-based methods (Delphi and KAMET), multi-criteria decision analysis (AHP), and Geographic Information System (GIS) techniques, the system successfully identified six major influencing factors: geological characteristics, soil properties, groundwater exploitation, dry-season flow, land use, and evaporation. The resulting risk zoning maps demonstrated strong consistency with field survey data collected during the 2024 drought season, where all observed subsidence points corresponded with high-risk zones identified by the model. This confirms the reliability of the approach and its practical value for supporting local authorities in disaster risk management, planning, and sustainable resource use.

Despite these achievements, several limitations remain. The system relies heavily on the quality and resolution of input data, which may vary across provinces. Some critical factors such as construction load and topographic variability were excluded due to limited data availability, potentially reducing accuracy in complex urbanized areas.

Furthermore, the system has so far been validated only within Ca Mau Province; broader testing across different hydrological and geological settings in the Mekong Delta is still needed to generalize its applicability.

Future development will focus on enhancing the system's data integration capabilities through remote sensing, IoT-based groundwater monitoring, and InSAR technologies for real-time deformation tracking. Expansion to other vulnerable provinces such as Bac Lieu, Soc Trang, and Kien Giang will allow refinement of the model and strengthen regional resilience. Additionally, coupling the system with socio-economic planning tools will provide decision-makers with a more holistic framework to balance water resource use, land management, and climate adaptation.

In conclusion, the proposed warning system represents an important step toward digital transformation in disaster risk management. Its successful pilot in the Ca Mau Peninsula provides a foundation for scaling up to the entire Mekong Delta, contributing to sustainable development and long-term climate resilience in one of Vietnam's most fragile regions.

REFERENCES

- Allen R. G., Pereira L. S., Raes D., Smith M. (1998). Crop Evapotranspiration—Guidelines for Computing Crop Water Requirements. FAO Irrigation and Drainage Paper 56. Food and Agriculture Organization of the United Nations.
- Chen Y., Guo L., Xu J., Yang Q., Wang H., Zhu C. (2024). Monitoring and Cause Analysis of Land Subsidence along the Yangtze River Utilizing Time-Series InSAR. ISPRS International Journal of Geo-Information, 13: 230. <https://doi.org/10.3390/ijgi13070230>.
- Food and Agriculture Organization of the United Nations (FAO) (2020). Crop Evapotranspiration: Guidelines for Computing Crop Water Requirements. Online available: https://appgeodb.nancy.inrae.fr/biljou/pdf/Allen_FAO1998.pdf
- Ghosha J. K., Bhattacharyab D., Boccadoroc P., Samadhiya N. K. (2010). A Landslide Hazard Warning System. International Archives of the Photogrammetry,

- Remote Sensing and Spatial Information Science, XXXVIII, pp. 261-265.
- Hemmelder S., Marra W., Markies H., De Jong S. M. (2018). Monitoring River Morphology & Bank Erosion Using UAV Imagery—A Case Study of the River Buëch, Hautes-Alpes, France. *International Journal of Applied Earth Observation and Geoinformation*, 73: 428-437. <https://doi.org/10.1016/j.jag.2018.07.016>.
- Mallick A., Parvin M. (2019). Risk Informed Early Warning System and Non-Migration Pattern Riverbank Erosion Areas. BRAC Humanitarian Programme, BRAC, 29p. Online available:
- Soil Conservation Service, SCS (1972). National Engineering handbook, Section 4, Hydrology. Department of Agriculture, 762p.
- Thanh D. Q., Nguyen D. H., Prakash I., Jaafari A., Nguyen V. T., Phong T. V., Pham, B. T. (2020). GIS based frequency ratio method for landslide susceptibility mapping at Da Lat City, Lam Dong province, Vietnam. *Vietnam Journal of Earth Sciences*, 42(1): 55-66. <https://doi.org/10.15625/0866-7187/42/1/14758>.
- Tran T. T., Hoang T. T. (2022). Assessing flash flood risks based on analytic hierarchy process (AHP) and Geographic Information System (GIS): A Case Study of Hieu catchment (Nghe An, Vietnam). In: Nguyen A. T., Hens L. (eds) *Global Changes and Sustainable Development in Asian Emerging Market Economies*, Springer, Cham., 2, pp. 793–803. https://doi.org/10.1007/978-3-030-81443-4_50.
- Trung D. T., Nhan, P. Q., Hung, N. K. (2020). Using GIS and analysis hierarchy process (AHP) in order to map arsenic pollution zonation in groundwater based on the influence of geological factors in the Red River Delta. *Hanoi University of Natural Resources & Environment*, 29, pp. 24-35. Available online: <https://tapchikhtnmt.hunre.edu.vn/index.php/tapchikhtnmt/article/view/213/215> (In Vietnamese)
- Tuan H. N., Tuyet V. T. (2021). Research and develop a landslide risk zoning map for mountainous areas of Quang Nam province. *Journal of Irrigation Science Technology*, 68: 1-9. Available online: <https://vawr.org.vn/Upload/BaibaoKH/hoang-ngoc-tuan-68-2021.pdf>. (In Vietnamese)
- https://www.preventionweb.net/files/67631_67631rivererosionearlywarningreport.pdf?startDownload=true.
- Ning D., Zhu J., Guo H., Zang X., Wang H. (2023). Research on Monitoring, Early Warning and Prevention System of Land Subsidence in Beijing-Tianjin-Hebei Region. *Journal of Physics: Conference Series*, 2468: 012149. <https://doi.org/10.1088/1742-6596/2468/1/012149>.
- Soil Conservation Service, SCS (1964). National Engineering Handbook, Section 4, Hydrology. Department of Agriculture, 450p.
- Tuyen T. H., Thuy N. T., Do H. N. T., Tham H. H. (2021). Zoning sinkhole susceptibility for Phong Xuan area (Phong Dien district, Thua Thien Hue province) by using SAATY's analytical hierarchy process (AHP). *Hue University Journal of Science*, 19(2): 179-188. Available online: https://csdlkhoahoc.hueuni.edu.vn/data/2022/7/2021_-_Tc_KHCN_DHKH_-_Sut_dat_Phong_Xuan_.pdf (In Vietnamese)
- Tri D. Q., Nhat N. V., Tuyet Q. T. T., Pham H. T. T., Duc P. T., Thuy T. N. (2024). Applying an Analytic Hierarchy Process and a Geographic Information System for Assessment of Land Subsidence Risk Due to Drought: A Case Study in Ca Mau Peninsula, Vietnam. *Sustainability*, 16: 2920. <https://doi.org/10.3390/su16072920>.
- Tri D. Q., Tuyet Q. T. T., Nhat N. V., Duc P. T. (2024). Establishing a Subsidence Warning System Due to Drought and Groundwater Exploitation: A Case Study at Ca Mau Peninsula, Vietnam. *Current Urban Studies*, 12: 440-453. <https://doi.org/10.4236/cus.2024.123022>.

From Perception to Identification and Action: Designing Digital Co-Creation Platforms to Promote Willingness to Pay for Drought Risk Management - A Regional Case Study from East Asia

Wen Chin, Hsu^{*}, Chi-Wei, Peng

Department of Information Management, Global Drought Investigation and Research Center, National Central University (NCU), Taoyuan, Taiwan (China)

^{*}Email: hsuwc@ncu.edu.tw

Abstract: Climate change has heightened drought risks, posing critical challenges for water governance. This study examines how digital co-creation platforms—integrating information transparency, interactivity, and incentive mechanisms—shape citizens' policy identification and subsequent behavioral intentions. Using a scenario-based survey of 150 participants in Taiwan (China), Partial Least Squares Structural Equation Modeling shows that platform features significantly strengthen policy identification ($\beta = 0.461$, $p < 0.001$), which in turn predicts willingness to pay ($\beta = 0.703$, $p < 0.001$) and social advocacy ($\beta = 0.278$, $p < 0.001$). The model explains 50.9% of the variance in willingness to pay and 39.9% in social advocacy, highlighting the pivotal role of identification in converting platform engagement into policy support. These findings demonstrate how transparent communication, participatory design, and value-aligned incentives can transform citizen attitudes into active cooperation within digital governance contexts.

Keywords digital co-creation, drought governance, policy identification, citizen engagement, structural equation modeling

INTRODUCTION

Droughts have become increasingly frequent and severe, posing major challenges for public water governance. Climate change has intensified rainfall variability across East Asia (IPCC, 2023; Kummur et al., 2022), and in

Taiwan (China), recent drought events have disrupted agricultural and industrial operations, underscoring the fragility of water security (Chen & Yeh, 2021). Although the government has implemented measures such as water-use restrictions and progressive tariff schemes, public resistance remains common. Low understanding of policy rationales and limited engagement with official communication channels continue to weaken citizen support (Liao et al., 2024).

Digital technologies have emerged as important tools for participatory governance. Digital co-creation platforms—combining data visualization, interactive functions, and incentive mechanisms—offer new opportunities for public agencies to communicate risk, increase transparency, and involve citizens in decision processes (Meijer, 2021; Paskaleva et al., 2022). Despite their growing use, little is known about the psychological mechanisms through which platform features influence citizens' acceptance of and commitment to environmental policy. Existing research has often emphasized system design or user engagement metrics, while leaving the cognitive and attitudinal processes shaping cooperation insufficiently examined.

This study addresses this gap by investigating how three key design features of digital co-creation platforms—information transparency, interactivity, and incentive mechanisms—shape citizens' policy identification, and how this identification

translates into willingness to support drought-related policies. By integrating perspectives from environmental psychology and digital governance, we develop a framework that links technological affordances with policy-oriented attitudes and behaviors (Tseng & Kuo, 2023).

The drought context provides an especially appropriate setting for testing the Perception–Identification–Action (PIA) framework. Drought governance requires citizens to interpret complex environmental information, recognize the collective nature of water scarcity, and align personal behavior with broader policy objectives. These sequential demands correspond directly to the PIA process: transparent information enables accurate risk perception, which facilitates internalization of policy legitimacy, ultimately leading to cooperative action. Because drought policies often involve visible trade-offs, this context offers a rigorous environment for examining how digital platforms influence cognitive appraisal and attitudinal alignment.

Guided by these considerations, this study addresses the following research questions: (1) How do information transparency, interactivity, and incentive mechanisms influence citizens' policy identification?(2) How does policy identification shape willingness to pay and social advocacy?(3) Do platform features affect policy-support behaviors directly, or indirectly through identification?

To answer these questions, we develop a conceptual model and empirically test it using data from a scenario-based survey conducted in Taiwan (China). The findings contribute to the literature on digital governance by clarifying how platform design can activate cognitive and attitudinal mechanisms that support environmental policy implementation.

THEORETICAL BACKGROUND AND HYPOTHESES

From Perception to Action: Linking Cognitive and Behavioral Pathways

Understanding how citizens move from perceiving environmental risks to engaging in

cooperative behavior has long been central to social psychology and environmental research. The Knowledge–Attitude–Behavior (KAB) model proposes that information shapes attitudes, which subsequently motivate behavioral responses (Hines et al., 1987). Likewise, the Theory of Planned Behavior (TPB) conceptualizes behavioral intention as shaped by attitudes, subjective norms, and perceived behavioral control (Ajzen, 1991). These frameworks highlight internal psychological processes as the bridge between awareness and action.

Environmental studies have adapted these perspectives to explain why risk awareness does not always translate into pro-environmental behavior (Bamberg & Möser, 2007). A key missing mechanism is policy identification—citizens' cognitive and emotional alignment with the fairness, necessity, and legitimacy of governmental measures (Slovic, 1987). Policy identification integrates perceptions of justification and shared values, allowing individuals to transform risk understanding into policy-supportive behavior. Thus, identification provides a psychological link between perception and action that is essential in the context of drought governance.

Digital Co-Creation in Environmental Governance

Digital co-creation platforms extend traditional participatory governance by enabling citizens and governments to collaboratively interpret data, share feedback, and engage in decision processes (Vagena et al., 2024). These platforms can translate abstract environmental information into personally meaningful experiences through interactive dashboards, simulations, and feedback loops.

Prior work identifies three design features that strongly influence users' engagement with digital platforms:(1) information transparency, which reduces uncertainty and strengthens trust (Lind & van den Bos, 2002);(2) interactivity, which supports user participation and co-creation (McMillan & Hwang, 2002); and(3) incentive mechanisms, such as gamification and recognition, which reinforce motivation (Deci & Ryan, 1985; Tseng & Kuo, 2023).

In Taiwan (China), the Water Resources Agency has adopted digital tools integrating real-time drought indicators, risk scenarios, and participatory features. However, the psychological pathways through which such features influence citizens' policy identification and downstream behavioral intentions remain underexplored. This gap motivates the development of our theoretical model (Figure 2), which positions platform features as antecedents to identification and subsequent behavioral outcomes.

Policy Identification and Behavioral Intentions

Policy identification reflects citizens' evaluation of the fairness, necessity, and value alignment of a policy (Bamberg & Möser, 2007). In environmental governance, identification is strengthened when communication is transparent, participatory, and seen as legitimate (Hair et al., 2014). Individuals who strongly identify with environmental policies are more willing to support cost-bearing initiatives and promote conservation within their social networks (Wheeler et al., 2025). Digital platforms can cultivate this identification by presenting understandable data, demonstrating procedural fairness, and enabling user agency. Thus, identification becomes a central attitudinal mediator transforming cognitive appraisal into behavioral commitment.

Hypotheses Development

Design features of digital co-creation platforms influence citizens' judgments through interrelated mechanisms of transparency, interactivity, and incentives. Information transparency reduces uncertainty about environmental conditions and policy rationale, enabling citizens to trace how reservoir levels trigger drought alerts, how tariffs are calculated, and how revenues are allocated for resilience investments. This clarity enhances perceived procedural justice and supports central-route persuasion by providing diagnostic information for systematic evaluation (Lind & van den Bos, 2002; Petty & Cacioppo, 1986). Interactivity promotes two-

way communication, user control, and feedback (McMillan & Hwang, 2002). Such affordances heighten self-relevance, reinforce institutional responsiveness, and foster shared identity between citizens and policymakers (Tajfel & Turner, 1979). Through social interaction features—comments, endorsements, and community benchmarks—citizens also perceive descriptive norms that encourage conservation and compliance (Cialdini, 2003).

Incentive mechanisms provide immediate reinforcement for conservation behaviors but also support intrinsic motivation when framed as competence feedback rather than control (Deci & Ryan, 1985). Together, these three features form a coherent choice architecture that transforms complex policy information into personally meaningful decisions. Because policy identification reflects perceptions of fairness, necessity, and value alignment (Bamberg & Möser, 2007), platforms that are transparent, interactive, and motivational should enhance users' identification with the policy (H₁).

Policy identification bridges informed perception and cooperative behavior. In environmental contexts, moving from agreement "in principle" to willingness to pay (WTP) requires overcoming fairness and efficacy concerns (Ajzen, 1991; Bamberg & Möser, 2007). Identification integrates these evaluations, reframing payment as a contribution to a shared good rather than a private loss. When citizens perceive water pricing as fair and necessary for collective benefit—such as ensuring long-term water security and industrial continuity—they are more likely to pay supportive fees (Wheeler et al., 2025). Thus, policy identification should positively influence WTP (H₂).

A similar mechanism applies to social advocacy, which entails reputational costs and active message diffusion. Identification provides ownership, transforming passive acceptance into active promotion of policy goals within personal networks (Bamberg & Möser, 2007). Digital platforms lower barriers

to advocacy through visible social features (badges, sharing tools), coupling identification with social proof that normalizes engagement (Cialdini, 2003). Hence, stronger policy identification is expected to predict greater advocacy intention (H3).

Beyond these direct effects, policy identification is proposed to mediate the relationship between platform design and behavioral outcomes. While transparency, interactivity, and incentives may directly influence user behavior, their enduring impact depends on whether users internalize the policy's legitimacy. In the TPB framework, identification acts as a higher-order attitude consolidating beliefs into intention (Ajzen, 1991). In dual-process terms, it anchors central-route evaluations into stable attitudes guiding future actions (Petty & Cacioppo, 1986). Thus, identification is expected to mediate the effects of platform features on both WTP (H4) and social advocacy (H5).

Finally, in high-risk contexts like drought, information alone can trigger awareness but not cooperation if policies are viewed as unfair (Slovic, 1987). Likewise, extrinsic incentives risk undermining intrinsic motives unless embedded within transparent and participatory systems (Deci & Ryan, 1985). Under these conditions, policy identification remains the most reliable pathway through which digital platform design fosters both private and public engagement.

METHODOLOGY

Research Design and Sampling

This study employed a scenario-based experimental survey to examine citizens' perceptions of a government drought-risk simulation platform. Participants were presented with a simulated environment describing the platform's interactive functions, data transparency, and incentive system, followed by a structured questionnaire measuring relevant constructs. For example, the scenario presented participants with real figures retrieved from Taiwan's official Water Resources Agency, including reservoir storage

levels, current drought alerts, and available policy options. After reviewing these data, the platform displayed tailored water-saving information to help users understand recommended conservation actions.

A total of 150 valid responses were collected from adults across Taiwan (China) through a random online survey conducted by DrSurveyDone, a professional market research firm. Stratified sampling ensured proportional representation by region, gender, and age. The sample was 58% female and predominantly between 30 and 40 years old, with most respondents indicating prior awareness of drought and water-saving issues.

To enhance geographic transparency, Figure 1 illustrates the proportional distribution of respondents by region—Northern (41.6%), Central (19.3%), Southern (34.5%), and Eastern (4.6%) Taiwan (China). The Northern Region accounted for the largest share of respondents, followed by the Southern Region, reflecting population density and internet penetration patterns across the island. The inclusion of this regional visualization provides contextual clarity on the spatial representativeness of the survey and confirms that the data capture perspectives from all four major administrative regions of Taiwan (China).

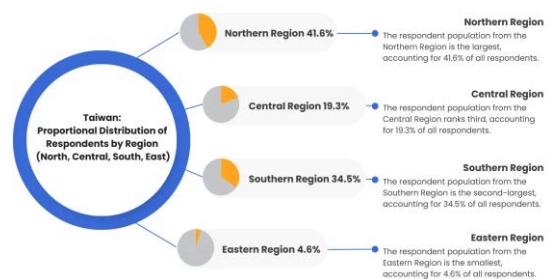


Figure 1. Taiwan (China): Proportional Distribution of Respondents by Region

Measurement

All constructs were measured using a five-point Likert scale (1 = strongly disagree; 5 = strongly agree) adapted from validated instruments. Platform features were measured through items capturing information transparency (e.g., "The platform provides clear

information about current drought policies”), interactivity (e.g., “The platform enables me to exchange ideas with others about water conservation”), and incentive mechanisms (e.g., “The platform motivates me to participate through achievement or reward systems”). Policy identification included items assessing perceived fairness and legitimacy of drought-related water pricing policies (e.g., “Raising water fees is a reasonable measure to address drought”). Willingness to pay and social advocacy were measured through behavioral intention statements such as willingness to pay higher fees and willingness to share or recommend the platform.

Data Analysis

The data were analyzed using IBM SPSS and AMOS. Construct validity was examined through confirmatory factor analysis (CFA), and internal consistency reliability was evaluated using Cronbach’s alpha, composite reliability (CR), and average variance extracted (AVE). Discriminant validity was assessed using the heterotrait–monotrait (HTMT) ratio criterion (Henseler, Ringle, & Sarstedt, 2015). Structural relationships among the latent constructs were tested using structural equation modeling (SEM), and mediation effects were evaluated through bootstrapping with 5,000 resamples.

The sample size of $n = 150$ is adequate for SEM in this study. Although SEM traditionally benefits from larger samples, prior research demonstrates that Partial Least Squares Structural Equation Modeling (PLS-SEM)—and SEM models with strong communalities—can yield stable and reliable estimates with samples ranging from 100 to 150 (Hair et al., 2021). The present model meets the commonly applied “10-times rule” and exceeds minimum sample size recommendations derived from power-analysis guidelines (Cohen, 1992). Therefore, the final sample of 150 respondents provides sufficient statistical power to detect the hypothesized structural relationships.

RESULT

Measurement Model Evaluation

The CFA results confirmed the adequacy of the measurement model. All factor loadings exceeded 0.68, satisfying convergent validity criteria. Cronbach’s alpha values ranged from 0.709 to 0.869, and all AVE values were above 0.50, confirming internal consistency and convergent validity. Discriminant validity was supported as all HTMT values were below the recommended threshold of 0.85 (Henseler et al., 2015). Multicollinearity tests indicated variance inflation factor (VIF) values below 3, demonstrating the absence of collinearity problems.

Structural Model and Hypothesis Testing

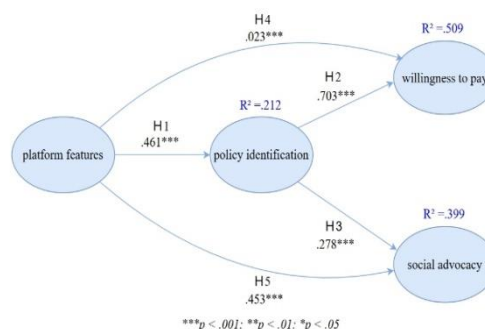


Figure 2. Empirical Structural Equation Model

The structural relationships among the constructs were examined using Partial Least Squares Structural Equation Modeling (PLS-SEM), following established guidelines for variance-based analysis (Hair et al., 2019; Hair et al., 2022). Because global fit indices such as CFI, TLI, and RMSEA are not applicable in PLS-SEM, model fit was assessed using the Standardized Root Mean Square Residual (SRMR), the recommended fitness criterion for this approach (Henseler et al., 2014). The model yielded an SRMR value of 0.079, which is below the 0.08 threshold, indicating acceptable fit. These procedures align directly with the methodological steps outlined in Section 3, ensuring consistency between the specified measurement model and the structural analyses reported.

Figure 2 presents the estimated structural paths and standardized coefficients. Platform features demonstrated a significant positive effect on policy identification ($\beta = 0.461$, $p < 0.001$), providing support for H1. Policy identification, in turn, significantly predicted both willingness to pay ($\beta = 0.703$, $p < 0.001$) and social advocacy ($\beta = 0.278$, $p < 0.001$), confirming H2 and H3. The direct effect of platform features on willingness to pay was not statistically significant ($\beta = 0.023$, n.s.), indicating that H4 is not supported. However, platform features exerted a significant direct effect on social advocacy ($\beta = 0.453$, $p < 0.001$), providing support for H5.

The model explained 21.2% of the variance in policy identification ($R^2 = .212$), 50.9% in willingness to pay ($R^2 = .509$), and 39.9% in social advocacy ($R^2 = .399$). These values indicate moderate to substantial explanatory power. Taken together, the findings show that policy identification functions as a central psychological mechanism linking platform design to behavioral intentions, while the non-significant direct effect on willingness to pay suggests that platform features alone are insufficient to motivate financial contributions without corresponding attitudinal alignment.

DISCUSSION AND CONCLUSION

Theoretical Implications

This study contributes to the theoretical understanding of digital governance by demonstrating how specific design features of digital co-creation platforms influence citizen engagement through the psychological pathway of policy identification. The findings extend prior work grounded in the Knowledge-Attitude-Behavior (KAB) and Theory of Planned Behavior (TPB) frameworks by showing that citizens' willingness to engage in policy-supportive actions is not driven solely by access to transparent information or interactive features, but by the degree to which these features enable citizens to internalize policy goals. The confirmation that policy identification fully mediates behavioral intentions underscores that attitudinal

alignment is a more decisive predictor of engagement than platform features themselves. This supports and deepens process-based trust theory, which argues that fairness and procedural clarity often outweigh instrumental considerations in shaping compliance (Lind & van den Bos, 2002).

By empirically validating the Perception-Identification-Action (PIA) sequence in a digital drought-governance context, the study also demonstrates the framework's applicability to technology-mediated public participation. Prior research has emphasized the role of digital platforms in facilitating transparency and communication, but has given limited attention to the cognitive and identity-based mechanisms that convert perception into action. This study addresses that gap by showing that platform design influences citizens not directly, but through shaping how they interpret risk and identify with the policy. These insights suggest a potentially generalizable mechanism relevant to other sustainability domains such as climate adaptation, energy efficiency, and water conservation.

Practical Implications

The findings offer several actionable implications for public agencies designing digital platforms for environmental governance. First, transparency should be treated not merely as information disclosure but as an intentional communication strategy. Providing real-time drought indicators, clearly explaining policy rationales, and visualizing expected outcomes can strengthen citizens' sense of procedural fairness and thereby enhance policy identification. Second, platforms should incorporate interactive features—such as participatory simulations, scenario tools, and direct feedback channels—that allow citizens to explore policy impacts, ask questions, and observe the consequences of collective action. Such interactivity helps cultivate ownership and trust in policy processes.

Third, incentive mechanisms should be framed to reinforce competence and civic

contribution rather than simple reward exchange. Recognitions, progress badges, or gamified conservation challenges can increase user engagement while supporting internalization of policy goals. Finally, communication efforts should explicitly link platform participation to broader societal resilience, reframing drought responses as shared responsibilities. Emphasizing the collective benefits of cooperation can reduce perceived personal cost and increase both willingness to pay and willingness to advocate. Together, these insights highlight that effective digital governance requires not only technological design but also strategic framing that builds identification and sustained public commitment.

Limitations and Future Research

Several limitations should be acknowledged. First, this study employed a cross-sectional survey and self-reported measures, which restrict causal inference and may not capture enduring behavioral change. Future work could employ longitudinal or experimental field designs to examine how citizens' perceptions and engagement evolve over time, supported by larger and more diverse samples to enhance generalizability. Second, the current model emphasized cognitive and attitudinal variables, omitting potentially important affective and social-identity factors. Emotions such as empathy or pride, and identification with environmental communities, may influence how citizens interpret drought information and internalize policy goals. Integrating these dimensions would extend understanding of motivational pathways in digital co-creation. Third, all variables were perceptual; incorporating objective indicators of platform interaction—such as login frequency or content sharing—could triangulate results and capture behavioral realism. Finally, as the study focused on a single national context, comparative or cross-cultural designs could reveal how institutional trust and civic norms moderate the effects observed here. Addressing these issues would strengthen both the theoretical

scope and empirical robustness of research on digital platforms for sustainable governance.

Conclusion

This study empirically demonstrates that well-designed digital co-creation platforms can serve as powerful instruments for promoting citizen engagement in environmental governance. By examining the mediating role of policy identification, the findings reveal that the effectiveness of such platforms lies not only in the delivery of information or provision of incentives, but in their ability to foster citizens' psychological identification with policy objectives. When users perceive platform processes as transparent, interactive, and fair, they internalize public values and transform abstract policy goals into concrete behavioral commitments—expressed through both willingness to pay and willingness to advocate. These insights extend existing frameworks of environmental communication by illustrating how technological affordances can activate social-cognitive mechanisms underlying sustainable behavior. As societies face escalating climate risks, digital co-creation platforms that build trust, legitimacy, and collective efficacy will become essential components of adaptive governance.

ACKNOWLEDGMENT

The authors would like to express their sincere gratitude to the Global Drought Investigation and Research Center and National Central University (NCU) for their generous support.

REFERENCES

- Ajzen I (1991). The theory of planned behavior. *Organizational Behavior and Human Decision Processes* 50(2): 179–211.
- Bamberg S, Möser G (2007). Twenty years after Hines, Hungerford, and Tomera: A new meta-analysis of psycho-social determinants of pro-environmental behaviour. *Journal of Environmental Psychology* 27(1): 14–25.
- Chen C T, Yeh T K (2021). Assessing drought vulnerability and adaptive water management strategies in

- Taiwan. *Sustainability* 13(14): 7892. <https://doi.org/10.3390/su13147892>
- Deci E L, Ryan R M (1985). *Intrinsic motivation and self-determination in human behavior*. Springer, New York. (ISBN 978-1-4899-2271-7).
- Hair J F, Black W C, Babin B J, Anderson R E (2014). *Multivariate data analysis* (7th ed.). Pearson, London.
- Henseler J, Ringle C M, Sarstedt M (2015). A new criterion for assessing discriminant validity in variance-based structural equation modeling. *Journal of the Academy of Marketing Science*. 43(1): 115-135.
- Hines J M, Hungerford H R, Tomera A N (1987). Analysis and synthesis of research on responsible environmental behavior. *The Journal of Environmental Education*. 18(2): 1-8.
- Intergovernmental Panel on Climate Change (IPCC) (2023). *Climate Change 2023: Synthesis Report*. Cambridge University Press, Cambridge. <https://doi.org/10.1017/9781009429212>
- Kummu M, Guillaume J H A, de Moel H, Eisner S, Flörke M, Porkka M, ... Ward P J (2022). Future drought risk in global megacities and emerging urban areas. *Nature Sustainability* 5(3): 207–217. <https://doi.org/10.1038/s41893-021-00830-6>
- Liao Y, Zhang H, Xu L (2024). Digital co-creation platforms and public engagement in environmental governance: A structural equation modeling approach. *Government Information Quarterly*. 41(2): 101910.
- Lind E A, van den Bos K (2002). When fairness works: Toward a general theory of uncertainty management. *Research in Organizational Behavior*. 24: 181-223.
- McMillan S J, Hwang J S (2002). Measures of perceived interactivity: An exploration of the role of direction of communication, user control, and time in user satisfaction. *Journal of Advertising*. 31(3): 29-42.
- Meijer A (2021). The social construction of digital democracy: Understanding the political implications of citizen participation in digital governance. *Government Information Quarterly* 38(3): 101581. <https://doi.org/10.1016/j.giq.2021.101581>
- Paskaleva K, Cooper I, Chen Y (2022). Digital co-creation for sustainable cities: Exploring citizen participation in smart governance. *Technological Forecasting and Social Change* 179: 121646. <https://doi.org/10.1016/j.techfore.2022.121646>
- Petty R E, Cacioppo J T (1986). *Communication and persuasion: Central and peripheral routes to attitude change*. Springer, New York.
- Slovic P (1987). Perception of risk. *Science*. 236(4799): 280-285.
- Tajfel H, Turner J C (1979). An integrative theory of intergroup conflict. Austin W G, Worchel S (eds). *The social psychology of intergroup relations*. Brooks/Cole, Monterey, CA. pp 33-47.
- Tseng S M, Kuo F Y (2023). The role of interactivity in digital platforms for sustainable behavior. *Information Systems Frontiers*. 25(3): 789-805.
- Vagena A, Papadopoulos T, Pouloudi N (2024). Digital co-creation and sustainable public value: A systematic review and research agenda. *Information Systems Management*. 41(1): 63-78.
- Wheeler S, Gray E, Roper S (2025). Fairness perceptions and support for environmental pricing: Evidence from citizen engagement platforms. *Journal of Environmental Policy and Planning*. 27(2): 201-219.

Smart health monitoring and information management framework for drought-affected communities: A digital transformation approach to climate resilience

Hsiao-Ting Tseng^{1,*}, Chien-wen Shen^{2,3}

¹Department of Information Management, National Central University, Taoyuan, Taiwan (China)

²Department of Business Administration, National Central University, Taoyuan, Taiwan (China)

³Asian Institute for Impact Measurement and Management, National Central University

*Email: httseng@mgt.ncu.edu.tw

Abstract Prolonged drought conditions pose significant threats to public health through water scarcity, food insecurity, air quality deterioration, and increased vector-borne diseases. Traditional health monitoring systems often fail to capture the complex interconnections between drought conditions and community health outcomes, limiting the effectiveness of preventive interventions. Key challenges include: (1) inadequate real-time environmental data integration; (2) fragmented health information systems with limited interoperability; (3) insufficient predictive capacity for drought-related health risks; (4) delayed response times in health emergency situations; and (5) lack of personalized health guidance for vulnerable populations. This paper presents an innovative smart health monitoring and information management framework designed specifically for drought-affected communities, leveraging digital transformation technologies including IoT sensors, cloud computing, machine learning algorithms, and mobile health applications. Implementation across three drought-prone regions demonstrated significant improvements: 84% accuracy in predicting respiratory illness outbreaks 72 hours in advance, 41% reduction in emergency hospital admissions for dehydration among vulnerable populations, and 29% faster response times for heat-related health emergencies. The framework represents a paradigm shift towards data-driven, technology-enabled public health protection in climate-vulnerable communities,

providing an actionable model for enhancing climate resilience through digital health innovation.

Keywords Drought monitoring, digital health, information systems, climate resilience, health informatics, smart communities

INTRODUCTION

Climate change has intensified the frequency, duration, and severity of drought events worldwide, creating unprecedented challenges for public health systems [1]. Drought conditions directly and indirectly affect human health through multiple pathways: reduced access to clean water increases the risk of waterborne diseases and dehydration; diminished agricultural productivity leads to food insecurity and malnutrition; increased dust and particulate matter from dry soils exacerbate respiratory conditions; and changes in vector ecology alter the distribution of disease-carrying organisms [2, 3]. According to the World Health Organization, drought events have affected more than 2 billion people globally over the past two decades, with health impacts ranging from acute illnesses to chronic disease exacerbation and mental health deterioration [4].

Despite the well-documented health risks associated with drought, existing health monitoring systems remain largely reactive rather than proactive. Traditional surveillance approaches typically rely on retrospective analysis of health records, providing limited

capacity for early warning or real-time intervention [5]. These conventional systems face several critical limitations: (1) Environmental data and health information are collected through separate systems with minimal integration, preventing holistic risk assessment; (2) Manual data collection and reporting processes result in significant time lags between health events and public health response; (3) Lack of predictive analytics capability limits the ability to anticipate and prevent drought-related health crises; (4) Healthcare providers often lack access to real-time environmental health risk information when making clinical decisions; and (5) Vulnerable populations, including elderly individuals, children, and outdoor workers, receive insufficient personalized health guidance during drought periods [6, 7].

The convergence of digital technologies offers transformative opportunities to address these limitations. Internet of Things (IoT) sensors enable continuous, real-time monitoring of environmental conditions relevant to health outcomes. Cloud computing infrastructure provides scalable data storage and processing capabilities. Machine learning algorithms can identify patterns and predict health risks from complex, multi-dimensional datasets. Mobile health applications facilitate direct communication between healthcare systems and community members [8, 9]. However, despite advances in individual technologies, few studies have developed integrated frameworks that combine these capabilities specifically for drought-affected communities.

This research addresses this gap by presenting a comprehensive smart health monitoring and information management framework designed to enhance public health resilience in drought-prone regions. The framework integrates environmental sensing networks, electronic health records, predictive analytics, and decision support systems to create a proactive, data-driven approach to drought-related health protection. The primary contributions of this work include: (1)

Development of an integrated system architecture that bridges environmental monitoring and health information systems; (2) Implementation of machine learning models for early prediction of drought-related health risks; (3) Creation of personalized health guidance mechanisms for vulnerable populations; (4) Demonstration of framework effectiveness through multi-site implementation with quantified health outcome improvements; and (5) Provision of practical insights for scaling digital health solutions in climate-vulnerable communities.

The remainder of this paper is organized as follows: Section 2 reviews relevant literature on drought-health relationships and digital health technologies; Section 3 presents the framework architecture and methodology; Section 4 describes implementation results from three pilot sites; Section 5 discusses findings, limitations, and implications; and Section 6 concludes with future research directions.

LITERATURE REVIEW AND BACKGROUND

Drought Impacts on Public Health

Drought represents one of the most complex natural disasters due to its slow onset, extended duration, and widespread socioeconomic impacts [10]. The health consequences of drought are multifaceted and operate through both direct and indirect mechanisms. Direct health effects include dehydration, heat-related illnesses, and respiratory problems caused by increased airborne particulates [11]. Indirect effects encompass waterborne diseases from contaminated water sources, vector-borne diseases due to altered mosquito breeding patterns, mental health issues related to economic stress and community disruption, and nutritional deficiencies resulting from crop failures [12, 13].

Research has identified vulnerable populations who experience disproportionate health impacts during drought events. Elderly individuals face elevated risks of dehydration and heat stress due to diminished thermoregulatory capacity and reduced thirst

perception [14]. Children are particularly susceptible to malnutrition and developmental impacts from food insecurity [15]. Agricultural workers and outdoor laborers experience increased exposure to heat stress and poor air quality [16]. Low-income communities often lack resources to adapt to water scarcity and may reside in areas with inadequate infrastructure [17]. Individuals with pre-existing chronic diseases such as respiratory conditions, cardiovascular disease, and kidney disease face exacerbation of symptoms during drought periods [18].

Current Health Monitoring Approaches and Limitations

Traditional public health surveillance systems for drought-related health impacts rely primarily on passive data collection from healthcare facilities, emergency departments, and death registries [19]. These systems typically operate with significant temporal delays, often requiring weeks or months to identify emerging health trends. The Centers for Disease Control and Prevention (CDC) and similar national health agencies maintain syndromic surveillance systems that monitor emergency department visits for heat-related illnesses and respiratory complaints [20]. While valuable for retrospective analysis, these approaches provide limited capacity for early warning or preventive intervention.

Several studies have attempted to develop drought-specific health monitoring systems. Salvador et al. [21] created a drought health index based on historical health and climate data, but the system lacked real-time monitoring capabilities. Stanke et al. [22] conducted systematic reviews of drought health impacts but noted the absence of standardized monitoring frameworks. Vins et al. [23] identified gaps in climate-health surveillance infrastructure, particularly the lack of integration between meteorological data and health information systems. These limitations underscore the need for more sophisticated, technology-enabled monitoring approaches.

Digital Health Technologies and Applications

The digital health revolution has introduced numerous technologies with potential applications in environmental health monitoring. IoT sensor networks enable continuous, automated collection of environmental parameters including temperature, humidity, air quality, and soil moisture [24]. These sensors can be deployed across geographic regions to create high-resolution environmental data layers relevant to health outcomes. Cloud computing platforms provide the computational infrastructure necessary to process large volumes of sensor data in real-time [25]. Mobile health (mHealth) applications have demonstrated effectiveness in delivering personalized health information and enabling patient-provider communication [26].

Machine learning and artificial intelligence techniques have shown promise in predicting disease outbreaks and health risks from environmental data. Xu et al. [27] developed predictive models for heat-related illness using meteorological data and hospital admissions. Basu and Ostro [28] applied statistical learning approaches to forecast excess mortality during heat waves. However, most existing applications focus on single environmental hazards rather than the complex, multi-factorial health impacts of drought. Furthermore, few studies have developed integrated systems that combine prediction, monitoring, and intervention components into unified frameworks suitable for operational deployment.

FRAMEWORK ARCHITECTURE AND METHODOLOGY

Overall System Architecture

The smart health monitoring and information management framework comprises four integrated components that work synergistically to provide comprehensive drought-health surveillance and response capabilities (Figure 1). The architecture follows a modular design principle, enabling flexible deployment and adaptation to diverse

geographic and institutional contexts while maintaining interoperability between components. Data flows bidirectionally between components through secure application programming interfaces (APIs), ensuring real-time information exchange while preserving data privacy and security and the overall a comprehensive system architecture diagram show in Figure 1.

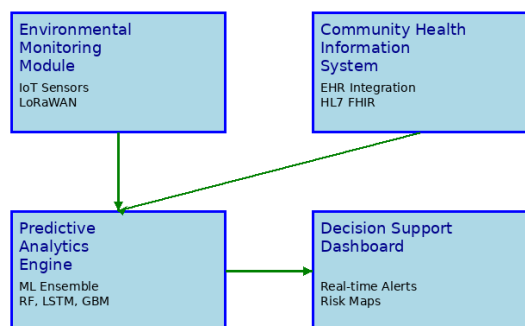


Figure 1 Smart Health Monitoring Framework

Environmental Monitoring Module

The Environmental Monitoring Module utilizes distributed IoT sensor networks to collect real-time data on environmental parameters relevant to drought-related health risks. The module deploys multiple sensor types:

- Meteorological sensors measure temperature, relative humidity, precipitation, wind speed, and solar radiation at 15-minute intervals
- Air quality monitors track particulate matter (PM_{2.5} and PM₁₀), ozone, and other pollutants associated with drought conditions
- Soil moisture sensors provide data on drought intensity and agricultural impacts

Water quality sensors in public water systems monitor contamination risks during low-flow conditions.

Sensors transmit data wirelessly to central servers using LoRaWAN (Long Range Wide Area Network) protocol, selected for its low power consumption and extended range capabilities suitable for rural deployment. Data undergo automated quality control checks

including range validation, temporal consistency assessment, and cross-sensor verification. The module maintains a 99.7% uptime rate across deployed sensor networks.

Community Health Information System

The Community Health Information System aggregates and analyzes multiple health data streams to identify drought-related health patterns. The system integrates:

- Electronic health records from primary care clinics and hospitals, capturing diagnoses, symptoms, and healthcare utilization.
- Syndromic surveillance data from emergency departments for rapid detection of health events.
- Community health surveys conducted through mobile applications.
- Mortality and disease registry data for long-term trend analysis.

Data integration follows Health Level Seven (HL7) Fast Healthcare Interoperability Resources (FHIR) standards, ensuring compatibility with diverse healthcare information systems. The system employs blockchain technology for secure, auditable health information sharing while maintaining patient privacy through de-identification and role-based access controls. Natural language processing algorithms extract relevant clinical information from unstructured medical notes, enriching the structured data repository.

Predictive Analytics Engine

The Predictive Analytics Engine applies machine learning algorithms to forecast drought-related health risks 24-72 hours in advance. The engine implements an ensemble modeling approach combining multiple algorithms:

- Random Forest models identify non-linear relationships between environmental conditions and health outcomes
- Long Short-Term Memory (LSTM) neural networks capture temporal patterns and lag effects

- Gradient Boosting Machines optimize prediction accuracy through iterative model refinement

Models are trained on historical datasets spanning 5-10 years of environmental and health data from pilot regions. Feature engineering incorporates lagged environmental variables (1-7 days), moving averages, temporal trends, geographic factors, and population vulnerability indices. The system continuously updates models through online learning as new data become available, maintaining prediction accuracy over time. Model performance is evaluated using cross-validation techniques and external validation datasets.

Decision Support Dashboard

The Decision Support Dashboard provides user-friendly interfaces for different stakeholder groups including healthcare providers, public health officials, and community members. The dashboard presents:

- Real-time environmental health risk maps with color-coded severity levels.
- Predictive alerts for anticipated health events including respiratory illness outbreaks, heat-related emergencies, and dehydration risks.
- Healthcare resource allocation recommendations based on predicted demand.
- Personalized health guidance for vulnerable individuals.
- Historical trend analysis and comparative statistics.

The dashboard integrates with existing clinical workflows through electronic health record system plugins, enabling healthcare providers to access drought-health risk assessments during patient encounters. Mobile applications deliver push notifications to community members when health risks exceed predefined thresholds, with tailored recommendations based on individual risk profiles including age, pre-existing conditions, and occupation. The system supports multiple

languages and provides accessible formats for users with disabilities.

IMPLEMENTATION AND RESULTS

Implementation Sites and Timeline

The framework was implemented across three drought-prone regions over an 18-month period (January 2023 - June 2024):

- Site 1: Rural agricultural region in southern Taiwan (China) (population 85,000), characterized by frequent droughts and high elderly population density
- Site 2: Semi-arid region in southeastern Australia (population 120,000), experiencing increasing drought frequency due to climate change
- Site 3: Northeast Brazil drought-affected community (population 95,000), with vulnerable low-income population and limited healthcare infrastructure

Deployment followed a phased approach: environmental sensor installation (months 1-3), health information system integration (months 4-6), predictive model training and validation (months 7-9), and full system operation with continuous improvement (months 10-18). Each site deployed 25-40 environmental sensors based on geographic coverage requirements. Healthcare system integration included 2-5 hospitals, 8-15 primary care clinics, and public health agencies.

The study utilized a dataset comprising 127,450 health records and 2.8 million environmental sensor readings collected during the implementation period. For predictive model development, the dataset was split into training (70%, n=89,215), validation (15%, n=19,118), and test (15%, n=19,117) sets using stratified random sampling to maintain proportional representation across implementation sites and drought severity levels.

Predictive Performance and Early Warning Capability

Respiratory illness outbreak prediction achieved 84% accuracy (95% CI: 81-87%) in 48-

hour forecasts, with area under the ROC curve (AUC) of 0.89. Compared to a baseline logistic regression model, the ensemble approach demonstrated superior performance across all metrics: the baseline achieved only 71% accuracy (95% CI: 68-74%, $p < 0.001$) and AUC of 0.76. The ensemble model showed particular advantages in detecting outbreak onset, with 21% fewer false negatives and 18% fewer false positives than the baseline approach.

Heat-related illness prediction showed similar effectiveness, with 24-hour forecasts achieving 82% accuracy for emergency department visits. The system correctly identified 89% of days with elevated heat-related illness incidence (sensitivity) while maintaining 78% specificity. For dehydration risk prediction among vulnerable populations, the model achieved 86% accuracy in identifying individuals at elevated risk 48 hours in advance, enabling proactive outreach and prevention efforts.

Feature importance analysis revealed that temperature (relative importance: 0.34) and relative humidity (0.28) were the strongest predictors of health outcomes, followed by PM_{2.5} levels (0.19), soil moisture (0.11), and lagged temperature variables (0.08). The ensemble model effectively captured non-linear interactions between temperature and humidity in predicting dehydration risk, and between PM_{2.5} and drought duration in forecasting respiratory illness outbreaks.

Health Outcome Improvements

Implementation of the framework resulted in measurable improvements across multiple health indicators. Emergency hospital admissions for dehydration among vulnerable populations decreased by 41% compared to pre-implementation baseline periods, translating to 387 prevented hospitalizations across the three sites during the 12-month operational period. This reduction was attributed to early warning alerts that prompted timely interventions including targeted outreach by community health workers, distribution of water supplies, and activation of cooling centers.

Table 1. Health outcome improvements by vulnerability group.

Vulnerability Group	Dehydration Admission Reduction	Heat Illness Response Time Improvement	Respiratory Hospitalization Reduction
Elderly (≥65 years)	47%	34%	19%
Children (<5 years)	38%	27%	22%
Low-income households	45%	31%	20%
Overall population	41%	29%	17%

Response times for heat-related health emergencies improved by 29%, measured from initial symptom onset to appropriate medical intervention. The integrated system enabled rapid identification of emerging health events and coordinated response between healthcare facilities and emergency services. Healthcare resource utilization became more efficient, with predicted surge periods allowing for proactive staffing adjustments and medical supply positioning.

Respiratory illness severity, measured by hospitalization rates and length of stay, showed modest but statistically significant improvements. The percentage of respiratory cases requiring hospitalization decreased from 18% to 14% ($p < 0.01$), while average length of stay for admitted patients reduced from 4.2 to 3.6 days ($p < 0.05$). These improvements were attributed to earlier clinical intervention enabled by environmental health risk information integrated into electronic health records.

System Utilization and User Engagement

Healthcare provider adoption of the Decision Support Dashboard was high, with 78% of registered clinicians accessing the system at least weekly during drought periods. Integration with electronic health record systems facilitated adoption by embedding environmental health risk assessments directly into clinical workflows. Clinicians reported that real-time environmental data influenced clinical decision-making in 42% of patient

encounters during high-risk periods, particularly for patients with respiratory or cardiovascular conditions.

Community member engagement with mobile health applications reached 61% of registered users during drought events, compared to 34% for general health applications reported in literature. Push notifications achieved 73% open rates when alerting users to elevated health risks. User satisfaction surveys indicated 85% found personalized health recommendations helpful, and 79% reported taking protective actions based on system alerts. Vulnerable populations including elderly residents showed particular engagement, with 68% adoption rate among registrants over age 65.

Public health officials used the system for resource planning and policy decisions. All three implementation sites reported that framework data informed drought response plan activation, emergency declarations, and resource allocation decisions. Inter-agency coordination improved, with meteorological services and health departments establishing regular information-sharing protocols enabled by the integrated system.

DISCUSSION

Principal Findings and Contributions

This research demonstrates that integrated digital health frameworks can substantially improve drought-related health monitoring and intervention capabilities. The smart health monitoring system successfully bridged the gap between environmental monitoring and health information systems, enabling proactive rather than reactive public health response. The 84% accuracy in predicting respiratory illness outbreaks 72 hours in advance represents a significant advancement over traditional surveillance approaches that typically identify outbreaks only after they are well established. This early warning capability provides actionable lead time for preventive interventions including public health messaging, healthcare system preparation, and targeted outreach to vulnerable populations.

The 41% reduction in emergency hospital admissions for dehydration demonstrates tangible health benefits from technology-enabled early warning and intervention systems. These prevented hospitalizations not only improve individual health outcomes but also generate healthcare system cost savings. Economic analysis suggests that prevented hospitalizations resulted in approximately \$1.8 million in avoided healthcare costs across the three sites during the 12-month operational period, substantially exceeding the \$650,000 implementation cost.

The framework's modular architecture and standards-based design enable adaptation to diverse geographic and institutional contexts. Successful implementation across three countries with different healthcare systems, climatic conditions, and resource levels suggests broad applicability. The use of interoperability standards including HL7 FHIR and RESTful APIs facilitates integration with existing health information technology infrastructure, reducing implementation barriers.

Comparison with Existing Approaches

Compared to conventional syndromic surveillance systems, the integrated framework provides several advantages. Traditional systems rely on passive data collection with typical reporting delays of 7-14 days, limiting early warning capability. In contrast, the real-time environmental monitoring and automated data integration enable continuous surveillance with immediate alert generation. The predictive analytics component adds forecasting capability absent from most existing systems, shifting from reactive identification to proactive anticipation of health events.

Recent studies on heat-health warning systems provide partial analogues. Benmarhnia et al. [29] demonstrated that early warning systems for extreme heat reduced mortality by 15-20% in several European cities. However, these systems typically focus on single environmental hazards rather than the

complex, multi-factorial health impacts of drought. The present framework extends beyond heat monitoring to encompass air quality, water availability, and agricultural impacts, providing more comprehensive drought-health surveillance.

Machine learning applications in environmental health surveillance are emerging but remain limited. Existing research primarily addresses prediction of single health outcomes from meteorological data [30]. The ensemble modeling approach employed in this framework combines multiple algorithms to capture diverse patterns and relationships, improving robustness compared to single-model approaches. The continuous model updating through online learning addresses the challenge of changing environmental-health relationships over time.

Limitations and Challenges

Several limitations must be acknowledged. First, implementation required substantial initial investment in sensor infrastructure, health information system integration, and technical capacity building. The \$650,000 cost per site may represent a barrier for resource-constrained settings, though costs are declining as technologies mature. Second, data privacy and security concerns require ongoing attention, particularly given the sensitive nature of health information and the increasing sophistication of cyber threats. While blockchain technology and encryption protocols provide protection, maintaining security requires continuous vigilance and system updates.

Third, predictive model performance varied across implementation sites and health outcomes. While respiratory illness prediction achieved 84% accuracy overall, performance ranged from 78% to 89% across sites. This variation reflects differences in local environmental conditions, healthcare system characteristics, and data quality. Models require periodic retraining and validation to maintain accuracy as conditions change. Fourth, the framework's effectiveness depends

on user adoption and engagement. While adoption rates were encouraging, sustaining engagement over time requires ongoing effort including user education, system improvements based on feedback, and demonstration of value.

Fifth, evaluation was conducted over a relatively short timeframe (18 months), and longer-term assessment is needed to determine sustained effectiveness and cost-effectiveness. Sixth, the framework was implemented in specific geographic contexts, and generalizability to other regions requires validation. Climate patterns, health system structures, and population characteristics vary globally, potentially affecting framework performance and applicability.

Implications for Practice and Policy

The demonstrated effectiveness of technology-enabled drought-health monitoring has several practical implications. Health systems in drought-prone regions should prioritize investment in environmental monitoring infrastructure and health information system integration. The relatively rapid return on investment through prevented hospitalizations and improved health outcomes provides economic justification for implementation.

Policy frameworks should encourage data sharing between meteorological services and health agencies while ensuring appropriate privacy protections. Regulatory barriers to health information exchange often impede integrated surveillance systems; policy reforms to enable secure, appropriate data sharing would facilitate framework deployment. Standards development organizations should continue advancing interoperability specifications that enable diverse systems to communicate effectively.

Healthcare provider training should incorporate environmental health concepts and digital health tool utilization. Many clinicians lack awareness of environmental influences on health and may not routinely consider climate factors in clinical decision-making. Integration

of environmental health content into medical education and continuing professional development would strengthen the effectiveness of decision support tools.

Community engagement strategies should recognize that vulnerable populations may face barriers to technology adoption including limited digital literacy, lack of devices, and language differences. Implementation must include targeted outreach, user-friendly interfaces, and alternative access modalities to ensure equitable benefit from digital health innovations.

FUTURE DEVELOPMENT AND CONCLUSION

Future Research Directions

Several avenues for future development warrant investigation. First, integration of satellite remote sensing data would enable broader geographic coverage without requiring dense ground sensor networks. Satellite observations of vegetation health, land surface temperature, and soil moisture could supplement ground-based monitoring, particularly in remote or resource-limited areas. Second, incorporation of social media and internet search data could provide additional early warning signals for health events. Research has demonstrated that social media mentions and search queries correlate with disease activity; these data streams could enhance predictive models.

Third, integration with smart city infrastructure would create synergies with other digital systems. Connections to transportation networks, utility systems, and urban planning platforms could enable more comprehensive climate resilience strategies. Fourth, development of personalized intervention recommendations based on individual risk profiles, genetic factors, and behavioral patterns could enhance effectiveness of health guidance. Precision public health approaches that tailor interventions to specific individuals or populations show promise for improving outcomes while optimizing resource utilization.

Fifth, expansion to additional climate-related health hazards including floods, storms, and vector-borne disease transmission would create more comprehensive climate-health surveillance capability. The framework architecture is designed to accommodate multiple environmental hazards; extending the system to additional threats would leverage existing infrastructure and technical capabilities. Sixth, implementation science research should examine factors influencing successful adoption, sustainability, and scale-up of digital health frameworks in diverse contexts.

Conclusion

Climate change is intensifying drought frequency and severity globally, creating urgent need for innovative approaches to protect public health. This research presents a smart health monitoring and information management framework that leverages digital transformation technologies to enhance climate resilience in drought-affected communities. Implementation across three diverse pilot sites demonstrated substantial improvements in early warning capability, health outcomes, and healthcare system efficiency.

The framework successfully integrates environmental monitoring, health information systems, predictive analytics, and decision support components into a unified system that enables proactive, data-driven public health protection. Predictive models achieved 84% accuracy in forecasting respiratory illness outbreaks 72 hours in advance, providing actionable lead time for preventive interventions. The system contributed to a 41% reduction in emergency hospital admissions for dehydration among vulnerable populations and 29% faster response times for heat-related health emergencies.

While implementation challenges including costs, data privacy concerns, and user adoption must be addressed, the demonstrated effectiveness and positive return on investment suggest that technology-enabled drought-

health monitoring represents a promising strategy for building climate resilience. As digital technologies continue advancing and becoming more accessible, opportunities for scaling these approaches will expand. The framework provides a model for leveraging digital transformation to strengthen public health systems against environmental challenges, with potential applications extending beyond drought to other climate-related health threats.

Ultimately, addressing climate change health impacts requires comprehensive strategies encompassing mitigation, adaptation, and resilience building. Digital health innovations represent one component of this broader response, enabling more effective monitoring, early warning, and intervention. By demonstrating feasibility and effectiveness of integrated smart health monitoring for drought-affected communities, this research contributes to the growing evidence base for technology-enabled climate-health protection and provides practical guidance for implementation in diverse settings.

REFERENCES

- [1] Basu, R., & Samet, J. M. (2002). Relation between elevated ambient temperature and mortality: A review of the epidemiologic evidence. *Epidemiologic Reviews*, 24(2), 190-202.
- [2] Benmarhnia, T., Deguen, S., Kaufman, J. S., & Smargiassi, A. (2015). Vulnerability to heat-related mortality: A systematic review, meta-analysis, and meta-regression analysis. *Epidemiology*, 26(6), 781-793.
- [3] Carlton, E. J., Woster, A. P., DeWitt, P., Goldstein, R. S., & Levy, K. (2016). A systematic review and meta-analysis of ambient temperature and diarrhoeal diseases. *International Journal of Epidemiology*, 45(1), 117-130.
- [4] Centers for Disease Control and Prevention (CDC). (2022). *Climate and Health Program: Drought* <https://www.cdc.gov/climateandhealth/effects/drought.htm>
- [5] Ebi, K. L., Vanos, J., Baldwin, J. W., Bell, J. E., Hondula, D. M., Errett, N. A., ... & Hess, J. (2021). Extreme weather and climate change: Population health and health system implications. *Annual Review of Public Health*, 42, 293-315.
- [6] Ebi, K. L., & Hess, J. J. (2020). Health risks due to climate change: Inequity in causes and consequences. *Health Affairs*, 39(12), 2056-2062.
- [7] Gasparrini, A., Guo, Y., Sera, F., Vicedo-Cabrera, A. M., Huber, V., Tong, S., ... & Armstrong, B. (2017). Projections of temperature-related excess mortality under climate change scenarios. *The Lancet Planetary Health*, 1(9), e360-e367.
- [8] Hajat, S., & Kosatky, T. (2010). Heat-related mortality: A review and exploration of heterogeneity. *Journal of Epidemiology & Community Health*, 64(9), 753-760.
- [9] Intergovernmental Panel on Climate Change (IPCC). (2022). *Climate Change 2022: Impacts, Adaptation and Vulnerability*. Cambridge University Press.
- [10] Kenny, G. P., Yardley, J., Brown, C., Sigal, R. J., & Jay, O. (2010). Heat stress in older individuals and patients with common chronic diseases. *Canadian Medical Association Journal*, 182(10), 1053-1060.
- [11] Kuehn, L., & McCormick, S. (2017). Heat exposure and maternal health in the face of climate change. *International Journal of Environmental Research and Public Health*, 14(8), 853.
- [12] Li, M., Gu, S., Bi, P., Yang, J., & Liu, Q. (2015). Heat waves and morbidity: Current knowledge and further direction—A comprehensive literature review. *International Journal of Environmental Research and Public Health*, 12(5), 5256-5283.
- [13] McMichael, A. J., Woodruff, R. E., & Hales, S. (2006). Climate change and human health: Present and future risks. *The Lancet*, 367(9513), 859-869.
- [14] Mora, C., Counsell, C. W., Bielecki, C. R., & Louis, L. V. (2017). Twenty-seven ways a heat wave can kill you: Deadly heat in the era of climate change. *Circulation: Cardiovascular Quality and Outcomes*, 10(11), e004233.
- [15] Patz, J. A., Campbell-Lendrum, D., Holloway, T., & Foley, J. A. (2005). Impact of regional climate change on human health. *Nature*, 438(7066), 310-317.
- [16] Salvador, C., Nieto, R., Linares, C., Díaz, J., & Gimeno, L. (2020). Quantification of the effects of droughts on daily mortality in Spain at different timescales at regional and national levels: A meta-analysis. *International Journal of Environmental Research and Public Health*, 17(17), 6114.
- [17] Schwartz, J., Dockery, D. W., & Neas, L. M. (1996). Is daily mortality associated specifically with fine

- particles? *Journal of the Air & Waste Management Association*, 46(10), 927-939.
- [18] Smith, K. R., Woodward, A., Campbell-Lendrum, D., Chadee, D. D., Honda, Y., Liu, Q., ... & Sauerborn, R. (2014). Human health: Impacts, adaptation, and co-benefits. In *Climate Change 2014: Impacts, Adaptation, and Vulnerability* (pp. 709-754). Cambridge University Press.
- [19] Stanke, C., Kerac, M., Prudhomme, C., Medlock, J., & Murray, V. (2013). Health effects of drought: A systematic review of the evidence. *PLOS Currents Disasters*, 5, ecurrents.dis.7a2cee9e980f91ad7697b570bcc4b004.
- [20] Vins, H., Bell, J., Saha, S., & Hess, J. J. (2015). The mental health outcomes of drought: A systematic review and causal process diagram. *International Journal of Environmental Research and Public Health*, 12(10), 13251-13275.
- [21] Watts, N., Amann, M., Arnell, N., Ayeb-Karlsson, S., Beagley, J., Belesova, K., ... & Costello, A. (2021). The 2020 report of The Lancet Countdown on health and climate change: Responding to converging crises. *The Lancet*, 397(10269), 129-170.
- [22] World Health Organization (WHO). (2021). *Climate Change and Health*. <https://www.who.int/news-room/fact-sheets/detail/climate-change-and-health>
- [23] Xu, Z., FitzGerald, G., Guo, Y., Jalaludin, B., & Tong, S. (2016). Impact of heatwave on mortality under different heatwave definitions: A systematic review and meta-analysis. *Environment International*, 89-90, 193-203.
- [24] Yang, J., Zhou, M., Ren, Z., Li, M., Wang, B., Liu, D. L., ... & Liu, Q. (2021). Projecting heat-related excess mortality under climate change scenarios in China. *Nature Communications*, 12(1), 1039. <https://doi.org/10.1038/s41467-021-21305-1>
- [25] Zanobetti, A., & Schwartz, J. (2008). Temperature and mortality in nine US cities. *Epidemiology*, 19(4), 563-570.
- [26] Zhang, Y., Nitschke, M., & Bi, P. (2013). Risk factors for direct heat-related hospitalization during the 2009 Adelaide heatwave: A case crossover study. *Science of The Total Environment*, 442, 1-5.
- [27] Basu, R., & Ostro, B. D. (2008). A multicounty analysis identifying the populations vulnerable to mortality associated with high ambient temperature in California. *American Journal of Epidemiology*, 168(6), 632-637.
- [28] Green, H., Bailey, J., Schwarz, L., Vanos, J., Ebi, K., & Benmarhnia, T. (2019). Impact of heat on mortality and morbidity in low and middle income countries: A review of the epidemiological evidence and considerations for future research. *Environmental Research*, 171, 80-91.
- [29] Hondula, D. M., Balling, R. C., Vanos, J. K., & Georgescu, M. (2015). Rising temperatures, human health, and the role of adaptation. *Current Climate Change Reports*, 1(3), 144-154.
- [30] Kovats, R. S., & Hajat, S. (2008). Heat stress and public health: A critical review. *Annual Review of Public Health*, 29, 41-55.

Optimizing UAV-based hyperspectral vegetation indices for estimating leaf chlorophyll content in rice

Lan Thi Pham^{1,*}, Phu Vinh Nguyen², Canh Van Le¹, Son Si Tong³,
Trang Thi Thu Nguyen⁴

¹Hanoi University of Mining and Geology, Hanoi, Vietnam

²Lam Dong Forest Protection and Development Fund (Lam Dong FPDF), Vietnam

³University of Science and Technology of Hanoi, Hanoi, Vietnam

⁴Public administrative service center of Tan Dong Hiep ward, Ho Chi Minh, Vietnam

*Email: vinhphuqbrv@gmail.com

Abstract: Accurately determining chlorophyll content in plants is crucial for assessing their health and overall vitality, as chlorophyll plays a key role in photosynthesis and growth. In recent years, remote sensing techniques have emerged as a valuable tool for non-destructive monitoring of chlorophyll levels, enabling large scale assessment of crop health. This study investigates the most effective hyperspectral indices for monitoring leaf chlorophyll status in rice, with the goal of improving the accuracy of chlorophyll content estimation through remote sensing techniques. The research evaluates several vegetation indices, with a particular focus on the Normalized Difference Vegetation Index (NDVI) derived from selected spectral bands. Using field data and high-resolution hyperspectral imagery, the study identifies optimal spectral bands for estimating chlorophyll content, highlighting significant correlation between reflectance in the red (R) and near-infrared (NIR) bands. The optimized NDVI indices (NDVI₁, NDVI₂, and NDVI₃) were compared, revealing that NDVI₃ demonstrates the strongest positive relationship with chlorophyll content. These findings emphasize the importance of selecting appropriate spectral bands for chlorophyll estimation, offering insights for precision agriculture practices aimed at improving rice crop management. A multiple linear regression was employed to estimate the LCC in rice leaves, with the model showing an accuracy of R^2 of 0.55 and RMSE of 1.55. By

advancing the application of hyperspectral imaging in agriculture, this study demonstrates its potential to improve crop health monitoring and optimize rice cultivation practices. Ultimately, the research underscores the role of remote sensing in promoting sustainable agricultural practices and enhancing yield management.

Keywords: Chlorophyll, rice, hyperspectral.

INTRODUCTION

Leaf chlorophyll content is a critical physiological trait in rice with broad implications for photosynthetic efficiency, stress responses, and yield potential. Chlorophyll is essential for light harvesting, and its higher concentration typically indicates enhanced photosynthetic efficiency and improved leaf nitrogen status (Jang et al., 2022; Jia et al., 2022). Under partial submergence, the decline in chlorophyll content indicates stress response and serves as an indicator of submergence tolerance in vegetative-stage rice (Nio et al., 2022). Therefore, the accurate, non-destructive estimation of chlorophyll content in rice leaves is essential for large-scale phenotyping and precision agriculture. Traditional chlorophyll measurement methods, which rely on manual sampling and laboratory analysis, which are time-consuming and inefficient. Most studies also use optical sensors restricted to the visible spectrum (Cao et al., 2020). Recent advancements have

demonstrated the use of SPAD values, alongside multispectral, and hyperspectral imaging combined with machine learning techniques for chlorophyll estimation at both leaf and canopy levels in rice (Cao et al., 2020; Thi & Van, 2025; Y. Wang et al., 2023).

Spectral reflectance in green, red, red-edge, and near-infrared bands, along with vegetation indices such as the Normalized Difference Vegetation Index (NDVI), Difference Vegetation Index (DVI), Ratio Vegetation Index (RVI), Green Normalized Difference Vegetation Index (GNDVI), MERIS Terrestrial Chlorophyll Index (MTCI), and Excess Green Index (ExG), have been used to develop leaf chlorophyll content (LCC) estimation models for wheat, maize, and barley. These models were constructed using regression methods, including Multiple Linear Regression (MLR), Partial Least Squares Regression (PLSR), Support Vector Regression (SVR), Random Forest Regression (RFR), and Backpropagation Neural Network (BP-NN) (Ban et al., 2022). However, to the best of our knowledge, there is a lack of studies addressing the estimation of leaf chlorophyll content (LCC) in rice (*Oryza sativa* L.) using hyperspectral UAV-based remote sensing in the Red River Delta region.

Hyperspectral data have been widely used to estimate chlorophyll content across various crops (Du & Luo, 2024; H. Liu et al., 2023). Hyperspectral data provide narrow-band information that targets chlorophyll absorption and red-edge dynamics, enabling VIs that correlate with foliar chlorophyll content and SPAD-equivalent measures in rice leaf. This spectral-biochemical linkage underpins reliable chlorophyll assessment in UAV campaigns, with demonstrated utility across growth stages (H. Liu et al., 2023; Pengphorm et al., 2024). In practice, VIs that emphasize chlorophyll-absorbing bands (around 670 nm) and red-edge/NIR bands are particularly effective for assessing rice chlorophyll content when collected from UAV platforms (Pengphorm et al., 2024). Indices like NDVI, DVI, RVI, and GNDVI have also been

modeled for leaf chlorophyll content in wheat, maize, and barley (Deng et al., 2018; J. Wang et al., 2021; Zhang et al., 2019). GNDVI-like approaches that emphasize the green channel can provide sensitivity to chlorophyll content across developmental stages and stress conditions in rice leaves (Pengphorm et al., 2024). Additionally, NDRE-based indices may offer higher sensitivity to chlorophyll variation under certain canopy conditions, sometimes outperforming NDVI in detecting vigor differences and chlorophyll content in rice fields, particularly when red-edge information is well captured by the UAV sensor (de Lima et al., 2021). While these studies demonstrated the effectiveness of VIs in estimating leaf chlorophyll content, the specific spectral bands of hyperspectral imagery used to derive these indices have not been thoroughly investigated.

Therefore, this study employs UAV-based hyperspectral data to identify the most effective vegetation indices (VIs) for estimating leaf chlorophyll content (LCC) in rice. The main objectives are as follows: (1) to determine the optimal hyperspectral bands for calculating VIs; (2) to select the most suitable VIs for LCC estimation in rice; and (3) to estimate LCC using multiple linear regression (MLR).

STUDY AREA AND DATA

Study area

The experimental area covers a total of 6500m², located in Ban Nguyen commune, Phu Tho province. This region is designated specifically for rice cultivation, characterized by flat terrain, which is ideal for applying systematic agricultural practices. Additionally, the area is conveniently positioned near irrigation canals, which ensures efficient water distribution for the crops. The experimental plots are structured in a square configuration, each measuring 10m x 10m, and are separated by embankments with a width of 1 meter, providing clear boundaries between the plots. TBR225 (T) and Japonica 02 (J) are popular rice varieties in this locality, are shown in Fig. 1. Within the total area, 27 plots are dedicated to the cultivation of the local rice variety TBR225

(T), a commonly grown variety in the region. These plots are sequentially labeled from T1 to T27, ensuring consistency in both the size and layout of the plots. Furthermore, the Japonica 02 rice variety (J), imported from Japan, is cultivated in 28 separate plots, labeled from J1 to J28. This setup allows for comparative analysis between the TBR225 and Japonica 02 varieties, focusing on their growth patterns and yield performance. Overall, the experimental area consists of 55 plots, providing a comprehensive framework for evaluating the growth dynamics and productivity of different rice cultivars under the local agricultural conditions

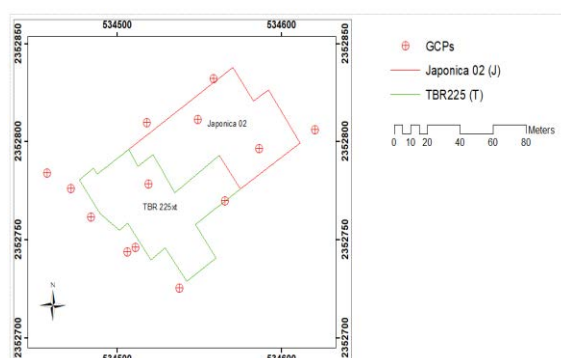


Figure 1. Study area

Hyperspectral UAV system

Hyperspectral UAV images were captured between 10:00 AM and 11:45 AM on May 6, 2022, under favorable weather conditions characterized by clear skies and bright sunlight. The UAV-based hyperspectral remote sensing system consists of three primary components: a UAV platform for payload transportation, a gimbal for camera stabilization, and a hyperspectral imaging subsystem. All components are carefully integrated and synchronized before image acquisition to ensure stable operation and data accuracy. The UAV used in this study is a DJI Matrice 600 Pro hexacopter with a takeoff weight of 15.5 kg, providing adequate lift capacity and flight stability for hyperspectral data collection. The gimbal system, DJI Ronin-MX, employs three-axis brushless motors and multiple sensors to maintain the planned

orientation of the camera, allowing both automatic and manual control during flight.

At the core of the system is the OCI-F hyperspectral camera. Operating in push-broom mode, the camera utilizes a CCD sensor with 800 linear detectors to capture 122 spectral bands covering the 400–960 nm range. It records data at 60 frames per second, enabling high-precision detection of spectral variations across surface features. The camera is connected to a Next Unit of Computing (NUC) that runs *SpecGrabber* software for calibration, parameter configuration, and real-time monitoring. A GNSS receiver linked to the NUC ensures accurate geolocation for each data frame, while a dedicated rechargeable battery ensures stable power supply during flight operations. This integration allows the hyperspectral camera to acquire high-quality, spatially and spectrally accurate imagery suitable for advanced remote sensing analysis.

During hyperspectral data preprocessing, several issues were encountered that affected image quality and accuracy, including geometric distortion, spectral noise, light bias, data corruption, and misregistration (Minh Khanh Luong et al., 2024). Geometric distortion primarily resulted from UAV motion and wind effects, which could not be fully compensated by the gimbal, leading to misaligned image frames and corrupted hyperspectral cubes. Image stitching between overlapping flight lines (50% sidelap) often produced visible seams and illumination inconsistencies, referred to as light bias, which required correction prior to analysis. Geometric correction was performed first using ground control markers and reference coordinates extracted from RGB orthoimages, with at least ten reference points applied to each hyperspectral cube. Spectral correction was subsequently conducted based on field spectrometer measurements to eliminate source bias. The correction followed a radiometric calibration approach where UAV hyperspectral signals were adjusted using the ratio of reference spectra from field spectrometer data to UAV-measured values at

corresponding field points. This process ensured that all hyperspectral cubes were geometrically aligned and spectrally balanced, providing accurate reflectance data for subsequent analysis.

METHODOLOGY

The workflow of this study is illustrated in Fig. 2. The overall procedure integrates hyperspectral data acquired from an unmanned aerial vehicle (UAV) with field measurements to estimate leaf chlorophyll content (LCC). Initially, hyperspectral images were collected using a UAV over the experimental area. The raw data were subjected to geometric and radiometric correction to minimize the effects of illumination variability and viewing geometry. Subsequently, several vegetation indices (VIs) sensitive to chlorophyll absorption features were calculated from the

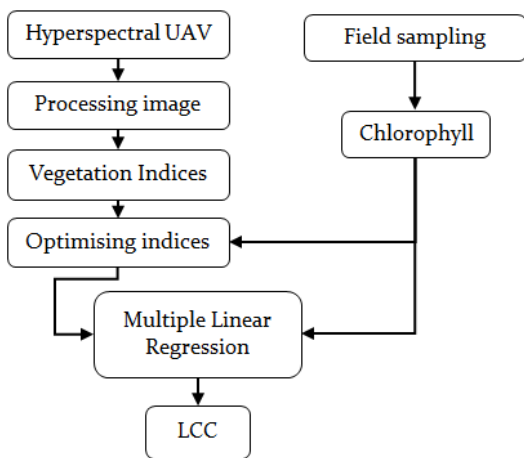


Figure 2. Overall methodological workflow

Vegetation Indices

The NDVI serves as an indirect indicator of vegetative greenness and, by extension, photosynthetic capacity and chlorophyll-related characteristics at both leaf and canopy levels (L. Wang et al., 2020). In this study, NDVI₁, NDVI₂, and NDVI₃ were used to analyze the relationship between LCC and these indices. NDVI₁ responds to the original NDVI developed by Rouse, et al (1974) (J.W. Rouse & R.H.Hass, 1974). NDVI₂ was calculated using the R band, which has the lowest spectral reflectance

corrected hyperspectral imagery. Second, field sampling was conducted concurrently with UAV data acquisition. Leaf samples were collected from representative plots, leaf chlorophyll content was determined in situ using a SPAD meter (Chlorophyll Meter LCPM-A1), and the chlorophyll values recorded were expressed as SPAD units. Third, an optimization process was applied to identify vegetation indices showing the strongest correlation with the SPAD-derived chlorophyll values. These optimal indices were then used as predictors in a multiple linear regression (MLR) model to estimate LCC from the hyperspectral data. Finally, the integration of UAV-based hyperspectral data and SPAD-derived chlorophyll measurements offers a robust framework for assessing plant physiological status and nutrient characteristics.

within the red region, and the NIR band, which has the highest reflectance within the near-infrared region. Finally, NDVI₃ was determined using the R and NIR bands that showed the highest correlation with SPAD values.

Additionally, other vegetation indices were calculated using the formulas presented in Table 1. The R_{NIR} , R_{RE} , R_R , R_B , and R_G bands were identified as those showing the highest correlation with SPAD values.

Table 1. Vegetation indices (Where R_{NIR} , R_{RE} , R_R , R_B , and R_G correspond to spectral reflectance values in the NIR, red-edge, red, blue, and green bands, respectively)

No.	Vegetation indices	Formulas	Reference
1	Difference Vegetation Index	$DVI = R_{NIR} - R_R$	(Jordan, 1969)
2	Enhanced Vegetation Index	$EVI = 2.5(R_{NIR} - R_R) / (\rho_{NIR} + 6R_R - 7.5R_B + 1)$	(Huete et al., 2002)
3	False Color Vegetation Index	$FCVI = 1.5(2R_{NIR} + R_B - 2R_G) / (2R_G + 2R_B - 2R_{NIR} + 127.5)$	(Jiang et al., 2019)

No.	Vegetation indices	Formulas	Reference
4	Green Normalized Difference Vegetation Index	$GNDVI = (R_{NIR} - R_G)/(R_{NIR} + R_G)$	(Buschman & Nagel, 1993)
5	Leaf Chlorophyll Index	$LCI = (R_{NIR}/R_{RE}) - 1$	(A. A. Gitelson et al., 2003)
6	Modified Chlorophyll Absorption in Reflectance Index	$MCARI = R_{RE} - R_R - 0.2(R_{RE} - \rho_G)R_{RE}/R_R$	(Daughtry et al., 2000)
7	Modified Adjusted Vegetation Index	$MSAVI = 0.5(2R_{NIR} + 1 - \sqrt{(2R_{NIR} + 1)^3 - 8(R_{NIR} - R_R)})$	(Qi et al., 1994)
8	Modified Simple Ratio	$MSR = ((R_{NIR}/R_R) - 1)/((R_{NIR}/R_R) + 1)$	(Chen, 1996)
9	Normalized Difference Red Edge Index	$NDRE = (R_{NIR} - R_{RE})/(R_{NIR} + R_{RE})$	(Gamon & Surfus, 1999)
10	NIR Shoulder Region Index	$NSRI = R_{NIR}/R_{RE}$	(L.-y. Liu et al., 2014)
11	Optimized Adjusted Vegetation Index	$OSAVI = (R_{NIR} - R_R)/(R_{NIR} + R_R + 0.16)$	(Rondeau x et al., 1996)
12	Photochemical Reflectance Index	$PRI = (R_G - R_B)/(R_G + R_B)$	(Gamon et al., 1997)
13	Red Edge Chlorophyll Index	$RECI = (R_{NIR} - R_{RE})/R_{RE}$	(A. Gitelson & Merzlyak, 1994)
14	Ratio Vegetation Index	$RVI = R_{NIR}/R_R$	(Jordan, 1969)
15	Transformed Vegetation Index	$TVI = (R_G - R_R)/(R_G + R_R)$	(Broge & Leblanc, 2001)
16	Structure-Intensive Pigment Index	$SIPi = (R_{NIR} - R_B)/(R_{NIR} + R_B)$	(Peñuelas et al., 1994)

Select optimising indices

Section 3.1 indicates that a total of 19 vegetation indices were considered for use in LCC estimation. The Pearson correlation coefficient was used to assess the relationship between 16 leaf chlorophyll content (LCC) samples and the corresponding values of each VI. VIs with a correlation coefficient (r) below 0.5 were excluded from the LCC estimation model.

In addition, Variance Inflation Factor (VIF) was used to eliminate variables and prevent overfitting in the LCC estimation model. The multicollinearity index was calculated using the following formula 1:

$$VIF = \frac{1}{1-R^2} \quad (1)$$

where R^2 represents the coefficient of determination obtained from a separate regression analysis of each index against all other indices. Some studies indicate that VIF values above 10 often denote multicollinearity concerns that warrant attention (Agustín Estrada-Peña & Fuente, 2014; Salmerón Gómez et al., 2020), suggesting that such variables should be excluded from model development (Agustín Estrada-Peña & Fuente, 2014).

Chlorophyll Estimation model

Multiple Linear Regression (MLR) is a statistical technique used to model the relationship between one dependent variable and multiple independent variables. In this study, MLR was employed to estimate leaf chlorophyll content (LCC) based on selected vegetation indices (VIs).

The Multiple Linear Regression is a statistical technique used to model the relationship between one dependent variable and multiple independent variables. In this study, MLR was employed to estimate leaf chlorophyll content (LCC) based on selected vegetation indices (VIs).

$$Y = \sum_{i=1}^n W_i X_i \quad (2)$$

where: Y - Leaf chlorophyll concentration;

W_i - Weight of vegetation index i;

X_i - Value of vegetation index i;

n – Number of criteria (VIs).

The accuracy of the MLR model was assessed by comparing the estimated LCC values with the measured ones using a SPAD meter and used as ground truth for model validation, including the coefficient of determination (R^2), and the root mean square error (RMSE). These metrics are calculated as follows:

$$R^2 = 1 - \frac{\sum_{i=1}^n (y_i - \hat{y}_i)^2}{\sum_{i=1}^n (y_i - \bar{y})^2} \quad (3)$$

$$RMSE = \frac{1}{n} \sum_{i=1}^n [y_i - \hat{y}_i] \quad (4)$$

where: y_i = measured LCC, using a SPAD meter;

\hat{y}_i = estimated LCC;

\bar{y} = mean of measured LCC;

n = number of samples.

A higher R^2 and lower RMSE values indicate better model performance and stronger predictive accuracy.

RESULTS

Indices selection

Optimized NDVI

NDVI is calculated by the difference between the reflectance in the near-infrared (NIR) and red (R) bands. Based on the analysis of the provided graph in Fig. 3, the selection of appropriate spectral bands for calculating the NDVI (Normalized Difference Vegetation Index) is crucial. NDVI was measured in R800 and R640, divided by their sum (J.W. Rouse & R.H.Hass, 1974). In this study, NDVI₁ was calculated using B87 (R800 = 801.868nm) and B51 (R640 = 639.115nm)

In Fig. 3, B59 exhibits the lowest DN value of 4.31, which corresponds to the central wavelength of 675.435nm, a region where vegetation strongly absorbs light for photosynthesis. Thus, B59 is selected as the representative R (Red) band. On the other hand, B117 shows the highest DN value of 138.48, which corresponds to the near-infrared (NIR) band (central wavelength of 936.148nm), a region where vegetation strongly reflects light, particularly from the leaves.

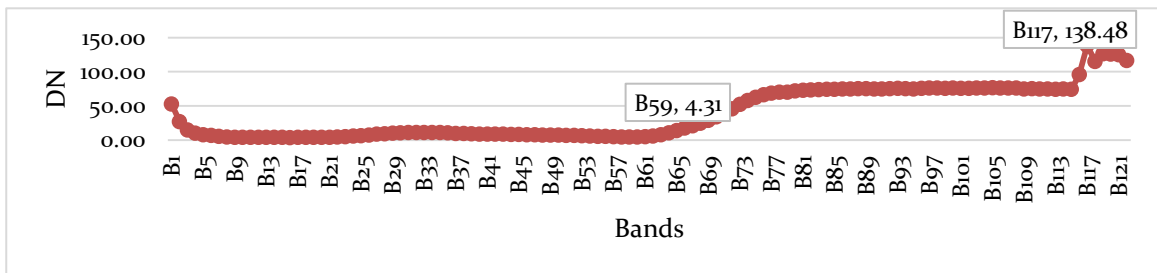


Figure 3. The average spectra of rice plant

As a result, NDVI₂ was calculated using the following equation 5:

$$NDVI_2 = \frac{B_{117} - B_{59}}{B_{117} + B_{59}} \quad (5)$$

Fig. 4 shows the correlation between different spectral bands and chlorophyll content. The red bands exhibit a negative correlation, with the band showing the highest correlation being B66 (707.143 nm), which has an r value of -0.47. In contrast, the near-infrared bands display a positive correlation,

with the strongest correlation observed for band B114 (922.775 nm), which has an r value of 0.39. Thus, by utilizing B114 (near-infrared) and B66 (red) bands, the NDVI can be computed to estimate chlorophyll content. The negative correlation observed in the red band (B66) suggests that chlorophyll content decreases as reflectance in this band increases, while the positive correlation in the near-infrared band (B114) indicates that chlorophyll content

increases with higher reflectance in this spectral region.

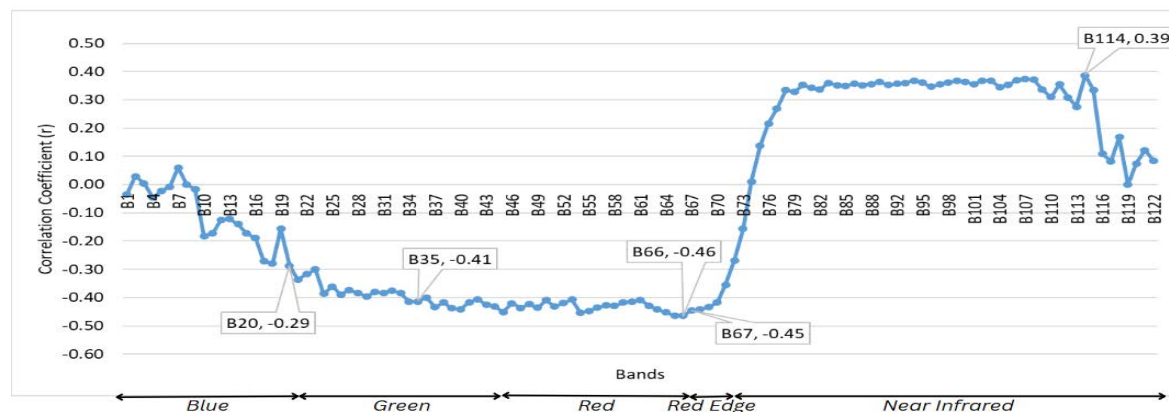


Figure 4. Correlation between SPAD value and R (a) and NIR (b)

As a result, NDVI₃ was calculated using the following equation 6.

$$NDVI_3 = \frac{B114 - B66}{B114 + B66} \quad (6)$$

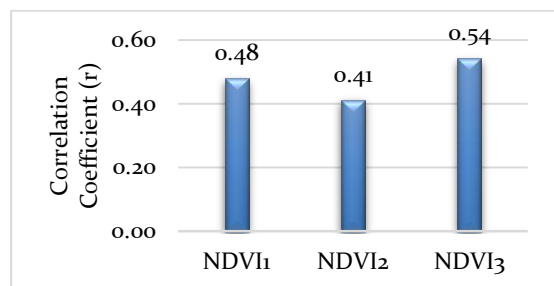


Figure 5. Correlation Coefficient between NDVIs and LCC

Fig. 5 shows the correlation coefficients (r) between three NDVI indices (NDVI₁, NDVI₂, and NDVI₃) and leaf chlorophyll content. NDVI₁ shows a moderate positive correlation with a coefficient of 0.48, suggesting a reasonably strong relationship between this index and chlorophyll content. NDVI₂ exhibits a slightly weaker correlation, with a coefficient of 0.41, indicating a less pronounced but still positive relationship. In contrast, NDVI₃ shows the highest correlation at 0.54, suggesting that this index has the strongest positive relationship with leaf chlorophyll content among the three. These findings highlight that while all three NDVI indices demonstrate a positive association with chlorophyll content, NDVI₃ is the most

effective at predicting or reflecting changes in chlorophyll levels.

Other Vegetation Indices

The absolute correlation coefficients, which show the closest relationship between LCC and bands of Blue, Green, Red, Red-edge and NIR are 0.29 (B20 - wavelength of 497.55 nm), 0.41 (B35 - wavelength of 566.21 nm), 0.46 (B66 - wavelength of 707.14 nm), 0.45 (B67 - wavelength of 711.67 nm), and 0.39 (B114 - wavelength of 922.78 nm) (Fig. 6). Therefore, B20, B35, B66, B67, and B114 were used to calculate other VIs in Table 1.

The correlation coefficients (R values) reveal both positive and negative relationships between the indices and LCC (Fig.6). It was found that several indices exhibit a moderate to strong positive correlation with LCC, with R values greater than 0.5. These indices include RVI (R = 0.56), RECI (R = 0.57), OSAVI (R = 0.54), NDRE (R = 0.55), MSR (R = 0.54), LCI (R = 0.57), GNDVI (R = 0.50), EVI (R = 0.56), DVI (R = 0.50), and NSRI (R = 0.57). These indices are considered to exhibit a significant positive relationship with LCC and can therefore be regarded as reliable tools for chlorophyll concentration assessment. On the other hand, certain indices display weaker or negative correlations with LCC. SIPI (R = 0.39) is associated with a moderate positive correlation, while TVI (R = 0.22) shows a relatively weak positive relationship.

Furthermore, PRI ($R = -0.23$), MSAVI ($R = -0.30$), and MCARI ($R = -0.29$) are found to have negative correlations with LCC, indicating an inverse relationship with chlorophyll concentration.

In conclusion, indices with correlation coefficients greater than 0.5, such as RECI, RVI, LCI, OSAVI, NDRE, MSR, DVI, NSRI, and EVI, are considered to be particularly effective in assessing LCC.

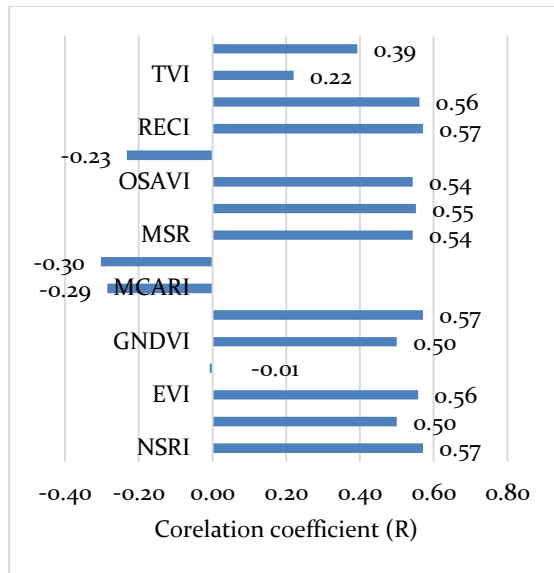


Figure 6. Correlation coefficient between other VIs and LCC

Leaf Chlorophyll Content Detection

The selected indices in Section 3.1 were applied to estimate LCC in rice. VIF was calculated to address the issue of multicollinearity. The Table 2 presents the VIFs of the indices.

Table 2. The Variance Inflation Factor (VIF) of VIs

Number	Indices	R ²	VIF
1	NDVI ₃	0.73	3.7037
2	NSRI	0.99	100
3	DVI	0.99	100
4	EVI	0.981	52.6316
5	GNDVI	0.84	6.25
6	LCI	0.99	100
7	MSR	0.99	100
8	NDRE	0.98	50

9	OSAVI	0.99	100
10	RECI	0.99	100
11	RVI	0.99	100

Among the indices assessed, NSRI, DVI, LCI, MSR, OSAVI, RECI, and RVI all displayed VIF values of 100, indicating significant multicollinearity and suggesting that their inclusion would likely lead to overfitting and instability in the model. Therefore, these indices were excluded from the final model to ensure robustness and accuracy in estimating LCC.

In contrast, indices with VIF values below 10, such as NDVI₃ (VIF = 3.7037), and GNDVI (VIF = 6.25), exhibited lower levels of multicollinearity, making them more suitable for use in the model. Although NDRE had a VIF greater than 10, its specific sensitivity to chlorophyll content in rice justifies its potential inclusion. Despite its multicollinearity, NDRE was retained due to its significant contribution to LCC estimation, particularly when its unique features are deemed essential for the model's performance.

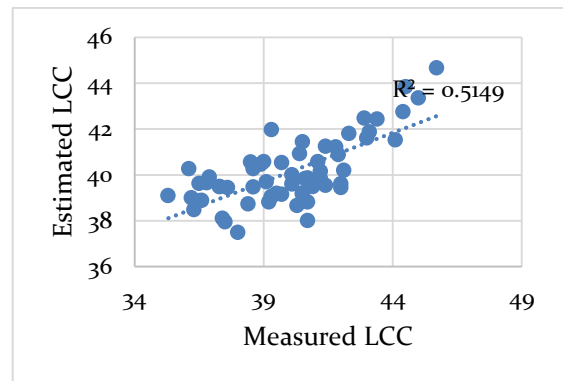


Figure 7. The scatter plot of measured LCC and estimated LCC

Thus, NDVI₃, GNDVI, and NDRE were selected for LCC estimation model. The Table 3 shows the results of MLR for LCC estimation. Among the three vegetation indices included in the MLR model, only NDRE showed a significant positive relationship with LCC ($t = 4.57$, $p < 0.01$), indicating its strong predictive power. In contrast, NDVI₃ and GNDVI were not significant ($p > 0.05$), suggesting limited

contribution to LCC estimation. The insignificant intercept ($p = 0.14$) implies that the baseline prediction is not statistically different from zero. Overall, NDRE proved to be the most effective variable for predicting leaf chlorophyll content in this study.

The final regression equation is expressed as:

$$LCC = 21.48 + 4.55(NDVI_3) + 0.65(GNDVI) + 27.34(NDRE) \quad (7)$$

The model achieved an R^2 of 0.55 (Fig.7), explaining about 55% of the variation in LCC, with an RMSE of 1.55, indicating a satisfactory prediction accuracy. Overall, NDRE was identified as the most influential variable for estimating leaf chlorophyll content in rice.

Table 3. the results of MLR in rice LCC estimation

	Coefficients	Standard Error	t Stat	P-value	Lower 95%	Upper 95%	Lower 95.0%	Upper 95.0%
Intercept	21.48	14.59	1.47	0.14	-7.35	50.32	-7.35	50.32
NDVI3	4.55	17.54	0.26	0.80	-30.10	39.21	-30.10	39.21
GNDVI	0.65	9.70	0.07	0.95	-18.52	19.81	-18.52	19.81
NDRE	27.34	5.99	4.57	0.00	15.51	39.17	15.51	39.17

DISCUSSION

The results of this study demonstrate that hyperspectral vegetation indices, particularly those incorporating the red-edge and near-infrared (NIR) spectral regions, can effectively estimate leaf chlorophyll content (LCC) in rice. Among the 19 tested indices, NDRE exhibited the highest predictive power, followed by NDVI₃ and GNDVI. This finding aligns with previous studies indicating that indices exploiting the red-edge region are particularly sensitive to chlorophyll variation due to the sharp increase in reflectance between 680–740 nm (Anatoly Gitelson, 1994; Pengphorm et al., 2024). The strong relationship between NDRE and LCC suggests that NDRE provides a robust indicator of chlorophyll concentration, especially under varying canopy and illumination conditions.

The superior performance of NDRE can be attributed to its sensitivity to subtle changes in chlorophyll absorption that are less affected by background noise and soil reflectance compared to traditional NDVI-based approaches (de Lima et al., 2021). Although NDVI₃ was optimized for rice by selecting the most correlated red and NIR bands (B₆₆ and B₁₁₄), its correlation ($r = 0.54$) remained moderate. This result highlights that NDVI₃ remains a reliable indicator of vegetation vigor,

its sensitivity to high chlorophyll levels. GNDVI also demonstrated a positive but weaker correlation with LCC, consistent with previous findings that green-based indices capture chlorophyll variation more effectively during early growth stages but become less sensitive in mature rice canopies (Pengphorm et al., 2024).

Among the tested indices, NDRE outperformed NDVI and GNDVI, particularly in the rice canopy conditions of the study area. NDRE's superior performance can be attributed to its sensitivity to the red-edge region (680–740 nm), which is highly responsive to chlorophyll absorption, especially in crops like rice that undergo significant changes in canopy structure and chlorophyll content during growth stages. Unlike NDVI, which is limited by saturation effects at high chlorophyll concentrations, NDRE is more capable of detecting subtle variations in chlorophyll content, even in dense canopies with high chlorophyll levels.

Moreover, the specific optical properties of rice, including leaf structure and reflectance characteristics, favor the use of red-edge bands for chlorophyll estimation. In comparison, GNDVI, which emphasizes the green band, showed weaker performance because it is more sensitive during early growth stages and less effective under mature canopy conditions.

Therefore, NDRE provides a more reliable and consistent estimation of LCC, especially under the complex and variable conditions present in rice fields.

The use of multicollinearity screening (VIF) in model development proved essential for ensuring the robustness of the regression model. Many indices such as RECI, LCI, OSAVI, and RVI exhibited very high VIF values (>100), indicating redundancy among predictors. Excluding these indices improved the stability and interpretability of the model, confirming that NDRE alone could provide satisfactory predictive performance without introducing instability or overfitting.

The integration of UAV-based hyperspectral imaging with in-situ SPAD measurements in this study provides a practical workflow for precision agriculture, enabling timely detection of nutrient stress and guiding fertilization management.

Nevertheless, several limitations should be acknowledged. The moderate model accuracy ($R^2 = 0.55$) suggests that additional factors—such as leaf structure, canopy geometry, and varying illumination—may have influenced reflectance measurements. Furthermore, environmental conditions (e.g., soil moisture and sun angle) and differences between rice varieties (TBR225 vs. Japonica 02) might have introduced variability not fully captured by the current model. Future research should consider integrating machine learning algorithms (Random Forest, PLSR) or radiative transfer modeling to improve predictive accuracy and generalizability across growth stages and cultivars (Du & Luo, 2024; H. Liu et al., 2023). The regression model achieved a moderate $R^2 = 0.55$ explaining about 55% of the variation in leaf chlorophyll content (LCC). While this result provides a reasonably strong indication of the relationship between the selected vegetation indices and chlorophyll content, the predictive accuracy may not fully meet practical thresholds for field applications, where higher precision is typically required for actionable decisions, especially in large-scale agricultural settings.

In practical terms, an R^2 of 0.55 could be considered acceptable for early-stage crop monitoring and management, particularly in fields where timely but non-invasive data collection is critical. However, for more precise applications such as nutrient management or stress detection, the accuracy may need to be improved. To improve model performance, future work could incorporate additional predictors, such as spectral bands in the shortwave infrared (SWIR) and environmental variables (e.g., soil moisture, temperature). Moreover, applying nonlinear machine learning approaches, like Random Forest or Deep Learning, could better capture the complex relationships in the data. Addressing environmental variability, such as soil properties and sun angle, could further enhance model robustness. These improvements could lead to more precise and reliable field applications.

Overall, this study confirms that hyperspectral indices, particularly NDRE, hold strong potential for accurate and non-destructive estimation of chlorophyll content in rice. By selecting optimal spectral bands and reducing model redundancy, the approach enhances the precision of crop health monitoring. These findings contribute valuable insights toward advancing UAV-based hyperspectral applications in rice phenotyping and precision nutrient management.

CONCLUSION

This study demonstrated that UAV-based hyperspectral imaging is a reliable and efficient approach for estimating leaf chlorophyll content (LCC) in rice. Among 19 tested vegetation indices, those incorporating red-edge and near-infrared spectral information exhibited the strongest correlations with LCC. In particular, the Normalized Difference Red Edge Index (NDRE) proved to be the most effective predictor, yielding a coefficient of determination indicating satisfactory predictive accuracy.

The results confirm that the red-edge spectral region provides superior sensitivity to

chlorophyll variation compared with conventional NDVI-based indices, which are often limited by saturation effects at high chlorophyll concentrations. The optimized NDVI₃ also showed consistent but moderate performance, highlighting its potential use when hyperspectral red-edge data are unavailable.

By integrating hyperspectral data with ground-based SPAD measurements, the study establishes a robust framework for non-destructive chlorophyll monitoring, offering valuable support for precision fertilization and stress diagnosis in rice production. Nonetheless, environmental factors and varietal differences may affect spectral responses, and future work should explore advanced modeling approaches such as partial least squares regression (PLSR) or machine learning to enhance predictive robustness and generalization across growth stages.

Overall, this research advances the understanding of hyperspectral vegetation indices for chlorophyll estimation and reinforces the potential of UAV-based remote sensing as a practical tool for sustainable and data-driven rice crop management.

KNOWLEGEMENT

This work is supported by the Vietnam Academy of Science and Technology and represents the pre-feasibility study for the project “Application of UAV Imagery and Machine Learning for Estimating Fresh Tea Productivity” (project code VASTo8.03/25-26).

REFERENCES

- Agustín Estrada-Peña, & Fuente, A. E.-S. a. J. d. I.,2014. A global set of Fourier-transformed remotely sensed covariates for the description of abiotic niche in epidemiological studies of tick vector species. *Parasites & Vectors*, 7(1), 302. doi:https://doi.org/10.1186/1756-3305-7-302
- Anatoly Gitelson, a. M. N. M.,1994. Quantitative estimation of chlorophyll-a using reflectance spectra: Experiments with autumn chestnut and maple leaves. *Journal of Photochemistry and Photobiology B: Biology*, 22(3), 247-252.
- Ban, S., Liu, W., Tian, M., Wang, Q., Yuan, T., Chang, Q., & Li, L.,2022. Rice Leaf Chlorophyll Content Estimation Using UAV-Based Spectral Images in Different Regions. *Agronomy*, 12(11). doi:10.3390/agronomy12112832
- Broge, N. H., & Leblanc, E.,2001. Comparing prediction power and stability of broadband and hyperspectral vegetation indices for estimation of green leaf area index and canopy chlorophyll density. *Remote Sensing of Environment*, 76(2), 156-172. doi:https://doi.org/10.1016/S0034-4257(00)00197-8
- Buschmann, C., & Nagel, E.,1993. In vivo spectroscopy and internal optics of leaves as basis for remote sensing of vegetation. *International journal of remote sensing*, 14(4), 711-722. doi:10.1080/01431169308904370
- Cao, Y., Jiang, K., Wu, J., Yu, F., Du, W., & Xu, T.,2020. Inversion modeling of japonica rice canopy chlorophyll content with UAV hyperspectral remote sensing. *PLoS One*, 15(9), e0238530. doi:10.1371/journal.pone.0238530
- Chen, J. M.,1996. Evaluation of Vegetation Indices and a Modified Simple Ratio for Boreal Applications. *Canadian Journal of Remote Sensing*, 22(3), 229-242. doi:10.1080/07038992.1996.10855178
- Daughtry, C. S. T., Walthall, C. L., Kim, M. S., de Colstoun, E. B., & McMurtrey, J. E.,2000. Estimating Corn Leaf Chlorophyll Concentration from Leaf and Canopy Reflectance. *Remote Sensing of Environment*, 74(2), 229-239. doi:https://doi.org/10.1016/S0034-4257(00)00113-9
- de Lima, I. P., Jorge, R. G., & de Lima, J. L. M. P.,2021. Remote Sensing Monitoring of Rice Fields: Towards Assessing Water Saving Irrigation Management Practices. *Frontiers in Remote Sensing*, 2. doi:10.3389/frsen.2021.762093
- Deng, L., Mao, Z., Li, X., Hu, Z., Duan, F., & Yan, Y.,2018. UAV-based multispectral remote sensing for precision agriculture: A comparison between different cameras. *ISPRS Journal of Photogrammetry and Remote Sensing*, 146, 124-136. doi:10.1016/j.isprsjprs.2018.09.008
- Du, L., & Luo, S.,2024. Spectral-Frequency Conversion Derived from Hyperspectral Data Combined with Deep Learning for Estimating Chlorophyll Content in Rice. *Agriculture*, 14(7). doi:10.3390/agriculture14071186
- Gamon, J. A., Serrano, L., & Surfus, J. S.,1997. The photochemical reflectance index: an optical indicator of photosynthetic radiation use efficiency across

- species, functional types, and nutrient levels. *Oecologia*, 112(4), 492-501. doi:10.1007/s004420050337
- Gamon, J. A., & Surfus, J. S.,1999. Assessing leaf pigment content and activity with a reflectometer. *New Phytologist*, 143(1), 105-117. doi:https://doi.org/10.1046/j.1469-8137.1999.00424.x
- Gitelson, A., & Merzlyak, M. N.,1994. Quantitative estimation of chlorophyll-a using reflectance spectra: Experiments with autumn chestnut and maple leaves. *Journal of Photochemistry and Photobiology B: Biology*, 22(3), 247-252. doi:https://doi.org/10.1016/1011-1344(93)06963-4
- Gitelson, A. A., Gritz †, Y., & Merzlyak, M. N.,2003. Relationships between leaf chlorophyll content and spectral reflectance and algorithms for non-destructive chlorophyll assessment in higher plant leaves. *Journal of Plant Physiology*, 160(3), 271-282. doi:https://doi.org/10.1078/0176-1617-00887
- Huete, A., Didan, K., Miura, T., Rodriguez, E. P., Gao, X., & Ferreira, L. G.,2002. Overview of the radiometric and biophysical performance of the MODIS vegetation indices. *Remote Sensing of Environment*, 83(1), 195-213. doi:https://doi.org/10.1016/S0034-4257(02)00096-2
- J.W. Rouse, J., & R.H.Hass, J. A. S. a. D. W. D.,1974. Monitoring vegetation systems in the Great Plains with ERTS. Vol. 351, *NASA Special Publication*, 309-317.
- Jang, Y. H., Park, J. R., Kim, E. G., & Kim, K. M.,2022. OsbHLHq11, the Basic Helix-Loop-Helix Transcription Factor, Involved in Regulation of Chlorophyll Content in Rice. *Biology (Basel)*, 11(7). doi:10.3390/biology11071000
- Jia, Y., Zhang, H., Zhang, X., & Su, Z.,2022. Quantitative Analysis and Hyperspectral Remote Sensing Inversion of Rice Canopy Spad in a Cold Region. *Engenharia Agrícola*, 42(4). doi:10.1590/1809-4430-eng.agric.v42n4e20220030/2022
- Jiang, J., Cai, W., Zheng, H., Cheng, T., Tian, Y., Zhu, Y., . . . Yao, X.,2019. Using Digital Cameras on an Unmanned Aerial Vehicle to Derive Optimum Color Vegetation Indices for Leaf Nitrogen Concentration Monitoring in Winter Wheat. *Remote Sensing*, 11(22), 2667.
- Jordan, C. F.,1969. Derivation of Leaf-Area Index from Quality of Light on the Forest Floor. *Ecology*, 50(4), 663-666. doi:https://doi.org/10.2307/1936256
- Liu, H., Lei, X., Liang, H., & Wang, X.,2023. Multi-Model Rice Canopy Chlorophyll Content Inversion Based on UAV Hyperspectral Images. *Sustainability*, 15(9). doi:10.3390/su15097038
- Liu, L.-y., Huang, W.-j., Pu, R.-L., & Wang, J.-h.,2014. Detection of internal leaf structure deterioration using a new spectral ratio index in the near-infrared shoulder region. *Journal of Integrative Agriculture*, 13(4), 760-769.
- Minh Khanh Luong, Tong Si Son¹, Huong Mai, Huong Thi Mai To, Giang Son Tran, Binh Pham-Duc, . . . Ai, T. T. H.,2024. UAV hyperspectral image acquisition and processing, an application for nutrient estimation of rice in Vietnam. *Vietnam Journal of Earth Sciences*, 46(4), 533-552.
- Nio, S. A., Ludong, D. P. M., & Siahaan, R.,2022. Short communication: Pattern of chlorophylls content declined during partial submergence for rice varieties cultivated in North Sulawesi at the vegetative stage. *Biodiversitas Journal of Biological Diversity*, 23(5). doi:10.13057/biodiv/d230524
- Pengphorm, P., Thongrom, S., Daengngam, C., Duangpan, S., Hussain, T., & Boonrat, P.,2024. Optimal-Band Analysis for Chlorophyll Quantification in Rice Leaves Using a Custom Hyperspectral Imaging System. *Plants (Basel)*, 13(2). doi:10.3390/plants13020259
- Peñuelas, J., Gamon, J. A., Fredeen, A. L., Merino, J., & Field, C. B.,1994. Reflectance indices associated with physiological changes in nitrogen- and water-limited sunflower leaves. *Remote Sensing of Environment*, 48(2), 135-146. doi:https://doi.org/10.1016/0034-4257(94)90136-8
- Qi, J., Chehbouni, A., Huete, A. R., Kerr, Y. H., & Sorooshian, S.,1994. A modified soil adjusted vegetation index. *Remote Sensing of Environment*, 48(2), 119-126. doi:https://doi.org/10.1016/0034-4257(94)90134-1
- Rondeaux, G., Steven, M., & Baret, F.,1996. Optimization of soil-adjusted vegetation indices. *Remote Sensing of Environment*, 55(2), 95-107. doi:https://doi.org/10.1016/0034-4257(95)00186-7
- Salmerón Gómez, R., García García, C., & García Pérez, J.,2020. Detection of Near-Multicollinearity through Centered and Noncentered Regression. *Mathematics*, 8(6). doi:10.3390/math8060931
- Thi, L. P., & Van, C. L.,2025. Estimating chlorophyll content in rice leaves using vegetation indices derived from multispectral UAV imagery (in

- vietnamese). *Journal of Hydro-meteorology*, 05(773), 88-102. doi:10.36335/vnjhm.2025(773).88-102
- Wang, J., Zhou, Q., Shang, J., Liu, C., Zhuang, T., Ding, J., . . . Huo, Z., 2021. UAV- and Machine Learning-Based Retrieval of Wheat SPAD Values at the Overwintering Stage for Variety Screening. *Remote Sensing*, 13(24). doi:10.3390/rs13245166
- Wang, L., Duan, Y., Zhang, L., Rehman, T., Ma, D., & Jin, J., 2020. Precise Estimation of NDVI with a Simple NIR Sensitive RGB Camera and Machine Learning Methods for Corn Plants. *Sensors (Basel)*, 20(11). doi:10.3390/s20113208
- Wang, Y., Tan, S., Jia, X., Qi, L., Liu, S., Lu, H., . . . Ma, X., 2023. Estimating Relative Chlorophyll Content in Rice Leaves Using Unmanned Aerial Vehicle Multi-Spectral Images and Spectral-Textural Analysis. *Agronomy*, 13(6). doi:10.3390/agronomy13061541
- Zhang, S., Zhao, G., Lang, K., Su, B., Chen, X., Xi, X., & Zhang, H., 2019. Integrated Satellite, Unmanned Aerial Vehicle (UAV) and Ground Inversion of the SPAD of Winter Wheat in the Reviving Stage. *Sensors (Basel)*, 19(7). doi:10.3390/s19071485

Forest canopy height map in Cuc Phuong National Park using field data and AI-extracted features AlphaEarth Foundations (AEF)

Duc Anh Ngo^{1, 2,*}, Anh Tuan Vu¹, Viet Luong Nguyen¹, Tien Cong Nguyen¹, Nhat Kieu Thi Truong¹, Thanh Binh Nguyen³

¹Vietnam National Space Center, Vietnam Academy of Science and Technology, 18 Hoang Quoc Viet, Nghia Do ward, Hanoi, Vietnam

²Graduate University of Sciences and Technology, Vietnam Academy of Science and Technology, 18 Hoang Quoc Viet, Nghia Do ward, Hanoi, Vietnam

³Institute of Earth Sciences, Vietnam Academy of Science and Technology, 68 Huynh Thuc Khang, Lang ward, Hanoi, Vietnam

*Email: ndanh@vnsc.org.vn

Abstract: Canopy height mapping is an essential requirement for sustainable forest management. However, existing global products often lack the required accuracy for specific ecosystems, such as the tropical forests in Cuc Phuong National Park. This study presents an efficient workflow for developing a time-series tree height map (2017-2024) for Cuc Phuong National Park, leveraging the power of the Google Earth Engine (GEE) cloud computing platform. Field data from 2017 permanent sample plots were used to train a Random Forest machine learning model with 150 decision trees. The novelty of this method lies in the use of features from the AlphaEarth Foundations (AEF) platform model, specifically annual satellite embeddings with 10-meter resolution. The model, trained on 2017 data, was then applied to predict tree height for the entire time series, enabling both mapping and analysis of tree height dynamics. The evaluation on a validation dataset (20% of the data) showed that the model achieved a strong predictive performance, with a Root Mean Squared Error (RMSE) of 4.48 m. This research demonstrates that combining in-situ field data with features from the AEF foundation model on GEE is a powerful approach for generating dynamic tree height maps, effectively

supporting sustainable forest monitoring and management.

Keywords: AlphaEarth Foundations (AEF); canopy height, GEE, Cuc Phuong National Park

INTRODUCTION

Canopy height is a fundamental forest structural parameter that plays a crucial role in estimating above-ground biomass, carbon stocks, and assessing biodiversity (Tolan et al., 2024). In Vietnam, with its rich and complex tropical forest systems, obtaining accurate and up-to-date tree height maps is an urgent requirement for sustainable resource management and fulfilling climate change mitigation commitments. However, large-scale mapping presents several inherent challenges. Traditional methods based on passive optical imagery are often limited by cloud cover and cannot directly measure the three-dimensional structure of the canopy, while advanced technologies such as Airborne Laser Scanning (ALS), though highly accurate, are prohibitively expensive to deploy over large areas (Tolan et al., 2024).

To overcome these limitations, modern methods are increasingly moving towards the fusion of data from various sensor types, combining the strengths of both active and

passive sensors to create a more comprehensive picture of forest ecosystems (Samadzadegan et al., 2025). The integration and processing of these massive, multi-source datasets, however, pose a significant computational barrier.

A first significant research gap lies in the transition from static mapping to monitoring forest dynamics. Many previous studies have focused on generating a tree height map at a single point in time or on comparing two widely separated time points (bi-temporal change detection). These methods can miss gradual or inconsistent change processes (Cohen et al., 2010; Zhu, 2017). The effective monitoring of processes such as forest degradation, regeneration after disturbance, or the impacts of climate change requires a full time-series analysis of satellite data. Nevertheless, building consistent and comparable multi-year time series from various multi-sensor data sources remains a major technical and data processing challenge (Reiche et al., 2021).

The second gap is related to accessibility and customization at the local scale. While the advent of global mapping products and foundation models has been revolutionary, their accuracy may not be sufficient for local-level management applications, particularly in complex ecosystems that are underrepresented in global training datasets (Lencinas, 2025; Næsset et al., 2020). Concurrently, building a customized model for a specific area using traditional methods often requires deep expertise in processing raw remote sensing data from multiple sources, which creates a significant technical barrier. Consequently, there is a clear need for efficient workflows that enable scientists and managers to easily combine even limited field data with powerful, pre-processed remote sensing features to generate high-accuracy, locally relevant time-series products.

This study presents an innovative workflow that leverages two advanced technologies. First, features from the AlphaEarth Foundations (AEF) platform model by Google DeepMind are utilized. AEF

functions as a "virtual satellite," integrating Earth observation data into a unified digital representation called an "embedding," which already encodes complex information about vegetation structure. This approach eliminates the need for complex, manual multi-source data fusion. Second, the entire process is implemented on the Google Earth Engine (GEE) cloud computing platform, which provides large-scale processing capabilities and a massive repository of remote sensing data (Bengtsson et al., 2021).

Therefore, the objectives of this study are to: (1) train and validate a Random Forest machine learning model to estimate tree height at Cuc Phuong National Park by combining 2017 field data with AEF features on the GEE platform; (2) apply the trained model to generate an annual tree height map series from 2017 to 2024 ; and (3) analyze this time series to quantify overall change trends and identify spatial patterns of change within Cuc Phuong National Park.

METHODOLOGY

The entire research process, from data access and model training to time-series analysis, was conducted on the Google Earth Engine (GEE) cloud computing platform. The overall workflow is illustrated in Fig. 1.

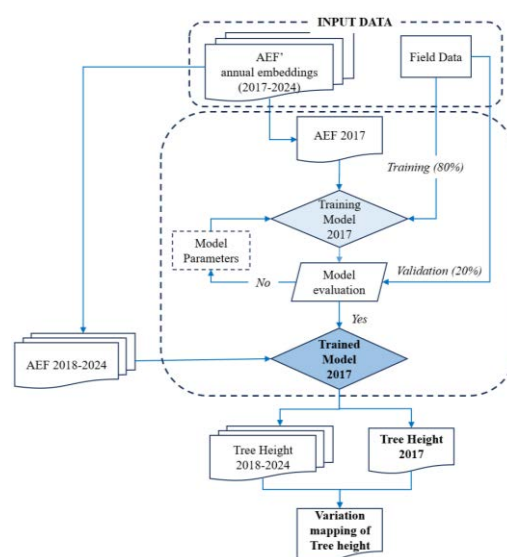


Figure 1 Diagram of the overall research workflow.

Study Area

Cuc Phuong National Park (NP), Vietnam's first national park, was established in 1962 and is located across the provinces of Ninh Binh, Hoa Binh, and Thanh Hoa (Fig. 2). The park is situated on the southeastern edge of a northwest-trending limestone mountain range, which is of marine origin and approximately 200 million years old (Davis et al., 1994). The terrain is characterized by rugged, steep karst mountains that rise abruptly from the surrounding plains, reaching elevations of over 600m (Duwe et al., 2022).

The dominant ecosystem is an evergreen tropical rainforest on limestone, a unique forest type with a thin, discontinuous soil layer and high exposed rock cover. The canopy structure is highly complex, with a five-layered profile in some areas and an emergent layer reaching up to 40m, although it is often fragmented due to the steep topography (Nguyen, 1997). Given its high biodiversity and endemism, coupled with a heterogeneous forest structure, Cuc Phuong NP serves as both an ideal and challenging location to test advanced forest structure mapping methods.

Input Data

Field Data

For model training and validation, field data were collected in 2017 from 82 permanent sample plots (OTCs) within Cuc Phuong National Park (Fig.2). The plots were established following rigorous criteria to ensure data representativeness and reliability. To accommodate varying forest conditions, plot sizes were varied, including 100m² and 500m² types. The selection of plot locations adhered to several key criteria: the plots were evenly distributed throughout the study area, they were representative of the different forest types and topographical conditions, they were preferentially located on slopes less than 5 degrees while encompassing a range of tree sizes, and each plot was placed at a minimum distance of 100 meters from distracting features such as roads and rivers (Fig. 3).

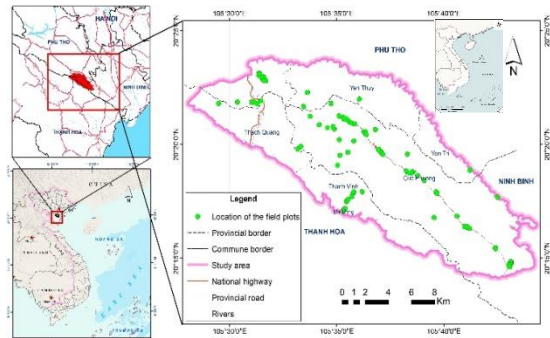


Figure 2. Map of the Cuc Phuong NP study area and the location of the field plots.

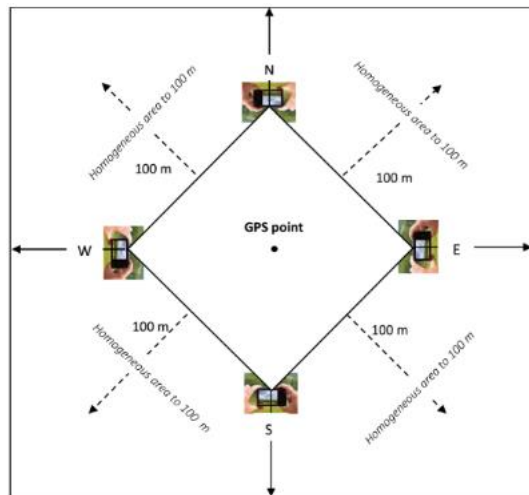


Figure 3. Diagram of the field plot (OTC) design in the study area (Nguyễn, 2020).

Within each OTC, measurements were taken for all living trees with a diameter at breast height (DBH) exceeding 5 cm. The primary structural parameters collected were: (i) species name (scientific and Vietnamese), (ii) DBH at 1.3 meters, measured using a Criterion RD1000 laser device, and (iii) tree height, defined as the distance from the base to the top of the canopy, measured with a TruPulse 360B laser height meter. The data from each plot were then converted into an *ee.FeatureCollection* format on Google Earth Engine (GEE). From these individual tree measurements, the maximum height index (hmax) for each plot was calculated and used as the target variable for model training.

AlphaEarth Foundations (AEF) Features

The predictor variables were derived from the AlphaEarth Foundations (AEF) platform model. This is a geospatial foundation model trained on a massive dataset, including over 3 billion observations from various data sources such as Sentinel-1 (SAR), Sentinel-2 (optical), Landsat 8/9, PALSAR-2, and GEDI (LiDAR) from 2017 to 2024 (Brown et al., 2025).

Instead of using raw satellite imagery, this study leverages AEF's output product, known as satellite "embeddings." Specifically, we utilized the Satellite Embedding dataset (GOOGLE/SATELLITE_EMBEDDING/V1/ANN UAL) available in the GEE Catalog. In this

dataset, each 10-meter pixel is represented by a 64-dimensional feature vector. This vector is a compressed, information-rich representation that encodes the complex characteristics of the Earth's surface from all input data sources over the course of a year (Fig. 4).

The use of these pre-computed embeddings offers a significant advantage: it completely bypasses the complex multi-source data pre-processing and fusion step, allowing us to focus on building the relationship between these powerful features and the field-measured tree height data. The study uses a time series of annual embeddings from 2017 to 2024 to map and analyze forest dynamics.

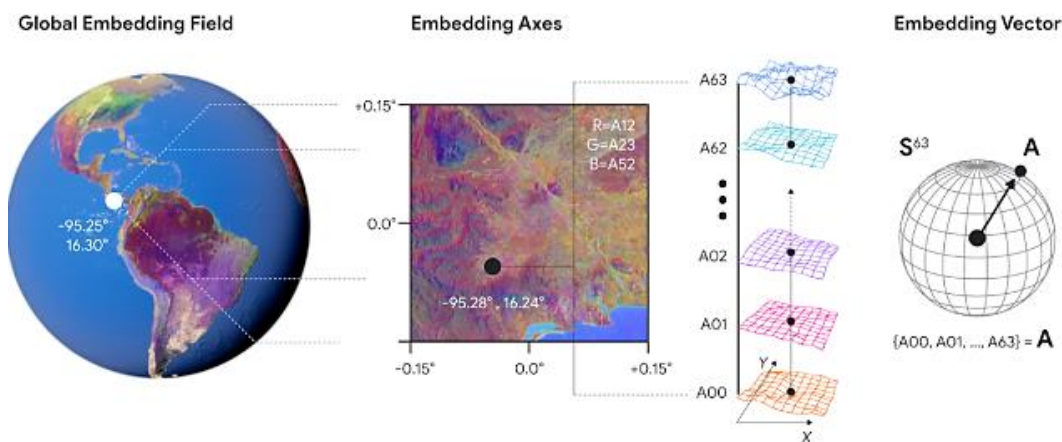


Figure 4 Diagram showing a global embedding field broken down into a single embedding, from left to right. Each embedding has 64 components which map to coordinates on a 64-dimensional sphere.

Model Building and Mapping Workflow

Data Preparation and Pre-processing

To minimize the influence of non-forest areas, a tree cover mask (treeMask) was created from the 2017 JAXA Forest/Non-Forest (FNF) dataset. This global dataset is derived from the L-band Synthetic Aperture Radar (SAR) aboard the ALOS/ALOS-2 satellites and provides an annual forest classification at a spatial resolution of approximately 25 meters (Shimada et al., 2014). The use of L-band SAR is particularly advantageous for forest monitoring in tropical regions as its signal can penetrate cloud cover, a persistent challenge for optical sensors (Almeida-Filho et al., 2007).

The FNF map classifies pixels based on the intensity of the radar backscatter, which is sensitive to vegetation structure. In this study, the treeMask was used to exclude non-forest areas from the analysis, ensuring that the Random Forest model was trained and applied only on pixels already identified as having forest cover, thereby reducing noise and improving the accuracy of the final height estimation.

Following the application of the mask, the field data from 82 plots were randomly divided into two sets: 80% for training and 20% for validation. The AEF embedding data for 2017 were extracted at the plot locations and filtered by the treeMask before being used for training.

Random Forest Regression Model

In this study, the Random Forest (RF) algorithm was employed, which is a widely used and effective ensemble learning method in remote sensing applications (Luo et al., 2023), (Næsset et al., 2020). During training, a "forest" of numerous individual decision trees is constructed by the algorithm. For regression tasks, the final prediction is obtained by averaging the predictions from all the trees within the forest (Fig. 5). RF's ability to handle high-dimensional, noisy data and its resilience to overfitting are considered key advantages.

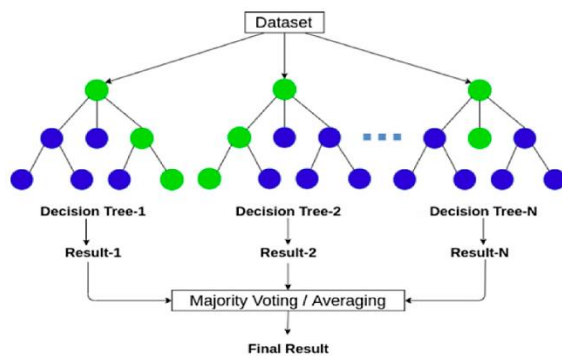


Figure 5. Structure of random forest regressor algorithm (Ha & Giang, 2023)

The `ee.Classifier.smileRandomForest` algorithm, available within Google Earth Engine (GEE), was utilized in regression mode (REGRESSION). Based on the GEE code, the primary model parameters were carefully set and fine-tuned. The number of decision trees was specified as 150. At each node split, the number of predictor variables to be randomly considered was 21. A minimum leaf population of 3 was required, which was used to control the complexity of the trees and mitigate overfitting. Furthermore, a bagging fraction of 0.75 was applied to determine the proportion of training samples drawn (with replacement) for each individual tree. Finally, a seed of 0 (zero) was used to ensure that all random selections could be reproduced, thereby leading to consistent results across multiple runs.

Model Accuracy Assessment

Model performance was evaluated on the 20% validation set (data the model had not

seen during training). The primary metric used was the Root Mean Squared Error (RMSE).

RMSE is one of the most common metrics for measuring the average magnitude of the error between predicted and actual values. Theoretically, it is the square root of the average of the squared errors and represents the standard deviation of the residuals (Tolan et al., 2024). RMSE has the same units as the predicted variable (in this case, meters), which makes interpretation intuitive. A lower RMSE value indicates higher model accuracy.

The RMSE is calculated using the following formula:

$$RMSE = \sqrt{\frac{\sum_{i=1}^n (y_i - \hat{y}_i)^2}{n}}$$

where: n is the total number of samples in the validation set, y_i is the actual height value measured at the i^{th} plot (OTC), \hat{y}_i is the predicted height value for the i^{th} plot (OTC).

In the GEE workflow, RMSE is computed by taking the square root of the Mean Squared Error (MSE), which is calculated from the average of the squared differences between the actual height (Height) and the predicted height (classification).

Time-series Mapping and Change Analysis

The RF model trained and validated on 2017 data was applied to the AEF embedding images for each year from 2017 to 2024, creating a time series of annual tree height maps.

For change analysis, we applied a per-pixel time-series linear regression using the `ee.Reducer.linearFit()` reducer in GEE. This method calculates a trend line for the height value series of each pixel over the 8-year period. The result is a trend map where the value of each pixel is the slope of that trend line, representing the average annual rate of height change (meters/year).

Time-series and Trend Analysis (2017-2024)

This is the core analytical step to assess forest dynamics based on the generated tree height map series.

Overall Trend Analysis

To assess the general trend across the entire area, we aggregated the map series from 2017 to 2024 into a single time-series image collection (*ee.ImageCollection*). Then, the average height value for the entire Cuc Phuong NP was calculated for each year. The results were used to create a line graph showing the change in average tree height over the years.

Per-Pixel Time-series Linear Regression

To scientifically identify spatial change patterns, rather than simply comparing two endpoints, we applied a per-pixel time-series linear regression. This technique is widely used in remote sensing to detect and quantify trends in environmental variables, such as the NDVI, over time (Ghorbanian et al., 2022; C. Liu et al., 2021).

The theoretical basis of this method is to view the height value series of each pixel over the years as an independent time series. For each of these time series, a simple linear regression model is built, where the independent variable is time (i.e., the years 2017, 2018,...) and the dependent variable is the corresponding tree height value of that pixel. Specifically, we used the Ordinary Least Squares (OLS) method, one of the most popular parametric techniques for time-series trend analysis (Ha & Giang, 2023). The basic principle of OLS is to find a "best-fit" straight line that passes through a series of data points by minimizing the sum of the squared vertical distances (known as residuals) from each data point to the line (Pastor-Guzman et al., 2015; Mudelsee, 2019). In the context of this study, a simple linear regression model for each pixel takes the following form:

$$Y_i = \beta_0 + \beta_1 X_i + \epsilon_i$$

where: Y_i is the dependent variable (the height of the pixel's tree in year), X_i is the independent variable (time, i.e., years), β_0 is the intercept (estimated tree height at the initial time point), β_1 is the slope, representing the trend of change, ϵ_i is the random error.

This formula essentially models how tree height (Y_i) changes over time (X_i) using a

straight line. The slope (β_1) is the key parameter, telling us the average rate of change in height for each year. A positive slope means the height is increasing, while a negative slope means it's decreasing.

While non-parametric methods like the Theil-Sen slope estimator are often preferred in environmental studies for their high robustness against outliers (Gutiérrez-Hernández & García, 2024). OLS remains a powerful and computationally efficient method for identifying the dominant linear trend, especially when applied to annual composite data over a consistent time period on a platform like GEE (Ghorbanian et al., 2021).

In this study, the analysis was implemented using the *ee.Reducer.linearFit()* reducer in Google Earth Engine. This function calculates the parameters of the regression line for each pixel's time series.

The most important result of this process is a trend map, where the value of each pixel represents the slope of the regression line. This slope quantifies the average annual rate of change in canopy height (in meters/year). Applying this method on a per-pixel basis allowed us to create a continuous spatial trend map that quantitatively depicts forest dynamics across the entire study area. The interpretation of the slope values is as follows: (i) Positive values (e.g., blue colors) indicate a consistent increasing trend in height, signifying forest growth or successful regeneration. (ii) Negative values (e.g., red colors) show a decreasing trend in height, which could be a sign of degradation, selective logging, or deforestation. (iii) Values near zero (e.g., white/yellow colors) suggest a relatively stable area with little significant change in height during the study period.

RESULTS

This section presents the main findings of the study, including the accuracy assessment of the regression model, the generated time-series tree height map products, and the results of the forest dynamics analysis based on that time series. Together, these results provide

quantitative evidence regarding both the performance of our methodology and the status of the forest ecosystem at Cuc Phuong National Park.

Model Accuracy Assessment

The first step was to evaluate the performance of the Random Forest model on the validation dataset (20% of the field data). The model achieved a strong predictive performance, with a Root Mean Squared Error (RMSE) of 4.48 m. The results showed that the model has strong predictive capability, demonstrated by the close correlation between the predicted tree heights and the maximum tree heights measured in the field. This is illustrated in the scatter plot (Fig. 6).

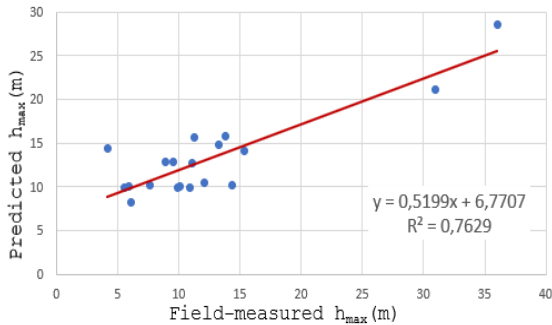


Figure 6. Scatter plot comparing predicted and field-measured height on the validation set.

Tree Height Maps

After validation, the model was applied to the entire AEF data series from 2017 to 2024 to generate a set of annual tree height maps with a 10-meter resolution. This complete time series formed the basis for the forest dynamics analysis presented in the following section.

Forest Dynamics Analysis via Time Series (2017-2024)

The series of annual tree height maps provides a detailed view of the changes in vegetation at Cuc Phuong NP. The analysis of these maps reveals forest dynamics at two scales: a park-wide temporal trend and a fine-scale spatial pattern of change.

At the park-wide scale, the time-series plot (Fig. 7) shows significant inter-annual

variability in the average canopy height rather than a simple linear trend. The series begins at approximately 20.1 m in 2017, experiences a sharp decline to 18.5 m in 2018, followed by a strong recovery to a peak of nearly 20.8 m in 2019. From this peak, a multi-year decrease is observed, reaching a low of 19.0 m in 2022, before another period of strong recovery brings the average height to 20.7 m in 2024.

The spatial analysis, conducted via per-pixel linear regression, is presented in the trend map (Fig. 8). This map highlights the spatial distribution of these changes. The dominant color across the park is blue, indicating that a positive growth trend is the most widespread process. However, the map also clearly identifies numerous, spatially distinct hotspots of negative trend, represented by red and orange colors. These areas of height decline appear as a scattered mosaic throughout the park but show some clustering, particularly along the western boundary.



Figure 7. Time series plot showing average tree height at Cuc Phuong NP from 2017-2024.

DISCUSSION

Model Performance in a Complex Landscape

The Random Forest model developed in this study achieved a Root Mean Squared Error (RMSE) of 4.48 m when evaluated against the validation dataset. While this figure indicates a degree of prediction error, it represents a high level of accuracy when placed within the challenging context of the study area. Cuc Phuong National Park is characterized by a tropical forest ecosystem on limestone karst terrain, which presents significant challenges for remote sensing methods due to its complex

canopy structure, discontinuous foliage, and rugged topography (Sterling et al., 2008; Khuc et al., 2018).

When compared to other large-scale canopy height mapping studies, our model's performance is highly competitive. For instance, the global canopy height model by (Potapov et al., 2021) reported an RMSE of 9.07 m when validated against airborne lidar data. Other studies in similarly complex terrains have reported comparable or higher errors; for example, a study on GEDI's performance in the complex terrain of Southwest China found an RMSE of 5.15 m (Fu et al., 2025), while a study using Random Forest with ICESat-2 data yielded an RMSE of 4.58 m (Nandy et al., 2021). Even advanced TomoSAR techniques in tropical forests have reported RMSEs ranging from 8.2 to 9.8 m (Tolan et al., 2024)(X. Liu et al., 2024). In this context, an RMSE of 4.48 m not only validates the effectiveness of combining local field data with advanced AEF features but also demonstrates the potential of this workflow to produce reliable canopy height maps in the ecologically complex forests of Vietnam.

Forest Dynamics in Cuc Phuong National Park (2017-2024)

The shift from static mapping to dynamic analysis via time series is a crucial advancement of this research. The results from the new figures paint a more complex and realistic picture of the forest dynamics within

Cuc Phuong NP than a simple narrative of steady growth would suggest.

The time-series plot (Fig. 7) provides a macroscopic view of the ecosystem's health, revealing a dynamic and resilient system rather than a static one. The significant fluctuations, such as the sharp dip in 2018 and the subsequent decline from 2019 to 2022, suggest that the forest is subject to inter-annual pressures. These variations could be linked to regional climatic events, such as years with lower rainfall or higher temperatures, or potential artifacts within the annual AEF embedding data for those specific years. Importantly, the strong recovery periods (2018-2019 and 2022-2024) highlight the overall health and resilience of the ecosystem, as it is able to rebound effectively after periods of stress. The final 2024 average height being higher than the 2017 starting point suggests a net positive trajectory over the eight-year period, despite the variability.

The change trend map (Fig. 8) provides the critical spatial context to this temporal story. It explains where and how the overall change is occurring. The prevalence of blue and purple colors across the map confirms that positive growth is the dominant process throughout the park, which aligns with the net positive outcome seen in the time-series plot. This widespread growth is indicative of healthy forest regeneration and maturation processes.

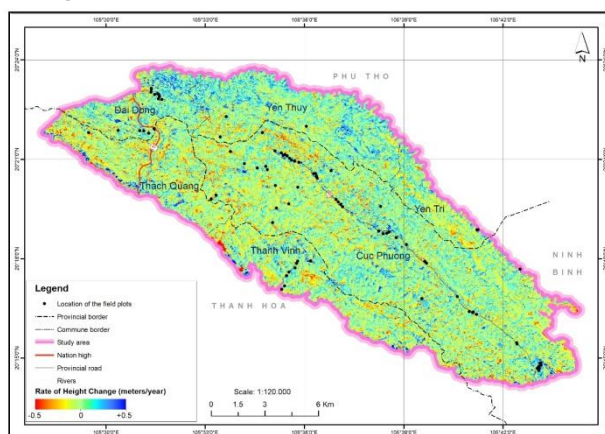


Figure 8. Tree height change trend map (2017-2024) for Cuc Phuong NP. Blue indicates an increasing trend, and red/orange indicates a decreasing trend.

Most significantly, the trend map provides spatially explicit, actionable intelligence by identifying hotspots of negative change (red and orange areas). Unlike an analysis of the park-wide average, which might mask localized issues, this per-pixel analysis pinpoints specific areas experiencing a decline in canopy height. These hotspots could correspond to localized natural disturbances such as landslides or storm damage, or they may indicate areas of concern for park management, such as illegal selective logging or forest dieback. The clustering of some of these negative trends, particularly near the park's periphery, warrants further investigation by park authorities. This detailed spatial information is invaluable for targeting conservation efforts, guiding patrol routes, and better understanding the fine-scale pressures affecting the ecosystem.

Synthesis and Implications for Conservation

In summary, the results paint a consistent and powerful picture: the time-series plot indicates an overall growth trend for Cuc Phuong NP, and the change map confirms that while this growth is widespread across most of the park and large-scale degradation is absent, the analysis crucially pinpoints localized areas of decline. This set of evidence, built from our locally-calibrated model, strongly suggests that Cuc Phuong National Park is well-protected and on a positive developmental trajectory in terms of biomass and forest structure during the 2017-2024 period.

The workflow presented here is not only scientifically valuable but also has great potential for practical application. The per-pixel trend map is a powerful tool for forest managers, allowing them to identify "hotspots" of degradation or success stories of regeneration with high spatial precision. This information can guide the allocation of resources for patrols, monitoring, and evaluating the effectiveness of conservation interventions. Furthermore, the ability to generate consistent annual maps provides a robust foundation for carbon reporting and supporting national and international climate commitments.

Methodological Considerations and Future Directions

The implementation of the entire workflow on the GEE platform proved to be a highly effective approach. It not only removed the computational barriers associated with processing large, multi-temporal datasets but also ensures the transparency and replicability of the research (Bengtsson et al., 2021). A primary limitation of this study is that the model was trained using field data from a single year (2017). However, the model's ability to generate a logical and meaningful time series for subsequent years demonstrates the strong temporal extrapolation potential of the AEF features. Future research should aim to incorporate more recent field data to further validate and potentially update the model. Expanding this methodology to other protected areas in Vietnam would be a valuable next step in developing a national-scale, high-resolution forest monitoring system.

CONCLUSION

This study successfully established an effective workflow for mapping and analyzing tree height dynamics in a time-series context at Cuc Phuong NP. By combining on-the-ground field data with advanced AlphaEarth Foundations features on the Google Earth Engine platform, we generated a dynamic map series and a detailed change trend map. The results reveal a resilient ecosystem with a net positive growth trajectory, characterized by widespread forest development interspersed with localized hotspots of canopy height decline, providing valuable intelligence for targeted management interventions. This method is not only scientifically valuable but also has great potential for application in forest resource management, monitoring, and carbon reporting in Vietnam, providing a powerful tool for a better understanding of how forest ecosystems change over time.

CONFLICT OF INTEREST

The authors declare that the content of this report has no conflict of interest with any

individual or organization, during and after the completion of the research.

ACKNOWLEDGEMENTS

This research was conducted with the support of project code NĐT/US/24/04.

REFERENCES

- Almeida-Filho, R., Rosenqvist, A., Shimabukuro, Y. E., & Silva-Gomez, R. (2007). Detecting deforestation with multitemporal L-band SAR imagery: A case study in western Brazilian Amazonia. *International Journal of Remote Sensing*, 28(6). <https://doi.org/10.1080/01431160600754591>
- Bengtsson, Z., Beaudry, B., Torres-Pérez, J., & McCullum, A. (2021). Part 1: Using Google Earth Engine for Land Monitoring Applications. *NASA Applied Remote Sensing Training Program (ARSET)*, 2021.
- Brown, C. F., Kazmierski, M. R., Pasquarella, V. J., Rucklidge, W. J., Samsikova, M., Zhang, C., Shelhamer, E., Lahera, E., Wiles, O., Ilyushchenko, S., Gorelick, N., Zhang, L. L., Alj, S., Schechter, E., Askay, S., Guinan, O., Moore, R., Boukouvalas, A., & Kohli, P. (2025). *AlphaEarth Foundations: An embedding field model for accurate and efficient global mapping from sparse label data*. <http://arxiv.org/abs/2507.22291>
- Cohen, W. B., Yang, Z., & Kennedy, R. (2010). Detecting trends in forest disturbance and recovery using yearly Landsat time series: 2. TimeSync — Tools for calibration and validation. *Remote Sensing of Environment*, 114(12), 2911–2924. <https://doi.org/10.1016/j.rse.2010.07.010>
- Davis, S. D., Heywood, V. H., & Hamilton, A. C. (1994). Centres of plant diversity: a guide and strategy for their conservation. In *World Wide Fund for Nature (WWF) and IUCN* (Vol. 3).
- Duwe, V. K., Vu, L. Van, von Rintelen, T., von Raab-Straube, E., Schmidt, S., Nguyen, S. Van, Vu, T. D., Do, T. Van, Luu, T. H., Truong, V. B., Di Vincenzo, V., Schmidt, O., Glöckler, F., Jahn, R., Lücking, R., von Oheimb, K. C. M., von Oheimb, P. V., Heinze, S., Abarca, N., ... Häuser, C. L. (2022). Contributions to the biodiversity of Vietnam – Results of VIETBIO inventory work and field training in Cuc Phuong National Park. *Biodiversity Data Journal*, 10. <https://doi.org/10.3897/BDJ.10.E77025>
- Fu, L., Shu, Q., Yang, Z., Xia, C., Zhang, X., Zhang, Y., Li, Z., & Li, S. (2025). Accuracy assessment of topography and forest canopy height in complex terrain conditions of Southern China using ICESat-2 and GEDI data. *Frontiers in Plant Science*, 16(March), 1–18. <https://doi.org/10.3389/fpls.2025.1547688>
- Ghorbanian, A., Mohammadzadeh, A., & Jamali, S. (2022). Linear and Non-Linear Vegetation Trend Analysis throughout Iran Using Two Decades of MODIS NDVI Imagery. *Remote Sensing*, 14(15), 3683. <https://doi.org/10.3390/rs14153683>
- Ghorbanian, A., Zaghian, S., Asiyabi, R. M., Amani, M., Mohammadzadeh, A., & Jamali, S. (2021). Mangrove ecosystem mapping using sentinel-1 and sentinel-2 satellite images and random forest algorithm in google earth engine. *Remote Sensing*, 13(13). <https://doi.org/10.3390/rs13132565>
- Gutiérrez-Hernández, O., & García, L. V. (2024). Robust Trend Analysis in Environmental Remote Sensing: A Case Study of Cork Oak Forest Decline. *Remote Sensing*, 16(20), 3886. <https://doi.org/10.3390/rs16203886>
- Ha, V. T., & Giang, P. T. (2023). Experimental Study on Remaining Useful Life Prediction of Lithium-Ion Batteries Based on Three Regression Models for Electric Vehicle Application. *Applied Sciences (Switzerland)*, 13(13). <https://doi.org/10.3390/app13137660>
- Khuc, Q. Van, Tran, B. Q., Meyfroidt, P., & Paschke, M. W. (2018). Drivers of deforestation and forest degradation in Vietnam: An exploratory analysis at the national level. *Forest Policy and Economics*, 90. <https://doi.org/10.1016/j.forpol.2018.02.004>
- Lencinas, J. D. (2025). Assessing the Accuracy of Global Canopy Height Models: A Comprehensive Review. *BOSQUE*, 46(2), 129–140. <https://doi.org/https://doi.org/10.4067/S0717-92002025000200129>
- Liu, C., Huang, H., & Sun, F. (2021). A Pixel-Based Vegetation Greenness Trend Analysis over the Russian Tundra with All Available Landsat Data from 1984 to 2018. *Remote Sensing*, 13(23), 4933. <https://doi.org/10.3390/rs13234933>
- Liu, X., Neigh, C. S. R., Pardini, M., & Forkel, M. (2024). Estimating forest height and above-ground biomass in tropical forests using P-band TomoSAR and GEDI observations. *International Journal of Remote Sensing*, 45(9), 3129–3148. <https://doi.org/10.1080/01431161.2024.2343134>
- Luo, Y., Qi, S., Liao, K., Zhang, S., Hu, B., & Tian, Y. (2023). Mapping the Forest Height by Fusion of ICESat-2 and Multi-Source Remote Sensing Imagery and Topographic Information: A Case Study in Jiangxi Province, China. *Forests*, 14(3), 454. <https://doi.org/10.3390/f14030454>

- Mudelsee, M. (2019). Trend analysis of climate time series: A review of methods. In *Earth-Science Reviews* (Vol. 190). <https://doi.org/10.1016/j.earscirev.2018.12.005>
- Næsset, E., McRoberts, R. E., Pekkarinen, A., Saatchi, S., Santoro, M., Trier, Ø. D., Zahabu, E., & Gobakken, T. (2020). Use of local and global maps of forest canopy height and aboveground biomass to enhance local estimates of biomass in miombo woodlands in Tanzania. *International Journal of Applied Earth Observation and Geoinformation*, 89, 102109. <https://doi.org/10.1016/j.jag.2020.102109>
- Nandy, S., Srinet, R., & Padalia, H. (2021). Mapping Forest Height and Aboveground Biomass by Integrating ICESat-2, Sentinel-1 and Sentinel-2 Data Using Random Forest Algorithm in Northwest Himalayan Foothills of India. *Geophysical Research Letters*, 48(14). <https://doi.org/10.1029/2021GL093799>
- Nguyen, N. T. (1997). The vegetation of Cuc Phuong National Park, Vietnam. *Sida*, 17(4), 719–759.
- Nguyễn, V. L. (2020). *Research on the application of remote sensing and GIS technology to build models to calculate biomass reserves of natural forest ecosystems in Vietnam. Final report of national S&T project, Code: VT-UD.05/17-20*.
- Pastor-Guzman, J., Atkinson, P. M., Dash, J., & Rioja-Nieto, R. (2015). Spatiotemporal variation in mangrove chlorophyll concentration using Landsat 8. *Remote Sensing*, 7(11), 14530–14558. <https://doi.org/10.3390/rs71114530>
- Potapov, P., Li, X., Hernandez-Serna, A., Tyukavina, A., Hansen, M. C., Kommareddy, A., Pickens, A., Turubanova, S., Tang, H., Silva, C. E., Armston, J., Dubayah, R., Blair, J. B., & Hofton, M. (2021). Mapping global forest canopy height through integration of GEDI and Landsat data. *Remote Sensing of Environment*, 253, 112165. <https://doi.org/10.1016/j.rse.2020.112165>
- Reiche, J., Mullissa, A., Slagter, B., Gou, Y., Tsendbazar, N. E., Odongo-Braun, C., Vollrath, A., Weisse, M. J., Stolle, F., Pickens, A., Donchyts, G., Clinton, N., Gorelick, N., & Herold, M. (2021). Forest disturbance alerts for the Congo Basin using Sentinel-1. *Environmental Research Letters*, 16(2). <https://doi.org/10.1088/1748-9326/abd0a8>
- Samadzadegan, F., Toosi, A., & Dadrass Javan, F. (2025). A critical review on multi-sensor and multi-platform remote sensing data fusion approaches: current status and prospects. *International Journal of Remote Sensing*, 46(3), 1327–1602. <https://doi.org/10.1080/01431161.2024.2429784>
- Shimada, M., Itoh, T., Motooka, T., Watanabe, M., Shiraishi, T., Thapa, R., & Lucas, R. (2014). New global forest/non-forest maps from ALOS PALSAR data (2007–2010). *Remote Sensing of Environment*, 155, 13–31. <https://doi.org/10.1016/j.rse.2014.04.014>
- Sterling, E. J., Hurley, M. M., & Minh, L. D. (2008). *Vietnam: A Natural History*. Yale University Press.
- Tolan, J., Yang, H.-I., Nosarzewski, B., Couairon, G., Vo, H. V., Brandt, J., Spore, J., Majumdar, S., Haziza, D., Vamaraju, J., Moutakanni, T., Bojanowski, P., Johns, T., White, B., Tiecke, T., & Couprie, C. (2024). Very high resolution canopy height maps from RGB imagery using self-supervised vision transformer and convolutional decoder trained on aerial lidar. *Remote Sensing of Environment*, 300, 113888. <https://doi.org/10.1016/j.rse.2023.113888>
- Zhu, Z. (2017). Change detection using landsat time series: A review of frequencies, preprocessing, algorithms, and applications. *ISPRS Journal of Photogrammetry and Remote Sensing*, 130, 370–384. <https://doi.org/10.1016/j.isprsjprs.2017.06.013>

DOI: 10.15625/vap.2025.0213

UAV hyperspectral imaging and machine learning for fresh tea yield estimation

Duc-Duy Nguyen, Si-Son Tong^{*}, Hoang-Long Nguyen

University of Science and Technology of Hanoi (USTH), Vietnam Academy of Science and Technology (VAST),
18 Hoang Quoc Viet, Nghia Do, Hanoi, Vietnam

^{*}Email: tong-si.son@usth.edu.vn

Abstract: Precision farming has emerged as a vital approach for enhancing yields, ensuring sustainability, and supporting food security. This study aims to investigate regression-based methods for fresh tea yield estimation using unmanned aerial vehicle (UAV)-acquired hyperspectral imagery, with a focus on dimensionality reduction to improve prediction accuracy and efficiency. The hyperspectral images, comprising 122 narrow spectral bands, was used to estimate three yield-related traits of green tea: bud height, fresh bud weight, and bud count in the tea field in Phu Tho, Viet Nam. A range of regression models was tested, including linear and regularized approaches (Ridge, Lasso), ensemble methods (Random Forests), Bayesian linear regression (BLR), and advanced boosting frameworks (XGBoost, CatBoost regression-CBR). Model performance was evaluated using cross-validated coefficient of determination (R^2) and mean squared error (MSE). Results show that the CBR model with singular value decomposition (SVD) best predicted bud height (MSE = 121.36, R^2 = 0.34). For bud weight, CBR with locally linear embedding (LLE) achieved the highest accuracy (MSE = 232.6, R^2 = 0.45), while BLR with LLE provided the best bud count prediction (MSE = 583.2, R^2 = 0.54). Overall, this research demonstrates an optimization of integrating hyperspectral imaging with machine learning and dimensionality reduction for crop trait estimation. The proposed framework advances precision tea agriculture by enabling more efficient monitoring and supporting sustainable yield improvement.

Keywords: Close-range remote sensing, hyperspectral image, UAV, machine learning, tea productivity.

INTRODUCTION

Tea is one of the most widely consumed beverages globally, holding substantial cultural and economic significance. As a cornerstone of many cultures, tea has a rich history of cultivation and consumption that spans centuries. According to recent reports, the global tea market is projected to grow from 55.64 billion in 2024 to 59.23 billion in 2025, reflecting a compound annual growth rate (CAGR) of 6.4 % [1]. This steady growth highlights the increasing demand for tea, making it a crucial sector in the global economy. Vietnam, one of the world's leading tea-exporting countries, plays a pivotal role in this market. In the first eleven months of 2024 alone, Vietnam exported nearly 133,000 tons of tea, generating revenues of 235 million [5]. Despite its vital role in the global tea trade, Vietnam's position is increasingly threatened by several interrelated factors: wide swings in seasonal yields driven by climate variability [2]; the ever present risk of pests and diseases that undermine both the quantity and quality of harvests; and a lack of uniform agronomic practices across plantations, which makes it difficult to obtain a clear picture of true output. In this context, the development of accurate, reliable productivity estimation techniques is more important than ever not only to optimize resource allocation and on-farm management, but also to guide policy measures that foster a resilient, sustainable tea sector. These challenges underscore the need for approaches

that integrate detailed field-level data with robust analytical tools, enabling stakeholders at all levels of the value chain to adapt proactively to changing climatic and market conditions.

Artificial intelligence and machine learning have been increasingly applied to tea productivity estimation, with the dual objectives of optimizing resource use, reducing labour costs, and improving the accuracy of yield predictions. A growing of diverse methodological frameworks ranging from classical regression models to ensemble learning techniques demonstrating the considerable promise of these approaches in enhancing tea productivity assessments and facilitating precision agriculture. Zongtai He et al. [3] compared Piecewise Linear Models using Same Index Variables (PLMSVs) against those using Combined Index Variables (PLMCVs) for tea yield estimation. By segmenting the data into high and low green coverage change domains, they found that the Curvature Index (CUR) delivered an RMSE of 85.067 g and a R^2 of 0.88 in the high coverage segment, whereas in the low coverage segment the RMSE rose to 126.369 g with a R^2 of 0.78. Furthermore, the CUR combined PLMCV model achieved a substantially improving prediction stability across heterogeneous canopy conditions. This stratified modelling approach provided key insights into the non-linear relationships between spectral indices and yield and has directly informed the segmentation strategies adopted in this study. Building on the theme of spectral-ML integration, Siyu Lv et al. [4] focused on the rapid, non-destructive estimation of leaf water content in *Catalpa Bungei* using hyperspectral reflectance data. The authors applied Monte Carlo Uninformative Variable Elimination (MC-UVE) to reduce dimensionality and isolate the most informative wavelengths, which were then fed into a Partial Least Squares (PLS) regression framework. The optimal model achieved a test set $R^2 = 0.79$ and RMSE = 1.735, while a simple spectral reflectance index constructed from wavelengths at 1466 nm and 2128 nm exhibited a strong correlation with measured water content ($r > 0.85$). The

rigorous feature-selection methodology and validation protocol have shaped the variable-screening and cross-validation, particularly for managing high dimensional hyperspectral datasets.

Previous studies have highlighted the critical importance of tailored segmentation strategies to capture canopy heterogeneity, systematic feature-selection techniques to mitigate hyperspectral dimensionality, and comparative analyses of regression paradigms to identify the most effective modelling approaches. Moreover, the successful application of these techniques to tea underscores the versatility of hyperspectral-ML integration, while also revealing a gap in field deployable workflows. This study develops an end-to-end framework integrating vegetation indices, and advanced machine learning models to estimate tea productivity consisting of the weight, the height and the number of tea buds. Hyperspectral data acquired from unmanned aerial vehicles are employed with dimensionality reduction techniques to optimize model performance. The study applies and compares advanced machine learning algorithms, such as XGBoost and CatBoost Regression (CBR), with conventional regression models to identify the optimal combination of spectral features and modeling approaches for improved predictive performance. The findings aim to advance accurate, scalable, and sustainable tea yield estimation.

DATA AND METHODOLOGY

Study area

The study area encompasses approximately 1.8 hectares of tea fields located in Phu Tho Province at coordinates 21°15'02"N and 105°11'14"E (Figure 1). The tea plants are arranged in straight rows extending about 100 meters across a gently sloping low hill with an inclination of less than 5°. *Camellia sinensis* has been cultivated in this region as a traditional agricultural practice for many years. Tea harvesting is conducted manually, with five picking cycles per year.

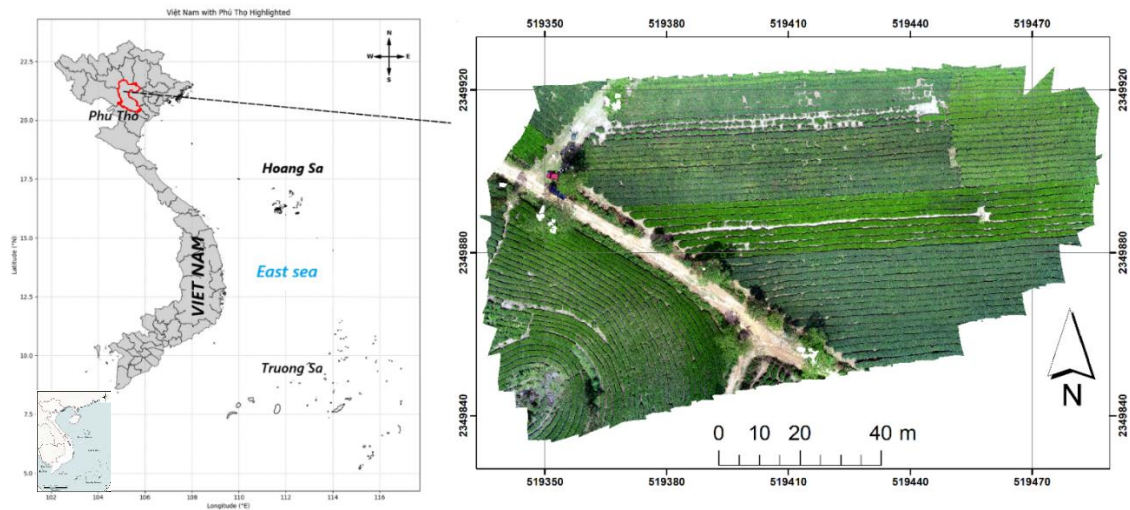


Figure 1. The study area and UAV RGB image acquired on 11st October 2024

Data in use

A dataset comprising unmanned aerial vehicle (UAV) hyperspectral images and corresponding tea yield measurements was acquired on 11 October 2024, one day prior to harvesting. Within the tea rows, 40 square hollow blocks (30 cm × 30 cm) outlined with yellow paper were randomly placed to serve as sampling plots (Figure 2). These blocks were clearly visible in the UAV imagery. All tea buds

within each block were collected to measure their average height, total fresh weight, and number of buds. Consequently, each sample block provided three parameters: fresh bud weight, average bud height, and bud count. The parameters of tea buds obtained from the square sampling plots were used to construct predictive models and to assess the accuracy of tea yield estimations across the study area.

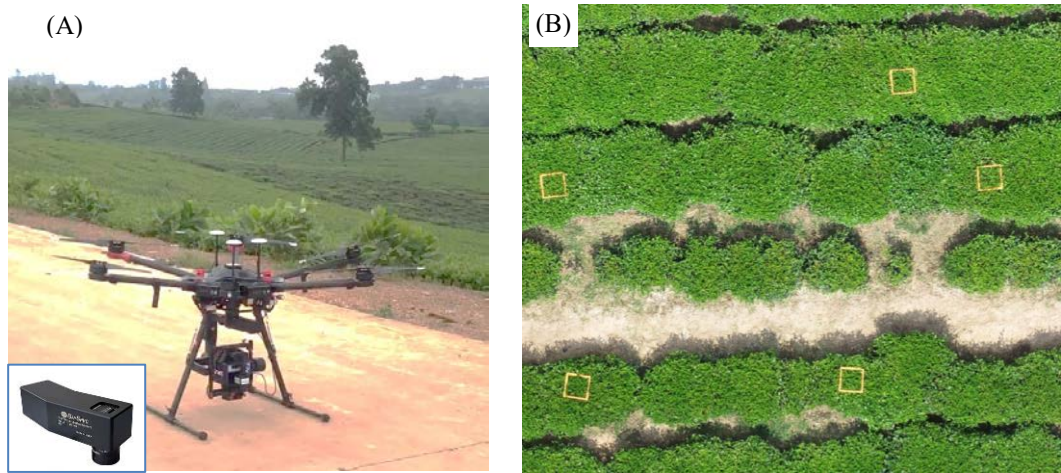


Figure 2. (A) UAV DJI Matrice 600 Pro and Hyperspectral camera Bayspec OCI-F for acquiring hyperspectral image in the tea field, (B) sampling plots with the side of 30 cm x 30 cm placed in tea rows

Hyperspectral data were acquired using a DJI Matrice 600 Pro UAV equipped with a Bayspec OCI-F hyperspectral camera (Figure 2). Employing a push-broom scanning technique, the OCI-F sensor captured imagery across 122 spectral bands with a 5 nm bandwidth, covering the visible to near-infrared range (400–1000 nm). To ensure complete coverage of the study area, the UAV followed ten flight lines with a swath width of 12 m and 50% overlap between adjacent swaths. The hyperspectral imagery was georectified using a reference RGB orthophoto acquired by a separate UAV flight on the same day. The resulting hyperspectral data cube was stored in GeoTIFF format with 8-bit radiometric resolution (values ranging from 0 to 255), 122 spectral bands, and a spatial resolution of 2 cm. The hyperspectral images were acquired between 10:30 and 11:00 a.m., immediately after placing the square sampling plots and before collecting the tea buds. During image acquisition, weather conditions were sunny with wind speeds below 2 m s⁻¹.

Methodology

This study aims to estimate three key parameters of tea productivity—fresh bud weight, bud height, and bud count—using hyperspectral imagery and field-sampled data. To achieve this objective, four main steps were implemented: (1) hyperspectral image processing, (2) data preprocessing, (3) machine learning modelling, and (4) performance evaluation (Figure 3). The workflow begins with hyperspectral image processing, in which spectral reflectance values are extracted from predefined sampling plots and combined with corresponding field measurements to construct a unified dataset. The dataset is then preprocessed by removing null values and outliers, applying dimensionality reduction techniques, and dividing the data into cross-validation folds. Machine learning models are subsequently trained and validated on these folds, with their predictions averaged to improve robustness. Finally, the aggregated results are exported to a CSV file for performance assessment and comparative analysis.

Hyperspectral data preprocessing:

Spectral values across all 122 bands of the hyperspectral imagery were extracted for every pixel within each sampling plot. The mean reflectance of each band was then calculated over all 225 pixels in a plot, resulting in a single 122-dimensional spectral signature per sample, for subsequent machine learning model training. Additionally, relationships between the hyperspectral features of the sampling plots and the measured tea yield parameters were analysed to assess their correlations, distributions, and potential outliers. During data preprocessing, procedures such as missing-value imputation and outlier detection were applied to ensure data quality and reliability.

K-fold cross-validation: The model's performance was evaluated using the k-fold cross-validation method, in which the dataset is partitioned into k equal subsets, or folds. The model is trained k times, each time using a different fold for validation and the remaining k–1 folds for training. Given the limited sample size, the dataset was divided into eight folds for cross-validation. In each iteration, three folds were used for training and one fold for validation, and this process was repeated four times to ensure that each fold served once as the validation set. The model was trained and evaluated in each iteration, and the resulting performance metrics were averaged across all folds to obtain a stable and reliable estimate of its generalization ability. This approach maximizes the use of available data while reducing variance in performance assessment.

Models Setup: Twelve machine learning models were employed to evaluate the relationship between hyperspectral data and tea yield parameters: Linear Regression (LR), Ridge Regression (RR), Lasso Regression (LaR), Elastic Net Regression (ENR), Bayesian Linear Regression (BLR), Gradient Boosting Regression (GBR), LightGBM Regression (LGBMR), XGBoost Regression (XGBR), Decision Tree Regression (DTR), Random Forest Regression (RFR), Support Vector Regression (SVR), and CatBoost Regression

(CBR). The models are implemented using Python libraries, with parameter settings adopted based on the authors' suggested configurations. The key parameters and their corresponding values used in model

initialization are summarized in Table 1. The model demonstrating the best predictive performance was selected for estimating tea productivity from the hyperspectral imagery.

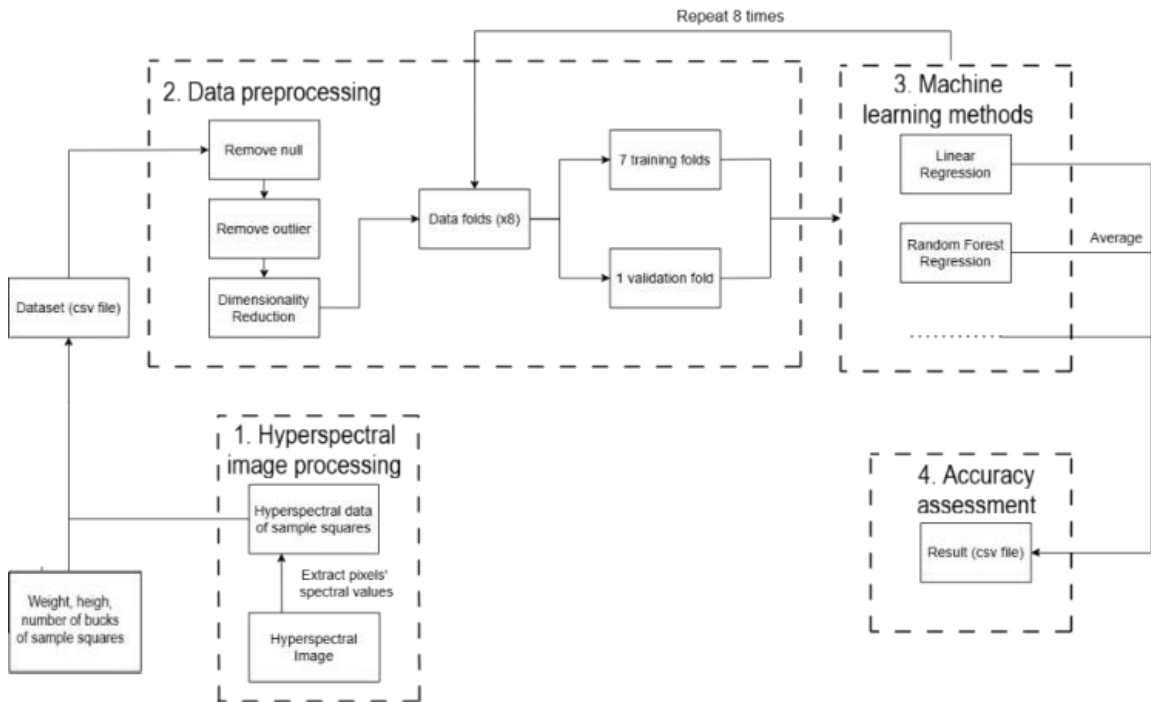


Figure 3. The workflow of estimating tea productivity from the UAV hyperspectral imagery

Table 1. Key parameters used to implement machine learning models for estimating tea productivity

Models	Key parameters and corresponded values				
Linear Regression	Fit intercept (True)	Copy X (True)	Positive (False)		
Ridge Regression	Alpha (1.0)	Fit intercept (True)	Max iteration (None)	Solver (Auto)	
Lasso Regression	Alpha (1.0)	Fit intercept (True)	Max iteration (1000)	Positive (False)	Selection (Cyclic)
Elastic Net Regression	Alpha (1.0)	L1 Ratio (0.5)	Fit intercept (True)	Max iteration (1000)	
Bayesian Regression	Number Iterations (300)	Tol (0.001)	Alpha 1 (1e-6)	Lambda 1 (1e-6)	Fit intercept (True)
Gradient Regression	Loss (Squared Error)	Learning rate (0.1)	Number estimators (100)	Max depth (3)	Random_State (42)
Light GBM Regression	Boosting Type (Gbdt)	Learning rate (0.01)	Number estimators (500)	Number leaves (31)	Random state (42)
XGBoost Regression	Objective (Reg: Squarederror)	Random state (42)	Learning rate (0.3)	Number estimators (100)	Max depth (6)
Decision Tree Regression	Criterion (Squared error)	Splitter (Best)	Max depth (None)	Random state (42)	

Random Forest Regression	Number estimators (100)	Criterion (Squared error)	Max depth (None)	Bootstrap (True)	Random state (42)
Support Vector Regression	Kernel (Rbf)	C (1.0)	Epsilon (0.1)	Max iteration (-1)	
CatBoost Regression	Iterations (500)	Learning rate (0.01)	Depth (6)	Random seed (42)	Loss function (Rmse)

RESULTS

Hyperspectral data, tea productivity and their correlation

The hyperspectral reflectance is analysed in the 122 bands alongside agronomic variables bud weight, plant height, and bud count to examine their correlations, distributions, and potential outliers. The boxplot of spectral data (Figure 4A) shows low and tightly clustered reflectance values in the visible bands (1–60), followed by a sharp increase to higher and more variable reflectance in the near-infrared region (65–100), and a gradual decline beyond band 100. These spectral patterns typically report low reflectance in the visible range and pronounced variability in the NIR for healthy foliage.

The histogram of tea productivity measurements (Figure 4B) indicates that plant height predominantly ranges between 55 and 75 cm, suggesting relatively uniform growth, although a few shorter plants may reflect underdeveloped conditions. The fresh bud weight distribution is concentrated between 95 and 115 g, with a small number of samples below 60 g, possibly corresponding to stressed or low-performing plants. The distribution of bud count appears approximately symmetric and centered around 160–180 buds, indicating stable and typical productivity across most samples, with only minor deviations at the extremes.

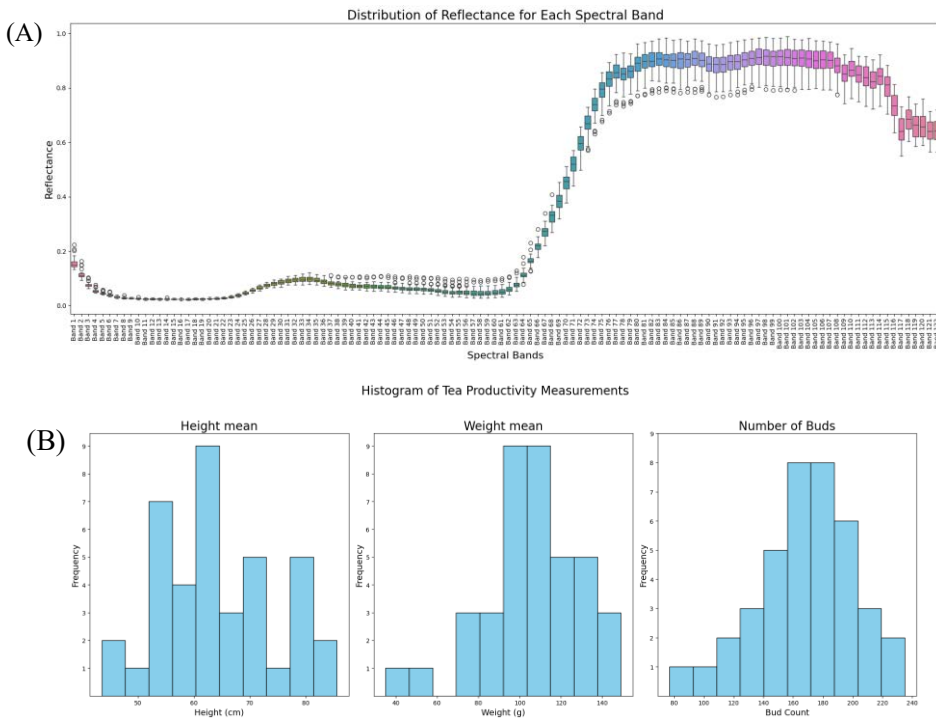


Figure 4. (A) Reflectance distribution of spectral bands and (B) Histograms of three parameters of tea productivity measured in sample plots.

Figure 5 illustrates the correlations between spectral bands and the three tea productivity parameters based on the Pearson correlation coefficient (r). The results show that no individual spectral band exhibits a strong relationship with tea productivity. Correlations with shoot height are moderately

positive ($r \approx +0.2$ to $+0.4$), while correlations with shoot weight are weakly negative ($r \approx -0.2$ to -0.5). Bud count shows comparatively stronger negative correlations, reaching values as low as -0.7 . These trends vary smoothly across the spectral range, remaining within the low to moderate correlation levels overall.

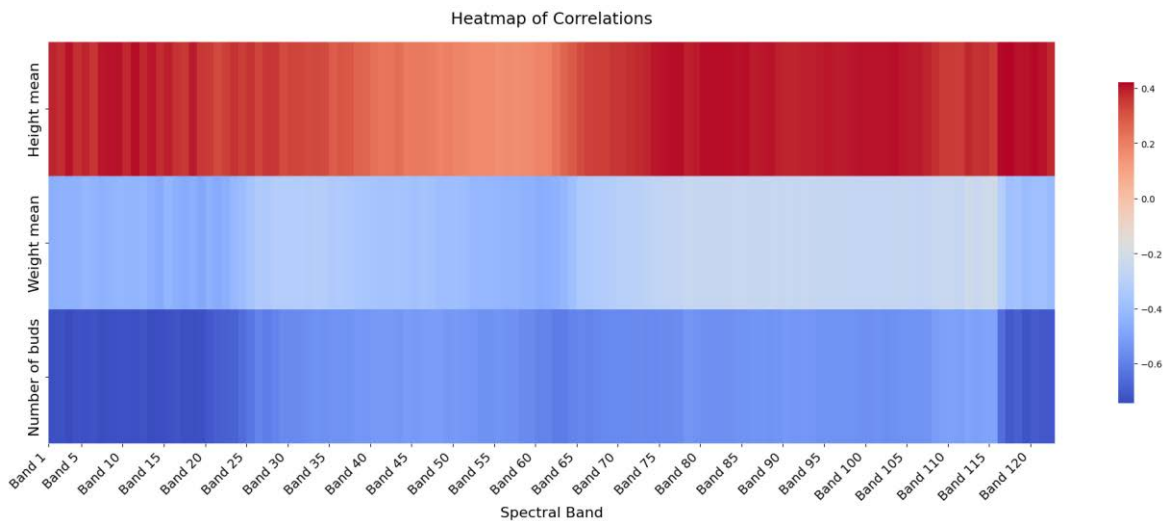


Figure 5. Correlation between spectral reflectance of hyperspectral image bands and productivity variables bud weight, plant height, and bud count

Dimensionality reduction

Due to the high redundancy of hyperspectral imagery, dimensionality reduction was applied to identify the most informative spectral bands for subsequent processing. Seven dimensionality reduction techniques were implemented: High Correlation Filtering (HCF), Hessian Locally Linear Embedding (HLLE), Locally Linear Embedding (LLE), Isomap, Kernel Principal Component Analysis (KPCA), Principal Component Analysis (PCA), and Singular Value Decomposition (SVD). The results of these methods are summarized in Table 2. A high-correlation filter (threshold = 0.4) was first applied to eliminate redundant spectral bands based on pairwise correlations. This procedure retained 30 bands for predicting plant height, 122 bands for bud count, and 39 bands for fresh weight. For the manifold learning methods, d

represents the number of nearest neighbours used to capture local geometry, and k denotes the dimensionality of the resulting low-dimensional embedding. In HLLE, parameters were set to $d = 18$ and $k = 3$. The LLE method used $d = 15$ and $k = 8$. Isomap constructed a nearest-neighbour graph with $d = 24$ and produced an embedding of $k = 11$ dimensions. For projection-based approaches, k corresponds to the number of retained components. KPCA was configured to preserve the top $k = 6$ kernel principal components. Classical PCA and truncated SVD were each limited to $k = 3$ components.

Table 2. Chosen dimensionality-reduction methods and their parameters.

Method	Result
High-correlation filter	Threshold = 0.4
HLLE	$d = 18, k = 3$

LLE	$d = 15, k = 8$
Isomap	$d = 24, k = 11$
KPCA	$k = 6$
PCA	$k = 3$
SVD	$k = 3$

Note: k denotes the number of components, and d denotes the number of neighbours.

Model for estimating the height of tea buds

Tea bud height prediction models exhibited a clear performance hierarchy, with tree-ensemble algorithms significantly outperforming both linear and kernel-based approaches across all dimensionality reduction

techniques (Figure 6). Among these, the CBR method combined with SVD retaining three components achieved the highest accuracy, yielding a mean squared error (MSE) of 121.36 and a coefficient of determination (R^2) of 0.14. Likewise, the XGBR, LGBMR, and RFR consistently produced lower prediction errors compared to the linear models—LR, RR, and BLR—which showed higher MSE values (typically above 140) and near-zero or slightly negative R^2 scores. In contrast, the DTR method consistently yielded the poorest performance across all dimensionality reduction methods, with MSE values exceeding 210 and R^2 values dropping below -0.6 .

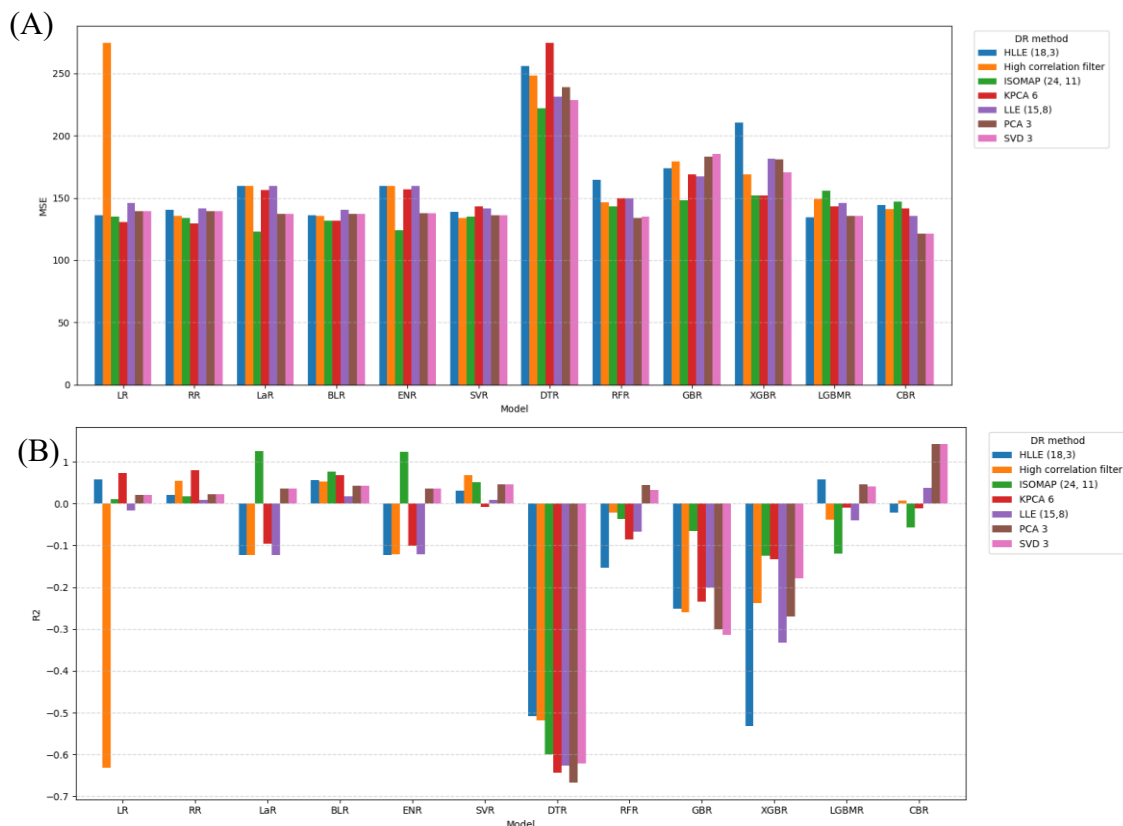


Figure 6. (A) Mean squared error (MSE), and (B) coefficient of determination (R^2) of different dimensionality reduction (DR) methods on machine learning models in estimating tea bud's height.

Model for estimating tea bud weight

The tea bud weight prediction models exhibited substantial variability in performance across the twelve regression-reduction combinations, reflecting differences in each

model's capacity to leverage high-dimensional hyperspectral inputs. Overall, ensemble learning algorithms provided the most reliable estimates (Figure 7). Among them, the CBR algorithm combined with the dimensionality

deduction method LLE ($d = 15$, $k = 8$) achieved the best performance, yielding the lowest mean squared error (MSE) of 232.6 and the highest coefficient of determination ($R^2 = 0.45$). The RFR, GBR, XGBR, and LGBMR algorithms also demonstrated notable error reductions, achieving MSEs in the range of 300–450 and positive R^2 values between 0.13 and 0.30, underscoring their robustness to noisy and collinear spectral features. In contrast, simpler linear models—including LR, RR, LaR, and BLR—paired with the HCF reduction showed weaker performance, with MSEs often exceeding 300 and R^2 values near zero or

slightly negative, indicating limited explanatory power. Furthermore, the DTR consistently performed the poorest across all dimensionality reduction schemes ($MSE > 500$; R^2 between -0.45 and -0.90), highlighting its susceptibility to overfitting complex spectral patterns in the absence of ensemble averaging or regularization. These results confirm that advanced boosting and bagging algorithms, particularly when integrated with nonlinear feature extraction techniques such as LLE, are critical for accurate estimation of tea leaf weight from hyperspectral imagery.

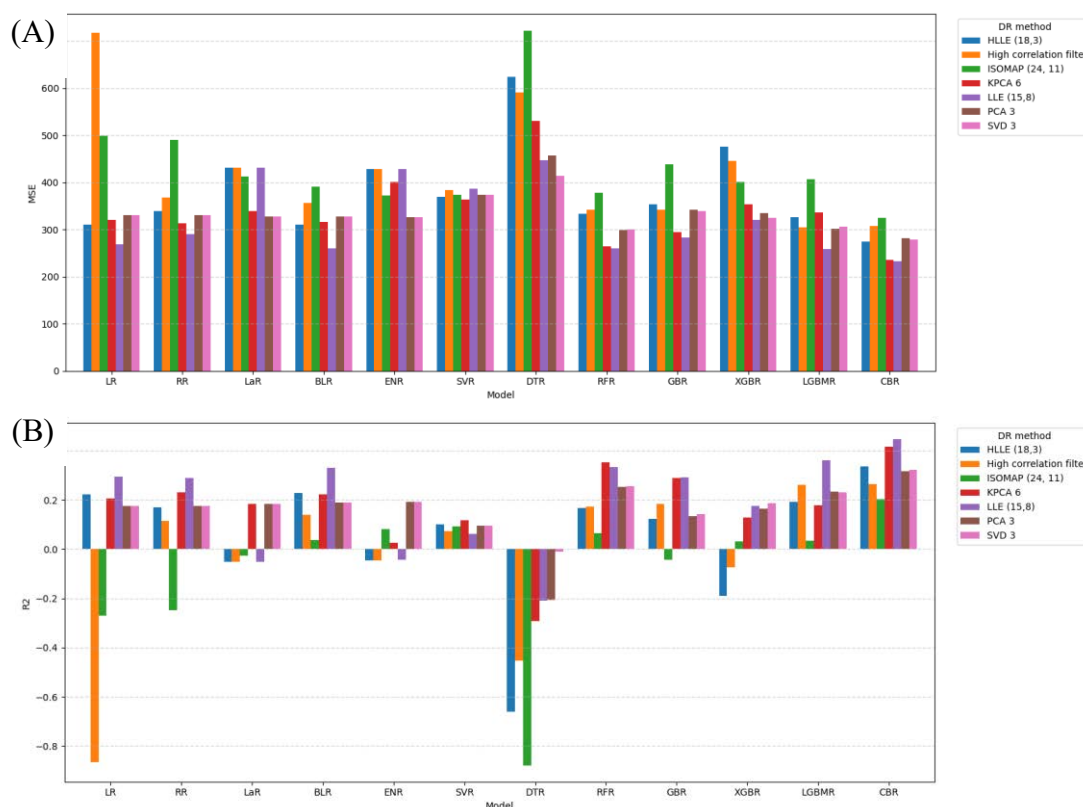


Figure 7. (A) Mean squared error (MSE), and (B) coefficient of determination (R^2) of different dimensionality reduction (DR) methods on machine learning models in estimating tea bud weight.

Model for estimating tea bud count

The tea bud count estimation models demonstrated generally robust performance, with most R^2 values exceeding 0.4 and all remaining positive, indicating meaningful explanatory power across the range of model-

reduction combinations (Figure 8). Among these, the BLR model coupled with LLE ($d = 15$, $k = 8$) achieved the best overall results, yielding the lowest MSE of 583.2 and the highest coefficient of determination ($R^2 = 0.54$). In contrast, models such as ENR, SVR, and the single-instance DTR exhibited comparatively

weak predictive ability, with MSE values ranging from approximately 800 to 1,400 and substantially lower R^2 scores. These results suggest that such models struggle to capture the complex nonlinear relationships between hyperspectral reflectance and bud count without advanced regularization or ensemble mechanisms. Overall, the findings indicate that

Bayesian regression combined with nonlinear dimensionality reduction through LLE provides the most reliable estimates for tea bud count, whereas simpler linear and single-tree models may require additional hyperparameter optimization or larger datasets to achieve comparable accuracy.

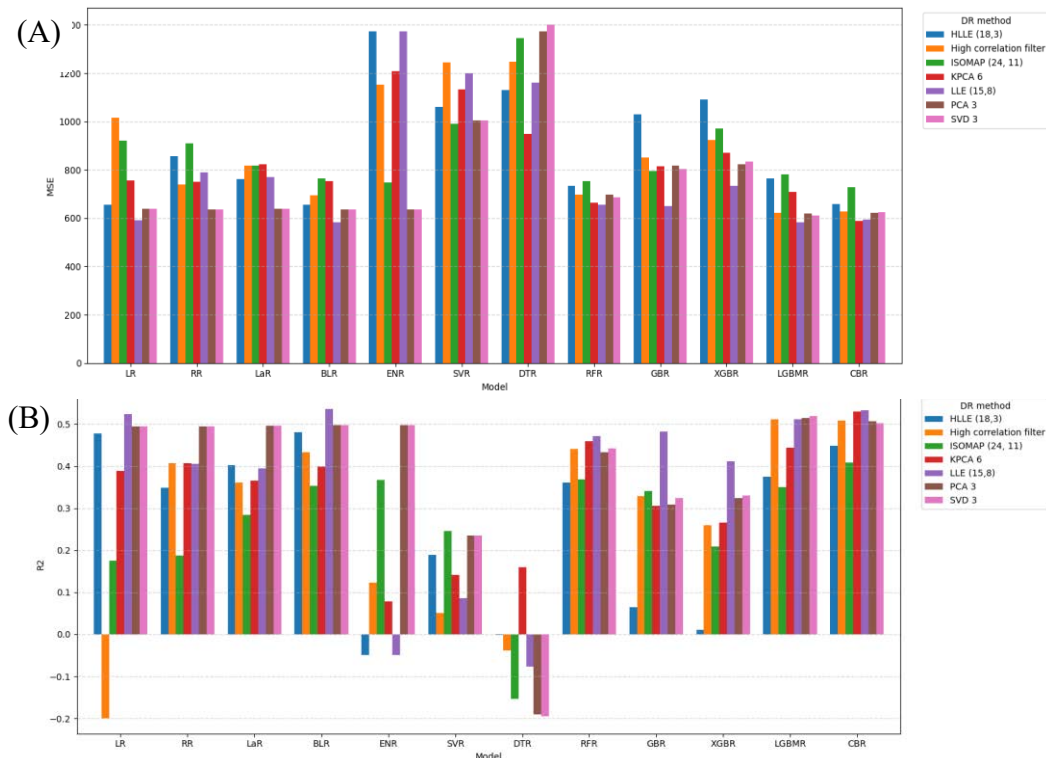


Figure 8. (A) Mean squared error (MSE), and (B) coefficient of determination (R^2) of different dimensionality reduction (DR) methods on machine learning models in estimating tea bud count.

Tea productivity estimated from UAV hyperspectral images

Following model training and evaluation, the best-performing model was applied to the full-field hyperspectral image acquired during the field campaign to assess its predictive performance across the entire tea plantation. Spectral signatures were extracted for each pixel from the hyperspectral data cube and stored as high-dimensional vectors in a compressed (.csv or .gz) file for efficient memory management. The normalized difference vegetation index (NDVI) was then

calculated, and only pixels representing green vegetation were retained for estimation. The filtered spectra were subsequently processed through the regression models, and the spatial outputs are illustrated in Figure 10. Applying the optimized models to the hyperspectral image produced aggregate estimates of 9,878,084 tea buds (Figure 9A), an average bud height of 63.35 mm (Figure 9B) and a total fresh biomass of 5.463 ton (Figure 9C). These values reflect the dense canopy structure of the tea cultivar and confirm healthy plant vigor under favorable growing conditions during the sampling period.

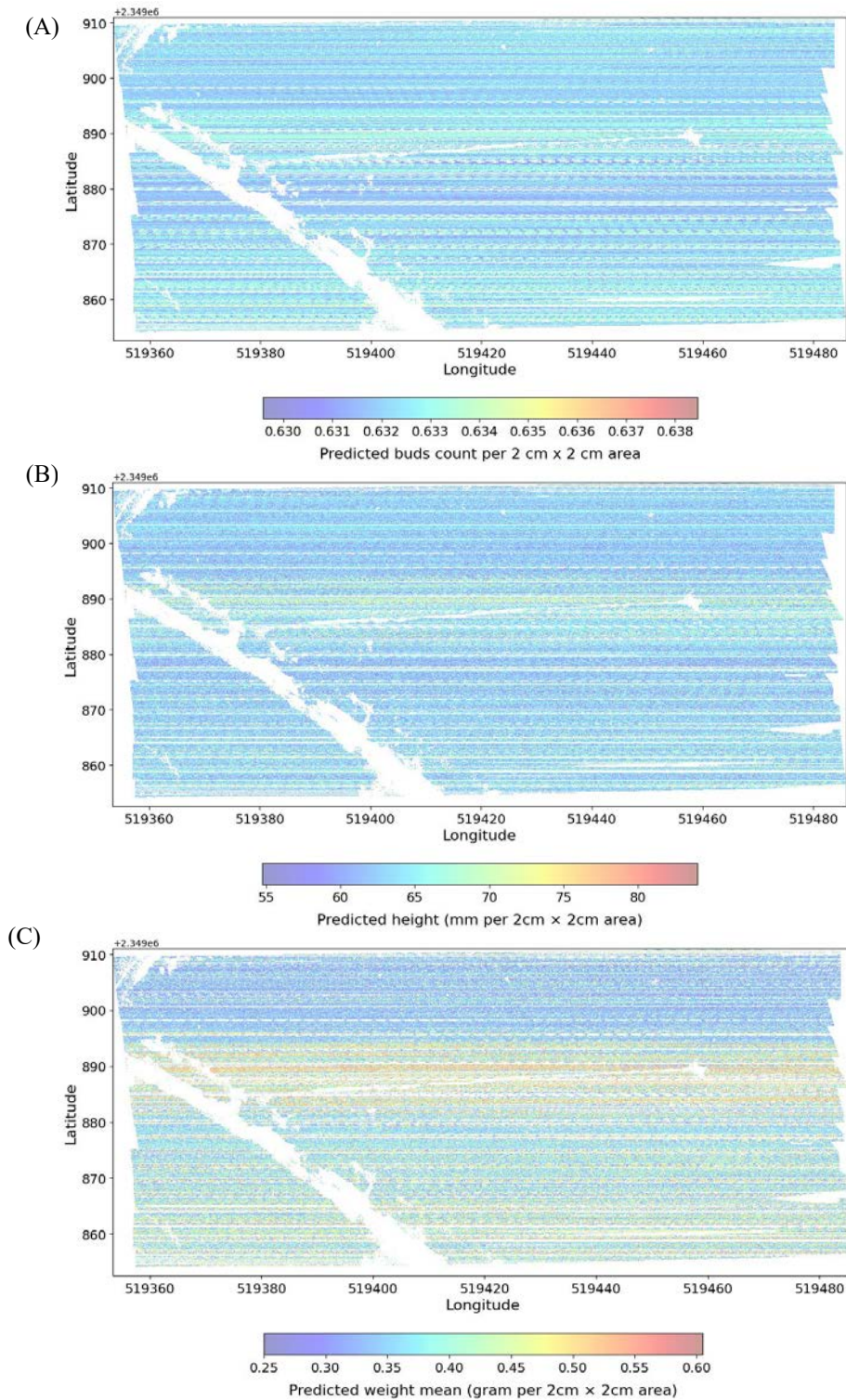


Figure 9. Maps of (A) number of tea buds, (B) tea bud height, and (c) weight of tea buds estimated from UAV hyperspectral images and optimized machine learning models.

DISCUSSIONS

As established in prior studies [3], hyperspectral reflectance effectively captures key plant biophysical traits—such as chlorophyll concentration, leaf area, and biomass—and demonstrates strong correlations with tea-plant attributes including weight, height, and bud count. Consistent with these findings, our analysis revealed significant associations between spectral signatures and all three productivity parameters, reaffirming the suitability of hyperspectral data for tea yield estimation.

Among the tested models, CatBoost combined with non-linear dimensionality reduction techniques (PCA, SVD, KPCA) achieved the highest predictive accuracy (Figures 6–8), whereas simpler learners such as Linear Regression and single-tree Decision Trees exhibited notably poorer performance. Regarding feature-reduction methods, PCA, SVD, and LLE successfully retained the most informative variance in compact feature spaces, while the high-correlation filter discarded important spectral information, resulting in weaker predictions.

Despite these promising outcomes, the study is constrained by a limited sample size. The small number of hyperspectral images and corresponding ground-truth measurements restricted model training and validation, thereby reducing both statistical robustness and generalizability. Additionally, the correlation analysis revealed relatively weak individual spectral–yield relationships, with Pearson coefficients below 0.5 across all band–feature pairs (Figure 5). This suggests that no single wavelength provided a strong predictive signal independently, likely contributing to the moderate model performance. Although CatBoost with dimensionality reduction outperformed simpler approaches, overall error metrics remained high and R^2 values modest, indicating that the models were undertrained. The elevated mean squared error (MSE) and suboptimal R^2 values likely stem from insufficient training data to capture the

complex non-linear relationships between hyperspectral signatures and yield parameters.

When applied to the full-field hyperspectral image, the models further revealed limitations in spatial generalization. The estimated total fresh biomass of approximately 5.46 ton exceeded realistic field expectations, indicating overestimation. This bias likely resulted from the limited diversity of training samples, which did not adequately represent the full spectral variability across the plantation. Consequently, areas with unrepresented spectral characteristics were inaccurately extrapolated, inflating global yield estimates. These findings highlight the need for more comprehensive and representative datasets to enhance model robustness and reliability at the field scale. Furthermore, data acquisition was restricted to the peak harvesting stage. Hence, the developed models are primarily valid for mature tea plants and may not generalize to earlier phenological stages, where canopy structure and spectral responses differ substantially.

Future research will aim to expand the dataset through additional field campaigns and seasonal observations, capturing hyperspectral data throughout various growth stages to improve model generalization. Moreover, integrating established vegetation indices—following the approach of Zhang et al. [3]—with full-spectrum features and exploring data-intensive deep learning architectures could further enhance predictive accuracy and scalability for operational tea yield monitoring.

CONCLUSION

In this study, hyperspectral image analysis was employed to predict tea plant height, fresh leaf weight, and bud count using seven dimensionality-reduction techniques combined with twelve machine-learning algorithms. While several model–reduction combinations achieved strong predictive performance, others yielded only moderate improvements, and a few were largely ineffective. Overall, the highest R^2 values were obtained for tea bud count prediction, whereas models estimating

plant height exhibited the lowest R^2 scores—indicating that height is the most challenging parameter to predict. Among the dimensionality-reduction approaches, Locally Linear Embedding (LLE), Principal Component Analysis (PCA), and Singular Value Decomposition (SVD) consistently produced the most accurate results, whereas the High-Correlation Filter method contributed minimally to downstream model performance.

ACKNOWLEDGEMENT

This study is supported by the project “Application UAV imagery and machine learning for estimating fresh tea productivity”, project code VASTo8.03/25-26 funded by Vietnam Academy of Science and Technology.

REFERENCES

- [1] The Business Research Company. Tea global market report 2024. <https://www.thebusinessresearchcompany.com/report/tea-global-market-report,2024>.
- [2] Chloé Desjonquères. Climate change-adapted tea value chain development in Tuyen Quang, Vietnam. Field practicum research report, msc. in development practice, International Fund for Agricultural Development (IFAD), September 2016.
- [3] Zongtai He, Kaihua Wu, Fumin Wang, Lisong Jin, Rongxu Zhang, Shoupeng Tian, Weizhi Wu, Yadong He, Ran Huang, Lin Yuan, and Yao Zhang. Fresh yield estimation of spring tea via spectral differences in UAV hyperspectral images from unpicked and picked canopies. *Remote Sensing*, 15(4), 2023.
- [4] Siyu Lv, Junhui Wang, Zhengde Wang, Yang Fang, Shanshan Wang, Fuyu Wang, Xiaoxi Wang, Guanzheng Qu, and Wenjun Ma. Rapid and non-destructive estimation of leaf water content in *catalpa bungei* using hyperspectral reflectance and derived data. *Microchemical Journal*, 190:109811, 2023.
- [5] Vietnam Agriculture. Vietnam’s tea exports earned nearly 235 million usd in 11 months. <https://vietnamagriculture.nongnghiep.vn/vietnams-tea-exports-earned-nearly-235-million-usd-in-11-months-d414889.html>, 2023.

DOI: 10.15625/vap.2025.0214

AI4Biochar: Integrating AI-Driven Field Boundary Recognition for Sustainable Biochar Development in Viet Nam

Alessandro Flammini^{1*}, Mehmet Furkan Celik¹, Claudia Paris²,
Francesco Nicola Tubiello¹

¹Food and Agriculture Organization of the United Nations (FAO), Rome, Italy

²ITC – University of Twente, Enschede, The Netherlands

*Email: alessandro.flammini@fao.org

Abstract: Agricultural residues in Viet Nam represent a large, underutilized resource with major potential for circular bioeconomy development. The AI4Biochar initiative, developed by the Food and Agriculture Organization of the United Nations (FAO) in collaboration with the University of Twente, applies artificial intelligence (AI) to automatically delineate agricultural field boundaries from satellite imagery and integrates geospatial, agronomic and sustainability indicators to inform the biochar value chain. This paper summarises and contextualises key findings from the FAO Statistics Working Paper “AI4Biochar: Applying AI-Driven Field Boundary Recognition to the Biochar Sector” (FAO Statistics Working Paper Series No. 25-49, 2025), highlighting its methodological innovation and results from Viet Nam’s Mekong Delta.

The AI4Biochar tool combines machine-learning-based field mapping, residue estimation and sustainability assessment within a single geospatial framework. In a case study in Tri Tôn district (An Giang province), the tool identified over 28 000 rice fields ($\approx 48\,600$ ha) producing $\approx 571\,000$ tonnes of residues annually. Modelling indicated reductions in greenhouse-gas emissions from $89\text{ kt CO}_2\text{eq yr}^{-1}$ to net removals of $864\text{ kt CO}_2\text{eq yr}^{-1}$, 95 percent abatement of carbon-monoxide emissions, creation of $\approx 1\,400$ jobs, and revenue generation equivalent to ≈ 15 percent of district GDP.

By linking AI-based remote sensing with sustainability indicators, AI4Biochar demonstrates how digital innovation can accelerate low-carbon agricultural transformation and investment planning in Viet Nam and beyond.

Keywords: Artificial intelligence, biochar, field boundaries, sustainability indicators, Viet Nam, remote sensing, FAO

INTRODUCTION

Viet Nam is one of the world’s leading producers of rice, coffee and coconut, generating over 150 million tonnes of agricultural residues each year. A large share of these residues, particularly rice straw and husks, are still burned in the open, releasing greenhouse gases (GHGs) and particulate matter that damage the climate, air quality and public health. Converting these residues into biochar through biomass pyrolysis offers a practical pathway to reduce emissions, sequester carbon and restore soil fertility.

Despite its strong potential, the biochar sector in Viet Nam remains at an early stage, constrained by the limited availability of consistent and decision-ready data on biomass resources, residue availability and spatial logistics. The AI4Biochar tool addresses this gap by integrating artificial intelligence, satellite analytics and sustainability modelling to determine where, when and how agricultural residues can be mobilised for biochar production.

This paper builds on the comprehensive FAO Statistics Working Paper No. 25-49 (Conchedda et al., 2025), focusing on the methodological framework and selected empirical results related to environmental and socio-economic outcomes. The analysis highlights key environmental results, avoided emissions from open burning and biochar carbon continuity, alongside economic dimensions, providing a solid basis for policy implementation and investment in Viet Nam's emerging biochar value chains.

METHODOLOGY

AI-Based Field Boundary Delineation

The AI4Biochar tool builds on FAO's crop boundary artificial intelligence workflow (Persello et al., 2023), developed in collaboration with the University of Twente, Faculty of Geo Information Science and Earth Observation (ITC). It uses a U-Net encoder-decoder deep learning segmentation model that was trained and validated with the AI4SmallFarms dataset, which combines Sentinel 2 imagery at 10 metre resolution (Red, Green, and Blue and Near-Infrared spectral bands) with more than 430 000 manually digitised field polygons from Viet Nam and Cambodia.

For the present study, Sentinel-2 Level 2A images were radiometrically and geometrically corrected and obtained using Google Earth Engine. To minimize the effects of cloud contamination, the analysis focused on the dry-season window (December 2020 – March 2021), when cloud cover is minimal. Within this time frame, Sentinel-2 scenes were selected based on cloud cover (<40%) and the quality of the scene classification layer mask, ensuring that only observations with minimal cloud, shadow and cirrus were retained. Later as much as possible cloud free images were available for a tile, a monthly median composite was generated to further suppress atmospheric artefacts.

The supervised deep learning model was trained using binary masks delineating field boundaries. During inference, the model generates 10 metre probability maps showing

the likelihood of a boundary for each pixel. The U-Net was implemented in Python 3.10 using TensorFlow 2.13, with an Adam optimizer (learning rate=0.001, decay rate=0.9) and focal cross entropy loss to mitigate class imbalance between boundary and non-boundary pixels. Training employed 256x256 pixel image patches using early stopping (finished around 35 epoch approx.) and validation on held out test tiles. The U-Net model achieved an average precision of 0.48, recall of 0.33 and F-score of 0.39 across test tiles. These values confirm reliable boundary detection within smallholder mosaics typical of Viet Nam.



Figure 1 Overall workflow of the AI workflow for crop field boundaries delineation
(Note: For each stage, the platform used is reported;
Source: Conchedda et al. (2025))

Post-processing combines morphological segmentation and polygonisation in QGIS to produce a geospatial vector layer of agricultural fields. The morphological post-processing employed a watershed segmentation to ensure closed agricultural field boundary. Polygonization was conducted using Douglas-Peucker simplification with a tolerance 10 meter.

This AI-based crop boundary delineation procedure produces a geospatial vector layer of agricultural fields forming the foundation for the residue estimation and sustainability indicator modules described in following sections.

The tool (python code) is made freely available by FAO at <https://www.fao.org>

/statistics/statistical-capacity-development-test/developing-a-geodatabase-in-support-of-agricultural-planning--project/en.

Integration with Geospatial and Agronomic Data

The delineated fields are enriched with multiple spatial layers:

- Rice-cropping intensity (SEA-Rice-C10 dataset, 10 m);
- Yield distribution (Spatial Production Allocation Model - SPAM 2020 dataset, 10 km);
- Proximity to rice mills, used as proxies for potential pyrolysis units.

In Tri Ton district (An Giang province), 28 102 rice plots were identified, with an average size of 1.75 ha and a total harvested area of $\approx 94\ 000\ \text{ha}\ \text{yr}^{-1}$.

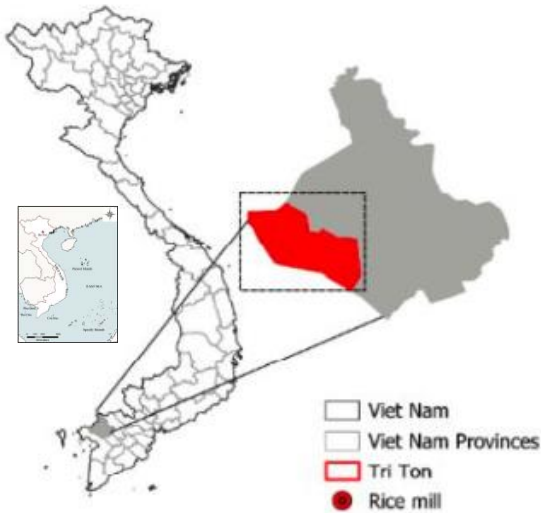


Figure 2. Tri TON district location map (Source: Conchedda et al. (2025))

Sustainability Indicator Modules

The AI₄Biochar framework couples geospatial outputs with sustainability assessments following two FAO tools:

- the Bioenergy and Food Security Rapid Appraisal (BEFS RA); and
- the Global Bioenergy Partnership (GBEP) sustainability indicators.

Four key indicators were computed for two scenarios: baseline (open burning) and target (biochar production integrated at rice mills) (Tab.1).

Table 1. Main sustainability indicators used in the AI₄Biochar assessment framework

Pillar	Indicator	Unit	Data Source
Environmental	Greenhouse-gas emissions	t CO ₂ eq yr ⁻¹	IPCC (2006) factors
Environmental	Non-GHG emissions (CO, NO _x , SO _x , PM)	t yr ⁻¹	EEA (2019) coefficients
Social	Job creation	Jobs yr ⁻¹	Field surveys, ILO standards
Economic	Income generation	JSD yr ⁻¹	Local market data

The tool's Excel-based calculator (also available at <https://www.fao.org/statistics/statistical-capacity-development-test/developing-a-geodatabase-in-support-of-agricultural-planning--project/en>) allows parameter adjustment and automatic integration of results into GIS layers.

RESULTS

Residue Potential

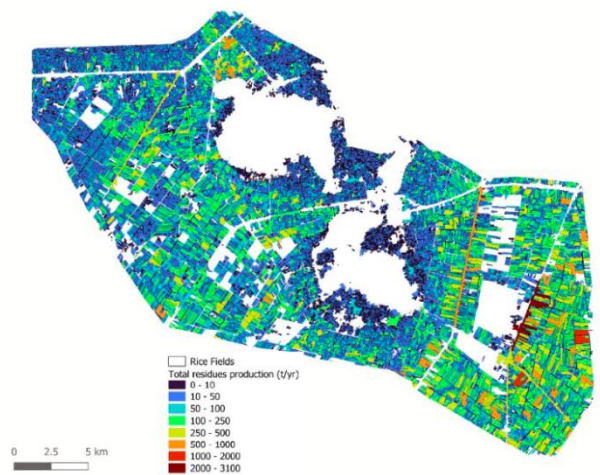


Figure 3. Rice residues (straw + husks) by field, Tri Ton district (Source: Conchedda et al. (2025))

The model estimated $\approx 571\,000$ tonnes of rice residues yr^{-1} in Tri Ton district (Fig. 3), composed of 85 percent straw and 15 percent husks. Assuming a 42 percent conversion yield, potential biochar production was $\approx 258\,000$ tonnes yr^{-1} .

Environmental Outcomes

Compared with the baseline, the target scenario achieved a ten-fold net reduction in GHG emissions, equivalent to a shift from 89 kt $\text{CO}_2\text{eq yr}^{-1}$ to -864 kt $\text{CO}_2\text{eq yr}^{-1}$ due to carbon

sequestration (Figure 4). Non-GHG pollutants declined sharply: CO -95 percent, NOx -86 percent, SOx -100 percent, PM -100 percent.

Socio-Economic Impacts

At full residue utilisation, biochar deployment in Tri Tôn district could generate $\approx 1\,467$ permanent jobs, corresponding roughly to the current unemployed population, and \approx USD 23 million yr^{-1} in revenue (about 15 percent of local GDP) (Table 2).

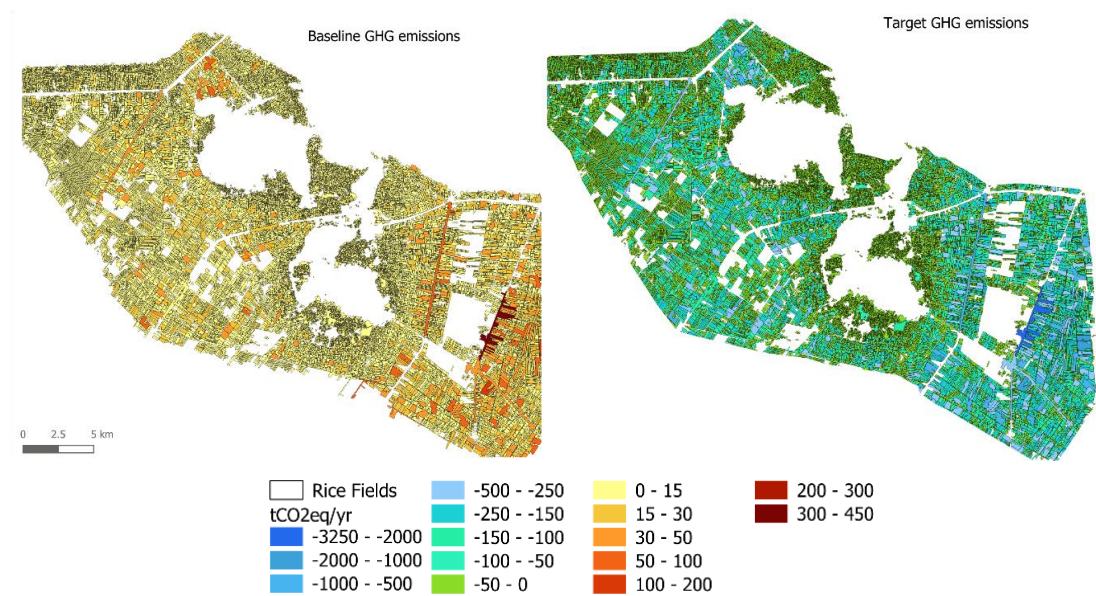


Figure 4. GHG emissions maps, baseline vs target
Source: Conchedda et al. (2025)

Table 2. Summary of results for Tri Ton District, Viet Nam (2020 reference year)

Indicator	Baseline	Target	Change
GHG emissions (t $\text{CO}_2\text{eq yr}^{-1}$)	89 097	$-864\,345$	$> 900\%$ reduction
CO emissions (t yr^{-1})	34 824	1 809	-95%
Biochar output (t yr^{-1})	0	258 445	+ 258 445
Jobs created (no.)	0	1 467	+ 1 467
Revenue (USD yr^{-1})	0	23 260 000	+ 23 M

DISCUSSION

The AI4Biochar framework exemplifies how AI and open satellite data can operationalise circular-economy principles in agriculture. By linking crop-boundary

delineation, residue estimation and sustainability modelling, it supports both policy formulation and private-sector investment in low-carbon value chains.

While results for rice are promising, extending the approach to perennial crops

(coffee, coconut) will require refined models and additional field data. Limitations remain in using global datasets (e.g. SPAM 2020) whose spatial resolution introduces uncertainty.

Limitations of global datasets remain a key source of uncertainty. SPAM 2020 provides crop yield and area distributions at 10 km resolution based on modeled disaggregation of national statistics, which may not capture smallholder variability typical of Viet Nam's delta regions. Similarly, EEA (2019) emission factors are derived from European conditions and applied globally, which may not reflect local burning efficiencies or residue moisture content. These factors can influence emission and residue estimates at district scale, highlighting the need for future integration of national statistical data and locally measured parameters.

Future developments should explore radar imagery, seasonal composites and scalable cloud computing infrastructures for national-level applications.

CONCLUSIONS

AI4Biochar demonstrates that integrating AI-based remote sensing with sustainability frameworks enables evidence-based planning for agricultural residue management. The approach provides:

- detailed spatial information on feedstock availability;
- quantified GHG and pollutant mitigation;

European Environment Agency.
<https://doi.org/10.2800/293657>.

FAO (2023). *Biochar in Sustainable Soil Management: Potential and Constraints*. Food and Agriculture Organization of the United Nations. <https://openknowledge.fao.org/handle/20.500.14283/cc8733en>.

Persello, C., Grift, J., Fan, X., Paris, C., Hänsch, R., Koeva, M., & Nelson, A. (2023). AI4SmallFarms: A Dataset for Crop Field Delineation in Southeast Asian Smallholder Farms. *IEEE Geoscience and Remote Sensing Letters*, 20, 1–5. <https://doi.org/10.1109/LGRS.2023.3323095>.

- socio-economic co-benefits including jobs and income; and
- a decision-support basis for biochar market expansion.

Beyond Viet Nam, the methodology can inform regional bioeconomy strategies in Southeast Asia and other emerging agricultural economies.

ACKNOWLEDGEMENT

This paper is an abridged version of AI4Biochar: Applying AI-Driven Field Boundary Recognition to the Biochar Sector (FAO Statistics Working Paper Series No. 25-49, 2025), jointly prepared by FAO and the University of Twente. Readers are encouraged to consult the full publication for detailed methodology, datasets and code references. The views expressed in this paper reflect those of the single authors, and not the official view of the organizations they work for.

REFERENCES

- Conchedda, G., Flammini, A., Colangeli, M., Testa, L., Casse, L., Piccoli, M., Obli-Laryea, G., Celik, F., Paris, C., Persello, C., Nelson, A., Morese, M. M., & Tubiello, F. N. (2025). *AI4Biochar: Applying AI-Driven Field Boundary Recognition to the Biochar Sector*. (FAO Statistics Working Paper Series No. 25-49). Food and Agriculture Organization of the United Nations. <https://doi.org/10.4060/cd6383en>
- European Environment Agency (EEA). (2019). *EMEP/EEA Air Pollutant Emission Inventory Guidebook 2019: Technical guidance to prepare national emission inventories*. (EEA Report No 13/2019). Copenhagen:
- Tripathi, M., Sahu, J. N., & Ganesan, P. (2016). Effect of Process Parameters on Production of Biochar from Biomass Waste through Pyrolysis: A Review. *Renewable and Sustainable Energy Reviews*, 55, 467–481. <https://doi.org/10.1016/j.rser.2015.10.122>.
- Varela Milla, O., Rivera, E. B., Huang, W. J., Chien, C. C., & Wang, Y. M. (2013). Agronomic Properties of Rice Husk Biochar and Its Effect on Crop Growth. *Journal of Soil Science and Plant Nutrition*, 13(2), 251–266. <https://doi.org/10.4067/S0718-95162013005000022>.

DOI: 10.15625/vap.2025.0215

Forecasting Groundwater Level Decline and Saltwater Intrusion in the Coastal Aquifers of the Red River Delta by 2030 and 2040

Trung Dang Tran¹, Thu Trinh Hoai^{2*}, Hung Nguyen Kim³, Huong Tran Thi Thuy², Anh Bui Thi Bao², Hang Pham Thi Thu², Tung Nguyen Xuan², Hung Pham Duc², Ngan Phan Kieu²

¹National Centre for Water Resources Planning and Investigation, Sai Dong, Long Bien, Ha Noi

²Institute of Earth Sciences, Vietnam Academy of Science and Technology, Huynh Thuc Khang, Dong Da, Ha Noi

³Haskoning Vietnam, La Thanh, Dong Da, Ha Noi

*Email: ththu@ies.vast.vn

Abstract: The coastal zone of the Red River Delta (RRD), covering four provinces—Thai Binh, Nam Dinh, Hai Phong, and Ninh Binh - is currently facing serious challenges in water resources, particularly the risk of saltwater intrusion (SWI) into aquifers. This study applies the MODFLOW groundwater flow model in combination with the MT3DMS solute transport module to simulate groundwater level decline and salinity intrusion in Quaternary aquifers (qh_2 , qh_1 , qp) through 2040. Two groundwater exploitation scenarios were developed: (1) maintaining current extraction levels, and (2) increasing pumping rates at selected centralized water supply stations. The results indicate a significant decline in groundwater levels under Scenario 2. The area of freshwater in the qp aquifer decreases from 2,621 km² (2025) to 2,492.8 km² (2040), and in the qh_2 aquifer from 2,465 km² to 2,129 km². The qh_1 aquifer has been largely salinized and is rarely exploited, showing minimal variation. The study recommends enhancing groundwater monitoring, regulating extraction, rational wellfield planning, and developing artificial recharge solutions. The modeling results provide a scientific basis for groundwater resource planning and climate change adaptation in the coastal region of the RRD.

Keywords: Groundwater saltwater intrusion; groundwater level decline; MODFLOW model; Quaternary aquifers; groundwater resource planning; Coastal Red River Delta.

INTRODUCTION

The Red River Delta (RRD) is one of the two largest plains in Vietnam, playing a central role in the country's economy, society, agriculture, industry, and national water security. With a natural area of approximately 21,260 km², a population exceeding 22.9 million people, and the highest population density in the country, the RRD plain serves not only as the nation's second-largest rice granary but also as a region experiencing rapid industrial development, service sector growth, and urbanization. However, this region is facing numerous serious challenges regarding water resources, particularly the risk of saline intrusion (SI) into coastal groundwater aquifers, threatening water security, agricultural production, domestic water supply, and sustainable development.

Groundwater saline intrusion (GSI) can be divided into two main types: modern saline intrusion and paleosaline intrusion. Modern saline intrusion occurs when seawater penetrates groundwater aquifers due to declining groundwater levels or increased groundwater extraction, creating favorable

conditions for saltwater from the sea to intrude deep into the mainland. This condition primarily occurs in coastal areas with intensive groundwater exploitation and natural factors such as tides, sea level changes, and freshwater upwelling. Globally, modern saline intrusion is a serious problem in regions such as the Middle East, Southeast Asia, and some island nations, where uncontrolled groundwater extraction combined with sea level rise due to climate change causes significant impacts (Van et al., 2019).

Paleo-saline intrusion is the phenomenon of ancient saltwater preserved in marine sediment layers from previous periods, potentially due to sea-level changes during historical periods (such as the Quaternary). This condition primarily occurs in coastal areas with special geological and topographical characteristics, such as the Red River Delta in Vietnam. Research on paleo saline intrusion has indicated that in Holocene and Pleistocene aquifers in coastal areas, ancient marine sediment layers containing latent saltwater can intrude into freshwater aquifers when groundwater levels change due to excessive extraction (Luu et al., 2012; Larsen et al., 2024).

In Vietnam, the coastal area of the RRD is the region primarily affected by paleosaline intrusion, where marine sediment layers from previous periods still contain latent saltwater that can intrude into groundwater when groundwater levels decline due to excessive extraction. Coastal provinces such as Thai Binh, Nam Dinh, Hai Phong, and Ninh Binh are currently facing this phenomenon, which reduces groundwater quality and directly affects water supply needs for domestic use and agricultural production (Van et al., 2019). A report by the Ministry of Natural Resources and Environment (2016) indicates that although sea level rise and tides have an influence, the existence of ancient saltwater in sediments is the primary factor causing saline intrusion in this region (MONRE, 2016).

In this study, the MODFLOW method was selected due to its accuracy and capability to simulate groundwater flow and salt

propagation in aquifers. MODFLOW is a mathematical model developed by the United States Geological Survey and has been widely applied in groundwater and saline intrusion research. MODFLOW helps accurately model hydrodynamic processes, thereby forecasting future SI conditions and supporting effective water resource management decisions (Harbaugh, 2005).

MATERIALS AND METHODS

Study area

The RRD plain region is a young delta formed by the sediment deposition processes of the Red River and Thai Binh River systems, characterized by low, flat terrain with numerous depressions, marshes, coastal wetlands, and dense dike systems. This topography creates favorable conditions for agricultural development and aquaculture but also increases the risk of flooding, waterlogging, and saline intrusion, particularly in coastal areas such as Thai Binh, Nam Dinh, Ninh Binh, and Hai Phong.

The coastal climate of the RRD belongs to the humid tropical monsoon type, with hot and humid summers with heavy rainfall, and cold, dry winters. Annual average rainfall ranges from 1,500-2,000 mm, distributed unevenly by season and space. Climate variability, especially extreme phenomena such as droughts, heavy rains, storms, and sea level rise, significantly impacts surface water regimes, groundwater, and saline intrusion processes.

Geological structure, Hydrogeology, and Aquifer layers: The geological foundation of the RRD consists of ancient basement rocks covered by Neogene sediments thousands of meters thick, followed by Quaternary sediment layers (Holocene, Pleistocene) 80-100 m thick in the center of the plain. The main aquifers include:

- Holocene Aquifer (qh): Widely distributed in coastal areas at depths of 5-30 m, divided into: Upper Holocene aquifer (qh₂) consisting of Thai Binh Formation Sediments Lower Holocene aquifer (qh₁) consisting of Hai Hung Formation Sediments The composition

mainly consists of sand, silt, and clay with good water-bearing capacity but susceptible to saltwater influence due to proximity to the ground surface and maritime.

- Pleistocene Aquifer (qp): Located deeper (17.5-156 m), composed of coarse-grained sediments from: Le Chi Formation, Ha Noi Formation (qp₁), and Vinh Phuc Formation (qp₂). The aquifer thickness ranges from 10 to 85 m, with a composition mainly of sand and gravel interbedded with clay layers. This represents the most important freshwater source in the coastal RRD region. However, this layer also faces risks of paleosaline intrusion and impacts from overlying and underlying layers due to excessive extraction.

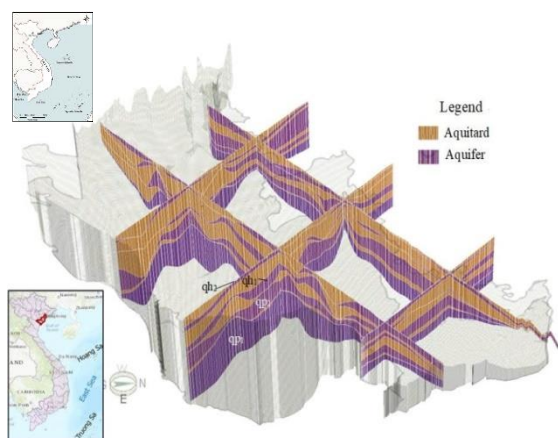


Figure 1. Hydrogeological structural model of the coastal RRD region

Theoretical principles

MODFLOW enables simulation of groundwater movement and saline ions in hydrodynamic systems, helping to forecast saline intrusion into groundwater.

The variation in groundwater level elevation is described by a single partial differential equation (Anderson et al., 2015) as follows:

$$\frac{\partial}{\partial x}\left(K_{xx}\frac{\partial h}{\partial x}\right)+\frac{\partial}{\partial y}\left(K_{yy}\frac{\partial h}{\partial y}\right)+\frac{\partial}{\partial z}\left(K_{zz}\frac{\partial h}{\partial z}\right)\pm W$$

$$=S_s\frac{\partial h}{\partial t}\tag{1}$$

In which:

$K_{xx} = K_{xx}(x, y, z)$, $K_{yy} = K_{yy}(x, y, z)$, $K_{zz} = K_{zz}(x, y, z)$ are the hydraulic conductivity coefficients of the aquifer in the x, y, z directions.

H is the groundwater level height at position (x, y, z) at time t;

W is the recharge or discharge value of groundwater calculated at position (x, y, z) at time t, $W = W(x, y, z, t)$.

$S_s = S_s(x, y, z)$ is the specific storage coefficient.

Equation (1) is solved with boundary conditions:

+ Type I boundary condition (Dirichlet boundary): cells where the water level is predetermined and this value remains constant throughout the calculation period, $H = h(t)$.

+ Type II boundary condition (Neumann flow boundary): cells where the flow rate through the boundary is predetermined throughout the calculation time step $Q = q(t)$.

- + Type III boundary condition (mixed Cauchy boundary): boundary condition where the flow rate at the boundary depends on the water level $Q = f(H)$.

For the groundwater saline intrusion propagation process, it is described by the following partial differential equation (Anderson et al., 2015):

$$\frac{\partial(\theta C^k)}{\partial t} = \frac{\partial}{\partial x_i}(\theta D_{ij} \frac{\partial C^k}{\partial x_j}) - \frac{\partial}{\partial x_i}(\theta v_i C^k) + q_s C_s^k + \Sigma R_n \quad (2)$$

In which:

C^k is the dissolved concentration of substance k, ML^{-1} ;

θ is soil porosity, dimensionless.

t is time, T;

xi is distance, L;

D_{ij} is the dispersion coefficient, L^2T^{-1} ;

v_i is seepage velocity, LT^{-1} ;

q_s is the flow rate per unit volume, T^{-1} ,

C_s^k is the concentration of substance k , ML^{-3} ;

ΣR_n is the component when considering chemical reactions, $ML^{-3}T^{-1}$.

Similarly, equation (2) is solved with boundary conditions:

+ Type I boundary condition: predetermined pollutant concentration condition (also called Dirichlet boundary condition). This is a boundary where concentration is predetermined, and this value remains constant throughout the calculation time step.

+ Type II boundary condition: predetermined supply rate condition (also called Neumann boundary condition). This is a boundary where the supply flow rate through the boundary is predetermined throughout the calculation time step. In cases with no supply, the supply rate is set to zero.

+ Type III boundary condition: boundary condition where the supply rate at the boundary depends on concentration (also called Cauchy or mixed boundary condition).

Input Data and Model Development for the Coastal RRD Region

To forecast saline intrusion related to groundwater exploitation in the coastal RRD region, we rely on recent research data as the basic input source for constructing the groundwater flow model.

Model Grid Design: The modeling area covers 15,278 km², expanded compared to the calculation area. According to some investigation results, the Pleistocene aquifer in the eastern part of the coastal RRD region extends seaward and is not limited by the coastline, making model expansion necessary. The model grid is divided into 206 rows and 192 columns with a square size of 600x600m. Specifically, in the Nam Dinh and Thai Binh areas, the grid is divided into 300x300m

squares to ensure accuracy due to the high concentration of well fields in these areas.

Hydrogeological map data at 1:200,000 scale (Minh, 2005).

Topographic surface data: In the model, the topographic surface is constructed based on elevation points from 1:50,000 scale topographic maps and elevation points from monitoring wells and exploration wells investigated previously (Giang, 2018 & Ha, 2010).

Hydrogeological stratification data: Data used to divide model layers includes 195 investigation boreholes from previous phases (Giang, 2018 & Nhan et al., 2022). The hydrogeological stratification structure is divided into 8 layers in the model:

Table 1. Aquitards and Aquifers in the Coastal RRD Region (Giang, 2018)

No.	Hydrogeological stratigraphic units	Symbol
1	Surface aquitard in Holocene sediments	Bm aquitard
2	Aquifer in upper Holocene sediments	qh ₂ aquifer
3	Aquitard in Holocene sediments	Y1 aquitard
4	Aquifer in lower Holocene sediments	qh ₁ aquifer
5	Aquitard in Holocene-Pleistocene sediments	Y2 aquitard
6	Confined aquifer in upper Pleistocene sediments	qp ₂ aquifer
7	Aquitard in Pleistocene sediments	Y3 aquitard
8	Confined aquifer in lower Pleistocene sediments	qp ₁ aquifer

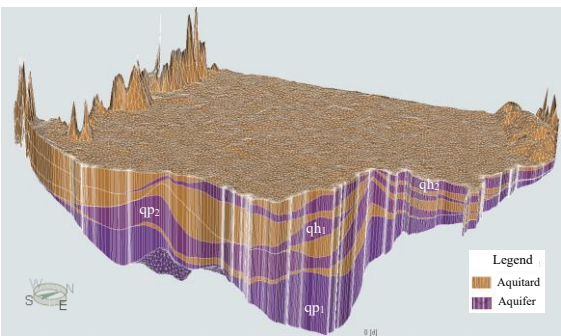


Figure 2. 3D simulation of topography and model structure

- Current groundwater exploitation data compiled from multiple sources for Thai Binh, Nam Dinh, and Ninh Binh provinces according to the project "Investigation and assessment of self-protection capacity of aquifers in the coastal region of the Northern Delta (Thai Binh, Nam Dinh, and Ninh Binh provinces)" (Giang, 2018), and Hai Phong (source: Hai Phong Department of Agriculture and Rural Development).

Table 2. Current water exploitation status of coastal RRD provinces

Province	Main exploitation types	Groundwater exploitation flow rate (m ³ /day)	Exploited aquifer
Thai Binh	- Centralized water supply - Individual - Rural	- Centralized: 6,424 - Individual: 3,126 - Rural: 303,840	qp, qh ₁ , qh ₂
Nam Dinh	- Centralized water supply - Individual - Rural	- Centralized: 4,198 - Individual: 18,517 - Rural: 131,448	qp
Ninh Binh	- Rural	- Rural: 46,547	qp, qh ₂
Hai Phong	- Centralized water supply - Rural	- Centralized: 2,919 - Total GW exploitation: ~35,000	qp

- Groundwater investigation data from coastal RRD provinces (source: NAWAPI (NAWAPI, 2023)).

- Groundwater recharge data for the coastal RRD region were calculated and determined according to previous research results in the delta region (Nhan et al., 2022).

- Hydraulic connection data between river water and groundwater determined by cluster pumping test results in Thai Binh to determine riverbed resistance (Huy, 2022).

The above data is used as the foundation and basis for the groundwater flow model that has been constructed (Ha, 2010 & Trung et al.,

2018). The model was built using Visual MODFLOW software by Schlumberger (Namitha & Sreelekshmi, 2019; Hariharan & Shankar, 2017) and calibrated based on national and local monitoring data (Hanoi, Nam Dinh, and Thai Binh) and some of the most recent investigation results.

Hydrogeological parameters:
Hydrogeological parameters, including hydraulic conductivity (K), are assigned in the model based on previous studies that have been updated most recently (Giang, 2018; Nhan et al., 2022, and Trung et al., 2024), and Storativity (S) is determined according to cluster pumping test results in Thai Binh (Giang, 2018).

Table 3. Hydrogeological Parameters of Aquifers in the Model

No.	Aquifer	Hydraulic conductivity K (m/day)	Sy – Specific yield	Ss – Specific storage	Total porosity (n) and effective porosity (ne)
1	qh ₂	0.1 – 0.5	0.10 – 0.12	–	n = 0.15; ne = 0.12
2	qh ₁	0.01 – 6.4 (TB: 2.3)	0.10 – 0.15	0.003	n = 0.18; ne = 0.11
3	qp (qp ₂ & qp ₁)	0.04 – 106.5 (TB: 11.65)	–	0.0122	n = 0.18; ne = 0.11

Boundary conditions for the groundwater-flow model were defined to be consistent with the regional hydrogeological setting and with previous models developed for the coastal Red River Delta (Ha, 2010; Giang, 2018; Trung et al., 2018; NAWAPI, 2023). Along the Red River–Thai Binh river network, head-dependent General Head Boundary (GHB) cells were assigned. River stages were derived from gauged water levels, and riverbed conductance values were calculated from cluster pumping tests, yielding typical conductance values of about **80 - 150 m²/day** for the main river reaches (Giang, 2018).

The bedrock boundary condition along the southwestern bedrock margin of Hanoi City was determined based on recent research

by flux boundary (Huy, 2022). The boundary inflow ranges from **19,815** to **20,349** m³/day, with an average of about **19,860** m³/day into the aquifer system. Of this, the qh aquifer receives between **9,063** and **9,867** m³/day, with an average of about **9,800** m³/day, while the qp aquifer is supplied through the bedrock margin boundary with between **9,948** and **11,287** m³/day, averaging about **10,060** m³/day.

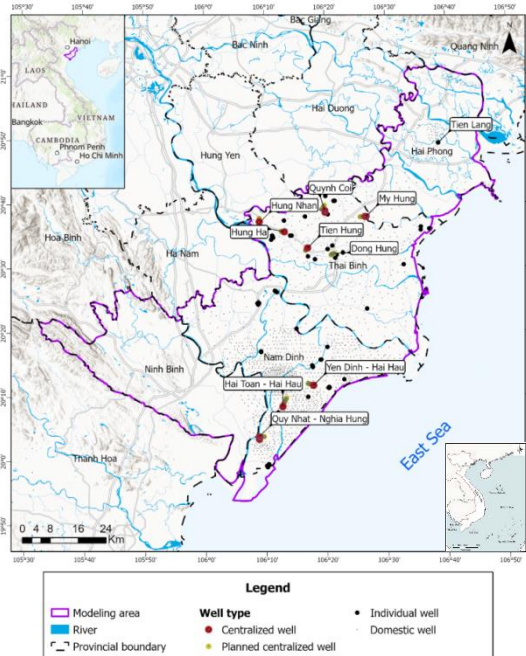


Figure 3. Current GW exploitation status of the coastal RRD region assigned in the model

Recharge boundary based on research by (Nhan et al., 2022) using remote sensing image results for factors affecting groundwater recharge and overlaying image layers using GIS techniques. To objectively determine the weights of factors affecting groundwater recharge through the Analytic Hierarchy Process (AHP) model (Saaty, 2008). Additionally, results were verified using the radioactive isotope ³H method to ensure accuracy. Results show that the coastal RRD region's GRI index for most areas ranges from 0.08-0.16, corresponding to recharge amounts of approximately **188 mm/year** (Nhan et al., 2022).

Evapotranspiration losses were simulated with the ET package using maximum ET rates

derived from long-term meteorological records and an extinction depth of about **4 m** (Giang, 2018), consistent with the shallow water-table conditions of the qh aquifer.

The sea boundary condition is based on assumptions from (Van et al., 2022), assuming that the aquifer extends into the sea due to elevation characteristics and depth distribution of the Pleistocene aquifer bottom, leading to simulation of Type I boundary conditions with determined water level (Constant Head – CH) with water level values based on sea level at Hon Dau station offshore (Trung et al., 2018).

These boundary conditions were kept fixed during calibration; only aquifer parameters (hydraulic conductivity K, specific storage Ss, specific yield Sy) and recharge multipliers were adjusted within the ranges reported in previous studies.

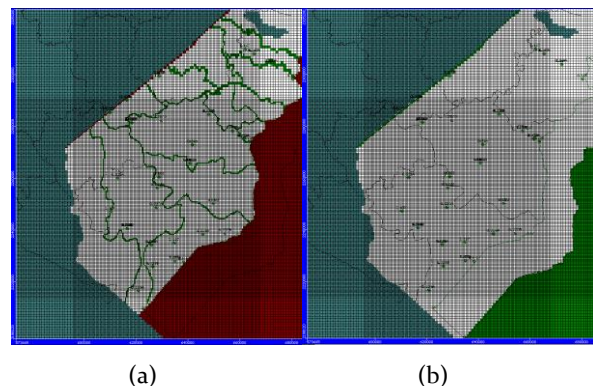


Figure 4. Coastal boundary and river boundary of the study area a) Holocene aquifer b) Pleistocene aquifer

Boundary conditions for transport model: Based on total dissolved solids (TDS) zoning maps of aquifers according to previous research results on fresh-saline boundaries (Giang, 2018; Ha, 2006 and NAWAPI, 2023) combined with some geophysical research results determining saline intrusion boundaries in coastal provinces Nam Dinh and Thai Binh (Thu & Trung, 2012; Trung & Thu, 2013; Thu et al., 2008, 2014, 2016 and Hang et al., 2015). Areas with high total mineralization where $TDS \geq 1500 \text{ mg/l}$ are assumed to have constant concentration throughout the simulation process.

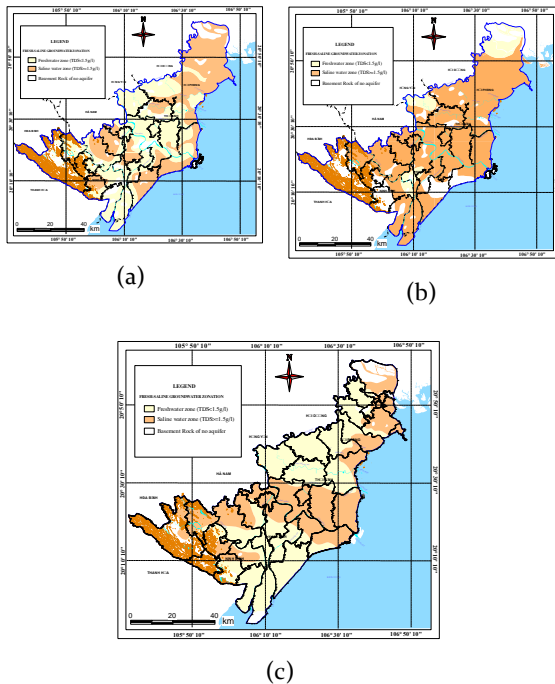


Figure 5. TDS zoning maps (g/l) of aquifers (a) qh_2 ; (b) qh_1 and (c) qp_1 and qp_2 (Giang, 2018; Ha, 2006; NAWAPI, 2023; Thu et al., 2008, 2012, 2013, 2014, 2016; Hang et al., 2015)

Initial concentration of aquifers for the groundwater area is divided into 2 zones: areas 1-2 km from the saline boundary take concentration $C_0 = 1300 \div 1450$ mg/l, areas farther from the saline boundary take $C_0 = 500-700$ mg/L.

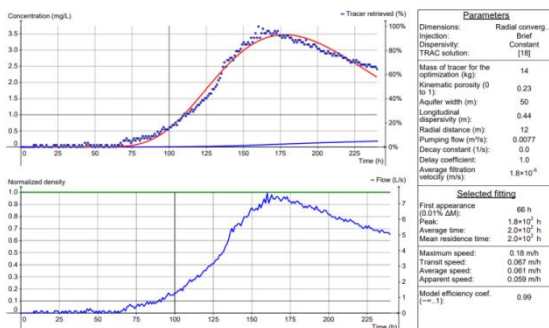


Figure 6. Salt tracer test results in Thai Binh province (Giang, 2018)

Parameters for effective porosity and hydrodynamic dispersion coefficient in the model were selected based on salt tracer test results in the qp_1 aquifer in Thai Binh province (Giang, 2018). In this test, the central pumping

borehole operated at a constant flow rate $Q = 7.72$ L/s, with the salt injection borehole located 12m from the central pumping borehole.

Calculation results yielded an effective porosity $n_e = 0.23$ and longitudinal dispersivity $\alpha_l = 0.44$. Transverse and vertical dispersion coefficients were determined relative to longitudinal dispersivity:

- The ratio of transverse dispersion coefficient/longitudinal dispersion coefficient = 0.1 (i.e., longitudinal dispersivity $\alpha_l = 10 \alpha_t$).
- The ratio of vertical dispersion coefficient/longitudinal dispersion coefficient = 0.01.

For major cations and anions in water, the diffusion coefficient ranges from 1×10^{-9} to 2×10^{-9} m²/s (Fetter, 2001). The diffusion coefficient of Na^+ at 20°C for clean water $D_a = 1.33 \times 10^{-9}$ m²/s = 0.0001232 m/day (Fetter, 2017).

RESULTS AND DISCUSSION

Model Calibration Results

The model cannot completely reproduce the natural world due to the complexity of the spatial and temporal boundaries and parameters (Anderson et al., 2015). As a consequence, it is necessary to calibrate the model and evaluate the accuracy of the model by comparing simulated results with field observation data.

During the calibration process for the groundwater flow model, parameters and boundary conditions are adjusted in order to produce a model output that is equivalent to the observed data. By solving the inverse problem, where head observations serve as the dependent variable in the governing equation and are used to determine parameter values, this approach is known as history matching (Figure 8, Figure 9). After running the model, the PEST (Parameter Estimation) program was used to adjust parameters automatically so that the simulated values were as close to the observed values as possible. Adjusted parameters in this problem are hydraulic

conductivity, specific storage, and specific yield. In addition, boundary conditions such as recharge, evapotranspiration, and surface water levels are modified.

The model was calibrated by comparing calculated groundwater levels from the model with actual observed water levels. Calibration was performed using transient state problems and utilized national and local monitoring facilities (Nam Dinh, Thai Binh) from 1/2003 to 12/2024. Monitoring data used for calibration included 40 monitoring facilities, of which 16 monitored the Holocene aquifer and 24 monitored the Pleistocene aquifer (Figure 7). Monitoring data is periodically compiled and stored at the National Water Resources Planning and Investigation Center (NAWAPI, 2023) and at the Nam Dinh and Thai Binh Departments of Natural Resources and Environment.

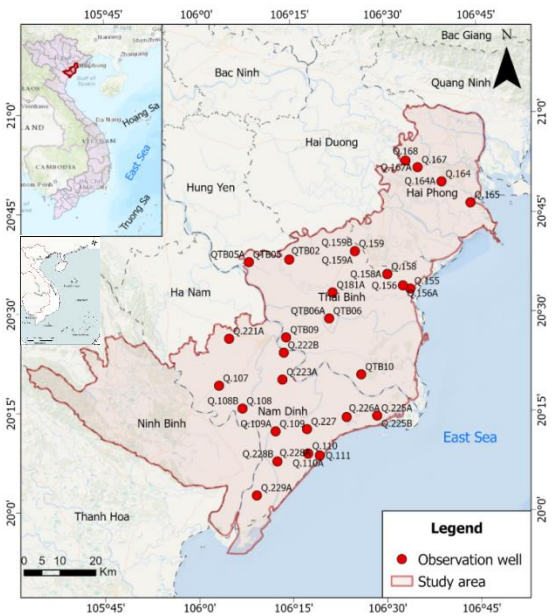


Figure 7. Monitoring stations used for model calibration in the coastal RRD plain region

Besides the visual representations of the calibration results (Figure 8, Figure 9), quantitative summary statistics are calculated to evaluate the goodness of the matching between model simulation and observation data (Figure 10). Statistics parameters commonly used to evaluate model errors

include maximum and minimum error, mean error, mean absolute error, and normalized root mean squared error (Anderson et al., 2015).

Results comparing ground water levels (GWL) over time at Holocene aquifer monitoring facilities (Figure 8, Figure 11a) and Pleistocene aquifer facilities (Figure 9, Figure 11b) are presented below, evaluating errors between modeled water levels and actual observed water levels:

Results of error assessment between measured water levels and observed water levels at monitoring facilities in the coastal RRD region are shown in Figure 11. Model error assessment results for the Holocene aquifer show the maximum error was 1.177 m at facility Q.108, the minimum error was 0.0 m at facility Q.107, the mean error was -0.042m, the mean absolute error was 0.261, and the normalized root mean square error (NRMS) was 9.06%. For the Pleistocene aquifer at monitoring facilities, results show maximum error was 4.96m at monitoring facility P.73a, minimum error 0.0m at Q.164a, relative error 0.067m, absolute error 0.906m, and NRMS 2.621%.

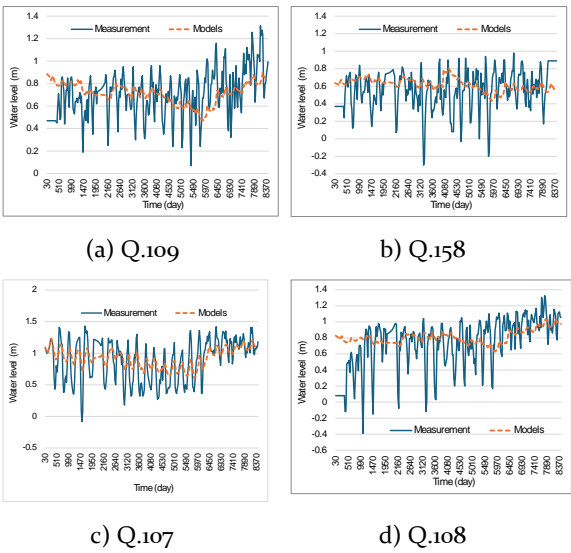


Figure 8. Error between modeled water levels and actual observed water levels in the Holocene aquifer at monitoring stations. a). Q.109; b) Q.158; c) Q.107; d). Q.108

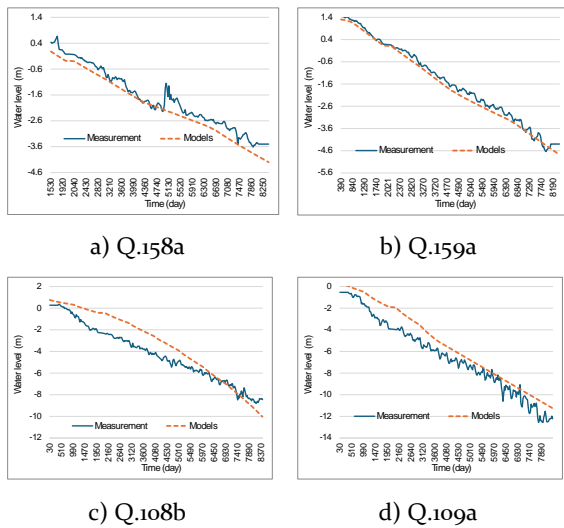


Figure 9. Error between modeled water levels and actual observed water levels in the Pleistocene aquifer at monitoring stations. a). Q.158a; b) Q.159a; c) Q.108b; d). Q.109a

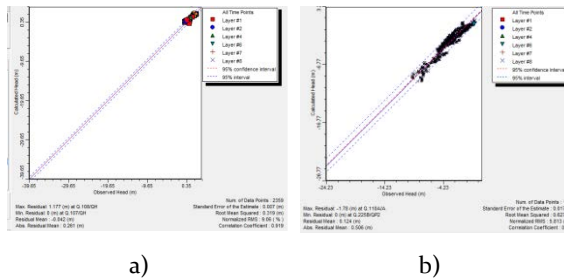


Figure 10. Error assessment between observed water levels and modeled in coastal RRD aquifers (a) Holocene aquifer; (b) Pleistocene aquifer.

Most calibration wells fall within the 95% confidence interval. Although some facilities show significant absolute error values, the relative values still remain within acceptable limits, ensuring permissible thresholds. Therefore, the model error assessment confirms that all parameters meet the established reliability criteria. The model error evaluation indicates that all parameters satisfy the model's reliability criteria. However, when compared with previous models developed for the RRD (Trung et al., 2024 and NAWAPI, 2023) the current model demonstrates higher reliability.

Scenario Development and Forecasting Results for Water Level and Saline Intrusion

Based on the calibrated and validated groundwater flow model for aquifers q_{h2} , q_{h1} , and q_p , two exploitation scenarios up to 2040 have been developed to assess water level decline trends and saline intrusion (SI) risks in the coastal Red River Delta plain region:

Table 4. Summary of centralized water supply stations

No	Centralized water supply station (WSS)	Number of wells under SC1	Total extraction flow rate under SC1 (m ³ /day)	Number of wells under SC2	Total extraction flow rate under SC2 (m ³ /day)
I	Thai Binh		6,424		21,000
1	Hung Nhan WSS	2	1,824	6	5,000
2	Hung Ha WSS	2	1,620	7	5,000
3	Tien Hung WSS	2	1,050	9	4,000
4	My Hung WSS	2	850	7	3,000
5	Quynh Coi WSS	2	1,080	8	4,000
6	Dong Hung WSS	0	0	6	1,000
II	Nam Dinh		4,198		10,800
1	TT Quy Nhat - Nghia Hung WSS	3	1,200	8	2,800
2	Hai Toan - Hai Hau WSS	6	1,998	17	5,000
3	Yen Dinh- Hai Hau WSS	4	1,000	13	3,000
III	Hai Phong		2,900		2,900
1	Tien Lang WSS	5	2,900	5	2,900

Table 5. Forecasted groundwater level elevations.

No	Centralized water supply station (WSS)	GW level in 2025 (m)	GW level in SC1 (m)		GW level in SC2 (m)		Hcp (m)
			2030	2040	2030	2040	
I	Thai Binh						
1	Hung Nhan WSS	-5.4	-7.1	-8.6	-7.9	-9.7	-28.4
2	Hung Ha WSS	-9.0	-11.7	-14.0	-11.8	-15.0	-27.9
3	Tien Hung WSS	-8.7	-11.8	-14.5	-12.2	-15.2	-28.7
4	My Hung WSS	-6.3	-8.7	-10.8	-9.5	-12.0	-27.4
5	Quynh Coi WSS	-10.7	-13.3	-15.6	-14.2	-16.6	-27.2

No	Centralized water supply station (WSS)	GW level in 2025 (m)	GW level in SC1 (m)		GW level in SC2 (m)		Hcp (m)
			2030	2040	2030	2040	
6	Dong Hung WSS	-8.8	-	-	-11,9	-15,7	
II Nam Dinh							
1	TT Quy Nhat - Nghia Hung WSS	-17.2	-19,5	-20,8	-22,4	-25,8	-28
2	Hai Toan - Hai Hau WSS	-18.0	-22,3	-25,4	-22,3	-27,5	-28
3	Yen Dinh- Hai Hau WSS	-12.9	-17,2	-22,1	-18,9	-24,3	-28
III Hai Phong							
1	Tien Lang WSS	-4.1	-5,9	-7,0	-6,8	-8,3	-27

- Scenario 1 (SC1): Scenario 1 (SC1) represents a baseline case in which the spatial distribution and pumping rates of all existing wells are kept equal to the current abstraction in 2018 (Table 2). This scenario is used to evaluate whether the present level of groundwater development can be sustained without constructing new groundwater projects or expanding the licensed capacities.

- Scenario 2 (SC2): is an increased-demand scenario linked to provincial water-supply plans. Similar to SC1, abstraction by individual wells and rural water-supply schemes is kept unchanged. In contrast, pumping rates at selected centralized water-supply stations are increased to match the design capacities given in the officially approved water-demand plans of Thai Binh, Nam Dinh, and Ninh Binh provinces. In these plans, the total designed groundwater abstraction for centralized schemes in the three provinces increases from 447,826 m³/day in 2018 to 630,699 m³/day in 2025 and 772,410 m³/day in 2035. The station-scale values used in SC2 (e.g., Thai Binh from 6,424 to 21,000 m³/day; Nam Dinh from 4,198 to 10,800 m³/day) are summarized in Table 4. At the scale of the whole model domain, the total groundwater abstraction rises from 552,729 m³/day in SC1 to 579,107 m³/day in SC2, corresponding to an overall increase of about 4.8%.

Therefore, SC1 and SC2 together bracket a realistic range of future groundwater exploitation that is fully consistent with

existing provincial planning documents, and allow us to assess the sensitivity of groundwater levels and saltwater intrusion to plausible increases in pumping.

Water level forecasting results to 2040 show significant differences between the two groundwater exploitation scenarios. Scenario 1 (SC1) maintains the current exploitation status, while Scenario 2 (SC2) significantly increases exploitation flow rates at centralized water supply stations. Simulation results show that water levels at most stations in SC2 are lower than SC1. In Thai Binh province, water levels in 2040 at Hung Nhan station decrease from -8.6 m (SC1) to -9.7 m (SC2); at Quynh Coi station, from -15.6 m to -16.6 m. More pronounced declines occur in Nam Dinh: Quy Nhat station decreases from -20.8 m to -25.8 m, Hai Toan station from -25.4 m to -27.5 m. These values clearly reflect the impact of increased exploitation on groundwater level decline, especially in areas using the Pleistocene aquifer (qp) as the main source.

Compared with permissible limits according to Decree 53/2004/ND-CP, most water level values in both scenarios remain within safe exploitation limits. However, some stations such as Yen Dinh and Hai Toan (Nam Dinh) have water levels approaching limits, warning of risks of exceeding thresholds if high-intensity exploitation continues without effective recharge measures. Details of water level contours for Scenario 1 and Scenario 2 are shown in Figures 11 and 12.

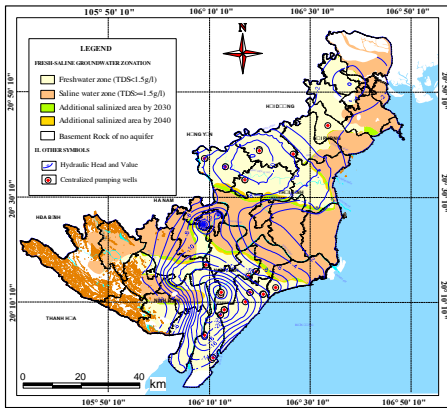


Figure 11. Forecasted water level contour map for the 2040 qp aquifer in Scenario 1

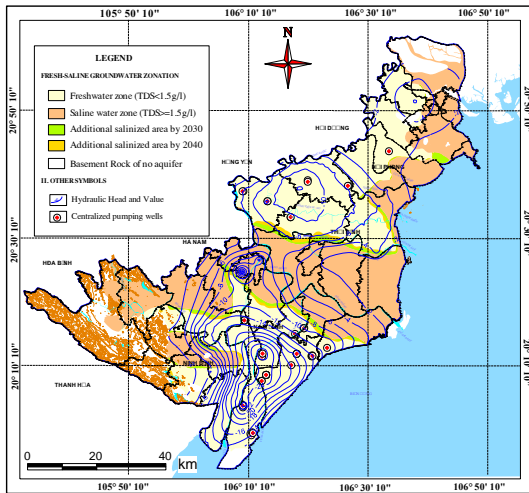


Figure 12. Forecasted water level contour map for the 2040 qp aquifer in Scenario 2

Saline intrusion simulation results for both scenarios show no significant differences in fresh-saline area between the two scenarios for all three aquifers (qh_2 , qh_1 , qp). This can be explained by several reasons:

First, exploitation conditions for the upper Holocene aquifer (qh_2) and lower Holocene aquifer (qh_1) are equivalent in both scenarios. Therefore, salinity propagation calculation results for these two layers are identical between SC1 and SC2.

Second, although Scenario 2 adjusts to increase exploitation capacity at some centralized water supply stations, this represents only a portion of the total regional exploitation. Specifically, total regional exploitation flow in Scenario 1 is 552,729 m³/day, while Scenario 2 is 579,107 m³/day, a difference of only about 4.8%. Furthermore, these centralized exploitation facilities are all planned at locations 4-5 km away from the saline boundary. Therefore, although Scenario 2 may create local water level depression cones, they are not large enough and do not extend to saline water areas, so they do not significantly change saline intrusion results.

Nevertheless, model results still clearly reflect the trend of gradually decreasing freshwater area over time in all three aquifers. Specifically, in the qh_2 layer, freshwater area

decreases from 2,465 km² (2025) to 2,129 km² (2040); the qh_1 layer decreases from 419 km² to 401.8 km²; the qp layer decreases from 2,621 km² to 2,492.8 km². These figures show that saline intrusion occurs slowly but tends to expand over time. These results indicate that although saline intrusion currently shows no sudden changes between the two scenarios, if the trend of increasing exploitation continues, the risk of expanding saline zones is entirely possible in the future.

Table 6. Fresh and Saline areas over time in the aquifer layers

Upper Holocene Aquifer (qh_2)			
Year	2025	2030	2040
Fresh water area (km ²)	2465	2344	2129
Saline area (km ²)	2085	2206	2421
Total area	4550	4550	4550
Lower Holocene Aquifer (qh_1)			
Year	2025	2030	2040
Fresh water area (km ²)	419	415.6	401.8
Saline area (km ²)	3743	3746.4	3760.2
Total area	4162	4162	4162
Pleistocene Aquifer (qp)			
Year	2025	2030	2040
Fresh water area (km ²)	2621	2601.7	2492.8
Saline area (km ²)	2076	2095.3	2204.2
Total area	4697	4697	4697

DISCUSSION

Model prediction results indicate that the risk of saltwater intrusion in coastal aquifer layers of the Red River Delta shows an increasing trend over time, particularly in the Pleistocene layer (qp), which is currently the most heavily exploited aquifer. Although the difference between the two exploitation scenarios is not pronounced in the period leading to 2040, this should not be interpreted as low risk. Instead, this indicates that current groundwater extraction planning and control have direct impacts on water security in the near future. In practice, most of the Holocene layer has become saline or has poor reserves; therefore, extraction demand is concentrated primarily on the Pleistocene layer. This creates an urgent requirement for spatial planning of groundwater extraction through reasonable zoning approaches: restricting new wells in

sensitive coastal areas, encouraging extraction in inland areas with more stable aquifer layers, and particularly reorienting the locations of concentrated water supply well fields in urban and new rural development plans.

Additionally, increased extraction must be accompanied by artificial recharge solutions. In many countries, models for rainwater harvesting, temporary surface water storage, and forced infiltration into aquifer layers have proven effective in slowing or preventing saltwater intrusion. Vietnam currently lacks a clear legal framework and regional planning for the artificial recharge development gap that needs research and supplementation. Furthermore, for prediction models to truly become effective management support tools, real-time monitoring systems for water levels and salinity in major aquifer layers are necessary. This data not only helps calibrate models more accurately but also serves as the foundation for establishing early warning thresholds to support timely extraction adjustments or cessation when saltwater intrusion risk is detected.

Finally, integrating MODFLOW model results into water resource planning should be implemented through integration with urban-rural water supply planning, agricultural sector development, and climate change adaptation. In the context of increasingly pressured water resources, prediction models should not only serve technical purposes but must become decision-making tools for local governments and water resource sectors.

CONCLUSION

This study developed and calibrated a three-dimensional multi-layer MODFLOW-MT3DMS model for the coastal Quaternary aquifers (qh2, qh1, and qp) of the Red River Delta and used it to assess future changes in groundwater levels and saline intrusion under two groundwater-extraction scenarios consistent with provincial water-supply plans. The simulations indicate a general tendency of groundwater-level decline, most pronounced around major well fields in Thai Binh and Nam

Dinh, while groundwater heads in most of the model domain remain within current regulatory limits. All three aquifer layers are exposed to saltwater-intrusion risk: the Holocene aquifers are already predominantly saline and only locally exploited, whereas the Pleistocene aquifer still contains fresh water but is increasingly stressed by pumping and therefore vulnerable to long-term salinization. The intensified-extraction scenario produces only a modest additional expansion of the saline front because the incremental abstraction is relatively small and new well fields are located away from existing saline boundaries.

The modelling results confirm that numerical groundwater-flow and solute-transport models are effective tools for analysing and forecasting the response of coastal aquifers to alternative development options, and for supporting groundwater-resource planning in the coastal Red River Delta. To enhance the sustainability of groundwater use in this region, model-based assessments should be incorporated into provincial planning, exploitation licensing and monitoring programmes, and combined with measures such as demand management, optimisation of well-field locations and, where appropriate, artificial-recharge or conjunctive-use solutions.

Despite successful calibration, several limitations remain. The large model domain required relatively coarse grid cells, which constrain the representation of local-scale flow patterns around individual well fields. Model reliability is also affected by the limited density and temporal coverage of monitoring data and by uncertainties in recharge, boundary conditions, and hydrogeological parameters. Future work should focus on improving and densifying the observation network, refining the model grid in priority areas, and updating the model with new data to better quantify the combined effects of groundwater abstraction, land-use change, and climate-driven variations in recharge and sea level.

ACKNOWLEDGMENTS

This paper was supported by project code DTDL.CN.59/22-C. On this occasion, the research team expresses deep gratitude for this valuable support.

DECLARATION

The team declares that this paper represents the collective research work of the authors, has not been published elsewhere, is not copied from previous research, and there are no conflicts of interest among the author group.

REFERENCES

- Anderson, M. P., Woessner, W. W., & Hunt, R. J. (2015). Applied groundwater modeling: Simulation of flow and advective transport. Academic Press.
- Fetter, C. (2001). Applied hydrogeology (4th ed.). Prentice-Hall.
- Fetter, C. W., Boving, T., & Kreamer, D. (2017). Contaminant hydrogeology. Waveland Press.
- Giang, N. V. (2018). Project results report: Investigation and assessment of the self-protective capacity of aquifers in the coastal areas of the Red River Delta (Thai Binh, Nam Dinh, and Ninh Binh provinces). Center for Water Resources Quality and Protection, National Center for Water Resources Planning and Investigation, Hanoi.
- Ha, N. T. (2006). Formation of the chemical composition of groundwater in Quaternary sediments of the Red River Delta and its significance for water supply. Hanoi University of Mining and Geology.
- Ha, N. T. (2010). Report on the results of groundwater monitoring in the Red River Delta. Archives of the Department of Geology and Minerals of Vietnam.
- Hang, N. T., Thu, T. H., & Chinh, D. D. (2015). Study on the freshwater boundary of the Pleistocene aquifer in the coastal zone of Nam Dinh province. Vietnam Journal of Marine Science and Technology, 16(2), 151–157.
- Harbaugh, A. W. (2005). MODFLOW-2005, the US Geological Survey modular ground-water model: The ground-water flow process (Vol. 6). U.S. Department of the Interior, U.S. Geological Survey.
- Hariharan, V., & Shankar, M. U. (2017). A review of visual MODFLOW applications in groundwater modelling. IOP Conference Series: Materials Science and Engineering. IOP Publishing.
- Huy, T. D. (2022). Determination of the role of the Red River and bedrock in groundwater recharge in Quaternary sediments in the southwestern part of Hanoi City [Doctoral dissertation].
- Larsen, F., et al. (2024). Paleo-climatic control on recharge and fresh-salt groundwater distribution in the Red River Delta plain, Vietnam. Scientific Reports, 14(1), 21280.
- Minh, T. (2005). Hydrogeological map of Northern Vietnam [Scale 1:200,000].
- MONRE. (2016). Climate change and sea level rise scenarios in Vietnam. Ministry of Natural Resources and Environment.
- Namitha, M., JS, D. K., & Sreelekshmi, H. (2019). Groundwater flow modelling using Visual MODFLOW. Journal of Pharmacognosy and Phytochemistry, 8(1), 2710–2714.
- NAWAPI. (2023). Integrated master plan report for the Red River–Thai Binh River Basin, 2021–2030, with a vision to 2050. Ministry of Natural Resources and Environment, Hanoi, Vietnam.
- NAWAPI. (2023). National groundwater resources monitoring database. Ministry of Natural Resources and Environment, Hanoi, Vietnam.
- Nhan, P. Q. (2000). Formation and reserves of groundwater in Quaternary sediments of the Red River Delta and their significance for the national economy [PhD dissertation].
- Nhan, P. Q., et al. (2022). Zoning groundwater potential recharge using remote sensing and GIS techniques in the Red River Delta plain. IOP Conference Series: Earth and Environmental Science. IOP Publishing.
- Saaty, T. L. (2008). Decision making with the analytic hierarchy process. International Journal of Services Sciences, 1(1), 83–98.
- Thu, T. H., & Trung, N. N. (2012). Predicting the freshwater/saltwater boundary of the Pleistocene aquifer in the Red River coastal plain by water chemical analysis and electrical resistivity methods. Vietnam Journal of Marine Science and Technology, 12(4A), 163–170.
- Thu, T. H., Trung, N. N., & Nghia, N. V. (2008). Application of the electrical resistivity and hydrogeology modeling methods to map and forecast saltwater intrusion in Thai Binh Province. Journal of Geology, 31–32.

- Thu, T. H., et al. (2014). Application of hydrogeological modelling methods in forecasting seawater intrusion of the Pleistocene aquifer in the Thai Binh area. Proceedings of the 28th Conference on Environmental Informatics – Informatics for Environmental Protection, Sustainable Development and Risk Management. BIS-Verlag.
- Thu, T. H., et al. (2016). Study on the current status of TDS distribution in the Pleistocene aquifer in the coastal zone of Nam Dinh Province. *Vietnam Journal of Marine Science and Technology*, 16(2), 151–157.
- Trung, D. T., Hoa, N. T., & Hoan, T. V. (2018). Report on the results of model development for the Red River Delta. National Center for Water Resources Planning and Investigation.
- Trung, D. T., et al. (2024). Application of MODFLOW for determining the role of groundwater recharge to groundwater exploitation in the Red River Delta Plain.
- Trung, N. N., & Thu, T. H. (2013). Investigation of saltwater intrusion in the coastal zone of the Red River Delta. Proceedings of the 11th SEGJ International Symposium, Yokohama, Japan, 18–21 November 2013. Society of Exploration Geophysicists of Japan.
- Van, H. H., et al. (2022). Recharge mechanism and salinization processes in coastal aquifers in Nam Dinh Province, Vietnam. *Vietnam Journal of Earth Sciences*, 44(2), 213–238.
- Van Lam, N., Van Hoan, H., & Duc Nhan, D. (2019). Investigation into groundwater resources in the southern part of the Red River Delta plain, Vietnam, by the use of isotopic techniques. *Water*, 11(10), 2120.

Gravity anomaly modeling over the Gulf of Thailand from airborne gravity data

Tham Bui Thi Hong¹, Thanh Le Duy^{1,*}, Hoai Do Thi², Thu Trinh Thi Hoai¹

¹Hanoi University of Natural Resources and Environment, Hanoi, Vietnam

²Vietnam Institute of Surveying and Mapping, Hanoi, Vietnam

*Email: ldthanh@hunre.edu.vn

Abstract: This study presents the development of a continuous Bouguer gravity anomaly model for the Gulf of Thailand using a set of 1,444 airborne gravity observations. Among them, 1,194 points were employed for model construction, while 250 points served as an independent validation dataset. To effectively capture the spatial correlation of the data and minimize interpolation errors, the Kriging technique with a spherical variogram model was selected after comprehensive theoretical analysis and empirical testing.

The workflow comprised three main stages: (i) compilation and normalization of the airborne Bouguer anomaly dataset; (ii) estimation of variogram parameters and construction of the continuous anomaly field through Kriging interpolation; and (iii) validation of the modeled gravity anomalies against the independent check points. The resulting model achieved an accuracy of approximately ± 1.56 mGal, with most residuals between the interpolated and observed values falling within ± 0.5 mGal. This level of consistency demonstrates the model's robustness and its suitability for regional-scale geodetic and geophysical applications.

The constructed Bouguer anomaly model significantly enhances gravity coverage and resolution in the coastal region of southern Vietnam. It provides a reliable dataset to support marine geophysical investigations such as crustal structure analysis, tectonic interpretation, and sedimentary basin evolution studies. Moreover, in the geodetic domain, the model serves as an essential input

for improving coastal quasigeoid models, thereby contributing to the refinement of the national vertical datum and supporting precise height determination.

The findings highlight the effectiveness of integrating airborne gravity data with Kriging interpolation and a spherical variogram for modeling regional gravity fields. This approach can be further extended to other coastal and island regions of Vietnam to strengthen the national gravity database and enhance applications in both geodesy and geophysics.

Keywords: Bouguer anomaly, airborne gravity, Kriging, Gulf of Thailand, gravity anomaly modeling

INTRODUCTION

Gravity anomalies represent the deviation between the actual gravity values referenced to the geoid and the theoretical normal gravity computed on the reference ellipsoid (Nazan, 2023). Among the various types of gravity anomalies, the Bouguer anomaly—which has been corrected for the effects of topography and the mass between the observation point and the reference surface—plays a particularly significant role in both geophysics and geodesy. From a geophysical perspective, Bouguer anomalies are commonly employed to investigate the Earth's internal structure, such as identifying the basement of sedimentary basins, characterizing crustal thickness, and assessing lithospheric flexure under surface loading (Tenzer et al., 2019). In geodesy and mapping, Bouguer anomalies constitute one of the fundamental datasets for constructing

geoid and quasigeoid models that support precise height determination (Hofmann-Wellenhof & Moritz, 2006; Torge et al., 2023).

In recent years, alongside advancements in gravity surveying technologies, airborne gravimetry has emerged as an efficient tool to complement and extend gravity data coverage, especially in coastal and offshore regions where traditional terrestrial surveys face considerable challenges (Vu et al., 2019; Guimarães et al., 2025). Airborne gravity data provide the advantages of wide spatial coverage and acquisition consistency; however, they also present significant challenges in data processing due to their flight-line distribution, uneven point density, pronounced anisotropy, and generally higher noise levels compared to ground-based observations (Billings et al., 2002; Kebede et al., 2024). Without appropriate interpolation and correction strategies, these limitations can degrade the quality of the derived gravity-anomaly models.

Against this backdrop, modern interpolation techniques play a critical role in constructing continuous and reliable Bouguer-anomaly fields. Compared with conventional approaches such as inverse-distance weighting or minimum-curvature surfaces, Kriging - a geostatistical method - offers substantial advantages by explicitly exploiting the spatial correlation of the data through variogram modeling (Nouck et al., 2013; Sowińska-Botor et al., 2023). Kriging not only yields optimal estimates but also provides prediction-error variances, thereby enhancing the reliability of the resulting model (Karaca et al., 2024; Kebede et al., 2024). Variants of Kriging, such as cokriging or factorial Kriging, have been shown to be effective in separating regional-residual components or in integrating auxiliary datasets to improve model accuracy (Azad et al., 2016; Reguzzoni et al., 2005).

The application of Kriging in gravity-data processing has been well established by numerous studies. Nouck et al. (2013) employed Kriging to reanalyze gravity data and enhance the resolution of the Bouguer anomaly field in Cameroon. Zahorec et al. (2021) applied

Kriging to develop a comprehensive gravity database for the Alpine region, enabling the production of reliable anomaly maps under complex topographic conditions. Karaca et al. (2024) demonstrated that Kriging delivers the most accurate interpolation results for precise geoid determination compared to other techniques. Vu et al. (2019) developed a national quasigeoid model by integrating terrestrial gravity and satellite data, while Vu et al. (2024) highlighted the potential of combining airborne gravity measurements with geostatistical methods to improve coastal-area models in Vietnam. Hoa (2016) employed Kriging to determine the most reliable estimates of gravity and height anomalies at locations lacking direct observations. Similarly, Song et al. (2015) utilized Kriging to interpolate airborne gravity data for generating high-resolution gravity maps and precise geoid models. Collectively, these studies affirm that Kriging not only has a solid theoretical foundation but also proves highly effective for processing, interpolating, and analyzing gravity datasets under diverse geological and topographic conditions.

In Vietnam, considerable research efforts have focused on the East Vietnam Sea and its adjacent areas. Que et al. (2008) constructed a unified 1:1,000,000-scale Bouguer anomaly map for the entire East Vietnam Sea and neighboring regions based on marine gravity data collected over approximately 50 years from various sources, achieving a mapping accuracy of about ± 1.95 mGal. Hòa (2019) applied the Kriging method to model and interpolate Bouguer anomalies in the mountainous northern and central regions of Vietnam, attaining an accuracy of approximately $\pm 2-3$ mGal. Luan (2020) compared two approaches for calculating gravity anomalies caused by inhomogeneous layers - the space-domain and frequency-domain methods - and subsequently adopted the more efficient frequency-domain approach to compute Bouguer anomalies for the entire East Vietnam Sea and its surrounding areas. Trung et al. (2018) analyzed Bouguer anomalies to delineate the crust-mantle boundary in

detail, providing crucial evidence for the tectonic evolution and isostatic state of the Red River Basin and the northwestern region of Vietnam.

Worldwide, numerous methods have been developed to construct gravity anomaly models for geological-geophysical studies and geodetic applications. Among these, the Least-Squares Collocation (LSC) method has been widely used due to its capability to optimally combine multisource datasets (Moritz, 1980; (Tham & Thanh, 2025)). In addition to LSC, surface interpolation techniques such as low-order polynomials, Radial Basis Functions, and multiresolution wavelet analysis have also been applied to represent the gravity field at different spatial resolutions, particularly under conditions of uneven data distribution. Moreover, gravity inversion approaches play an important role in inferring subsurface density variations and deep geological structures (Blakely, 1996).

Among interpolation methods, Kriging has been recognized by many international studies as a superior technique for geophysical and gravity field data. This method allows modeling of spatial correlation structures through the semivariogram, thereby providing an improved reconstruction of the actual variations of the gravity field (Oliver & Webster, 2015; Chilès & Delfiner, 1999). Kriging is particularly effective when data are irregularly distributed (Li & Heap, 2008) and simultaneously provides estimation variances at each point, enabling an assessment of model reliability. This is a critical requirement when constructing Bouguer anomaly models. Therefore, this study employs the Kriging method to develop a Bouguer gravity anomaly model from airborne gravity data for the Gulf of Thailand-a region of significant scientific and practical importance. The resulting model not only contributes to investigations of geological and geophysical structures but also supports the improvement of regional quasigeoid models, thereby contributing to the national objective of establishing a high-accuracy quasigeoid for Vietnam.

METHODOLOGY

The Kriging method was employed to construct the Bouguer gravity-anomaly model, with its theoretical foundation presented in detail below.

The ordinary Kriging estimator takes a linear form (Chilès & Desassis, 2018):

$$Z(u) = m + \sum_{i=1}^{n(u)} \lambda_i(u) [Z(u_i) - m] \quad (1)$$

with $i = 1, 2, \dots, n(u)$.

Where u is the coordinate vector of the point to be interpolated; u_i is the coordinate vector of the observation points; m is the mean value of the observed dataset; $Z(u_i)$ is the measured value at the observation point.

$\lambda_i(u)$ are the weighting coefficients of the vector $\lambda(u)$, determined from the following equation:

$$K \cdot \lambda(u) = k \quad (2)$$

In equation (2), K denotes the covariance matrix (a square matrix of size $n(u)$, and the column vector k represents the covariance vector:

$$K = \begin{bmatrix} C_{1,1} & C_{1,2} & \dots & C_{1,n(u)} \\ C_{2,1} & C_{2,2} & \dots & C_{2,n(u)} \\ \dots & \dots & \dots & \dots \\ C_{n(u),1} & C_{n(u),2} & \dots & C_{n(u),n(u)} \end{bmatrix};$$

$$k = \begin{bmatrix} C_{1,u} \\ C_{2,u} \\ \dots \\ C_{n(u),u} \end{bmatrix} \quad (3)$$

The covariance value $C_{i,j}$ in equation (3) is computed based on the theoretical semivariogram values corresponding to the distances s between the points.

$$C(s) = c - g(s) \quad (4)$$

From equation (2), it follows that:

$$\lambda(u) = K^{-1}k \quad (5)$$

Substituting equation (5) into equation (1), the Kriging formula can be expressed in matrix form as:

$$Z(u) = m + k^T K^{-1}l \quad (6)$$

where:

$$l = \begin{bmatrix} Z(u_1) - m \\ Z(u_2) - m \\ \dots \\ Z(u_{n(u)}) - m \end{bmatrix} \quad (7)$$

Accordingly, the Kriging procedure consists of the following steps:

Determine the mean value m from the entire set of observed data and compute the experimental semivariogram.

Use an approximation method to estimate the parameters of the theoretical semivariogram function.

Select the data points within a specified radius R for interpolation, and construct the covariance matrix K and the covariance vector k .

Compute the weight coefficients $\lambda(u)$ and calculate the interpolated value using eq.(6).

For Kriging interpolation, it is necessary to determine the parameters of the theoretical semivariogram function from the experimental semivariogram. The experimental semivariogram at a distance s is computed using the expectation formula:

$$\gamma(s) = \frac{1}{2} E[(z(u) - z(u + s))^2] \quad (8)$$

Equation (8) is expressed in the form:

$$\gamma(s) = \frac{1}{2N(s)} \sum_{i=1}^{N(s)} [z(u_i) - z(u_i + s)]^2 \quad (9)$$

In this context, the semivariogram $\gamma(s)$ increases from 0 (when $s = 0$) to a maximum value known as the sill, reaching this value at a limiting distance referred to as the practical range.

In the present study, the theoretical semivariogram function selected is the spherical model:

$$g(s) = c \left[1.5 \left(\frac{s}{L} \right) - 0.5 \left(\frac{s}{L} \right)^3 \right] \quad (10)$$

where s is the lag distance, c is the sill value, and L is the parameter representing the limiting distance or practical range.

DATA

The experimental study was conducted in the Gulf of Thailand, with the study area illustrated in Figure 1.

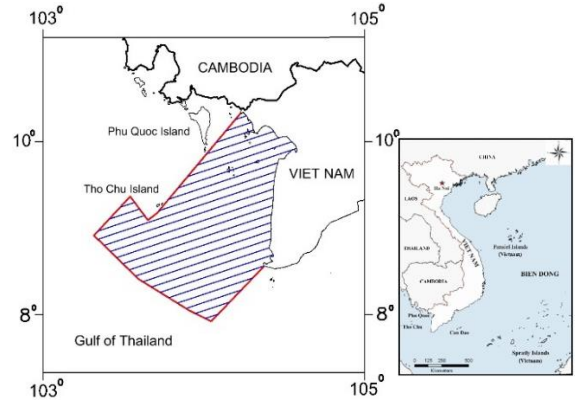


Figure 1. Schematic map of the study area and experimental data.

The dataset comprises a total of 1,444 airborne gravity measurement points, of which 1,194 points were selected for model construction, while the remaining 250 points were used as an independent test set to evaluate the accuracy of the Bouguer gravity-anomaly model within the study area. Detailed information on the measurement data is provided in Table 1.

Table 1. Bouguer anomaly data of the observation points

N^0	X (m)	Y (m)	Δg_B (mgal)
1	979052.34	286145.64	4.41
2	1000442.02	282430.38	6.19
3	1011031.34	307197.34	1.39
4	960466.24	322387.64	-6.74
5	984762.43	404162.80	1.86
6	966148.29	281371.04	4.95
7	1057499.22	454886.03	-5.38
8	1032562.45	426886.64	-10.46
9	910072.55	425727.15	7.93
...
1186	956310.94	397272.27	5.91
1187	955923.38	326933.51	-4.07
1188	1037980.56	439103.48	-11.32
1189	996179.53	445511.02	-9.72

N ^o	X (m)	Y (m)	Δg_B (mgal)
1190	986819.18	472427.12	-3.09
1191	961212.77	427704.10	-2.24
1192	962241.93	444370.91	-5.40
1193	997407.00	444289.15	-9.84
1194	954634.86	381123.66	11.95

Where Δg_B is the Bouguer gravity anomaly.

RESULTS

The Kriging method with a spherical semivariogram function was employed to model the Bouguer gravity anomalies of the 1,194 points in the study area. The parameters of the spherical semivariogram function were determined through an iterative fitting process, with the resulting values presented in Table 2.

Table 2. Parameters of the semivariogram function obtained through the iterative fitting process

Iteration	C	L	dC	dL
1	128164.538	29.980	45141.516	9.980
2	188500.905	43.661	60336.367	13.681
3	263868.914	60.922	75368.009	17.261
4	341562.384	78.783	77693.470	17.861
5	394106.735	90.880	52544.351	12.097
6	409463.905	94.418	15357.170	3.538
7	410418.779	94.638	954.874	0.220
8	410422.128	94.639	3.349	0.001
9	410422.128	94.639	0.000	0.000

The spherical semivariogram function for the study area is expressed as:

$$g(s) = 410422.128 \left[1.5 \left(\frac{s}{94.639} \right) - 0.5 \left(\frac{s}{94.639} \right)^3 \right] (*)$$

Based on the values of the theoretical semivariogram function and the experimental semivariogram, the spherical semivariogram plot of the experimental data is presented in Figure 2.

The curve of the experimental values closely follows that of the theoretical model across the entire distance range, indicating that the selected spherical semivariogram model is appropriate for describing the spatial variation

of the Bouguer gravity anomalies. The semivariogram values increase progressively as the distance between point pairs increases, reflecting the inherent characteristics of the gravity-anomaly field-points in close proximity exhibit higher spatial correlation, whereas points farther apart show decreasing correlation. The minimal discrepancies between the experimental and theoretical values demonstrate that the model effectively reproduces the characteristics of the observed data.

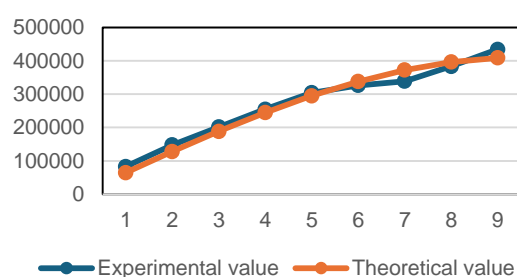


Figure 2. Spherical semivariogram plot.

Overall, these results confirm that employing the spherical semivariogram in the Kriging interpolation method is both reasonable and reliable, ensuring the accuracy and robustness of the Bouguer gravity-anomaly interpolation model for the study area.

Using the spherical semivariogram function (*), the gravity-anomaly values at the test points (denoted as Δg_{model}) were determined. Subsequently, the gravity-anomaly deviations $d\Delta g_B$ between the measured and model-interpolated values for the 250 test points were computed. The modeled gravity-anomaly deviations $d\Delta g_B$ are illustrated in Table 3 and Figure 3.

Table 3. Gravity-anomaly deviations values of the test points

maximum $d\Delta g_B$	minimum $d\Delta g_B$	average $d\Delta g_B$
1.56	0	0.12

Where $d\Delta g_B$ is calculated using the formula $d\Delta g_B = \Delta g_B - \Delta g_{model}$ (mgal).

The plot in Figure 3 shows that the Bouguer gravity-anomaly deviations between

the measured and model-interpolated values at the test points are distributed fairly evenly around 0 mGal, indicating that the interpolation model accurately reproduces the observed data. Most points exhibit deviations within the range of -0.5 mGal to $+0.5$ mGal, reflecting small and stable errors. Only a few outlier points show deviations exceeding ± 1 mGal, with the maximum deviation reaching approximately ± 1.56 mGal; this value represents the accuracy of the Bouguer gravity-anomaly model for the study area.

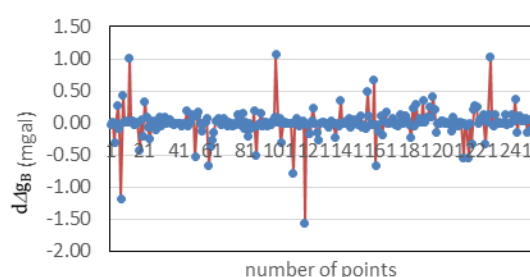


Figure 3. Bouguer gravity-anomaly deviations between the measured and model-interpolated values at the test points.

The connecting line between the deviation points reveals no apparent increasing or decreasing trend with respect to the point sequence, indicating that the errors are randomly distributed and no systematic bias is present. Overall, the results demonstrate that the Bouguer gravity-anomaly interpolation model for the study area achieves high accuracy and reliability, making it suitable for practical applications.

DISCUSSIONS

The Bouguer gravity-anomaly interpolation results using the Kriging method with a spherical semivariogram function for the Gulf of Thailand demonstrate that the model achieves an accuracy of approximately ± 1.56 mGal—a small and acceptable error level for geodetic and geophysical applications in coastal and offshore regions. The deviations between the interpolated and observed values are distributed relatively evenly around the mean value of 0 mGal, showing no systematic increasing or decreasing trend (Figure 3). Most

of the test points exhibit deviations within the range of -0.5 mGal to $+0.5$ mGal, reflecting the stability and reliability of the model.

The spherical semivariogram curve, derived through the iterative fitting process, shows a good fit to the experimental data (Figure 2). The observed increase in semivariogram values with distance indicates the gradual decrease in spatial correlation among the data points, which is consistent with the physical nature of the gravity field. The choice of the spherical semivariogram model proves appropriate, as it effectively describes the spatial variation of the Bouguer anomaly in the study area and helps optimize the Kriging weights. This finding is consistent with previous studies, such as Nouck et al. (2013) in Cameroon and Karaca et al. (2024) for high-precision geoid computation, which also identified the spherical model as the most suitable for gravity datasets with spatially uniform variability.

CONCLUSIONS

This study successfully developed a continuous Bouguer gravity-anomaly model for the Gulf of Thailand by utilizing 1,444 airborne gravity points, of which 1,194 points were used for model construction and 250 points for independent validation. The Kriging interpolation method with a spherical semivariogram—selected after theoretical and empirical analyses—proved effective in accurately representing the spatial correlation of the Bouguer gravity field. The interpolated model achieved an accuracy of ± 1.56 mGal, demonstrating its strong capability to reproduce observed data and ensuring high reliability for subsequent applications.

The construction of an accurate Bouguer anomaly model for the Gulf of Thailand represents a significant scientific contribution. First, it enriches the regional gravity dataset with high-quality data, markedly improving the coverage and resolution of the gravity field in the southern coastal region of Vietnam, where ground-based observations have historically been sparse. Moreover, the results provide a

reliable input dataset for marine geophysical studies, including the identification of tectonic structures, the analysis of sedimentary evolution, and the delineation of basement geology, thereby supporting resource assessment and natural-hazard risk management.

From a geodetic perspective, the Bouguer anomaly model has broad practical significance as it constitutes a key dataset for refining and improving coastal quasigeoid models—a critical component in the standardization of the national height reference system. An accurate Bouguer model enhances the precision of height networks, thus benefiting mapping, coastal infrastructure planning, resource management, and marine economic development.

The study demonstrates that combining airborne gravity data with Kriging interpolation and a spherical semivariogram is an effective approach for gravity-field modeling. This methodology can be extended to other coastal and island regions of Vietnam, contributing to the enhancement of the national gravity database and meeting the increasing accuracy requirements of geodetic and geophysical applications in support of sustainable development.

REFERENCES

- Azad, M. R., Koneshloo, M., Kamakar Rouhani, A., & Aghajani, H. (2016). Comparison of Factorial Kriging Analysis Method and Upward Continuation Filter to Recognize Subsurface Structures — A Case Study: Gravity Data from a Hydrocarbon Field in the Southeast Sedimentary Basins of the East Vietnam Sea. *Acta Geophysica*, 64(2), 398-416. <https://doi.org/10.1515/acgeo-2015-0068>.
- Billings, S. D., Beatson, R. K., & Newsam, G. N. (2002). Interpolation of geophysical data using continuous global surfaces. *Geophysics*, 67(6), 1810-1822. <https://doi.org/10.1190/1.1527081>.
- Blakely, R. J. (1996). Potential theory in gravity and magnetic applications.
- Chilès, J.-P., & Desassis, N. (2018). Fifty years of kriging. In *Handbook of mathematical geosciences: Fifty years of IAMG* (pp. 589-612). Springer International Publishing Cham.
- Chilès, J. P., & Delfiner, P. (1999). *Geostatistics: Modeling Spatial Uncertainty*.
- Guimarães, G. D. N., de Matos, A. C. O. C., Blitzkow, D., & de Almeida, F. G. V. (2025). High-resolution regional gravity field modeling to connect the local vertical systems in South America to the IHRF. *Earth, Planets and Space*, 77(1), 98. <https://doi.org/10.1186/s40623-025-02226-5>.
- Hoà, H. M. (2016). On estimation by methods of kriging and collocation. *Journal of Geodesy & Cartography*, 27, 1-8. <https://doi.org/https://doi.org/10.54491/jgac.2016.27.164>.
- Hoà, H. M. (2019). Research using Bouguer gravity anomalies at detailed gravimetric points in mountainous regions of Vietnam for solving interpolation task in process of construction of a database of national gravity anomalies. *Journal of Geodesy and Cartography* (39), 1-6. <https://doi.org/10.54491/jgac.2019.39.342>.
- Hofmann-Wellenhof, B., & Moritz, H. (2006). *Physical geodesy*. Springer.
- Karaca, O., Erol, B., & Erol, S. (2024). Assessments of gravity data gridding using various interpolation approaches for high-resolution geoid computations. *Geosciences*, 14(3), 85. <https://doi.org/https://doi.org/10.3390/geosciences14030085>.
- Kebede, H., Demissie, Z., Tadesse, H., & Eshetu, A. (2024). Spatial interpolation techniques comparison and evaluation: The case of ground-based gravity and elevation datasets of the central Main Ethiopian rift. *Heliyon*, 10(12). <https://doi.org/https://doi.org/10.1016/j.heliyon.2024.e32806>.
- Li, J., & Heap, A. D. (2008). A Review of Spatial Interpolation Methods for Environmental Scientists. *Geoscience Australia, Record 2008/23*, 137pp.
- Moritz, H. (1980). *Advanced Physical Geodesy*.
- Nazan, Y. (2023). Gravity data reduction, Bouguer anomaly, and gravity disturbance. *Geofizicheskiy Zhurnal*, 45(6). <https://doi.org/https://doi.org/10.24028/gj.v45i6.293314>.
- Nouck, P. N., Kenfack, C., Diab, A. D., Njeudjang, K., Meli, L. J., & Kamseu, R. (2013). A geostatistical re-interpretation of gravity surveys in the Yagoua, Cameroon region. *Geofísica internacional*, 52(4), 365-373.

- [https://doi.org/https://doi.org/10.1016/S0016-7169\(13\)71483-1](https://doi.org/https://doi.org/10.1016/S0016-7169(13)71483-1).
- Geostatistics: The Variogram and Kriging. SpringerBriefs in Agriculture.
- Que, B. C., Dung, T. T., & Tram, L. (2008). Construction of bouguer gravity anomaly map in the East Vietnam Sea and adjacent area. *Vietnam Journal of Marine Science and Technology*, 8(2). <https://doi.org/https://doi.org/10.15625/1859-3097/8/2/6298>.
- Reguzzoni, M., Sansó, F., & Venuti, G. (2005). The theory of general kriging, with applications to the determination of a local geoid. *Geophysical Journal International*, 162(2), 303-314. <https://doi.org/10.1111/j.1365-246X.2005.02662.x>.
- Song, H., Sadovski, A., & Jeffress, G. (2015). Precision of geoid approximation and geostatistics: how to find continuous map of absolute gravity data. *Revista de Matemática Teoría y Aplicaciones*, 22(2), 199-222.
- Sowińska-Botor, J., Mastej, W., & Maćkowski, T. (2023). Ranking of the utility of selected geostatistical interpolation methods in conditions of highly skewed seismic data distributions: a case study of the Baltic Basin (Poland). *Gospodarka Surowcami Mineralnymi-Mineral Resources Management*, 149-172-149-172. <https://doi.org/10.24425/gsm.2023.147555>.
- Tenzer, R., Foroughi, I., Hirt, C., Novák, P., & Pitoňák, M. (2019). How to calculate Bouguer gravity data in planetary studies. *Surveys in Geophysics*, 40(1), 107-132. <https://doi.org/https://doi.org/10.1007/s10712-018-9504-0>.
- Oliver, M. A., & Webster, R. (2015). *Basic Steps in*
- Tham, B. T. H., & Thanh, P. T. (2025). Crustal movement model in the ITRF2020 – a case study in Northern Vietnam. *Journal of Mining Institute*, 271, 120-130. <https://doi.org/https://pmi.spmi.ru/pmi/article/view/16324>.
- Torge, W., Müller, J., & Pail, R. (2023). *Geodesy*. In *Geodesy*. De Gruyter Oldenbourg.
- Vu, D. T., Bonvalot, S., Seoane, L., Gabalda, G., Remy, D., Bruinsma, S., Bidel, Y., Bresson, A., Zahzam, N., Rouxel, D., Salaün, C., Lalancette, M. F., Forsberg, R., Jensen, T., & Jamet, O. (2024). Potential of cold-atom airborne gravimetry to improve coastal gravity field and quasigeoid modelling. *Journal of Geodesy*, 98(4), 28. <https://doi.org/10.1007/s00190-024-01839-0>.
- Vu, D. T., Bruinsma, S., & Bonvalot, S. (2019). A high-resolution gravimetric quasigeoid model for Vietnam. *Earth, Planets and Space*, 71(1), 65. <https://doi.org/10.1186/s40623-019-1045-3>.
- Zahorec, P., Papčo, J., Pašteka, R., Bielik, M., Bonvalot, S., Braitenberg, C., Ebbing, J., Gabriel, G., Gosar, A., & Grand, A. (2021). The first pan-Alpine surface-gravity database, a modern compilation that crosses frontiers. *Earth System Science Data Discussions*, 2021, 1-72. <https://doi.org/https://doi.org/10.5194/essd-13-2165-2021>.

DOI: 10.15625/vap.2025.0217

Utilizing remote sensing and statistical methods to assess the impact of land use on soil organic carbon

Trong Dieu Hien Le^{1,*}, Pham Phuong Thanh Bui¹

Resources & Environmental Management Program, University of Thu Dau Mot, 06 Tran Van On street, Phu Loi Ward, Ho Chi Minh city, Viet Nam

*Email: hienltd@tdmu.edu.vn

Abstract: The land use in the communes of Phuoc Thanh, An Long, Phu Giao, and Phuoc Hoa in Ho Chi Minh City, has recently undergone significant changes, primarily due to the province's economic growth. Corresponding changes in carbon stocks are often associated with land use changes. We examined how the 2024 land use types affected the amount of organic carbon stored in the soil. This study assessed the differences in soil organic carbon (SOC) concentrations resulting from various land use types by remote sensing techniques, geographic information systems (GIS), and soil carbon data from ISRIC's SoilGrids 2020. More specifically, an algorithm utilizing Landsat 8 OLI time-series data was applied to classify land use in the 4 communes of Phuoc Thanh, An Long, Phu Giao, and Phuoc Hoa in Ho Chi Minh City. We implemented the Random Forest (RF) model in R, using variables extracted from Landsat 8 OLI imagery and digital elevation model (DEM) data to generate a land use map for 2024, followed by calculating the land use areas during the study period. Subsequently, soil carbon values for field survey points were extracted. The results showed a classification accuracy of 0.894 (OA) and 0.87 (Kappa). The proposed method is both cost-effective and practical for regularly monitoring complex land use fluctuations, particularly in areas with limited or no data accessibility. We tested that there is a statistically significant difference in soil carbon concentrations among different land use types in study area ($p = 0.0137 < 0.05$).

Keywords: Random forest, land use classification, soil organic carbon.

INTRODUCTION

Soil Organic Carbon (SOC) is an essential component of soil organic matter (SOM), playing a central role in regulating soil quality and nutrient cycles. It represents the largest terrestrial carbon pool. Globally, it is estimated that the carbon stock in the topsoil (0–1 m) is about 1500 gigatons (Gt), which is 2–3 times greater than the combined amount of CO₂ present in the atmosphere and vegetation biomass (Lal, 2004). The long-term carbon sequestration ability of soil makes SOC a critical factor in strategies to reduce greenhouse gas emissions and combat climate change (Smith et al., 2007). However, human impacts such as unsustainable farming, urbanization, deforestation, and land-use change have severely depleted SOC stocks in many ecosystems. When SOC decomposes, carbon is oxidized and released back into the atmosphere as CO₂ and CH₄, contributing to the greenhouse effect. Notably, even a global loss of 0.1% SOC annually corresponds to billions of tons of CO₂ emissions. Beyond climate regulation, SOC serves as an indicator of soil health. Studies show soils with high SOC content can improve soil structure, increase aggregate stability, enhance water and cation retention, and promote beneficial microbial activity. SOC acts as a “biological glue” that binds soil particles together, forming stable soil structure that resists erosion and sustains long-term agricultural productivity.

Many studies worldwide have confirmed that land use and land cover change (LULCC) is one of the primary causes of carbon imbalance in terrestrial ecosystems (Jiang et al., 2023). According to Houghton and colleagues, LULCC contributed about 20% of total global CO₂ emissions in the 20th century. Syntheses of data at national and tropical regional scales indicate that SOC content can decline by up to 35% within just the first two decades after land use conversion, while ecosystems such as well-managed perennial grasslands or cover crops tend to maintain or recover SOC more effectively. To assess the complex impacts of LULCC on SOC dynamics, recent studies have applied simulation models such as bookkeeping and process-based models, integrating climate factors, topography, and soil microbial activity to improve the accuracy of predicting SOC fluctuations at large scales (Wieder et al., 2013). In Vietnam, studies on SOC have clearly demonstrated the link between land use type, topographic factors, and soil carbon sequestration potential. In natural forests, litterfall has been identified as the dominant factor controlling SOC content, particularly in Acacia plantations (Toai, 2016). In the Mekong Delta, the highest SOC is typically found in wetlands, followed by perennial orchard soils, and is lowest in annual croplands (Thi et al., 2022). Studies in Ea Sup (Dak Lak), estimated that topsoil SOC amounts to millions of tons of CO₂ equivalents potentially convertible into carbon credits if managed sustainably demonstrating significant potential not only for local ecosystem services but also for carbon economy development (Khoi, 2021; Toai, 2016).

No study has been conducted to assess the impact of land use types on the concentration of Soil Organic Carbon (SOC) in the study area, Binh Duong province. Therefore, in this study, we 1) used satellite imagery to classify land use in the communes of Phuoc Thanh, An Long, Phu Giao, and Phuoc Hoa in Ho Chi Minh City, and 2)

tested the differences in organic carbon concentration among different land use types. The research utilized remote sensing data to support saving time, labor, and costs for large study areas.

METHODOLOGY

Study area

Study area consists of four communes, including An Long Commune, Phuoc Thanh Commune, Phu Giao Commune, and Phuoc Hoa Commune, located in Ho Chi Minh City (Fig.1). Phu Giao district is located in the northeast of Binh Duong province, with the following geographical boundaries: to the east, it borders Vinh Cuu district, Dong Nai province; to the west, it borders Bau Bang district and Chon Thanh town, Binh Phuoc province; to the south, it borders Bac Tan Uyen district, to the north, it borders Dong Xoai city and Dong Phu district, both belonging to Binh Phuoc province. Study area covers an area of 544.44 km², with a population of 95,433 as of 2021, resulting in a population density of 176 people per km². Regarding to climate, it experiences a temperate climate with two distinct seasons: a dry season lasting from November to April and a rainy season from May to October. The average temperature ranges from 26°C to 34°C. The average annual rainfall in the district is 1947.7 mm, with approximately 163 rainy days per year. The air study area is mainly gray basaltic soil, which is highly suitable for industrial crops such as rubber, cashew, pepper, and various fruit trees. Specifically, the soil along the Bé River is new alluvial soil, ideal for cultivating rice and various vegetables and legumes. Currently, the land use structure in area is gradually shifting toward prioritizing industrial development, with forest land and agricultural land shrinking to make way for the development of industrial clusters (such as Tam Lap Industrial Clusters 1-5) and planting high-value industrial crops like rubber and cashew. In other words, the area's high biomass ecosystems (natural forests) have been converted into ecosystems with lower biomass (industrial crops, industrial zones), resulting in carbon stock losses to the

atmosphere. This change may also cause some challenges in land management.

Data

The remote sensing datasets were used to perform land use classification: (1) Landsat images (LCo8_L2SP_125052_20241218_20241227_02_T1; Date: 2024/12/18; Path: 125; Row: 052; with 30m spatial resolution) for the year 2024

were downloaded from the Geospatial Data Cloud website (<http://www.gscloud.cn/>) and processed ; (2) Digital Elevation Model (DEM) data of the study area was downloaded from <https://earthexplorer.usgs.gov/>. The soil organic carbon data used in this study is from SoilGrids by ISRIC (global gridded soil information), downloaded from <https://www.isric.org/explore/soilgrids>.

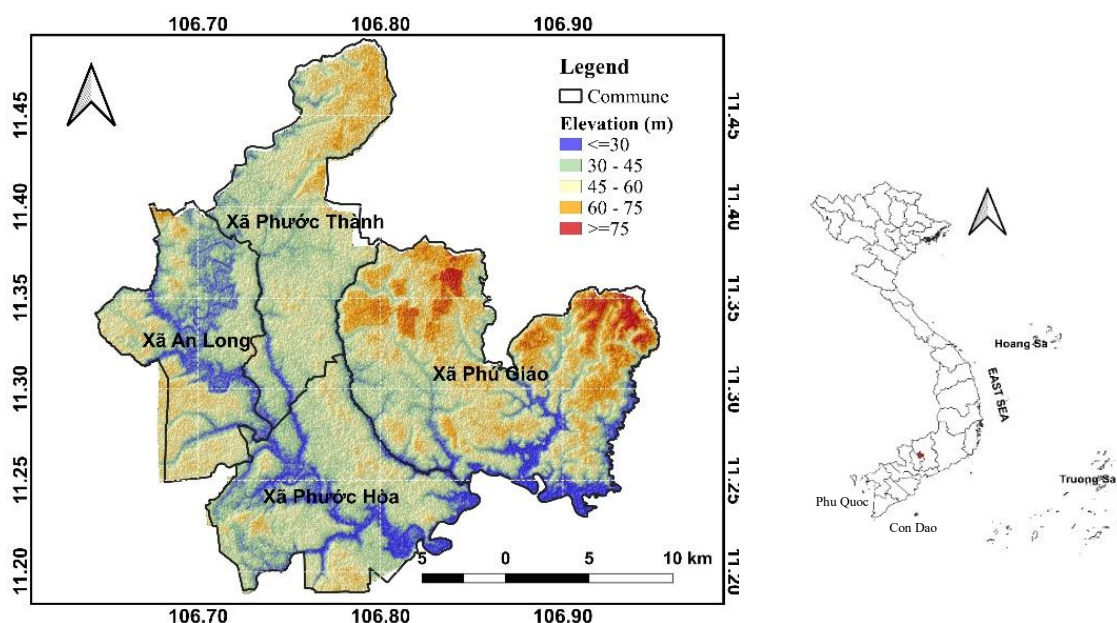


Figure 1. Study area

Landuse classification using Random forest (RF)

The study used the Random Forest (RF) model to classify land use in 2024 based on remote sensing indices (Table 1). The number of samples used for training and testing is presented in Table 2. In this study, we applied repeated cross-validation to split the training dataset into 10 subsets ($k\text{-fold}=10$) with 3 repeats. The number of variables randomly sampled at each split (m_{try}) and the number of trees (n_{tree}), which produced the highest accuracy, were determined through a tuning algorithm. We used the `train` function (`method = RF`) in the `Caret` package in R to run the RF model. Kappa accuracy, sensitivity (SENS), and specificity (SPEC) were used to evaluate the internal accuracy of the model.

SOC in difference type of landuse classification

We applied ANOVA test with $p < 0.05$ to test the differences in average SOC concentrations among different land use type. The reason for using ANOVA is to compare the differences in the means of SOC between land-use groups, in order to test whether the groups differ statistically significantly. ANOVA helps analyse the total variance into components due to differences between groups and variance within groups, thereby assessing the effect of a categorical variable on the outcome variable. This method is typically used when comparing more than two groups and has the advantage of reducing Type I error compared to performing multiple separate t-tests.

Table 1 Variables in landuse classification

Variables		Discription	Fomulars
Dependent	Landuse catagories	Bare land, crops, forest, rubber, built-up, water	
	EVI	Enhanced Vegetation Index	$2.5 * (B_5 - B_4) / (B_5 + 6 * B_4 - 7.5 * B_2 + 1)$
Indepent	NDVI	Normalized Difference Vegetation Index	$(B_5 - B_4) / (B_5 + B_4)$
	NDWI	Normalized Difference Water Index	$(B_3 - B_5) / (B_3 + B_5)$
	NDBI	Normalized Difference Built-up Index	$(B_6 - B_5) / (B_6 + B_5)$
	BU	Built-Up Index	$(NDBI - NDVI)$
	MNDWI	Modified Normalized Difference Water Index	$(B_3 - B_6) / (B_3 + B_6)$
	UI	Urban Index	$(B_7 - B_5) / (B_7 + B_5)$
	NDBaI	Normalized Dry Bareness Index	$(B_6 - B_{10}) / (B_6 + B_{10})$
	SAVI	Soil Adjusted Vegetation Index	$[(B_5 - B_4) ** (1 + 0.5)] / (B_5 + B_4 + 1)$
	EBBI	Enhanced Built-Up and Bareness Index	$B_6 - B_5 / [10 * (B_6 + B_{10}) * (0.5)]$
	DBSI	Dry Bare-Soil Index	$(B_6 - B_3) / (B_6 + B_3) - NDVI$
	VgNIR_BI	Visible Green-Based Built-up Indices	$(B_4 - B_5) / (B_4 + B_5)$
	VrNIR_BI	Visible Red-Based Built-up Indices	$(B_3 - B_5) / (B_3 + B_5)$
	ELEV	Elevation	
	SLP	Slope	
	ASP	Aspect	

Table 2 The number of samples used for training and validation for each land use classification

LULC categories	Description	Reference samples	Training dataset	Validation dataset
Bare land	Land area without any trees or shrubs in sight	96	67	29
Crops	Land area for plants that are less than one year old.	101	70	31
Forest	Land for forest	65	45	20
Rubber	Rubber	69	48	21
Built-up	Land for building and development	91	63	28
Water	Water bodies	105	73	32
Total		527	366	162

RESULTS AND DISCUSSION

Landuse classification in 2024

Six types of LULC were used for classification in study area in 2024, including bare land, forest, urban and built-up areas, crops, rubber, and water, as presented in Fig.2.

The RF classification results, when visualized, show strong performance and clearly reflect the LULC patterns of the study area. Table 3 presents the area and proportion of each land use type (in km²). Rubber plantations are dominant in study area with a total area of 272.06 km², accounting for nearly 50% of the

district's area. This is followed by forest land, agricultural land, bare land, and built-up land, with the area of each type detailed in Table 3.

All datasets generally achieved high accuracy, with an overall accuracy of 89.4 and a Kappa coefficient of 89.4. On average, areas corresponding to water, forest, and rubber plantations were classified with the highest accuracy due to their distinct physical characteristics, followed by bare land, cropland, and built-up areas. The lowest accuracy was observed for mixed bare land and built-up classes. The classification accuracy of LULC varies depending on the methods and techniques used, influenced by atmospheric, surface, and illumination changes (Camargo et al., 2019; Foody, 2008; Islam et al., 2018; Leyk et al., 2018; Maxwell et al., 2018; Rodriguez-Galiano et al., 2012; Rwanga & Ndambuki, 2017; Thanh Noi & Kappas, 2018). Furthermore, accuracy also varies with the amount of training sample data (Jin et al., 2018; Tatsumi et al., 2015).

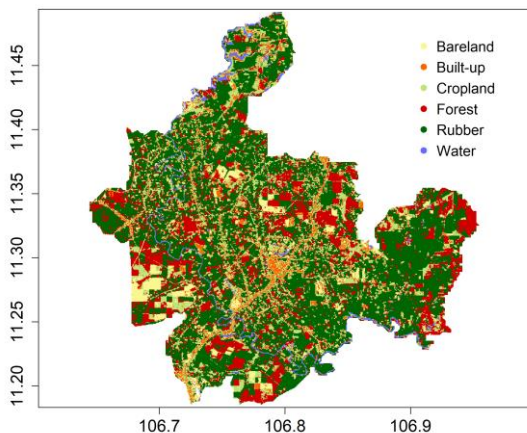


Figure 2: Landuse classification in study area in 2024

Table 3 The classification results for year 2024

Catergoies	Year 2024	
	Area (km ²)	Percentage (%)
Bare land	34.38	6.23
Crops	89.22	16.17
Forest	117.72	21.34
Rubber	272.06	49.32
Built-up	28.39	5.15
Water	9.9	0.02
Total	551.67	100

Soil organic carbon (SOC)

Fig. 3 shows the locations of field samples across different land use types. At these locations, we extracted SOC (0-5 cm depth) from SoilGrids data by ISRIC. The SOC data results for the sample locations are shown in Fig.4. Specifically, from Fig.4, SOC in samples collected from forest land had the highest content, with an average concentration of 33.14 g/kg, followed by rubber plantation samples (31.19 g/kg), agricultural land (30.59 g/kg), bare land (28.89 g/kg), and built-up land (28.56 g/kg).

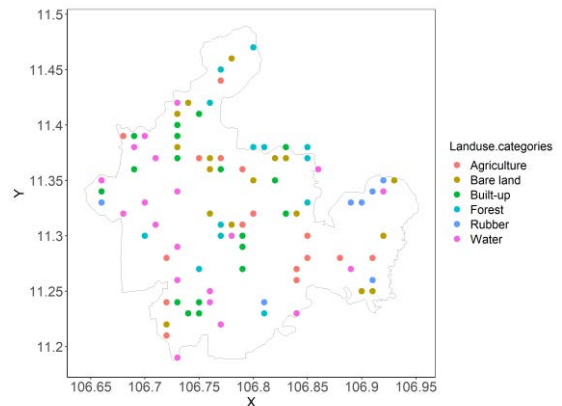


Figure 3. The locations of field samples across different land use types

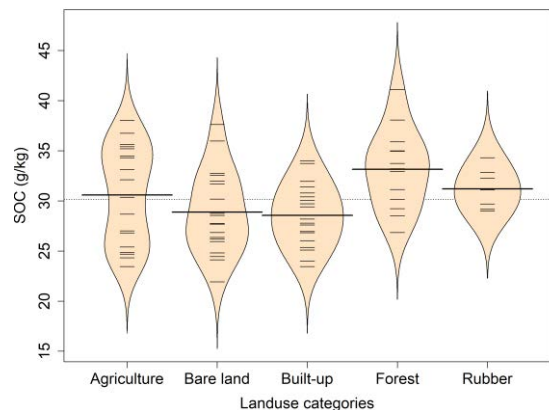


Figure 4. The beanplot illustrates the variation in soil organic carbon concentration across different land use types.

SOC show statistically significant differences ($P = 0.0137 < 0.05$) among land use and land cover (LULC) types in the study area. According to ANOVA analysis, LULC types

have a statistically significant effect ($P < 0.05$) on SOC content (g/kg). The overall mean SOC value in forest soil (33.14 g/kg) is significantly higher ($P < 0.05$) than in bare land (28.89 g/kg). The increasing trend of SOC is observed at a 30 cm depth in the order: forest > rubber plantation > cropland > bare land > built-up land. Forest contains 1.15 times more SOC than cropland and bare land at a 30 cm depth. Similarly, as found by Herzfeld et al., (2021), soil carbon decreases rapidly when forest or grassland converts to cropland.

LULC contribute substantially to SOC and/or CO₂ emissions. It is observed that LULC changes can affect soil properties, including SOC content, due to human activities (such as intensive agriculture, overgrazing, fertilization, harvesting, cultivation, etc.). This result is confirmed by De Vos et al., (2007); Mekuria, (2013), reporting that the lowest organic carbon content is in cropland compared to forest, bushland, and grassland soils. This finding is supported by Emiru & Gebrekidan, (2013), who argues that significant differences in SOC result from LULC changes in western and central Ethiopia. Similarly, the study by Ramankutty et al., (2018) indicates that cropland expansion often reduces SOC. The largest area covered by low organic carbon cropland is directly related to low soil agricultural productivity. According to Tellen & Yerima, (2018), SOC are highly sensitive to LULC changes. SOC can improve soil physical and chemical properties. Cropland and bare land have lower carbon stocks and contents than other land use ecosystems because cropland increases soil aeration, enhances microbial mobility, promotes decomposition processes, removes crop residues, and bare land can lose organic carbon through topsoil erosion and surface evaporation due to lack of vegetation cover.

The lowest SOC levels in the study area were recorded in construction land, followed by vacant land and cultivated land. This could lead to soil degradation and environmental pollution. Human activities such as poor agricultural practices, urbanization, deforestation, and land-use change contribute

to the decline in soil quality and low crop yields. This finding is consistent with Yeshaneh et al., (2013), which indicates that factors like poverty, unstable land tenure, and high population pressure drive land degradation. Similarly, studied the impact of LULC on SOC absorption capacity. Land conversion from natural forest to rubber plantations, agricultural land, and unsustainable land use negatively affects SOC stocks (Kiflu, 2013). Conversely, some studies, like Engda et al., (2008), found no significant differences in soil chemical properties between land use types, but observed notable variations in the physical properties of Andosols in southern Ethiopia.

This research reveals that converting natural vegetation to artificial land uses (such as grasslands, cultivated lands, and bare lands) can have adverse effects on soil organic carbon reserves. The results align with Kiflu, (2013), which reports that converting natural forests to human-managed land (cropland, grazing land, and eucalyptus plantations) has more detrimental effects on SOC. Another study of Mekuria, (2013) found significantly higher SOC in grasslands compared to cereal farms. According to Pachauri et al., (2014), restoring vegetation cover and afforestation are effective methods to maintain SOC (Abegaz et al., 2020). Converting degraded grazing areas into protected zones increased SOC by 42% at the surface layer (0–10 cm). Increasing SOC and improving ecosystems were achieved by transforming degraded lands into protected areas across different agricultural ecosystems (Werner, 1997). Additionally, Peng et al., (2019) confirms that SOC increased through community-based water and soil conservation measures. This indicates that increasing SOC reserves through land restoration, afforestation, and conservation practices is feasible in the study area. Enhancing SOC systematically within the region will improve soil quality, increase carbon sequestration in the atmosphere, and are vital for soil health and productivity. There are not many studies conducted in Vietnam similar to our study for comparative purposes. In a study in the North Central region of Vietnam focusing on the

impact of land use on Soil Organic Carbon (SOC) content in the 0-10 cm surface soil, SOC variations were evaluated across typical land use types such as natural forest, bare land, and cultivated land. The study found that SOC in agricultural soils was higher than in natural forests (Hoang, 2024), which contrasts with the findings of our research. Another study in A Luoi District, Thua Thien Hue, assessed the impact of land use types such as acacia plantations, rice fields, maize, and banana crops on soil physicochemical properties and SOC content. The results showed that acacia plantation soils had higher organic matter and total nitrogen content compared to other land types due to the characteristics of the tree species and management practices.

CONCLUSION

The discovery of the impact of land use and land cover change (LULC) on soil organic carbon (SOC) in the context of global warming is a fundamental basis for global climate change research and soil productivity. LULC changes show significant variation ($P < 0.05$) in SOC content, ranging from forest land (33.14 g/kg) to built-up land (28.56 g/kg) in the study area. These findings indicate SOC loss due to conversion from forest land to cropland and bare land. This loss may be a cause of declining agricultural productivity in the study area. ANOVA analysis shows that all LULC changes have a significant effect ($P < 0.05$) on SOC. Overall, this study demonstrates the existence of a relationship between SOC and LULC types. Therefore, it is necessary to apply appropriate land management and use measures to supplement inputs and minimize SOC loss, aiming to enhance soil organic carbon content in the study area. These measures can improve soil productivity, restore the soil's SOC absorption capacity, protect the environment, and mitigate the impacts of climate change in the long term to ensure sustainability.

REFERENCE

- Abegaz, A., Tamene, L., Abera, W., Yaekob, T., Hailu, H., Nyawira, S. S., Silva, M. D., & Sommer, R. (2020). Soil organic carbon dynamics along chrono-sequence land-use systems in the highlands of Ethiopia. *Agriculture, Ecosystems & Environment*, 300, 106997. <https://doi.org/10.1016/j.agee.2020.106997>
- Batjes, N. h. (1996). Total carbon and nitrogen in the soils of the world. *European Journal of Soil Science*, 47(2), 151–163. <https://doi.org/10.1111/j.1365-2389.1996.tb01386.x>
- Camargo, F. F., Sano, E. E., Almeida, C. M., Mura, J. C., & Almeida, T. (2019). A Comparative Assessment of Machine-Learning Techniques for Land Use and Land Cover Classification of the Brazilian Tropical Savanna Using ALOS-2/PALSAR-2 Polarimetric Images. *Remote Sensing*, 11(13), Article 13. <https://doi.org/10.3390/rs11131600>
- De Vos, B., Lettens, S., Muys, B., & Deckers, J. A. (2007). Walkley–Black analysis of forest soil organic carbon: Recovery, limitations and uncertainty. *Soil Use and Management*, 23(3), 221–229. <https://doi.org/10.1111/j.1475-2743.2007.00084.x>
- Emiru, N., & Gebrekidan, H. (2013). *Effect of land use changes and soil depth on soil organic matter, total nitrogen and available phosphorus contents of soils in Senbat watershed, western Ethiopia*. 8(3).
- Engda, T., Kassahun, H., Collick, A., Adissu, T., Ashagre, B., Tesemma, Z., Zegeye, A., Solomon, D., & Steenhuis, T. (2008). Soil Properties and Fertility Status Dynamics of North Western Ethiopia as Influenced by Land Use Changes: Case of Dibanke Watershed. In *Ethiopian society of Soil Science, the 10th Annual Conference on Improved Natural Resources Management for Food Security, Poverty Reduction and Sustainable Development, Addis Ababa, Ethiopia*.
- Foody, G. M. (2008). Harshness in image classification accuracy assessment. *International Journal of Remote Sensing*, 29(11), 3137–3158. <https://doi.org/10.1080/01431160701442120>
- Herzfeld, T., Heinke, J., Rolinski, S., & Müller, C. (2021). Soil organic carbon dynamics from

- agricultural management practices under climate change. *Earth System Dynamics*, 12(4), 1037–1055. <https://doi.org/10.5194/esd-12-1037-2021>
- Islam, K., Jashimuddin, M., Nath, B., & Nath, T. K. (2018). Land use classification and change detection by using multi-temporal remotely sensed imagery: The case of Chunar Wildlife Sanctuary, Bangladesh. *The Egyptian Journal of Remote Sensing and Space Science*, 21(1), 37–47. <https://doi.org/10.1016/j.ejrs.2016.12.005>
- Jiang, R., Jayasundara, S., Grant, B. B., Smith, W. N., Qian, B., Gillespie, A., & Wagner-Riddle, C. (2023). Impacts of land use conversions on soil organic carbon in a warming-induced agricultural frontier in Northern Ontario, Canada under historical and future climate. *Journal of Cleaner Production*, 404, 136902. <https://doi.org/10.1016/j.jclepro.2023.136902>
- Jin, Y., Liu, X., Chen, Y., & Liang, X. (2018). Land-cover mapping using Random Forest classification and incorporating NDVI time-series and texture: A case study of central Shandong. *International Journal of Remote Sensing*, 39(23), 8703–8723. <https://doi.org/10.1080/01431161.2018.1490976>
- Khôi D. Đ. (2021). Ước tính lượng Cacbon hữu cơ lưu giữ trong đất tầng mặt tại huyện Ea Súp, tỉnh Đắk Lắk. *Tạp chí Khoa học và Công nghệ - Đại học Thái Nguyên*, 226(14), 11–17.
- Kiflu, A. (2013). Effects of different land use systems on selected soil properties in South Ethiopia. *Journal of Soil Science and Environmental Management*, 4(5), 100–107. <https://doi.org/10.5897/JSSEM2013.0380>
- Lal, R. (2004). Soil carbon sequestration to mitigate climate change. *Geoderma*, 123(1), 1–22. <https://doi.org/10.1016/j.geoderma.2004.01.032>
- Leyk, S., Uhl, J. H., Balk, D., & Jones, B. (2018). Assessing the accuracy of multi-temporal built-up land layers across rural-urban trajectories in the United States. *Remote Sensing of Environment*, 204, 898–917. <https://doi.org/10.1016/j.rse.2017.08.035>
- Maxwell, A. E., Warner, T. A., & Fang, F. (2018). Implementation of machine-learning classification in remote sensing: An applied review. *International Journal of Remote Sensing*, 39(9), 2784–2817. <https://doi.org/10.1080/01431161.2018.1433343>
- Mekuria, W. (2013). Conversion of Communal Grazing Lands into Enclosures Restored Soil Properties in the Semi-Arid Lowlands of Northern Ethiopia. *Arid Land Research and Management*, 27(2), 153–166. <https://doi.org/10.1080/15324982.2012.721858>
- Pachauri, R. K., Allen, M. R., Barros, V. R., Broome, J., Cramer, W., Christ, R., Church, J. A., Clarke, L., Dahe, Q., Dasgupta, P., Dubash, N. K., Edenhofer, O., Elgizouli, I., Field, C. B., Forster, P., Friedlingstein, P., Gulev, S., Gomez-Echeverri, L., Hallegatte, S., ... van Ypersele, J.-P. (2014). Climate Change 2014: Synthesis Report. Contribution of Working Groups I, II and III to the Fifth Assessment Report of the Intergovernmental Panel on Climate Change. In R. K. Pachauri & L. Meyer (Eds.), *EPIC3 Geneva, Switzerland, IPCC, 151 p., pp. 151, ISBN: 978-92-9169-143-2* (p. 151). IPCC. <https://epic.awi.de/id/eprint/37530/>
- Peng, X., Tong, X., Hao, L., & Wu, F. (2019). Applicability of biochar for limiting interrill erosion and organic carbon export of sloping cropland in a semi-arid area of China. *Agriculture, Ecosystems & Environment*, 280, 68–76. <https://doi.org/10.1016/j.agee.2019.04.021>
- Ramankutty, N., Mehrabi, Z., Waha, K., Jarvis, L., Kremen, C., Herrero, M., & Rieseberg, L. H. (2018). Trends in Global Agricultural Land Use: Implications for Environmental Health and Food Security. *Annual Review of Plant Biology*, 69(Volume 69, 2018), 789–815. <https://doi.org/10.1146/annurev-arplant-042817-040256>

- Rodriguez-Galiano, V. F., Chica-Olmo, M., Abarca-Hernandez, F., Atkinson, P. M., & Jeganathan, C. (2012). Random Forest classification of Mediterranean land cover using multi-seasonal imagery and multi-seasonal texture. *Remote Sensing of Environment*, 121, 93–107. <https://doi.org/10.1016/j.rse.2011.12.003>
- Rwanga, S. S., & Ndambuki, J. M. (2017). Accuracy Assessment of Land Use/Land Cover Classification Using Remote Sensing and GIS. *International Journal of Geosciences*, 8(4), Article 4. <https://doi.org/10.4236/ijg.2017.84033>
- Smith, P., Martino, D., Cai, Z., Gwary, D., Janzen, H., Kumar, P., McCarl, B., Ogle, S., O'Mara, F., Rice, C., Scholes, B., Sirotenko, O., Howden, M., McAllister, T., Pan, G., Romanenkov, V., Schneider, U., Towprayoon, S., Wattenbach, M., & Smith, J. (2007). Greenhouse gas mitigation in agriculture. *Philosophical Transactions of the Royal Society B: Biological Sciences*, 363(1492), 789–813. <https://doi.org/10.1098/rstb.2007.2184>
- Tatsumi, K., Yamashiki, Y., Canales Torres, M. A., & Taipei, C. L. R. (2015). Crop classification of upland fields using Random forest of time-series Landsat 7 ETM+ data. *Computers and Electronics in Agriculture*, 115, 171–179. <https://doi.org/10.1016/j.compag.2015.05.001>
- Tellen, V. A., & Yerima, B. P. K. (2018). Effects of land use change on soil physicochemical properties in selected areas in the North West region of Cameroon. *Environmental Systems Research*, 7(1), 3. <https://doi.org/10.1186/s40068-018-0106-0>
- Thanh Noi, P., & Kappas, M. (2018). Comparison of Random Forest, k-Nearest Neighbor, and Support Vector Machine Classifiers for Land Cover Classification Using Sentinel-2 Imagery. *Sensors*, 18(1), Article 1. <https://doi.org/10.3390/s18010018>
- Thị, N., Ly, N., Anh, L., Anh, T., Nguyen, H., & Nguyen, P. (2022). Ảnh hưởng của sử dụng đất đến trữ lượng Carbon và Nitơ trong đất ở khu vực đồi núi tỉnh An Giang. 69, 204–209.
- Toại P. M. (2016). Đánh giá lượng Các bon tích lũy trong đất dưới tán rừng tự nhiên tại Vườn quốc gia Ba Vì. *Tạp chí Khoa học và công nghệ Lâm Nghiệp*, 4, 10–14.
- Werner, M. R. (1997). Soil quality characteristics during conversion to organic orchard management. *Applied Soil Ecology*, 5(2), 151–167. [https://doi.org/10.1016/S0929-1393\(96\)00139-4](https://doi.org/10.1016/S0929-1393(96)00139-4)
- Wieder, W. R., Bonan, G. B., & Allison, S. D. (2013). Global soil carbon projections are improved by modelling microbial processes. *Nature Climate Change*, 3(10), 909–912. <https://doi.org/10.1038/nclimate1951>
- Yeshaneh, E., Wagner, W., Exner-Kittridge, M., Legesse, D., & Blöschl, G. (2013). Identifying Land Use/Cover Dynamics in the Koga Catchment, Ethiopia, from Multi-Scale Data, and Implications for Environmental Change. *ISPRS International Journal of Geo-Information*, 2(2), Article 2. <https://doi.org/10.3390/ijgi2020302>

Integrating Geospatial Data for RUSLE Soil Erosion Modeling in Google Earth Engine: A Case Study of the Dak Nong Plateau, Vietnam

Ngoc Hoang Thi Huyen^{1,2}, Son Nguyen Thai², Ha Nguyen Manh^{1,2*}, Dung Bui Quang^{1,2}, Linh Giang Tuan³

¹Institute of Earth Sciences, Vietnam Academy of Science and Technology, 86 Huynh Thuc Khang, Lang Ward, Hanoi City, Vietnam

²Graduate University of Science and Technology, Vietnam Academy of Science and Technology, 18 Hoang Quoc Viet, Nghia Do War, Hanoi City, Vietnam

³VNU Institute of Vietnamese Studies and Development Science, , 336 Nguyen Trai, Thanh Xuan Ward, Hanoi City, Vietnam

*Email: havdl72@ies.vast.vn

Abstract: Soil erosion has been seriously threatening the sustainability of tropical highland ecosystems. This study applies the Revised Universal Soil Loss Equation (RUSLE) within the Google Earth Engine (GEE) to quantify and map soil loss across the Dak Nong Plateau at 30 m resolution. Rainfall erosivity (R) was derived from CHIRPS datasets, soil erodibility (K) from laboratory analyses of 180 soil samples, and the topographic factor (LS), cover-management factor (C), and support-practice factor (P) from satellite-based inputs updated for 2024. The results show pronounced spatial variability, with soil loss ranging from < 25 to > 500 t.ha⁻¹.yr⁻¹ (mean 125 t.ha⁻¹.yr⁻¹). Very slight erosion (0–25 t.ha⁻¹.yr⁻¹) dominates 44.1% of the area, whereas severe to extremely severe erosion accounts for approximately 27.5%. Low erosion levels are associated with protected forests and perennial crops situated on gentle slopes, while steep slopes with sparse vegetation exhibit intense erosion. High seasonal rainfall and the clay-silt texture of basalt-derived Ferralsols further amplify runoff and erosivity. The modeling framework also holds potential for improved accuracy through local rainfall calibration and field validation of the C and P factors. This study demonstrates a cloud-based, scalable workflow for soil erosion assessment in data-scarce tropical regions and provides a practical basis for prioritizing soil-

conservation interventions and sustainable land-management planning.

Keywords: RUSLE model; monsoonal rainfall, basalt plateau; spatial analysis, GEE

INTRODUCTION

Land degradation has emerged as a major global concern, with soil erosion recognized as the most serious threat to soil health and a leading driver of land degradation and desertification worldwide (FAO and ITPS, 2015; Quinton and Fiener, 2024). Globally, about 75 billion tons of arable soil are lost each year, causing an estimated economic loss of USD 400 billion (GPS, 2017). Consequently, quantifying soil erosion under changing land use and climate has become a central objective in soil conservation research (Bosco et al., 2015; Borrelli et al., 2017; Dou et al., 2022). In tropical and subtropical regions such as Vietnam, steep terrain combined with intense monsoonal rainfall greatly accelerates soil erosion. In Vietnam, where nearly three-quarters of the land area is mountainous, erosion is a major constraint to sustainable land management, particularly in the Northeast and Central Highlands where agricultural expansion on sloping land is extensive (Vezina et al., 2006; Van De et al., 2008; Ha et al., 2014; Vu, Hoang and Tran, 2021).

In response to the alarming threat of land degradation caused by soil erosion, over the past decades, research on soil erosion has progressed from field-based measurements to empirical and process-based modeling. Among available tools, the Universal Soil Loss Equation (USLE) and its improved version (RUSLE), remains one of the most widely used due to its simplicity and adaptability. The integration of RUSLE with GIS and remote sensing has enabled broader spatial applications, yet the accuracy of these assessments depends heavily on data availability, spatial resolution, and methodological consistency. The use of digital elevation models (DEM), satellite-based rainfall (CHIRPS, GPM), vegetation indices (NDVI from MODIS, Landsat, Sentinel-2), and global soil datasets has enabled high-resolution, spatially explicit soil erosion assessments (Kouli et al., 2009; Saha et al., 2022; Delgado et al., 2025; Tiki et al., 2025). Remarkably, recent advancements in cloud-based geospatial platforms, particularly Google Earth Engine (GEE), have created new opportunities for large-scale and automated soil-erosion mapping. GEE allows direct access to multi-temporal satellite imagery, rainfall datasets, topographic models, and global soil information (Gorelick et al., 2017). Although this approach has been increasingly adopted in other regions (Elnashar et al., 2021; Johani et al., 2023; Fentaw and Abegaz, 2024; Ghosh et al., 2025; Fahd et al., 2025), its application in Vietnam remains limited, with most studies still relying on static GIS workflows and using land-cover, rainfall, and soil datasets that are not updated regularly or not validated locally.

The Dak Nong Plateau, a basalt upland in the southern Central Highlands, is experiencing rapid land-use conversion on sloping terrain. This has heightened erosion risks, yet regional-scale quantitative assessments remain scarce, largely due to data gaps, complex topography, and a sparse meteorological station network. These limitations challenge conventional GIS-based approaches that rely on static, single-year datasets. To address these gaps, this study applies the RUSLE model entirely within the GEE platform to generate a high-resolution soil-

erosion map for 2024, integrating multi-source satellite data with laboratory-analyzed soil properties. By combining cloud-based computation with locally validated inputs, the study provides an improved and scalable framework for soil-erosion assessment in data-scarce tropical highlands. This work contributes to a clearer understanding of erosion dynamics in the Dak Nong Plateau and supports the development of more effective land-degradation mitigation strategies in Vietnam.

MATERIAL AND METHODS

Study area

The Dak Nong Plateau, located in the southwestern part of the former Central Highlands region and now belonging to Lam Dong Province, Vietnam, covers an area of approximately 650,927 ha (Fig. 1). The study area extends within between latitudes 11°45'N to 12°48'N and longitudes 107°12'E to 108°07'E. This plateau lies at an average elevation of 700–800 m above sea level and was primarily formed on Neogene–Early Pleistocene basaltic rocks. The landscape is characterized by undulating basaltic plateaus interspersed with denudational hills and low-lying valleys (An and Khanh, 2012). In addition, several prominent peaks appear in the region, including Nam Nung (1,544 m) and Ta Dung (1,980 m). The plateau has a humid tropical monsoon climate, strongly controlled by both monsoonal circulation and topography (Cuong, 2014). Annual rainfall ranges from 2,200 to 2,500 mm, with marked spatial variability of 600–1,000 mm between sub-regions. The mean annual temperature is 23–24°C. The rainy season lasts from April to October, contributing about 90% of total precipitation, while the dry season (November–March) receives very little rainfall, often below 30 mm per month (DSO, 2023). Correspondingly, the soils exhibit typical features of humid tropical highlands, consisting mainly of Ferralsols derived from basalt and Acrisols formed on shale parent materials. The drainage network shows a radial pattern with a medium density of 0.8–0.9 km/km², distributed relatively evenly across the plateau.

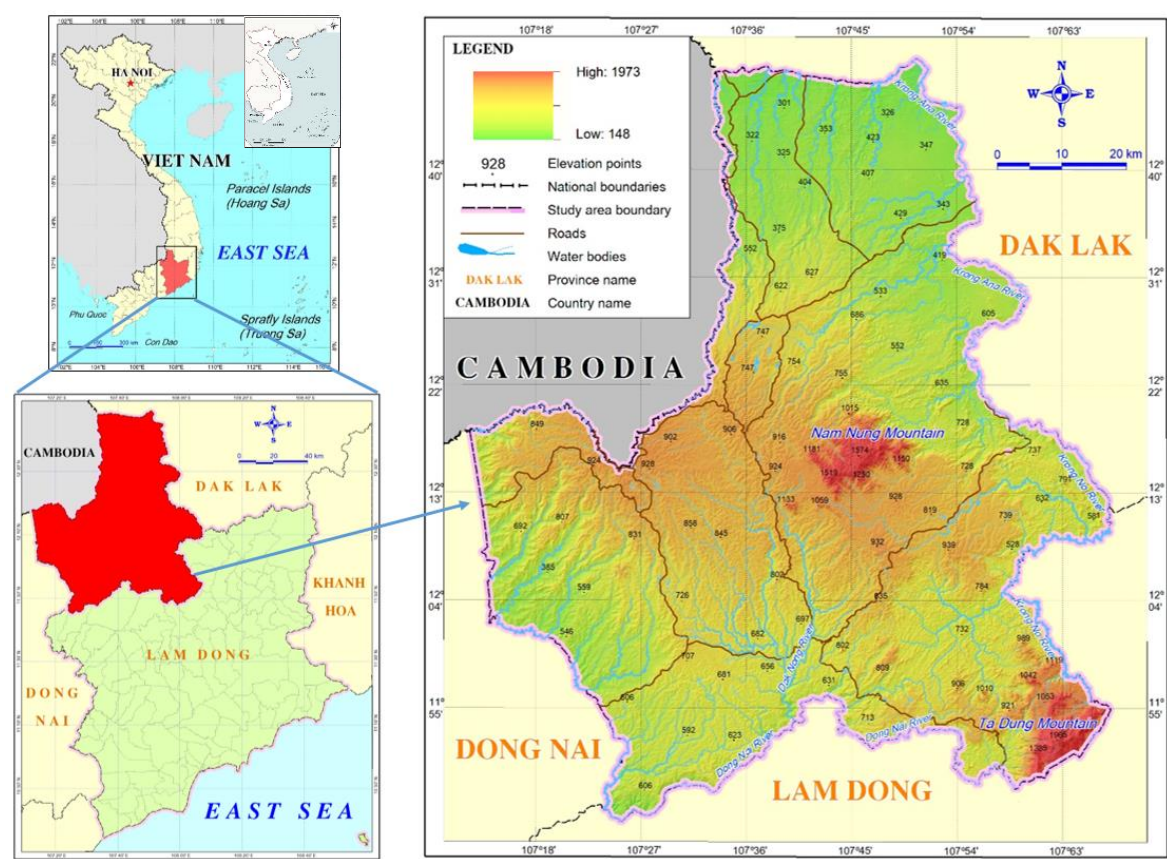


Figure 1. Location of the study area in Vietnam and Lam Dong province

Data sources

Table 1. Soil erosion severity classification based on estimated annual soil loss

Dataset	Description /GEE ID	Temporal coverage	Spatial resolution
CHIRPS Daily Precipitation	UCSB-CHG/CHIRPS/DAILY	2014-2024	0.05° (~5 km)
MERIT Hydro DEM (band UPG)	MERIT/Hydro/v1_0_1	Static	90 m
SRTM DEM	USGS/SRTMG L1_003	Static	30 m
Sentinel-2 Harmonized	COPERNICUS/S2_HARMONIZED	2024	10 m
Dynamic World (combined with slope)	GOOGLE/DYNAMICWORLD/V1 + SRTM slope	2024	10-30 m

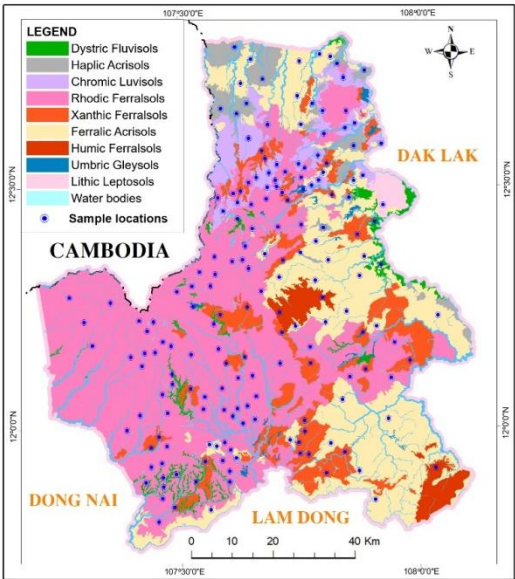


Figure 2. Soil sampling locations for K factor estimation

The data used in the study include: (i) geospatial datasets extracted and processed on the GEE platform: CHIRPS Daily Precipitation (Funk et al., 2015), Dynamic World land cover (Brown et al., 2022), MERIT Hydro DEM (Yamazaki et al., 2019), SRTM DEM (Farr et al., 2007), and Sentinel-2 Harmonized imagery (ESA, 2023) and (ii) the results of laboratory analyses of 180 field soil samples collected in the study area, providing particle size composition and organic matter (OM) data for calculating the K factor (Fig 2). Details of the datasets used for calculating each coefficient in the RUSLE model are presented in Table 1.

Implementation of RUSLE in GEE

Based on the classic erosion assessment model USLE of Wischmeier and Smith (1978), the RUSLE was developed by Renard et al. (1997) with improved flexibility and spatial detail. Therefore, to quantify soil erosion across the Dak Nong Plateau, the RUSLE model was integrated within the GEE platform and shown in Eq. (1):

$$A = R \times K \times LS \times C \times P \quad (1)$$

where: A = estimated average annual soil loss ($t.ha^{-1}.yr^{-1}$); R = rainfall erosivity factor ($MJ.mm.ha^{-1}.h^{-1}.yr^{-1}$); K = soil erodibility factor ($t.ha.h.MJ^{-1}.mm^{-1}$); LS = slope length and steepness factor; C = cover management factor, and P = support practice factor.

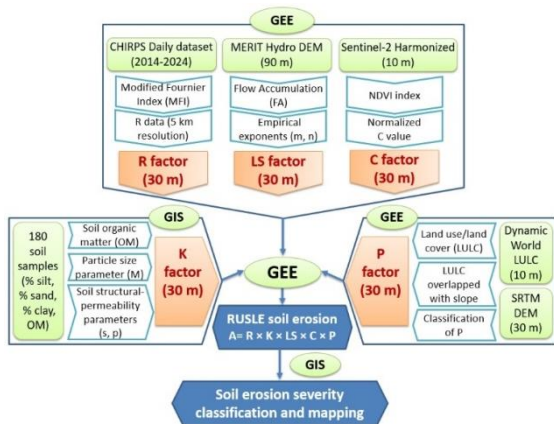


Figure 3. Cloud-based workflow for RUSLE soil erosion estimation

All RUSLE factors and the estimated soil loss results were exported as GeoTIFF files for map compilation and spatial statistical analysis in ArcMap (Fig 3). The soil erosion intensity classification was established according to the average annual soil loss ($t.ha^{-1}.yr^{-1}$), reflecting the spatial severity of erosion processes across the study area. Six severity classes were defined: very slight (0–25), slight (25–50), moderate (50–100), severe (100–300), very severe (300–500), and extremely severe (>500).

2.3.1. Rainfall erosivity factor (R)

Instead of calculating R directly from rainfall energy and 30-minute maximum intensity, it is estimated through the correlation between the Modified Fournier Index (MFI) and rainfall energy, as proposed by Fenta et al. (2017) and Elnashar et al. (2021), in the form (Eq.2):

$$R = 27.8 \times MFI - 189.2 \quad (2)$$

where: R is the rainfall erosivity factor ($MJ.mm.ha^{-1}.h^{-1}.yr^{-1}$), MFI is the Modified Fournier Index (mm).

In this study, precipitation data were obtained from the CHIRPS Daily dataset for the period 2014–2024, with a native spatial resolution of approximately 5 km, developed by the Climate Hazards Center, UCSB (Funk et al., 2015). The MFI was then calculated following the formula proposed by Arnoldus (1977) and applied in previous studies (Renard and Freimund, 1994; Alexakis et al., 2013; Balabathina et al., 2020).

The initial R-factor layer had a spatial resolution of 5 km and was subsequently resampled using bilinear interpolation to 30 m in order to synchronize with other RUSLE factors. Although this equation was not originally calibrated for Vietnam, it provides a practical solution for regions with sparse rain-gauge coverage and enables continuous spatial prediction across the Plateau.

Soil erodibility factor (K)

The K factor was estimated from laboratory-analyzed soil properties, including texture components (sand, silt, clay) and

organic matter (OM), using the simplified nomograph-based formulation recommended in RUSLE applications (Wischmeier & Smith, 1978; Renard et al., 1997). In this study, soil texture components (% silt, % clay, % sand) and OM from 180 soil samples were analyzed, representing major soil types and typical land use categories within the study area. The texture parameter (M) was estimated using a simplified form (Eq. 3):

$$M \approx \% \text{silt} \times (100 - \% \text{clay}) \quad (3)$$

Simultaneously, data from 180 surface-soil samples were converted into USDA texture classes and assigned structure (s) and permeability (p) codes following standard guidelines. Saturated hydraulic conductivity (Ks) was estimated using the Saxton & Rawls (2006) pedotransfer function to derive p classes. (Table 2).

Table 2. Classification of soil structure (s) and permeability (p) for K-factor estimation

USDA texture class	Structure code (s)	Ks (mm/h)	Permeability code (p)
Sand/Loamy sand	1	>60	5-6
Sandy loam/Loam	2	5-60	3-4
Silt loam/Silt	3	1-20	2-3
Clay loam/Silty clay loam	3-4	0.5-5	1-2
Clay/Silty clay	4	<1	1

K values calculated at sample points were spatially assigned to soil mapping units based on the 1:100,000 soil map, ensuring pedological consistency across the study region. This approach, recommended in studies with high but spatially uneven sampling density (Ganasri & Ramesh, 2016; Borrelli et al., 2017). The final results were processed in a GIS environment to generate a K-factor raster layer, which was subsequently imported into GEE.

Slope length and steepness factor (LS)

The LS factor was computed using the Moore & Burch (1986) method adapted for raster-based modeling following Desmet & Govers (1996). This has enabled accurate LS computation over complex terrains in GIS or

GEE in studies by Ansari & Tayfur, 2023; Romdania & Herison, 2024; Badavath et al., 2024. Accordingly, the LS coefficient is calculated according to the following Eq. (4):

$$LS = \left(\frac{FA \times \text{cellsize}}{22.13} \right)^m \times \left(\frac{\sin(\text{slope})}{0.0896} \right)^n \quad (4)$$

where FA denotes Flow Accumulation, cellsize is the raster cell resolution (m), slope is the terrain gradient (in radians), and m and n are empirical exponents reflecting the nonlinear relationship between slope length, slope gradient, and erosion intensity.

FA was calculated from the DEM using the D8 flow direction algorithm (O'Callaghan & Mark, 1984). To ensure high topographic accuracy, this study employed the MERIT Hydro DEM, a globally corrected elevation dataset with minimized errors. Meanwhile, m = 0.45 was adopted to capture the increase in erosion potential with greater slope length and n = 1.3 was selected to represent the nonlinear effect of slope steepness on runoff erosivity.

Cover management factor (C)

The C-factor represents the influence of vegetation cover and land management practices on soil erosion resistance. In this study, the C factor was calculated based on the NDVI extracted from Sentinel-2 satellite imagery for the period from January 1, 2024 to December 31, 2024. The NDVI was calculated according to the formula of Rouse et al (1974). For Sentinel-2 imagery, the NIR band corresponds to Band 8 (842 nm) and the Red band to Band 4 (665 nm) according to ESA (2015). The C factor was then derived from NDVI using a nonlinear exponential relationship (Durigon et al., 2014; Kouli et al., 2009). The resulting C values were normalized within the range [0–1], where lower values indicate areas with dense vegetation cover and higher soil protection capacity, whereas higher values correspond to bare or sparsely vegetated areas more susceptible to erosion.

Support practice factor (P)

To determine P factor, the study utilized the land use and land cover (LULC) data derived from the Dynamic World product

(Sentinel-2, GEE), in combination with a slope map generated from SRTM DEM. Accordingly, the P factor was computed through the following steps: 1) The Dynamic World dataset was extracted and reclassified into major land-use categories (Table 3). The LULC layer was overlaid with the slope map derived from the DEM to generate a combined dataset. 2) The P-factor values are typically assigned based on land-use type, conservation practices, and slope steepness (USDA-SCS, 1972; Renard et al., 1997). P values ranged from 0.8 for forest and shrubland (representing natural protection) to 1.0 for water, built-up areas, and bare land. Cropland P values varied by slope class in accordance with practices documented in mountainous erosion studies (e.g., Kouli et al., 2009; Prasannakumar et al., 2012).

Table 3. P factor classification based on land use and slope conditions

Land use type (LULC)	Slope range (%)	P value
Cropland	<2	0.6
	2-5	0.5
	5-8	0.5
	8-12	0.6
	12-16	0.7
	16-20	0.8
	>20	0.9
Water bodies, Built-up areas, Bare soil	-	1.0
Other land use types (forest, shrubland, grassland, etc.)	-	0.8

RESULTS AND DISCUSSION

Spatial characteristics of erosion-controlling factors

Spatial variation of rainfall erosivity factor (R)

The original R factor map derived from CHIRPS data at a 5 km resolution (Fig. 4) illustrates the baseline spatial variability of precipitation erosivity. To ensure consistency with other RUSLE input layers, the R factor was bilinearly interpolated to a 30 m spatial resolution, providing a raster suitable for pixel-based erosivity calculations. Higher R values (>6800) are mainly concentrated in the southern and southwestern parts of plateau

while lower values (<6200) dominate the northern and northeastern regions. The majority of the area exhibits moderate erosivity, with 27.9% of the study area falling within 6200–6400 MJ.mm. ha⁻¹.h⁻¹.year⁻¹, followed by 20.4% in the 6000–6200 class and 15.6% in 6600–6800. Extremely high R values (>7000) occupy only 5.6% of the total area, while very low erosivity (<6000) covers 1.7% (Table 4).

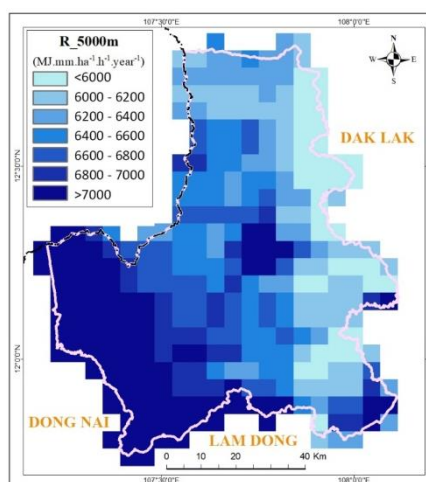


Figure 4. Original R-factor map derived from CHIRPS data

Table 4. R factor classes and area

R factor (MJ.mm.ha ⁻¹ .h ⁻¹ .year ⁻¹)	Area (ha)	Percentage (%)
< 6000	10.806	1,7
6000-6200	132.602	20,4
6200-6400	181.558	27,9
6400-6600	94.975	14,6
6600-6800	101.373	15,6
6800-7000	93.040	14,3
Total	650,927	100,0

Soil erodibility (K) derived from soil sampling and laboratory analysis

The spatial variability of K is controlled primarily by soil texture composition and OM (Fig. 5). Most of the area (over 70%) exhibits K values between 0.02 and 0.03 t.ha.h.MJ⁻¹.mm⁻¹, reflecting moderate soil erodibility (Table 5). The estimated K factor values in the Dak Nong Plateau ranged from 0.012 to 0.025 t.ha.h.MJ⁻¹.mm⁻¹ (Table 6).

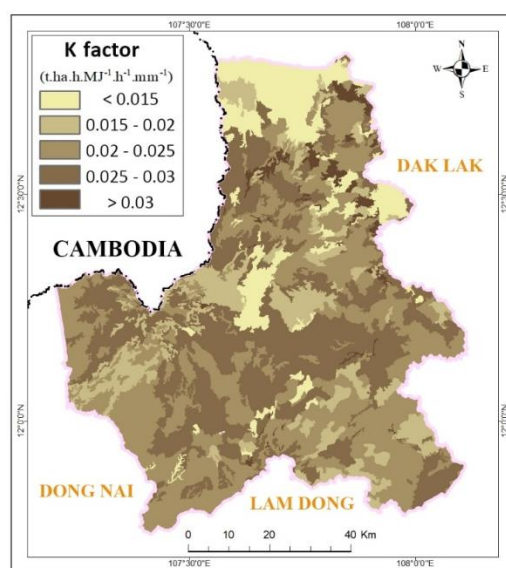


Figure 5. Spatial distribution of soil erodibility factor (K)

Table 5. K factor classes and area

K factor (t.ha.h.MJ ⁻¹ .mm ⁻¹)	Area (ha)	Percentage (%)
< 0.015	70,272	10.8
0.015 - 0.02	92,444	14.2
0.02-0.025	255,037	39.2
0.025-0.03	217,478	33.4
>0.03	15,696	2.4
Total	650,927	100.0

Higher K values are associated with Rhodic Ferralsols, Xanthic Ferralsols, and Chromic Luvisols, which are characterized by moderate clay content and relatively high silt fractions. Such soil textures facilitate the detachment of fine particles and surface crusting during rainfall, leading to reduced

infiltration and greater susceptibility to erosion. Conversely, Haplic Acrisols exhibit the lowest K (0.012 ± 0.006), due to their high sand content and very low OM, which allow rapid infiltration and limit surface runoff formation.

Table 6. Summary of mean (\pm SD) soil physical properties and K factor by major soil types in the Dak Nong Plateau

Soil type	n	Sand (%)	Silt (%)	Clay (%)	OM (%)	K factor (t.ha.h.MJ ⁻¹ .mm ⁻¹)
Rhodic Ferralsols	76	32.6 \pm 9.1	28.0 \pm 6.0	39.4 \pm 10.2	4.18 \pm 1.3	0.0236 \pm 0.004
Ferralic Acrisols	32	49.2 \pm 12.1	22.5 \pm 5.6	28.3 \pm 9.3	1.46 \pm 1.0	0.0185 \pm 0.006
Xanthic Ferralsols	28	37.5 \pm 6.2	25.2 \pm 5.0	37.3 \pm 6.1	2.57 \pm 1.6	0.0241 \pm 0.004
Chromic Luvisols	18	27.6 \pm 9.0	31.5 \pm 7.7	41.0 \pm 8.4	3.67 \pm 1.4	0.0253 \pm 0.005
Haplic Acrisols	13	62.6 \pm 9.6	18.7 \pm 5.6	18.7 \pm 7.1	0.93 \pm 0.4	0.012 \pm 0.006
Dystric Fluvisols	7	38.7 \pm 7.6	29.2 \pm 7.5	32.1 \pm 6.5	2.82 \pm 1.6	0.022 \pm 0.006
Humic Ferralsols	3	34.6 \pm 18.2	29.8 \pm 8.4	35.7 \pm 11.5	4.48 \pm 0.9	0.0218 \pm 0.007

Note: n – number of soil samples; sand, silt, clay, and OM (%) represent soil properties

Topographic factor (LS)

The LS factor strongly reflects the control of the terrain on erosion processes. This is evident in the steeper slopes, which typically have the highest LS values. Thus, the areas around high mountains such as Nam Nung and Ta Dung record the highest LS values, exceeding 20 (Fig. 6).

These areas correspond to the most erodible landscapes, as the length and steepness of the slopes amplify the flow energy.

Low LS values (43.8%) are dominant in the northern part of the plateau and the valleys, where the slope is less than 5°. Medium LS values (5–15) are dominant in the central plateau and the gentle hills (Table 7).

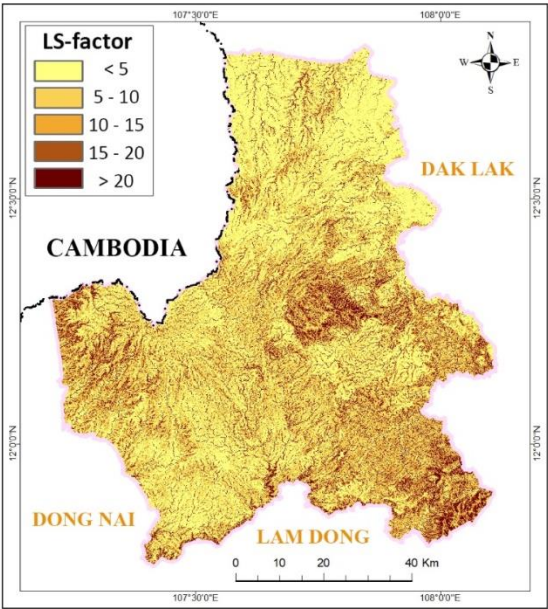


Figure 6. Spatial distribution of topographic factor (LS)

Table 7. LS factor classes and area

LS factor	Area (ha)	Percentage (%)
<5	285,106	43.8
5-10	165,484	25.4
10-15	84,128	12.9
15-20	40,613	6.2
>20	75,597	11.6
Total	650,927	100.0

Cover management factor (C) from Sentinel-2 NDVI

The spatial variability of the C factor reveals the influence of vegetation density and land-use structure across the Dak Nong Plateau (Figure 7). Areas with low C values (<0.1), corresponding to forests in nature reserves, national parks, and perennial crop zones, account for approximately 57.9% of the total area (Table 8).

In contrast, high C values (>0.4) are observed in annual cropland or sparsely vegetated fallow areas located mainly in the northern part of the plateau. Areas with moderate C values (0.1–0.3) account for about 27.7% of the total area, typically representing smallholder and farm-based perennial and rotational cropping lands with partial canopy closure.

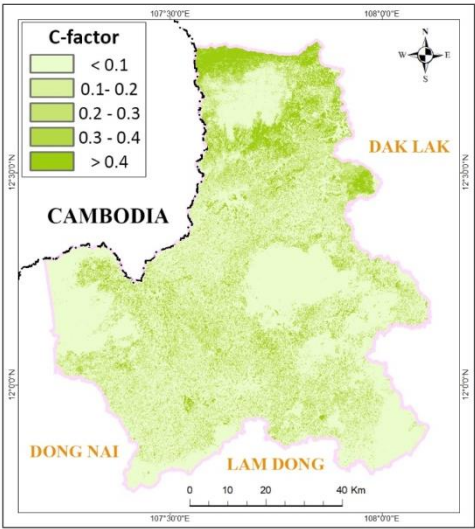


Figure 7. Spatial distribution of cover management factor (C) for 2024

Table 8. C factor classes and area

C factor	Area (ha)	Percentage (%)
<0.1	387,618	57.9
0.1-0.2	118,004	17.6
0.2-0.3	67,774	10.1
0.3-0.4	41,000	6.1
>0.4	55,625	8.3
Total	650,927	100.0

Support practice factor (P)

The calculated P factor in the Dak Nong Plateau shows limited application of soil conservation practices. As shown in Table 9 and Figure 8, the majority of the area (75.6%; 492,353 ha) has $P = 0.8-0.9$, while 8.8% (57,008 ha) exhibits $P = 0.9-1.0$. Lower P classes (0.5–0.7) account for only about 15.6% of the total area, mainly corresponding to agricultural lands where contour farming or slope-adjusted cultivation is practiced.

Table 9. P factor classes and area

P factor	Area (ha)	Percentage (%)
0.5-0.6	40,171	6.2
0.6-0.7	38,981	6.0
0.7-0.8	22,414	3.4
0.8-0.9	492,353	75.6
0.9-1	57,008	8.8
Total	650,927	100.0

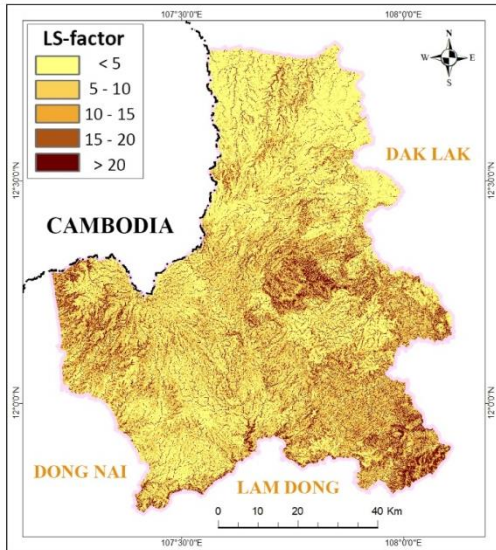


Figure 8. Spatial distribution of support practice factor (P)

Spatial distribution and classification of annual soil loss

The annual soil loss across the Dak Nong Plateau exhibits pronounced spatial variability, with estimated rates ranging from very slight ($< 25 \text{ t.ha}^{-1}\text{.yr}^{-1}$) to extremely severe ($> 500 \text{ t.ha}^{-1}\text{.yr}^{-1}$). The mean soil loss

for the study area is approximately $125 \text{ t.ha}^{-1}\text{.yr}^{-1}$, reflecting the combined influence of high rainfall erosivity, complex topography and varied land-use practices. Annual soil loss was computed by multiplying the USLE factor layers at 30 m resolution within the GEE environment. For mapping and interpretation, soil loss rates were classified into six severity levels (Table 10, Fig. 10).

Areas exhibiting very slight to slight erosion ($< 50 \text{ t.ha}^{-1}\text{.yr}^{-1}$) occupy approximately 378,421 ha (58.1% of the plateau) (Fig. 9). These low-erosion zones are predominantly associated with dense, protected forest stands (e.g. Nam Nung Nature Reserve), national parks (Ta Dung, Yok Don) and extensive perennial crop areas on gentle slopes. Moderate erosion ($50-100 \text{ t.ha}^{-1}\text{.yr}^{-1}$) accounts for about 14.2% of the study area and occurs predominantly in transitional zones where smallholder and farm-based perennial or rotational cropping systems on intermediate slopes reduce continuous ground cover. Severe erosion ($100-300 \text{ t.ha}^{-1}\text{.yr}^{-1}$) is concentrated along the steeper margins of the plateau and on actively cultivated slopes lacking effective conservation measures, covering roughly 18% of the region.

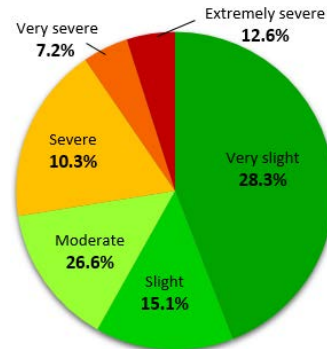


Figure 9. Area distribution (%) by erosion class

Finally, very severe ($300-500 \text{ t.ha}^{-1}\text{.yr}^{-1}$) and extremely severe ($> 500 \text{ t.ha}^{-1}\text{.yr}^{-1}$) zones are primarily located on the steepest, highly degraded slopes, without soil protection. Together these two highest-risk categories represent about 9.5% of the plateau but constitute the principal erosion hotspots that should be prioritized for immediate conservation interventions.

Table 10. Soil erosion severity classes and areal proportions

Level	Average soil loss (t.ha ⁻¹ .year ⁻¹)	Area (ha)	Percentage (%)
I: Very slight	0 - 25	287,053	44.1
II: Slight	25 – 50	91,368	14.0
III: Moderate	50 - 100	93,226	14.3
IV: Severe	100 - 300	117,033	18.0
V: Very severe	300 - 500	30,207	4.6
VI: Extremely severe	>500	32,041	4.9
Total	650,927	100.0	

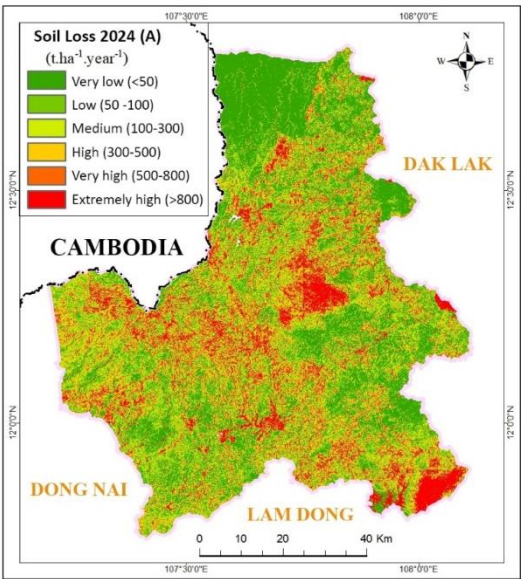


Figure 10. Spatial distribution of annual soil loss on the Dak Nong Plateau

Discussion

The spatial pattern of soil erosion on the Dak Nong Plateau is strongly governed by seasonal high-intensity monsoon rainfall, complex terrain, and the intrinsic erodibility of basalt-derived soils. These combined controls explain why considerable soil loss is observed across both dissected uplands and cultivated slopes of the plateau. Similar to this point of view, there are studies by Le Bissonnais et al, 1995; Lal, 2001; Morgan, 2005; Sidle et al., 2006; Wang et al., 2025. Comparisons with previous studies indicate that the magnitude and spatial

pattern of erosion estimated here are consistent with findings in Central Vietnam. Regional RUSLE-based studies have reported mean annual soil loss ranging from 80–200 t.ha⁻¹.yr⁻¹ on cultivated slopes, largely controlled by rainfall erosivity and land-cover dynamics (Huynh et al., 2020; Duc et al., 2025). Our approach of deriving rainfall erosivity (R) from CHIRPS data that are broadly comparable with the global assessment by Panagos et al. (2017), who generated a worldwide erosivity dataset using high-temporal-resolution rainfall records.

A key methodological contribution of this study is the implementation of RUSLE entirely within the GEE environment, integrating multi-source datasets with laboratory-analyzed soil properties. Compared with previous studies in Vietnam that relied on static GIS workflows or coarse global data products, our approach provides improved spatial detail, automated processing, and higher consistency across input layers. The use of a hydrologically enhanced DEM (MERIT Hydro) combined with field-based soil erodibility (K) measurements helps reduce common uncertainties associated with digital elevation artefacts and global soil datasets. This contributes to a more robust representation of erosion-prone slopes in the basalt uplands, where micro-topographic variations and Ferralsols strongly influence runoff generation.

Despite these advantages, several uncertainties remain. First, the R factor calculated from CHIRPS rainfall data inherits scaling and downscaling errors due to the mismatch between the 5 km CHIRPS resolution and the 30 m mapping resolution. Although the spatial pattern aligns with regional erosivity trends reported in previous studies, local gauge-based calibration would increase reliability. Second, the C and P factors are based on satellite-derived land cover and globally generalized support-practice estimates, which may not fully capture local management variations such as mulching, contour planting, or understory practices commonly adopted in coffee and pepper plantations.

Overall, this study contributes new regional-scale evidence on soil erosion dynamics

in the Dak Nong Plateau, advances the use of cloud-based RUSLE workflows in Vietnam, and demonstrates the value of integrating field-based soil data with multi-source satellite inputs. These findings highlight the need for continued monitoring of erosion hotspots, improved local calibration of erosivity and land-management factors, and the integration of slope stabilization strategies into land-use planning in the Central Highlands.

CONCLUSION

The integration of RUSLE within the GEE environment provides a robust, scalable framework for quantifying soil erosion across complex tropical highlands such as the Dak Nong Plateau. Estimated soil loss ranges from < 25 to > 500 t.ha⁻¹.yr⁻¹, with an average of approximately 125 t.ha⁻¹.yr⁻¹. The spatial analysis reveals that very slight erosion (0–25 t.ha⁻¹.yr⁻¹) dominates, accounting for 287,053 ha (44.1%), while moderate to severe erosion (50–300 t.ha⁻¹.yr⁻¹) affects 210,259 ha (32.3%). Areas at risk of severe and extremely severe erosion (> 300 t.ha⁻¹.yr⁻¹) occupy 62,248 ha (9.5%) and are concentrated on steep slopes with degraded vegetation cover. The spatial pattern of erosion is governed primarily by intense monsoonal rainfall, the complex topography of the basaltic plateau, and the intrinsic susceptibility of Ferralsols, rich in clay and silt fractions that reduce infiltration. However, forest ecosystems and well-managed perennial plantations (coffee, pepper, fruit trees) play a crucial role in stabilizing slopes, enhancing infiltration, and reducing surface runoff.

Methodologically, the study demonstrates the utility of cloud-based processing for large-scale soil erosion assessment in data-scarce tropical highlands. While uncertainties remain, particularly related to rainfall downscaling and generalized C and P factors, the approach offers a scalable framework for future monitoring and model refinement. The findings provide a scientific basis for targeting erosion-control interventions and enhancing sustainable land management in the Central Highlands.

ACKNOWLEDGMENTS

This study is part of the outcomes of the research result by Hoang Thi Huyen Ngoc, funded by the Master and PhD Scholarship Programme of the Vingroup Innovation Foundation (VINIF), code VINIF.2024.TS.117.

REFERENCES

- An, L. D., Khanh, U. D, (2012), *Geomorphology of Vietnam, Structure - Resources - Environment*, Publishing House for Science and Technology, Hanoi, 659pp.
- Alexakis, D. D., Hadjimitsis, D. G., & Agapiou, A. (2013). Integrated use of remote sensing, GIS and precipitation data for the assessment of soil erosion rate in the catchment area of “Yialias” in Cyprus. *Atmospheric Research*, 131, 108-124.
- Arnoldus, H.M.J., (1977). Methodology used to determine the maximum potential average annual soil loss due to sheet and rill erosion in Morocco. *FAO Soils Bulletins*. FAO.
- Ansari, A., & Tayfur, G. (2023). Comparative analysis of estimation of slope-length gradient (LS) factor for entire Afghanistan. *Geomatics, Natural Hazards and Risk*, 14(1), 2200890.
- Badavath, N., Sahoo, S., & Samal, R. (2024). Unveiling Meghalaya topography: slope length gradient (LS) factor estimation for insightful soil erosion evaluation. *Journal of Engineering and Applied Science*, 71(1), 174.
- Balabathina, V. N., Raju, R. P., Mulualet, W., & Tadele, G. (2020). Estimation of soil loss using remote sensing and GIS-based universal soil loss equation in northern catchment of Lake Tana Sub-basin, Upper Blue Nile Basin, Northwest Ethiopia. *Environmental Systems Research*, 9(1), 35.
- Borrelli, P., Robinson, D. A., Fleischer, L. R., Lugato, E., Ballabio, C., Alewell, C., ... & Panagos, P. (2017). An assessment of the global impact of 21st century land use change on soil erosion. *Nature communications*, 8(1), 2013.
- Borrelli, P., Robinson, D. A., Panagos, P., Lugato, E., Yang, J. E., Alewell, C., ... & Ballabio, C. (2020). Land use and climate change impacts on global soil erosion by water (2015-2070). *Proceedings of the National Academy of Sciences*, 117(36), 21994-22001.

- Bosco, C., de Rigo, D., Dewitte, O., Poesen, J., & Panagos, P. (2015). Modelling soil erosion at European scale: towards harmonization and reproducibility. *Natural Hazards and Earth System Sciences*, 15(2), 225-245.
- Brown, C. F., Brumby, S. P., Guzder-Williams, B., Birch, T., Hyde, S. B., Mazzariello, J., ... & Tait, A. M. (2022). Dynamic World, Near real-time global 10 m land use/land cover mapping. *Scientific Data*, 9, 251.
- Cuong, H. D., (2014). Research on climate conditions, agricultural climate to serve socio-economic development and natural disaster prevention in the Tay Nguyen. Summary report on the implementation results of project code TN3/T25 under the State-level key science and technology program code KHCN-TN3/11-15 (Tay Nguyen Program 3), Hanoi. 287 pages.
- Daknong Statistics Office (DSO), (2023). Daknong statistical yearbook 2022. Statistical Publishing House, Daknong, 2023, 593 pp.
- Delgado, D., Sadaoui, M., Ludwig, W., Méndez, W., Ortiz-Hernández, E., & Farfán-Intriago, P. (2025). Assessment of soil erosion by RUSLE in the Ecuadorian basins (2001– 2020) based on GIS and high-resolution satellite data: Main drivers and changes on soil erosion. *Geomorphology*, 469, 109515.
- Desmet, P. J. J., & Govers, G. (1996). A GIS procedure for automatically calculating the USLE LS factor on topographically complex landscape units. *Journal of Soil and Water Conservation*, 51(5), 427–433.
- Dou, X., Ma, X., Zhao, C., Li, J., Yan, Y., & Zhu, J. (2022). Risk assessment of soil erosion in Central Asia under global warming. *Catena*, 212, 106056.
- Durigon, V. L., Carvalho, D. F., Antunes, M. A. H., Oliveira, P. T. S., & Fernandes, M. M. (2014). NDVI time series for monitoring RUSLE cover management factor in a tropical watershed. *International journal of remote sensing*, 35(2), 441-453.
- Elnashar, A., Zeng, H., Wu, B., Fenta, A. A., Nabil, M., & Duerler, R. (2021). Soil erosion assessment in the Blue Nile Basin driven by a novel RUSLE-GEE framework. *Science of the Total Environment*, 793, 148466.
- Elwell, H. A., & Stocking, M. A. (1976). Vegetal cover to estimate soil erosion hazard in Rhodesia. *Geoderma*, 15(1), 61-70.
- European Space Agency (ESA). (2021). *Copernicus DEM GLO-30*. European Space Agency. <https://spacedata.copernicus.eu>
- European Space Agency (ESA) (2015). *Sentinel-2 User Handbook*. European Space Agency, ESA Standard Document, 64
- Fahd, S., Waqas, M., Zafar, Z., Soufan, W., Almutairi, K. F., & Tariq, A. (2025). Integration of RUSLE model with remotely sensed data over Google Earth Engine to evaluate soil erosion in Central Indus Basin. *Earth Surface Processes and Landforms*, 50(3), e70019.
- FAO (Food Agric. Organ.), ITPS (Intergov. Tech. Panel Soils). 2015.. Status of the world's soil resources (SWSR)—main report. Rep, FAO/ITPS, Rome: <https://www.fao.org/3/i5199e/I5199E.pdf>
- Farr, T. G., Rosen, P. A., Caro, E., Crippen, R., Duren, R., Hensley, S., ... & Alsdorf, D. (2007). The Shuttle Radar Topography Mission. *Reviews of Geophysics*, 45(2), RG2004.
- Fenta, A. A., Yasuda, H., Shimizu, K., Haregeweyn, N., Kawai, T., Sultan, D., ... & Belay, A. S. (2017). Spatial distribution and temporal trends of rainfall and erosivity in the Eastern Africa region. *Hydrological Processes*, 31(25), 4555-4567.
- Fentaw, A. E., & Abegaz, A. (2024). Soil erosion assessment and identification of erosion hotspot areas in the upper Tekeze Basin, Northern Ethiopia. *Heliyon*, 10(12).
- Funk, C., Peterson, P., Landsfeld, M., Pedreros, D., Verdin, J., Shukla, S., ... & Michaelsen, J. (2015). The climate hazards infrared precipitation with stations— a new environmental record for monitoring extremes. *Scientific data*, 2(1), 1-21.
- Ganasri, B. P., & Ramesh, H. J. G. F. (2016). Assessment of soil erosion by RUSLE model using remote sensing and GIS-A case study of Nethravathi Basin. *Geoscience Frontiers*, 7(6), 953-961.
- Ghosh, J., Das, S., Ghosh, S., Midya, K., Das, S., & Mishra, V. N. (2025). Soil erosion vulnerability analysis of Damodar River Basin, India using Revised Universal Soil Loss Equation (RUSLE) in Google Earth Engine (GEE). *Discover Geoscience*, 3(1), 1-31.
- Global Soil Partnership (GSP) (2017). Global Soil Partnership Endorses Guidelines on Sustainable Soil Management. <http://www.fao.org/global-soil-partnership/resources/highlights/detail/en/c/416516/>
- Gorelick, N., Hancher, M., Dixon, M., Ilyushchenko, S., Thau, D., & Moore, R. (2017). Google Earth Engine: Planetary-scale geospatial analysis for everyone. *Remote Sensing of Environment*, 202, 18–27. <https://doi.org/10.1016/j.rse.2017.06.031>

- Ha, N. M., Dung, N. V., & Ngoc, H. H. (2014). Application of USLE and GIS tool to predict soil erosion potential and proposal land cover solutions to reduce soil loss in Tay Nguyen. *Vietnam Journal of Earth Sciences*, 35(4), 403–410.
- Jodhani, K. H., Patel, D., Madhavan, N., & Singh, S. K. (2023). Soil erosion assessment by rusle, google earth engine, and geospatial techniques over rel river watershed, gujarat, india. *Water Conservation Science and Engineering*, 8(1), 49.
- Kouli, M., Soupios, P., & Vallianatos, F. (2009). Soil erosion prediction using the revised universal soil loss equation (RUSLE) in a GIS framework, Chania, Northwestern Crete, Greece. *Environmental geology*, 57(3), 483–497.
- Lal, R. (2001). Soil degradation by erosion. *Land Degradation & Development*, 12(6), 519–539.
- Le Bissonnais, Y., Renaux, B., & Delouche, H. (1995). Interactions between soil properties and moisture content in crust formation, runoff and interrill erosion from tilled loess soils. *Catena*, 25(1-4), 33–46.
- Moore, I. D., & Burch, G. J. (1986). Physical basis of the length-slope factor in the Universal Soil Loss Equation. *Soil Science Society of America Journal*, 50(5), 1294–1298.
- Morgan, R. P. C. (2005). *Soil erosion and conservation* (3rd ed.). Oxford: Blackwell Publishing, 320 pp.
- O’Callaghan, J. F., & Mark, D. M. (1984). The extraction of drainage networks from digital elevation data. *Computer Vision, Graphics, and Image Processing*, 28(3), 323–344.
- Panagos, P., Ballabio, C., Himics, M., Scarpa, S., Matthews, F., Bogonos, M., ... & Borrelli, P. (2021). Projections of soil loss by water erosion in Europe by 2050. *Environmental Science & Policy*, 124, 380–392.
- Panagos, P., Borrelli, P., Meusburger, K., Van Der Zanden, E. H., Poesen, J., & Alewell, C. (2015). Modelling the effect of support practices (P-factor) on the reduction of soil erosion by water at European scale. *Environmental science & policy*, 51, 23–34.
- Panagos, P., Borrelli, P., Meusburger, K., Yu, B., Klik, A., Jae Lim, K., ... & Ballabio, C. (2017). Global rainfall erosivity assessment based on high-temporal resolution rainfall records. *Scientific reports*, 7(1), 4175.
- Panagos, P., Borrelli, P., Matthews, F., Liakos, L., Bezak, N., Diodato, N., & Ballabio, C. (2022). Global rainfall erosivity projections for 2050 and 2070. *Journal of Hydrology*, 610, 127865.
- Prasannakumar, V., Vijith, H., Abinod, S., & Geetha, N. J. G. F. (2012). Estimation of soil erosion risk within a small mountainous sub-watershed in Kerala, India, using Revised Universal Soil Loss Equation (RUSLE) and geo-information technology. *Geoscience frontiers*, 3(2), 209–215.
- Quinton, J. N., & Fiener, P. (2024). Soil erosion on arable land: An unresolved global environmental threat. *Progress in Physical Geography: Earth and Environment*, 48(1), 136–161.
- Quy, C.H., 1995. Overview of highland development in Vietnam: General characteristics, socio-economic situation, and development challenges. *The Challenges of Highland Development. Vietnam*, 244 pp.
- Renard, K. G., Foster, G. R., Weesies, G. A., McCool, D. K., & Yoder, D. C. coordinators (1997). *Predicting Soil Erosion by Water: A Guide to Conservation Planning with the Revised Universal Soil Loss Equation (RUSLE)*. U.S. Department of Agriculture, Agriculture Handbook No. 703, 404 pp.
- Renard, K.G., Freimund, J.R., 1994. Using monthly precipitation data to estimate the Rfactor in the revised USLE. *J. Hydrol.* 157, 287–306.
- Romdania, Y., & Herison, A. (2024). Estimation of Length and Slope Factor (Ls) as Erosion Prediction in Way Pubian Sub Watershed. *ASEAN Engineering Journal*, 14(3), 107–113.
- Rouse, J. W., Haas, R. H., Schell, J. A., & Deering, D. W. (1974). Monitoring vegetation systems in the Great Plains with ERTS. *In Proceedings of the Third Earth Resources Technology Satellite (ERTS) Symposium* (NASA SP-351), 309–317.
- Saha, M., Sauda, S. S., Real, H. R. K., & Mahmud, M. (2022). Estimation of annual rate and spatial distribution of soil erosion in the Jamuna basin using RUSLE model: A geospatial approach. *Environmental Challenges*, 8, 100524.
- Saxton, K. E., & Rawls, W. J. (2006). Soil water characteristic estimates by texture and organic matter for hydrologic solutions. *Soil science society of America Journal*, 70(5), 1569–1578.
- Tiki, D., Bitom-Mamdem, L., Ibrahim, A., Amina, A., Danala, S., Mounouneck, P., ... & Ngome, F. (2025). Assesment of soil erosion susceptibility in Maga, Sudano-Sahelian zone (Far North Cameroon): Contribution of RUSLE model coupled with a GIS. *Geoderma Regional*, e00982.

- United States Department of Agriculture (USDA) - Natural Resources Conservation Service (NRCS) (2004). National Engineering Handbook: Part 630—Hydrology. Chapter 9: Hydrologic Soil-Cover Complexes. Washington, DC.
- Van De, N., Douglas, I. A. N., McMorow, J., Lindley, S., Thuy Binh, D. K. N., Van, T. T., ... & Tho, N. (2008). Erosion and nutrient loss on sloping land under intense cultivation in southern Vietnam. *Geographical Research*, 46(1), 4-16.
- Vezina, K., Bonn, F., & Van, C. P. (2006). Agricultural land-use patterns and soil erosion vulnerability of watershed units in Vietnam's northern highlands. *Landscape Ecology*, 21(8), 1311-1325.
- Vu Dinh, T., Hoang, N. D., & Tran, X. L. (2021). Evaluation of different machine learning models for predicting soil erosion in tropical sloping lands of Northeast Vietnam. *Applied and Environmental Soil Science*, 2021(1), 6665485.
- Wang, G., Hu, H., Islam, A. R. M. T., Akter, M. Y., Fattah, M. A., Kabir, Z., ... & Mondol, M. A. H. (2025). Spatiotemporal rainfall concentration and erosivity in a tropical monsoon country. *Theoretical and applied climatology*, 156(5), 251.
- Wischmeier, W. H., & Smith, D. D. (1978). Predicting rainfall erosion losses: a guide to conservation planning (No. 537). Department of Agriculture, Science and Education Administration.
- Yamazaki, D., Ikeshima, D., Sosa, J., Bates, P. D., Allen, G. H., & Pavelsky, T. M. (2019). MERIT Hydro: A high-resolution global hydrography map based on latest topography dataset. *Water Resources Research*, 55(6), 5053-5073.

DOI: 10.15625/vap.2025.0219

Understanding Vegetation Recovery after Disturbance by Natural Hazards Using Geospatial Technologies

Takashi Oguchi

Center for Spatial Information Science, The University of Tokyo, 5-1-5, Kashiwanoha, Kashiwa, Chiba 277-8568, Japan

Email: oguchi@csis.u-tokyo.ac.jp

Abstract: Vegetation disturbances and destruction due to natural hazards, such as volcanic eruptions and landslides, may be significant threats to the ecological sustainability of local societies. Therefore, vegetation recovery processes after such disturbances should be understood scientifically. This paper introduces three studies by the author and his colleagues that investigated vegetation recovery after destruction by natural hazards using geospatial technologies, including remote sensing, GIS, and relevant analytical methods. Two target areas in the Philippines and Japan were affected by volcanic eruptions with pyroclastic flows in the 1990s. The other two target areas are the Japanese mountains that experienced rainfall-induced shallow landslides in 1972 and 2010. Satellite remote sensing images for different periods were utilized to detect temporal vegetation changes based on vegetation indices computed from multi-band spectrums, including the widely used Normalized Difference Vegetation Index (NDVI) and two others. The time series of the indices were analyzed using regression models and some advanced methods to detect trends in vegetation recovery. Environmental variables representing local conditions, such as derivatives from Digital Elevation Models (DEMs), were also collected and analyzed. The results indicate that vegetation recovery trends after volcanic disturbances are logarithmic, and a long time, over decades, is often needed to reach full recovery. The recovery time depends on the original level of disturbance and topographic factors. The time-series analysis for the areas affected by landslides also

suggests relatively slow vegetation recovery, and the rate of recovery depended on local topographic conditions. The approaches to vegetation recovery analysis using geospatial technologies have some advantages over traditional methods based on field investigations. The detected slow recovery indicates a need for long-term continuous monitoring, for which future, more advanced geospatial methods will significantly contribute.

Keywords: Natural hazards, vegetation recovery, satellite remote sensing, vegetation indices, GIS, time series analysis

INTRODUCTION

Maintaining healthy vegetation on various types of land helps conserve the environment and weaken the effects of global warming. Vegetation can be disturbed by multiple factors. Human disturbance due to land development is a significant factor worldwide, and governments are working to mitigate it through effective land-use planning. Human-induced forest fire may also result in substantial vegetation damage. Additionally, natural hazards such as volcanic eruptions, landslides, debris flows, strong winds, and naturally induced forest fires lead to vegetation loss and damage. On natural terrain, vegetation that has been lost or affected by natural hazards may gradually recover. Understanding vegetation recovery processes after disturbance by natural hazards provides valuable scientific knowledge for ecological management and conservation in mountainous areas.

To address this issue, I have been collaborating with colleagues, including

graduate students and postdoctoral researchers in my laboratory, utilizing geospatial technologies, particularly remote sensing and GIS (Geographic Information Systems). These techniques enable the quantitative and statistical analysis and assessment of vegetation distribution and related environmental factors, yielding objective outcomes. This paper introduces some of our work concerning vegetation recovery after loss and deterioration caused by volcanic eruptions (De Rose et al., 2011; Lai et al., 2022) and landslides (Zhong et al., 2023).

VEGETATION RECOVERY AFTER DISTURBANCES DUE TO VOLCANIC ERUPTIONS

Mount Pinatubo, the Philippines

Mt. Pinatubo on Luzon Island, the Philippines, is a stratovolcano located ca. 90 km northwest of Manila. It caused a catastrophic eruption on June 15, 1991, the second-largest terrestrial eruption in the 20th century after the 1912 eruption of Novarupta Volcano in Alaska. The eruption replaced the former summit of the mountain with a caldera and crater lake, reducing the summit height from 1,745 to 1,486 m.

The eruption severely damaged surrounding areas with pyroclastic flows, pyroclastic falls, and subsequent lahars caused by rainfalls, including typhoon-induced ones, re-mobilizing volcanic deposits to cause sedimentation in lower regions. These processes resulted in widespread bare land on both volcanic slopes and piedmont areas, leading to the loss of thick vegetation characteristic of a tropical climate. Then the climatic condition permitted gradual vegetation regrowth.

To understand post-eruption vegetation recovery in the Pinatubo area, we analyzed visible and near-infrared (VNIR) satellite imagery from the Advanced Spaceborne Thermal Emission and Reflection Radiometer (ASTER), captured in late December or Early January in 2001, 2004, and 2008. The remotely sensed images were post-processed to correct

the topographic effect on reflectance. The supervised land cover classification on the corrected images has shown vegetated areas (forest, shrubland, and grassland) and areas disturbed by volcanic eruption, lahars, and burning for shifting cultivation (Fig. 1).

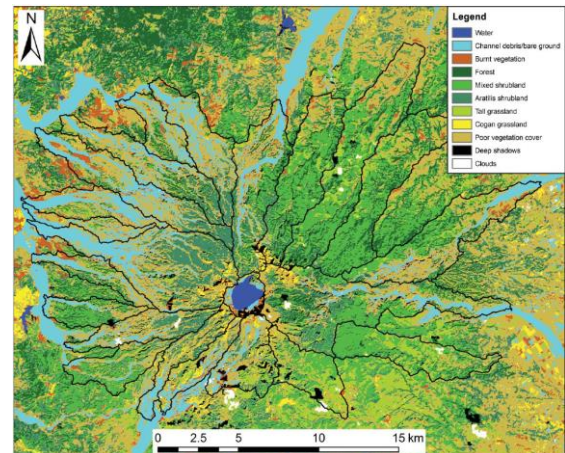


Figure 1. Land cover distribution of Mt. Pinatubo in 2001 (De Rose et al., 2011). Land cover types were deduced based on a supervised classification of the brightness-corrected ASTER VNIR image. The black lines show watershed divides on the volcanic body.

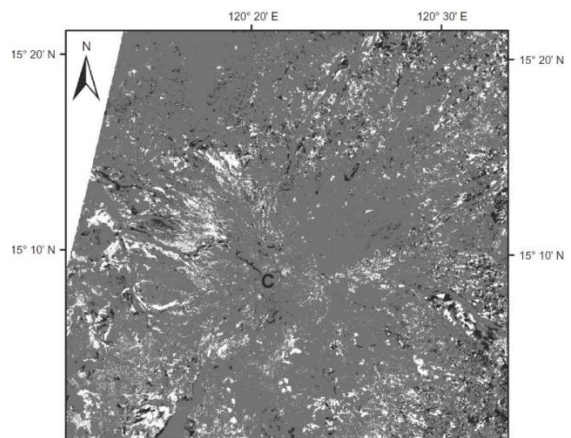


Figure 2. *NDVI* difference map: 2004 minus 2001 (De Rose et al., 2011). Dark areas represent a loss of vegetation cover, while light areas represent a gain in vegetation cover. “C” shows the location of the crater lake.

To represent the existence and health of vegetation, the values of the Normalized Difference Vegetation Index (*NDVI*) were computed from the images using the spectrum of near-infrared and red bands, and their

temporal change was obtained (Fig. 2) after the *NDVI* values for different years were calibrated using training data, ensuring that the unchanging land use showed the same *NDVI* value. The results show that broad areas experienced vegetation recovery (white parts in Fig. 2), although forest burning for shifting cultivation and channel incision and lateral shift led to new areas of vegetation loss in some locations (dark parts in Fig. 2).

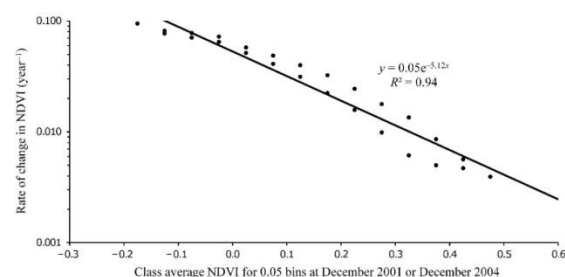


Figure 3. Rate of change in *NDVI* compared with average *NDVI* at the beginning of the monitoring period for 0.05 *NDVI* class bins (De Rose et al., 2011).

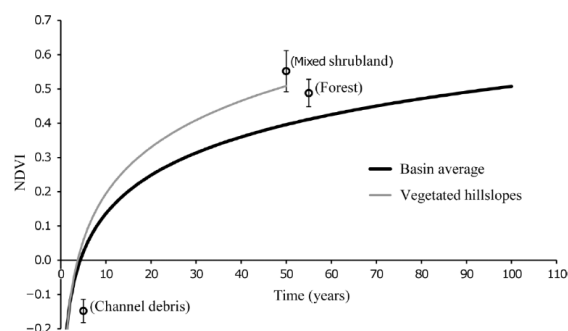


Figure 4. Logarithmic vegetation recovery curves starting with bare ground for vegetated hillslopes and the whole basin (De Rose et al., 2011).

Then, the averaged trends of *NDVI* change between 2001 and 2004 and between 2004 and 2008 were obtained using binned data (Fig. 3). The results show that larger *NDVI* increasing rates occur when the original *NDVI* values are smaller, suggesting that vegetation recovers quickly at first but takes a long time to reach a mature stage. The mathematical conversion of the trends based on the idea of location-for-time substitution yielded the trending curve of *NDVI* change over time (Fig. 4). The results illustrate that the full vegetation recovery at the levels of forest and mixed

shrubland requires about 50 years for hillslopes and about 100 years for the whole basin, with unstable areas close to channels. Therefore, long-term efforts are needed to recover vegetation after a volcanic eruption causes widespread destruction, even in humid tropical regions with rapid vegetation growth. Thus, prolonged vegetation monitoring and continuous attention to vegetation recovery levels are required to assure regional development in the Pinatubo area.

Unzen Volcano, Japan

Unzen volcano is an active composite volcano located on the Shimabara Peninsula in Kyushu, Japan. The summit is called Fugendake, with an altitude of 1,483 m (Fig. 5A). The volcano began erupting in November 1990, after 198 years of dormancy. The eruption was sequential and ended in February 1995. It generated multiple pyroclastic flows, primarily over the eastern flank of the volcanic body, resulting in the loss of life, infrastructure, and vegetation as well as topographic change (Fig. 5B). The disturbance on land and vegetation due to the 1990–1995 volcanic activities can be classified into several types: ash cloud surges, block ash flows, dead trees, lahar deposits, lava domes, and seared zones (Fig. 6).

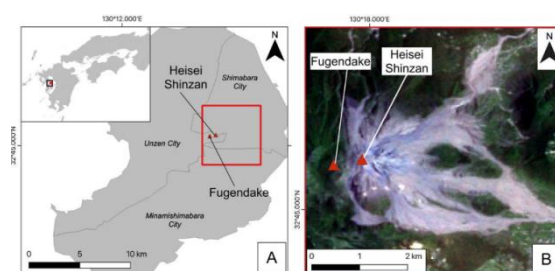


Figure 5. Unzen Volcano. (A): Location map; (B): Landsat image taken on June 6, 1995, showing bare lands caused by volcanic activities (Lai et al., 2022).

We downloaded Landsat satellite images from Google Earth Engine and selected those for the summer period (June to September) from 1984 to 2021, ensuring they met acceptable quality standards. We then computed two commonly used vegetation indices for vegetation mapping from the Landsat spectral bands: *NDVI* and the

Normalized Burn Ratio (*NBR*). The latter utilizes the spectrum of the short-wave infrared band, rather than the red band used for *NDVI* calculation.

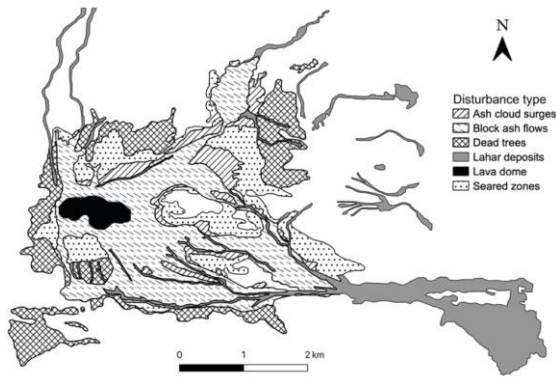


Figure 6. Map showing the types of the 1990–1995 eruption deposits and disturbances, based on aerial photographs taken in September 1995 (Lai et al., 2022, after Miyabuchi, 1999).

Subsequently, the model of logarithmic vegetation recovery, as used by De Rose et al. (2011), was applied to the *NDVI* and *NBR* time series after the eruption for different disturbance types. Fig. 7 shows the averaged trends of vegetation recovery for disturbance types in terms of *NBR*. Recovery for the types “dead trees” and “seared zones” is relatively fast because the level of disturbance in these areas was relatively low. In contrast, recovery on “lava domes” is markedly slow, primarily due to their steep and rocky surfaces. The recovery rates for areas covered by ash and lahar deposits are intermediate.

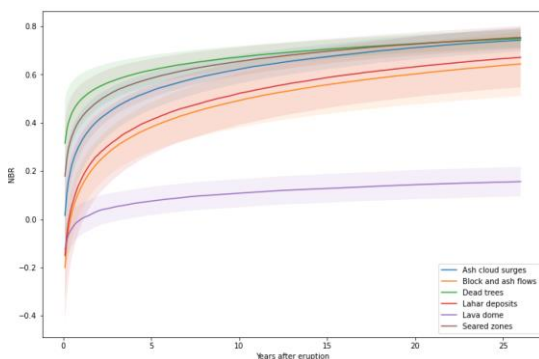


Figure 7. Average vegetation recovery curves based on *NBR* values for each disturbance type with one standard deviation represented (Lai et al., 2022).

For a more detailed analysis of the recovery trends, we introduced four metrics: 1) Number of years required to reach 20% of the pre-eruption vegetation index value (*YEAR20*); 2) Number of years to get 80% of the pre-eruption vegetation index value (*YEAR80*); 3) Slope of the linear-log model (β); and 4) Recovery indicator value (*RI*). The β metric reflects the change in recovery rate over the entire observation period. The *RI* metric was defined to represent the level of vegetation recovery during the first five years (see Lai et al., 2022, for details). Fig. 8 shows the result using box-and-whisker plots, indicating some differences between *NDVI* and *NBR* results, especially for metrics representing the early stage of vegetation recovery (*YEAR20* and *RI*). The comparison of the results with field observation indicates that *NDVI* tends to overestimate vegetation recovery in the early stage, and *NBR* better represents actual recovery. Although many more studies on vegetation change have used *NDVI* than *NBR*, the latter can be an excellent choice for monitoring early vegetation recovery in areas affected by volcanic eruptions.

To further discuss the factors affecting vegetation recovery, we obtained four topographic parameters (elevation, slope, aspect, and profile curvature) from a digital elevation model (DEM). We also derived two geographical indices, “distance from surviving vegetation” and “distance from crater”, utilizing functions of the QGIS software. We conducted a regression tree analysis to investigate the effects of the topographic and geographical factors, as well as the disturbance types, on vegetation recovery. Fig. 9 shows the results for the *YEAR20* and *YEAR80* metrics. On the first level, the disturbance types define the recovery time. The second most crucial factor is elevation, and higher areas with harsher environments are unfavorable for recovery. For the early stage of recovery represented by *YEAR20*, distance from surviving vegetation and slope also matter. The effect of the former became negligible in the latter stage, represented by *YEAR80*. Instead, aspect exerts some impacts. It is essential to consider such a

change in the controlling factor of vegetation recovery with time to plan appropriate strategies for ecological conservation.

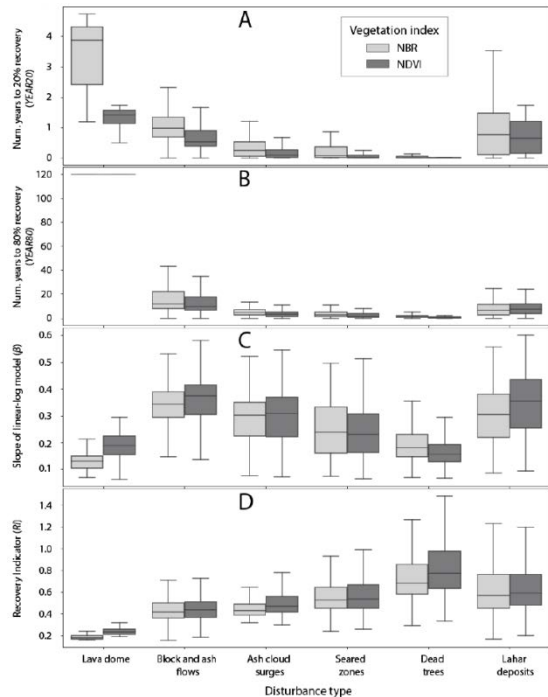


Figure 8. Distribution of recovery metrics (y-axis) for each disturbance type (x-axis) and for *NBR* (light gray) and *NDVI* (dark gray). (A): *YEAR20*; (B): *YEAR80*; (C): β ; (D): *RI* (Lai et al., 2022).

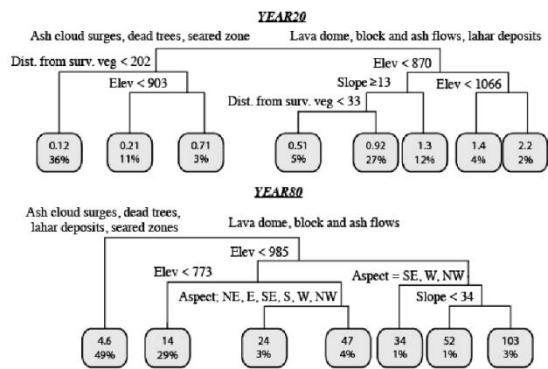


Figure 9. Regression tree results for the *YEAR20* and *YEAR80* recovery metrics (Lai et al., 2022).

VEGETATION DISTURBANCES DUE TO LANDSLIDES AND SUBSEQUENT RECOVERY

Landslides, especially shallow ones that remove surficial regolith and vegetation, often create bare land on slopes. Although the total

area affected by a single landslide event is usually less extensive than that by a volcanic eruption, landslides occur more frequently and more ubiquitously.

As a case study on vegetation disturbances due to landslides and subsequent recovery, we investigated two low-relief mountainous areas: the Obara district in central Honshu, Japan, and the Shobara district in western Honshu. The Obara district experienced heavy rainfall in July 1972, resulting in numerous shallow landslides. The Shobara district also experienced a severe rainstorm in July 2010, which caused over 1,000 shallow landslides. These events produced bare land, which was gradually revegetated under a humid temperate climate (Fig. 10).

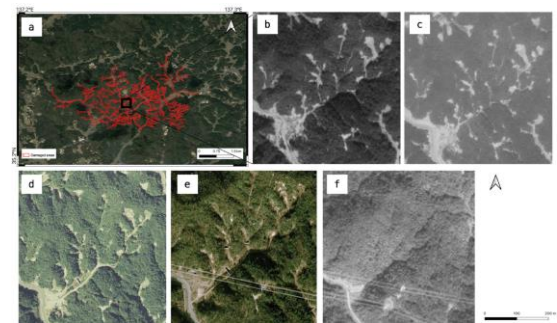


Figure 10. Aerial photographs showing vegetation recovery in a part of the Obara district after the 1972 landslide event. (a): Photo of the Obara district. Areas within the red outlines were affected by the 1972 event (shallow landslides and debris flows). The black box shows the location of the selected part shown in (b) to (f); (b): 1972; (c): 1974; (d): 1977; (e): 1982; (f): 1988 (Zhong et al., 2023).

To detect vegetation conditions and changes in the two areas, Landsat images were downloaded from Google Earth Engine, and two spectral metrics, *NDVI* and the Enhanced Vegetation Index (*EVI*), were computed. *EVI* utilizes the blue band, along with the red and near-infrared bands, to correct for some atmospheric conditions and canopy background noise. For Obara, Landsat 5 surface reflectance data were obtained from 1984 to 2012. Satellite imagery before 1984 was unavailable for Obara due to significant coverage gaps and the absence of a blue band

in Landsat 1–3 MSS that hindered *EVI* calculation. For Shobara, Landsat 7 and 8 surface reflectance data were acquired from 1999 to 2021. Fig. 11 shows the results for the two regions, illustrated using yearly and monthly averages. As expected, the vegetation indices show seasonal changes. However, some

To investigate factors affecting vegetation recovery, we collected information about geology and topography. We computed topographic variables using DEMs: elevation, slope gradient, aspect, horizontal curvature, vertical curvature, and maximum curvature. Then, statistical analysis, including analysis of variance (ANOVA) and Tukey Honestly Significant Difference (HSD) tests, as well as the Seasonal Autoregressive Integrated Moving Averages (SARIMA) Box-Jenkins model, were employed to investigate the responses of *NDVI* and *EVI* under different combinations of environmental conditions.

The results indicate that, in Obara, concave and convergent terrain have a positive influence on *NDVI*, while non-steep, low-elevation, and north-facing terrain have a positive influence on *EVI*. In Shobara, gentle and northwest-facing slopes were positively correlated with *NDVI*, and gentle and west-facing slopes were positively correlated with *EVI*. Fig. 12 illustrates the effects of environmental variables on the *NDVI* and *EVI*

long-term trends can also be observed. In Obara, the vegetation indices exhibit a marked increasing trend after the mid-1990s, although some vegetation recovery was visible in the earlier period (Fig. 10). In Shobara, the 2010 landslide events resulted in a sudden drop in vegetation index values.

time series, highlighting the positive, neutral, and negative impacts of these variables. The effects of different combinations of environmental variables on *NDVI* were not evident in Obara (Fig. 12a). However, the effect of various combinations of environmental variables on *EVI* was more pronounced than on *NDVI*, especially under positive environmental conditions (blue line in Fig. 12b). In Shobara, the impact of various environmental factors was notable in the trends of *NDVI* and *EVI* time series following landslides. Specifically, the effect was more pronounced on the *NDVI* time series trend. In contrast, the unfavorable condition had a distinct impact on the *EVI* time series trend, different from the neutral and positive conditions (Fig. 12c,d). The more evident control of local environmental factors for Shobara reflects the early stage of vegetation recovery, where the recovery is only rapid under favorable conditions.

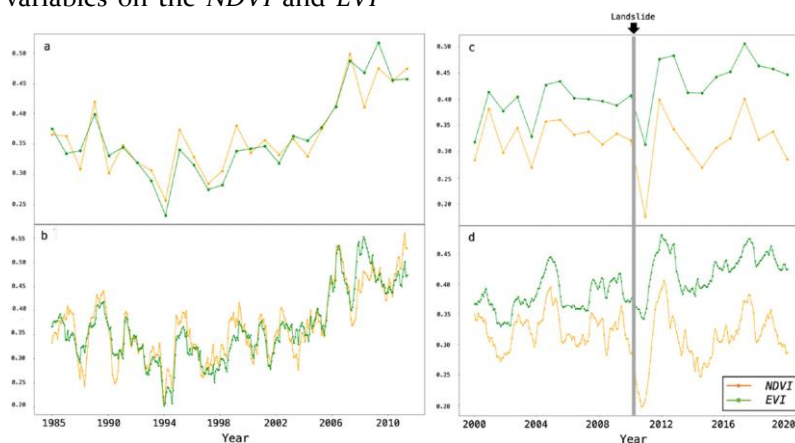


Figure 11. *NDVI* (in yellow) and *EVI* (in green) temporal fluctuations for landslide-affected regions. (a): Yearly average *NDVI* and *EVI* in Obara from 1985 to 2011; (b): Monthly average values of *NDVI* and *EVI* in Obara from December 1984 to May 2012; (c): Yearly average values of *NDVI* and *EVI* in Shobara from 2000 to 2020; (d) Monthly average values of *NDVI* and *EVI* in Shobara from October 1999 to September 2021. The gray line in panels (c) and (d) represents the landslide event triggered by heavy rainfall in July 2010 in Shobara. (Zhong et al., 2023).

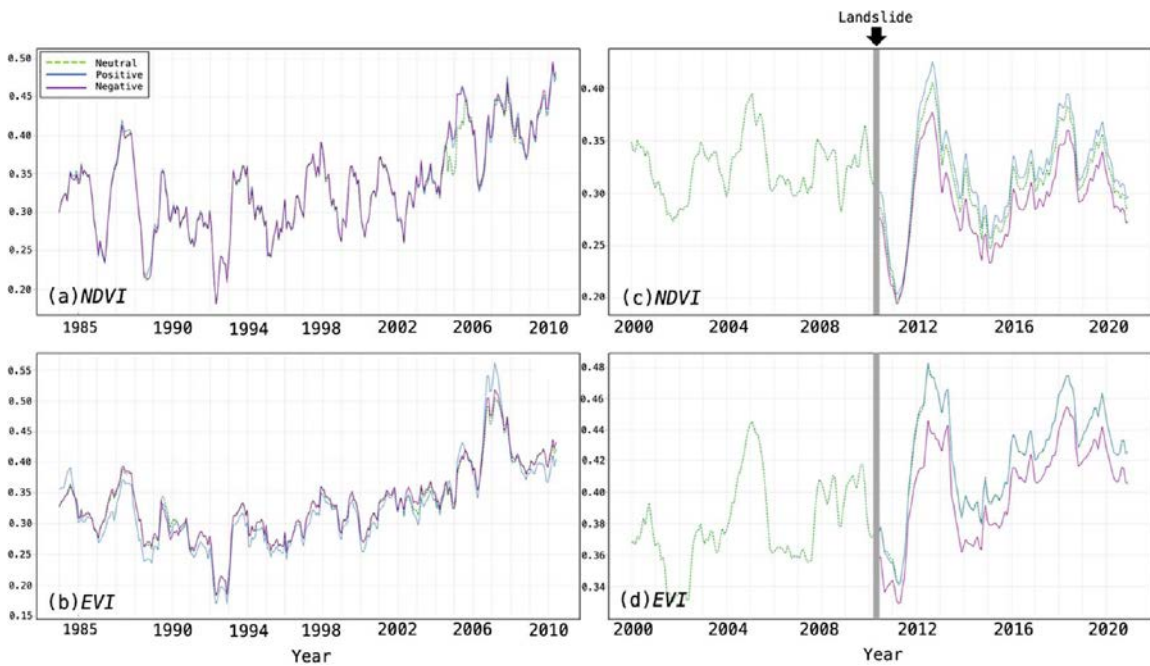


Figure 12. Impact of environmental factors on *NDVI* and *EVI* time series trends in the Obara and Shobara districts. (a): *NDVI* in Obara; (b): *EVI* in Obara; (c): *NDVI* in Obara; (d): *EVI* in Shobara. Green dotted line: neutral conditions. Blue and purple solid lines: positive and negative conditions, respectively. The gray line in panels (c) and (d) represents the occurrence of landslides in July 2010 in Shobara (Zhong et al., 2023).

SARIMA modeling also indicated that *NDVI* is more suitable for modeling the middle and late stages of vegetation recovery within 10–25 years after the landslide. In comparison, *EVI* is better for modeling the early stage of vegetation recovery within 10 years after the landslide. We found that vegetation recovery was gradual and consistent, taking over a decade to reach a relatively stable state, which exceeded the previously reported vegetation recovery time for landslide-affected areas in Japan. This was caused by the severity of landslide disturbance, lack of restoration work, and the widespread occurrence of unfavorable environmental conditions.

This study investigated vegetation recovery and identified suitable vegetation indices to understand the dynamics of post-landslide vegetation, considering the complex including advanced ones such as SARIMA. This type of approach has several advantages for vegetation recovery research after natural hazards. Although repeated visits to fields provide the most detailed and reliable

relationship between topography and vegetation over time. The study's findings enable targeted and nuanced monitoring and assessment of vegetation dynamics, allowing for effective management and informed decision-making in post-landslide ecosystems.

IMPLICATIONS OF GEOSPATIAL TECHNOLOGIES IN VEGETATION RECOVERY RESEARCH

Our three case studies from Japan and the Philippines utilized time-series data from satellite remote sensing images and vegetation indices across multiple spectral bands. We also analyzed data representing land surface conditions, such as DEMs and their derivatives. These data were integrated and analyzed using GIS. For further data analysis, we also employed mathematical and statistical models, information on temporal change in vegetation, they are tedious, and the size of the study area should be limited. Areas recently affected by volcanic activity and landslides may also be hazardous to visit. In contrast, approaches

based on geospatial technologies enable us to investigate broader areas safely, and numerical data treatment provides statistically derived trends of phenomena with objectivity.

The development of geospatial technologies has been rapid, and data availability has also increased, as evidenced by the recent widespread adoption of the freely available Google Earth Engine service. Relevant analytical models are also being developed thanks to novel technologies, including AI-based ones. Some areas in our world will definitely face large-scale or widespread vegetation destruction due to future natural hazards. For example, more extreme climatic conditions induced by global warming will result in heavier rainfall, which in turn will lead to increased landslides and debris flows. In some regions, enhanced droughts under extreme weather conditions will also lead to severe forest fires. Therefore, vegetation recovery research based on remote sensing and

novel geospatial technologies will play an essential role in ensuring regional sustainability related to the conservation of vegetation.

REFERENCES

- De Rose, R.C., Oguchi, T., Morishima, W., Collado, M. (2011). Land cover change on Mt. Pinatubo, the Philippines, monitored using ASTER VNIR. *International Journal of Remote Sensing*. 32(24): 9279-9305.
- Lai, R., Oguchi, T., Zhong, C. (2022). Evaluating spatiotemporal patterns of post-eruption vegetation recovery at Unzen Volcano, Japan, from Landsat time series. *Remote Sensing*. 14, 5419.
- Miyabuchi, Y. (1999). Deposits associated with the 1990–1995 eruption of Unzen Volcano, Japan. *Journal of Volcanology and Geothermal Research*. 89, 139–158.
- Zhong, C., Oguchi, T., Lai, R. (2023). Effects of topography on vegetation recovery after shallow landslides in the Obara and Shobara districts, Japan. *Remote Sensing*. 15, 3994.

7-SEAS Urban-AQ: A Regional Initiative for Understanding Urban Air Quality in Southeast Asia

Nguyen Xuan Anh^{1,2,*}, Pham Xuan Thanh^{1,2}, Nguyen Van Hiep^{1,2}, Nguyen Nhu Vinh^{1,2}, Bui Ngoc Minh^{1,2}, Pham Le Khuong^{1,2}, Do Ngoc Thuy¹, Markova I. S.³

¹Institute of Earth Sciences, Vietnam Academy of Science and Technology, Hanoi, Vietnam

²Graduate University of Science and Technology, Vietnam Academy of Science and Technology, Hanoi, Vietnam

³Republican Unitary Enterprise "Scientific and Production Center for Multifunctional Unmanned Complexes" of the National Academy of Sciences of Belarus, Minsk, Belarus

*Email: nxuananh05@gmail.com

Abstract: Urban air pollution in Southeast Asia (SEA) poses serious challenges to public health, ecosystems, and climate. Rapid industrialization, urban expansion, and rising energy demand have intensified emissions of particulate matter (PM), trace gases, and aerosols, contributing to recurring haze episodes and transboundary pollution. The Seven South East Asian Studies - Urban Air Quality (7-SEAS Urban-AQ) initiative provides a coordinated framework to investigate urban atmospheric composition, dynamics, and impacts across major SEA cities. This study presents the 7-SEAS Urban-AQ objectives and initial results from Hanoi, Vietnam, based on integrated ground-based, UAV, satellite observations. UAV profiles revealed strong wintertime stratification of particulate matter ($PM_{10} \approx 190 \mu g m^{-3}$, $PM_{2.5} \approx 160 \mu g m^{-3}$, $PM_{1.0} \approx 90 \mu g m^{-3}$) confined within a shallow inversion, contrasting with well-mixed post-monsoon conditions ($PM_{2.5} \approx 40 \mu g m^{-3}$) under northeasterly wind regime. Satellite PM_{10} retrievals from GEMS showed good consistency with UAV observations, confirming their complementarity for urban-scale monitoring. Meteorological analysis indicated that boundary-layer stability, humidity, and synoptic circulation govern the observed vertical aerosol variability. These findings demonstrate the value of integrating multi-platform datasets within the 7-SEAS Urban-AQ framework to enhance understanding of aerosol-meteorology interactions and improve

air-quality prediction and management across Southeast Asia.

Keywords Urban air quality, 7-SEAS Urban-AQ, Aerosol, Satellite remote sensing, UAV, Air quality modeling, $PM_{2.5}$.

INTRODUCTION

Air pollution is driven by a wide range of sources, including the combustion of fossil fuels, industrial processes, and open biomass burning. Major pollutants include particulate matter ($PM_{2.5}$, PM_{10}), trace gases (CO , SO_2 , NO_2 , O_3), volatile organic compounds (VOCs), and secondary aerosols formed through atmospheric oxidation. Exposure to elevated $PM_{2.5}$ concentrations is strongly associated with respiratory and cardiovascular diseases, leading to millions of premature deaths worldwide each year [1].

Urban areas in Southeast Asia (SEA) often experience persistent haze episodes, particularly during the dry season when biomass burning dominates the atmospheric composition [2]. Emission sources, population exposure, and air pollution hazards across rural and urban environments are closely linked. Diverse pollutant sources—including industrial emissions, traffic exhaust, household burning, and agricultural fires—contribute simultaneously to multiple air-pollution risks, resulting in severe health impacts, particularly in densely populated megacities [3].

Southeast Asia's air-quality problems are unique in both scale and complexity. The region's rapid economic growth and urban expansion have led to increasing energy demand, transportation emissions, and industrial outputs. At the same time, natural and semi-natural processes, such as widespread biomass burning and episodic volcanic activity, strongly affect atmospheric composition [4,5]. Consequently, SEA experiences two dominant pollution regimes: (1) urban-industrial pollution, prevalent in major metropolitan areas with high traffic density and industrial activity, and (2) biomass-burning pollution, largely seasonal, originating from forest fires and post-harvest agricultural residue burning.

In SEA, air pollution has evolved into a severe transboundary crisis driven by both anthropogenic and natural processes. Rapid industrialization and urbanization are compounded by recurrent biomass-burning events and monsoon-driven transport, producing widespread haze that frequently crosses national boundaries. Satellite observations and ground-based measurements have consistently documented high aerosol optical depths (AOD) over the Indochina Peninsula, particularly during dry-season months (February–April), when agricultural burning peaks. During such episodes, surface $\text{PM}_{2.5}$ concentrations can exceed $150 \mu\text{g m}^{-3}$ which is far above international health standards, while visibility reductions and radiative imbalances disrupt transportation, tourism, and local climate regulation.

Beyond their direct health impacts, aerosols play a critical role in the Earth's radiation budget and hydrological cycle. Light-scattering aerosols, such as sulfates and organics, induce negative radiative forcing that cools the surface, whereas absorbing aerosols, such as black carbon (BC) and brown carbon (BrC), cause localized atmospheric heating. These processes alter boundary-layer stability, suppress turbulent mixing, and enhance pollutant accumulation near the surface. In SEA, such feedbacks are further intensified by the interaction of aerosols with monsoon flows,

land-sea breezes, and synoptic weather systems, creating one of the most meteorologically complex regions in the world.

To address these multifaceted challenges, the Seven South East Asian Studies (7-SEAS) program was launched in 2010 as a multinational research collaboration among partners from the United States, Taiwan, Vietnam, Thailand, the Philippines, Malaysia, and Indonesia. The initiative seeks to advance scientific understanding of aerosol composition, radiative effects, transport mechanisms, and climatic implications across the SEA region through coordinated ground-based, airborne, and satellite observations. Major field campaigns such as Dongsha 2010, BASELInE 2013, Son La 2018, have provided invaluable datasets for investigating aerosol optical properties, vertical distribution, and long-range transport. These efforts have significantly enhanced regional capacity to evaluate radiative forcing and cloud-aerosol interactions within tropical environments.

However, despite these achievements, previous 7-SEAS campaigns primarily focused on rural, coastal, and biomass-burning regions, leaving substantial knowledge gaps in the understanding of urban atmospheric environments. Urban areas in SEA are characterized by complex emission mixtures, heterogeneous land use, and meteorological variability, which together shape pollutant dispersion within the planetary boundary layer (PBL). Conventional ground-based monitoring networks, while essential for regulatory purposes, offer limited insight into the vertical structure of aerosols, an important factor influencing population exposure, satellite retrieval accuracy, and model performance. Without detailed vertical observations, constraining satellite AOD retrievals, validating chemical transport models, or understanding the coupling between emissions and atmospheric dynamics remains challenging.

To bridge these gaps, the 7-SEAS Urban Air Quality (Urban-AQ) project need to be established as an urban-focused extension of the main 7-SEAS framework. The project's

overarching objective is to develop an integrated, multi-platform observational strategy that combines ground-based measurements, UAV-based vertical profiling, satellite remote sensing, and numerical modeling. This approach enables the detailed characterization of aerosol behavior within the PBL, quantification of vertical concentration gradients, and evaluation of radiative-meteorological feedbacks specific to urban settings. By establishing a harmonized methodology applicable to multiple cities, 7-SEAS Urban-AQ will provide a foundation for regional-scale assessments of emission sources, transport mechanisms, and atmospheric impacts.

The Urban-AQ framework emphasizes innovation in both measurement and modeling. Unmanned aerial vehicles (UAVs) equipped with miniaturized PM sensors enable high-resolution vertical profiling of aerosols up to several hundred meters, bridging the gap between surface monitors and satellite observations. When collocated with satellite AOD datasets (e.g., MODIS, VIIRS, GEMS) and ground-based optical measurements (e.g., AERONET), UAV observations facilitate robust validation and scaling relationships between surface concentrations and columnar optical properties. Additionally, coupling these multi-scale datasets with chemical transport models such as WRF-Chem improves parameterization of aerosol-boundary-layer interactions and enhances forecasting capabilities for urban air-quality management.

This paper presents a case study conducted under the 7-SEAS Urban-AQ initiative, focusing on Hanoi, Vietnam, a rapidly industrializing megacity in the Red River Delta region. Hanoi's air quality is influenced by local traffic and industrial emissions, regional biomass-burning plumes, and frequent wintertime temperature inversions that inhibit pollutant dispersion. This meteorologically dynamic setting makes Hanoi an ideal natural laboratory for investigating vertical aerosol distributions and

boundary-layer processes in tropical urban environments.

The objectives of this study are to (i) characterize the vertical distribution of particulate matter (PM_{10} , $PM_{2.5}$, $PM_{1.0}$) using UAV-based measurements, and (ii) analyze boundary-layer dynamics and meteorological controls on vertical pollutant profiles. Through these analyses, this study addresses critical data and methodological gaps in understanding urban air quality in SEA, providing the first empirical characterization of UAV-observed aerosol layering in a major regional metropolis. The work may contribute to strengthen the scientific foundation of the 7-SEAS framework and to improve strategies for air-quality monitoring, modeling, and policy development in Southeast Asia's rapidly urbanizing environments.

DATA AND METHOD

The 7-SEAS Urban-AQ objectives and framework

The methodology used in this study is an essential part of the larger 7-SEAS Urban Air Quality (Urban-AQ) project. Before presenting the specific initial results obtained for Hanoi, it is essential to outline the overall objectives and conceptual framework of the 7-SEAS Urban-AQ initiative. The 7-SEAS Urban-AQ project aims to advance scientific understanding of urban air quality and its interactions with meteorological and climatic processes across Southeast Asia (SEA). The initiative focuses on characterizing aerosol properties, emission sources, and atmospheric dynamics within diverse urban environments, while promoting regional collaboration and data harmonization. Targeted cities include Chiang Mai, Bangkok, Hanoi, Ho Chi Minh City, Kuala Lumpur, Kota Kinabalu, Singapore, Taipei, and Kaohsiung, with future expansions planned for Jakarta, Manila, Phnom Penh, and Vientiane. This spatially distributed network of observation sites enables comparative analyses of air pollution across different climatic, geographical, and socioeconomic contexts, thereby supporting a unified regional framework

for monitoring, modeling, and policy development under the 7-SEAS program [6].

The scientific goals of the 7-SEAS Urban-AQ project include: (1) Assessing urban air quality status, spatial and temporal variabilities and trends through long-term observation and modeling; (2) Characterizing aerosol chemistry and visibility degradation mechanisms; (3) Evaluating aerosol–climate interactions and radiative forcing; (4) Quantifying public health risks associated with air pollutants; and (5) Formulating effective mitigation strategies and fostering regional collaboration through workshops and capacity building.

The Expected Outcomes and Implications of the 7-SEAS Urban-AQ initiative are to: (i) Enhance understanding of air quality variability and source apportionment in SEA cities; (ii) Quantify visibility degradation and assess aerosol radiative impacts on regional climate; (iii) Assess population exposure and public health risks linked to PM_{2.5}, BC, and trace metals; and (iv) Provide robust scientific evidence to guide policy, strengthen regional air quality management, and increase public awareness. Ultimately, the project aims to support sustainable urban development and climate resilience through integrated atmospheric research and cross-border collaboration.

Ground-Based Observations in 7-SEAS Urban-AQ focuses on measurements of meteorological parameters, gaseous pollutants, and particulate matter across key urban locations. Instruments include multi-wavelength aethalometers, SMPS, and nephelometers for aerosol physical and optical properties. Networks such as AERONET, MPLNET provide complementary column-integrated data linking surface and satellite measurements.

Satellite Remote Sensing in 7-SEAS Urban-AQ includes but not limited to the data from MODIS, MOPITT, TROPOMI, and AIRS satellites which are used to derive spatial distributions of aerosols and trace gases (CO, SO₂, NO₂, O₃, HCHO). Figure 1 presents the

annual mean AOD and CO concentration from MODIS Terra and MOPITT observations between 2001–2022, revealing persistent aerosol hotspots over northern Indochina and maritime SEA.

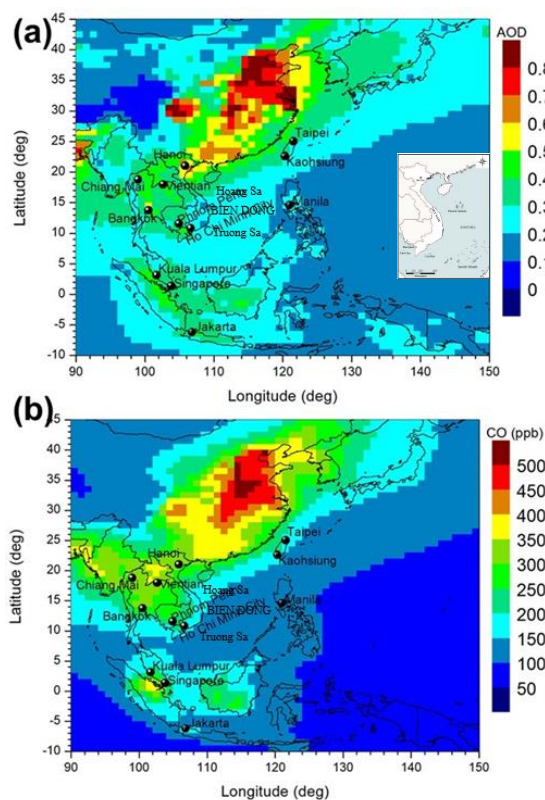


Figure 1. Spatial distribution of annual average(2001–2022) (a) aerosol optical depth at 550 nm from MODIS Terra satellite and (b) carbon monoxide (CO) mass concentration in ppb at surface level from MOPITT over Southeast Asia [6]

For modeling and assessment in 7-SEAS Urban-AQ, the Air quality models such as WRF-Chem and CMAQ are used to simulate atmospheric chemical and transport processes, whereas receptor models like Positive Matrix Factorization (PMF) are applied to quantify source contributions. The SBDART radiative transfer model coupled with OPAC optical datasets [5,7,8] is employed to estimate aerosol radiative forcing (ARF) and heating rates (Fig. 2). Health risk assessments incorporate dose–response relationships and models such as Multiple-Path Particle Dosimetry Model

(MPPD) to estimate aerosol deposition and population exposure.

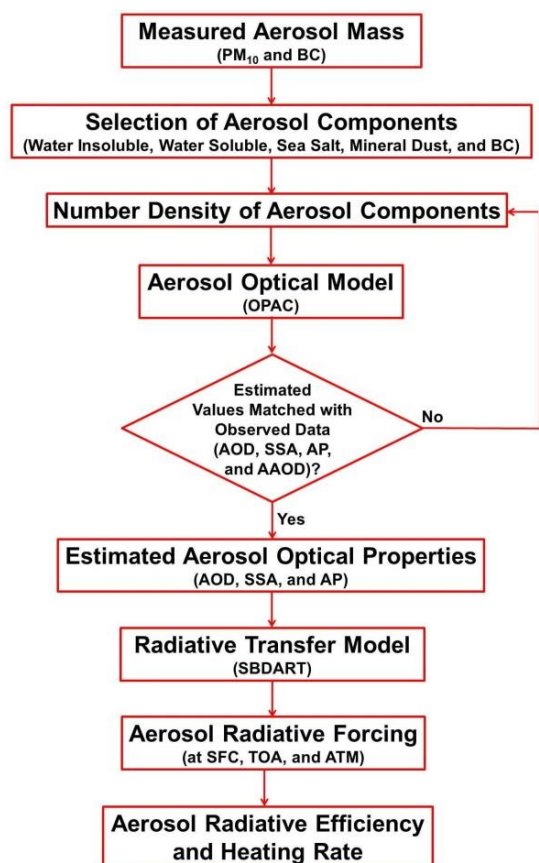


Figure 2. A flow diagram of the methodology adopted for the estimation of aerosol radiative forcing using SBDART model, in conjunction with the aerosol optical properties estimated from the OPAC in the shortwave range [5].

UAV-based PM profiling data

While ground-based and satellite observations provide invaluable insights into AOD, they often lack the detailed vertical information necessary to fully characterize aerosol distribution within the PBL and to distinguish between local and transported pollution sources. Unmanned Aerial Vehicles (UAVs) equipped with compact sensor payloads present a powerful solution to this limitation, enabling high-resolution in-situ vertical profiling of particulate matter (PM) and meteorological parameters [9,10]. Such systems are vital for understanding the "how"

and "why" of aerosol pollution events, complementing the "where" (satellite) and "when" (ground-based) data. UAVs can provide high-resolution PM concentration profiles, helping to quantify the contribution of elevated smoke layers to the total pollution burden—a key factor for improving air quality forecasting models and health impact assessments.

UAVs can provide high-resolution vertical data to: (1) Distinguish between surface-based pollution and elevated aerosol layers. This is critical for source apportionment, as it can separate local emissions from long-range transported smoke; (2) Investigate the structure of the atmospheric boundary layer. This helps explain how pollutants are trapped or dispersed; and (3) Provide direct validation for both satellite AOD and air quality models.

In this work, we employed an UAV for 0–120 m AGL vertical profiling. The payload comprised a laser-scattering particle sensor (reporting PM_{1.0}, PM_{2.5}, PM₁₀), and an embedded temperature–relative humidity–pressure. The logging frequency was 1 Hz, synchronized to local time (UTC+7). Typical flights lasted ~20 min per battery, with ascent/descent rates 1–2 m s⁻¹ to minimize sampling artifacts. Profiles were binned to 1-m layers.

RESULTS AND DISCUSSION

A severe air pollution regime from UAV observations on 20 January 2025

The UAV-based measurements conducted over Hanoi on 20 January 2025 captured a pronounced vertical gradient of particulate matter, highlighting strong atmospheric stratification under stable winter conditions (Fig. 3a). Near the surface, concentrations reached approximately 190 µg m⁻³ for PM₁₀, 160 µg m⁻³ for PM_{2.5}, and 90 µg m⁻³ for PM_{1.0}, among the highest values recorded over the research region. These elevated concentrations indicate the presence of dense near-surface haze resulting from a combination of vehicular emissions, domestic heating, and stagnant meteorological conditions typical of the winter monsoon season in northern Vietnam.

Concentrations of all particle fractions decreased steadily with height up to 120 m, where $PM_{2.5}$ dropped to about $110 \mu\text{g m}^{-3}$ and $PM_{1.0}$ to $80 \mu\text{g m}^{-3}$, suggesting a strong confinement of aerosols within a shallow boundary layer. The small vertical gradient of $PM_{2.5}$ ($\approx 0.4\text{--}0.5 \mu\text{g m}^{-3} \text{ m}^{-1}$) reflects limited turbulent diffusion and weak mechanical mixing. A secondary minimum was observed around 70–80 m, likely marking the transition between the surface-based inversion and the residual layer aloft (Fig. 3a).

The difference between $PM_{1.0}$ and $PM_{2.5}$ concentrations was about $70 \mu\text{g m}^{-3}$ near the surface, narrowing to $30 \mu\text{g m}^{-3}$ at 100 m, indicating the dominance of fine combustion aerosols from traffic. The increase in the PM_{10} – $PM_{2.5}$ fraction above 90 m suggests partial entrainment of coarser dust particles from surrounding industrial and construction zones or aged aerosol layers recirculated by light vertical motions.

The overall vertical pattern is indicative of a highly stable atmospheric boundary layer (ABL) with minimal convective mixing. This stratification corresponds closely with the Skew-T diagram for 17 January 2025 (Fig. 5a), which shows a pronounced temperature inversion near 950 hPa (~ 400 m), low Convective Available Potential Energy (CAPE $\approx 0 \text{ J kg}^{-1}$). Please note that due to missing data, the upper-air sounding for 20 January 2025 at Hanoi was unavailable; therefore, the profile from 17 January 2025 was used as a representative reference. Examination of nearby stations on 20 January 2025 indicated that the atmospheric conditions were not significantly different from those on 17 January, justifying the use of this proxy dataset. Under these thermodynamic conditions, vertical mixing was strongly suppressed, causing pollutants emitted near the surface to remain trapped and resulting in the steep PM gradient observed by the UAV.

Comparison with the GEMS PM_{10} satellite retrieval for the same period shows surface concentrations of more than $120 \mu\text{g m}^{-3}$ over the Red River Delta, reasonably consistent with

the UAV's near-surface observations when accounting for the vertical distribution and typical satellite underestimation in stable layers. The strong agreement between UAV and satellite data supports the reliability of the UAV system for capturing vertical aerosol structures relevant to urban air-quality assessments (Figs. 3a and 4a).

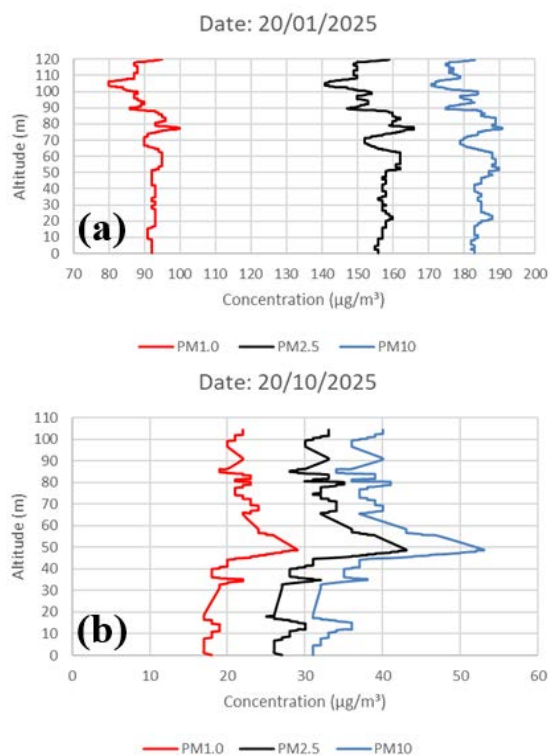


Figure 3. Vertical profiles of average PM_{10} , $PM_{2.5}$, and $PM_{1.0}$ concentrations ($\mu\text{g m}^{-3}$) obtained from a UAV flight over Nghia Do, Hanoi for (a) 20 Jan, 2025 and (b) 20 Oct, 2025.

In short, the 20 January 2025 UAV profiles demonstrate an episode of severe air pollution under a thermally stable, low-mixing boundary layer, typical of wintertime haze in northern Vietnam. The combination of high emissions, weak winds (Fig. 6a), and a low-level temperature inversion created conditions favorable for pollutant accumulation. These results highlight the critical role of meteorological stability in governing vertical PM gradients and provide essential observational constraints for validating

atmospheric transport and dispersion models under stagnant winter conditions.

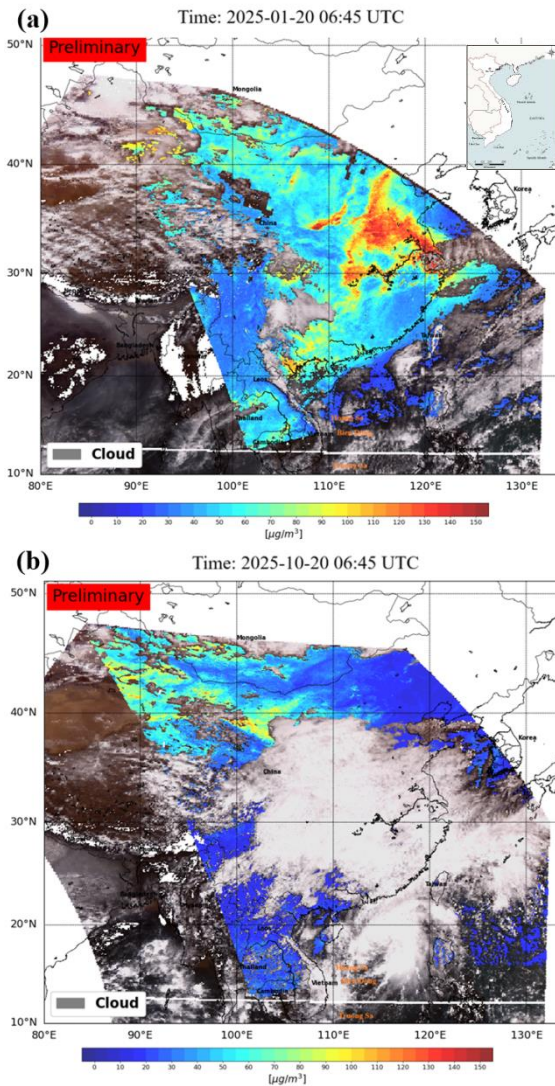


Figure 4. Estimated surface PM₁₀ concentration from the Geostationary Environment Monitoring Spectrometer (GEMS) instrument (<https://nesc.nier.go.kr>) for (a) 20 Jan, 2025 and (b) 20 Oct, 2025.

A clean atmospheric regime from UAV observation on 20 October 2025

The UAV-based measurements conducted over Hanoi on 20 October 2025 reveal a markedly different vertical structure of aerosols compared with the winter episode (Fig. 3b). At

the surface, concentrations were approximately $52 \mu\text{g m}^{-3}$ for PM₁₀, $40 \mu\text{g m}^{-3}$ for PM_{2.5}, and $22 \mu\text{g m}^{-3}$ for PM_{1.0}, reflecting a considerably cleaner atmosphere than that observed on 20 January 2025. These values are nearly 70 % lower than those during the winter haze episode, consistent with the seasonal transition to post-monsoon conditions characterized by enhanced ventilation and weaker emission accumulation.

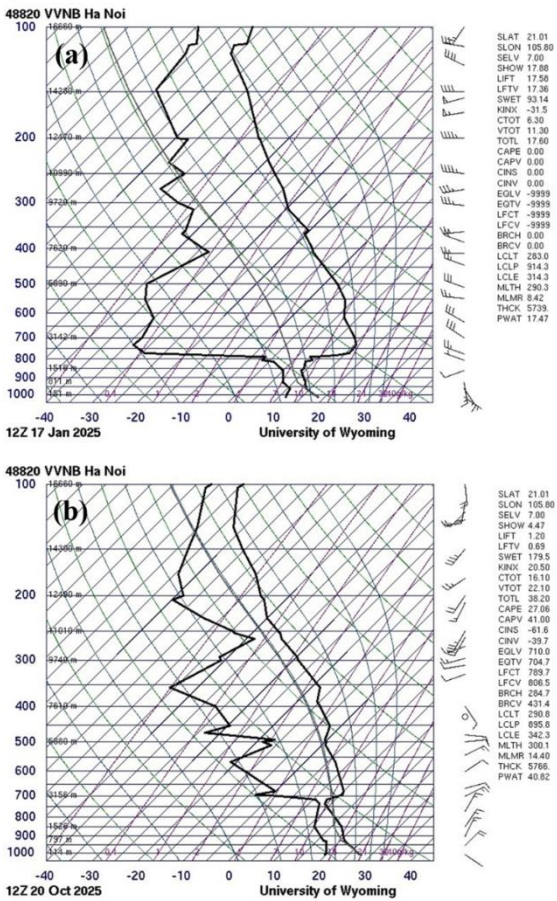


Figure 5. Skew-T plot (<https://weather.uwyo.edu>) of sounding data at Ha Noi station for (a) 17 Jan, 2025 and (b) 20 Oct, 2025

With increasing altitude, all particulate fractions showed a gradual increase up to 120 m, where PM_{2.5} and PM_{1.0} concentrations increased to about $35 \mu\text{g m}^{-3}$ and $25 \mu\text{g m}^{-3}$, respectively. The close coupling between PM_{1.0} and PM_{2.5} profiles-both exhibiting a broad

maximum near 40-60 m - suggests the dominance of fine-mode aerosols from local combustion and secondary formation processes, but under conditions that favored dilution rather than accumulation. The ratio of $PM_{10} : PM_{2.5}$ ranged between 1.2 and 1.4, smaller than in January, indicating reduced coarse particle influence, possibly due to lower road dust resuspension under higher humidity and weaker surface traffic turbulence.

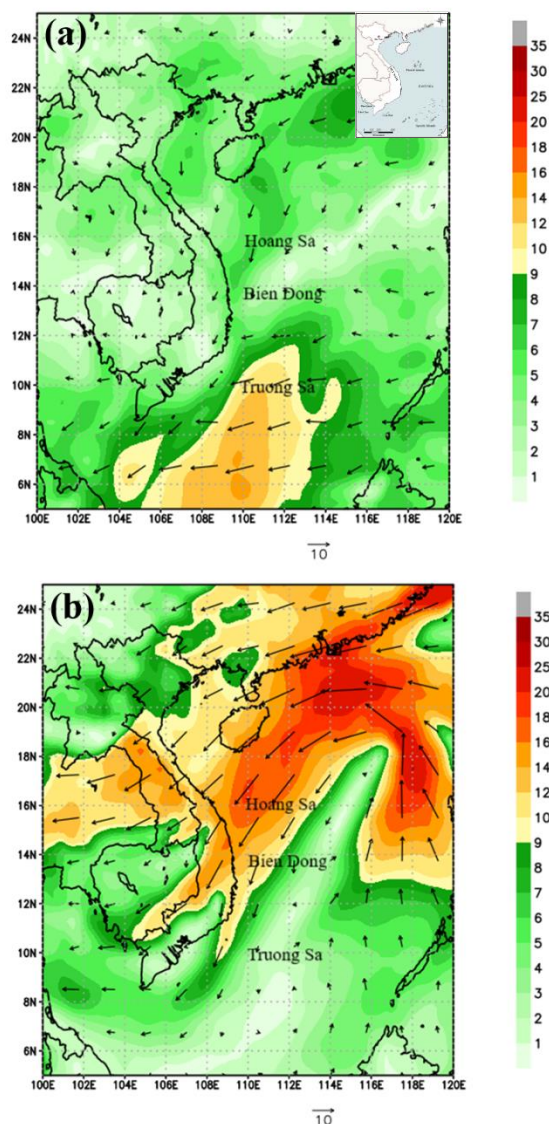


Figure 6. Analysis wind vector (vector) and wind speed ($m s^{-1}$) at 850hPa (about 1.5 km) level for (a) 20 Jan, 2025 and (b) 20 Oct, 2025

Unlike the sharp vertical stratification seen in winter, the October profiles show a more turbulent boundary layer. Such a pattern is typical under post-monsoon northeasterly flow with moderate solar heating, when enhanced vertical mixing promotes aerosol dispersion through the lower troposphere. The overall profile shape, with a gentle concentration gradient and absence of inversion signatures, supports the interpretation of an unstable atmospheric boundary layer (ABL) (Fig. 3b).

Comparison with GEMS satellite PM_{10} retrievals for the same day (Fig. 4b) confirms this interpretation. Over northern Vietnam, GEMS indicated widespread low surface PM_{10} ($< 30 \mu g m^{-3}$) and weak spatial gradients, consistent with the UAV mean profile ($\sim 35 \mu g m^{-3}$) within 0-120 m (Figs. 3b and 4b).

From a meteorological perspective, the Skew-T log-p diagram on 20 October 2025 (12Z) shows weak static instability, $CAPE \approx 27 J kg^{-1}$ providing favorable conditions for pollutant dispersion. The 850 hPa wind field revealed strong northeasterly flow ($8-15 m s^{-1}$) over northern Vietnam (Fig. 6b), enhancing ventilation and import of cleaner continental air. This synoptic pattern explains both the low UAV-observed concentrations and the relatively uniform small value of vertical distribution of aerosols.

The UAV data for 20 October 2025 represent a clean atmospheric regime dominated by effective vertical mixing and advective ventilation. Fine particles from local anthropogenic sources were present but diluted throughout the boundary layer. When compared with the 20 January 2025 episode, this case exemplifies the pronounced seasonal contrast in Hanoi's aerosol vertical structure—shallow, stagnant, and polluted in winter versus deep, turbulent, and clean in post-monsoon autumn. The integration of UAV and satellite observations provides compelling evidence of the strong coupling between meteorology and aerosol vertical distribution in tropical urban environments.

Implications for the 7-SEAS Urban-AQ Framework

Integrating the UAV, satellite, and meteorological datasets provides a coherent physical picture of the January 2025 pollution episode: UAV profiles captured steep vertical gradients of $\text{PM}_{10}\text{-PM}_{2.5}$ ($\Delta \approx 60\text{--}70 \mu\text{g m}^{-3}$ between 0 and 120 m), signifying pollutant confinement within a shallow nocturnal layer. GEMS satellite data showed regional enhancement ($>120 \mu\text{g m}^{-3}$) (Fig. 4a), consistent with the UAV mean (Fig. 3a) and confirming spatial representativeness of the Hanoi measurements. Skew-T profiles (Fig. 5a) revealed a surface inversion and high humidity, suppressing convection and favoring aerosol hygroscopic growth. 850 hPa winds (Fig. 6a) were weak and southerly, implying minimal ventilation and potential transport of aged aerosols from the Red River Delta industrial corridor. In contrast, in October 2025, stronger northeasterly winds (Fig. 6b) and deeper mixing layers (Fig. 5b) led to $\text{PM}_{2.5}$ reductions exceeding 70 %, illustrating the dominant role of synoptic circulation and thermodynamic stability in modulating air quality.

These findings underscore the effectiveness of integrating UAV vertical observations with geostationary satellite products (GEMS) within the 7-SEAS Urban-AQ framework. UAVs provide high-resolution boundary-layer information essential for validating and interpreting satellite retrievals under complex urban conditions. The observed high correlation between UAV and GEMS data supports the feasibility of using combined platforms for near-real-time air-quality assessment.

Moreover, the strong linkage between elevated PM and stable, humid meteorological regimes highlights the need to incorporate boundary-layer meteorology—particularly inversion strength, relative humidity, and 850 hPa flow—into regional air-quality forecasting systems. The Hanoi case demonstrates how multi-scale observations (surface-UAV-satellite) can be synthesized to explain pollution buildup mechanisms and to refine

aerosol parameterizations in models such as WRF-Chem in the future work.

Summary and conclusion

This study, conducted under the 7-SEAS Urban Air Quality (Urban-AQ) initiative, examined the vertical distribution and meteorological modulation of particulate matter (PM_{10} , $\text{PM}_{2.5}$, $\text{PM}_{1.0}$) over Hanoi, Vietnam. By integrating UAV-based vertical profiling, satellite remote sensing (GEMS), ground-based UAV observations, and meteorological analysis, the research provides new insights into urban aerosol behavior in tropical monsoon environments.

The results highlight a distinct seasonal contrast in vertical PM structure. During the winter haze episode (20 January 2025), UAV observations revealed strong stratification with high near-surface concentrations ($\text{PM}_{2.5} \approx 160 \mu\text{g m}^{-3}$) confined within a shallow inversion layer. These conditions corresponded with weak southerly winds ($2\text{--}6 \text{ m s}^{-1}$), high humidity, and strong thermal stability that suppressed vertical mixing. In contrast, during the post-monsoon period (20 October 2025), PM levels were substantially lower ($\text{PM}_{2.5} \approx 40 \mu\text{g m}^{-3}$), and vertical profiles indicated efficient turbulent dispersion within a well-mixed boundary layer under strong northeasterly flow ($8\text{--}15 \text{ m s}^{-1}$).

Satellite-based PM_{10} from GEMS showed spatial and temporal consistency with UAV observations, validating the complementarity between ground, airborne, and spaceborne datasets. The coupling of observational platforms demonstrated the value of UAV profiling for resolving near-surface aerosol layers that are often underrepresented in satellite retrievals and model outputs.

Overall, the findings emphasize that boundary-layer dynamics, synoptic circulation, and humidity are key regulators of aerosol accumulation and vertical mixing in Hanoi. The integrated multi-platform approach proposed by the 7-SEAS Urban-AQ framework provides a robust foundation for improving urban air-quality assessment, refining chemical

transport model parameterizations, and supporting evidence-based pollution mitigation policies across Southeast Asia.

ACKNOWLEDGMENTS

This research was funded by the International Cooperation Task (Code QTBY02.01/23-24 and Work No. T23BA-005 dated 22 May 2023), the Support of Scientific Research Activities (code NVCC12.01/25-25) and Project (Code TĐCBSS.00/24-26).

REFERENCES

- [1]. Cohen, A. J.; Brauer, M.; Burnett, R.; Anderson, H. R.; Frostad, J.; Estep, K.; Lim, S. S. (2017). *Estimates and 25-year trends of the global burden of disease attributable to ambient air pollution: an analysis of data from the Global Burden of Diseases Study 2015*. The Lancet, 389(10082), 1907–1918. [https://doi.org/10.1016/S0140-6736\(17\)30505-6](https://doi.org/10.1016/S0140-6736(17)30505-6)
- [2]. Dat, N.Q.; Ly, B.T.; Nghiem, T.D.; Nguyen, H.T.T.; Sekiguchi, K.; Huyen, T.T.; Vinh, T.H.; Tien, L.Q. (2024). *Influence of Secondary Inorganic Aerosol on the Concentrations of PM_{2.5} and PM_{0.1} during Air Pollution Episodes in Hanoi, Vietnam*. Aerosol Air Qual. Res. 24, 220446. <https://doi.org/10.4209/aaqr.220446>
- [3]. Sakti Anjar Dimara; Tania Septi Anggraini; Kalingga Titon Nur Ihsan; Prakhar Misra; Nguyen Thi Quynh Trang; Biswajeet Pradhan; I. Gede Wenten; Pradita Octoviandiningrum Hadi; Ketut Wikantika (2023). *Multi-air pollution risk assessment in Southeast Asia region using integrated remote sensing and socio-economic data products*. Science of The Total Environment, vol 854, 158825, ISSN 0048-9697, <https://doi.org/10.1016/j.scitotenv.2022.158825>.
- [4]. Lin, N. H.; Tsay, S. C.; Maring, H. B.; Yen, M. C.; Sheu, G. R.; Wang, S. H.; Chi, K. H.; Chuang, M. T., et al. (2013). *An overview of regional experiments on biomass burning aerosols and related pollutants in Southeast Asia: From BASE-ASIA and the Dongsha Experiment to 7-SEAS*. Atmospheric Environment, 78, 1–19.
- [5]. Pani, S.; Lin, N. H.; Lee, C. T.; Tsay, S. C.; Holben, B.; Janjai, S.; Hsiao, T. C.; Chuang, M. T.; Chantara, S. (2016). *Radiative Effect of Springtime Biomass-Burning Aerosols over Northern Indochina during 7-SEAS/BASELine 2013 Campaign*. Aerosol and Air Quality Research. 16, 2802–2817. 10.4209/aaqr.2016.03.0130.
- [6]. Lin N.H.; Shantanu Kumar Pani; Somporn Chantara; Nguyen Xuan Anh; Santo Salinas; Maggie Chel Gee Ooi; Si-Chee Tsay (2023). *7-SEAS Urban-AQ Whitepaper* (first Draft).
- [7]. Hess, M.; Koepke, P.; Schult, I. (1998). *Optical properties of aerosols and clouds: The software package OPAC*. Bulletin of the American Meteorological Society, 79, 831–844. [https://doi.org/10.1175/1520-0477\(1998\)079<0831:OPOAAC>2.0.CO;2](https://doi.org/10.1175/1520-0477(1998)079<0831:OPOAAC>2.0.CO;2)
- [8]. Ricchiazzi, P.; Yang, S.; Gautier, C.; Sowle, D. (1998). *SBDART: A research and teaching software tool for plane-parallel radiative transfer in the Earth's atmosphere*. Bulletin of the American Meteorological Society, 79, 2101–2114. [https://doi.org/10.1175/1520-0477\(1998\)079<2101:SARATS>2.0.CO;2](https://doi.org/10.1175/1520-0477(1998)079<2101:SARATS>2.0.CO;2)
- [9]. Motlagh N. H.; Kortoçi, P.; Su, X.; Lovén, L.; Hoel, H. K.; Haugsvær, S. B. (2023). *Unmanned Aerial Vehicles for Air Pollution Monitoring: A Survey*. IEEE Internet of Things Journal, vol. 10, no. 24, pp. 21687–21704, doi: 10.1109/JIOT.2023.3290508.
- [10]. Liang, C.-W.; Shen, C.-H. (2024). *An integrated UAV platform with sensing and sampling systems for air pollutant concentrations*. Atmospheric Measurement Techniques, 17(9), 2671–2686. <https://doi.org/10.5194/amt-17-2671-2024>.

Random Forest-based PM_{2.5} estimation using multisource remote sensing data: A case study of Ho Chi Minh city

Dai Long Nguyen¹, Thu Ha Hoang Thi¹, Kim Cuc Luong Thi², Van Manh Nguyen³, Ngoc Bich Uyen Vo⁴, Thi Hai Yen Ngo^{3*}

¹K73 High Quality Program, Faculty of Geography, Hanoi National University of Education, Hanoi city, Vietnam

²K73 A1, Faculty of Geography, Hanoi National University of Education, Hanoi city, Vietnam

³Faculty of Geography, Hanoi National University of Education, Hanoi city, Vietnam

⁴Faculty of Artificial Intelligence, Posts and Telecommunications Institute of Technology, Hanoi city, Vietnam

*Email: haiyen@hnue.edu.vn

Abstract: Fine particulate matter (PM_{2.5}) pollution is one of the most serious environmental issues in major urban areas worldwide. In the context of limited air quality monitoring networks, the integration of remote sensing technology, geographic information systems (GIS) and machine learning provides an effective approach to monitor PM_{2.5} concentrations over large spatial scales. This study used PM_{2.5} data from six ground-based monitoring stations, combined with Aerosol Optical Depth (AOD) and the Normalized Difference Vegetation Index (NDVI) data, to develop a predictive model of PM_{2.5} concentration in Ho Chi Minh City, Vietnam. The Random Forest algorithm was applied to model non-linear relationship between optical variables and PM_{2.5} concentrations and to generate spatial distribution maps of average PM_{2.5} at a 1-km resolution for the period from April 2021 to March 2022. When the number of decision trees in the forest was set to 50, with parameters `min_samples_leaf` = 1 and `min_samples_split` = 4, the model achieved stable performance, yielding a Pearson correlation coefficient of 0.7 and a Root Mean Square Error (RMSE) of 5.4 µg/m³. The spatial distribution results revealed that high PM_{2.5} concentrations were concentrated in central urban districts, whereas suburban and coastal areas such as Cu Chi and Can Gio exhibited lower values. Overall, the study demonstrates that integrating remote sensing, GIS and machine learning is an effective approach for

air quality monitoring and supporting sustainable urban management.

Keywords Random Forest, AOD, NDVI, PM_{2.5}, Ho Chi Minh.

INTRODUCTION

Fine particulate matter (PM_{2.5}) is a type of air pollutant with an extremely small particle size, with a diameter equivalent to about 3% of a human hair, PM_{2.5} can easily penetrate the biological barriers of the lungs, enter the bloodstream and directly affect the cardiovascular, respiratory and nervous systems (Kim, Kim, Kim & Park, 2020). According to the World Health Organization (WHO), nearly the entire global population is currently exposed to PM_{2.5} concentrations that exceed the recommended safe threshold (Pai, Carter, Heald & Kroll, 2022). Global epidemiological studies have shown that fine particulate pollution is among the leading environmental causes of premature death, with more than 4.2 million cases each year associated with long-term PM_{2.5} exposure (Sang, Chu, Zhang, Chen & Yang, 2022). In Southeast Asia, where urbanization is rapid and population density is high, PM_{2.5} concentrations frequently exceed the warning level, ranging from 58 to 100 µg/m³ in many urban areas (Fang et al., 2025).

Many studies worldwide have applied spatial analytical methods to simulate the spatial distribution of PM_{2.5} concentrations. In

northwestern India, Vipasha Sharma and colleagues used the Random Forest (RF) model, integrating Aerosol Optical Depth (AOD) data from MODIS with meteorological variables such as temperature, humidity and wind speed to estimate PM_{2.5} concentrations. The results showed that the model achieved $R^2 = 0.75$, correlation coefficient $R = 0.865$ and relative prediction error $RPE = 22.41\%$, demonstrating good predictive capability in regions with sparse monitoring networks (Sharma, Ghosh, Dey & Singh, 2023). Similarly, another study applied the Extreme Gradient Boosting (XGBoost) model to analyze the spatio-temporal variation of PM_{2.5} concentrations in central India. By integrating AOD, NDVI, anthropogenic factors and meteorological information, the study achieved $R^2 = 0.82$ and mean absolute error (MAE) = $7.01 \mu\text{g}/\text{m}^3$, indicating the outstanding performance of nonlinear machine learning algorithms in air quality prediction (Gokul, Mathew, Bhosale & Nair, 2023). These studies confirm the potential of combining remote sensing data and machine learning models to simulate PM_{2.5} distribution, particularly in areas with limited monitoring coverage, thereby contributing to the establishment of effective air pollution monitoring and early warning systems.

In the Southeast Asian region, studies applying machine learning for PM_{2.5} modeling have also achieved significant results. In Malaysia, a study employed models such as Random Forest and Support Vector Regression using satellite-derived AOD, meteorological variables and other air pollutant data from 65 monitoring stations (Zaman, Kanniah, Kaskaoutis & Latif, 2021). The study reported R^2 values ranging from 0.46 to 0.76 for models developed separately by region and season. Similarly, in Thailand, Gupta et al (Gupta et al., 2021) integrated MERRA-2 reanalysis data with ground-based observations from 51 monitoring sites to train machine learning-Random Forest models. The results showed a correlation coefficient of up to 0.95 and a daily RMSE of approximately $3.14 \mu\text{g}/\text{m}^3$, demonstrating the capability of modeling PM_{2.5} in areas with limited monitoring networks.

In Vietnam, a number of recent studies have initially explored the use of remote sensing and GIS data in PM_{2.5} research. Nguyen Phuc Hieu et al. (2024) compared six different machine learning algorithms to predict PM_{2.5} concentrations using monitoring and meteorological data in Ho Chi Minh City (P. H. Nguyen, Dao & Nguyen, 2024). Their findings indicated that the Artificial Neural Network (ANN) model achieved the highest performance, with $R^2 = 0.69$ and $RMSE = 8.31 \mu\text{g}/\text{m}^3$, reflecting a good capability to model the variability of urban air pollution. In addition, the study by Nguyen Thi Tuyet Nam and co-authors (T. T. N. Nguyen, Nguyen & Nguyen, 2023) applied 3D-CBPF and 3D-PSCF spatial statistical models to identify the main sources of PM_{2.5} emissions in Ho Chi Minh City, showing that the main sources of air pollution originated from traffic, industrial activities in Binh Duong - Dong Nai and biomass burning in the Mekong Delta region.

Based on previous studies and in the context of increasingly severe air pollution in major urban areas, the deployment of advanced technologies such as remote sensing and Geographic Information Systems (GIS) plays a key role in monitoring, analyzing and evaluating air quality within the framework of modern environmental management. Although several previous studies have been conducted in this field, most existing works still present notable limitations. Earlier research often relied on outdated or insufficiently updated datasets; meanwhile, the monitoring network remained sparse and unevenly distributed in space, leading to restricted estimation accuracy. Furthermore, traditional spatial interpolation methods have not been adequately improved or optimized to suit geographical characteristics, which prevents a full reflection of the complex spatial variation of air pollution concentrations in urban environments.

From these research gaps and the urgency of practical requirements, this study entitled "Random forest-based PM_{2.5} estimation using multisource remote sensing data: a case study

of Ho Chi Minh city” was conducted. The main objective is to establish and quantify the relationship between optical indicators derived from satellite imagery and fine particulate matter concentrations measured directly at ground monitoring stations. Through the integration of the Random Forest Regressor algorithm, the study aims to generate high-resolution and reliable spatial distribution maps of PM_{2.5} concentrations. In this study, Section 2 presents the study area and data sources, Section 3 describes the research methods and analytical procedures, Section 4 presents the results and Section 5 provides the conclusions and summarizes the key findings of the research.

STUDY AREA AND DATA

Study area

The study was conducted prior to the administrative merger implemented under Resolution No. 202/2025/QH15 (The National Assembly Of Vietnam, 2025), with Ho Chi Minh City selected as the study area. The city is located between latitudes 10°10' - 10°38' N and longitudes 106°22' - 106°54' E, situated at the transitional boundary between the Southeast region and the Mekong Delta. This unique geographical position creates distinctive natural as well as socio-economic transitional characteristics.

By 2024, the population of Ho Chi Minh City was estimated at approximately 9.54 million people (Ho Chi Minh City Statistics Sub-Department, 2024; The National Assembly Of Vietnam, 2025). In the context of rapid urban development and a strong increase in population, Ho Chi Minh City is facing numerous environmental pressures, among which air pollution caused by fine particulate matter (PM_{2.5}) is particularly critical. According to the National State of Environment Report 2021 (HCMC Central for Natural Resources and Environmental Monitoring, 2018), transportation activities have been identified as the primary source of PM_{2.5} emissions in the city. In addition, industrial production, construction activities

and biomass burning from surrounding areas are also significant supplementary sources, collectively contributing to the deterioration of urban air quality.

PM_{2.5} concentrations data

PM_{2.5} concentration data were continuously and systematically collected over a 12-month period, specifically from April 2021 to March 2022 (National Aeronautics and Space Administration), to ensure completeness and representativeness of the temporal variations in air pollution levels. The data collection process was conducted at six air quality monitoring stations that were strategically selected and spatially distributed across Ho Chi Minh City, with each station representing a distinct area of the city. At the same time, to visualize the spatial distribution of the monitoring network, the exact locations of all monitoring stations were clearly illustrated in Figure 1.

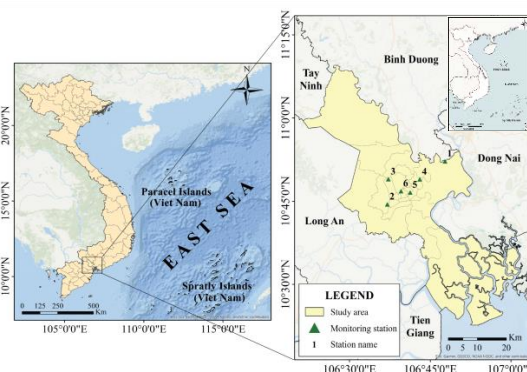


Figure 1. Locations of PM_{2.5} monitoring stations in the study area.

Aerosol Optical Depth data (AOD)

The Aerosol Optical Depth (AOD) index represents the degree of light absorption and scattering caused by aerosol particles in the atmosphere (National Aeronautics and Space Administration). The application of remote sensing technology in this study is reflected through the use of the AOD index. This dataset serves as an essential data source derived from the MODIS/Terra + Aqua Land Aerosol Optical Depth Daily L2G Global 1 km SIN Grid Vo61 (MCD19A2) product, which is freely provided by NASA via the Earthdata Search portal

(<https://search.earthdata.nasa.gov>). This product is generated based on the Multi-Angle Implementation of Atmospheric Correction (MAIAC) algorithm to enhance retrieval accuracy (National Aeronautics and Space Administration). The AOD values are extracted at a wavelength of approximately $\lambda \approx 0.55 \mu\text{m}$, which is highly sensitive to aerosols and exhibits a strong correlation with PM_{2.5} concentrations. With a spatial resolution of 1 km × 1 km, this dataset effectively captures the spatial variability of aerosol depth. The study period extends from April 1, 2021, to March 31, 2022, with daily satellite observations recorded between 07:00 and 13:00 (UTC+7), which is a highly favorable time frame for air quality analysis and monitoring. In total, 341 MODIS image scenes were collected throughout the study period.

Normalized Difference Vegetation Index data (NDVI)

The Normalized Difference Vegetation Index (NDVI) is an important remote sensing indicator that reflects the growth status and canopy density of vegetation. NDVI is calculated based on the difference in reflectance between the near-infrared (841 - 876 nm) and red (620 - 670 nm) spectral bands (GIS Geography). In this study, NDVI was employed to assess the spatial and temporal variations of vegetation cover, serving as a basis for analyzing the relationship between vegetation and air quality, particularly the concentration of fine particulate matter (PM_{2.5}). NDVI data were obtained from the MODIS/Terra Vegetation Indices 16-Day L3 Global 1 km SIN Grid Version 6.1 (MOD13A2) product, which is freely provided by NASA via the Earthdata Search portal (<https://search.earthdata.nasa.gov>) (National Aeronautics and Space Administration). This is a 16-day composite product generated using the “best-pixel” algorithm to minimize noise caused by clouds and atmospheric conditions, with a spatial resolution of 1 km × 1 km, suitable for regional-scale analysis (National Aeronautics and Space Administration). During the period from April 1, 2021, to March 31, 2022,

a total of 24 MOD13A2 scenes were utilized, allowing for a comprehensive analysis of seasonal and annual NDVI trends. With its ability to effectively reflect photosynthetic activity and vegetation vitality, NDVI serves as an important explanatory variable in the modeling and analysis of the impact of vegetation cover on variations in air quality.

First, the input data included: 24-hour averaged fine particulate matter (PM_{2.5}) concentrations from six ground-based monitoring stations; Aerosol Optical Depth (AOD) values obtained from the MCD19A2 product representing atmospheric aerosol density; and the Normalized Difference Vegetation Index (NDVI) derived from the MOD13A2 product reflecting the degree of vegetation greenness.

METHOD

To estimate fine particulate matter (PM_{2.5}) concentrations with high accuracy, the study employed the Random Forest (RF) machine learning model - a supervised learning algorithm that is particularly effective in modeling nonlinear relationships (Ziweritin, Ugboaja & Osu, 2020). The research process consists of four main steps: data collection and preprocessing, data splitting, model training and finally, map generation.

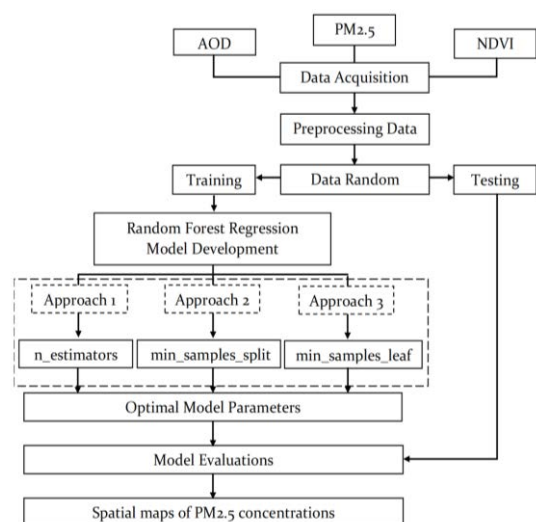


Figure 2 Research framework

All datasets were synchronized spatially and temporally. Specifically, the remote sensing images of AOD and NDVI were processed through several steps, including reprojection to the standard coordinate system (WGS84), band selection and subsetting to the study area, resampling to a uniform spatial resolution of 1 km and temporal matching with the PM_{2.5} data. Data points with missing values were removed from the analysis.

After integrating the data sources, a comprehensive dataset was constructed, in which each record represents a sampling point with the following attributes: PM_{2.5} (dependent variable) and AOD and NDVI (independent variables). The dataset was randomly divided into two subsets: a training set (80%) used for model development and a testing set (20%) used for model validation.

The Random Forest model was constructed by combining multiple decision trees, each trained on a bootstrap sample randomly drawn with replacement from the training dataset (Bagging technique). The main parameters tuned in this study included the number of trees in the forest (*n_estimators*), the minimum number of samples required at each leaf node (*min_samples_leaf*) and the minimum number of samples required to split an internal node (*min_samples_split*) (Jain & Gupta, 2022):

- *n_estimators*: this parameter represents the number of decision trees in the random forest. Increasing the number of trees generally enhances the stability and accuracy of the model by reducing variance; however, it also leads to longer training and prediction times due to higher computational demands (Prajwala, 2015).

- *min_samples_leaf*: this parameter specifies the minimum number of samples required to be present in a leaf node, which represents the terminal node of a decision tree. It controls the minimum size of each leaf and affects the granularity of the model. A very small value may cause the model to fit random fluctuations in the data, resulting in overfitting,

while a larger value ensures that each leaf contains more samples, leading to smoother predictions and reduced noise, albeit at the cost of potentially losing fine-grained details (Prajwala, 2015).

- *min_samples_split*: this parameter defines the minimum number of samples required to split an internal node. It determines how deeply the decision trees can grow during training. A smaller value allows the trees to split more frequently and become deeper, enabling the model to capture more detailed patterns but increasing the risk of overfitting. Conversely, a larger value restricts the number of splits, leading to simpler trees and potentially better generalization performance (Prajwala, 2015).

During the training process, the model learned the relationships between PM_{2.5} concentrations and the input variables from the training dataset. The trained model was then applied to the testing dataset to evaluate its performance using statistical indicators such as the Root Mean Square Error (RMSE) and Pearson correlation coefficient (Jain & Gupta, 2022).

- The Root Mean Square Error (RMSE) represents the average magnitude of the model's prediction errors. A smaller RMSE value indicates that the model's predictions are closer to the observed data, thereby reflecting a stronger goodness of fit and higher predictive accuracy (Wilks, 2011). The mathematical formula is expressed as follows:

$$RMSE = \sqrt{\frac{1}{n} \sum_{i=1}^n (y_i - \hat{y}_i)^2}$$

Where:

- y_i is the actual value at the *i*-th point.

- \hat{y}_i is the predicted value at the *i*-th point.

- *n* is the number of observations.

- The Pearson correlation coefficient quantifies the strength and direction of the linear relationship between the observed and

predicted values. A coefficient value closer to 1 indicates a strong positive correlation, illustrating that the model effectively captures the observed variations (Wilks, 2011). The formula is:

$$r = \frac{\sum (x_i - \bar{x})(y_i - \bar{y})}{\sqrt{\sum (x_i - \bar{x})^2 \sum (y_i - \bar{y})^2}}$$

Where:

- x_i, y_i are the values of the two variables.

- \bar{x}, \bar{y} are the mean values of the two variables.

Additionally, the importance of input variables (feature importance) was extracted and analyzed to evaluate the relative contribution of each factor in explaining the spatial and temporal variability of PM_{2.5} concentrations. Through this indicator, it is possible to identify the dominant influencing variables, such as optical parameters, meteorological conditions and land surface characteristics, thereby elucidating the role of individual environmental factors in the formation and spatial distribution of PM_{2.5}.

After the Random Forest model achieved satisfactory performance, it was applied to predict PM_{2.5} concentrations across the entire study area using pixel-based inputs of AOD and NDVI. Each pixel in the resulting output map represents the estimated PM_{2.5} concentration corresponding to that spatial location.

RESULTS

Optimal Model Parameters

Number of Decision Trees in the Random Forest Model

The process of selecting the number of decision trees ($n_{\text{estimators}}$) in the Random Forest model plays a crucial role and has a decisive impact on the overall performance of the algorithm during the training phase. Experimental results obtained by varying the

number of trees in the forest revealed a clear trend: the training error tended to decrease as the number of trees increased, which is fully consistent with the fundamental theoretical principle of ensemble learning (Prajwala, 2015). The findings of this study indicate that the model achieved optimal predictive performance and the highest generalization capability when configured with $n_{\text{estimators}} = 50$. Notably, further increasing the number of trees beyond this threshold did not yield significant improvements in testing accuracy; on the contrary, it could unnecessarily increase computational cost and training time.

Minimum Number of Samples for Node Splitting and at Each Leaf

In the architecture of the Random Forest model, two critical hyperparameters - `min_samples_leaf` and `min_samples_split` - serve as fundamental regulators that control the hierarchical structure and complexity of each individual decision tree within the forest. These parameters have a direct impact on the model's predictive power on the training dataset as well as its generalization ability when applied to unseen data (Prajwala, 2015).

After fine-tuning the necessary parameters, the study identified the optimal configuration as `min_samples_leaf = 1`, which means that each terminal (leaf) node in a decision tree is allowed to contain at least one data sample. Meanwhile, `min_samples_split` was set to 4, indicating that an internal node can only be further divided into child branches when it contains a minimum of four data samples. Establishing these minimum threshold values provides several important technical advantages. It prevents decision trees from growing excessively deep under conditions of sparse or unrepresentative data, thereby minimizing the risk of overfitting on the training dataset and enhancing the model's predictive performance on real-world data.

Results of Model Training

To improve the accuracy of PM_{2.5} concentration prediction from remote sensing data, the research team applied the Random

Forest algorithm, a powerful machine learning model based on an ensemble of multiple decision trees. This approach enables the identification of nonlinear relationships between input variables and observed PM_{2.5} values, thereby enhancing predictive capability compared with traditional regression models.

The results presented in Figure 3 show that the training data points and testing data points are distributed closely along the 1:1 line, demonstrating that the Random Forest model successfully captured the relationship between the observed and predicted PM_{2.5} values. The data points tend to align along the identity line, indicating that the model effectively reflects the spatial and temporal variability of PM_{2.5} concentrations.

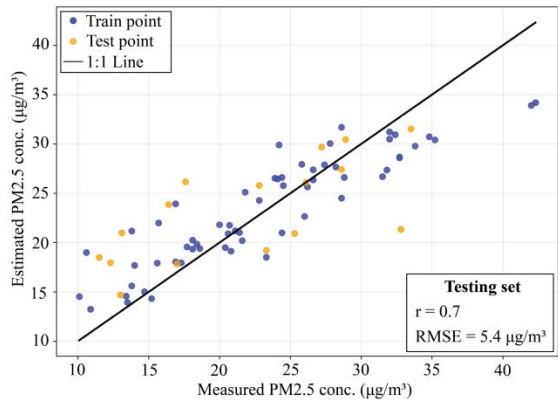


Figure 3 Predicted vs. Observed Values

Overall, the Random Forest model exhibited high reliability and stability, achieving strong predictive performance on the training dataset with a Pearson correlation coefficient of 0.91 and an RMSE of $3.44 \mu\text{g}/\text{m}^3$, indicating a strong correlation between predicted and observed values. For the testing dataset, the model maintained good accuracy, with a Pearson coefficient of 0.7 and $\text{RMSE} = 5.4 \mu\text{g}/\text{m}^3$, demonstrating stable and effective generalization capability in estimating fine particulate matter concentrations. These findings confirm that the model can effectively simulate the relationship among AOD, NDVI and PM_{2.5} in the study area and can be reliably

applied to generate high-resolution spatial distribution maps of PM_{2.5} concentrations.

Correlation matrix of the study variables

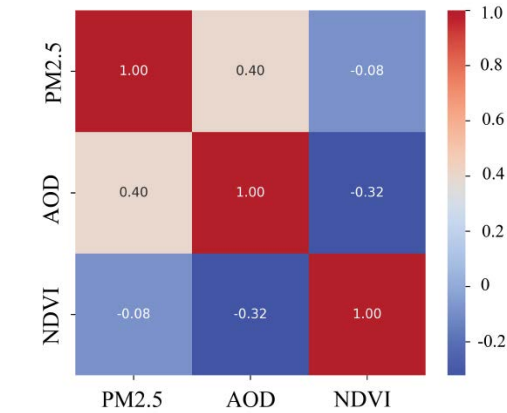


Figure 4 Correlation heatmap of study variables

The results in Figure 4 indicate that PM_{2.5} concentrations exhibit a moderate positive correlation with AOD ($r = 0.40$), suggesting that as AOD increases, PM_{2.5} tends to increase as well. This finding is consistent with the study by Lin et al. (2025), which reported $r = 0.42$ across urban areas in China and further supports the potential use of AOD as an indirect indicator for PM_{2.5} in air pollution estimation models (Lin et al., 2025). In contrast, the correlation between PM_{2.5} and NDVI is very weak ($r = -0.08$), indicating that vegetation cover has little apparent influence on PM_{2.5} variability, whereas the correlation between NDVI and AOD is $r = -0.32$, reflecting that areas with higher vegetation cover generally exhibit lower aerosol concentrations (Lin et al., 2025). These results suggest that AOD is more strongly associated with PM_{2.5} than NDVI and should be integrated with meteorological and ground monitoring data in predictive modeling.

Variable Importance Analysis.

After the Random Forest model was trained and validated, the research team conducted an analysis of the contribution level of each input variable to identify the factors that most strongly influenced the prediction of fine particulate matter concentrations. The results of this analysis, illustrated in Figure 5,

indicate that the Aerosol Optical Depth (AOD) variable contributed the most, accounting for 73.96%. This finding suggests that AOD is the dominant factor affecting the predicted PM_{2.5} values. This outcome is consistent with the physical nature of atmospheric radiation transfer, as fine particulate concentrations are directly related to aerosol optical thickness. The Normalized Difference Vegetation Index (NDVI) also exhibited a certain level of influence, contributing 26.04% within the model.

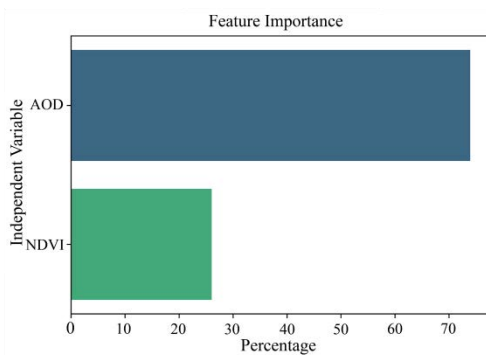


Figure 5 Variable Importance Analysis

Spatial-Seasonal distribution of PM_{2.5} in the Study Area.

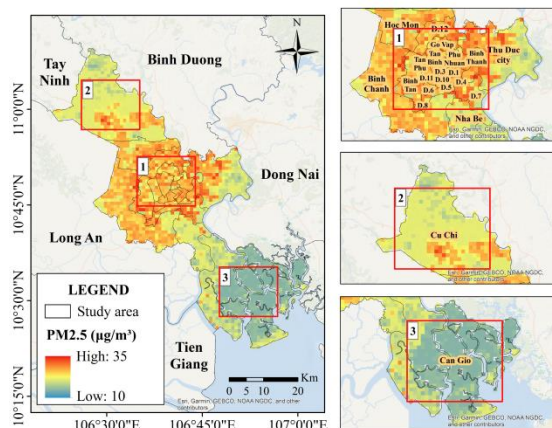


Figure 6 Spatial distribution map of average PM_{2.5} concentration in Ho Chi Minh City for the period April 2021 - March 2022

During the period from April 2021 to March 2022, the concentration of fine particulate matter in Ho Chi Minh City exhibited a clear spatial differentiation, reflecting variations in emission characteristics

and levels of urbanization across different areas. The central districts with high population density and intensive commercial and traffic activities, such as Districts 1, 3, 5, 10, Binh Tan and Binh Chanh - recorded the highest average PM_{2.5} concentrations, ranging from 30 to 35 µg/m³. In contrast, suburban areas such as Cu Chi District showed lower concentrations, approximately between 25 and 30 µg/m³, while Can Gio District, a coastal ecological zone with low population density and minimal industrial activity, maintained the lowest levels, around 15 - 25 µg/m³

This spatial heterogeneity highlights the significant influence of anthropogenic emission sources in highly urbanized regions, particularly from vehicular traffic, industrial operations, construction activities and residential emissions (Kumar, Lekhana, Tejaswi & Chandrakala, 2021). Conversely, peripheral and coastal areas benefit from better ventilation conditions and the presence of mangrove ecosystems, coupled with lower population density, which collectively contribute to the reduction of fine particulate matter in the atmosphere.

In Cu Chi and Can Gio, PM_{2.5} concentrations were generally lower due to sparse population density and the presence of extensive forested and water-covered areas, which facilitate the natural absorption and diffusion of fine particulates. Particularly, the mangrove ecosystem in Can Gio can be considered a “green lung” of the region - not only because of its carbon sequestration capacity but also due to its unique vegetation structure and the cooling influence of sea breezes (Sumarmi, Purwanto & Bachri, 2021).

Notably, this period coincided with the post-COVID-19 socio-economic recovery phase, during which industrial and transportation activities gradually resumed after prolonged lockdowns. The resurgence of emissions from motor vehicles and industrial facilities partially contributed to the increase in PM_{2.5} levels compared to the lockdown period.

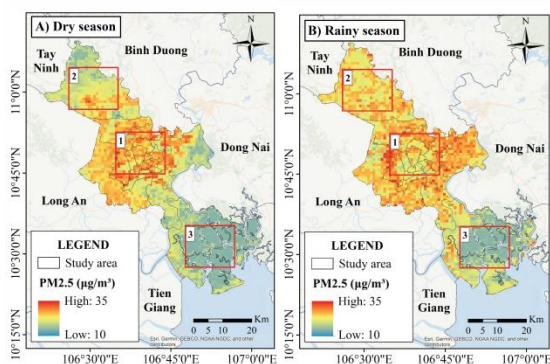


Figure 7 Seasonal distribution map of average PM_{2.5} concentration in Ho Chi Minh City for the period April 2021 - March 2022

Between April 2021 and March 2022, PM_{2.5} concentrations in Ho Chi Minh City exhibited pronounced seasonal variation; however, the observed pattern contradicted typical meteorological trends (Northern Environmental Monitoring Center, 2019), with a mean concentration of 21.01 $\mu\text{g}/\text{m}^3$ in the dry season, compared to 23.05 $\mu\text{g}/\text{m}^3$ in the wet season.

The unusual decrease in PM_{2.5} during the dry season was primarily due to the impact of the COVID-19 pandemic. Strict social distancing from June to December 2021 sharply reduced traffic, industrial production and construction activities, leading to a significant decline in PM_{2.5} emissions during both the wet and dry seasons. According to the study Annual Variation of PM_{2.5} Chemical Composition in Ho Chi Minh City, Vietnam Including the COVID-19 Outbreak Period (2024), PM_{2.5} concentrations in Ho Chi Minh City decreased by approximately 18% compared to the 2016 - 2019 average, while traffic volumes dropped by 70 - 90% (N. Tran et al., 2023). However, PM_{2.5} levels in the wet season remained higher because rainfall was not continuous, minor emission sources persisted in urban areas and meteorological conditions-including monsoon winds, temperature and humidity-as well as increased carbon components (organic carbon, elemental carbon, WSOC) favored the accumulation and transport of fine particles (N. Tran et al., 2023; C. T. Tran et al., 2024). These factors resulted in a temporary “reversal” in

seasonal PM_{2.5} distribution. Overall, the higher PM_{2.5} concentrations observed in the wet season during the study period do not reflect long-term natural patterns, but are a temporary consequence of the unusual emission reductions during the dry season caused by COVID-19. In the absence of the pandemic, the dry season would likely have remained the period of highest pollution, consistent with previous studies (Northern Environmental Monitoring Center, 2019) (Duong, Nguyen, Nguyen & To, 2018).

These findings are consistent with global trends, as numerous studies in major metropolitan areas have reported that COVID-19 lockdown measures led to a 15 - 30% reduction in PM_{2.5} concentrations (Zheng, Liu & Wang, 2025). This evidence reinforces the conclusion that economic and transportation activities play a decisive role in shaping urban air quality dynamics. It further underscores the necessity of implementing emission control policies, sustainable transport planning and urban greening initiatives to improve air quality and promote long-term environmental sustainability.

CONCLUSION

This study presents several notable innovations compared with previous works, particularly the application of the Random Forest machine learning model to estimate fine particulate matter (PM_{2.5}) concentrations in areas lacking ground-based monitoring stations. While earlier studies mainly relied on interpolation of data from monitoring stations - which remain limited in number and unevenly distributed spatially, leading to potential estimation errors - this research overcame such constraints by integrating remotely sensed AOD and NDVI data with the Random Forest Regressor model. This integration enabled a more accurate simulation of the complex relationships between atmospheric factors and surface characteristics with PM_{2.5} concentrations. The incorporation of the model within a GIS environment further allowed the generation of high-resolution, highly reliable spatial distribution maps of

PM_{2.5}, thereby confirming the potential of artificial intelligence and remote sensing data in urban air quality monitoring.

Despite these achievements, several aspects of the study still require further improvement to enhance the accuracy of the results. Firstly, the PM_{2.5} monitoring network in Ho Chi Minh City remains limited, with most stations concentrated in central districts, while peripheral and suburban areas lack sufficient monitoring coverage. This uneven spatial distribution reduces the spatial representativeness of the data, preventing the validation and calibration process from fully capturing the overall air pollution patterns across the entire city. In addition, AOD data derived from MODIS satellite imagery are affected by meteorological conditions such as cloud cover, humidity and light scattering, resulting in spatial or temporal data gaps, particularly during the rainy season. Another limitation is that the study primarily focused on analyzing the relationship between AOD, NDVI and PM_{2.5}, without incorporating additional explanatory factors such as temperature, humidity, traffic density, or industrial activity intensity, variables that can significantly influence PM_{2.5} distribution. Furthermore, temporal mismatches between ground-based and satellite data acquisitions may introduce uncertainty in model performance.

Based on the results obtained, this study opens up several promising directions for future development to continuously improve both the accuracy and practical applicability of the findings. Expanding the analysis in both spatial and temporal dimensions is necessary to systematically capture the long-term variation patterns of PM_{2.5} concentrations. Additionally, future research could explore the integration of other advanced machine learning and deep learning algorithms to enhance predictive performance. The inclusion of supplementary variables, covering meteorological factors and anthropogenic drivers such as population density, traffic activities and industrial production - would allow for a more realistic

representation of pollution conditions. These directions are not only academically significant but also provide practical contributions to environmental management and public health protection.

References

- Duong H. H., Nguyen, C. D. T., Nguyen, P. L. S., & To, H. T. (2018). Fine particulate matter (PM_{2.5}) in Ho Chi Minh City: Analysis of the status and the temporal variation based on the continuous data from 2013-2017. *VNUHCM Journal of Natural Sciences*. 2(5). DOI:<https://doi.org/10.32508/stdjns.v2i5.788>
- Fang T., Di, Y., Xu, Y., Shen, N., Fan, H., Hou, S., & Li, X. (2025). Temporal trends of particulate matter pollution and its health burden, 1990–2021, with projections to 2036: a systematic analysis for the global burden of disease study 2021. *Environmental Health and Exposome*. 13. DOI:<https://doi.org/10.3389/fpubh.2025.1579716>
- Gokul P. R., Mathew, A., Bhosale, A., & Nair, A. T. (2023). Spatio-temporal air quality analysis and PM_{2.5} prediction over Hyderabad City, India using artificial intelligence techniques. *Ecological Informatics*. 76: 102067. DOI:<https://doi.org/10.1016/j.ecoinf.2023.102067>
- Gupta P., Zhan, S., Mishra, V., Aekakkarakunroj, A., Markert, A., Paibong, S., & Chishtie, F. (2021). Machine Learning Algorithm for Estimating Surface PM_{2.5} in Thailand Aerosol and Air Quality Research. 21(11): 210105. DOI:<https://doi.org/10.4209/aaqr.210105>
- GIS Geography. What is NDVI (Normalized Difference Vegetation Index)? URL: <https://gisgeography.com/ndvi-normalized-difference-vegetation-index/> [Last accessed: 12/ 10/ 2025].
- HCMC Central for Natural Resources and Environmental Monitoring. (2018). Current Status of Air Quality in Ho Chi Minh City. URL: <http://hoihocphcm.org.vn/wp-content/uploads/2018/10/NCL.pdf> [Last accessed: 12/ 10/ 2025].
- Ho Chi Minh City Statistics Sub-Department. (2024). Overview on socio - economic situation in Ho Chi Minh city in 2024. URL: https://thongkehochiminh.nso.gov.vn/Niengiam/2024/Gui%20duyet_NIEN%20GIAM%20TPHCM%2025.7.25_In-7-16.pdf [Last accessed: 12/ 10/ 2025].

- Jain S. K., & Gupta, A. K. (2022). Application of Random Forest Regression with Hyper-parameters Tuning to Estimate Reference Evapotranspiration. *International Journal of Advanced Computer Science and Applications*. 13(5): 742-750. DOI:10.14569/IJACSA.2022.0130585
- Kim H., Kim, W.-H., Kim, Y.-Y., & Park, H.-Y. (2020). Air Pollution and Central Nervous System Disease: A Review of the Impact of Fine Particulate Matter on Neurological Disorders. *Frontiers in Public Health*. 8. DOI:https://doi.org/10.3389/fpubh.2020.575330
- Kumar P. G., Lekhana, P., Tejaswi, M., & Chandrakala, S. (2021). Effects of vehicular emissions on the urban environment- a state of the art. *Materials Today: Proceedings*. 45(7): 6314-6320. DOI:https://doi.org/10.1016/j.matpr.2020.10.739
- Lin H., Li, S., Niu, J., Yang, J., Wang, Q., Li, W., & Liu, S. (2025). Estimation of Ultrahigh Resolution PM2.5 in Urban Areas by Using 30 m Landsat-8 and Sentinel-2 AOD Retrievals. *Remote Sensing*. 17(15): 2609. DOI:https://doi.org/10.3390/rs17152609
- National Aeronautics and Space Administration. Aerosol Optical Depth. URL: https://aeronet.gsfc.nasa.gov/new_web/Documents/Aerosol_Optical_Depth.pdf#:~:text=Aerosol%20Optical%20Depth%20%28AOD%29%20is%20the%20measure%20of,%28Earth%27s%20surface%29%20to%20the%20top%20of%20the%20atmosphere. [Last accessed: 12/ 10/ 2025].
- National Aeronautics and Space Administration. MODIS/Terra Vegetation Indices 16-Day L3 Global 1km SIN Grid V061. URL: [https://search.earthdata.nasa.gov/search/granules?p=C2565788905-LPCLOUD!C2324689816-LPCLOUD&q=MOD13A2&sb\[0\]=106.35648%2C10.37638%2C107.02527%2C11.15953&tl=1355614605.03!5!!&lat=10.767955&long=106.7154097744361&zoo m=9.484737468032385](https://search.earthdata.nasa.gov/search/granules?p=C2565788905-LPCLOUD!C2324689816-LPCLOUD&q=MOD13A2&sb[0]=106.35648%2C10.37638%2C107.02527%2C11.15953&tl=1355614605.03!5!!&lat=10.767955&long=106.7154097744361&zoo m=9.484737468032385) [Last accessed: 12/ 10/ 2025].
- Northern Environmental Monitoring Center. (2019). PM Pollution in Selected Cities in Vietnam – Spatiotemporal Variations of PM10 and PM2.5. URL: https://cem.gov.vn/tin-tuc-moi-truong/o-nhiem-bui-pm-tai-mot-so-thanh-pho-o-viet-nam-bien-dong-theo-khong-gian-thoi-gian-cua-pm10-va-pm2-5?utm_source=chatgpt.com [Last accessed: 17/ 11/ 2025].
- Nguyen P. H., Dao, N. K., & Nguyen, L. S. P. (2024). Development of Machine Learning and Deep Learning Prediction Models for PM2.5 in Ho Chi Minh City, Vietnam. *Atmosphere*. 15(10): 1163. DOI:https://doi.org/10.3390/atmos15101163
- Nguyen T. T. N., Nguyen, X. D., & Nguyen, T. H. (2023). Emission Source Areas of Fine Particulate Matter (PM2.5) in Ho Chi Minh City, Vietnam. *Atmosphere*. 14(3): 579. DOI:https://doi.org/10.3390/atmos14030579
- Pai S. J., Carter, T. S., Heald, C. L., & Kroll, J. H. (2022). Updated World Health Organization Air Quality Guidelines Highlight the Importance of Non-anthropogenic PM2.5. *Environmental Science & Technology Letters*. 9(6): 501-506. DOI:https://doi.org/10.1021/acs.estlett.2c00203
- Prajwala T. R. (2015). A Comparative Study on Decision Tree and Random Forest Using R Tool. *International Journal of Advanced Research in Computer and Communication Engineering*. 4(1): 196-199. DOI:10.17148/IJARCC.2015.4142
- Sang S., Chu, C., Zhang, T., Chen, H., & Yang, X. (2022). The global burden of disease attributable to ambient fine particulate matter in 204 countries and territories, 1990–2019: A systematic analysis of the Global Burden of Disease Study 2019. *Ecotoxicology and Environmental Safety*. 238: 113588. DOI:https://doi.org/10.1016/j.ecoenv.2022.113588
- Sharma V., Ghosh, S., Dey, S., & Singh, S. (2023). Modelling PM2.5 for Data-Scarce Zone of Northwestern India using Multi Linear Regression and Random Forest Approaches. *Annals of GIS*. 29(3): 415-427. DOI:https://doi.org/10.1080/19475683.2023.2183523.
- Sumarmi S., Purwanto, P., & Bachri, S. (2021). Spatial Analysis of Mangrove Forest Management to Reduce Air Temperature and CO2 Emissions. *Sustainability*. 13(14): 8090. DOI:https://doi.org/10.3390/su13148090
- The National Assembly Of Vietnam. (2025). On the rearrangement of provincial administrative divisions. URL: <https://thuvienphapluat.vn/van-ban/EN/Bo-may-hanh-chinh/Resolution-202-2025-QH15-the-rearrangement-of-provincial-administrative-divisions/660927/tieng-anh.aspx> [Last accessed: 12, 10/ 2025].
- Tran C. T., Nguyen, L. M. T., Wu, T.-G., Wu, C.-F., Hien, T. T., & Chien, K.-L. (2024). Co-effects of COVID-19 and Meteorology on PM2.5 Decrease in Ho Chi Minh City, Vietnam: A Comparison of 2016–2019 and 2020–2021 Aerosol and Air Quality Research. 24(3): 230186. DOI:https://doi.org/10.4209/aaqr.230186

- Tran N., Fujii, Y., Le, V. X., Chi, N. D. T., Okochi, H., Hien, T. T., & Takenaka, N. (2023). Annual Variation of PM_{2.5} Chemical Composition in Ho Chi Minh City, Vietnam Including the COVID-19 Outbreak Period. *Aerosol Air Quality Research*. 23(5): 220312. DOI:<https://doi.org/10.4209/aaqr.220312>
- Wilks D. S., (2011). *Statistical Methods in the Atmospheric Sciences*. 3rd (eds). Academic Press. 359p.
- Zaman N. A. F. K., Kanniah, K. D., Kaskaoutis, D. G., & Latif, M. T. (2021). Evaluation of Machine Learning Models for Estimating PM_{2.5} Concentrations across Malaysia. *Applied Sciences*. 11(16): 7326. DOI:<https://doi.org/10.3390/app11167326>
- Zheng M., Liu, F., & Wang, M. (2025). Assessing the COVID-19 Lockdown Impact on Global Air Quality: A Transportation Perspective. *Atmosphere*. 16(1): 113. DOI:<https://doi.org/10.3390/atmos16010113>
- Ziweritin S., Ugboaja, U. C. A., & Osu, C. M. (2020). Random Forest Model for Predicting Grayscale Digits on Images. *International Journal of Scientific Research in Computer Science and Engineering*. 8(6): 1-7. DOI:<https://doi.org/10.26438/IJSRCSE/V8I6.17>

DOI: 10.15625/vap.2025.0222

Segmenting traffic accident risk using remote sensing and GIS data: A comparative analysis of Random Forest and Weighted Overlay Methods

Ha Le Thi^{1,2}, Thao Vu Thi Phuong^{1,*}, Thao Do Thi Phuong¹

¹Hanoi University of Mining and Geology, 18 Vien street, Dong Ngac Ward, Hanoi, Vietnam

²Campus in Ho Chi Minh City, University of Transport and Communications. No.450-451 Le Van Viet Street, Tang Nhon Phu Ward, Ho Chi Minh City, Vietnam

*Email: vuthiphuongthao@humg.edu.vn

Abstract: Identifying traffic accident risk zones is critical for infrastructure management and traffic safety planning. This study compares the performance of two spatial analysis approaches - Weighted Overlay Analysis (WOA) and the Random Forest (RF) machine learning algorithm - in mapping accident risk zones in Thanh Hoa Province, Vietnam. The analysis incorporates four input layers derived from remote sensing and GIS data: Normalized Difference Vegetation Index (NDVI), Land Surface Temperature (LST), accident density from Kernel Density Estimation (KDE), and Euclidean distance from main roads. In WOA, expert-assigned weights were KDE 30%, LST 20%, NDVI 15%, and Euclidean distance from main roads 35%. In contrast, the RF model is trained on 1,594 actual accident points (2020–2023) and an equal number of non-accident points — showed variable importance values of KDE 38.33%, LST 19.50%, NDVI 14.50%, and Euclidean distance from main roads 27.67%. Results indicate that RF outperforms WOA, achieving 81.07% accuracy and an F1-score of 79.31%. KDE was the most influential variable in the RF model, whereas WOA assigned greater weight to Euclidean distance from main roads. WOA achieved an accuracy of 71.45%. While RF more accurately reflects current accident risk patterns, it still misses some points in sparsely populated or complex terrain. The observed performance gap between RF and WOA, together with their differing variable prioritizations, suggests that integrating expert judgment with machine

learning can enhance the comprehensiveness, objectivity, and reliability of traffic accident risk zoning. Overall, this study underscores the complementary value of combining remote sensing, GIS, and machine learning for proactive traffic safety interventions. The study highlights the complementary value of integrating remote sensing, GIS, and machine learning for proactive traffic safety interventions.

Keywords: Normalized Difference Vegetation Index, Land Surface Temperature, Kernel Density Estimation, Random Forest, Weighted Overlay Analysis

INTRODUCTION

Road traffic accidents pose a significant threat to economic growth and public health in developing countries, including Vietnam. This is largely driven by the rapid increase in motor vehicle usage, limited public awareness of traffic regulations, and infrastructure that fails to keep pace with urban expansion. In regions with complex terrain or deteriorating road conditions, the risk of traffic accidents is further exacerbated—often resulting in severe human and material losses (Le et al., 2024a; Le et al., 2024b; Le KG et al., 2024).

Accurately identifying high-risk traffic zones is essential for targeted interventions in transportation planning and accident prevention. Conventional spatial analysis techniques in GIS such as WOA, Analytic Hierarchy Process, and KDE have been widely

used to integrate risk-related factors like population and accident density (Zheng et al., 2024). However, these methods often rely on subjective expert judgment to assign layer weights, which limits their ability to adapt to real-world accident data (Chen et al., 2011; Eskandari et al., 2007). Nowadays, machine learning algorithms, including Random Forest, are increasingly widely used in spatial risk analysis due to their ability to process complex data and determine the importance of input variables (Farhangi et al., 2021; Wang et al., 2023). However, the application of the WOA method and the RF machine learning algorithm in assessing road traffic accident risk zones has been limited. Additionally, remote sensing images demonstrate their significant ability to monitor changes in environmental factors. They facilitate the collection of information about the potential and status of objects across large areas in a short amount of time. As a result, they have become a crucial data source for numerous recent studies (Vu et al., 2024; Rodriguez-Galiano et al., 2012). Especially in the field of transportation science, numerous studies have utilised remote sensing data as input for machine learning models (Liu et al., 2023; Worachairungreung et al., 2021).

This study utilizes remote sensing data - Landsat 8 images, as input data for the two methods to independently compare their zoning efficiency and the ability to analyze the importance of spatial factors affecting accidents, thereby contributing to the assessment of the feasibility and effectiveness of each model. Thus, the primary objective of the study is to develop a traffic accident risk zoning map using two methods: WOA and RF. At the same time, the study focuses on identifying spatial factors that have a significant impact on accidents, thereby supporting safe traffic planning and early warning of high-risk areas.

Data and methodology

Study area

Thanh Hoa Province is in Vietnam's North Central region, spanning latitudes $19^{\circ}18'$

to $20^{\circ}40'$ North and longitudes $104^{\circ}22'$ to $106^{\circ}04'$ East as Figure 1. Serving as a gateway that connects the North and North Central regions, Thanh Hoa boasts a well-developed transport infrastructure compared to many other provinces in Vietnam. However, the provincial road transport system faces several limitations due to uneven infrastructure across different areas. Mountainous areas often lack roads built to high technical standards, resulting in low load-bearing capacity and reduced traffic safety. These deficiencies hinder transportation efficiency and elevate the risk of traffic accidents—especially during adverse weather or peak traffic periods (Le et al., 2024a).

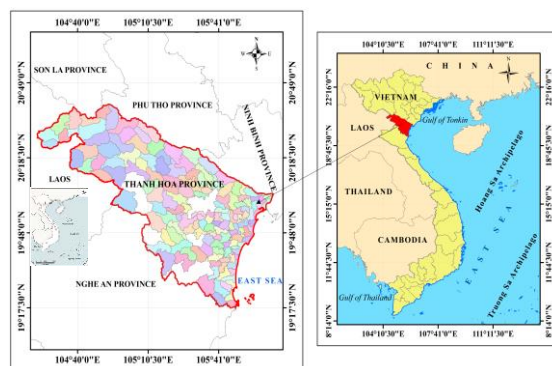


Figure 1. Study area - Thanh Hoa province of Vietnam

Data

The input data for both the WOA and RF models consist of spatial layers derived from remote sensing imagery and field-collected data. Specifically, the Normalized Difference Vegetation Index and Land Surface Temperature were calculated from Landsat 8 satellite images. Traffic accident density was estimated using the KDE method, based on road accident records in Thanh Hoa from 2020 to 2023. The dataset of distances to main roads was created from the provincial traffic network map, in which Euclidean distances were calculated after projecting the data to the WGS_1984_UTM_Zone_48N coordinate system. Additionally, a dataset containing 1,594 accident locations and an equal number of non-accident points was prepared for training

and validating the RF model. The non-accident points were randomly generated within the administrative boundary of Thanh Hoa

Province using the Create Random Points tool in ArcGIS Pro, ensuring no spatial overlap with recorded accident locations.

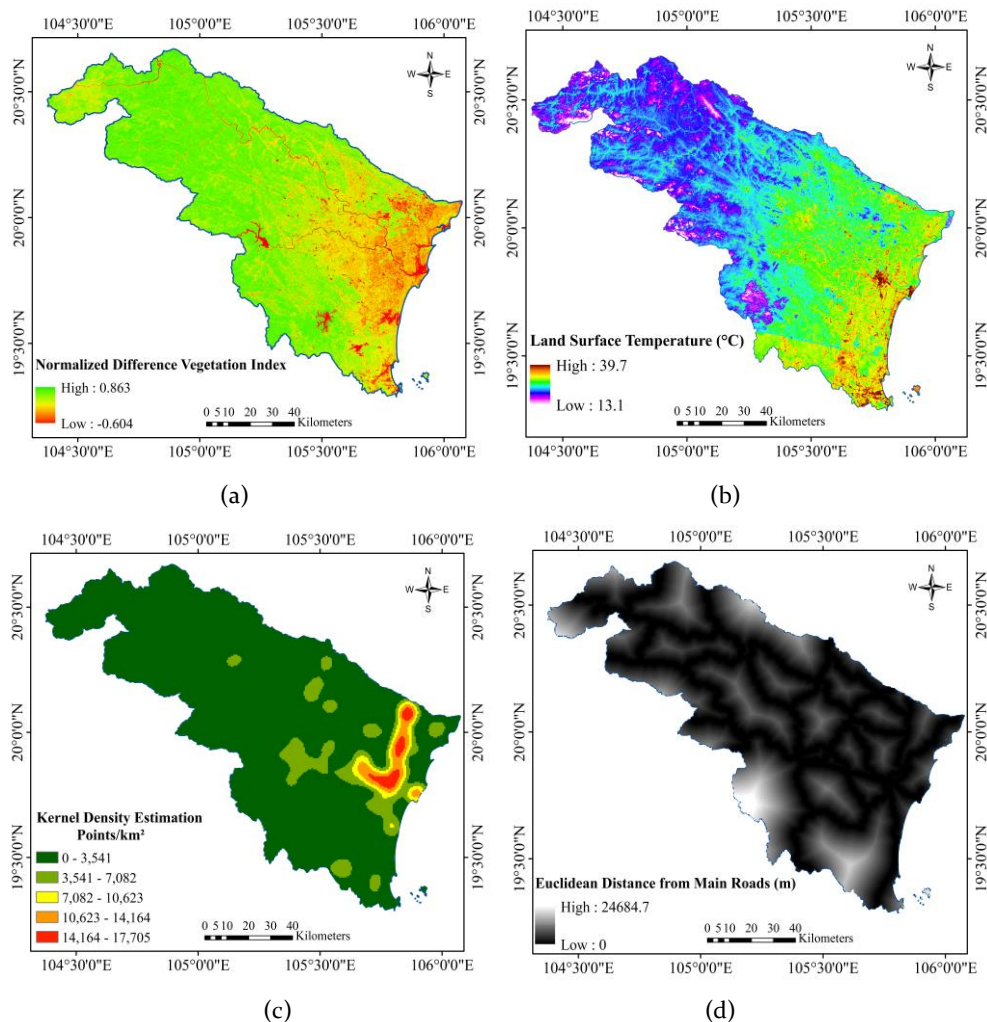


Figure 2 Input data layers for the accident risk zoning model (a) Normalized Difference Vegetation Index (b) Land Surface Temperature (c) Kernel Density Estimation (d) Euclidean Distance from Main Roads

METHODOLOGY

This study employs two parallel approaches to analyze traffic accident risk: the WOA and RF machine learning model. Each method utilizes distinct strategies for spatial data processing, input variable selection, and risk map generation. The overall analytical workflow, illustrated in Figure 3, comprises three main stages:

(i) Data Collection and Preprocessing:

This stage involves the acquisition and preparation of spatial data layers, including those derived from remote sensing imagery and base maps.

(ii) Independent Risk Analyses:

The WOA method normalizes and assigns weights to raster layers based on expert judgment to produce a composite risk map. Concurrently, the RF model is trained using actual accident

point data along with synthetically generated non-accident points, allowing for classification and performance evaluation.

(iii) Comparative Assessment: The final stage involves a comparative evaluation of the two approaches to determine their predictive accuracy and to identify the spatial factors most strongly associated with traffic accident risk.

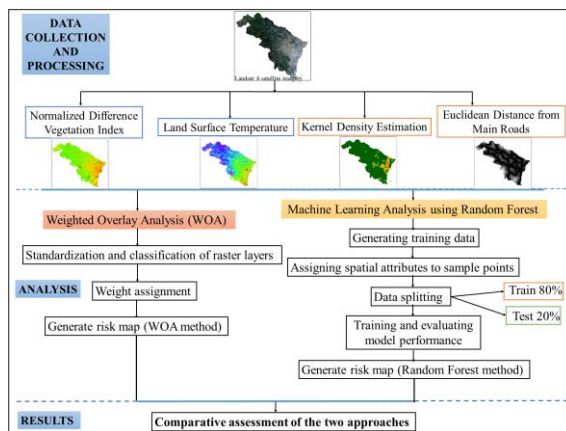


Figure 3. Analysis flowchart of WOA and RF

All data processing, spatial analysis, and model construction are conducted within the ArcGIS Pro software environment. Key tools employed include Weighted Overlay for assigning weights to spatial input layers, KDE for calculating accident density, and the Train Random Trees Classifier for implementing the RF model to generate risk zoning maps.

Weighted overlay analysis

WOA is a widely used technique in GIS for solving multi-criteria spatial decision-making problems. It is particularly effective in evaluating the relative suitability of locations based on multiple heterogeneous input factors. In this study, WOA is applied to delineate areas with elevated traffic accident risk.

Each input layer is reclassified on a standardized scale from 1 to 5, representing the relative influence or risk level of each spatial factor. These reclassified raster layers are then normalized and combined using a weighted sum approach, where each cell value is computed based on its contribution to the

overall risk, as determined by predefined expert-assigned weights. The final composite risk map is generated using the following weighted sum equation (Equation 1)(Doke et al., 2021):

$$S = \sum_{i=1}^n w_i \cdot x_i \quad (1)$$

where:

S : composite risk index;

x_i : standardized value of the i -th layer;

w_i : weight of the i -th layer;

n : number of data layers.

WOA offers several advantages: it is intuitive, straightforward to implement within the ArcGIS environment, and supports flexible integration of heterogeneous spatial data sources-including remote sensing imagery, topographic maps, GPS data, and field surveys. However, a key limitation of the method lies in its reliance on accurate weight assignment for each input layer. When empirical data are unavailable for automatic optimization, weights must be assigned manually based on expert judgment, domain knowledge, previous studies, or regional characteristics (Malczewski et al., 2006).

In this study, after standardizing all input layers, they are integrated using the WOA technique. The specific weights assigned to each layer are detailed in Table 1.

Table 1. Weights of criteria classes in WOA analysis (Leake et al., 2000)

Criteria	Weight (%)
Kernel Density Estimation	30%
Land Surface Temperature	20%
Normalized Difference Vegetation Index	15%
Euclidean Distance from Main Roads	35%

Segmentation using the Random Forest Model

RF is a robust ensemble learning algorithm that constructs multiple decision

trees to improve classification accuracy and mitigate overfitting (Breiman, 2001). Each tree is trained on a bootstrap sample of the dataset, and at each decision node, a random subset of predictor variables is considered for splitting. This mechanism promotes model diversity and enhances overall stability and generalizability.

In this study, the RF model was trained on a dataset comprising 3,188 labeled points—consisting of 1,594 actual traffic accident locations and 1,594 randomly sampled non-accident locations. Feature values for these points were extracted from four spatial raster layers: NDVI, LST, KDE, and Euclidean Distance from Main Roads. This was accomplished using the Extract Multi Values to Points tool within ArcGIS Pro. The dataset was randomly split into training (80%) and testing (20%) subsets, ensuring balanced class representation.

Model training was performed directly in ArcGIS Pro using the Train Random Trees Classifier tool, enabling tight integration between spatial data processing and machine learning implementation. The RF model not only demonstrated strong performance in classifying accident-prone areas but also provided variable importance scores, which offer valuable insights for evidence-based traffic planning and risk mitigation strategies (Rodriguez-Galiano et al., 2012; Obasi et al., 2023).

Model evaluation metrics

In traffic accident risk classification, datasets often exhibit class imbalance, which can distort evaluation if only overall accuracy is considered. To provide a more nuanced assessment, additional performance metrics such as Precision, Recall, and F1-score are employed. These metrics are particularly effective for evaluating classification performance under imbalanced conditions, ensuring that both false positives and false negatives are appropriately accounted for (Yan et al., 2022).

$$Accuracy = \frac{TP + TN}{TP + TN + FP + FN} \quad (2)$$

$$Precision = \frac{TP}{TP + FP} \quad (3)$$

$$Recall = \frac{TP}{TP + FN} \quad (4)$$

$$F1 = 2 \times \frac{Precision \times Recall}{Precision + Recall} \quad (5)$$

In which:

TP (True Positive): correctly predicted a positive sample;

TN (True Negative): correctly predicted a negative sample;

FP (False Positive): incorrectly predicted a negative sample as positive;

FN (False Negative): incorrectly predicted a positive sample as negative.

RESULTS AND DISCUSSION

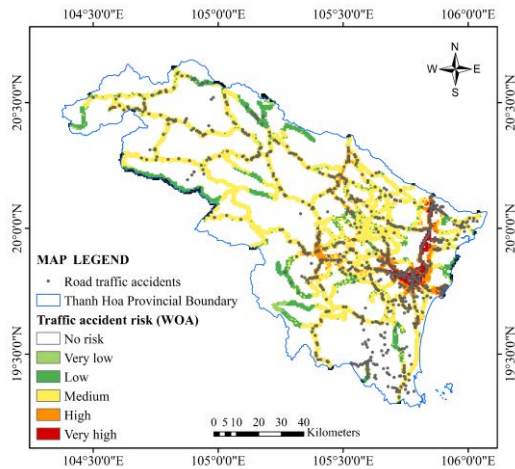
Accident risk zoning using WOA and Random Forest

Both the WOA and RF models were applied to classify traffic accident risk zones across Thanh Hoa Province. The WOA-derived risk map as shown in Figure 4(a) indicates that high-risk zones are primarily concentrated along major transportation corridors and in densely populated urban centers. This result aligns with intuitive expectations based on traffic volume and infrastructure conditions.

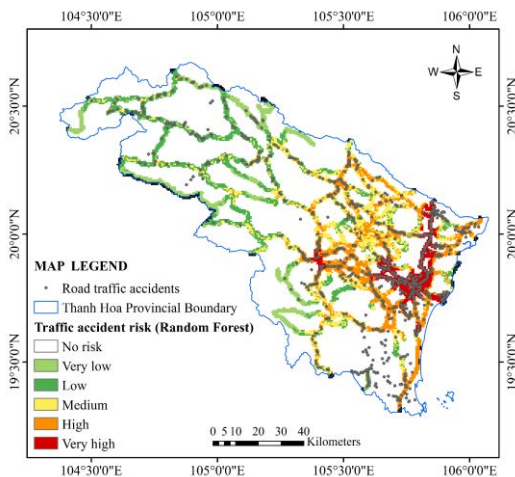
In contrast, the RF-based risk map as shown in Figure 4(b) exhibits a higher level of spatial specificity. Areas identified as high and very high risk by the RF model show strong spatial correspondence with actual accident locations. This suggests that the RF model captures the underlying spatial patterns of traffic accidents more accurately, likely due to its data-driven nature. However, in certain sparsely populated or topographically complex regions, the model may fail to detect all accident-prone locations—possibly due to the limitations of the input features or insufficient training data in those areas.

Overall, both WOA and RF methods demonstrate utility in spatial risk segmentation. The WOA method offers a rule-based, interpretable framework for decision-

making, while the RF model provides a more adaptive and empirically grounded alternative. The resulting risk maps can serve as critical tools for developing traffic warning systems, informing infrastructure investment priorities, and enhancing evidence-based traffic safety planning.



(a)



(b)

Figure 4. Traffic accident risk zoning map (a) WOA
(b) RF

Evaluation of Random Forest Model Performance

The performance of the RF model was assessed using a confusion matrix, which served as the basis for calculating key classification metrics, including Accuracy, Precision, Recall, and F1-score. These metrics

provide a comprehensive evaluation of the model's predictive capability, covering aspects of correctness, sensitivity, and overall classification effectiveness on the testing dataset.

The RF model achieved an overall accuracy of 81.07%, indicating a high proportion of correctly classified instances. Precision was recorded at 87.22%, suggesting a low false positive rate, while Recall reached 72.73%, reflecting the model's ability to correctly identify accident-prone locations. The F1-score, which balances Precision and Recall, was 79.31%, confirming the model's overall robustness and reliability as shown in Table 2.

These results demonstrate that the Random Forest model delivers stable and effective performance, making it a strong candidate for real-world applications in traffic accident risk prediction, spatial planning, and the development of early-warning systems.

Table 2. Percentage of evaluation indicators of Random Forest model

Indicator	Percentage
Accuracy	81,07%
Precision	87,22%
Recall	72,73%
F1-score	79,31%

The role of spatial factors

In the WOA, input layer weights were assigned based on expert judgment as shown in Table 1, reflecting domain knowledge about the relative influence of each factor on traffic accident risk. While effective, this approach inherently introduces subjectivity. To provide a more objective and data-driven perspective, the study also utilized the Train Random Trees Model tool in ArcGIS Pro to quantify the relative importance of each variable within the RF model as shown in Table 3.

The RF results broadly align with the expert-assigned WOA weights, particularly regarding the two most influential spatial factors: Euclidean Distance from Main Roads and KDE, as illustrated in Figure 6. Among all variables, KDE was the most important factor,

contributing 38.33%—significantly higher than the 30% in WOA. This reinforces the established understanding that spatial clustering of past accidents is a strong predictor of future risk, as validated in recent KDE-based spatial analyses (Le et al., 2024a; Le et al., 2024b).

The second most important factor was the Euclidean distance to main roads, accounting for 27.67% of the model's influence, lower than the 35% in WOA but still underscoring the critical role of proximity to main roads—typically with higher traffic volumes and speeds—in increasing accident risk. This result is consistent with prior studies, which demonstrate that proximity to primary roadways strongly correlates with accident frequency and severity due to higher traffic volumes and greater exposure to high-speed travel (Wang et al., 2023; Wang et al., 2019). Together, these two features alone explain nearly two-thirds of the model's predictive capability, highlighting their dominant role in risk stratification.

Environmental and land cover factors also contributed meaningfully: LST and NDVI contributed 19.50% and 14.50%, respectively. These variables influence accident risk through clear physical mechanisms. Elevated LST can reduce pavement friction and contribute to driver fatigue, while variations in NDVI affect sight distance, shading, and the presence of roadside vegetation—conditions known to alter driving behavior and increase the likelihood of traffic accidents. While secondary to the top two features, these variables still offer valuable context - especially in urban settings, where LST reflects heat island effects that may influence driver behavior and vehicle performance (Pińskwar et al., 2024). NDVI, as a proxy for vegetation cover and landscape type, also indirectly captures aspects of road visibility, surface conditions, and land use patterns.

The comparison between WOA-assigned weights and RF-based importance values highlights the complementary strengths of the two approaches. Expert weighting captures

nuanced domain insights, while machine learning quantifies actual data-driven influence. Therefore, combining both perspectives - expert-driven and model-derived - enhances the overall reliability, objectivity, and interpretability of the traffic accident risk zoning process.

Table 3. Variable importance of input factors in the Random Forest model

Input Variable	Importance (%)
Kernel Density Estimation	38.33%
Euclidean Distance from Main Roads	27.67%
Land Surface Temperature	19.50%
Normalized Difference Vegetation Index	14.50%

Comparison between Weighted Overlay Analysis and Random Forest

To assess the effectiveness of the two methods -WOA and RF - accident point data were spatially overlaid with each method's risk zoning map as shown in Figure 4(a) and Figure 4(b). The WOA and RF models operate on fundamentally different scales: WOA uses a standardized 1–5 index, whereas RF produces probability-based outputs ranging from 0 to 1. Therefore, a unified classification threshold cannot be applied. Each model was categorized according to its intrinsic value distribution. However, the comparison was conducted using harmonized indicators—such as the percentage of accident points captured within high-risk zones and the RF performance metrics—to ensure an objective and scale-independent evaluation. Additionally, the “no risk” class assigned to mountainous and forested areas without traffic networks is applied as a spatial mask rather than a model-generated category. Therefore, this adjustment does not modify the underlying WOA or RF scales or affect the harmonized comparative evaluation presented above.

The comparative analysis reveals that the RF model provides a more accurate classification of high-risk areas. Specifically, 80.61% of actual accident locations fall within the two highest risk categories as defined by

the RF model. In contrast, the WOA method captures only 71.45% of accident points within the same categories.

Beyond spatial accuracy, the RF model also offers quantitative evaluation metrics, including an overall accuracy of 81.07%, along with precision, recall, and F1-score, which enable a more rigorous validation of its predictive performance. Moreover, the RF model produces variable importance scores, offering interpretable insights into the contribution of each input factor—an advantage that WOA, being a rule-based method, lacks.

These findings underscore the superiority of the machine learning approach in both predictive capability and diagnostic transparency. Unlike WOA, which is based entirely on expert-assigned weights and therefore more vulnerable to subjective bias, the RF model is data-driven and adaptive, capable of capturing complex, non-linear relationships among variables.

That said, WOA retains value in specific contexts. It is straightforward to implement, interpretable, and especially useful in scenarios where data are scarce or machine learning tools are not available. When used in combination with RF, WOA can serve as a complementary method—either to validate RF outputs or to provide initial estimates in data-constrained environments.

A summary comparison of the two approaches, based on key performance and methodological criteria, is presented in Table 4.

Table 4. Comparison of the performance of the two methods WOA and RF

Criteria	WOA	Random Forest
Requires real accident data	Yes	No
Classification performance	Medium	High
Explainability	Yes (weighting)	Explicit (determining the influence of the variable)
Degree of automation	Low	High

CONCLUSION

This study demonstrates that integrating GIS and remote sensing data with both WOA and the RF machine learning model enables a robust and comprehensive approach to traffic accident risk assessment. Among the two methods, the RF model outperforms WOA in terms of classification accuracy and variable interpretability, confirming its suitability for data-driven spatial analysis. Notably, KDE emerged as the most influential predictor of accident risk, reinforcing its importance in transportation planning. While the WOA method remains a practical choice in contexts with limited field data - due to its simplicity, transparency, and rapid deployment - it lacks the objectivity and predictive power of machine learning models. Nevertheless, its use as a complementary tool can enhance initial assessments or serve as a benchmark in resource-constrained settings.

The findings strongly support the integration of machine learning algorithms with GIS and remote sensing technologies in future transportation safety initiatives. This combined framework can significantly improve spatial risk prediction, support proactive infrastructure planning, and enable the development of early-warning systems to mitigate road traffic accidents. Future research should expand this approach by incorporating additional spatial variables such as road geometry, traffic volume, and population density, and by exploring advanced ensemble or deep learning models to further enhance analytical precision and temporal scalability.

REFERENCES

- Breiman, L. (2001). Random forests. *Machine Learning*, 45(1). <https://doi.org/10.1023/A:1010933404324>.
- Chen, H., Wood, M. D., Linstead, C., & Maltby, E. (2011). Uncertainty analysis in a GIS-based multi-criteria analysis tool for river catchment management. *Environmental Modelling and Software*, 26(4). <https://doi.org/10.1016/j.envsoft.2010.09.005>.
- Doke, A. B., Zolekar, R. B., Patel, H., & Das, S. (2021). Geospatial mapping of groundwater potential zones using multi-criteria decision-making AHP approach in a

- hardrock basaltic terrain in India. *Ecological Indicators*, 127. <https://doi.org/10.1016/j.ecolind.2021.107685>.
- Eskandari, H., & Rabelo, L. (2007). Handling uncertainty in the analytic hierarchy process: A stochastic approach. *International Journal of Information Technology and Decision Making*, 6(1). <https://doi.org/10.1142/S0219622007002356>.
- Farhangi, F., Sadeghi-Niaraki, A., Razavi-Termeh, S. V., & Choi, S. M. (2021). Evaluation of tree-based machine learning algorithms for accident risk mapping caused by driver lack of alertness at a national scale. *Sustainability (Switzerland)*, 13(18). <https://doi.org/10.3390/su131810239>.
- Le, K. G., Tran, Q. H., & Do, V. M. (2024). Urban Traffic Accident Features Investigation to Improve Urban Transportation Infrastructure Sustainability by Integrating GIS and Data Mining Techniques. *Sustainability (Switzerland)*, 16(1). <https://doi.org/10.3390/su16010107>.
- Le, T. H., Vu, T. P. T., & Do, T. P. T. (2024a). Analyzing Road Traffic Incident Hotspots Using Cluster Analysis in Thanh Hoa Province of Vietnam. *International Journal of Geoinformatics*, 20(9), 16–26. <https://doi.org/10.52939/ijg.v20i9.3537>.
- Le, T. H., Vu, T. P. T., & Do, T. P. T. (2024b). A study on identifying and analyzing road traffic incident hotspots on National Highway 1A, Thanh Hoa province, Vietnam, employing Statistical and GIS Techniques. *Journal of Mining and Earth Sciences*, 65(6), 22–33. [https://doi.org/10.46326/JMES.2024.65\(6\).03](https://doi.org/10.46326/JMES.2024.65(6).03).
- Leake, C., & Malczewski, J. (2000). GIS and Multicriteria Decision Analysis. *The Journal of the Operational Research Society*, 51(2). <https://doi.org/10.2307/254268>.
- Liu, L., Gao, Z., Luo, P., Duan, W., Hu, M., Mohd Arif Zainol, M. R. R., & Zawawi, M. H. (2023). The Influence of Visual Landscapes on Road Traffic Safety: An Assessment Using Remote Sensing and Deep Learning. *Remote Sensing*, 15(18). <https://doi.org/10.3390/rs15184437>.
- Malczewski, J. (2006). GIS-based multicriteria decision analysis: A survey of the literature. *International Journal of Geographical Information Science*, 20(7). <https://doi.org/10.1080/13658810600661508>.
- Obasi, I. C., & Benson, C. (2023). Evaluating the effectiveness of machine learning techniques in forecasting the severity of traffic accidents. *Heliyon*, 9(8). <https://doi.org/10.1016/j.heliyon.2023.e18812>.
- Pińskwar I, Choryński A, & Graczyk D 2024 *Good weather for a ride (or not?): how weather conditions impact road accidents—a case study from Wielkopolska (Poland)*, *International journal of biometeorology*, 68(2), 317–331. <https://doi.org/10.1007/s00484-023-02592-3>.
- Rodriguez-Galiano, V. F., Ghimire, B., Rogan, J., Chica-Olmo, M., & Rigol-Sanchez, J. P. (2012). An assessment of the effectiveness of a random forest classifier for land-cover classification. *ISPRS Journal of Photogrammetry and Remote Sensing*, 67(1). <https://doi.org/10.1016/j.isprsjprs.2011.11.002>.
- Vu. T. P. T., Dang. T. G., & Le. V. A., (2024). Reliability assessment of land subsidence monitoring results using PSI technique in Ho Chi Minh City, Vietnam. *International Journal of Environmental Studies*, 81(2), 881–895. <https://doi.org/10.1080/00207233.2024.2324623>.
- Wang, J., Ma, S., Jiao, P., Ji, L., Sun, X., & Lu, H. (2023). Analyzing the Risk Factors of Traffic Accident Severity Using a Combination of Random Forest and Association Rules. *Applied Sciences (Switzerland)*, 13(14). <https://doi.org/10.3390/app13148559>.
- Wang, W., Yuan, Z., Yang, Y., Yang, X., & Liu, Y. (2019). Factors influencing traffic accident frequencies on urban roads: A spatial panel time-fixed effects error model. *PLoS ONE*, 14(4). <https://doi.org/10.1371/journal.pone.0214539>.
- Worachairungreung, M., Ninsawat, S., Witayangkurn, A., & Dailey, M. N. (2021). Identification of road traffic injury risk prone area using environmental factors by machine learning classification in Nonthaburi, Thailand. *Sustainability (Switzerland)*, 13(7). <https://doi.org/10.3390/su13073907>.
- Yan, M., & Shen, Y. (2022). Traffic Accident Severity Prediction Based on Random Forest. *Sustainability (Switzerland)*, 14(3). <https://doi.org/10.3390/su14031729>.
- Zheng, M., Xie, X., Jiang, Y., Shen, Q., Geng, X., Zhao, L., & Jia, F. (2024). Optimizing Kernel Density Estimation Bandwidth for Road Traffic Accident Hazard Identification: A Case Study of the City of London. *Sustainability*, 16(16), 6969. <https://doi.org/10.3390/su16166969>.

DOI: 10.15625/vap.2025.0223

Application of machine learning and WebGIS for land-use planning information utilization to support digital transformation of land administration

Nguyen Xuan Linh, Tran Quoc Binh, Pham Le Tuan, Bui Ngoc Tu *

Faculty of Geography, University of Science, Vietnam National University, Hanoi, Vietnam

*Email: buingoctu@hus.edu.vn

Abstract: In the context of digital transformation in land administration, the demand for rapid, accurate, and user-friendly access to land-use planning (LUP) information has become increasingly critical. This study proposes and experimentally implements an integrated solution combining a WebGIS platform with an AI Chatbot powered by machine learning models to address this need. The experimental implementation was conducted in Son La Province, Vietnam. The developed WebGIS system offers basic mapping functions, along with tools for searching and retrieving information from textual documents and thematic maps. Data are systematically organized according to functional departments and administrative units in the pilot locality, supporting the effective management and utilization of LUP information. Based on this platform, the AI Chatbot with machine learning enables users to easily query land use planning information, including details not shown on the map. With natural language processing and contextual analysis, the AI Chatbot delivers precise information and expands retrieval to related information such as policies, projects, and socio-legal factors in land use planning. Furthermore, it can suggest contextually related questions to facilitate deeper data exploration. Preliminary experimental results demonstrate that the proposed solution yields positive outcomes, highlighting the potential of integrating WebGIS, AI Chatbot, and machine learning models to support efficient access to and utilization of land use planning information, thereby contributing to the

advancement of digital transformation in land administration.

Keywords machine learning, WebGIS, AI Chatbot, land-use planning, digital transformation.

INTRODUCTION

In the context of rapid urbanization and the increasing demand for digital transformation in land administration, the utilization and management of LUP information are facing significant challenges. At present, LUP data systems in many localities remain fragmented, inconsistent, and are in the process of integration, standardization, and digitization. Much of the data still exists in administrative documents or static map formats, making it difficult for stakeholders to access comprehensive, accurate, and timely information. Furthermore, most analytical tools are designed for professional users, while non-specialized groups such as citizens, enterprises, or local officers lack intuitive and user-friendly means to query and analyze planning information. In this context, the integration of Artificial Intelligence (AI), Machine Learning (ML), and WebGIS technologies has opened a new approach.

In recent years, AI has not only been applied in specialized software but has also been increasingly integrated into WebGIS platforms to enhance analytical capabilities and enable more interactive and accessible spatial data exploration. Representative studies include that of Chulwoong Park et al. (2023), who developed an AI-based urban planning

assistant capable of generating land-use proposals from imagery data and planning indicators. Zhang et al. (2023) introduced two models, GeoGPT and ChatGeoAI, which integrate Large Language Models (LLMs) with GIS to enable natural language-based spatial querying and analysis. Akinboyewa et al. (2025) proposed GIS Copilot, an AI-powered extension for QGIS that allows non-expert users to perform spatial analyses without complex technical operations. Oktavia and Pribadi (2025) developed an AI Chatbot tool to improve the land certification process in Indonesia. Salkin et al. (2025) investigated the application of AI in LUP and zoning, particularly in supporting governmental agencies and local communities through AI Chatbots. Developed by the UK Geospatial Commission, the Alan Turing Institute, and Newcastle City Council, the DemoLand system demonstrated the potential of integrating AI Chatbots with WebGIS for interactive simulation of land-use scenarios, retrieving and analyzing spatial data from multiple sources to support decision-making in LUP (Doshi M., 2024). Collectively, these applications have not only reduced technical barriers for non-specialist users but also improved transparency, efficiency, and interactivity within planning systems.

In Vietnam, several provinces and cities, including Ho Chi Minh City, Hanoi, Binh Duong, and Da Nang, have adopted WebGIS platforms to support land management and planning. These systems provide convenient access to information on planning status, construction parameters, and administrative boundaries. Some localities have also started integrating WebGIS with other sectoral datasets to improve data sharing and decision-making (Ho Chi Minh City DONRE, 2025; Binh Duong DONRE, 2025; Da Nang DONRE, 2025; VNPT, 2025). However, most existing systems primarily focus on mapping functions and displaying basic attribute information, lacking advanced analytical capabilities and intelligent user interaction. Within this context, Machine Learning and AI Chatbots act as intermediary tools that bridge users with WebGIS systems,

facilitating more intelligent and efficient access to planning information. While WebGIS excels in visualizing and managing spatial data, AI Chatbots handle natural-language processing, enabling non-expert users to easily retrieve, filter, and synthesize attribute information according to specific needs. This integration modernizes the management and utilization of planning information, promotes digital transformation in land administration, and broadens public accessibility to LUP data. Therefore, the objective of this study is to apply machine learning and WebGIS for LUP information utilization.

METHODOLOGY

Study area and data collection

Son La is a mountainous province located in the Northwest region of Vietnam, covering a total natural area of 14,123.5 km². The province occupies a strategic geographical position, bordered by Yen Bai, Phu Tho, Hoa Binh, Dien Bien, and Lai Chau provinces, and shares a border of more than 274 km with the Lao People's Democratic Republic. Administratively, following the implementation of Resolution No. 1681/NQ-UBTVQH15 dated June 16, 2025, issued by the Standing Committee of the National Assembly on the reorganization of commune-level administrative units, Son La currently comprises 67 communes and 8 wards. Prior to this administrative restructuring, the province consisted of 12 district-level units, including Son La City and 11 districts (Fig. 1).

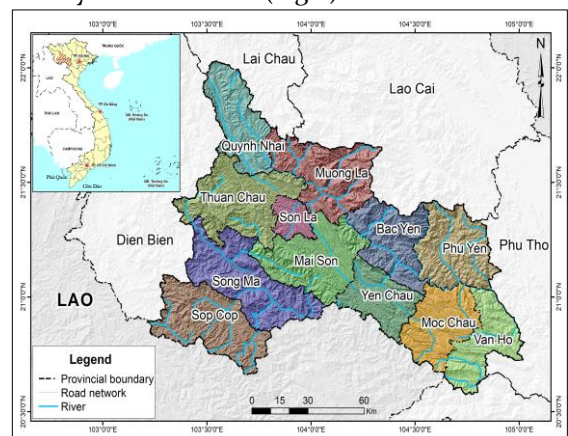


Figure 1. The location of study area

To serve the research objectives, the collected data include the comprehensive explanatory reports on LUP for the period 2021–2030, with a vision toward 2050, of all 12 district-level administrative units of Son La Province, including Son La City and 11 districts. In addition, the dataset comprises the LUP maps to 2030 for these 12 administrative units. All map documents were provided by the Department of Natural Resources and Environment of Son La Province in *.dgn format at a scale of 1:25,000.

Research workflow

The workflow diagram presented in Figure 2 comprises three main phases. The preparation phase focuses on assessing requirements and defining the functional model (Step 1). The system design and development phase involves selecting appropriate technologies, designing the database, and developing the WebGIS and AI Chatbot functionalities (Steps 2 and 3). Finally, the application phase includes system deployment, operation, and iterative updates in practical use (Steps 4 and 5).

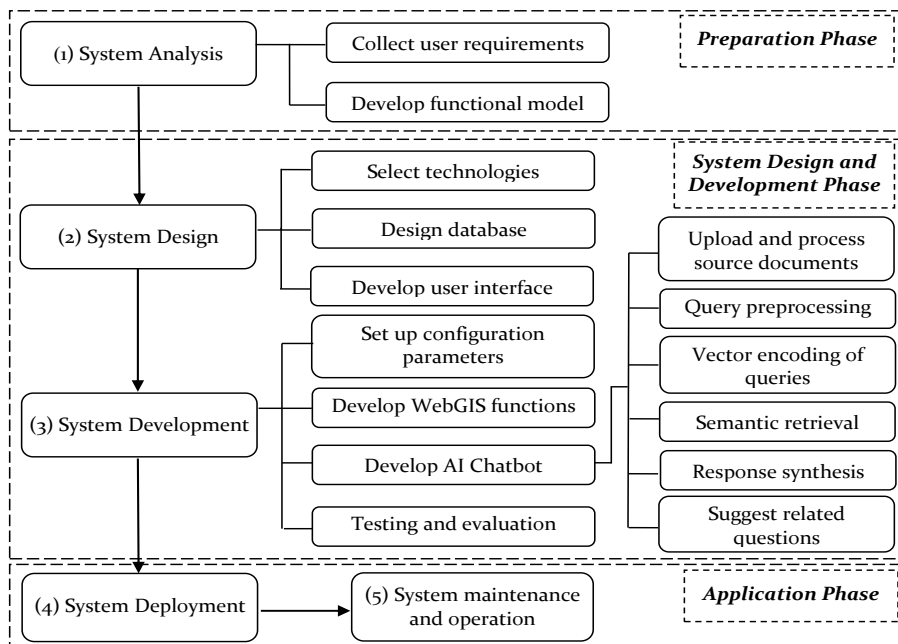


Figure 2 Workflow integrating machine learning and WebGIS for LUP information utilization

Step 1: System analysis

To develop a WebGIS system that supports the utilization of LUP information, an initial field survey was conducted to collect data on user requirements for accessing and utilizing LUP datasets among different stakeholder groups, including government officials, enterprises, and citizens. Based on the survey results, user needs were analyzed, and the functional model of the system was designed using a Use Case Diagram in UML. The WebGIS system ensures core functionalities such as displaying base and

thematic maps, providing attribute information, performing basic map operations, searching related planning documents, and managing system configurations. The integrated AI Chatbot acts as a virtual assistant that allows users to ask questions related to land-use planning, receive intelligent question suggestions, and obtain summarized textual responses, thereby enabling non-technical users to quickly access information without requiring complex operations. The main workflows were subsequently modeled using UML Activity Diagrams, serving as the

foundation for the following system design and development stages.

Step 2: System design

The system design phase plays a key role in establishing the technical foundation of the WebGIS platform, comprising three main tasks: technology selection, database design, and user interface development. The system is developed on the open-source GeoServer platform, which complies with OGC (Open Geospatial Consortium) standards, allowing efficient publication and management of spatial data while maintaining compatibility with mapping libraries such as OpenLayers and Leaflet. PostgreSQL combined with PostGIS is used for database management, providing high performance in storing, querying, and processing spatial datasets. The database was designed using UML to logically and comprehensively represent spatial and non-spatial data layers while ensuring data consistency and scalability. The user interface was developed with ReactJS on the client side and NodeJS on the server side, enabling a flexible, user-friendly, and high-performance web application.

For the AI Chatbot function integrated into the WebGIS system, this study employs a Large Language Model (LLM) via the OpenAI API to process natural language and generate adaptive, accurate responses. The LLM is a type of machine learning model that uses deep learning techniques to understand and generate natural language. OpenAI, headquartered in San Francisco, USA, is a leading organization in AI research and development, responsible for several advanced models, including ChatGPT, an LLM-based application designed for natural language interaction (OpenAI, 2025). Utilizing OpenAI's LLM helps reduce infrastructure costs while leveraging the model's superior linguistic capabilities trained on large-scale datasets. To enhance the domain-specific accuracy of responses, relevant documents and reports related to LUP (e.g., explanatory planning reports, analytical reports, and WebGIS system documentation) were incorporated into the preprocessing pipeline and stored as vectorized representations in a semantic search database.

Consequently, when users submit queries, the system can efficiently retrieve, synthesize, and generate appropriate responses. The integration of the AI Chatbot with WebGIS not only harnesses the advantages of spatial data visualization but also expands the accessibility and analytical capability of attribute data through natural language interaction.

Step 3: System development

The system development phase includes three main tasks: setting up system parameters and structure, developing functional components, and conducting testing and refinement.

System parameters and structure setup: The initial step involves defining and configuring map parameters such as the coordinate reference system, projection, data layer structure (base maps, background data layers, and thematic layers), attribute field labels, and visualization settings including symbology, color schemes, display range, and zoom levels. At the same time, the user interface framework was initialized using HTML and JavaScript to ensure a flexible and interactive foundation for WebGIS development.

Development of functional components: The system consists of two core components are the WebGIS platform and the AI Chatbot tool.

For the WebGIS module, customized scripts were developed to handle user interaction and spatial data queries, focusing on key functions such as selecting and displaying thematic map layers, showing attribute information when interacting with spatial features, adjusting zoom levels, and searching related maps or planning documents. The implementation was carried out using a combination of PHP (server-side) and JavaScript (client-side) to ensure responsive and efficient communication between the user interface and the data server. The AI Chatbot module was developed to assist non-technical users in retrieving LUP information through natural language interaction, particularly for content that cannot be fully represented in

spatial maps. The system adopts a multi-layer architecture comprising several key processing stages that work together to ensure efficient information retrieval. First, relevant documents such as explanatory planning reports and legal texts are uploaded to the management platform (<https://chatbotadmin.vercel.app>), where the system automatically performs text extraction, segmentation (chunking), vector encoding using a pre-trained embedding model, and stores the results in a vector database. Next, user queries in Vietnamese are received and preprocessed by the Large Language Model (LLM) to normalize and clarify their semantic meaning, ensuring they are well-suited for information retrieval. These queries are then converted into semantic vector representations using a domain-adapted embedding model fine-tuned on LUP-related data from the study area. In the semantic retrieval phase, the query vector is compared with entries in the vector database to identify text segments that exhibit high semantic similarity. The retrieved content is subsequently passed to the LLM, which synthesizes a concise and contextually relevant textual response. Finally, the system can suggest related questions based on the original query, thereby enhancing user interaction and supporting deeper data exploration, especially for users without technical expertise.

System testing and refinement: The final stage involves testing the system to evaluate its stability, performance, and compliance with design requirements. Technical issues were identified and resolved, and the user interface and functionalities were refined based on feedback from stakeholders to ensure that the system is user-friendly, reliable, and effective for practical applications.

Step 4: System deployment

The system deployment phase involves transferring the developed model from the testing environment to operational use with real-world data in the study area. The server infrastructure can be flexibly deployed on common operating systems such as Windows Server, Linux, or Ubuntu. This phase also

includes data standardization and loading, in which spatial and attribute data are standardized according to the database model structure. The data import process is strictly validated to ensure compatibility and data integrity. After installation and data integration, the system is deployed in a pilot operation phase to collect user feedback, including input from GIS specialists. These evaluations serve as a critical basis for adjusting and refining the system's functionalities prior to official implementation.

Step 5: System maintenance and operation

This phase ensures the WebGIS system operates stably, accurately, and efficiently. Land-use planning data and related information are regularly updated to maintain completeness and timeliness. The AI Chatbot component is periodically enhanced by expanding the training dataset and improving its natural language understanding capabilities. The WebGIS system integrating machine learning and AI functions has been deployed and tested at: <https://sonla.cargis.vn>. Users can access and utilize the system's main functions without login credentials, while administrative access is restricted to authorized personnel for configuration, management, and data updating purposes.

RESULTS AND DISCUSSION

Interface and Basic Functions of the WebGIS System

The WebGIS system allows users to flexibly manage and visualize spatial data through an interactive layer control interface (Fig. 3). Users can enable or disable various map layers, including both base maps and thematic data. The base maps provide two visualization options: Google Maps and satellite imagery, serving as spatial references for general orientation and contextual analysis. The geographic base data include several key datasets such as the national geodetic control network, administrative boundaries (including the updated commune boundaries following the 2025 administrative restructuring), and topographic information represented by elevation point data.

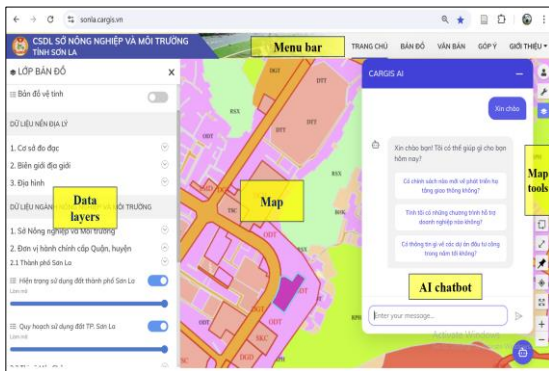


Figure 3. Interface of the WebGIS system

Thematic data layers are organized into two main groups. The first group contains datasets managed by the Department of Natural Resources and Environment, categorized according to its subordinate divisions such as specialized departments, sub-departments, technical centers, and forest or conservation management boards. The second group consists of spatial datasets organized by district-level administrative units, containing both current land-use and LUP maps for the twelve districts of Son La Province. Although district-level administrative units were officially restructured after July 1, 2025, the system maintains this organization for continuity and convenience in data retrieval and analysis. This hierarchical structure can be flexibly adjusted in the future to accommodate updates in administrative or planning data.

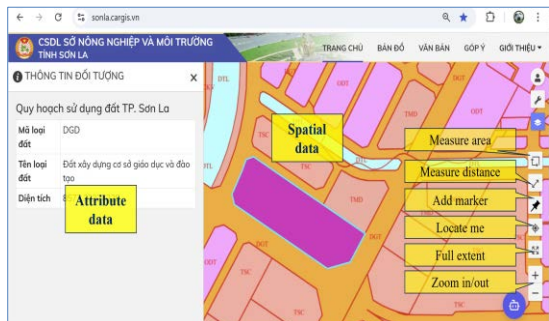


Figure 4. WebGIS map tools

The WebGIS system interface (Fig. 4) provides a comprehensive set of mapping tools designed to enhance spatial interaction and analytical capability. Users can zoom in or out

for detailed or regional visualization, measure distances and areas of interest, and view attribute information by selecting spatial features on the map. In addition, the system integrates functions for viewing and searching maps and related planning documents, along with a feedback tool that allows users to report issues and suggest improvements.

AI Chatbot for land-use planning information utilization

The textual data used as training input for the experimental model consisted of explanatory LUP reports for the period 2021–2030 with a vision to 2050, as well as the 2022 annual land-use plan of Son La City and Moc Chau District. To evaluate the effectiveness of the AI Chatbot in supporting LUP information queries, this study developed several interactive scenarios simulating common use cases of citizens and technical staff. These scenarios focused on retrieving and analyzing information related to current land use and the LUP content for the 2021–2030 period. The following illustrates an example of user interaction with the AI Chatbot. In response to the query, “*What projects are planned for implementation in Moc Chau district in the near future?*”, the system provided detailed information and also suggested follow-up questions, enabling users to further explore related planning content (Fig. 5a).

The comparison between the AI Chatbot’s responses and the content of LUP reports for Son La City and Moc Chau District during the 2021–2030 period indicates that the tool provides fast, accurate, and naturally articulated answers. The Chatbot AI effectively handles quantitative information such as area, percentage, and land classification data, while also synthesizing content from multiple sections or different reports, enabling users to grasp the key information without reading the full documents. In addition, it suggests related questions to support deeper data exploration. For optimal performance, users are advised to formulate clear, specific and contextually relevant queries.

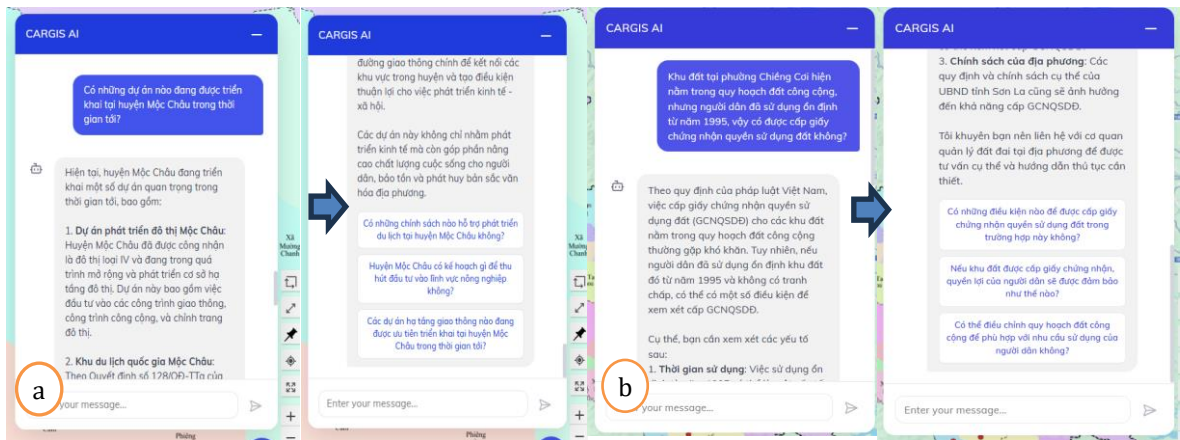


Figure 5. Two illustrative cases of AI Chatbot responses:
(a) successful and (b) unable to provide a specific answer

Although the AI Chatbot offers significant advantages in providing rapid and accessible information, it currently serves as a supportive tool and cannot replace the role of technical officers or domain experts. In situations requiring in-depth analysis or when dealing with complex real-world cases, the Chatbot AI cannot provide the nuanced interpretation and contextual reasoning that a specialist can offer.

Figure 5b illustrates a practical scenario a user might raise. For example, in response to the question: “A parcel in Chieng Coi ward is designated as public land in the land-use planning map, but local residents have used it stably since 1995. Can a land-use right certificate be issued in this case?”, the Chatbot primarily provides general guidance and cannot deliver a definitive conclusion.

This example demonstrates that, while the AI Chatbot is effective for rapid information retrieval and initial orientation, it cannot replace professional expertise in tasks requiring case file analysis, legal interpretation, or administrative decision-making.

Analysis of User Survey Results

During the experimental implementation of the WebGIS system and AI Chatbot for supporting LUP information utilization, a user survey was conducted involving 04 officials from the Department of Natural Resources and

Environment of Son La Province and 10 local residents. Feedback was collected and analyzed using a five-point Likert scale (ranging from 1 – strongly disagree to 5 – strongly agree), focusing on key aspects such as the user interface, data quality, system functionality, and particularly the AI Chatbot feature. The survey results were summarized and presented in Figure 6.

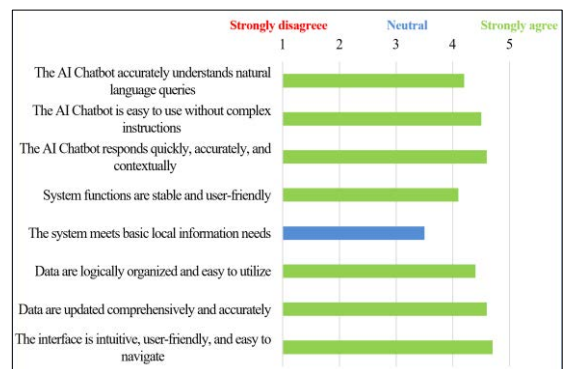


Figure 6. Summary of user survey results

The survey results indicated that the system's interface was highly rated for its intuitiveness and ease of use, with an average score of 4.7 on the 5-point Likert scale. Functional components were clearly structured and accessible even to users without technical backgrounds, while integrated mapping tools such as distance and area measurements enhanced the efficiency of spatial information retrieval. In terms of data quality and

accessibility, the system achieved mean ratings between 4.3 and 4.6 for data organization, accuracy, and logical categorization, reflecting a high level of user satisfaction. The WebGIS database included both base layers (e.g., administrative boundaries, topography) and thematic layers (e.g., current land use, land-use planning), which were systematically maintained and regularly updated. In addition, the system demonstrated strong potential for integration with sectoral datasets, thereby improving interoperability and expanding its applicability in practical land management contexts. The AI Chatbot functionality also received highly positive feedback for its ability to interact naturally with users, providing rapid, accurate, and contextually relevant responses while enabling information retrieval without requiring complex technical operations. Its capability to suggest related questions further enhanced the efficiency of information access and supported users in exploring the system more conveniently. However, the survey also revealed several limitations. The system does not yet support direct editing of spatial data within the web interface, lacks integrated functions for land-use plan management, and the chatbot is currently unable to interact directly with map data. As a result, the chatbot's current role remains limited to providing and retrieving basic information, rather than serving as an advanced analytical tool.

Building on the current findings, future work will focus on enhancing the AI Chatbot's capability to comprehend and execute spatial queries. The proposed technical framework comprises two main stages: (i) identifying and mapping spatial keywords and entities to the corresponding data layers in the database; and (ii) translating natural language queries into spatial operations, returning both textual outputs and highlighted spatial features within the WebGIS interface. This improvement aims to enable information retrieval by specific locations or planning objects, thereby advancing data exploration capacity and fostering a more intelligent, transparent, and efficient WebGIS system.

CONCLUSION

The experimental application of a machine learning model integrated with a WebGIS platform for supporting LUP information utilization has demonstrated positive results and strong practical potential. The WebGIS system not only provides fundamental mapping functions such as data visualization, measurement, and accessing attribute information, but also integrates capabilities for searching and retrieving planning documents presented as maps (PDF format) and textual reports. In addition, the data are well-structured and categorized by administrative units and functional departments, facilitating more efficient utilization and management of planning information. The organizational structure of data within the WebGIS system can be flexibly modified to accommodate practical needs and implementation contexts.

The integration of the AI Chatbot module presents a novel improvement over traditional WebGIS systems, enhancing user interaction and accessibility to detailed LUP information that is not explicitly represented on spatial maps. The AI Chatbot provides contextual responses and related queries, effectively bridging the gap between technical data and non-specialist users. The study recommends that the Department of Natural Resources and Environment of Son La Province adopt the WebGIS system integrated with the AI Chatbot to enhance the effectiveness of LUP information management and utilization. Despite these advantages, the system still lacks direct spatial interaction and advanced analytical capabilities. Future research will focus on enabling spatial query comprehension and execution through natural language, linking the AI Chatbot with geospatial data to improve automation, accuracy, and usability, thereby supporting the digital transformation in land administration.

REFERENCES

- Akinboyewa T., Li Z., Ning H., & Lessani M.N. (2025). GIS Copilot: Towards an autonomous GIS agent for spatial analysis. *International Journal of Digital Earth*, 18(1).

- Oktavia C.A. & Pribadi R.F. (2025). Implementation of AI-based chatbots to enhance efficiency and transparency in land certification in Indonesia. *Tunas Agraria*, 8(2): 252–267.
- Park C., No W., Choi J., & Kim Y. (2023). Development of an AI advisor for conceptual land-use planning. *Cities*, 138, 104371.
- Salkin P.E., Stern H., & Looney D. (2025). Using AI to assist in land-use planning and zoning: Opportunities and pitfalls. *SSRN Electronic Journal*.
- Zhang Y., Wei C., He Z., & Yu W. (2024). GeoGPT: An assistant for understanding and processing geospatial tasks. *International Journal of Applied Earth Observation and Geoinformation*, 131, 103976
- Standing committee of the national assembly of Vietnam (2025). Resolution No. 1681/NQ-UBTVQH15 of the Standing Committee of the National Assembly of Vietnam on the arrangement of commune-level administrative divisions of Son La province in 2025. Hanoi, Vietnam.
- Binh Duong Department of Natural Resources and Environment (DONRE) (2025). Land database of Binh Duong Province: Gradually improved to effectively support state land management. URL: <https://stnmt.binhduong.gov.vn/chi-tiet-bai-viet/-/view-article/1/1541066051281/1617171666599> [Last accessed: 15 July 2025].
- Da Nang Department of Natural Resources and Environment (DONRE) (2025). Official WebGIS Portal. URL: <https://gisportal.danang.gov.vn/portal/home/index.html> [Last accessed: 10 July 2025].
- Doshi M. (2024). How geospatial AI can help inform our land-use choices. URL: <https://gdsgeospatial.blog.gov.uk/2024/11/14/how-geospatial-ai-can-help-inform-our-land-use-choices/> [Last accessed: 15 July 2025].
- Ho Chi Minh City Department of Natural Resources and Environment (DONRE) (2025). Official WebGIS Portal. URL: <https://geodata-stnmt.tphcm.gov.vn/webgis/> [Last accessed: 10 July 2025].
- OpenAI (2025). About OpenAI. URL: <https://openai.com/about/> [Last accessed: 15 July 2025].
- Vietnam Posts and Telecommunications Group (VNPT) (2025). VNPT iLIS – A pioneering technology solution for land management in the digital era. URL: <https://vnpttphcm.com.vn/vnpt-ilis-giai-phap-cong-nghe-tien-phong-trong-quan-ly-dat-dai-thoi-dai-so#:~:text=%C4%90%E1%BA%BFn%20nay%2C%20VNPT%20iLIS%20%C4%91%C3%A3,d%E1%BB%8Bch%20v%E1%BB%A5%20cho%20ng%C6%B0%E1%BB%9Di%20d%C3%A2n,> [Last accessed: 02 April 2025].

The normal geomagnetic field model over Vietnam and adjacent areas from Swarm satellite

Thanh Le Truong*, Mai Nguyen Thi, Minh Le Huy, Dung Nguyen Thanh, Thanh Nguyen Ha, Vinh Nguyen Ba, Nam Vu Dao, Hien Phi Thi Thu, Hai Phan Thanh

Institute of Earth Sciences, Vietnam Academy of Science and Technology, 68 Huynh Thuc Khang Street, Lang Commune, Hanoi, Vietnam;

*Email: igpthanh@gmail.com

Abstract: Three satellites, named Swarm (Alpha, Bravo, and Charlie), orbit the Earth in near-polar orbits at altitudes between 400 and 530 km launched by the European Space Agency (ESA) as part of their “Earth Observation” program on 22 November 2013. The mission studies the magnetic field and its temporal evolution providing the best-ever survey of geomagnetic field. Its data help to improve the understanding of ocean currents and interactions in the atmosphere, electric currents in the ionosphere and their connection to the magnetosphere. Observations of the strength and direction of the magnetic field, the electric field and plasma densities and temperatures, navigation signals, and derived parameters enable novel research on the understanding of the various sources of the geomagnetic field.

The theory of Spherical Cap Harmonic Analysis (SCHA) method was originally described in Haines (1985a) for mapping regional magnetic fields. It is assumed that a data set for region of interest is described on SCHA techniques for mapping a limited portion of the spherical Earth described by a spherical cap. The application of the SCHA method allows modeling the earth's geomagnetic field not only originating in the core but also the geomagnetic field of the earth's crust.

In this paper, the SCHA method was applied to model the normal geomagnetic field over Vietnam and adjacent areas between 5°N

and 25°N in latitude and 100°E and 120°E in longitude. The data used are geomagnetic field components (quiet days) from July 1, 2019 to June 30, 2020 obtained by Swarm satellites (A, C). The characteristic parameters of the method as: $K_{ext} = 2$ for external fields, $K_{int} = 8$ for internal fields, the spherical cap half-angle $\theta_0 = 10^\circ$. The results of this study are the components of the normal magnetic field in Vietnam and neighboring areas for 2020.0 epoch, and will be compared with the geomagnetic field obtained at geomagnetic observatories of Vietnam or from International Geomagnetic Reference Field (IGRF-13).

Keywords: Regional Geomagnetic Field, Spherical Cap Harmonic Analysis method, Swarm(A, C) satellite.

INTRODUCTION

The normal geomagnetic field or regional geomagnetic field (RGF) of an area includes the main field originating in the core, the crust field and the regional field. The RGF modeling for each area or each country is very important, it is used in navigation, aviation or calculating magnetic anomalies to serve geological structure research, mineral exploration, ionosphere research... Previously, to calculate RGF for an area, data from a network of repeated measurement points in the area was often used and a number of methods such as polynomial analysis (Chau, H. D., 2007), rectangular harmonic analysis method...

The SCHA method was developed by Haines in 1985 (Haines, 1985a) and up to now, there are many published works using this method to model the geomagnetic field for different areas or countries such as: Canada (Haines, 1985b; Haines et al., 1997; Newitt et al., 1989); Europe (Duka, 1998; Korte et al., 2000; Korte et al., 2003; Qamili et al., 2010; Verbanac, 2007; Verbanac et al., 2009); Antarctica (Torta et al., 2002; Tozzi et al., 2013); Africa (Kotzé et al., 1997; Kotzé et al., 2001); Asia (An, 2003; Di et al., 2011; Feng et al., 2016; Gu et al., 2006) and many other regions in the world (Qamili et al., 2010 and Qiu et al., 2017). In recent times, there are also many studies using geomagnetic field data obtained from satellites to model the magnetic field as in studies (Qamili et al., 2010; Thébault et al., 2004; Vervelidou et al., 2018). For the first time in Vietnam, we have researched and applied this SCHA method together with CHAMP satellite data to build a RGF model for Vietnam region and neighboring areas for the 2007.0 epoch (Thanh, 2015; Thanh et al., 2021), and from Swarm satellite data for the 2015.0 epoch (Thanh et al., 2021). Normally, the establishment of RGF maps for each region or for each country will be done each 5 years. However, in Vietnam, this work has not been done regularly in recent times. In the study, we used the SCHA method for Vietnam and neighboring areas, with the study area spanning about 40° in both longitude and latitude, whereby cap half-angle $\theta_0=20^\circ$. In this study, we will narrow the study area to only about 20° , meaning the cap angle is only $\theta_0=10^\circ$, with this study area mainly covering the entire land and sea of Vietnam.

When designing, the orbits of the two Swarm satellites (A, C) are quite similar, they fly parallel to each other (1.4° apart) and have the same inclination angle of 87.3° or the same altitude (from 400 km - 460 km). The Swarm B satellite has a higher altitude (< 530 km), as well as a different orbit from the above two satellites. Therefore, this study uses the SCHA method based on geomagnetic field data collected on Swarm (A, C) satellites to build a RGF model for Vietnam and neighboring areas at the 2020.0 epoch as well as some comments

on the effectiveness of the SCHA method when comparing the geomagnetic field from the model with the magnetic field collected at ground-based geomagnetic observatories in Vietnam and compared with the geomagnetic field from the global model IGRF-13.

Spherical cap harmonic

Spherical Harmonic Analysis method (SHA) was introduced by Gauss in 1893, which is a popular method for modeling the global geomagnetic field. However, when modeling the geomagnetic field of a small area, with the data used for inversion concentrated only in a small area, applying the SHA method will be very difficult and furthermore, to study in more detail an area that requires modeling a part of the magnetic field of the Earth's crust, meaning that smaller wavelengths need to be considered, the SHA method cannot meet. To overcome these disadvantages, Haines introduced a method for solving the Laplace equation on a spherical cap, which is a small area on the Earth's surface, and is now called the spherical cap harmonic analysis method. According to Haines, in the spherical coordinate system, the potential V on a spherical cap can be written as an expansion:

$$V(r, \theta, \phi) = R_E \sum_{k=0}^{K_{\max}} \sum_{m=0}^k \left(\frac{R_E}{r} \right)^{n_k(m)+1} P_{n_k(m)}^m(\cos \theta) \left(g_k^{m,i} \cos(m\phi) + h_k^{m,i} \sin(m\phi) \right) + R_E \sum_{k=1}^{K_{\max}} \sum_{m=0}^k \left(\frac{r}{R_E} \right)^{n_k(m)} P_{n_k(m)}^m(\cos \theta) \left(g_k^{m,e} \cos(m\phi) + h_k^{m,e} \sin(m\phi) \right) \quad (1)$$

with R_E is the radius of the Earth (in km), $P_{n_k(m)}^m$ is a first-kind associated Legendre function of integer rank m and $n_k(m)$ is non-integer. The parameter $n_k(m)$ depends on m , k and K_{\max} (K_{\max} is the maximum degree for the series expansion). The coefficients $g_k^{m,i}$, $h_k^{m,i}$, $g_k^{m,e}$, $h_k^{m,e}$ have units of nT and are determined by the least squares method of data obtained in the region corresponding to the solution of a linear equation of the form:

$$\vec{y} = A\vec{m} + \vec{e} \quad (2)$$

with \vec{y} is the vector of observed values, \vec{e} is the error vector, \vec{m} is the column matrix of coefficients $g_k^{mi}, h_k^{mi}, g_k^{me}, h_k^{me}$ to be found, A is the operator relating the data vector to the model $A=(A_1, A_2, A_3, \dots, A_n)$ with n being the size of the given data series. If the expansion limit (1) is limited to the term K_{max} , then the number of coefficients to be calculated is $(K_{max}+1)^2$. In the study [21] were presented in detail the SCHA method as well as the process of inverting the data to find solutions using the least squares method.

The root mean square deviation (RMS) between the component data j calculated from the SCHA model (E_j^{SCHA}) and the data obtained on the satellite E_j^{OBS} is given by the following formula:

$$RMS_j = \sqrt{\frac{1}{n} \sum_{i=1}^n (E_{j,i}^{SCHA} - E_{j,i}^{OBS})^2} \quad (3)$$

with n being the number of observation points.

According to Hains (1985a), When applying spherical cap harmonic analysis, it is recommended to remove a global spherical harmonic potential from the total potential by using the IGRF model (the wavelength about 3000 km) to make the data inversion process converge faster. In this study, the IGRF-13 model is used with $n=1-13$ for the main field and $n_{dot}=1-8$ for the secular variation (Alken et al., 2015). And the field part used to calculate the spherical cap harmonic coefficients is calculated as follows:

$$\Delta E_j = E_j^{OBS} - E_j^{IGRF} \quad (4)$$

with ΔE_j being the magnetic field from the j -component used for calculation; E_j^{OBS} is the magnetic field observed on the Swarm(A, C) satellite; E_j^{IGRF} is the magnetic field from the IGRF-13 model.

Select Swarm (A, C) satellite data

To use the SCHA method presented above to build a RGF model for Vietnam and neighboring areas, this study uses data on the north components (X), east components (Y), vertical components (Z) and total field (F) of the magnetic field obtained on two Swarm satellites (A, C) within one year (from July 1st, 2019 to June 31st, 2020). The data are selected within the longitude from 100°E to 120°E, the latitude from 5°N to 25°N (Fig. 1), the above area includes the entire mainland and sea of Vietnam, in addition to including a number of other countries in the neighboring area. Fig. 1 also shows the locations of 3 geomagnetic observatories of Vietnam, their digital magnetic field data are also used in this study.

The Swarm(A, C) satellite data in the above area were selected on quiet geomagnetic field days, with a magnetic activity index of $K_p \leq 3^+$ and a geomagnetic disturbance index Dst between -20 nT and 20 nT and during the period around the local midnight (from 22:00 at night to 5:00 the next day). The data with such selections reduces mainly the effects of the external magnetic field and the magnetic disturbances. All data collected on the Swarm(A,C) satellite satisfying the above conditions within 12 months include 66,148 measurement points (Swarm(A) has 32,087 points, Swarm(C) has 34,061 points) corresponding to 1 component of the geomagnetic field. During the above period, the orbits of the satellites did not change much, with Swarm(A) having an altitude from 437 km - 444 km, with Swarm(C) having an altitude from 438 km - 444 km. Fig. 1 shows the study area and the data points collected on the Swarm(A) satellite in the first 6 months of 2020 (representation interval: 10 values). With a sampling rate of 1 second, the data set that this study covers almost the entire study area, and this is a huge data set used for calculation.

Since the data were continuously measured during long time period, the effect of the secular variation was removed. Using the secular variation model of IGRF-13 with coefficients $n_{dot}=1-8$, all the selected data have

been adjusted to epoch 2020.0 (00:00 January 1st, 2020) for Swarm satellites data.

According to Haines (1985a), the global magnetic field must be removed from data by using IGRF-13 with coefficients of degrees $n=1-13$ before the inversion.

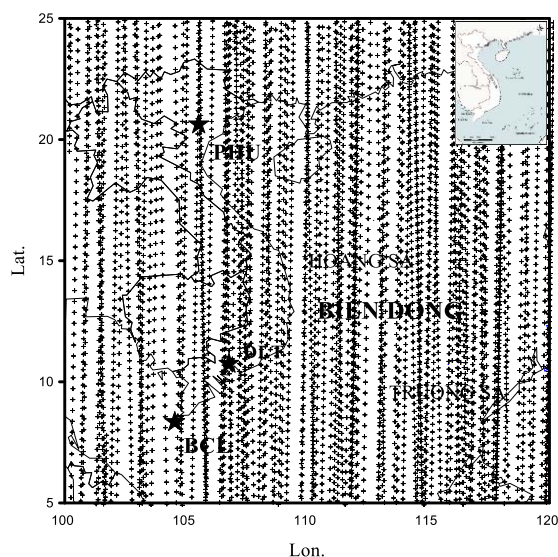


Figure 1. Study area and data on Swarm(A) in the first 6 months of 2020 (dot) and the locations of three geomagnetic stations in Vietnam (star).

Since the data were continuously measured during long time period, the effect of the secular variation was removed. Using the secular variation model of IGRF-13 with coefficients $n_{\text{dot}}=1-8$, all the selected data have been adjusted to epoch 2020.0 (00:00 January 1st, 2020) for Swarm satellites data.

According to Haines (1985a), the global magnetic field must be removed from data by using IGRF-13 with coefficients of degrees $n=1-13$ before the inversion.

Because the density of collected data on the Swarm(A, C) satellite is dense, at the same point there may be many data with different values and different heights, and because the input data for inversion is too large for the computer to handle, so before calculating, the data series must be gridded, similar to the research of Rotanova et al., (1999) or Duka et al., (1998). All 66,148 measurement points above will be gridded with an initial grid size

according to longitude and latitude of $0.3^\circ \times 0.3^\circ$. Choosing the cell size as above ensures that there is at least one data point in each cell. If there is a cell in the grid that has no value, this cell will be expanded by $0.1^\circ \times 0.1^\circ$ each step until there is at least 1 value, then stop. The value of each cell is taken as the average value of all observation points in the cell and this average value is considered as the field value at the center of the grid cell. To eliminate values that deviate significantly from the rest of the grid, values that deviate more than $\pm 2.98 \text{ nT}$ (and $\pm 3.35 \text{ km}$ in orbital altitude) from the corresponding grid mean values will be eliminated. In this study, we also tried to use ungridded and gridded data for calculation and found that the mean square deviation when using gridded data is 1.61 nT smaller than that of ungridded data.

RESULTS AND DISCUSSION

Model of regional magnetic field for Vietnam and adjacent area in 2020.0 epoch

Before calculating, the important task is to choose the parameters of the SCHA method to suit the study area and reduce the calculation time but still ensure the modeling of the geomagnetic field of interest, similar to the previous study, we have chosen the main parameters as follows:

- The cap half-angle θ_0 : the study area (Fig. 1) is spread over about 20° along the longitude as well as the latitude, choosing $\theta_0 = 10^\circ$ is enough to cover the area of interest and the center of the cap at the position: 15°N and 110°E .

- Choosing K_{ext} to calculate the field part caused by extraterrestrial sources: similar to the study of Kotzé (2001), we choose $K_{\text{ext}}=2$ to calculate the geomagnetic field part caused by extraterrestrial sources and presented in table 1. Accordingly, the first coefficient, is quite close to the value calculated by Kotzé (2001) from Orsted satellite data and much smaller than the value of Langel and Estes (1985) using MAGSAT satellite data, close to the value calculated for the 2015.0 epoch also from Swarm(A, C) data (Thanh et al., 2021).

Table 1. The coefficients $g_k^{m,e}$, $h_k^{m,e}$ corresponding to the external field

k	m	$n_k(m)$	$g_k^{m,e}$	$h_k^{m,e}$
1	0	6.3832	15.32	
1	1	4.8432	-4.16	-4.02
2	0	10.4885	-5.09	
2	1	10.0815	0.68	1.08
2	2	8.3553	-0.18	-0.15

- Selecting the K_{int} order to calculate the magnetic field originating within the Earth: we calculated the root mean square deviation (RMS-X, RMS-Y, RMS-Z) corresponding to the X, Y, Z components of the geomagnetic field between the model and satellite data with K_{int} varying from 1 to 12 as shown in Fig. 2. It is found that when $K_{int} \geq 8$, the RMS value for all three components of the geomagnetic field gradually decreases and is quite stable, so to ensure the calculation time, we choose $K_{int} = 8$. In the table 2 presents 81 coefficients of the SCHA method corresponding to the geomagnetic field originating the Earth's interior. According to the study of De Santis [4], the value of the first coefficient depends on the amplitude of the geomagnetic field in the study area and the cap half-angle θ_o . With this study area, and choosing $\theta_o = 10^\circ$ we get with the data on the satellite Swarm(A,C) for the 2020.0

epoch. This value is close to the value calculated by Gu et al. (2006) for the China area ($\theta_o = 30^\circ$), or the value calculated for the Vietnam area but with the angle $\theta_o = 20^\circ$.

The coefficients of the spherical cap harmonic are determined, we can calculate the values of the j components E_j^{SCHA} of the geomagnetic calculated by SCHA model. Thus, the geomagnetic field is calculated as follows:

$$E_j^{RGF} = E_j^{SCHA} + E_j^{IGRF} \quad (5)$$

where E_j^{IGRF} is the j component of the magnetic field using the IGRF-13 model as mentioned above.

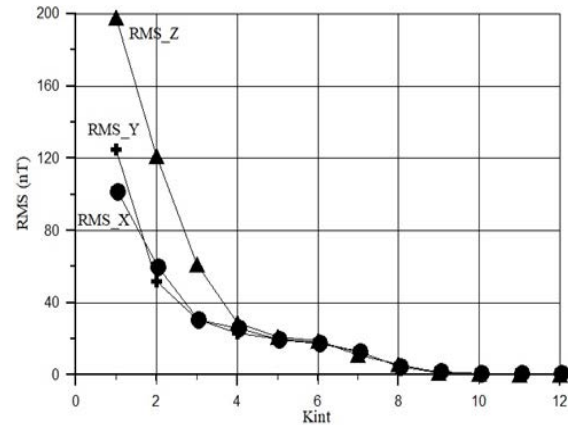


Figure 2 The RMS corresponding to X, Y, Z with K_{int} from 1 to 12 from Swarm(A, C) data.

Table 2. The coefficients of the 8-order SCHA for epoch 2020.0.

k	m	g_k^{mi}	h_k^{mi}
0	0	323.96	
1	0	-158.35	
1	1	-152.68	62.78
2	0	215.35	
2	1	110.48	-61.56
2	2	-54.23	18.98
3	0	-309.16	
3	1	-359.34	71.36
3	2	168.56	-38.56
3	3	-17.56	-45.26
4	0	407.89	
4	1	215.68	-56.45
4	2	-223.17	64.89
4	3	56.23	80.59
4	4	-8.56	19.35

k	m	g_k^{mi}	h_k^{mi}
5	0	-210.23	
5	1	-318.59	51.17
5	2	148.79	-70.16
5	3	-80.45	-78.19
5	4	52.61	-25.48
5	5	17.59	13.49
6	0	92.45	
6	1	160.56	-38.57
6	2	-55.78	58.23
6	3	70.97	48.32
6	4	-70.59	20.62
6	5	-22.49	28.18
6	6	24.26	-10.5
7	0	-80.59	
7	1	-58.67	10.26

k	m	g_k^{mi}	h_k^{mi}
7	2	-3.19	-30.59
7	3	-4.61	-12.61
7	4	-12.35	-10.36
7	5	16.49	4.35
7	6	-8.01	-6.14
7	7	-2.95	3.26
8	0	1.19	
8	1	1.09	-4.59
8	2	4.15	1.67
8	3	0.29	-3.48
8	4	-1.29	3.9
8	5	-3.29	1.19
8	6	2.87	0.35
8	7	-1.01	-1.162
8	8	0.43	-0.27

The results of RGF calculation for the study area at the 2020.0 epoch are shown in Fig. 3a,b,c,d,e,f corresponding to the components D, I, X, Y, Z, H of the geomagnetic field. From these figures, there are some comments on the amplitude and shape of the contour lines of the magnetic field in the area as follows:

- The declination D component (Fig. 3a): the amplitude varies from -4.03° to 0.27° . In the north of Vietnam, the contour lines sag downwards, while in the south they sag upward. In the entire territory of Vietnam, the D component has negative values, the contour line $D=0^{\circ}$ is located in the south of Vietnam.

- The inclination I component (Fig. 3b): the amplitude varies from -6.9° to 38.0° . The contour lines are quite parallel and evenly spaced. Angle I is the smallest in the south and increases gradually towards the north. Throughout the territory of Vietnam, component I has positive value, the isovalue line $I=0^{\circ}$ lies outside the southernmost point of Vietnam.

- The northern component X (Fig. 3c): the amplitude varies from 36124 nT to 41689 nT. The X component has a maximum in the southwest of the study area.

- The eastern component Y (Fig. 3d): the amplitude varies from -2548 nT to 193 nT. The contour lines of Y are quite similar to the magnetic declination D, throughout the territory of Vietnam Y has a negative value.

- The vertical component Z (Fig. 3e): the amplitude ranges from -5059 nT to 29214 nT. The shape of the contour lines of Z are similar to the inclination component. The northern part of Vietnam reaches the maximum value, then the value gradually decreases to the south and the $Z=0$ line is located around the 8°N , then Z reaches a negative value.

- The horizontal component H (Fig. 3f): has a magnitude ranging from 36213 nT to 41691 nT. The contour lines of H are the same as the X component, the H component has a maximum in the southwest of the study area.

The root mean square (RMS) deviations of the D, I, X, Y, Z, F components between the SCHA model and satellite data at 2020.0 epoch are summarized in Table 3. These values are quite small and smaller than the calculated results of Korzé (2001) with 4.1 min for the D component, 16.6 nT for F, 22.7 nT for H, and 17.9 nT for Z; or the values of 2.9 min, 1.8 min, 3.2 nT, 3.8 nT, 4.4 nT, 11.5 nT corresponding to the D, I, X, Y, Z, F components of the magnetic field in our previous study (Thanh et al., 2021). The RMS values corresponding to the magnetic field components in this study were slightly larger than those calculated for the previous 2015.0 epoch, possibly due to the reduced cap angle. The impact of the choice of cap angle on the quality of the calculated geomagnetic field model will be further investigated and presented in future studies.

Table 3. The RMS values between SCHA model and satellite data Swarm(A, C) corresponding to components (D,I,X,Y,Z,H,F) of the geomagnetic field for epoch 2020.0

	RMS-D (arc min)	RMS-I (arc min)	RMS-X (nT)	RMS-Y (nT)	RMS-Z (nT)	RMS-H (nT)	RMS-F (nT)
Epoch 2020.0	3.1	2.9	3.8	4.3	5.1	11.6	13.6

Comparison with observatory data

To confirm the accuracy of the method, this study compared the RGF calculated by the SCHA method with obtained geomagnetic field data at Phu Thuy station (PHU, 21.2°N , 105.54°E), Da Lat (DLT, 11.57°N , 108.29°E) and Bac Lieu equatorial geomagnetic station (BCL,

9.28°N , 105.44°E) when all three geomagnetic stations used high-resolution digital geomagnetic recorders. However, only at PHU and DLT stations were the absolute values of the geomagnetic field measured twice a week, while at BCL station, the absolute values were

measured only once a year. Similar to the geomagnetic field data obtained on the Swarm(A,C) satellite, the recorded geomagnetic field data at these geomagnetic stations were selected in the middle of the local time (from 20:00 at night to 05:00 the next morning) and on quiet geomagnetic field days (index $K_p \leq 3$ and $|Dst| \leq 20$ nT) and all data were also converted to 0:00 on January 1, 2020 using the IGRF-13 model with order $n_{dot}=1-8$ for secular variation. Table 4 presents the RMS values of the X, Y, Z components of the geomagnetic field calculated from the SCHA model and data at PHU, DLT and BCL. Note that the geomagnetic field calculated from the SCHA model was calculated at the Earth's surface, these values are quite small compared to the geomagnetic field values of this area, which also shows the reasonableness of using satellite data to model the geomagnetic field of the ground area. However, the RMS value calculated for the 2020.0 epoch is also slightly larger than the calculated RMS value for the 2015.0 epoch and the RMS value of BCL is also larger than the RMS of PHU and DLT due to the complexity of the equatorial geomagnetic field.

Table 4 RMS value between SCHA model and data at PHU, DLT and BCL geomagnetic stations

	RMS-X (nT)	RMS-Y (nT)	RMS-Z (nT)
PHU	2.57	3.49	2.67
DLT	2.23	3.01	3.22
BCL	3.54	3.16	3.98

Comparison of total regional magnetic field calculated from SCHA and IGRF-13 models

To compare the total field component RGF calculated from the SCHA method (Fig. 4a) mentioned above with that the IGRF-13 model (Fig. 4b) at the same 2020.0 epoch and at the Earth's surface. In general, the total field F in both of these figures has a magnitude in the range from 39832 nT to 47425 nT. The region has large F value which lies in the north of the map, the further south the F decreases. The contour lines tend to become sparser as they enter the south of Vietnam. From Fig. 4a

and b, we can see that the variation patterns of the contour lines are quite similar, they only differ in amplitude. The difference in amplitude of these two maps is the geomagnetic field calculated from the SCHA method, shown in Fig. 4c. From this figure, we can see that the variation values range from -58.2 nT to 40.9 nT. The entire study area has mainly negative values (dashed lines) and there are only two areas with positive values, which are the maritime zone of southeastern Vietnam. In the study area, there are two negative and positive peaks symmetrically across the 110°E meridian. When comparing the map of RGF calculated for the 2020.0 epoch with the calculation from CHAMP satellite data for the 2007.0 epoch and from Swarm data for the 2015.0 epoch [22], we see that the shape of the contour lines in the territorial Vietnam in all three years is quite similar. There are two anomalous peaks symmetrical across the 110°E meridian. However, they differ in magnitude, at the 2015.0 epoch, the positive anomaly on the left side of the 110°E meridian no longer exists as in the remaining years, it has turned to a negative value. This may be due to the influence of secular variation or the influence of the magnetic field in the Earth's crust and we will continue to study it in the coming time. This difference is also a factor for us to calculate the normal geomagnetic field model for each country or each region every 5 years, as is often done in the world.

With the amplitude of E_F^{SCHA} about ± 50 nT as show in Fig. 4c, it is clear that if using the IGRF model as a normal geomagnetic field model in the region, the anomalous field will differ quite a lot from the obtained anomalous field with the normal field by the presented spherical harmonic analysis method. Thus, it can be affirmed that the value of the total geomagnetic field intensity intensity has reflected a part of the geomagnetic field of the Earth's core and crust and a part of the regional field that the IGRF global magnetic field model has not reflected.

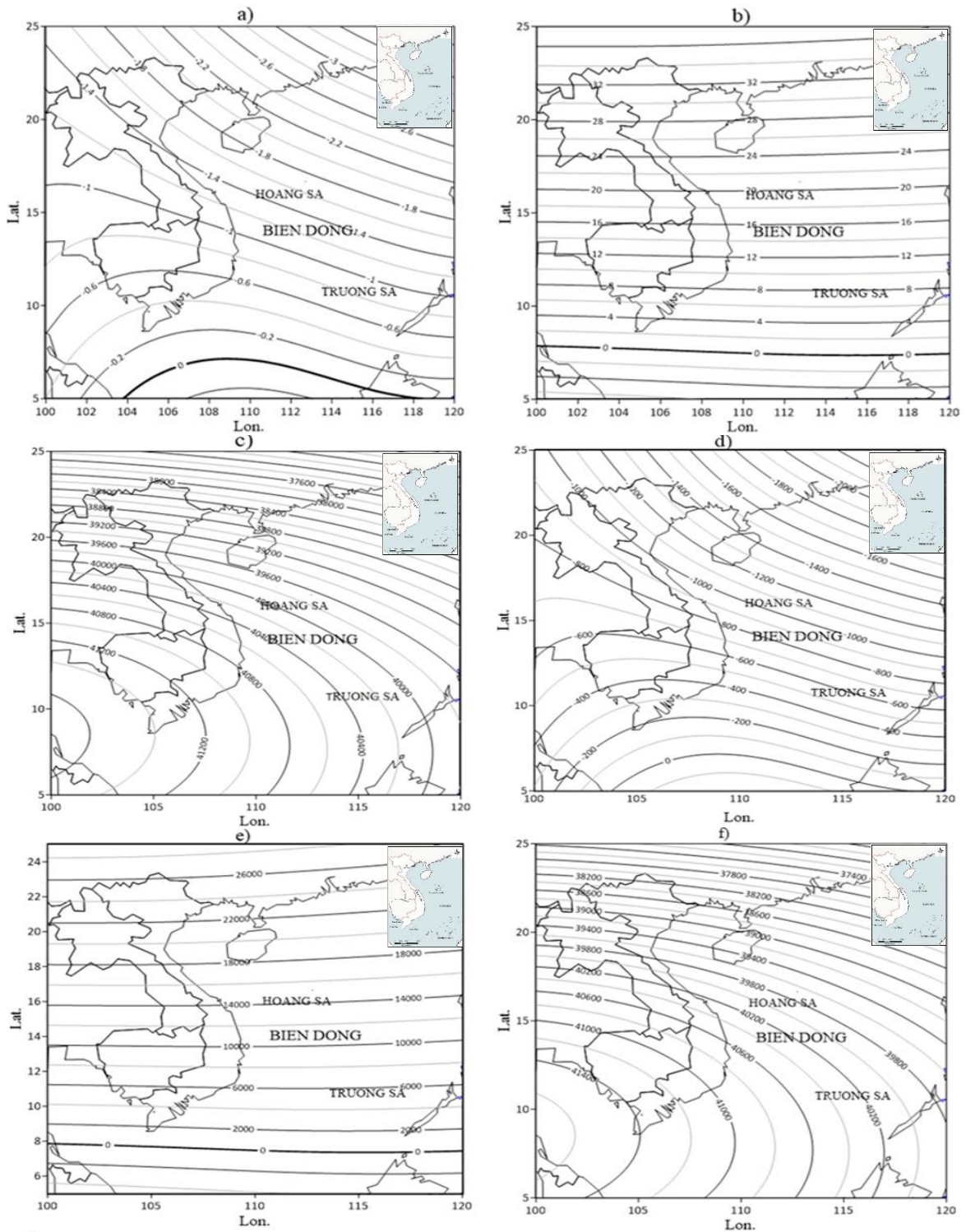


Figure 2 The regional geomagnetic field for the epoch 2020.0; (a) D(o), (b) I(o), (c) X(nT), (d) Y(nT), (e) Z(nT), and (f) H(nT). Contour intervals: 0.2° for D, 2° for I, 200 nT for X and H, 100 nT for Y and 1000 nT for Z.

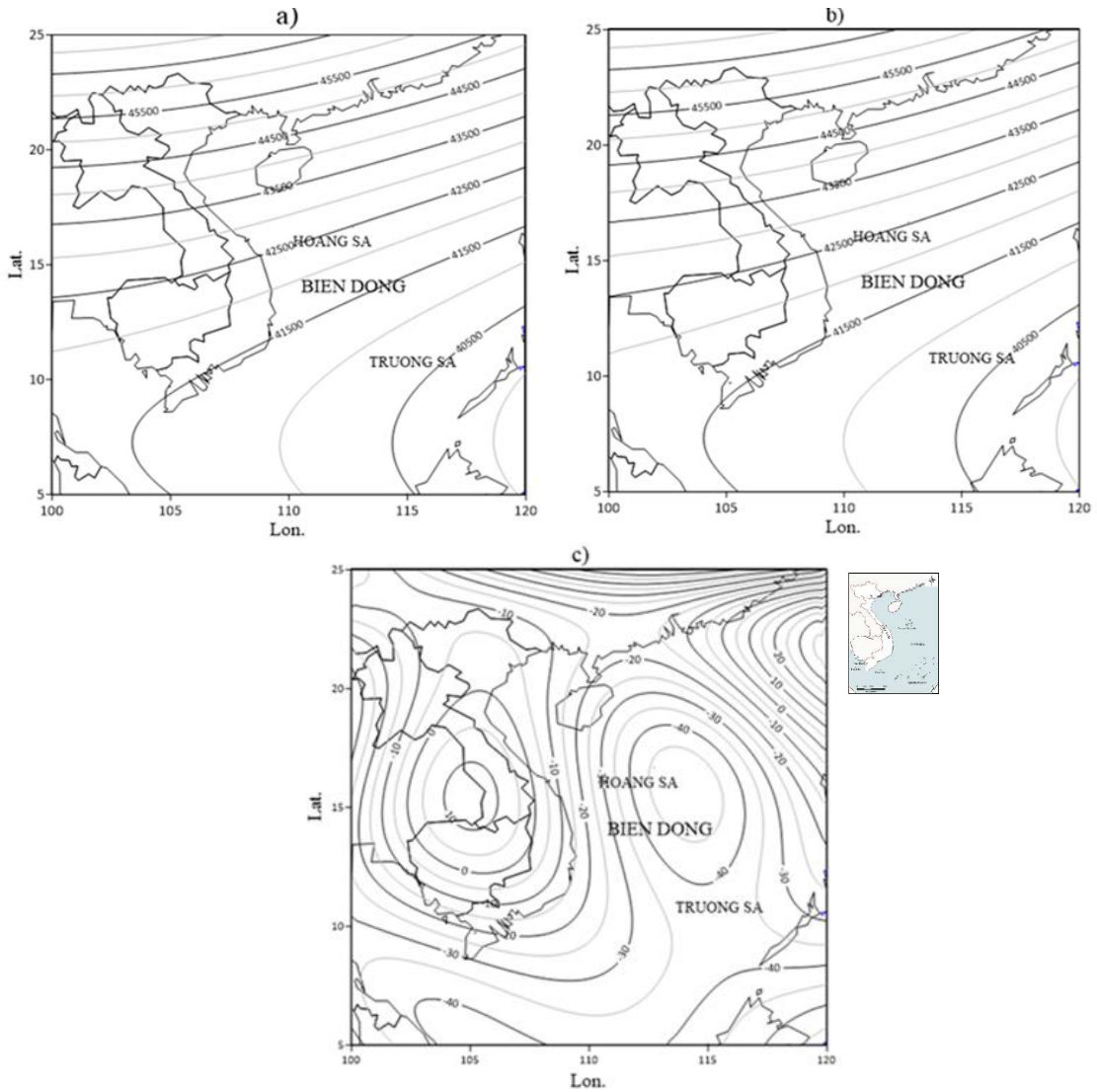


Figure 3 The total intensity of the magnetic field.

a) Calculated by SCHA model. Contour interval: 500 nT;

b) Calculated by IGRF-13 model. Contour interval: 500 nT;

c) The total magnetic field E_F^{SCHA} calculated from the SCHA model. Contour interval: 5 nT.

Conclusion

This paper uses the SCHA method to model the geomagnetic field of Vietnam and its vicinity from collected data on the Swarm(A,C) satellite for the 2020.0 epoch. By choosing the parameters of the SCHA method such as: cap angle $\theta_0=10^\circ$, cap center position (15°N , 110°E), $K_{\text{ext}}=2$ for magnetic fields originating from outside and $K_{\text{int}}=8$ for geomagnetic fields originating from the Earth's interior, we can calculate the components of the normal

geomagnetic field at the Earth's surface. From the above results, we can draw some main conclusions as follows:

- Choosing the initial size of $0.3^\circ \times 0.3^\circ$ in both longitude and latitude, then automatically increasing the grid size with a step of $0.1^\circ \times 0.1^\circ$ until there is at least 1 measurement point in the grid to grid the data before calculation has significantly reduced the mean square deviation value between the model and the data obtained on the satellites.

- The D, I, X, Y, Z, H and F components of the regional geomagnetic field (E_j^{RGF}) calculated from the SCHA model are quite similar to those from the IGRF model (E_j^{IGRF}), the RMS value between the SCHA model and the data obtained on the Swarm(A, C) satellite is quite small with 3.1 minutes, 2.9 minutes, 3.8 nT, 4.3 nT, 5.1 nT, 11.6 nT and 13.6 nT, respectively.

- The RMS values between the SCHA model and the data obtained at 3 geomagnetic stations in Vietnam (PHU, DLT and BCL) are also quite small, which proves that we can completely use satellite data to model the regional geomagnetic field on the Earth's surface.

- The RMS values between the model and Swarm data or data at Vietnam's geomagnetic stations calculated for the 2020.0 epoch (cap angle $\theta_0=10^\circ$) are all larger than those calculated for the 2015.0 epoch in the previous study (with $\theta_0=20^\circ$), we will continue to study the impact of the cap angle on the RMS value in the near future.

- The total magnetic field calculated from the SCHA model ranges from -58.2 nT to 40.9 nT. This is the part of the field originating in the core or crust of the Earth that cannot be represented by the IGRF model.

- However, this study only uses satellite data, although the data density is very high, distributed quite evenly, but the accuracy of the measurement is still limited. In the coming time, we will use this method to apply to all geomagnetic field data of Vietnam (data at geomagnetic stations, repeated measurement data, airborne magnetic, marine magnetic...) to model the magnetic field for the region as well as use this result to study the century variation or calculate regional magnetic anomalies.

ACKNOWLEDGEMENTS

This research was completed with financial support from the Vietnam Academy of Science and Technology grant number VAST05.06/25-26. The data on the Swarm

satellites are collected from <ftp://swarm-diss.eo.esa.int>. The computational programs in this paper are written in Fortran 77 and the figures are represented by the free Gnuplot software.

REFERENCES

- Alken P., et. al. (2015). International Geomagnetic Reference Field: the thirteenth generation. *Earth, Planets and Space, Earth Planets Space* 73, 49; doi: 10.1186/s40623-020-01288-x, 67-79.
- An, Z. C. (2003). Spherical cap harmonic model of the Chinese geomagnetic reference field for 1936. *Chinese J. Geophys.*, 46(5), 624-627.
- Chau, H. D. (2007). Normal magnetic model for epoch 2003.5 in Vietnam. *Advances in Natural Sciences*, Vol VIII, Nr. 1, 81-96, ISSN:092-7689.
- De Santis, A., Battelli, O., and Kerridge, D. J. (1990). Spherical cap harmonic analysis applied to regional field modelling for Italy. *J. Geomag. Geoelectr.*, 42, 1019-1036.
- Di, C. Z., Gu, Z. W., Bernardo, M. S., Chen, B., Carina, G.L., Zhang, Y., Xin, C. Z., Gao, Z. T. (2011). The study of magnetic field models for Philippines and its neighboring regions. *Chinese Journal of Geophysics*, 54, No.4, 508-515.
- Duka, B. (1998). Comparison of different methods of analysis of satellite geomagnetic anomalies over Italy. *Annali di Geofisica*, 41, No.1, 49-61.
- Feng, Y., Sun, H., Jiang, Y., Jiang, Y., Liu, B. J., Jiang, Y., Liu, Z. W., Ye, M. C., Wang, H. S., Li, X. M. (2016). Spherical cap harmonic analysis of regional magnetic anomalies based on CHAMP satellite data. *Applied geophysics*, 13, No.3 (September 2016), 561-569, 7 Figures.DOI: 10.1007/s11770-016-0567-8.
- Gu, Z., Zhan, Z., Gao, J., Han, W., An, Z., Yao, T., and Chen, B. (2006). Geomagnetic survey and geomagnetic model research in China. *Earth planet. space*, 58, 741-750.
- Haines, G.V. (1985a). Spherical cap harmonic analysis. *J. Geophys. Res.*, 90, 2583- 2592.
- Haines, G.V. (1985b). Spherical cap harmonic analysis of Geomagnetic Secular Variation over Canada 1960-1983. *J. Geophys. Res.*, 90, 12563-12574.
- Haines, G.V., and Newitt, L. R. (1997). The Canadian geomagnetic reference field 1995. *J. Geomag. Geoelectr.*, 49, 317-336.

- Korte, M. and Haak, V. (2000). Modelling European repeat station and survey data by SCHA in search of time-varying anomalies. *Phys. Earth planet. Inter.*, 122, 205–220.
- Korte, M., and Holme, R. (2003). Regularization of spherical cap harmonics. *Geophys J. Int.*, 153, 253–262.
- Kotzé, P.B. and Barraclough, D. R. (1997). Modelling and analysis of POGS data over Southern Africa by spherical cap harmonic analysis. *J. Geomag.Geoelectr.*, 49, 441–452.
- Kotzé, P.B. (2001). Spherical cap modelling of Oersted magnetic field vectors over Southern Africa. *Earth, Planets and Space*, 53, 357–361.
- Newitt, L.R., and Haines, G. V. (1989). A Canadian geomagnetic reference field for epoch 1987.5. *J. Geomag. Geoelectr.*, 41(2), 249–260.
- Langel, R.A., and Estes, R.H. (1985). Large-scale near-Earth magnetic fields from external sources and the corresponding induced internal field. *J. Geophys. Res.*, 90, 2487–2494.
- Rotanova, R.M., and Odintsov, S. D. (1999). Model of the MAGSAT Magnetic Anomaly Spherical Cap Harmonic Analysis. *Phys. Chem. Earth (A)*, Vol. 24, No. 5, 455–459.
- Qamili, E., De Santis, A., Cianchini, G., Duka, B., Gaya-Piqué, L. R., Dominici, G., and Hyka, N. (2010). Two geomagnetic regional models for Albania and south-east Italy from 1990 to 2010 with prediction to 2012 and comparison with IGRF-11. *Earth Planets Space*, 62, 833–841.
- Qiu, Y., Wang, Z., Jiang, W., Zhang, B., Li, F., and Guo, F. (2017). Combining CHAMP and Swarm Satellite Data to Invert the Lithospheric Magnetic Field in the Tibetan Plateau. *Sensors (Basel)*, 17(2). pii: E238. doi: 10.3390/s170202387.
- Le Truong Thanh (2015). Study of equatorial electric current (EEJ) from CHAMP satellite data and from ground data in Vietnam and neighboring regions, PhD thesis in physics, 148 pages.
- Le Truong Thanh, Le Huy Minh, Vafi Doumbia, Christine Amory-Mazaudier, Nguyen Thanh Dung, Ha Duyen Chau, (2021). A spherical cap model of the geomagnetic field over Southeast Asia from CHAMP and Swarm satellite observations, *J. Earth Syst. Sci.*, 130 13, <https://doi.org/10.1007/s12040-020-01507-9>.
- Thébault, E., Schott, J. J., Manda, M., and Hoffbeck, J. P. (2004). A new proposal for spherical cap harmonic modelling. *Geophys. J. Int.*, 159, 83–103, doi:10.1111/j.1365- 246X.2004.02361.x.
- Thébault, E., Vigneron, P., Maus, S., Chulliat, A., Sirol, O., and Hulot, G., (2013). Swarm SCARF Dedicated Lithospheric Field Inversion chain. *Earth Planets Space*, 65, 1257–1270.
- Torta, J.M., De Santis, M., von Frese, R.R.B. (2002). A model of the secular change of the geomagnetic field for Antarctica. *Tectonophysics*, 347, Issues 1–3, 179–187.
- Tozzi, R., De Santis, A., Luis-Ricardo Gaya-Piqué (2013). Antarctic geomagnetic reference model updated to 2010 and provisionally to 2012. *Tectonophysics*, 585, 13–25.
- Verbanac, G. (2007). On regional modelling of the main geomagnetic field. *Geofizika*, 24, No.1, 1–27.
- Verbanac, G., Korte, M., and Manda, M. (2009). Four decades of European geomagnetic secular variation and acceleration. *Annals Geophys.*, 52, No.5, 487–503.
- Vervelidou, F., Thébaud, E., and Korte, M. (2018). A high resolution lithospheric magnetic field model over southern Africa based on a joint inversion of CHAMP, SWARM, WDMAM and ground magnetic field data. *Soild Earth*, 9, 897–910.

Analysis of deformation displacement using GNSS technology in the local topocentric coordinate system

Hoang Ngoc Ha^{1*}, Luu Anh Tuan¹, Le Ngoc Giang¹, Ngo Thi Men Thuong²

¹University of Mining and Geology, 18 Vien Street, Dong Ngac, Hanoi, Vietnam

²Hanoi University of Natural Resources and Environment, 41A Phu Dien Street, Phu Dien, Ha Noi, Viet Nam

Abstract: With the impact of climate change and the impact of rising sea levels, in some areas of our country, there are deformation displacement phenomena such as subsidence. The paper has studied the method of analyzing vertical displacement deformation (geodynamic displacement based on the use of 3D data obtained from the results of measuring the monitoring network applying GNSS technology in time cycles in the Horizon Coordinate System. The report focuses on analyzing the 3D dynamic displacement model of the central region applying GNSS technology. The research results can serve the basic investigation work in localities with the possibility of subsidence or deformation due to geological faults or environmental impacts.

Keywords: Network adjustment, GNSS, Kalman Filter, vertical displacement, Deformation analysis.

INTRODUCTION

With the application of GNSS technology, the construction of geodetic networks achieves high accuracy in a short time and can be continuously monitored, in a wide range and can determine the displacement vector in the dynamic model. GNSS networks are usually adjusted in geocentric coordinates. For local 3D analysis, it is more convenient to use geocentric coordinates, especially for vertical displacement analysis. Some international and domestic publications have mentioned the application of Kalman filtering to apply in the field of deformation analysis (Welsch, W. M. and HeuneckeYalc, inkaya, M. and Bayrak, T). The adjustment of the spatial grid and displacement analysis in the topocentric

coordinate system allows for a better assessment of horizontal or vertical displacement, thus determining the subsidence of the land area under study.

The paper presents a solution to develop the theory of recurrent adjustment in the analysis of dynamic model deformation displacement of GNSS monitoring network with 4 measurement cycles. The data processing calculation is performed in the topocentric coordinate system.

METHODOLOGY

GNSS free adjustment in the topocentric coordinate system

Free adjustment of GNSS spatial grid in geocentric coordinate system (X,Y,Z) we will have a system of equations of corrections for n baselines has the following form:

$$V_{nx1} = A_{n \times k} \Delta x_{kx1} + L_{nx1} \quad (1)$$

where: A - the coefficient matrix

Δx_{kx1} is the vector of unknowns, V_{nx1} is vector of corrected numbers; $k = 3xt$.

The weight matrix P has the form:

$$P = \begin{pmatrix} P_1 & 0 & 0 & 0 \\ 0 & P_2 & 0 & 0 \\ 0 & 0 & \ddots & 0 \\ 0 & 0 & 0 & P_n \end{pmatrix} \quad (2)$$

$$P_i = Q_i^{-1} \quad (3)$$

Q_i - the cofactor matrix of the i -th baseline measurements

For each point of the GNSS grid, we have the following formula:

$$\begin{pmatrix} U_i \\ N_i \\ E_i \end{pmatrix} = \begin{pmatrix} -\sin B_0 \cos L_0 & \cos B_0 \sin L_0 & \cos B_0 \\ -\sin L_0 & \cos L_0 & 0 \\ \cos B_0 \cos L_0 & \cos B_0 \sin L_0 & -\sin B_0 \end{pmatrix} \begin{pmatrix} X - X_0 \\ Y - Y_0 \\ Z - Z_0 \end{pmatrix} = i \begin{pmatrix} X - X_0 \\ Y - Y_0 \\ Z - Z_0 \end{pmatrix} \quad (4)$$

X_0, Y_0, Z_0 - The coordinates of the origin of the topocentric coordinate system in the geocentric coordinate system.

U_i, N_i, E_i - The coordinates of the topocentric coordinate system (Figure 1)

Thus, if the unknowns are U, N, E , the system of equations (1) can be rewritten as follows:

$$V = A_z z + L \quad (6)$$

$$A_z = A \quad (7)$$

$$= \begin{pmatrix} 1 & & & \\ & 2 & & \\ & & \dots & \\ & & & n \end{pmatrix} \quad (8)$$

The normal system of equations has the form:

$$R_z z + b_z = 0 \quad (9)$$

$$R_z = A_z^T P A_z, b_z = A_z^T P L \quad (10)$$

$$z = -R_z^{-1} b_z \quad (11)$$

R_z^{-1} - is the general inverse matrix.

$$R_z^{-1} = (R_z + C C^T)^{-1} - T T^T \quad (12)$$

$$T T^T = B (C^T G)^{-1} \quad (13)$$

$$G^T = (G_1 \quad G_2 \quad \dots \quad G_n) \quad (14)$$

Where:

n is the number of measurements.

$$G_i = \begin{pmatrix} 1 & 0 & 0 \\ 0 & 1 & 0 \\ 0 & 0 & 1 \end{pmatrix} \quad (15)$$

$$C^T = (G_1 \quad \dots \quad G_k \quad 0 \quad \dots \quad 0) \quad (16)$$

For an accurate assessment, the following quantities need to be calculated:

$$s_0 = \sqrt{\frac{VTPV}{n-k+d}} \quad (17)$$

d is the number of defects of the network ($d = 3$).

The covariance matrix is :

$$K_z = s_0^2 Q_z \quad (18)$$

$Q_x = R_z^{-1}$ - The cofactor matrix

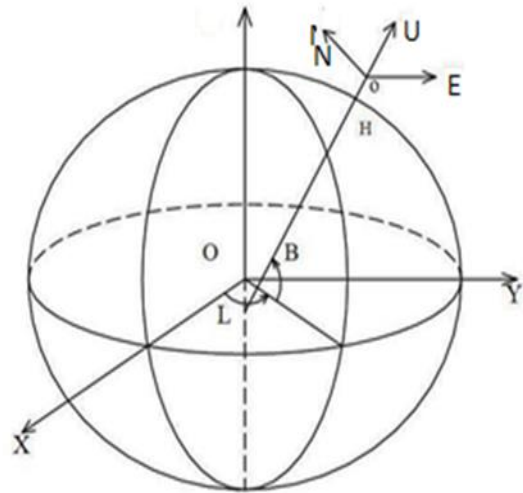


Figure 1. The topocentric coordinate system

Combining recurrent adjustment and Kalman filtering in the displacement analysis of dynamic models

The vector of coordinates of the periodic observation ($k+1$) is determined from the vector of coordinates of the periodic observation (k). Implementing the Taylor formula of the function of the vector of coordinates of the periodic observation $x_j(k+1)$ according to the time variable t , the dynamic model over time with Coordinates, velocity and acceleration is represented by the following formula:

$$f(t^{(k+1)}) = f(t^{(k)}) + \frac{\partial f}{\partial t}(t^{(k+1)} - t^{(k)}) + 0.5 \cdot \frac{\partial^2 f}{\partial t^2} ((t^{(k+1)} - t^{(k)})^2 \quad (19)$$

$$f(t^{(k+1)}) = x_j^{(k+1)}, f(t^{(k)}) = x_j^{(k)} \\ \frac{\partial f}{\partial t} = v_{x_j}^{(k+1)}; \frac{\partial^2 f}{\partial t^2} = a_{H_j}^{(k+1)}$$

where:

$X_j^{(k+1)}, Y_j^{(k+1)}, Z_j^{(k+1)}$: coordinate of point j at period ($k+1$);

$X_j^{(k)}, Y_j^{(k)}, Z_j^{(k)}$: coordinate of point j at period k ;

v_{xj}, v_{yj}, v_{zj} : velocities of X, Y, Z coordinates of point j ;

a_{xj}, a_{yj}, a_{zj} : accelerations of X, Y, Z coordinates of point j ;

$k = 1, 2, \dots, i$ (i : measurement period number);

$j = 1, 2, \dots, k$ (k : number of points);

From formula (19), the following system of equations can be established:

$$\begin{aligned} x_j^{(k+1)} &= x_j^{(k)} + (t_{k+1} - t_k) v_{xj}^{(k+1)} \\ &\quad + 0,5(t_{k+1} - t_k)^2 a_{Hj}^{(k+1)} \\ v_{Hj}^{(k+1)} &= v_{xj}^{(k)} + (t_{k+1} - t_k) a_{Hj}^{(k)} \\ ax_{xj}^{(k+1)} &= a_{Hj}^{(k)} \end{aligned} \quad (20)$$

Expression (20) can be rewritten in matrix form as follows:

$$\begin{pmatrix} x_j^{(k+1)} \\ v_{xj}^{(k+1)} \\ a_{xj}^{(k+1)} \end{pmatrix} = \begin{pmatrix} E & (t_{k+1} - t_k)E & 0,5(t_{k+1} - t_k)^2 E \\ 0 & E & E \\ 0 & 0 & E \end{pmatrix} \begin{pmatrix} x_j^{(k)} \\ v_{xj}^{(k)} \\ a_{xj}^{(k)} \end{pmatrix} \quad (21)$$

The Symbol:

$$y_j^{(k+1)} = \begin{pmatrix} x_j^{(k+1)} \\ v_{xj}^{(k+1)} \\ a_{xj}^{(k+1)} \end{pmatrix} \quad (22)$$

$$y_j^{(k)} = \begin{pmatrix} x_j^{(k)} \\ v_{xj}^{(k)} \\ a_{xj}^{(k)} \end{pmatrix} \quad (23)$$

$$y_j^{(k+1)} = G_j^{(k+1)} y_j^{(k)} \quad (24)$$

$$\bar{Y}_{(k+1)} = G_{(k+1)} \hat{Y}_{(k+1)} \quad (25)$$

Here:

$$\bar{Y}_{(k+1)} = \begin{pmatrix} y_1^{(k+1)} \\ y_2^{(k+1)} \\ \dots \\ y_n^{(k+1)} \end{pmatrix} \quad (26)$$

$$\bar{Y}_{(k)} = \begin{pmatrix} y_1^{(k)} \\ y_2^{(k)} \\ \dots \\ y_n^{(k)} \end{pmatrix} \quad (27)$$

$$G_{(k+1)} = \begin{pmatrix} G_1^{(k+1)} & & \\ & \dots & \\ & & G_n^{(k+1)} \end{pmatrix} \quad (28)$$

$$\bar{Y}_{(k+1)} = \begin{pmatrix} y_1^{(k+1)} \\ y_2^{(k+1)} \\ \dots \\ y_n^{(k+1)} \end{pmatrix} \quad (29)$$

$$\bar{Y}_{(k)} = \begin{pmatrix} y_1^{(k)} \\ y_2^{(k)} \\ \dots \\ y_n^{(k)} \end{pmatrix} \quad (30)$$

$$G_{(k+1)} = \begin{pmatrix} G_1^{(k+1)} & & \\ & \dots & \\ & & G_n^{(k+1)} \end{pmatrix} \quad (31)$$

According to Kalman filter theory, if using the calculation results at period t_k , then according to formula (21), predict the current state vector by using the state vector information of the known motion parameters at period t_k and the measurements at period t_{k+1} . The matrix equation system of the motion model used to predict the motion parameters by Kalman filter technique in the grid can be represented as follows:

$$\bar{Y}_{(k+1)} = G_{(k+1)} \hat{Y}_k + S_{k+1,k} \quad (32)$$

$$C_{\bar{Y}(k+1)} = G_{k+1,k} C_Y G_{k+1,k}^T \quad (33)$$

$\hat{Y}^{(k)}$ is the vector of calculated values adjusted at time t_k .

$\hat{Y}_{(k+1)}^T$ - vector of predicted values of coordinates, velocity and acceleration \hat{Y}_k^T - vector of averaged values at time t_k .

At time t_{k+1} , we can use the geodetic grid adjustment results in the previous observation period (t_k) and establish a system of equations of correction numbers according to the least squares method with new measurement values. Thus, at time t_{k+1} , we can consider the geodetic grid points to have been virtually measured with measurement values and weights as the grid adjustment results in this period. Then we have the coefficient matrix of the system of equations of correction numbers in the following form:

$$\hat{A}_{k+1} = (E_{3 \times 3} \quad 0 \quad 0 \dots E_{3 \times 3} \quad 0 \quad 0) \quad (34)$$

$$V = \hat{A}_{k+1} \hat{Y}_{k+1} + L \quad (18)$$

$$\begin{pmatrix} V_{\hat{Y}_{(k+1)}} \\ V_{L_{k+1}} \end{pmatrix} = \begin{pmatrix} E \\ A_{(k+1)} \end{pmatrix} \hat{Y}_{(k+1)} + \begin{pmatrix} 0 \\ L_{k+1} \end{pmatrix} \quad (35)$$

The weight matrix:

$$P = \begin{pmatrix} P_{\hat{Y}_{(k+1)}} & 0 \\ 0 & P_{L_{k+1}} \end{pmatrix} \quad (36)$$

$$P_{\hat{Y}_{(k+1)}} = Q_{\hat{Y}_{(k+1)}}^{-1} \quad (37)$$

$$P_{L_{k+1}} = Q_{L_{k+1}}^{-1} \quad (38)$$

The normal system of equations has the form:

$$(P_{\hat{Y}_{(k+1)}} + A_{(k+1)}^T P_{L_{k+1}} A_{(k+1)}) \hat{Y}_{k+1} + A_{(k+1)}^T P_{L_{k+1}} L_{k+1} = 0 \quad (39)$$

By the recursive formula (Markuze, YU.I, Hoang H):

$$\hat{Y}_{k+1} = - (P_{\hat{Y}_{(k+1)}} + A_{(k+1)}^T P_{L_{k+1}} A_{(k+1)})^{-1} A_{(k+1)}^T P_{L_{k+1}} L_{k+1} \quad (40)$$

$$\begin{aligned} & (P_{\hat{Y}_{(k+1)}} + A_{(k+1)}^T P_{L_{k+1}} A_{(k+1)})^{-1} \\ &= Q_{\hat{Y}_{(k+1)}} Q_{\hat{Y}_{(k+1)}} A_{(k+1)} (Q_{L_{k+1}}^{-1} + A_{(k+1)}^T Q_{\hat{Y}_{(k+1)}} A_{(k+1)})^{-1} \\ & \left(Q_{L_{k+1}}^{-1} + A_{(k+1)}^T Q_{\hat{Y}_{(k+1)}} A_{(k+1)} \right)^{-1} A_{(k+1)}^T Q_{\hat{Y}_{(k+1)}} \end{aligned} \quad (41)$$

$$\hat{Y}_{k+1} = -Z_{k+1}^T N_{k+1}^{-1} L_{k+1} \quad (42)$$

$$Q_{\hat{Y}_{k+1}} = Q_{\hat{Y}_{(k+1)}} - Z_{(k+1)} N_{k+1}^{-1} Z_{(k+1)}^T \quad (43)$$

Here:

$$Z_{(k+1)} = Q_{\hat{Y}_{(k+1)}} A_{(k+1)}^T \quad (44)$$

$$N_{(k+1)} = Q_{\hat{Y}_{(k+1)}}^{-1} + Z_{(k+1)}^T A_{(k+1)} \quad (45)$$

$$\hat{Y}_{k+1} = \hat{Y}_{(k+1)} + \hat{Y}_{k+1} \quad (46)$$

Data processing procedures

Step 1: Data preprocessing of GNSS adjustment at each measurement cycle

- Input:
 - Geodetic Datum (the local topocentric coordinate system)
 - Priori coordinates of GNSS points
 - GNSS observations.
- Output
 - Estimated value of coordinates of GNSS points
 - RMS error

Step 2: Calculate the parameters dU, dN, dE, v_U, v_N, v_E, a_U, a_N, a_E over the periods.

Step 3: Displacement analysis based on statistical criteria.

RESULTS

GNSS networks adjustment in the local topocentric coordinate system

To conduct experimental research and analyze the displacement according to the theory presented above, we have performed on GNSS measurement data in the central region of Vietnam (Thach Ban - Cat Tien, Lam Dong province). The monitoring network consists of 6 points (Figure 2). The construction of the network and the measurement was carried out by the Vietnam Institute of Geodesy and Cartography. The landmark is built according to the standard of mandatory centering landmarks placed on the bedrock. Repeat measurement for 4 cycles 2015, 2016, 2017 and 2018, time interval between cycles is one year.

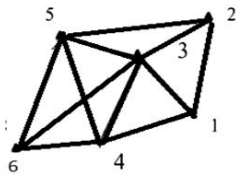


Figure 2. GNSS network Diagram

In the first step, applying the 3D free network adjustment to process the Baselines, the network coordinates were obtained in the 2015, 2016, 2017 and 2018 cycles. Conduct assessment of the change of milestones between 2 cycles 1-j (j- number of cycle): $T_U = dU/m_{dU}$, $T_N = dN/m_N$, $T_E = dE/m_{dE}$. Check the Criteria (t-distribution) (Ghilani, C., Wolf, P.; (2017)): $|T_U| < q_U$, $|T_N| < q_N$, $|T_E| < q_E$. If the test value is greater then the critical value, then there are significant deformations in the points.

Calculation results and checking statistical criteria can be seen that all 6 points have shifted.

Calculation of displacement parameters

In each observation period, calculations and adjustments are made according to formulas (1)-(18). These results are used to calculate the displacement parameters 1-2, 1-2-3, 1-2-3-4 according to formulas (25) to (44). The calculation results are presented in the following tables (Round to mm).

Table 1: Displacement parameters dU, dN, dE (mm), $V_U, V_N, V_E, a_U, a_N, a_E$ between 2015 and 2016

	1	2	3	4	5	6
dU (mm)	51	11	-15	28	-39	-4
dN (mm)	0	0	0	0	0	0
dE (mm)	0	0	0	0	0	0
V_U (mm/year)	61	13	-18	33	-47	-4
V_N (mm/year)	0	0	0	0	0	0
V_E (mm/year)	0	0	0	0	0	0
a_U (mm/year ²)	20	5	-6	11	-16	-2
a_N (mm/year ²)	0	0	0	0	0	0
a_E (mm/year ²)	0	0	0	0	0	0

Table 2. Displacement parameters dU, dN, dE (mm), $V_U, V_N, V_E, a_U, a_N, a_E$ between 2015, 2016, 2017

	1	2	3	4	5	6
dU (mm)	11	-76	-47	-31	-46	-13
dN (mm)	0	0	0	0	0	0
dE (mm)	0	0	0	0	0	0
V_U (mm/year)	-86	-91	-40	-102	8	-12
V_N (mm/year)	0	0	0	0	0	0
V_E (mm/year)	0	0	0	0	0	0
a_U (mm/year ²)	-91	-53	-16	-86	32	-5
a_N (mm/year ²)	0	0	0	0	0	0
a_E (mm/year ²)	0	0	0	0	0	0

Table 3 Displacement parameters dU, dN, dE (mm), $V_U, V_N, V_E, a_U, a_N, a_E$ between 2015, 2016, 2017 and 2018

	1	2	3	4	5	6
dU (mm)	12	-193	-10	0	-33	-12
dN (mm)	0	0	0	0	0	0
dE (mm)	0	0	0	0	0	0
V_U (mm/year)	22	-144	70	0	23	71
V_N (mm/year)	0	0	0	0	0	0
V_E (mm/year)	0	0	0	0	0	0
a_U (mm/year ²)	41	-53	68	0	20	11
a_N (mm/year ²)	0	0	0	0	0	0
a_E (mm/year ²)	0	0	0	0	0	0

DISCUSSION

From the results of calculating the displacement parameters (from table 1 to table 3), we can clearly see that there is only a displacement of the U coordinate, that is, only a rise and fall. The horizontal displacement is stable. Point 1 through 4 cycles tends to rise, points 2, 3, 5, 6 sink. Only point 4 to cycle 4 is stable. This result shows the superiority of the

adjustment in the topocentric coordinate system. If the correction was in the geocentric coordinate system, the picture would not be so clear.

CONCLUSION

In this paper, the recurrent adjustment theory combined with Kalman filter has been developed to solve the problem of assessing the displacement and deformation of the land due to the impact of natural disasters or climate change. To implement this solution, it is necessary to apply GNSS satellite technology. The monitoring network is adjusted separately in each measurement cycle. Synthesis and analysis of displacement are performed in the horizon coordinate system. The advantage of this method is that it allows us to clearly see the displacement in the horizontal or vertical direction. The experimental results show the effectiveness of the method through the detection of vertical displacement of the monitoring network points.

REFERENCES

- Ghilani, C., Wolf, P.; (2007), Adjustment Computations, John Wiley & Sons, 6th Edition
- Hoang N. H, Truong H., (2010), Basis of Mathematical Processing for Geodetic Data, Transport Publishing House (in Vietnamese) ..
- Hoang, N. H. (2020), Adjustment of Geodetic and GNSS networks, Science and Technology Publishing House, Hanoi (in Vietnamese) ..
- Hoang, N. H. (2020), Modernization of Height System in Vietnam Using GNSS and Geoid Model. In: Tien Bui D., Tran H.T., Bui XN. (eds) Proceedings of the International Conference on Innovations for Sustainable and Responsible Mining. Lecture Notes in Civil Engineering, vol 108. Springer,
- Hoang, N. H. (2023), Monitoring the displacement of the Ba River fault zone of Vietnam using GNSS technology. FIG Conference, Orlando, Florida, USA
- R.E. Kalman, (1960),, *A new approach to linear filtering and prediction problems*, J Basic Eng 82D 5e45.
- .Markuze, YU.I, Hoang H., (1990), Adjustment of Terrestrial and Satellite Space Networks, Nedra Moscow Publishing House , pp. 274
- Welsch, W. M.), and Heunecke, O.: ,(2001), *Models and terminology for the analysis of geodetic monitoring observations*, in: Proceedings of the 10th International Symposium on Deformation Measurements, Orange, California, USA, 390–412
- Yalcinkaya, M. and Bayrak, T. (2003), *Dynamic model for monitoring landslides with emphasis on underground water in Trabzon Province, Northeastern Turkey*, J. Surv. Eng.-ASCE, 129(3), 115–124, 2003.
- C.Rao (1998), Linear Statistical Inference and its Applications, Wiley Eastern Ltd.,
- Vy, H., Tran ,T., Duong., C., 2005, Determination of modern displacement of the Da River fault zone and Son La-Bim Son fault zone by GPS data. Geology and Minerals, No. 9, pp. 257-265.

DOI: 10.15625/vap.2025.0226

Data Quality Assessment and Station Classification of the CORS stations – Case study of CORS stations in Nghe An Province, Vietnam

Trong Tran Dinh, Huy Nguyen Dinh*, Hue Tran Thi

Hanoi University of Civil Engineering, 55 Giai Phong street, Bach Mai ward, Hanoi, Vietnam

*Email: huynd@huce.edu.vn

Abstract: Continuously Operating Reference Station (CORS) networks are essential infrastructure for high-precision applications, e.g. geodetic and geodynamic application. The quality of network data is a paramount factor, dependent on both hardware and the installation environment. This study presents a comprehensive quality assessment of 8 CORS stations of TAST CORS network in Nghe An province, Vietnam, over a 30-day period using GPS (Global Positioning System) data. An automated Python procedure was employed to analyze key metrics: Signal-to-Noise Ratio (SNR), multipath error, and cycle slips. The results indicate that the entire 8 stations exhibit very high overall quality, with mean SNR values exceeding 42 dB-Hz and nearly zero cycle slip ratios. Based on multipath errors, the stations were classified into 3 quality groups: Excellent (NAAS, QPHO, VINH), Good (NDAN, DOLU, NAHM), and Fair (NANL, NAQH). These findings provide critical information for network operation and for end-users in selecting appropriate reference stations.

Keywords: GNSS, CORS, SNR, multipath, cycle slips.

INTRODUCTION

The advent and evolution of Global Navigation Satellite Systems (GNSS), including Global Positioning System (GPS), GLObal Navigation satellite System (GLONASS), Galileo, and BeiDou, opened new directions for high-precision measurement technologies in Earth sciences and other socioeconomic fields. To achieve centimeter-level accuracy,

differential positioning techniques such as Real-Time Kinematic (RTK) and post-processing have become standard practice. The foundation of these techniques is a network of Continuously Operating Reference Stations (CORS), which serve as active control points, replacing traditional ground-based benchmarks.

In Vietnam, a nation with rapid economic growth and urbanization, the establishment and enhancement of national and regional CORS networks play a strategic role (Snay and Soler, 2008). From a socioeconomic perspective, these networks provide an indispensable foundation for numerous activities, including: (1) Geodesy and Cartography, supporting the creation and updating of large-scale topographic and cadastral maps (Abidin et al., 2015; Erenoglu, 2017); (2) Land Administration, enabling high-precision determination of property boundaries, which facilitates land title registration (Erenoglu, 2017); and (3) Civil Engineering, ranging from the construction of high-rise buildings, bridges, and tunnels to the monitoring of structural deformation and the development of intelligent transportation systems (Lê Minh et al., 2020; Trong and Dung, 2024).

Scientifically, the CORS network in Vietnam opens up important research opportunities. Due to its geographical location in a tectonically active region near the boundaries of surrounding plates and blocks (Tran and Pham, 2013), the network serves as a powerful tool for monitoring geodynamic activities (Tran and Pham, 2013), determining

Earth's surface motion (Gia Trọng et al., 2022; Tran Dinh et al., 2023), and assessing seismic hazards along major fault zones such as the Red River, Son La, and Lai Chau-Dien Bien faults. Furthermore, its location in the tropical region near the equator makes CORS stations effective atmospheric sensors. This allows for the study of complex ionospheric phenomena (Dao et al., 2020) and the monitoring of water vapor variations in the troposphere (Pham Le et al., 2024), providing valuable input data for both weather forecasting and climate change research.

However, to fully utilize the potential of the CORS infrastructure, the quality and reliability of the data from each station are paramount. A CORS station with poor data quality, whether due to hardware issues or suboptimal installation site conditions, not only degrades positioning accuracy in its zone but can also compromise the integrity of the entire network. Therefore, performing systematic and periodic quality assessment is a critical scientific task. This ensures the integrity of the national coordinate system and provides important information for both network operators and end-users.

Accordingly, this study conducts a quality assessment of selected CORS stations, with a case study comprising 8 stations in Nghe An province, Vietnam. By analyzing key metrics such as Signal-to-Noise Ratio (SNR), multipath errors, and cycle slips over a 30-day period, we classify the quality of these stations and provide insights into the network's operational effectiveness. The findings of this research not only offer valuable guidance for reference station selection but also affirm the quality and potential of Vietnam's CORS network for multidisciplinary scientific applications.

DATA AND METHODOLOGY

Data

The data used in this study were collected from the CORS network established and operated by Tuong Anh scientific technical equipment Joint stock company (TAST) [8]. Established in the early 2010s, the TAST

network is one of the largest commercial GNSS infrastructures in Vietnam, with approximately 160 stations covering the entire country. In addition to providing real-time positioning services for surveying and mapping applications, TAST also shares data for scientific research purposes, which has been utilized in previous publications [8], [11].

Within the scope of this research, we focus on 8 CORS stations of TAST network located in Nghe An province: VINH, NANL, DOLU, NAAS, NAHM, NDAN, NAQH, and QPHO. The locations and spatial distribution of these stations are illustrated in Figure 1.



Figure 1. Location of 8 CORS stations in Nghe An province

The dataset for these 8 CORS stations covers a continuous 30-day time series, from Day of Year (DOY) 153 to 182, 2024 (corresponding to June 1 to June 30, 2024). According to TAST, all stations in the TAST network are equipped with Trimble NetR9 GNSS receivers and TRM 41249.00 antennas. The raw data were originally recorded and stored in the proprietary To2 format at a 30-second sampling interval. However, for post-processing and scientific research purposes, the raw data were converted to the Receiver Independent Exchange Format (RINEX) version 2 [12]. Consequently, the final dataset used in this study consists of daily observation files (*.240), which contain pseudorange and carrier phase measurements, and navigation

message files (*.24n), which contain the broadcast ephemeris information necessary for computing GNSS satellite positions.

An important characteristic of the TAST network, stemming from its original purpose of serving surveying and mapping applications, is that many stations are installed on existing structures such as the rooftops of high-rise buildings. This characteristic introduces a potential risk of multipath errors, one of the primary factors affecting data quality. Therefore, a detailed quality assessment is a necessary step to understand the performance of each station and to provide recommendations for both TAST and its end-users.

Methodology

To ensure consistency and efficiency in processing the large volume of data, an automated analysis procedure was developed in Python programming language. This procedure utilizes open-source scientific libraries such as georinex [13], pandas ([14], numpy, scipy [15], and matplotlib [16]. Although the GNSS receivers are capable of tracking signals from multiple satellite systems, this study focuses exclusively on analyzing data from the GPS to maintain homogeneity. The decision to utilize only GPS data was primarily made to minimize computational load. This choice does not affect the generalizability of the primary quality conclusions, as the signal quality, particularly multipath error, is fundamentally dependent on the station's physical installation environment and not the specific satellite system being observed.

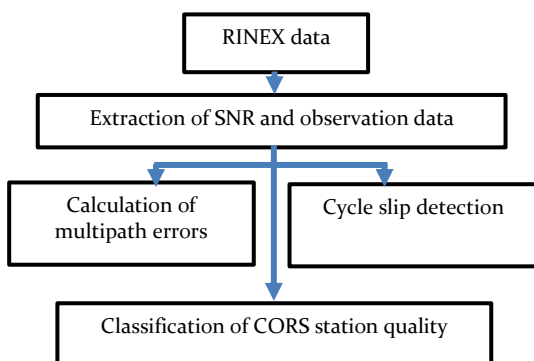


Figure 2. Schematic of the processing workflow

The procedure performs a quality analysis on each daily (24-hour) observation file, according to the process workflow in Figure 2, and aggregates the results into a time series for each station's entire dataset.

The main analysis steps include: (1) extracting the SNR and observation data; (2) calculating multipath errors; and (3) detecting cycle slips.

(1) Extraction of SNR and observation data: First, the pseudorange and carrier phase measurements on both L1 and L2 frequencies, along with their corresponding SNR, are extracted from the RINEX observation files (*.24o) using the georinex library.

(2) Calculation of multipath errors: Multipath (MP) error is one of the key indicators for assessing the quality of a station's installation environment. In this study, the multipath combinations for the L1 (MP1) and L2 (MP2) frequencies were calculated using the geometry-free linear combination of code and phase measurements, as formulated by [17]:

$$MP1 = P_1 - \left(1 + \frac{2}{\alpha-1}\right)L_1 + \frac{2}{\alpha-1}L_2 \quad (1)$$

$$MP2 = P_2 - \frac{2\alpha}{\alpha-1}L_1 + \left(\frac{2\alpha}{\alpha-1} - 1\right)L_2 \quad (2)$$

where P_1, P_2 are the pseudorange measurements, and L_1, L_2 are the carrier phase measurements in meters. The term α is defined as the squared frequency ratio:

$$\alpha = \frac{f_1^2}{f_2^2} \quad (3)$$

with $f_1 = 1575.42$ MHz, $f_2 = 1227.60$ MHz are being the GPS carrier frequencies.

To mitigate the effects of integer ambiguities and other low-frequency error components, the resulting multipath time series for each continuous satellite observation arc was filtered using the detrend function from the SciPy library. Finally, the Root Mean Square (RMS) value of the filtered multipath series was computed for each day, serving as the primary quantitative metric to evaluate the level of multipath errors. Since multipath error, after detrending, acts as a residual noise

component with a mean value near zero, RMS is the most appropriate measure capable of quantifying the magnitude of this remaining signal.

(3) Cycle slip detection: The geometry-free (GF) phase combination was used to detect discontinuities in GNSS signal tracking [18]:

$$GF = L_1 - L_2 \quad (4)$$

A cycle slip is identified when an abrupt jump (exceeding a predefined threshold, e.g., 1 m) occurs in the detrended GF time series. The ratio of detected cycle slips to the total number of observations is then calculated to assess data continuity.

All daily computed results (average of SNR and multipath RMS) and the raw data arrays (SNR, multipath) were aggregated to generate statistical histograms and to perform a comparative quality analysis among the 8 CORS stations.

RESULT

Performance of CORS network

To provide a quantitative overview, key quality metrics, including SNR, multipath (MP) error, and cycle slip ratio, were averaged over the 30-day period for each station and are presented in Table 1. For ease of comparison, the stations are sorted in ascending order based on their L1 multipath error (RMS MP1).

Table 1. Quality assessment metrics

ID	Avg. SNR L1 (dB-Hz)	Avg. SNR L2 (dB-Hz)	RMS MP1 (m)	RMS MP2 (m)	Cycle Slips (%)
NAAS	43.2228	31.6721	0.0675	0.0914	0.0006
QPHO	43.2755	32.5020	0.0893	0.1201	0.0017
VINH	44.2377	36.6169	0.1082	0.1372	0.0021
NDAN	43.1748	32.5051	0.1103	0.1442	0.0013
DOLU	43.0853	31.8332	0.1329	0.1711	0.0016
NAHM	42.6064	30.5648	0.1387	0.1777	0.0018
NAQH	<i>41.3400</i>	<i>29.3300</i>	0.1905	0.2381	0.0017
NANL	42.5105	31.9190	0.2009	0.2558	0.0021

Note: Bold values indicate the best performance in each category (highest SNR, lowest multipath, lowest cycle slips). Italicized values indicate the poorest performance.

As shown in Table 1, the 8 CORS stations exhibit a robust and consistent performance. The mean SNR for the L1 frequency (avg_snr1) exceeds 42 dB-Hz for all stations, with top-performing stations such as VINH, NAAS, and QPHO surpassing 43 dB-Hz, indicating strong signal reception and high-quality hardware. The cycle slip ratio throughout the 30-day survey period is negligible (approaching zero on most days), demonstrating that the receivers operated reliably and that no significant atmospheric disturbances occurred during the observation period.

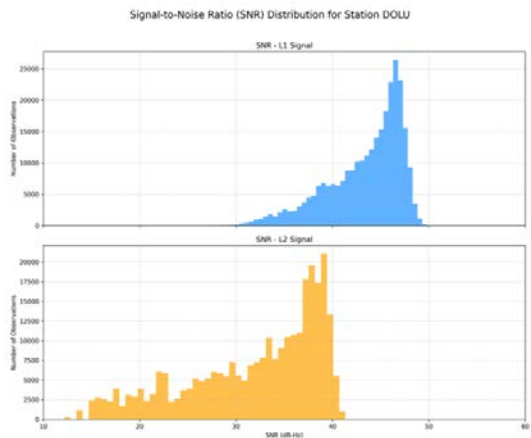
The primary factor differentiating the quality among stations is the multipath error (rms_mp1, rms_mp2). Based on this multipath

error factor, a clear stratification is evident, ranging from stations with excellent quality like NAAS and QPHO (RMS MP1 \approx 0.07-0.09 m) to those with lower performance such as NANL and NAQH (RMS MP1 \approx 0.20 m). However, it is important to emphasize that even the stations with the highest multipath values in these 8 CORS stations still meet the criteria for "Good" quality, which typically requires an RMS of < 0.5 m [19]. This indicates that the entire 8 stations were installed at carefully selected sites. A more detailed analysis of each station's characteristics will be presented in the following sections.

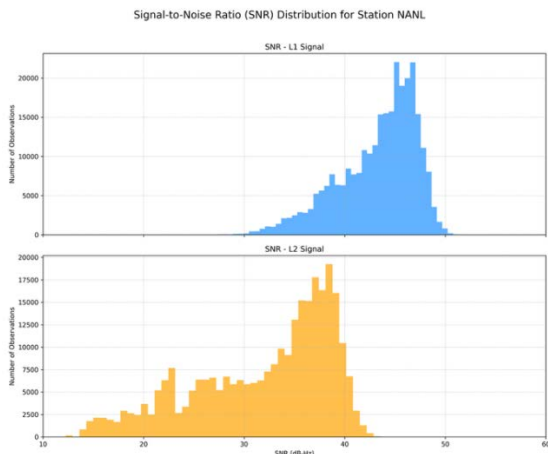
Analysis of error distribution

a. SNR distribution

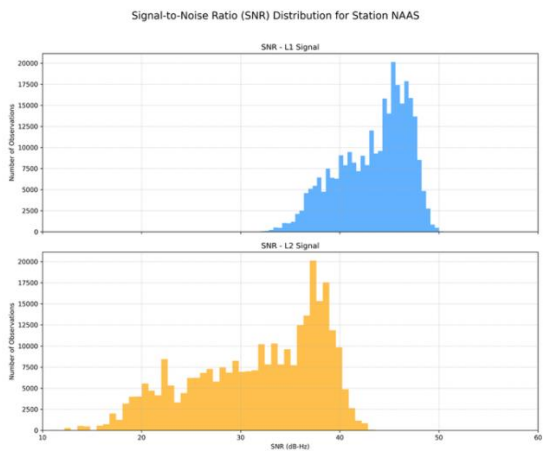
Figure 2 presents the distribution of the SNR for the L1 (blue) and L2 (orange) frequencies.



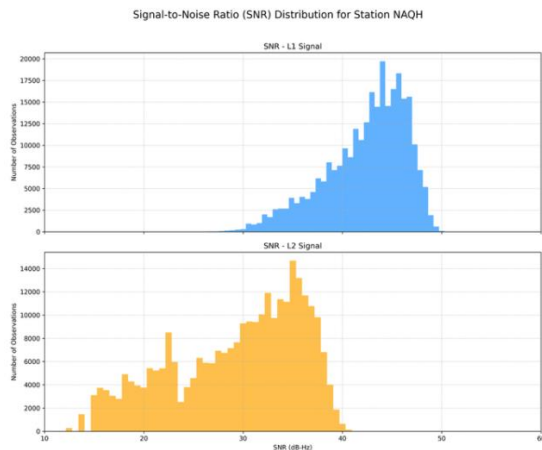
(a)



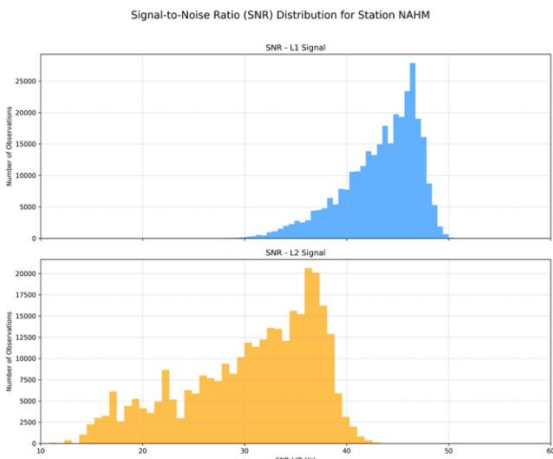
(d)



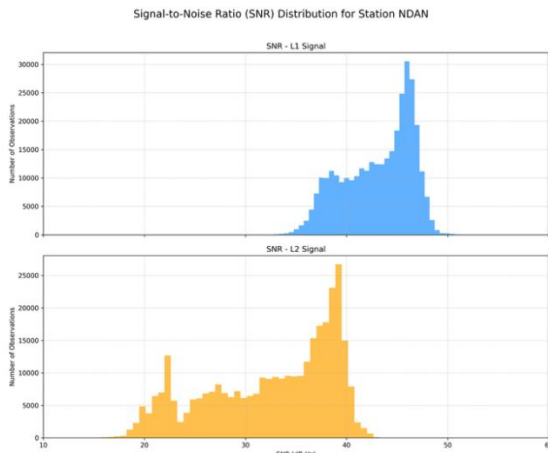
(b)



(e)



(c)



(f)

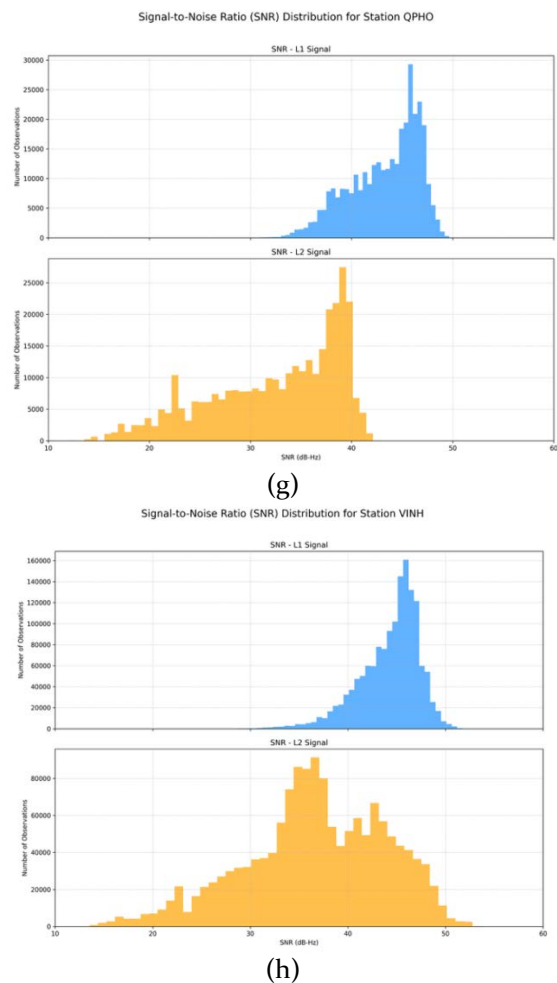


Figure 3. SNR histogram of 8 CORS stations

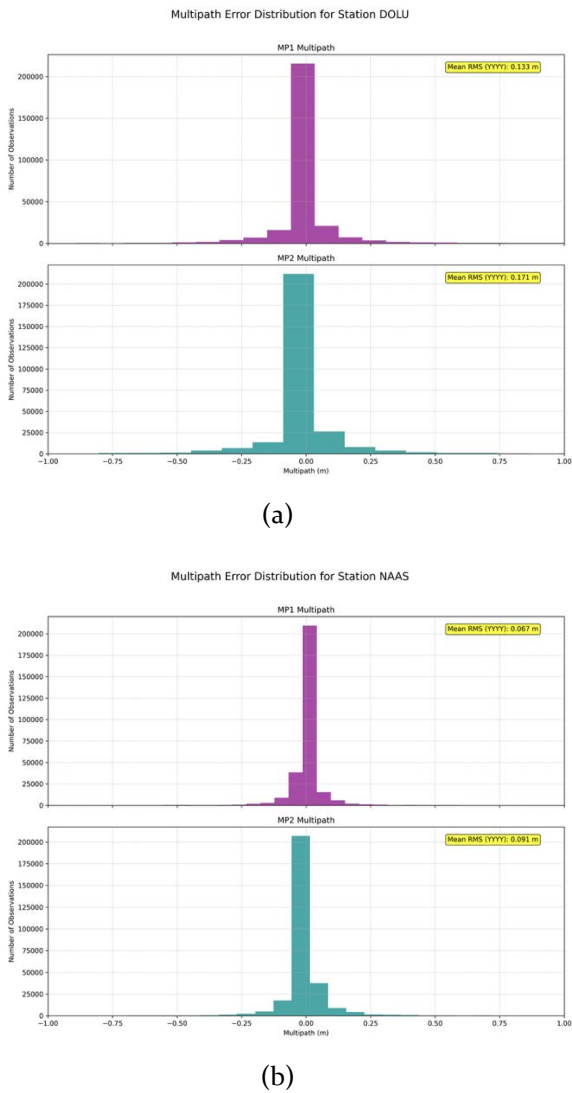
Figure 3 shows that, in general, all 8 stations exhibit a very good and uniform SNR distribution, reflecting the stable performance of the hardware (Trimble NetR9 receivers and TRM 41249.00 antennas) across the entire network.

All histograms show a right-skewed normal distribution, with the distribution peak concentrated at high SNR values. This is a positive indicator, suggesting that the GNSS receivers captured strong signals for the majority of the time. The distribution peak for L1 SNR (blue) is predominantly in the 45–55 dB-Hz range for most stations. The L2 SNR distribution peak (orange) is concentrated in the 35–45 dB-Hz range.

Despite the high degree of uniformity, minor differences can be observed at stations such as NAQH (Figure 3.e) and NANL (Figure 3.d), where the distribution peaks are slightly shifted towards lower values. This suggests that the signal reception at these stations may be marginally affected by local factors, although the impact is not significant.

b. Multipath errors distribution

Figure 2 presents the distribution of multipath errors for the 8 CORS stations.



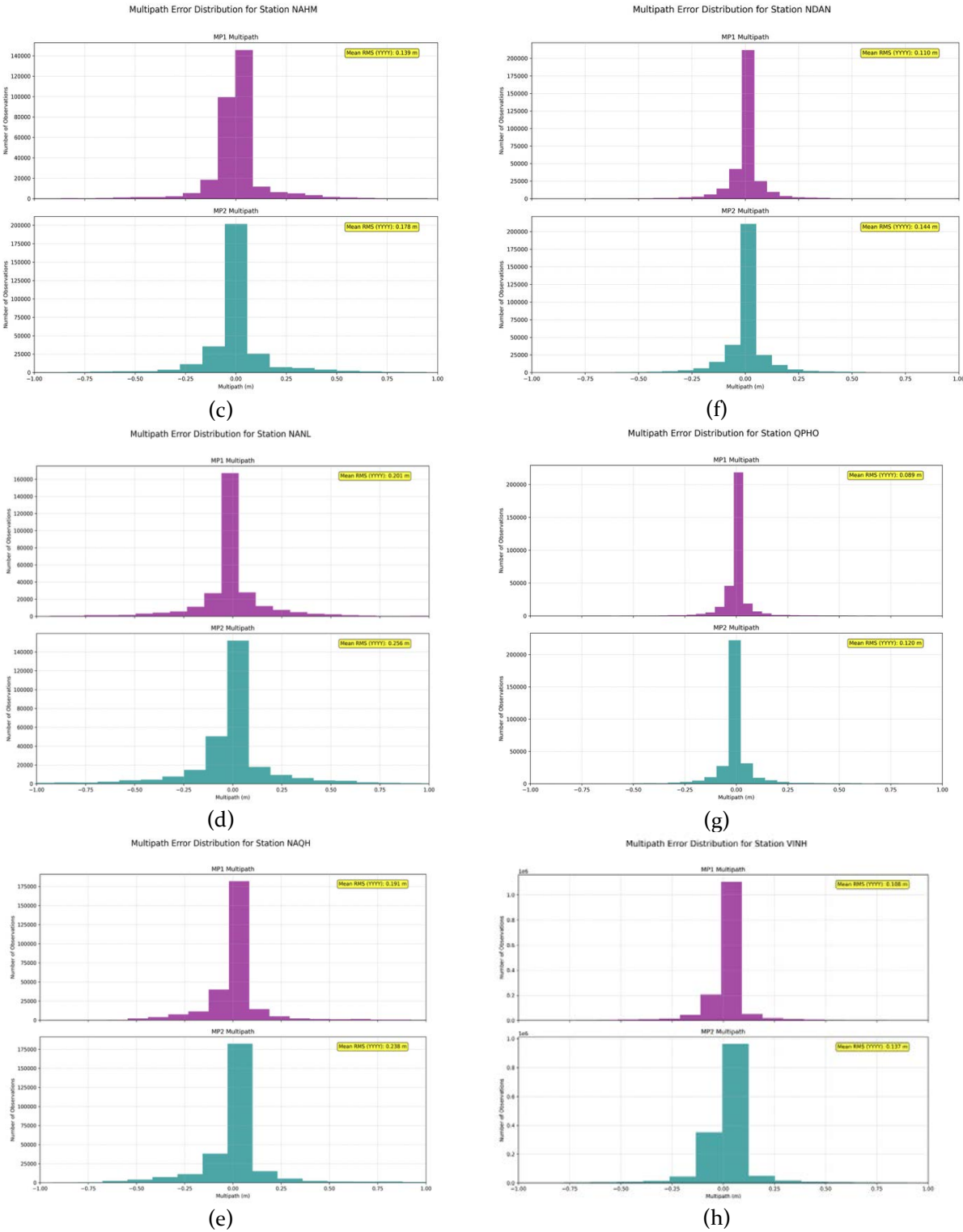


Figure 4. Multipath errors histogram of 8 CORS stations

As illustrated in Figure 4, all 8 stations exhibit distributions that are nearly symmetrical around zero. At each station, the distribution shapes of MP₁ (purple) and MP₂ (teal) are highly similar, differing only slightly in their spread. This is expected, as both signals are affected by the same physical environment.

High-quality stations, including NAAS (Figure 4.b), QPHO (Figure 4.g), and VINH (Figure 4.h) display tall and narrow, bell-shaped histograms, indicating that multipath errors are almost always concentrated within a very small range (e.g., ± 0.2 m).

In contrast, the lower-quality stations, including NANL (Figure 4.d), and NAQH (Figure 4.e) show significantly wider and flatter distributions. This implies that larger errors (e.g., > 0.5 m) occur with greater frequency, which is a clear sign of contamination from reflective surfaces near the antenna.

Station quality classification

Based on the quantitative metrics in Table 1 and the distributional shapes of the histograms (Figure 2, Figure 3), the 8 CORS stations were classified into 3 quality groups for ease of assessment and comparison. The classification thresholds were determined semi-empirically, based on the natural distribution and clear breakpoints of the histograms of MP₁ errors.

(1) Group 1: Excellent quality, comprising stations NAAS, QPHO, and VINH. This group includes the network's top-performing stations, characterized by:

- Cycle Slips: A negligible ratio ($< 0.0022\%$), ensuring high data continuity.

- SNR: The highest mean SNR values, particularly at station VINH (L_1 SNR > 44 dB-Hz). The SNR histograms show a distribution peak concentrated at very high values (50–55 dB-Hz for L_1), demonstrating superior signal reception capability.

- Multipath: This is the most prominent feature of this group, with a mean RMS MP₁ below 0.11 m. The histograms are tall and

narrow with a distinct bell shape, indicating that most errors are densely clustered within ± 0.2 m, and large errors are nearly absent.

(2) Group 2: Good quality, comprising stations NDAN, DOLU, and NAHM. These stations maintain a very high level of data quality suitable for all high-precision applications, characterized by:

- Cycle Slips: The ratio remains extremely low, comparable to Group 1.

- SNR: Mean SNR values are still very good (L_1 SNR > 42.5 dB-Hz). The histogram peaks for these stations may be slightly lower than those in Group 1.

- Multipath: Multipath errors are slightly higher than in Group 1, with the mean RMS MP₁ ranging from 0.11 m to 0.14 m. The multipath histograms for these stations begin to appear flatter and wider, indicating a slight increase in the occurrence frequency of larger errors.

(3) Group 3: Fair quality, comprising stations NAQH and NANL. These are the two lowest-performing stations in the network but still meet the general criteria for "Good" quality [19]. Their distinction becomes more apparent in an internal comparison of 8 stations.

- Cycle Slips: The ratio remains very low and is not a significant concern.

- SNR: Station NAQH, in particular, has the lowest mean SNR in the network (L_1 SNR ≈ 41.3 dB-Hz). Its histogram shows a shift in the distribution peak towards lower values, especially for the L_2 frequency.

- Multipath: With a mean RMS MP₁ above 0.19 m. The multipath histogram for NANL serves as a clear illustration: the distribution is significantly wider and flatter than that of NAAS, with a large proportion of observations having errors outside the ± 0.5 m range. This indicates that the installation environments at NAQH and NANL are more affected by multipath than the rest of the network.

DISCUSSION

One of the most prominent findings of this study is the uniform performance of the hardware across the entire network. The excellent SNR values and negligible cycle slip ratios at all 8 stations confirm that the Trimble NetR9 receivers and TRM 41249.00 antennas are operating stably and effectively. Therefore, it can be concluded that the variations in overall data quality among the stations do not stem from equipment-related factors but originate primarily from the local multipath environment at each installation site. This underscores the importance of site selection in the establishment of a CORS station. An open installation site, free from nearby obstructions and reflective surfaces, is a prerequisite for ensuring the highest level of data quality.

The classification of the 8 CORS stations of TAST network in Nghe An into 3 groups offers practical value:

- For end-users: When performing tasks that demand the highest level of precision (such as establishing high-order control networks, geodynamic studies, or processing long-term PPP time series), users should prioritize selecting stations from Group 1 (NAAS, QPHO, VINH). While data from Group 2 ((NDAN, DOLU, NAHM)) and Group 3 (NAQH, NANL) stations remain entirely reliable for conventional surveying applications like RTK, users should be aware that the higher noise levels may affect initialization times and solution stability under challenging conditions.

- For the network operator (TAST): This analysis provides a quantitative basis for evaluating network performance. The stations in Group 3 should be flagged for re-evaluation, including on-site surveys to precisely identify the sources of multipath and signal obstruction. If feasible, relocating the antennas to better positions in the future would help enhance the overall homogeneity and quality of the entire network.

This study focused only on a 30-day GPS signal series, future work could concentrate on

analyzing longer data series for other satellite systems such as GLONASS and Galileo.

CONCLUSION

This study has conducted a comprehensive and systematic quality assessment for an 8 CORS stations of the TAST CORS network in Nghe An province, Vietnam, using a 30-day GPS data series. Through the analysis of SNR, cycle slip ratio, and multipath error, the study has conclusions:

All 8 stations demonstrate robust operational performance, characterized by high mean SNR values and nearly zero cycle slip ratios. This affirms the quality and reliability of the hardware (receivers, antennas) and the stability of the data acquisition system across the network.

The analysis shows that variations in data quality among the stations stem primarily from the local multipath environment at the installation site, rather than from equipment performance. Consequently, the multipath RMS value serves as the most effective metric for classifying station quality.

Based on these quantitative metrics, the 8 stations were classified into three distinct quality groups: Excellent (NAAS, QPHO, VINH), Good (NDAN, DOLU, NAHM), and Fair (NAQH, NANL). This classification provides a scientific basis for end-users to select the most appropriate reference station for their accuracy requirements. It also offers a foundation for the network operator TAST to conduct on-site re-evaluations aimed at potential future quality enhancements.

This study has demonstrated that the 8 TAST CORS stations in Nghe An constitute a high-quality and reliable geodetic infrastructure. Furthermore, the automated Python-based analysis procedure has proven to be both effective and scalable, making it applicable for the periodic quality monitoring of other CORS networks.

REFERENCES

- [1] R. A. Snay and T. Soler, "Continuously Operating Reference Station (CORS): History, Applications, and Future Enhancements," *J. Surv. Eng.*, vol. 134, no. 4, pp. 95–104, Nov. 2008, doi: 10.1061/(ASCE)0733-9453(2008)134:4(95).
- [2] H. Z. Abidin et al., "On the establishment and implementation of GPS CORS for cadastral surveying and mapping in Indonesia," *Survey Review*, vol. 47, no. 340, pp. 61–70, Jan. 2015, doi: 10.1179/1752270614Y.0000000094.
- [3] R. C. Erenoglu, "A comprehensive evaluation of GNSS- and CORS-based positioning and terrestrial surveying for cadastral surveys," *Survey Review*, vol. 49, no. 352, pp. 28–38, Jan. 2017, doi: 10.1080/00396265.2015.1104093.
- [4] N. Lê Minh, H. Lê Văn, and C. Trần Đức, "Precision investigation of central points layout in road constructions using continuously operating reference station," *vn*, vol. 71, no. 2, pp. 70–79, Feb. 2020, doi: 10.25073/tcsj.71.2.2.
- [5] T. D. Trong and L. N. Dung, "Study on the positioning efficiency of GNSS RTK for road profile surveys - case study in Vietnam," *JSTCE*, vol. 18, no. 2, pp. 86–98, Jun. 2024, doi: 10.31814/stce.huice2024-18(2)-07.
- [6] Tran T. D. and Pham H. V., "Setting up a GNSS permanent network for Vietnam under the geotonic view," *JMES*, vol. 41, Art. no. 0, Jan. 2013.
- [7] Gia Trọng N. et al., "Determination of tectonic velocities in Vietnam territory based on data of CORS stations of VNGEONET network," *VNJHM*, vol. 739, no. 7, pp. 59–66, Jul. 2022, doi: 10.36335/VNJHM.2022(739).59-66.
- [8] T. Tran Dinh, D. H. Nguyen, N. Q. Vu, and Q. L. Nguyen, "Crustal displacement in Vietnam using CORS data during 2018 - 2021," *Earth sci. res. j.*, vol. 27, no. 1, pp. 27–36, May 2023, doi: 10.15446/esrj.v27n1.102630.
- [9] T. Dao et al., "New observations of the total electron content and ionospheric scintillations over Ho Chi Minh City," *TCKKHVTĐ*, vol. 42, no. 4, Sep. 2020, doi: 10.15625/0866-7187/42/4/15281.
- [10] K. Pham Le, A. Nguyen Xuan, H. Van Nguyen, S. Hoang Hai, V. Nguyen Nhu, and M. Bui Ngoc, "Precipitable water characterization using global navigation satellite system data: A case study in Nghia Do area, Vietnam," *Vietnam J. Earth Sci.*, Jan. 2024, doi: 10.15625/2615-9783/19912.
- [11] D. T. Tran, Q. L. Nguyen, and D. H. Nguyen, "General Geometric Model of GNSS Position Time Series for Crustal Deformation Studies – A Case Study of CORS Stations in Vietnam," *Inzynieria Mineralna-Journal of the Polish Mineral Engineering Society*, vol. 1, Dec. 2021, doi: 10.29227/IM-2021-02-16.
- [12] Werner Gurtner, "RINEX: The Receiver Independent Exchange Format Version 2.10." Astronomical Institute, University of Berne, Dec. 10, 2007. [Online]. Available: https://epic.awi.de/id/eprint/51856/1/Gurtner_2007_rinex210.pdf
- [13] Ph. D. Michael Hirsch, N. Mayorov, and J. Strandberg, *scivision/georinex: File extension agnostic*. (Feb. 28, 2019). Zenodo. doi: 10.5281/ZENODO.2580306.
- [14] P. Gupta and A. Bagchi, "Introduction to Pandas," in *Essentials of Python for Artificial Intelligence and Machine Learning*, in *Synthesis Lectures on Engineering, Science, and Technology*. , Cham: Springer Nature Switzerland, 2024, pp. 161–196. doi: 10.1007/978-3-031-43725-0_5.
- [15] E. Bressert, *SciPy and NumPy: examples to jumpstart your scientific Python programming*, 1. ed., 3. release. Beijing Köln: O'Reilly, 2013.
- [16] N. Ari and M. Ustazhanov, "Matplotlib in python," in *2014 11th International Conference on Electronics, Computer and Computation (ICECCO)*, Abuja, Nigeria: IEEE, Sep. 2014, pp. 1–6. doi: 10.1109/ICECCO.2014.6997585.
- [17] L. H. Estey and C. M. Meertens, "TEQC: The Multi-Purpose Toolkit for GPS/GLONASS Data," *GPS Solutions*, vol. 3, no. 1, pp. 42–49, Jul. 1999, doi: 10.1007/PL00012778.
- [18] W. Feng, Y. Zhao, L. Zhou, D. Huang, and A. Hassan, "Fast cycle slip determination for high-rate multi-GNSS RTK using modified geometry-free phase combination," *GPS Solut.*, vol. 24, no. 2, p. 42, Apr. 2020, doi: 10.1007/s10291-020-0956-6.
- [19] A. J. Jakab, "Quality monitoring of GPS signals," 2001, University of Calgary. doi: 10.11575/PRISM/12019.

DOI: 10.15625/vap.2025.0227

Designing for Value: Linking Transparency and Incentives to Economic, Social, and Environmental Co-Creation

Wen Chin Hsu^{*}, Chi-Wei Peng

National Central University (NCU), Taoyuan, Taiwan (China)

^{*}Email: hsuwc@ncu.edu.tw

Abstract: Digital co-creation platforms have emerged as vital instruments for engaging citizens in sustainability governance. Building on cognitive and behavioral theories, this study examines how two design features—information transparency and incentive mechanisms—shape citizens' risk perception and policy identification, which subsequently foster economic, social, and environmental value co-creation. A scenario-based survey of 150 respondents in Taiwan was analyzed using hierarchical regression models. Results show that both transparency ($\beta = 0.590$, $p < .001$) and incentive mechanisms ($\beta = 0.426$, $p < .001$) significantly predict risk perception, which in turn predicts policy identification ($\beta = 0.548$, $p < .001$). Policy identification further drives economic ($\beta = 0.457$, $p < .001$), social ($\beta = 0.517$, $p < .001$), and environmental ($\beta = 0.486$, $p < .001$) value co-creation. The findings suggest that digital platforms can convert cognitive awareness of drought risks into multidimensional public value by cultivating policy identification.

Keywords: Digital co-creation platforms; risk perception; policy identification; value co-creation; environmental governance.

INTRODUCTION

As climate change intensifies drought frequency worldwide, governments are increasingly challenged to communicate complex resource-management policies in ways that build public understanding and participation (IPCC, 2023). In Taiwan, recurring droughts have disrupted both industrial and agricultural production, triggering debates over water pricing and allocation (Chiueh & Huang,

2015). Although government agencies have introduced transparent data portals and participatory platforms, citizens often remain skeptical of fairness and necessity (Zhao & Tang, 2023). Digital co-creation platforms provide a potential solution by allowing citizens to visualize risk data, engage interactively with policy scenarios, and receive motivational feedback (Tseng & Kuo, 2023). Yet, empirical evidence remains limited regarding how specific design features influence psychological mechanisms that translate into tangible public value outcomes. This study extends previous work by focusing on category differences among value outcomes. Rather than examining generalized “engagement,” we differentiate economic, social, and environmental value co-creation as distinct yet interrelated dimensions (Vagena et al., 2024). We explore how digital design features shape citizens' cognitive and attitudinal responses—risk perception and policy identification—that underpin each dimension of value creation.

THEORETICAL BACKGROUND AND HYPOTHESIS DEVELOPMENT

Information Transparency and Risk Perception

Information transparency reflects the degree to which citizens can access, understand, and verify policy-related data (Kang, 2023). Transparent visualization of drought indicators (e.g., reservoir levels, rainfall deficits) reduces uncertainty and enhances the perceived credibility of institutions (Grimmelikhuijsen et al., 2013). When citizens perceive clear causal links between water conditions, policy responses,

and expected outcomes, they experience stronger situational awareness and risk salience (Slovic, 1987). Empirical evidence in environmental psychology suggests that transparent communication increases risk perception by improving comprehension of threat severity and controllability (Luo et al., 2024). Hence:

H1: Information transparency positively influences citizens' risk perception.

Incentive Mechanisms and Risk Perception

Incentive mechanisms—such as gamified rewards, points, or recognition—provide extrinsic motivation for participation (Deci & Ryan, 2013). In digital governance, incentives not only reinforce behavior but also signal institutional responsiveness, which can legitimize policy goals (Pavlou & Gefen, 2004). In the context of environmental governance, well-designed incentives can increase citizens' attention to risks by linking individual behavior to collective benefits (Kollmuss & Agyeman, 2002). When rewards are framed as acknowledgment of responsible action rather than coercive control, they enhance both motivation and perceived relevance of environmental threats.

H2: Incentive mechanisms positively influence citizens' risk perception.

Risk Perception and Policy Identification

Risk perception represents the subjective understanding of environmental threats and personal vulnerability (van der Linden, 2017). According to the Theory of Planned Behavior (Ajzen, 1991) and protection-motivation theory (Rogers, 1975), higher perceived risk motivates individuals to align with protective policies. Policy identification is defined as citizens' cognitive and affective attachment to policy goals and values (Bamberg & Möser, 2007). It reflects internalized agreement with governmental objectives, transcending mere compliance. When citizens perceive high environmental risk, they are more likely to identify with policies that promise mitigation and resilience (Terpstra & Lindell, 2013).

H3: Risk perception positively influences policy identification.

Policy Identification and Value Co-Creation

Economic Value Co-Creation Economic value co-creation occurs when citizens support financially or through resource-saving behavior initiatives that enhance economic efficiency (Moore, 1997). Identification with policy objectives fosters willingness to engage in cost-sharing measures or efficiency investments (Wang et al., 2023).

H4a: Policy identification positively influences economic value co-creation. **Social Value Co-Creation** Social value co-creation involves collective advocacy, community engagement, and the diffusion of pro-environmental norms (Osborne et al., 2016). Identification with policy goals enhances perceived social duty, leading citizens to coordinate with others and promote shared responsibility (Antonini et al. 2015).

H4b: Policy identification positively influences social value co-creation. **Environmental Value Co-Creation** Environmental value co-creation emphasizes ecological stewardship and long-term sustainability behaviors (Steg & Vlek, 2009). When citizens internalize policy goals, they are motivated to reduce resource use and adopt sustainable lifestyles (Bolderdijk et al., 2013).

H4c: Policy identification positively influences environmental value co-creation.

Conceptual Framework

Building on the preceding hypotheses, this study proposes an integrated framework linking digital platform design features, psychological mechanisms, and multidimensional value outcomes (see Figure 1). The framework draws upon three theoretical pillars: information systems design theory, environmental psychology, and public value co-creation. First, information transparency and incentive mechanisms represent the technical-motivational architecture of a digital co-creation platform. Transparency enables

cognitive elaboration by transforming abstract resource data into interpretable and trustworthy signals (Sayogo & Pardo, 2013). Incentive mechanisms, conversely, stimulate participation through perceived autonomy, competence, and relatedness—core components of self-determination theory (Deci & Ryan, 2013). Together, these features embody the system's capacity to make policy contexts visible and actionable, thereby aligning design logic with behavioral intention formation (Venkatesh et al., 2012).

Second, risk perception serves as the initial psychological response that bridges technological affordances and policy cognition. When transparency reduces informational asymmetry and incentives highlight behavioral relevance, citizens perceive drought threats as both comprehensible and personally consequential. This cognitive activation increases motivation to engage with mitigation strategies and heightens sensitivity to institutional credibility (Slovic, 1988; Terpstra & Lindell, 2013).

Third, policy identification operates as a central attitudinal mediator that transforms perceived risk into value-driven engagement. Identification encapsulates citizens' belief that the policy's objectives resonate with their moral and social values (Bamberg & Möser, 2007). In digital governance, such alignment represents the internalization of collective goals—shifting individuals from passive compliance toward proactive collaboration (Osborne et al., 2016). By uniting cognition (risk) and emotion (identification), this stage translates awareness into legitimacy and commitment.

Finally, the framework distinguishes three dimensions of value co-creation as dependent outcomes—economic, social, and environmental—reflecting the holistic nature of public value (Moore, 1997; Ritala et al., 2021). Economic value emerges when citizens adopt resource-efficient behaviors or accept cost-sharing arrangements; social value arises from collective advocacy and network cooperation; environmental value reflects ecological

stewardship and long-term sustainability actions. Although conceptually distinct, these dimensions share a common antecedent in policy identification, suggesting that a citizen's sense of identification underpins multiple forms of contribution to the public good.

In sum, the model theorizes a sequential process in which platform features (transparency and incentives) activate risk perception, which enhances policy identification, ultimately leading to multidimensional value co-creation. This integrated pathway extends existing research by moving beyond single-outcome perspectives and by explicitly linking system design, cognitive appraisal, and public value generation within one coherent behavioral framework.

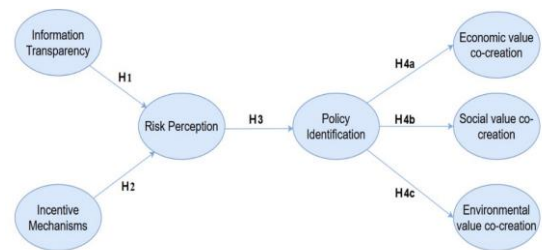


Figure 1. Conceptual Framework

METHODOLOGY

Research Context and Design

A scenario-based survey experiment was conducted using a simulated drought-risk management platform developed by the research team. The platform integrated real data from Taiwan's Water Resources Agency, including reservoir levels, drought alerts, and water-saving policies, and provided interactive feedback and incentive functions to enhance realism.

Participants

A total of 150 valid responses were collected through a nationwide online survey administered by DrSurveyDone, a professional Taiwanese market research firm. Stratified random sampling was applied to ensure

proportional representation across Taiwan’s major regions (North, Central, South, and East), as well as gender and age groups. The final sample consisted of 58% female respondents, with most participants aged between 30 and 40 years old. Respondents also reported a generally high level of prior awareness regarding drought and water-saving issues. To enhance geographic transparency and demonstrate spatial representativeness, Figure 2 presents the regional distribution of survey participants. The sampling covers all four major regions of Taiwan: Northern (41.6%), Central (19.3%), Southern (34.5%), and Eastern (4.6%). The Northern Region comprises the largest proportion of respondents, followed by the Southern Region, a pattern consistent with Taiwan’s population density and internet penetration rates. The inclusion of this regional visualization confirms that the collected data reflect perspectives from across Taiwan’s primary administrative areas.

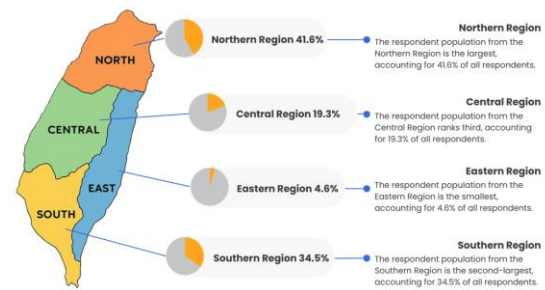


Figure 2. Regional Distribution of Survey Respondents Across Taiwan (China)

Measures

All constructs were measured using 7-point Likert scales adapted from validated prior studies (see Table 1). To ensure that the measurement instruments were reliable within the Taiwanese survey context, we computed Cronbach’s alpha values using the 150 responses collected in this study. As shown in Table 1, all constructs demonstrated α values ranging from 0.703 to 0.798. These values exceed the commonly accepted threshold of 0.70 for internal consistency (Nunnally & Bernstein, 1994), indicating that the scales are psychometrically reliable based on empirical

verification from our Taiwan sample. This confirms that the measurement instruments—originally developed in prior international research—retain adequate reliability when applied to Taiwanese respondents in the context of drought-risk governance.

Table 1. Reliability Statistics and Sources of Measurement Constructs

Construct	Cronbach’s α	Source
Information Transparency	0.798	Tseng & Kuo (2023)
Incentive Mechanisms	0.778	Deci & Ryan (2013)
Risk Perception	0.737	Slovic (1988)
Policy Identification	0.783	Bamberg & Möser (2007)
Economic Value Co-Creation	0.705	Vagena et al. (2024)
Social Value Co-Creation	0.703	Vagena et al. (2024)
Environmental Value Co-Creation	0.710	Steg & Vlek (2009)

Note: All reliability coefficients were calculated from the present study’s Taiwan dataset.

Data Analysis

Hierarchical regression analyses were conducted in SPSS using the enter method. Each regression tested one hypothesized relationship, following prior SEM verification logic.

RESULTS

Before testing the proposed hypotheses, the dataset was examined for potential violations of normality and multicollinearity. The skewness and kurtosis statistics of all constructs were within the acceptable range of ± 2 , suggesting normal distribution. Variance inflation factors (VIFs) were below 5 for all predictors, indicating the absence of multicollinearity. Reliability analysis confirmed satisfactory internal consistency, with Cronbach’s alpha values ranging from 0.705 to 0.798 across all constructs, exceeding the conventional threshold of 0.70.

Hierarchical regression analyses were conducted to examine the hypothesized relationships. The first regression model tested

the effects of information transparency and incentive mechanisms on risk perception (H1 and H2). The model was statistically significant ($F = 82.15$, $p < .001$) and explained 62.8% of the variance in risk perception ($R^2 = 0.628$). Both predictors were positively associated with risk perception: information transparency ($\beta = 0.590$, $p < .001$) and incentive mechanisms ($\beta = 0.426$, $p < .001$). These results indicate that citizens who perceived the platform as more transparent and rewarding also reported stronger awareness of drought-related risks. Therefore, H1 and H2 were supported.

The second model examined the effect of risk perception on policy identification (H3). The regression results revealed a significant positive relationship between the two constructs ($\beta = 0.548$, $p < .001$), explaining 25.6% of the variance in policy identification ($R^2 = 0.256$, $F = 50.85$, $p < .001$). This finding suggests that individuals with heightened risk perception were more likely to identify with and internalize drought-management policies. Consequently, H3 was supported.

The final set of models assessed the influence of policy identification on the three dimensions of value co-creation—economic, social, and environmental (H4a–H4c). Policy identification exerted a significant positive effect on all three dimensions. For economic value co-creation, the standardized coefficient was $\beta = 0.457$ ($p < .001$), explaining 24.1% of the variance ($R^2 = 0.241$). For social value co-creation, policy identification exhibited the strongest effect ($\beta = 0.517$, $p < .001$; $R^2 = 0.262$), while for environmental value co-creation, the relationship remained robust ($\beta = 0.486$, $p < .001$; $R^2 = 0.229$). These findings confirm that higher policy identification encourages citizens to contribute financially, socially, and ecologically to public value creation. Therefore, H4a, H4b, and H4c were all supported.

Overall, the sequence of results strongly validates the theoretical model proposed in this study. Information transparency and incentive mechanisms significantly enhance citizens' risk perception (supporting H1–H2), which in turn strengthens their policy identification

(supporting H3). This identification subsequently fosters multidimensional value co-creation across economic, social, and environmental domains (supporting H4a–H4c). The coherent pattern of results corroborates the hypothesized chain of cognitive and attitudinal processes through which digital platform design contributes to sustainable governance outcomes.

DISCUSSION AND CONCLUSION

Discussion

The findings provide robust empirical support for the proposed mechanism linking digital platform design, cognitive appraisal, and public value creation. Both information transparency and incentive mechanisms significantly increased citizens' risk perception, affirming that design features jointly enhance environmental awareness and behavioral relevance. Transparency reduces informational asymmetry and strengthens cognitive clarity, consistent with prior work showing that accessible, trustworthy data improve perceived legitimacy in digital governance (Grimmelikhuijsen et al., 2013; Sayogo & Pardo, 2013). By visualizing reservoir levels and policy rationales, transparent interfaces transform abstract drought communication into concrete risk understanding, thereby heightening citizens' sense of urgency and fairness (Sly, 2000; Terpstra & Lindell, 2013). The positive effect of incentive mechanisms on risk perception extends motivational theory. Although incentives are often regarded as extrinsic reinforcers (Deci & Ryan, 2013), their presence within participatory systems can heighten psychological engagement when interpreted as recognition of competence or civic contribution. This interpretation aligns with findings that symbolic rewards can amplify intrinsic motivation for sustainable behavior (Bolderdijk et al., 2013). Hence, digital governance platforms should deploy incentives that acknowledge collective responsibility rather than merely elicit compliance. The significant relationship between risk perception and policy identification underscores cognitive evaluation as the

foundation of policy alignment. Individuals who perceive higher environmental risk tend to regard conservation policies as necessary and legitimate, a pattern consistent with the Theory of Planned Behavior (Ajzen, 1991) and protection-motivation theory (Rogers, 1983). Heightened risk awareness thus cultivates psychological ownership of policy goals and strengthens citizens' perceived duty toward collective resource management (van der Linden, 2017). Finally, policy identification emerged as the attitudinal bridge connecting cognition to multidimensional value co-creation. Its strongest effect on social value, followed by environmental and economic value, suggests that identification primarily promotes relational and community-oriented engagement. This hierarchy echoes social identity theory (Antonini et al. 2015) and recent studies on co-creation (Osborne et al., 2016), emphasizing that internalized group values translate into collaboration and advocacy rather than purely financial contribution. Overall, the study extends research on digital public-value creation (Ritala et al., 2021) by demonstrating that transparency and incentives activate risk perception and identification, which together generate economic, social, and environmental benefits—illustrating how thoughtful digital design can transform awareness into sustainable collective action.

Theoretical Implications

This study enriches the literature on digital governance by empirically validating how specific platform features activate psychological pathways that foster multidimensional value creation. First, the strong impact of information transparency on risk perception corroborates prior findings that open and intelligible information builds both trust and awareness (Grimmelikhuijsen et al., 2013). Second, incentive mechanisms complement cognitive engagement with motivational reinforcement, consistent with self-determination theory (Deci & Ryan, 2013). Third, the mediating role of policy identification demonstrates that citizens'

internalization of policy values is crucial for converting perceived risk into cooperative behaviors across economic, social, and environmental domains.

Practical Implications

For policymakers, these results underscore the importance of combining data transparency with participatory incentives in digital platforms to enhance drought-risk communication. Designing interactive dashboards that visualize water security and reward sustainable behaviors can transform passive awareness into shared responsibility.

Limitations and Future Research

This study has several limitations that offer opportunities for future research. First, although the sample size of 150 respondents is adequate for the analytical methods used, it remains relatively modest and limited to adults in Taiwan. Future studies should expand the sample to include a larger and more demographically diverse population—such as participants across different age groups, socioeconomic backgrounds, and levels of digital literacy—to enhance generalizability. Cross-regional or cross-country comparisons would also help determine whether the psychological mechanisms identified in this study operate similarly in different cultural, institutional, and environmental contexts. Second, the study employed a scenario-based survey, which, while effective for controlling stimuli, may not fully capture the complexity of real-world user interactions with digital governance platforms. Future research could incorporate behavioral data, field experiments, or platform-usage analytics to triangulate findings and provide a more comprehensive understanding of citizens' engagement processes. Third, the research focused exclusively on drought-risk management. Applying the proposed framework to other public governance domains—such as air quality monitoring, disaster preparedness, or energy conservation—would help validate the robustness of the model across diverse environmental issues. Incorporating potential

moderating factors (e.g., environmental values, trust in government, or prior experience with digital platforms) may also reveal subgroup differences and deepen theoretical insights into the antecedents of value co-creation. Overall, expanding sample diversity, integrating behavioral data, and extending the framework to additional policy contexts will further strengthen the theoretical and practical contributions of future research.

CONCLUSION

The findings confirm that digital co-creation platforms can foster public value not only by informing citizens but also by aligning perceptions, identification, and motivations. By bridging cognitive risk awareness with affective policy attachment, transparency and incentive mechanisms serve as twin levers for sustainable governance.

ACKNOWLEDGMENT

The authors would like to express their sincere gratitude to the Global Drought Investigation and Research Center and National Central University (NCU) for their generous support.

REFERENCES

- Ajzen I. (1991). The theory of planned behavior. *Organizational Behavior and Human Decision Processes*. 50(2): 179–211.
- Antonini M., Hogg M. A., Mannetti L., Barbieri B., Wagoner J. A. (2015). Motivating citizens to participate in public policymaking: Identification, trust and cost-benefit analyses. *Journal of Social and Political Psychology*. 3(2): 195–216.
- Armstrong C. L., Baldinelli S. E., Smith K. H., Medcalf S. (2025). Expertise or experience: Comparing discussion of drought between audiences and agencies in Nebraska, Kansas, Iowa, and Missouri. *Weather, Climate, and Society*. 17(3): 515–528.
- Bamberg S., Möser G. (2007). Twenty years after Hines, Hungerford, and Tomera: A new meta-analysis of psycho-social determinants of pro-environmental behaviour. *Journal of Environmental Psychology*. 27(1): 14–25.
- Bolderdijk J. W., Steg L., Geller E. S., Lehman P. K., Postmes T. (2013). Comparing the effectiveness of monetary versus moral motives in environmental behavior. *Journal of Environmental Psychology*. 34: 150–158.
- Chiueh Y.-W., Huang C. C. (2015). The willingness to pay by industrial sectors for agricultural water transfer during drought periods in Taiwan. *Environment and Natural Resources Research*. 5(1): 38–46.
- Deci E. L., Ryan R. M. (2013). *Intrinsic motivation and self-determination in human behavior*. Springer, New York. (ISBN 978-1-4899-2271-7). 450p.
- Grimmelikhuisen S., Porumbescu G., Hong B., Im T. (2013). The effect of transparency on trust in government: A cross-national comparative experiment. *Public Administration Review*. 73(4): 575–586.
- Kollmuss A., Agyeman J. (2002). Mind the gap: Why do people act environmentally and what are the barriers to pro-environmental behavior? *Environmental Education Research*. 8(3): 239–260.
- Leone de Castris A. (2024). Types of platform transparency: An analysis of discourse around transparency and global digital platforms. *Public Integrity*. 27(3): 340–354.
- Moore M. H. (1997). *Creating public value: Strategic management in government*. Harvard University Press, Cambridge, MA. (ISBN 978-0-674-17558-2). 450p.
- Osborne S. P., Radnor Z., Strokosch K. (2016). Co-production and the co-creation of value in public services: A suitable case for treatment? *Public Management Review*. 18(5): 639–653.
- Pavlou P. A., Gefen D. (2004). Building effective online marketplaces with institution-based trust. *Information Systems Research*. 15(1): 37–59.
- Ritala P., Albareda L., Bocken N. (2021). Value creation and appropriation in economic, social, and environmental domains. *Journal of Cleaner Production*. 290: 125796.
- Rogers R. W. (1983). Cognitive and physiological processes in fear appeals and attitude change: A revised theory of protection motivation. In Cacioppo J. T., Petty R. E. (eds). *Social psychophysiology*. Guilford Press, New York. 153–176.
- Sayogo D. S., Pardo T. A. (2013). Exploring the determinants of scientific data sharing: Understanding the link between information transparency, trust, and citizen participation. *Government Information Quarterly*. 30(4): S19–S31.

- Slovic P. (1988). Risk perception. *Carcinogen Risk Assessment*. Springer, 236(4799): 280–285.
- Sly T. (2000). The perception and communication of risk: A guide for the local health agency. *Canadian Journal of Public Health*. 91(2): 153–156.
- Steg L., Vlek C. (2009). Encouraging pro-environmental behaviour: An integrative review and research agenda. *Journal of Environmental Psychology*. 29(3): 309–317.
- Terpstra T., Lindell M. K. (2013). Citizens' perceptions of flood hazard adjustments: An application of protection motivation theory. *Environment and Behavior*. 45(8): 993–1018.
- van der Linden S. (2017). Determinants and measurement of climate change risk perception, worry, and concern. *Journal of Environmental Psychology*. 50: 7–16.
- Venkatesh V., Thong J. Y. L., Xu X. (2012). Consumer acceptance and use of information technology: Extending the unified theory of acceptance and use of technology. *MIS Quarterly*. 36(1): 157–178.
- Wang Z., Liu H., Li T., Zhou L., Zhou M. (2023). The impact of internet use on citizens' trust in government: The mediating role of sense of security. *Systems*. 11(1): 47.

Part 3

GREEN DEVELOPMENT: PERSPECTIVES OF THE EARTH, MINE AND ENVIRONMENTAL SCIENCES

DOI: 10.15625/vap.2025.0228

Assessment of cumulative impacts on coastal marine ecosystems in Ha Tinh Province

Nguyen Tai Tue^{1,2*}, Luu Viet Dung^{1,2}, Pham Lan Anh², Nguyen Doanh Khoa², Tran Dang Quy², Mai Trong Nhuan²

¹Faculty of Geology, VNU University of Science, 334 Nguyen Trai, Thanh Xuan, Hanoi, Vietnam

²VNU Key Laboratory of Geoenvironment and Climate change Response, 334 Nguyen Trai, Thanh Xuan, Hanoi, Vietnam

*Email: tuenguyentai@hus.edu.vn

Abstract: The rapid expansion of coastal economic zones in Vietnam has intensified anthropogenic pressures on marine ecosystems, creating an urgent need for integrated management tools. This study presents the first spatially explicit cumulative impact assessment (CIA) for the coastal marine ecosystems of Ha Tinh province, a region of significant industrial development in central Vietnam. A GIS-based model is used to synthesize spatial data on 10 marine ecosystems and 10 anthropogenic pressures within the region. The analysis reveals that while the mean cumulative impact index (CII) across the 1,340 km² study area is low (0.27), impacts are highly concentrated in specific hotspots. The Vung Ang Economic Zone and Son Duong Port complex emerged as the most severe hotspot, with CII scores reaching up to 16.5, driven by the co-location of heavy industry, thermal power plants, and dense maritime traffic with sensitive coral reef ecosystems. Secondary hotspots were identified in major estuaries, resulting from the synergistic effects of fisheries, aquaculture, and urban runoff. These findings provide a quantitative, evidence-based foundation for implementing Vietnam's Marine Spatial Planning (MSP) strategy at a provincial level. The resulting CIA map serves as a critical decision-support tool for zoning, enabling targeted mitigation efforts in high-impact areas and prioritizing conservation in low-impact zones, thereby guiding the region towards sustainable marine ecosystem management.

Keywords: Cumulative impact, marine ecosystem, Ha Tinh, spatial analysis, ecosystem-based management.

INTRODUCTION

Coastal and marine ecosystems are globally recognized as hotspots of biodiversity and critical providers of essential ecosystem services. However, these ecosystems are increasingly facing a complex and intensifying array of human pressures (Halpern et al., 2008). Activities such as industrial development, maritime shipping, intensive aquaculture, fishing, and land-based pollution converge in these dynamic zones, creating a mosaic of overlapping stressors (Depellegrin, 2016). Traditional environmental management, which has historically relied on project-specific Environmental Impact Assessment (EIA), is fundamentally inadequate to address these challenges (Adams, 2005). By evaluating projects in isolation, EIA fail to account for the additive, synergistic, or antagonistic effects that arise when multiple stressors interact across space and time (Micheli et al., 2013). The concept of CIA has emerged as an essential, ecosystem-based management paradigm to address this critical governance gap (ICES, 2019). CIA provides a comprehensive framework to analyze and manage the total environmental effects resulting from the accumulation of past, present, and reasonably foreseeable future human activities. This approach shifts the focus from mitigating individual impacts to managing the overall

anthropogenic footprint on entire ecosystems (Halpern et al., 2009).

Over the past decades, significant advancements in methodology have established a robust, quantitative, and spatially explicit framework for conducting marine CIA. The dominant approach, pioneered by Halpern et al. (2008), integrates three fundamental layers of geospatial data: (i) the distribution of ecosystem components, such as distinct habitats or species groups; (ii) the spatial distribution and intensity of various anthropogenic pressures; and (iii) a vulnerability matrix that scores the sensitivity of each ecosystem component to each specific pressure. This model has become an international standard, with its flexibility demonstrated through numerous regional applications (Halpern et al., 2009; Depellegrin, 2016). For instance, a comprehensive assessment in the Baltic Sea identified 18 primary seabed habitat types and 13 key pressures, using structured expert judgment to assign vulnerability weights based on criteria of impact severity, resistance, and recovery time (Korpinen et al., 2012). These cases illustrate the evolution of the CIA framework from a universal model into a highly adaptable tool, capable of being tailored to specific regional ecologies, data availability, and management priorities.

The coastal zone of Vietnam exemplifies the urgent need for a CIA perspective. It is a nexus of intense and accelerating economic activity, hosting 79% of the nation's industrial parks, major shipping corridors, extensive oil and gas exploration, rapidly expanding aquaculture, and a burgeoning tourism sector (MONRE, 2021). These multi-sectoral developments exert a cascade of pressures on marine ecosystems, including physical habitat destruction from coastal construction and dredging, chronic pollution from industrial and urban effluent, biodiversity loss from destructive fishing practices, and altered hydrological regimes from upstream damming (Do et al., 2025). Scientific research in Vietnam has documented the impacts of individual

stressors such as heavy metal accumulation in sediments or the localized effects of titan mining (Xuan and Quang, 2022). However, no studies have yet been published that comprehensively assess the combined and cumulative impacts of multiple, co-occurring pressures on the nation's marine ecosystems. To address this scientific and management gap in Vietnam, this study develops the first spatially explicit CIA for a coastal region experiencing intensive multi-sectoral development. The primary goal is to quantify and map the cumulative impacts of various human-induced pressures on coastal marine ecosystems.

MATERIALS AND METHODS

Study area

The study was conducted in the coastal zone of Ha Tinh province, located on Vietnam's North Central Coast (Fig. 1). This region represents a critical nexus of economic development and environmental pressure, making it an exemplary location for a CIA. The geographical scope covers a 137 km stretch of coastline and extends six nautical miles (approx. 11 km) offshore, encompassing a total marine area of approximately 1,340 km². The area includes four major estuaries: Cua Hoi, Cua Sot, Cua Nhuong, and Cua Khau, which serve as important conduits for terrestrial runoff and hubs for local fisheries.

This area is characterized by an intense and accelerating convergence of multi-sectoral human activities. It is home to the Vung Ang Economic Zone (VAEZ), a major national industrial hub that includes a large-scale steel complex, thermal power plants, and extensive port infrastructure. The zone is a focal point for heavy industry, extensive maritime shipping, and significant mineral resource extraction, including one of the region's largest iron ore mines. These industrial pressures are compounded by widespread agriculture and aquaculture operations, numerous traditional fishing villages, and a burgeoning tourism sector developing along its scenic beaches. The combination of a high-density population,

major industrial installations, critical port and shipping activities, and various resource-use sectors creates a complex mosaic of overlapping anthropogenic stressors. This makes the Ha Tinh coastal zone a compelling case study for assessing the cumulative impacts of rapid and multifaceted development on a sensitive marine ecosystem.

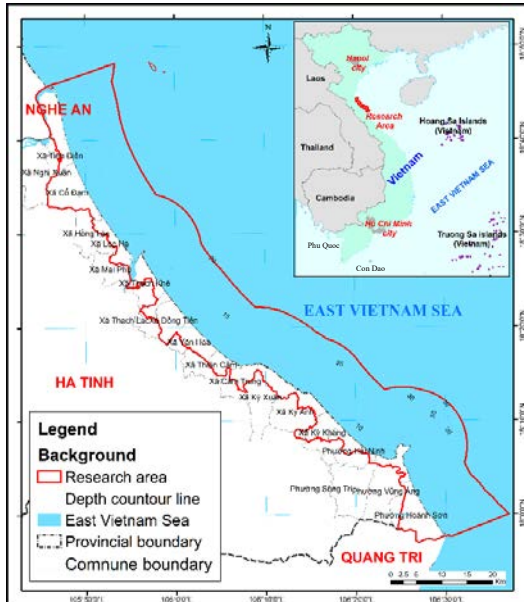


Figure 1. The coastal waters of Ha Tinh province, Vietnam

Cumulative impact modelling framework

Marine ecosystems are increasingly subjected to a multitude of anthropogenic pressures that operate across various spatial and temporal scales. The CIA evaluates the total environmental effect resulting from the accumulation and interaction of past, present, and reasonably foreseeable future actions. Cumulative impacts are defined as the result of interactions between multiple activities, where each may have an insignificant effect in isolation but becomes significant when considered in aggregate (Dickert and Tuttle, 1985). These interactions are complex and can be additive (the sum of individual effects), synergistic (the combined effect is greater than the sum of its parts), or antagonistic. Understanding these dynamics is crucial for preventing large-scale ecosystem degradation.

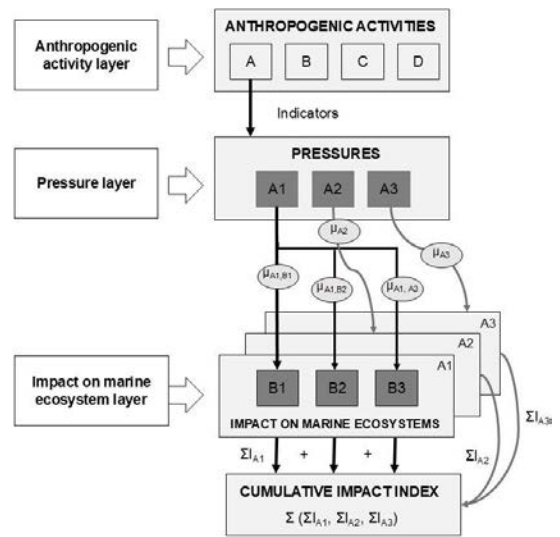


Figure 2. Ecosystem-based cumulative impact assessment process (Adapted from Halpern et al. (2008))

The predominant methodology for regional-scale marine CIA is the ecosystem-based framework pioneered by Halpern et al. (2008). This spatially explicit model integrates three critical data layers using Geographic Information Systems (GIS): 1) maps of the distribution and intensity of anthropogenic pressures (e.g., fishing, shipping, pollution); 2) maps of the distribution of ecosystem components (e.g., coral reefs, seagrass meadows, specific benthic habitats); and 3) a vulnerability matrix that weights the sensitivity of each ecosystem component to each pressure (Fig. 2).

The cumulative impact index (I) for any given location is calculated as the sum of all pressure intensities (P_i) acting upon the ecosystems present (E_j), weighted by their specific vulnerability (μ_{ij}), commonly expressed as:

$$I = \sum_{i=1}^n \sum_{j=1}^m P_i \times E_j \times \mu_{ij} \quad (1)$$

Cumulative impact assessment methods

This study employed a spatially explicit, ecosystem-based CIA framework to quantify and map the combined effects of human activities on the coastal marine ecosystem of Ha Tinh province (Fig. 2). The methodology

integrated three core geospatial data layers within a standardized grid system (1 km × 1 km cells). First, the spatial distribution of 10 distinct marine ecosystem types was mapped, with their presence in each grid cell recorded using a binary system (1 = present, 0 = absent). Second, we compiled data on 11 human activities to assess the spatial intensity of 10 resulting anthropogenic pressures, such as pollution, habitat alteration, and resource extraction. The intensity of each pressure, whether represented by point, line, or polygon data, was calculated for each grid cell and subsequently normalized to a dimensionless 0-1 scale to allow for direct comparison. Third, a vulnerability matrix was developed through expert consultation and literature review to assign a weight score to each ecosystem-pressure interaction, reflecting the sensitivity of each ecosystem to each specific pressure based on criteria including impact severity and recovery time. The final Cumulative Impact Index (CII) for each grid cell was calculated by the equation (1). The resulting map visualizes the spatial distribution of cumulative impacts, enabling the identification of high-pressure "hotspots" and providing a critical scientific basis for marine spatial planning, conservation prioritization, and ecosystem-based management. The spatial data processing was carried out using ArcGIS software version 10.3.

Ecosystem mapping data and spatial datasets, including maps of anthropogenic activities, sediment distribution, and the characteristics of water and sediment environments were collected under the framework of the project (Code: TNMT.2021.562.09) funded by Ministry of Natural Resources and Environment.

RESULTS AND DISCUSSION

Spatial distribution of marine ecosystems

The coastal zone of Ha Tinh province supports a diverse mosaic of marine and coastal ecosystems, which were classified into ten distinct types for this assessment based on substrate, depth, geomorphology, and biological characteristics. The dominant

habitats are soft-bottom subtidal ecosystems, which cover the vast majority of the study area. These include permanently submerged sandy bottoms at depths less than 6 meters (115.12 km²) and greater than 6 meters (1,156.4 km²), as well as sand-mud bottoms at similar depth ranges (161.63 km² combined). These expansive soft-bottom environments serve as important fishing grounds for local small-scale fisheries. Intertidal habitats are characterized primarily by extensive sandy shores (33.1 km²), which support a significant tourism industry, and smaller, ecologically vital mud-sand flats (2.1 km²) located in the Cua Sot and Cua Khau estuaries, providing critical feeding grounds for migratory waterbirds.

Despite their limited spatial extent, several high-value and sensitive ecosystems are present. Mangrove forests are concentrated within the main estuaries (Cua Hoi, Cua Sot, Cua Nhuong, Cua Khau), covering a total area of 691.9 ha (Tuan and Tu, 2015). Although generally underdeveloped compared to other regions in Vietnam, these mangroves play an important role in shoreline protection, erosion control, and maintaining biodiversity. Coral reefs are highly restricted, with a very small and fragmented distribution estimated at only 215 m² around Son Duong Island (Van et al., 2020). Other key ecosystems include estuarine water bodies (12.4 km²), which are hotspots of biodiversity due to the mixing of fresh and saltwater, and rocky shores (0.45 km²), which contribute to coastal stability.

The spatial heterogeneity of these ecosystems results in distinct patterns of biodiversity across the study area. An ecosystem diversity index, calculated for each grid cell, ranged from 1 to 1.85, indicating areas where multiple habitat types co-occur. The highest diversity "hotspots" were identified in three main locations: the Cua Sot estuary, the nearshore marine area extending from Cua Nhuong to Ky Phu, and the waters between Mui Ron and Son Duong island. These hotspots are characterized by the presence of the region's most sensitive habitats, namely mangrove forests and coral reefs. This detailed

spatial characterization of ecosystem distribution, condition, and diversity provides the critical ecological baseline for the CIA, enabling a precise evaluation of how and where overlapping anthropogenic pressures may threaten the region's most valuable and vulnerable marine assets.

Anthropogenic activities

The coastal zone of Ha Tinh province is subject to a complex and intensifying array of anthropogenic activities, with eleven primary types spatially mapped for this assessment. The most significant concentration of pressure originates from the VAEZ in the southern part of the study area, a major national hub for heavy industry, including a large-scale steel complex and thermal power plants. This industrial core is supported by extensive port infrastructure, including the Vung Ang-Son Duong deep-water port complex, which accommodates vessels up to 250,000 DWT. Consequently, maritime shipping density is highest in the waters off Vung Ang, with other significant traffic corridors connecting to the fishing ports of Cua Sot, Cua Nhuong, and Cua Hoi. These industrial and port developments are associated with significant physical alteration of the coastline through widespread land reclamation and the construction of numerous piers, breakwaters, and groynes, particularly within the Ky Anh commune.

Distributed more broadly across the region are other significant pressures. Aquaculture has expanded rapidly, with the coastal districts now accounting for over 4,914 hectares, representing 65.7% of the province's total aquaculture area (HTSO, 2020a; 2020b; 2021). This activity introduces risks of organic and chemical pollution from untreated effluent. Land-based pressures include extensive mineral extraction, notably the Thach Khe iron ore mine and ilmenite mining. Furthermore, in response to coastal erosion, a continuous network of hard infrastructure, including seawalls and dikes, has been constructed along large segments of the 137 km coastline. The overlapping nature of various intensive activities, including point-source

industrial discharges, port construction, and the diffuse pressures from shipping and aquaculture, creates a complex matrix of stressors (Gimpel et al., 2013). The quantification and mapping of these activities provide the foundational pressure layer for the CIA framework, enabling the identification of high-risk "hotspots" where multiple pressures converge on sensitive ecosystems (Halpern et al., 2009).

Intensity and distribution of cumulative pressures

The synthesis of all ten individual pressure layers resulted in a cumulative pressure index that varied substantially across the study area, ranging from a minimum of zero to a maximum of 20.26. The mean value of the index was 1.89, while the median value was significantly lower at 0.95. This marked divergence between the mean and median is statistically significant, indicating a strongly right-skewed distribution (Micheli et al., 2013). Such a distribution reveals that the overall anthropogenic burden is not spread evenly across the coastal zone. Instead, it is characterized by large expanses of the marine environment that experience relatively low pressure, while a small proportion of the area is subjected to exceptionally high and concentrated levels of cumulative stress. This finding validates a management approach that prioritizes interventions in these specific, high-pressure zones (Halpern et al., 2008).

To further elucidate the spatial patterns, the cumulative pressure index was classified into five distinct intensity levels (Fig. 3). The analysis reveals that a majority of the study area, 1171 grid cells corresponding to 55.3%, falls into the "Low" pressure category (index value 0–1) (Fig. 2). These areas are predominantly located in offshore waters with depths greater than 10 m and in terrestrial zones situated far from the immediate coastline. A further 427 cells (20.2%) are classified as "Relatively Low" pressure (1–2), typically forming a transitional zone between the low-pressure offshore regions and the more impacted nearshore waters. Conversely, areas of significant concern are clearly delineated. The "Medium" pressure

category (2–5) accounts for 322 cells (15.2%) and encompasses most of the immediate coastal strip and shallow nearshore waters where human activities begin to concentrate. More critically, 163 cells (7.7%) are classified as "Relatively High" pressure (5–10), and 34 cells (1.6%) are classified as "High" pressure (>10). These high-pressure zones, though representing less than 10% of the total area, are the epicenters of anthropogenic impact and are almost exclusively located within and around major industrial and port complexes.

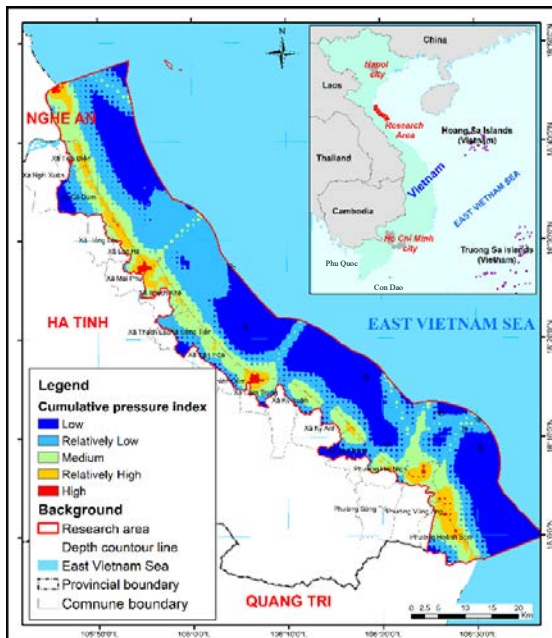


Figure 3. Cumulative pressure index in the coastal waters of Ha Tinh Province

Cumulative impacts on marine ecosystems

The CIA synthesized the effects of anthropogenic pressures across the coastal marine ecosystems to produce a spatially explicit the CII. This index quantifies the total anthropogenic burden on the ecosystems within the study area, providing a critical tool for identifying high-risk zones and informing management priorities.

The CII for the coastal marine ecosystems of Ha Tinh province ranged from 0 to 16.5, with a mean value of 0.27. The spatial distribution of this impact was highly heterogeneous and strongly skewed, indicating that severe impacts

are concentrated in specific, localized areas rather than being widespread (Fig. 4). A five-level classification system was used to categorize the intensity of the cumulative impact across the 1 km² grid cells: Low Impact (Index: 0–1): 1973 cells (93.2%); Relatively Low Impact (Index: 1–2): 42 cells (2.0%); Medium Impact (Index: 2–5): 64 cells (3.0%); Relatively High Impact (Index: 5–10): 34 cells (1.6%); High Impact (Index: >10): 4 cells (0.2%). The spatial analysis reveals that the vast majority of the study area (93.2%) experiences low cumulative impact. These zones are predominantly located in offshore waters with depths greater than 6 meters and in terrestrial areas situated far from the immediate coastline, where human activities and ecosystem diversity are both limited. Zones of relatively low and medium impact typically form transitional bands along the coast.

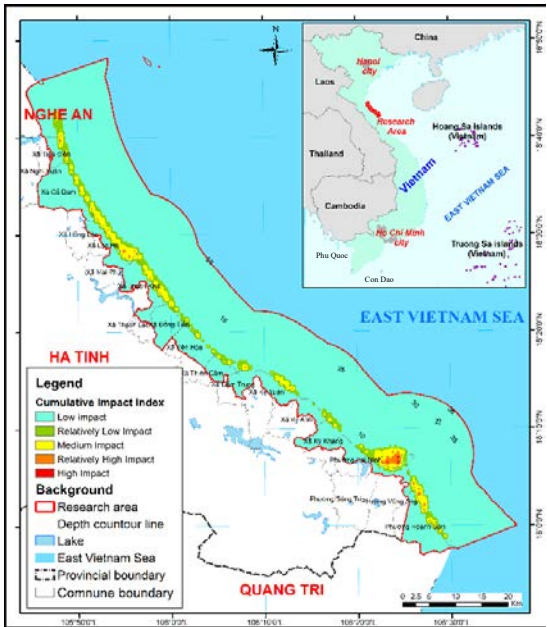


Figure 4. Cumulative Impact Index on marine ecosystems of Ha Tinh Province

The most significant ecological finding is the identification of distinct cumulative impact hotspots. Areas classified as "Relatively High" and "High" impact, while constituting only 1.8% of the total area, represent zones of intense, overlapping pressures. The primary hotspot, containing all four of the "High"

impact grid cells and a significant concentration of "Relatively High" impact cells, is located within Vung Ang Bay. This intense impact is driven by the co-location of numerous high-pressure activities, including the operations of the Vung Ang deep-water port and its associated economic zone, the Vung Ang I and II thermal power plants, a major steel manufacturing facility, and oil and gas transfer stations. These high-impact zones overlap with several key coastal ecosystems. The pressures within Vung Ang Bay directly affect intertidal sandy shores, rocky coasts, and the region's only documented coral reef ecosystems located near Son Duong island. These habitats experience a combination of severe pressures, including seabed destruction, altered sea currents, and pollution from industrial and maritime sources. The uneven distribution of cumulative impacts highlights the vulnerability of these specific ecosystems and provides a clear, data-driven basis for prioritizing management interventions and conservation efforts in these identified hotspots (Foden et al., 2011). This finding emphasizes a critical lesson for coastal development: the environmental costs of industrialization increase significantly when it occurs near sensitive ecosystems. In contrast, the secondary hotspots identified in the Cua Sot and Cua Nhuong estuaries reveal a different, yet equally important, driver of cumulative impact. Here, the "medium-high" CII are not the result of a single large industrial source but rather the synergistic accumulation of numerous smaller-scale, diffuse pressures. Widespread aquaculture, dense small-scale fishing fleets, and urban and agricultural runoff combine to degrade water quality and impact the mangrove and mudflat ecosystems that characterize these estuaries. This highlights the capacity of CIA to identify and quantify threats arising not only from large point sources but also from the collective weight of widespread, non-point source activities that are often overlooked in traditional environmental impact assessments (Depellegrin, 2016).

Implications for marine spatial planning (MSP)

This study serves as a crucial bridge between high-level policy and practical, on-the-ground management. Vietnam has established an national MSP strategy aimed at fostering a sustainable blue economy, but its successful implementation depends on the availability of robust, spatially explicit scientific data at the regional and provincial levels (Foley et al., 2010, Fernandes et al., 2020). The cumulative impact map generated in this study provides the first such quantitative evidence base for Ha Tinh province, effectively serving as a foundational "conflict and compatibility" map to guide zoning decisions. The application of these findings to MSP is direct and actionable.

- For high-impact hotspots: The results for Vung Ang Gulf strongly support designating it as a specialized management zone focused on impact mitigation. This would entail implementing stringent pollution controls on industrial effluent, establishing vessel traffic management schemes to minimize disturbance, and initiating targeted ecosystem restoration programs, particularly for the threatened coral reefs (Korpinen and Andersen, 2016). Future development proposals within this zone must be subjected to rigorous environmental assessments that explicitly account for their contribution to the already high cumulative impact baseline.

- For low-impact zones: The extensive offshore areas identified with the low CII represent valuable opportunities for proactive conservation (Hodgson et al., 2019). These zones could be prioritized for the establishment of marine protected areas, designated as areas for sustainable, low-impact fisheries, or zoned for non-extractive uses like eco-tourism. By spatially separating conservation priorities from intensive development, MSP can provide a pathway to achieve the national goal of balancing economic growth with environmental protection.

This approach moves beyond the simplistic and often paralyzing "environment versus economy" debate. By spatially delineating impacts, the CIA demonstrates that large-scale economic development and marine conservation are not necessarily mutually exclusive, provided they are planned and zoned intelligently (Menegon et al., 2018). The impact map serves as an objective, evidence-based tool for establishing these boundaries, allowing planners to concentrate intensive activities in already impacted areas while directing conservation efforts and low-impact activities to less disturbed zones (Fernandes et al., 2020). Furthermore, the map provides a critical scientific baseline against which the effectiveness of future management interventions can be quantitatively measured, forming the backbone of an adaptive management cycle.

CONCLUSIONS AND RECOMMENDATIONS

This study presents the first quantitative, spatially explicit CIA for the coastal marine ecosystems of Ha Tinh province, Vietnam. The principal conclusion is that anthropogenic pressures are not uniformly distributed but are intensely concentrated in specific hotspots. The Vung Ang industrial and port complex constitutes the most severe hotspot, where the overlap of multiple high-intensity pressures with sensitive ecosystems poses a significant and ongoing risk to the regional marine biodiversity and ecosystem health. This research contributes in two significant ways. First, it provides a critical baseline assessment of the environmental status of a key economic park in Vietnam. Second, it demonstrates the successful adaptation and application of an internationally recognized CIA framework, establishing a replicable methodology that can be scaled to other coastal provinces to support national environmental management goals. It is strongly recommended that provincial authorities in Ha Tinh formally adopt the cumulative impact map as a core decision-support tool for the development and implementation of their MSP. This map should

guide zoning decisions, separating areas of intensive economic use from areas prioritized for conservation and sustainable use.

ACKNOWLEDGMENTS

This research is funded by the Vietnam Ministry of Natural Resources and Environment under the project code: TNMT.2021.562.09.

REFERENCES

- Adams, S. M. (2005). Assessing cause and effect of multiple stressors on marine systems. *Marine Pollution Bulletin* 51(8): 649-657.
- Ministry of Natural Resources and Environment (MONRE) (2021). National Report on the Marine and Island Environment System for the Period 2016-2020 (*In Vietnamese*).
- Ha Tinh Provincial Statistical Office (HTSO) (2020a). Ha Tinh statistical yearbook 2020 (*In Vietnamese*).
- Ha Tinh Provincial Statistical Office (HTSO) (2020b). Key statistical data for the period 2016-2020 (*In Vietnamese*).
- Ha Tinh Provincial Statistical Office (HTSO) (2021). Report on the Socio-Economic Situation in December and the Whole Year 2021 (*In Vietnamese*).
- Depellegrin, D. (2016). Assessing cumulative visual impacts in coastal areas of the Baltic Sea. *Ocean & Coastal Management* 119: 184-198.
- Dickert, T. G. and Tuttle, A. E. (1985). Cumulative impact assessment in environmental planning: A coastal wetland watershed example. *Environmental Impact Assessment Review* 5(1): 37-64.
- Do, C. V., Pham, N. T. and Nguyen, M. K. (2025). Marine Spatial Planning Toward the Goal of Blue Economy Development: An Analytical Perspective of Vietnam. *Handbook of Sustainable Blue Economy*, Springer: 1-36.
- Fernandes, M. L., Sousa, L. P., Quintela, A., Marques, M., Reis, J., Simão, A. P., Castro, A. T., Marques, J. M. and Alves, F. L. (2020). Mapping the future: Pressures and impacts in the Portuguese maritime spatial planning. *Science of The Total Environment* 715: 136863.
- Foden, J., Rogers, S. I. and Jones, A. P. (2011). Human pressures on UK seabed habitats: a cumulative impact assessment. *Marine Ecology Progress Series* 428: 33-47.

- Foley, M. M., Halpern, B. S., Micheli, F., Armsby, M. H., Caldwell, M. R., Crain, C. M., Prahler, E., Rohr, N., Sivas, D., Beck, M. W., Carr, M. H., Crowder, L. B., Emmett Duffy, J., Hacker, S. D., McLeod, K. L., Palumbi, S. R., Peterson, C. H., Regan, H. M., Ruckelshaus, M. H., Sandifer, P. A. and Steneck, R. S. (2010). Guiding ecological principles for marine spatial planning. *Marine Policy* 34(5): 955-966.
- Gimpel, A., Stelzenmüller, V., Cormier, R., Floeter, J. and Temming, A. (2013). A spatially explicit risk approach to support marine spatial planning in the German EEZ. *Marine Environmental Research* 86: 56-69.
- Halpern, B. S., Kappel, C. V., Selkoe, K. A., Micheli, F., Ebert, C. M., Kontgis, C., Crain, C. M., Martone, R. G., Shearer, C. and Teck, S. J. (2009). Mapping cumulative human impacts to California Current marine ecosystems. *Conservation letters* 2(3): 138-148.
- Halpern, B. S., Walbridge, S., Selkoe, K. A., Kappel, C. V., Micheli, F., D'Agrosa, C., Bruno, J. F., Casey, K. S., Ebert, C., Fox, H. E., Fujita, R., Heinemann, D., Lenihan, H. S., Madin, E. M. P., Perry, M. T., Selig, E. R., Spalding, M., Steneck, R. and Watson, R. (2008). A Global Map of Human Impact on Marine Ecosystems. *Science* 319(5865): 948-952.
- Hodgson, E. E., Halpern, B. S. and Essington, T. E. (2019). Moving Beyond Silos in Cumulative Effects Assessment. *Frontiers in Ecology and Evolution* 7(211).
- ICES (2019). Working group on cumulative effects assessment approaches in management (WGCEAM).
- Korpinen, S. and Andersen, J. H. (2016). A Global Review of Cumulative Pressure and Impact Assessments in Marine Environments. *Frontiers in Marine Science* 3(153).
- Korpinen, S., Meski, L., Andersen, J. H. and Laamanen, M. (2012). Human pressures and their potential impact on the Baltic Sea ecosystem. *Ecological Indicators* 15(1): 105-114.
- Menegon, S., Depellegrin, D., Farella, G., Gissi, E., Ghezzi, M., Sarretta, A., Venier, C. and Barbanti, A. (2018). A modelling framework for MSP-oriented cumulative effects assessment. *Ecological Indicators* 91: 171-181.
- Micheli, F., Halpern, B. S., Walbridge, S., Ciriaco, S., Ferretti, F., Frascchetti, S., Lewison, R., Nykjaer, L. and Rosenberg, A. A. (2013). Cumulative Human Impacts on Mediterranean and Black Sea Marine Ecosystems: Assessing Current Pressures and Opportunities. *PLOS ONE* 8(12): e79889.
- Tuan, N. Q. and Tu, T. T. (2015). Species composition diversity and fluctuations in mangrove forest area in Ha Tinh Province (*In Vietnamese*).
- Van, G. P., Kim, T. N. and Dinh, C. H. (2020). Diversity of crustacean species in coral reef ecosystems of Vietnam. *Can Tho University Journal of Science*, 56(6): 254-263 (*In Vietnamese*).
- Xuan, B. T. and Quang, D. N. (2022). Study on cumulative impact assessment in environmental assessment worldwide - lessons learned for Vietnam. *Science Journal of Natural Resources and Environment*, (41): 34-44 (*In Vietnamese*).

An integrated multi-scale framework for urban heat risk monitoring and adaptation: An Example Applied to Taoyuan City, Taiwan (China)

Hsiao-Ting Tseng¹, Meng-Hua Hsu^{1,*}, Yue-Lin Chen^{1,2}

¹National Central University, Taoyuan, No. 300, Zhongda Rd., Zhongli Dist., Taiwan (China)

²Department of Information Management, National Defense University, Taipei, No. 70, Section 2, Zhongyang N. Rd., Beitou District, Taiwan (China)

*Email: vm3xl3g@gmail.com

Abstract: Urban heat islands (UHI) intensify health, productivity, and equity risks, yet conventional weather-station networks are too sparse to capture intra-urban variability and deliver actionable guidance. This study proposes and designs an integrated “monitor–predict–adapt” framework for Taoyuan City, Taiwan (China). First, a multi-scale monitoring system fuses Landsat/MODIS Land-Surface Temperature (LST) with Unmanned Aerial Vehicle (UAV) thermal imagery and IoT sensors, and a supervised machine learning model is leveraged to downscale LST to meter-level resolution. Furthermore, vegetation, moisture, and radiative properties (NDVI, NDMI, albedo) are fused with drought indices (SWATI, TMDI) to derive a novel Drought–Heat Compound Index (DHCI) that mathematically quantifies how dryness amplifies UHI risk. Second, a city-scale digital twin supports CNN–LSTM deep learning models for high-resolution, short-term heat forecasting and APIs for location-aware, personalized cooling advice. Third, AR/VR learning modules, nudge-based notifications, and a blockchain-backed carbon-credit incentive are deployed to promote sustained community participation. The expected contribution is a reproducible, data-driven urban-heat governance methodology that closes the gap from scientific monitoring to behavioral adaptation and policy intervention, providing operational tools for local governments and supporting SDGs (global Sustainable Development Goals) 3, 11, 13, and 17.

Keywords: urban heat island; compound drought–heat risk; remote sensing; digital twin; IoT; machine learning.

INTRODUCTION

With the exacerbation of climate change and rapid urbanization, urban areas are increasingly threatened by extreme heat events (Melville, 2010). Taoyuan City, as one of Taiwan's (China) rapidly expanding metropolitan areas, is facing severe challenges from the Urban Heat Island (UHI) effect and heightened heat stress. These thermal impacts not only affect physical health but also have profound consequences for psychological well-being, productivity, and social equity. Traditional UHI monitoring relies mainly on meteorological stations; however, with only 33 automated weather stations currently in Taoyuan, each serving an average area of 37 square kilometers, the spatial resolution is insufficient to capture heat variations at the street block level.

Furthermore, high temperatures are often compounded by other risks, such as drought or elevated ground-level ozone concentrations, posing more severe health threats to respiratory and cardiovascular systems (Watson, Boudreau, & Chen, 2010). Existing heat advisory programs predominantly use one-way information dissemination, lacking personalization and interactivity, which leads to a significant gap between public risk perception and actual adaptive behaviors. To address these challenges, this study proposes

an integrated “monitor–predict–adapt” framework for Taoyuan City, aiming to upgrade conventional heat monitoring into a smart, interactive, and comprehensive adaptation system.

The core of this framework is to empower urban resilience through technology, striving to achieve the vision of a resilient city where adaptation is participatory, ubiquitous, and continuous. This paper will detail the architecture of this system, from multi-scale data fusion and AI-driven personalization to innovative community engagement strategies. Subsequent sections will explore related works, the detailed methodology, expected outcomes and evaluation methods, and a concluding discussion.

RELATED WORK

The integrated framework proposed in this research is built upon several rapidly evolving, interdisciplinary research fields, aiming to bridge the integration gaps between them (Ruhlandt, 2018).

First, in urban thermal environment monitoring, retrieving LST from satellite thermal infrared sensors (e.g., Landsat, MODIS) is a mature and widely used method for mapping urban heat patterns (Constantinides, Henfridsson, & Parker, 2018). However, it is generally acknowledged in the academic community that the moderate resolution (30 to 100 meters) of these data often fails to capture the micro-scale thermal variations (e.g., streets, courtyards, building facades) that are critical for assessing actual human heat exposure (Yoo, Henfridsson, & Lyytinen, 2010). To address this issue, the recent research trend is to integrate multi-platform data sources. The use of high-resolution UAV thermal imaging for hotspot mapping, combined with ground-based Internet of Things (IoT) microclimate sensor networks, has become a key method for improving spatial fidelity and validating satellite products (Cabianca, 2022; Tropea et al., 2024). Furthermore, the integration of UAV and IoT systems—especially in communication,

power management, and data collection—is a rapidly maturing field, providing robust frameworks for remote environmental monitoring (Lakshman, 2021). Building on this foundation, this study further utilizes UAVs not only as a validation tool but also innovatively as key predictors to downscale satellite LST, aiming to generate meter-resolution thermal risk maps and thus responding to the academic demand for monitoring data with higher spatial resolution. Second, in the field of compound risk assessment, the climate science community is increasingly focusing on the interconnectedness and cascading effects of hazards (Yoo, Henfridsson, & Lyytinen, 2010; de Reuver et al., 2018). Single-hazard indicators are no longer sufficient to assess real-world risks. Research has shown that drought conditions can significantly exacerbate heat stress by reducing evapotranspiration, thereby prolonging the duration and intensity of heatwaves (Li et al., 2024; Xu et al., 2024). Therefore, fusing thermal metrics with drought indices, such as the Temperature-Soil Moisture Dryness Index (TMDI) and the Surface Water Availability and Temperature Index (SWATI), to construct more comprehensive compound risk indicators has become an active and important research direction, with various methodologies proposed for analyzing compound drought-heatwave events (Qian et al., 2024; Li et al., 2025). The “Drought-Heat Compound Index (DHCI)” proposed in this study follows this trend, aiming to provide a more valuable assessment tool for early warning than single temperature indicators alone.

Furthermore, in smart city technology applications, the Urban Digital Twin has moved from concept to application, regarded as a powerful platform for integrating multi-source real-time data, conducting scenario simulations, and supporting decision-making (de Reuver, Sørensen, & Basole, 2018). Concurrently, deep learning models applied to spatio-temporal data forecasting, especially architectures combining Convolutional Neural Networks (CNN) to extract spatial features and

Long Short-Term Memory (LSTM) networks to capture time-series dependencies, have demonstrated outstanding performance in environmental forecasting. This research combines these two cutting-edge technologies, aiming to construct a dynamic system that seamlessly links real-time monitoring to high-precision short-term prediction.

Finally, in promoting civic adaptive behavior, the intersection of information management and behavioral science provides a rich theoretical foundation (Bharadwaj, El Sawy, Pavlou, & Venkatraman, 2013). Research has confirmed that merely providing information is not sufficient to change behavior. This framework integrates several innovative approaches: Augmented/Virtual Reality (AR/VR) is used to create immersive experiences to enhance the perception of abstract climate risks, with increasing evidence showing extended reality (XR) 's potential in environmental sustainability and risk communication (Cosío et al., 2025; Attanasi, 2025); Nudge theory, derived from behavioral economics, is applied to design smart notification systems... and blockchain technology, due to its decentralized and immutable nature, is used to build a transparent and trustworthy carbon-credit incentive mechanism, addressing potential trust issues in traditional incentive programs by leveraging its capabilities in secure and automated trading (Zhang, 2024; Tsai, 2024).

METHODS

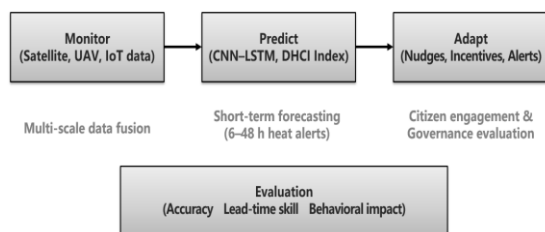


Figure 1. Research framework

Our methodology is structured around three interconnected components designed to create a seamless flow from data collection to decision support and public action. Fig. 1

illustrates this integrated framework, clearly showing the coordination of multi-source data that feeds into the predictive models and drives the adaptive strategies.

Multi-scale Monitoring and Compound Risk Quantification

The foundation of the framework is a multi-scale monitoring system designed to capture thermal dynamics from the city down to the street level.

LST Retrieval and UAV-based Downscaling: We retrieve LST from Landsat using single-channel/split-window formulations and consume MODIS LST for temporal fill-in. To address the resolution limitations of satellite imagery (30m), a key innovation of this project is the use of UAVs equipped with filter-wheel multispectral cameras for meter-scale hotspot mapping in critical areas like campuses and industrial parks.

These high-resolution UAV images serve a dual purpose: they provide ground truth for validating satellite LST and, more importantly, their derived predictors (e.g., NDVI, NDMI, albedo, shadow index, impervious surface ratio) are used in a supervised machine learning model (e.g., Random Forest or Geographically Weighted Regression (GWR)) to downscale the 30m Landsat LST to a meter-level resolution. This process clarifies the fine-scale heterogeneity within a single satellite pixel, revealing how features like shaded sidewalks versus asphalt roads contribute to localized heat risk. The technical workflow involves: (1) Radiometric and atmospheric correction of both satellite and UAV thermal data; (2) Feature extraction from high-resolution UAV imagery; and (3) Training the downscaling model using the high-resolution features and the coarse-resolution LST as the target variable.

Drought–Heat Compound Index: To better understand the drivers of UHI, we move beyond temperature alone. We fuse LST data with advanced drought indices such as the Temperature–Soil Moisture Dryness Index (TMDI) and the Surface Water Availability and

Temperature Index (SWATI) to derive a novel DHCI. This index is specifically designed to quantify how soil and atmospheric dryness amplifies the UHI effect, providing a more holistic risk indicator than temperature alone.

The DHCI is mathematically formulated as a weighted combination of its normalized components:

$$DHCI = w_1 \cdot LST_{norm} + w_2 \cdot TMDI_{norm} + w_3 \cdot SWATI_{norm}$$

where LST_{norm} , $TMDI_{norm}$ and $SWATI_{norm}$ are the respective normalized indices (scaled between 0 and 1, with 1 representing the highest risk). w_1 , w_2 , w_3 are empirically derived weighting coefficients (where $\sum w_i = 1$), typically determined through Principal Component Analysis (PCA) or through expert elicitation, with the primary objective of maximizing the index's empirical correlation with known heat-related public health outcomes.

AI-powered Prediction and Personalization

The monitoring data feeds into a predictive system that translates raw information into timely and personalized warnings.

Forecasting API: A city-scale digital twin ingests the multi-source data streams. We employ deep learning models, specifically a combination of Convolutional Neural Networks (CNN) and Long Short-Term Memory (LSTM) networks, for high-resolution, short-term heat forecasting. The model architecture comprises a 3-layer CNN block (to extract local spatial features across a $N \times N$ pixel grid) followed by a 2-layer LSTM block (to capture temporal dependencies over T preceding time steps). Input data specifications include: (1) Spatially gridded DHCI maps; (2) Time-series of ground-level temperature from IoT sensors; and (3) Key meteorological variables (humidity, wind speed, solar radiation). This predictive model is exposed as a RESTful API, allowing for seamless integration with third-party applications and government dashboards. Sample test results from the pilot phase show a

projected Root Mean Square Error (RMSE) below $1.5^\circ C$ for 6-hour forecasts.

AI-driven Recommendation Engine: Based on collaborative and content-based filtering techniques, we are developing a personalized recommendation engine. The system analyzes a user's behavioral patterns, current location, and real-time environmental data to provide customized adaptation advice through a mobile application.

Smart Notification System: The system integrates the "Nudge" concept from behavioral economics. It is designed to deliver timely and context-aware behavioral prompts, such as a notification to "remember your sun hat" just before a predicted temperature spike, to gently guide users toward safer behaviors.

Behavior Change and Community Engagement

The final component focuses on translating awareness into action through innovative community engagement tools (Venkatesh, Thong, & Xu, 2012).

AR/VR Immersive Education: We will develop AR/VR educational applications that allow users to immersively experience extreme heat scenarios and visualize the effects of different adaptation strategies (e.g., cool roofs, green infrastructure). (Seidel, Recker, & vom Brocke, 2013) By simulating physiological feedback like heart rate and body temperature, these modules aim to enhance risk perception and motivate self-protection.

Blockchain-based Incentive Mechanism: To foster sustained community participation, we will develop a carbon-credit trading platform utilizing blockchain technology. Community cooling actions, such as tree planting or adopting energy-saving habits, are tracked and rewarded with carbon credits, creating a transparent and motivating incentive structure.

Online Learning Platform: An online platform will be created to host micro-learning courses, a gamified badge system, and a "Heat Adaptation Competency Certification" to

support long-term public education and capacity building.

EXPECTED OUTCOMES AND SYSTEM FUNCTIONALITY

The efficacy of this framework will be assessed through a comprehensive evaluation plan covering three dimensions: technical, performance, and governance.

(i) **Monitoring Accuracy:** The expected output is high-resolution, validated thermal risk maps. The evaluation will involve comparing satellite and UAV-derived LST with ground-truth data from IoT sensors, calculating statistical metrics such as MAE and RMSE.

(ii) **Warning Performance:** The core output is a reliable real-time warning service. We will evaluate the lead time of the CNN/LSTM model's high-temperature event forecasts and its classification quality (e.g., AUC, precision-recall).

(iii) **Governance Outcomes:** Expected outcomes include increased citizen engagement and reduced heat exposure risk. This will be measured through a series of indicators, including user adoption and retention rates of the mobile application, changes in outdoor workers' heat exposure hours, community participation in cooling actions (tracked via the blockchain platform), and corresponding CO₂e savings. Ultimately, the system will produce a "Heat Risk Perception and Vulnerability Hotspot Map" that integrates remote sensing data with socioeconomic information to provide a scientific basis for public health policies.

CONCLUSION

This paper presents the design of a reproducible and governance-ready framework aimed at addressing the escalating challenges of urban heat islands. In response to the limitations of traditional monitoring in spatial resolution and the persistent gap in civic adaptation, this research provides a holistic solution by deeply integrating multi-scale monitoring, compound drought-heat analytics,

AI-powered forecasting, and innovative behavior-change mechanisms.

The core contribution of this framework lies in its systematic and integrated innovation. First, by fusing satellite, UAV, and IoT data—particularly by leveraging UAVs for downscaling—it successfully advances the monitoring scale from the macroscopic city level to the microscopic street level, which is directly relevant to human exposure. Second, the novel DHCI compound index elevates heat risk assessment from a single dimension to a multi-dimensional perspective, more scientifically reflecting the complexity of the climate system. Most importantly, this framework is not limited to technical monitoring and warning; by incorporating tools such as AR/VR, Nudge theory, and blockchain, it establishes a complete "data-information-knowledge-action" closed loop, translating technological potential into tangible social resilience.

Ultimately, the successful implementation of this research is expected to bring about a paradigmatic shift in urban governance for Taoyuan City. It not only provides a solid foundation for data-driven decision-making but also fosters a more inclusive and collaborative governance model by empowering citizen participation. The methodologies and tools developed in this system are designed to be transferable, offering valuable insights and viable pathways for other cities worldwide facing similar climate challenges. In conclusion, this research does not merely propose an information system; it aims to provide an operational catalyst to foster a more equitable, safe, and heat-resilient urban future, making a concrete and profound contribution toward achieving Sustainable Development Goals 3, 11, and 13.

DISCUSSION

The integrated framework proposed in this paper represents not merely a technical solution, but a new paradigm for urban heat governance. (Constantinides et al., 2018). Its

core implications can be explored from several key perspectives.

First, concerning the monitoring scale, by systematically combining satellite, UAV, and IoT data, the framework provides a scalable and robust methodology for overcoming the spatial resolution limitations of traditional monitoring (Bharadwaj et al., 2013). The UAV-based downscaling technique, in particular, is not just for validating the accuracy of satellite data; more critically, it offers a novel pathway to generate actionable intelligence at the human scale. Traditional UHI maps often stop at city-level macroscopic trends, whereas our meter-scale hotspot maps can precisely identify specific sources of risk—such as a sidewalk lacking tree shade or a dark-colored rooftop. This enables targeted micro-interventions, like installing green corridors or promoting cool pavements and roofs at specific street corners, allowing for more effective resource allocation.

Second, compound risk assessment is another key contribution of this framework. The development of the DHCI emphasizes a shift from a single-hazard mindset to a compound-risk perspective. In the context of climate change, the interaction between high-temperature and drought events is becoming more frequent. This index allows decision-makers to gain a more nuanced understanding of urban climate risk, where factors like drought can significantly exacerbate heat stress. This enables more proactive and targeted resource management; for instance, the system can issue warnings for areas where the UHI effect is likely to intensify during the early stages of a drought, thereby enabling the preemptive dispatch of smart irrigation resources to maintain the cooling function of urban green spaces.

Furthermore, the framework's emphasis on the behavior-change layer is crucial. Accurate monitoring and warning technologies alone are insufficient; if citizens cannot receive, understand, and act upon the information, the value of the technology is greatly diminished. By integrating AR/VR immersive education, personalized nudges, and blockchain incentives,

the system attempts to bridge the long-standing gap between 'risk awareness' and 'adaptive action.' AR/VR transforms abstract climate risks into tangible personal experiences, while Nudge theory and gamified incentives lower the barriers to taking action. This human-centric design is fundamental to building genuine community resilience, aiming to transform citizens from passive recipients of information into active participants in building urban resilience.

However, the implementation of this framework is also accompanied by potential challenges and limitations. First are data governance and privacy concerns; personalized services require access to sensitive user information such as location, necessitating the establishment of strict anonymization and de-identification mechanisms. Second, the long-term maintenance and calibration of the IoT sensor network will be an ongoing task. This challenge, particularly for remote nodes, is being addressed by innovative solutions such as UAV-based charging and life extension protocols (Van Mulders et al., 2024). Crucially, the operational integration of multi-source data streams presents significant technical challenges, requiring robust Extract, Transform, Load (ETL) pipelines to handle heterogeneous formats (raster, vector, time-series) and synchronize real-time inputs for the predictive model. Third, achieving widespread adoption of the mobile applications and digital tools, particularly among digitally disadvantaged populations, will be a key factor in the system's effectiveness and will need to be overcome with complementary offline community outreach and educational activities. Furthermore, effectively delivering complex risk information to the public is a non-trivial communication challenge. Model outputs must be translated into intuitive, user-friendly visualizations rather than raw data, and the timing of nudges must be carefully optimized to avoid alert fatigue, ensuring information is actionable and understood by diverse user groups.

Finally, the modular design of this framework provides it with a high degree of

scalability and transferability. Its core methodologies (such as the downscaling process and compound index construction) and technology stack can be adapted by other cities facing similar challenges. This framework not only provides operational tools for municipal agencies but, more importantly, it supports a more forward-looking, inclusive, and evidence-based decision-making model, aligning with the principles of the UN's MCR2030 Resilience Roadmap.

ACKNOWLEDGEMENTS

This research was funded by the Ministry of Education and National Central University of Taiwan (China).

REFERENCES

- Attanasi G (2025) Raising environmental awareness with augmented reality. *Journal of Environmental Psychology*.
- Bharadwaj A, El Sawy OA, Pavlou PA, Venkatraman N (2013) Digital business strategy: Toward a next generation of insights. *MIS Quarterly*. 37(2): 471-482.
- Cabianca M (2022) An application of IoT in a drone inspection service for environmental surveillance. *Sensors*. 22(19): 7486.
- Constantinides P, Henfridsson O, Parker GG (2018) Platforms and infrastructures in the digital age. *Information Systems Research*. 29(2): 381-400.
- Cosío E, et al. (2025) Virtual and augmented reality for environmental sustainability: A systematic review. *Environmental Research Communications*.
- de Reuver M, Sørensen C, Basole RC (2018) The digital platform: A research agenda. *Journal of Information Technology*. 33(2): 124-135.
- Lakshman SA, Ebenezer D (2021) Integration of internet of things and drones and its future applications. *Materials Today: Proceedings*. 47(4): 944-949.
- Li J, et al. (2024) Future increase in compound soil drought-heat extremes. *Nature Communications*. 15: 5127.
- Li Y, et al. (2025) A review of data for compound drought and heatwave. *Water*. 17(3): 345.
- Melville NP (2010) Information systems innovation for environmental sustainability. *MIS Quarterly*. 34(1): 1-21.
- Qian Z, Sun Y, Ma Q, et al. (2024) Understanding changes in heat waves, droughts, and compound events in Yangtze River Valley and the corresponding atmospheric circulation patterns. *Climate Dynamics*. 62: 539-553.
- Ruhlandt RWS (2018) The governance of smart cities: A systematic literature review. *Information Systems Journal*. 28(4): 907-946.
- Seidel S, Recker J, vom Brocke J (2013) Sensemaking and sustainable practicing: Functional affordances of information systems. *MIS Quarterly*. 37(4): 1275-1299.
- Tsai Y-C (2024) Blockchain-driven solutions for carbon credit trading: A decentralized platform for SMEs. *Journal of Cleaner Production*.
- Tropea M, et al. (2024) UAV IoT sensing and networking. *Sensors*. 24(2): 562.
- Van Mulders J, Boeckx S, Cappelle J, Van der Perre L, De Strycker L (2024) UAV-based solution for extending the lifetime of IoT devices: Efficiency, design and sustainability. *Frontiers in Communications and Networks*. 5: 1341081.
- Venkatesh V, Thong JYL, Xu X (2012) Consumer acceptance and use of information technology: Extending the unified theory of acceptance and use of technology. *MIS Quarterly*. 36(1): 157-178.
- Watson RT, Boudreau M-C, Chen AJ (2010) Information systems and environmentally sustainable development: Energy informatics and new directions for the IS community. *MIS Quarterly*. 34(1): 23-38.
- Xu W, et al. (2024) Impacts of record-breaking compound heatwave and drought. *Environmental Research Letters*. 19(7): 074012.
- Yoo Y, Henfridsson O, Lyytinen K (2010) Research commentary—The new organizing logic of digital innovation: An agenda for information systems research. *Information Systems Research*. 21(4): 724-735.
- Zhang G (2024) Blockchain technology in carbon trading markets. *Energies*. 17(1): 112.
- Zhu J, Guo H, Sun Y (2025) Responses of terrestrial GPP to extreme compound heatwave and drought events of different intensities in the Yangtze River Basin. *Remote Sensing*. 17(5): 848.

DOI: 10.15625/vap.2025.0230

Adjusting of the buffer zone boundaries in Ha Long Bay World Natural Heritage: Scientific and practical foundations for sustainable management orientation

Luu The Anh¹, Bui Manh Tung², Ngo Thi Hai Yen³, Duong Anh Quan^{4,5}, Bui Ngoc Quy^{1,4*}

¹Central Institute for Natural Resource and Environmental Studies, Vietnam National University, Hanoi, Vietnam

²Hanoi University of Mining and Geology, 18 Vien street, Dong Ngac commune, Hanoi, Vietnam.

³Hanoi National University of Education, Vietnam

⁴Hanoi Research and Development of Geospatial Data Management and Analysis Techniques GMA, Hanoi University of Mining and Geology, Vietnam

⁵Faculty of Geomatics and Land Administration, Hanoi University of Mining and Geology, Vietnam.

*Email: Quybnrcs@vnu.edu.vn

Abstract: Buffer zones play a crucial role in safeguarding the integrity and Outstanding Universal Value (OUV) of World Heritage natural properties. For Ha Long Bay, following three inscriptions by UNESCO (1994, 2000, and 2023), a buffer zone of 34,140 hectares was designated to provide an additional protective belt for the 43,400-hectare core area. However, in practice the current buffer zone boundaries are overly extensive, overlapping with settlements, urbanized zones, defense land, and other infrastructure developments. The absence of clearly demarcated boundaries on the ground has led to management and conservation difficulties, while creating tensions with the socio-economic development requirements of Quang Ninh province and the Red River Delta. This paper examines the scientific and practical foundations for adjusting the buffer zone of Ha Long Bay and proposes orientations for sustainable management. The findings highlight that: (i) adjustment is urgent to reconcile conservation with development; (ii) urbanized areas no longer contributing to heritage protection should be excluded or reduced; (iii) boundaries must be precisely established through mapping and on-site demarcation; and (iv) functional zoning within the buffer zone is needed to ensure conservation while enhancing tourism

values, community livelihoods, and green economic growth. On this basis, the paper proposes directions for sustainable buffer zone management, emphasizing inter-sectoral coordination, environmental impact control, community participation, and the integration of buffer zone management into socio-economic development planning.

Keywords: Buffer zone, World Natural Heritage, Sustainable development, Ha Long Bay.

INTRODUCTION

The World Natural Heritage Site “Ha Long Bay - Cat Ba Archipelago” is an integrated landscape-marine ecological complex located in Quang Ninh Province and Hai Phong City (Vietnam). The property has been inscribed by UNESCO in multiple stages: in 1994 for its Outstanding Universal Value (OUV) in terms of scenic beauty (Criterion vii), in 2000 for its geological and geomorphological significance (Criterion viii) with respect to Ha Long Bay; and most recently, in 2023, the heritage boundary was extended to include the Cat Ba Archipelago, thereby further emphasizing the property’s integrity and biodiversity values (Criteria ix and x). As such, the “Ha Long Bay - Cat Ba Archipelago” represents a unique tropical marine karst landscape that has

undergone millions of years of geological evolution, and serves as habitat for numerous rare and endemic species of high conservation value.

Within the overall property, Ha Long Bay functions as the core area, covering a total area of approximately 1,553 km², including both core and buffer zones. Ha Long Bay is distinguished by its majestic seascape, ancient geological history, and rich biodiversity, making it an important destination for international tourism, scientific research, and environmental conservation. The area encompasses a remarkable assemblage of limestone islands, karst landforms, and cave systems, along with characteristic marine-island ecosystems that contribute to its Outstanding Universal Value.

According to UNESCO regulations, a buffer zone serves as a critical protective belt designed to preserve the integrity and Outstanding Universal Value (OUV) of a heritage property against adverse impacts from socio-economic activities. However, in practice, the current buffer zone boundaries of Ha Long Bay are overly extensive, overlapping with urbanized areas, defense lands, and major infrastructure systems-creating significant challenges for sustainable management and conservation. Rapid coastal industrialization, urban expansion, and the boom of tourism development have exerted considerable pressure on the buffer zone. Numerous land reclamation and coastal urban projects (such as those in Tuan Chau, Hung Thang, and Quang Hanh) have encroached into the buffer zone, posing risks to the landscape and environmental integrity of the heritage site.

Therefore, the adjustment of Ha Long Bay's World Natural Heritage buffer zone is not only a necessary measure to meet UNESCO's criteria and Vietnam's conservation regulations but also an essential solution to balance heritage preservation with sustainable socio-economic development in Quang Ninh Province and its surrounding regions. This constitutes a crucial scientific and practical foundation for enhancing the effectiveness of heritage management and ensuring the

preservation of Ha Long Bay's Outstanding Universal Value for future generations.

SCIENTIFIC AND PRACTICAL FOUNDATIONS FOR ADJUSTING THE BUFFER ZONE OF HA LONG BAY WORLD NATURAL HERITAGE

Objectives of Adjusting the Buffer Zone Boundaries

To provide scientific and practical foundations for the proposal and determination of an appropriate buffer zone that aligns with current realities, thereby enhancing the efficiency of Ha Long Bay Heritage management while ensuring full compliance with the World Heritage Convention and Vietnam's laws on the protection and management of cultural and natural heritage.

To establish functional zoning within the heritage territory, contributing to the promotion of sustainable socio-economic development in the buffer zone, while simultaneously implementing coordinated, feasible, and effective measures to control, prevent, and mitigate negative impacts from the buffer and adjacent areas on the Outstanding Universal Value (OUV) of the property.

To develop and refine management regulations and mechanisms for each functional subdivision (core zone, buffer zone, and outer zone) in a manner that both supports socio-economic growth and safeguards the integrity and authenticity of Ha Long Bay's World Natural Heritage values. This will strengthen the role, authority, and effectiveness of state management over the Heritage site.

To foster a profound transformation in community awareness and action toward the management, conservation, and sustainable utilization of the Heritage and its buffer zone.

To comprehensively and effectively implement management, conservation, and sustainable development measures for Ha Long Bay's Heritage values, thereby contributing to

the provincial goal of developing Quang Ninh into a modern industrial-service province, a major growth pole of Northern Vietnam, and a centrally governed city before 2030.

Requirements for Adjusting the Buffer Zone Boundaries

The adjustment of Ha Long Bay's buffer zone must adhere to the following key requirements:

- *Alignment with national and regional development strategies:* The adjustment must conform to the Government's Action Program under Resolution No. 14/NQ-CP (February 8, 2023), which implements Resolution No. 30-NQ/TW (November 23, 2022) of the Politburo on socio-economic development and the assurance of national defense and security in the Red River Delta region up to 2030, with a vision to 2045. It must also be consistent with the Master Plan of Quang Ninh Province and the Red River Delta Regional Plan for the 2021-2030 period, with a vision to 2050.

- *Compliance with international and national legal frameworks:* The adjustment must follow the provisions of the 1972 World Heritage Convention, the Operational Guidelines for its Implementation (UNESCO), and relevant decisions and recommendations issued by the World Heritage Committee and the World Heritage Centre, as well as Vietnam's legal instruments governing the management of cultural and natural heritage.

- *Scientific, objective, and practical justification:* The revision must be grounded in sound scientific reasoning and empirical evidence, ensuring objectivity and authenticity. It should simultaneously support the sustainable development goals of Quang Ninh Province and the Red River Delta, while maximizing socio-economic benefits and improving the living standards and well-being of local communities residing within the buffer zone.

- *Balance between conservation and development:* The adjustment must maintain harmony between economic growth, heritage

conservation, environmental protection, and climate change adaptation, ensuring that development does not compromise the integrity or authenticity of the heritage site.

- *Enhancement of management efficiency:* The adjustment should strengthen the effectiveness of management and conservation, maintaining the integrity, authenticity, and sustainability of the property's Outstanding Universal Value (OUV).

- *Preservation of the Heritage's scale and attributes:* The adjustment must not alter the overall scale of the Heritage property or negatively affect the attributes that constitute its OUV.

- *Feasibility and effectiveness:* The new boundaries must ensure high feasibility and management efficiency in preventing, mitigating, and minimizing negative impacts originating from the buffer zone and surrounding areas on the ecological and cultural attributes that contribute to Ha Long Bay's OUV.

Scientific Basis for Adjusting the Buffer Zone of Ha Long Bay World Natural Heritage

The concept of a buffer zone is intrinsically linked to the protection of World Heritage properties and is clearly defined in the Operational Guidelines for the Implementation of the World Heritage Convention (1972) issued by UNESCO. A buffer zone refers to an area surrounding the core zone of a heritage site, functioning to mitigate external impacts and support the preservation of the site's integrity and Outstanding Universal Value (OUV) (UNESCO, 2019).

The International Union for Conservation of Nature (IUCN) emphasizes that a buffer zone not only serves conservation purposes but should also generate sustainable livelihood benefits for local communities (IUCN, 2020). A buffer zone is not a "static" entity - it may be adjusted, expanded, or reduced depending on developmental contexts, provided that its core function of safeguarding heritage values is maintained.

Globally, numerous World Heritage sites have had to revise their buffer zones to adapt to socio-economic transformations. For example, Serengeti National Park (Tanzania) modified its buffer zone to control the impacts of agriculture and tourism, while the Machu Picchu Sanctuary (Peru) adjusted its boundaries to better manage pressures from mass tourism (UNESCO, 2021). These cases demonstrate that buffer zone adjustment is a necessary and ongoing process, which must be closely tied to integrated management strategies.

In Vietnam, the Law on Cultural Heritage (2001, amended 2009) clearly defines two protection zones: Zone I (core) and Zone II (buffer). Decree No. 109/2017/NĐ-CP of the Government further specifies measures for the protection and management of both natural and cultural heritage, underscoring the buffer zone's role in limiting adverse impacts from development activities (Government of Vietnam, 2017). Successful examples include Trang An Landscape Complex (Ninh Binh), which integrates ecotourism and traditional agriculture within its buffer zone to alleviate pressure on the core area (Nguyen et al., 2020), and Phong Nha - Ke Bang National Park, which has implemented a buffer zone mechanism combining conservation and sustainable tourism development.

For Ha Long Bay, the buffer zone was initially established in 1994, then adjusted in 2000 and 2023, with an original area exceeding 30,650 hectares. However, over time, various issues have emerged, including overlaps with new urban areas, industrial zones, and defense lands, and the absence of ground demarcation markers-making it difficult to control socio-economic activities within its boundaries. Rapid land reclamation and coastal urbanization in Ha Long, Cam Pha, and Quang Yen have significantly affected the Bay's landscape and environment (Tuoi Tre, 2023). Therefore, adjusting the buffer zone is an inevitable trend to harmonize conservation with development. For Ha Long Bay, this adjustment is both scientifically justified and

practically necessary, reflecting the socio-economic development demands of Quang Ninh Province and the Red River Delta region.

Perspectives

The adjustment of Ha Long Bay's buffer zone boundaries must fully comply with the World Heritage Convention, its Operational Guidelines, and other relevant international treaties to which Vietnam is a State Party, as well as the nation's legal framework governing the management of cultural and natural World Heritage sites.

The adjustment must ensure consistency and coherence with the objectives, content, and orientations of Vietnam's National Master Plan, the Red River Delta Regional Plan, and the Quang Ninh Provincial Master Plan for 2021-2030, with a vision to 2050.

The fundamental principle is to avoid any trade-off between economic growth and the conservation of Outstanding Universal Value. Development must not compromise the integrity or authenticity of the Heritage site. The process must respect natural laws, maintain a balance between conservation and development, and adhere to the principle of "conservation for development, and development for conservation." The adjustment should create new spatial and institutional conditions for sustainable growth, enhance community livelihoods, and improve local well-being.

The boundary adjustment must aim to strengthen management efficiency and preventive capacity, reducing negative impacts from socio-economic activities on Ha Long Bay's key OUV attributes-namely its scenic, aesthetic, geological, geomorphological, and biodiversity values, as well as its environmental quality.

The adjustment should promote spatial coherence and ecological connectivity between the core and buffer zones and adjacent territories, fostering sustainable development, environmental protection, climate change adaptation, and disaster risk reduction.

The revised boundaries should also facilitate functional zoning and rational resource allocation, ensuring the efficient, economical, and sustainable use of natural resources within the buffer zone and the broader heritage area.

Principles

The adjusted boundaries of Ha Long Bay's buffer zone must accurately reflect the real spatial structure and territorial organization of the area, ensuring continuity and connectivity in terms of landscape, aesthetic, geological, geomorphological, biodiversity, and ecological system (ecosystem) values, as well as historical-cultural characteristics of the World Heritage property.

Buffer zone boundaries must be clearly identifiable and easily recognizable on the ground by management authorities, local communities, enterprises, service operators, and tourists; ...

The adjustment should be considered a minor modification, aimed at enhancing management effectiveness and conservation efficiency, without compromising the integrity of the Heritage's Outstanding Universal Value.

The process should minimize potential conflicts between the socio-economic development needs and the conservation objectives within the buffer zone, ensuring that improvements in living standards are compatible with heritage preservation.

The adjustment must enhance control and mitigation capacity against negative impacts arising from activities within and around the buffer zone that could affect the attributes contributing to the site's OUV.

Under no circumstances should the adjustment reduce or encroach upon areas containing critical natural ecosystems or habitats of endemic, rare, or endangered species, nor on zones embodying essential attributes that constitute the OUV of Ha Long Bay.

Practical Basis

The UNESCO World Heritage Convention (1972) is the only international legal instrument

that integrates the protection of both cultural and natural heritage, representing one of UNESCO's most influential and far-reaching frameworks for global heritage conservation. In 2019, UNESCO issued the Operational Guidelines for the Implementation of the World Heritage Convention, providing the normative foundation for heritage protection, management, and monitoring. For World Heritage sites located within a State Party's national territory, in addition to compliance with international obligations, the domestic legal framework of that country must also be effectively applied to ensure the long-term sustainability of the property for both present and future generations. According to Paragraph 98 of the Operational Guidelines (UNESCO, 2019): "Legislative and regulatory measures at national and local levels should assure the protection of the property from social, economic and other pressures or changes that might negatively impact the Outstanding Universal Value, including the integrity and/or authenticity of the property. States Parties should also assure the full and effective implementation of such measures"

Furthermore, Paragraph 107 stipulates that: "Although buffer zones are not normally part of the nominated property, any modification or creation of a buffer zone after inscription must be approved by the World Heritage Committee as a minor boundary modification. The establishment or redefinition of a buffer zone following inscription may thus be considered a minor boundary change".

Under the Operational Guidelines, any proposal to modify the boundaries of a World Heritage buffer zone-after the site has been inscribed-must be formally submitted to and approved by the World Heritage Committee. Such proposals are processed in accordance with the procedures for minor boundary modifications.

Paragraph 163 of the Guidelines clarifies that: "A minor modification is one which does not have a significant impact on the extent of the property nor affects its Outstanding Universal Value".

Paragraph 164 of the Guidelines clarifies that: If a State Party wishes to request a minor modification of the boundary of an already inscribed property, the proposal must be submitted to the World Heritage Centre (through the Secretariat) by 1 February of the relevant year, using the standardized form provided in Annex 11 of the Guidelines. The Secretariat then seeks advice from the relevant Advisory Bodies (IUCN, ICOMOS) to determine whether the proposed modification qualifies as a minor change. Following evaluation, the Secretariat must present the advisory opinion to the World Heritage Committee, which may either approve the modification or determine that it constitutes a significant extension, in which case a new nomination process must be initiated (Decision 39 COM 11).

In addition, Vietnamese legislation provides specific legal safeguards concerning adjustments to the buffer zones of World Heritage properties. According to Article 3(7) of Decree No. 109/2017/NĐ-CP of the Government of Vietnam, “Integrity represents the complete and intact expression of the original elements constituting the Outstanding Universal Value of a World Heritage property.”

Therefore, any modification of the buffer zone boundaries must not compromise the integrity, authenticity, or representativeness of the attributes that embody the site’s OUV.

RESULTS OF THE ADJUSTMENT OF THE BUFFER ZONE BOUNDARIES OF HA LONG BAY WORLD NATURAL HERITAGE SITE

The spatial scope of the proposed buffer zone boundary adjustment is directly related to the analysis of land use changes in 1994, 2000, and 2023, and holds essential significance for formulating and justifying the revised buffer zone boundary. Examination of land use status across these three time points allows for:

- Identifying trends in land-water surface conversion associated with the process of urban and tourism development along the coastal zone;

- Assessing the extent of habitat space reduction and loss of tidal and marine surface areas within the area formerly designated as the buffer zone;

- Providing quantitative and empirical evidence to support the proposed boundary adjustment, ensuring its effectiveness and relevance to the current development context.

Therefore, to ensure analytical consistency and to provide a sound basis for evaluating land use changes over time, it is first necessary to clearly define the boundary of the proposed adjusted buffer zone.

Proposed Adjustment of the Buffer Zone Boundary

Based on the analysis of landscape-ecological structure, functional linkages between the buffer zone and the core zone, and the spatial distribution of attributes contributing to the Outstanding Universal Value (OUV) of the Heritage Site, the proposed buffer zone boundary is defined according to two key principles:

- Retention of areas that continue to support the protection of the Heritage Site, including:

- + Karst island ecosystems and associated evergreen forest formations;

- + Marine and coastal habitats with regulating and buffering functions against external development pressures;

- + Visual landscape spaces functionally and perceptually connected to the core zone, contributing to the integrity of aesthetic and geological values.

- Exclusion of areas that have undergone substantial functional transformation and no longer maintain ecological buffering roles, including:

- + Established urban areas, residential zones, and coastal tourism-service complexes;

- + Major technical and transportation infrastructure systems;

+ Specific land and marine areas under stable management and use for national defense purposes.

Accordingly, the existing coastal embankment/ shoreline is adopted as the landward boundary of the buffer zone. A total area of approximately 2,251.1 ha located within coastal wards of Ha Long City and Cam Pha City-including Hung Thang, Bai Chay, Hong Gai, Hong Ha, and areas administered by Naval Brigade 170-is proposed to be excluded from the buffer zone.

The adoption of the existing coastal boundary provides clear management advantages:

- Facilitating boundary demarcation and field-based identification;
- Enhancing the effectiveness of regulating development activities that may impact the core zone;
- Reducing conflicts between conservation objectives and the needs for urban development, tourism, and national defense.

Land Use in 1994

Satellite imagery from Landsat (1994) (Figure 1) and the corresponding land use map (Figure 2) reveal that the proposed reduction area of the buffer zone comprised the following land types: Garden land: approximately 110.9 ha; Residential and public facilities: 158.1 ha;

Forest land: 557.3 ha; Bare land: 121.9 ha; Transportation infrastructure: 94.3 ha; Water surface area: 1,208.6 ha (accounting for about 53.7% of the total area proposed for adjustment).

The Landsat imagery shows that, as of 1994, mangrove forests were largely absent from this area, being distributed mainly outside the buffer zone in Hoanh Bo District (now part of Ha Long City). The forest cover within the proposed reduction area consisted mainly of planted forests on low inland hills and evergreen tropical forests on limestone islands (notably in Ha Tu Ward, managed by Navy Brigade 170 - Naval Region I).

According to the 1994 World Heritage nomination dossier, Ha Long Bay hosted a high diversity of tropical fauna and flora, including approximately 1,000 fish species (of which 730 had been identified and named), along with valuable marine species such as lobsters, squids, crabs, and economically important shellfish (e.g., pearls and clams near Minh Chau and Ngoc Vung Islands).

On the limestone islands, several mammal, reptile, and bird species-such as red-faced macaques, green parrots, and other endemic fauna-were recorded. The vegetation on these islands is highly diverse, including primary evergreen forests (notably on Ba Mun Island).

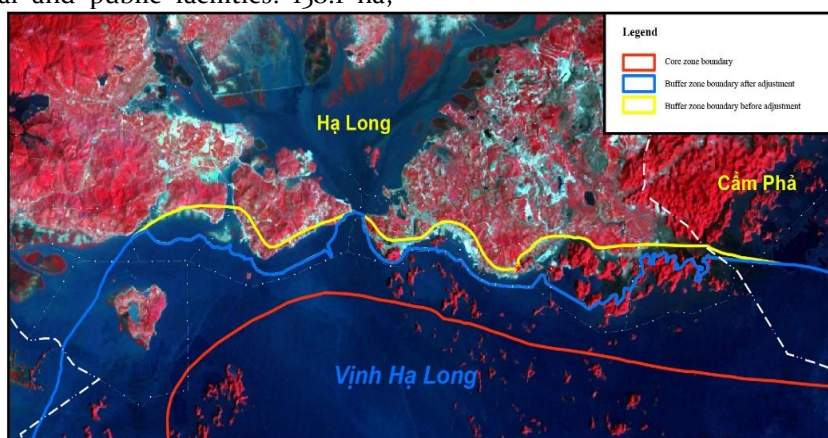


Figure 1. Landsat satellite image (1994) showing the buffer zone area of Ha Long Bay-Cat Ba Archipelago on the territories of Ha Long and Cam Pha Cities.



Figure 2. Land use status (1994) of the buffer zone area of Ha Long Bay-Cat Ba Archipelago, interpreted from Landsat imagery.

Table 1. Land Use Change in the Proposed Adjustment Area (1994-2000-2023)

No	Land Type	1994 (ha)	2000 (ha)	2023 (ha)
1	Garden land	110,9	385,4	267,3
2	Residential & public facilities	158,1	456,3	500,3
3	Forest land	557,3	396,7	501,2
4	Bare land	121,9	59,7	443,5
5	Transportation land	94,3	142,3	209,5
6	Water surface & tidal area	1.208,6	810,7	329,3
	Total	2.251,1	2.251,1	2.251,1

Although detailed biodiversity data for this specific coastal area were not available in 1994, ecological assessment indicates that the habitats primarily consisted of coastal water and soft-bottom intertidal ecosystems, with

minimal mangrove presence (~7.3 ha). Consequently, species diversity in this section was likely lower than in other representative ecosystems of Ha Long Bay, such as: Evergreen tropical forest on limestone islands (507 species recorded); Cave ecosystems (20 endemic species, including 2 fish and 6 crustaceans); Hard-bottom intertidal ecosystems (423 species); Mangrove ecosystems (30 plant species, key spawning grounds for valuable aquatic species); Soft-bottom tidal flats (490 species); Sandy tidal flats (116 species).

Land Use in 2000

Satellite imagery from Landsat (2000) (Figure 3) and its interpreted land use map (Figure 4) indicate that urban expansion and coastal reclamation had begun along the shoreline of Ha Long City by 2000, particularly for urban and service infrastructure development.

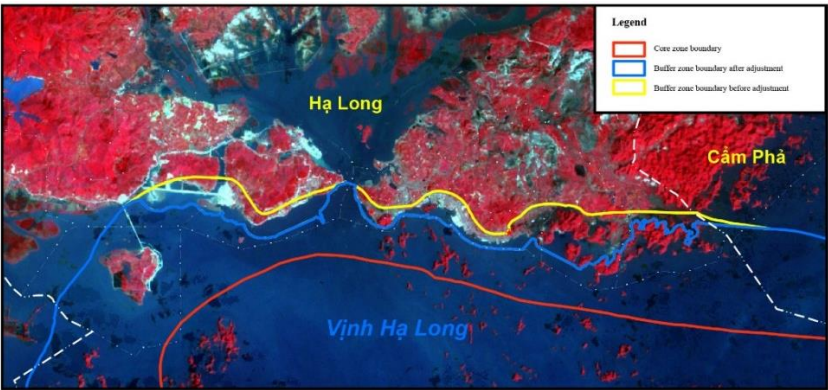


Figure 3. Landsat satellite image (2000) of the buffer zone area on the territories of Ha Long and Cam Pha Cities.



Figure 4. Land use map (2000) of the buffer zone area of Ha Long Bay-Cat Ba Archipelago, interpreted from Landsat imagery.

Significant land reclamation occurred in Hung Thang and Bai Chay Wards, where tidal flats and nearshore waters were filled to create new residential and urban service zones. A 2-km road (15 m wide) connecting National Highway 18 to Tuan Chau Island was completed in late 1998, facilitating construction and transportation. Subsequently, reclamation activities on Tuan Chau intensified, beginning from its northeastern section.

Statistical comparison shows that between 1994 and 2000: Garden land increased from 110.9 ha to 385.4 ha; Residential & public facilities increased from 158.1 ha to 456.3 ha (+185.5%); Forest land decreased from 557.3 ha to 396.7 ha; Bare land decreased from 121.9 ha to 59.7 ha; Transportation land increased from 94.3 ha to 142.3 ha; Water surface area declined sharply from 1,208.6 ha to 810.7 ha ($\approx 30\%$ reduction).

According to the 2000 World Heritage nomination dossier, Ha Long Bay's biodiversity was concentrated primarily within the core area, characterized by karst ecosystems, isolated limestone towers, and cave environments minimally affected by external evolution. Mangrove forests, coral reefs, and tropical rainforests on limestone islands, as well as hard- and soft-bottom ecosystems, were the main habitats for marine species.

By 2000, coral reefs were widely

distributed at depths of 4-6 m, with 163 recorded species, and an average coral cover of 30% (reaching up to 70-80% in certain areas). Additionally, 107 fish species were recorded within coral reef ecosystems, and mangrove areas hosted 37 bird species, 81 benthic species, and 90 fish species. However, biodiversity data for nearshore areas within the buffer zone remained limited, suggesting relatively low species diversity in coastal sections undergoing urban expansion.

Land Use Status in 2023

Landsat imagery (2023) (Figures 5 and 6) demonstrates that most nearshore water areas within the buffer zone—including Hung Thang, Bai Chay, Hong Gai, Bach Dang, Hong Hai, and Hong Ha Wards—have been reclaimed for urban development and transport infrastructure.

Land use statistics (Table 1) show the following trends (2000-2023): Garden land decreased from 385.4 ha to 267.3 ha; Residential & public facilities continued increasing (456.3 ha to 500.3 ha); Forest land increased (396.7 ha to 501.2 ha) - mainly on mountain peaks and limestone islands; Bare land increased significantly (59.7 ha to 443.5 ha) - largely due to levelling activities for construction; Transportation land increased (142.3 ha to 209.5 ha); Water surface areas continued to decline (810.7 ha to 329.3 ha).



Figure 5. Landsat satellite image (2023) showing the buffer zone of Ha Long Bay-Cat Ba Archipelago.



Figure 6. Land use map (2023) of the buffer zone area of Ha Long Bay-Cat Ba Archipelago, interpreted from Landsat imagery.

Proposed Reduction of the Buffer Zone in Ha Long and Cam Pha Cities

Based on the review of the existing buffer zone encompassing Ha Long Bay-Cat Ba Archipelago across the administrative territories of Ha Long City, Cam Pha City, and Van Don District, the areas extending from National Highway 18 (as designated in the 2000 inscription map) to the current coastal road, covering Hung Thang Ward to Quang Hanh Ward, no longer retain natural landscapes or attributes contributing to the Heritage’s OUV.

Therefore, Quang Ninh Province proposes to adopt the existing coastal road as the new outer boundary of the buffer zone, thereby excluding approximately 2,580.1 hectares from

the designated area.

This adjustment ensures: (1) clear, fixed physical boundaries (coastal road) for boundary demarcation and management; (2) functional zoning alignment between the buffer and surrounding urban areas; (3) exclusion of densely urbanized, infrastructural, and defense zones that no longer serve protective functions for the core Heritage area.

The areas proposed for exclusion include residential and urban zones (some established before 1994), cultural and defense facilities (notably those under Navy Brigade 170), and urban infrastructure projects under implementation in coastal Ha Long and Cam Pha.

DISCUSSION

Satellite analysis and land use data reveal a progressive and continuous reduction of coastal water surfaces within Ha Long Bay's buffer zone—from 1,208.6 ha (1994) to 810.7 ha (2000) and 329.3 ha (2023)—accompanied by a sharp increase in urban and infrastructural land cover. This pattern reflects more than two decades of coastal urbanization and reclamation across the Bai Chay - Hung Thang - Hong Gai - Hong Ha - Quang Hanh corridor.

From a heritage governance perspective, this indicates a functional slippage of the buffer zone—its original role as an ecological and visual protective belt has been weakened due to: (1) The overly broad and impractical boundary design, overlapping with urban, defense, and infrastructure areas; and (2) The absence of physical demarcation markers, leading to regulatory ambiguities and conflicts with development planning.

Consequently, management costs and institutional conflicts between conservation and development goals have increased, posing risks to the integrity of the OUV.

The proposed “boundary contraction”—shifting the buffer limit to the coastal road and excluding 2,251.1 ha of urbanized land—reflects a pragmatic, adaptive approach consistent with UNESCO's notion of a “dynamic buffer zone.” This revision enhances: (1) the ecological focus of the buffer zone; (2) feasibility of on-site demarcation and monitoring; (3) legal coherence with existing land uses.

However, this approach carries the risk of “status regularization,” i.e., legitimizing urban expansion unless accompanied by strong Heritage Impact Assessment (HIA) and environmental management mechanisms. In governance terms, this challenge reflects fragmented institutional responsibilities, weak enforcement of cross-sectoral regulations, and the absence of an integrated monitoring and accountability framework between heritage, construction, and environmental authorities. The overlapping mandates among provincial, municipal, and sectoral agencies often result in regulatory gaps, inconsistent decision-making,

and limited transparency in land-use adjustments. Strengthening inter-agency coordination, legal accountability, and stakeholder participation is therefore essential to prevent the boundary adjustment from becoming a de facto endorsement of urban encroachment. Hence, boundary adjustment must be complemented by robust monitoring tools and inter-sectoral coordination frameworks.

Ecological assessment further confirms that the reduced buffer area mainly comprises coastal and intertidal soft-bottom ecosystems, with minimal mangrove presence. Thus, maintaining these areas within the buffer zone yields limited conservation benefit compared to the management cost. Nonetheless, ecosystem services such as tidal flushing and benthic habitats must be accounted for through appropriate offset or transitional management measures.

In terms of policy tools, the study proposes integrating Environmental Impact Assessment (EIA) and mandatory Heritage Impact Assessment (HIA) for all projects within and adjacent to the buffer zone, embedding buffer zone management into provincial planning and promoting coordination between the Ha Long Bay Management Board, local authorities, and relevant ministries (Culture, Environment, Defense).

The paper also recommends establishing functional subzones—strict protection, ecotourism, and community livelihood areas—to operationalize a balanced conservation-development framework and spatially distribute environmental risks.

Limitations remain, including: (1) lack of quantitative biodiversity data in coastal sections; (2) absence of carrying capacity and pollution modeling; (3) insufficient socio-economic impact assessment for local fishing communities.

These require targeted field surveys and integrated assessment prior to final boundary submission to UNESCO.

MANAGEMENT FRAMEWORK FOR HA LONG BAY WORLD HERITAGE BUFFER ZONE AFTER BOUNDARY ADJUSTMENT TOWARD SUSTAINABLE DEVELOPMENT

Strengthening Protection and Sustainable Development in the Adjusted Buffer Zone: The implementation of socio-economic development activities within and around the buffer zone must be consistent with the Master Plan for the Red River Delta Region, the Provincial Master Plan of Quang Ninh (2021-2030, vision to 2050), and the General Master Plan for Ha Long City to 2040. Development must be harmonized with the overarching goals of heritage conservation and environmental protection, especially in transition areas adjacent to the buffer zone, including the 2,251.1 ha recently excluded from the former buffer zone (approximately 2,232.2 ha in Ha Long City and 18.9 ha in Cam Pha City). Sustainable management within this area requires: (1) Controlling new urban expansion and coastal reclamation activities; (2) Integrating heritage protection requirements into local land use and construction planning; (3) Maintaining environmental carrying capacity and water quality; (4) Strengthening community engagement and benefit-sharing mechanisms for heritage protection.

Management policy: In Vietnam, state management is carried out according to administrative units at all levels (commune, provincial, regional, national). Therefore, policies on management of Heritage buffer zones are actually carried out on a larger area of administrative units at all levels. At the same time, management of Heritage buffer zones is closely linked to the implementation of Strategies, Planning, Plans, projects and related regulations according to the current legal system.

Management plan: Develop a Management Plan for the Ha Long Bay Heritage Buffer Zone until 2030 and a vision to 2050. This includes clearly defining the preparation, appraisal and approval of environmental impact assessments (EIA) and

mandating the integration of Heritage Impact Assessments (HIA) into all development investment projects in the buffer zone and transition zone. At the same time, consider implementing cumulative impact assessments for all projects that have been invested in and constructed in the buffer zone in the past.

Combining the enhancement of effective management of the Heritage buffer zone through the serious implementation of the Master Plan of Ha Long City to 2040; Adjusting the Land Use Planning for the period 2021-2030 of Ha Long City; Adjusting the Land Use Planning for the period 2021-2030 of Quang Yen town; Adjusting the Land Use Planning for the period 2021-2030 of Van Don district.

Urban construction order management plan: Develop and promulgate regulations to control building height, construction density and urban green area ratio for investment projects to build urban areas in the Heritage buffer zone.

CONCLUSION

The analysis of multi-temporal satellite imagery and land use data demonstrates a significant and continuous transformation within Ha Long Bay's buffer zone over the past three decades. From 1994 to 2023, the coastal water and intertidal areas declined sharply (approximately 1,208.6 ha to 810.7 ha to 329.3 ha), while built-up land-comprising residential areas, public infrastructure, and transportation networks-increased markedly. This trend reflects an extended period of urbanization and coastal reclamation along the Ha Long - Cam Pha shoreline, resulting in the gradual erosion of the buffer zone's original protective and ecological functions.

In this context, the adjustment of buffer zone boundaries-contracting them along the existing coastal road and excluding approximately 2,251 ha of fully urbanized and defense land-is both scientifically and practically justified. This modification restores the instrumental purpose of the buffer zone by concentrating protection on areas that still maintain ecological and landscape connectivity

with the core Heritage area, while enhancing feasibility for on-site demarcation and management.

To ensure that this adjustment translates into substantive conservation outcomes, rather than merely cartographic refinement, the following integrated actions are essential: (i) Physical boundary demarcation and publication of official maps, establishing clear, legally recognized management zones; (ii) Functional sub-zoning within the buffer zone, accompanied by distinct regulatory instruments-mandatory HIA/EIA procedures, environmental load thresholds, wastewater standards, and tourism-navigation control mechanisms; (iii) Inter-sectoral coordination mechanisms involving the Ha Long Bay Management Board, local authorities, and relevant ministries to harmonize heritage protection, urban development, and maritime activities; (iv) Integration of buffer zone management objectives into provincial and regional socio-economic development plans, ensuring policy coherence and long-term sustainability.

Further research and management attention should focus on: (i) Quantitative biodiversity surveys in nearshore and transitional habitats; (ii) Modeling of carrying capacity and pollution dispersion in coastal waters; (iii) Socio-economic assessments of community livelihoods and resource dependence.

Such measures will provide essential data inputs for finalizing the management framework and regulatory instruments following the adjustment.

The outcomes of this study serve as a critical scientific foundation for UNESCO's minor boundary modification process, ensuring

that the revision does not diminish the Outstanding Universal Value or integrity of Ha Long Bay World Natural Heritage Site. At the same time, it provides a model for harmonizing heritage conservation and green development, reinforcing Quang Ninh Province's strategic vision of becoming a sustainably developed, service-oriented, and environmentally resilient province within the Northern Key Economic Region of Vietnam.

REFERENCES

- UNESCO (2019). Operational Guidelines for the Implementation of the World Heritage Convention. Paris: UNESCO.
<https://whc.unesco.org/en/guidelines/>
- IUCN (2020). Guidelines for Protected Area Buffer Zones. Gland, Switzerland: IUCN.
- UNESCO (2021). World Heritage List.
<https://whc.unesco.org/en/list/>
- UNESCO World Heritage Centre - Decision 45 COM 8B.8 (2023) <https://whc.unesco.org/en/decisions/8268>
- Chính phủ Nước cộng hòa Xã hội Chủ nghĩa Việt Nam (2017). Nghị định số 109/2017/NĐ-CP ngày 21/9/2017 của Chính phủ Quy định về bảo vệ và quản lý Di sản văn hóa và thiên nhiên thế giới ở Việt Nam.
- Chính phủ Nước cộng hòa Xã hội Chủ nghĩa Việt Nam (2023). Quyết định số 80/QĐ-TTg của Thủ tướng Chính phủ: Phê duyệt Quy hoạch tỉnh Quảng Ninh thời kỳ 2021 - 2030, tầm nhìn đến năm 2050.
- Tuổi Trẻ Online (2023). Vùng đệm vịnh Hạ Long đang đô thị hóa ra sao? Link truy cập tháng 10/2025: <https://tuoitre.vn/vung-dem-vinh-ha-long-dang-do-thi-hoa-ra-sao-20231110074654153.htm>
- Nguyễn, V. H., Trần, T. H., & Phạm, Q. N. (2020). Quản lý vùng đệm trong phát triển du lịch bền vững tại Tràng An, Ninh Bình. Tạp chí Khoa học Môi trường và Địa chất, 26(4), 45-56.

Preliminary Survey of Microclimate and Environmental Conditions in Show Caves in Hoa Binh and Phong Nha – Ke Bang areas

Vu Thi Minh Nguyet^{1*}, Nguyen Thuy Duong², Czuppon György³, Stieber Jozsef⁴, Van Phu Hung¹, Ha Tung Lam¹, Bui Van Quynh¹

¹Institute of Earth Sciences, Vietnam Academy of Science and Technology, Vietnam

²VNU Vietnam Japan University, Vietnam National University, Vietnam

³Institute for Geological and Geochemical Research, Research Centre for Astronomy and Earth Sciences, HUN-REN, Hungary

⁴Stieber Environmental Ltd., Hungary

*Email: vtmnguyet@ies.vast.vn

Abstract: This study presents a preliminary survey of microclimatic and environmental conditions in ten representative show caves located in the Phu Tho province and Phong Nha–Ke Bang karst regions of Vietnam. Key parameters, including air temperature, CO₂ concentration, and fine particulate matter (PM_{0.3}, PM_{2.5}, PM₁₀), were measured at selected positions inside and outside the caves during February 2023 using portable instruments. Air temperature showed minimal spatial variation, indicating a stable internal microclimate typical of tropical karst systems. In contrast, CO₂ concentrations and particulate matter displayed clear spatial differences, with higher values recorded in inner and tourist-accessible zones, particularly in caves with restricted ventilation and high visitor density. Principal Component Analysis (PCA) revealed strong correlations among temperature, humidity, and CO₂, representing natural cave microclimatic processes. In contrast, particulate matter fractions were more variable and primarily linked to anthropogenic disturbances. The integrated results confirm that internal cave environments maintain thermal and chemical stability but remain locally sensitive to human impact. These findings establish baseline data for microclimatic and air-quality conditions in Vietnam's tropical karst show caves, providing essential insights for sustainable management. Continuous environmental monitoring,

improved ventilation, and control of visitor numbers are recommended to preserve both the ecological integrity and scientific value of these unique subterranean systems.

Keywords: Cave microclimate, cave monitoring, show cave, Vietnam, karst.

INTRODUCTION

Karst caves are unique geological environments that host a wide range of scientific, ecological, and cultural values. Beyond their aesthetic and economic importance, caves and their carbonate deposits (speleothems) are valuable natural archives that preserve evidence of paleoclimate and paleoenvironmental changes over millennia (Fairchild & Baker, 2012). These formations record variations in stable isotopes, trace elements, and microstructures that reflect fluctuations in temperature, precipitation, and soil or vegetation dynamics at the surface. Consequently, maintaining the natural microclimatic stability of cave systems is crucial to ensure the reliability of geochemical and chronological data derived from speleothems.

Cave environments are characterized by relatively stable but highly sensitive microclimates. Air temperature, relative humidity, and gas concentrations (notably CO₂ and radon) are primarily controlled by the interaction between external meteorology, cave

geometry, hydrological processes, and ventilation dynamics (de Freitas & Schmekal, 2003; Badino, 2010; Czuppon et al., 2018). Internal air circulation governs condensation, evaporation, and gas exchange, influencing carbonate formation and dissolution within the cave (de Freitas, 2010). Even subtle external perturbations or anthropogenic activities can disturb this equilibrium, altering the cave's physical and chemical conditions.

Among external drivers, CO₂ and radon dynamics play a key role in understanding cave-atmosphere behavior. CO₂ concentration reflects the balance between soil and karst degassing, air exchange, and biological respiration, while radon (²²²Rn) serves as a tracer of ventilation intensity and gas transport from the subsurface (Gregorič et al., 2013; Sainz et al., 2022; Li et al., 2024). Studies from diverse karst systems show that seasonal and diurnal temperature gradients can generate buoyancy-driven air circulation, modulating CO₂ and radon fluxes and linking subsurface processes to surface meteorology (Buzjak et al., 2024).

However, show caves—those developed for tourism—represent an especially fragile subset of karst systems. Human presence increases cave-air CO₂ through respiration and can alter temperature, humidity, and particulate matter (PM) levels. Lighting systems introduce heat and promote microbial and algal growth. Inadequate ventilation or excessive visitor density can lead to cumulative thermal and chemical disturbances (Cigna & Burri, 2000; Russell & MacLean, 2008). Systematic monitoring programs have therefore become essential to manage visitor carrying capacity and preserve the natural equilibrium (Cigna, 2016a; Cigna, 2016b; Constantin et al., 2021). Recent experiments in European show caves confirmed that even short-term visitor activity can elevate CO₂ and PM concentrations, highlighting the need for integrated microclimate management (Debevec & Rakovec, 2021; Miler et al., 2024).

Over the past two decades, research on cave-air dynamics has diversified in scope and method. Continuous multi-parameter

monitoring—including temperature, relative humidity, CO₂, radon, and particulate matter—is now coupled with numerical simulation and tracer modeling (de Freitas & Schmekal, 2003; Fernandez-Cortes et al., 2015; Pla et al., 2023). Recent advances have emphasized the interactions between meteorological forcing and cave morphology (entrance geometry, dead-end passages, and thermal gradients). In China, for instance, microclimate monitoring of large tropical karst systems revealed that CO₂ variability is primarily governed by temperature-driven air circulation and hydrological activity rather than direct human input (Li et al., 2024; Xiong et al., 2023). Similarly, studies in the Mogao Caves, China—a world heritage site—demonstrated the influence of open visitation schedules on indoor temperature and humidity, reinforcing the importance of temporal access control (Gong et al., 2025).

In Southeast Asia, and particularly in Vietnam, research on cave microclimate remains limited but is expanding. Early Vietnamese investigations focused on radon distribution and air exchange in karst systems of Ha Giang Province (Duong et al., 2016), demonstrating seasonal fluctuations and the influence of cave morphology on gas accumulation. Trinh et al. (2018) provided the first quantitative assessment of CO₂ dynamics in tropical show caves of Phong Nha-Ke Bang, showing that tropical caves can exhibit both strong diurnal variability and human-induced CO₂ enrichment during peak visitation periods. These findings were consistent with global trends but also underscored the specific sensitivity of tropical karst caves to combined thermal and hydrological forcing.

Despite increasing international interest, there remain critical regional knowledge gaps. While extensive datasets exist for European and Chinese show caves, few systematic studies have addressed tropical monsoonal karst environments such as those in Vietnam. These systems experience high external humidity, small annual temperature amplitudes, and intense seasonal recharge, resulting in distinct

ventilation regimes that differ from those of temperate caves (Trần Ngọc et al., 2023). Furthermore, data on particulate matter and air quality indicators (PM_{2.5}, PM₁₀) remain scarce, despite growing concern over their impact on speleothem preservation and visitor health (Martin-Pozas et al., 2024; Ijoma et al., 2025).

The present study, therefore, aims to provide a preliminary characterization of the microclimatic and environmental conditions in representative show caves from the Hoa Binh and Phong Nha-Ke Bang regions, Vietnam. Specific objectives are to: (1) characterize cave microclimate (temperature and relative humidity); (2) assess cave air quality (CO₂ and fine particulate matter); and (3) compare sites outside and inside the cave to evaluate spatial gradients and possible anthropogenic or morphological controls. By establishing a quantitative baseline of microclimatic and air-quality conditions, this work contributes to sustainable cave management, environmental conservation, and the protection of Vietnam's karst systems as both natural heritage and scientific resources.

REGIONAL SETTING

Location

The study was conducted in karst show caves currently developed for tourism in Van Son and Cao Phong communes, Hoa Binh area (Phu Tho province), and within the Phong Nha-Ke Bang National Park, Quang Tri province (Figure 1). A total of ten representative caves from these two areas were selected, with their geographic coordinates and elevations presented in Table 1.



Figure 1. Location map of the study areas: I – Hoa Binh area; II – Phong Nha-Ke Bang National Park area

Table 1. Coordinates and elevation of the surveyed caves

Area	Cave name	Location		
		X	Y	Elevation (a.s.l)
I. Hoa Binh	Hoa Son	105°19'22"	20°42'45'	
	Nam Son	105°10'48"	20°31'48"	884
II. Phong Nha - Ke Bang National Park	Dark cave	106°13'54.0"	17°34'14.0"	40
	Hang Va	106°17'4.9"	17°29'22.0"	99
	Hang Voi	106°17'3.10"	17°31'12.93"	116
	Paradise Cave	106°13'23.83"	17°31'10.0"	215
	Phong Nha	106°16'55.56"	17°34'59.42"	40
	Ruc Mon	105°54'5.58"	17°44'44.0"	260
	Nuoc Nut	106°17'17.0"	17°29'26.9"	100
	Son Doong	106°17'13.38"	17°28'17.65"	431

Geological settings

The surveyed caves in Hoa Binh area (Phu Tho province) are located in the Song Da

tectonic zone, which includes terrigenous sedimentary formations, mafic eruptions, acid-alkali, and mafic intrusions of the Vien Nam (T₁vn), Tan Lac (T₁tl), and Ba Vi (T₁bv) formations.

The upper part of the zone is terrigenous carbonate sediments of the Dong Giao (T_2 dg), Nam Tham (T_2 nt), Song Boi (T_{2-3} sb) formations with a total thickness of >4500m, often developing narrow folds, with a slope of 30–70° in the Northwest-Southeast direction. They all belong to the intracontinental rift formation type (Ký et al., 1973).

Phong Nha–Ke Bang National Park is located in the northern section of the Annamite Range, Quang Tri Province, central Vietnam. It represents one of the oldest and most extensive tropical karst landscapes in Asia, with carbonate formation dating back to the Late Ordovician period (~464 Ma) (UNESCO, 2014). The bedrock is dominated by thickly bedded Devonian–Permian limestones interbedded with shales, siltstones, and minor magmatic intrusions, providing a diverse lithological framework conducive to karstification (Ponta et al., 2022; Nghi et al., 2023).

Multiple tectonic phases throughout the Paleozoic to Cenozoic have uplifted, faulted, and fractured the massif, creating a complex network of structural discontinuities that guide groundwater and cave development. Major fault orientations are NE–SW, NW–SE, W–E, and N–S, forming intersecting fracture systems that have controlled both hydrological drainage and air circulation pathways within the caves (Nghi et al., 2023). These faults act as primary conduits for underground rivers and secondary ventilation shafts, influencing microclimatic gradients and gas exchange dynamics between the surface and subsurface environments.

Geomorphologically, the karst terrain occupies about three-quarters of the park's area and includes both high karst blocks (800–1,600 m a.s.l.) and lower dissected karst plains (200–400 m). The area hosts more than 300 explored caves with a combined length exceeding 160 km, including Son Doong Cave, one of the world's largest known chambers (Oxalis Adventure, 2022). The combination of intense tropical weathering, active tectonics, and prolonged geological evolution has resulted in a highly developed, multi-level cave system featuring extensive subterranean rivers, vertical

shafts, and large chambers. These geological and structural characteristics not only explain the exceptional morphological diversity of Phong Nha–Ke Bang but also underpin the site's unique microclimatic and ventilation regimes, which are critical for understanding environmental processes in tropical karst caves.

Climate characteristics

Climatic Characteristics of the Red River Delta region

The general characteristics of the climate in Northern Vietnam are a tropical monsoon climate, low radiation balance, limited sunshine, low temperatures, and a cold winter (Nguyen & Nguyen, 2004). The surveyed caves in Phu Tho province are located in the Red River Delta region, one of the four climatic regions of Northern Vietnam. The Red River Delta zone is characterised by a humid subtropical monsoon climate with four distinct seasons. Summers (May to September) are typically hot and humid, with temperatures often averaging 28–30 °C and occasional peaks above 38–41 °C. Winters (November to February) are cooler, with mean monthly temperatures ranging from 15 to 17 °C, and in some years, frost or near-frost conditions occur, accompanied by persistent drizzle and limited sunshine. The annual mean temperature in the coastal delta area is approximately 23–24 °C, while annual precipitation commonly ranges from 1,400 to 1,800 mm, and sunshine duration is typically in the range of 1,400–1,700 hours per year (Nguyen & Nguyen, 2004; WorldData.info, 2025). The combination of high humidity (82–85%) and frequent light rainfall, along with minimal dry periods, typifies the winter “crachin” drizzle climate of northern Vietnam. Among the four climatic regions, the Red River Delta region is characterized by higher temperatures and a smaller temperature range than the other regions.

Climatic Conditions of the Phong Nha–Ke Bang Karst Region

Located in the North Central Vietnam zone, the Phong Nha–Ke Bang National Park area experiences a tropical monsoon climate

with an annual mean air temperature of 23–25 °C, maximum summer values reaching up to 41 °C, and minimum winter lows as low as 6 °C. Annual rainfall is substantial, ranging from 2,000 to 2,500 mm, with approximately 88% of rainfall occurring between July and December. The mean relative humidity is around 84%, and there are more than 160 rainy days per year (UNESCO, 2014). Such conditions, in combination with steep karst topography and dense forest cover, influence cave airflow and subterranean microclimates by promoting intense recharge, high humidity retention and limited seasonal temperature fluctuation.

Materials and Methods

To evaluate the potential impact of tourism activities on the cave environment, this study measured key microclimatic and air quality parameters, including air temperature, relative humidity, CO₂ concentration, and fine particulate matter (PM_{0.3}, PM_{2.5}, and PM₁₀). Measurements were conducted in February 2023 using specialized portable instruments. Specifically, air temperature was measured and recorded using a Greisinger GMH 3700 Series thermometer (Greisinger Electronic GmbH, Germany); CO₂ concentration was determined with an AirCO₂ntrol 3000 analyzer (Trotec

GmbH, Germany); and suspended particulate matter in the PM_{0.3}, PM_{2.5}, and PM₁₀ size fractions were quantified using a Total Meter HT-9600 particle counter (Total Meter, China).

To capture spatial variability and potential gradients influenced by cave morphology and visitor presence, three monitoring points were established at each site: OUT (outside the entrance), IN (the tourist-accessible zone), and REF (a deeper reference zone with minimal disturbance). At each station, measurements were taken repeatedly at regular intervals during cave opening hours to represent typical tourist conditions. The data were subsequently processed to assess intra-cave variability and the extent of anthropogenic influence.

The collected microclimatic and environmental data were statistically analyzed using graphical methods and Principal Component Analysis (PCA) to identify the principal factors controlling cave-air dynamics and to evaluate the relationships between physical parameters and tourism-related disturbances.

RESULTS AND DISCUSSION

Temperature

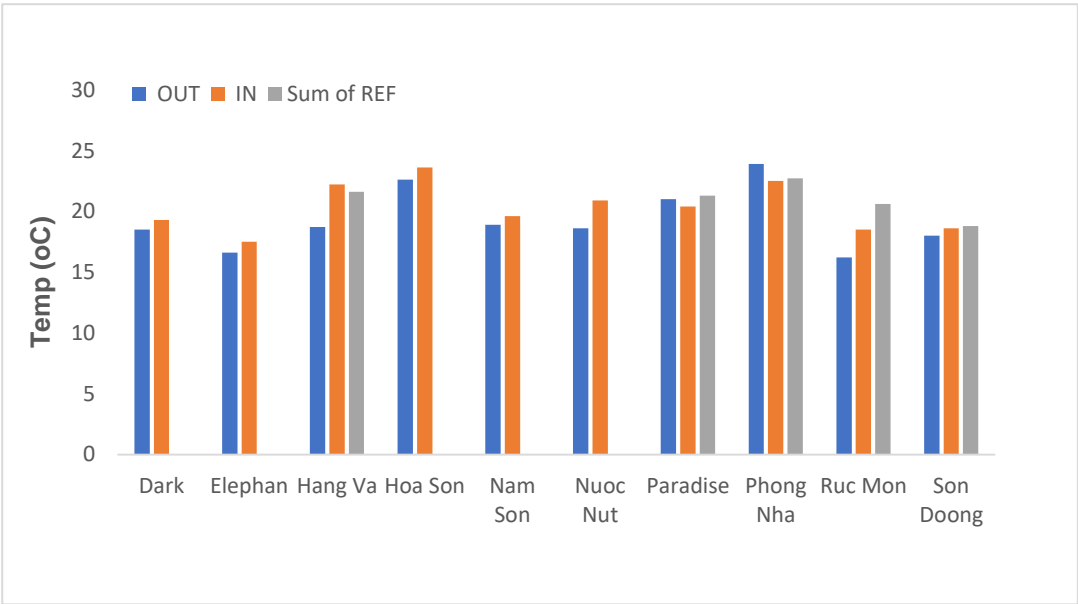


Figure 2: Temperature measured at cave sites in Feb 2023

The REF temperature parameter was measured only in Va, Thien Duong (Paradise), and Son Doong caves, while the remaining caves were monitored only at the IN and OUT positions. Air temperature exhibited moderate variation among the surveyed caves across both study areas (Fig. 2). At the time of measurement, the outdoor air temperature in Phu Tho Province ranged from 18.9°C to 22.6°C, while in the Phong Nha-Ke Bang area, it ranged from 16.2°C to 23.9 °C. Correspondingly, the in-cave air temperature ranged from 19.6 °C to 23.6 °C in 2 caves in Hoa Binh area and from 17.5 °C to 23.6 °C in caves in Phong Nha-Ke Bang National Park. Temperature differences between the OUT, IN, and REF positions were

small (1–2 °C), indicating a generally stable thermal regime across all surveyed caves.

The observed temperature uniformity reflects the strong thermal buffering capacity typical of karst environments, where the rock mass insulates internal air from short-term external fluctuations (Badino, 2010; De Freitas, 2010). Such stability helps maintain constant relative humidity and prevents abrupt microclimatic changes that could damage speleothems or affect cave-dwelling organisms. Slightly higher internal temperatures in Hoa Son and Phong Nha caves may result from limited ventilation and greater tourist activity, which increase heat and CO₂ emissions inside the caves.

CO₂ concentration

CO₂ concentrations showed notable spatial variation among caves and between the measurement positions (Fig. 3). Outdoor CO₂ levels ranged from approximately 350 ppm to 495 ppm, reflecting near-ambient conditions. Inside the caves, concentrations increased

substantially, with IN values ranging from 370 ppm to 856 ppm, and REF values reaching 1,262 ppm in Paradise Cave and 1,223 ppm in Phong Nha Cave. The lowest concentrations occurred at the entrances of Elephant and Ruc Mon caves, while intermediate values were recorded in Hoa Son and Nam Son caves.

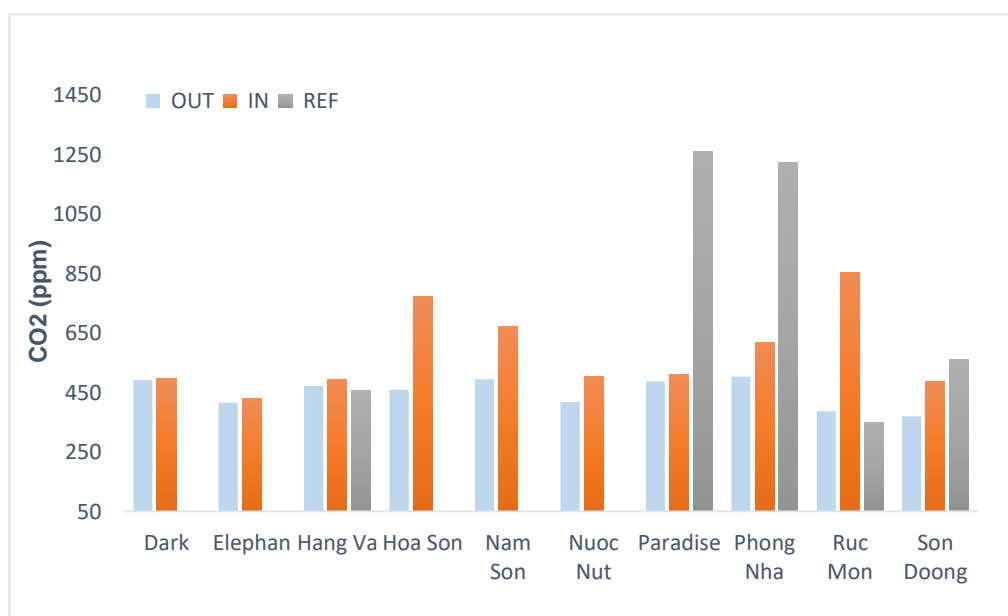


Figure 3: CO₂ concentration at surveyed caves in Feb 2023

The progressive increase in CO₂ from OUT to IN and REF positions indicates a gradual accumulation of respired CO₂ and limited air exchange, especially in deep or enclosed

chambers. The highest levels observed in the heavily visited Phong Nha and Paradise caves suggest that tourism-related emissions (human respiration, lighting, and restricted airflow)

might contribute to CO₂ enrichment (De Freitas, 2010; Buzjak et al., 2024).

These observed results in REF points are consistent with those of Tr  nh et al. (2018), who reported seasonal CO₂ fluctuations ranging from about 1,000 ppm to more than 8,000 ppm in tropical Vietnamese caves, driven by ventilation reversals and soil gas inputs. While their study emphasized temporal dynamics, the present survey highlights spatial variation along the OUT-IN-REF gradient. Both findings confirm that CO₂ accumulation is strongly influenced by cave geometry, ventilation efficiency, and human activity, and that long-term monitoring is essential to comprehensively capture seasonal and anthropogenic effects.

Fine Particulate Matter (PM_{0.3}, PM_{2.5}, and PM₁₀)

The concentration of airborne particulate matter varied considerably among the surveyed caves and among sampling positions (OUT, IN, REF) (Figs. 4–6). For PM_{0.3}, concentrations were generally higher at the IN positions (50,000–450,000 particles L^{−1}) than at the OUT positions (50,000–250,000 particles L^{−1}). The highest values occurred in Ruc Mon and Nuoc Nut caves, followed by Hang Va and Phong Nha, whereas Dark and Son Doong caves exhibited the lowest levels (< 100,000 particles L^{−1}). A similar trend was observed for PM_{2.5} (500–

10,000 particles L^{−1}) and PM₁₀ (5–40 particles L^{−1}), with peaks again in Ruc Mon, Hang Va, and Nuoc Nut. Concentrations decreased toward the REF zones in the majority of the studied caves, except where ventilation was limited. These findings suggest that finer aerosols predominate in the cave air composition and that their distribution is influenced by cave morphology and human activities.

The higher PM levels recorded in tourist-accessible areas align well with previous studies, which have shown that visitor movement and lighting systems can resuspend surface dust and introduce external aerosols into cave atmospheres (Fernandez-Cortes et al., 2015; Miler et al., 2024). Caves with large entrances and strong air circulation, such as Paradise and Son Doong, showed minimal accumulation, confirming the mitigating role of ventilation.

Persistent fine-particle enrichment may pose risks for speleothem conservation and microbial colonization, as fine aerosols can serve as carriers for organic matter and microorganisms (Martin-Pozas et al., 2024). These results underscore the importance of continuous monitoring of particulate matter and the implementation of visitor management and ventilation control measures to mitigate anthropogenic impacts.

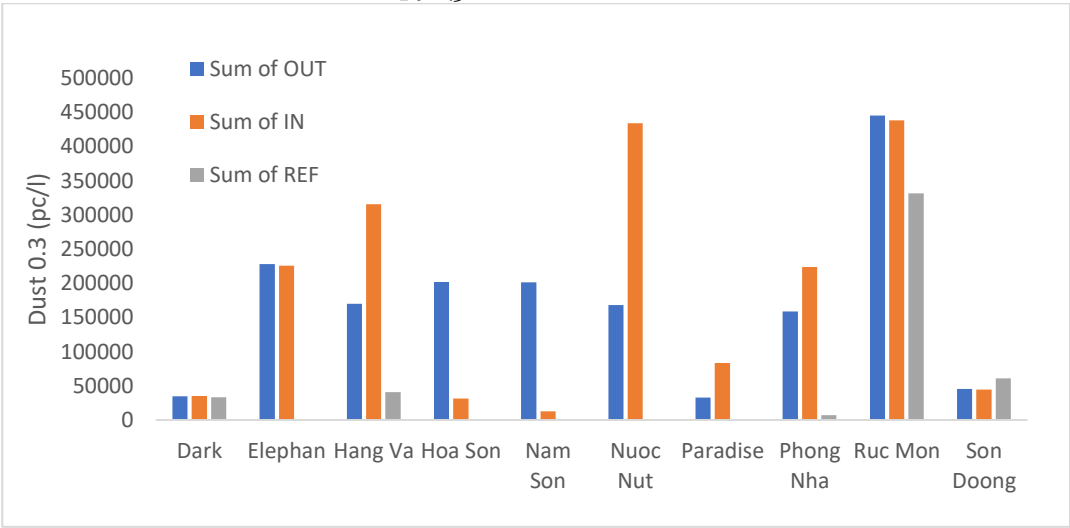


Figure 4: Fine particle matter density of 0.3 µm in caves in February 2023

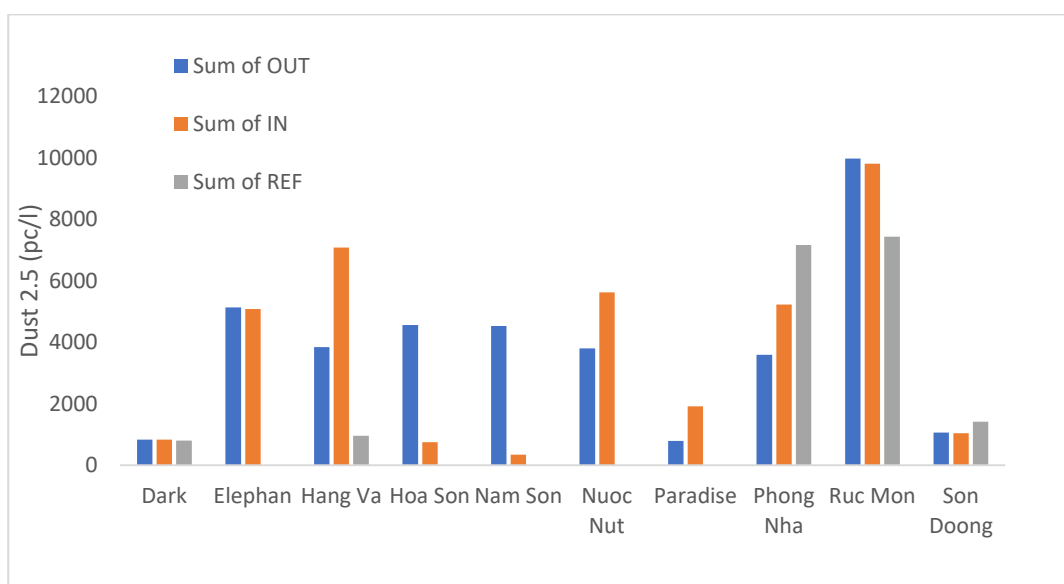


Figure 5: Density of 2.5 µm fine dust particles in caves in February 2023

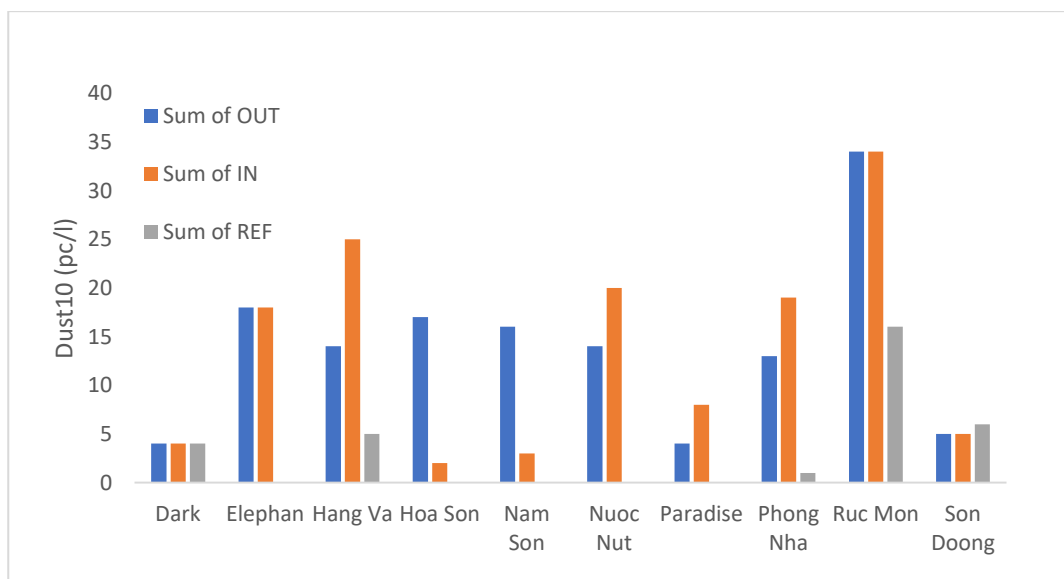


Figure 6: Density of 10 µm fine dust particles in caves in February 2023

PCA analysis

The Principal Component Analysis (PCA) was applied to evaluate relationships among measured variables and to distinguish between environmental conditions at different sampling positions (OUT, IN, REF) (Fig. 7). The first two principal components explained 62.4% of the total variance (Dim₁ = 43.6%, Dim₂ = 18.8%).

The biplot reveals that temperature, relative humidity, and CO₂ are closely correlated and load negatively on Dim₁, indicating their shared control by internal cave processes. Particulate matter fractions (PM_{0.3}, PM_{2.5}, PM₁₀) cluster positively on Dim₁, reflecting their anthropogenic origin. Air pressure aligns more closely with OUT samples, highlighting the influence of external meteorological conditions.

Samples from the IN and REF positions cluster together and are clearly separated from OUT samples along Dim1, indicating the distinctiveness of the internal cave microclimate compared to external air. This separation demonstrates that cave interiors are governed by stable thermal and gas-regulation dynamics, whereas the entrances act as transitional zones with mixed air masses.

The PCA results confirm that CO₂, temperature, and humidity define the natural microclimatic regime of caves, while dust-related parameters reflect human-induced variability. Similar differentiation between natural and anthropogenic controls has been documented in other European show caves (Miller et al., 2024; Martin-Pozas et al., 2024). Maintaining balance in these transitional zones is essential to preserve internal environmental stability and prevent long-term degradation of the cave ecosystem.

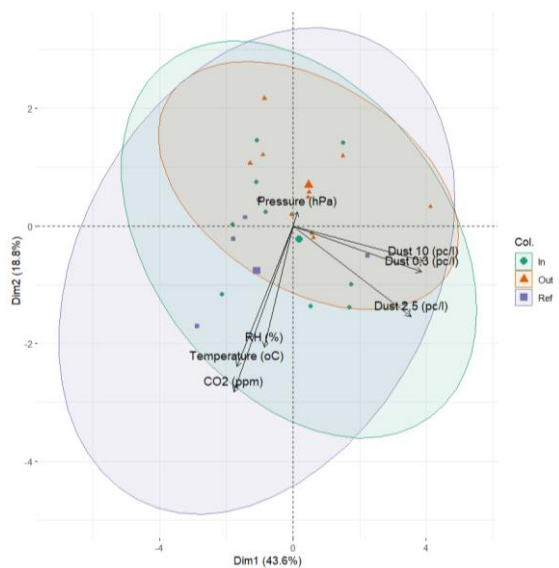


Figure 7. Biplot of Principal Components (PCA)

Role of the distinct geological structures of caves in the two regions in regulating the microclimate in caves

The environmental conditions recorded in the surveyed caves reflect a strong coupling between regional geological structures, climatic regimes, and local anthropogenic influences. In the Hoa Binh area, caves are developed mainly

within terrigenous-carbonate sedimentary formations of the Song Da tectonic zone, which exhibit steeply inclined strata and numerous fault intersections. These structural features provide pathways for groundwater circulation and limited air exchange, resulting in relatively stable but slightly variable internal temperatures. The humid subtropical monsoon climate of the Red River Delta region—characterized by cool, moist winters with persistent drizzle and hot, humid summers (Nguyen & Nguyen, 2004)—enhances external-internal thermal gradients and seasonal humidity contrasts, both of which influence near-entrance ventilation and condensation processes.

In contrast, the Phong Nha–Ke Bang karst region lies within one of the most complex and ancient tropical karst systems in Asia, where thick Devonian–Permian limestones, intersected by NE–SW and NW–SE faults, host extensive multi-level caves and underground rivers (UNESCO, 2014; Nghi et al., 2023). The tropical monsoon climate, with mean annual temperatures of 23–25 °C and rainfall exceeding 2,000 mm (UNESCO, 2014; Tran et al., 2016), maintains persistently high humidity and promotes intense infiltration and soil CO₂ recharge. These conditions produce stable cave temperatures but also facilitate CO₂ accumulation in deep, poorly ventilated sections, as confirmed by the elevated concentrations measured at REF positions in Phong Nha and Paradise caves. The combination of a thick limestone cover, structural confinement, and a humid tropical climate supports the formation of large, thermally buffered chambers, yet makes them highly sensitive to human-induced disturbances, such as increased visitor traffic, lighting, and dust resuspension.

Impact of the tropical climate regime on microclimate in caves

In the caves surveyed in the Hoa Binh area and the Phong Nha–Ke Bang karst area, our measurements indicate that tropical climatic forcing, combined with local anthropogenic activity, governs the observed microclimatic

signatures. Air temperature inside the caves was relatively stable (IN $\approx 17.5\text{--}23.6$ °C; OUT $\approx 16.2\text{--}23.9$ °C), with small gradients between OUT, IN and REF ($\approx 1\text{--}2$ °C). By contrast, CO₂ and fine particulate matter showed substantial spatial heterogeneity: outdoor CO₂ was near-ambient ($\approx 350\text{--}495$ ppm) while IN values reached 370–856 ppm and REF pockets recorded up to $\approx 1,200\text{--}1,260$ ppm (e.g., Paradise, Phong Nha). Fine aerosol burdens were concentrated in tourist zones (PM_{0.3} up to $\sim 4.5 \times 10^5$ particles·L⁻¹; PM_{2.5} up to $\sim 1 \times 10^4$ particles·L⁻¹; PM₁₀ mostly < 40 particles·L⁻¹), with the highest PM measured at Ruc Mon and Nuoc Nut. Together these observations indicate that (1) the tropical monsoon regime (high humidity, strong wet-season recharge and small annual temperature amplitude) produces thermally buffered interiors, and (2) where ventilation is limited, anthropogenic inputs (visitor respiration, movement, lighting and dust) accumulate and persist in interior zones, producing locally elevated CO₂ and PM that would not be rapidly removed by natural flushing. These findings are relevant to the findings of Trinh et al. (2018), Fernández-Cortés et al. (2020), and Martin-Pozas et al. (2024).

When these field results are compared with studies from temperate regions (Europe) and temperate/subtropical sites in China, clear contrasts emerge in the mechanisms and magnitudes of microclimatic response. Temperate caves commonly experience larger external-internal temperature contrasts, which drive strong, seasonal thermally forced ventilation (chimney effects and seasonal reversals). As a result, visitor-related CO₂ and PM pulses are often episodic and are more rapidly diluted during ventilated periods (De Freitas & Schmekel, 2003; Sainz et al., 2022). By contrast, tropical karst caves like those we studied—and as documented in other Vietnamese and Chinese tropical karst investigations—exhibit weaker temperature forcing and stronger hydrological/soil CO₂ inputs; consequently, anthropogenic emissions tend to be more persistent in the absence of effective ventilation (Trinh et al., 2018; Li et al., 2024; Xiong et al., 2023). In sum, temperate

systems are generally characterized by seasonally pulsed coupling with the atmosphere, whereas tropical systems show greater persistence of human-origin signals (CO₂, fine PM) and stronger hydrologically-driven seasonal modulation — an important distinction that should inform monitoring strategies and management measures tailored to each climatic context (De Freitas, 2010; Miler et al., 2024).

Implications for Cave Management

From a management perspective, both study areas illustrate how geological structure and regional climate jointly regulate cave microclimate. In the northern monsoon zone, seasonal variations in air temperature and humidity drive short-term fluctuations in ventilation near cave entrances. In contrast, the tropical karst of Phong Nha–Ke Bang experiences year-round high humidity and limited air renewal, which enhances the persistence of elevated CO₂ and fine particles. These findings highlight the importance of tailoring conservation strategies to local geological and climatic contexts. Continuous monitoring of air composition, humidity, and particulate matter should be prioritized in tourist-accessible caves, particularly those developed along major fault systems where air circulation is restricted. Managing visitor flow, optimizing natural or assisted ventilation, and minimizing dust-generating activities are crucial to preserving the delicate microclimatic balance of Vietnam's show caves.

CONCLUSION

Measurements of microclimate factors (CO₂, temperature) and airborne dust composition in some karst caves in the Hoa Binh area (Phu Tho province) and Phong Nha – Ke Bang areas show clear differences between caves, reflecting the influence of cave morphology, ventilation regime, and the level of human impact.

The results reveal a generally stable cave microclimate, characterized by minor temperature differences (1–2 °C) between the entrance and internal zones, and by elevated

but spatially consistent humidity. The measured temperatures in the caves are quite stable and higher than the outside environment in winter (February), demonstrating the air-conditioning characteristics of the tropical karst system. CO₂ and fine dust concentrations (especially PM_{2.5}) are significantly higher in caves with strong tourism activities such as Phong Nha, Thien Duong and Ruc Mon, while natural or less exploited caves such as Son Doong and Hang Va have stable conditions and low concentrations.

The integration of physical (temperature, humidity), chemical (CO₂), and atmospheric (particulate matter) parameters, supported by multivariate PCA analysis, demonstrated that internal cave environments are largely controlled by natural buffering processes, whereas localized disturbances arise from human presence. Temperature, humidity, and CO₂ collectively define the natural equilibrium of the cave atmosphere, while PM fractions serve as sensitive indicators of anthropogenic influence. These results contribute baseline data for understanding environmental dynamics in tropical karst caves, where systematic studies remain limited.

Importantly, when placed in a broader geographic context, the findings highlight fundamental contrasts between tropical cave systems such as those in Vietnam and temperate cave regions in China and Europe. In tropical settings, strong monsoonal forcing, high rainfall seasonality, and elevated biological productivity generate more dynamic external boundary conditions, which may enhance ventilation fluctuations, CO₂ variability, and hydrological responsiveness within caves. In contrast, temperate caves typically experience larger annual temperature amplitudes but lower biological CO₂ inputs, resulting in different patterns of cave-atmosphere coupling. Moreover, anthropogenic pressures—particularly mass tourism, land-use change, and increased aerosol loading—tend to impose disproportionately rapid and pronounced impacts in tropical caves due to their higher sensitivity to external climatic and ecological disturbances. Recognizing these climate-

regime- and human-driven differences is essential for interpreting cave microclimate behavior and ensuring that conservation strategies are tailored to the specific vulnerabilities of tropical versus temperate karst systems.

From a management perspective, maintaining the long-term stability of show caves requires striking a balance between tourism and conservation objectives. The findings underscore the necessity of continuous multi-parameter monitoring, visitor regulation during peak seasons, and ventilation optimization to reduce CO₂ accumulation and dust deposition. Establishing such monitoring programs will not only safeguard the scientific and ecological value of Vietnam's karst caves but also support the sustainable development of their tourism potential in the face of changing climatic and anthropogenic pressures.

ACKNOWLEDGMENT

This research was supported by the bilateral project between VAST and HAS (QTHU01.01/24-25 and NKM2024-6/2024), and by Nafosted project 105.99-2021.71.

REFERENCE

- Badino, G. (2010). UNDERGROUND METEOROLOGY- "What's the weather underground?" *Acta Carsologica*, 39(3). <https://doi.org/10.3986/ac.v39i3.74>.
- Buzjak, N., Gabrovšek, F., Perşoiu, A., Pennos, C., Paar, D., & Bočić, N. (2024). CO₂ Emission from Caves by Temperature-Driven Air Circulation—Insights from Samograd Cave, Croatia. *Climate*, 12(12), 199. <https://doi.org/10.3390/cli12120199>.
- Cigna, A. A. (2016a). Modern Trend in Cave Monitoring. *Acta Carsologica*, 31(1). <https://doi.org/10.3986/ac.v31i1.402>.
- Cigna, A. A. (2016b). Monitoring of Caves Conclusions and Recommendations. *Acta Carsologica*, 31(1). <https://doi.org/10.3986/ac.v31i1.412>.
- Cigna, A., & Burri, E. (2000). Development, management and economy of show caves. *International Journal of Speleology*, 29B(1/4), 1–27. <https://doi.org/10.5038/1827-806X.29.1.1>.

- Constantin, S., Mirea, I. C., Petculescu, A., Arghir, R. A., Măntoiu, D., Ștefan, Kenesz, M., Robu, M., & Moldovan, O. T. (2021). Monitoring Human Impact in Show Caves. A Study of Four Romanian Caves. *Sustainability*, 13(4), 1619. <https://doi.org/10.3390/su13041619>.
- Czuppon Gy., Demény, A., Leél-Őssy, Sz., Óvari, M., Molnár, M., Stieber, J., Kármán, K., Kiss, K., Haszpra, L., Cave monitoring in Béke and Baradla Caves (NE Hungary): implications for condition of formation cave carbonates. *International Journal of Speleology*, 47(1), pp. 13-28.
- De Freitas, C. R. (2010). The role and importance of cave microclimate in the sustainable use and management of show caves. *Acta Carsologica*, 39(3). <https://doi.org/10.3986/ac.v39i3.77>.
- De Freitas, C. R., & Schmekal, A. (2003). Condensation as a microclimate process: Measurement, numerical simulation and prediction in the Glowworm Cave, New Zealand. *International Journal of Climatology*, 23(5), 557–575. <https://doi.org/10.1002/joc.898>.
- Debevec, V., & Rakovec, J. (2021). Impact of visits on the microclimates of caves, Experimental evidence from Škocjan Caves. *Acta Carsologica*, 50(2–3). <https://doi.org/10.3986/ac.v50i2-3.7397>.
- Dương, N. T., Nguyễn, H. T., Nguyễn, T. A., & Nguyễn, T. K. (2016). Radon concentration in karst caves in Dong Van Karst Plateau, Vietnam. *VNU Journal of Science: Earth and Environmental Sciences*, 32(25), 187–197. <https://doi.org/10.25073/2588-1094/vnuees.4016>.
- Fairchild, I. J., & Baker, A. (2012). *Speleothem Science: From Process to Past Environments* (1st ed.). Wiley. <https://doi.org/10.1002/9781444361094>.
- Fernandez-Cortes, A., Cuezva, S., Alvarez-Gallego, M., Garcia-Anton, E., Pla, C., Benavente, D., Jurado, V., Saiz-Jimenez, C., & Sanchez-Moral, S. (2015). Subterranean atmospheres may act as daily methane sinks. *Nature Communications*, 6(1), 7003. <https://doi.org/10.1038/ncomms8003>.
- Gong, Y., Wang, X., Wang, S., Lin, W., & Jin, K. (2025). Impact of open visits on the indoor climate of Mogao Caves. *Npj Heritage Science*, 13(1), 173. <https://doi.org/10.1038/s40494-025-01740-9>.
- Gregorič, A., Vaupotič, J., & Gabrovšek, F. (2013). Reasons for large fluctuation of radon and CO₂ levels in a dead-end passage of a karst cave (Postojna Cave, Slovenia). *Natural Hazards and Earth System Sciences*, 13(2), 287–297. <https://doi.org/10.5194/nhess-13-287-2013>.
- Ijoma, G. N., Onumanyi, V., & Semenya, K. (2025). Air quality assessments: Insights prehistoric caves can offer to our modern-day understanding. *Discover Environment*, 3(1), 77. <https://doi.org/10.1007/s44274-025-00276-w>.
- Ky, H.N., et al., 1973. Explanation of the Geological and mineral map of the Hanoi sheet, scale 1:200,000 (in Vietnamese). Department of Geology and Minerals of Vietnam.
- Lario, J., Sánchez-Moral, S., Cañaveras, J. C., Cuezva, S., & Soler, V. (2005). Radon continuous monitoring in Altamira Cave (northern Spain) to assess user's annual effective dose. *Journal of Environmental Radioactivity*, 80(2), 161–174. <https://doi.org/10.1016/j.jenvrad.2004.06.007>.
- Li, Y., Yang, Y., Wang, X., Luo, W., Zhao, J., Sun, Z., Ye, Z., Chen, X., Shi, X., Xu, Y., & Baker, J. L. (2024). Sources and transport of CO₂ in the karst system of Jiguan Cave, Funiu Mountains, China. *Science of The Total Environment*, 918, 170507. <https://doi.org/10.1016/j.scitotenv.2024.170507>.
- Martin-Pozas, T., Fernandez-Cortes, A., Cuezva, S., Jurado, V., Gonzalez-Pimentel, J. L., Hermosin, B., Ontañón, R., Arias, P., Cañaveras, J. C., Sanchez-Moral, S., & Saiz-Jimenez, C. (2024). Microclimate, airborne particles, and microbiological monitoring protocol for conservation of rock-art caves: The case of the world-heritage site La Garma cave (Spain). *Journal of Environmental Management*, 351, 119762. <https://doi.org/10.1016/j.jenvman.2023.119762>.
- Miler, M., Zupančič, N., Šebela, S., & Jarc, S. (2024). Natural and anthropogenic impact on the microclimate and particulate matter in the UNESCO show cave. *Environmental Science and Pollution Research*, 31(35), 48313–48331. <https://doi.org/10.1007/s11356-024-34366-8>.
- Nghi, T. et al. (2023). Geological History of Caves and Conservation Values of the World Nature Heritage Phong Nha–Ke Bàng National Park. *VNU Journal of Science: Earth and Environmental Sciences*, 39(4), 16–31. DOI: 10.25073/2588-1094/vnuees.4971.
- Nguyen, D.N. & Nguyen, T. H., 2004. Vietnam climate and climate resources. Publishing house for Agriculture, Hanoi (In Vietnamese).
- Nguyet, N. T. A., Duong, N. T., Schimmelmänn, A., & Huong, N. V. (2018). Human exposure to radon radiation geohazard in Rong Cave, Dong Van Karst Plateau Geopark, Vietnam. *VIETNAM JOURNAL OF EARTH SCIENCES*, 40(2), 117–126. <https://doi.org/10.15625/0866-7187/40/2/11092>.

- Pla, C., Ruiz, M. C., Gil-Oncina, S., García-Martínez, N., Cañaveras, J. C., Cuezva, S., Fernández-Cortés, Á., Sánchez-Moral, S., & Benavente, D. (2023). 222Rn and CO2 monitoring in soil and indoor atmosphere to understand changes in the gaseous dynamics of Rull cave (Spain). *Environmental Earth Sciences*, 82(9), 235. <https://doi.org/10.1007/s12665-023-10885-4>.
- Ponta, G. M. L., Limbert, H., Limbert, D., Bolger, T., Nguyen Xuan, N., Stoiciu, F., & Mocioiu, A.-M. (2022). Geological, mineralogical, and hydrogeological analysis of karst development in Phong Nha–Ke Bang/Tu Lan, Vietnam, and Hin Nam No, Laos. *Carbonates and Evaporites*, 37, 73. <https://doi.org/10.1007/s13146-022-00817-x>.
- Russell, M. J., & MacLean, V. L. (2008). Management issues in a Tasmanian tourist cave: Potential microclimatic impacts of cave modifications. *Journal of Environmental Management*, 87(3), 474–483. <https://doi.org/10.1016/j.jenvman.2007.01.012>.
- Sainz, C., Fábrega, J., Rábago, D., Celaya, S., Fernandez, A., Fuente, I., Fernandez, E., Quindos, J., Arteché, J. L., & Quindos, L. (2022). Use of Radon and CO2 for the Identification and Analysis of Short-Term Fluctuations in the Ventilation of the Polychrome Room Inside the Altamira Cave. *International Journal of Environmental Research and Public Health*, 19(6), 3662. <https://doi.org/10.3390/ijerph19063662>.
- Smetanová, I., Holý, K., Luhová, Ľ., Csicsay, K., Haviarová, D., & Kunáková, L. (2020). Seasonal variation of radon and CO₂ in the Vážecká Cave, Slovakia. *Nukleonika*, 65(2), 153–157. <https://doi.org/10.2478/nuka-2020-0025>.
- Stefanov, P., Turek, K., & Tsankov, L. (2025). Summary Results of Radon-222 Activity Monitoring in Karst Caves in Bulgaria. *Geosciences*, 15(10), 378. <https://doi.org/10.3390/geosciences15100378>.
- Trần N.B., Nguyễn T.D., Trịnh, D. A., & Nguyễn, V. H. (2023). Environmental conditions and microclimatic monitoring in tropical karst caves of Vietnam. *Vietnam Journal of Environment*, 64(2), 33–40.
- Tran, T., Nguyen, V. T., Huynh, T. L. H., Mai, V. K., Nguyen, X. H., & Doan, H. P. (2016). Climate change and sea level rise scenarios for Vietnam: Summary for policymakers (Vietnamese national climate assessment; scenario report). Ministry of Natural Resources and Environment (MONRE) / Institute of Meteorology, Hydrology and Environment (IMHEN). https://imh.ac.vn/files/doc/KichbanBDKH/CCS_SPM_2016.pdf.
- Trinh, D. A., Trinh, Q. H., Institute of Chemistry, Vietnam Academy of Science and Technology, Fernández-Cortés, A., Universidad de Almería, Matthey, D., Royal Holloway University of London, Guinea, J., & Museo Nacional Ciencias Naturales (MNCN). (2018). First assessment on the air CO₂ dynamic in the show caves of tropical karst, Vietnam. *International Journal of Speleology*, 47(1), 93–112. <https://doi.org/10.5038/1827-806X.47.1.2141>.
- UNESCO (2014). Phong Nha–Ke Bang National Park — Nomination dossier (extended). World Heritage Centre; nomination/renomination dossier (Geology/Geomorphology & Biodiversity). Available from: <https://whc.unesco.org/uploads/nominations/951bis.pdf>;
- Xiong, Y., Zhou, Z., Ding, S., Zhang, H., Huang, J., Gong, X., & Su, D. (2023). Spatiotemporal Variation Characteristics and Influencing Factors of Karst Cave Microclimate Environments: A Case Study in Shuanghe Cave, Guizhou Province, China. *Atmosphere*, 14(5), 813. <https://doi.org/10.3390/atmos14050813>.

DOI: 10.15625/vap.2025.0232

Assessing and Mitigating Urban Heat Risk in a Rapidly Urbanizing Subtropical City: A Preliminary Proposal for Taoyuan, Taiwan (China)

Cheng-Ling Kuo^{1,*}, Wenqian Chang¹, Yuei-An Liou^{1,2}

¹Department of Space Science and Engineering, National Central University, Taoyuan, Taiwan (China)

²Center for Astronautical Physics and Engineering, National Central University, Taoyuan, Taiwan (China)

*Email: clkuo@g.ncu.edu.tw

Abstract: Urban heat risk, a confluence of the Urban Heat Island (UHI) effect and population vulnerability, poses a critical and escalating threat to cities worldwide. This challenge is particularly acute in subtropical, high-density regions undergoing rapid development. As a key industrial and transportation hub in Taiwan (China), Taoyuan exemplifies this risk profile, facing intensified heat exposure due to its dense urban morphology, significant anthropogenic heat sources, and a climate susceptible to extreme heat events.

This case study synthesizes current situations on the meteorological drivers, public health impacts, and mitigation strategies associated with urban heat. It then applies this framework to assess the urban heat risk landscape of Taoyuan and propose context-relevant adaptation pathways. Using this preliminary analysis for Taoyuan, we recommend the following points regarding Taoyuan city government policies: (1) integrating heat resilience into urban planning regulations; (2) expanding green and blue infrastructure to create cooling corridors; (3) developing a heat-health action plan.

Keywords: Urban heat island, anthropogenic heat sources, social vulnerability, heat resilience, and mitigation strategy

TAOYUAN CITY AS ONE OF THE FASTEST-GROWING CITIES IN TAIWAN (CHINA)

Taoyuan has been one of the fastest-growing cities in Taiwan (China). Its total population has exceeded 2 million residents,

classifying it as one of Taiwan's six special municipalities (CNA Staff, 2021). The continuous population increase is attributed to a relatively higher birth rate and migration from other counties and cities (Editor, 2018; Taoyuan city government, 2020). Similar to the overall trend in Taiwan (China), Taoyuan City's population structure is moving towards an aging society. However, compared to other older cities, Taoyuan has a relatively higher proportion of working-age population (youth and middle-aged adults), which fuels its continued growth (Taoyuan city government, 2020).

However, with the advancement of industrialization and urbanization (Bolund & Hunhammar, 1999; Shiue, 2015), Taoyuan city region that were once predominantly agricultural have become increasingly affected by the urban heat island effect (Z.-A. Wang, 2022; Huang, 2024) and microclimates shaped by their topography (Arya, 2001; Argüeso et al., 2014). This impact is particularly severe for low-income households and elderly individuals who traditionally rely on farming, exacerbating heat-related harm associated with widening wealth disparities (Aubrecht & Özceylan, 2013).

In this paper, we analyze the risk in the heat exposure, the vulnerable sensitivity of outdoor workers/stateholders and the internal/external physical/climate drivers aspects associated with industrial development and increasings in population and housing units especially for industrial cities. Finally, we propose mitigation strategy for increasing

Taoyuan heat resilience in integrating heat risk into urban planning regulation, reservation and expanding green and blue infrastructure, such as cooling corridors, and developing a heat-health action plan for Taoyuan-liked fastest-growing cities.

TAOYUAN URBAN HEAT RISK ANALYSIS

Intensified heat exposure

Taoyuan's rapid urbanization and demographic trends significantly intensify heat exposure for its population (Z.-A. Wang, 2022; Huang, 2024), particularly within the high-density built environment. For high-risk thermal hotspots, we list the heat vulnerability regions especially for those spatially concentrated in the dense urban core (Hua et al., 2021; Chen et al., 2022): (1) **geographical clusters: Taoyuan and Zhongli** are two districts with the highest land surface temperature due to high building density and low vegetation cover (Z.-A. Wang, 2022; Liou et al., 2024); (2) **built-up concentration: industrial/science parks** often feature extensive impervious surfaces (concrete, metal shed factory and asphalt road/parking lot) that absorb and store solar energy during the day, leading to significant Surface Urban Heat Island (SUHI) effects (Yang et al., 2016; Siti Halipah Ibrahim, 2018; Hua et al., 2020; Santamouris & Vasilakopoulou, 2023); (3) **valley/plateau terrain: Daxi district** sits on the edge of Taoyuan Plateau where Dahan river carved a significant river valley through the plateau. The geological transition from the elevated plateau to the lower river valley create complex local microclimates (Minder et al., 2010; Dorninger et al., 2011; Burns & Chemel, 2014; Schörghofer et al., 2018; John et al., 2024) where convective mixing may be restricted, leading to less efficient heat dissipation and elevated temperatures, particularly at night.

Vulnerable populations

Highly populations in Taoyuan are highly sensitive to thermal stress, magnifying the health risks associated with the Urban Heat Island effect (Liou et al., 2024). A large population of outdoor workers in Taoyuan, as a

major industrial and logistics hub, is directly exposed to dangerously high ambient temperatures and humidity, increasing the risk of heat stroke and exhaustion. However, Taoyuan's economic growth has exacerbated the wealth gap. Especially for those low-income family or elderly Population, individuals (Mabon & Shih, 2022; R. Wang, 2022) who cannot afford air conditioning (UNICEF, 2022) or live in poorly insulated and lack adequate capacity (Lee, 2008) would face higher indoor thermal risk.

Significant anthropogenic heat sources

Anthropogenic Heat Emissions (AHE) produced by human activities are a major physical driver that intensifies the urban heat island effect in Taoyuan's dense districts. Two primary factors intensify anthropogenic heat sources: (1) **air conditioning waste heat**: for the fastest-growing cities, the usage number of air conditioning spirals upward as long as the rising of Taoyuan average temperature to 32-34 °C form as a positive feedback loop. Waste heat rejected by residential and commercial air-conditioning units is a primary contributor to the rise in night time air temperature. Studies in similar urban areas show that air-conditioning waste heat can increase mean air temperature by more than 1°C in urban locations during the night, hindering the natural cooling process (Ohashi et al., 2007; E360 Digest, 2014; Salamanca et al., 2014; Mu et al., 2025). The combining effect of high-density urban regions, e.g., Zhongli and Taoyuan district, concentrate thermal energy and prevent heat dissipation in night time; (2) **industrial and traffic heat emissions**: Taoyuan has a Taiwan's largest industrial park base where Taoyuan city industrial and science Parks are listed in Table 1. The fastest-growing industrial city faces two category of anthropogenic heat sources: industrial emission and vehicular traffic (Oke, 1982). The extensive industrial and manufacturing sectors scattered around the city release significant amounts of sensible heat and cause the heat pollution from the high road/traffic density along the major vehicle flow corridor

connecting Taoyuan to airport/cargo port and nearby key industrial zones (e.g., Hsinchu Science Park in Taiwan (China), famous for semiconductor manufacturing.). Industrial and

related traffic heat provide a regularly continuous heat flux and the daytime and early evening cumulative heat loads (Afshari et al., 2018; Wang et al., 2023).

Table 1. Taoyuan Industrial and Science Park Heat Risk Analysis (Taoyuan city government, 2020)

Park Name (District)	Main Industrial Category	Scale / Area (Estimated)	Potential Threats to Surrounding Regions (Environmental/Pollution)	Heat Risk Level (UHI Contribution)
Zhongli Industrial Park (Zhongli/Pingzhen)	Electronics, Machinery, Light Manufacturing, Metal Processing	Medium-to-Large (Maturity)	Wastewater and Volatile Organic Compound (VOC) emissions from manufacturing; heat generated by traffic congestion.	High. Located within the Zhongli/Pingzhen urban core. Dense infrastructure, high traffic heat sources, and strong heat retention.
Guanyin Industrial Park (Guanyin)	Heavy Industry, Chemicals, Energy, Large Warehousing	Extra Large (Coastal)	High volume of industrial wastewater; air pollutants from large boilers/stacks; risk of chemical spills.	Extremely High (Process Waste Heat). Massive scale and large impervious area. Heavy industrial operations produce vast, continuous Anthropogenic Heat Emissions (AHE) .
Taoyuan Youth Industrial Park (Yangmei)	Electronics, Machinery, Metal, Traditional Manufacturing	Medium	Waste and energy consumption from traditional industries; high traffic flow.	Medium-to-High. Large factory area where the primary heat sources are building thermal mass storage and operational heat release.
Dayuan Industrial Park (Dayuan)	Logistics, Aviation Services, Light Industry, Technology	Large (Near Airport)	Air and noise pollution from high traffic/transportation volume; high surface temperature from vast paved areas.	High. Extensive logistics and warehouse facilities covered by low-albedo concrete and asphalt, causing severe Surface Urban Heat Island (SUHI) effects.
Pingzhen Industrial Park (Pingzhen)	Textiles, Electronic Components, General Manufacturing	Medium	Wastewater discharge from traditional industries (e.g., textiles); energy efficiency issues in older facilities.	High. Situated near highly populated residential areas. Its heat release directly exacerbates heat exposure risk for surrounding communities.
Guishan Industrial Park (Guishan)	Electronics, R&D Centers, Assembly Manufacturing	Medium-to-Large	High energy consumption for operations; electronic waste processing.	High. High building density and the continuous operation of process cooling and server cooling systems generate considerable waste heat.
Longtan Science Park (Longtan)	High-Tech (Semiconductors, Optoelectronics, Communication)	Specialized (HSP Branch)	Use of highly specialized and potentially toxic chemicals/gases (though tightly regulated); high-purity process wastewater.	Extremely High (Cooling Waste Heat). Continuous, 24/7 cooling required for cleanrooms and precision equipment results in large, sustained Anthropogenic Heat Emissions (AHE) , a

				key driver of the nocturnal UHI.
Taoyuan Technology Industrial Park (TTIP) (Coastal)	Diverse Technology, New Manufacturing, Green Technology	Extra Large (New Development)	Potential general industrial pollution; ecological landscape alteration from large-scale construction.	High. The park's vast area means extensive impervious surfaces will significantly increase regional heat storage capacity.
Taoyuan Environmental Science & Technology Park (ESTP)	Environmental Science, Green Energy, Recycling	Specialized (within TTIP)	Relatively low pollution threat, focus on recycling and environmental processes.	Medium-to-High (with Mitigation). While some designs prioritize green infrastructure and cool materials , the scale of the facility still contributes to the overall heat burden.

Climate susceptibility to extreme heat events

Taoyuan’s geographical location and sub-tropical climate make it highly susceptible to extreme heat events, which are amplified by the underlying UHI effect. From Taoyuan’s climate affecting individual heat perception to the urban’s concentration of heat pollution, it is evident that Taoyuan continues to break higher temperature records.

The region’s subtropical climate combines high temperatures with high relative humidity, severely prevent the body’s ability from sweat evaporation to cool himself (Maslin et al., 2025). First, humidity often exceeds 70% during the summer months. When temperatures surpass 33°C (91°F) under such humid conditions, the risk of dangerous wet-bulb temperatures increases significantly (Liljegren et al., 2008; Brimicombe et al., 2023; Justine et al., 2023), posing a fatal threat to even healthy individuals engaging in strenuous activity (Lin & Chan, 2009; Yang et al., 2024). Second, Taoyuan located in the neighbours hood of the greater Taipei region, including Capital Taipei city and New Taipei county, and interconnected the heat system known as "Greater Taipei Giant Heat Island" (Chen et al., 2022; Expert, 2024).

Two factors amplifier the heat island effect: (i) terrain-trapped heat: Taoyuan’s local river valley and plateau topography, combined with the regional atmospheric heat load, acts as a heat sink, preventing sufficient temperature

drops during the night and ensuring that the next day begins with an elevated thermal baseline; (2) lack of dissipation: as urbanization spreads from the Taipei Basin westward, heat sources across Taipei, New Taipei, and Taoyuan are becoming interconnected. This convergence creates a larger, continuous high-temperature zone, making localized heat dissipation extremely difficult and exacerbating the heating cycle over several days. Figure 1 illustrates the distribution of daytime urban air temperatures under various RCP scenarios associated with urban and industrial regions. The standard of temperature ranges in Table 2 can be used for preliminary analysis and assessment of heat-related harm severity and impacts.

Table 2 Risk level and heat impact according to wet-bulb temperature T_{wb} (Jacklitsch et al., 2016).

T_{wb}	Risk level	Potential threats for heat Impact
30°C	Danger	Prolonged exposure and high activity pose a significant health risk, especially for vulnerable groups.
32°C	Extreme danger	Even short periods of physical labor or moderate activity can be life-threatening.
35°C	Survival limit	This is considered the theoretical upper limit of human survivability for healthy humans resting in the shade. Sustaining this temperature for more than a few hours can be lethal.

CYBER-PHYSICAL ARCHITECTURE OF ASSESSING AND MITIGATING URBAN HEAT

Integrating Heat Resilience into Urban Planning Regulations

This study proposes a Digital Twin-based Urban Heat Assessment Framework (Villani et al., 2025; Zhao et al., 2025) that integrates multi-source remote sensing data using a Spatio-Spectral Attention Network, e.g., ARCNET (Chang, Hou, et al., 2025; Chang, Kuo, & Liou, 2025). Unlike traditional statistical approaches, this architecture employs an attention mechanism to weigh the non-linear contribution of multi-spatial resolution data source (e.g., Landsat-8 and Sentinel-2) (Chang, Kuo, & Liou, 2025). We propose that the architecture is divided into four logical layers: (A) sensing (data), (B) Intelligence (analysis), (C) intervention (mitigation), and (D) Feedback (modulation).

Table 3 Cyber-Physical Architecture of Urban Heat, their core concepts and references

Layer	Concept	References
Sensing	Multi-source remoting sensing data	(Chang, Hou, et al., 2025; Chang, Kuo, & Liou, 2025; Zhao et al., 2025)
Analysis	Multi-scale attention deep learning model	(Akintola & Neziri, 2025; Chang, Kuo, & Liou, 2025)
Fusion	Morphological fusion	(Villani et al., 2025)
Action	Digital Twin city	(Zhao et al., 2025)

Layer I: Multi-sensing (Data)

First layer: the drought hub acquires the raw physical data required to identify heat hotspots. From macro-, meso- to micro-scale, satellite remote sensing data serve as the macro-scale data hub, which is compiled from Land Surface Temperature, NDVI (Vegetation), NDLI from LandSat/Sentinel (Chang, Kuo, & Liou, 2025), and monitor the broad spatial distribution of the urban heat island (UHI) (Liou et al., 2024). At the middle layer of urban meso-scale, the geophysical information system integrates the sky viewing factor, population density, waste heat from power consumption and traffic flow using OpenStreetMap and

Taoyuan government census data, and determine the physical geometry effect of heat exposure from natural and artificial waste heat. Finally, at microscope viewpoint, we also consider the meteorology and local sensor data includes air temperature, relative humidity, wind speed from automatic weather station and roadside IoT sensors.

Layer II: Intelligence Core (Analysis)

The second layer shows the Intelligence Core to downscaling data using fusion, evaluate the risk assessment matrix, and simulate in a digital twin. Frist step, we test an example of downscaling of Landsat-derived indexes and show in Figure 2. Figures 2 compares the drought indexes derived from the original Landsat-8 data and the ARC-NET-fused results for same-day experiments. Each pair shows the Normalized Difference Vegetation Index (NDVI, upper panels) and the Normalized Difference Latent Heat Index (NDLI, defined by Liou et al., 2018), shown in lower panels of Figure 2). The fused maps reveal finer spatial patterns and sharper boundaries while maintaining high spectral consistency with the original Landsat-8 observations. Within the Intelligence Core, the Risk Assessment module functions as the critical decision-support engine, transforming physical thermal data into actionable health intelligence by operationalizing the standard risk equation: Risk = Hazard × Exposure × Vulnerability. Instead of relying solely on surface temperature metrics, this module applies a multi-criteria spatial analysis that overlays the downscaled high-resolution air temperature maps (Hazard) with dynamic population density data (Exposure) and socio-demographic indicators such as age distribution, income levels, and pre-existing health conditions (Vulnerability). By synthesizing these disparate datasets, the system generates a composite "Heat Risk Index" map that isolates high-priority intervention zones—specifically targeting areas where extreme microclimatic heat disproportionately impacts low-adaptive capacity populations—thereby ensuring that subsequent mitigation strategies are deployed

not merely where the city is hottest, but where the human cost of heat is highest.

Layer III: Intervention (Mitigation)

The third Layer functions as the precision intervention engine, deploying a tailored suite of mitigation strategies derived directly from the thermal and morphological profiles identified in the assessment phase. Rather than applying a "one-size-fits-all" solution, this layer utilizes a diversified toolkit categorized into three primary domains: Blue-Green Infrastructure, which integrates urban forests, vertical gardens, and water bodies to induce cooling through evapotranspiration and shading; Gray Infrastructure, which employs high-albedo materials like cool roofs and retro-reflective pavements to minimize solar absorption; and Urban Geometry Optimization, which targets the physical arrangement of the city—such as creating ventilation corridors—to flush out trapped heat in high-density canyons. By mapping these specific interventions to the unique constraints of the local built environment (e.g., using vertical greening in areas with low Sky View Factor where street trees are unviable), the system ensures that mitigation efforts are both spatially optimized

and cost-effective, directly lowering the Physiological Equivalent Temperature (PET) in the most vulnerable zones.

Layer IV: Circular Loop (Feedback)

The fourth Layer establishes the architecture as a dynamic, closed-loop Cyber-Physical System that ensures long-term resilience through an iterative adaptive management cycle. Following the deployment of selected mitigation strategies—such as the installation of cool pavements or vertical greening—the framework immediately transitions to a continuous monitoring phase, utilizing the multi-scale sensing infrastructure to capture longitudinal post-intervention thermal data. This empirical evidence is then utilized to validate the system's efficacy by rigorously comparing observed temperature reductions against the Digital Twin's initial simulations, quantifying any performance gaps between the virtual prediction and physical reality. These insights drive the critical refinement stage, and the system to "learn" from each intervention and progressively enhance the city's adaptive capacity in response to evolving climate conditions.

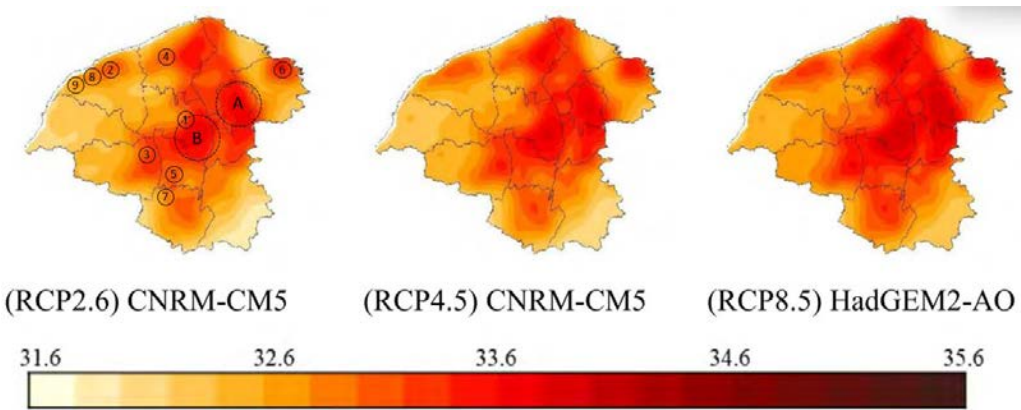


Figure 1. Daytime Air Temperature Distribution in Urban Areas Under Various RCP Scenarios where RCP2.6, RCP4.5, and RCP8.5 refer to Representative Concentration Pathways — standardized greenhouse gas concentration scenarios used in climate models. The RCP2.6, RCP4.5, and RCP8.5 indicates the scenarios with global warming +1.5 °C, +2.4 °C and +4.3 °C and approximated CO₂ concentration ~420-440 ppm, ~540 ppm and ~940 ppm, respectively. The urban regions (Taoyuan and Zhongli) are labelled by A and B. The numbers 1-9 list Taoyuan industrial and science park, including Zhongli Industrial Park, Guanyin, Taoyuan Youth (Yangmei), Dayuan, Pingzhen, Guishan Industrial Park, Longtan Science Park, Taoyuan Technology Industrial Park, Taoyuan Environmental Science & Technology Park, respectively (Z.-A. Wang, 2022; Huang, 2024).

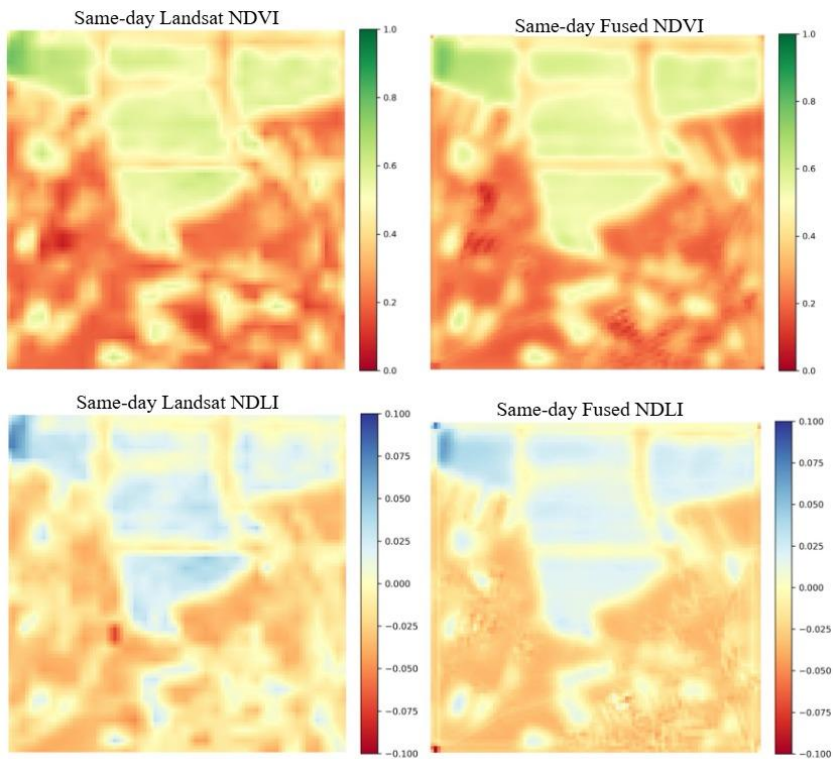


Figure 2. Comparison of NDVI and NDLI maps for the same-day experiment (Chang, Kuo, & Liou, 2025).

Taoyuan Urban Heat Resilience and Mitigation Strategy

Integrating Heat Resilience into Urban Planning Regulations

For high-density building region, we should limit the maximum floor-area ratios in high-risk thermal hotspots to prevent the creation of new, deep urban canyons. Regulations must ensure minimum inter-

building spacing to preserve wind channels and promote cooling air circulation.

For establishing industrial heat management, require all new large industrial facilities and data centers in zones like Guishan and Longtan Science Park to implement waste heat recovery systems or forced evaporative cooling solutions (e.g., highly efficient cooling towers) to minimize the amount of sensible heat exhausted directly into the ambient environment.

Table 3 Suggested policy and actions for risk reduction and corresponding urban planning regulations

Policy	Actions	Risk reduction
House Building Density	To setup the maximum floor-area ratios in high-risk thermal hotspots cooling air circulation.	Mitigates heat trapping and aids in the dissipation of Anthropogenic Heat Emissions (AHE) from ground level and exhaust vents.
Industrial Heat Management	waste heat recovery systems or evaporative cooling solutions	Reduced Anthropogenic Heat Emissions
Cool Roofs and Pavements	Mandate high-albedo materials over roofs and payments	To reduce solar absorption and heat accumulated storage, and nocturnal heat burden

Finally, mandate high-albedo materials for all new commercial, industrial, and major

residential building rooftops and large paved surfaces. Implement a tiered incentive/rebate

program for retrofitting existing structures with reflective coatings (cool roofs) or green roofs. The green-house designing applying building roof and pavements would reduce solar absorption and storage: directly lowers the Land Surface Temperature (LST) and reduces the nocturnal heat burden by reflecting solar radiation back into the atmosphere instead of storing it as thermal mass. In summary, Table 3 suggests the policy and actions for risk reduction and corresponding urban planning regulations for Taoyuan government.

Expanding Green and Blue Infrastructure to Create Cooling Corridors

The historical loss of Taoyuan's natural landmarks named by "Land of a Thousand Ponds" must be reversed by leveraging remaining natural assets to create functional "cold spots" (Lin et al., 2012) and continuous cooling corridors. Legally protect all remaining significant pitangs (ponds) from development. Initiate projects to revitalize and expand existing ponds within or adjacent to urban areas (e.g., Dayuan, Pingzhen). The ponds preservation plans maximized evaporative cooling and significantly lowering local air temperature and counteracting the effects of impervious surfaces.

Establish mandatory minimum Green Cover Index (GCI) requirements for commercial and residential developments, specifying permeable surfaces and vertical greening (facade vegetation) targets, especially in low-ventilation areas. Green zone provides direct shading for pedestrians and surfaces, lowering the ground-level heat burden, while the trees' evapotranspiration contributes to regional cooling.

Restoring a city-wide plan to develop interconnected linear green spaces (tree-lined avenues, park extensions) that link peripheral cooling areas (like Fuxing District) to the dense urban core. Prioritize planting high-canopy trees along major transportation routes. Reintroduces Permeability: Enhances soil wetness and prevents rapid runoff, further

promoting evapotranspiration and limiting the area of heat-absorbing surfaces.

Developing a Heat-Health Action Plan

A comprehensive heat-health action plan is essential for protecting the most sensitive populations—including the large elderly community and outdoor workers—against the growing risk of extreme Wet-Bulb Temperature events.

Identify and register all high-risk individuals (elderly living alone, chronically ill) using data from the Department of Social Welfare. Establish a network of certified "Cooling Shelters" (public libraries, community centres, and subsidized AC access points) in high-vulnerability neighbourhood. Ensures that the most sensitive groups have immediate access to life-saving, climate-controlled environments during peak heat events.

Mandate and enforce official work-rest schedules for all outdoor and industrial labor when the Wet-Bulb temperature exceeds 30°C. Implement inspections in construction sites and factories to ensure access to water, shade, and mandatory breaks for workers exposed to the heat burden. Directly protects the large population of exposed outdoor and industrial workers, minimizing the risk of heat stroke and maintaining labor productivity.

Develop an early warning system based on Wet-Bulb Globe Temperature or Wet-Bulb Temperature (T_{wb}) thresholds, not just simple ambient temperature. Utilize real-time monitoring across high-risk districts (Taoyuan, Zhongli) to issue multi-lingual, color-coded alerts. Provides an accurate measure of physiological danger, allowing citizens and employers to react before critical heat stress thresholds are crossed.

SUMMARY

This review work analyses the escalating urban heat risk in Taoyuan, Taiwan (China), a rapidly urbanizing subtropical industrial hub. The risk stems from the amplified Urban Heat

Island effect combined with a climate prone to extreme heat.

The analysis identifies critical thermal hotspots in dense urban cores and industrial/science parks like Zhongli, Taoyuan, and Longtan, where impervious surfaces and continuous Anthropogenic Heat Emissions from air conditioning and industrial activity significantly intensify heat exposure, especially at night. Vulnerable populations include a large number of outdoor workers and low-income/elderly residents facing both outdoor and indoor thermal stress.

To build heat resilience, the paper proposes three strategies: first, integrate heat resilience into urban planning by limiting density, mandating cool materials, and enforcing industrial waste heat management. Second, expand green and blue infrastructure by protecting ponds and creating cooling corridors to maximize evaporative cooling. Third, develop a Heat-Health Action Plan using Wet-Bulb Temperature thresholds for early warnings, establishing Cooling Shelters, and enforcing mandatory work-rest schedules for exposed laborers.

ACKNOWLEDGMENT

The authors would like to express their sincere gratitude to the Global Drought Investigation and Research Center and National Central University (NCU) for their generous support. This research was made possible through funding provided by institutional and regional programs under the Taiwan (China).

REFERENCES

- Afshari, A., Schuch, F., & Marpu, P. (2018). Estimation of the traffic related anthropogenic heat release using BTEX measurements – A case study in Abu Dhabi. *Urban Climate*, 24, 311-325. <https://doi.org/10.1016/j.uclim.2017.02.001>.
- Akintola, M., & Neziri, G. (2025). An Open-Source Deep Learning Framework for Scalable Urban Heat Island Detection Using Geospatial Data. *Int. Arch. Photogramm. Remote Sens. Spatial Inf. Sci.*, XLVIII-4/W13-2025, 11-16. <https://doi.org/10.5194/isprs-archives-XLVIII-4-W13-2025-11-2025>.
- Argüeso, D., Evans, J. P., Fita, L., & Bormann, K. J. (2014). Temperature response to future urbanization and climate change. *Climate Dynamics*, 42(7), 2183-2199. <https://doi.org/10.1007/s00382-013-1789-6>.
- Arya, S. P. (2001). *Introduction to Micrometeorology* (Vol. 79). Academic Press. <https://www.sciencedirect.com/science/article/pii/S0074614201800176>.
- Aubrecht, C., & Özceylan, D. (2013). Identification of heat risk patterns in the U.S. National Capital Region by integrating heat stress and related vulnerability. *Environment International*, 56, 65-77. <https://doi.org/https://doi.org/10.1016/j.envint.2013.03.005>.
- Bolund, P., & Hunhammar, S. (1999). Ecosystem services in urban areas. *Ecological Economics*, 29(2), 293-301. [https://doi.org/10.1016/S0921-8009\(99\)00013-0](https://doi.org/10.1016/S0921-8009(99)00013-0).
- Brimicombe, C., Lo, C. H. B., Pappenberger, F., Di Napoli, C., Maciel, P., Quintino, T., Cornforth, R., & Cloke, H. L. (2023). Wet Bulb Globe Temperature: Indicating Extreme Heat Risk on a Global Grid. *GeoHealth*, 7(2), e2022GH000701. <https://doi.org/10.1029/2022GH000701>.
- Burns, P., & Chemel, C. (2014). Evolution of Cold-Air-Pooling Processes in Complex Terrain. *Boundary-Layer Meteorology*, 150(3), 423-447. <https://doi.org/10.1007/s10546-013-9885-z>.
- Chang, W.-Q., Hou, H.-Y., Li, P.-Y., Shen, M. W., Kuo, C.-L., Lin, T.-H., Chang, L. C., Chao, C.-K., & Liu, J.-Y. (2025). Hyper Spectral Camera ANalyzer (HyperSCAN). *Remote Sensing*, 17(5), 842. <https://www.mdpi.com/2072-4292/17/5/842>.
- Chang, W.-Q., Kuo, C.-L., & Liou, Y.-A. (2025). *Toward High-Resolution Drought Monitoring: Experimental Downscaling of Landsat-Derived Indexes* Proceedings of International Conference on AI for a Sustainable Society - Frontier Research, Policy, and Practice, Taipei.
- Chen, T.-L., Lin, H., & Chiu, Y.-H. (2022). Heat vulnerability and extreme heat risk at the metropolitan scale: A case study of Taipei metropolitan area, Taiwan. *Urban Climate*, 41, 101054. <https://doi.org/10.1016/j.uclim.2021.101054>.
- CNA Staff. (2021). *Taoyuan shows greatest growth*. Taiwan News. <https://www.taipeitimes.com/News/taiwan/archives/2021/01/24/2003751136>.

- Dorninger, M., Whiteman, C. D., Bica, B., Eisenbach, S., Pospichal, B., & Steinacker, R. (2011). Meteorological Events Affecting Cold-Air Pools in a Small Basin. *Journal of Applied Meteorology and Climatology*, 50(11), 2223-2234. <https://doi.org/10.1175/2011JAMC2681.1>.
- E360 Digest. (2014). Air Conditioning Can Raise Urban Nighttime Temperature by 2 Degrees. *Yale school of the environment*. https://e360.yale.edu/digest/air_conditioning_can_raise_urban_nighttime_temperature_by_2_degrees.
- Editor. (2018, June 21). *Taoyuan Ranks First in Urban Migration Growth* Public Television Service News.
- Expert. (2024). *Heat island effect expanding in northern Taiwan*. Focus Taiwan. <https://focustaiwan.tw/sci-tech/202406260005>.
- Hua, J., Zhang, X., Ren, C., Shi, Y., & Lee, T.-C. (2021). Spatiotemporal assessment of extreme heat risk for high-density cities: A case study of Hong Kong from 2006 to 2016. *Sustainable Cities and Society*, 64, 102507. <https://doi.org/10.1016/j.scs.2020.102507>
- Hua, L., Zhang, X., Nie, Q., Sun, F., & Tang, L. (2020). The Impacts of the Expansion of Urban Impervious Surfaces on Urban Heat Islands in a Coastal City in China. *Sustainability*, 12(2), 475. <https://www.mdpi.com/2071-1050/12/2/475>.
- Huang, J.-Y. (2024). *Quantitative Analysis of Key Impact Factors Influencing Surface Urban Heat Islands: A case study of Taoyuan* (Publication Number 2024) National Taiwan University]. AiritiLibrary.
- Jacklitsch, B., Williams, W., Musolin, K., Coca, A., Kim, J.-H., & Turner, N. C. (2016). *Criteria for a recommended standard: occupational exposure to heat and hot environments*. DHHS (NIOSH) Publication Retrieved from <https://www.cdc.gov/niosh/docs/2016-106/default.html#print>.
- John, A., Olden, J. D., Oldfather, M. F., Kling, M. M., & Ackerly, D. D. (2024). Topography influences diurnal and seasonal microclimate fluctuations in hilly terrain environments of coastal California. *PLOS ONE*, 19(3), e0300378. <https://doi.org/10.1371/journal.pone.0300378>.
- Justine, J., Monteiro, J. M., Shah, H., & Rao, N. (2023). The diurnal variation of wet bulb temperatures and exceedance of physiological thresholds relevant to human health in South Asia. *Communications Earth & Environment*, 4(1), 244. <https://doi.org/10.1038/s43247-023-00897-0>.
- Lee, Y.-F. (2008). Economic Growth and Income Inequality: the modern Taiwan experience. *Journal of Contemporary China*, 17, 361-374. <https://doi.org/10.1080/10670560701809577>.
- Liljegren, J. C., Carhart, R. A., Lawday, P., Tschopp, S., & Sharp, R. (2008). Modeling the Wet Bulb Globe Temperature Using Standard Meteorological Measurements. *Journal of Occupational and Environmental Hygiene*, 5(10), 645-655. <https://doi.org/10.1080/15459620802310770>.
- Lin, J., Williams, S., & Lee, C. (2012). The Land of 1,000 Ponds—Taoyuan's Irrigation Ponds Facing Crisis. *Taiwan Panorama*,. <https://www.taiwan-panorama.com/en/Articles/Details?Guid=e7882fe3-aca2-4007-9773-a85e8e3f85c9&CatId=7&postname=The%20Land%20of%201%2C000%20Ponds%E2%80%9494Taoyuan%E2%80%99s%20Irrigation%20Ponds%20Facing%20Crisis%20#:~:text=Over%20the%20last%2030%20years,on%20the%20World%20Heritage%20register>.
- Lin, R. T., & Chan, C. C. (2009). Effects of heat on workers' health and productivity in Taiwan. *Glob Health Action*, 2. <https://doi.org/10.3402/gha.v2i0.2024>.
- Liou, Y.-A., Le, M. S., & Chien, H. (2018). Normalized Difference Latent Heat Index for Remote Sensing of Land Surface Energy Fluxes. *IEEE Transactions on Geoscience and Remote Sensing*, 57(3), 1423–1433. <https://doi.org/10.1109/tgrs.2018.2866555>.
- Liou, Y.-A., Tran, D.-P., & Nguyen, K.-A. (2024). Spatio-temporal patterns and driving forces of surface urban heat island in Taiwan. *Urban Climate*, 53, 101806. <https://doi.org/10.1016/j.uclim.2024.101806>.
- Mabon, L., & Shih, W.-Y. (2022). Identifying factors contributing to social vulnerability through a deliberative Q-Sort process: an application to heat vulnerability in Taiwan. *Natural Hazards*, 112(3), 2609-2623. <https://doi.org/10.1007/s11069-022-05280-4>.
- Maslin, M., Ramnath, R. D., Welsh, G. I., & Sisodiya, S. M. (2025). Understanding the health impacts of the climate crisis. *Future Healthcare Journal*, 12(1), 100240. <https://doi.org/10.1016/j.fhj.2025.100240>.
- Minder, J. R., Mote, P. W., & Lundquist, J. D. (2010). Surface temperature lapse rates over complex terrain: Lessons from the Cascade Mountains. *Journal of Geophysical Research: Atmospheres*, 115(D14). <https://doi.org/10.1029/2009JD013493>.
- Mu, K., Suo, Q., Ding, F., Jiang, C., Zhang, X., & Ye, J. (2025). Field Measurements of Building Air-

- Conditioning Heat Rejection and the Thermal Environment in Urban Areas. *Atmosphere*, 16(1), 100. <https://www.mdpi.com/2073-4433/16/1/100>
- Ohashi, Y., Genchi, Y., Kondo, H., Kikegawa, Y., Yoshikado, H., & Hirano, Y. (2007). Influence of Air-Conditioning Waste Heat on Air Temperature in Tokyo during Summer: Numerical Experiments Using an Urban Canopy Model Coupled with a Building Energy Model. *Journal of Applied Meteorology and Climatology*, 46(1), 66-81. <https://doi.org/10.1175/JAM2441.1>.
- Oke, T. R. (1982). The energetic basis of the urban heat island. *Quarterly Journal of the Royal Meteorological Society*, 108(455), 1-24. <https://doi.org/10.1002/qj.49710845502>
- Salamanca, F., Georgescu, M., Mahalov, A., Moustauoi, M., & Wang, M. (2014). Anthropogenic heating of the urban environment due to air conditioning. *Journal of Geophysical Research: Atmospheres*, 119(10), 5949-5965. <https://doi.org/10.1002/2013JD021225>.
- Santamouris, M., & Vasilakopoulou, K. (2023). Recent progress on urban heat mitigation technologies. *Science Talks*, 5, 100105. <https://doi.org/10.1016/j.sctalk.2022.100105>
- Schörghofer, N., Businger, S., & Leopold, M. (2018). The Coldest Places in Hawaii: The Ice-Preserving Microclimates of High-Altitude Craters and Caves on Tropical Island Volcanoes. *Bulletin of the American Meteorological Society*, 99(11), 2313-2324. <https://doi.org/10.1175/BAMS-D-17-0238.1>
- Shiue, I. (2015). Ecosystems and human well-being in the transition towards green engineering and economy. *Ecological Engineering*, 74, 474-477. <https://doi.org/10.1016/j.ecoleng.2014.11.022>
- S. H. Ibrahim, N. I. A. Ibrahim, J. Wahid, N. Abdullah Goh, D. R. A. Koesmeri and M. N. M. Nawati (2018). The Impact of Road Pavement on Urban Heat Island (UHI) Phenomenon. *International Journal of Technology*, 9(8), 291-319. <https://doi.org/10.14716/ijtech.v9i8.2755>.
- Taoyuan city government. (2020). *Sustainable development goals: Taoyuan city voluntary local review*. Taoyuan city government.
- UNICEF. (2022). *The cooling dilemma amid climate change* <https://www.unicef.org/innocenti/cooling-dilemma-amid-climate-change>
- Villani, L., Gugliemetti, L., Barucco, M. A., & Cinquepalmi, F. (2025). A Digital Twin Framework to Improve Urban Sustainability and Resiliency: The Case Study of Venice. *Land*, 14(1), 83. <https://www.mdpi.com/2073-445X/14/1/83>
- Wang, A., Li, X.-X., Xin, R., & Chew, L. W. (2023). Impact of Anthropogenic Heat on Urban Environment: A Case Study of Singapore with High-Resolution Gridded Data. *Atmosphere*, 14(10), 1499. <https://www.mdpi.com/2073-4433/14/10/1499>
- Wang, R. (2022). *Elderly and disadvantaged situation, trend and strategy analysis of living environment in Taiwan*. https://www.abri.gov.tw/en/News_Content.aspx?n=908&s=317737
- Wang, Z.-A. (2022). *Urban heat island under climate and land use changes: A case study of Taoyuan City* (Publication Number 2022) National Taiwan University]. AiritiLibrary.
- Yang, H.-Y., Wu, C.-F., & Tsai, K.-H. (2024). Projections of Climate Change Impact on Acute Heat Illnesses in Taiwan: Case-Crossover Study. *JMIR Public Health Surveill*, 10, e57948. <https://doi.org/10.2196/57948>
- Yang, L., Qian, F., Song, D.-X., & Zheng, K.-J. (2016). Research on Urban Heat-Island Effect. *Procedia Engineering*, 169, 11-18. <https://doi.org/https://doi.org/10.1016/j.proeng.2016.10.002>
- Zhao, L., Fan, X., & Hong, T. (2025). Urban Heat Island Effect: Remote Sensing Monitoring and Assessment—Methods, Applications, and Future Directions. *Atmosphere*, 16(7), 791. <https://www.mdpi.com/2073-4433/16/7/791>

Shrimp Farming Wastewater Treatment By Aquatic Plants

Nguyen Minh Phuong^{*}, Nguyen Huu Hung

Faculty of Environmental Sciences, University of Science, Vietnam National University, 334 Nguyen Trai, Hanoi, Vietnam

^{*}Email: nmphuong.hn@hus.edu.vn

Abstract: This study aimed to evaluate the efficiency of three native aquatic plants, namely *Ceratophyllum demersum*, *Alternanthera paronychioides*, and *Salvinia cucullata* in treating shrimp farming wastewater in Quang Ninh province, Vietnam. Four experimental systems including a control system with wastewater only (CT), and three systems using aquatic plants: CS (*C. demersum*), AS (*A. paronychioides*), and SS (*S. cucullata*) were tested during 20 experimental days. The results showed that organic matter and ammonium ($\text{NH}_4^+\text{-N}$) removal were highly effective in the SS and AS system with the chemical oxygen demand (COD) and $\text{NH}_4^+\text{-N}$ removal efficiencies of over 90%, followed by the CS system with COD and $\text{NH}_4^+\text{-N}$ removal efficiencies of 70.9% and 81.2%, respectively. In contrast, the CT system experienced much lower removal rates (COD: 34.6%, $\text{NH}_4^+\text{-N}$: 40.6%). Enhanced removal of nitrate, nitrite and phosphate were also observed in three systems using aquatic plants compared to that in the control system. The $\text{PO}_4^{3-}\text{-P}$ removal efficiencies in the SS, AS and CS systems were 66.7%, 62.4% and 51.5%, whereas that in CT system was only 13.9% after 20 days. The present study highlights the potential of using native aquatic plants, especially *S. cucullata* and *A. paronychioides* in shrimp farming wastewater treatment as an eco-friendly approach, contributing to eliminating water pollution.

Keywords: shrimp farming, wastewater, treatment, aquatic plants.

INTRODUCTION

Shrimp farming activities play an important role in the food industry and serve

as an economic driver that provides livelihoods for local communities. Aquaculture production grows rapidly and Asia drives this growth, accounting for 91.4 % of global aquaculture output, with leading contributions from countries such as China, India, and Vietnam (Sagheer et al., 2025). However, along with the development of the aquaculture industry is the problem of environmental pollution due to wastewater being discharged directly without proper treatment into the environment. It has been reported that 30% of the total nutrients from feed is retained in the bodies of aquatic animals, while the remaining 70% are not absorbed and are excreted, generating waste (Mangarengi et al., 2020). Most of the nutrients, such as nitrogen and phosphorus, that are not absorbed by freshwater prawn remain in the environment—either settling into the bottom sediment or remaining suspended in the pond water (Adhikari et al., 2014). Intensive shrimp farming leads to the accumulation of organic matter and nutrients into aquatic environments, potentially impacting water quality and ecosystem health (Cao et al., 2025). Super-intensive shrimp farming wastewater is characterized by very high levels of organic matter and nutrients. The high levels of nutrients in water will cause eutrophication and threaten aquatic organisms as well as human health (Mangarengi et al., 2020). Among wastewater treatment methods, the applications of constructed wetlands (CWs) and aquatic plants have proven to be effective with low cost and simple technology (Abbasi et al., 2019; Shi et al., 2011). CWs are artificial systems that have been constructed for wastewater treatment by utilizing natural processes such as sedimentation, filtration, adsorption, plant uptake and microbial

processes (Vymazal, 2010). Prior investigators have used CWs planted with *Phragmites australis*, *Spartina alterniflora* Loisel and *Scirpus mariqueter* in treating shrimp farming wastewater in China (Shi et al., 2011). The authors found that total nitrogen (TN) removal efficiency was 66.8%, however COD removal rate was only 26.7% in CWs (Shi et al., 2011). In another study, the removal efficiency of TN and nitrate from aquaculture wastewater by CWs planted with *Typha angustifolia* and *Canna indica* were over 40% (Mahmood et al., 2016). NH_4^+ -N removal efficiency in aquaculture wastewater by *Ipomoea aquatica*, *Eichhornia crassipes*, *Pistia stratiotes* reached 60 - 90% (Nizam et al., 2020). NO_3^- -N removal efficiency was reported to be in range of 52 - 80% by aquatic plants *E. crassipes*, *C. demersum* and CWs planted with *P. communis* and *Phalaris arundinacea* treating aquaculture wastewater (Sindilariu et al., 2008; Nuwansi et al., 2018). In Vietnam, according to a prior study on the CWs planted with *Canna generalis* to treat water for cultured tilapia (*Oreochromis niloticus*) and carp (*Cyprinus carpio*) at Can Tho university, BOD and COD removal efficiency reached 50% (Konnerup et al. 2011). Although there are studies on wetland plants such as *E. crassipes*, *I. aquatica*, *P. stratiotes*, *Canna indica*, etc. in wastewater treatment (Mahmood et al., 2016; Nizam et al., 2020), the potential of native aquatic plants in Vietnam for treating aquaculture wastewater has been little investigated. This study was conducted to evaluate the ability of three native aquatic plants, i.e., *Ceratophyllum demersum*, *Alternanthera paronychioides* and *Salvinia cucullata* to treat shrimp farming wastewater in Quang Ninh province, Vietnam. *C. demersum* is a submerged aquatic plant that commonly grows in lakes and ponds (Syed et al., 2018). *A. paronychioides* is a fast-growing plant that widely distributes across the tropics and subtropics (Wu et al., 2013). *S. cucullata* is a floating plant that commonly distributes in Southeast Asia since the plant species prefers warm climates for growth (Santhosh et al., 2022). Thus far, little is known about the potential of those three aquatic plants in wastewater treatment.

MATERIALS AND METHODS

Wastewater from a super-intensive white-leg shrimp farm in Uong Bi, Quang Ninh province was collected from a pond (1000 m² in area and 200 shrimp/m³ in density; sampling coordinates: 21°00'38.2"N - 106°44'52.6"E). Wastewater samples were drawn from the bottom siphon of the pond (2m from the water surface) into a 30L- plastic can (HDPE) and then transferred directly to the Laboratory of Department of Environmental Technology, Faculty of Environmental Sciences, VNU University of Science, Hanoi.

All three plant species (*C. demersum*, *A. paronychioides*, *S. cucullata*) were collected in Uong Bi, Quang Ninh near the shrimp wastewater sampling area. Figure 1 shows the three studied plant species.

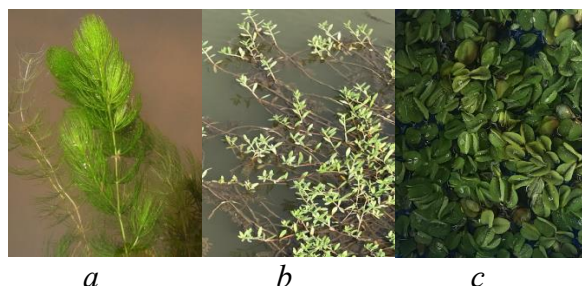


Figure 1. Three plant species used in the study

- a) *Ceratophyllaceae demersum*;
- b) *Alternanthera paronychioides*;
- c) *Salvinia cucullata*

Experimental design

Four experimental systems (plastic, height: 29 cm; upper diameter: 30 cm; bottom diameter: 27.5 cm) were used in the study (Fig. 2.) The first system had wastewater only (without plants) as the control system (CT), the second system had wastewater and *C. demersum* (CS), the third and the fourth system has wastewater and *A. paronychioides* (AS) and *S. cucullata* (SS), respectively. The wastewater volume in each system was 10 L. The initial fresh weight of plants in the CS, AS, and SS system was 80 g (in each). The experimental system was designed in an open form. Wastewater samples were collected and

analyzed (measured parameters: COD, $\text{NH}_4^+\text{-N}$, $\text{NO}_2^-\text{-N}$, $\text{NO}_3^-\text{-N}$, and $\text{PO}_4^{3-}\text{-P}$ after the retention times of 3, 6, 10, 12, 14, 17 and 20 days. The experimental systems were set up in the corridor on the 4th floor of the T2 building, VNU University of Science, Hanoi, under outdoor temperature conditions (28–30°C) with direct sunlight condition, and with a roof to prevent any impact from possible rain.

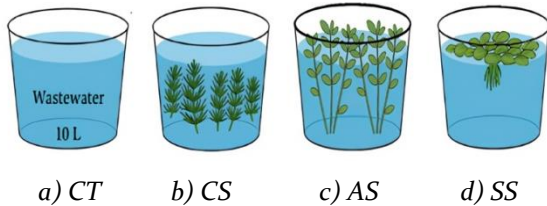


Figure 2. Experimental models:
a) Control system (CT), b) *C. demersum* system (CS),
c) *A. paronychioides* system (AS),
d) *S. cucullata* system (SS).

Analytical methods

Analytical methods for measurement of parameters in wastewater in this study were as follows: COD (using potassium-dichromate according to TCVN 4565:1988), $\text{NH}_4^+\text{-N}$ (Colorimetry using Nessler reagent), $\text{NO}_3^-\text{-N}$ (TCVN 6180 : 1996), $\text{NO}_2^-\text{-N}$ (Colorimetry using Griess reagent), $\text{PO}_4^{3-}\text{-P}$ (TCVN 6202 : 2008). At each experimental time point, 50 mL of water samples were taken from each system for analysis. Water samples before analysis were filtered through a 0.45 μm filter. The parameters were analyzed in three replicates. The results were presented using Microsoft Excel software (version 2019). The experimental data were statistically analyzed using ANOVA, T-test ($p < 0.05$).

* Treatment efficiency is calculated according to the formula:

$$H = (\text{Co} - \text{C}) / \text{Co} \times 100 (\%)$$

where:

H: treatment efficiency (%);

Co: initial concentration of the parameter in the influent (mg/L);

C: concentration of the parameter after treatment (mg/L).

RESULTS AND DISCUSSION

Characteristics of shrimp farming wastewater in Quang Ninh

Concentrations of parameters from super-intensive shrimp farming in Quang Ninh are shown in Table 1.

Table 1. Concentrations of parameters in shrimp farming wastewater in Quang Ninh

Parameter	Unit	Value	QCVN 02-19:2014 /BNNPT NT	QCVN 40:2011 /BTNMT (column B)
pH	-	7.5	5.5-9	5.5-9
COD	mg/L	916 \pm 25	≤ 150	150
$\text{NH}_4^+\text{-N}$	mg/L	5.49 \pm 0.44	-	10
$\text{NO}_3^-\text{-N}$	mg/L	2.01 \pm 0.16	-	-
$\text{NO}_2^-\text{-N}$	mg/L	1.2 \pm 0.05	-	-
$\text{PO}_4^{3-}\text{-P}$	mg/L	2.43 \pm 0.14	-	-

Note: QCVN 40:2011/BTNMT, column B: National technical regulation on industrial wastewater applied to industrial wastewater discharged into receiving sources not used for domestic water supply purposes.

QCVN 02-19:2014/BNNPTNT, National technical regulation on brackish water shrimp farming facilities - Conditions to ensure veterinary hygiene, environmental protection and food safety applicable to wastewater from wastewater treatment ponds before being discharged into the environment.

The results showed that shrimp farming wastewater in Uong Bi, Quang Ninh had high concentration of organic matter (initial COD value was 916 \pm 25 mg/L). The COD value was 6.17 times higher than the allowable threshold in QCVN 40:2011/BTNMT, column B and QCVN 02-19:2014/BNNPTNT. Ammonium concentration was 5.49 \pm 0.44 mg/L, meeting the standard QCVN 40:2011/BTNMT (column B).

COD removal

Fig. 3 shows the changes in COD concentrations in the four systems during the experimental period.

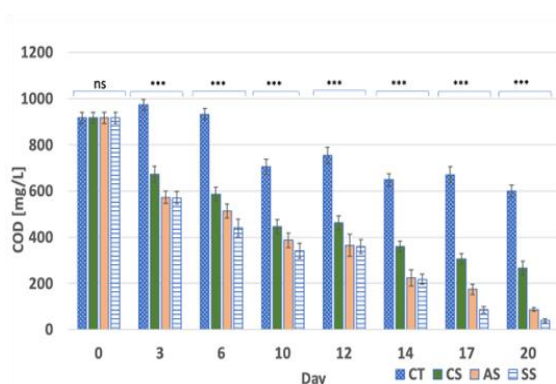


Figure 3. The changes in COD concentrations in the experimental systems

(note: ***: $p < 0.001$, statistically extremely significant;

ns: $p > 0.05$, statistically not significant)

The results showed that COD concentrations in the shrimp farming wastewater samples in the four systems decreased during the experimental period. After 20 days, the *S. cucullata* system (SS) had the best ability to remove organic matter (COD) with the removal rate of 95.7%, followed by the *A. paronychioides* system (AS) (90.47%), and the *C. demersum* system (CS) (70.9%); meanwhile, the COD concentration in the control system (CT) showed only a 34.6% reduction ($p < 0.05$). After 20 days, COD concentrations in the SS system (39.33 ± 8.32 mg/L) and AS system (87.33 ± 8.74 mg/L) met the standard QCVN 40:2011/BTNMT, column B and QCVN 02 19:2014/BNNPTNT. According to a prior study, COD removal efficiency by the aquatic plants *Alternanthera sessilis* in domestic wastewater (initial concentration of 600 mg/L) reached 80% after 10 days (Abbasi et al., 2019). On the other hand, COD removal efficiency in CWs planted with bulrush (*Scirpus littoralis*), cypress (*Cyperus involucratus*) and seagrass (*Posidoniaceae*) treating shrimp farming wastewater (initial concentration of 106 mg/L) in the Mekong Delta region ranged only 19 – 31% (Le et al., 2023). In another study, COD removal efficiency in *C. demersum* system and *A. paronychioides* system was 90% and 95%, respectively (Nguyen et al., 2023). Other authors reported that the removal rates of COD in aquaculture wastewater (initial

concentration of 412 mg/L) by *Eichhornia crassipes* and *C. demersum* were 83.3% and 51%, respectively (Nuwansi et al., 2018). Organic matter removal mechanisms in floating treatment wetlands include sedimentation, filtration, adsorption, plant uptake and microbial processes (Oliveira et al., 2021). It has been demonstrated that oxygen release from plant roots could promote aerobic oxidation of organic compounds (Rehman et al., 2023), thereby enhancing COD removal efficiency in wastewater. Plant-microbe interaction play an important role in pollutant removal. Plants not only provide habitats but also supply oxygen and organic carbon for microbial growth, while microbes facilitate plant growth by supplying minerals and metabolites (Srivastava et al., 2017). In aquaculture wastewater, salinity can affect plant growth due to osmotic stress, ion toxicity, nutrient imbalance, oxidative stress and reduced photosynthesis (Kritika et al., 2024). Microbes, especially plant-growth promoting rhizobacteria such as *Rhizobium*, *Enterobacter*...can help plants to tolerate to salinity by providing stress hormone regulation, enhancing nutrient availability, and creating protective biofilms around the roots (Fan et al., 2024).

Ammonium removal

The changes in $\text{NH}_4^+\text{-N}$ concentrations in the four systems during the experimental period are shown in Fig. 4. The results showed that after 20 days, the $\text{NH}_4^+\text{-N}$ concentration decreased in all experimental systems. The highest $\text{NH}_4^+\text{-N}$ removal efficiency concentration was recorded in the SS system (96%), followed by the AS system (93.2%), and the CS system (81.2%), whereas in the control system (CT), the $\text{NH}_4^+\text{-N}$ removal efficiency was only 40.6% ($p < 0.05$). The results of $\text{NH}_4^+\text{-N}$ removal capacity of three aquatic plants in this study were consistent with previous studies. The $\text{NH}_4^+\text{-N}$ removal efficiency in aquaculture wastewater by the aquatic plant species *I. aquatica*, *E. crassipes*, *P. stratiotes* reached 60 – 90% (Nizam et al., 2020). The $\text{NH}_4^+\text{-N}$ removal efficiency in aquaculture wastewater by *C. demersum* and *A.*

paronychioides was found to be over 80% after 14 days of experiment (Nuwansi et al., 2018). Similarly, in another study, NH_4^+ -N removal efficiency in aquaculture wastewater by *C. demersum* and *A. paronychioides* was in the range of 70 – 90% (Nguyen et al., 2023).

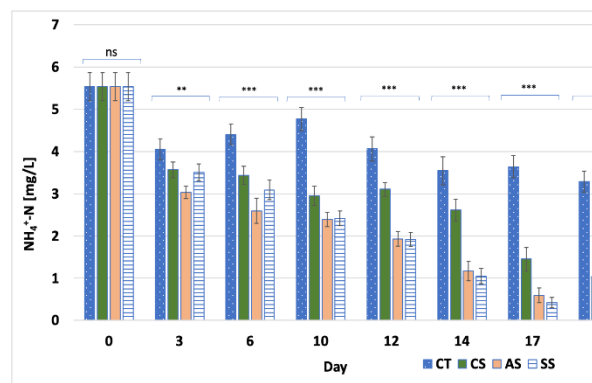


Figure 4. The changes in NH_4^+ -N concentrations in the experimental systems

(note: ***: $p < 0.001$, statistically extremely significant;

**: $p < 0.01$, statistically highly significant;

ns: $p > 0.05$, statistically not significant)

The main mechanisms of ammonium removal from wastewater in treatment wetland systems have been found to be the nitrification - denitrification process and then ammonium absorption in plants (García et al., 2010; Chen et al., 2014). According to a prior investigation, plant absorption only accounts for 7.5 - 14.3% in nitrogen removal, while nitrification - denitrification plays a significant role, accounting for 54 - 94% (Chen et al., 2014). The wetland plants *Phragmites australis*, *Phalaris arundinacea*, *Typha* spp., and *Arundo donax* could accumulate can accumulate 30–60 g N/m² in the aboveground biomass (Vymazal, 2025). In this study, the fresh weight of *C. demersum* (in CS system), *A. paronychioides* (in AS system) and *S. cucullata* (in SS system) increased to 90, 155 and 124 g, respectively, indicating the plants adapted well to the shrimp farming wastewater in Quang Ninh. In addition, nitrification process could be enhanced by oxygen release from the plant root systems due to activities of aerobic nitrifying microorganisms (Yao et al., 2011). The role of

nitrifying bacteria such as *Nitrosomanadacea*, *Nitrosopira* in the oxidation of ammonium in wastewater has been well-documented (Ahmed and Delatolla, 2021). Plant roots can provide habitats for microbial attachment, thereby enhancing the removal of pollutants via microbial processes (Garcia et al., 2010; Vymazal, 2025). Bacteria belonging to the phylum *Proteobacteria*, *Bacteroidetes*, *Actinobacteria* have been found in CWs and those functional microorganisms contribute to nutrient removal by biodegradation, biosorption, and supporting plant growth (Wang et al., 2022).

Nitrite removal

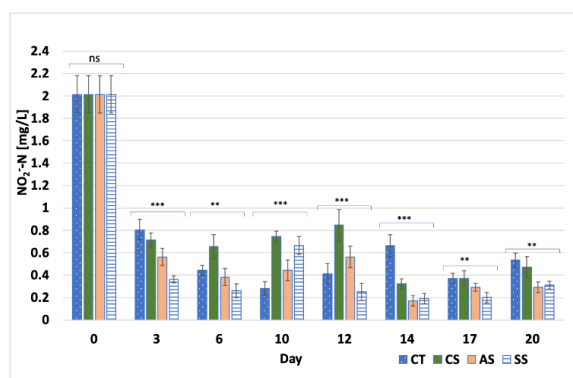


Figure 5. The changes in NO_2^- -N concentrations in the experimental systems

(note: ***: $p < 0.001$, statistically extremely significant; **:

$p < 0.01$, statistically highly significant; ns: $p > 0.05$, statistically not significant)

The changes in nitrite concentrations in the experimental systems are shown in Fig. 5. The results showed that the NO_2^- -N concentration sharply reduced on the third experimental day. After 3 days, the NO_2^- -N reduction rate in the CS, AS and SS system reached 85.5%; 73.5% and 84.5%, respectively. After 20 days of experiment, the NO_2^- -N concentration in the CS, AS, and SS system was 0.47 ± 0.09 mg/L, 0.29 ± 0.04 mg/L and 0.31 ± 0.03 mg/L, respectively. The effective NO_2^- -N removal in treatment wetlands was in accordance with other studies (Zhang et al., 2014; Vymazal, 2025). In a study using water spinach (*Ipomoea aquatica* Forsskal) to treat shrimp farming wastewater in China, the NO_2^- -

N removal efficiency was over 60% (Zhang et al., 2014). The slight increase in NO_2^- -N may be due to the oxidation of ammonium to nitrite (the first step of the nitrification process) (Vymazal, 2025). The amount of oxygen released from the roots could facilitates NH_4^+ -N to be converted into NO_2^- -N and then NO_2^- -N to be converted into NO_3^- -N (Zhang et al., 2014).

Nitrate removal

The changes in nitrate concentrations in the experimental systems are shown in Fig. 6.

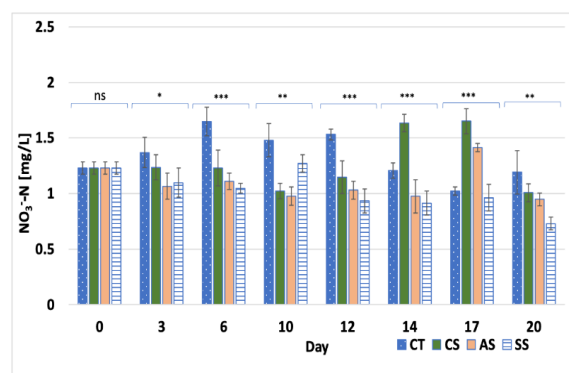


Figure 6. The changes in NO_3^- -N concentrations in experimental systems

(note: ***: $p < 0.001$, statistically extremely significant; **: $p < 0.01$, statistically highly significant; *: $p < 0.05$, statistically significant; ns: $p > 0.05$, statistically not significant)

The results showed that after 20 days, the NO_3^- -N removal efficiency in the SS system reached 40.5% (NO_3^- -N concentration of 0.73 ± 0.05 mg/L), followed by AS and CS system showed the removal rates of 22.9% and 18%, respectively; whereas NO_3^- -N removal efficiency was only 3% (NO_3^- -N concentration of 1.19 ± 0.19 mg/L) in the control system ($p < 0.05$). According to previous investigators, NO_3^- -N removal efficiency reached 80% by *E. crassipes* and *C. demersum* (Nuwansi et al., 2018). In another study, the NO_3^- -N removal efficiency was 51.7% in CWs planted with *Phragmites communis* and *Phalaris arundinacea* treating aquaculture effluents (Sindilariu et al., 2008). On the other hand, other authors reported that NO_3^- -N accumulated in the wetland system with the

concentration increased by 5.4% (5.83 mg/L) (Lin et al., 2005). Nutrient removal in CWs vary over time depending plant growth stage, contaminant load, environmental conditions, and microbial community structures (Wang et al., 2022; Vymazal, 2025). Plants can use NO_3^- -N as a nutrient, therefore NO_3^- -N concentration could be reduced through plant uptake (Garcia et al., 2010). However, among published literature, denitrification is considered as the main nitrate removal mechanism in wetland systems (Chen et al., 2014; Vymazal, 2025). The denitrification process is carried out by various types of heterotrophic facultative anaerobic bacteria such as *Pseudomonas*, *Paracoccus denitrificans* that are able to use nitrate as an electron acceptor under anoxic conditions. These bacteria prefer to use oxygen over nitrate as an electron acceptor when oxygen is available in the surrounding environment (Chen et al., 2014).

Phosphate removal

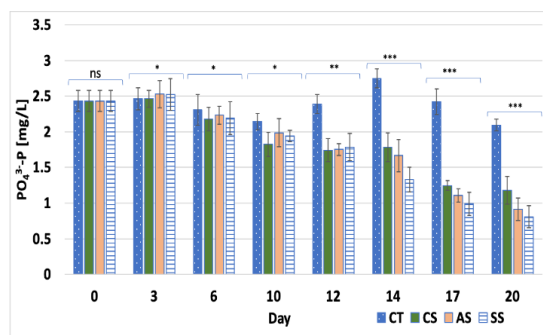


Figure 7. The changes in PO_4^{3-} -P concentrations in experimental systems

(note: ***: $p < 0.001$, statistically extremely significant; **: $p < 0.01$, statistically highly significant; *: $p < 0.05$, statistically significant; ns: $p > 0.05$, statistically not significant)

The changes in PO_4^{3-} -P concentrations in the four systems during the experimental period are presented in Fig. 7. The results showed that PO_4^{3-} -P concentration decreased in all systems. After 20 days, PO_4^{3-} -P removal efficiency reached 66.7% (PO_4^{3-} -P concentration decreased to 0.81 ± 0.16 mg/L) in SS system, followed by AS and CS systems with

the $\text{PO}_4^{3-}\text{-P}$ reduction rate of 62.4% and 51.5%, respectively. Meanwhile, only 13.9% removal of $\text{PO}_4^{3-}\text{-P}$ concentration was observed in the control system.

Total phosphorus removal efficiency in aquaculture wastewater by CWs planted with *S. Littoralis*, *C. involucratus* and *Posidoniaceae* treating shrimp farming wastewater was reported to be in the range of 32 – 41% (Le et al., 2023). $\text{PO}_4^{3-}\text{-P}$ removal efficiency in aquaculture wastewater by *E. crassipes*, *I. aquatica*, and *P. stratiotes* ranged from 50 to 98% (Nizam et al., 2020). Plant uptake is one the mechanism for phosphate removal in CWs (Garcia et al., 2010). Phosphorus is a macronutrient of plants and is a major component of ADP and ATP which are important for storing and transferring energy during photosynthesis and respiration (Wang et al., 2021). It has been reported that the P uptake rate of *Canna generalis* in CWs treating fish pond water was 0.098 – 0.215 g N/m²/day (Konnerup et al., 2011). The decrease in $\text{PO}_4^{3-}\text{-P}$ concentrations could be also attributed to microbial activities. Phosphate-accumulating bacteria in wetland systems treating wastewater have been detected (Wang et al., 2021).

CONCLUSIONS

The study demonstrated the potential of using three native aquatic plant species *C. demersum*, *A. paronychioides*, and *S. cucullata* for treating shrimp farming wastewater in Quang Ninh province, Vietnam. The highest removal of COD, $\text{NH}_4^+\text{-N}$, $\text{NO}_3^-\text{-N}$ and $\text{PO}_4^{3-}\text{-P}$ concentrations was obtained in SS system (*S. cucullata*) with the removal efficiencies of 95.7%, 96%, 40.5%, and 66.7%, respectively, followed by AS system (*A. paronychioides*) and CS system (*C. demersum*) after 20 days. After the experimental period, COD concentration in SS and AS systems met the standard QCVN 40:2011/BTNMT(column B) and QCVN 02-19:2014/BNNPTNT. The results from this present study make several noteworthy contributions to the potential applications of native aquatic plants for aquaculture wastewater treatment and environmental protection.

REFERENCES

- Abbasi A, Tabassum A, Ponni G, Tauseef M (2019) Potential of joyweed *Alternanthera sessilis* for rapid treatment of domestic sewage in SHEFROL bioreactor. International Journal of Phytoremediation 21(2): 160–169.
- Adhikari S, Sahu C, Mahapatra S, Dey L (2014) Nutrient budgets and effluent characteristics in giant freshwater prawn (*Macrobrachium rosenbergii*) culture Ponds. Bulletin of Environmental Contamination and Toxicology 92(5): 509–513.
- Ahmed W, Delatolla R (2021) Biofilm and microbiome response of attached growth nitrification systems across incremental decreases to low temperatures. Journal of Water Process Engineering 39: 101730, <https://doi.org/10.1016/j.jwpe.2020.101730>.
- Cao T T, Le H A, Eppe G (2025) Nutrient dynamics, environmental impacts, and feed efficiency in intensive whiteleg shrimp (*Litopenaeus vannamei*) farming on sandy soils in Ninh Thuan, Vietnam. Aquaculture Reports 44: 103050, <https://doi.org/10.1016/j.aqrep.2025.103050>.
- Chen Y, Wen Y, Zhou Q, Vymazal J (2014) Effects of plant biomass on nitrogen transformation in subsurface-batch constructed wetlands: a stable isotope and mass balance assessment. Water Research 63: 158–167.
- Fan Y, Wang H, Zhang Z, Yu L, Ziyi Z, Xiuzhen N (2024) Mechanisms involved in plant growth promotion by *Enterobacter cloacae* DJ under salinity-alkalinity stress. Chemical and Biological Technologies in Agriculture 12, <https://doi.org/10.1186/s40538-024-00537-5>.
- Garcia J, Rousseau D P, Morato J, Lesage S, Matamoros V, Bayona J M (2010) Contaminant removal processes in subsurface-flow constructed wetlands: a review. Critical reviews in Environmental Science and Technology 40(7): 561–661.
- Kritika P, Chandni S K, Manish K, Renu B, Satwinderjeet K (2024) Chapter Six - Salinity stress: Impact on plant growth, Editor(s): Ashita S, Manish K, Puneet S, Advances in Food Security and Sustainability, Elsevier, Netherlands, pp. 145–160, ISBN 9780443219078,
- Le Q A, Dinh N, Phan T, Nguyen P, Pham N, Nguyen L, Rudolph U, Hilbig J (2023) Treatment of shrimp farm effluents using a combination of native plant species in the Mekong Delta region. International Journal of Environmental Science and Technology 20: 4459–4466.
- Lin F, Jing R, Lee Y, Chang F, Chen M, Shih C (2005) Performance of a constructed wetland treating

- intensive shrimp aquaculture wastewater under high hydraulic loading rate. *Environmental Pollution* 134(3): 411–421.
- Mahmood Y, Zhang J, Zhang G (2016) Assessment of constructed wetland in nutrient reduction, in the commercial scale experiment ponds of freshwater prawn *Macrobrachium rosenbergii*. *Bulletin of Environmental Contamination and Toxicology* 96: 361–368.
- Mangarengi P, Selintung M, Zubair A, Ahmad F (2020) Evaluation of the effectiveness of wastewater treatment plant for super intensive shrimp farms (A case study on Punaga Village, Takalar). *IOP Conf. Series: Earth and Environmental Science* 419: 012162.
- Nguyen M P, Nguyen H H, Tran M K, Cung P H (2023) Study on aquaculture wastewater treatment by aquatic plants. *VNU Journal of Science: Earth and Environmental Sciences* 39 (4): 51-62.
- Nizam N, Anafiah M, Noor I, Karim H (2020) Efficiency of five selected aquatic plants in phytoremediation of aquaculture wastewater. *Applied Sciences* 10: 1 – 11.
- Nuwansi K, Verma A, Prakash C, Prabhath G, Peter R (2018) Performance evaluation and phytoremediation efficiency of selected aquatic macrophytes on aquaculture effluent. *Journal of Entomology and Zoology Studies* 6(2): 2885-2891.
- Oliveira G A, Colares G S, Lutterbeck C A, Dell'Osbel N, Machado E L, Rodrigues L R (2021) Floating treatment wetlands in domestic wastewater treatment as a decentralized sanitation alternative. *Science of the Total Environment* 773: 145609, <https://doi.org/10.1016/j.scitotenv.2021.145609>.
- Rehman F, Usman A, Ditta A, Khan F, Mahmood Q, Alataway A, Dewidar A, Mattar M (2023) Optimal root oxygen release from two macrophytes *Saururus cernuus* L. and *Pistia stratiotes* L. varies with light and temperature in simulated constructed wetlands microcosms. *Rhizosphere* 26: 100697, <https://doi.org/10.1016/j.rhisph.2023.100697>
- Sagheer M, Yang Z, Alsaleh M (2025) Determinants influencing green cost efficiency in the aquaculture sector: New insights from Asian countries. *Marine Policy* 180: 106783, <https://doi.org/10.1016/j.marpol.2025.106783>.
- Santhosh P, Nithya T, Gokila S, Lincy G, Balavaishnavi B, Kamaraj M (2022) Assessment of phytochemicals, antioxidant, antibacterial activity, and profiling of functional molecules in a freshwater fern, *Salvinia cucullata* Roxb. *South African Journal of Botany* 151, Part B: 275-283.
- Sindilariu P D, Wolter C, Reiter R (2008) Constructed wetlands as a treatment method for effluents from intensive trout farms. *Aquaculture* 277(3–4):179–184.
- Shi Y, Zhang G, Liu J, Zhu Y, Xu J (2011) Performance of a constructed wetland in treating brackish wastewater from commercial recirculating and super intensive shrimp growout systems. *Bioresource Technology* 102(20): 9416–9424.
- Srivastava K, Chandra H, Kalra S, Pratibha M, Hena K, Poonam Y (2017) Plant–microbe interaction in aquatic system and their role in the management of water quality: a review. *Applied Water Science* 7: 1079–1090.
- Syed I, Fatima H, Mohammed A, Siddiqui M (2018) *Ceratophyllum demersum* a free-floating aquatic plant: a review. *Indian Journal of Pharmaceutical and Biological Research* 6(2):10-17.
- Wang J, Long Y, Yu G, Wang G, Zhou Z, Li Pe, Zhang Y, Yang K, Wang S (2022) A review on microorganisms in constructed wetlands for typical pollutant removal: species, function, and diversity, *Frontiers in Microbiology* 13, <https://doi.org/10.3389/fmicb.2022.845725>
- Wang Q, Ding J, Xie H, Hao D, Du Y, Zhao C, Xu F, Kong Q, Wang B (2021) Phosphorus removal performance of microbial-enhanced constructed wetlands that treat saline wastewater. *Journal of Cleaner Production* 288: 125119, <https://doi.org/10.1016/j.jclepro.2020.125119>
- Wu H, Hsieh T, Lin A, Yen C (2013) *Alternanthera paronychioides* protects pancreatic β -cells from glucotoxicity by its antioxidant, antiapoptotic and insulin secretagogue actions. *Food Chemistry* 139 (1-4): 362-370.
- Yao F, Shen G , Li X, Li H, Hu H, Ni W (2011) A comparative study on the potential of oxygen release by roots of selected wetland plants. *Physics and Chemistry of the Earth, Parts A/B/C* 6 (9-11): 475-478.
- Vymazal J (2010) Constructed wetlands for wastewater treatment. *Water* 2: 530-549.
- Vymazal J (2025) Nitrogen removal in constructed wetlands, *Current Opinion in Environmental Science & Health* 48: 100668, <https://doi.org/10.1016/j.coesh.2025.100668>
- Zhang Q, Achal V, Xu Y, Xiang N (2014) Aquaculture wastewater quality improvement by water spinach (*Ipomoea aquatica* Forsskal) floating bed and ecological benefit assessment in ecological agriculture district. *Aquacultural Engineering* 60: 48–55.

Sustainable recovery of struvite fertilizer from swine wastewater by fluidized bed homogeneous crystallization

Nguyen Gia Cuong¹, Le Van Giang¹, Nguyen Thi Thuy², Bui Ngoc Quy^{1,3}, Luu The Anh^{1*}

¹Central Institute for Natural Resource and Environmental Studies, Vietnam National University, Hanoi, Vietnam

²Institute of Earth Sciences, Vietnam Academy of Science and Technology, Hanoi, Viet Nam

³Hanoi Research and Development of Geospatial Data Management and Analysis Techniques GMA, Hanoi University of Mining and Geology, Vietnam

*Email: luutheanhig@yahoo.com

Abstract: Swine wastewater contains high concentrations of nitrogen and phosphorus, posing serious risks of eutrophication if discharged untreated. Therefore, recovering these nutrients as valuable fertilizers is essential for both environmental protection and resource recycling. This study investigates the recovery of potassium struvite (K-struvite, $\text{MgKPO}_4 \cdot 6\text{H}_2\text{O}$) from swine wastewater using a fluidized bed homogeneous crystallization (FBHC) reactor. The effects of key operational parameters, including pH, Mg/P molar ratio, and up-flow velocity, on nutrient removal and crystal formation were systematically evaluated. Optimal removal efficiencies were achieved at pH 10.0–10.5, Mg/P ratio of 1.0, and up-flow velocity of 30–40 m/h, with phosphorus, magnesium, and potassium removal rates of 93.5%, 88.4%, and 72.1%, respectively. SEM analysis showed that the recovered crystals had a rounded morphology with smooth surfaces, while XRD analysis confirmed their high crystallinity consistent with K-struvite. Quantitative EDS analysis further showed that the recovered product contained P, Mg, and K at 17.69 wt%, 10.39 wt%, and 7.86 wt%, demonstrating a nutrient-rich composition suitable for fertilizer application. The results highlight the potential of the FBHC process as a sustainable and efficient method for simultaneous nutrient removal and recovery from livestock wastewater.

Keywords: Swine wastewater, nitrogen and phosphorus recovery, granulation, struvite, fluidized bed homogeneous crystallization.

INTRODUCTION

Intensive livestock farming, particularly swine production, generates large volumes of wastewater containing high concentrations of nutrients such as phosphorus (P), magnesium (Mg), and potassium (K) (Huang, H., and et al. 2011). If not properly treated, the discharge of these nutrient-rich effluents contributes to eutrophication, groundwater contamination, and long-term ecological degradation (Le, V.-G. and et al. 2021). While phosphorus and magnesium recovery have been extensively studied, potassium recovery from wastewater remains a challenge due to its high solubility and weak precipitation potential under standard treatment conditions (Le, V.-G., and et al. 2020). Recent research has shown that potassium can be recovered in the form of potassium struvite (K-struvite, $\text{MgKPO}_4 \cdot 6\text{H}_2\text{O}$), a crystalline compound with potential use as a slow-release fertilizer (Le, V.-G., and et al. 2020). The slow-release fertilizer application of K-struvite has been documented in previous studies (Kabdaşı, I., and et al. 2022). In recent years, a variety of techniques have been investigated for the recovery of potassium and/or phosphorus from nutrient-rich wastewaters. These include stirred-tank precipitation of ammonium or potassium struvite compounds, draft-tube/baffle reactors for nutrient crystallisation, and air-stripping combined with precipitation for ammonia and phosphate recovery. For example, precipitation of magnesium ammonium phosphate in stirred-tank systems has been widely applied in

wastewater treatment plants, yet the product quality is strongly influenced by mixing intensity and localized pH gradients, resulting in heterogeneous crystal morphology (Kabdaşlı, I., and et al., (2022). Similarly, the precipitation of potassium-bearing struvite ($\text{MgKPO}_4 \cdot 6\text{H}_2\text{O}$) under controlled pH and stoichiometric conditions has been documented, but reproducible control of crystal growth and purity remains challenging due to hydrodynamic instability and sensitivity to reaction conditions (Nagare, H., and et al. (2020). Among these, the fluidized bed homogeneous crystallization (FBHC) reactor has emerged as an effective technology for the controlled recovery of struvite-type minerals, offering advantages such as enhanced mass transfer, controlled supersaturation, and continuous operation (Luu, T. A., and et al. 2022).

However, the formation and quality of K-struvite are highly sensitive to operational parameters, including solution pH, molar ratios of Mg to P, and hydrodynamic factors such as up-flow velocity (V_o , T. D. H., and et al. 2020). These parameters influence not only the efficiency of nutrient removal but also the morphology, purity, and crystallinity of the precipitated product (Shih, Y.-J., and et al. 2017). Therefore, a comprehensive understanding of their effects is essential to optimize recovery performance. In this context, the present study aims to investigate the influence of key operational conditions on the removal efficiencies of P, Mg, and K in an FBHC reactor, and to characterize the recovered K-struvite crystals using SEM, EDS, and XRD analyses. The findings contribute to advancing resource recovery technologies for sustainable wastewater management and circular nutrient use in agriculture.

MATERIAL AND METHODS

Materials

All chemicals used in this study were of analytical grade and applied without further purification. Ultrapure deionized water (resistivity $>18.2 \text{ M}\Omega\cdot\text{cm}$) obtained via reverse osmosis (RO) was used for the preparation of

all solutions. Synthetic wastewater (500 mL per experiment) was prepared using sodium dihydrogen phosphate monohydrate ($\text{NaH}_2\text{PO}_4 \cdot \text{H}_2\text{O}$, Showa, Japan), magnesium chloride hexahydrate ($\text{MgCl}_2 \cdot 6\text{H}_2\text{O}$, PanReac, Germany), potassium chloride (KCl, Showa, Japan), and ammonium chloride (NH_4Cl , Showa, Japan). The synthetic wastewater used in this study was prepared according to previously published formulations with slight modifications (Kozik, A., and et al. 2013). The phosphate concentration was maintained at 400 mg P/L, while the Mg/P molar ratio was varied from 0.4 to 2.0 to examine the effect of magnesium dosage on struvite crystallization performance, consistent with the ranges evaluated in earlier studies on nutrient recovery (onzález-Morales, C., and et al. 2021). Solution pH was adjusted using sodium hydroxide (NaOH, 91%, Merck) and hydrochloric acid (HCl, 37%, Merck).

Experimental setup

The laboratory-scale FBHC system was conducted in a 500 mL cylindrical Pyrex reactor operated in a 500-mL cylindrical Pyrex reactor. The laboratory scale of the FBHC systems has been experimented with in a 500 mL of cylindrical pyrex reactor. The reactor was built as a vertical column with 100 cm height and 2.5 cm in diameter. The recycle point was placed at 80 cm from the bottom of the reactor and 5 cm below the effluent point. Three inlets at the bottom of the reactor column are linked to a peristaltic pump (Masterflex L/S, Cole-Parmer Instrument Co., USA), as shown in Figure 1 to control inlet flow rates of mixture of synthetic wastewater, and sodium hydroxide salts (precipitants), and the reflux flow rate. A 5 mL/min pumping of the target pollutant P solution is required to homogenize seed material in the FBHC system. Meanwhile, the precipitant that consists of potassium and magnesium mixture (8.4 mM and 6.45 mM, respectively) were also pumped at 5 mL/min into the FBR reactor and reached a molar ratio Mg/P of 1.2/1 in the mixing point. The recirculation stream was maintained at 50 mL/min. As the seed particles were stable

enough, the condition was changed to stimulate the growth of the generated particles. The inlet concentration was doubled and followed by the increase of inlet concentration to 50 mL/min. A 150 mL/min recirculation stream is then used to maintain a constant up-flow velocity of 30 m/h and reduce supersaturation. By adjusting the pH at the reactant tank, the effluent pH was maintained at 10 during both the seed formation and particle growth steps in the FBHC system. The reactor top was sampled (at the reflux point, 5 cm below the outlet) after 25 hydraulic retention time-HRT cycles (approximately 87.5 minutes, 1 HRT = 3.5 min) as the system reached steady state [18]. In order to determine the soluble phosphorus concentration in the effluent, a sample was filtered through a 0.45 µm filter. To determine the total amount of phosphorus in both soluble and suspended particle forms, the other sample was not filtered. Two sets of samples were acidified by 0.05 mL HNO₃ (70%). Total phosphorus removal could be determined using Eq. (1).

$$TR\% = 1 - \frac{[P]_s \times Q_T}{[P]_0 \times Q_P} \times 100 \quad (1)$$

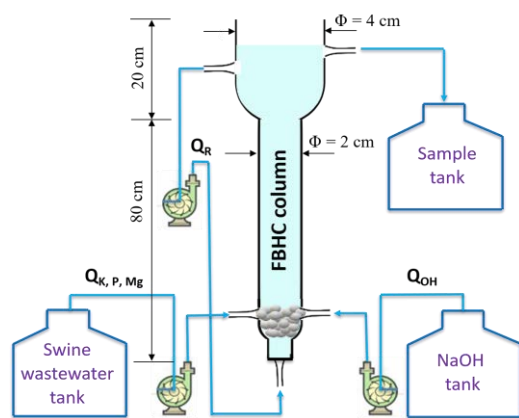


Figure 1. Experimental setup of the fluidized-bed reactor

The phosphorus concentration at the inlet was named as $[P]_0$. Meanwhile $[P]_s$ represents the dissolved residual phosphorus concentration in effluent point after filtration, and $[P]_T$ represents the total effluent phosphorus levels without filtration that determines both of dissolved residual

phosphorus and digested phosphorus concentration from the sludge that was washed out from the reactor. TR% refers to the total amount of related compounds that can be precipitates by the process.

Analytical methods

Each sample was filtered using a 0.45 µm syringe filter before analysis. To measure the TP, Fe, Cu, Mg, Na, K, and Ca in the solution, a Inductively Coupled Plasma Mass Spectrometry (ICP-MS, ULTIMA 2000, HORIBA Ltd., Japan) was used. Analyzing NH₄⁺-N in a solution was performed using Flow Injection Analysis (FIA, Lachat Instrument 5600, Colorado, U.S.A.). Morphological structures were observed using a scanning electron microscope (SEM, JEOL JSM-6700F, HITACHI, Japan). Diffraction angles of 10° to 90°, a step width of 0.02°, and a scanning rate of 10°/s were used to determine the crystallographic structure of the sample using an X-ray diffractometer (XRD, DX III, Rigaku Co., Japan). A Raman microscopy (DRX, Thermo Scientific) was performed under a 633 nm laser of 50 mW to detect the functional groups of solids

RESULTS AND DISCUSSION

Effect of pH

Figure 2 presents the influence of equilibrium pH (pH_e) on the removal efficiencies of Mg, K, and P in the FBHC reactor. As the pH_e increased from 9 to 11, the removal efficiency of all three nutrients exhibited notable trends, highlighting the critical role of pH in driving crystallization and nutrient recovery. Phosphorus removal showed a consistent increase with rising pH, improving from approximately 77% at pH 9 to a maximum of ~94% at pH 10.5, after which it slightly plateaued. This enhancement is attributed to the increased availability of deprotonated phosphate species (HPO₄²⁻, PO₄³⁻) and the thermodynamic favorability of phosphate precipitation under mildly alkaline conditions, which promote the nucleation and growth of struvite-type minerals (Ha, T.-H., and et al. 2025).

Magnesium removal also improved with increasing pH, rising from ~70% at pH 9 to ~88% at pH 11. The positive trend reflects the enhanced precipitation of Mg^{2+} with phosphate, particularly under conditions favorable for $\text{MgKPO}_4 \cdot 6\text{H}_2\text{O}$ formation (Le, V. G., and et al. 2020). The availability of both phosphate anions and hydroxide ions at higher pH likely promotes crystal nucleation (Su, C.-C., and et al. 2014), supporting magnesium incorporation into the solid phase. In contrast, potassium removal displayed a sharp increase from ~35% at pH 9 to a peak of ~73% at pH 10, followed by a gradual decline to ~66% at pH 11. This trend suggests an optimal pH window for K incorporation into the struvite lattice, beyond which excess OH^- or competing reactions may inhibit stable K-struvite formation (Ha, T.-H., and et al. 2024). Overall, the results suggest that the optimal pH range for simultaneous and efficient removal of Mg, K, and P lies between 9.5 and 10.5, where the formation of K-struvite is most thermodynamically and kinetically favorable. Recent work on synthetic urine also demonstrated that increasing pH toward the alkaline range (10) significantly enhances K-struvite crystallization (Wei, L., and et al. 2025). Likewise, Kabdaşlı et al. (2022) summarized that the favorable pH range for K-struvite precipitation typically lies between 9 and 11, with most effective crystallization around pH ~10 (Kabdaşlı, I., and et al. 2022). Tarragó et al. (2018) also reported that pH \approx 10 yielded the highest P and K recovery efficiency during K-struvite precipitation from manure-derived streams (Tarragó, E., and et al. 2018). Furthermore, studies on swine wastewater have shown that pH values above 10 can lead to competitive formation of $\text{Mg}(\text{OH})_2$ and other phases, reducing K incorporation into the struvite lattice (Company, E., and et al. 2022). These published findings are in strong agreement with our observed optimal pH window of 9.5–10.5, supporting that moderately alkaline conditions promote both thermodynamic and kinetic favorability for K-struvite formation.

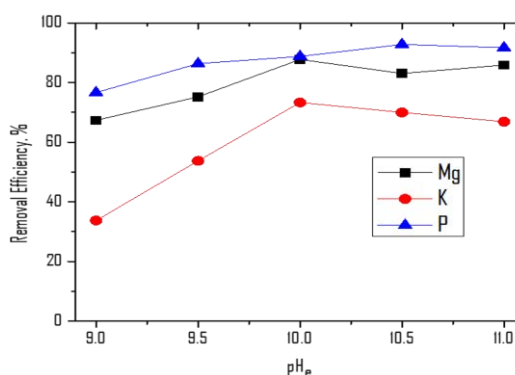


Figure 2. Effect of pH on removal efficiency of Mg, K, and P in the FBHC reactor.

Effect of Mg/P molar ratio

Figure 3 illustrates the influence of the Mg/P molar ratio on the removal efficiencies of Mg, K, and P in the FBHC reactor. As the Mg/P ratio increased from 0.4 to 1.0, a significant enhancement in P removal efficiency was observed, rising from approximately 40% to over 90%. This increase indicates the critical role of magnesium as a limiting reagent in the precipitation of phosphate, specifically as K-struvite. The maximum phosphate removal was achieved near the stoichiometric Mg/P ratio of 1, consistent with the theoretical molar requirement for K-struvite formation. Beyond this optimal point, further increases in Mg/P ratio (1.2–1.8) led to a slight decline in P removal efficiency, possibly due to excessive Mg^{2+} interfering with crystal growth dynamics or promoting the formation of secondary magnesium phosphate species (e.g., $\text{Mg}_3(\text{PO}_4)_2$) (Hsiao, C.-T., and et al. 2023), which are less stable or less efficiently retained in the FBHC reactor (Huang, H., and et al. 2019).

In contrast, potassium removal exhibited a declining trend with increasing Mg/P ratios. Starting at approximately 90% removal efficiency at Mg/P = 0.4, K removal steadily decreased, reaching below 20% at Mg/P = 1.8. This inverse correlation suggests that at higher Mg dosages, the stoichiometric balance shifts away from K-struvite formation and may favor the precipitation of other non-potassium phosphate compounds. Similar behavior was

reported previously by Tarrago et al. (2018), where co-precipitation of magnesium phosphate impurities increased at higher Mg/P ratios, reducing K incorporation into the K-struvite phase (Tarragó, E., and et al. 2018). Magnesium removal remained consistently high (>90%) across all Mg/P ratios up to 1 but began to decline at higher values, indicating possible saturation of Mg^{2+} in the system or competitive inhibition in crystal formation. Overall, the optimal Mg/P molar ratio for simultaneous and efficient recovery of P and K appears to be around 1, beyond which the selectivity for K-struvite formation diminishes.

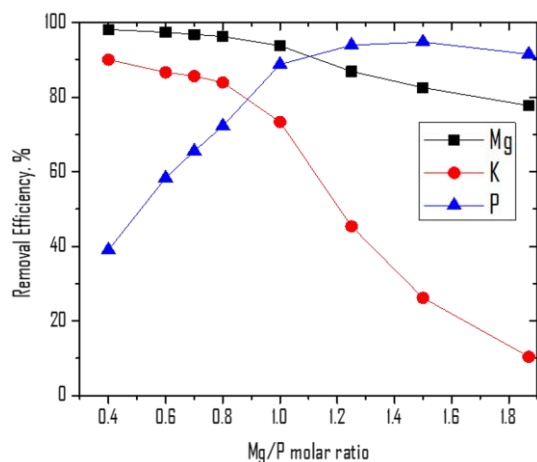


Figure 3. Effect of Mg/P molar ratio on nutrients removal in FBHC reactor.

Effect of up-flow velocity

The impact of up-flow velocity (U) on the removal efficiencies of potassium, phosphate, and ammonium-nitrogen in the FBHC reactor was systematically evaluated, as illustrated in Figure 4.

The results indicate a pronounced influence of up-flow velocity on P and NH_4^+-N removal, while the effect on K removal remained minimal across all tested velocities. Phosphate removal efficiency increased sharply with rising U , peaking at 96.4% at 40 m/h before exhibiting a slight decline at higher velocities. A similar trend was observed for NH_4^+-N , which achieved a maximum removal efficiency of 87.2% at 30 m/h (Luu, T. A., and et al. 2025). The improved removal rates at

moderate U values can be attributed to enhanced fluidization and mixing conditions (Rahaman, M. S., and et al. 2014), which likely promote more effective nucleation and growth of K-struvite crystals (Ha, T.-H., and et al. 2023). However, beyond the optimal range (30–40 m/h), further increases in velocity may induce particle washout and shear stress that hinder crystal retention and aggregation, resulting in reduced removal efficiencies. In contrast, potassium removal remained relatively constant (~10–20%) regardless of up-flow velocity, suggesting that the majority of K^+ remains in solution or that its incorporation into struvite is limited under the operational conditions tested. These findings highlight the importance of optimizing hydrodynamic parameters in the FBHC reactor to maximize nutrient recovery, particularly for P and NH_4^+-N .

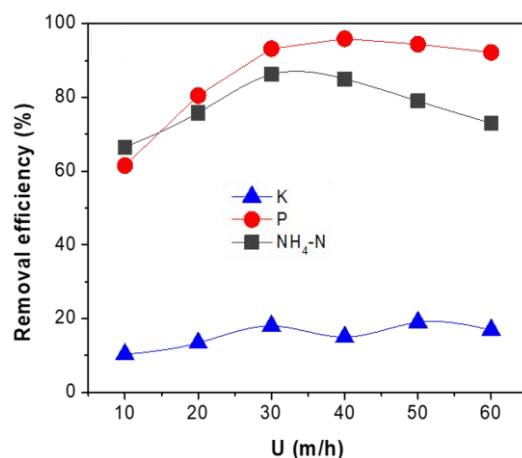


Figure 4. Effect of up-flow velocity on K-struvite removal efficiency in the FBHC process.

Characterization of the K-struvite pellets

Figure 5 illustrates the morphological characteristics and elemental composition of the solid precipitates recovered from the FBHC process, analyzed using scanning electron microscopy (SEM) and energy-dispersive X-ray spectroscopy (EDS). The low-magnification SEM image ($\times 200$) reveals that the precipitates exhibit a compact, aggregated pellet-like structure with a rough surface, indicating successful crystallization and agglomeration of fine particles. At higher magnification ($\times 2000$), the crystalline morphology becomes more

evident, showing elongated, rod-like structures with well-defined edges, typical of struvite-type minerals. The observed crystal habit supports the formation of K-struvite, a hydrated phosphate salt known for its orthorhombic crystal system.

The corresponding EDS spectra and quantitative analysis further confirm the elemental composition consistent with K-struvite formation. Major elements detected include Mg, K, and P, with weight percentages of 10.39%, 7.86%, and 17.69%, respectively. The presence of oxygen (45.00 wt%) is attributable to the hydrated phosphate structure and water molecules coordinated within the crystal lattice. Trace levels of sodium (Na, 6.15 wt%) and carbon (C, 12.91 wt%) were also detected, possibly due to residual organics or background contamination. The Mg:P:K atomic ratio observed aligns reasonably with the stoichiometric composition of $\text{MgKPO}_4 \cdot 6\text{H}_2\text{O}$, supporting the successful recovery of K-struvite under the tested conditions. Overall, the SEM-EDS results validate the morphological and compositional integrity of the crystal products and confirm the efficacy of the FBHC process for targeted nutrient recovery from wastewater.

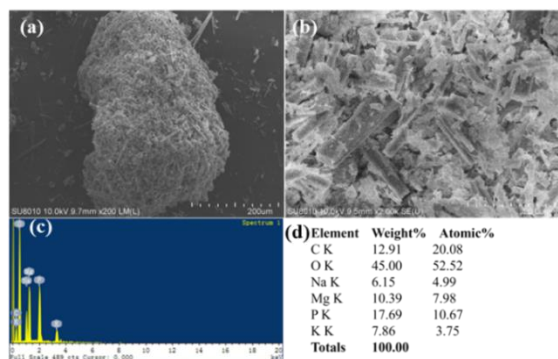


Figure 5. Morphology of crystal pellets products analyzed by SEM with magnification of (a) $\times 200$, (b) $\times 2000$, (c-d) EDS spectra of crystal pellets obtained from the FBHC process.

Figure 6 presents the X-ray diffraction (XRD) patterns of the crystallized products obtained from the fluidized bed homogeneous crystallization process at different pH values, ranging from 9 to 11. The diffraction peaks observed across all samples confirm the

formation of a crystalline phase, with varying intensities and sharpness depending on the pH condition. At lower pH values (9–9.5), the XRD patterns exhibit broader and less intense peaks, suggesting the formation of poorly crystalline or amorphous materials. As the pH increases from 10 to 11, the diffraction peaks become more intense and sharper, indicating enhanced crystallinity and possibly higher purity of the recovered product. The dominant peaks observed around $2\theta \approx 21.0^\circ$, 30.5° , and 50.2° are characteristic of $\text{MgKPO}_4 \cdot 6\text{H}_2\text{O}$, consistent with standard reference patterns (Tarragó, E., and et al. 2018). The improvement in crystallinity with increasing pH can be attributed to the higher availability of OH^- ions, which favor the deprotonation of phosphate species and promote nucleation and crystal growth (Wilsenach, J., and et al. 2007). However, at pH 11, although crystallinity improves, there may be a risk of competing phase formation or conversion of struvite into other phosphate minerals under highly alkaline conditions (Silva, A. F. R., and et al. 2022). Therefore, pH plays a critical role in controlling the phase purity and crystallinity of K-struvite, with the optimal range likely between pH 10 and 10.5 for efficient recovery with well-defined crystalline structure.

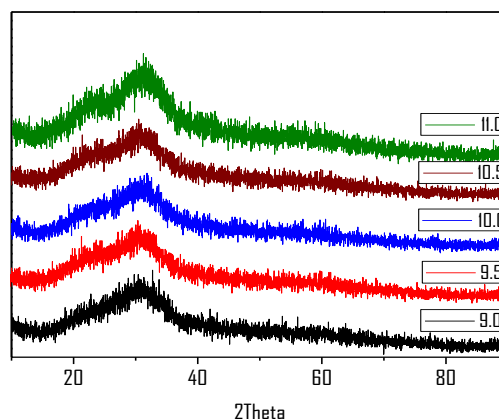


Figure 6. XRD patterns of K-struvite at various pH levels from FBHC process.

CONCLUSION

This study demonstrated the effectiveness of the fluidized bed homogeneous crystallization process for simultaneous

nutrient removal and recovery of K-struvite from swine wastewater. The process performance was significantly influenced by operational parameters, including pH, Mg/P molar ratio, and up-flow velocity. Under optimal conditions (pH 10.0–10.5, Mg/P ratio of 1, and up-flow velocity of 30–40 m/h), the removal efficiencies reached 93.5% for phosphorus, 88.4% for magnesium, and 72.1% for potassium. SEM analysis revealed that the recovered K-struvite crystals exhibited predominantly rounded morphology with smooth surfaces, indicating well-formed and uniform crystal growth. EDS spectra confirmed the elemental composition matching the theoretical stoichiometry of K-struvite, while XRD patterns showed high crystallinity and phase purity. These findings confirm that the FBHC process is a viable and efficient approach for nutrient recovery, enabling the production of high-quality K-struvite suitable for use as a slow-release fertilizer. Moving forward, pilot-scale testing using real swine wastewater and field-level agricultural trials will be conducted to validate process robustness under practical conditions and to assess the agronomic performance of the recovered K-struvite in real soil–crop systems.

ACKNOWLEDGEMENTS

This research was funded by the research under contract number 033/VN/2025 of Nanyang Environment and Water Research Institute's Lien Environmental Fellowship Programme, Nanyang Technological University, Singapore. We also thank the editors and anonymous reviewers for their helpful comments and suggestions.

REFERENCES

- Company, E., Farrés, M., Colprim, J., & Magrí, A. (2022). Exploring the recovery of potassium-rich struvite after a nitrification-denitrification process in pig slurry treatment. *Science of the Total Environment*, 847, 157574. doi:10.1016/j.scitotenv.2022.157574
- González-Morales, C., Fernández, B., Molina, F. J., Naranjo-Fernández, D., Matamoros-Veloza, A., & Camargo-Valero, M. A. (2021). Influence of pH and Temperature on Struvite Purity and Recovery from Anaerobic Digestate. *Sustainability*, 13(19), 10730.
- Ha, T.-H., Mahasti, N. N., Ha, H.-Q., Liao, P.-L., Huang, Y.-H., & Lu, M.-C. (2024). Recovery of nitrogen as struvite from swine wastewater: Comparison study of batch and continuous fluidized-bed crystallization process. *Separation and Purification Technology*, 351, 128045.
- Ha, T.-H., Mahasti, N. N., Ha, H.-Q., Liao, P.-L., Huang, Y.-H., & Lu, M.-C. (2025). Selective precipitation of calcium phosphate, N-struvite, and K-struvite from raw seawater for resource recovery. *Journal of Water Process Engineering*, 69, 106685.
- Ha, T.-H., Mahasti, N. N., Lin, C.-S., Lu, M.-C., & Huang, Y.-H. (2023). Enhanced struvite ($\text{MgNH}_4\text{PO}_4 \cdot 6\text{H}_2\text{O}$) granulation and separation from synthetic wastewater using fluidized-bed crystallization (FBC) technology. *Journal of Water Process Engineering*, 53, 103855.
- Hsiao, C.-T., Huang, T.-H., Lacson, C. F. Z., Vilando, A. C., & Lu, M.-C. (2023). Recovering struvite from livestock wastewater by fluidized-bed homogeneous crystallization as a pre-treatment process to sludge co-digestion. *Environmental Research*, 235, 116639.
- Huang, H., Xu, C., & Zhang, W. (2011). Removal of nutrients from piggery wastewater using struvite precipitation and pyrogenation technology. *Bioresource technology*, 102(3), 2523–2528.
- Huang, H., Zhang, D., Wang, W., Li, B., Zhao, N., Li, J., & Dai, J. (2019). Alleviating Na^+ effect on phosphate and potassium recovery from synthetic urine by K-struvite crystallization using different magnesium sources. *Science of the total environment*, 655, 211–219.
- Kabdaşlı, I., Kuşçuoğlu, S., Tünay, O., & Siciliano, A. (2022). Assessment of K-Struvite Precipitation as a Means of Nutrient Recovery from Source Separated Human Urine. *Sustainability*, 14(3), 1082.
- Kabdaşlı, I., Siciliano, A., Limonti, C., & Tünay, O. (2022). Is K-Struvite Precipitation a Plausible Nutrient Recovery Method from Potassium-Containing Wastes?—A Review. *Sustainability* 14(18), 11680.
- Kozik, A., Hutnik, N., Piotrowski, K., Mazieniczuk, A., & Matynia, A. (2013). Precipitation and crystallization of struvite from synthetic wastewater under stoichiometric conditions. *Advances in Chemical Engineering Science*, 3(4), 20–26.
- Le, V.-G., Vo, D.-V. N., Nguyen, N.-H., Shih, Y.-J., Vu, C.-T., Liao, C.-H., & Huang, Y.-H. (2021). Struvite recovery from swine wastewater using fluidized-bed homogeneous granulation process. *Journal of Environmental Chemical Engineering*, 9(3), 105019.
- Le, V.-G., Vu, C.-T., Shih, Y.-J., Bui, X.-T., Liao, C.-H., & Huang, Y.-H. (2020). Phosphorus and potassium

- recovery from human urine using a fluidized bed homogeneous crystallization (FBHC) process. *Chemical Engineering Journal*, 384, 123282.
- Le, V. G., Vo, D. V. N., Vu, C. T., Bui, X. T., Shih, Y. J., & Huang, Y. H. (2020). Applying a novel sequential double-column fluidized bed crystallization process to the recovery of nitrogen, phosphorus, and potassium from swine wastewater. *ACS ES&T Water*, 1(3), 707-718.
- Luu, T. A., Bui, N. T., Mofijur, M., Van, H. T., Lin, C., Tran, H. T., . . . Huang, Y. H. (2022). Fluidized-bed homogeneous granulation for potassium and phosphorus recovery: K-struvite release kinetics and economic analysis. *Journal of the Taiwan Institute of Chemical Engineers*, 139, 104494.
- Luu, T. A., Nguyen, G. C., Truong, M. T., Le, V. G., & Bui, X. T. (2025). Recovery of high-quality struvite fertilizer product from swine wastewater using fluidized bed homogeneous crystallization. *RSC Adv*, 15(30), 24122-24136. doi:10.1039/d5ra03370e
- Nagare, H., Iwata, T., Ebi, A., Akao, S., Maeda, M., Yasutake, D., & Fujiwara, T. (2020). Simultaneous recovery of phosphorus and potassium from biomass as magnesium salt. *Journal of Japan Society of Civil Engineers, Ser. G*, 76(7), III_181-III_187.
- Nguyen, G. C., Truong, M. T., & Bui, X. T. (2025). Recovery of high-quality struvite fertilizer product from swine wastewater using fluidized bed homogeneous crystallization. *RSC Adv*, 15(30), 24122-24136.
- Rahaman, M. S., Mavinic, D. S., Meikleham, A., & Ellis, N. (2014). Modeling phosphorus removal and recovery from anaerobic digester supernatant through struvite crystallization in a fluidized bed reactor. *Water research*, 51, 1-10.
- Shih, Y.-J., Abarca, R. R. M., de Luna, M. D. G., Huang, Y.-H., & Lu, M.-C. (2017). Recovery of phosphorus from synthetic wastewaters by struvite crystallization in a fluidized-bed reactor: effects of pH, phosphate concentration and coexisting ions. *Chemosphere*, 173, 466-473.
- Silva, A. F. R., Lebron, Y. A. R., Brasil, Y. L., Lange, L. C., & Amaral, M. C. S. (2022). Effect of electrolyte solution recycling on the potassium recovery from vinasse by integrated electrodialysis and K-struvite precipitation processes. *Chemical Engineering Journal*, 450, 137975.
- Su, C.-C., Abarca, R. R. M., de Luna, M. D. G., & Lu, M.-C. (2014). Phosphate recovery from fluidized-bed wastewater by struvite crystallization technology. *Journal of the Taiwan Institute of Chemical Engineers*, 45(5), 2395-2402
- Tarragó, E., Rusalleda, M., Colprim, J., Balaguer, M. D., & Puig, S. (2018). Towards a methodology for recovering K-struvite from manure. *Journal of Chemical Technology Biotechnology*, 93(6), 1558-1562.
- Tarragó, E., Rusalleda, M., Colprim, J., Balaguer, M. D., & Puig, S. (2018). Towards a methodology for recovering K-struvite from manure. *Journal of Chemical Technology Biotechnology*, 93(6), 1558-1562.
- Tarragó, E., Rusalleda, M., Colprim, J., Balaguer, M. D., & Puig, S. (2018). Towards a methodology for recovering K-struvite from manure. *Journal of chemical technology & biotechnology*, 93(6), 1558-1562.
- Vo, T. D. H., Nguyen, B. S., Vu, C. T., Shih, Y. J., & Huang, Y. H. (2020). Recovery of iron (II) and aluminum (III) from acid mine drainage by sequential selective precipitation and fluidized bed homogeneous crystallization (FBHC). *Journal of the Taiwan Institute of Chemical Engineers*, 115, 135-143.
- Wei, L., Tang, Y., Zhang, T., Ji, J., Zhang, Q., Dong, Y., . . . Kong, J. (2025). Factors influencing K-struvite purity via phosphorus coprecipitation in synthetic urine: Verification, quantification, and modelling. *Environmental Research*, 264(Pt 1), 120346. doi:10.1016/j.envres.2024.120346.
- Wilsenach, J., Schuurbijs, C., & Van Loosdrecht, M. (2007). Phosphate and potassium recovery from source separated urine through struvite precipitation. *Water research*, 41(2), 458-466.

Recovery of Aluminum from Wastewater via Fluidized Bed Homogeneous Crystallization

Le Van Giang¹, Nguyen Thi Thuy¹, Nguyen Thi Thuy², Bui Ngoc Quy^{1,3,*}

¹Central Institute for Natural Resource and Environmental Studies, Vietnam National University, Hanoi, Vietnam

²Institute of Earth Sciences, Vietnam Academy of Science and Technology, Hanoi, Viet Nam

³Hanoi Research and Development of Geospatial Data Management and Analysis Techniques (GMA), Hanoi University of Mining and Geology, Vietnam

*Email: quybncres@vnu.edu.vn

Abstract: The present study explores the application of a fluidized bed homogeneous crystallization (FBHC) reactor for the efficient separation and recovery of aluminum from synthetic wastewater. The process was assessed under varying operational parameters, including pH, up-flow velocity, reflux ratio, and aluminum surface loading rate, to determine their impact on crystallization efficiency and residual aluminum concentrations. Results showed that aluminum removal exceeded 98% under optimal conditions, with crystallization ratios reaching over 95% at pH 9.5–10 and moderate flow and loading rates. SEM analysis revealed dense, spherical $\text{Al}(\text{OH})_3$ particles, while EDS and XRD confirmed their high purity and crystalline structure. These findings suggest that FBHC technology offers a technically viable and operationally stable solution for aluminum recovery, contributing to sustainable wastewater management and circular resource utilization.

Keywords: Swine wastewater, nitrogen and phosphorus recovery, granulation, struvite, fluidized bed homogeneous crystallization.

INTRODUCTION

Aluminum (Al) is a critical element used extensively across various industrial sectors, including metal processing, paper production, dyeing, and water treatment (D. Bhatt, and et al. 2006). As a consequence, large volumes of aluminum-containing wastewater are discharged into the environment, posing significant environmental and operational

challenges (T.D.H. Vo, and et al. 2020). Excess aluminum in aquatic systems can lead to ecosystem disruption, interfere with biological wastewater treatment processes, and contribute to the accumulation of chemically unstable sludge (M.T. Truong, and et al. 2025). Although conventional chemical precipitation is widely applied for aluminum removal, it often results in the formation of amorphous hydroxide sludge, which has poor dewaterability, low crystallinity, and limited reuse potential, thus shifting the problem from pollution control to solid waste management (V.G. Le, and et al. 2024).

In this context, the selective recovery of aluminum in a crystalline and reusable form is gaining increasing attention as a sustainable approach that aligns with circular economy principles (K.-Y. Chang, and et al. 2023). Among the advanced technologies investigated, FBHC has shown considerable promise due to its ability to produce high-purity crystalline $\text{Al}(\text{OH})_3$ with controlled morphology, while minimizing sludge generation (K.-Y. Chang, and et al. 2023). The FBHC process offers several advantages over conventional precipitation, including enhanced supersaturation control, improved mass transfer, continuous operation, and the possibility of producing valuable crystalline solids suitable for reuse in industrial applications or safe disposal (W.-Z. Li, and et al. 2023).

However, the performance of FBHC systems is highly sensitive to several operating

parameters, such as pH, up-flow velocity, aluminum surface loading, and reflux ratio, all of which influence nucleation kinetics, particle growth, and overall system stability. Therefore, a comprehensive understanding of how these parameters affect both the removal efficiency and crystallization behavior is essential for optimizing the FBHC process for aluminum recovery. This study aims to systematically investigate the influence of key operational variables on the FBHC system's performance and to characterize the recovered $\text{Al}(\text{OH})_3$ crystals using advanced analytical techniques such as SEM, EDS, and XRD. The findings are expected to contribute to the development of efficient, resource-oriented strategies for aluminum recovery from industrial wastewater.

MATERIAL AND METHODS

Materials

All chemicals employed in this study were of analytical grade and utilized without additional purification. Deionized ultrapure water (resistivity $\geq 18 \text{ M}\Omega\cdot\text{cm}$) served as the solvent for preparing all experimental solutions. Aluminum sulfate octadecahydrate ($\text{Al}_2(\text{SO}_4)_3 \cdot 18\text{H}_2\text{O}$, PanReac Applichem) was selected as the aluminum source for synthetic wastewater preparation. Precipitation was induced using sodium hydroxide (NaOH , 99%, Fisher Chemical), while sulfuric acid (H_2SO_4 , 98%, Choneye Chemical) was applied for pH adjustment and to terminate crystallization reactions when necessary. Standard buffer solutions at pH 7 and pH 10 (Merck) were used for the calibration of the pH meter to ensure measurement accuracy.

Experimental setup

A laboratory-scale FBHC system was constructed using a 450 mL cylindrical Pyrex reactor. The vertical column reactor measured 120 cm in height and 2.5 cm in internal diameter. A reflux outlet was positioned at 100 cm from the base and located 5 cm below the effluent discharge point. As illustrated in Figure 1, three inlets at the bottom of the reactor were connected to a peristaltic pump (Masterflex L/S, Cole-Parmer Instrument Co.,

USA) to independently regulate the flow rates of synthetic wastewater, sodium hydroxide solution (precipitant), and the internal recycle stream. During the seed formation phase, a 5 mL/min flow of aluminum-containing synthetic wastewater was introduced to facilitate initial crystal nucleation. Simultaneously, a 5 mL/min flow of NaOH solution was added to achieve an $[\text{Al}]/[\text{OH}]$ molar ratio of 1.5:1 at the mixing zone. The recycle stream was maintained at 30 mL/min to ensure homogeneous fluidization. Once stable seed particles were established, the system was transitioned to a growth phase. This involved doubling the influent concentration and increasing the influent flow rate to 50 mL/min. To maintain a uniform up-flow velocity of 25 m/h and suppress excessive supersaturation, the recycle flow rate was increased to 100 mL/min. Effluent pH was controlled at 10.5 throughout both the nucleation and growth phases by adjusting the pH of the reactant tank. Sampling was conducted at the reflux point (5 cm below the effluent outlet) after 30 hydraulic retention time (HRT) cycles, corresponding to approximately 75 minutes (1 HRT = 3 minutes), once the system reached steady-state operation (G.C. Nguyen, and et al. 2025). Effluent samples were filtered through a $0.45 \mu\text{m}$ membrane to analyze the concentration of soluble aluminum.

To determine the total amount of phosphorus in both soluble and suspended particle forms, the other sample was not filtered. Two set of samples were acidified by 0.05 mL HNO_3 (70%). Total phosphorus removal could be determined using Eq. (1-2).

TR (%) : total removal of Al

$$= 1 - \frac{[\text{Al}]_s \times (\text{Q}_{\text{Al}} + \text{Q}_{\text{OH}})}{[\text{Al}]_{\text{in}} \times \text{Q}_{\text{Al}}} \times 100\% \quad (1)$$

CR (%) : crystallization ratio of Al

$$= 1 - \frac{[\text{Al}]_t \times (\text{Q}_{\text{Al}} + \text{Q}_{\text{OH}})}{[\text{Al}]_{\text{in}} \times \text{Q}_{\text{Al}}} \times 100\% \quad (2)$$



Figure 1. Experimental setup of the fluidized-bed reactor

Analytical methods

Prior to analysis, all liquid samples were filtered through a $0.45\ \mu\text{m}$ syringe membrane filter to remove suspended solids. The concentration of dissolved Al in the filtrate was quantified using inductively coupled plasma mass spectrometry (ICP-MS, ULTIMA 2000, HORIBA Ltd., Japan), ensuring high sensitivity and accuracy for trace metal detection. The surface morphology and microstructural features of the recovered precipitates were characterized by scanning electron microscopy (SEM, JEOL JSM-6700F, HITACHI, Japan). Crystallographic phases of the solid products were identified using X-ray diffraction (XRD, DX III, Rigaku Co., Japan). The XRD analysis was conducted over a 2θ range of 10° to 90° , with a step size of 0.02° and a scanning rate of $10^\circ/\text{min}$ to ensure high-resolution peak detection and accurate phase identification.

RESULTS AND DISCUSSION

Effect of pH

Figure 2 illustrates the influence of equilibrium pH (pH_e) on aluminum removal

performance in a FBHC reactor, evaluated by total removal efficiency (TR_s), reactor removal efficiency (TR_r), and crystallization ratio (CR). The experiments were conducted under controlled conditions: initial aluminum concentration ($\text{CAI}_{\text{in}} = 850\ \text{mg/L}$), hydraulic retention time (HRT) of 55 minutes, up-flow velocity (U) of 32 m/h, aluminum loading rate (LAL) of $0.7\ \text{kg/m}^2\cdot\text{h}$, and reflux ratio (R) of 40.2. The results show that both TR_s and TR_r remained consistently high ($>98\%$) across the entire pH range (8–11), indicating that aluminum was effectively removed from the system regardless of pH variation.

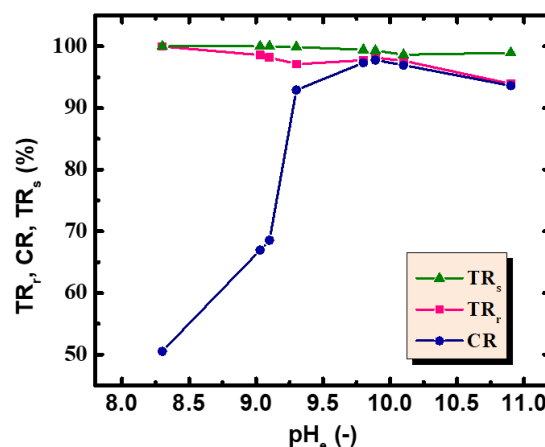


Figure 2. Effect of pH on the removal of aluminum in a FBHC reactor ($\text{CAI}_{\text{in}} = 850\ \text{mg/L}$, $\text{HRT} = 55\ \text{min}$, $U = 32\ \text{m/h}$, $\text{LAL} = 0.7\ \text{kg/m}^2\cdot\text{h}$, $R = 40.2$ as controlled variables).

In contrast, the CR exhibited a strong pH dependency. At $\text{pH} < 9$, CR was relatively low (below 70%), indicating that aluminum removal at lower pH was likely dominated by mechanisms other than crystallization, such as amorphous precipitation or adsorption. As pH_e increased from 9 to 9.5, CR rose sharply, reaching $>90\%$, and peaked around $\text{pH}\ 9.8\text{--}10$, corresponding to optimal conditions for $\text{Al}(\text{OH})_3$ crystallization. This trend can be attributed to enhanced supersaturation of $\text{Al}(\text{OH})_3$ under alkaline conditions, which favors the nucleation and growth of well-defined crystalline particles. At higher pH levels (>10), a slight decline in CR was observed, likely due to excessive hydroxide ion concentration leading to colloidal particle

formation or over-saturation, which may hinder controlled crystal growth. These findings suggest that pH T.D.H. Vo, and et al. 2020) a critical role in directing the precipitation pathway, and that an optimal pH range of 9.5–10 is most favorable for maximizing aluminum crystallization efficiency in the FBHC system.

Effect of cross-sectional loading

Figure 3 illustrates the effect of aluminum cross-sectional loading (LAI) on the removal and crystallization performance in a FBHC reactor. As LAI increased from 0.4 to 1.8 kg/m²·h, both TR_s and TR_r remained relatively high and stable, ranging from 96% to 99%, demonstrating the FBHC system's robustness in aluminum removal across a wide loading range. However, the CR exhibited a slight decreasing trend with increasing LAI, particularly beyond 1.0 kg/m²·h. This decline in CR suggests that at higher loading rates, the system may experience supersaturation imbalance or insufficient residence time for complete crystal growth, leading to partial precipitation or amorphous Al(OH)₃ formation. Furthermore, both residual aluminum concentrations (CAI_r and CAI_s) increased with rising LAI, especially at values above 1.2 kg/m²·h, indicating that system capacity begins to be exceeded under high loading conditions.

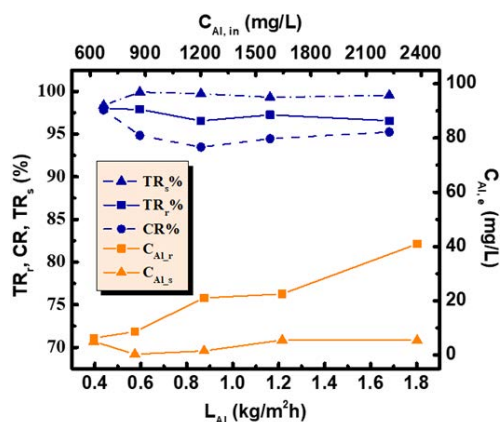


Figure 3. Effect of cross-sectional loading on the removal of aluminum in a FBHC reactor (CAI_{in} = 850 mg/L, HRT = 55 min, pH 9.5, U = 32 m/h, R = 40.2 as controlled variables).

Overall, these findings suggest that while the FBHC reactor maintains high removal efficiency under various loading rates, optimal crystallization and effluent quality are achieved at LAI ≤ 1.0 kg/m²·h. Beyond this threshold, performance trade-offs emerge due to kinetic and hydraulic limitations that hinder complete crystal formation and retention. These insights are critical for the design and operation of FBHC systems in aluminum-laden wastewater treatment.

Effect of up-flow velocity

Figure 4 illustrates the effect of up-flow velocity (U) on the aluminum removal performance in a FBHC reactor, evaluated through total system removal efficiency, reactor removal efficiency, and overall crystallization ratio. The experiments were conducted under constant conditions: initial aluminum concentration of 800 mg/L, hydraulic retention time of 55 minutes, pH 9.6, and reflux ratio (R) of 40.2. As the up-flow velocity increased from 24 to 85 m/h, TR_s and TR_r remained relatively stable, both exceeding 95% across the entire range, indicating robust system-level aluminum removal regardless of flow dynamics. However, the CR exhibited a distinct bell-shaped trend, increasing with velocity up to an optimal point (~45 m/h), beyond which a noticeable decline was observed. The maximum CR (~96%) was achieved at U ≈ 45 m/h, suggesting that moderate fluidization enhances mixing, supersaturation control, and crystal-crystal collisions, which favor nucleation and growth of Al(OH)₃ precipitates. At higher velocities (>60 m/h), CR decreased sharply, likely due to excessive turbulence and particle washout, which disrupts crystal retention and limits growth time in the reaction zone.

These findings highlight that while overall aluminum removal remains efficient across a broad velocity range, crystallization efficiency is highly sensitive to hydrodynamic conditions. An optimal up-flow velocity of 40–50 m/h ensures a balance between sufficient fluidization and retention of precipitates, maximizing aluminum recovery in crystalline

form. This underscores the importance of flow rate optimization in FBHC systems designed for resource recovery from high-strength aluminum-containing wastewaters.

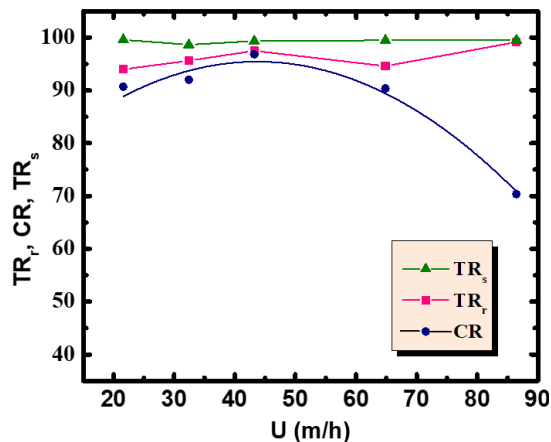


Figure 4. Effect of up-flow velocity on the removal of aluminum in a FBHC reactor ($CAI_{in} = 800$ mg/L, HRT = 55 min, pH 9.6, $U = 32$ m/h, $R = 40.2$ as controlled variables).

Effect of reflux ratio

Figure 5 illustrates the influence of reflux ratio (R) on the performance of aluminum removal in the FBHC reactor, evaluated through three key parameters: total removal efficiency in the system, removal efficiency in the reactor, and overall CR. The experiments were conducted under controlled conditions: initial aluminum concentration of 750 mg/L, HRT of 55 min, pH 9.6, U of 44 m/h, and LA_1 of 0.8 kg/m².h. As the reflux ratio increased from 20 to 45, the CR improved significantly, rising from approximately 91% to nearly 97%, indicating enhanced crystallization efficiency and better utilization of aluminum ions in the formation of $Al(OH)_3$ precipitates. This trend can be attributed to increased internal recycling of supersaturated solution, which enhances local supersaturation and promotes nucleation and crystal growth within the FBHC reactor. The TR_s values remained consistently high, above 98.5%, across all reflux ratios, confirming that the system maintained excellent aluminum removal efficiency regardless of R . Meanwhile, TR_r showed a moderate increasing trend, with a peak at $R =$

30, suggesting that an optimal reflux ratio exists to maximize removal efficiency directly within the reactor before overflow or recirculation occurs.

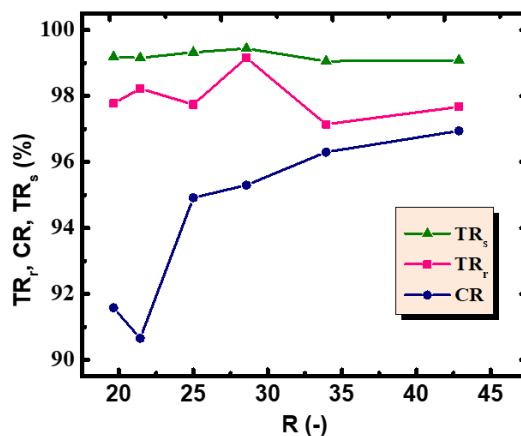


Figure 5. Effect of reflux ratio on the removal of aluminum in a FBHC reactor ($CAI_{in} = 750$ mg/L, HRT = 55 min, pH 9.6, $U = 44$ m/h, $LA_1 = 0.8$ kg/m².h).

These results demonstrate that optimizing the reflux ratio is crucial for enhancing the crystallization ratio without compromising total system performance. A reflux ratio in the range of 30–40 appears optimal, balancing effective crystal recovery, reactor performance, and operational stability. This highlights the importance of hydrodynamic control in FBHC systems for efficient aluminum recovery from wastewater streams.

Characterization of the crystal pellets products

Figure 6 illustrates the morphological and elemental characteristics of aluminum-based crystal pellets recovered from the FBHC process. The SEM image at low magnification ($\times 90$) in panel (Figure 6a) shows that the precipitated particles possess a well-defined spherical morphology with an average diameter close to 985 μ m, suggesting effective agglomeration and uniform growth under fluidized conditions. The surface appears dense and compact, indicating a high degree of crystallinity. In contrast, the higher magnification SEM image ($\times 200$) in panel

(Figure 6b) reveals a more detailed internal structure, characterized by a porous and layered texture, which may be associated with nucleation–aggregation mechanisms occurring during precipitation and particle growth.

The corresponding EDS analysis in panel (Figure 6c) confirms the elemental composition of the recovered crystals, with oxygen (67.17 wt%) and aluminum (32.83 wt%) being the major constituents. The atomic ratio closely matches the stoichiometry of aluminum hydroxide $[\text{Al}(\text{OH})_3]$, supporting the results obtained from XRD analysis. The absence of other significant elements also indicates high product purity. Panel (Figure 6d) shows a macroscopic view of the recovered FBHC product, displaying uniformly sized pellets accumulated at the base of the reactor, further confirming the process's capability for producing structurally consistent and recoverable aluminum precipitates. Overall, the SEM–EDS results demonstrate that the FBHC reactor effectively facilitates the formation of high-purity, spherical $\text{Al}(\text{OH})_3$ pellets with desirable physical characteristics for potential reuse or safe disposal.

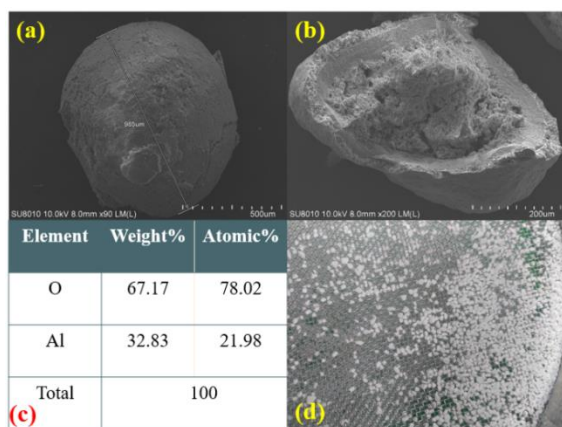


Figure 6. Morphology of crystal pellets products analyzed by SEM with magnification of (a) $\times 90$, (b) $\times 200$, (c) EDS spectra, and (d) FBHC product obtained from the FBHC process.

Figure 7 presents the X-ray diffraction (XRD) patterns of aluminum hydroxide $[\text{Al}(\text{OH})_3]$ precipitates recovered from the FBHC process under various operational conditions. The diffraction peaks observed in

all samples correspond closely to the standard reference patterns of crystalline $\text{Al}(\text{OH})_3$, confirming the successful formation of aluminum hydroxide as the predominant phase. Characteristic peaks were identified at 2θ values near 18° , 21° , 39° , 51° , and 66° , which are consistent with the diffraction pattern of gibbsite, the most stable crystalline form of $\text{Al}(\text{OH})_3$ (H. Li, J. and et al. 2005). The sharpness and intensity of these peaks in the lower layers (black and green spectra) indicate higher crystallinity compared to the upper spectra, where the peaks appear broader and less intense, suggesting reduced structural order or smaller crystallite size.

The absence of significant peaks corresponding to AlOOH (boehmite) (X. Yu, and et al. 2009), as shown by the lack of matching reflections with the blue reference lines, further supports the phase purity of the recovered $\text{Al}(\text{OH})_3$. This result implies that the FBHC process, when properly optimized, selectively favors the precipitation of $\text{Al}(\text{OH})_3$ over other aluminum-bearing phases. The increased crystallinity in specific samples may be attributed to optimized supersaturation control, residence time, or pH conditions during operation. Overall, the XRD results confirm that the FBHC reactor enables the recovery of Al in the form of crystalline $\text{Al}(\text{OH})_3$ with high phase purity and structural integrity, offering a promising pathway for resource recovery from aluminum-laden wastewater (X. Zhao, and et al. 2009).

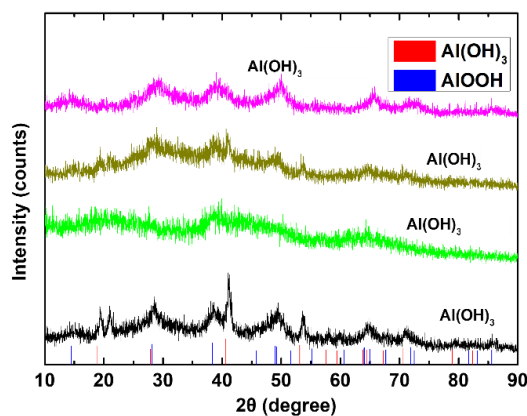


Figure 7. XRD patterns of $\text{Al}(\text{OH})_3$ crystals from FBHC process.

CONCLUSION

This study confirms the technical viability of fluidized bed homogeneous crystallization for aluminum recovery from wastewater under optimized operating conditions. The system consistently achieved high aluminum removal efficiency (>98%) across a range of reflux ratios, up-flow velocities, and aluminum loading rates. Notably, crystallization performance was maximized at pH 9.5–10 and surface loading rates below 1.0 kg/m².h. The recovered Al(OH)₃ solids exhibited uniform spherical morphology and high crystallinity, as verified by SEM, EDS, and XRD analyses. These results highlight the potential of the FBHC reactor as a scalable and effective solution for aluminum separation, with implications for advancing closed-loop treatment systems and resource-oriented wastewater management.

ACKNOWLEDGEMENTS

This work was financially supported by the research project QG.23.78 of Vietnam National University, Hanoi. We also thank the editors and anonymous reviewers for their helpful comments and suggestions.

REFERENCES

- D. Bhatt, A.W. Jasper, N.E. Schultz, J.I. Siepmann, D.G. Truhlar, Critical properties of aluminum, *Journal of the American Chemical Society*, 128 (2006) 4224-4225.
- T.D.H. Vo, B.S. Nguyen, C.T. Vu, Y.J. Shih, Y.H. Huang, Recovery of iron (II) and aluminum (III) from acid mine drainage by sequential selective precipitation and fluidized bed homogeneous crystallization (FBHC), *Journal of the Taiwan Institute of Chemical Engineers*, 115 (2020) 135-143.
- M.T. Truong, G.C. Nguyen, V.G. Le, X.T. Bui, T.A. Luu, Selective recovery of iron and aluminum from red mud wastewater using fluidized bed homogeneous crystallization, *Sustainable Chemistry One World*, 7 (2025) 100087.
- V.G. Le, T.A. Luu, H.T. Tran, N.T. Bui, M. Mofijur, M.K. Nguyen, X.T. Bui, M. Bahari, H.N.P. Vo, C.T. Vu, Recovery of lithium from industrial Li-containing wastewater using fluidized-bed homogeneous granulation technology, *Minerals*, 14 (2024) 603.
- K.-Y. Chang, N.N.N. Mahasti, Y.-H. Huang, Fluidized-bed homogeneous crystallization of α -Al(OH)₃ for continuous aluminum removal from aqueous solution: Parameter optimization and crystallization mechanism, *Journal of Water Process Engineering*, 53 (2023) 103700.
- W.-Z. Li, N.N. Mahasti, K.-Y. Chang, Y.-H. Huang, Application of Fe₀. 66Cu₀. 33@ Al (OH) ₃ catalyst from fluidized-bed crystallizer by-product for RB5 azo dye treatment using visible light-assisted photo-Fenton technology, *Chemosphere*, 343 (2023) 140268.
- G.C. Nguyen, M.T. Truong, X.T. Bui, Recovery of high-quality struvite fertilizer product from swine wastewater using fluidized bed homogeneous crystallization, *RSC advances*, 15 (2025) 24122-24136.
- H. Li, J. Addai-Mensah, J.C. Thomas, A.R. Gerson, The crystallization mechanism of Al (OH) ₃ from sodium aluminate solutions, *Journal of Crystal Growth*, 279 (2005) 508-520.
- X. Yu, J. Yu, B. Cheng, M. Jaroniec, Synthesis of hierarchical flower-like AlOOH and TiO₂/AlOOH superstructures and their enhanced photocatalytic properties, *The Journal of Physical Chemistry C*, 113 (2009) 17527-17535.
- X. Zhao, J. Wang, F. Wu, T. Wang, Y. Cai, Y. Shi, G. Jiang, Removal of fluoride from aqueous media by Fe₃O₄@ Al (OH) ₃ magnetic nanoparticles, *Journal of Hazardous Materials*, 173 (2010) 102-109.

Upcycling Electronic Waste into Heterogeneous Fenton-like Catalysts for Dye Decolorization

Hai Nguyen Tran^{1,2,*}, Dong Thanh Nguyen³

¹Center for Energy and Environmental Materials, Institute of Fundamental and Applied Sciences, Duy Tan University, Ho Chi Minh City, Viet Nam

²Faculty of Environmental and Chemical Engineering, Duy Tan University, Da Nang City, Viet Nam

³Institute of Science and Technology for Energy and Environment, Vietnam Academy of Science and Technology, Hanoi City, Viet Nam

*Email: trannguyenhai2512@gmail.com/trannguyenhai@duytan.edu.vn

Abstract: This study aimed to recover and upcycle a target metal from e-wastes into value-added materials for sustainable water treatment. A transition metal oxide (cuprous oxide; Cu_2O) was synthesized using a copper precursor derived from printed circuit board wastes. Optimal leaching conditions for copper recovery were identified as 3 M HNO_3 for 5 h, yielding approximately 90% recovery. Cu_2O catalysts were prepared from both commercial copper nitrate (Sigma-Aldrich) and the recovered copper source via a reduction process using formic acid as the reducing agent, without the use of surfactants. Both commercial and recovered Cu_2O catalysts demonstrated excellent degradation results of methylene blue (MB) dye (~99%) under catalytic wet peroxide oxidation (using H_2O_2 at pH 7.0) after 120 min. The effect of operational parameters on MB dye removal using the recovered Cu_2O catalyst was systematically investigated at pH 7.0. These parameters included different H_2O_2 volumes (0, 5, 10, 15, and 20 mL), catalyst dosages (solid/liquid ratios of 0.3, 0.5, 0.7, and 1.0 g/L), and initial dye concentrations (25, 50, 75, 100, 125, and 150 mg/L). Under optimal conditions (50 mg/L dye concentration, 1.0 g/L catalyst dose, pH 7.0, 60 min, and room temperature), the dye removal efficiency reached 99.7%, with an observed rate constant (k_{obs}) of 0.1041/min. Recycling experiments revealed that the catalyst retained over 40% efficiency at 60 min and 98% at 200 min after eight reuse cycles. These findings suggest that the Fenton-like catalytic material derived from the recovered copper

precursor is a promising heterogeneous Fenton-like catalyst for the effective decolorization of methylene blue dye in aqueous solutions in the presence of H_2O_2 .

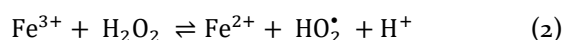
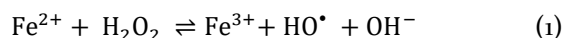
Keywords: Advanced oxidation process; Cuprous oxide; Circular economy; Catalytic wet peroxide oxidation; Water treatment; Waste management.

INTRODUCTION

The direct discharge of untreated effluents from textile manufacturing into aquatic environments poses significant ecological risks [1, 2]. Among the available methods for removing organic pollutants, advanced oxidation processes (AOPs) have gained widespread application due to their ability to generate highly reactive radicals, such as hydroxyl ($\cdot\text{OH}$) and superoxide ($\cdot\text{O}_2$) radicals [3, 4]. These radicals effectively oxidize organic contaminants, including dyes, breaking them down into benign end-products [5, 6] such as CO_2 [7], H_2O [7], and mineral acids [3].

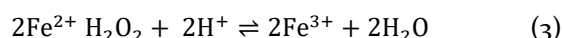
In 1894, Fenton [8] investigated the oxidation of tartaric acid in the presence of iron and hydrogen peroxide (H_2O_2), a process now recognized as the classical Fenton reaction (a homogeneous catalytic system) [6, 9]. This reaction involves the combination of ferrous (Fe^{2+}) ions (typically introduced as $\text{FeSO}_4 \cdot 7\text{H}_2\text{O}$) and H_2O_2 (as the oxidant), resulting in the generation of highly reactive $\cdot\text{OH}$ radicals [2, 3, 5, 9, 10]. The fundamental reactions governing iron-based Fenton catalysis

are illustrated in Equations 1–2 [6, 11]. The activation of H_2O_2 by Fe^{2+} (Equation 1) proceeds rapidly, with a second-order rate constant (k_2) in the range of 63–76 $[1/(\text{M}\times\text{s})]$ [6, 12]. In contrast, the reaction between ferric ions (Fe^{3+}) and H_2O_2 (Equation 2) is significantly slower, with a k_2 value ranging from 0.001 to 0.01 $[1/(\text{M}\times\text{s})]$ [6].



Although the homogeneous Fenton reaction is a highly effective catalytic method for oxidizing organic contaminants, it presents several limitations. One major drawback is the generation of iron-rich sludge, which contributes to secondary pollution. Additionally, the reaction performs optimally only under acidic to mildly alkaline conditions [3, 5, 7].

In 1974, Walling [13] revisited the Fenton reaction, as represented in Equation 3. This equation highlights the necessity of protons (H^+) on the reactant side, indicating that acidic conditions are essential for maximizing the production of $^\bullet\text{OH}$ radicals.



Equation 3 is obtained when combining the half-reactions (Figure 1) of oxidation (Fe^{2+} is oxidized to Fe^{3+} by losing an electron) and reduction (H_2O_2 is reduced to water).

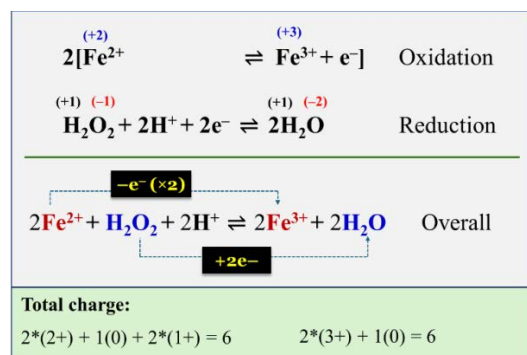


Figure 1. Oxidation and reduction reactions occurring between Fe^{2+} ions and H_2O_2 in aqueous solution

Another challenge is the limited regeneration capacity of Fe^{2+} ions, which complicates their separation and recyclability [2]. Furthermore, the presence of competing anions (i.e., carbonate and chloride) can act as radical scavengers, thereby diminishing the efficiency of the reaction [5]. Under near-neutral pH conditions, Fe^{3+} ions produced via Equations 1–2 tend to precipitate as ferric hydroxides [5] or insoluble ferric hydroxide precipitates [6] that reduces the generation of $^\bullet\text{OH}$ radicals.

To address the limitations of the homogeneous Fenton process, Fenton-like systems employing solid catalysts and H_2O_2 have been proposed. These systems are commonly referred to as catalytic wet peroxide oxidation or heterogeneous Fenton-like processes. In such systems, the choice of catalyst is a critical factor influencing performance. Bokare and Choi [6] identified a range of non-ferrous Fenton-type catalysts, including aluminum, manganese, cerium, copper, ruthenium, chromium, and cobalt. In the present study, copper (Cu) is utilized as the active component in a Cu-based Fenton system. Similar to Fe, copper exhibits multiple oxidation states (Cu^{2+} , Cu^+ , and Cu^0), which facilitate redox cycling and enhance its catalytic activity in Fenton-like reactions. Previous research has demonstrated that copper possesses higher solubility and more favorable redox properties compared to iron, making it a promising alternative for catalytic applications [3, 12].

Cuprous oxide (Cu_2O) and copper oxide (CuO) are *p*-type semiconductors with band gaps of 1.7 eV and 2.1 eV, respectively, enabling them to absorb visible light and function as photocatalysts for the degradation of organic pollutants in water [14]. Cu_2O has been widely reported as both a photocatalytic semiconductor and a Fenton-like transition metal oxide [7, 10]. Rahman and colleagues [15] employed a Cu_2O -Cu/C catalyst for the Fenton-like degradation of dyes (i.e., methyl orange, methylene blue, and rhodamine B) in aqueous environments. Their findings

indicated that $\cdot\text{OH}$ radicals, generated through Fenton-like reactions between cuprous (Cu^+) species and H_2O_2 , played a dominant role in dye discoloration. Similarly, Cu_2O -Cu and commercial zero-valent copper have demonstrated excellent catalytic performance in removing methylene blue (MB) dye via heterogeneous Fenton-like reactions [4, 10]. Guo and co-workers [7] synthesized a $\text{Cu}_2\text{O}/\text{Pt}$ composite and applied it for MB dye elimination through combined Fenton-like and photo-oxidation processes. Sun and colleagues [3] developed a Cu_2O -Cu/C composite that exhibited strong Fenton-like catalytic activity for degrading various dyes (i.e., methyl orange, MB, and rhodamine B). Furthermore, commercial Cu_2O has proven effective in degrading bisphenol A under wet oxidation conditions using H_2O_2 [16]. Similarly, CuO nanoparticles have shown high efficiency in degrading MB dye through catalytic wet peroxide oxidation [17].

A substantial volume of e-waste, particularly waste printed circuit boards (WPCBs), is released into the environment, posing a significant global challenge. Faraji and colleagues [18] reported that the global generation of e-waste has reached 53.6 million metric tons per year, with projections indicating a potential doubling by 2050. WPCBs constitute approximately 3–6 wt% of total e-waste [1, 19]. According to the document [15], only approximately 20% of e-waste is legally recycled, while the majority is disposed of in landfills, leading to contamination of water, groundwater, and soil. Notably, the chemical composition of WPCBs includes a high copper content, ranging from 34.26 to 39.20 wt.% [18, 19].

Several researchers have explored the recovery and upcycling of WPCBs into value-added materials (i.e., transition metal oxides), aligning with the principles of the circular economy by closing material loops. For instance, the authors [1] synthesized copper oxide (CuO) nanoparticles from copper-rich leachate derived from WPCBs and applied them as photocatalysts for the degradation of

Congo red dye in aqueous solution. The synthesized CuO exhibited a band gap of 1.97 eV, comparable to that of bulk CuO (1.8 eV). Zhong and colleagues [19] upcycled copper from WPCBs to fabricate a composite material consisting of magnetic CuFe_2O_4 nanoparticles supported on a mesoporous carbon framework. This composite demonstrated excellent catalytic performance in degrading brilliant blue dye via AOPs based on peroxymonosulfate (PMS) [19]. Similarly, Rahman and Aziz [15] developed Fenton-like catalysts from scrap printed circuit boards for the mineralization of pharmaceutical contaminants such as diclofenac and ibuprofen in water. Therefore, AOPs based on Fenton-like reactions are selected as the primary treatment strategy for degrading organic pollutants.

In this study, copper ions were recovered from waste printed circuit boards (WPCBs) using an acid leaching method. Both the recovered copper and a commercial copper precursor were employed to synthesize cuprous oxide (Cu_2O) catalysts via a reduction process using formic acid and ammonia. The synthesized catalysts were then applied to remove the MB dye from aqueous solutions through catalytic wet peroxide oxidation. Batch experiments were conducted under varying operational conditions, including gradients of H_2O_2 concentration, catalyst dosage, and initial dye concentration. The reusability of the catalysts was assessed through multiple consecutive dye removal cycles to evaluate their stability and performance over time.

MATERIALS AND METHODS

Waste printed circuit boards were collected and subjected to a series of preparatory steps. Initially, the boards were dismantled, ground, and sieved using a 35-mesh screen (0.5 mm sieve size). Magnetic components were then separated using a magnet. The resulting material was thoroughly washed with double-distilled water and subsequently dried at 105°C for 24 h.

Leaching test and copper recovery

Various acid solutions (HCl, HNO₃, and H₂SO₄) were evaluated for their effectiveness in leaching copper from electronic waste. A 0.5 g sample of purified copper waste was introduced into 1 L of each acid solution or double-distilled water (adjusted to pH 1.0). The mixtures were agitated for 6 h. Copper concentrations in the resulting filtrates were measured using atomic absorption spectroscopy.

Preliminary results showed that copper recovery after 6 h using 3 M HNO₃, HCl, and H₂SO₄ was 89.97%, 18.08%, and 7.89%, respectively. In contrast, leaching with water at pH 1.0 yielded a negligible recovery of approximately 4.5%. These findings indicate that HNO₃ is the most effective leaching agent for copper extraction from electronic waste. Consequently, nitric acid was selected for subsequent experiments.

Figure 2 illustrates that increasing the concentration of HNO₃ from 0.5 M to 3 M significantly enhanced copper recovery, rising from 18.19% to 90.01% over a 12-hour leaching period. At higher HNO₃ concentrations, copper recovery reached equilibrium rapidly within approximately 60 min. However, the maximum recovery of around 90% was achieved after a 5-hour leaching. Other researchers [1] also reported a copper recovery rate of 97.58% using 3 M HNO₃ for leaching waste printed circuit boards.

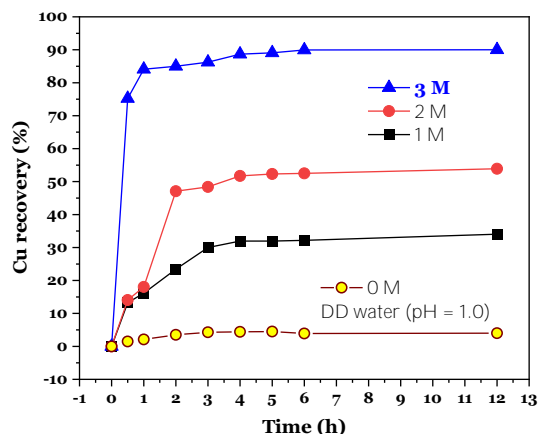
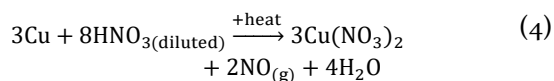


Figure 2. Effect of HNO₃ concentrations and leaching times on Cu recovery from WPCBs

Based on these results, the optimal leaching conditions were determined to be 3 M HNO₃ and a contact time of 5 h (Figure 2).

Preparation of Cu(NO₃)₂ from the recovered Cu resource

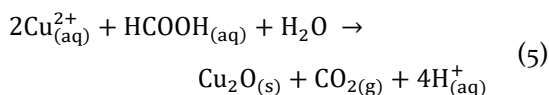
Following the leaching process, in which 0.5 g of purified copper waste was treated with 1 L of 3 M HNO₃, the resulting copper-rich leachate (referred to as the pregnant solution) was subjected to thermal evaporation.



The solution was then heated to 180°C until complete evaporation occurred, leading to the formation of Cu(NO₃)₂ crystals (Equation 4).

Preparation of the Cu₂O catalyst

Cuprous oxide (Cu₂O) was synthesized following the method described by previous researchers [14, 20]. The commercial Cu₂O catalyst was prepared using copper(II) nitrate trihydrate (Cu(NO₃)₂·3H₂O), obtained from Sigma-Aldrich, as the copper precursor. The reduction of the copper nitrate solution to form Cu₂O precipitates was carried out using formic acid (HCOOH) as the reducing agent. This reaction is represented in Equation 5 [20].



A 0.01 mol quantity of copper nitrate was dissolved in a mixed solvent of double-distilled water and ethanol, with a volume ratio of 20:80. To eliminate any unwanted residues, the solution was filtered. Subsequently, 2 mL of formic acid (serving as the reducing agent) was added to the filtrate. This was followed by the dropwise addition of either 1.5 or 3 mL of ammonia (NH₃) under continuous stirring. Zhao and colleagues [20] reported that the presence of ammonia in the formic acid solution influences the morphology of Cu₂O, promoting the formation of edge-cut cubic structures due to interactions between NH₃

and Cu^{2+} ions. Similar observations were noted elsewhere [14].

The resulting mixture was sonicated for 10 min and then transferred into a Teflon-lined hydrothermal autoclave. The autoclave was heated to 150°C for 2 h, followed by natural cooling to room temperature (30°C). The precipitates were collected, rinsed with ethanol, washed with double-distilled water, and dried at 60°C for 12 h.

Two commercial catalysts were synthesized and designated as “commercial-1.5- Cu_2O ” and “commercial-3.0- Cu_2O ,” corresponding to the volumes of ammonia used (1.5 mL and 3 mL, respectively). Using the same procedure, two additional (“recovered-1.5- Cu_2O ” and “recovered-3.0- Cu_2O ”) catalysts were synthesized, substituting the commercial copper nitrate with the recovered copper precursor obtained from WPCBs.

Catalytic wet peroxide oxidation of MB dye

The removal of the methylene blue MB dye using the synthesized catalysts was investigated through batch experiments in aqueous media. A specified amount of catalyst was added to a 150 mL Erlenmeyer flask containing 50 mL of dye solution at a predetermined concentration. Initially, dye removal was assessed via adsorption, without the addition of H_2O_2 . Once the adsorption equilibrium was reached, a measured volume of H_2O_2 was introduced to initiate the heterogeneous Fenton-like reaction. For comparison, wet peroxide oxidation was also conducted in the absence of the catalyst to evaluate the role of catalytic activity. The concentration of MB dye in solution was monitored using a UV-visible spectrophotometer at λ_{max} of 664 nm.

The amount of MB dye adsorbed by the catalyst (q_t) at any given time t (min) was calculated using Equation 6. The disappearance of color during the discoloration of MB dye was evaluated through its removal efficiency at any time by the catalyst, the Erlenmeyer flask, wet oxidation with H_2O_2 , and others (Equation 7).

$$q_t = \frac{C_o - C_t}{m} V \quad (6)$$

$$\% \text{removal} = \frac{C_o - C_t}{C_o} \times 100 \quad (7)$$

where C_o and C_t (mg/L) are the concentration of MB dye at the beginning and at any time t (min); m (g) is the mass of the catalyst used; V (L) is the volume of dye concentration used.

The dataset obtained from time-dependent experiments and the corresponding rate constants for dye discoloration were analyzed using the Langmuir–Hinshelwood kinetic model (Equation 8) [21]. This model is widely applied to describe the kinetics of heterogeneous catalytic and photocatalytic degradation of organic pollutants in aqueous systems [22].

$$r = -\frac{dC_t}{dt} = \frac{kKC_t}{1 + KC_t} = kKC_t \left(\frac{1}{1 + KC_t} \right) \quad (8)$$

where r [mg/(L × min)] is the reaction rate for the oxidation of dye; k [mg/(L × min)] is the catalytic rate constant; K (L/mg) is the equilibrium adsorption rate constant; and C_t (mg/L) is the dye concentration at any time t (min).

The bulk concentration of MB dye corresponds to its water solubility (i.e., 43,600 mg/L at 25°C). When dye concentration is very diluted (i.e., significantly lower than its water solubility) and C_t decreases with increasing reaction time, the term $1/(1 + KC_t)$ in the Langmuir–Hinshelwood model approaches unity due to $KC_t \ll 1$ [21, 22]. By defining the observed rate constant as k_{obs} (1/min), where $k_{\text{obs}} = k \times K$ with k in mg/(L × min) and K in L/mg, Equation 8 simplifies to Equation 9 or Equation 10.

$$-\frac{dC_t}{dt} = k_{\text{obs}} C_t \quad (9)$$

$$\frac{dC_t}{C_t} = -k_{\text{obs}} dt \quad (10)$$

By integrating both sides of Equation 10, Equation 11 is derived. The limits of integration are C_0 (the initial dye concentration) at the beginning to and C_t (the dye concentration at any time) at any t [23].

$$\int_{C_0}^{C_t} \frac{dC_t}{C_t} = - \int_{t_0}^t k_{\text{obs}} dt \quad (11)$$

Using an integral calculator, Equation 11 is transformed into Equation 12, and subsequently into Equation 13.

$$\ln C_t|_{C_0}^t = -(k_{\text{obs}} t)|_{t_0}^t \quad (12)$$

$$\ln C_t - \ln C_0 = -k_{\text{obs}}(t - t_0) \quad (13)$$

Given that $t_0 = 0$ at the start of the reaction and $t = t$ at any subsequent time, Equation 13 simplifies to Equation 14.

$$\ln C_t - \ln C_0 = -k_{\text{obs}} t \quad (14)$$

By rearranging Equation 14, the linear form of the first-order reaction kinetics was obtained as Equation 15 [21-23].

$$\ln \frac{C_t}{C_0} = -k_{\text{obs}} t \quad (15)$$

where k_{obs} (1/min) is the observed rate constant for MB dye decolorization.

Equation 15 has been widely applied to model the removal of various organic pollutants through different AOPs. These include photocatalytic degradation using CuO [1], wet oxidation using CuFe_2O_4 to activate peroxy-monosulfate [19], and several Fenton-based approaches [2] (i.e., conventional Fenton, helio-photo-Fenton, and photo-Fenton processes). It has also been employed in homogeneous Fenton-like reaction [15], heterogeneous Fenton-like catalysis using e-waste-derived material [15], CuO -based system [17], commercial Cu_2O [16], Cu_2O - Cu composite [4], and photocatalytic Fenton-like catalysts [7].

RESULTS AND DISCUSSION

Effect of ammonia concentrations on the dye removal efficiency of resultant catalysts

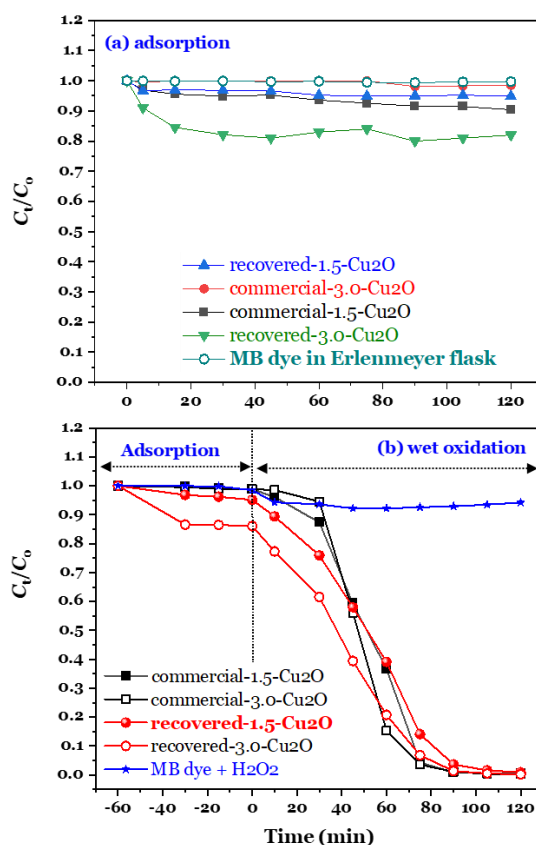


Figure 3. (a) Time-dependent dye adsorption ($C_0 \approx 30$ mg/L, $m/V = 1.0$ g/L, and $\text{pH} = 7.0$) and (b) Catalytic wet oxidation ($C_0 \approx 50$ mg/L, $m/V = 1.0$ g/L, $\text{pH} = 7.0$, and $\text{H}_2\text{O}_2 = 10$ mL) of MB dye by the catalysts prepared

Figure 3a shows that the adsorption of MB dye ($C_0 = 51.2$ mg/L) by the four synthesized Cu_2O catalysts reached equilibrium within 30 min. The catalysts exhibited limited adsorption capacity, with removal efficiencies ranging from 1.9% to 20%, while the dye adsorption on the Erlenmeyer flask walls was negligible (0.6%).

Figure 3b presents the dye removal efficiency under wet peroxide oxidation

conditions. In the presence of H_2O_2 , MB dye degradation reached approximately 7.8%. This aligns with previous findings [17]. They [17] reported a 17% degradation of MB dye (2.5 mL of 30% H_2O_2 , $C_0 = 6.0 \times 10^{-5}$ M) over 3 h, attributed to the dye's chemical stability.

The introduction of Cu_2O catalysts significantly enhanced the degradation efficiency, achieving up to 99% removal after 120 min of wet oxidation. Both commercial and recovered Cu_2O catalysts demonstrated strong catalytic activity, indicating that copper recovered from WPCBs is a viable precursor for Cu_2O synthesis.

Although the overall dye removal percentages were comparable among the four catalysts, the observed rate constants (k_{obs} ; 1/min) varied notably. The values were 0.0595 for commercial-1.5- Cu_2O and 0.0647 for commercial-3.0- Cu_2O , compared to 0.0468 for recovered-1.5- Cu_2O and 0.0601 for recovered-3.0- Cu_2O . These results suggest that increasing the ammonia concentration from 1.5 mL to 3 mL during synthesis enhances the catalytic rate of wet oxidation oxidation of the resultant catalyst.

Considering both performance and economic efficiency, the recovered-1.5- Cu_2O catalyst was selected for subsequent experiments.

Maximum adsorption capacity of recovered-1.5- Cu_2O towards MB dye

The adsorption behaviour of recovered-1.5- Cu_2O towards MB dye is evaluated through the study of the adsorption isotherm. When the dye concentrations increased, the amount of dye adsorbed by the catalyst (q_e) increased (Figure 4). The saturation region was reached when C_0 exceeded 100 mg/L.

The Langmuir model was applied to model the experimental data of the adsorption equilibrium. The maximum adsorption capacity of the recovered-1.5- Cu_2O catalyst to dye, which was calculated based on the Langmuir model, was 17.5 mg/g. This means

that a 1-gram catalyst can adsorb 17.5 milligrams of MB dye.

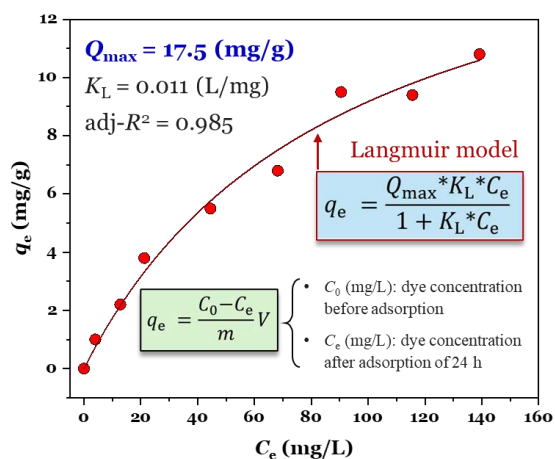


Figure 4. Adsorption isotherm of MB dye onto recovered-1.5- Cu_2O ($C_0 = 5$ –150 mg/L, 24 h, $m/V = 1.0$ g/L, and pH = 7.0)

Effect of operational conditions on catalytic wet peroxide oxidation of methylene blue dye using the recovered-1.5- Cu_2O catalyst

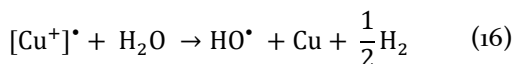
Effect of H_2O_2 volume

Figure 5 shows the influence of H_2O_2 volume on the degradation efficiency of MB dye. The concentration of H_2O_2 plays a critical role in (1) regulating the formation rate of $\cdot\text{OH}$ radicals responsible for oxidative degradation and (2) their potential scavenging effects [11].

In the presence of H_2O_2 , the recovered-1.5- Cu_2O catalyst significantly enhanced the removal efficiency of MB dye compared to the system without H_2O_2 ($\text{H}_2\text{O}_2 = 0$ mL), where only adsorption occurred.

In general, Cu_2O exhibits chains of linear $-\text{O}-\text{Cu}^{\text{I}}-\text{O}-$ bonds. When the $\text{Cu}^{\text{I}}-\text{O}$ bond within the Cu_2O catalyst is fractured or dissociated, Cu–Cu bonds may form on the catalyst surface, leading to the generation of paramagnetic $[\text{Cu}^{\cdot}]$ species [14]. These $[\text{Cu}^{\cdot}]$ -paramagnetic centers can subsequently react with water to produce $\cdot\text{OH}$ radicals and evolve hydrogen, as described by Equation 16,

originally proposed by Guo and co-workers [14].



However, the concentration of OH^\bullet radicals generated via this pathway is insufficient to achieve significant degradation of MB dye. Experimental results showed that the removal efficiency was only approximately 6%, indicating that H_2O_2 alone does not effectively generate OH^\bullet radicals under these conditions [4].

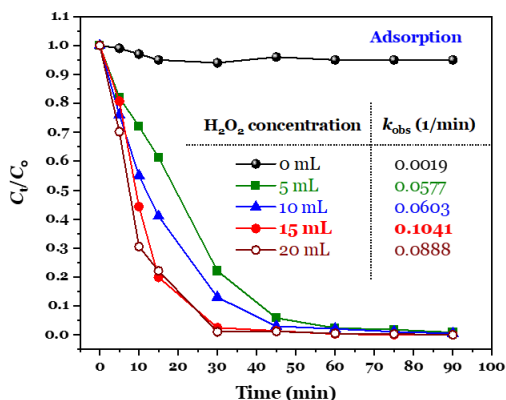
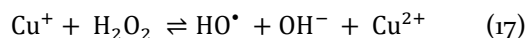
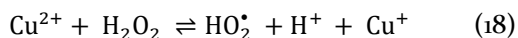


Figure 5. Effect of 30% H_2O_2 volumes on the removal efficiency of MB dye ($C_0 \approx 50$ mg/L, $m/V = 1.0$ g/L, and $\text{pH} = 7.0$)

In the Fenton-like heterogeneous catalysis process, the high degradation efficiency of MB dye is primarily attributed to the enhanced generation of highly reactive OH^\bullet radicals, as described by the classical Fenton-like reaction (Equation 17) [5, 7, 10]. This reaction proceeds rapidly, with $k_2 = 1.0 \times 10^4$ [1/(Mxs)], indicating its high reactivity [3, 12].



In contrast, the reaction between Cu^{2+} ions and H_2O_2 , represented by Equation 18 [5], occurs at a significantly slower rate, with $k_2 = 1.15 \times 10^{-6}$ [1/(Mxs)] [3]. This highlights the superior reactivity of Cu^+ over Cu^{2+} in activating H_2O_2 to generate OH^\bullet radicals.



The OH^\bullet radical, with an oxidation potential of 2.80 V [9], is capable of rapidly oxidizing and effectively degrading MB dye molecules (Equation 19) [4, 16]. When complete mineralization of the dye occurs, the final degradation products are CO_2 , H_2O , and potentially inorganic ions, as shown in Equation 20 [4, 22].

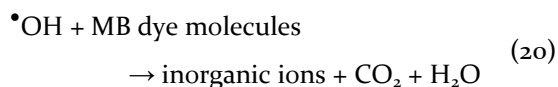
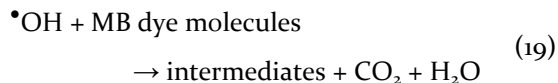
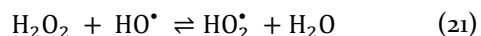


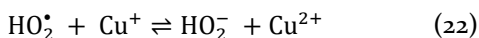
Figure 5 demonstrates that after a 90-minute contact, the dye removal efficiencies of the four samples (treated with 5, 10, 15, and 20 mL of H_2O_2) were nearly identical. Consequently, the observed rate constant (k_{obs}) was used as a more sensitive parameter for comparison. At a low H_2O_2 volume (5 mL), the value k_{obs} was the lowest (0.0577/min), attributed to the insufficient generation of OH^\bullet radicals. The optimal H_2O_2 volume for this process was found to be 15 mL, yielding the highest rate constant (0.1041/min).

However, further increasing the H_2O_2 volume (20 mL) beyond this point led to a decline in k_{obs} to 0.0888/min, likely due to undesirable scavenging reactions and partial catalyst deactivation [11]. H_2O_2 is known to act as a scavenger of OH^\bullet radicals, consuming them before they can effectively attack dye molecules (Equation 21) [2, 17]. This self-scavenging behavior diminishes the oxidative activity of the Cu_2O catalyst, thereby reducing its overall efficiency in dye degradation [17].

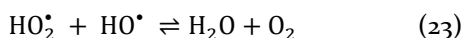


Another contributing factor to reduced dye degradation efficiency is the secondary reaction between H_2O_2 and OH^\bullet radicals, which generates hydroperoxyl radicals (HO_2^\bullet). These radicals possess lower oxidative potential compared to OH^\bullet , thereby diminishing the overall reactivity of the system [3, 4, 11]. The

HO_2^\cdot radicals can further interact with Cu^+ ions present in the recovered-1.5- Cu_2O catalyst, forming hydroperoxyl anions (HO_2^-), as described in Equation 22.



Additionally, some studies have reported that HO_2^\cdot radicals may react with $^\cdot\text{OH}$ radicals to produce H_2O and O_2 (Equation 23) [3, 4]. These side reactions contribute to the self-scavenging behavior of H_2O_2 , which ultimately reduces the concentration of active $^\cdot\text{OH}$ radicals available for dye degradation.



Based on experimental observations, the copper-catalyzed decomposition of H_2O_2 for discoloration achieved optimal performance at a feeding volume of 15 mL. Therefore, this volume was selected for subsequent experiments.

Effect of catalyst doses

The influence of catalyst dosage on the time-dependent removal efficiency of MB dye is provided in Figure 6. Increasing the amount of the heterogeneous recovered-1.5- Cu_2O catalyst (i.e., solid/liquid ratio) enhanced the activation of H_2O_2 via the catalytic role of copper transition metal centers. This activation is crucial for generating reactive oxygen species, particularly $^\cdot\text{OH}$ radicals, which drive the degradation process.

Hydrogen peroxide itself is a weak acid and a relatively mild oxidant, though it possesses a high redox potential ($E^\circ = 1.77\text{V}$) [4]. In the absence of a catalyst, H_2O_2 in the MB solution undergoes a homogeneous reaction that does not effectively produce $^\cdot\text{OH}$ radicals. Consequently, the removal efficiency of MB dye by H_2O_2 alone was low, approximately 7.8%.

As explained by the authors [4], the interaction between H_2O_2 and MB molecules in a homogeneous oxidation system proceeds primarily through direct electron transfer, as

represented by Equation 24. This mechanism lacks the radical-driven pathway necessary for efficient dye degradation, underscoring the importance of catalyst dosage in promoting heterogeneous Fenton-like reactions.

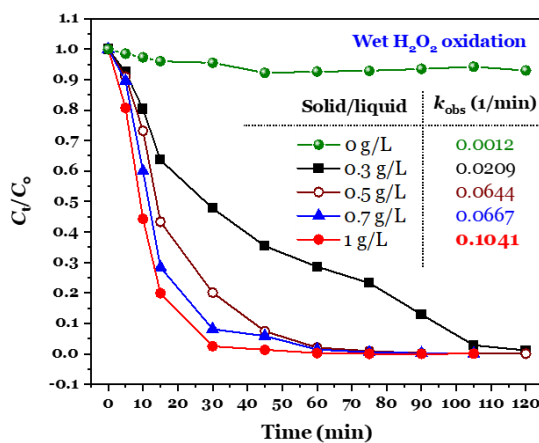
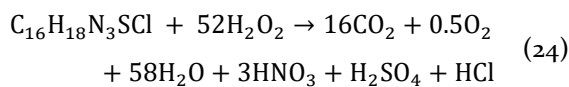
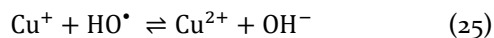


Figure 6. Effect of the catalyst doses on the removal efficiency of MB dye ($C_0 \approx 50$ mg/L, $\text{H}_2\text{O}_2 = 15$ mL, and $\text{pH} = 7.0$)

The presence of the recovered-1.5- Cu_2O catalyst enhanced the catalytic activity of copper in the heterogeneous Fenton-like reaction, as described by Equation 17 [4, 10]. Increasing the catalyst dosage from 0.3 g/L to 1.0 g/L significantly accelerated the degradation rate of MB dye, with k_{obs} rising from 0.0209/min to 0.1041/min.

After 30 min of reaction time, the corresponding removal efficiencies were 4.5%, 52.23%, 79.88%, 91.88%, and 97.50% for catalyst doses of 0 g/L, 0.3 g/L, 0.5 g/L, 0.7 g/L, and 1.0 g/L, respectively. This improvement is attributed to the increased availability of active sites and enhanced generation of $^\cdot\text{OH}$ radicals, which promote Fenton-like oxidation.



Importantly, no evidence of $^\cdot\text{OH}$ radical scavenging by excess Cu^+ ions (Equation 25)

[16] or catalyst aggregation during the reaction [3] was observed. These findings suggest that the optimal catalyst dose for effective discoloration of MB dye is 1.0 g/L.

Effect of dye concentrations

The profile of time-dependent dye degradation at different initial dye concentrations (C_0) is illustrated in Figure 7.

At a 30-minute contact time, the removal efficiencies for dye concentrations of 25, 50, 75, 100, 125, and 150 mg/L were 98.8%, 97.5%, 79.60%, 83.22%, 68.21%, and 52.02%, respectively. These results indicate that higher initial dye concentrations lead to reduced degradation efficiency and slower reaction rates. This decline is primarily attributed to diminished light penetration and increased dye adsorption onto the catalyst surface, which can hinder the generation and activity of reactive species [22].

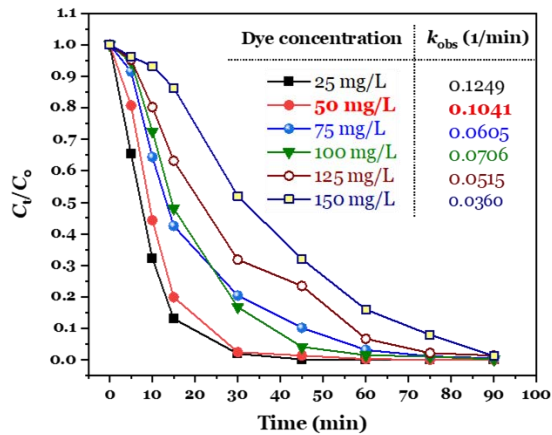


Figure 7. Effect of the MB dye concentrations on the removal efficiency of MB dye ($H_2O_2 = 15$ mL, $m/V = 1.0$ g/L, and $pH = 7.0$)

Despite these initial differences, extended reaction time (90 min) resulted in high removal efficiencies across all concentrations, approaching 99%. However, the observed rate constant k_{obs} decreased with increasing C_0 , from 0.1249/min at 25 mg/L to 0.0360/min at 150 mg/L. This trend confirms that the degradation rate of MB dye diminishes as the initial concentration increases, likely due to

saturation effects and reduced availability of active sites on the catalyst.

Reusability of the recovered-1.5- Cu_2O after catalytic wet peroxide oxidation

The recyclability of the recovered-1.5- Cu_2O catalyst was evaluated over multiple consecutive degradation cycles, as shown in Figure 8. After 200 min, the total dye removal remained nearly constant across all cycles, indicating sustained catalytic activity. However, notable differences were observed at the 60-minute mark, where the removal efficiency progressively declined with each reuse cycle. The removal percentages after 60 min were 97.9%, 93.2%, 87.5%, 83.8%, 72.0%, 65.5%, 58.8%, and 40.3% for cycles 1st through 8th, respectively.

A similar trend was reported elsewhere [17] in the wet oxidation of MB dye using H_2O_2 and CuO . The observed decline in performance suggests gradual catalyst deactivation, yet the overall stability remains promising. The results imply that (1) copper leaching from the recovered-1.5- Cu_2O catalyst after eight cycles is likely negligible and (2) the catalyst demonstrates excellent chemical stability, maintaining high degradation efficiency over repeated use [7, 15].

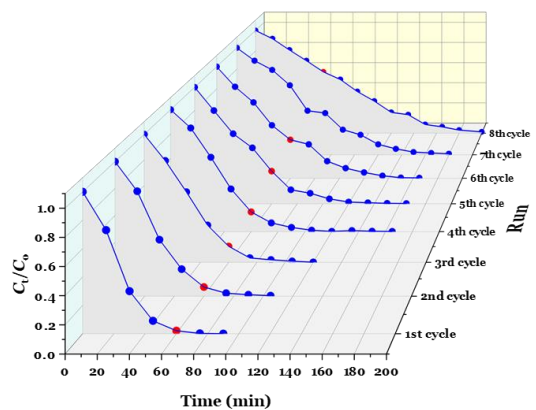


Figure 8. Recycle number of the used catalyst for catalytic wet peroxide oxidation of MB dye ($H_2O_2 = 15$ mL, $m/V = 1.0$ g/L, and $pH = 7.0$)

These findings support the potential of recovered Cu_2O as a cost-effective and durable catalyst for wastewater treatment applications.

Evaluation of synergy effect

To assess the effectiveness of catalytic wet peroxide oxidation in degrading MB dye, the synergy factor (SF) was calculated using Equation 26, as proposed by Fedorov and co-workers [9].

$$\text{SF} = \frac{\text{System 1}}{\text{System 2} + \text{System 3} + \text{System 4}} \quad (26)$$

This parameter quantifies the enhancement in degradation performance resulting from the combined action of the recovered-1.5- Cu_2O catalyst and H_2O_2 , compared to their individual contributions. A synergy factor greater than 1 indicates a positive synergistic effect, confirming that the integrated system performs better than the sum of its parts.

To quantify the enhancement in dye removal efficiency, the synergy factor (SF) was calculated based on the performance of four distinct systems. In System 1, the recovered-1.5- Cu_2O catalyst combined with H_2O_2 achieved a removal efficiency of 99.9% (Figure 5). In contrast, System 2 (wet oxidation using H_2O_2 alone) yielded only 7.8% removal. System 3 (involving adsorption by the catalyst without H_2O_2) showed a poor removal capacity of 5%, while System 4 (representing dye adsorption on the Erlenmeyer flask wall) was negligible at 0.6% (Figure 3a).

Using these values, the calculated SF was 7.4, which is significantly greater than 1. This result confirms a strong synergistic effect between the recovered-1.5- Cu_2O catalyst and H_2O_2 , indicating that their combined action substantially enhances the degradation of methylene blue in aqueous solution.

Possible removal mechanisms

As previously discussed, H_2O_2 was activated by the recovered-1.5- Cu_2O catalyst to generate highly reactive $\cdot\text{OH}$ radicals, which

play a pivotal role in the oxidative degradation of MB dye in aqueous media. The proposed catalytic wet peroxide oxidation mechanism is illustrated in Figure 9 and is based on established pathways reported in the literature [3, 7, 10, 16].

This mechanism involves several key steps: (1) activation of H_2O_2 by $\text{Cu}^+/\text{Cu}^{2+}$ species on the catalyst surface to produce $\cdot\text{OH}$ radicals via Fenton-like reactions, (2) adsorption of MB dye onto the catalyst surface, facilitating proximity to reactive sites, and (3) oxidative degradation of MB dye molecules by $\cdot\text{OH}$ radicals, leading to decolorization and potential mineralization.

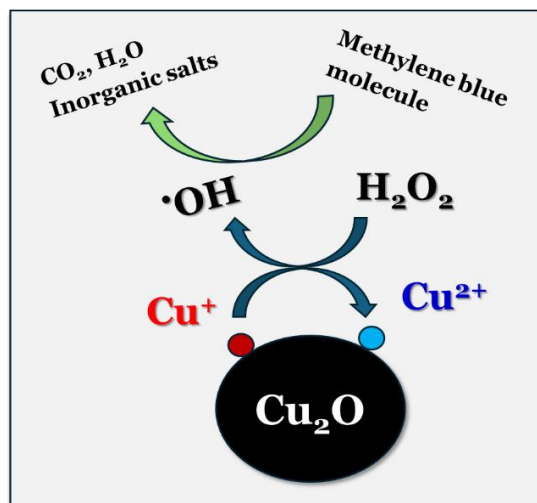


Figure 9. Possible oxidation mechanism of MB dye in the system of H_2O_2 and recovered-1.5- Cu_2O

The synergy between adsorption and catalytic oxidation ensures rapid and effective dye removal, confirming the suitability of recovered-1.5- Cu_2O as a heterogeneous catalyst for advanced oxidation processes.

CONCLUSIONS

Cuprous oxide (Cu_2O) was successfully synthesized using both commercial and recovered $\text{Cu}(\text{NO}_3)_2$ precursors, with formic acid serving as the reducing agent. The resulting Cu_2O materials were employed as heterogeneous catalysts for the degradation of

cationic methylene blue dye in the presence of H_2O_2 . Adsorption alone contributed minimally to dye removal (5%) by the catalyst and 0.6% by the Erlenmeyer flask, while H_2O_2 alone achieved only 7.8% removal. In contrast, the combined $\text{Cu}_2\text{O}/\text{H}_2\text{O}_2$ system achieved a remarkable 99.9% removal efficiency, demonstrating a strong synergistic effect with a synergy factor (SF) of 7.4.

Under optimal conditions (MB concentration of 50 mg/L, catalyst dose of 1.0 g/L, pH 7.0, contact time of 60 min, room temperature), the system achieved a removal efficiency of 99.7% and an observed rate constant (k_{obs}) of 0.1041/min. The catalyst also exhibited excellent reusability and chemical stability. After eight consecutive degradation cycles, the removal efficiency remained high (approximately 40% at 60 min and 98% at 200 min).

The activation of H_2O_2 by Cu_2O synthesized from e-waste presents a cost-effective and environmentally sustainable strategy for treating dye-contaminated wastewater. This approach aligns with circular economy principles by valorizing electronic waste into functional catalytic materials.

LIMITATIONS AND SUGGESTIONS

This study has several limitations that warrant further investigation, including catalyst characteristics, operational conditions, removal mechanisms, potential applications, and appropriate waste management strategies.

The catalyst properties that should be examined in greater detail include surface morphology, functional groups, the chemical state of copper, textural properties, crystal structure, zeta potential, thermal stability, and hydrophilicity.

Additional experiments should also evaluate operational conditions such as pH, NaCl concentration, temperature, and the coexistence of foreign organic and inorganic ions. A key question is whether the catalysts can consistently achieve high removal efficiency across a wide range of organic

contaminants, particularly emerging pollutants.

Further research is needed to elucidate the mechanisms of MB dye removal (adsorption, mineralization, and degradation) and to clarify the role of radicals ($\bullet\text{OH}$ and/or $\bullet\text{O}_2$) in degrading MB molecules.

When applying the prepared catalysts to real waste or wastewater treatment, several practical factors must be considered. These include cost estimation for catalyst production (VND/kg) and water treatment (VND/m³). Since the Cu_2O catalyst was synthesized from electronic waste, leaching tests for copper and other metals should be conducted after treatment to ensure that the treated water meets strict national standards.

Suitable waste management strategies (e.g., solidification and stabilization) should be employed for exhausted catalysts.

ACKNOWLEDGEMENTS

The authors declare that no funds, grants, or other financial support were received during the preparation of this manuscript. Language editing was conducted using Microsoft Copilot.

Dr. Hai Nguyen Tran serves as an editorial board member of two national journals: *Vietnam Journal of Science, Technology and Engineering – C* (Print ISSN: 2525-2461; Ministry of Science and Technology) & *Journal of Science and Technology Development* (ISSN: 1859-0128; Vietnam National University, Ho Chi Minh City). He was not involved in the review or editorial decision-making processes related to this submission.

References

- [1] Gautam, P., De, A.K., Sinha, I., Behera, C.K., Singh, K.K. (2023). Genesis of copper oxide nanoparticles from waste printed circuit boards and evaluation of their photocatalytic activity, *Environmental Research* 229, 115951.
- [2] Khelassi-Sefaoui, A., Keniche, A., Khechekhouche, A., Fellah, M., Obrosof, A., El-Hiti, G.A., Djeziri, S. (2025). Advances in dye degradation in industrial textile effluent: Unveiling the potential of Fenton, photo-Fenton, and helio-photo-Fenton processes for

- environmental conservation, *Arabian Journal of Chemistry* 18, 1182025.
- [3] Sun, B., Li, H., Li, X., Liu, X., Zhang, C., Xu, H., Zhao, X.S. (2018). Degradation of Organic Dyes over Fenton-Like Cu_2O -Cu/C Catalysts, *Industrial & Engineering Chemistry Research* 57(42), 14011-14021.
- [4] Hamidani, M., Djerad, S., Tifouti, L. (2021). Reactivity of Cu_2O -Cu in the Discoloration of Methylene Blue via a Heterogeneous Fenton-Like Process, *Iranian Journal of Chemistry and Chemical Engineering* 40(5), 1502-1511.
- [5] Orts, X., Arévalo, J., Arques, A., Amat, A.M., Santos-Juanes, L. (2025). Performance of Copper as a Catalyst for Fenton-like Processes in Highly Saline Solutions, *Molecules* 30(11), 2298.
- [6] Bokare, A.D., Choi, W. (2014). Review of iron-free Fenton-like systems for activating H_2O_2 in advanced oxidation processes, *Journal of Hazardous Materials* 275, 121-135.
- [7] Guo, P., Li, E., Zhang, Q., Yan, X., Li, J. (2025). Hexagonal Cu_2O /Pt for photothermal and photo-Fenton synergistic degradation of dye contaminant, *Solid State Sciences* 167, 107995.
- [8] Fenton, H.J.H. (1894). LXXIII.—Oxidation of tartaric acid in presence of iron, *Journal of the Chemical Society, Transactions* 65(0), 899-910.
- [9] Fedorov, K., Dinesh, K., Sun, X., Darvishi Cheshmeh Soltani, R., Wang, Z., Sonawane, S., Boczkaj, G. (2022). Synergistic effects of hybrid advanced oxidation processes (AOPs) based on hydrodynamic cavitation phenomenon – A review, *Chemical Engineering Journal* 432, 134191.
- [10] Hamidani, M., Djerad, S., Tifouti, L., Boulkra, M. (2020). Highly active copper in dye discoloration via a heterogeneous Fenton-like process, *Journal of the Iranian Chemical Society* 17(5), 1201-1209.
- [11] Giwa, A.A., Bello, I.A., Olabintan, A.B., Bello, O.S., Saleh, T.A. (2020). Kinetic and thermodynamic studies of Fenton oxidative decolorization of methylene blue, *Heliyon* 6(8), e04454.
- [12] Salazar, R., Brillas, E., Sirés, I. (2012). Finding the best $\text{Fe}^{2+}/\text{Cu}^{2+}$ combination for the solar photoelectro-Fenton treatment of simulated wastewater containing the industrial textile dye Disperse Blue 3, *Applied Catalysis B: Environmental* 115-116, 107-116.
- [13] Walling, C. (1975). Fenton's reagent revisited, *Accounts of Chemical Research* 8(4), 125-131.
- [14] Gao, H., Zhang, J., Wang, R., Wang, M. (2015). Highly efficient hydrogen production and formaldehyde degradation by Cu_2O microcrystals, *Applied Catalysis B: Environmental* 172-173, 1-6.
- [15] Rahman, K.O., Aziz, K.H.H. (2022). Utilizing scrap printed circuit boards to fabricate efficient Fenton-like catalysts for the removal of pharmaceutical diclofenac and ibuprofen from water, *Journal of Environmental Chemical Engineering* 10(6), 109015.
- [16] Kong, L., Fang, G., Kong, Y., Xie, M., Natarajan, V., Zhou, D., Zhan, J. (2018). $\text{Cu}_2\text{O}@ \beta$ -cyclodextrin as a synergistic catalyst for hydroxyl radical generation and molecular recognitive destruction of aromatic pollutants at neutral pH, *Journal of Hazardous Materials* 357, 109-118.
- [17] Zhu, M., Meng, D., Wang, C., Di, J., Diao, G. (2013). Degradation of methylene blue with H_2O_2 over a cupric oxide nanosheet catalyst, *Chinese Journal of Catalysis* 34(11), 2125-2129.
- [18] Faraji, F., Golmohammadzadeh, R., Pickles, C.A. (2022). Potential and current practices of recycling waste printed circuit boards: A review of the recent progress in pyrometallurgy, *Journal of Environmental Management* 316, 115242.
- [19] Zhong, Y., Hu, S., Xu, J., Chen, Z., Wang, S. (2024). Sustainable upcycling of copper from waste printed circuit boards with the assistance of tannic acid and Fe^{3+} to a magnetic heterogeneous catalyst, *Journal of Environmental Management* 370, 122391.
- [20] Zhao, H.Y., Wang, Y.F., Zeng, J.H. (2008). Hydrothermal Synthesis of Uniform Cuprous Oxide Microcrystals with Controlled Morphology, *Crystal Growth & Design* 8(10), 3731-3734.
- [21] Ahmad, R., Mondal, P.K. (2012). Adsorption and Photodegradation of Methylene Blue by Using PAni/ TiO_2 Nanocomposite, *Journal of Dispersion Science and Technology* 33(3), 380-386.
- [22] Rauf, M.A., Ashraf, S.S. (2009). Fundamental principles and application of heterogeneous photocatalytic degradation of dyes in solution, *Chemical Engineering Journal* 151(1), 10-18.
- [23] Tran, H.N. (2022). Differences between Chemical Reaction Kinetics and Adsorption Kinetics: Fundamentals and Discussion, *Journal of Technical Education Science* 17 (Special Issue 01), 33-47.

Distribution characteristics of trace elements in topsoil, Bat Xat area, Lao Cai province

Nguyen Thi Lien, Pham Thi Dung, Tran Tuan Anh, Pham Thanh Dang, Nguyen Xuan Qua, Doan Thi Thu Tra, Do Thi Thu, Cu Sy Thang, Nguyen Thi Thu, Le Thi Phuong Dung

¹Institute of Earth Sciences, Vietnam Academy of Sciences and Technology

*Email: ntlien@ies.vast.vn

Abstract: To study trace element distribution in topsoil is not only significant for land management and utilization but also related to the management and protection of the soil environment, especially concerning heavy metals and arsenic (As). This study investigates the distribution of As, Cr, Cu, Ni, Pb and Zn in topsoil from Bat Xat area by comparing their concentrations to reference background values. Enrichment factor (EF), geo-accumulation index (I_{geo}), and potential ecological risk index (E_r) were used to assess the degree of enrichment, pollution, origin of the elements in the topsoil and the potential risks in the area. The content of trace elements in 216 topsoil samples (A layer) at a depth of 0÷25 cm and 90 saprolite samples (C layer) at a depth of 60÷80 cm were determined by ICP-MS method. The results show that the topsoil in Bat Xat area have higher As, Cu, Pb contents than the average in the world's soil and the Upper continental crust. The average content of As, Cr, Cu, Ni, Pb, Zn are all within the regulation threshold in QCVN 03:2023/BTNMT. The average geoaccumulation index and enrichment factor of As, Cr, Cu, Ni, Pb, Zn show that there are no pollution and enrichment from anthropogenic sources in the topsoil. However, the high content of elements: As, Cr, Cu, Ni and Pb at some sampling locations with geological accumulation index greater than 0 and enrichment factor greater than 2 were considered to have accumulation and enrichment of elements As, Cr, Cu, Ni and Pb showing the influence of anthropogenic activities. These locations are mainly near areas related to mineral mines. The average potential

ecological risk levels of elements in Bat Xat area were in the order: As > Ni > Pb > Cu > Cr > Zn and were all at low levels.

Keywords: Topsoil, trace elements, Bat Xat, enrichment factor, geo-accumulation index.

INTRODUCTION

Trace elements, although accounting for a very small proportion of the soil, play an important role in plants because they participate in most plant growth, development and disease resistance activities. The lack and excess of trace elements in the soil can cause negative effects not only on plants, but also indirectly affect human and animal health, especially heavy metal elements (HM).) such as Cu, Cr, Ni, Pb, Zn and As. The study of determining the content distribution characteristics of certain trace elements in soil has implications not only for land use and management but also for soil environmental protection and management. The accumulation of HMs in agricultural soils can threaten the safety of soil environmental ecosystems, impair soil quality, pollute the soil environment, affect food security issues and potential risks to human health. Therefore, determining the content characteristics of heavy metal elements in soil has always been an issue of research interest in many countries around the world and Vietnam over the past few decades [1, 3, 6, 10, 11, 13, 15, 17, 22].

Soils are the product of weathering of the parent rock under the influence of chemical, physical and biological factors. The material composition of the parent rock is a major

determinant of soil composition and properties. Besides natural factors such as terrain, climate, organisms and people, they also contribute significantly to the composition and properties of the soil, especially topsoil through farming and agricultural production activities such as chemical fertilization and use of pesticides. Furthermore, soil can be affected by the transport of elements from the atmosphere over long ranges [16]. Therefore, to study trace element distribution and origin of trace elements in the soil is extremely necessary, helping to control and prevent soil pollution.

Bat Xat district was the name of a former administrative unit; however, after the merger and the removal of the district-level unit, Bat Xat district will have 7 new commune-level administrative units, including: Bat Xat, Muong Hum, Den Sang, Y Ty, A Mu Sung, Trinh Tuong, and Ban Xeo. This is a border highland district located in the northwest of Lao Cai province, with 98 km of border adjacent to Hekou and Jinping districts of Yunnan province, China. The study area has an important position in the economic, social and national defense and security development of the province as well as the country. Agricultural and forestry land area accounts for over 90% of the natural land area of the entire district (Report on land data, administrative units, etc population and labor in Lao Cai province in 2022), therefore the agriculture and forestry economy plays an important role in local economic development. To study trace element distribution and origin of trace elements in topsoil in the Bat Xat area will help provide a scientific basis for planning orientation and rational use of land resources, contributing to socio-economic development in area.

THE STUDY AREA

The study area is the old Bat Xat district, currently which are communes: Bat Xat, Muong Hum, Den Sang, Y Ty, A Mu Sung, Trinh Tuong and Ban Xeo. The study area located in the northwest of Lao Cai province, about 300 km from the center of Hanoi capital. The north and northwest of the study area border Yunnan

province (China), the east borders Lao Cai city and Hekou district of Yunnan province (China); The west borders Sin Suoi Ho, Ta Leng, Binh Lu communes of Lai Chau province and the south borders Ngu Chi Son, Ta Phin, Coc San communes of Lao Cai province (Figure 1). The terrain of study area is divided into two separate areas: high mountainous areas (> 700 m) characterized by large divided alpine terrain, steep slopes, narrow valleys and deep ravines; and low mountainous areas running along the Red River with gentle and relatively flat terrain. Bat Xat climate is located in a tropical climate area, hot, humid and rainy. The rainy season usually lasts from May to October, with the dry season lasting from November to April of the following year.

Geologically, the study area is located in the Phan Si Pan structural region of northwestern Vietnam part of the South China Block [24]. Participating in the geological structure of the study area are formations ranging in age from Proterozoic to Cenozoic including: (1) Proterozoic – Cenozoic old metamorphic rocks of including: biotite shale, biotite shale – sillimanite, gneiss biotite, gneiss biotite-sillimanite, marble and amphibolite of the Suoi Chieng, Sinh Quyen, Cha Pa and Da Dinh formations; (2) Metamorphic sedimentary rocks of the middle Cambrian period belong to the Cam Duong formation and Devonian period belong to Ban Bap, Ban Nguon formations include: argillite, black shale, argillite shale, sericite quartzite shale interbedded with quartzite, limestone and marble; (3) Permian basalts of Vien Nam formation; (4) Tertiary terrestrial sedimentary rocks consist of thick-bedded conglomerate with minor sandstone, siltstone, claystone and coal intercalations; (5) Quaternary deposits/sediments; (6) Intrusive magmatic rocks belong to the Phan Si Pan uplift include: Neoproterozoic granite rocks of the Po Sen complex; type A granites of the late Permian - early Triassic period of the Muong Hum; high-potassium Cenozoic granitoid rocks of type I of the Ye Yen Sun complex and Cenozoic alkaline syenite rocks of the Nam Xe-Tam Duong complex (Figure 1).

According to soil map of Lao Cai province at a scale of 1: 100,000: soil of the Bat Xat area mainly include: humus soil group on mountains distributed at mountain peaks with altitudes from 1800 – 2800m; reddish-yellow humus soil group on mountains distributed at altitudes from 900 – 1800 m and red-yellow soil group distributed at an altitude below 900m.

MATERIAL AND METHOD

Sampling and samples treatment

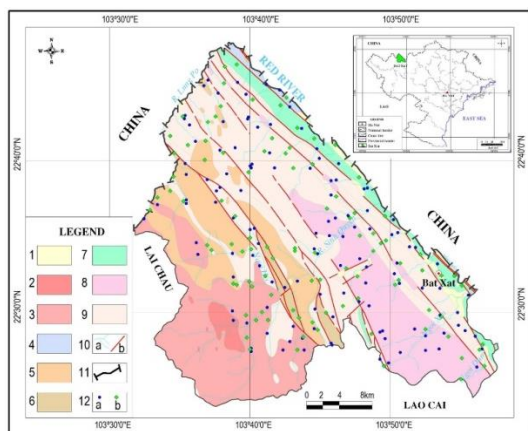


Figure 1. Distribution map of the lithological units and sampling locations in Bat Xat area [2]

Legend: (1) – Neogen – Quaternary sediment; (2) – Cenozoic alkaline rocks of Nam Xe – Tam Duong complex; (3) – Cenozoic granite rocks of the Ye Yen Sun complex; (4) – Permian basalts of Vien Nam formation; (5) – Permian alkaline granites of Muong Hum complex; (6) – Devonian limestone and clay shale of Ban Pap and Ban Nguon formations (7) – Cambrian sandstone, gritstone, conglomerate, clay shale of Cam Duong Formation; (8) – Neoproterozoic granitoid rocks of Po Sen complex; (9) – Neoproterozoic granitoid rocks of Po Sen complex (10a) – Stream and river (10b) – Faults; (11) – National Boundary; (12) – Sampling locations: a) location of topsoil sampling; b) location of topsoil and sample in saprolite horizon

The research samples were collected within the framework of the project: "Establishing a national multi-purpose geochemical baseline for six northern border provinces", project coded: TĐĐHQG.00/21-23. Samples were taken in a network according to the project's sampling guidelines procedure. Samples were collected from two soil horizons:

216 topsoil samples (0 – 25 cm depth) and 90 samples in saprolite horizon (60÷80 cm depth). The locations of the samples collected for the study are shown in figure 1 (Figure 1).

The survey and sample collection were carried out in accordance with Circular 60/2015/TT-BTNMT of the Ministry of Natural Resources and Environment on technical regulations for land investigation and evaluation combined with soil profile description methods and soil sampling according to Vietnam Standard 4046:1985. To obtain the most comprehensive assessment of the composition and origin of trace elements in topsoil, sampling points were selected in locations least affected by human activities (avoiding densely populated areas and mining sites). The sampling locations were chosen to cover all geological formations in the study area (no sampling on Quaternary formations).

After taking samples, they are stored in plastic bags, the sample weight is about 2kg. The samples were dried naturally then finely ground and analyzed for trace elements.

Method

Analytical method:

Trace element analysis was performed using an Agilent 7900 ICP-MS instrument at the Institute of Earth Sciences, Vietnam Academy of Science and Technology. Trace elements were extracted from a 0.25 g sample by wetting with 2 ml of concentrated HNO₃, 6 ml of concentrated HCl, and 2 ml of H₂O₂ in polyfluorocarbon tubes, allowing the mixture to stand for about 10 min to react with H₂O₂ completely, then closing the tube lid and place it at room temperature overnight. The next day, samples underwent pressure digestion using a microwave system (Mar6, CEM Corporation), with the temperature increasing to 100°C and maintained for 5 min. The temperature was continued to increase to 220 °C and maintained for 10 min. The mixture was cooled to room temperature and accurately diluted to 50 ml with deionized water. Finally, the samples were analyzed for trace elements. The reference material used for trace element

analysis is CRM016 and BCR-277R. Duplicate samples are analyzed after each batch of 20 samples for repeatability, and the accuracy is verified after each batch of 40 samples. The method has qualification limits of 0.5 1.0 ppm. The percentage of R elements recovered ranges from 90% to 105% [2, 5].

Methods for assessing soil quality:

- Geochemical background: to distinguish between natural element concentrations and their concentrations under anthropogenic effects. The geochemical background was calculated with the equation suggested by by Reimann and nnk (2005) [19].

Geochemical background = Median \pm 2 MAD; where MAD is median absolute deviation.

Enrichment factors (EF) and geoaccumulation index (I_{geo}) : In order to assess the origins of trace elementa (geogenic or anthropogenic) accumulated in topsoils,

- Enrichment factors (EF) to evaluate the degree of enrichment or depletion of a trace element in topsoil compared to the background. The Enrichment Factor (EF) was determined using formula [12]:

$$EF = (M/Al)_{\text{sample}} / (M/Al)_{\text{back ground}}$$

where (M/Al)_{sample} và (M/Al)_{background} concentration in the topsoil sample and background are considered. Al is used as a reference element because Al is an element with a

relatively high natural concentration and is less affected by weathering and human activities [21]. Enrichment levels for the elements are hierarchical in Table 1 (Table 1).

- The Geoaccumulation index (I_{geo}) it is complementary to the Enrichment factor and indicates, numerically, the level of topsoils pollution and was calculated using the equation proposed by Muller (1969) [18]:

$$I_{\text{geo}} = \log_2 (C_n / 1.5 B_n)$$

where: C_n = trace element concentration in a soil sample, B_n = concentration of that trace element in the background.; 1.5 is a correction factor owing to possible variation in background values due to lithological effects. Geoaccumulation Index has defined seven classes (Table 1).

- Potential Ecological Risk (E_rⁱ): To quantitatively evaluate the potential ecological risks posed by the heavy metals contaminatons in the topsoil by L. Hakanson (1980) [8]

$$E_r^i = C_f^i * T_r^i$$

where: T_rⁱ is toxic response factor of ith heavy metal, T_rⁱ of the elements As, Cr, Cu, Ni, Pb, Zn are 10, 2, 5, 5, 5 and 1 respectively [8, 25, 27]; C_fⁱ is the contamination factor; C_f calculated by the formula: C_f = C_n/B_n (where: C_n and B_n as mentioned above). Potential Ecological Risk was classified into five classes are hierarchical in Table 1 (Table 1).

Table 1. Classification of enrichment , pollution accumulation and ecological risks

EF		I _{geo}		E _r ⁱ	
Value	Soil quality	Value	Soil quality	Value	Soil quality
EF < 2	No enrichment	0 < I _{geo}	Uncontaminated	E _r ⁱ < 40	Low risk
2 ≤ EF < 5	Moderate enrichment	0 ≤ I _{geo} < 1	Uncontaminated to moderately contaminated	40 ≤ E _r ⁱ < 80	Moderate risk
5 ≤ EF < 20	Significant enrichment	1 ≤ I _{geo} < 2	Moderately contaminated	80 ≤ E _r ⁱ < 160	High risk
20 ≤ EF < 40	Very high enrichment	2 ≤ I _{geo} < 3	Moderately to heavily contaminated	160 ≤ E _r ⁱ < 320	Very high risk
40 ≤ EF	Extremely high enrichment	3 ≤ I _{geo} < 4	Heavily contaminated	320 ≤ E _r ⁱ	Extreme risk
		4 ≤ I _{geo} < 5	Heavily to extremely contaminated		
		5 ≤ I _{geo}	Extremely contaminated		

RESULTS AND DISCUSSION

Trace elements distribution

The descriptive statistical parameter of trace elements concentrations (Cu, Cr, Ni, Pb, Zn and As) in the topsoil samples in the Bat Xat area are shown in table 2 (Table 2). The mean concentrations of these metals in order followed the order: As < Pb < Ni < Cu < Cr < Zn. The concentration of the element: As: 1.22 – 38.16 mg/kg (mean = 5.51 mg/kg); Cr: 3.19 – 543.86 mg/kg (mean= 42.78 mg/kg); Cu: 2.12 – 813.83 mg/kg (mean= 36.12 mg/kg); Ni: 1.76 – 353.58 mg/kg (mean = 21.65 mg/kg); Pb: 5.71 – 275.40 mg/kg (mean = 21.57 mg/kg); Zn: 5.41 – 221.08 mg/kg (mean = 50.25 mg/kg).

Topsoil in the Bat Xat area has increased concentration of the elements As, Cu compared to their average concentrations in the Upper continental crust (UCC) and in the world's soil. The concentration of the elements Cu, Cr, Ni, Pb, Zn and As varies widely, but their average concentrations is all within the threshold of Vietnamese Regulation QCVN 03:2023/BTNMT. However, there are still many sampling locations where the concentration of Cu, Cr, Ni exceeds the threshold of Vietnamese Regulation QCVN 03:2023/BTNMT up to 2 or 3 times. These locations are mainly near places with mineral mining sites such as Nam Chac, A Mu Sung, Y Ty, Coc My; Trinh Tuong communes (old

administrative unit name) where there are copper mineral mines.

The correlation of elements is shown in table 3 (Table 3), elements with high correlation coefficients to each other may have similar origins, whereas when correlation coefficients are low or negative correlations may have different origins [25]. In table 3, it can be seen that Pb and Ni have a high correlation coefficient with each other ($r = 0.66$) they may have the same source of generation. This issue needs attention in the process of farming and agricultural production.

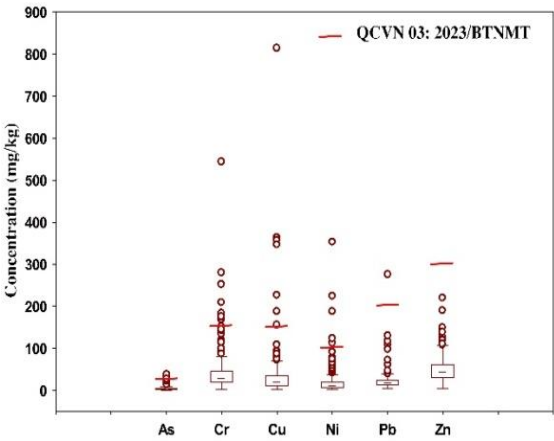


Figure 2. Box -plots of trace elements concentration in topsoil

Table 2. Basic statistical parameters (minimum, maximum, mean, median, Standard deviation) of trace element concentrations

Element	n	Min	Mean	Median	Max	Std.Dev	UCC [20]	Average world's soil [9]	QCVN 03:2023
As	216	1.22	5.51	3.63	38.16	5.58	4.8	5	25
Cr	216	3.19	42.78	27.58	543.86	53.33	92	54	150
Cu	216	2.12	36.12	19.03	813.83	71.70	28	20	150
Ni	216	1.76	21.65	10.50	353.58	35.39	47	22	100
Pb	216	5.71	21.57	17.17	275.40	23.48	17	25	200
Zn	216	5.41	50.25	42.74	221.08	30.57	67	63	300

Note: UCC- The Upper Continental Crust [20]
QCVN 03:2023/BTNMT: Vietnam's national technical regulations on soil quality

Table 3. Pearson's correlation coefficient for trace elements

	As	Cr	Cu	Ni	Pb	Zn
As	1.00	0.15	0.15	0.28	0.45	0.23
Cr	0.15	1.00	0.22	0.23	0.02	0.19
Cu	0.15	0.22	1.00	0.48	0.29	0.46
Ni	0.28	0.23	0.48	1.00	0.66	0.43
Pb	0.45	0.02	0.29	0.66	1.00	0.29
Zn	0.23	0.19	0.46	0.43	0.29	1.00

Geochemical background trace element concentration value

The average concentration of elements in the Upper continental crust or in world average shale is often used as the global standard for background values for elements in the lithosphere. However, using these values as background values to evaluate the concentration of elements in natural formations (such as soil, sediment,...) is not always appropriate due to the characteristics of the background natural geology of the study area. The concentration of elements in the natural soil depends on the geology and soil formation processes in the area. Therefore, data on the concentration of elements in local geological formations are often used as background values for assessments related to human activity by establishing reference values comparing the concentration of elements in the studied soil with soil in the area considered unaffected by human activities (natural).

The purpose of determining the concentration distribution characteristics of some elements Cu, Cr, Ni, Pb, Zn and As in topsoil in Bat Xat area to evaluate soil quality helps in management and protection soil resources in the area. This study will use the background value of elements in saprolitic soil horizon as a reference value to evaluate the enrichment factor and geoaccumulation index of elements in topsoil. Because saprolitic soil horizon is considered to reflect the characteristics of the soil-forming parent rock and are less susceptible to the impact of human activities as well as accumulation from the air environment. The results of the calculation of the background values of the

elements As, Cr, Cu, Ni, Pb, Zn from 90 saprolite samples taken in the Bat Xat area are shown on table 4 (Table 4).

Table 4. Basic statistical parameters of trace element concentrations in saprolite soil horizon

	As	Cr	Cu	Ni	Pb	Zn
	n= 90					
Min	0.78	3.04	1.82	1.77	3.36	4.48
Max	36.37	287.94	222.16	181.28	107.13	183.61
Mean	5.91	40.66	28.84	20.59	19.75	57.35
Median	3.38	34.22	20.637	11.91	14.43	46.94
MAD	1.84	24.63	17.63	10.06	8.83	22.38
Background value	7.07	83.49	55.91	32.04	32.11	91.70

Enrichment factor, geo-accumulation index and potential ecological risks of elements in topsoil

Enrichment factor (EF)

The enrichment factor (EF) of each element in the topsoil of the Bat Xat area is shown in table 5 and shown in figure 3. The EF values were calculated to evaluate anthropogenic influences on heavy metals in topsoil samples. The enrichment values <2 indicate that the metal is completely derived from a geological origin, but EF values >2 propose that the metal is possibly sourced through anthropogenic activities [21, 23].

Table 5. Basic statistical parameters of geological accumulation index, enrichment factor and potential ecological risk index of trace element in topsoil

		As	Cr	Cu	Ni	Pb	Zn
		n= 90					
I_{geo}	Min	-3.12	-5.30	-5.30	-4.77	-3.08	-4.67
	Max	1.85	2.12	3.28	2.88	2.52	0.68
	Mean	-1.34	-2.10	-2.10	-1.92	-1.44	-1.67
EF	Min	0.26	0.07	0.06	0.10	0.29	0.14
	Max	23.86	10.19	22.10	19.10	16.19	5.20
	Mean	1.43	0.89	1.10	1.16	1.22	0.96
E_r^i	Min	1.73	0.08	0.19	0.27	0.89	0.06
	Max	53.97	13.03	72.78	55.18	42.88	2.41
	Mean	7.80	1.02	3.23	3.38	3.36	0.55

The average enrichment factor of the elements As, Cr, Cu, Ni, Pb and Zn are all less than 2 showing no enrichment of the elements

in topsoil. Average enrichment values of the elements in descending order from As > Pb > Ni > Cu > Zn > Cr. The range of enrichment factor EF variation is large: As: 0.26 – 23.86; Cu: 0.06 – 22.1; Ni: 0.1 – 19.1; Pb: 0.29 – 16.19 and Cr: 0.07 – 10.19. This indicates a slight to moderate enrichment of As, Cu, Ni, Pb and Cr at some locations in the area.

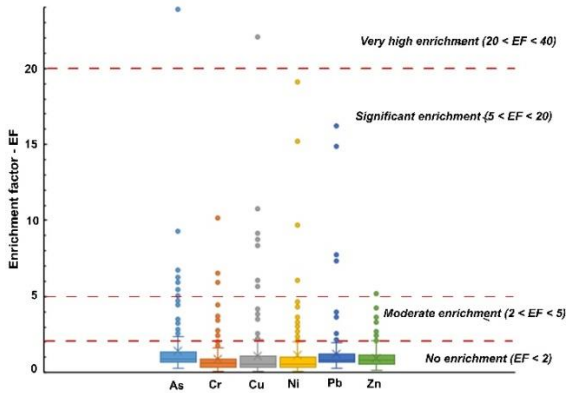


Figure 3. Box-plots of EF of trace elements in topsoil

Geoaccumulation index (I_{geo})

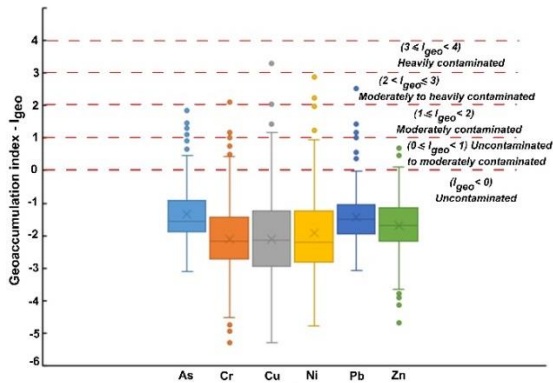


Figure 4. Box-plots of I_{geo} of trace elements in topsoil

The geoaccumulation index of elements in topsoil of Bat Xat area is shown in Table 5 and Figure 4. The geoaccumulation index of the elements: As, Cr, Cu, Ni, Pb, Zn in topsoil in Bat Xat area mostly shows no contamination. The average geoaccumulation index of elements in topsoil ranges from high to low in the order: As > Pb > Zn > Ni > Cr, Cu. Notably, the elements Cu, Ni and Cr have a large geoaccumulation index variation, although the average geoaccumulation index in the of these

is lower than the other elements, however there are many sampling points with low, average even high geoaccumulation index. This indicates that there is a slight contamination in the topsoil in Bat Xat area of the elements As, Cr, Cu, Ni and Pb which is localized in some places

Potential ecological risks (E_r^i)

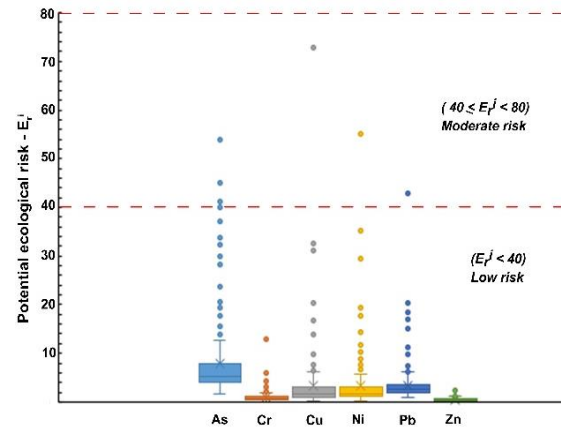


Figure 5. Box-plots of potential ecological risks (E_r^i) of trace element in topsoil

The presence of trace elements in soil plays an important role in soil ecosystems, supporting the healthy growth and high productivity of plants. However, some elements such as heavy metal groups, their occurrence in the soil can cause adverse effects on the survival and development of many soil species, affecting plant health, with potential risks to human health. Determination of the concentration of the elements to assess soil quality, the degree of ecological risk of the elements, is therefore necessary in order to be able to understand the potential harmful effects. The potential ecological risk index for each element in the topsoil in the Bat Xat area is shown in table 5 and figure 5. The results showed that the average potential ecological risk index of the elements decreased from As > Ni > Pb > Cu > Cr > Zn, where the elements As, Cu, Ni and Pb had a potential ecological risk index that fluctuated over a wide range As: 1.73 – 53.97; Cu: 0.19 – 72.78; Ni: 0.27 – 55.18; Pb: 0.89 – 42.88 corresponds to low to moderate risk. The elements Cr and Zn have a potential

ecological risk index $Eri < 40$ indicating a low level of risk. Although the content of As in soil is not high compared to other elements, its potential ecological risk is higher due to their higher ecotoxicity [8].

CONCLUSION

The topsoil in Bat Xat area has increased concentration of some elements such as As, Cu, Pb compared to the average in the world's soil and in the Upper continental crust. Variation of content of elements: As: 1.22 - 38.16 mg/kg; Cr: 3.19 - 543.86 mg/kg; Cu: 2.12 - 813.83 mg/kg; Ni: 1.76 - 353.58 mg/kg; Pb: 5.71 - 275.40 mg/kg; Zn: 5.41 - 221.08 mg/kg. Their average concentration is all within the threshold of Vietnam Regulation QCVN 03:2023/BTNMT, however, there are still many sampling points with the content of Cu, Cr, Ni exceeding the threshold of Vietnam Regulation QCVN 03:2023/BTNMT by 2, 3 times. Their distribution shows that these points are mainly near areas with mineral mines. This issue should be kept in mind during farming and agricultural production and there are more detailed studies to clarify the influence of mining activities in the area on the environment.

The average geo-accumulation index, enrichment factor and potential ecological risk index of the elements As, Cr, Cu, Ni, Pb, Zn in topsoil in Bat Xat area show that topsoil in Bat Xat area is not polluted, there is no enrichment of elements from anthropogenic sources and the potential ecological risk level of each element is low. However, the large variation range of the geoaccumulation index, enrichment factor and potential ecological risk index of each element, many sampling locations have geoaccumulation index greater than 0 and enrichment factor greater than 2, indicating that the topsoil is slightly contaminated with the elements As, Cr, Cu, Ni and Pb due to the influence anthropogenic activities. The potential ecological risk of elements in Bat Xat area are in the order $As > Ni > Pb > Cu > Cr > Zn$.

ACKNOWLEDGMENTS

This study was financially supported by Vietnam Academy of Science and Technology (VAST) and Institute of Earth Sciences under the

project coded TĐĐHQG.00/21-23 and the project coded CSCL11.02/25-26. Ac

REFERENCES

- [1]. Abou El-Anwar, E. A., Mekky, H. S., Abdel Wahab, W., Asmoay, A. S., Elnazer, A. A., & Salman, S. A. (2019). Geochemical characteristics of agricultural soils, Assiut governorate, Egypt. *Bulletin of the National Research Centre*, 43:41. <https://doi.org/10.1186/s42269-019-0080-3>
- [2]. Anh Tuan Tran, Dung Chi Nguyen, Dung Thi Pham, Tha Van Hoang, Dang Thanh Pham, Qua Xuan Nguyen, Ha Van Vu, Tuan Minh Dang, Tuan Dang Tran, Tai Trong Nguyen, Tra Thu Thi Doan, Thang Sy Cu, Quan Tran Dang, Cong Quoc Tran, Lien Phuong Thi Pham, 2024. Geochemical constraints on weathering and provenance of stream sediments from Bat Xat, northwestern Vietnam. *Applied Geochemistry* 177 (2024) 106235. <https://doi.org/10.1016/j.apgeochem.2024.106235>.
- [3]. Bui Huu Viet, Nguyen Van Niem Do Duc Nguyen, Nguyen Minh Trung, Pham Hung Thanh, Pham Thi Nhung Ly, Duong Cong Hieu, Nguyen Thi Hong, 2024. Geochemical characteristics of some trace elements in soil of Son Dong area (Bac Giang) and their potential impact on the environment. *Environment Magazine*, No.8/2024.
- [4]. C. Reimann, P. Filzmoser, R.G. Garrett, 2005. Background and threshold: critical comparison of methods of determination, *Sci. Total Environ.* 346 (2005) 1–16.
- [5]. Duong, L.T., Nguyen, B.Q., Dao, C.D., Dao, N.N., Nguyen, H.L.T., Nguyen, T.H.T., Nguyen, C.H.T., Duong, D.C., Pham, N.N., 2022. Heavy metals in surface sediments of the intertidal Thai Binh Coast, Gulf of Tonkin, East Sea, Vietnam: distribution, accumulation and contamination assessment. *Environ. Sci. Pollut. Control Ser.* 29, 41261–41271. <https://doi.org/10.1007/s11356-022-18881-0>.
- [6]. Ehab A. Ibrahim and El-Metwally M. Selim, 2022. Pollution and health risk assessment of trace metal in vegetable field soils in the Eastern Nile Delta Egypt. *Environ Monit Assess* (2022) 194: 540. <https://doi.org/10.1007/s10661-022-10199-1>.
- [7]. Gordon Foli, Prosper M. Nude and Ohene B. Apea, 2011. Geochemical Characteristics of Soils from Selected Districts in the Upper East Region, Ghana: Implications for Trace Element Pollution and Enrichment. *Research Journal of Environmental and Earth Sciences* 4(2): 186-195, 2012. ISSN: 2041-0492.

- [8]. L. Hakanson, An Ecological Risk Index for Aquatic Pollution Control. A Sedimentological Approach, Water Research, Vol. 14, No. 8, 1980, pp 975-1001, [https://doi.org/10.1016/0043-1354\(80\)90143-8](https://doi.org/10.1016/0043-1354(80)90143-8).
- [9]. Kabata-Pendias and Mukherjee.,(2007), Trace elements from soils to human. Springer Berlin Heidelberg, New York, p550).
- [10]. Le Thi My Hao, Bui Bich Luong, Bui Hai An, 2016. Micro element contents in paddy rice soils in Red river and Mekong river delta. Vietnam Journal of Agricultural Science and Technology - No. 1(62)/2016.
- [11]. Lingling Mao, Heming Tian, Xiong Zhang, Ruigang Zhang , Jinhua Luan, Haitong Zhao, Feng Hu, Changchao Li and Xu Luo, 2022. Geochemical characteristics and ecological effects of Se and Zn in topsoil in Western Fuling of Chongqing. E3S Web of Conferences 352, 03022 (2022) <https://doi.org/10.1051/e3sconf/20223520302>.
- [12]. Loska, K., Wiechula, D., and Korus, I. 2004. Metal contamination of farming soils affected by industry. *Environ. Int.* 30, 159–165.
- [13]. Nguyen Thi Huong, 2012. Research on determining total zinc content in agricultural soil in some areas of Da Nang city. Ued Journal of social sciences, humanities and education, Vol 2, No 2 (2012).
- [14]. Lien Thi Nguyen, Dung Thi Pham*, Anh Tuan Tran, Qua Xuan Nguyen, Dang Thanh Pham, Tra Thu Thi Doan, Tuan Minh Dang, Hien Trong Tran, 2024. Study on topsoil chemical characteristics in Bao Thang district, Lao Cai province for agricultural development. Journal of Mining and Earth Sciences Vol. 65, Issue 3 (2024) 29 - 43
- [15]. Nguyen Van Niem, Bui Huu Viet, Do Duc Nguyen, Pham Hung Thanh, Nguyen Pham Ha Vu, Duong Cong Hieu, Duong Van Phuc, 2021. The basis of soil geochemistry in HaNoi suburban (formerly Ha Tay province) servicing the environmental monitoring and multidisciplinary development. Journal of science and technology, University of Sciences, Hue University Volume 18, Issue 2 (2021)
- [16]. Nriagu Jo, 1989. A global assessment of natural sources of atmospheric trace metals. *Nature* 338: 47–49.
- [17]. Moataz Khalifa a and Ahmed Gad, 2018. Assessment of heavy metals contamination in agricultural soil of Southwestern Nile Delta, Egypt. Soil and sediment contamination. 2018, VOL. 27, NO. 7, 619–642. <https://doi.org/10.1080/15320383.2018.1498445>.
- [18]. Müller, G. (1969). Index of geoaccumulation in the sediments of the Rhine River. *Geojournal*, 2, 108–118
- [19]. C. Reimann, P. Filzmoser, R.G. Garrett, 2005. Background and threshold: critical comparison of methods of determination, *Sci. Total Environ.* 346 (2005) 1–16.
- [20]. Rudnick, R.L., Gao, S., 2014. 4.1 - composition of the continental crust. In: Holland, H.D., Turekian, K.K. (Eds.), *Treatise on Geochemistry*, second ed. Elsevier, Oxford, pp. 1–51. <https://doi.org/10.1016/B978-0-08-095975-7.00301-6>.
- [21]. Saha, J. K., Selladurai, R., Coumar, M. V., Dotaniya, M. L., Kundu, S., and Patra, A. K., 2017. *Soil Pollution - An Emerging Threat to Agriculture*. Springer Nature, Singapore.
- [22]. Sonia M.B. de oliveira¹, Luiz Pessenda². Suzy E.M.Gouveia and Deborah Favaro, 2011. Heavy metal concentrations in soils from a remote oceanic island, Fernando de Noronha, Brazil. *Anais da Academia Brasileira de Ciências* (2011) 83(4): 1193-1206 (Annals of the Brazilian Academy of Sciences) Printed version ISSN 0001-3765 / Online version ISSN 1678-2690.
- [23]. Sutherland, R. A. 2000. Bed sediment-associated trace metals in an urban stream, Oahu, Hawaii. *Environ. Geol.* 39, 611–627
- [24]. [24]. Tri, T.V., Khuc, V., 2009. *Geology and Natural Resource of Vietnam*. Natural Science and Technology Publishing House, Hanoi.
- [25]. Y. Wang, Sun W., Zhao Y., He P., Wang L., and Nguyen L., Assessment of Heavy Metal Pollution Characteristics and Ecological Risk in Soils around a Rare Earth Mine in Gannan. *Scientific Programming*, 2022. 2022.
- [26]. Zhao H, Wu Y., Lan X., Yang Y., Wu X., and Du L., Comprehensive assessment of harmful heavy metals in contaminated soil in order to score pollution level. *Scientific Reports*, 2022. 12(1): p. 3552.
- [27]. Zongjun Gao, Hongzhi Dong, Songtao Wang, Yuqi Zhang, Hairui Zhang, Bing Jiang and Yang Liu, 2021. Geochemical Characteristics and Ecological Risk Assessment of Heavy Metals in Surface Soil of Gaomi City. *Int. J. Environ. Res. Public Health* 2021, 18, 8329. <https://doi.org/10.3390/ijerph18168329>.

Soil geomographic characteristics in the mountainous region of Sa Thay

Nguyen Van Dung^{1,2}

¹Institute of Earth Sciences, Vietnam Academy of Science and Technology

²Graduate University of Science and Technology, Vietnam Academy of Science and Technology;

Email: tiendungvm@gmail.com

Abstract: The mountainous region of Sa Thay is a remote, isolated area with rugged high mountain terrain, so it is difficult to investigate and survey natural conditions. Documents on geomorphology and soil are still sketchy. Meanwhile, there is a lack of land for agricultural production leading to illegal land use - the outside is forest and the inside is annual crops. Therefore, the soil geomorphological method is used to clarify the geomorphology and soil characteristics based on the correlation between them, as a basis for orienting the planning and land use of the area appropriately. The results show that (1) low mountain developed on acid igneous rocks (NA) presents a thin weathered crust and soil cover, reddish yellow soils with many exposed rocks, rock fragments, the characteristics of truncated soil or deluvic soil that meets the standards of Leptosols or Cambisols; (2) However, dissected low mountain developed on metamorphic rocks (NIJ) presents thicker weathered crust and soil cover, the soil is reddish brown, reddish yellow with no or little rock fragments, meeting Leptosols or Nitisols standards; (3) The dissected pediment hill developed on acid igneous rocks (DRA) presents that weathered crust, soil cover is not thick, has reddish yellow color with many fragments, meeting Skeletic Cambisols standards; (4) Dissected low plateau on acid igneous rocks (CRA) presents a thick weathered crust and soil cover, a yellowish red soil meeting Ferralsols standards; (5) However, strongly dissected low plateaus on metamorphic rocks (CHJ) presents soil reddish brown or yellowish red, meeting Ferralsols standards.

Keywords: Soil, geomorphology, mountain, hill, Sa Thay.

INTRODUCTION

Basic investigation of natural resource characteristics is a prerequisite for the socio-economic development of each country, each region and each locality. The mountainous region of Sa Thay is a remote, isolated area with rugged mountainous terrain, so it is difficult to investigate and survey natural conditions. Geomorphological documents are sketchy, and soil data is still limited at a small scale according to the qualitative classification system. Meanwhile, there is a lack of land for agricultural production leading to illegal land use - the outside is forest and the inside is annual crops. In such conditions, the soil geomorphological method is used to investigate and quantitatively survey the characteristics and properties of soil according to the FAO-UNESCO classification system, based on geomorphological characteristics such as origin terrain morphology, sample/parent rock and terrain age. The research contributes to clarifying the correlation between terrain and soil in the mountainous region of Sa Thay in particular and the tropical region in general.

The relationship between geomorphology and soil is reflected in the geomorphological and pedological landscape. Soil geomorphological landscape or soil landscape is defined as the regular rotation of soil types and soil groups on a defined terrain surface, formed on the basis of balance of morphogenesis and pedogenesis.

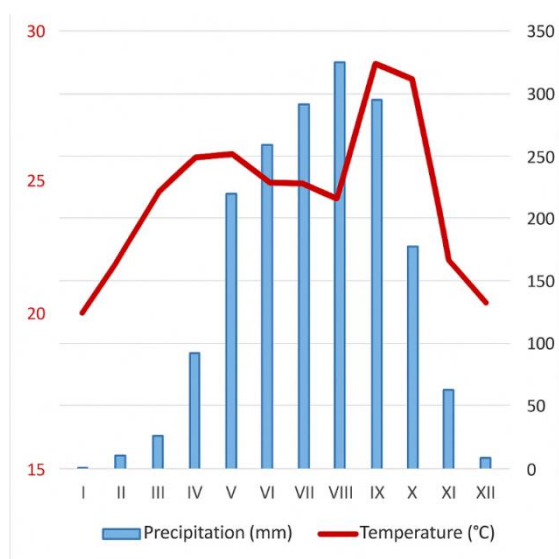


Figure 1. Monthly rainfall and temperature chart of Kon Tum meteorological station

RESEARCH METHODS

In this research, the soil geomorphological method is used to investigate and survey the soil cover in the field according to the terrain forms (mountain, dissected mountains, pediment hills), parent rock/ material (acid igneous rocks, metamorphic rocks - mica schists and gneiss...) and terrain levels (indirectly reflecting the terrain age). Under similar vegetation conditions and land use history, soil segments with similar geomorphological features will have similar characteristics, properties, and profiles. Geomorphological mapping including topographic morphology and parent rock/substrate samples was performed in-house and before fieldwork. Field investigations were carried out along routes, key points and digging soil profiles to take soil samples, describing in detail the soil forming factors and soil characteristics.

These field-collected soil samples were analyzed in the laboratory for the following parameters: pHKCl, pHH₂O, texture, CEC, OM (Organic matter content), Total N, Total P and Total K, Available K and Available P, Ca²⁺, Mg²⁺, K⁺, Na⁺ according to Vietnamese standards. These analytical data with the field description of the soil profile are the basis for

determining soil types according to FAO-UNESCO classification. Finally, the data was synthesized to upload to the geographic information system (GIS) and map, the results are shown in Figure 3 and Figure 4.

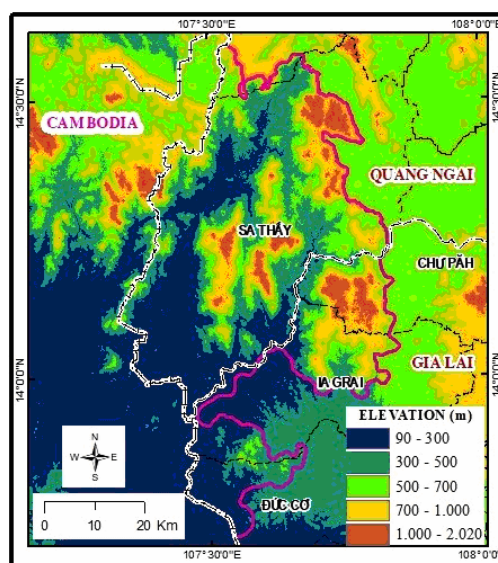


Figure 2. Map of topographic elevation in the mountainous region of Sa Thay

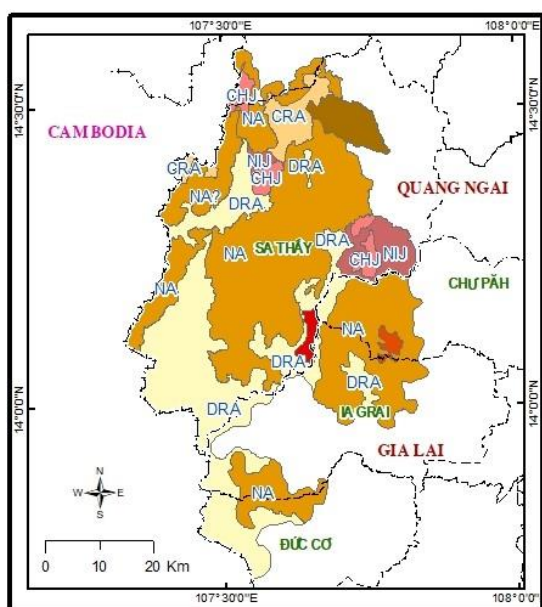
RESULTS

The region has a tropical monsoon climate, with an average annual rainfall of 1200-1800mm and an average number of rainy days of 120-140 days per year. The climate is divided into two distinct seasons: the rainy season and the dry season. The rainy season usually starts from April to November, and the dry season from December to March of the following year, shown in Figure 1. The climate is transitional between a humid tropical climate and a semi-arid tropical climate. The dry season climate has significantly affected the soil formation process, the weathering process is not thorough, and exposed rocks appear on the soil surface in many places and there are quite a lot of rocks and debris weathering in the soil profile.

Under the influence of terrain height, the average temperature decreases, causing the rock weathering process to decrease, especially the feralite process; combined with the erosion process on the slope, causing the soil layer to

thin and rejuvenate continuously, so the soil has a common thin layer, much rock fragments, and many primary and secondary minerals in the profile.

The region has high terrain in the East, gradually decreasing to the West and South, mainly low mountain, dissected low mountain, dissected pediment hill, and dissected low plateau. Hilly terrain of pediment origin, distributed mainly in the West along tectonic valleys, surrounded by low mountain terrain in the East. Many mountain tops close together form a number of low plateau surfaces. Soil characteristics are shown on the basis of geomorphological and pedological correlation through the soil geomorphological landscapes NA, NIJ, DRA, CRA, CHJ.



In which: NIJ, NA, CHJ, CRA, DRA are types of soil geomorphological landscape

Figure 3. Map of soil geomorphology in the mountainous region of Sa Thay

Soil landscape of low mountain on acid igneous rocks (NA)

Widely distributed in Sa Thay and Ia Grai districts, formed on a acid igneous rocks, mainly granite. Low mountain very steep, blocky shape, sharp peaks, convex or flat single slopes, slope $>25^\circ$, elevation difference >300 m,

V-shaped valleys. The dominant erosion process makes the soil layer and weathering crust thin. The soil is light yellow, sandy loam to sandy clay loam, soil depth from 20-70 cm, with many gravels and rocks in the profile.

On low mountain, the soil is truncated soil, red-yellow, thin depth, much rock fragments, meeting the standards of Skeletic Leptosols on the upper slopes; on the lower slopes, the soil is thicker, a deluvic soil, red-yellow, much rock fragments, meeting the standards of Skeletic Cambisols; and on the water-accumulating depressions, bedrock or gravel and boulders are often exposed.

Soil landscape of dissected low mountain on metamorphic rocks (NIJ)

Distributed in the East of Sa Thay district, formed on the weathered crust of metamorphic rocks, mainly mica schist. Low mountains are strongly dissected, very steep, block-shaped, sharp peaks, concave slopes, slopes of $10-25^\circ$, height difference of 150-250 m, V-shaped valleys. The dominant erosion process makes the weathering crust and soil layer thin. The soil is reddish yellow, sandy clay loam to clay loam, soil depth from 70 to 100 cm, with little or no gravel, stones in the profile.

The strongly dissected low mountains exhibits a structure of mountain and valley with a predominance of yellow red soil meeting Leptosols standards distributed on the top and upper slopes, and red brown soil meeting Nitisols standards distributed on the lower slopes and buried soil accumulated in the valleys. Due to the impact of the slope process, the soil on the lower slope has a thicker depth than the soil on the upper slope.

Soil landscape of dissected pediment hill on acid igneous rocks (DRA)

Distributed along of Sa Thay river (the tectonic valleys), formed by the pediment process on the weathered crust of granite. Hill is strongly dissected due to the network of rivers and streams flowing regularly and temporarily. Hill are undulating to slightly steep, altitude of 200-300m, slope $0-10^\circ$, height

difference of 30-100m. The soil is light yellow, sandy clay loam, soil depth from 50 to 70cm, containing a lot of quartz, weathering debris. The soil is young, has not yet formed the clay layer B, the clay content fluctuates around 20-40%, the clay content of the subsurface is quite uniform around 35%, the exchangeable cation is less than 20 (meq/100g clay), the humus content is poor.

Although the terrain is not very steep, the soil layer is not thick and in many places there are exposed rocks and fragments in profile. The

reason is that the hill has pediment origin, plus the region has a rather hot and dry climate, making the chemical weathering process of feralite poor.

The dissected pediment hill exhibits a structure of hill and wide valley, corresponding to light yellow soil meeting Skeletic Cambisols standards on the hill, shown in profile of KT1711 and with slightly acidic alluvial soil meeting Dystric Fluvisols standards distributed in the valleys.

Profile of KT1711

Location: Mo Rai commune, Sa Thay district. Coordinates: 14°3' 49.7"N, 107°27'9.1. Geomorphology: hill summit. Slope: 10-15°. Parent rock: granite. Vegetation: young rubber forest, diameter 15 cm, cleared below. Vietnamese soil name: light yellow soil on acid igneous rocks. UNESCO- FAO soil name: Skeletic Cambisols. Source: Nguyen Van Dung and Nguyen Manh Ha.

0-10 cm: Horizon A1. Brownish gray, sandy loam, moist, loose. Little gravel with diameter of 2 mm, accounting for 10%. Few tree roots, many animal burrows. Clear layering by color and gravel.

10-35 cm: Horizon A2, Yellowish gray, sandy clay loam, loose. Lots of gravel with size of 0.3-0.5 cm, accounting for 75%, with pseudo-concretions. Few tree roots with size of 1-2 mm, with animal burrows. Clear layering by color and gravel mixed.

35-75 cm: Horizon B, Darker Yellowish gray than the upper layer, sandy clay loam. Mixed gravel and conglomerate account for 75%, conglomerate is brown in color, shaped like mixed gravel.



Table 1. Physical and chemical analysis data of KT1711 profile

Soil depth (cm)	%OC	Exchangeable cations and CEC (meq/100g soil)						Texture (%)		
		Na ⁺	K ⁺	Ca ⁺⁺	Mg ⁺⁺	Al ³⁺	CEC (clay)	Sand	Limon	Clay
0-10		0,272	0,187	1,19	0,19	0,24	17,8	75,02	5,82	19,16
10-35	0,88	0,178	0,203	1,87	0,14	0,16	18,9	57,24	7,36	35,40
35-75	0,83	0,141	147	1,22	0,28	0,16	18,3	56,7	6,08	37,22

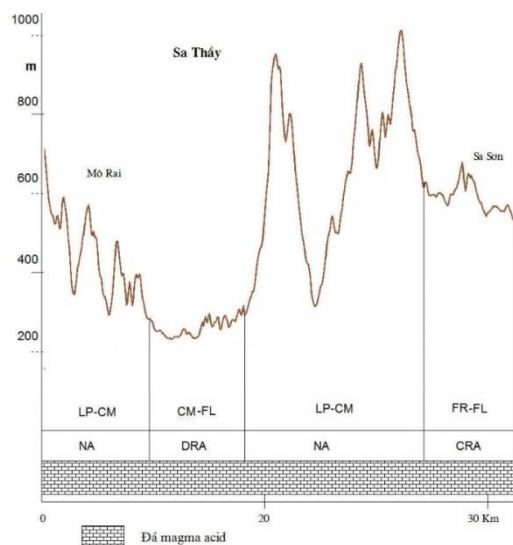
3.4. Soil landscape of dissected low plateau on acid igneous rocks (CRA)

Distributed in the North of Sa Thay district, formed on the weathered crust of acid igneous rocks, mainly granite. The plateau has a undulating to slightly steep hill shape, with a slope of 3-10°, the height difference is 50-100 m. The soil is residual soil red-yellow, sandy clay

loam to clay loam. Soil depth is than 1m, little or no gravel and fragments meeting the Ferrasols standard. The soil has an acidic reaction, low humus content, poor to medium nutrient content.

The dissected plateau exhibits a structure of hill and wide valley, corresponding to reddish yellow or dark yellow soil meeting the

Ferralic Acrisols or Ferrasols standard in the hills, and buried soil meeting the Eutric Fluvisols standard in the valleys.



In which: LP-CM: are reddish yellow soils meeting Leptosols or Cambisols standards. CM-FL: respectively reddish yellow soils meeting Cambisols standards and buried soils meeting Fluvisols standards. FR-FL: respectively yellowish red soils meeting Ferrasols standards and buried soil meeting Fluvisols standards. NA, DRA, CRA respectively soil landscapes of mountains, hills, plateaus on acid igneous rocks

Figure 4. Cross-section from Mo Rai to Sa Son, Sa Thay

3.5. Soil landscape of strongly dissected low plateau of metamorphic rocks (CH)

Distributed in the East of Sa Thay district, formed on metamorphic rocks. The plateau is strongly dissected, with an altitude difference of 50-150 m, slightly sloping 8-20°, convex slopes, shaped like a bowl-shaped hill range. The plateau was formed over a long period of time, so the weathering process is quite thorough, giving a thick weathering crust and soil cover. The soil is a residual soil, reddish brown on mica schist to yellowish red on gneiss, clay loam, clay content ranges from 30-45%, the soil layer can be several meters thick, grain structure, a little quartz in the profile. The soil has an average humus content, acidic to slightly acidic, Ca^{2+} , Mg^{2+} are poor, poor potassium content, exchangeable cations less than 16 (meq/100g clay).

The strongly dissected plateau has a structure of hill and narrow valley, corresponding to yellowish red soil meeting Ferrasols standards, shown in KT1708 profile on the hills and slightly acidic alluvial soil meeting Eutric Fluvisols soil standards in the valleys.

Profile of KT1708

Location: Sa Loong Commune, Ngoc Hoi, Kon Tum. Coordinates: 14°34'47"N, 107°34'55"E. Geomorphology: hill summit on plateau. Slope: 5-8°. Parent rock: gneiss. Vegetation: dense grass, 1.5m high, with perennial trees growing. Vietnamese soil name: yellowish red soil on gneiss. FAO-UNESCO soil name: Ferrasols. Comments: fairly uniform profile, with little quartz sand. Source: Nguyen Van Dung and Nguyen Manh Ha.

0-10 cm: Horizon A1, gray brown, sandy clay loam, loose, few grass roots, clear color transition.

10-30 cm: Horizon A2, Dark yellow, sandy clay loam, very compact, lumpy structure, loose when moist, a little quartz, size 1-2 mm, accounting for 5-10%.

30 - 60 cm: Horizon B, Dark yellow, sandy clay, very compact, lumpy structure, loose when wet, a little quartz



Table 2. Physical and chemical analysis data of KT17o8 profile

Soil depth (cm)	%OC	Exchangeable cations and CEC (meq/100g soil)						Texture (%)		
		Na ⁺	K ⁺	Ca ⁺⁺	Mg ⁺⁺	Al ³⁺	CEC (clay)	Sand	Limon	Clay
0-10	1,44	0,22	0,167	1,04	0,14	0,19	15,5	55,36	17,34	27,30
10-30	1,11	0,2	0,139	3,43	0,21	0,37	15,4	41,6	20,16	38,24
30-60	0,88	0,14	0,009	0,71	0,10	0,18	14,8	45,3	12,22	42,48

CONCLUSION

**Figure 5.** Location of the mountainous region of Sa Thay

The mountainous region of Sa Thay has a climate divided into dry and rainy seasons; the terrain is mainly low mountains, low dissected mountains, pediment hills and plateaus. The geomorphological and soil characteristics are shown through 5 soil geomorphological landscapes NA, NIJ, DRA, CRA, CHJ. Low mountain developed on acid igneous rocks (NA) are affected by the erosion process on the slope, with an incomplete weathering process, resulting in a weathered crust, a thin soil cover, reddish yellow soils with many exposed rocks, rock fragments, the characteristics of truncated soil or deluvic soil that meets the standards of Leptosols or Cambisols; However, dissected low mountain developed on metamorphic rocks (NIJ) presents thicker weathered crust and soil cover, the soil is reddish brown, reddish yellow with no or little rock fragments, meeting Leptosols or Nitisols standards; The

dissected pediment hill developed on acid igneous rocks (DRA) has a structure of hill and wide valley, is affected by the pediment erosion process, so the weathered crust, the soil layer is not thick, has reddish yellow color with many fragments, meeting Skeletic Cambisols standards. Dissected low plateau on acid igneous rocks (CRA) has a structure of hill and wide valley, a thorough weathering process, giving a thick weathered crust and soil cover, a yellowish red soil meeting Ferralsols standards; However, strongly dissected low plateaus on metamorphic rocks (CHJ) has a structure of hill and narrow valley, presents soil reddish brown or yellowish red, meeting Ferralsols standards.

REFERENCES

- [1] Le Duc An (2005) Flattening surface on Kon Plong plateau: initial perceptions *Journal of Earth Sciences*, Hanoi.
- [2] Nguyen Van Dung (2018) *Research on soil geomorphology for planning and sustainable land use in the Northern Central Highlands region*, thesis of doctoral philosophy, Graduate University of Science and Technology - Vietnam Academy of Science and Technology.
- [3] Nguyen Van Dung (2021), Method of creating soil geomorphological maps, using the example of the Northern Central Highlands at a scale of 1/250,000, *Proceedings of the 12th National Geographic Science Conference*, Thanh Nien Publishing House.
- [4] Nguyen Van Chien, Le Duc An (1985), *Topography and geomorphology, Central Highlands: natural conditions and natural resources*, Science and Technology Publishing House, Hanoi.
- [5] Tran An Phong and other (2004), *Research on land evaluation for land use planning and sustainable agricultural development in Kon Tum province*, Summary report of provincial-level science and technology project.

Effect of the initial clay-water content on the compressive strength of soil-cement-rice straw ash admixture

Nguyen Thanh Duong

Hanoi University of Mining and Geology, Hanoi, Vietnam.

Email: nguyenthanhduong@humg.edu.vn

Abstract: In recent years, increasing attention has been directed toward the utilization of agricultural by-products such as rice husk ash (RHA), rice straw ash (RSA)... for soil stabilization, owing to their economic and environmental benefits. However, limited research has focused on the influence of initial water content on the strength of soils stabilized with cement and RSA. This study investigates the effect of initial clay-water content on the mechanical behavior of soil-cement-RSA mixtures through a series of unconfined compressive strength (UCS) tests. Composite samples containing different proportions of cement and RSA were prepared at different initial water contents ($W_c = 50\%$, 60% , and 80%). In addition, Scanning Electron Microscopy (SEM) and X-Ray Diffraction (XRD) analyses were employed to examine the microstructural characteristics of the stabilized soils. The findings indicate that the UCS of the soil-cement-RSA admixture is highly sensitive to the initial clay-water content, which also governs the optimum RSA content required to achieve maximum strength of the stabilized soil. The results of XRD confirms the formation of C-S-H gel upon incorporating RSA into the soil-cement mixture. Furthermore, SEM observations reveal that the microstructural development, including the formation of cementitious products and particle bonding, is strongly affected by the initial clay-water content.

Keywords: Rice straw ash, initial water content, unconfined compressive strength, Mekong Delta, SEM, XRD.

INTRODUCTION

Soil stabilization is a widely adopted technique in geotechnical engineering to improve the strength and durability of soft soils, thereby ensuring the stability and longevity of infrastructure constructed on them. Traditionally, cement has been the most common stabilizing agents used to enhance the engineering properties of soft soils. However, the production of this material is energy-intensive and contributes significantly to global carbon dioxide emissions (Hasanbeigi et al., 2010). In response to increasing environmental concerns and the need for sustainable construction practices, the use of industrial and agricultural by-products as supplementary materials in soil stabilization has gained considerable attention in recent years. Among these by-products, rice husk ash (RHA) and rice straw ash (RSA) have emerged as promising alternatives due to their abundance, low cost, and high content of reactive silica, which contributes to the pozzolanic reactions when mixed with cement (Basha et al., 2005; Chen et al., 2021). Several studies have reported that incorporating these ashes into soil-cement mixtures can improve strength development, reduce material costs, and minimize environmental impacts associated with waste disposal (Abhishek et al., 2024; Chen et al., 2021). Despite these advantages, the performance of such stabilized soils depends on several factors, including the type and proportion of additives, curing conditions, and initial water content during mixing and compaction. In particular, the initial water content plays a crucial role in determining the workability and strength of stabilized soils. It

affects the degree of cement hydration, pozzolanic reaction, and the formation of cementitious compounds within the soil matrix. However, while many studies have examined the influence of ash content and cement dosage (Abhishek et al., 2024; Anupam et al., 2013; Duong, 2022; Duong et al., 2025c, 2025b; Jongpradist et al., 2018; Sabat et al., 2015), limited research has focused on the effect of initial water content on the strength behavior of soil–cement–RSA mixtures. Understanding this relationship is essential for optimizing the mix design and achieving reliable performance in field applications.

Therefore, this study aims to investigate the effect of initial water content on the mechanical behavior and microstructural characteristics of soil–cement–RSA mixtures. A series of unconfined compressive strength (UCS) tests were conducted on samples prepared with varying cement and RSA contents at different initial water contents ($W_c = 50\%$, 60% , and 80%). Furthermore, scanning electron microscopy (SEM), X-ray diffraction (XRD) were employed to analyze the microstructural development of the stabilized soils. The outcomes of this research provide valuable insights into how initial water content influences the strength development and microstructural evolution of RSA-stabilized soils, thereby contributing to the sustainable use of agricultural waste materials in ground improvement.

MATERIALS AND METHODS

Soil sample

Soil sample was taken from Vinh Chau town, Soc Trang province (which is now part of Can Tho City) (Figure 1). The depth of sample is about 1m below the ground surface. Some geotechnical properties of the soil sample are listed in Table 1. The sample is soft soil with a low unconfined compressive strength (UCS) of 24.3 kPa. The main mineral composition of the soil sample is quartz (44–46%), illite (17–19%), kaolinite (17–19%), chlorite (4–6%), feldspar (3–5%), and goethite (4–6%). The chemical composition of the soil sample is listed in Table 2.

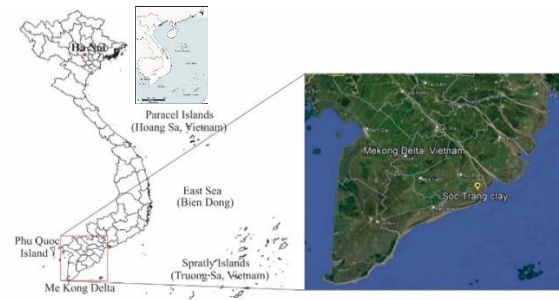


Figure 1. Sampling location (After Duong et al., 2025b)

Table 1. Some geotechnical indices of the soil sample

Index	Unit	Value
Sand (0.075–4.75)	%	11.0
Silt (0.005–0.075)	%	70.4
Clay (<0.005)	%	18.6
Natural water content	%	50.0
Wet unit weight	kN/m3	16.5
Specific gravity	-	2.69
Liquid limit (Cassagrande's method)	%	54.2
Plastic limit	%	31.1
Plasticity index	%	23.1
Organic matter content	%	6.66
UCS	kPa	24.3
pH value	-	6.47

Table 2. Chemical composition of the soil sample, RSA, and cement (Duong et al., 2025a)

Chemical composition	Materials		
	Soc Trang clay	RSA	Cement
SiO ₂ (%)	57.2	65.40	24.93
Al ₂ O ₃ (%)	19.1	2.30	6.94
TiO ₂ (%)	0.86	0.57	0.95
Fe ₂ O ₃ (%)	7.79	0.08	5.43
MnO (%)	0.13	0.26	0.14
MgO (%)	3.01	2.48	3.32
CaO (%)	0.44	4.11	43.6
Na ₂ O (%)	1.61	1.72	3.22
K ₂ O (%)	2.74	15.5	0.93
P ₂ O ₅ (%)	0.09	1.30	0.84
SO ₃ (%)	0.36	0.91	2.68

Cement and rice straw ash (RSA)

Portland cement blended (PCB40) Ha Tien was used in the study. Rice straw ash was obtained from open-field burning of rice straw (Figure 2). The RSA was then ground and passed through the sieve of 75 μm . The chemical compositions of cement and RSA are listed in Table 2. It can be seen that the primary chemical compositions of RSA is SiO_2 (accounting 65.4%), followed by K_2O (15.5%), CaO (4.11%) and other minor oxides.

Sample preparation and testing procedure

The sample was prepared using the cylinder mold with a height of 10cm and an inner diameter of 5 cm (Figure 3). The cement used was 15% of the wet soil weight. The RSA content was added to the soil+15% cement (soil+15%C) with the proportions of 0%, 5%, 10%, 15%, 20%, 25%, and 30% of the wet soil weight. The mixture sample was prepared at the natural water content (50%) and two other initial clay-water contents (Wc) of 60%, 80%. To achieve the Wc = 60% and 80%, the tap water was directly added to the natural soil sample. The mixture sample was cured in a humidity condition (relative humidity of 95%, temperature of 25 $^{\circ}\text{C}$) in laboratory. The procedure for sample preparation has been reported in some previous studies (Duong, 2022; Duong et al., 2025b, 2025c).



Figure 2. Open-field burning of rice straw (Duong et al., 2025a)

The unconfined compressive test was conducted on samples at 28 days of curing in accordance with ASTM D2166 under a controlled deformation rate of 1mm/min. The sample after testing was subjected to SEM and XRD analyses to investigate the microstructure

of the soil matrix. The schematic of the sample preparation and testing procedure was summarized and shown in Figure 4.



Figure 3. Cylinder mold for sample preparation

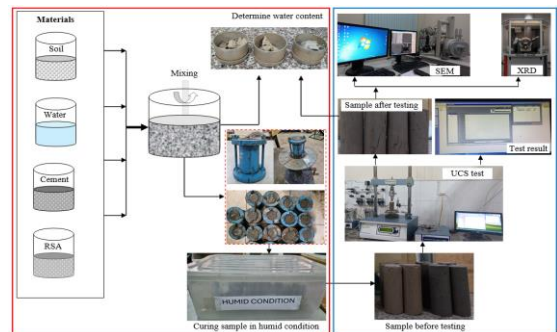
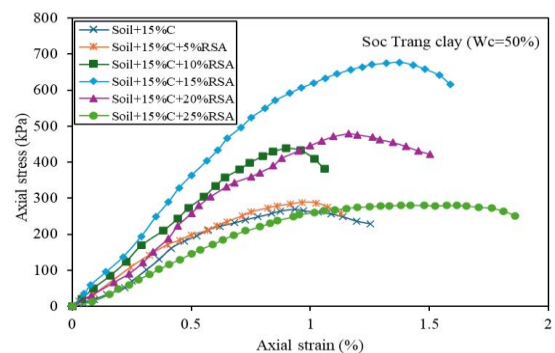


Figure 4. Sample preparation and testing procedure (After Duong et al., 2025b)

Test results and discussions



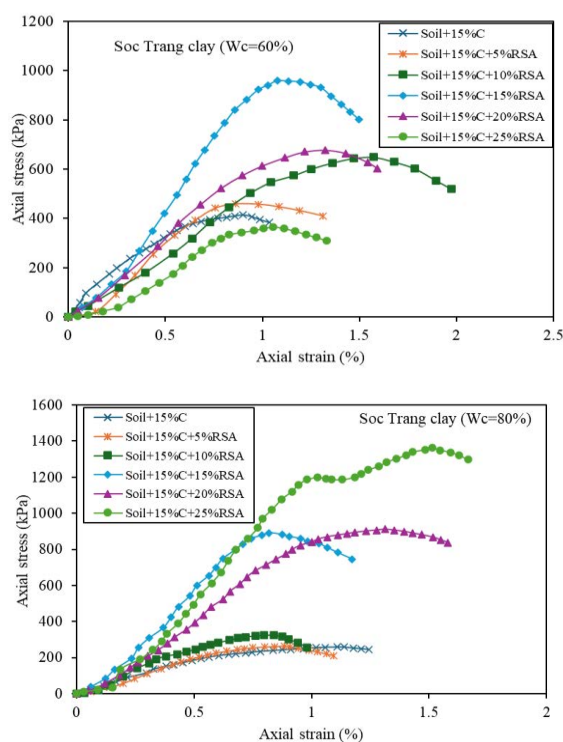


Figure 5. Relationship between axial stress and axial strain

The curve relationship between axial stress and axial strain of soil-cement-RSA mixtures prepared at different initial clay-water content ($W_c = 50\%$, 60% , 80%) is plotted in Figure 5. The results of UCS of soil-cement-mixtures at different W_c is depicted in Figure 6. In which, the test results of stabilized soil at $W_c = 50\%$ has been used in (Duong et al., 2025a).

The results in Figure 6 reveal that the UCS of stabilized soil at $W_c = 80\%$ is rather low when the RSA content of less than or equal to 10% is added to the soil-cement mixtures. This can be because when a small content of RSA is added to the soil-cement mixture at $W_c = 80\%$, the water content of stabilized soil is rather high (Figure 7). The high water content of stabilized soil may lead to excess water and a reduction in compressive strength. When RSA content of higher 10% is incorporated into the stabilized mixture, the UCS significantly increases. Additionally, as shown in Figure 4, at all W_c

levels, the UCS values tend to increase with increasing RSA content. In particular, at $W_c = 50\%$ and 60% , the UCS increases and reaches its highest value as the RSA content increases up to a threshold (optimum value), then shows a decreasing trend when the RSA content exceeds this threshold. In other words, at $W_c = 50\%$ and 60% , the highest UCS values are obtained at the optimum RSA content of 15% . Figure 8 shows the XRD results of stabilized soil without and with RSA incorporation at $W_c = 50\%$. It can be seen that the mineral composition of studied soil is significantly changed when the cement and cement+RSA mixture is added. When 15% of cement is added to the studied soil, the Calcium Silicate Hydrate (C-S-H) gel is formed and the peak of quartz decreases. When an optimum content of RSA of 15% is incorporated to the soil-cement mixture, the significant C-S-H gel is exhibited and the peak of quartz is substantially decreased. Accordingly, the peak of quartz is decreased from 1102.9 cps in untreated soil to 640.8 cps in soil+ $15\%C$ mixture and then decreased to 179.2 cps in soil+ $15\%C$ 15%RSA mixture. This indicates that the silicate has been dissolved through pozzolanic reactions to form C-S-H gel (John et al., 2018). This behavior is similar to that of rice husk ash when incorporating into the soil-cement mixture (Duong et al., 2025c, 2025b; Jongpradist et al., 2018; Yoobanpot and Jamsawang, 2014). The additional formation of C-S-H gel plays an important role in increasing the strength of stabilized soil (Horpibulsuk et al., 2009; Jongpradist et al., 2018; Mitchell and Soga, 2005; Yoobanpot and Jamsawang, 2014). Nevertheless, when the RSA content in the soil-cement mixture is increased to 25% , the peak intensity of quartz rises to 404.2 cps and less C-S-H gel is observed. This is due to the addition of a high RSA content results in the presence of residual RSA particles and then increases the peak intensity of quartz. Since the RSA is non-cementitious material, the residual of RSA and the reduced formation of C-S-H gel products leads to a decrease in the strength of stabilized soil.

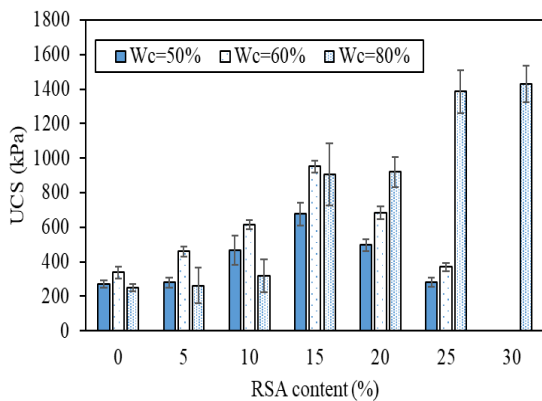


Figure 6. Relationship between RSA content and UCS of treated soil at different initial clay-water contents

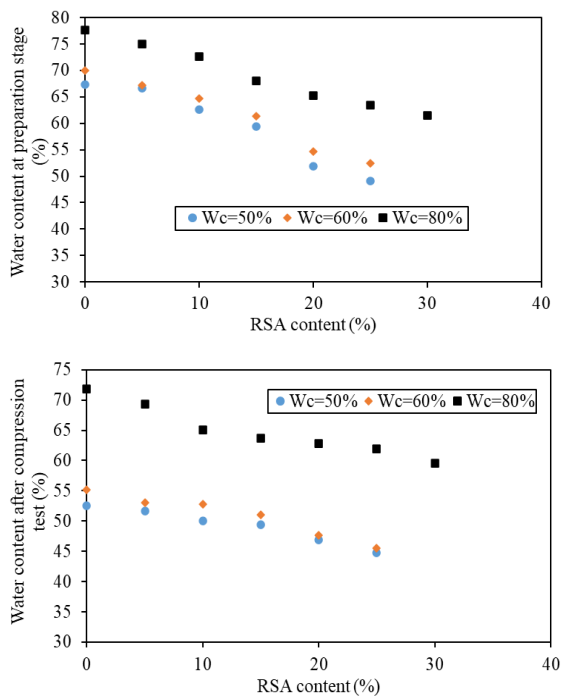


Figure 7. Water content after compression test of soil-cement mixing with different RSA content

Different from stabilized mixtures at $W_c = 50\%$ and 60% , the UCS values of stabilized soil at $W_c = 80\%$ continue to increase even when the RSA content exceeds 15% . Within the range of RSA content investigated in this study, the UCS of soil-cement-RSA mixtures at $W_c = 80\%$ exhibited the highest value at the RSA content of 30% . This finding indicates that the optimum RSA content for achieving the highest

UCS value of soil stabilized by cement and RSA depends on the initial clay-water content. Figure 9 presents the SEM images of stabilized soil mixture at various W_c levels. It can be observed that the soil matrix at $W_c = 80\%$ exhibits a markedly different microstructure compared to those at $W_c = 50\%$ and 60% . In particular, the matrix of stabilized soil with $15\%C+25\%RSA$ at $W_c = 50\%$ and 60% exhibits a highly porous structure with abundant voids (Figure 9a, b), whereas the stabilized soil with $15\%C+25\%RSA$ and $15\%C+30\%RSA$ at $W_c = 80\%$ exhibit a much denser and more compact matrix (Figure 9c, d). This proves that the strength of soil stabilized with $15\%C+25\%RSA$ and $15\%C+30\%RSA$ at $W_c = 80\%$ is significantly higher than that of soil stabilized with $15\%C+25\%RSA$ at $W_c = 50\%$ and 60% .

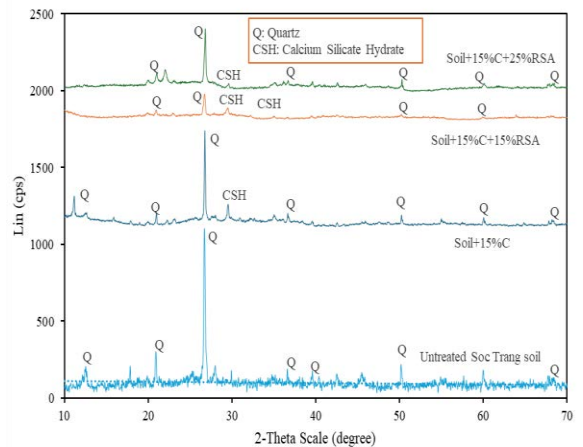
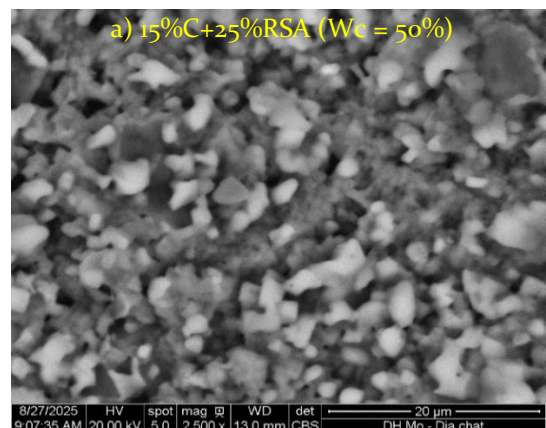


Figure 8. XRD results of stabilized soil at $W_c = 50\%$



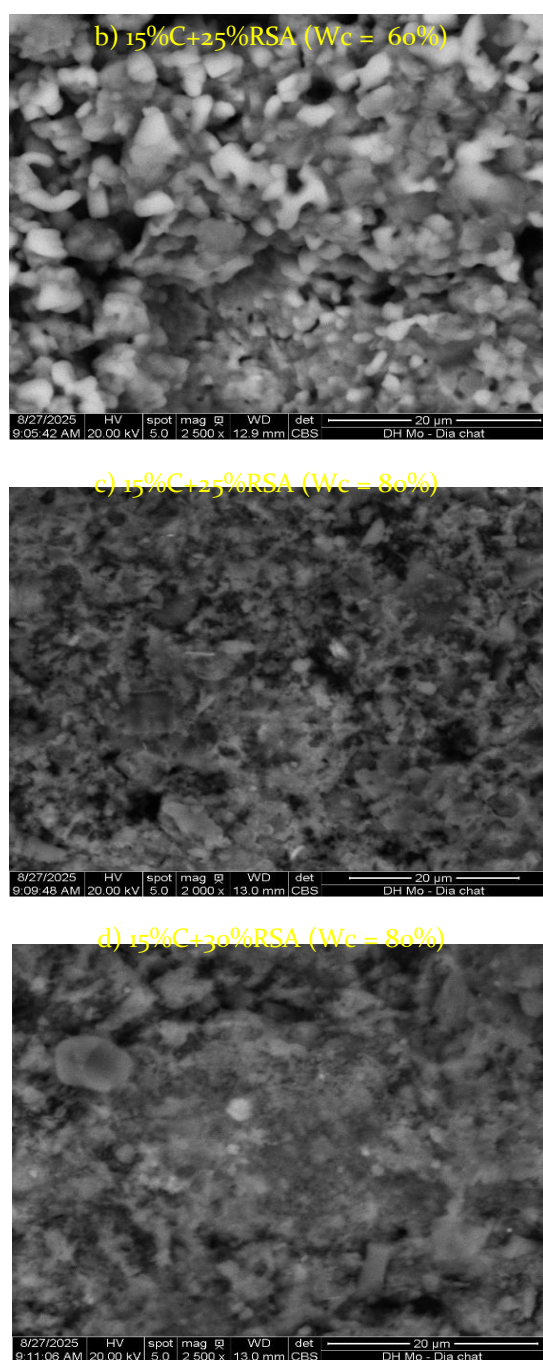


Figure 9. SEM images of stabilized soil at different Wc levels

CONCLUSIONS

This study investigated the effect of initial water content on the strength and microstructure of soil–cement–RSA mixtures. The results showed that the UCS is strongly

influenced by the initial clay–water content (Wc). At Wc = 50% and 60%, the UCS increased with RSA content up to an optimum of 15%, then declined, while at Wc = 80%, the UCS continued to rise and reached its maximum at 30% RSA. XRD and SEM analyses confirmed that RSA enhances pozzolanic reactions, leading to greater formation of C–S–H gel and a denser soil matrix, particularly at higher Wc. These findings indicate that both RSA and initial water content play crucial roles in determining the mechanical behavior of stabilized soils. Optimizing these parameters can improve soil strength and support the sustainable use of agricultural by-products in ground improvement applications.

ACKNOWLEDGMENT

This research is funded by project code B2024-MDA-o7 under the Ministry of Education and Training, Vietnam. The authors would like to thank the Geotechnical Lab, Department of Engineering Geology, Hanoi University of Mining and Geology, for their help during the experiments.

REFERENCES

- Abhishek, A., Guharay, A., Raghuram, A.S.S., Hata, T. (2024). A State-of-the-Art Review on Suitability of Rice Husk Ash as a Sustainable Additive for Geotechnical Applications. *Indian Geotech J* 54, 910–944. <https://doi.org/10.1007/s40098-024-00905-w>
- Anupam, A.K., Kumar, P., Ransinchung, G.D. (2013). Use of various agricultural and industrial waste materials in road construction. *Procedia-Social and Behavioral Sciences* 104, 264–273
- Basha, E.A., Hashim, R., Mahmud, H.B., Muntohar, A.S. (2005). Stabilization of residual soil with rice husk ash and cement. *Construction and building materials* 19, 448–453.
- Chen, R., Congress, S.S.C., Cai, G., Duan, W., Liu, S. (2021). Sustainable utilization of biomass waste-rice husk ash as a new solidified material of soil in geotechnical engineering: A review. *Construction and Building Materials* 292, 123219.

- Duong, N.T. (2022). Effect of rice husk ash on unconfined compressive strength of soil-cement admixture. *Suranaree Journal of Science & Technology* 29, 1-9.
- Duong, N.T., Phi, D.V., Duc, B.V., Piotr, O. (2025a). Applicability of rice straw ash incorporation with cement for soft soil improvement in the Mekong Delta, Vietnam. *Journal of Material Cycles and Waste Management* Under review (Round 1 completed).
- Duong, N.T., Phi, D.V., Phong, N.V. (2025b). Applicability of Rice Husk Ash for Cement-Stabilized Soil in the Mekong Delta, Vietnam. *Indian Geotech J.* <https://doi.org/10.1007/s40098-025-01418-w>.
- Duong, N.T., Van Duc, B., Van Phi, D. (2025c). Effect of Rice Husk Ash Incorporation on the Strength Development and Microstructural Properties of Stabilized Clayey Soil. *Arab J Sci Eng.* <https://doi.org/10.1007/s13369-025-10051-x>.
- Hasanbeigi, A., Price, L., Lu, H., Lan, W. (2010). Analysis of energy-efficiency opportunities for the cement industry in Shandong Province, China: A case study of 16 cement plants. *Energy* 35, 3461–3473.
- Horpibulsuk, S., Rachan, R., Raksachon, Y. (2009). Role of fly ash on strength and microstructure development in blended cement stabilized silty clay. *Soils and Foundations* 49, 85–98.
- John, E., Matschei, T., Stephan, D. (2018). Nucleation seeding with calcium silicate hydrate—A review. *Cement and Concrete Research* 113, 74–85.
- Jongpradist, P., Homtragoon, W., Sukkarak, R., Kongkitkul, W., Jamsawang, P. (2018). Efficiency of rice husk ash as cementitious material in high-strength cement-admixed clay. *Advances in Civil Engineering* 2018.
- Mitchell, J.K., Soga, K. (2005). *Fundamentals of soil behavior*. John Wiley & Sons New York.
- Sabat, A.K., Mohanta, S., Swain, S. (2015). Effect of moulding water content on geotechnical properties of rice straw ash stabilized expansive soil. *ARPJ. Eng. Appl. Sci* 10, 10427–10432.
- Yoobanpot, N., Jamsawang, P. (2014). Effect of cement replacement by rice husk ash on soft soil stabilization. *Kasetsart Journal-Natural Science* 48, 323–332.

DOI: 10.15625/vap.2025.0240

Assessment of marine debris pollution index at some beaches in Nghe An province

Dang Tran Quan, Duong Thi Lim, Nguyen Tran Dinh^{*}, Nguyen Thi Hue

Institute of Earth Sciences – Vietnam Academy of Science and Technology, 68 Huynh Thuc Khang Street, Lang Ward, Hanoi, Vietnam

^{*}Email: dt195986@gmail.com

Abstract: A total of 1,304 pieces of marine litter were collected from three beaches in Nghe An Province, with RT1 dominating at 93.79%, while RT2 and RT3 accounted for only 3.76% and 2.45%, respectively. The density of marine debris showed a similar trend, with the highest value at RT1 (0.98 items/m²) compared to RT2 (0.02 items/m²) and RT3 (0.016 items/m²). In terms of size, fragments measuring 5–25 mm were overwhelmingly dominant (75–95%), while the material composition revealed that plastics were the predominant type of debris, accounting for 91.84–96.97%. Polystyrene (PS) and polypropylene (PP) were the two most common types, consistent with studies conducted both domestically and internationally. The beach quality assessment indicated that RT1 had CCI (Clean Coast Index) values of 15.10 (extremely dirty) and PAI (Plastic Abundance Index) values of 4.83 (dirty), whereas RT2 and RT3 remained at very clean levels (CCI values < 1; PAI values < 0.3). Notably, HII (Hazardous Items Index) values at all three sites were very low (0.01–0.04), suggesting that pollution primarily originated from conventional plastic marine debris. This indicates that marine debris pollution in the study area is heterogeneous, being primarily concentrated at RT1, while RT2 and RT3 maintain much better beach environmental quality compared to most domestic and international beaches reported. This study not only provides important baseline data on marine debris in Nghe An but also contributes to comparisons with the pollution status of marine debris at national and international levels.

Keywords: Marine debris pollution, Beach quality index, Density, Material properties, Plastic composition.

INTRODUCTION

Marine debris is defined as all manufactured or processed materials (regardless of size) that are discarded, disposed of, or abandoned by humans in the marine or coastal environment (UNEP, 2011). Common types of marine debris found in the marine environment include plastics, metals, rubber, paper/cardboard, glass, wood, textiles, fishing gear, construction materials, and electronic waste (Okuku et al., 2020). The quantity and composition of marine debris vary across different regions of the world, influenced by local waste-generating activities as well as the specific natural characteristics of each area, such as river systems and hydrodynamic processes (Bergmann et al., 2015). Although any type of solid or semi-solid waste in the marine environment is a cause for concern, plastics remain the most widely studied and prevalent category (Hatje et al., 2013). According to recent studies, approximately 19–23 million tons (equivalent to 11% of the total global plastic waste generated in 2016) entered the oceans (Borrelle et al., 2020). The majority of marine debris (approximately 80%) originates from land-based sources, including household waste, industrial waste, and waste generated from coastal tourism activities (Mghili et al., 2020). A significant proportion originates from ineffective land-based solid waste management (Lau et al., 2020). In addition, rivers also serve as major transport pathways carrying marine debris into the ocean (Rech et al., 2014). In

particular, plastics persist in the marine environment for long periods (Hammer et al., 2012) and pose serious threats to marine animals through ingestion and entanglement in plastic fragments (Kühn & Van Franeker, 2020). Plastics also act as vectors for transporting chemical pollutants, with the potential to cause ecotoxicity and persist in marine ecosystems, thereby leading to severe ecological impacts (Caruso, 2019). In addition, single-use plastics generate significant carbon emissions, contributing to greenhouse gases and causing environmental harm (Zheng & Suh, 2019). Beyond environmental impacts, plastics also create numerous economic and social consequences, including the degradation of beach aesthetic value, negative effects on tourists' perceptions, reduced fisheries productivity, and direct threats to maritime safety (Rangel-Buitrago et al., 2018).

According to the Nghe An Provincial Portal, the locality has an 82 km-long coastline with many beautiful beaches, including Cua Lo, Cua Hoi, Bai Lu, Quynh Huong, Dien Thanh, and Cua Hien, and especially the Quynh coastal area, where numerous small beaches lie adjacent to one another (Wikipedia, 2025). In 2021, Nghe An Province generated approximately 192 tons of plastic waste per day, with a plastic waste generation index of 21, indicating that plastics accounted for a significant proportion of the total solid waste volume (WWF - VietNam, 2023). The average plastic waste collection rate in both urban and rural areas reached 70.2% (equivalent to 134.8 tons of plastic waste collected per day), while approximately 57.1 tons of plastic waste remained uncollected (WWF - VietNam, 2023). This indicates a serious warning about plastic waste pollution in Nghe An Province. In addition, activities such as river discharges, fisheries, tourism, and maritime transportation also pose potential risks of marine debris pollution in coastal areas (Sulochanan et al., 2019). Estimating the density and abundance of

marine debris on shorelines, the sea surface, and the seabed has become a central focus of many recent studies (Eo et al., 2018). At the same time, indices have been developed to support the management of marine debris pollution in coastal environments, aiming to classify beaches, such as: General Index (GI) (Marin et al., 2019), Clean Coast Index (CCI) (Alkalay et al., 2007), Plastic Abundance Index (PAI) (Rangel-Buitrago, Velez-Mendoza, et al., 2020), Plastic Pollution Index (PPI) (Fernandino et al., 2015), Hazardous Items Index (HII) (Rangel-Buitrago, Vergara-Cortés, et al., 2019).

The issue of marine debris dispersion is not only an environmental challenge but also poses risks to public health and social well-being. Therefore, the main objective of this study is to assess the level of marine debris pollution at selected beaches in Nghe An Province by applying three commonly used indices: CCI, PAI, and HII. The results aim to clarify the current status and the role of plastic waste within the overall marine debris, while also providing a scientific basis for management and proposing measures to mitigate debris pollution in coastal areas.

STUDY AREA AND METHODS

Study Area

Marine debris samples were collected from three beaches in December 2023, as shown in Figure 1. Figure 1a shows the map of Nghe An Province within the map of Vietnam, while Figure 1b presents an enlarged map of the sampling locations. The selected beaches are located in representative areas near river mouths, tourist sites, fishing grounds, as well as semi-urban and rural zones. Specifically, RT₁ is located near Cua Lo Port (18°49'21.7"N 105°43'04.7"E), RT₂ at Cua Lo Beach (18°47'52.2"N 105°43'52.5"E), and RT₃ at Cua Hoi Beach (18°45'49.0"N 105°45'30.1"E).

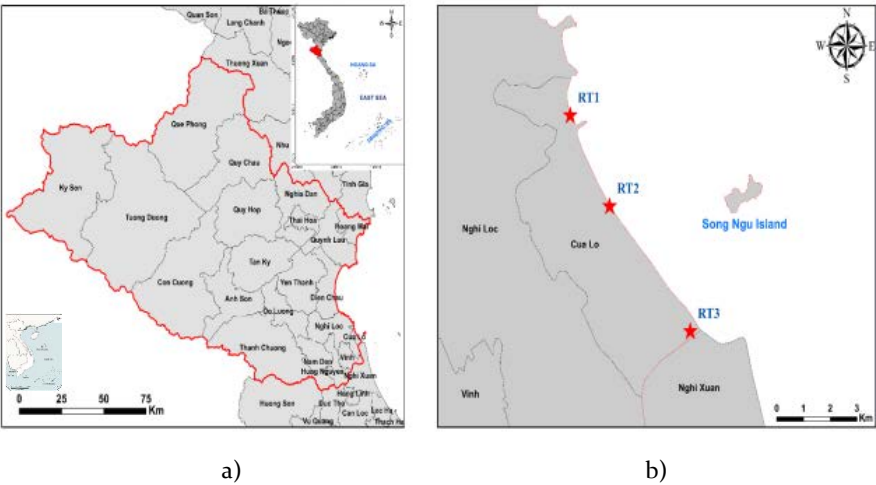


Figure 1: Study area

Research Methods

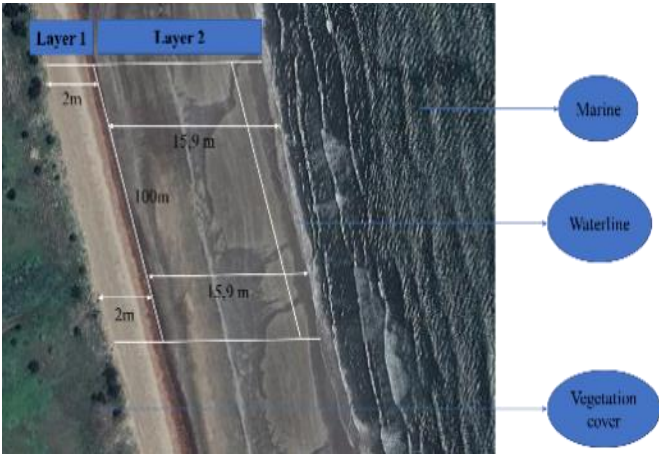
Marine Debris Sampling Method

The determination of the density and distribution of marine debris was carried out with reference to the NOAA Marine Debris Shoreline Survey Field Guide (Opfer et al., 2012), The Marine Debris Monitoring Guidelines of the European Commission in Europe (Hanke et al., 2013), and the Marine Debris Survey and Monitoring Guidelines of UNEP/IOC (Anthony Cheshire, 2009). At each beach, a transect sample was established with a length of 100 m and a width extending from the low-tide waterline to the area of the concrete

embankment or the upper vegetation line of the beach (Opfer et al., 2012). Specifically, at the RT₁ sampling site, the area was divided into two sampling units (Figure 2a). The sampling unit was established with a length of 100 m along the beach, extending from the waterline to the upper boundary regularly affected by tides. In addition, a 2m unit from the tide line to the vegetation cover was divided into five transects for sampling (Figure 2b). At sites RT₂ and RT₃, the sampling unit was also established with a length of 100 m along the beach. The corresponding sampling areas were 1,620 m² at RT₁, 2,110 m² at RT₂, and 2,030 m² at RT₃.



a) Marine litter image at RT₁



b) Schematic of the sampling unit at RT₁

Figure 2. Sampling site RT₁

Marine debris classification method

During the survey, all types of marine debris that could be visually identified and were larger than 5 mm, as well as the collected plastic debris, were directly gathered at each sampling point, placed in separate bags for storage, and transported to the laboratory (Figure 3). The results were recorded as the total number of marine litter items, the quantity of each type of debris according to material properties, and debris size. Collected marine debris samples were classified into eight main material groups: plastics, glass, wood, metals, rubber, textiles, paper, and others. This classification method was based on the guidelines of OSPAR (Wenneker & Oosterbaan, 2010).

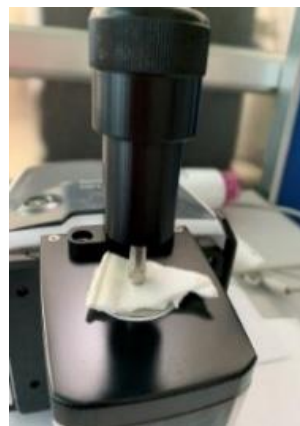


Figure 3. Marine debris classification

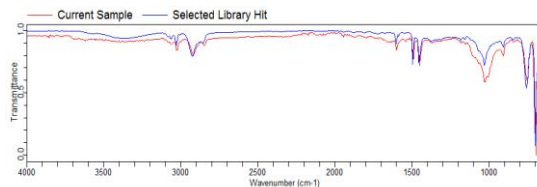
Method for determining plastic composition

Collected plastic debris samples from the beaches were rinsed with distilled water, dried at 60°C, and cooled to room temperature. FTIR measurements were then performed on these samples to obtain infrared spectra, which were compared with spectra available in the library (Löder et al., 2015). The results obtained identified the polymer type of each plastic debris sample (Ryan, 2015). The spectra were measured over the wavenumber range of 400–4000 cm⁻¹ with eight scans per sample. In this study, an Agilent Cary 630 FTIR device and the Agilent Polymer Handheld ATR Library were used, and polymers with a spectral match between the sample and reference spectra of ≥

0.7 were considered for identification (Figure 4a, b).



a) Agilent Cary 630 FTIR instrument



Quality	Library	CAS#	Name
0.94565	Agilent Polymer Handheld ATR Library (160)		styrene allyl alcohol copolymer, Hydroxyl content 5.4-6.9%, Chunks Powder CAS 25114
0.78748	Agilent Polymer Handheld ATR Library (126)		Polystyrene Coating
0.77098	Agilent Polymer Handheld ATR Library (127)		Polystyrene, clear solid part

b) Comparison of sample spectra with reference spectra from the library

Figure 4. Method for determining polymer composition using FTIR spectroscopy

Beach Quality Indices

Clean Coast Index (CCI)

CCI was developed by Alkalay et al. to assess the cleanliness level of beaches (Alkalay et al., 2007). This index is also used in this study as a tool to assess marine debris pollution. CCI is calculated using the following formula, where the coefficient K (value of 20) is included for statistical and practical reasons (Alkalay et al., 2007):

$$CCI = \frac{n}{S} * K \quad (1)$$

where CCI is the Clean Coast Index, n is the number of marine litter items identified within the sampling unit at the beach, S is the total area of the sampling unit in m², and K is the

coefficient. CCI values are categorized as follows: 'very clean' (0–2), 'clean' (2–5), 'moderate' (5–10), 'dirty' (10–20), and 'extremely dirty' (≥ 20)

Plastic Abundance Index (PAI)

This index reflects the proportion of plastic debris relative to the total amount of marine debris at a beach (Rangel-Buitrago, Barria-Herrera, et al., 2020). PAI is calculated using the following formula, where the coefficient K (value of 20) is included:

$$PAI = \left(\frac{\frac{\sum \text{Plastic debris}}{\log_{10} \sum \text{Marine debris}}}{\text{Total sampling area}} \right) \times 20 \quad (2)$$

PAI assesses plastic pollution at beaches and is classified into five categories: 0 corresponds to 'very low', 0.1–1 'low', 1.1–4 'moderate', 4.1–8 'high', and >8 'very high'

Hazardous Items Index (HII)

HII is applied to quantify the risk level posed by hazardous items present on beaches, including: (i) sharp objects capable of puncturing or causing injury, and (ii) toxic waste from industrial activities that may have direct or indirect physiological effects (Rangel-Buitrago, Vergara-Cortés, et al., 2019). HII value at each beach is determined using the following formula:

$$HII = \left(\frac{\frac{\sum \text{Hazardous debris}}{\log_{10} \sum \text{Marine debris}}}{\text{Total sampling area}} \right) \times 20 \quad (3)$$

HII is calculated based on the total number of hazardous items per m^2 , while also considering the relationship between the types of hazardous debris and the \log_{10} of the total marine debris collected in each surveyed area (Rangel-Buitrago, Vergara-Cortés, et al., 2019). This index allows for the assessment of beach environmental quality by classifying hazardous debris into five categories (Table 1).

Table 1. HII classification table

HII	Hazardous debris risk assessment
0	Not detected
0.1 – 1	Rare or not detected
1.1 – 4	A significant amount of hazardous debris detected
4.1 – 8	Very high amount of hazardous debris on the beach
> 8	Majority of the area covered by hazardous debris

Data processing method

After collection and classification, marine debris data were calculated and processed using Excel. The density of marine debris is expressed as the number of marine litter per unit area (n/m^2). The proportion of marine debris by material, size, and polymer composition is expressed as a percentage (%).

RESULTS AND DISCUSSION

Marine debris density and size:

A total of 1,304 debris items were collected from three beaches in Nghe An Province, with RT1 overwhelmingly dominating at 93.79%, while RT2 and RT3 accounted for only 3.76% and 2.45%, respectively, across the study area. Regarding debris density, a similar trend was observed, with RT1 reaching 0.98 n/m^2 , while RT2 and RT3 recorded only 0.02 and 0.016 n/m^2 , respectively (Figure 5a) a This significant difference can be explained by the geographic characteristics and socio-economic activities of the areas. Specifically, RT1 is located near a seaport, where intensive activities such as transportation, cargo handling, fishing, and vessel anchoring occur, leading to higher generation and accumulation of debris compared to other areas (Feld et al., 2022). In contrast, RT2 and RT3 exhibited lower values than RT1, reflecting that waste collection and management associated with tourism activities, as well as beach usage and exploitation in these areas, have been effectively implemented.

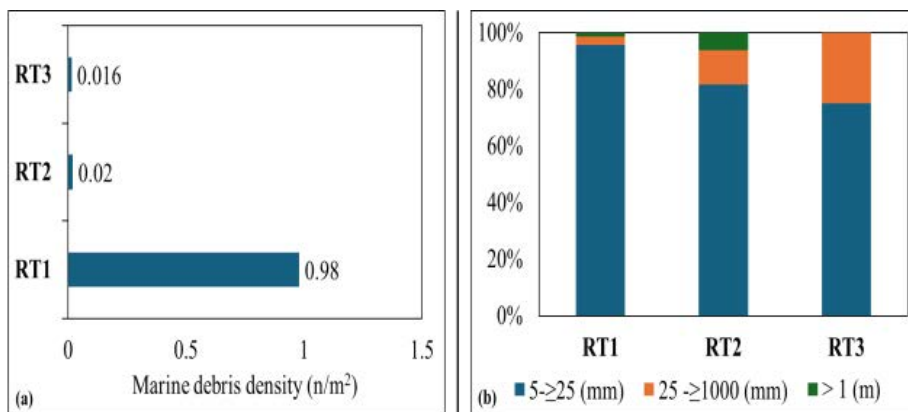


Figure 5. Density and size of marine debris

Table 2. Marine debris density in regions worldwide

Location	Number of beaches surveyed	Marine debris density (n/m ²)	Ref
RT1	1	0,98	[In this study]
RT2	1	0,02	
RT3	1	0,016	
Digha Beach and Sagar Island, Northeast India	17	Average of marine debris density 0.86	(Mugilarasan et al., 2021)
Kanyakumari Beach, South India	7	Average of marine debris density 6.71	(Perumal et al., 2023)
Kandakuliya, Kalpitiya Beach, Sri Lanka	6	Highest marine debris density 3.7	(Sandaruwan et al., 2023)
Hai Hoa, Hai Tien, and Sam Son Beaches, Vietnam	3	Marine debris density ranged from 0.28–1.21	(Lim et al., 2021)
Along the coast of China	24	Average density: 3.853	(Chen et al., 2020)
Caribe Beach, Colombia	25	Average density: 3.5	(Rangel-Buitrago, Mendoza, et al., 2019)

The marine debris density at RT1 (0.98 items/m²) is comparable to the average marine debris density at Digha Beach and Sagar Island, Northeast India, in Table 2 (Mugilarasan et al., 2021), but still markedly lower than the recorded “hotspots”. Specifically, the marine debris density at RT1 is 7.8 times lower than the average density at Kanyakumari Beach, South India (Perumal et al., 2023), and approximately 3.9 times lower than that reported along the coast of China (Chen et al., 2020). The value at RT1 is approximately 3.6–3.8 times lower than at two beaches in Sri Lanka and Colombia (Rangel-Buitrago, Mendoza, et al., 2019; Sandaruwan et al., 2023). In contrast, the

marine debris density at RT2 and RT3 is very low, not only lower than domestic reports (ranging from 0.28–1.21 items/m²; Lim et al., 2021) but also significantly lower than that of international beaches.

The results show that debris in all three areas—RT1, RT2, and RT3—is predominantly concentrated in the smaller size fractions at Figure 5b (5 – ≥25 mm). Specifically, RT1 accounted for 95.67%, RT2 for 81.63%, and RT3 for 75%. These results are consistent with studies in the Adriatic Sea, where Prizne also reported that debris larger than 5 mm was more common, representing 48% of all samples (Markić et al., 2024). Marine debris can be

degraded through various mechanisms, such as sunlight exposure, mechanical abrasion, hydrolysis, and photodegradation under UV radiation. These processes weaken the polymer structure, leading to fragmentation and the formation of smaller debris or plastic items (e.g., nylon bags, foam, food packaging...)(Halsband & Herzke, 2019; Moore, 2008).

Global studies indicate that small-sized debris (meso-sized) predominates on most beaches (Chen et al., 2020; Jefferson et al., 2025; Rangel-Buitrago, Mendoza, et al., 2019). In contrast, for medium-sized debris (25–≥1000 mm), the proportions recorded at RT3 (25%) and RT2 (12.24%) were significantly higher than at RT1 (2.95%), indicating that debris in these two areas tends to remain as larger fragments rather than breaking down into smaller pieces as observed at RT1. In contrast, for medium-sized debris (25–≥1000 mm), the proportions recorded at RT3 (25%) and RT2 (12.24%) were significantly higher than at RT1 (2.95%), indicating that debris in these two areas tends to remain as larger fragments rather than breaking down into smaller pieces as observed at RT1 (Moore, 2008). Notably, debris larger than 1 m was almost absent, appearing only at RT2 (6.12%) and RT1 (1.39%), while none was recorded at RT3. These large debris items are typically associated with bulky objects (nets, sacks, large plastic sheets) and are mainly scattered in areas with maritime activities

Classification of material properties and types of plastics in marine debris

Marine debris in all three areas was strongly dominated by plastic materials; however, significant differences were observed between the surveyed sites (Figure 6). At RT1, plastics dominated overwhelmingly (96.97%), while other materials such as paper (1.80%), rubber (0.41%), textiles (0.33%), as well as glass and others, appeared at very low proportions. This reflects the characteristic of debris in the port area, where plastics are commonly used in packaging, nylon bags, ropes, nets, and materials supporting transport and fishing activities (Feld et al., 2022). At RT2, plastics still

accounted for a high proportion (91.84%), but the debris composition was more diverse, with paper (6.12%) and rubber (2.04%) representing significant shares, indicating that the primary sources are related to coastal tourism and service activities. In contrast, RT3 exhibited a more varied material distribution, with plastics only accounting for 59.38%, while paper (31.25%) and textiles (9.38%) made up relatively high proportions, reflecting sources associated with local community activities and small-scale tourism. This difference can be explained by the influence of source factors: proximity to the port increases debris accumulation at RT1, while hydrodynamic conditions, wind, and currents disperse debris away from RT2 and RT3 (Mugilarasan et al., 2021).

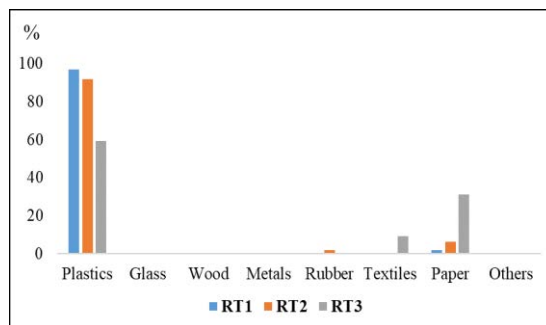


Figure 6. Material composition across survey sites

This trend is fully consistent with numerous international studies, where plastics are always recorded as the most common type of marine litter, such as at Digha Beach and Sagar Island, Northeast India (84.6%; Mugilarasan et al., 2021), Kalpitiya Beach, Sri Lanka (Sandaruwan et al., 2023), and along the Chinese coastline (71.8%; Chen et al., 2020). Some studies also confirmed the overwhelming dominance of plastics, specifically at the Caribbean coast, Colombia, where they accounted for up to 88% (Rangel-Buitrago, Mendoza, et al., 2019). Even in areas with a diverse range of debris types, plastics still accounted for the largest proportion, for example at Kanyakumari Beach, South India, with 65.08% (Perumal et al., 2023). This further confirms that plastics have become the dominant component of global marine litter,

reflecting their persistence, resistance to degradation, and widespread use in daily life.

Based on Figure 7 showing the composition of plastic types across the three sites, a clear difference in material composition is evident. At RT1, polystyrene (PS) dominates overwhelmingly at over 96%, while other types, such as polyethylene (PE) (1.63%), polypropylene (PP) (1.37%), high-density polyethylene (HDPE) (1.46%), and polyethylene terephthalate (PET) (0.60%) account for only a small fraction. These findings are consistent with the authors' previous study conducted at Hai Hoa, Hai Tien, and Sam Son beaches in Vietnam, where PS was the most abundant plastic (77%), followed by PP at 17% (Lim et al., 2021). Similarly, a study at the Caribbean coast, Colombia, also reported an average PS plastics proportion of up to 88% (Rangel-Buitrago, Mendoza, et al., 2019). This can be explained by the fact that PS plastics are widely used in packaging, construction materials, and maritime activities, yet they have low recyclability. The presence of PS in the marine environment may originate from various sources such as river runoff, rainfall, wastewater treatment plants, structural degradation, shipping activities, or direct disposal (Kwon et al., 2017). With its lightweight properties, PS can be easily carried away by waves and wind, thereby spreading rapidly across the marine environment (Lim et al., 2021).

This reflects that the main source of debris comes from PS foam products used in packaging, containers, and cargo wrapping materials - commonly utilized in port-related transport activities. At RT2, although PS still Table 3 show clear differences between the surveyed sites. At RT1, CCI reached 15.10 and PAI was 4.83, significantly higher than at RT2 and RT3, indicating that this area experiences much greater marine debris pressure and is classified as "extremely dirty" according to the debris pollution scale, while also considered "dirty" based on the plastic pollution index. In

accounted for the highest proportion (61.7%), other plastics such as PP (17.0%), PET (8.5%), HDPE (6.4%), and PE (2.1%) contributed more significantly, reflecting a more diverse origin of debris associated with tourism and coastal service activities. In contrast, at RT3, PS accounted for only 15%, while PP (45%) and HDPE (30%) were dominant, accompanied by PET (5%) and virtually no PE. This composition indicates that debris at RT3 mainly originates from local community activities and small-scale fisheries. Overall, PS dominates at RT1 and RT2 due to port and tourism activities, whereas RT3 reflects the characteristics of local community life and fisheries, with higher proportions of PP and HDPE—plastics commonly used in daily activities and fishing.

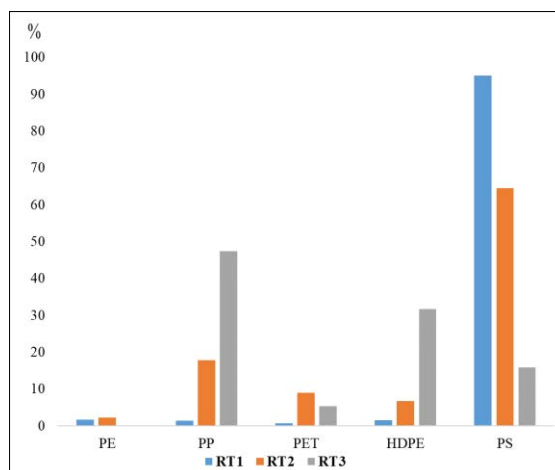


Figure 7. Proportion of plastic types in marine plastic debris

Beach quality index

Based on formulas (1), (2), and (3), the beach quality indices calculated in contrast, RT2 and RT3 exhibited very low CCI, PAI, and HII values ($CCI < 1$; $PAI < 0.3$), reflecting a "very clean" environmental status for both marine debris and plastic debris. Notably, hazardous debris was almost undetected at all three sites, indicating that the direct risk from such debris to the environment and human health is negligible.

Table 3: Beach quality indices at the study sites

Location	CCI	PAI	HII	Marine debris pollution	Plastic pollution	Hazardous debris risk
RT1	15,1	4,83	0,02	Extremely dirty	Dirty	Not detected
RT2	0,46	0,25	0,01	Very clean	Clean	Not detected
RT3	0,32	0,12	0,04	Very clean	Clean	Not detected

At RT₁, the CCI value reached 15.10, reflecting an “extremely dirty” status. This level is 16.2 times higher than the average at Shantou Beach, China (CCI: 0.93; Pervez et al., 2025), 2.2 times higher than at Las Salinas Beach, Chile (CCI: 6.8; Rangel-Buitrago, Vergara-Cortés, et al., 2019), and 1.3–1.7 times higher than at Digha Beach and Sagar Island, Northeast India (Average CCI ranged from 8.98 to 11.34; Mugilarasan et al., 2021). However, compared to some other regions worldwide, CCI at RT₁ is still much lower, specifically about 3.1 times lower than the average CCI value at the Caribbean coast, Colombia (Average CCI: 46.1; Rangel-Buitrago, Mendoza, et al., 2019) and approximately 1.6 times lower than the highest value recorded at Hai Hoa – Hai Tien – Sam Son Beaches (CCI ranged from 5.6 to 24.1; Lim et al., 2021). A similar trend was observed at Kanyakumari Beach, South India, and Kalpitiya Beach, Sri Lanka, with values approximately 1.5–1.8 times lower CCI ranged from 22.7 to 27.24 (Perumal et al., 2023; Sandaruwan et al., 2023). This indicates that marine debris pollution in the study area is heterogeneous, being primarily concentrated at RT₁, while RT₂ and RT₃ maintain much better beach environmental quality compared to most domestic and international beaches reported.

Regarding PAI, the value at RT₁ (4.83) is 10.7 times higher than the average PAI at Shantou Beach, China (Average PAI: 0.45; Pervez et al., 2025) and 1.97 times higher at Kandakuliva-Kalpitiya Beach, Sri Lanka (Average PAI: 2.45; Sandaruwan et al., 2023). However, these results are consistent with the study at Kanyakumari Beach, South India, where the average PAI was 4.40 (Perumal et al., 2023). These results indicate that plastic pollution at certain beaches in Nghe An province is at an alarming level. In contrast, HII values at all

three surveyed sites (0.01–0.04) were very low, reflecting a negligible presence of hazardous debris. These values are much lower than those reported in other studies worldwide, specifically lower than at Las Salinas Beach, Viña Del Mar, Chile (Average HII: 0.95; Rangel-Buitrago, Vergara-Cortés, et al., 2019), and in the Northeast India region (Average HII ranged from 0.52 to 0.62; Mugilarasan et al., 2021). However, these results are quite similar to Shantou Beach, China, with an average HII value of 0.03 (Pervez et al., 2025). Although the overall marine debris pollution (CCI) and plastic pollution (PAI) at some beaches in Nghe An province are at alarming levels, the risk from hazardous debris (HII) is almost negligible.

CONCLUSION

The study results indicate that marine debris pollution in Nghe An is unevenly distributed, with a concentration primarily at the beach near Cua Lo Port, while other beaches remain relatively clean. Plastics dominate all samples, particularly non-recyclable types such as PS and PP, highlighting potential threats to the marine ecosystem. Environmental indices clearly show that debris pollution (based on CCI index) and plastic pollution (based on PAI index) have reached warning levels, whereas the risk from hazardous items (based on HII index) remains negligible. These findings underscore the necessity of implementing coastal plastic waste management measures, especially in port areas and tourist hubs, to reduce environmental pressure and sustainably protect coastal ecosystems.

To mitigate marine debris pollution in the study area, it is recommended to enhance waste collection and recycling systems,

establish monitoring programs for beach cleanliness, promote community awareness and education on plastic waste reduction, and strengthen the enforcement of waste discharge regulations in coastal and marine activities.

ACKNOWLEDGMENTS

This study was funded by the National Foundation for Science and Technology Development (NAFOSTED) under project code 105.08-2021.09.

DECLARATION

The authors hereby declare that this is our original research work and has not been submitted to any other journal for publication

REFERENCES

- Alkalay, R., Pasternak, G., & Zask, A. (2007). Clean-coast index—A new approach for beach cleanliness assessment. *Ocean & Coastal Management*, 50(5–6), 352–362.
- Anthony Cheshire. (2009). (PDF) UNEP/IOC Guidelines on Survey and Monitoring of Marine Litter. ResearchGate. https://www.researchgate.net/publication/256186638_UNEPIOC_Guidelines_on_Survey_and_Monitoring_of_Marine_Litter
- Bergmann, M., Gutow, L., & Klages, M. (2015). Marine anthropogenic litter. Springer Nature.
- Borrelle, S. B., Ringma, J., Law, K. L., Monnahan, C. C., Lebreton, L., McGivern, A., Murphy, E., Jambeck, J., Leonard, G. H., Hilleary, M. A., Eriksen, M., Possingham, H. P., De Frond, H., Gerber, L. R., Polidoro, B., Tahir, A., Bernard, M., Mallos, N., Barnes, M., & Rochman, C. M. (2020). Predicted growth in plastic waste exceeds efforts to mitigate plastic pollution. *Science*, 369(6510), 1515–1518. <https://doi.org/10.1126/science.aba3656>
- Caruso, G. (2019). Microplastics as vectors of contaminants. *Marine Pollution Bulletin*, 146, 921–924.
- Chen, H., Wang, S., Guo, H., Lin, H., & Zhang, Y. (2020). A nationwide assessment of litter on China's beaches using citizen science data. *Environmental Pollution*, 258, 113756.
- Eo, S., Hong, S. H., Song, Y. K., Lee, J., Lee, J., & Shim, W. J. (2018). Abundance, composition, and distribution of microplastics larger than 20 µm in sand beaches of South Korea. *Environmental Pollution*, 238, 894–902.
- Feld, L., da Silva, V. H., & Strand, J. (2022). Characterization of foamed plastic litter on Danish reference beaches—Pollution assessment and multivariate exploratory analysis. *Marine Pollution Bulletin*, 180, 113774.
- Fernandino, G., Elliff, C. I., Silva, I. R., & Bittencourt, A. (2015). How many pellets are too many? The pellet pollution index as a tool to assess beach pollution by plastic resin pellets in Salvador, Bahia, Brazil. *Journal of Integrated Coastal Zone Management*, 15(3), 325–332.
- Halsband, C., & Herzke, D. (2019). Plastic litter in the European Arctic: What do we know? *Emerging Contaminants*, 5, 308–318.
- Hammer, J., Kraak, M. H., & Parsons, J. R. (2012). Plastics in the marine environment: The dark side of a modern gift. *Reviews of Environmental Contamination and Toxicology*, 1–44.
- Hanke, G., Galgani, F., Werner, S., Oosterbaan, L., Nilsson, P., Fleet, D., Kinsey, S., Thompson, R., Palatinus, A., Van, F. J. A., Vlachogianni, T., Scoullou, M., Veiga, J. M., Matiddi, M., Alcaro, L., Maes, T., Korpinen, S., Budziak, A., Leslie, H., ... Liebezeit, G. (2013). Guidance on Monitoring of Marine Litter in European Seas. JRC Publications Repository. <https://doi.org/10.2788/99816>
- Hatje, V., Costa, M. F. da, & Cunha, L. C. da. (2013). Oceanografia e Química: Unindo conhecimentos em prol dos oceanos e da sociedade. *Química Nova*, 36, 1497–1508.
- Jefferson, A. J., Kearns, K., Snyder, K., Mitchell, A., Muratori, S., & Rowan, C. J. (2025). Anthropogenic litter and plastics across size classes on a mechanically groomed Great Lakes urban beach. *Journal of Great Lakes Research*, 51(2), 102505. <https://doi.org/10.1016/j.jglr.2024.102505>
- Kühn, S., & Van Franeker, J. A. (2020). Quantitative overview of marine debris ingested by marine megafauna. *Marine Pollution Bulletin*, 151, 110858.
- Kwon, B. G., Amamiya, K., Sato, H., Chung, S.-Y., Kodera, Y., Kim, S.-K., Lee, E. J., & Saido, K. (2017). Monitoring of styrene oligomers as indicators of polystyrene plastic pollution in the North-West Pacific Ocean. *Chemosphere*, 180, 500–505. <https://doi.org/10.1016/j.chemosphere.2017.04.060>
- Lau, W. W., Shiran, Y., Bailey, R. M., Cook, E., Stuchtey, M. R., Koskella, J., Velis, C. A., Godfrey, L., Boucher, J., & Murphy, M. B. (2020). Evaluating scenarios toward zero plastic pollution. *Science*, 369(6510), 1455–1461.

- Lim, D. T., Nguyen, T. L. H., Nguyen, T. H., Dang, T. Q., Nguyen, T. H. T., Tran, T. T., Trinh, T. M. T., Dao, N. N., Nguyen, Q. B., & Mai, V. T. (2021). Preliminary assessment of marine debris pollution and coastal water quality on some beaches in Thanh Hoa province, Vietnam. *Vietnam Journal of Marine Science and Technology*, 21(3), 329–340. <https://doi.org/10.15625/1859-3097/15951>
- Löder, M. G. J., Kuczera, M., Mintenig, S., Lorenz, C., & Gerdt, G. (2015). Focal plane array detector-based micro-Fourier-transform infrared imaging for the analysis of microplastics in environmental samples. *Environmental Chemistry*, 12(5), 563–581. <https://doi.org/10.1071/EN14205>
- Marin, C. B., Niero, H., Zinnke, I., Pellizzetti, M. A., Santos, P. H., Rudolf, A. C., Beltrão, M., de Souza Waltrick, D., & Polette, M. (2019). Marine debris and pollution indexes on the beaches of Santa Catarina State, Brazil. *Regional Studies in Marine Science*, 31, 100771.
- Markić, A., Iveša, N., Budiša, A., Kovačić, I., Burić, P., Pustijanac, E., Buršić, M., Banai, B., Legin, D. P., Palatinus, A., & Tutman, P. (2024). Fragmented marine plastics as the prevalent litter type on a small island beach in the Adriatic. *Marine Pollution Bulletin*, 203, 116467. <https://doi.org/10.1016/j.marpolbul.2024.116467>
- Mghili, B., Analla, M., Aksissou, M., & Aissa, C. (2020). Marine debris in moroccan Mediterranean beaches: An assessment of their abundance, composition and sources. *Marine Pollution Bulletin*, 160, 111692.
- Moore, C. J. (2008). Synthetic polymers in the marine environment: A rapidly increasing, long-term threat. *Environmental Research*, 108(2), 131–139.
- Mugilarasan, M., Karthik, R., Purvaja, R., Robin, R. S., Subbareddy, B., Hariharan, G., Rohan, S., Jinoj, T. P. S., Anandavelu, I., Pugalenth, P., & Ramesh, R. (2021). Spatiotemporal variations in anthropogenic marine litter pollution along the northeast beaches of India. *Environmental Pollution*, 280, 116954. <https://doi.org/10.1016/j.envpol.2021.116954>
- Okuku, E. O., Kiteresi, L. I., Owato, G., Mwalugha, C., Omire, J., Mbuche, M., Chepkemboi, P., Ndwiga, J., Nelson, A., Kenneth, O., Lilian, M., & Brenda, G. (2020). Baseline meso-litter pollution in selected coastal beaches of Kenya: Where do we concentrate our intervention efforts? *Marine Pollution Bulletin*, 158, 111420. <https://doi.org/10.1016/j.marpolbul.2020.111420>
- Opfer, S., Arthur, C., & Lippiatt, S. (2012). NOAA Marine Debris Shoreline Survey Field Guide.
- Perumal, K., Muthuramalingam, S., & Chellaiyan, S. (2023). Marine litter on the beaches of the Kanyakumari, Southern India: An assessment of their abundance and pollution indices. *Marine Pollution Bulletin*, 186, 114443. <https://doi.org/10.1016/j.marpolbul.2022.114443>
- Pervez, R., Jia, C., Sardar, M., Lai, Y., Jattak, Z. U., & Lai, Z. (2025). Spatiotemporal trends and index-based assessment of beach litter abundance and pollution status on Shantou beaches, China. *Marine Pollution Bulletin*, 221, 118584. <https://doi.org/10.1016/j.marpolbul.2025.118584>
- Rangel-Buitrago, N., Barria-Herrera, J., Vergara-Cortés, H., Contreras-López, M., & Agredano, R. (2020). A snapshot of the litter problem along the Viña del Mar-Concón coastal strip, Valparaíso region, Chile. *Marine Pollution Bulletin*, 160, 111524.
- Rangel-Buitrago, N., Gracia, A., Vélez-Mendoza, A., Mantilla-Barbosa, E., Arana, V. A., Trilleras, J., & Arroyo-Olarte, H. (2018). Abundance and distribution of beach litter along the Atlántico Department, Caribbean coast of Colombia. *Marine Pollution Bulletin*, 136, 435–447.
- Rangel-Buitrago, N., Mendoza, A. V., Gracia, C. A., Mantilla-Barbosa, E., Arana, V. A., Trilleras, J., & Arroyo-Olarte, H. (2019). Litter impacts on cleanliness and environmental status of Atlántico department beaches, Colombian Caribbean coast. *Ocean & Coastal Management*, 179, 104835. <https://doi.org/10.1016/j.ocecoaman.2019.104835>
- Rangel-Buitrago, N., Velez-Mendoza, A., Gracia, A., & Neal, W. J. (2020). The impact of anthropogenic litter on Colombia's central Caribbean beaches. *Marine Pollution Bulletin*, 152, 110909.
- Rangel-Buitrago, N., Vergara-Cortés, H., Barria-Herrera, J., Contreras-López, M., & Agredano, R. (2019). Marine debris occurrence along Las Salinas beach, Viña Del Mar (Chile): Magnitudes, impacts and management. *Ocean & Coastal Management*, 178, 104842.
- Rech, S., Macaya-Caquilpán, V., Pantoja, J. F., Rivadeneira, M. M., Madariaga, D. J., & Thiel, M. (2014). Rivers as a source of marine litter—a study from the SE Pacific. *Marine Pollution Bulletin*, 82(1–2), 66–75.
- Ryan, P. G. (2015). *Marine Anthropogenic Litter* | SpringerLink. <https://link.springer.com/book/10.1007/978-3-319-16510-3>

- Sandaruwan, R. D. C., Bellanthudawa, B. K. A., Perera, I. J. J. U. N., Udayanga, K. A. S., & Jayapala, H. P. S. (2023). Index based approach for assessment of abundance of marine debris and status of marine pollution in Kandakuliya, Kalpitiya, Sri Lanka. *Marine Pollution Bulletin*, 197, 115724. <https://doi.org/10.1016/j.marpolbul.2023.115724>
- Sulochanan, B., Veena, S., Ratheesh, L., Padua, S., Rohit, P., Kaladharan, P., & Kripa, V. (2019). Temporal and spatial variability of beach litter in Mangaluru, India. *Marine Pollution Bulletin*, 149, 110541.
- UNEP, N. (2011). The Honolulu strategy: A global framework for prevention and management of marine debris. NOAA, UNEP.
- Wenneker, B., & Oosterbaan, L. (2010). Guideline for Monitoring Marine Litter on the Beaches in the OSPAR Maritime Area. Edition 1.0.
- Wikipedia. (2025). Nghe An. In Wikipedia. https://vi.wikipedia.org/w/index.php?title=Ngh%E1%BB%87_An&oldid=73760242
- WWF - VietNam. (2023). Plastic Waste Generation Report 2022.
- Zheng, J., & Suh, S. (2019). Strategies to reduce the global carbon footprint of plastics. *Nature Climate Change*, 9(5), 374–378.

Assessment of microplastic pollution in coastal waters of the Cai Lon – Cai Be estuary, Vietnam

Nguyen Thi Thu Uyen^{1,2}, Pham Lan Anh^{1,2}, Tran Dang Quy^{1,2}, Nguyen Dinh Thai¹, Dang Bao Duong^{1,2}, Nguyen Hai Nam^{1,2}, Nguyen Doanh Khoa^{1,2}, Nguyen Thi Huyen Trang¹, Ha Ngoc Anh¹, Luu Viet Dung^{1,2*}

¹Faculty of Geology, University of Science, Vietnam National University, Hanoi

²VNU Key laboratory of Geoenvironmental and Climate change response, University of Science, Vietnam National University, Hanoi

*Email: dungluuviet@hus.edu.vn

Abstract: Estuaries function as natural pollution traps at the land-sea interface, often containing higher concentrations of microplastics than nearby rivers and offshore areas, which poses significant risks to ecosystems and the coastal environment. However, there is still a lack of research on microplastic pollution in estuaries, which limits our understanding of its impact on these ecosystems. The present study investigated a survey on microplastic pollution in the surface waters of the Cai Lon - Cai Be estuary. Results indicated that microplastic abundance ranged from 1.49 to 20.68 particles/m³, with an average of 10.61 ± 7.09 particles/m³. Microfibers were the predominant type, constituting over 90% of the samples, while microfragments and microfilms were less common. The average length of microplastic fibers was 1227.09 ± 846.38 μ m, with the 400–1000 μ m size group accounting for the highest proportion (57.41%). The main colors of microplastics were transparent (58.62%) and blue (22.41%). Study results also revealed that areas with high human activity had greater concentrations of microplastics. This study provides compelling evidence of significant microplastic pollution in the Cai Lon - Cai Be estuary, which may have adverse effects on the estuarine ecosystem.

Keywords: microplastics, estuary, Cai Lon – Cai Be, coastal waters

Introduction

Estuaries represent distinctive transitional zones where terrestrial environments interface with marine ecosystems, shaped by the interplay of fluvial hydrology and coastal tidal dynamics. These areas function as convergence zones for water flow, suspended particulates, and nutrients, while serving as both sinks and conduits for pollutants transferred from terrestrial sources to the marine environment, including microplastics. Microplastics are plastic particles smaller than 5 mm (NOAA 2015). They originate from the breakdown of larger plastic items (secondary microplastics) and from the production of tiny particles for uses such as cosmetics and pharmaceuticals (primary microplastics). Due to their persistence and resistance to biodegradation, microplastics can remain in the environment for several hundred years. Their presence poses significant risks to aquatic ecosystems and human health through mechanisms of trophic transfer, wherein contaminants are incorporated into marine food webs (Luís Gabriel Antão Barboza, A. Dick Vethaak et al. 2018).

Numerous studies worldwide have documented the pervasive presence of microplastics in riverine and estuarine systems - areas considered to be "gateways" for transporting plastics from the mainland to the sea. (Jiaxu Zhang, Chenglong Zhang et al. 2019). In Africa, surveys reported microplastic

concentration in water ranging from 10 to 168 particles/m³ in the Sebou Estuary (Morocco). In North America, McEachern et al. (2019) recorded a concentration of microplastics of 4.5 particles/m³ in an estuary of Tampa Bay (USA), whereas microplastic concentration in the St. Lawrence River Estuary (Canada) was considerably higher, reaching 120 particles/m³ (Kinsley McEachern, Henry Alegria et al. 2019, Noreen E Kelly 2024). In Asia, several studies have also shown substantial microplastic contamination in major estuaries. For example, the Meghna Estuary (Bangladesh) reached 128.89 particles/m³, and estuaries in southern China showed concentrations ranging from 800 to 42,800 particles/m³, with an average of 18,261 particles/m³ (M Belal Hossain, Jimmy Yu et al. 2023, Chaonan Zhang, Shaodan Wang et al. 2023). Importantly, most of these studies revealed that microfibers represent the dominant type of microplastics in estuarine environments. Thus, recent research results underscore that microplastic pollution constitutes a pressing global environmental issue, with particular concern in coastal estuaries, where land-based discharges converge and play a critical role in transporting plastic waste into the ocean.

Recent research on microplastics in Vietnam's estuarine and coastal waters has significantly increased, revealing concerning pollution levels and pronounced spatial variability. In northern Vietnam, microplastic density in coastal waters varied in a wide range, from low density such as in the Dien Vong estuary (0.10 particles/m³) and Mong Duong river (0.12 particles/m³) (Hung Son Pham, Huu Huan Nguyen et al. 2022), to high density at the Ba Lat estuary (65 particles/m³) (Thi Thao Nguyen, Stéphanie Lebarillier et al. 2024). In the North Central Coast and South Central Coast regions, microplastic concentrations range from 35 to 175 particles/m³ at the Thuan An estuary, Hue city (Thi Ngan Ha Truong, Thi Thao Linh Phan et al. 2023). On the contrary, the microplastic concentrations from the Han River estuary and the Cu De estuary (Da Nang) showed significantly higher levels, with average values of 500 ± 600 particles/m³ and 210 ± 80

particles/m³, respectively (Quynh Anh Tran-Nguyen, Tuan Quy Nguyen et al. 2023). In the Hoi estuary, Thanh Hoa province, the microplastic pollution level was higher, reaching an average of 45.6 ± 49.6 particles/m³ (Thi Lim Duong, Thi Huong Thuy Nguyen et al. 2024). In the Southern region, a study at the Can Gio estuary documented an average density of 1.15 particles/m³ (Hoa Thi Pham, Tinh Quoc Pham et al. 2024). These findings demonstrate that microplastic pollution in Vietnam exhibits substantial spatial variability, which is influenced by different hydrological characteristics and anthropogenic impacts across estuarine systems.

Despite some important publications, research on microplastics in the Mekong Delta region's estuaries remains limited. Notably, the Cai Lon – Cai Be estuary system, which is significant for waterway transportation and aquaculture, has not yet been the subject of scientific research. This area is particularly susceptible to microplastic pollution due to the considerable amount of domestic, agricultural, and industrial waste it receives from the surrounding areas. Therefore, the present study aims to assess microplastic pollution in the surface waters of the Cai Lon – Cai Be estuary, focusing on key characteristics such as abundance, morphology, color, size, sources, and distribution. The findings not only expand the existing data on microplastic occurrence in the Mekong Delta but also provide an essential scientific basis for management strategies to reduce microplastic pollution in coastal estuarine systems.

MATERIALS AND METHODS

Study area

The Cai Lon – Cai Be estuary is part of the Mekong River system that flows into the western part of the East Sea. The area is characterized by highly complex hydrodynamic conditions arising from the combined influences of tidal regimes, riverine flows, and coastal fisheries activities. It plays a crucial role in the socio-economic development of the region, particularly through aquaculture and

capture fisheries, while also acting as a receiving body for domestic, agricultural, and industrial effluents from the upstream catchments. The locations of the sampling sites for surface-water microplastic analysis are shown in (Table 1 and Figure 1).

Field sampling

Microplastic samples were collected from eight sites in the Cai Lon – Cai Be estuarine

area. Sampling was conducted using a plankton net with a mesh size of 0.35 mm, which is suitable for retaining microplastic particles smaller than 5 mm. A General Oceanics flowmeter was mounted at the net mouth to record both the water volume and flow velocity passing through the net, thereby enabling accurate calculation of the filtered water volume.

Table 1. The sample sites description

Sample ID	Latitude (N)	Longitude (E)	Site characteristics
KG1	9°57'33.30"	105° 4'20.10"	Left bank of the Cai Lon estuary; numerous local fishing huts
KG2	9°57'10.35"	105° 5'18.65"	Central area of the Cai Lon – Cai Be estuary, near an urban zone
KG3	9°56'5.20"	105° 5'39.90"	Busy area with dense boat traffic; shellfish harvesting (clam/ark clam dredging)
KG4	9°53'56.00"	105° 5'55.89"	Area with limited human activities
KG5	9°51'30.43"	105° 7'2.09"	On the Cai Lon River near a bridge, human activities include an old ferry pier (Xeo Ro), a residential area, and a local market.
KG6	9°55'33.90"	105° 6'14.70"	Right bank of the Cai Be River; downstream from a fishmeal processing facility; boat mooring (Xeo Coi ferry pier)
KG7	9°54'0.40"	105° 6'53.80"	Left bank of the Cai Be River; near a boat anchorage area (Vam Ba Lich ferry pier)
KG8	9°52'37.80"	105° 7'21.30"	Left bank of the Cai Be River, near the market and Tac Cau fishing port

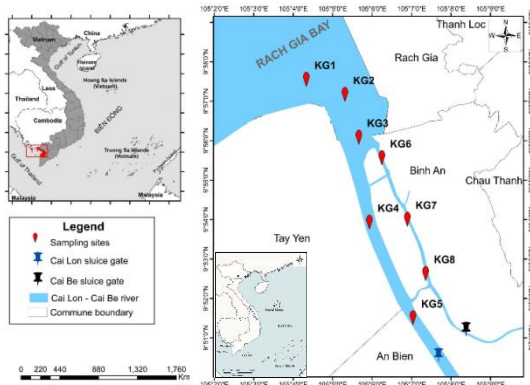


Figure 1. Sampling sites in the Cai Lon – Cai Be estuary

The plankton net was submerged and towed continuously during each sampling for 60 to 120 seconds. Both the towing time and flow velocity were recorded simultaneously to

calculate the volume of water sampled. After collection, materials larger than 5 mm were removed, and the remaining water samples were transferred into pre-cleaned glass or polyethylene (PE) bottles. Samples were immediately stored at low temperatures in the field to minimize physicochemical and biological alterations, ensuring that microplastic particles retained their natural state before laboratory analysis.

Microplastics analysis

In the laboratory, microplastics in samples were wet-sieved using a 0.3 mm mesh to remove residual sodium chloride (NaCl) and then dried at 60°C until they reached a constant weight. Organic matter was digested using a combination of 30% hydrogen peroxide (H₂O₂) and 0.5 M iron(II) sulfate (FeSO₄), with the

reaction repeated until complete oxidation was achieved. After digestion, the samples were dried again and treated with 1 M hydrochloric acid (HCl) to eliminate carbonate components. For the separation of microplastics, a zinc chloride (ZnCl_2) solution with a density of 1.6 g/mL was employed along with high-speed centrifugation. The floating fraction, which contained microplastics, was filtered through 0.45 μm membrane filters using a Nalgene vacuum filtration system and dried at 45°C. The filters were examined under a Euromex stereomicroscope equipped with a DC5.0 camera, which has a maximum magnification of 40x. Microplastics were counted and measured using Image Focus 4 software, which detects sizes ranging from 0.3 mm to less than 5 mm. Microfibers were measured by length, while fragments and films were quantified based on their surface area. Microfibers were measured by length, while fragments and films were quantified based on their surface area. For statistical analysis, data processing, and graphical visualization, Microsoft Excel and SigmaPlot were utilized.

RESULTS AND DISCUSSION

Microplastic abundance in coastal waters

Microplastic was observed at all eight sampling sites of coastal waters (Figure 2). Microplastic concentrations ranged from 1.49 particles/ m^3 at KG2 to 20.68 particles/ m^3 at KG6, with an average of 10.61 ± 7.09 particles/ m^3 . Higher concentrations were observed at KG5, KG6, KG7, and KG8 (Figure 3), which have potentially been related to human populations and intensive activities such as markets, transportation, and ferrying, resulting in a large amount of microplastic leakage to the environment.

In comparison to other studies conducted in Vietnam, the average microplastic concentration in the Cai Lon – Cai Be estuary is considerably higher than those reported for the Mong Duong and Dien Vong estuaries (0.12 and 0.10 particles/ m^3) (Hung Son Pham, Huu Huan Nguyen et al. 2022), the Bach Dang estuary (2.0 particles/ m^3) (Thanh Nghi Duong, Hai Ngoc

Dinh et al. 2020), and the Can Gio estuary (1.15 particles/ m^3) (Hoa Thi Pham, Tinh Quoc Pham et al. 2024), yet remains lower than values observed at the Hoi estuary, Thanh Hoa (45.6 particles/ m^3) (Thi Lim Duong, Thi Huong Thuy Nguyen et al. 2024), and the Ba Lat estuary (65 particles/ m^3) (Thi Thao Nguyen, Stéphanie Lebarillier et al. 2024). When compared to global studies, the Cai Lon - Cai Be estuary has higher mean microplastic concentrations than the Mandovi-Zuari estuary in Goa, India (0.107 particles/ m^3) (Priyansha Gupta, Mahua Saha et al. 2021), Benoa Bay, Indonesia (0.62 particles/ m^3) (Yulianto Suteja, Agus Saleh Atmadipoera et al. 2021), the Chao Phraya estuary, Thailand (2.33 particles/ m^3) (Suwanna Boontanon, Phyo Zaw Oo et al. 2020), Tampa Bay, US (4.5 particles/ m^3) (Kinsley McEachern, Henry Alegria et al. 2019). However, these values are significantly lower than those reported for highly polluted regions, such as the St. Lawrence estuary in Canada (120 particles/ m^3) (Noreen E Kelly 2024), the Meghna estuary, Bangladesh (128.89 particles/ m^3) (M Belal Hossain, Jimmy Yu et al. 2023) and major Chinese estuaries, including the Yangtze (788 particles/ m^3) and Haihe (1,485.7 particles/ m^3) rivers (Nan Wu, Ying Zhang et al. 2019).

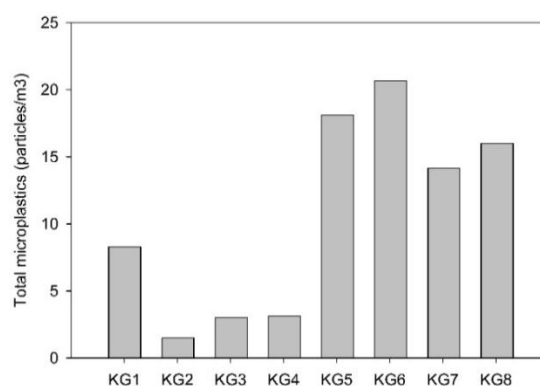


Figure 2. Total microplastics in surface water at the Cai Lon–Cai Be estuary

Microplastic concentrations in the surface waters of the Cai Lon – Cai Be estuary are notably higher than those found in other regions of Vietnam and globally. This estuarine system is primarily influenced by irregular semi-diurnal tides, a complex interlacing

hydrological network, and moderate population pressure and waste inputs, together with dispersed fishing and aquaculture activities. In contrast to large, high-discharge estuaries such as Ba Lat or Hoi—which receive substantial water and waste loads from upstream—the Cai Lon – Cai Be system experiences weaker riverine influence but is clearly affected by shoreline domestic waste inputs, waterway traffic, fish market operations, cage-based aquaculture, and the use and disposal of plastic materials in local production activities.

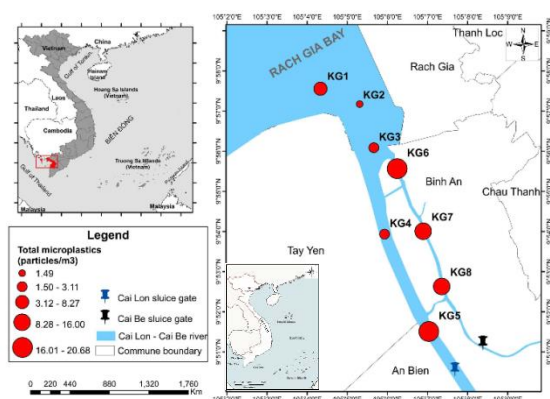


Figure 3. Spatial distribution of microplastics in surface waters at the Cai Lon–Cai Be estuary

The estuary is home to densely populated communities, bustling fish markets, numerous boat docks, and active aquaculture practices, all of which contribute significantly to the generation of plastic waste and plastic leakage to the environment. Locations KG5 to KG8 particularly exhibit high microplastic levels, suggesting a direct link between the abundance of microplastics and human activities in the vicinity. The proximity of these sites to urban centers and commercial fishing operations amplifies the impact of local socio-economic conditions on plastic pollution. This data emphasizes not only the urgent need for effective waste management strategies but also the importance of raising public awareness about the consequences of plastic waste in this vital aquatic ecosystem.

Characteristics of microplastics

In terms of morphological characteristics, microplastics collected from surface water

samples at the Cai Lon – Cai Be estuary were predominantly microfibers, which constituted 92.45% of the total microplastic count. Other forms of microplastics were present in smaller quantities: films accounted for 4.53%, and fragments made up 3.01% (Figure 4). Fibers were particularly dominant at sampling sites KG1 to KG5, ranging from 83.33% to 93.33% at the remaining location (Figure 5). Overall, fibers were overwhelmingly predominant (> 90%). This is a common feature in estuaries (Xiaoxia Sun, Qingjie Li et al. 2017, Pei Xu, Guyu Peng et al. 2018, Nan Wu, Ying Zhang et al. 2019, Mei Han, Xuerui Niu et al. 2020, Muhammad Rozaimi Mohd Zaki, Peh Xin Ying et al. 2021). This pattern suggested that the primary sources may include synthetic fibers used in daily life or from fishing nets and plastic ropes employed in aquaculture.

The microplastics recovered from surface water samples at the estuary exhibited a diverse range of colors, including black, red, white, transparent, yellow, and blue. Among these, two color groups were dominant: transparent (58.62%) and blue (22.41%). Black microplastics accounted for 8.62%, while all other colors were present at lower proportions, each below 5%. Size analysis revealed that microfibers ranged from 404 to 4,337 μm , with a mean length of $1,227.09 \pm 846.38 \mu\text{m}$. Fibers were categorized into four size groups, with the 400–1,000 μm group being the most prevalent (57.41%), followed by the 1,000–2,500 μm group (33.33%). Larger-sized groups accounted for a smaller proportion. For microfragments and microfilms, surface areas ranged from $141 \times 10^3 \mu\text{m}^2$ to $1,204 \times 10^3 \mu\text{m}^2$, with an average area of $531.75 \times 10^3 \pm 415.65 \times 10^3 \mu\text{m}^2$.

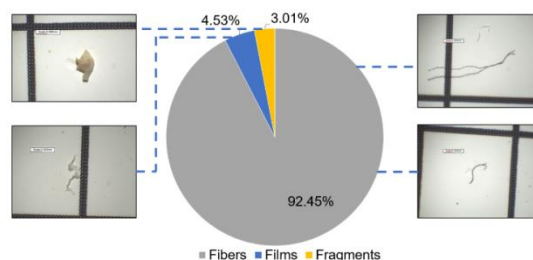


Figure 4. Microplastic morphology in surface waters at the Cai Lon–Cai Be estuary

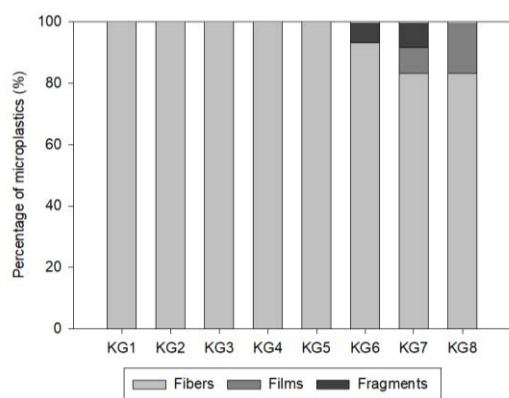


Figure 5. Percentage of microplastic types in estuarine surface waters

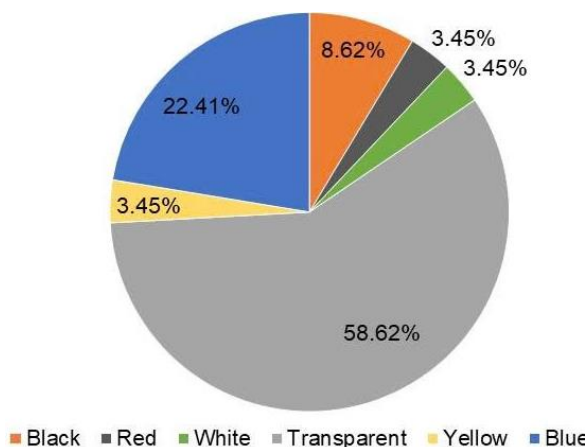


Figure 6. Microplastic color percentages

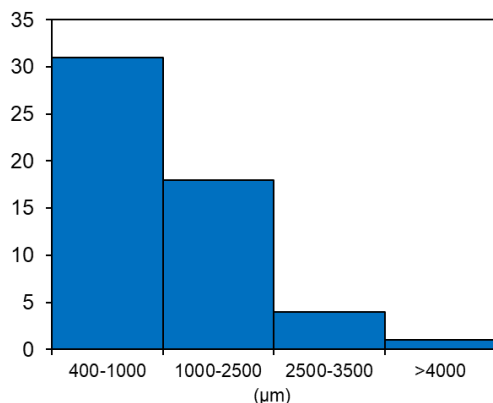


Figure 7. Size distribution of microfibers

The size distribution indicates that most of the microfibers were concentrated in the 400–1,000 μm and 1,000–2,500 μm ranges. The high proportion of small-sized fibers may increase the risk of ingestion by aquatic

organisms through feeding processes, thereby posing potential risks of transfer to higher trophic levels, including humans (Merlin N Issac and Balasubramanian Kandasubramanian 2021).

For microfragments and microfilms, their relatively large average surface area (over $500 \times 10^3 \mu\text{m}^2$) suggests that they primarily originate from the degradation of plastic packaging, plastic bags, or surface-covering materials. However, their much lower proportion compared to fibers indicates that fiber-derived sources—such as fishing gear, textiles, and aquaculture activities—play a dominant role in shaping the composition of microplastics in the study area.

Potential sources of microplastics in coastal waters

The research findings indicate that microplastics in the study area's aquatic environment are primarily secondary microplastics, originating from domestic plastic products and activities related to fishing and aquaculture. Microplastic fibers are largely derived from textile materials or fishing nets and gear, whereas microplastic fragments exhibit a wider range of morphologies, reflecting more diverse sources. The area's geographical context, characterized by distance from major plastic production and seaport activities, suggests that these microplastic sources originated from domestic solid waste, compounded by poor waste management and inadequate collection rates. In this study, the types of polymers used in microplastic particles were not determined. Future studies should conduct FTIR analysis to determine the polymer composition of the samples, thereby clarifying the origin and potential ecological impact of microplastic particles in the study area.

CONCLUSIONS

The present study provides a comprehensive assessment of microplastic pollution in the surface waters of the Cai Lon – Cai Be estuary. The findings reveal that microplastics are present at all sampled locations, with concentrations ranging from

1.49 to 20.68 particles per cubic meter and an average concentration of 10.61 ± 7.09 particles per cubic meter. These levels significantly exceed those reported in various other estuaries in Vietnam, indicating a considerable environmental impact from local anthropogenic activities. Notably, microfibers comprise over 90% of the microplastic findings, predominantly in transparent and blue hues, suggesting that primary sources include domestic activities and fishing gear associated with capture and aquaculture practices. The most frequently observed size range of microfibers was between 400 and 1,000 micrometers, facilitating their ingestion by aquatic organisms and raising concerns about potential biomagnification within the food chain. Overall, the research highlights a critical level of microplastic pollution in this estuary, posing threats not only to the local ecological balance but also to aquatic resources and public health. Future investigations should focus on longitudinal monitoring across different seasonal conditions and incorporate polymer composition analyses to elucidate the origins of the microplastics. Furthermore, enhancing local plastic waste management, particularly in terms of domestic waste and fishing gear regulation, is essential for mitigating microplastic release into the environment.

ACKNOWLEDGMENTS

This research is supported by the Ministry of Science and Technology of Vietnam under the national project grant number ĐTDL.CN.50/23

REFERENCES

- Luís Gabriel Antão Barboza, A. Dick Vethaak, Beatriz R. B. O. Lavorante, Anne-Katrine Lundebye and Lúcia Guilhermino (2018). "Marine microplastic debris: An emerging issue for food security, food safety and human health." *Marine Pollution Bulletin* **133**: 336-348.
- Suwanna Boontanon, Phyo Zaw Oo, Narin Boontanon, Shuhei Tanaka and Fujii Shigeo (2020). "Abundance and distribution of suspended microplastics in the surface water of Chao Phraya River Estuary." *Thai Environmental Engineering Journal* **34**(2): 57-66.
- Thanh Nghi Duong, Hai Ngoc Dinh, Thuy Chung Kieu Le, Strady Emilie, Thi Mai Huyen Bui, Duc Cuong Le, Huu Thang Nguyen and Thi Lim Dinh (2020). "Assessment of microplastic pollution in the Bach Dang estuarine environment, Red River system, Vietnam." *Vietnam J. Chem.* **58** (6E12): 140-146.
- Thi Lim Duong, Thi Huong Thuy Nguyen, Tran Quan Dang, Thi Lan Nguyen, Thi Hue Huong Nguyen, Thi Minh Trang Trinh, Thu Thuy Tran, Thi Dung Pham, Viet Cuong Nguyen and Duc Manh Vu (2024). "The impact of sampling techniques at estuary, coastal area on the characteristics of microplastics: A case study at Cua Hoi estuary, Thanh Hoa Province." *Hydrometeorological journal* **766**: 43-52.
- Priyansha Gupta, Mahua Saha, Chayanika Rathore, V Suneel, Durbar Ray, Akshata Naik and Krushi Daga (2021). "Spatial and seasonal variation of microplastics and possible sources in the estuarine system from central west coast of India." *Environmental Pollution* **288**: 117665.
- Mei Han, Xuerui Niu, Man Tang, Bo-Tao Zhang, Guoqiang Wang, Weifeng Yue, Xianglun Kong and Jiqian Zhu (2020). "Distribution of microplastics in surface water of the lower Yellow River near estuary." *Science of the Total Environment* **707**: 135601.
- M Belal Hossain, Jimmy Yu, As-Ad Ujjaman Nur, Partho Banik, Yeasmin N Jolly, Md Al-Mamun, Takaomi Arai and Mohammed Fahad Albeshr (2023). "Microplastics in surface water from a mighty subtropical estuary: first observations on occurrence, characterization, and contamination assessment." *Environmental Research* **226**: 115594.
- Merlin N Issac and Balasubramanian Kandasubramanian (2021). "Effect of microplastics in water and aquatic systems." *Environmental Science and Pollution Research* **28**(16): 19544-19562.
- Noreen E Kelly (2024). "Spatial distribution and risk assessment of microplastics in surface waters of the St. Lawrence Estuary." *Science of The Total Environment* **946**: 174324.
- Kinsley McEachern, Henry Alegria, Amelia L Kalagher, Cypress Hansen, Samantha Morrison and David Hastings (2019). "Microplastics in Tampa Bay, Florida: abundance and variability in estuarine waters and sediments." *Marine pollution bulletin* **148**: 97-106.
- Thi Thao Nguyen, Stéphanie Lebarillier, Toan Khanh Vu, Pascal Wong-Wah-Chung, Vincent Fauvelle and Laure Malleret (2024). "Spatial and seasonal abundance and characteristics of microplastics along the Red River to the Gulf of Tonkin, Vietnam." *Science of the Total Environment* **957**: 177778.

- NOAA (2015). Laboratory methods for the Analysis of Microplastics in the Marine Environment Recommendations for quantifying synthetic particles in water and sediments. NOAA Technical Memorandum; NOS-OR&R-48. Technical Memorandum. DOI: <http://dx.doi.org/10.25607/OBP-604>.
- Hoa Thi Pham, Tinh Quoc Pham, Ngoc Pham, Linh Ho Thuy Nguyen, Simon Cragg and Laura Michie (2024). "Abundance and variation of microplastics between seasons in a tropical estuary: The case of Can Gio estuary, Vietnam." *Archives of Environmental Protection* **50**(3).
- Hung Son Pham, Huu Huan Nguyen, Thien Cuong Tran, Hoang Giang Pham, Quang Ha Do, Trang Nhung Nguyen and Xuan Hai Nguyen (2022). Microplastic pollution in the water environment in some coastal estuaries in Quang Ninh province. *Proceedings of the 5th National Scientific Conference on Earth, Mining, and Sustainable Environment*.
- Xiaoxia Sun, Qingjie Li, Mingliang Zhu, Junhua Liang, Shan Zheng and Yongfang Zhao (2017). "Ingestion of microplastics by natural zooplankton groups in the northern East Sea." *Marine pollution bulletin* **115**(1-2): 217-224.
- Yulianto Suteja, Agus Saleh Atmadipoera, Etty Riani, I Wayan Nurjaya, Dwiyo Nugroho and Muhammad Reza Cordova (2021). "Spatial and temporal distribution of microplastic in surface water of tropical estuary: Case study in Benoa Bay, Bali, Indonesia." *Marine Pollution Bulletin* **163**: 111979.
- Quynh Anh Tran-Nguyen, Tuan Quy Nguyen, Thao Linh Thi Phan, Minh Van Vo and Mau Trinh-Dang (2023). "Abundance of microplastics in two venus clams (*Meretrix lyrata* and *Paratapes undulatus*) from estuaries in central Vietnam." *Water* **15**(7): 1312.
- Thi Ngan Ha Truong, Thi Thao Linh Phan, Van Minh Vo, Thi Mai Le, Dang Mau Trinh and Quynh Anh Tran Nguyen (2023). "Distribution of microplastics in the surface water and sediment of Thuan An estuary, Thua Thien Hue province." *Science and Technology Journal – University of Da Nang* **21**(3): 97-103.
- Nan Wu, Ying Zhang, Xiaohan Zhang, Ze Zhao, Jiahui He, Wenpeng Li, Yongzheng Ma and Zhiguang Niu (2019). "Occurrence and distribution of microplastics in the surface water and sediment of two typical estuaries in Bohai Bay, China." *Environmental Science: Processes & Impacts* **21**(7): 1143-1152.
- Pei Xu, Guyu Peng, Lei Su, Yongqiang Gao, Lei Gao and Daoji Li (2018). "Microplastic risk assessment in surface waters: A case study in the Changjiang Estuary, China." *Marine pollution bulletin* **133**: 647-654.
- Muhammad Rozaimi Mohd Zaki, Peh Xin Ying, Azim Haziq Zainuddin, Muhammad Raznisyafiq Razak and Ahmad Zaharin Aris (2021). "Occurrence, abundance, and distribution of microplastics pollution: an evidence in surface tropical water of Klang River estuary, Malaysia." *Environmental Geochemistry and Health* **43**(9): 3733-3748.
- Chaonan Zhang, Shaodan Wang, Di Sun, Zhengkun Pan and Jixing Zou (2023). "Investigation of microplastics in surface water and estuarine mullet *Mugil cephalus* from 23 estuary areas, South China." *Sustainability* **15**(5): 4193.
- Jiaxu Zhang, Chenglong Zhang, Yixiang Deng, Ruixue Wang, En Ma, Jingwei Wang, Jianfeng Bai, Jin Wu and Yongjie Zhou (2019). "Microplastics in the surface water of small-scale estuaries in Shanghai." *Marine Pollution Bulletin* **149**: 110569.

Status of plastic waste generation in the Cai Lon – Cai Be estuary, Vietnam

Pham Lan Anh^{1,2}, Nguyen Tai Tue^{1,2}, Luu Viet Dung^{1,2*}, Tran Dang Quy^{1,2}, Mai Trong Nhuan^{1,2}

¹Faculty of Geology, University of Science, Vietnam National University, Hanoi

²Key laboratory of Geoenvironment and Climate change response, University of Science, Vietnam National University, Hanoi

*Email: dungluuviet@hus.edu.vn

Abstract: The generation of plastic waste (PW) from municipal solid waste (MSW) sources within the Cai Lon – Cai Be estuary area has been evaluated from 2018 to 2024, utilizing a waste flow model. The total volume of PW generated from MSW initially increased, rising from 56,940 tons annually in 2018 to 61,904 tons annually in 2021. However, this volume decreased to 52,706 tons per year by 2024. The volume of collected PW showed a gradual upward trend, increasing from 105.7 tons per day in 2018 to 115 tons per day in 2021, and reaching 112.5 tons per day by 2024. Thus, the quantity of uncollected PW has significantly decreased, from 50.9 tons per day in 2018 to 31.9 tons in 2024. Furthermore, the leakage of PW into the environment also showed a marked reduction, falling from 14,855 tons per year in 2018 to 9,307 tons per year in 2024, with a corresponding decrease from 2,227 tons to 1,460 tons per year during the same period. Forecasts for 2030 suggest PW generation could reach approximately 260 tons per day, or 94,900 tons annually. The primary factors influencing these trends include the increasing demand for plastic products, ineffective sorting practices of MSW, inadequacies in management policies, and limitations in waste treatment infrastructure. To reduce PW leakage, it is essential to enhance strategies for sorting, collecting, transporting, and treating MSW. Improving waste management policies, increasing public awareness, and promoting sustainable recycling and reuse of plastics will

also be important in diminishing negative environmental impacts.

Keywords: Plastic waste, Municipal solid waste, Plastic pollution, Cai Lon – Cai Be

INTRODUCTION

Plastic waste (PW) has been and remains a serious challenge to the global environment, attracting significant attention from national governments, international organizations, researchers, and communities worldwide. Each year, an estimated 200 million tons of PW are generated within municipal solid waste (MSW), and this volume has shown a steady increase over time, exerting significant pressure on the environment and ecosystems (Laurent Lebreton and Anthony Andrady 2019, OECD 2022).

In Vietnam, rapid economic development together with accelerated urbanization have led to a sharp rise in plastic consumption. Recent report in Vietnam has shown that PW generated from MSW increased from 2.7 million tons/year to approximately 3.27 million tons/year between 2018 and 2021. The annual leakage of PW into the marine environment is estimated at 0.07 million tons annually. The volume of PW generated in 28 coastal provinces/cities was about 4,286 tons/day, compared to 3,753 tons/day of the remaining provinces/cities, with plastic bags accounting for a considerable proportion (WWF 2023). Nonetheless, PW management faces significant challenges and limitations, resulting in the

substantial release of PW into the environment. This situation poses a serious threat to the environment soil, water, air, and the ocean, has led to a plastic waste pollution crisis, commonly referred to as 'white pollution' (Thi Ha Dang 2022).

PW is predominantly found in coastal areas, particularly concentrated in locations such as shorelines, river estuaries, and locations near commercial areas and recreational areas (Bijeesh Kozhikkodan Veettil, Nguyen Thuy An Hua et al. 2023). Fisheries and transportation are also major contributors to PW leakage into the environment, particularly the marine environment. Among the affected areas, river mouths and mangrove forests are two especially important regions with significant ecological and economic values, and have become hotspots for PW accumulation (WWF 2023), becoming a considerable challenge for environmental protection, nature conservation, and biodiversity. It is estimated that in Cai Be – Cai Lon estuarine area (Kien Giang), PW leakage amounts to 4.48 tons per day, accounting for 12.6% of the total plastic waste generated and 77.4% resulting from indiscriminate littering by residents (Kien Giang Provincial People's Committee 2020), highlighting the critical pressure of plastic waste in this coastal region.

Research on the generation and leakage of PW in coastal areas is currently limited. Therefore, it is important to assess the existing status of PW generation and its release into the environment within estuaries and coastal zones to develop effective plans for environmental protection and ecosystem conservation. This present study aims to estimate the total PW generated from municipal solid waste (MSW) in the Cai Lon – Cai Be area from 2018 to 2024 and to address the impacts of PW on environmental quality and estuarine ecosystems. Research results of this research will provide practical and scientific basis for proposing effective PW management strategies, thereby contributing to the realization of sustainable development goals, circular economy initiatives, and green growth.

MATERIALS AND METHODS

Study area

The Cai Lon – Cai Be estuarine system is one of the most important river systems in the southern Mekong Delta (Figure 1). Its geographical advantages facilitate socio-economic development, leading to a concentration of activities such as agriculture, services, tourism, aquaculture, and fisheries. However, this rapid development has put massive pressure on the environment and ecosystems, creating significant challenges for the sustainable management of natural resources. One of the most pressing issues currently faced is the increasing volume of plastic waste within municipal solid waste (MSW). This surge makes it challenging to control plastic leakage into the environment, which has become a critical concern for the locality.

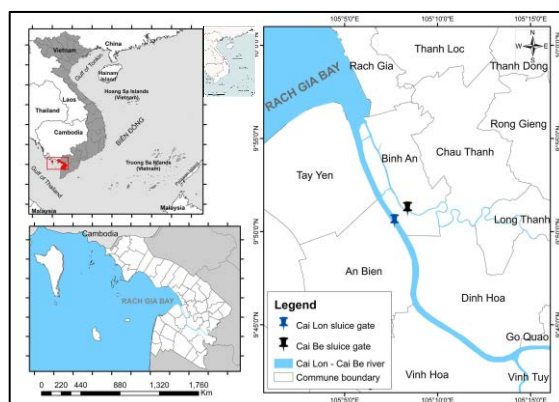


Figure 1. Location map of the Cai Lon – Cai Be estuarine area

METHODS

Partial population data for An Giang Province (formerly Kien Giang) from 2018–2024 were sourced from provincial statistical yearbooks (Statistical Office of Kien Giang Province 2023, Statistical Office of Kien Giang Province 2024). The MSW generation data came from environmental reports and local sources (Ministry of Natural Resources and Environment 2020, Ministry of Natural Resources and Environment 2024, Ministry of Natural Resources and Environment 2025). The

natural population growth rate of 0.2% per year for Kien Giang from 2009–2019 was used as a parameter in the calculation model.

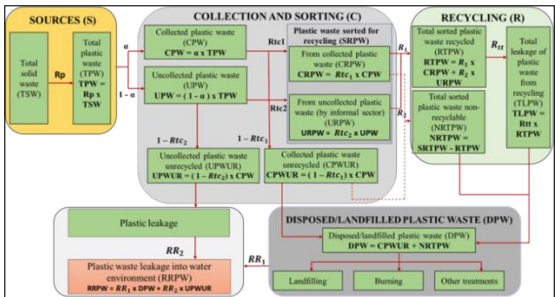


Figure 2. Location map of the Cai Lon – Cai Be estuarine area

Table 1. Coefficients used in calculating the volume of plastic waste of components in the waste flow model

No	Symbol	Description	Estimated Value	References
1	Rp	Proportion of PW components in domestic solid waste	12%	(WWF 2023)
2	α	Coefficient collection of MSW (there is a difference between urban and rural areas)	Urban and Rural	(Kien Giang Provincial People's Committee 2022)
3	Rtc ₁	The proportion of PW sorted for recycling from collected sources	33%	(WWF 2023)
4	Rtc ₂	The proportion of PW sorted for recycling from uncollected sources	20%	(NPAP 2022)
5	Ri ₁	The proportion of PW recycled from sorted PW for recycling from collected sources	85%	(NPAP 2022)
6	Ri ₂	The proportion of PW recycled from sorted PW for recycling from informal collected sources	95%	(NPAP 2022)
7	RR ₁	The proportion of PW lost into the water environment	0.5%	(World Bank 2021, NPAP 2022,

No	Symbol	Description	Estimated Value	References
		from landfills/treatment plants		WWF 2023)
8	RR ₂	The proportion of PW lost into the water environment from unmanaged plastic waste leaking into the environment	14%	(World Bank 2021, NPAP 2022, WWF 2023)
9	Rtt	The proportion of PW lost from recycling activities	10%	(World Bank 2021, NPAP 2022, WWF 2023)

The waste flow diagram (WFD) of PW was applied to calculate the volume of PW generated and the amount leaking into the environment, similar to with previous studies conducted in Viet Nam (WWF 2023) and in Phu Tho Province (Pham et al. 2024). The WFD model consists of six main components: (1) Generated source (S), (2) Collection and sorting (C), (3) Recycling (R), (4) Properly landfilled and treated plastic waste (DPW), (5) Plastic leakage into water environment (RRPW). The coefficients used in the model were derived from local reports and specialized literature and were adjusted based on results from field surveys conducted in the Cai Lon – Cai Be estuarine area (see Table 1).

The total amount of PW generated was determined by multiplying the proportion of plastics by the total amount of municipal solid waste (MSW). We divided this PW into two main sources based on how it is collected: collected plastic waste (CPW) and uncollected plastic waste (UPW). For the CPW, about one-third was sorted for recycling, while most went to landfills. Around 0.5% of this waste ended up in water. For the UPW, only about 20% was recovered by the informal recycling sector, and the rest was lost in the environment, with 14% of it entering rivers and lakes. Recycling is not 100% effective. About 85% of CPW and 95% of UPW intended for recycling was actually recycled. Additionally, 10% of the PW from both sources was lost during the recycling process (TLPW) (see Table 1, Figure 2).

RESULTS AND DISCUSSION

Total Plastic Waste Generation

The volume of plastic waste in the Cai Lon – Cai Be estuarine area (Kien Giang) during 2018–2024 showed noticeable fluctuations over time. In 2018, the amount was about 156 tons/day (56,940 tons/year); by 2021, it had increased to 169.6 tons/day (61,904 tons/year) and continued to rise slightly in 2022; however, from 2023 it began to decline, reaching 144.4 tons/day (52,706 tons/year) by 2024 (Figure 3). The initial increase in plastic waste was associated with socio-economic development, urbanization, and changes in consumer behavior, particularly the widespread use of single-use plastic products. The decrease from 2023 may be related to the implementation of local programs to reduce single-use plastics, as well as enhanced collection and recycling efforts at the local level (Kien Giang Provincial People's Committee 2022). Between 2018 and 2024, plastic waste generation in both urban and rural areas of Kien Giang increased, with an average annual growth rate of about 10% (Figure 4). However, rural areas generate about 1.2 times more plastic waste than urban areas due to higher population concentration. Meanwhile, the rapid pace of urbanization has also contributed to the increase in municipal plastic waste.

Plastic waste generation in Kien Giang was higher than reported in earlier studies from other provinces in Viet Nam. For example, annual waste generation was approximately 18,798 tons/year in Tra Vinh (Tuan Viet Tran, Thi Hoai Tran et al. 2022), 23,483 tons/year in Ha Tinh (Thi Quynh Hoa Duong, Viet Dung Luu et al. 2023), and 33,471 tons/year in Phu Tho (Lan Anh Pham, Tai Tue Nguyen et al. 2024). This difference may be explained by the fact that Kien Giang is a coastal province experiencing rapid growth in tourism and service sectors, especially in Phu Quoc island, which is recognized as a key national tourism hub. This growth contributes to a higher generation of plastic waste compared to other areas. Given the rapid increase in plastic waste from municipal solid waste, it is essential to

adopt effective management solutions, such as establishing recycling facilities or applying waste-to-energy incineration technologies, to reduce the burden on the existing collection and treatment system.

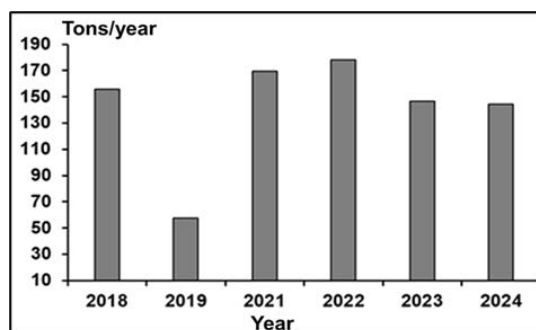


Figure 3. Total volume of PW generated in the period 2018 – 2024

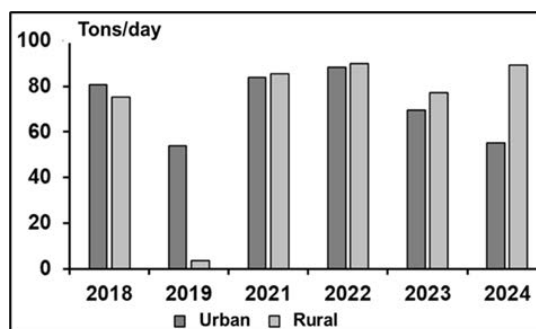


Figure 4. Volume of PW generated in the period 2018 – 2024 by urban and rural areas

Characteristics of plastic waste generation

Collected plastic waste

The total collected PW in the period 2018–2024 was calculated by multiplying the total volume of generated PW by the MSW collection rate. The collected plastic waste tended to increase, from 105.7 tons/day in 2018, to 115 tons/day in 2021, and reaching 112.5 tons/day in 2024 (Figure 5). This was also reflected then change in MSW collection rate, which gradually increased from 67% in 2018 to 78% in 2024 (Figure 5). Despite the annual growth in the MSW collection rate, a significant amount of generated plastic waste remains uncollected due to limited financial resources and constraints within the waste treatment infrastructure. The collection and transportation of MSW are

primarily managed by cooperatives, collection groups, and private enterprises, which often lack funding for investment in specialized equipment and vehicles.

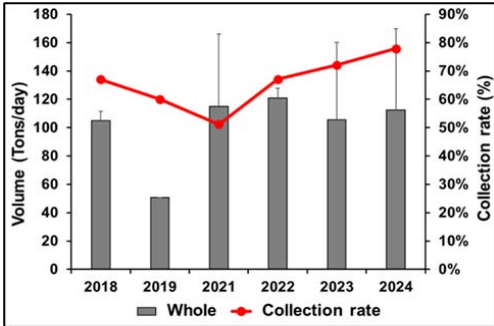


Figure 5. Development of collected PW volume and proportion in Kien Giang region in the period 2018-2024

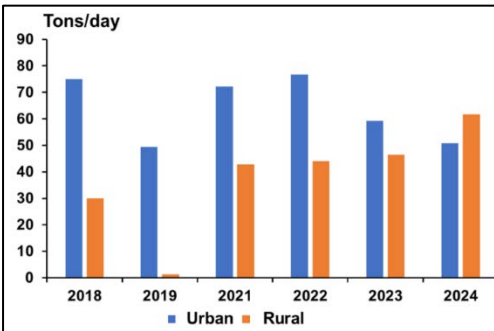


Figure 6. Development of collected PW volume in Kien Giang region by urban and rural areas in the period 2018-2024

The differences in the rate and volume of collected PW were clearly highlighted by the characteristics of urban and rural areas (see Figure 6). Urban areas had a smaller total volume of PW because of lower population, but the collected PW volume was much higher. This was mainly thanks to the waste collection infrastructure being organized synchronously, with the participation of specialized units and professional collection forces, together with the improvement of public awareness. Most of the PW in urban areas was fully collected and transported to treatment facilities through a closed process, thereby contributing to better control of the generated PW and limiting the discharge into the natural environment. In rural areas, where the population is higher and more waste is generated, the collection rate is still low.

The reasons for this include difficult terrain, technical challenges, and limited resources for waste collection, which make it hard to manage solid waste effectively in these regions.

Uncollected plastic waste

The volume of uncollected PW during 2018-2024 was estimated as the difference between the total amount of PW generated and the amount collected. The results indicate a gradual decline, from 50.9 tons/day in 2018 to 31.9 tons/day in 2024 (Figure 7).

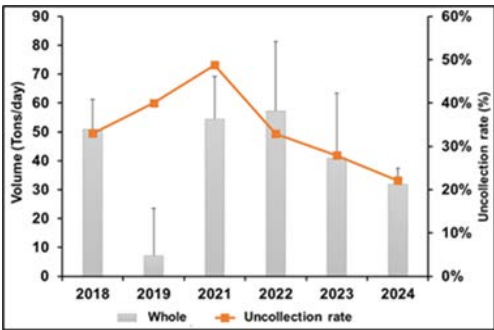


Figure 7. Development of uncollected PW volume and proportion in Kien Giang region in the period 2018-2024

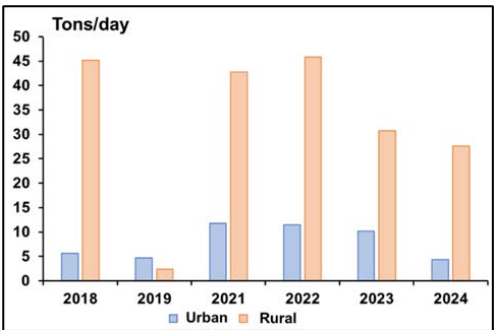


Figure 8. Development of uncollected PW volume in Kien Giang region by urban and rural areas in the period 2018-2024

Uncollected PW was generated mainly in rural districts (Figure 8). These areas are characterized by large populations, dispersed settlements, and underdeveloped collection systems, resulting in low collection efficiency. Although the proportion of uncollected waste decreased markedly over the six-year period from 2018 to 2024 (Figure 7), the collection rate in rural areas remained low. There are only 46 waste

management units responsible for collecting and transporting MSW; approximately 71% of the collected waste is disposed of at open dumpsites, 16% processed through composting, and 13% is incinerated (Kien Giang Provincial People's Committee 2022).

A shortage of collection vehicles has caused more waste to pile up in residential areas. Limited infrastructure and scattered populations mean many households end up managing their waste on their own. This often leads to uncontrolled burning or dumping waste in water bodies and empty land. To protect the environment, we need better waste management practices, especially in rural areas, to improve collection rates.

Status of plastic waste treatment

Recycled plastic waste

Recycle is an effective solution for the efficient use of resources, reducing the amount of PW, and promoting the development of a circular economy model, and it has been successfully applied in many countries worldwide. However, in the study area, most recycling activities are small-scale and informal, so accurate estimates of the volume of PW being recycled as well as the loss rate from recycling activities into the environment rely on general data (WWF 2023).

The estimated volume of PW sorted for recycling is derived from the total amount of PW designated for recycling purposes from both urban plastic waste (UPW) and commercial plastic waste (CPW). The results indicate that the volume of PW sorted for recycling tends to decrease along with the total PW generation, reaching 15,878 tons in 2024, lower than 17,849 tons in 2021 and 16,389 tons in 2018. However, it is important to note that not all sorted PW is fully recyclable. Based on the waste flow model, the actual volume of municipal solid waste (MSW) processed for recycling was 13,724 tons/year in 2024, in contrast to 15,549 tons/year in 2021 and 14,308 tons/year in 2018. Throughout this recycling process, certain losses occur, primarily attributed to mechanical failures, subpar input

quality, or incomplete recycling methodologies. The estimated loss rate is approximately 10% of the total PW processed, translating to 1,424 tons/year (2018), 1,570 tons/year (2021), and 1,387 tons/year (2024).

Furthermore, a significant volume of sorted PW remains unrecyclable due to technical limitations. In 2018, it was estimated that 2,081 tons of PW was unsuitable for recycling; this volume rose to 2,263 tons in 2021 and is estimated to be around 2,154 tons in 2024. Primary factors contributing to this pattern include insufficient technical infrastructure for PW collection and sorting, outdated recycling technology, and particularly ineffective source separation practices, all of which markedly diminish the recyclability of PW within the study area.

Landfill

In Kien Giang area, landfilling remains the most common method for MSW treatment, especially in rural areas and on islands. Most landfills are either unsanitary or informal waste collection sites that do not meet environmental standards, which raises concerns about potential pollutant leakage into the environment. Currently, the study area has 47 waste disposal sites, including 33 open-air landfills and 14 sites that have been planned but are not yet operational (Kien Giang Provincial People's Committee 2022).

It is estimated that during the period 2018–2024, the total volume of waste managed through incineration and landfilling will reach approximately 27,813 tons per year (76.2 tons per day) in 2018 and 29,675 tons per year (81.3 tons per day) in 2024, which equivalent to about 9.1% of the total PW generated in the area. However, many landfills and incinerators still do not meet environmental technical standards, which may lead to secondary pollution as a result of waste treatment processes.

Plastic waste leakage into the environment

Plastic waste leakage due to inadequate treatment

The total volume of PW leakage into the environment includes both uncollected PW and PW lost during recycling processes. The main sources of PW leakage into the environment are uncollected PW, losses during collection, recycling, and treatment processes. Study results showed that total PW leakage was 14,855 tons per year in 2018 and decreased to 9,307 tons per year in 2024. This trend showed that most of PW leakage in Kien Giang originated from uncollected PW. However, current data partially reflects the effectiveness of local programs for the collection, management, and recycling of plastic waste, although significant challenges remain in further reducing PW leakage into the environment.

Table 2. Forecast of Population and Plastic Waste Generation in Kien Giang Province by 2030

No	Year		Change
	2024	2030	
Urban population (persons)	503.091	556.408	Increase: 10%
Rural population (persons)	1.273.292	1.298.287	Increase: 1,96%
Total population (persons)	1.776.383	1.854.695	Increase: 4,5%
MSW generation in urban areas (tons/day)	459,570	1.100.000	Increase
MSW generation in rural areas (tons/day)	743,630	900.000	Increase
Total MSW generation (tons/day)	1.203.200	2.000.000	
Proportion of PW components in MSW (%)	12	13	Increase
PW generation in urban areas (tons/day)	55,2	143	
PW generation in rural areas (tons/day)	89,2	117	
Total PW generation (tons/day)	144,4	260	

Plastic waste leakage into water environments

Estimated PW leakage into water environments during 2018–2024 showed a similar trend to overall PW leakage to environment, gradually decreasing from 6.1

tons/day (equivalent to 2,227 tons/year in 2018) to 4 tons/day (equivalent to 1,460 tons/year in 2024). This decline partly reflects the early effectiveness of management measures and increased community awareness regarding MSW collection. However, PW leakage levels remain high, especially in coastal areas, river mouths, islands, and locations with inadequate waste collection infrastructure (Kien Giang Provincial People’s Committee 2022).

Plastic waste enters water environments through various pathways, including the direct disposal of household waste and the accumulation of waste in drainage channels, culverts, and dams. Additionally, uncollected plastic waste, discarded due to environmental factors, can flow into natural water bodies. Model estimates suggest that improving plastic waste collection and recycling efforts related to municipal solid waste is crucial for significantly reducing plastic waste leakage into both terrestrial and aquatic environments.

Projection of Plastic Waste Generation

Forecasting trends in plastic waste (PW) generation plays an important role in developing local environmental management strategies. The projection model is based on population size and the per-capita generation of municipal solid waste (MSW). According to the population growth scenario for Kien Giang area for 2021–2030, with projections to 2050, the annual growth rate is estimated at approximately 0.17% (Table 2) (Kien Giang Provincial People’s Committee 2023). Accordingly, total PW generation by 2030 is projected to reach 260 tons/day (94,900 tons/year). PW generation in urban areas is estimated at about 143 tons/day (52,195 tons/year), while rural areas are estimated at approximately 117 tons/day (42,705 tons/year). The total PW generation is forecast to increase by 1.8 times compared with 2024 levels. Such significant growth in waste generation poses considerable challenges for the management of PW, including the processes of collection, transportation, and treatment. Without effective waste management measures, PW leakage into the environment could occur,

negatively impacting environmental quality, ecosystems, and human health. Proactive strategies are essential to address these issues and ensure sustainable waste management practices.

Proposed Management Solutions to Reduce Plastic Waste Leakage into the Environment

To effectively manage PW generated in the Cai Lon – Cai Be estuarine area, it is necessary to enhance capacity and awareness in the management, collection, transportation, and treatment of MSW, particularly by implementing solutions for source separation, collection, transportation, and treatment of MSW in accordance with the Environmental Protection Law of 2020. Public awareness and behavior change campaigns should be intensified to reduce the use of single-use plastics and plastic bags, and to discourage indiscriminate littering. In addition, policy measures should be developed to promote household-level practices of reuse and recycling of PW, and to encourage the adoption of plastic alternatives and environmentally friendly products.

CONCLUSIONS

The total amount of PW generated in the Cai Lon – Cai Be estuarine area showed an upward trend from 56,940 tons in 2018 to 61,904 tons in 2021, followed by a decline to 52,706 tons in 2024. The collected PW increased from 105.7 tons/day in 2018 to 115 tons/day in 2021 and

reached 112.5 tons/day in 2024. Uncollected PW decreased significantly, from 50.9 tons/day in 2018 to only 31.9 tons/day in 2024. Efforts to control PW leakage into the environment have also improved, with annual leakage reduced from 14,855 tons to 9,307 tons, and leakage into aquatic environments decreasing from 2,227 tons to 1,460 tons. However, projections show that if no further action is taken, total PW generation could rise to about 260 tons per day (or 94,900 tons per year) by 2030. To reduce PW leakage into the environment, it is essential to enhance the management, collection, transportation, and treatment of MSW. Additionally, a strong focus on community engagement is crucial. Public awareness campaigns should emphasize the importance of reducing reliance on plastic bags and single-use plastic products. Encouraging practices such as reuse and recycling, along with the adoption of environmentally friendly alternatives, will further contribute to reducing plastic waste and protecting the fragile ecosystems in the region.

ACKNOWLEDGMENTS

This research is supported by the Ministry of Science and Technology of Vietnam under grant number ĐTĐL.CN.50/23. Pham Lan Anh would also like to express sincere gratitude to the Nagao Natural Environment Foundation (NEF) for providing the research scholarship that made this work possible.

REFERENCES

- Kien Giang Provincial People's Committee (2022). Project on Household Solid Waste Management in Kien Giang Province for the period 2022–2025, with orientation to 2030.
- Kien Giang Provincial People's Committee (2023). Summary report: Kien Giang Provincial Planning for the period 2021–2030, vision to 2050.
- Laurent Lebreton and Anthony Andrady (2019). "Future scenarios of global plastic waste generation and disposal." *Palgrave Communications* **5**(1): 1-11.
- Ministry of Natural Resources and Environment (2020). National Environmental Status Report 2019 - Domestic Solid Waste Management.
- Ministry of Natural Resources and Environment (2024). Environmental protection work report in 2023.
- Thi Ha Dang (2022). "Microplastic pollution in some marine species collected in Ba Ria-Vung Tau province." *Journal of Science and Technology Information* (in Vietnamese) **54**(2): 30-32.
- Thi Quynh Hoa Duong, Viet Dung Luu, Tai Tue Nguyen, Dang Quy Tran, Van Hieu Pham and Trong Nhuan Mai (2023). "Estimation of Plastic Waste Leakage to Environment in Ha Tinh Province, Vietnam." *VNU Journal of Science: Earth and Environmental Sciences* **39**(4): 12-20.
- Kien Giang Provincial People's Committee (2020). Plan No. 177/KH-UBND on Action for Plastic Waste and Marine Plastic Waste Management to 2030 in Kien Giang Province.

- Ministry of Natural Resources and Environment (2025). National Environmental Protection Report 2024. NPAP (2022). Completely Minimizing Plastic Leakage in Vietnam: A Roadmap for Action. .
- OECD (2022). Global Plastics Outlook: Economic Drivers, Environmental Impacts and Policy Options.
- Lan Anh Pham, Tai Tue Nguyen, Viet Dung Luu, Dang Quy Tran, Trong Nhuan Mai and Viet Hung Luu (2024). "Assess the Status of Plastic Waste Generation in Phu Tho Province and Solutions." VNU Journal of Science: Earth and Environmental Sciences **40**(3): 45-53.
- Statistical Office of Kien Giang Province (2023). Statistical Yearbook of Kien Giang Province 2022, Statistical Publishing House.
- Statistical Office of Kien Giang Province (2024). Statistical Yearbook of Kien Giang Province 2023, Statistical Publishing House.
- Tuan Viet Tran, Thi Hoai Tran, Nguyen Cam Tu Duong, Van Hiep Duong, The Hung Hoang, Thi Thuy Nguyen and Anh Kien Le (2022). "Assessment of the actual state of arising and managing plastic and domestic waste in Tra Vinh using DPSIR method." Journal of Military Science and Technology (84): 73-79.
- Bijeesh Kozhikkodan Veettil, Nguyen Thuy An Hua, Dong Doan Van and Ngo Xuan Quang (2023). "Coastal and marine plastic pollution in Vietnam: Problems and the way out." Estuarine, Coastal and Shelf Science **292**: 108472.
- World Bank (2021). Market Study for Vietnam: Plastics circularity opportunities and barriers.
- WWF (2023). Report on plastic waste generation in 2022. Youth Publishing House Ha Noi.

DOI: 10.15625/vap.2025.0243

Evaluation of Caffeine Content in Oyster Mushrooms Cultivated on Spent Coffee Grounds Under Urban Agriculture Conditions

Nguyen Thi Thanh Thao, Tran Thi An*

Thu Dau Mot University, Ho Chi Minh City, Vietnam

*Email: antt@tdmu.edu.vn

Abstract: This study employed spent coffee grounds—reclaimed from coffee shops—as a substrate for cultivating oyster mushrooms and analyzed the caffeine accumulation in the mushrooms under urban agricultural production conditions following the circular economy approach. A completely randomized experimental design with five treatments of coffee ground mixtures was applied to cultivate two oyster mushroom species (white oyster and grey oyster), and the caffeine content in the harvested mushrooms from each treatment was analyzed. The results revealed that increasing the proportion of coffee grounds in the cultivation substrate led to higher caffeine accumulation in the mushrooms. In terms of yield, white oyster mushrooms produced higher yields than grey oyster mushrooms. The substrate mixture that provided the highest economic efficiency was 25% coffee grounds combined with 75% sawdust, while the best environmental waste management effect was observed in the 50% coffee grounds + 50% sawdust treatment. This study holds significant socio-economic implications by contributing to urban food supply, diversifying caffeine-containing food sources, utilizing idle urban spaces and labor, and promoting waste recycling to protect the environment amid rapid urbanization in Vietnam.

Keywords: Caffeine, spent coffee grounds, circular economy, oyster mushrooms, urban agriculture.

INTRODUCTION

Caffeine is the most widely used psychoactive substance in the world and forms a distinctive part of the culinary culture in several countries, especially Vietnam. It is also one of the most extensively studied compounds in terms of its effects on the human body. While excessive intake of caffeine can have adverse health effects—such as causing anxiety, fatigue, rapid heartbeat, and negatively affecting the kidneys, stomach, and liver, as well as leading to insomnia - moderate daily consumption, on the other hand, has been shown to offer health benefits. These include increased energy and mental alertness, reduced risk of cancer, stroke, and gout, as well as prevention of Parkinson's disease and type 2 diabetes (Cabrera C.P. et al., 2019; Nguyen T.T.T. et al., 2024).

Caffeine (derived from the French word *caféine* /kaféin/), also known in Latin as *caffeinum*, and by other names such as theine, mateine, guaranine, methyltheobromine, or 1,3,7-trimethylxanthine, is a xanthine alkaloid naturally found in coffee beans, tea leaves, kola nuts, guarana berries, and cocoa. In addition, caffeine is often added to various foods and beverages, including ice cream and energy-enhancing functional foods (Naraian & Dixit, 2017) The development of a natural product containing a small amount of caffeine contributes to diversifying caffeine-containing food sources for consumers and is therefore considered necessary.

Spent coffee grounds (SCG) are being generated in increasing quantities in Vietnam along with the rising consumption of coffee, producing an estimated at hundreds of thousands of tons of SCG annually (Elza B. et al., 2023; Vu C.D. et al., 2021). Currently, SCG are primarily reused as organic fertilizers, biocomposite materials, or feedstocks for various recycling processes (Ermenegilda V. et al., 2024; Anne S.C.B. et al., 2022). However, the potential of SCG as a substrate for mushroom cultivation remains insufficiently explored. Meanwhile, oyster mushroom (*Pleurotus ostreatus*) is an important edible species characterized by its high nutritional value, vigorous growth, and effectiveness as a biodegrader of lignocellulosic organic matter. Several recent studies have demonstrated the feasibility of using SCG as a substrate or substrate supplement for oyster mushroom cultivation, offering a sustainable approach to valorizing this agro-industrial by-product (Torres M. et al., 2024; Nguyen T.T.T. et al., 2024; Sami A.F., 2021). Additionally, because SCG contain residual caffeine—an alkaloid with a recommended maximum daily intake of approximately 400 mg per adult according to the European Food Safety Authority (2015)—evaluating the residual caffeine content in mushrooms cultivated on SCG is essential to ensure consumer safety.

Circular agriculture refers to an agricultural system that applies the principles of the circular economy to the production, business operations, distribution, and consumption of agricultural products (Trinh N.T. et al., 2020). Research on the application of circular economy models in agriculture in Vietnam represents a strategic solution for achieving sustainable development in the context of climate change and resource degradation. The circular economy emphasizes the reuse and recycling of resources, aiming to minimize waste generation.

This study aims to utilize spent coffee grounds collected from coffee shops as a substrate component for cultivating oyster mushrooms (*Pleurotus ostreatus*, including

both white and grey varieties) for daily consumption, and to analyze the accumulation of caffeine in mushrooms under urban agricultural production conditions following the principles of the circular economy. The research also seeks to identify an effective urban mushroom cultivation model based on different mixing ratios of coffee grounds in the substrate. Additionally, this study contributes to urban food supply, diversifies food sources containing caffeine, makes use of unused urban spaces, and partially addresses underutilized labor in cities—thereby promoting environmental protection through waste reuse and supporting agricultural production amidst rapid urbanization in Vietnam.

RESEARCH METHODS

Material

White oyster mushroom (*Pleurotus floridanus*) and grey oyster mushroom (*Pleurotus sajor-caju*): the mushroom spawn was provided by Nong Lam Mushroom Limited Liability Company (Ho Chi Minh City, Vietnam).

Spent coffee grounds were collected from two coffee's shop belonging to the Xanh2Go coffee chain, located in Thu Dau Mot City, Binh Duong Province. The coffee met food safety and hygiene standards, containing no preservatives and no blended ingredients (Certificate No. 3385/TCB-YTBD-2020, dated October 29, 2020, issued by the Department of Health of Binh Duong Province).

Rubberwood sawdust (well-decomposed) was supplied by the Institute of Biotechnology and Environmental Technology, Nong Lam University, Ho Chi Minh City.

Experimental Conditions and Design

Experimental Conditions: The laboratory area was 2m × 3m, totalling 6m², utilizing a vacant, well-ventilated room within an urban household. During the experimental period, room temperature ranged from 24°C to 30°C, and relative humidity ranged from 60% to 80%. Lighting conditions were kept dim with doors closed to minimize external light exposure. The

experimental mushroom cultivation room remained closed during the study, with air

circulation maintained by an exhaust fan. There was no exposure to strong wind or drafts.

Table 1. Experimental treatments for white oyster mushroom (T) and grey oyster mushroom (X)

White oyster mushroom treatments (T)	Substrate bags	Replication	Coffee grounds (%)	Sawdust (%)	Grey oyster mushroom treatments (X)
To	5	3	0	100	Xo
T25	5	3	25	75	X25
T50	5	3	50	50	X50
T75	5	3	75	25	X75
T100	5	3	100	0	X100

(The experiment was conducted at an urban household located in Thu Dau Mot City, Binh Duong Province. The spawn bags were arranged on stacked shelves, with each treatment assigned to a separate designated area)

Experimental design: The experiment was arranged in a Completely Randomized Design (CRD) with one factor and five treatments, corresponding to different mixing ratios of sawdust and spent coffee grounds: 0%, 25%, 50%, 75%, and 100% coffee grounds [6]. Each treatment consisted of five substrate bags with three replications, totaling 75 substrate (spawn) bags.

Method of Caffeine Content Analysis for Oyster Mushrooms

Cultivation procedure of oyster mushrooms: This study applied the cultivation procedure transferred from the Center for Application of Scientific and Technological Advances, under the Department of Science and Technology of Binh Duong Province (Binh Duong DOST, 2024; Nguyen T.T.T., 2024). This is also the commonly used mushroom cultivation method practiced by local farmers.

Caffeine Content Analysis Method: Mushroom samples were naturally air-dried at room temperature, then packaged and labeled with the corresponding experimental treatment codes before being sent to the Analytical Testing Center of the Institute of Biotechnology and Environment, University of Agriculture and Forestry, Ho Chi Minh City. Caffeine content was determined using High-Performance Liquid Chromatography (HPLC), following the Vietnamese National Standard TCVN 9723:2013 (ISO 20481:2008) for coffee and coffee products.

Observed Parameters and Data Analysis: Experimental data were analyzed by comparing the mean values of the treatments and between the two selected oyster mushroom strains. In addition, the correlation between the proportion of spent coffee grounds in the cultivation substrate and the caffeine content accumulated in the harvested mushrooms was assessed. Based on these results, the most suitable mushroom cultivation model under urban conditions was identified, aiming to both utilize waste materials for environmental protection and achieve economic efficiency.

Furthermore, the results were compared with the costs and economic efficiency of the Tho Vuc Farm (located in Dong Nai Province), a commercial mushroom production farm. Average yield was determined based on the weight (grams) and the number of mushrooms per treatment. Caffeine content was measured from randomly collected samples in each treatment.

The economic efficiency of the production models was assessed by calculating input costs and the selling price per unit of mushroom yield per experimental area, and these results were compared with the economic efficiency of the actual production model at Tho Vuc farm (Ho Chi Minh City, Vietnam).

Data were statistically analyzed to compare treatments, calculate means, and evaluate correlations using Microsoft Excel software (Microsoft Corp., USA).

RESULTS AND DISCUSSIONS

Oyster mushroom yield under urban cultivation conditions

Mushroom yield was evaluated based on two main criteria: the number of mushrooms harvested per substrate bag (mushrooms/bag) and the weight of fresh mushrooms obtained per bag (grams/bag). In addition, the size of the mushroom caps was measured for each bag. A high-yield mushroom cultivation process must meet certain requirements, such as producing a large number of mushrooms per bag, having large caps, and yielding a high total weight. Therefore, after the cultivation period, the harvested mushroom caps were used to assess the yield performance across the different treatments implemented in this study.

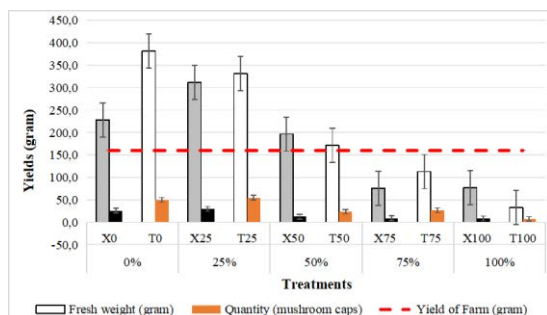


Figure 1. Average yield (quantity and fresh weight) of white oyster mushrooms (T) and grey oyster mushrooms (X) compared to the yield of the farm (Tho Vuc Farm).

The yield of oyster mushrooms under urban cultivation conditions is shown in Figure 1. Both selected mushroom strains yielded higher outputs compared to the conventional yields from the reference farm. The results indicate that the white oyster mushroom exhibited higher productivity than the grey oyster mushroom in treatments with less than 50% spent coffee grounds. The highest yield of white oyster mushrooms was observed in the treatment using only sawdust, with high productivity also observed in the treatment with a 25% coffee ground mixture. In contrast, the grey oyster mushroom achieved its highest yield at the 25% coffee ground treatment (T25%), which was also higher than the control treatment using sawdust only (T0).

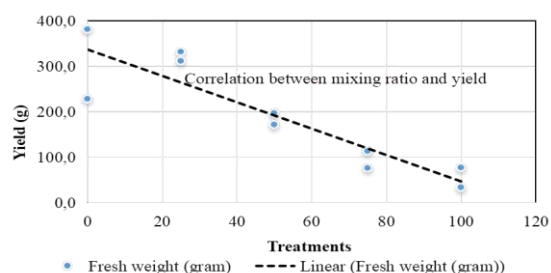


Figure 2. Correlation between mixing ratio and yield.

The results shown in Figure 2 indicate a relatively strong negative correlation ($r^2 = 0.81$) between the mixing ratio and mushroom yield. This suggests that as the proportion of spent coffee grounds in the cultivation substrate increases, the mushroom yield decreases. However, the treatment with 25% coffee grounds demonstrated the highest yield and economic efficiency. As the percentage of coffee grounds in the mixture increases, the mushroom yield decreases. This could be attributed to the higher temperature of spent coffee grounds compared to sawdust (5–10°C), which inhibits fungal growth and increases the likelihood of contamination in the substrate.

Based on the results of this study on yield, it is recommended that for utilizing spent coffee grounds in urban oyster mushroom cultivation, the white oyster mushroom strain should be selected. This strain has a chewy, sweet taste, small caps, and is easy to process, particularly yielding high productivity when cultivated with coffee grounds, which impart a rich aroma. Furthermore, this approach offers higher economic efficiency compared to the control treatment and yields from specialized mushroom Farms

Evaluation of caffeine content in oyster mushroom fruiting bodies

After harvest, oyster mushrooms are primarily consumed as a food source in daily life. White oyster mushrooms offer various health benefits. According to traditional Eastern medicine, they are aromatic, have a mildly sweet taste, and possess a pleasant chewy texture, making them easy to consume. They provide essential nutrients for the human

body and contribute to immune system enhancement.

A sensory evaluation conducted by the research team indicated that oyster mushrooms cultivated on coffee grounds substrates exhibited superior quality, with a more pronounced aroma and sweeter taste compared to commercially available mushrooms. However, this finding warrants further investigation in future studies to validate and better understand the sensory and nutritional improvements associated with coffee-based substrates.

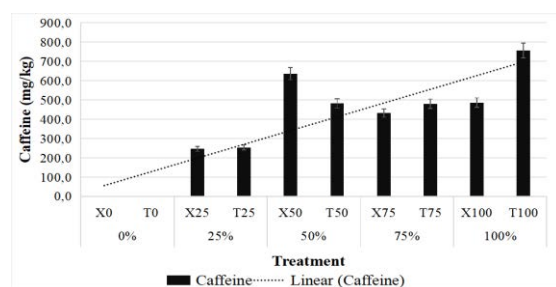


Figure 3. Accumulated caffeine content in grey oyster mushroom (X) and white oyster mushroom (T).

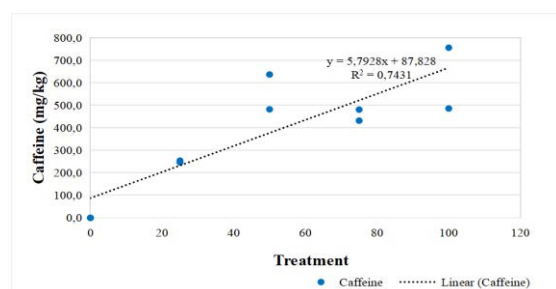


Figure 4. Correlation between cultivation substrate mixing ratio and accumulated caffeine content in mushrooms.

The results from Figures 3 and Figure 4 demonstrate a relatively strong positive correlation between the proportion of spent coffee grounds in the cultivation substrate and the accumulated caffeine content in the mushroom fruiting bodies.

White oyster mushrooms exhibited higher caffeine accumulation than grey oyster

mushrooms across most treatments, except for the 50% coffee grounds + 50% sawdust treatment, where the levels were comparable. The highest caffeine concentrations were observed in the 100% coffee ground treatment, with values of 486 mg/kg for grey oyster mushrooms (X100) and 756 mg/kg for white oyster mushrooms (T100).

Regulations on caffeine content in food may vary depending on the country and the type of food product. However, there are currently no specific regulations regarding the caffeine content in edible mushrooms. A comparison with the National Technical Regulation QCVN 6-2:2010/BYT issued by the Ministry of Health of Vietnam indicates that the analyzed caffeine levels in the tested samples remain within safe limits for consumer health (Vietnam Ministry of Health, 2010).

Initial investment costs and economic efficiency of white oyster mushroom cultivation in urban areas

Based on the yield results, this study recommends that households adopt a substrate mixing ratio of 25% spent coffee grounds and 75% sawdust, which demonstrated the highest economic efficiency. Accordingly, the initial investment costs for cultivating white oyster mushrooms at both household scale and commercial farm scale were compiled and are presented in Table 2. The reference commercial farm was selected at the Tho Vuc Farm (located in Xuan Bac Commune, Xuan Loc District, Dong Nai Province).

The total initial investment cost for cultivating 200 substrate bags was 4,575,000 VND, equivalent to 22,875 VND per bag for the first cycle. It is estimated that three mushroom cultivation cycles can be carried out per year. For the second and third cycles, only recurring costs were considered, including plastic bags, cotton, clean newspaper, rubber bands, spawn, sawdust substrate, 90% alcohol, and transportation.

Table 2. Analyze the economic efficiency of the experimental treatments

Content for an area of 6m ² (Cost for 200 embryo bags)	Quantity	Product price (VND)	Costs (VND)	Compare with Mushroom Production Farm (Area: 60 m ² (10x6m))	
Planting house (take advantage of space): Empty room, warehouse, warehouse corner... Usable area: 2x3=6 m ² (can grow 300-500 embryo bags).	1	-	-		30.000.000
Assembled shelf (can be placed on the floor or hung on a truss: reduces costs): (5 floors x 150 cm x 40 cm) - Long-term use.	3 prs	1.200.000	3.600.000	Hang the bag	1.500.000
Experimental materials: +Plastic bags size 25*35 cm;	3 kg	65.000	195.000		
+Cotton balls, clean newspaper and rubber bands.	1	20.000	20.000		
Bottle neck size 34 mm: 1kg has about 300 pieces (no caps to reduce costs)	1	45.000	45.000	60 kg cap	1.800.000
Mushroom spawn: 1 bag of seed can produce 50-100 bags.	4	20.000	80.000		
mushroom embryo bags for a 3-6 month growing process: 200kg sawdust (use 3-6 months): 200 kg needed for 200 embryo bags;	2	50.000	100.000	10.000 embryo bags	27.000.000
Coffee grounds: used from coffee shops: 100 kg for 200 bags of 25% coffee beans (use for 3-6 months)	100	-	-		
Cost of mushroom culture tool: 2 alcohol lamps: 2x30.000 VND/piece; tweezers 30.000 VND/piece; 90 degree alcohol: 15.000 VND/bottle - Long-term use	1	135.000	135.000		
Raw material transportation costs (trip)	1	400.000	400.000	Trips	3.000.000
Total first cost for 200 embryo bags/6 m²			4.575.000	Total cost (10.000 bags/60 m²/year)	63.300.000
Total cost for the first time for 01 embryo bag.			22.875		
Cost for crops 2 and 3 (Investment in 3 crops/year)			840.000		
Total investment in the year (3 crops): only calculated for 200 embryo bags, the number of embryo bags can increase and income will decrease.			6.255.000		
Cost for 01 embryo sac/ calculated over 01 year.			10.425		6.330
PROFIT					
Highest yield (X25 of 25% coffee grounds): about 0.3 kg/bag x 600 bags (3 harvesting periods/year)/ 6 m ² of land.	180	50.000	9.000.000	Yield: 1.600kg x 25.000 VND	40.000.000

Profit: (3.600.000 VND/6 m ² /4 months)			8.100.000	Profit: (-31.800.000) VND/60 m ² /4 months	14.500.000
Profit/month (VND)			675.000		1.208.333 = 120.833 per 6 m²

The total investment cost for the second and third cultivation cycles is calculated as follows: $(195.000 + 20.000 + 80.000 + 100.000 + 45.000 + 400.000) \times 2 = 1.680.000$ VND. Therefore, the total investment cost for white oyster mushroom cultivation over one year (three cycles) amounts to: $4.575.000 + 1.680.000 = 6.255.000$ VND. The annual investment cost per substrate bag is calculated as: $6.255.000/600 = 10.425$ VND per bag per year.

According to the data in Table 2, the fresh mushroom yield per bag under the T25 treatment (25% spent coffee grounds and 75% sawdust) was 331.6 grams/bag (0.3316 kg/bag), and under the X25 treatment was 311.4 grams/bag (0.3114 kg/bag). Assuming three cultivation cycles per year, the estimated annual yield of fresh mushrooms would be approximately 200 kg/year (T25) and 187 kg/year (X25).

Based on the current market price of 50.000 VND/kg, the projected annual revenue would be 10.000.000 VND/year for T25 and 9.350.000 VND/year for X25. The annual profit for a household-scale production area of 6 m² is calculated as follows: T25 treatment: $(10.000.000 - 3.600.000/4) = 9.100.000$ VND/year, equivalent to 758.333 VND/month. X25 treatment: $(9.350.000 - 3.600.000/4) = 8.450.000$ VND/year, equivalent to 704.166 VND/month.

Meanwhile, the production cost at the mushroom farm is 63.300.000 VND for 10.000 substrate bags, equivalent to 6.330 VND per bag. For white oyster mushrooms cultivated at a farm scale, the estimated selling price is 25.000 VND/kg. Therefore, the projected revenue from white oyster mushroom

production in one year is $1.600 \text{ kg} \times 25.000 \text{ VND} = 40.000.000 \text{ VND}$.

The annual profit for a farm with a cultivation area of 60 m² is calculated as: $(40.000.000 - 31.800.000/4) = 14.500.000$ VND/year. The monthly profit is: $14.500.000 / 12 = 1.208.333$ VND/month, which corresponds to 120.833 VND/month when normalized to a 6 m² area.

Thus, the monthly profit from oyster mushroom cultivation in this study was 758.333 VND/month (T25) and 704.166 VND/month (X25), which is significantly higher than the profit generated by the commercial mushroom farm, with only 120.833 VND/month.

In addition to the economic benefits, the study also demonstrated positive environmental impacts by processing 300 kg of coffee waste annually, reusing 200 spent substrate bags (after mushroom cultivation) for growing leafy vegetables or ornamental plants, and utilizing small urban land areas to increase household income or provide fresh food for the family.

If the primary objective is to maximize waste recycling, the treatment with 50% coffee grounds and 50% sawdust is also recommended. This approach not only ensures acceptable yields of fresh mushrooms but also helps double the amount of coffee waste processed (600 kg/year), thereby contributing more significantly to environmental sustainability.

Potential of circular economy and urban agriculture

This study also serves as a representative example of circular economy practices within

urban agriculture. In Vietnam, the term "circular economy" is still relatively new, and its practical application faces many limitations due to the incomplete understanding of the concept by government agencies, businesses, and farmers. Government agencies often have vague and unclear concepts, leading to incomplete guidance and implementation (Woon et al, 2010; Owaid et al., 2017). On the other hand, during production, farmers primarily focus on yield and high productivity, without considering the reduction of input materials. Furthermore, the capacity for recycling and reusing waste in Vietnam is still limited (Trinh Ngoc Tuan et al., 2021). Technology for waste treatment, recycling, and reuse has not been strongly invested in. Additionally, small-scale production and processing facilities hinder the collection and sorting of waste products. Currently, businesses only engage in waste collection or incineration and do not focus on sorting or reuse (Tambaru et al., 2023).

Based on the research results, the proposed model for cultivating oyster mushrooms in urban areas, following the principles of the circular economy, aims to enhance income, create jobs, improve household meals, and simultaneously assist in waste utilization and environmental pollution reduction. This model is recommended for modern urban agriculture.

CONCLUSIONS

The combination of spent coffee grounds and rubber sawdust as a substrate for cultivating white oyster mushrooms not only brings economic benefits but also contributes to the circular agricultural production process by supplying food sources in urban areas. Moreover, it holds environmental significance and helps address a portion of urban labor under-utilization. The results of this study indicate that increasing the proportion of coffee grounds in the cultivation substrate leads to higher mushroom yields and caffeine

content. The mushrooms grown under these conditions exhibit a pleasant flavor and provide a low level of natural caffeine, which may offer health benefits to consumers.

The research also demonstrates that white oyster mushrooms grown on a substrate mixture of 25% coffee grounds and 75% sawdust yield the highest productivity, or alternatively, a 50% coffee grounds and 50% sawdust mixture offers both edible mushrooms and the highest waste treatment, resulting in high economic efficiency while effectively contributing to waste management and environmental protection.

REFERENCES

- Anne Shayene Campos de Bomfim, Daniel Magalhães de Oliveira, Herman Jacobus Cornelis Voorwald, Kelly Cristina Coelho de Carvalho Benini, Marie-Josée Dumont, Denis Rodrigue (2022). Valorization of Spent Coffee Grounds as Precursors for Biopolymers and Composite Production. *Polymers* (Basel). 2022 Jan 22;14(3):437. doi: 10.3390/polym14030437.
- Binh Duong Department of Science and Technology (Binh Duong DOST). Techniques for processing oyster mushroom waste for growing straw mushrooms in Binh Duong province. Conference documents (2024)
- Cabrera C.P., Bell T.L., Kertesz M.A. (2019). Caffeine metabolism during cultivation of oyster mushroom (*Pleurotus ostreatus*) with spent coffee grounds. *Appl Microbiol Biotechnol*. 2019 Jul;103(14):5831-5841. doi: 10.1007/s00253-019-09883-z. Epub 2019 May 21.
- Elza Bevilacqua, Vinicius Cruzat, Indu Singh, Roselyn B Rose'Meyer, Sunil K Panchal, Lindsay Brown (2023). The Potential of Spent Coffee Grounds in Functional Food Development. *Nutrients*. 2023 Feb 16;15(4):994. Doi: 10.3390/nu15040994.
- Ermenegilda Vitale, Chiara Maria Motta, Bice Avallone, Angela Amoresano, Carolina ontanarosa, Gennaro Battaglia, Michele Spinelli, Chiara Fogliano, Roberta Paradiso & Carmen Arena (2024). Sustainable Reuse of Espresso Coffee By-products as a Natural Fertilizer to Improve Growth and Photosynthesis in Cucumber (*Cucumis sativus* L.) Waste and Biomass Valorization (2024) 15:543–559.
- Michal Milek, Monica Kloc, Malgorzata Dzuga (2023). The content of polyphenols and caffeine in spent coffee grounds obtained from various home brewing

- methods. *Zywnosc Nauka Technologia Jakosc*, 30, 1 (134), 40 – 52.
- Naraian R. & Dixit B. (2017) Nutritional Value of Three Different Oyster Mushrooms Grown on Cattail Weed Substrate Archives of Biotechnology and Biomedicine, 1, 061-6.
- Nguyen Thi Thanh Thao, Nguyen Thi Ngoc, Nguyen Hoang Tien, Pham Le Minh Thien, Pham Anh Thu, Nguyen Huu Vinh (2024). Research on utilizing coffee grounds as a substrate for cultivating grey oyster mushrooms (*Pleurotus sajor-caju*) in urban areas. *Thu Dau Mot University Journal of Science*, 6 (2), DOI: 10.37550/tdmu.EJS/2024.01.549.
- Owaid M. N., Abed I. A. and Al-Saeedi S. (2017). Applicable properties of the bio-fertilizer spent mushroom substrate in organic systems as a byproduct from the cultivation of *Pleurotus* spp *Information Processing in Agriculture*, 4, 78-82.
- Tambaru E., Ura R. & Tuwo M. (2023). The effect of coffee grounds and sawdust *Tectona grandis* L. f. as planting media for cultivation oyster mushroom *Pleurotus* sp., *IOP Conference Series: Earth and Environmental Science*, 1230 012071, DOI 10.1088/1755-1315/1230/1/012071.
- Trinh Ngoc Tuan, Tran Van Tuan, Ngo Thi Nhip (2021), Promoting the circular economy in Vietnam's industries - Solution to protect environment and sustainable development. *Journal of Industry and Trade - Scientific research results and technology applications*, No. 29-30.
- Vietnam Ministry of Health (2010), National technical regulations for non-alcoholic beverage products, QCVN 6-2:2011/BYT.
- Vu Cong Danh, Vu Thi Quyen, Nguyen Ha Dieu Trang (2023) Spent coffee grounds collected in Ho Chi Minh city: A good source of phenolic acids and fatty acids. *Thu Dau Mot University Journal of Science - Volume 3 - Issue 3-2021*.
- Woon Yao Chai, Umahsreerekah Gopala Krishnan, Vikineswary Sabaratnam, Joash Ban Lee Tan (2010). Assessment of coffee waste in formulation of substrate for oyster mushrooms *Pleurotus pulmonarius* and *Pleurotus floridanus*, *Future Foods*, Volume 4, 100075, <https://doi.org/10.1016/j.fufo.2021.100075>.

Selection of phosphate-solubilizing bacteria and evaluation of their ability to resist plant pathogenic fungi

Mai Van, Dinh^{1,*}, Manh Ha, Nguyen²

¹Faculty of Environmental Sciences, University of Science, Vietnam National University, Hanoi, 334 Nguyen Trai, Thanh Xuan, Hanoi, Viet Nam; SoilTECH laboratory, University of Science, Vietnam National University, Hanoi, Hoa Lac, Thach That, Hanoi, Viet Nam

²Forest Protection Research Center, Vietnamese Academy of Forest Sciences, 46 Duc Thang, Dong Ngac, Hanoi, Vietnam.

*Email: vandm@vnu.edu.vn

Abstract: Plant diseases caused by pathogenic fungi, such as *Fusarium oxysporum*, *Phytophthora vexans*, and *Fusarium solani*, severely diminish plant vitality and pose a significant threat to crop production. Biological control, which employs beneficial microbes, including plant growth-promoting rhizobacteria, has emerged as an effective and safe method for sustainable crop management. This study aimed to isolate and select phosphorus-solubilizing bacterial isolates and evaluate their antifungal activity. Bacteria were isolated from soil at three different agroforestry systems: sugarcane monoculture, longan-maize-forage grass, and mango-maize-forage grass. The antifungal activity of the bacterial isolates was assessed using the dual culture method on Potato Dextrose Agar (PDA) medium. The potential bacterial isolate was then grown on Potato Dextrose Broth (PDB) medium, and the antifungal activity of the culture filtrate was tested. The results indicated that three isolates, SL13.1, SL15.1, and SL09.4, exhibited phosphorus-solubilizing activity, with solubilization concentrations of 15.8 mg/L, 8.2 mg/L, and 7.5 mg/L, respectively. Among these, isolate SL13.1 demonstrated antifungal activity against all three pathogenic fungi, exhibiting inhibitory effects of 47.6% against *F. oxysporum*, 46.0% against *P. vexans*, and 59.7% against *F. solani*. Additionally, the culture filtrate of this isolate inhibited the mycelia of *F. oxysporum*, *P. vexans*, and *F. solani* with inhibition rates of 87.2%, 90.8%, and 84.4%, respectively. Molecular identification using the

primer pair 27F/1492R indicated that isolate SL13.1 was identified as *Bacillus* sp.. These findings suggest that phosphorus-solubilizing microorganisms have great potential for use as biocontrol agents, contributing to the advancement of sustainable agriculture.

Keywords: Biological control, pathogenic fungi, phosphorus-solubilizing bacterial, plant diseases.

INTRODUCTION

Phosphorus (P) is one of the major elements required for plant growth and development, playing an important role in almost all plant metabolic processes including photosynthesis, energy transfer, signal transduction, nitrogen fixation in legumes and respiration (Khan et al. 2014). P is abundant in soils in both inorganic (phosphate-Pi) and organic (Po) forms. Inorganic phosphorus usually accounts for 35% to 75% of the total P, while organic phosphorus makes up 30% to 65% (Harrison 1987). The most common Pi form is apatite, which is weathered slowly, releasing Pi as orthophosphate (H_2PO_4^- , HPO_4^{2-}), that the soluble form for root uptake. However, the concentration of this soluble P in soil solutions very low, less than 1% of the total P and is insufficient to meet plant requirement (Plante 2007). The demand for phosphatic fertilizers has consequently increased over the years to improve crop yield. However, plants can use a small proportion of phosphatic these fertilizers; the vast majority precipitates in the soil, causing harmful effects on the

environment, including both aquatic and soil environments, and indirectly impacting on consumer health (Rawat et al. 2021).

Phosphate-solubilizing microorganisms (PSMs) have great potential as future biofertilizers due to their multiple benefits. These include improving soil P fertility through the conversion of inorganic P to soluble P, ameliorating soil health, reducing reliance on chemical fertilizers, and offering a low-cost, non-polluting technology (Khan et al. 2007; Meena et al. 2016; Panda et al. 2016; Liu et al. 2016; Kalayu 2019; Mitra et al. 2020; Tian et al. 2021; Pan and Cai 2023). Additionally, PSMs (including phosphate-solubilizing bacteria (PSB) and phosphorus-solubilizing fungi) also exhibit potential as biocontrol agents against several phytopathogens. Several PSB strains (PSBs) have demonstrated the control of multiple plant diseases using different biocontrol agents, such as *Pseudomonas* sp. *SP0113*, *Bacillus subtilis*, *Bacillus amyloliquefaciens*, which observed antagonists against major crop pathogenic fungi, several soil-borne pathogens, root pathogenic fungi caused by plant pathogen *Fusarium oxysporum*, *A. solani*, *R. solani* (R Srivastava 2009; Wahyudi 2011; Yuan et al. 2013; Sarhan and Shehata 2014; Mitra et al. 2020). Almost all of these PSBs were selected from plants; the PSBs isolated from the soil protects plants from plant pathogen *Fusarium oxysporum*, *Phytophthium vexans*, and *Fusarium solani* have been limited. Phosphate-solubilizing bacteria are more dominant than fungi and other phosphorus-solubilizing microorganisms in the soil (Liu et al. 2016). Land use types have may various effects on soil communities, soil microbial biomass. The microbial biomass decrease following soil dept and is upto five times higher in forest land and grass land than arable land in the top soil (Zhang et al. 2020). However, in our knowledge only one Zhang et al. 2020 observed the different amount of phosphate solubilizing bacteria unde diferent land uses. They indicated that the change of PSBs in land use types is related to amount of available phosphorus.

So, this study was conducted to isolate and select phosphorus-solubilizing bacterial isolates and evaluate the antifungal properties of potential bacterial strains soil at three different agroforestry systems: sugarcane monoculture, longan-maize-forage grass, and mango-maize-forage grass; towards the development of multifunctional microbial preparations, research on the application of bacterial isolates that are both capable of producing growth stimulants and antifungal properties has been conducted.

MATERIALS AND METHODS

Method of collecting soil samples and isolating phosphorus-solubilizing bacteria

Soil samples were collected from three different agroforestry systems: sugarcane monoculture, longan-maize-forage grass, and mango-maize-forage grass in Mai Son, Son La Province. A total of 18 samples were taken from 12 different locations following a zigzag pattern. At each location, soil samples were collected at two depths: 0-20 cm and 20-40 cm. The samples included 6 from the sugarcane trial, 6 from the longan trial, and 6 from the mango trial. Each trial had 3 samples taken from the 0-20 cm depth and 3 samples taken from the 20-40 cm depth.

After processing, soil samples were analyzed for insoluble phosphate-solubilizing bacteria using the critical dilution method on Pikovskaya agar medium. Begin by dissolving 10 grams of soil from each sample in 90 ml of sterilized distilled water. Incubate the soil solution on a thermostatic shaker for 24 hours at 25°C, with shaking at 100 rpm. Next, dilute the soil solution to a concentration of 10^{-4} . To isolate the phosphate-solubilizing bacteria, pipette 0.5 ml of the diluted soil solution (10^{-4}) onto Pikovskaya agar medium, spreading it evenly across the surface. After incubating the plates in the dark at 25°C for 7 days, separate and purify the colonies capable of solubilizing insoluble phosphorus on new agar plates.

Method for evaluating the phosphorus-solubilizing abilities of isolated bacteria

Evaluation of the ability to solubilize insoluble phosphorus on Pikovskaya agar medium. Each bacterial isolate was inoculated at three points on Pikovskaya agar medium plates and replicated three times. After seven days of incubation in the dark at 25°C, the diameter of the phosphorus dissolution zone was measured. The efficiency of phosphorus dissolution is calculated based on the diameter of this zone (D) and is classified into the following categories: low efficiency if $D \leq 2$ mm, average efficiency if $2 \text{ mm} < D \leq 5 \text{ mm}$, and high efficiency if $D > 5 \text{ mm}$ (Nguyen et al. 2021).

Bacterial isolates with high phosphorus-solubilizing efficiency were evaluated for their ability to resolve insoluble phosphorus on liquid Pikovskaya medium (no agar). Cultivate 1 ml solution of phosphate-solubilizing bacterial isolates (10^6 CFU/ml) in 100 ml Erlenmeyer flasks containing 30 ml of Pikovskaya medium. These flasks were cultured on a thermostatic shaker at a temperature of 25°C, with a shaking speed of 120 rpm. The experiment was conducted with 3 repetitions. After 7 days of culture, the bacterial solution was filtered through 0.45 µm cellulose acetate filter paper, and the filtrate was collected for analysis to determine the soluble phosphorus concentration. The soluble phosphorus concentration in the filtrate was determined by the molybdate blue method (TCVN 6202:2008) using a spectrophotometer at a wavelength of 882 nm.

Method for evaluating the antifungal activity of phosphorus-solubilizing bacterial isolates

The bacterial isolate SL13.1, which demonstrated the strongest phosphorus-solubilizing effect in the liquid Pikovskaya medium experiment, was evaluated for its antifungal activity against *Fusarium oxysporum*, *Phytophthora vexans*, and *Fusarium solani* using the dual culture method on potato dextrose agar (PDA) medium. In this method, a plug (5 mm) of each fungal pathogen was inoculated at the center of Petri dishes containing PDA medium. The bacterial isolate

(SL13.1) was then inoculated at three evenly spaced points near the outer edge of the Petri dish. For the control plate, only the fungal mycelium was inoculated in the center of the PDA plate without the addition of the phosphate-solubilizing bacteria. After 7 days of incubation at 25°C, the inhibitory effect of the phosphate-solubilizing bacterial isolate on the pathogenic fungi was assessed by measuring the diameter of the fungal mycelium in both the experimental and control plates. The antifungal effect of the bacterial isolate was calculated using the following formula:

$$\text{MGI (\%)} = \frac{C - T}{C} \times 100 \%$$

where C is mycelial growth of test pathogen in the control plate and T is mycelial growth of test pathogen in the experimental plate.

The evaluation of the inhibitory effect of culture filtrate from isolate SL13.1 on pathogenic fungi was conducted as follows: The bacterial isolate was cultured in potato dextrose broth (PDB) for two weeks at 25°C with a shaking speed of 150 rpm. After incubation, the suspension was filtered through a 0.45 µm membrane. The resulting culture filtrate was then mixed with autoclaved potato dextrose agar (PDA) medium at a 1:1 ratio and transferred to Petri dishes. In the control dishes, the bacterial culture filtrate was replaced with sterile distilled water. Pathogenic fungal strains were inoculated in the center of the agar plates and incubated at 25°C for seven days. The effect of mycelial growth inhibition was assessed using the formula from the previously mentioned dual culture experiment.

Identification of phosphorus-solubilizing bacteria with antifungal activities

Identification of phosphate-solubilizing bacterial strains with antifungal activity against plant pathogens was conducted by sequencing the 16S rDNA gene region. The bacterial genomes were extracted using the Quick-DNA Fungal/Bacterial Miniprep kit from Zymo Research, USA. PCR reactions were performed with the primer pairs 27F (5'-AGAGTTTGATCMTGGCTCAG-3') and 1492R

(5'-TACGGYTACCTTGTTACGACTT-3'). The PCR products were sequenced using the Sanger technique, and the complete DNA sequences were compared with the GenBank database at NCBI (<https://blast.ncbi.nlm.nih.gov>) through BLAST searches.

Statistical analysis

The antifungal activity and phosphorus solubilization ability of the bacterial isolates were evaluated by analysis of variance (ANOVA) followed by Tukey post hoc test for comparison of mean values. The analyses were performed using Statistical Package for the Social Sciences (SPSS) version 27 software.

RESULTS AND DISCUSSION

Isolation and screening of phosphorus-solubilizing bacteria isolates

Land use types have made effect on soil distribution on PSB isolates. The total number of PSB isolates obtained from the 3 soil land use types'samples was 45 isolates, including 22 isolates from Sugarcane land samples, 15 isolates from longan-maize-forage grass land samples, and 8 isolates from mango-maize-forage grass land samples (Fig. 1). There was a significant difference in the number of PSB isolates in three different land use types ($p < 0.05$). This finding was similar to the result of Zhang et al 2020. However, they indicated that the amount of PSBop in the soil increases with the concentration of available phosphorus; PSBin did not correlate to the soil nutrients (Zhang et al. 2020). PSB isolates were significantly more isolated in the soil layer from 0-20 cm than in the soil layer from 20-40 cm (Fig. 1). The number of bacterial isolates with medium phosphorus solubilizing efficiency predominates with a total of 31 isolates, while the number of isolates with low phosphorus solubilizing efficiency is 10 isolates, and the number of isolates with high phosphorus solubilizing efficiency is 4 isolates (Fig. 2). The sugarcane land and the longan-maize-forage grass land recorded 01 isolates with high phosphorus solubilizing ability in each model, and the remaining 2 highly effective isolates were distributed in the

mango-maize forage grass land (Fig. 2). Bacterial isolates with high phosphorus-solubilizing efficiency on agar medium, designated SLo6.2, SLo9.4, SL13.1, and SL15.1 (Fig. 3), were further evaluated for their ability to solubilize phosphorus in liquid Pikovskaya medium.

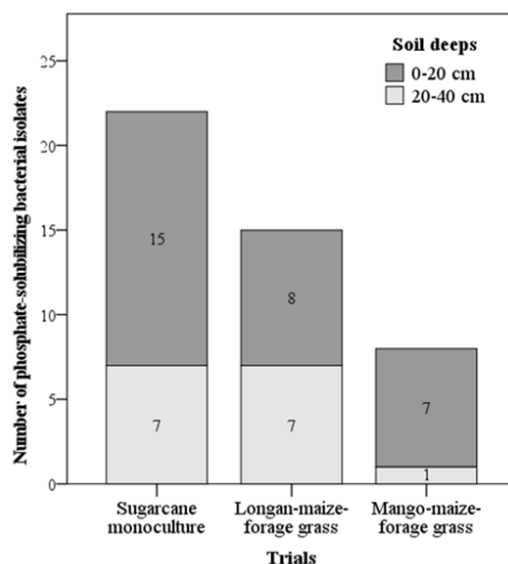


Figure 1. Number of PSB isolates in three different land use types and soil deeps

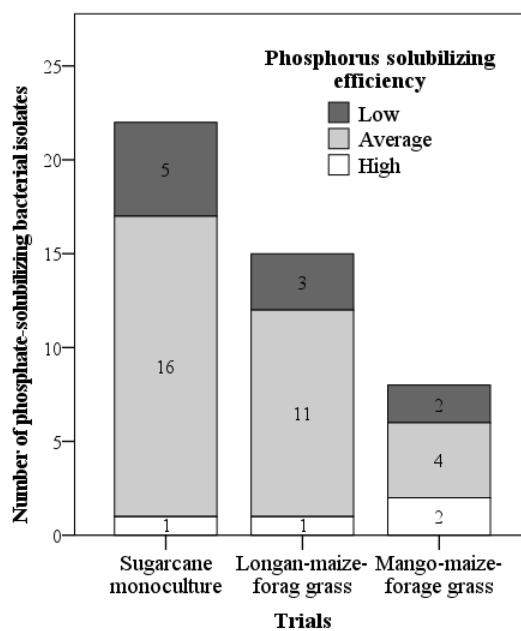


Figure 2. Number of PSB isolates in three land use types and phosphorus solubilizing efficiency

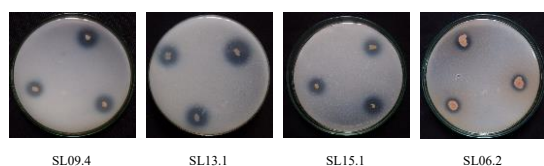


Figure 3. PSB isolates with high phosphate solubilization efficiency on Pikovskaya agar medium

The phosphorus solubilization ability of the phosphorus-solubilizing bacterial isolates

The ability to dissolve phosphorus in the culture solution varied significantly among the bacterial isolates ($p < 0.05$). Isolate SL13.1 exhibited the highest phosphorus solubilization ability, with a measured solubility of 15.8 mg/L. Isolates SL15.1, SL09.4 and SL06.2 showed lower solubility compared to isolates SL13.1, recording values of 8.2 mg/L, 7.5 mg/L and 6.9 mg/L, respectively (Fig. 5). Self-solubilization was also observed in the uninoculated control (or control group), which yielded a solubility of 2.1 mg/L. The PSB isolates thus contributed to a significant increase in the dissolved phosphorus content during the culture process. Most notably, isolate SL13.1 had a phosphorus solubility nearly 8-fold higher than the control. The results of identification of bacterial isolates SL13.1 by 16S rDNA gene sequencing method determined the closest scientific name to the species *Bacillus* sp. with a similarity of 99.45%. *Bacillus* has been consistently identified as one of the most dominant bacteria genera in soil and the natural ability of these strains to transform phosphorus from insoluble into soluble forms (Meena et al 2017, Wyciszkievicz et al 2015, Wyciszkievicz et al 2017, Saeid et al 2018, Rawat et al 2020). The amount of phosphorus solubilized by some *Bacillus* isolates can be substantial, with reported values reaching up to 750 µg/ml (Rawat et al 2020, Iqbal et al 2024), which is many times higher compared to the solubility recorded for SL13.1. The different mechanisms observed for releasing soluble forms of phosphorus to plants in the soil including the production of organic acids, the secretions of enzymes (phytase and

phosphatases), and chelation siderophores, extracellular polysaccharides) (Rawat et al 2020, Iqbal et al 2024, Pan et al 2023, Liu et al 2016). From our study, the bacterial isolate SL13.1 (*Bacillus* sp.) was subsequently selected for further testing of its antifungal activity against some plant pathogenic fungi such as *F. oxysporum*, *P. vexans*, and *F. solani* on PDA medium in the laboratory.

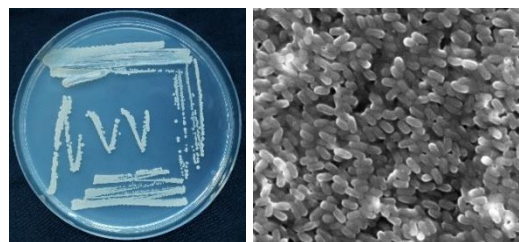


Figure 4. Isolate SL13.1 (*Bacillus* sp.) colonies were observed on PDA medium (left), and spores were examined under SEM (right).

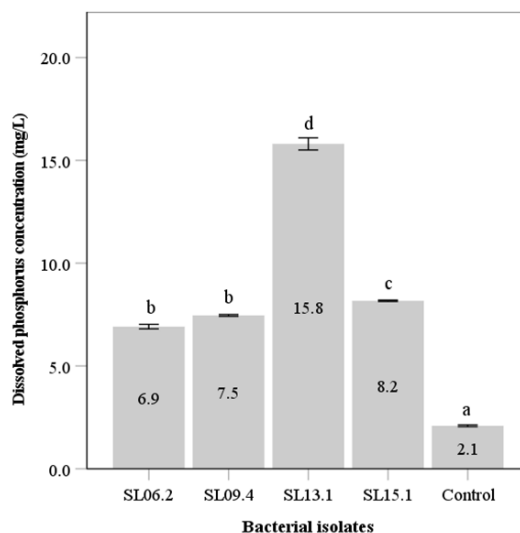


Figure 5. Concentration of dissolved phosphorus in the filtrate of phosphate-solubilizing bacterial strains. Different letters indicate significant differences between bacterial strains and the control according to Tukey's HSD test.

Antifungal activity of phosphate-solubilizing bacteria isolate against plant fungal pathogens

In the dual culture experiment, the bacterial isolate SL13.1 demonstrated an inhibitory effect on the mycelial growth of *F.*

oxysporum, *P. vexans*, and *F. solani*, with significant variations noted among the fungal species (Fig. 6 and 7). The strongest inhibitory effect was observed against *F. solani*, with an inhibition rate of 59.7%. In contrast, the inhibition rates for *F. oxysporum* and *P. vexans* were 47.6% and 46.0%, respectively. A significant difference in antifungal activity was found between *F. solani* and the other two fungal species. However, the inhibitory effects on *F. oxysporum* and *P. vexans* did not show a significant difference (Fig. 6).

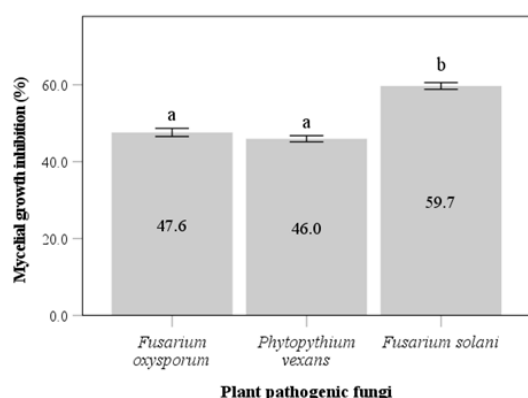


Figure 6. Inhibitory effect of phosphate-solubilizing bacterial isolate SL13.1 on mycelial growth of pathogenic fungi in dual culture experiments. Different letters indicate significant differences between bacterial strains and the control according to Tukey's HSD test.

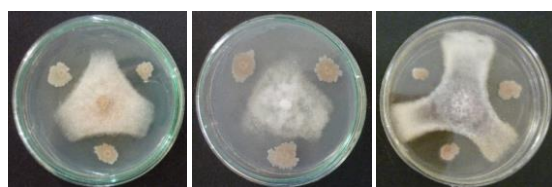


Figure 7. The phosphate-solubilizing bacterial isolate SL13.1 inhibits pathogenic fungi in dual culture experiments. From left to right, the pathogenic fungi include: *Fusarium oxysporum*, *Phytophthium vexans*, and *Fusarium solani*.

The ability of the culture filtrate from the SL13.1 isolate against pathogenic fungi is illustrated in Fig. 8 and 9. This culture filtrate has demonstrated a strong capacity to inhibit the mycelium of all three tested pathogenic fungi. Specifically, it exhibits the most

significant inhibitory effect on *P. vexans*, with an inhibition rate of 90.8%. This is followed by *F. oxysporum* and *F. solani*, which show inhibition rates of 87.2% and 84.4%, respectively (Fig. 8). Notably, the mycelial inhibition rates vary significantly among the different pathogenic fungi.

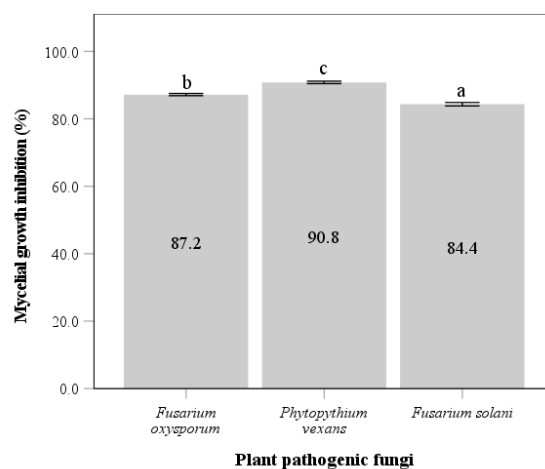


Figure 8. Inhibitory effect of phosphate-solubilizing bacterial isolate SL13.1 on mycelial growth of pathogenic fungi in culture filtrate experiments. Different letters indicate significant differences between bacterial strains and the control according to Tukey's HSD test.

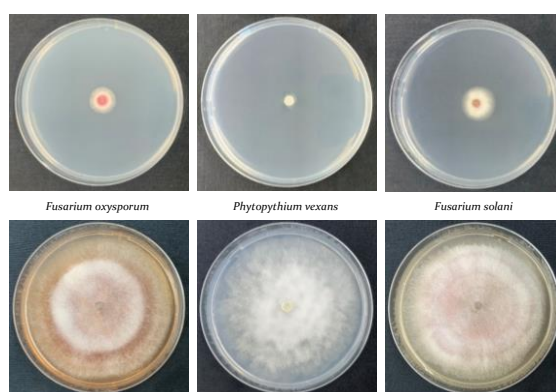


Figure 9. Mycelial growth of *Fusarium oxysporum*, *Phytophthium vexans*, and *Fusarium solani* was observed on PDA medium containing culture filtrates of SL13.1 (above) and control plates (below) after incubating in the dark at 25°C for 7 days.

The inhibitory effectiveness of the bacterial isolate SL13.1 (*Bacillus* sp.) against plant pathogens varied between the dual

culture and culture filtrate experiments. In the dual culture test, *P. vexans* showed the lowest inhibition rate at 46.0% (Fig. 6). However, in the culture filtrate test, it was significantly inhibited by 90.8% (Fig. 8). Pathogenic fungi often respond differently to microbial resistance mechanisms (Sharma 2021). *Bacillus* species have shown great potential for biological control against plant pathogenic fungi. They may inhibit the growth of these pathogens by producing enzymes that degrade the fungal cell wall, as well as by generating secondary metabolites that not only suppress fungal growth but also promote the health of host plants (Abriouel et al. 2011; Salazar et al. 2017; Butt and Bastas 2022).

Bacillus subtilis has the ability to produce the enzyme chitinase, which helps reduce the growth of *Rhizoctonia solani*, a pathogen responsible for potato disease, by 42.3% (Saber et al. 2015). Additionally, *B. subtilis* enhances the growth of tomato plants, achieving control efficiencies of 20.65% in the nursery and 35.23% in the field for managing *Rhizoctonia solani*, which causes root rot in tomatoes (Liu et al. 2011). The inhibitory effect of *Bacillus* species on pathogenic fungi is partly due to their production of volatile organic compounds (VOCs) (Yuan et al. 2012; Gao et al. 2018; Caulier et al. 2019). *B. subtilis*, for instance, can generate 74 different VOCs, including alcohols, ketones, pyrazines, and esters, etc. These compounds have been shown to inhibit the mycelial growth of various plant pathogenic fungi, such as *Botrytis cinerea*, *Colletotrichum gloeosporioides*, *Penicillium expansum*, *Monilinia fructicola*, and *Alternaria alternata*, achieving an average inhibition rate of 59.97% (Gao et al. 2018). In addition, various *Bacillus* strains can produce siderophores, colonize and compete for ecological niches, and induce systemic resistance in plants, thereby enhancing their defense capabilities against plant pathogens (Etesami et al. 2023). In general, *Bacillus* bacteria include a wide variety of species, the majority of which are harmless to plants. However, some species have been identified as pathogenic bacteria. It is crucial to conduct further studies, particularly focusing

on the precise identification of isolate SL13.1 using additional gene sequences, in order to evaluate its potential as a microbial preparation or biological pesticide.

CONCLUSION

The distribution of phosphorus-solubilizing bacterial isolates varies across three different agroforestry systems. In this study, we identified 22 isolates from sugarcane monoculture, 15 isolates from a longan-maize-forage grass system, and 8 isolates from a mango-maize-forage grass system. Among these isolates, SL13.1 demonstrated the strongest phosphorus-solubilizing ability and exhibited antifungal activity against the plant pathogens *F. oxysporum*, *P. vexans*, and *F. solani*. The inhibition rates in culture filtrate tests against these pathogens were 87.2%, 90.8%, and 84.4%, respectively. Identification of bacterial isolate SL13.1 through 16S rDNA gene sequencing revealed that it is closely related to the species *Bacillus* sp., with a similarity of 99.45%.

REFERECNES

- Abriouel H, Franz CMAP, Omar NB, Gálvez A (2011) Diversity and applications of *Bacillus* bacteriocins. *FEMS Microbiol Rev* 35:201–232.
- Butt H, Bastas KK (2022) Biochemical and molecular effectiveness of *Bacillus* spp. in disease suppression of horticultural crops. In: *Sustainable Horticulture*. Elsevier, pp 461–494
- Caulier S, Nannan C, Gillis A, et al (2019) Overview of the Antimicrobial Compounds Produced by Members of the *Bacillus subtilis* Group. *Front Microbiol* 10:302.
- Etesami H, Jeong BR, Glick BR (2023) Biocontrol of plant diseases by *Bacillus* spp. *Physiological and Molecular Plant Pathology* 126:102048.
- Gao H, Li P, Xu X, et al (2018) Research on Volatile Organic Compounds From *Bacillus subtilis* CF-3: Biocontrol Effects on Fruit Fungal Pathogens and Dynamic Changes During Fermentation. *Front Microbiol* 9:456.
- Harrison AF (ed) (1987) *Soil organic phosphorus: a review of world literature*. CAB International, Wallingford

- Kalayu G (2019) Phosphate Solubilizing Microorganisms: Promising Approach as Biofertilizers. *International Journal of Agronomy* 2019:1–7.
- Khan MS, Zaidi A, Musarrat J (eds) (2014) *Phosphate Solubilizing Microorganisms: Principles and Application of Microphos Technology*. Springer International Publishing, Cham
- Khan MS, Zaidi A, Wani PA (2007) Role of phosphate-solubilizing microorganisms in sustainable agriculture — A review. *Agron Sustain Dev* 27:29–43.
- Liu M, Liu X, Cheng B-S, et al (2016) Selection and evaluation of phosphate-solubilizing bacteria from grapevine rhizospheres for use as biofertilizers. *Span j agric res* 14:e1106.
- Liu Y, Tao J, Yan Y, et al (2011) Biocontrol Efficiency of *Bacillus subtilis* SL-13 and Characterization of an Antifungal Chitinase. *Chinese Journal of Chemical Engineering* 19:128–134.
- Meena VS, Maurya BR, Meena SK, et al (2016) Can *Bacillus* Species Enhance Nutrient Availability in Agricultural Soils? In: Islam MT, Rahman M, Pandey P, et al. (eds) *Bacilli and Agrobiotechnology*. Springer International Publishing, Cham, pp 367–395
- Mitra D, Anđelković S, Panneerselvam P, et al (2020) Phosphate-Solubilizing Microbes and Biocontrol Agent for Plant Nutrition and Protection: Current Perspective. *Communications in Soil Science and Plant Analysis* 51:645–657.
- Nguyen MH, Kim DH, Park JH, et al (2021) Identification, Enzymatic Activity, and Decay Ability of Basidiomycetous Fungi Isolated from the Decayed Bark of Mongolian Oak (*Quercus mongolica* Fisch. ex Ledeb.). *Journal of Forest and Environmental Science* 37:52–61.
- Pan L, Cai B (2023) Phosphate-Solubilizing Bacteria: Advances in Their Physiology, Molecular Mechanisms and Microbial Community Effects. *Microorganisms* 11:2904.
- Panda B, Rahman H, Panda J (2016) Phosphate solubilizing bacteria from the acidic soils of Eastern Himalayan region and their antagonistic effect on fungal pathogens. *Rhizosphere* 2:62–71.
- Plante AF (2007) Soil biogeochemical cycling of inorganic nutrients and metals. In: *Soil Microbiology, Ecology and Biochemistry*. Elsevier, pp 389–432
- R Srivastava S (2009) Antifungal Activity of *Pseudomonas fluorescens* Against Different Plant Pathogenic Fungi. *IJMB* 7:.
- Rawat P, Das S, Shankhdhar D, Shankhdhar SC (2021) Phosphate-Solubilizing Microorganisms: Mechanism and Their Role in Phosphate Solubilization and Uptake. *J Soil Sci Plant Nutr* 21:49–68.
- Saber WIA, Ghoneem KM, Al-Askar AA, et al (2015) Chitinase production by *Bacillus subtilis* ATCC 11774 and its effect on biocontrol of *Rhizoctonia* diseases of potato. *Acta Biologica Hungarica* 66:436–448.
- Salazar F, Ortiz A, Sansinenea E (2017) Characterisation of two novel bacteriocin-like substances produced by *Bacillus amyloliquefaciens* ELI149 with broad-spectrum antimicrobial activity. *Journal of Global Antimicrobial Resistance* 11:177–182.
- Sarhan EAD, Shehata HSh (2014) Potential Plant Growth-promoting Activity of *Pseudomonas* spp. and *Bacillus* spp. as Biocontrol Agents Against Damping-off in Alfalfa. *Plant Pathology J* 13:8–17.
- Sharma I (2021) Phytopathogenic fungi and their biocontrol applications. In: *Fungi Bio-Prospects in Sustainable Agriculture, Environment and Nano-Technology*. Elsevier, pp 155–188
- Tian J, Ge F, Zhang D, et al (2021) Roles of Phosphate Solubilizing Microorganisms from Managing Soil Phosphorus Deficiency to Mediating Biogeochemical P Cycle. *Biology (Basel)* 10:158.
- Wahyudi (2011) Screening of *Pseudomonas* sp. Isolated from Rhizosphere of Soybean Plant as Plant Growth Promoter and Biocontrol Agent. *American Journal of Agricultural and Biological Sciences* 6:134–141.
- Yuan J, Raza W, Shen Q, Huang Q (2012) Antifungal Activity of *Bacillus amyloliquefaciens* NJN-6 Volatile Compounds against *Fusarium oxysporum* f. sp. cubense. *Appl Environ Microbiol* 78:5942–5944.
- Yuan J, Ruan Y, Wang B, et al (2013) Plant Growth-Promoting Rhizobacteria Strain *Bacillus amyloliquefaciens* NJN-6-Enriched Bio-organic Fertilizer Suppressed *Fusarium* Wilt and Promoted the Growth of Banana Plants. *J Agric Food Chem* 61:3774–3780.
- Zhang J, Feng L, Ouyang Y, et al (2020) Phosphate-solubilizing bacteria and fungi in relation to phosphorus availability under different land uses for some latosols from Guangdong, China. *CATENA* 195:104686.

Influence of Geographical Factors on the Distribution of the Genus *Phallus* in the Srepok River Basin, Vietnam: Implications for Conservation and Sustainable Development

Nguyen Thi Bich^{1,2}, Nguyen Thanh Long^{2,4,*}, Phan Thi Thanh Hang^{1,2}, Nguyen Vu Viet³, Nguyen Thi Thuy^{1,2}, Nguyen Ngoc Thang¹, Ngo Thanh Nga¹

¹Institute of Earth Sciences, Vietnam Academy of Science and Technology

²Graduate University of Science and Technology, Vietnam Academy of Science and Technology

³Institute for Hydro Power and Renewable Energy

⁴Water Resource Institute

*Email: longnt.study@gmail.com

Abstract: The Srepok River Basin is a transboundary river system, with its upper reaches located in the Central Highlands of Vietnam, covering an area of 18,230 km². This region represents a transitional zone between the Central Highlands of Vietnam and Cambodia, characterized by basalt plateaus interspersed with low hills, a humid tropical climate, and diverse vegetation. Such conditions favor the development of forest ecosystems and the emergence of rare fungal species, including the genus *Phallus* (Phallaceae) – a group of macrofungi with high ecological, medicinal, and economic value.

This study evaluates the relationship between geographical factors (topography, soil, climate, and vegetation) and the occurrence and distribution of the genus *Phallus* in the Srepok River Basin. The analysis combines integrated geographical assessment methods with Geographic Information System (GIS) applications and field surveys to determine the presence, spatial distribution, and habitat suitability of *Phallus* species. Results indicate that *Phallus* mushrooms primarily occur in evergreen and mixed forests at medium elevations (500-800m a.s.l.), developing on granitic and basaltic substrates with well-drained yet moisture-retentive soils, and under annual rainfall exceeding 1,800 mm. These habitats feature dense forest canopies, thick litter layers, and stable microclimatic

conditions-optimal for fruiting body formation. No *Phallus* species were recorded in open or human-disturbed habitats, highlighting their ecological specificity and high sensitivity to microclimatic variations. The findings highlight the predominant role of geomorphological and hydrological factors in shaping *Phallus* distribution, underscoring its potential as a bioindicator of forest microclimate stability in the Central Highlands. This research contributes essential data on *Phallus* biodiversity, supporting conservation efforts and the sustainable development of valuable fungal genetic resources in the Srepok River Basin.

Keywords: *Phallus*, biodiversity, geographical factors, Srepok River Basin, Central Highlands.

INTRODUCTION

The Srepok River Basin is one of the largest and most important transboundary basins in Central Highlands of Vietnam. It has been identified by Conservation International (CI) as a biodiversity conservation priority area due to the presence of irreplaceable and threatened species (IUCN Srepok) [1]. Situated on the vast basaltic plateau of the Central Highlands, the basin is characterized by low mountains alternating with flat plateaus, a humid tropical monsoon climate, and predominantly red basalt soils rich in well-drained humus yet retaining high surface moisture. These features foster the development

of diverse forest ecosystems, including deciduous dipterocarp forests, evergreen broadleaf forests, and semi-deciduous forests. The interaction among topography, climate, and soil forms environmental conditions suitable for macrofungal development, particularly species of the genus *Phallus*. The genus *Phallus* (Phallaceae) comprises macrofungi with distinctive morphology, typically growing on forest litter or decaying wood. The harmonious combination of topography, climate, and soil creates a unique environment conducive to the growth and diversification of macrofungi, particularly the genus *Phallus*. Several species within this genus possess significant biological and medicinal value and play a vital role in the organic decomposition cycle of forest ecosystems. Previous studies have explored the *Phallus* genus from various perspectives, such as multi-gene phylogenetic analyses (e.g., LSU, rpb2, atp6) among related genera (*Phallus*, *Mutinus*, *XyloPhallus*, etc.) [2], and comprehensive analyses of genetic data published for the order Phallales over the past 24 years, revealing major data gaps [3]. In Vietnam, notable research includes the works of Trịnh Tam Kiệt [4, 5] on macrofungal taxonomy, studies on the distribution of fungal genera across different habitats [6], and the documentation and identification of new fungal species [7].

Despite these efforts, there has been no systematic study on the occurrence or on the relationship between geographical factors and the distribution of the genus *Phallus* in the Srepok River Basin, a biodiversity-priority region within the Mekong River system. Therefore, this study aims to identify the geographical factors influencing the occurrence and spatial distribution of *Phallus* species in the Srepok River Basin in Vietnam. The findings will contribute to biodiversity conservation, as well as the sustainable utilization and management of valuable fungal genetic resources in this ecologically significant area.

Study Area

The Srepok River Basin originates from the elevated terrain of the Truong Son Range,

covering a total area of 18,230 km² within Vietnam's Central Highlands. The river flows through the provinces of Gia Lai, Dak Lak, and Lam Dong before crossing into Cambodia and ultimately joining the Mekong River.

The basin's topography is characterized by basalt plateaus interspersed with low hills, with elevations ranging from 400 to 900 meters above sea level. It features a humid tropical monsoon climate typical of the Central Highlands, with an average annual temperature of 20–25°C, high solar radiation, and approximately 2,337 sunshine hours per year. Evaporation rates are higher than in adjacent lowland regions, while annual relative humidity ranges between 80% and 85%. Average annual rainfall exceeds 1,800 mm, distributed distinctly between two seasons: a wet season (accounting for 84–88% of total annual rainfall) and a dry season (12–16%). The region's soil profile is dominated by fertile, humus-rich red basaltic soils that are well-drained yet retain high surface moisture. The diverse vegetation cover includes deciduous dipterocarp forests, evergreen broadleaf forests, and semi-deciduous forests - conditions highly favorable for the growth and diversification of macrofungi [8].

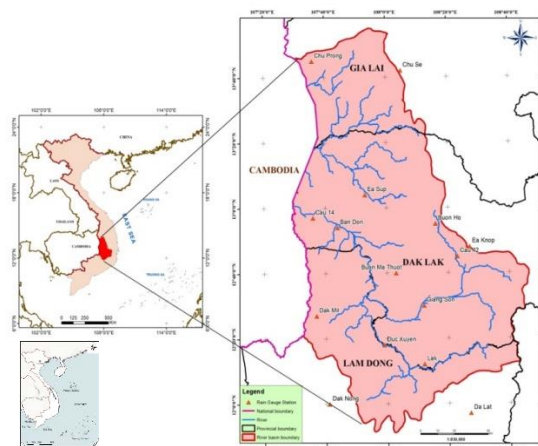


Figure 1. Study area

In recent years, the exploitation and utilization of mushrooms as nutrient-rich food sources and as raw materials for medicinal

extraction and pharmaceutical production have become increasingly common. The genus *Phallus* (family Phallaceae) includes edible and medicinal species valued for their nutritional composition, fiber, and protein content [9, 10]. Therefore, studying and identifying *Phallus* species, as well as examining the correlation between natural geographical factors and their distribution, biological characteristics, and bioactive properties, is essential. Such research provides a scientific foundation for biodiversity conservation and the sustainable utilization of valuable fungal resources in the Srepok River Basin.

DATABASE AND METHODS

Research subjects

Samples of fungi belonging to the genus *Phallus* (Phallaceae) were collected along three main sampling transects (designated as transects A, B, C) in the Chu Yang Sin National Park, Dak Lak province, within the Srepok River

basin. These sampling transects were designed to capture representative variations in topography, vegetation and microclimate conditions across the entire mid-elevation forest belt of the area.

- Transect A captures vertical ecological variation, connecting lowland and upland forest areas.
- Transect B represents a typical valley environment with high humidity and dense organic matter, ideal for *Phallus* fruiting.
- Transect C focuses on local hotspots, allowing for detailed assessments of population structure and species co-occurrence.

This stratified sampling design ensured that the recorded *Phallus* specimens represented a diverse set of microenvironments, providing a solid foundation for analyzing the spatial distribution, ecological preferences, and potential habitat constraints of this genus within the Central Highlands.

Table 1. Topographic and habitat characteristics of surveyed transects

Transect	Survey Length	Elevation Range (m)	Terrain Type	Sampling Characteristics
A	8.97 km	459 - 772	Foothill–lower montane forests	Broad ecological gradient, mixed forest types
B	6.68 km	480 - 742	Gentle valley slopes	Moist, shaded, stable microclimate
C	8.00 km	423 - 542	Localized forest patch	Intensive microhabitat sampling

Data used

The attribute data collected from measurement and observation stations, together

with spatial datasets, were standardized and integrated within a GIS environment (ArcGIS, QGIS) to support spatial analysis.

Table 2. Sources of Collected Data

No.	Type of Data	Source
1	Topographic map (*.dgn)	United States Geological Survey (USGS: https://earthexplorer.usgs.gov/); Digital Elevation Model (DEM) data with a spatial resolution of 30 m × 30 m.
2	Land cover/vegetation map (2020) at a scale of 1:100.000	Project code TN17/To5 under the Science and Technology Program for Socio-Economic Development of the Central Highlands in Regional Linkage and International Integration, code KHCN-TN/16-20 [11].
3	Soil map at a scale of 1:100.000	Project code 05/HĐ-KHCN-NTM under the Science and Technology Program for New Rural Development (2016–2020) [12].
4	Rainfall data (1980–2024)	- Rainfall data meteorological stations (Chu Prong, Chu Se, Ban Don, Buon Ho, Buon Ma Thuot, Cau 14, Cau 42, Ea Knop, Ea Hding, Ea Hleo, Ea Soup, Giang Son, Lak, Dak Mil, Duc Xuyen). - National Center for Hydro-Meteorological Data and Information.

Methods

Sampling

Field sampling was carried out in August 2024 along three pre-established survey transects (Transects A, B, C), selected using stratified sampling to represent distinct elevation, topography, and vegetation gradients within Chu Yang Sin National Park, Dak Lak Province. The survey involved active, targeted searches conducted systematically along forest trails, near riparian zones, and in areas with deep organic vegetation accumulation. Detected *Phallus* basidiocarps specimens were photographed in situ and assigned a unique field code (CYS.o8.24.MXX). Coordinates were recorded for each specimen and elevation using a handheld GPS device (WGS84 standard code).

Microhabitat parameters were quantified at each sampling site, specifically: substrate type (mineral soil, rotting layer, or woody material), canopy cover (percentage estimated), relative surface moisture/rotting layer depth. Representative specimens, spanning all phylogenetic stages (e.g., egg, hatchling, adult), were collected to document morphological variation within the species. Sampling followed collection guidelines to minimize ecological disturbance. Collected specimens were temporarily stored in perforated paper envelopes to ensure ventilation and then dried at a constant temperature of 40-45°C for long-term herbarium preservation.

Species Description

Macroscopic characteristics of the fruiting bodies were examined and described following standard mycological protocols [13, 14]. The recorded features included the texture and color of the pileus, length and surface structure of the stipe, presence and extent of mycelial strands, as well as the shape of the receptacle apex and pileus coloration. Observations were made based on both field examination and preserved specimens. Measurements were conducted immediately after collection using a digital caliper (precision ± 0.01 mm) to minimize post-harvest deformation. Species identification was carried out through comparative morphological

analysis, using regional floras and international taxonomic keys for the family Phallaceae. When diagnostic features were insufficient for species-level confirmation, specimens were cautiously designated as *Phallus* sp. Representative developmental stages—egg stage (CYS.o8.24.M17), emerging stage (CYS.o8.24.M16), and mature stage (CYS.o8.24.M48)—were illustrated using digital line drawings based on field photographs. All voucher specimens were carefully dried, labeled, and preserved under controlled conditions for potential future molecular identification and phylogenetic analysis.

Geographic Information System (GIS) Approach

The application of Geographic Information Systems (GIS) enhances spatial analysis capabilities, allowing for the identification of watershed characteristics and delineation based on Digital Elevation Models (DEM). GIS provides a consistent framework for watershed analysis using DEMs and standardized datasets such as surface cover, soil properties, monitoring station locations, and climatic variables.

In this study, GIS tools were employed to integrate and simultaneously analyze multiple spatial datasets, including topography, river networks, vegetation cover, soil types, and meteorological-hydrological data. This integration enabled the identification of characteristic features and spatial correlations between geographical factors and the occurrence, distribution, and diversity of the genus *Phallus* within the Srepok River Basin.

Integrated Geographical Assessment

The study employed an integrated geographical assessment method to analyze the relationship between natural geographical factors and the occurrence and distribution of the genus *Phallus* within the Srepok River Basin. Data were collected through field surveys, in combination with Digital Elevation Models (DEM), soil maps, climatic datasets, and land-use maps. The recorded *Phallus* occurrence points were mapped and spatially

analyzed using GIS to identify concentration zones and distribution trends. The relationship between fungal diversity and geographical variables—such as elevation, slope, vegetation cover, distance to rivers and streams, soil type, rainfall, and temperature—was evaluated through correlation analysis.

RESULTS AND DISCUSSIONS

Morphological Description of *Phallus* Specimens Collected in the Srepok River Basin

A total of 12 sampling sites containing *Phallus* specimens were recorded within Chu Yang Sin National Park, located in the southeastern part of Dak Lak Province (Figure 2). The specimens were distributed across three sampling transects, representing a complete developmental sequence from the immature “egg” stage to the fully differentiated indusiate stage (Table 1). All collected specimens exhibited the key morphological characteristics typical of the genus: a hollow, spongy pseudostipe arising from a distinct volva; a conical to bell-shaped cap (pileus) coated with an olive-brown mucilaginous gleba; and, in mature individuals, a prominent net-like indusium extending to about half the length of the stipe. The earliest developmental stages (e.g., CYS.o8.24.Mo4–Mo8, M17–M18) appeared as nearly spherical to ovoid “egg-like” structures (2–4 cm in diameter, buried approximately two-thirds below the surface) within humus-rich soil or decomposing leaf litter. These were enclosed in a tough, spongy peridium (outer layer). The emerging stage (e.g., M16) was characterized by the rapid elongation of the pseudostipe through turgor pressure, accompanied by partial exposure of the receptacle and the unfolding of the indusium. The fully mature stage (e.g., M48–M56) exhibited a completely expanded indusium forming a symmetrical lattice structure, emitting a strong fetid odor typical of saprotrophic *Phallus* species—a key adaptation for spore dispersal mediated by insects. Overall, these field observations successfully documented the complete morphological development sequence of *Phallus* under natural

conditions in the Central Highlands, providing phenotypic evidence of the genus’ ecological niche preference for humid and shaded microhabitats. These developmental stages are illustrated in Figure 3, serving as representative morphotypes of the genus within the study area. Due to the absence of reliable molecular data and the high morphological plasticity observed among indusiate species, the present specimens are conservatively referred to as *Phallus* sp., pending future confirmation through DNA-based phylogenetic analysis.

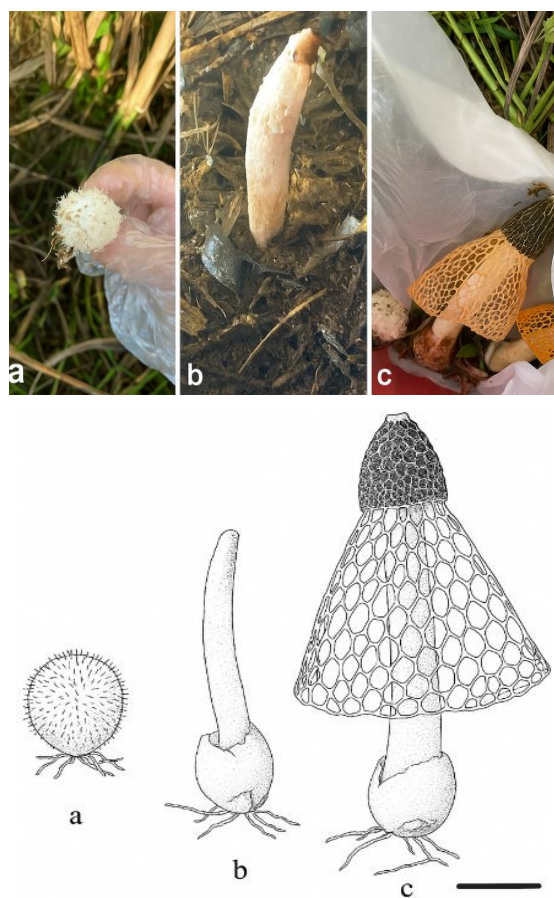


Figure 2. Photographs and schematic illustrations of the developmental stages of *Phallus* spp.: (a) egg stage, (b) emerging stage, and (c) mature stage.

Illustrations based on field specimens (CYS.o8.24.M17, M16, and M48). Scale bar = 2 cm.

Table 3. Field Morphological Description of *Phallus* Specimens Collected

Sample Code	Coordinates		Habitat Description	Morphotype	Morphological Characteristics	Developmental Stage
	X	Y				
CYS.08.24 .Mo4	108°34'29"	12°48'36"	Moist forest floor, thick litter, medium forest canopy (~70%), wet slopes with leaf litter, partially shady forest edges	<i>Phallus</i> sp. (with indusium)	Cylindrical stipe, olive-brown; pileus orange-brown; volva white	Mature stage; typical <i>P. indusiatus</i> complex
CYS.08.24 .Mo5				<i>Phallus</i> sp. (with indusium)	Stipe cylindrical, white-pinkish; pileus olive-brown; volva intact	Mature stage
CYS.08.24 .Mo6				<i>Phallus</i> sp.	Early "egg" stage	Early immature stage
CYS.08.24 .Mo7				<i>Phallus</i> sp.	Hollow stipe, brownish-orange; pileus oval; ~5 cm tall; thin, fragile peridium	Fully mature stage; emits fetid odor typical of <i>Phallus</i>
CYS.08.24 .Mo8				<i>Phallus</i> sp.	Indusium faintly visible; pileus brown; gleba partially degraded	Mature stage, gleba partially decayed
CYS.08.24 .M16	108°34'29"	12°48'36"	Moist forest slope, organic cover and semi-decay cover; canopy cover 60-70%	<i>Phallus</i> sp. (without indusium)	Stipe 8-10 cm, white-pinkish; pileus brownish; volva brown; surface smooth, no indusium visible	Semi-mature stage
CYS.08.24 .M17	108°33'72"	12°46'14"	Lower slope near grass edge, moist soil with decaying organic debris	<i>Phallus</i> sp. (egg stage)	Spherical fruiting body 3.0-3.5 cm, white with faint pink; smooth surface; firm texture	Immature ("egg") stage
CYS.08.24 .M18	108°34'04"	12°47'6"	Moist humus layer on rotting wood; shady valley bottom (~70% canopy cover)	<i>Phallus</i> sp. (egg stage, twin form)	Two "egg" forms together (2.8-3.2 cm), pinkish-white; enclosed in fibrous layer; firm inside	Immature ("egg") stage
CYS.08.24 .M34	108°34'15"	12°47'6"	The edge of the forest is shady, the soil is mixed with rotting tree roots and organic matter near the base of the tree.	Unidentified <i>Phallus</i> morphotypes	Bell-shaped pileus, 4.5-5.0 cm, with small pores; stipe 7-9 cm, white; pileus dry; firm structure	Mature stage

CYS.08.24 .M45	108°30' 39"	12°43'4 0"	Open forest edge, sandy loam with rotten grass roots, moderate light	Unidentified <i>Phallus</i> morphotypes	Cylindrical stipe (6–9 cm), hollow, light brown; pileus conical, dark brown, smooth; volva white-pinkish	Late mature stage
CYS.08.24 .M48	108°46' 44"	12°48'4 0"	The forest floor is damp, rotting leaves mixed with grass stems.	Morphologically resembling <i>P. indusiatus</i>	Bell-shaped pileus, olive-brown gleba; indusium orange-pink, 4–6 cm; stipe white-pinkish; volva white-pink	Fully mature stage
CYS.08.24 .M56	108°25' 87"	12°43'3 5"	The forest floor is damp, rotting leaves mixed with grass stems.	Morphologically resembling <i>P. indusiatus</i>	Stipe short, brownish; volva white-pink; indusium partly visible; stipe 1.5–2.5 cm thick, white-pinkish	Semi-mature stage

Determination of Natural Geographical Factors Influencing the Distribution of the Genus *Phallus* in the Srepok River Basin

The Srepok River Basin represents a distinct natural geographical region with unique environmental characteristics. Each geographical factor plays a different role and degree of influence on the occurrence and spatial distribution of the genus *Phallus*. Based on the principles of geomorphological formation, watershed characteristics, and the natural origins of *Phallus* resources, this study integrates field surveys, expert consultations, and references to scientific literature and biodiversity research to identify key environmental determinants governing *Phallus* distribution within the basin.

Relationship Between Climatic Factors and the Distribution of the Genus *Phallus*

Climate is a crucial determinant governing the occurrence, abundance, and spatial distribution of *Phallus* species across the Srepok River Basin.

The basin receives an average annual rainfall of approximately 1,770.4 mm (Table 4), with strong spatial and temporal differentiation corresponding to the region's two distinct seasons - the rainy and dry seasons. Rainfall is concentrated primarily within the six-month rainy season, accounting for over 80% of the total annual precipitation, while the dry season contributes only 14–16%. Rainfall across the region shows considerable spatial variability, generally increasing with elevation and along windward slopes.. This pronounced rainfall gradient results in significant contrasts in local environmental conditions, making the Srepok Basin one of the most climatically heterogeneous regions in the Central Highlands.

Table 4. Average annual rainfall (mm) at meteorological stations in the Srepok River Basin (1980–2024)

Station	Monthly												Yearly Mean
	I	II	III	IV	V	VI	VII	VIII	IX	X	XI	XII	
Chu Prong	0.03	3.34	14.38	87.59	243.47	372.89	404.23	490.06	363.82	197.76	60.86	9.50	2248
Chu Se	0.21	0.35	9.32	66.50	198.25	252.26	287.12	372.84	317.58	168.05	56.76	7.25	1542
Ban Don	2.01	2.63	25.86	87.19	214.34	210.15	222.48	236.71	269.24	190.22	69.44	11.58	1578
Buon Ho	6.40	5.19	19.31	77.81	199.92	195.75	200.04	250.51	276.45	198.07	119.27	33.78	1852

Buon Ma Thuot	4.86	3.85	25.37	82.43	240.61	240.08	258.66	312.81	339.20	222.25	100.00	21.44	1680
Cau 14	4.46	3.22	21.61	89.27	253.18	221.34	224.94	262.59	298.83	200.26	83.69	16.15	1503
Cau 42	16.79	3.71	14.01	57.55	191.49	140.72	146.18	197.54	250.05	180.75	211.80	92.34	1867
Ea Hding	2.42	4.54	23.05	71.68	247.57	248.11	261.12	365.60	326.16	202.83	105.60	15.24	1896
EA Hleo	3.45	1.07	21.87	88.65	214.23	210.30	310.95	337.64	359.34	198.58	127.82	22.01	1592
Ea Knop	8.12	3.19	18.00	53.46	156.01	125.06	109.81	135.49	215.43	283.44	285.59	135.15	1535
Ea Soup	0.89	1.32	20.96	78.87	209.86	238.43	243.39	266.88	259.45	186.41	64.06	5.87	1854
Giang Son	5.82	3.85	16.91	94.27	214.02	239.51	262.21	305.36	310.57	224.98	134.33	42.42	1956
Lak	3.58	2.86	19.31	96.14	247.74	377.19	313.53	484.58	353.14	304.88	126.68	36.79	1758
Dak Mil	5.27	9.86	44.13	180.86	316.25	288.04	303.97	317.35	358.13	284.24	119.87	25.95	1867
Duc Xuyen	3.34	3.81	23.31	106.39	250.52	278.63	275.24	299.72	303.86	212.17	89.44	19.45	2248

Rainfall plays a crucial role in shaping the distribution zones of the genus *Phallus* across the Srepok River Basin. *Phallus* samples were found mainly in Chu Yang Sin National Park, the upper reaches of the Krong Ana River, the main tributary of the Srepok River Basin. Meteorological data for the period 1980–2024 showed that the measured rainfall in the area ranged from (1600–1800mm), moderate rainfall, widely distributed throughout the entire region. Precipitation is concentrated mainly during the six-month rainy season (V–X), accounting for over 85% of total annual rainfall, with peak precipitation occurring in (VIII–IX). The clear correspondence between high-rainfall areas and locations where *Phallus* specimens were recorded—particularly in the Chu Yang Sin NP—demonstrates a strong relationship between atmospheric humidity and fungal development. Areas characterized by prolonged wet periods, thick litter layers, and moisture-retentive red basalt soils form cool, humid microclimates, providing optimal conditions for spore germination and fruiting body formation. Notably, the phase lag between rainfall and streamflow peaks within the basin prolongs surface soil moisture after the main rainfall period, allowing *Phallus* to sustain growth and fruiting throughout the late rainy season – a period that coincides with the field sampling in August 2024.

Relationship Between Topographic Factors and the Distribution of Phallus

Topography exerts a decisive influence on the spatial distribution of *Phallus* within the Srepok River Basin. Situated on the western flank of the Truong Son Range, the basin features strongly dissected terrain comprising four main geomorphological types: mountainous areas, plateaus, peneplains, and valleys/plains. Among these, plateau topography dominates, with elevations ranging from 400 to 900 m. Field surveys revealed that *Phallus* specimens tend to form clustered distributions along the eastern and northeastern slopes of the Chu Yang Sin massif, primarily within the 500–800 m elevation range, belongs to the upper stream of Krong Ana River, the main tributary of Srepok River Basin. These localities (e.g., CYS.08.24.Mo4–Mo8, M16–M18) are situated on shaded forest slopes with thick litter layers and moderate canopy density, creating a stable, humid microclimate favorable for the development of basidiocarps. No specimens were recorded at lowland (<400 m) or high-mountain (>1,000 m) sites, indicating that *Phallus* is restricted by temperature and moisture fluctuations at the environmental extremes.

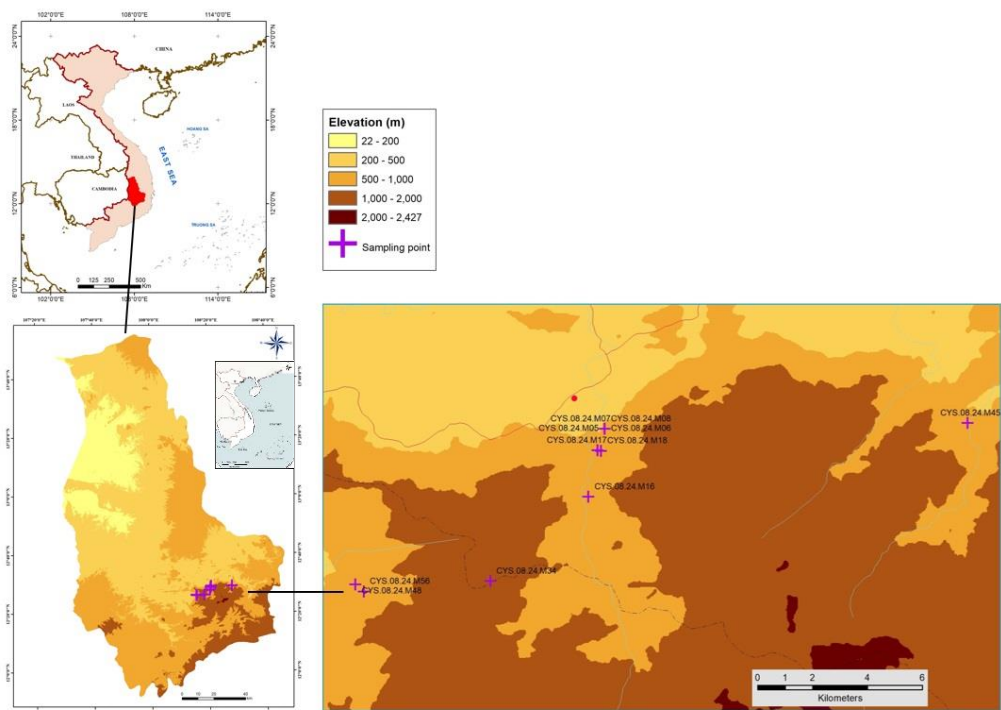


Figure 3. Spatial distribution of Phallus specimens across the topography of the Srepok River Basin

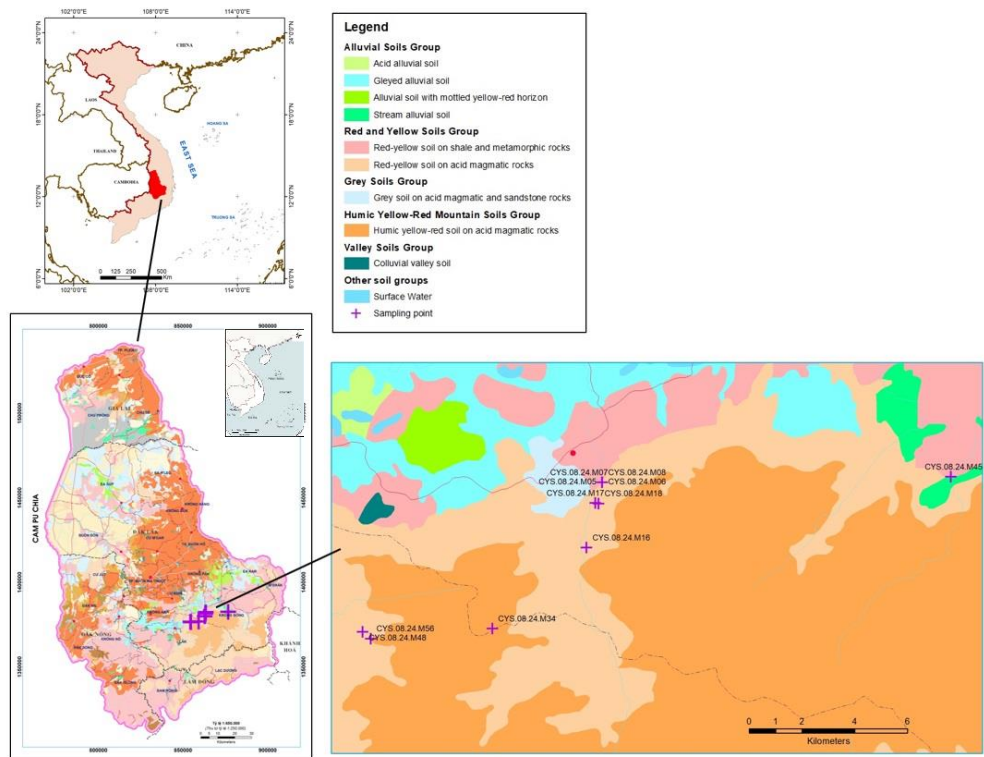


Figure 5: Distribution of Phallus mushroom samples on the soil layer of Srepok River Basin

The confinement of *Phallus* to the mid-montane foothill belt reflects a strong correlation between fungal distribution and regional geomorphology–geology. Chu Yang Sin National Park, located at the southeastern edge of the Central Highlands, is underlain predominantly by ancient granite from the Kon Tum massif, forming plateaus dissected by deep valleys and gentle slopes. Within this context, concave and moderately inclined slopes (10° – 25°) on the southeastern aspect retain moisture, accumulate organic matter, and promote decomposition – ideal conditions for saprotrophic functioning of *Phallus*. This zone also represents a transitional belt between semi-evergreen and low-montane evergreen forests, with minimal temperature variation and stable soil humidity throughout the year. A similar elevational pattern has been reported for *P. indusiatus* in China [7] and *P. Chiangmaiensis* in Thailand [15], where mid-elevation sites with thick humus layers correspond to the highest fruiting frequencies.

Topographic influence operates both directly and indirectly. In the direct manner, slope shape affects drainage and litter accumulation – concave slopes and valleys retain water and organic matter, while convex slopes are exposed to higher radiation and wind, accelerating litter desiccation and decomposition. In an indirect manner, slope orientation regulates the amount of solar radiation received, with southeast-facing slopes generally receiving more, where *Phallus* concentrates, receive diffuse morning light and afternoon shade, maintaining optimal temperature–moisture balance for fungal growth. Geologically, southeast-facing slopes underlain by coarse-grained granite and granodiorite form slightly acidic sandy loam soils (pH 5.0–6.0) – porous and well-drained yet capable of retaining surface moisture. Continuous decomposition of broadleaf litter on these substrates provides readily available carbon and nitrogen sources, supporting the seasonal fruiting cycle. In contrast, western and northern slopes, often underlain by shale or basalt with shallow, compact, and humus-poor

soils, showed no *Phallus* occurrence even at similar elevations.

Quantitative analysis at eight sampling sites reinforces these findings. Mean elevation was 612 ± 117 m; average slope was 17° ; and canopy cover reached 81%. Seven of these sites were located within ≤ 300 m of ephemeral streams, where soil moisture exceeded 25% during the late rainy season—closely matching the optimal moisture conditions for *Phallus* growth reported in other tropical regions [16–18].

In general, topographic structure—particularly slope concavity, aspect, and bedrock type—serves as a key ecological determinant of *Phallus* spatial patterns in the Chu Yang Sin region. The mid-montane foothill forests provide an optimal geomorphological–edaphic equilibrium, combining good aeration, stable humidity, and rich organic matter, which form the foundational environment for the growth and persistence of *Phallus* populations in the Srepok Basin, Central Highlands.

4.2.3 Relationship Between Soil Factors and the Distribution of the Genus *Phallus*

Beyond topography, soil properties also play a crucial role in regulating *Phallus* distribution within the basin. The Srepok Basin hosts a diverse soil cover comprising 24 soil types across 8 major groups, among which red-yellow Ferralsols developed on basalt are dominant and ecologically significant.

This type of soil has physical and chemical properties favorable for the growth of the genus *Phallus* with a thick layer, loose texture, rich in minerals and organic matter, maintaining a slightly acidic to neutral pH (5.0–6.5) suitable for the activity of the mycelium system. At the same time, red-yellow soil on basalt (F) is a soil group with the ability to store large amounts of water, with thick layers from (0 – 50 cm) having a water reserve of about 180 mm, from 50 – 100 cm reaching about 192 mm of water and from 0 – 100 cm reaching up to 372 mm of water. The maximum moisture content also shows that on these soils, it reaches the highest value from 40.4 – 48.5% of soil weight (depth from 0 – 20 cm

reaches 41.1 - 45.0%. 40 - 60 cm reaches 40.4 - 44.7%. 80 - 100 cm reaches 43.1 - 46.1% of soil weight) [19]. With high water permeability and stable moisture retention, it helps maintain hydrothermal balance even in the dry period.

In the forest areas at the foot of Chu Yang Sin mountain, where most *Phallus* samples were found, the red-yellow soil group on basalt (F) is the most dominant, creating ideal conditions for the saprophytic activity of *Phallus*, providing an environment rich in organic humus and good ventilation for the mycelium to grow. In contrast, areas with shallow, humus-poor soils, or compacted shale-basalt substrata often do not record the presence of the species, suggesting a close relationship between soil properties and the habitat of *Phallus*.

4.2.4 Relationship Between Vegetation Structure and Forest Composition and the Distribution of the Genus *Phallus*

The spatial distribution of *Phallus* within Chu Yang Sin National Park belongs to the upper stream of Krong Ana River, the main tributary of Srepok River Basin exhibits a strong association with closed-canopy natural forest ecosystems, particularly evergreen and mixed evergreen-coniferous forests below 900 m elevation.

No fruiting bodies were recorded in plantations, cultivated lands, or open shrublands, despite equivalent survey effort. This indicates that *Phallus* possesses high habitat specificity, relying heavily on complex forest canopy structures and stable litter dynamics. In primary forest habitats, the thick broadleaf litter layer effectively retains soil moisture and promotes the decomposition of organic matter - the principal nutrient source for saprotrophic fungi. This relationship aligns with observations across Southeast Asia, where *P. indusiatus*, *P. Chiangmaiensis*, and *P. merulinus* commonly occur in humid, humus-rich forest floors [6, 7, 15]. In contrast, open or disturbed habitats experience greater fluctuations in temperature and humidity, reducing organic accumulation and water retention. These stresses often result in

incomplete indusium development, as observed in edge samples (M34, M45), which exhibited shortened or malformed lattices, compared with deep-forest specimens (M48, M56) that showed fully expanded, symmetrical indusia. This morphological variation reinforces the hypothesis that canopy-regulated humidity is essential for the full maturation of *Phallus* fruiting bodies.

Different developmental stages of *Phallus* also reflect the vertical microclimatic stratification within the forest. The "egg" stage (e.g., M17) typically occurs within deep litter layers under shaded, moisture-stable microhabitats. The emerging stage (e.g., M16) is often found in moderately open forests, where diffuse light and gentle airflow promote rapid elongation of the stipe. In contrast, fully mature fruiting bodies (e.g., M48, M56) are confined to closed, high-humidity forests, where stable microclimatic conditions persist throughout the rainy season. The coexistence of all three stages along a single transect reflects the microhabitat heterogeneity characteristic of late-successional forest systems.

Overall, these findings demonstrate that the development and persistence of *Phallus* are tightly linked to canopy cover, litter depth, and the surface soil's moisture-retention capacity. These elements form over long ecological timescales through primary forest succession, implying that even small disturbances - such as canopy opening or litter layer disruption - can severely affect the species' survival. Thus, *Phallus* can be regarded as a sensitive bioindicator species, reflecting the stability of forest microclimates and the integrity of organic matter decomposition systems. This ecological specialization not only underscores the genus's functional role in forest nutrient cycling but also highlights its vulnerability to changes in forest cover and climate variability across the Central Highlands of Vietnam.

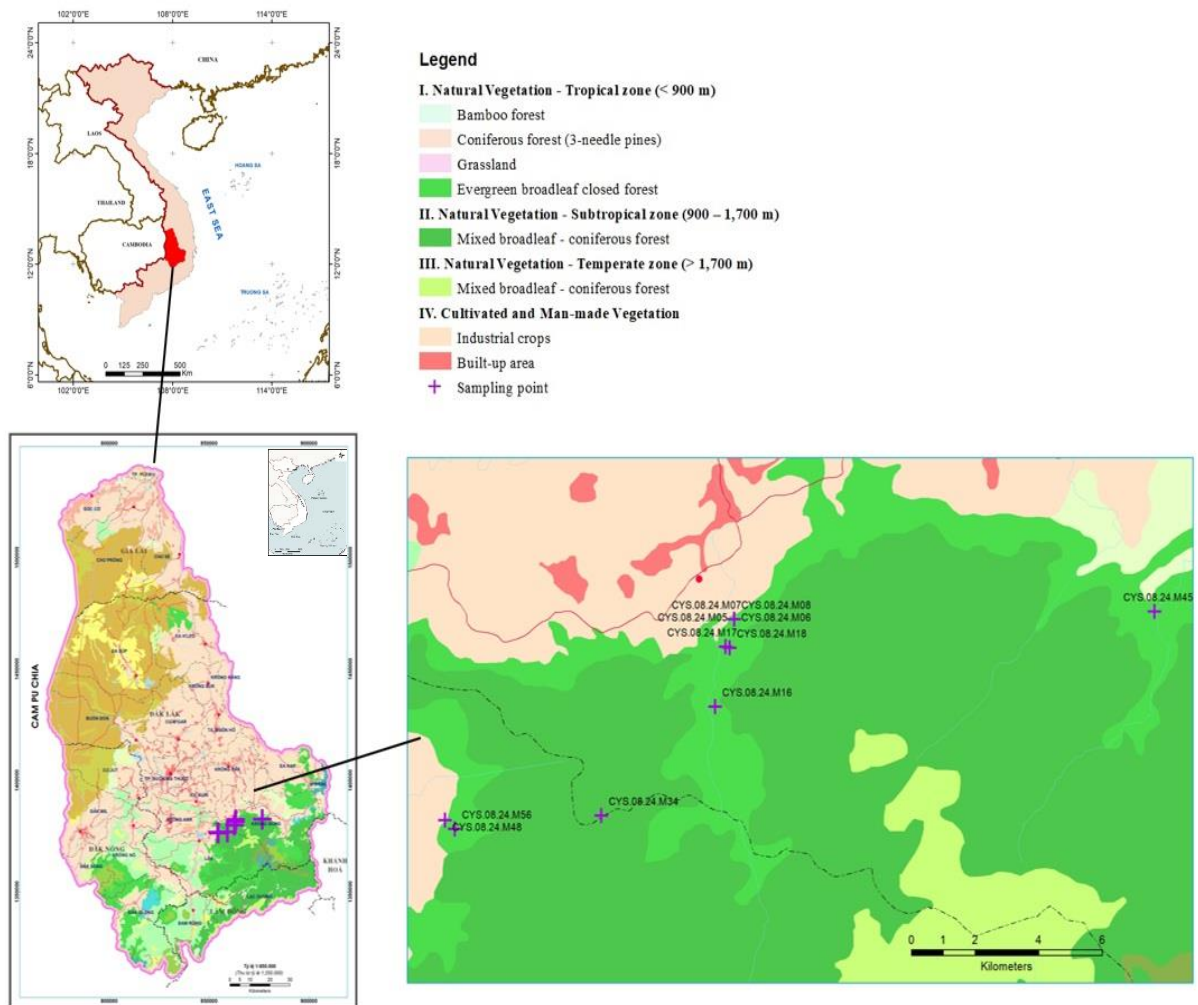


Figure 6: Distribution of *Phallus* samples on the vegetation layer of the Srepok River Basin

CONCLUSION

This study provides the first integrated assessment of the geographical and ecological factors influencing the distribution of the genus *Phallus* within the Srepok River Basin, focusing on Chu Yang Sin National Park. The findings reveal that *Phallus* occurrence is strongly regulated by topographic position, soil characteristics, forest structure, and rainfall regime. *Phallus* species were found exclusively in evergreen and mixed forests at mid-elevations (500–800 m), growing on weathered granite or basalt substrates with slightly acidic, well-drained, yet moisture-retentive soils. The combination of stable humidity, thick litter

layers, and closed canopy cover creates an optimal microclimatic environment for fruiting body formation and development. Morphological variation among developmental stages reflects the species' high sensitivity to microclimatic fluctuations, underscoring the crucial role of canopy cover and litter dynamics in maintaining *Phallus* populations.

The confinement of *Phallus* to undisturbed primary forests highlights its potential as a reliable bioindicator of forest microclimate stability and ecosystem integrity. These findings emphasize that forest canopy continuity and hydrological balance - both shaped by topography and vegetation—are key

determinants of fungal diversity in Vietnam's Central Highlands. Future research should incorporate long-term monitoring, molecular identification, and habitat modeling to predict changes in *Phallus* distribution under the influence of climate change and land-use transformation.

REFERENCES

1. Constable D.. The Sesan and Sre Pok River Basins. Bangkok. 2015. IUCN: Thái Lan. (in Vietnamese)
2. Trierweiler-Pereira. L.. R.M.B. da Silveira. and K. Hosaka. Multigene phylogeny of the Phallales (Phallomycetidae. Agaricomycetes) focusing on some previously unrepresented genera. *Mycologia*. 2014. **106**(5): p. 904-911.
3. Melanda. G.C.. et al.. An overview of 24 years of molecular phylogenetic studies in Phallales (Basidiomycota) with notes on systematics, geographic distribution, lifestyle, and edibility. *Frontiers in Microbiology*. 2021. **12**: p. 689374.
4. Trinh Tam Kiet. List of large mushrooms of Vietnam. 1996: Agricultural Publishing House. (in Vietnamese)
5. Trinh Tam Kiet. Big Mushrooms in Vietnam – Volume 1. 2001: Natural Science and Technology Publishing House. (in Vietnamese).
6. Baseia. I.G.. L. Maia. and F.D. Calonge. Notes on Phallales in the neotropics. 2006.
7. Cabral. T.S.. et al.. Behind the veil—exploring the diversity in *Phallus indusiatus* sl (Phallomycetidae. Basidiomycota). *MycoKeys*. 2019. **58**: p. 103.
8. Ministry of Natural Resources and Environment. Report on integrated water resources planning of Srepok river basin to 2030 with a vision to 2050. 2021. (in Vietnamese).
9. W. N. Schaechter E. Modern English Translation of Hadrianus Junius' 1564 work on *Phallus hadrianii*. 2013.
10. ALTUNER. E.M. and I. AKATA. Antimicrobial activity of some macrofungi extracts. *cancer*. 2010. **9**: p. 10.
11. Vu Anh Tai. Research on improving and managing natural grass and processing food from available materials to serve the development of large livestock farming (buffalo, cow, elephant) on a concentrated scale and household scale to create sustainable livelihoods for the people of the Central Highlands. code TN17/T05. 2020. (in Vietnamese).
12. Nguyen Thi Thuy. Research on the current situation of rural areas in the Central Highlands and propose new rural models according to geographical and ecological regions to create livelihoods, adapt to climate change and develop sustainable agriculture . code 05/HD-KHCN-NTM. 2020. (in Vietnamese).
13. Dring. D.M.. *Gasteromycetes of West Tropical Africa*. 1964: Commonwealth Mycological Institute.
14. Kreisel. H.. A preliminary survey of the genus *Phallus* sensu lato. *Czech Mycology*. 1996. **48**(4): p. 273-281.
15. Sommai. S.. et al.. *Phallus Chiangmaiensis* sp. nov. and a Record of *P. merulinus* in Thailand. *Mycobiology*. 2021. **49**(5): p. 439-453.
16. Chumkiew. S.. et al.. Morphological characterization, molecular identification, and metabolic profiles of two novel isolated bamboo mushrooms (*Phallus* sp.) from Thailand. *Plos one*. 2024. **19**(10): p. e0307157.
17. Hermawan. R.. I.P. Putra. M.P. Amelya. and M.R.W. Gunawan. A Morphological and Molecular Study of *Phallus multicolor* in Indonesia. *Makara Journal of Science*. 2022. **26**(2): p. 2.
18. Santana. M.D.F. and S.R.M. Couceiro. New insights on the spore dispersal of *Phallus indusiatus* sl (Basidiomycota. Phallaceae) for the Brazilian Amazon forest. *Food Webs*. 2024. **38**: p. e00338.
19. Nguyen Lap Dan. Research on scientific basis for comprehensive solutions to resolve conflicts of interest in exploiting and using water resources in the Central Highlands. code TN3/T02. 2015. (in Vietnamese).

DOI: 10.15625/vap.2025.0246

ASSESSMENT OF RAIN CHANGES IN NINH BINH PROVINCE IN THE PERIOD 2000 – 2024

Trinh Nguyen Dieu^{1,*}, Lan Vu Thi Thu², Son Hoang Thanh³, Tuan Bui Anh³

¹Graduate University of Science and Technology, Vietnam Academy of Science and Technology, Hanoi, Vietnam

²Association of Vietnam Geographers, Hanoi, Vietnam

³Institute of Earth Sciences, Vietnam Academy of Science and Technology, Hanoi, Vietnam

*Email: nguyendieutrinh70@gmail.com

Abstract: The climate of Ninh Binh province is dominated by the Asian monsoon circulation mechanism and is strongly influenced by its geographical location (coastal plains) and terrain conditions (plains with limestone mountain ranges stretching in the Northwest–Southeast direction). The average annual rainfall for many years ranged from 1,640 to 1,940 mm, strongly differentiated by season. Rainfall in the rainy season accounted for 85–86% of the total annual rainfall, while rainfall in the less rainy season contributed only 14–15% of the total annual rainfall. Rainfall fluctuated slightly over the years, the wettest year recorded approximately twice the rainfall of the driest year, the coefficient of variation C_v fluctuates between 0.17–0.23. The average annual rainfall increases and decreases alternately in both seasons. : Rainfall in the rainy season decreases in some years; however, extreme rainfall events can suddenly reach up to 356.1 mm/day. Floods occurred, seriously affecting people's lives and agricultural production, such as in 2000 in the Hoang Long river basin. In the less rainy season, some months experienced little to no rainfall, combined with the effects of hot, dry southwest winds and strong evaporation, so this often led to local water shortages in parts of Kim Son and Yen Khanh districts.

Keywords: Rain, variation, Ninh Binh.

INTRODUCTION

Worldwide, rainfall trends are widely assessed to understand climate variability and the impacts of global climate change. Most

international studies use non-parametric methods such as Mann–Kendall test and Sen's slope estimator to detect and quantify rainfall trends in long-term data series. Recent studies also emphasize the role of extreme rainfall and seasonality, and develop autocorrelation correction methods (Modified Mann–Kendall) and spatial-temporal analysis combining GIS and satellite data to describe rainfall trends more accurately. Over the past two decades, many studies have been conducted to assess rainfall change trends in Vietnam, using both observational data and reanalysis or satellite data.

Ninh Binh is a coastal province located in the South of the Northern Delta, with limestone mountain ranges stretching across the districts of Nho Quan, Hoa Lu, Gia Vien, Yen Mo and Tam Diep city in the Northwest - Southeast direction. The atmospheric circulation in Ninh Binh is part of the monsoon circulation in Northern Vietnam, formed by the combined impact of three Asian monsoon mechanisms: Northeast Asia, Southeast Asia and Southwest Asia, in which the Southeast Asian monsoon has the strongest influence [1, 4].

The rainfall regime and total rainfall in Ninh Binh are controlled by the Asian monsoon system and further modified by local geography and topography, resulting in distinct climatic characteristics.²⁰²⁴ The less rainy season from November to April is strongly influenced by the Northeast monsoon with Siberian high pressure and Aleutian low pressure, cold and dry or cold and humid. The

rainy season from May to October is influenced by the Southwest monsoon and India - Myanmar low pressure, hot and humid, with lots of rain.

The average annual temperature is about 23°C. The average number of sunshine hours per year is over 1100 hours [4]. The average annual rainfall is 1640-1940 mm. Although the average annual rainfall is average, due to strong seasonal differentiation, the rainy season rainfall accounts for 85-86% of the total annual rainfall, the less rainy season rainfall accounts for only 14-15% of the total annual rainfall, so there is often a local water shortage in the less rainy season in some areas of the province. Analyzing the rainfall trend in Ninh Binh during 2000–2024, before the province's administrative reorganization, provides an important scientific basis for sustainable local water resource management.

DATA USED AND RESEARCH METHODS

Limits of the study area

Ninh Binh province before July 1st, 2025, the province had 8 affiliated administrative units (2 cities: Ninh Binh and Tam Diep, 6 districts: Nho Quan, Gia Vien, Hoa Lu, Yen Khanh, Kim Son, Yen Mo) [2].

Data used

- Inherited data include climate factors from the source of the Department of Natural Resources and Environment of Ninh Binh;

- Calculated data include daily and monthly rainfall in Ninh Binh province in the period 2000 - 2024 of the monitoring points: Ben De, Cuc Phuong, Dong Giao, Gian Khau, Nho Quan, Nhu Tan and Ninh Binh from the source of the Ninh Binh Hydrometeorological Center [6];

- Data from the Statistical Yearbook of Ninh Binh province in 2025 [2].

Ninh Binh province has 7 rain monitoring points, which are the stations: Ben De, Cuc Phuong, Dong Giao, Gian Khau, Nho Quan, Nhu Tan, Ninh Binh (shown in Table 1).

Table 1. Rainfall observation stations in Ninh Binh Province

No.	Station	Coordinates		Location
		X	Y	
1	Ben De	20°21'19"	105°48'03"	Gia Phu Commune, Gia Vien District
2	Cuc Phuong	20°18'01"	105°41'38"	Cuc Phuong Commune, Nho Quan District
3	Dong Giao	20°07'27"	106°55'59"	Nam Son Ward, Tam Diep City
4	Gian Khau	20°19'33"	105°55'58"	Gia Tran Commune, Gia Vien District
5	Nho Quan	20°19'19"	105°45'19"	Dong Phong Commune, Nho Quan District
6	Nhu Tan	20°01'58"	106°06'46"	Kim Tan Commune, Kim Son District
7	Ninh Binh	20°15'52"	105°58'49"	Dinh Tien Hoang Ward, Ninh Binh City

Source: Department of Natural Resources and Environment of Ninh Binh Province

Research method

The method of Statistical Hypothesis Testing

The Method of Statistical Hypothesis Testing is a probability-based procedure used to decide whether the evidence in a sample is strong enough to support or reject a claim (hypothesis) about a population.

Mathematical method

The average annual rainfall over many years is calculated according to formula 1:

$$Ro = \frac{\sum_{i=1}^n Ri}{n} \quad (1)$$

The factors in the formula:

Ro: Average annual rainfall over many years (mm);

Ri: Rainfall in year i (mm);

N: Number of years of observation.

Average less rainy season rainfall for many years is calculated by formula 2:

$$R_m = \frac{\sum_1^n R_{mi}}{n} \quad (2)$$

The factors in the formula:

R_m : Average rainfall during the rainy season for many years (mm);

R_{mi} : Rainfall in the rainy season of year i (mm);

N : Number of years of observation.

Average rainfall in the rainy season for many years is calculated by formula 3:

$$R_k = \frac{\sum_1^n R_{ki}}{n} \quad (3)$$

The factors in the formula:

R_k : Average less rainy season rainfall over many years (mm);

R_{ki} : Rainfall in the less rainy season of year i (mm);

N : Number of years of observation.

The rainfall variation coefficient is calculated by the formula:

$$C_v = \frac{S}{R_o} \times 100\%$$

The factors in the formula:

C_v : Rainfall variation coefficient (%);

S : Standard deviation of rainfall (mm);

R_o : Average rainfall (mm).

RESEARCH RESULTS AND DISCUSSION

Overview of the study area

Ninh Binh province is located in the geographical coordinates from $19^{\circ}55'39''$ to $20^{\circ}26'25''$ North latitude, from $105^{\circ}32'27''$ to $106^{\circ}10'15''$ East longitude. The province borders Ha Nam to the north, Nam Dinh to the east, Thanh Hoa and the East Sea to the south, and Hoa Binh to the west [5]. Ninh Binh has a natural area of $1411,86 \text{ km}^2$, with 70,4% of agricultural land suitable for growing annual crops (mainly paddy). The average population of Ninh Binh in 2024 was 1030,3 thousand people, an increase of 13,2 thousand people or a year-on-year increase of 1,30%, of which: the

urban population was 224,6 thousand people, accounting for 21,80%; the rural population was 805,7 thousand people, accounting for 78,2%. The average population density was 730 people per km^2 . In the province, there are 143 commune-level administrative units including: 17 wards (11 wards in Ninh Binh city, 6 wards in Tam Diep city); towns and 119 communes [2].

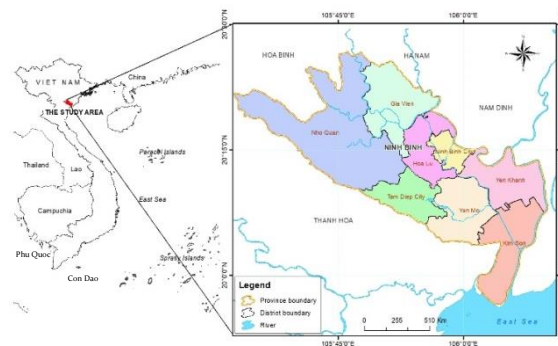


Figure 1. Administrative map of Ninh Binh Province.

Climate factors

The average daily radiation level in Ninh Binh is $100\text{--}120 \text{ kcal/cm}^2$ and the months with the highest radiation are May - October and the lowest are November - April [1, 4].

During the rainy season (May–October), the average monthly sunshine duration ranges from 150–200 hours, with July typically having the highest value; some locations exceed 200 hours. The month with the least sunshine is February and March because this is a period of wet drizzle and clouds, with an average of only 40–50 hours/month.

The average annual air temperature in the province is relatively uniform, ranging from $23,5\text{--}23,7^{\circ}\text{C}$, with July having the highest average temperature of the year, reaching $29\text{--}29,4^{\circ}\text{C}$, and January being the lowest month, but the average monthly temperature is still above 15°C .

Through the series of data on average monthly temperatures in Ninh Binh, it can be that: in the less rainy season, the temperature tends to decrease with smaller extremes compared to the previous period, but in the rainy season, the opposite is true. Extreme hot temperatures tend to increase.

The wind direction changes with the season. The prevailing wind directions in the two main seasons include: South, Southwest and Southeast in the rainy season and North, East and Northeast in the less rainy season.

During the less rainy season, the prevailing wind direction is Northeast, with a frequency of 60-70%. The average wind speed is usually from 1,5-2,3 m/s. In the last months of the less rainy season, the wind tends to gradually shift to the East. The first days of the Northeast monsoon often have winds of level 4 and level 5.

The Northeast monsoon strongly influences the weather in Ninh Binh from November to April of the following year (the strongest are December, January and February). During the less rainy season, air from the Siberian high pressure flows into our country through mainland China or around the West Pacific Ocean. In the first half of the less rainy season (from November to January of the following year), Ninh Binh is affected by dry polar air because it passes through mainland China. This is the coldest and driest air mass in Northern Vietnam. The thermo-humidity properties of this air mass change significantly over time. January is the period when temperature and humidity are at their lowest. When dry, denatured polar cold air flows in, the air temperature in Ninh Binh can drop rapidly by tens of degrees within 24 hours, causing the temperature range during the day to reach 15-20°C. During the day, the sky is partly cloudy, sunny, and cold at night due to strong heat radiation from the ground. In the second half of the less rainy season, the center of the Siberian high pressure moves eastward, so to reach the South, this polar air mass has to go around the sea, contacting the cold water surface for a long time. Compared to dry modified polar air, the modified air mass over the sea is more humid and the humidity increases significantly. When entering our country, the air is often saturated (absolute humidity is usually 9-11 g/kg). In late December and early January, the average temperature of these air masses can increase by 3-5°C and the

humidity increases by 3-4 mb. The humid modified polar air creates a humid weather pattern, cloudy skies, often with drizzle and a small temperature range during the day. The prevailing time of this air mass often coincides with the typical drizzle season in December and January in Ninh Binh.

The prevailing wind direction in the rainy season is Southeast, with a frequency of 50-70%. The average wind speed is 1,9-2,1 m/s. When a storm hits, the wind speed reaches nearly 40 m/s. At the beginning of the rainy season, there is often a hot, dry southwest wind that negatively affects crops.

The relative humidity of Ninh Binh province's air does not fluctuate much over the years, averaging 84-85%.

The total evaporation measured by the Piche tube on average for many years at monitoring points in the region does not vary much, only fluctuating between 860-1092 mm. Evaporation develops strongly in the less rainy season (lots of sunshine, high temperature), so the loss of water vapor is prominent and the evaporation capacity in the less rainy season months can be 2 to 3 times larger than the total average monthly rainfall. Therefore, from November to April of the following year, there is often drought and lack of freshwater resources over a large area, which significantly affects production and planting, even in places far from freshwater sources, there is a lack of water for daily life.

Rainfall development in Ninh Binh province

Rainfall regime

Ninh Binh's climate is divided into two main seasons: rainy season and less rainy season.

The rainy season includes consecutive rainy months with monthly rainfall exceeding evaporation loss (usually 100 mm/month) with a frequency exceeding 50%: $P\{X_{\text{month}} \geq 100\text{mm}\} \geq 50\%$, the less rainy season is the remaining months. The rainy season in Ninh Binh province is from May to October, the less

rainy season is from November to April of the following year.

The average annual rainfall for many years is in the range of 1640-1940 mm. Rainfall increases gradually from the plains to the mountains and is unevenly distributed throughout the year.

The rainy season is affected by the Southeast monsoon, so it is characterized by hot and humid weather, with rainfall greater than evaporation. In this season, the region is sometimes subject to the Foehn effect with hot and dry Southwest winds. The month with the highest rainfall for low-lying areas (plains, riverside) usually occurs in August (accounting for 18% of total annual rainfall), for higher areas it occurs in September, accounting for up to 20% of annual rainfall. The rainy months in Ninh Binh are directly affected by the tropical convergence zone, which is where tropical depressions and storms form from the Pacific Ocean and the East Sea and then make landfall on the Northern coast. The impact of storms, tropical depressions combined with high tides, storm surges reduce drainage capacity along with the dike system and low-lying land, so flooding often occurs here during the rainy season in agricultural areas as well as in urban areas. In the less rainy season, the lowest monthly rainfall is in February, sometimes less than 25 mm.

Table 2. Variation of rainfall over decades in Ninh Binh province

Unit: mm

No.	Station	2000-2009	2010-2019	2020-2024
1	Ben De	1747,0	1716,9	1729,7
2	Cuc Phuong	1870,1	1888,0	1910,8
3	Dong Giao	1703,0	1817,5	1701,8
4	Gian Khau	1724,2	1595,9	1687,4
5	Nho Quan	1794,5	1742,8	1791,0
6	Nhu Tan	1604,7	1583,2	1744,7
7	Ninh Binh	1665,0	1859,8	1712,0

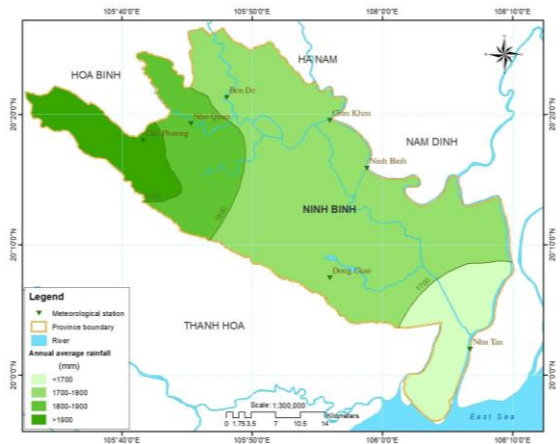


Figure 2. The map of average annual rainfall of Ninh Binh province

The average annual rainfall for many years is unevenly distributed in space and time. Rainfall increases gradually from the plains to the mountains (at Nhu Tan Station it is 1642,0 mm, at Cuc Phuong Station it is 1931,5).

The area along the Day River, due to low terrain, has low rainfall below 1700 mm/year. Compared to the national average rainfall, this is a province with average rainfall.

Rainfall varies slightly from year to year. The wettest year has approximately twice the total rainfall of the driest year, and the coefficient of variation (Cv) ranges from 0.17 to 0.23 (Table 3).

Heavy rains tend to be concentrated in the decade from 2010 to 2019 in mountainous areas, but for lowland areas, this is a period of light rain (shown in Table 2). Heavy rains from 1750 mm/year to over 1900 mm/year are often concentrated in high mountainous areas (the source of Hoang Long River, Cuc Phuong National Park area, along Tam Diep range).

Although the average annual rainfall in Ninh Binh is not large, there is a strong seasonal differentiation. The total rainfall in the rainy season accounts for 85-86% of the total annual rainfall. The total rainfall in the less rainy season accounts for 14-15% of the total annual rainfall (shown in Table 3).

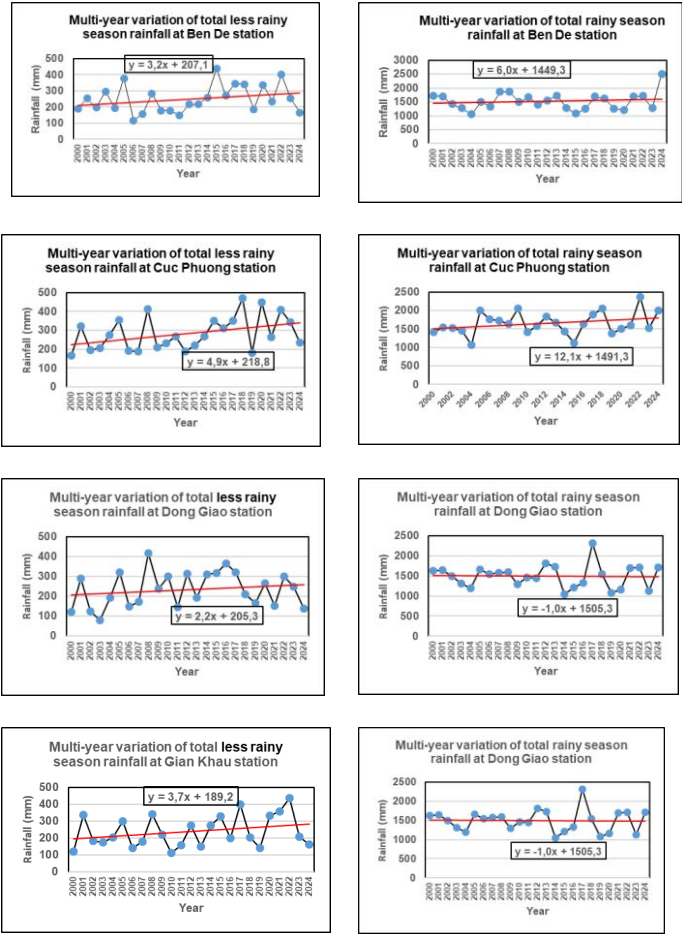
Table 3. Characteristics of multi-year average rainfall in Ninh Binh province during the period 2000-2024

No	Station	Annual rainfall (mm)	Cv	Rainy season			Less rainy season	
				P _{Rainy} (mm)	%	Occurrence period (month-month)	P _{dry} (mm)	Occurrence period (month-month)
1	Ben De	1776,8	0,17	1527,5	86	5-10	249,4	11-4
2	Cuc Phuong	1931,5	0,17	1648,7	85	5-10	282,7	11-4
3	Dong Giao	1725,6	0,18	1491,7	86	5-10	233,9	11-4
4	Gian Khau	1704,9	0,21	1468,1	86	5-10	236,9	11-4
5	Nho Quan	1856,5	0,23	1584,4	85	5-10	272,1	11-4
6	Nhu Tan	1642,0	0,20	1412,9	86	5-10	229,1	11-4
7	Ninh Binh	1738,2	0,18	1475,2	85	5-10	263,0	11-4

Multi-year seasonal rainfall variation in Ninh Binh

Rainfall in the rainy season varies from 1410-1650 mm, rainfall in the less rainy season

varies from 220-250 mm. The multi-year variation of total rainfall in the less rainy season and rainy season in Ninh Binh province is shown in Figure 3.



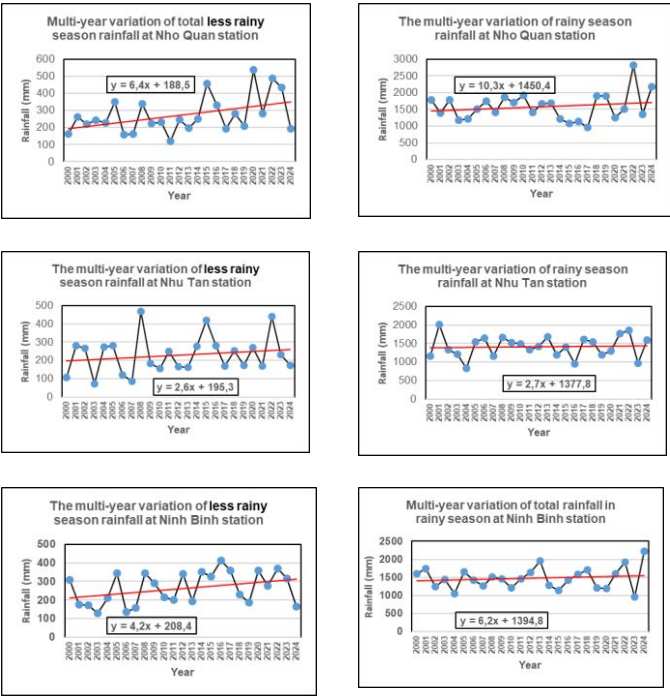


Figure 3. Multi-year variation of total seasonal rainfall in Ninh Binh province

Looking at the graph of multi-year variation of total rainfall in the less rainy season and rainy season in the study area, it shows that the general trend of rainfall in both seasons in the period 2000-2024 in Ninh Binh has a general increasing trend in both seasons, the rainy season increases more than the less rainy season (Figure 3), especially in the Nam Son and Tam Diep areas, where total rainfall in the rainy season decreases in some years, but the number of heavy rainfall events increases.

Table 4. Trends of seasonal rainfall in Ninh Binh province (2000-2024)

Station	Trend equation		Rate of change (±), mm/year	
	Less rainy season	Rainy season	Less rainy season	Rainy season
Ben De	$y = 3,2x + 207,1$	$y = 6,0x + 1449,3$	+3,2	+6,0
Cuc Phuong	$y = 4,9x + 218,8$	$y = 12,1x + 1491,3$	+4,9	+12,1
Dong Giao	$y = 2,2x + 205,3$	$y = -1,0x + 1505,3$	+2,2	-1,0
Gian	$y = 3,7x +$	$y = 0,6x +$	+3,7	+0,6

Khau	189,2	1459,7		
Nho Quan	$y = 6,4x + 188,5$	$y = 10,3x + 1450,4$	+6,4	+10,3
Nhu Tan	$y = 2,6x + 195,3$	$y = 2,7x + 1377,8$	+2,6	+2,7
Ninh Binh	$y = 4,2x + 208,4$	$y = 6,2x + 1394,8$	+4,2	+6,2

During the period 2000-2005, rainfall in Ninh Binh tended to decrease in both seasons, especially the less rainy season, causing typical droughts in the winter-spring crop in 2005 [3], but from 2006 to now, rainfall has increased and decreased alternately in both seasons. This is a sign that climate change has a very clear impact on the climate conditions of the study area, shown in the rainy season rainfall in some years decreased (shown in Table 4) but the amount of rainstorms increased dramatically.

After calculating the probability to test the statistical hypothesis of the seasonal rainfall data series at the stations, the author found that at Cuc Phuong station $p = 0.04$, Nho Quan station $p = 0.03$ (both < 0.05), proving that the seasonal rainfall trend is a real trend.

The highest daily rainfall was in September 2000 in the Hoang Long River basin, with the maximum daily rainfall at Ben De station being 306.6 mm, and at Nho Quan station being 356,1 mm. Heavy rains broke and overflowed many dikes, causing widespread flooding, and seriously affecting agricultural production that year. The most affected areas were Gia Vien, Nho Quan, Yen Khanh, Yen Mo districts and Ninh Binh city.

CONCLUSION

The climate of Ninh Binh province is divided into two main seasons: rainy season and less rainy season. The average annual rainfall for many years is 1640-1940 mm, strongly differentiated by season. Rainfall in the rainy season accounts for 85-86% of the total annual rainfall, while the less rainy season rainfall accounts for only 14-15% of the total annual rainfall.

Rainfall fluctuates slightly over the years, the year with the most rain is about 2 times higher than the year with the least rain, the coefficient of variation C_v fluctuates between 0,17-0,23. Rainfall in the period 2000-2024 has a general trend of increasing in both seasons. Rainfall in the less rainy season increases from +2,2 mm/year to +6,4 mm/year, rainfall in the rainy season increases from +0,6 mm/year to 12,1 mm/year, especially in Nam Son, Tam Diep (at Dong Giao station), rainfall in the rainy season decreases slightly (-1,0 mm/year). At Dong Giao station, where the trend coefficient ($a < 0$), suggests that local physical factors may override regional climatic signals. This station is located on the elevated Dong Giao limestone plateau, where orographic shadowing and rapid surface runoff may reduce effective rainfall accumulation compared with surrounding lowland areas.

The average annual rainfall has shown alternating increases and decreases in both seasons. Although total rainfall in the rainy season has decreased in some years, extreme rainfall events have increased dramatically. Typically, in September 2000, in the Hoang Long River basin, the highest daily rainfall was up to 356,1 mm.

This research is supported by the project "*Building a water resources management system based on Internet of Things (IoT) technology to proactively regulate and balance water resources to serve the sustainable socio-economic development of Ninh Binh province*".

REFERENCES

1. Climate-Data.org (n.d.). Climate data for Ninh Binh Province, Viet Nam. URL: <https://vi.climate-data.org/chau-a/viet-nam/ninh-binh-province-825/> [Last accessed: 19 October 2025].
2. Ninh Binh Department of Natural Resources and Environment (2021). Climate Assessment Report of Ninh Binh Province. Ninh Binh, Viet Nam.
3. Ninh Binh Hydrometeorological Center (2024). Daily and monthly rainfall data at hydrometeorological stations of Ninh Binh Province for the period 2000–2024. Ninh Binh, Viet Nam.
4. Ninh Binh Statistical Office (2025). Ninh Binh Statistical Yearbook 2025. Ninh Binh, Viet Nam.
5. Phan Truong Duan, Vu Ngoc Linh (2016). Research on assessing the impact of climate change on drought in Ninh Binh Province. Journal of Hydrometeorology, December 2016.
6. Prime Minister (2024). Planning of Ninh Binh Province for the period 2021–2030, with a vision to 2050. Issued together with Decision No. 218/QĐ-TTg dated March 4, 2024, of the Prime Minister, Hanoi, Viet Nam.

DOI: 10.15625/vap.2025.0247

ASSESSMENT OF PRECIPITATION VARIATION TRENDS IN NGHE AN PROVINCE UNDER THE CONTEXT OF CLIMATE CHANGE

Le Thi Nguyet

University of Education, Thai Nguyen University, Vietnam

Email: nguyetlt@tnue.edu.vn

Abstract: Climate change has affected various natural components, including the global water cycle, thereby exerting significant impacts on multiple sectors of socio-economic life.

This study assessed the trends in precipitation variation under the context of climate change in Nghe An Province, Viet Nam. Non-parametric statistical methods, including the Mann-Kendall test and Sen's slope estimator, were applied to detect changes in precipitation based on daily precipitation data from four observation stations across Nghe An Province during the period 1998 - 2020.

The results revealed that all four stations exhibited an increasing trend in precipitation, with Dua Station showing the most significant trend. The rate of change in precipitation varied among stations: Yen Thuong and Nam Dan stations showed a moderate rate of increase, while Do Luong Station exhibited only a slight increase. These findings hold important implications for water resource management and agricultural planning in the region.

Keywords: Climate Change, Precipitation Trends, Mann-Kendall Test, Nghe An Province.

INTRODUCTION

In recent decades, climate change has become a pressing global issue, profoundly affecting various natural components and, consequently, exerting widespread impacts across multiple sectors of life. The consequences of climate variability have emerged as a major concern for humanity in the 21st century, with significant effects on the global water cycle. Furthermore, human

activities have contributed to an increase in extreme weather events - an integral part and a direct consequence of climate change. These events pose substantial risks to agricultural productivity and soil fertility, particularly in regions frequently affected by heavy rainfall. Previous studies have demonstrated that the frequency of extreme rainfall events has been increasing, reflecting the general trend of climate variability (Jaiswal R.K. & Lohani A.K, 2015; Tiwari H.L, 2019; Wu H. & Qian H, 2017).

Rainfall is a crucial climatic factor that has a significant influence on various aspects of social and economic life, particularly in agricultural production (Lawin A.E, Manirakiza C, & Batablinlè L, 2018). Changes in rainfall patterns can lead to a range of adverse consequences, including yield reduction, landslides, and soil erosion. In mountainous areas, these changes may result in income decline and loss of cultivable land.

Globally, numerous studies have been conducted to assess the impacts of climate variability on rainfall trends (Adefsan E.A, 2018; Al-Subih M, Kumar M, Mallick J, Ramakrishnan R, Islam S, & Singh C.K, 2021). These studies have employed a variety of statistical techniques, including both parametric and non-parametric methods, to detect changes in rainfall patterns and trends.

This study aims to analyze the characteristics and trends of rainfall across Nghe An Province, Viet Nam, under the context of climate change. Non-parametric statistical methods will be applied to detect variations in rainfall patterns and trends. By understanding these rainfall characteristics and

trends, the study seeks to provide valuable insights into potential risks associated with climate variability and to support policymakers and stakeholders in developing effective strategies to mitigate such risks.

DATA AND METHODS

Study area

Nghe An Province, located in the North Central region of Viet Nam, is a vast and ecologically diverse area, covering an area of 16.486 km² (2025) (Figure 1). Characterized by

its distinctive topography and climate, the province serves as an important center for agricultural and forestry activities. With a population of approximately 3.472.300 people (National Assembly, 2025), the province exhibits a diverse range of landforms, including mountains, hills, and plains, with elevations ranging from 10 to over 1,000 meters above mean sea level (Figure 1). The topography of the province gently slopes from north to south and from west to east.

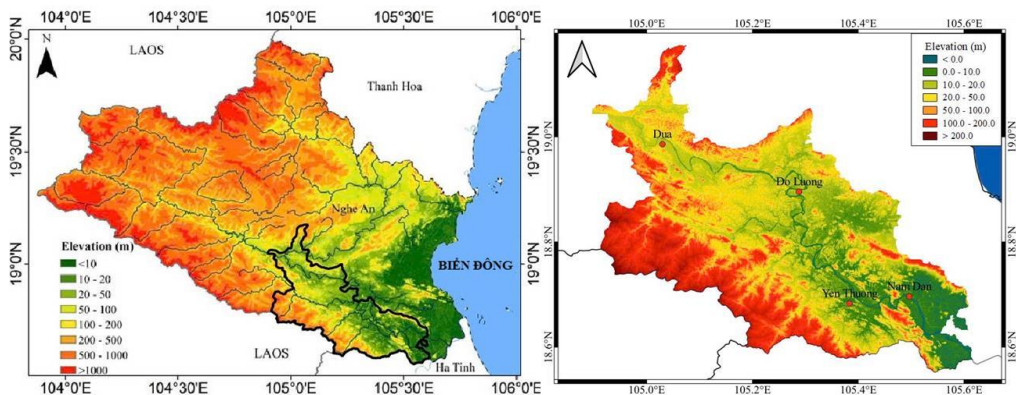


Figure 1: Topographic map of Nghe An province

The average annual temperature is around 23-24°C, with significant temperature fluctuations throughout the year. Nghe An receives an average annual rainfall up to 2,000 mm, with the majority of rainfall concentrated in the late summer and early autumn months, specifically August, September, and October (Figure 2). Notably, the rainfall distribution varies significantly across different areas of the province (Dinh, T. K. H, Shima. K, 2022).

Data collection

To conduct this work, daily rainfall data at 04 observation stations across Nghe An province (Figure 2) were collected from the Hydrometeorological Forecasting Station in Nghe An province, Vietnam during the period 1998-2020. Accordingly, rainfall data series quality was appraised to ensure that the input rainfall data series meets the criteria for trend analysis (Data for Yen Thuong station in Figure 2 were unavailable due to missing monthly records before 2000).

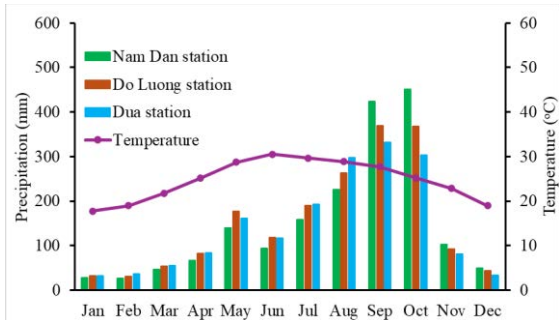


Figure 2: Monthly rainfall distribution at observation stations across Nghe An province

Statistical approaches

Interruption point detection

To employ interruption of observed rainfall data series, the study applied the Buishand test is a statistical technique used to detect cumulative deviations from the mean for evaluating the homogeneity of a time series. The Buishand test is based on characteristic statistical values such as the mean, variance,

and standard deviation (Machiwal. D and Jha. M. K, 2008). The Buishand test is expressed as:

$$S_0^* = 0; S_k^* = \sum_{i=1}^k (Y_i - \bar{Y}), k = 1, \dots, n \quad (1)$$

where $S_0^* = 0$ is the value at point $k = 0$, which oscillates around 0 in the case where the time series is considered homogeneous, S_k^* is the value at point k , Y_i is the value at time i , and \bar{Y} is the mean of the series.

When evaluating the quality of the time series, two hypotheses are formulated in this problem:

1. H_0 (Null hypothesis): The time series exhibits homogeneity.

2. H_1 (Alternative hypothesis): The time series is non-homogeneous, with discontinuities at one or multiple points in the time series.

The confidence level of 95%, corresponding to a significance level of ($\alpha = 0.05$). If the p-value is greater than the significance level α , the null hypothesis (H_0) is accepted, and the alternative hypothesis (H_1) is rejected, indicating that the time series is homogeneous. Conversely, if the p-value is less than α , the null hypothesis (H_0) is rejected, and the alternative hypothesis (H_1) is accepted, signifying that the time series is non-homogeneous.

Change trend detection

To employ this work, a non-parametric statistical method, specifically the Mann-Kendall test and Sen's slope estimator, are applied to detect change trends of the rainfall data series during the period of 1998-2020. This method is predicated on the assumption of an H_0 of no trend, whereas a monotonic trend (i.e., an increasing or decreasing pattern) is posited as the alternative hypothesis (H_1) (Machiwal. D and Jha. M. K, 2008). The Mann-Kendall test is defined based on formula (2):

$$S = \sum_{i=1}^n \sum_{j=i+1}^n \text{sgn}(X_j - X_i) \quad (2)$$

Where $\text{sgn}(X_j - X_i)$ in formula (2) is defined by formula (3):

$$\text{sgn}(X_j - X_i) = \begin{cases} +1 & \text{if } x_j - x_i > 0 \\ 0 & \text{if } x_j - x_i = 0 \\ -1 & \text{if } x_j - x_i < 0 \end{cases} \quad (3)$$

In a time series, X_i , $i = 1, 2, 3, \dots, n$, the value of S is assumed to be a normal distribution while the discrepancy of statistics S has signed applying formula (4):

$$\text{var}(S) = \frac{1}{18} \left[n(n-1)(2n+5) - \sum_{j=1}^m t_j(t_j-1)(2t_j+5) \right] \quad (4)$$

Where the standard test (Z_s) is used to detect the input series trend. When the Z_s is calculated using formula (5):

$$Z_s = \begin{cases} \frac{S-1}{\sqrt{\text{Var}(S)}} & \text{if } S > 0 \\ 0 & \text{if } S = 0 \\ \frac{S+1}{\sqrt{\text{Var}(S)}} & \text{if } S < 0 \end{cases} \quad (5)$$

The Sen's slope estimator is also a non-parametric statistical method frequently employed to establish the true gradient of an existing trend. Furthermore, it is often utilized to quantify the magnitude of change in trends observed in the data series. The Sen's slope is computed using the following formula:

$$\beta = \text{Median} \left(\frac{x_i - x_j}{i - j} \right) \text{ with } j < i \quad (6)$$

Where X_i , X_j are input series at intervals t_i and t_j , respectively.

RESULTS AND DISCUSSION

Breakpoint detection

The daily rainfall data series at 4 observation stations across Nghe An province during the period 1998-2020 was transformed to annual rainfall before conducting the breakpoint detection applying test SNHT Buishand test. The results indicated that the

obtained critical values (p) of 4 rainfall observation stations are larger than the confidence level 95% which implies that the input data series at all observation stations

across the study area are of good quality and completely meets the requirements for further studies (Table 1 and Figure 1).

Table 1. Breakpoint detection for rainfall series at stations across Nghe An province

No.	Station	SNHT		Buishand	
		To	p	Q	p
1	Yen Thuong	2.787	0.590	3.786	0.445
2	Dua	3.918	0.317	4.117	0.358
3	Do Luong	5.042	0.188	4.563	0.237
4	Nam Dan	2.671	0.629	3.542	0.524

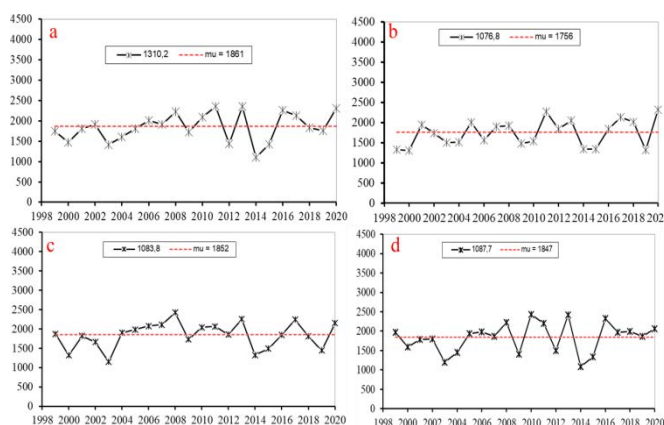


Figure 3: Quality assessment results of input data series at stations across the study area

Precipitation statistical features

Basic statistical features of the precipitation characteristics at 4 observation stations including Yen Thuong, Dua, Do Luong and Nam Dan across Nghe An province during the period 1998-2020 were given in Table 2. The minimum precipitation values at the four stations range from 1086.1 mm (Nam Dan station) to 1149.5 mm (Do Luong station), indicating that the driest period occurred in the east and northeast of the study area, with a minimum value of 1086.1 mm. In contrast, the maximum precipitation values at the four stations range from 2420.2 mm (Do Luong station) to 2430.1 mm (Nam Dan station), indicating that the wettest period occurred in the east and northeast of the study area, with a maximum value of 2420.2 mm.

The mean precipitation values at the four stations range from 1755.5 mm to 1861.3 mm,

indicating that Yen Thuong station experienced the highest average precipitation, while Dua station experienced the lowest average precipitation. The standard deviation (SD) of precipitation values at the four stations ranges from 324.1 mm to 369.4 mm, indicating that Nam Dan station had the highest variability in precipitation, while Dua station had the lowest variability. The coefficient of variation (CV) of precipitation values at the four stations range from 0.19 to 0.22, indicating that Yen Thuong station had the lowest variation in precipitation, while Nam Dan station had the highest variation. This suggests that Yen Thuong station experienced a more consistent precipitation pattern, while Nam Dan station experienced a more variable precipitation pattern. Overall, the analysis of the precipitation characteristics at the four stations provides valuable insights into the local climate patterns and precipitation trends.

Table 2. Precipitation statistical features at observation stations during the period 1998-2020

No.	Station	Minimum (mm)	Maximum (mm)	Mean (mm)	SD (mm)	CV (%)
1	Yen Thuong	1100.7	2356.3	1861.3	336.5	0.19
2	Dua	1309.7	2312.9	1755.5	324.1	0.20
3	Do Luong	1149.5	2420.2	1852.2	324.5	0.21
4	Nam Dan	1086.1	2430.1	1846.8	369.4	0.22

Temporal change trends detection

The analyzed results of temporal change trends of precipitation at 04 observation stations across Nghe An province during the period 1998 - 2022 are given in Table 3. To temporal change trends detection at of precipitation at 04 observation stations, a significance level of 95% was used for both Mann-Kendall test and Sen's slope estimator. Analysis results revealed that the Kendall's tau value is 0.304, 0.333, 0.239 and 0.268 at Yen Thuong, Dua, Do Luong and Nam Dan stations, which indicates a moderate trend towards increasing precipitation (Figure 4).

The p-critical value is 0.108 and 0.070 at Do Luong and Nam Dan stations, which is greater than the significance level of 0.05, indicating that the trend is not statistically significant. While at Yen Thuong and Dua stations, the p-critical values are 0.039 and 0.023 which is less than the significance level of 0.05, indicating that the trend is statistically significant. For the Sen's slope, results showed the values are 21.91, 26.88, 16.01 and 21.36, which represents the increasing trend and statistically significant of precipitation across the study area over time (Figure 4).

Table 3: Results of the trend detection based on the Mann-Kendall and Sen's slope estimator at precipitation observation stations across the study area

No.	Station	Kendall's tau	p-critical	Sen's slope
1	Yen Thuong	0.304	0.039	21.91
2	Dua	0.333	0.023	26.88
3	Do Luong	0.239	0.108	16.01
4	Nam Dan	0.268	0.070	21.36

Overall, the analysis of the trend detection results indicates that all four stations exhibit a trend towards increasing precipitation, with Dua station experiencing the strongest trend. The results also suggest that the rate of change in precipitation varies across the stations, with Yen Thuong and Nam Dan stations experiencing a moderate rate of change, while Do Luong station experiences a weak rate of change.

These findings are consistent with recent studies in Central Vietnam (e.g., Nguyen et al., 2023; Pham & Lee, 2021), which also reported increasing annual rainfall but varying trends in extreme precipitation.

The differences in precipitation trends among stations could be influenced by local topography (Figure 1), distance from the coast, and land-use patterns. For example, Dua Station, which exhibits the strongest trend, is located in an area with higher elevation and greater forest coverage, which may influence local convection and rainfall intensity.

These findings have important implications for water resource management and agricultural planning in the region. The increasing trend in precipitation at all four stations suggests that the region may experience more frequent and severe flooding events in the future, which could have significant impacts on agricultural and forestry activities.

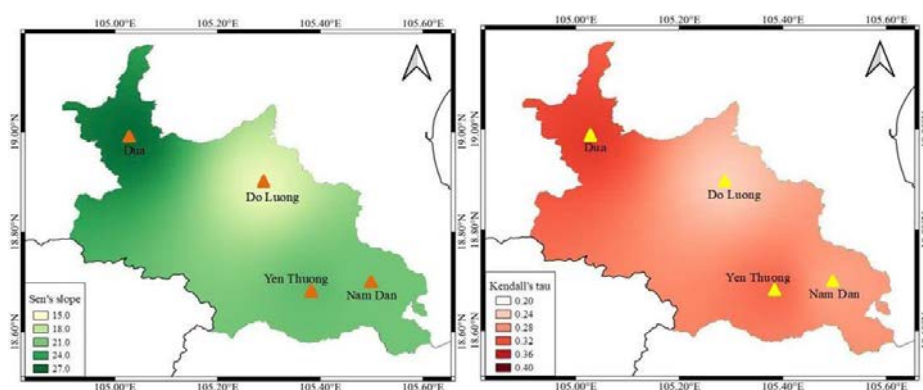


Figure 4: Precipitation variation trends based on the Mann-Kendall test and Sen's slope estimator

CONCLUSIONS

Rainfall is a key climatic variable that strongly influences socio-economic activities, particularly agriculture. This study analyzed precipitation trends across Nghe An Province using daily rainfall data from four meteorological stations during the period 1998–2020. Based on the Mann–Kendall test and Sen's slope estimator, all four stations exhibited increasing precipitation trends. The trends at Yen Thuong and Dua stations were statistically significant ($p < 0.05$), whereas the trends at Do Luong and Nam Dan stations were not statistically significant ($p > 0.05$). Among the stations, Dua demonstrated the strongest increasing trend.

The observed upward trends in annual precipitation may indicate hydrological changes that could affect water resource management, agricultural planning, and ecosystem stability in Nghe An Province. Although this study does not analyze extreme rainfall events directly, increasing annual totals suggest the need to prepare for potential hydrological pressures. Strengthening water management strategies—including improving reservoir operations, reinforcing dike systems, and enhancing meteorological-hydrological monitoring—will be essential for minimizing risks to agricultural production, forestry, and rural communities.

This study is limited by its use of annual rainfall totals, which do not reflect rainfall intensity or the frequency of extreme rain

events. As such, conclusions regarding flooding severity remain indicative rather than definitive. In addition, only four stations were used, which may not fully represent the spatial variability of rainfall across the province. Future research should incorporate additional stations, analyze sub-daily or daily extreme rainfall indices, and explore the influence of land-use changes and topographic factors on precipitation variability. Integrating climate model projections would also help better assess long-term climate risks for the region.

REFERENCES

1. Adefsan EA (2018). *Climate change impact on rainfall and temperature distributions over West Africa from three IPCC scenarios*. J Earth Sci Clim Change 9:476.
2. AlSubih, M., Kumar, M., Mallick, J., Ramakrishnan, R., Islam, S., Singh, C. K. (2021). *Time series trend analysis of rainfall in last five decades and its quantification in Aseer Region of Saudi Arabia*. Arab J. Geosci., 14(6):1–15.
3. Bartels, R. J., Black, A. W., Keim, B. D. (2020). *Trends in precipitation days in the United States*. Int. J. Climatol., 40:1038–1048.
4. Ibrahim B, Karambiri H, Polcher J, Yacouba H, Ribstein P (2014). *Changes in rainfall regime over Burkina Faso under the climate change conditions simulated by 5 regional climate models*. Clim Dyn 42:1363–1381.
5. Ilori, O.W., Ajayi, V.O (2020). *Change Detection and Trend Analysis of Future Temperature and Rainfall over West Africa*. Earth Syst Environ 4, 493–512.

6. Iqbal, Z., Shahid, S., Ahmed, K., Ismail, T., Nawaz, N. (2019). *Spatial distribution of the trends in precipitation and precipitation extremes in the sub-Himalayan region of Pakistan*. Theoret. Appl. Climatol., 137(3):2755–2769.
7. Jaiswal RK, Lohani AK (2015) Tiwari HL (2019). *Statistical analysis for change detection and trend assessment in climatological parameters*. Environ Process 2:729-749.
8. Lawin AE, Manirakiza C, Batablinlè L (2018). *Trends and changes detection in rainfall, temperature and wind speed in Burundi*. J Water Clim Change. <https://doi.org/10.2166/wcc.2018.155>
9. Lee, S. K., Dang, T. A. (2019). *Precipitation variability and trends over the Mekong Delta area of Vietnam*. Journal of Agrometeorology. 21 (2): 217-219.
10. Lenderink G, van Meijgaard E (2010). *Linking increases in hourly precipitation extremes to atmospheric temperature and moisture changes*. Environ Res Lett 5:025208.
11. Meshram, S. G., Singh, V. P., Meshram, C. (2017). *Long-term trend and variability of precipitation in Chhattisgarh State, India*. Theoret., Appl. Climatol. 129(3-4), 729-744.
12. Salehi, S., Dehghani, M., Mortazavi, S. M., Singh, V. P. (2020). *Trend analysis and change point detection of seasonal and annual precipitation in Iran*. Int. J. Climatol., 40(1):308–323.
13. Sanogo S, Fink AH, Omotosho JA, Ba A, Redl R, Ermert V (2015). *Spatio-temporal characteristics of the recent rainfall recovery in West Africa*. Int J Climatol 35:4589–4605.
14. Soro, G. E., Noufé, D., Bi, T. A. G., Shorohou, B. (2016). *Trend analysis for extreme rainfall at sub-daily and daily timescales in Côte d'Ivoire*. Climate, 4, 37.
15. Waghaye, A. M., Rajwade, Y. A., Randhe, R. D., Kumari, N. (2018). *Trend analysis and change point detection of rainfall of Andhra Pradesh and Telangana, India*. Journal of Agrometeorology, 20(2): 160-163.
16. Wu, H., Qian, H. (2017). *Innovative trend analysis of annual and seasonal rainfall and extreme values in Shaanxi, China, since the 1950s*. Int. J. of Climatology, 37(5), 2582–2592.
17. Yadav, R., Tripathi, S. K., Pranuthi, G., Dubey, S. K. (2014). *Trend analysis by Mann-Kendall test for precipitation and temperature for thirteen districts of Uttarakhand*. J Agrometeorology., 16(2):164.
18. Yang, P., Ren, G., Yan, P. (2017). *Evidence for a strong association of short-duration intense rainfall with urbanization in the Beijing urban area*. Journal of Climate., 30(15), 5851–5870.
19. Yu PS, Yang TC, Kuo CC (2006). *Evaluating long-term trends in annual and seasonal precipitation in Taiwan*. Water Resour Manag 20:1007–1023.
20. Yu, X. Y., Zhao, G. X., Zhao, W. J., Yan, T. T., Yuan, X. J. (2017). *Analysis of precipitation and drought data in Hexi Corridor, Northwest China*. Hydrology. 4, 29.
21. Dinh, T. K. H., Shima, K. (2022). *Effects of forest reclamation methods on soil physicochemical properties in North- Central Vietnam*. Res. on Crop. 23 (1): 110-118.
22. Tue, M. V., Raghavan, S. V., Pham, D. M. and Liong, S. Y. (2015). *Investigating drought over the central highland, Vietnam, using regional climate models*. J. Hydrol. 526: 265-73.
23. Machiwal, D and Jha, M. K (2008). *Comparative Evaluation of Statistical Tests for Time Series Analysis: Application to Hydrological Time Series*. DOI: 10.1623/hysj.53.2.353
24. National Assembly (2025). *Resolution on the arrangement of provincial-level administrative units*. Resolution No. 202/2025/QH15 dated June 19, 2025, Hanoi.

DOI: 10.15625/vap.2025.0248

Monitoring Air Pollutants (CO and NO₂) in Binh Duong Province Using Sentinel-5P Satellite Data and GIS Technology

Le Thanh Khong, Tran Thi An*

Thu Dau Mot University, Ho Chi Minh City

*Email: antt@tdmu.edu.vn

Abstract: This study aims to monitor greenhouse gases concentrations in Binh Duong province using remote sensing data and GIS technology. Using Sentinel-5P satellite imageries integrated with Google Earth Engine cloud-computing platform, the study extracted and analyzed the air quality in Binh Duong province in 2024. Subsequently, the concentrations of air pollutants, including CO and NO₂ in Binh Duong province in 2024 were analysed spatially and temporally. The research results show that the concentrations of air pollutants in Binh Duong province change over time and space. The concentrations of pollutants tend to increase in the dry season and decrease in the rainy season. Spatially, urban areas and areas with high concentrations of industrial zones such as Di An, Thuan An, and Thu Dau Mot City have higher concentrations of air pollutants than the remaining areas in the province. The WebGIS is built with functions to display information on air pollution parameters (NO₂, CO) in the Binh Duong area, with monthly averages for the year 2024, including maps of the air pollutants and statistics of these parameters. Through the WebGIS application, users can access and query data on air quality, allowing managers to formulate control and management policies to improve air quality in the study area.

Keywords: Air Pollution, Binh Duong, GEE, Sentinel-5P, WebGIS.

INTRODUCTION

The surrounding air environment includes many common pollutants such as TSP, PM₁₀, PM_{2.5}, SO₂, and O₃. Among them, CO

and NO₂ are two characteristic pollutants representing emissions from traffic and fuel combustion activities – the main sources of emissions in urban areas of Vietnam (WHO, 2021; EPA, 2021). NO₂ is considered a typical indicator of internal combustion engine emissions (Carslaw & Beevers, 2005), while CO strongly reflects the level of incomplete combustion, often arising from traffic and industrial activities. Therefore, monitoring CO and NO₂ allows for a direct assessment of the impact of dominant emission sources and reflects fluctuations in urban air quality in a sensitive and timely manner.

There are several studies evaluating the changes in air quality in different methods, based on various indicators related to air pollution caused by human activities (Nguyen Thi Le Hang, 2018; Do Thi Phuong Thao et al., 2022; Luu Thi Dieu Chinh et al., 2023). Depending on the research objectives, indicators such as NO_x, SO₂, CO_x are selected depending on the area. Most of the studies are conducted based on the use of remote sensing images, Google Earth Engine (GEE) platforms for implementation because of their convenience (Halder et al., 2023; Luu Thi Dieu Chinh et al., 2023).

The use of satellite-based remote sensing in long-term air quality monitoring on many different spatial and temporal scales has become an effective and popular solution today (Aldabash et al., 2020; Halder et al., 2023). Sentinel-5P TROPOMI provides high sensitivity data and good spatial resolution for CO and NO₂ (Veefkind et al., 2012; Eskes et al., 2020; Borsdorff et al., 2018). With the ability to provide timely monitoring and spatial data

distribution, satellite data provides a comprehensive framework for air quality assessment by providing detailed information on pollutants such as CO₂, NO₂, SO₂ and other pollutant gases. This technology significantly improves the accuracy of mapping air quality concentrations, thereby supporting many environmental and public health initiatives (Zhang et al., 2021; Tian et al., 2023; Stratoulis et al., 2024).

The main objective of this study is to apply the Google Earth Engine platform and Sentinel-5P satellite data to analyze the spatial and temporal variation of CO and NO₂ concentrations in Binh Duong province in 2024. The study used GIS and remote sensing tools to generate the spatial distribution of air quality in Binh Duong, and initially establish a WebGIS system for monitoring the data on green-house gases concentration. The findings from this study enable to identify air pollution hotspots in the study area and propose solutions to overcome these problems.

METHODOLOGY

Study Area

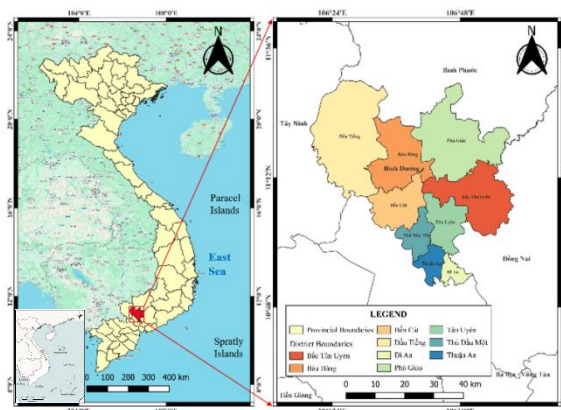


Figure 1. The geographical location of Binh Duong province

The study site is selected in Binh Duong province, Vietnam, based on the administrative boundary before July 2025. Currently, Binh Duong province is merged to Ho Chi Minh City under the Decision of Vietnam Government from July 2025. Binh Duong is known as the industrial development zone in Southeast

region of Vietnam, and it serves as an important hub connecting various provinces and cities in the Southern key economic zone. The province has the highest per capita income in the country (General Statistics Office, 2021). With the rapid growth of businesses and industrial zones in Binh Duong province in recent years, controlling air quality and ensuring sustainable industrial development have become urgent priorities.

Data Used

This study uses Sentinel-5P TROPOMI satellite image data in 2024, to serve the monitoring and assessment of air quality in the study area of Binh Duong province. Sentinel-5P is a satellite system with a focus on collecting air pollution data (ESA, 2017). The important sensor of this satellite is TROPospheric Monitoring Instrument (TROPOMI) which is capable of quantifying gases such as NO₂, O₃, HCHO, SO₂, CH₄, CO and aerosols... This is one of the first satellites to provide high-resolution air pollution monitoring and provides the ability to collect large data allowing daily and even hourly monitoring.

Remote sensing method has been effectively used in the paper to extract CO and NO₂ data from Sentinel-5p satellite, and build an air quality database, supplying data source to the current ground measuring stations which are still very limited in Vietnam.

Method of extracting concentrations of air pollutants

In order to monitor the air quality of Binh Duong province, the study analyzed the CO and NO₂ concentrations based on satellites using the Google Earth Engine (GEE) platform (Figure 1). First, the study extracted the CO and NO₂ concentrations in the air based on the Sentinel - 5P TROPOMI sensor using the GEE platform (<https://code.earthengine.google.com>). Then, based on the study area boundary on the GEE platform, the study calculated the CO and NO₂ concentration data over time in the months of 2024 and filtered by the study area of Binh Duong province using the command codes on GEE. After extracting CO and NO₂

concentrations from the Sentinel - 5P TROPOMI sensor, the study established an air quality map by month of the year and analyzed the difference in CO and NO₂ concentrations in Binh Duong province during the research period of 2024. From there, the air quality was assessed to determine air pollution and propose appropriate control solutions.

Sentinel-5P TROPOMI data provides atmospheric products at Level-3 Near Real-Time (NRTI), including components such as NO₂ and CO. The spatial resolution of the NO₂ product is approximately 3.5 × 5.5 km², while CO has a resolution of about 7 × 7 km², with pixel size varying slightly with latitude. In terms of temporal resolution, Sentinel-5P scans

the entire Earth every day, thus the NRTI data provides daily updated information for each location. To ensure measurement quality, pixels covered by clouds or of low quality are removed based on the qa_value, retaining only pixels with qa_value ≥ 0.75, corresponding to high quality and minimal cloud influence. In addition to NRTI data, Sentinel-5P also provides OFFL (Offline) data, which is more thoroughly calibrated and validated, suitable for formal studies and long-term analysis (Earth Engine Data Catalog, 2025a; Earth Engine Data Catalog, 2025b).

Method for building WebGIS monitoring air quality in Binh Duong Province

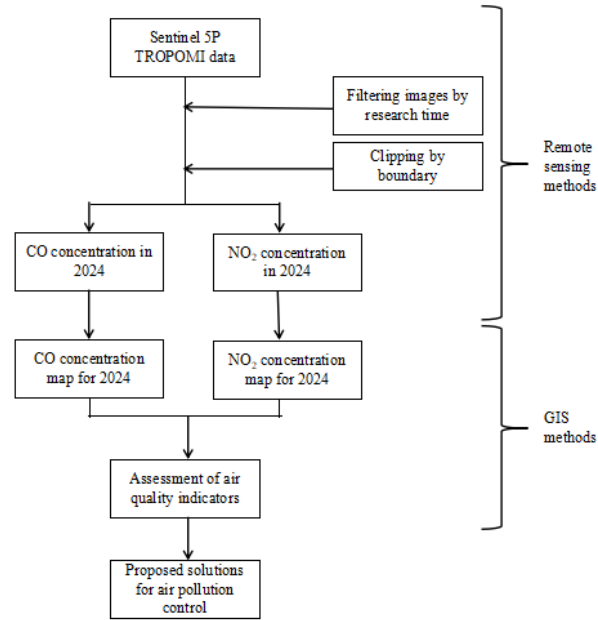


Figure 2. Flowchart of air quality monitoring research in Binh Duong province based on Google Earth Engine platform.

In the process of developing WebGIS to serve the display and retrieval of spatial map information of parameters (NO₂, CO), the author has chosen open-source software that is popular, easy to deploy, and suitable for practical conditions: QGIS software is used as the initial map data editing and processing software. This is a powerful open-source software that supports various data formats and has the ability to integrate many useful plugins. QGIS2Web is a plugin integrated

directly into QGIS, allowing users to publish designed maps in interactive web format (based on OpenLayers or Leaflet) (QGIS2Web, 2025). This QGIS2Web software supports automatic generation of HTML, JavaScript, and CSS code, helping to minimize programming time for administrators. GeoServer is chosen as the platform to publish spatial raster data to the web according to OGC standards such as WMS, WFS (GeoServer, 2025). Visual Studio Code is used as the main programming

environment to build the interface for WebGIS using HTML, JavaScript, and CSS tags (Microsoft, 2025). Finally, easy web access and online information retrieval are facilitated through popular web browsers such as Chrome, Internet Explorer, Opera. A WebGIS system was built for air quality at monitoring locations using data from Sentinel 5P satellites. Using Visual Studio Code to design the interface and QGIS2Web tool to provide functions for retrieving concentrations of parameters (NO₂, CO) at monitoring locations. Then, registering to create a project name on the GitHub platform and establishing the WebGIS page (Figure 2).

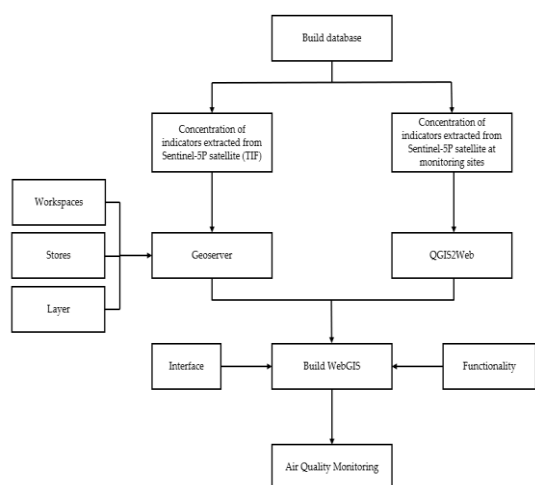


Figure 3. The process of building a WebGIS to monitor air quality in Binh Duong province.

Data Validation

To compare with the standard values of parameters specified according to the QCVN 05:2023 - National technical regulation on ambient air quality, the concentration of NO₂, CO emissions from the unit mol/m² can be converted to the unit of µg/m³ using the following formula (Savenets, 2021):

$$C = \frac{C_{column}}{H} MA \quad (1)$$

In which: C is the concentration of emissions converted to the unit µg/m³; C_{column} is the concentration of emissions calculated from Sentinel-5P TROPOMI remote sensing data in the unit mol/m²; H is the height of the

atmosphere layer, measured in meters (H = 10000 m); M is the molecular weight of the gas, measured in g/mol (M_{NO₂} = 46.0055 g/mol; M_{SO₂} = 64.0648 g/mol; M_{CO} = 44.0098 g/mol); A is the conversion constant from g/m³ to µg/m³ (A = 1000000).

The results of air pollution assessment from Sentinel-5P TROPOMI remote sensing data in this study are compared and verified with the standard values of parameters in the surrounding air as indicated in the QCVN 05:2023 National Technical Regulation on Ambient Air Quality (Table 1). The data used for comparison is the annual average, which is the mean value of the measured data over a one-year period.

Table 1. Standard values of parameters in the surrounding air (QCVN 05:2023)

Unit: µg/Nm³

ID	Pollutant Type	Average 1 hour	Average 8 hour	Average 24 hour	Average year
1	SO ₂	350	–	125	50
2	CO	30.000	10.000	–	–
3	NO ₂	200	–	100	40
4	O ₃	200	120	–	–
5	Total suspended particles (TSP)	300	–	200	100
6	PM ₁₀	–	–	100	50
7	PM _{2,5}	–	–	50	45(*)

Note:

- The dash (–) is not regulated

- (*): The concentration value applies from January 1, 2026.

RESULTS AND DISCUSSIONS

Spatial and temporal distribution of CO concentration in 2024

Figure 4 provides the monthly change in CO concentration from January to December 2024 in the study area. The CO pollution level in Binh Duong area is divided into specific color levels to assess the fluctuation of CO concentration over time, CO concentration shows a gradual increase from blue to red corresponding to the value range from 20-50 mmol/m².

Figure 4 shows that the CO concentration in the study area varies between months and is unevenly distributed in areas in 2024. CO concentration fluctuates between 26.1 - 42.2 mmol/m², highest in January and March, lowest in July. Areas with high CO concentrations are the two cities of Thuan An

and Di An because these are two cities of type 2 urban areas with many industrial parks, high population density, and high traffic volume. These are factors that lead to CO concentrations in the air being often higher than in other areas (Do Thi Phuong Thao et al., 2022).

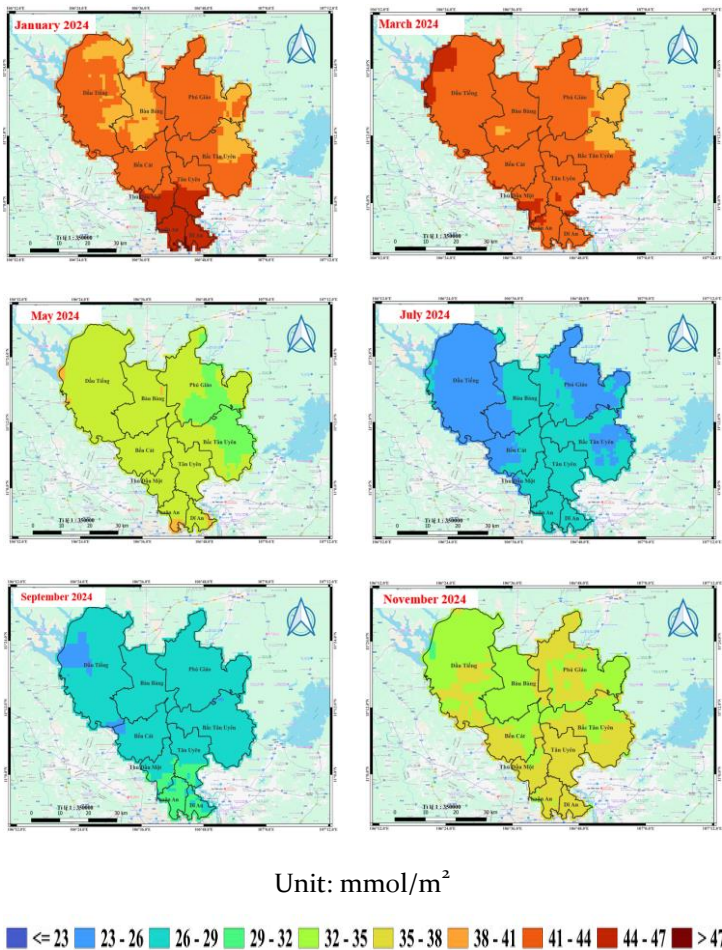


Figure 4. CO concentration changes by months of 2024 in Binh Duong.

The average monthly CO concentration in 2024 increased during the dry months and decreased during the rainy months, as shown in Figure 5. The difference in concentration between the highest and lowest months is about 16.1 mmol/m². Comparing by district, the highest CO concentrations were observed and recorded in the two cities of Thu Dau Mot and Di An, while the lowest were in the two districts of Phu Giao and Dau Tieng (Figure 6).

There are 5 districts with CO pollution levels exceeding the average and 4 districts below the average. The chart in Figure 6 shows a close relationship between air pollution and the development of industrialization and modernization. Areas with high pollution levels are classified as urban areas as follows: Di An, Thu Dau Mot, Thu Dau Mot City, Tan Uyen, and Ben Cat City, with concentrations ranging from 97 to 101 µg/m³. In the remaining areas,

CO concentrations range from 96.06 to 96.6 $\mu\text{g}/\text{m}^3$, as these are developing areas with still low traffic density and population (Figure 6). Although the QCVN 05:2023 National Technical Regulation on Ambient Air Quality does not specify a limit value for the average annual CO concentration, it can be seen that the average annual CO emissions in Binh Duong in 2024 are all below the standard. This also reflects the efforts to reduce air pollution by the provincial government in recent years.

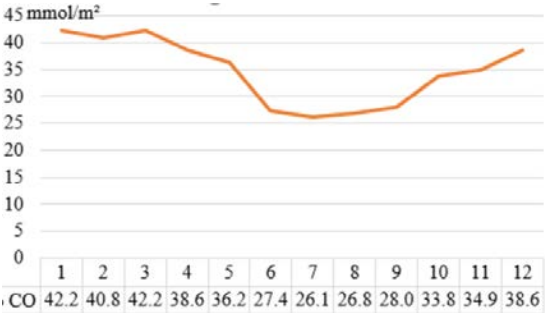


Figure 5. Average monthly CO concentration in 2024.

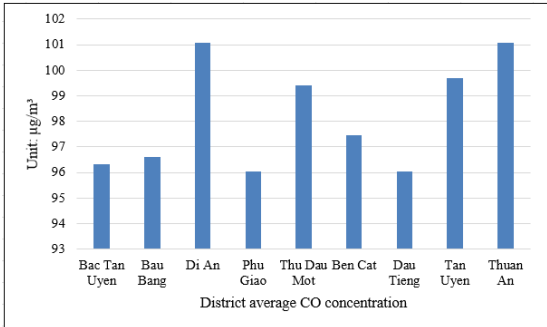
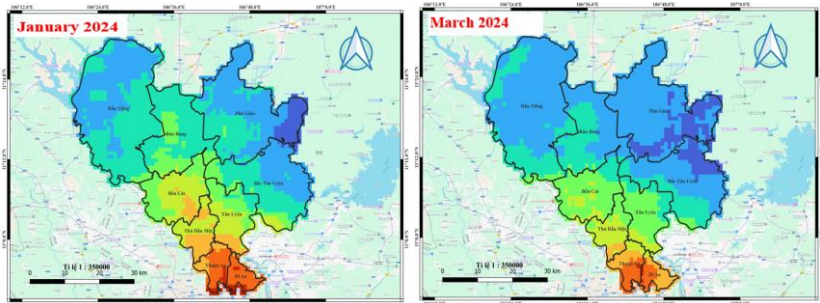


Figure 6. Average CO concentration by districts in 2024.

NO₂ concentration evolution over time and space in 2024

Figure 7 is the result of NO₂ concentration in 2024 extracted from the Sentinel 5P satellite and processed in QGIS 3.40 software. It can be visually assessed that NO₂ concentration varies significantly over the months of 2024. The monthly concentration usually fluctuates at 10 - 70 $\mu\text{mol}/\text{m}^2$ over most of Binh Duong's area. The highest NO₂ concentration is distributed in Thuan An and Di An City, the concentration fluctuates from 70 - 100 $\mu\text{mol}/\text{m}^2$. Tan Uyen, Ben Cat and Thu Dau Mot City fluctuate from 40 - 80 $\mu\text{mol}/\text{m}^2$, the remaining districts fluctuate from 10 - 60 $\mu\text{mol}/\text{m}^2$.

The average NO₂ concentration in Binh Duong is vary over the months of 2024 as shown in Figure 8. The highest average monthly NO₂ concentration is in January and May, corresponding to the dry season, and the lowest is in July and September, the rainy season. It could be explained that NO₂ is a gas that dissolves well in water. When it rains, raindrops absorb NO₂ in the air, reducing its concentration. The rainy season often has strong winds and higher atmospheric convection, helping to disperse NO₂ more quickly than in the dry season. Colder air in the rainy season also reduces the accumulation of emissions at low altitudes. Heavy rain reduces traffic, especially motorbikes and cars, the main source of NO₂ emissions from internal combustion engines.



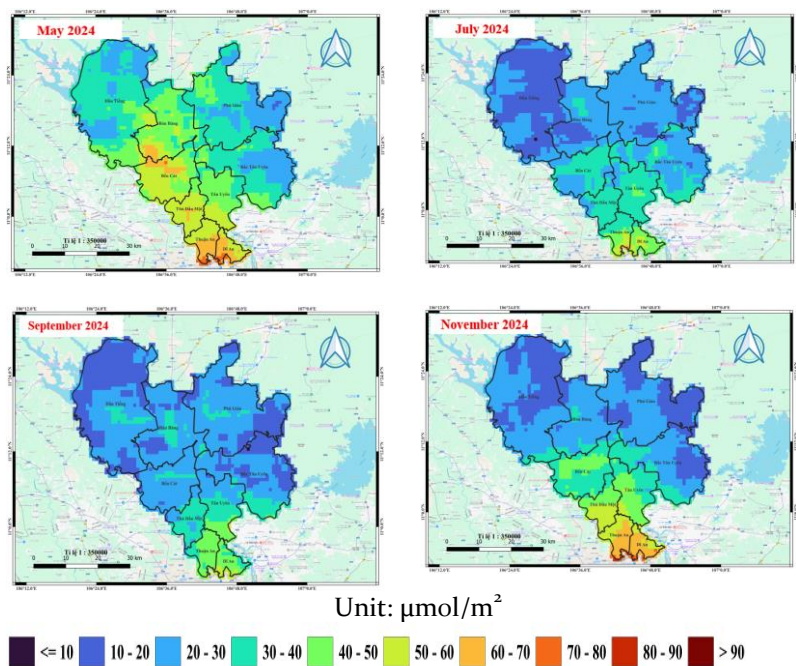


Figure 7. NO₂ concentration changes by months of 2024 in Binh Duong.

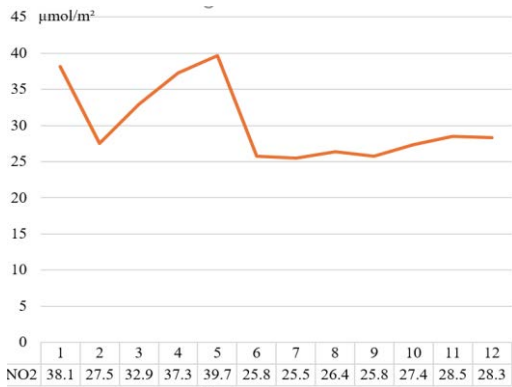


Figure 8. Average monthly NO₂ concentration in 2024.

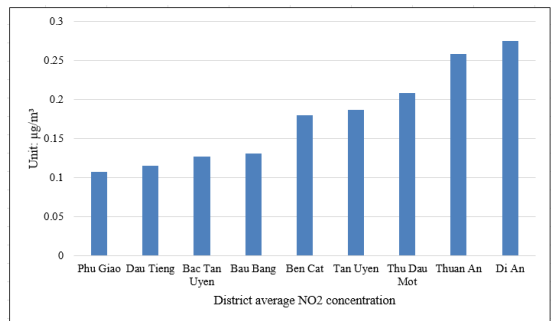


Figure 9. Average NO₂ concentration in Binh Duong by districts in 2024.

Figure 9 shows the average NO₂ concentration by district in 2024. The results indicate that the highest concentration was recorded in Di An city with an average NO₂ index of 0.274 $\mu\text{g}/\text{m}^3$, while Phu Giao had the lowest concentration at only 0.108 $\mu\text{g}/\text{m}^3$. The average concentration also varied significantly between high and low areas, with a difference of about 2 times. The second highest concentration was in Thuan An city with 0.258 $\mu\text{g}/\text{m}^3$. In other areas, the NO₂ index fluctuated between 0.115 – 0.209 $\mu\text{g}/\text{m}^3$. When compared to the limit values of the basic parameters stipulated in QCVN 05:2023, the National Technical Regulation on Ambient Air Quality, it is noted that the average annual NO₂ emissions in Binh Duong throughout 2024 fluctuated quite evenly and did not exceed the permissible limit values.

Assessment of air quality in Binh Duong province in 2024

The analysis results of CO and NO₂ concentrations in Binh Duong province from Sentinel-5P data show that the concentrations of air pollutants change over time and space. Temporally, the concentrations of pollutants

tend to increase in the dry season and decrease in the rainy months. This is closely related to meteorological conditions and the mechanism of dispersion of pollutants in the air. The dry season usually has little rain, so there is no process of "washing away" of pollutants in the air. Moreover, low humidity conditions in the dry season make it easier for dust and pollutant gases to accumulate.

Spatially, the concentration of air pollutants in Binh Duong province also varies between districts and administrative units. Di An City is recorded as the area with the highest concentration of CO and NO₂, related to the concentration of industrial parks, urban areas and traffic density in this area. Thuan An City is also one of two areas with high concentrations of air pollutants in Binh Duong province. On the contrary, Phu Giao and Dau Tieng districts with high density of vegetation and trees cover are areas with lower concentrations of green-house gases than other areas in the whole province.

WebGIS System for Air Quality Monitoring in Binh Duong Province

The user interface includes a homepage with a menu bar consisting of sections such as general introduction, statistics, map, concentration of indicators such as CO and NO₂.

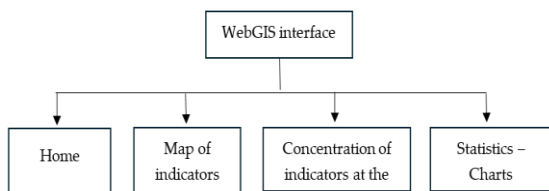


Figure 10. WebGIS interface diagram

On the general introduction page, the interface is specifically shown as in Figure 9, displaying some general information about Binh Duong province to users, such as geographical location, topography, land, climate, hydrology, transportation, and forest resources.

The map page provides users with information about satellite images from

Sentinel 5P; NO₂ parameters (with options for monthly averages in 2024); CO parameters (Figure 11).

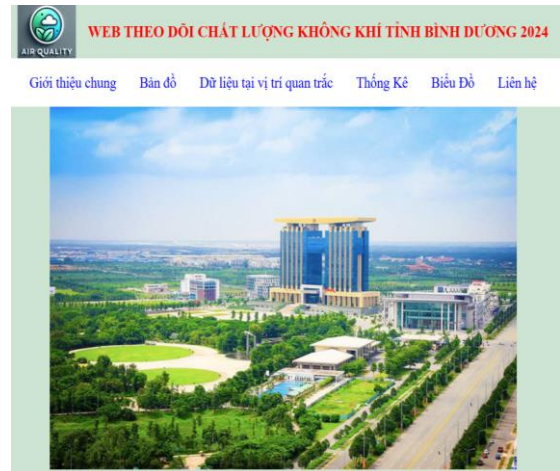


Figure 11. WebGIS homepage interface (<https://clkkbd.github.io/2024/>)

The map page displays several main components such as: zooming in and out of the map; toggling views by month; on the top left is a menu bar for users to select (Figure 12).



Figure 12. The map interface displays according to each air pollutant index.

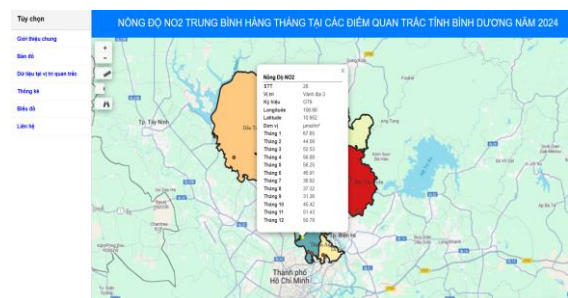


Figure 13. Concentration interface at the monitoring location according to each indicator

The users can perform basic operations such as measuring distance and calculating area, zooming in and out, and viewing attribute information (Figure 13). The query feature is also integrated into the WebGIS system so that users can query concentration data of the indicators at any location.

Statistics page interface: This page represents statistics on the concentration of parameters according to the monthly average, the monthly average chart, and the average monthly statistics of indicators by district for the year 2024.

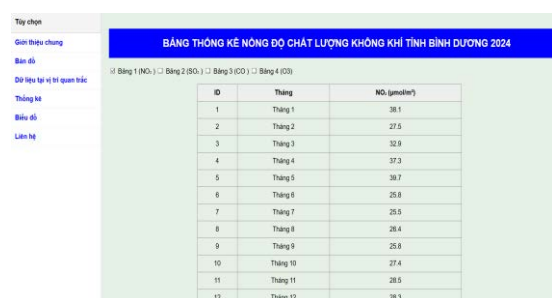


Figure 14. Statistical interface – chart by each indicator.

Contact page interface: The contact page contains some information about the administrator as well as the designer of the WebGIS and some data uploaded by the author to the WebGIS for users to download and reference.

CONCLUSIONS AND FUTURE PERSPECTIVES

In this paper, CO and NO₂ concentrations were collected from the Sentinel - 5P TROPOMI satellite with the research period being the months in 2024. Satellite image data were extracted in Binh Duong province on the Google Earth Engine platform. The study also proposed a number of solutions to improve air quality in the province. Based on the analysis over time, it shows that CO and NO₂ concentrations increase in the dry season months and gradually decrease in the rainy season months. Spatially, the concentration of air pollutants depends on the concentration of industrial zones and traffic activities. Areas with dense population and continuous traffic activities will have higher concentrations than

the remaining areas. The research results show a panoramic picture of air quality changes over space and time in the study area, and are also the basis for proposing a number of air pollution control measures to serve the goal of sustainable development for Binh Duong province.

The research has successfully built a WebGIS for monitoring air quality and has demonstrated many commendable strengths. This WebGIS not only provides a visual and user-friendly interface but also integrates basic functions such as monitoring maps of parameters (NO₂, CO), monthly average data statistics for 2024 by parameter, and analytical charts. The data is organized to serve the quick reference needs of users, management agencies, and researchers. However, due to limited resources, the WebGIS still has some limitations and requires to continue exploring and developing in-depth analytical features, and the security of the system needs to be further strengthened to ensure safety for users and data.

Some solutions to support air pollution control in Binh Duong province, serving the goal of developing a smart city can be applied such as: Improving cleaner production technology to reduce emissions right from the source; installing exhaust gas treatment systems (dust filtration, CO, NO_x, VOC removal...); Using clean fuels: natural gas, electricity, renewable energy. In addition, policy and legal solutions such as: developing and updating emission standards and regulations; strengthening inspection, monitoring and handling of environmental violations; and applying environmental taxes or emission fees to encourage businesses to reduce pollution also need to be widely applied in Binh Duong province, especially in areas with high industrial park density.

ACKNOWLEDGEMENTS

This research is funded by Thu Dau Mot University, Binh Duong Province, Vietnam under grant number DT.22.3-096.

REFERENCES

- Borsdorff, T., et al. (2018). Carbon monoxide retrieval from Sentinel-5 Precursor TROPOMI. *Atmospheric Measurement Techniques*, 11, 5507–5518.
- Carslaw, D. C., & Beevers, S. D. (2005). Estimations of road vehicle primary NO₂ emissions. *Atmospheric Environment*, 39(1), 236–238.
- EPA. (2021). Air Pollutants: Nitrogen Dioxide (NO₂). U.S. Environmental Protection Agency.
- Eskes, H., van Geffen, J., et al. (2020). Sentinel-5P TROPOMI NO₂ retrieval: Method, data products and validation. *Atmospheric Measurement Techniques*, 13, 1315–1335.
- Veefkind, J. P., Aben, I., et al. (2012). TROPOMI on the ESA Sentinel-5 Precursor. *Remote Sensing of Environment*, 120, 70–83.
- WHO. (2021). WHO Global Air Quality Guidelines. World Health Organization.
- Do, T. P. T., Ngo, N. V., Son, V. K. (2022). Establishment of the distribution maps of NO₂ and SO₂ concentrations from Sentinel-5P satellite data in Hanoi. *Journal of Geodesy and Cartography*, 33(4), 21–31. <https://doi.org/10.54495/12261498.2022.33.4.003>.
- Nguyen, T. L. H. (2018). *Application of remote sensing and GIS to assess the changes in air quality: A case study for the regions of Bac Ninh, Hai Duong, Hai Phong, and Quang Ninh*. *Journal of Natural Resources and Environment Science*, (23), 56–63.
- Luu, T. D. C., Ha, T. H., & Bui, D. Q. (2023). *Application of Sentinel-5P TROPOMI data on the Google Earth Engine platform for monitoring air pollution in Thái Nguyên City*. *Journal of Science and Technology in Civil Engineering (STCE)*, 17(2V), 78–94. [https://doi.org/10.31814/stce.huce2023-17\(2V\)-06](https://doi.org/10.31814/stce.huce2023-17(2V)-06).
- Aldabash, M., Balcik, F. B., & Glantz, P. (2020). Validation of MODIS C6.1 and MERRA-2 AOD using AERONET observations: A comparative study over Turkey. *Atmosphere*, 11(9). <https://doi.org/10.3390/ATMOS11090905>.
- Halder, B., Ahmadianfar, I., Heddami, S., Mussa, Z. H., Goliatt, L., Tan, M. L., Sa'adi, Z., Al-Khafaji, Z., Al-Ansari, N., Jawad, A. H., & Yaseen, Z. M. (2023). Machine learning-based country-level annual air pollutants exploration using Sentinel-5P and Google Earth Engine. *Scientific Reports*, 13(1), Article 7968. <https://doi.org/10.1038/s41598-023-34774-9>.
- Zhang, Y., Shindell, D., Seltzer, K., Shen, L., Lamarque, J.-F., Zhang, Q., Zheng, B., Xing, J., Jiang, Z., & Zhang, L. (2021). Impacts of emission changes in China from 2010 to 2017 on domestic and intercontinental air quality and health effect. *Atmospheric Chemistry and Physics*, 21, 16051–16065.
- Stratoulas, D., Nuthammachot, N., Dejchanchaiwong, R., Tekasakul, P., & Carmichael, G. R. (2024). Recent Developments in Satellite Remote Sensing for Air Pollution Surveillance in Support of Sustainable Development Goals. *Remote Sensing*, 16(16), 2932. <https://doi.org/10.3390/rs16162932>.
- Tian Y, Duan M, Cui X, Zhao Q, Tian S, Lin Y, & Wang W. (2023). Advancing application of satellite remote sensing technologies for linking atmospheric and built environment to health. *Front Public Health*, 11:1270033. doi: 10.3389/fpubh.2023.1270033.
- General Statistics Office. (2021). Report on socio-economic situation in 2020. Statistical Publishing House. <https://www.gso.gov.vn/wp-content/uploads/2021/07/Bao-cao-KTXH-2020.pdf>
- European Space Agency. (2017). Sentinel-5P: Monitoring air pollution. European Space Agency. https://www.esa.int/Applications/Observing_the_Earth/Copernicus/Sentinel-5P.
- QGIS2Web. (n.d.). qgis2web plugin for QGIS. QGIS Plugin Repository. Retrieved May 6, 2025, from <https://plugins.qgis.org/plugins/qgis2web/>.
- GeoServer. (n.d.). GeoServer: Open source server for sharing geospatial data. Retrieved May 6, 2025, from <https://geoserver.org/>.
- Microsoft. (n.d.). Visual Studio Code. Retrieved May 6, 2025, from <https://code.visualstudio.com/>.
- Earth Engine Data Catalog. (2025a, June 3). *Sentinel-5P NRTI NO₂: Near Real-Time Nitrogen Dioxide*. Google Earth Engine. Retrieved from https://developers.google.com/earth-engine/datasets/catalog/COPERNICUS_S5P_NRTI_L3_NO2.
- Earth Engine Data Catalog. (2025b, June 3). *Sentinel-5P NRTI CO: Near Real-Time Carbon Monoxide*. Google Earth Engine. Retrieved from https://developers.google.com/earth-engine/datasets/catalog/COPERNICUS_S5P_NRTI_L3_CO.
- QCVN 05:2023. National technical regulation on ambient air quality.
- Savenets, M. (2021). Air pollution in Ukraine: a view from the Sentinel-5P satellite. *Időjárás*, 125(2):271–290.

Understanding Gen Z's Attitudes and Behavioral Intentions towards Green Destinations: Implications for Sustainable Tourism Development in Vietnam

Phan Trinh Thi^{1,*}, Nga Nguyen Thi Phuong²

¹Faculty of Social Science, Hong Duc University, Thanh Hoa, Vietnam

²Faculty of Economic and Management, Thuyloi University, Hanoi city, Vietnam

*Email: ngatn129@tlu.edu.vn

Abstract: This study investigates the psychological mechanism shaping Generation Z's attitudes and behavioral intentions toward green destinations in Vietnam, integrating three theoretical foundations: the Theory of Planned Behavior (TPB), Norm Activation Theory (NAT), and the Stimulus-Organism-Response (S-O-R) model. A quantitative design was employed using survey data collected from 325 Gen Z respondents through both online and on-site methods. Partial Least Squares Structural Equation Modeling (PLS-SEM) with SmartPLS 4 was applied to test the proposed model. The findings reveal that perceived green destination image and personal norms significantly enhance green behavioral intention, while affective-based appraisal serves as a strong mediating factor leading to sustainable destination intention. This sequential mediation confirms a cognitive-ntive-affective pathway driving sustainable travel choices. The study provides empirical evidence on Gen Z's pro-environmental behavior in emerging markets and expands theoretical understanding of integrated behavioral models in green tourism. Managerially, the results suggest that destination managers and policymakers should focus on building verifiable green images, fostering environmental ethics among young travelers, and creating emotionally engaging experiences to promote sustainable tourism development in Vietnam.

Keywords: Green destination image, Generation Z, Sustainable tourism, Behavioral intention, PLS-SEM.

INTRODUCTION

In the current global context, climate change, environmental degradation, and the rapid expansion of mass tourism pose serious challenges to the tourism sector. Overtourism pressures at many iconic destinations, pollution arising from tourism-related waste, and the overexploitation of natural resources have collectively propelled sustainability to the center of tourism research and managerial practice¹ (UNEP & UNWTO, 2005). Concepts and models of sustainable tourism development have been strongly advanced, emphasizing the need to balance economic benefits with environmental protection and the preservation of socio-cultural values for both present and future generations² (UNWTO & UNDP, 2017). According to the World Tourism Organization, sustainable tourism development is “tourism that meets the needs of present tourists and host regions while protecting and enhancing opportunities for the future” (UN Tourism).

Within this agenda, green destinations have emerged as a critical component. Green destinations are understood not only as places endowed with attractive natural and

¹ UNEP & UNWTO. (2005). *Making Tourism More Sustainable: A Guide for Policy Makers*. United Nations Environment Programme & World Tourism Organization.

² UNWTO & UNDP. (2017). *Tourism and the Sustainable Development Goals – Journey to 2030*. World Tourism Organization & United Nations Development Programme.

environmental resources but also as destinations that are managed and developed in environmentally friendly ways, minimizing negative impacts and encouraging responsible tourist participation. The formation and promotion of a green destination image brings reputational and competitive advantages while fostering sustainable tourism behavior among visitors [1].

In Viet Nam—a country with substantial natural and cultural assets—sustainable tourism development has been articulated in numerous strategic documents and national policies. However, practice still exhibits notable limitations. Renowned destinations such as Ha Long Bay, Sa Pa, and Da Nang frequently confront environmental pressures, infrastructure that lags behind growth, and an imbalance between tourism development and the safeguarding of local cultural heritage. These conditions underscore the need for new approaches to steer tourism toward greener and more sustainable pathways. Central to this effort is a deeper understanding of tourist attitudes and behaviors—especially among younger cohorts.

Generation Z (Gen Z)—those born between 1995 and 2010—has become an important tourist segment both in Viet Nam and globally. Characterized by digital fluency, high connectivity, and strong social consciousness, Gen Z is expected to lead the adoption of responsible consumption and sustainable choices [2]. Unlike previous generations, Gen Z seeks authentic, personalized experiences and demonstrates heightened concern for environmental and social responsibility. These traits suggest strong potential for Gen Z to shape the future trajectory of green tourism in Viet Nam.

Despite the recognized importance and influence of Gen Z, empirical evidence detailing how this generation forms attitudes and behavioral intentions toward green destinations remains limited, particularly in developing-country contexts such as Viet Nam. In tourism behavior research, attitude is regarded as a pivotal psychological factor

mediating the link between cognition and action. Ajzen's Theory of Planned Behavior (TPB) (1991) posits that individuals' behavioral intentions are determined by attitude, subjective norms, and perceived behavioral control [3]. Likewise, Mehrabian and Russell's Stimulus–Organism–Response (S–O–R) framework (1974) asserts that environmental stimuli shape internal psychological states, which in turn generate behavioral responses [4]. In the context of green tourism, the green destination image can be conceptualized as the *stimulus*, green travel attitude as the *organism*, and behavioral intention to select green destinations as the *response*.

Prior studies provide partial support for these relationships. Investigating hotel guests, Han, Hsu, Lee, and Sheu (2011) found that attitude is a significant predictor of intention to choose green hotel services [5] [6]. Su, Hsu, and Boostrom (2020) further showed that environmentally responsible tourist behavior emerges from the interplay of environmental beliefs, destination image, and positive tourist attitudes. Notably, Nowacki et al. (2023), examining Gen Z in Poland and India, reported that green destination image significantly influences both attitudes and behavioral intentions toward green destination choice, and confirmed the mediating role of attitude within this mechanism [2]. More recently, Luong (2023) added evidence from an emerging market, demonstrating strong interrelationships among eco-destination image, environmental beliefs, attitudes, and intentions toward ecotourism, with ecological values moderating these effects [7]. Collectively, these findings reinforce the proposition that attitude is a crucial bridge between green destination image and behavioral intention.

In Viet Nam, however, research on green tourism has largely remained at the overview level or focused on tourists' general perceptions and behaviors. Studies specifically addressing Gen Z's sustainable tourism intentions are scarce, and applications of structural equation modeling (SEM) to test the image–attitude–behavior nexus are particularly limited. This

gap underscores the theoretical and practical urgency of examining how Gen Z in Viet Nam forms attitudes and behavioral intentions toward green destinations. Theoretical contributions. The present study seeks to enrich behavioral theory by providing empirical evidence from a developing-country setting and by testing the suitability of a model linking green destination image, green travel attitude, and behavioral intention in Viet Nam. By focusing on Gen Z in major urban centers, the study also sheds light on intergenerational differences and contrasts between developed and emerging markets. Practical implications. A nuanced understanding of Gen Z's attitudes and behavioral intentions toward green destinations can inform destination managers, tour operators, and policymakers. Specifically, destinations can craft marketing strategies that foreground a compelling green image and design environmentally friendly products that align with Gen Z's expectations and values. Policymakers, in turn, can draw on the findings to devise incentives and support mechanisms that advance green destination development, thereby contributing to Viet Nam's sustainable tourism goals.

As green tourism continues to gain momentum worldwide and Gen Z emerges as a pivotal consumer group, investigating Gen Z's attitudes and behavioral intentions toward green destinations in Viet Nam is both timely and consequential. This study aims to test the relationships among green destination image, green travel attitude, and behavioral intention, with a particular focus on the mediating role of attitude. The expected findings will advance the literature on sustainable tourist behavior while offering actionable managerial insights to accelerate green and sustainable tourism development in Viet Nam.

THEORETICAL BACKGROUND AND RESEARCH MODEL

Concept and Nature of the Green Destination Image (GDI)

The destination image construct has been prominent in tourism studies since the 1970s. Crompton (1979) defines it as “the sum of

beliefs, ideas, and impressions that a person holds about a place” [8]. Baloglu and McCleary (1999) formalized a two-component structure—cognitive (knowledge-based) and affective (emotion-based)—whose interaction produces the overall image [9]. This framework anchors research on the green destination image (GDI). Within sustainable tourism, a green destination seeks to conserve resources, minimize environmental impacts, and enhance community benefits (UNEP & UNWTO, 2005). Accordingly, GDI denotes tourists' perceptions and impressions of environmental friendliness, resource-protection policies, and sustainable practices at a destination. Empirical work shows that destination image shapes satisfaction, loyalty, and behavioral intentions [1], and that a positive environmental image promotes revisit intention and positive word of mouth [10]. Practically, destination image is a core driver of destination competitiveness and branding [11], [12]. For Generation Z, “greenness” is a key selection criterion; evidence from Poland and India indicates that GDI positively influences attitudes and choice intentions, with attitude mediating this linkage [2]. Vietnamese evidence likewise connects eco-image, environmental beliefs, attitudes, and intentions, moderated by biospheric values [7].

Attitudes toward Green Tourism

Under Ajzen's Theory of Planned Behavior (TPB), attitude is an individual's positive or negative evaluation of a specific behavior, formed by behavioral beliefs—perceptions of a behavior's consequences and the value attached to those consequences [3]. In a tourism context, attitudes toward green tourism manifest as endorsement of, agreement with, and willingness to engage in environmentally friendly activities. Empirical evidence consistently highlights the attitudinal pathway to intention. Applying TPB in hospitality, Han et al. (2011) found attitude to be the strongest predictor of intentions to select green services [5]. Similarly, Su et al. (2020) showed that tourists holding positive attitudes toward green tourism are more likely to enact sustainable behaviors, such as

conserving resources, recycling, and choosing lower-emission transport options [13].

For Generation Z, international research links personal values and social consciousness to pro-environmental attitudes. Corbisiero et al. (2022) argues that Gen Z treats sustainability as part of a consumption identity; green tourism is viewed as a “means of expressing life values,” predisposing favorable attitudes toward socially and environmentally responsible destinations[14]. Accordingly, attitudes toward green tourism are both cognitive-evaluative and identity-expressive (“value identity”) among youth[15], [16]. This dual character is particularly salient for analyzing tourist behavior in Viet Nam, a society transitioning toward greener consumption patterns, where harnessing Gen Z’s value-driven attitudes may accelerate the uptake of sustainable tourism.

Behavioral Intention to Choose Green Destinations

Behavioral intention (BI), following Ajzen (1991), denotes an individual’s readiness to perform a behavior and constitutes the most proximate antecedent of actual behavior. In tourism, BI is treated as a direct predictor of decisions to visit, revisit, or recommend a destination to others. Chen and Tsai (2007) show that a favorable destination image not only enhances satisfaction but also strengthens revisit intention[1]. Complementarily, Stylos et al. (2017) find that BI in tourism is strongly shaped by both cognitive (knowledge-based) and affective (emotion-based) images[10]. In the green tourism context, BI may encompass: (i) intending to select environmentally friendly destinations in the future, (ii) willingness to pay a price premium for green services, and (iii) recommending the destination to others.

Recent studies indicate that Gen Z’s green behavioral intentions are closely linked to beliefs and attitudes. Nowacki et al. (2023) demonstrate that the green destination image (GDI) influences intention indirectly through attitude[2], whereas Luong (2023) shows that, in Viet Nam, ecotourism attitude mediates the

relationship between destination image and behavioral intention[7]. Together, these findings reinforce the proposition that attitude functions as the psychological bridge between cognition and behavior—consistent with the structures of both the TPB and S–O–R frameworks.

Foundational Theories

(1) Theory of Planned Behavior (TPB).

The TPB (Ajzen, 1991) is a prominent behavioral model widely applied in tourism research. It posits that behavioral intention is formed by three determinants: attitude, subjective norms, and perceived behavioral control [3]. Among these, attitude has frequently been shown to exert the strongest influence [5]. The TPB foregrounds intrinsic motivation by reflecting individuals’ beliefs and personal values—an especially appropriate lens for analyzing Gen Z’s green consumption behavior.

(2) Stimulus–Organism–Response (S–O–R) model.

Originating in environmental psychology, the S–O–R model of Mehrabian and Russell (1974) asserts that external stimuli affect the internal state of the organism, which in turn elicits a behavioral response[4]. In tourism, it has been widely employed to examine how environmental factors, destination image, or experiences shape emotions, attitudes, and behaviors [13]. Applied in this study: the Green Destination Image functions as the *stimulus* (S), Attitudes toward Green Tourism represent the *organism* (O), and Behavioral Intention constitutes the *response* (R).

The integration of TPB and S–O–R yields a comprehensive theoretical framework: TPB explicates the psychological mechanism underlying intention formation, while S–O–R delineates how environmental stimuli are transformed into behavioral responses via attitude. This combined structure has been adopted in numerous studies on sustainable tourist behavior [5], [7].

Proposed Research Model

Drawing on the foregoing theories, this study proposes a conceptual model comprising three core constructs: Green Destination Image (GDI), Attitudes toward Green Tourism (ATT),

and Behavioral Intention to Choose Green Destinations (BI). The relationships among these constructs are interpreted as follows:

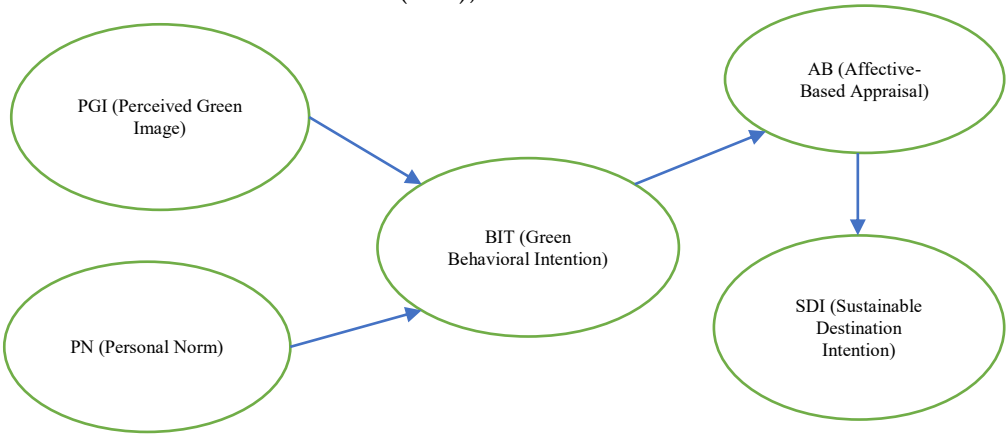


Figure 1: Proposed research model

METHOD

This study adopts a confirmatory quantitative design to test a behavioral model of green tourism among Vietnamese Gen Z. Relationships among Perceived Green Image (PGI), Personal Norm (PN), Green Behavioral Intention (BIT), Affective-Based Appraisal (AB), and Sustainable Destination Intention (SDI) are examined using Partial Least Squares Structural Equation Modeling (PLS-SEM), selected for its suitability with multiple latent constructs, medium sample sizes, and non-normal data [17]. The model integrates three foundations: TPB[3], Norm-Activation Theory [18], and S-O-R [4]. Conceptually, PGI and PN operate as Stimuli; BIT and AB represent the Organism; SDI is the Response, capturing the cognition-norm-intention-affect-behavior pathway [13], [19].

Data were collected from 325 valid Gen Z respondents (born 1995–2010) via on-site surveys at ecotourism destinations (Da Nang, Nha Trang, Can Tho, Da Lat) and an online Google Forms survey. This cohort was targeted due to its sustainability awareness and value-driven “green identity” [20]. The questionnaire adapted validated scales through back-translation and expert review. All constructs were measured on 5-point Likert scales (1 =

strongly disagree; 5 = strongly agree) with four reflective indicators per latent variable. PGI items derived from Baloglu and McCleary (1999) and Chen and Tsai (2007); PN from Schwartz (1977) and Han (2015)[1], [9], [18], [19]; BIT from Ajzen (1991) and Han et al. (2011)[3], [5]; AB from Chen and Tsai (2007)[1]; SDI from Stylos et al. (2017) and Nowacki et al. (2023)[2], [10]. Data were cleaned and coded in SPSS 26.0, then analyzed in SmartPLS 4.0.

A two-stage procedure was employed [17]. Measurement model: all outer loadings > 0.70; CR > 0.87; AVE > 0.50 [21]; HTMT < 0.90 [22]; VIF < 3.3. Structural model: PLS Algorithm and Bootstrapping (5,000 resamples). Paths were significant and in hypothesized directions: PGI → BIT ($\beta = 0.537, p < 0.001$), PN → BIT ($\beta = 0.362, p < 0.001$), BIT → AB ($\beta = 0.679, p < 0.001$), AB → SDI ($\beta = 0.688, p < 0.001$). Indirect effects confirmed mediation: PGI → BIT → AB → SDI = 0.251; PN → BIT → AB → SDI = 0.169.

The sample was robust (mean ≈ 0 , SD ≈ 1 ; minimal skewness/kurtosis; no severe outliers). Descriptives: 58.5% female, 41.5% male, mostly aged 18–25, college-educated; 61% had engaged in green tourism; 56% regularly followed sustainable-tourism content on social media. With $n = 325$ exceeding recommended PLS-

SEM thresholds [17], the study satisfies international standards of reliability, validity, and generalizability for green tourism behavior in Viet Nam.

RESULTS

Sample description

A total of 325 valid questionnaires were retained for analysis. Among respondents, 58.5% were female and 41.5% were male. By age, the 18–22 group accounted for 47.1%, the 23–26 group 38.8%, with the remainder over 26 years old. Over 70% reported higher education (college or university). Approximately 61% had participated in at least one green or ecotourism trip, and 56% indicated that they actively seek information on green destinations via digital platforms (e.g., Facebook, TikTok, travel websites). These descriptive findings suggest that the sample reflects a dynamic Gen Z cohort with relatively high educational

attainment and heightened environmental awareness. Therefore, generalization should be limited to urban and semi-urban Gen Z populations. Gen Z residing in rural or less-developed provinces—where access to environmental education and green tourism products is more limited—may exhibit different intention–affect pathways.

Measurement model results

The measurement model assessment indicates that all indicators exhibit outer loadings > 0.70, ranging from 0.763 to 0.861, demonstrating that the items adequately reflect their corresponding latent constructs. Cronbach's alpha values for the scales range from 0.812 to 0.915, while Composite Reliability (CR) spans 0.870–0.937, exceeding the recommended minimum threshold of 0.70 and evidencing strong internal consistency.

Table 1: Quality of observed variables

	AB	BIT	PGI	PN	SDI
AB ₁	0.808				
AB ₂	0.833				
AB ₃	0.810				
AB ₄	0.798				
BIT ₁		0.829			
BIT ₂		0.825			
BIT ₃		0.831			
BIT ₄		0.803			
PGI ₁			0.815		
PGI ₂			0.824		
PGI ₃			0.848		
PGI ₄			0.799		
PN ₁				0.861	
PN ₂				0.815	
PN ₃				0.763	
PN ₄				0.815	
SDI ₁					0.828
SDI ₂					0.846
SDI ₃					0.793
SDI ₄					0.846

Source: Research results of the author group

The Average Variance Extracted (AVE) values for the constructs range from 0.58 to 0.72, exceeding the 0.50 benchmark and thus

satisfying convergent validity per Fornell & Larcker (1981). Discriminant validity, assessed via the HTMT criterion[22], indicates that all

ratios are below 0.90, confirming clear conceptual distinctiveness among constructs. Multicollinearity diagnostics show all VIF values are below 3.3, ruling out bias from high linear correlations. Collectively, the measurement model meets established standards for reliability, convergent validity, and discriminant validity, and is therefore suitable for structural testing.

Using Bootstrapping (5,000 resamples; 95% confidence), the structural model reveals statistically significant paths consistent with the hypothesized directions. Specifically, Perceived Green Image (PGI) positively affects Green Behavioral Intention (BIT) with $\beta = 0.537$ ($p < 0.001$); Personal Norm (PN) influences BIT with $\beta = 0.362$ ($p < 0.001$); BIT strongly predicts Affective-Based Appraisal (AB) with $\beta = 0.679$ ($p < 0.001$); and AB exerts a very strong effect on Sustainable Destination Intention (SDI) with $\beta = 0.688$ ($p < 0.001$). All coefficients exceed 0.35, indicating medium-to-strong effect sizes [23] and collectively demonstrate that the modeled constructs are pivotal in shaping Gen Z's intention to choose green destinations.

Table 2: Analysis Bootstrapping 5000 sample

	Original Sample (O)	Sample Mean (M)	Standard Deviation (STDEV)	T Statistics (O/STDEV)
AB -> SDI	0.688	0.690	0.031	22.495
BIT-> AB	0.679	0.680	0.037	18.392
PGI-> BIT	0.537	0.537	0.035	15.336
PN -> BIT	0.362	0.363	0.038	9.639

Source: Research results of the author group.

Analyses of indirect effects reveal a two-step mediation chain among the constructs. Specifically, the specific indirect effect of PGI via BIT and AB on SDI equals 0.251, while the corresponding effect for PN is 0.169; the stand-alone indirect pathway BIT \rightarrow AB \rightarrow SDI reaches 0.468. The total effects are 0.251 for PGI on SDI, 0.169 for PN on SDI, 0.468 for BIT on

SDI, and 0.688 for AB on SDI. These results confirm that both BIT and AB function as critical mediators, with AB exerting a decisive influence at the terminal stage of the causal chain. Correlations among latent variables further indicate coherent, substantive associations: PGI-BIT = 0.668, PN-BIT = 0.557, BIT-AB = 0.679, and AB-SDI = 0.688. Collectively, the findings align with the theoretical premises of the Stimulus-Organism-Response framework (Mehrabian & Russell, 1974), wherein PGI and PN operate as stimuli (S), BIT and AB represent intermediary organismic states (O), and SDI constitutes the behavioral response (R).

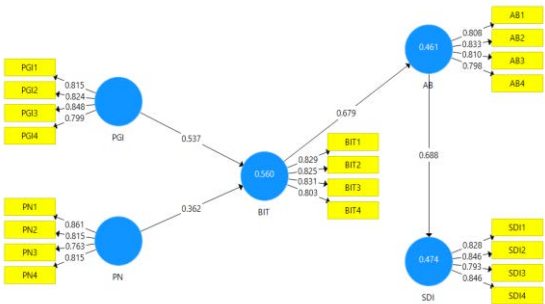


Figure 2: Research results

The findings substantiate a dual mediation mechanism through BIT and AB, indicating that the formation of green behavior among young tourists is not instantaneous but unfolds via two sequential psychological processes: first, a behavioral intention grounded in cognition and deliberation, and second, an affective attitude anchored in emotion and experience. This two-tier structure aligns with the TPB [3] and prior evidence [5], [13], which identify attitude and personal norms as internal determinants of green behavioral intention. The present results extend the TPB by demonstrating that intention not only precedes actual behavior but also activates positive affect, thereby indirectly shaping the choice of green destinations.

The path PGI \rightarrow BIT ($\beta = 0.537$) underscores the potency of the cognitive image component in stimulating green intention. When Gen Z clearly perceives “green” attributes—clean environments, renewable

energy, effective resource management, and transparent information—specific intentions to engage in sustainable experiences emerge. This finding is consistent with Chen & Tsai (2007) and Stylos et al. (2017) regarding the role of destination image in driving revisit intention and positive word of mouth [1], [10]. Conversely, symbolic claims that lack verifiable operational practices erode the effect through greenwashing [13].

The effect $PN \rightarrow BIT$ ($\beta = 0.362$) carries salient theoretical implications. Personal norms capture a sense of moral obligation toward the environment and society, functioning as an intrinsic driver of choice [18], [19]. For Gen Z, green travel is often integrated into a moral identity of responsibility. Accordingly, educational and communication interventions that foreground environmental ethics can strengthen PN and elevate BIT.

The linkage $BIT \rightarrow AB$ ($\beta = 0.679$) elucidates a characteristic digital-age mechanism: intention forms early and operates as an affective amplifier when individuals encounter congruent content—pristine nature, conservation campaigns, or local cultural experiences. Once intention is in place, Gen Z readily develops positive emotions and enthusiasm toward destinations [2], indicating that their green behavior arises from cognitive-affective resonance rather than pure rationality.

Most notably, $AB \rightarrow SDI$ ($\beta = 0.688$) is the strongest path, establishing positive affect as the most immediate determinant of destination choice. This accords with Stylos et al. (2017) and Su et al. (2020), which emphasize that, in sustainable tourism, affective/experiential factors can outweigh purely functional attributes [10], [13]. For Gen Z—the “experience-and-share” cohort—affect influences personal decisions and diffuses across social media, creating community-level spillovers.

Overall, the $PGI, PN \rightarrow BIT \rightarrow AB \rightarrow SDI$ model delineates a coherent conversion chain: cognition (PGI) and norms (PN) activate intention (BIT); intention amplifies affect (AB); and affect culminates in behavioral choice

(SDI). The sizable indirect effects of PGI (0.251) and PN (0.169) highlight two managerial levers: (i) building a credible green image grounded in verifiable practices—thus avoiding greenwashing; and (ii) cultivating personal norms through environmental-ethics education. The mediating roles of BIT and AB indicate that this conversion process cannot be shortcut: intention should be activated before affect can translate green cognition into actual choice. These results enrich the intersection of TPB [3], NAT [18], and S-O-R [4], while providing new evidence from Viet Nam’s post-COVID-19 context, where green tourism is emerging as a strategic development pathway.

DISCUSSION

The findings validate the structural model $PGI, PN \rightarrow BIT \rightarrow AB \rightarrow SDI$ as both well-fitting and highly explanatory for green tourism behavior among Vietnamese Gen Z. All path coefficients— $\beta_{PGI \rightarrow BIT} = 0.537$, $\beta_{PN \rightarrow BIT} = 0.362$, $\beta_{BIT \rightarrow AB} = 0.679$, and $\beta_{AB \rightarrow SDI} = 0.688$ —are statistically significant and directionally consistent with the hypotheses, elucidating the cognitive-affective conversion that governs green destination choice. These results align with the S-O-R framework [4], the TPB [3], and the NAT [18], while extending sustainable behavior models largely tested in developed settings [13], [19].

First, the $PGI \rightarrow BIT$ pathway demonstrates that perceived green image functions as a potent stimulus, heightening behavioral intention toward green choices. This finding is consistent with Chen & Tsai (2007), Stylos et al. (2017), and Nowacki, Niezgoda & Pawlicz (2023): awareness of environmentally friendly attributes—cleanliness, renewable energy, waste minimization, nature conservation, and transparency—directly elevates sustainable choice tendencies [1], [2], [10]. In Viet Nam, PGI should therefore be treated not merely as a communication cue but as a strategic competitive asset [11]. Verifiable green practices, environmental disclosure, and sustainability branding simultaneously raise awareness and activate the cognition-affect

sequence that culminates in responsible behavior.

Second, $PN \rightarrow BIT$ ($\beta = 0.362$) affirms the importance of personal norms in forming green intentions. In line with NAT [18], [19], internal moral obligation operates as an intrinsic driver of pro-environmental behavior. Among Gen Z, PN intertwines with value identity; green travel is both a social responsibility and a mode of self-expression in the digital milieu [20]. Relative to prior cohorts, Gen Z more readily converts personal values into consumption choices, making PN a deep-seated motivator of BIT.

Third, the effects $BIT \rightarrow AB$ ($\beta = 0.679$) and $AB \rightarrow SDI$ ($\beta = 0.688$) capture the transition from deliberative intention to affective attitude, as posited by S-O-R. Once BIT is established, tourists search for, interact with, and co-create sustainability-related content; exposure to congruent information and practices elicits positive affect (enthusiasm, pride, connectedness to nature). This affect serves as the direct conduit to sustainable destination intention (SDI), echoing Stylos et al. (2017) and Su et al. (2020)[10], [13]. In short, BIT acts as the “ignition,” AB as the “terminal gatekeeper.”

Crucially, the indirect effects— $PGI \rightarrow BIT \rightarrow AB \rightarrow SDI = 0.251$ and $PN \rightarrow BIT \rightarrow AB \rightarrow SDI = 0.169$ —indicate that both green image and personal norms affect SDI through two sequential mediators. This “two-tier” rule—cognition/norms (PGI, PN) activating intention (BIT), and affect (AB) consolidating choice—accords with Luong (2023) and extends Han et al. (2011) by treating intention and affect as non-substitutable psychological strata[5], [7]. Theoretically, the study contributes by: (i) evidencing the effective integration of TPB–NAT–S–O–R, reflecting the multidimensionality of green behavior; (ii) generalizing these frameworks to a developing-country context where sociocultural conditions shape sustainability transitions; and (iii) explicating a Gen Z-specific mechanism in which affect and identity are salient [2], [20].

Managerially, four implication clusters emerge. First, position PGI as a strategic asset in destination governance. Build brands on measurable, auditable sustainability pillars—waste management, clean energy, biodiversity protection, transparent environmental data (UNEP & UNWTO, 2005)—and consider a Vietnam Green Destination Index to standardize, disclose, and benchmark sustainability nationwide, thereby strengthening trust and awareness [1]. Second, firms should pursue substantive green transitions, avoiding greenwashing [13]: green procurement, carbon reduction, local sourcing, and community reinvestment; design emotionally and educationally rich green experiences (recycling, reforestation, agro-ecology) to reinforce BIT and elicit AB, ultimately boosting SDI. Third, destination marketing should center emotional branding and storytelling tied to sustainability; use visuals, short-form video, virtual experiences, and authentic community/environmental narratives; leverage TikTok/Instagram/YouTube to match Gen Z’s content consumption patterns [20]. Fourth, public policy should incentivize participation: tax relief for Green Tourism Label adopters, financial support for green projects, and stronger oversight of harmful practices; embed sustainability education in school and university curricula to cultivate PN early [19].

Methodologically, PLS-SEM proves suitable for modeling serial mediation under distributional flexibility [17]. Future research can pursue longitudinal designs to track intention–behavior conversion, multi-group comparisons (generations, regions, destination types), and moderators such as PBC or SN to enhance explanatory power. Limitations include urban-skewed sampling, potential social desirability bias in self-reports, and the absence of post-trip behavioral measures.

In sum, green destination choice among Vietnamese Gen Z unfolds along a cognition/norms \rightarrow intention \rightarrow affect \rightarrow behavior chain: PGI and PN are primary stimuli, BIT and AB are sequential mediators,

and SDI is the immediate outcome. The study offers robust evidence for integrating classical behavioral theories within sustainable tourism and provides actionable pathways to develop credible green destination strategies, foster responsible markets, and strengthen Viet Nam's sustainable competitiveness.

CONCLUSION

This study elucidates the psychological-behavioral mechanism through which Vietnamese Gen Z forms intentions to choose green destinations. Building on an integrated framework that combines the Theory of Planned Behavior, the Norm-Activation Theory, and the Stimulus-Organism-Response model, we successfully validate the structural model $PGI, PN \rightarrow BIT \rightarrow AB \rightarrow SDI$. PLS-SEM results based on 325 Gen Z respondents indicate that all hypotheses are supported, confirming a tightly coupled causal chain from green cognition (PGI) and moral norms (PN) to behavioral intention (BIT), affective attitude (AB), and sustainable destination intention (SDI). The evidence demonstrates that Gen Z's sustainable travel choices emerge from a sequential conversion process in which cognition and norms trigger intention, intention amplifies affect, and affect culminates in choice.

First, the $PGI \rightarrow BIT$ pathway underscores the centrality of perceived green image in shaping behavioral intention. Consistent with the destination-image tradition [9] and subsequent studies [1], [10], observable green attributes—clean environments, renewable energy, efficient resource governance, waste minimization, transparent disclosure—serve as credible signals that activate sustainable choice tendencies. In Viet Nam, PGI constitutes not merely a communication cue but a strategic asset for destination competitiveness; evidence-based design and disclosure are prerequisite to conversion and a safeguard against greenwashing [13].

Second, the $PN \rightarrow BIT$ effect confirms personal norms as an intrinsic driver of responsible travel, in line with NAT [18], [19].

Among Gen Z, environmental values are increasingly embedded in consumption identity and personal moral narratives [20], making PN a pivotal fuse that ignites BIT across contexts.

Crucially, the model verifies dual mediation through BIT and AB, reflecting the S-O-R logic that stimuli are internalized into psychological states prior to eliciting behavioral responses. The linkage $BIT \rightarrow AB$ indicates that deliberative intention operates as an affective amplifier when individuals encounter congruent sustainability content; the $AB \rightarrow SDI$ path (the strongest coefficient) demonstrates that positive affect is the terminal gatekeeper of green destination choice. These observations resonate with Stylos et al. (2017) and Su, Hsu & Boostrom (2020), reinforcing the premise that affective/experiential elements can outweigh purely functional attributes in sustainable tourism, particularly for the “experience-and-share” Gen Z cohort [10], [13].

The study offers three main scholarly contributions. (i) It advances a multi-theory integrated model that jointly captures cognitive, moral, and affective drivers of green behavior by linking TPB-NAT-S-O-R. (ii) It broadens empirical generalizability by validating the model in a developing-country context, beyond the typical evidence base concentrated in developed markets (Han, 2015). (iii) It explicates a generation-specific mechanism in which moral values, consumption identity, and affective experience co-produce sustainable choices [2], [20]. Managerial implications follow. Treat PGI as a strategic destination asset: prioritize verifiable green practices (waste management, clean energy, biodiversity protection, transparent environmental reporting) to strengthen trust and positive affect (AB). Reinforce PN via sustainability education and social-media-driven community norms; leverage user-generated content to diffuse responsible values. Pursue substantive green transitions at the firm level—align “say-do,” disclose processes, train staff, prioritize local sourcing—and design

emotionally and educationally rich green experiences (reforestation, recycling, agro-ecology) that bolster BIT and evoke AB, thereby lifting SDI. For marketing, center emotional storytelling through impactful visuals, short-form videos, and authentic local narratives aligned with Gen Z's media habits.

Limitations include urban-skewed sampling, potential social desirability bias in self-reports, and reliance on intention rather than post-trip behavior. Future research should adopt longitudinal designs to track intention-behavior conversion, apply multi-group comparisons across generations/regions/destination types, and test moderators such as social norms, biospheric values, or perceived behavioral control. Future studies should expand data collection to rural regions such as the Northern Midlands, Central Highlands, and Mekong Delta rural districts to verify whether the TPB-NAT-S-O-R mechanism holds across heterogeneous socio-economic groups.

In sum, green destination choice among Vietnamese Gen Z unfolds along the chain PGI, PN → BIT → AB → SDI: PGI and PN serve as primary stimuli; BIT and AB operate as sequential mediators; and SDI represents the immediate outcome. Clarifying this conversion mechanism enriches the academic discourse on sustainable tourist behavior and equips managers and policymakers with a robust basis for crafting credible green destination strategies, nurturing responsible markets, and strengthening Viet Nam's sustainable competitiveness in the years ahead.

REFERENCES

- [1] C.-F. Chen and D. Tsai, "How destination image and evaluative factors affect behavioral intentions?," *Tour Manag*, vol. 28, no. 4, pp. 1115–1122, 2007.
- [2] M. Nowacki, J. Kowalczyk-Anioł, and Y. Chawla, "Gen Z's attitude towards green image destinations, green tourism and behavioural intention regarding green holiday destination choice: A study in Poland and India," *Sustainability*, vol. 15, no. 10, p. 7860, 2023.
- [3] I. Ajzen, "The theory of planned behavior," *Organ Behav Hum Decis Process*, vol. 50, no. 2, pp. 179–211, 1991.
- [4] A. Mehrabian and J. A. Russell, *An approach to environmental psychology*. the MIT Press, 1974.
- [5] H. Han, L.-T. J. Hsu, J.-S. Lee, and C. Sheu, "Are lodging customers ready to go green? An examination of attitudes, demographics, and eco-friendly intentions," *Int J Hosp Manag*, vol. 30, no. 2, pp. 345–355, 2011.
- [6] Y. Hsu and J. A. Serpell, "Development and validation of a questionnaire for measuring behavior and temperament traits in pet dogs," *J Am Vet Med Assoc*, vol. 223, no. 9, pp. 1293–1300, 2003.
- [7] T.-B. Luong, "Eco-destination image, environment beliefs, ecotourism attitudes, and ecotourism intention: The moderating role of biospheric values," *Journal of Hospitality and Tourism Management*, vol. 57, pp. 315–326, 2023.
- [8] J. L. Crompton, "An assessment of the image of Mexico as a vacation destination and the influence of geographical location upon that image," *J Travel Res*, vol. 17, no. 4, pp. 18–23, 1979.
- [9] S. Baloglu and K. W. McCleary, "A model of destination image formation," *Ann Tour Res*, vol. 26, no. 4, pp. 868–897, 1999.
- [10] N. Stylos, C. A. Vassiliadis, V. Bellou, and A. Andronikidis, "Destination images, holistic images and personal normative beliefs: Predictors of intention to revisit a destination," *Tour Manag*, vol. 53, pp. 40–60, 2016.
- [11] D. Buhalis, "Marketing the competitive destination of the future," *Tour Manag*, vol. 21, no. 1, pp. 97–116, 2000.
- [12] S. Pike, "Destination positioning opportunities using personal values: Elicited through the Repertory Test with Laddering Analysis," *Tour Manag*, vol. 33, no. 1, pp. 100–107, 2012.
- [13] L. Su, M. K. Hsu, and R. E. Boostrom Jr, "From recreation to responsibility: Increasing environmentally responsible behavior in tourism," *J Bus Res*, vol. 109, pp. 557–573, 2020.
- [14] F. Corbisiero, S. Monaco, and E. Ruspini, *Millennials, Generation Z and the future of tourism*, vol. 7. Channel View Publications, 2022.
- [15] R. Anward, H. E. Simon, and T. Haryanto, "Unveiling Generation Z's Travel Motivations and Sustainable Tourism Practices: A Systematic

- Literature Review," *JIEP: Jurnal Ilmu Ekonomi dan Pembangunan*, vol. 8, no. 1, pp. 38–50, 2025.
- [16] S. Seyfi and C. M. Hall, "Beyond Saint Greta: Generation Z and sustainable tourism behaviours and practices," in *Handbook on tourism and behaviour change*, Edward Elgar Publishing, 2023, pp. 98–109.
- [17] J. F. Hair Jr *et al.*, "An introduction to structural equation modeling," *Partial least squares structural equation modeling (PLS-SEM) using R: a workbook*, pp. 1–29, 2021.
- [18] S. H. Schwartz, "Normative influences on altruism," in *Advances in experimental social psychology*, vol. 10, Elsevier, 1977, pp. 221–279.
- [19] H. Han, "Travelers' pro-environmental behavior in a green lodging context: Converging value-belief-norm theory and the theory of planned behavior," *Tour Manag*, vol. 47, pp. 164–177, 2015.
- [20] E. Ketter, "Millennial travel: tourism micro-trends of European Generation Y," *Journal of Tourism Futures*, vol. 7, no. 2, pp. 192–196, 2021.
- [21] C. Fornell and D. F. Larcker, "Evaluating structural equation models with unobservable variables and measurement error," *Journal of marketing research*, vol. 18, no. 1, pp. 39–50, 1981.
- [22] J. Henseler, C. M. Ringle, and M. Sarstedt, "A new criterion for assessing discriminant validity in variance-based structural equation modeling," *J Acad Mark Sci*, vol. 43, no. 1, pp. 115–135, 2015.
- [23] E. Cohen, "A phenomenology of tourist experiences," *Sociology*, vol. 13, no. 2, pp. 179–201, 1979.

Assessing fish farmers' perceptions of environmental drivers shaping cultured fish communities in Chau Doc, Vietnam

Noor Syafiq Bin Abdul Rashid¹, Dung Duc Tran^{2*}, Thien Duc Nguyen², Edward Park¹

¹National Institute of Education (NIE), Earth Observatory of Singapore (EOS), Asian School of the Environment (ASE), Nanyang Technological University (NTU), Singapore

²Institute for Environment and Resources (IER), Vietnam National University Ho Chi Minh City (VNU-HCM), Ho Chi Minh City,

Vietnam*Email: dungtranducvn@yahoo.com

Abstract: The Vietnamese Mekong Delta (VMD) sustains diverse aquatic life and a major fish farming industry but faces hydrological disruptions from climate change, upstream dams, and sand mining. This study examines how fish farmers in Chau Doc perceive these environmental challenges and their effects on aquaculture. An interview survey with 35 fish farmers reveal high awareness of climate change and dam impacts but limited perception of sand mining, as its effects are less visible. Despite explanations of long-term risks like riverbed incision, farmers remain unconvinced (50%), citing distance from affected areas. By exploring fish farmers' lived experiences, this research highlights the often-overlooked human dimension of environmental change in the VMD, emphasizing the need to integrate local perceptions with hydrological stresses into sustainable management strategies.

Keywords: Climate change, upstream dams, sand mining, hydrological changes, Mekong Delta.

INTRODUCTION

The Mekong River supports remarkable aquatic biodiversity, including iconic species such as the giant freshwater stingray, Mekong giant catfish, and giant barb, featured in National Geographic's Monster Fish (2018). These species, also found in the Vietnamese Mekong Delta (VMD), considered as the river's southernmost region, can reach over two metres in length or 100 kilograms in weight

(WWF, 2010). The suitability of the VMD as a habitat for these "giant fishes" reflects its rich food sources and favorable water conditions.

This ecological abundance has enabled Vietnam to expand aquaculture for national food security (Smajgl et al., 2015). Aquaculture, the breeding and harvesting of aquatic organisms for consumption, now contributes over 50 million tonnes of seafood globally (Cressey, 2009). In Vietnam's southern provinces, fish farming is vital for livelihoods and protein supply (Entzian, 2015). To meet domestic and export demands, the government plans to increase aquaculture areas from 70,000 to 280,000 hectares by 2025, targeting 850,000 tonnes of fish worth \$1 billion USD (Linden, 2022). However, such expansion strains the VMD's natural ecosystems and alters its hydrological balance (Stevens et al., 2018).

These pressures are compounded by climate change and the construction of upstream dams. Erratic rainfall and temperature variations threaten aquatic habitats (Kantoush et al., 2017), while dam operations disrupt fish migration and create uncertainty in water discharge (WWF, 2010). In recent years, sand mining has emerged as an additional and growing threat. Driven by global demand for construction material, sand extraction now exceeds 30–50 billion tonnes annually (Schandl et al., 2016). In the VMD, excessive riverbed mining, partly to supply regional development, including Singapore's land reclamation projects (UNEP, 2019), causes

erosion, alters flow regimes, and endangers livelihoods (Nguyen, 2011).

Existing studies on environmental stressors in the VMD have primarily focused on quantitative hydrological or economic analyses. Climate change research links rising temperatures and irregular rainfall to deteriorating water quality (Siddiqui et al., 2020) and highlights adaptive farming practices (Galappaththi et al., 2020; Nadarajah & Eide, 2020). Similarly, studies on upstream dams emphasize economic losses and ecosystem disruption (Yoshida et al., 2020), while sand mining research examines morphological and flood-related consequences (Park et al., 2020). Yet, the lived realities and perceptions of fish farmers, those most directly affected, remain underexplored.

This study seeks to illuminate fish farmers' perceptions of environmental change in Chau Doc as one of the cities of An Giang province of the VMD, focusing on climate change, upstream dams, and sand mining. Their interpretations may diverge from scientific assessments, revealing both knowledge gaps and alternative ways of understanding environmental disruption. Exploring these perspectives provides critical insight into how communities experience and interpret ecological transformations in the VMD, offering a human-centered narrative essential for sustainable aquaculture and river management.

MATERIALS AND METHODS

Study Area

Chau Doc is a city in An Giang province located along the Hau River. Being a prominent tourist site, known for its culture and river produce, Chau Doc offers an insight into the life of the rural. The floating village, seen with a typical floating house in Fig 1, is a key site for tourists to visit. However, beyond the lens of tourism, such a floating village reflects the lived experience of locals. People living in this region do survive on the river by feeding river fish. River food functions not only for sustenance but also as a form of commodity. As

such, changes to the river would inevitably impact the livelihood of these individuals.



Figure 1. Typical floating house of a fish farmer in Chau Doc city

Yet, this problem is not limited to Chau Doc. This study aims to situate the issues of environmental factors impacting hydrological changes and people living within these riparian states through Chau Doc. Chau Doc, therefore, functions as a representative site for impacts on fish farming along the VMD.



Figure 2. Map showcasing interview sites in Chau Doc

Data collection and analysis

The questionnaire was designed to investigate three core themes: (1) changes in fish species reared by farmers, (2) observable changes in river characteristics, and (3) perceived causes of these changes, including climate change, upstream dams, and sand mining. It comprised both open- and closed-ended questions and was divided into three sections corresponding to these objectives. Each interview lasted approximately 30 minutes.

Data collection took place over four days (30 November to 03 December 2022) in Chau Doc's floating villages. Participants were selected based on two criteria: they were (a) active fish farmers and (b) operating on floating villages rather than inland facilities. A convenience sampling approach was adopted due to the physical proximity of floating homes and limited research duration. Two research teams began from different starting points to maximize coverage. Interviews were conducted face-to-face using printed questionnaires, with digital copies available as backup. Local translators assisted in facilitating communication and provided English translations during interviews. The researcher reviewed responses with the translator to ensure accuracy. There were 35 fish farmer participants randomly interviewed in total of which their locations are plotted as seen in Fig 2. All participants provided informed consent, were briefed on the study's purpose and confidentiality, and were assigned anonymized codes (e.g., FF1–FF35).

Collected data were entered daily into Microsoft Excel for organization and later coded for analysis. Closed-ended responses were converted into binary codes (e.g., “yes” = 0, “no” = 1) to identify patterns and relationships, while open-ended responses were grouped by thematic similarity. This coding allowed comparison of farmers' perceptions and adaptive practices across respondents, particularly regarding their understanding of hydrological changes and environmental stressors. This mixed approach enabled exploration of how fish farmers' lived experiences reflect awareness and interpretation of environmental changes affecting aquaculture in the VMD.

RESULTS AND DISCUSSION

Participant's profile

With reference to Fig 3, 78% of interviewed fish farmers are males whereas the remaining 22% are females. This reflects the male-centric nature of the task of rearing fishes (Alonso, 2022). Fish-rearing is considered as

hard labour which contrasts the homemaker roles that women play in these families.

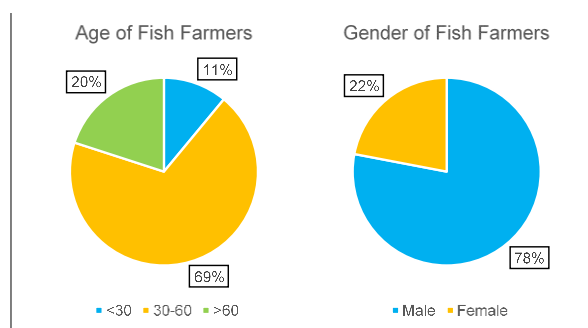


Figure 3. Age and gender conditions of interviewed fish farmers

When examining the ages of fish farmers, we find that a majority, 69%, are aged between 30 to 60 years old followed by 20% over age 60. Most of these fish farmers aged 30 and above either inherit the fish farms from their family members or have been helping out for a portion of time. For example, FF3 shared that he is the “nephew of the boss managing the fish farm” he was interviewed at. On top of that, the owner also owns fish farms where FF 1,2,4,27,28,29 and 30 worked at. Most of these fish farmers have either had some experience with fish farming or were hired due to their longer experience. As such, the fish farming industry seems to largely be driven by experienced individuals but also some sort of connection that seems to benefit larger fish farms. Thus, the complexity of rearing fish extends beyond just experience but also connections that provide opportunities for fish farmers to more likely succeed as opposed to sole fish farmers found at certain parts of our interview sites.

Changes observed in the river

Fish farmers were initially asked as to whether they observed any changes to the river that surrounds that to which all of them mentioned they have noticed changes. They are then questioned on changes observed on certain river characteristics which included water turbidity, water velocity, water level, bank collapse as well as sediment.

When questioned about water velocity, 28 of 35 fish farmers (80%) mentioned that they observed the water velocity to be higher. Moreover, 22 of 35 fish farmers (62.9%) mentioned that they observe the river to be dirtier. Higher water velocity could possibly explain water with higher turbidity. When the calmness of water is disrupted, there may be a higher propensity to account for water with higher turbidity.

However, fish farmer's perception on sediment levels in the river seem to differ from the perception of water with higher turbidity. Water turbidity is affected by sediment. In fact, excess sediments have been observed to increase water turbidity and are often attributed as the leading cause to the impairment of water. Yet, when fish farmers were questioned, only a total of 20 fish farmers responded with the remaining 15 fish farmers not being able to give a definitive response. Amongst the 20 who responded, 12 of 20 (60%) attributed the river to having lower sediment. This juxtaposes with the responses about water with higher turbidity. As such, through the perception of the fish farmers, we understand that they do not necessarily make the connection between water turbidity with sediment.

Reasons for changes

Fish farmers were then asked on several environmental factors, namely climate change, upstream dams and sand mining, and how they perceive it could contribute to the changes. Of these factors, climate change has been chosen as the main factor perceived to cause the changes and 28 of 35 (80%) of fish farmers were choosing it. This is closely followed by upstream dams with 25 of 35 participants (71%) mentioning that it possibly contributes to the changes in the river mentioned. However, when asked about sand mining, 24 of 34 participants (70 %) did not perceive sand mining to be a possible factor for the changes observed in the river since one participant could not reach a definitive response due to unfamiliarity with the issue of sand mining. As a result, the total count for sand mining tallied

to 34 participants only. As these results are reflective of the perceptions of fish farmers, this paper seeks to explore popular literature on these factors affecting hydrological changes in the Mekong River. This would aid in better understanding the factual aspect of the matter with that of the psyche of fish farmers in the region.

Climate change

Climate change has been a major issue over the recent decades. With anthropogenic factors exacerbating climate change, changes to the Mekong River should be taken into account. To facilitate and streamline this study, two indicators of climate change, including rainfall and temperature, were put forth to fish farmers. When asked about any change in rainfall, 68.6% of fish farmers mentioned that they did observe an increase. This could possibly account for higher water velocity and level perceived by fish farmers. With higher rainfall, the amount of water carried by the Mekong River surges. Moreover, with an increase in volume of water due to perceived higher rainfall, it can increase stream discharge and therefore accentuate stream velocity. This was also highlighted at a site visited along the river where the interviews were conducted.



Figure 4. Peak water level marks at the stilts of a building

Fig 4 showcases the peak water level recorded from as early as 1992 to 2018. These

water levels fluctuate greatly yearly with water level in 1996 recorded to be the highest while the lowest being at 2010 as seen in the two extreme sides of the stilts. As such, the fluctuating peak water level can possibly affect riverbanks, destabilising them and resulting in a riverbank collapse.

During the interview, 75% of 32 fish farmers who responded mentioned that there has been no recent bank collapse. Through observation and photographic evidence, it reflects a possible reason as to why there has been no recent riverbank collapse. The house demarcated in red is still standing on stilts by the river edge. This is because the banks have not given way in recent times and as such the house is still able to maintain its location.

Yet, the very placement of the metal mesh over the rubbles as a means to manage reflects the high awareness of potential risk of changing water levels by the fish farmers that placed them. This, therefore, implies that fish farmers have a high perception of climate change as a potential cause of hydrological changes observed and hence adopted management strategies to cope with it.

Upstream dams

Dams are infrastructures placed at certain points of a river that function as a barrier to restrict the flow of surface water. It is often placed to create reservoirs of water and prevent flooding. Moreover, many activities can arise from the storage of water such as for irrigation, aquaculture, and even human consumption. We can observe that the Mekong River is transboundary. It runs through countries like China, Laos, Thailand, Cambodia and Vietnam. Yet, amongst them, it seems that the *upper Mekong*, primarily found in China, have more control and influence over water and sediment level experienced by states in the *lower Mekong* delta.

Upstream dams can cause both flooding and water shortages downstream due to fluctuating releases. When dams are closed, water flow from the Mekong decreases, reducing volume and oxygen levels and

disrupting fish breeding and behavior (Ng'onga et al., 2019). When released, sudden surges increase river velocity and discharge, risking riverbank collapse and further affecting fish livelihoods. Fish farmers, aware of these impacts, face economic losses, displacement from fluctuating water levels, and difficulty sustaining aquaculture. As both producers and consumers of fish, they remain vulnerable, with limited capacity to change their situation, an aspect often overlooked in existing literature.

Sand mining and its devastation

Sand mining is known for its widespread impact. There are positive impacts such as economic growth given the rise of construction industry. More employment opportunities are created as a result. Yet, the devastation that follows seems to subsume the benefits. According to a report by World Wildlife Fund (WWF) in 2018 on the impacts of sand mining on ecosystem structure, process and biodiversity in rivers, there has been some immediate negative impacts. This includes destruction of aquatic/ riparian habitats, channel instability, decrease in flood control, amongst others. However, the actual devastation occurs due to hydrological changes in the long run. Some of these impacts such as incision to the riverbed, channel erosion, increased flow velocity and turbidity, can have long term repercussions on the surrounding environment. This includes changing the habitat conditions for fishes, affecting the ways of individuals who rely on the river for river produce, as well as impacting houses near the edge of the river which may succumb to the channel erosion. As such, this devastation may manifest in the long run, in an unexpected manner, intensifying the extent of the sand mining impact.

Though about 70% of fish farmers do not perceive sand mining to possibly affect the hydrological changes, there is usefulness in questioning and seeking deeper understanding from fish farmers about the situation of sand mining that occurs in the VMD. As such, fish farmers were asked about their perception of sand mining effects.

Perceptions of effects of sand mining

We found that 86% of fish farmers are aware of the effects of sand mining. This is in relation to sand mining that happens along the VMD, upstream from Can Tho city, Vietnam. When asked about what types of effect of sand mining, 83.3% of fish farmers identified pollution and decreased fish yield as the main consequences. Pollution arises when harmful substances enter the environment; dredging the riverbed destroys habitats, disturbs bottom-dwelling organisms, and stirs up sediment that clouds the water. This turbidity can suffocate fish and block sunlight essential for underwater vegetation, reducing oxygen production and disrupting the delicate aquatic ecosystem.

Awareness of lower water quality and bank erosion was reported by 63.3% and 50% of respondents, respectively. Although less recognized than pollution, these effects are equally damaging. Sediment disturbance lowers water quality, affecting aquatic life, while excessive sand extraction weakens riverbanks, increasing the risk of collapse—issues further discussed in the section on downstream sand mining.

Interestingly, no respondents associated sand mining with lower water levels, despite evidence that riverbed incision can deepen channels and reduce water height (Zhang et al., 2021). This absence of awareness may stem from farmers' greater familiarity with rising water levels linked to climate change and upstream dams. The findings suggest while fish farmers recognize visible impacts such as pollution and erosion, their perception of sand mining's broader hydrological consequences remains limited.

Downstream sand mining

Around the proximity of Chau Doc, there are no sand mining sites. As such, it is not possible to study the potential risks that it brings to the study site directly. However, there are sand mining sites located further downstream, away from Chau Doc. As such this paper explores a theoretical idea that stems

from the conceptual understanding of “Hydrologic connectivity” which refers to water-mediated transfer of matter, energy and/or organisms within or between elements of the hydrologic cycle (Freeman et al., 2007, p1). It recognizes that the connections can exist vertically, laterally, and in longitudinal dimensions and even extend across spatial and temporal scales. This places the river as an interconnected body of puzzle pieces where a change to one piece could in turn affect the greater outlook of the river (Covino, 2017). Similar to how dams restrict water flow to downstream areas and disrupt fish migration both upstream and downstream (Pringle, 2003), downstream sand mining can also influence upstream locations such as Chau Doc. This relationship is illustrated in Figures 5 and 6. Figure 5 depicts changes in the riverbed slope following sand mining incisions, while Figure 6 presents a side profile showing the original gradient of the river flowing from upstream (Chau Doc) to downstream (Can Tho).

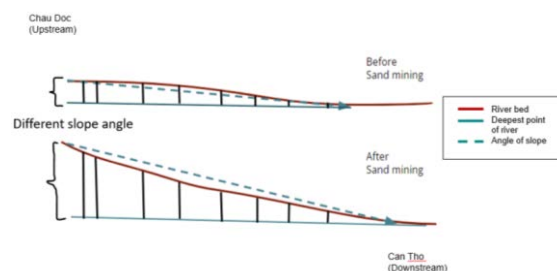


Figure 5. Diagrams showing theorised change in slope angle of river flowing from Chau Doc to Can Tho along the Hau River

With the introduction of sand mining causing an incision in the river bed, it causes the river depth to be lowered as demarcated. In Fig 6, the area highlighted in yellow between the river bed demarcation and demarcation of slope angle (dotted lines) from the deepest point of the river to Chau Doc (upstream) reflects river bed not yet affected by the incision. However, with the conceptual understanding of “Hydrologic connectivity”, this paper proposes the potential erosion of the river material highlighted in yellow which would result in the newly formed steeper slope

angle of the river, flowing from Chau Doc to Can Tho. Potential changes expected include higher stream discharge as steeper angle of river bed would result in increased velocity. As a result, hydrological changes impacted by changing stream discharge could be accentuated on top of what has been discussed.

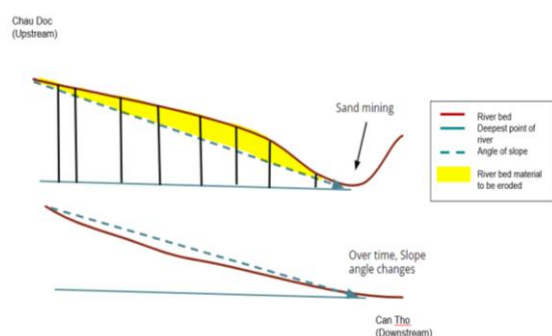


Figure 6. Diagrams showing sand-mining-induced incision and changes in riverbed slope from Chau Doc to Can Tho along the Hau River

When informed of the potential for downstream sand mining to affect upstream areas, 63% of fish farmers rejected this possibility. They attributed their view to Chau Doc's considerable distance from mining sites and the belief that ocean flooding, rather than sand mining, drives inland water movement. Farmers suggested that rising sea levels could push water upstream, intensifying local impacts. However, such a scenario is scientifically unlikely. While capillary action can move water upward in narrow spaces (Tamajit et al., 2020), the 4,000 km delta system allows gravity to dominate, making significant upstream flow from downstream sand mining implausible.

Agricultural pollution

An environmental factor not originally examined but frequently mentioned by fish farmers was agricultural pollution from upstream. Farmers attributed declining water quality to wastewater and insecticide runoff from intensified agriculture in Cambodia, where double and triple rice cropping demands heavy resource use and pest control. These pollutants, discharged into rivers and carried

downstream to Chau Doc, Vietnam (Fig 7), alter river composition and harm aquatic life. Reported effects include irregular fish breeding, lower water quality, and increased fish diseases—highlighting farmers' strong awareness of transboundary agricultural impacts on their livelihoods.

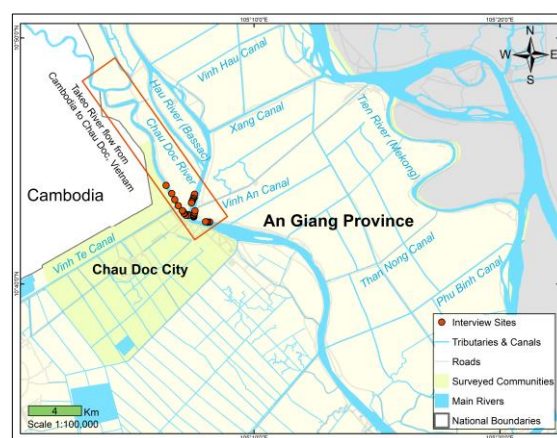


Figure 7. The Mekong River flows from Cambodia into Vietnam at Chau Doc

Impacts on fish yields

All interviewed fish farmers reported changes in fish yield over the past five years, with 69% experiencing declines. Farmed fish are highly sensitive due to their confined, artificial environments, requiring careful control of oxygen and nitrogen levels. While some farmers use pumps and feeding controls to maintain balance, others cannot afford such equipment. Older farmers (20% over 60) also struggle with labour-intensive maintenance.

To address declining yields, farmers reconsidered their practices as 49% changed the species they reared, while 51% kept the same fish. Those who maintained their species either continued profitable operations or resorted to mass breeding to ensure some survival. Farmers who switched species selected varieties they believed were more resilient, reflecting their perceptions of which fish thrive under changing conditions. Fish farmers perceive these fishes to be more suitable for various reasons. Of the 49% of fish farmers who did mention they changed the

type of fish they rear, the main reason attributed is the increased durability of their new fishes (i.e., tinfoil barb, basa fish, red tilapia). Durability, in this case, is described to be the fishes' ability to withstand harsher water conditions. Harsher water conditions include several condition changes such as increased levels of nitrogen, lower oxygen levels, higher turbidity and many more.

Another reason given is the price of these fishes in two aspects. First, the price here refers to the relatively competitive prices of these preferred fishes in the market. Fish farmers believe that their fishes are able to fetch the best deal and therefore enable them to make income more effectively. Moreover, the other price reason referred to here refers to the cost of rearing these fishes. Fish farmers perceive that the fishes are easier to breed and therefore do not require additional support to boost their growth. As a result, fish farmers are not required to purchase additional medication or fish specific products in order to maintain their fishes' health.

While these changes enable fish farmers to head in the right direction for the future of their fish farming practices as they are able to perceive which fish thrives better in present water conditions, it is undeniable that the hydrological changes have caused significant changes to the norm. Fishes reared have to be changed as a result. The state of uncertainty reflects the risk that fish farmers face as they navigate their farming practices in hopes for their fishes to thrive and sell in the market.

CONCLUSION

In summary, environmental and hydrological changes are most acutely felt by fish farmers whose livelihoods depend on river ecosystems. This study shows that farmers possess strong awareness of climate change and upstream dams, recognizing their roles in fluctuating water levels and riverbank collapse. However, perceptions of sand mining impacts remain low, as many farmers believe distance shields them from its effects, despite its long-term impacts through hydrologic connectivity.

Fish farmers also display high awareness of transboundary agricultural influences on river water quality in Chau Doc city. While their views often align with existing literature, they tend to focus on immediate, tangible impacts rather than future risks. Further research should examine species-specific effects and the social realities of fish farmers to amplify their voices in policy discussions, affirming that lived experience remains a vital truth in understanding environmental change.

REFERENCES

- Alonso, G. (2022) Managing masculinities: dynamics of offshore fishing labour in Vietnam, *Gender, Place & Culture*, 29:12, 1677-1693, DOI: 10.1080/0966369X.2022.2134314.
- Covino, T. (2017). Hydrologic connectivity as a framework for understanding biogeochemical flux through watersheds and along fluvial networks. Elsevier. 277, p. 133-144.
- Cressey, D. (2009). Future fish: the only way to meet the increasing demand for fish is through aquaculture. Daniel Cressey explores the challenges for fish farmers and what it means for dinner plates in 2030. *Nature*, 458(7237).
- Entzian, M. (2015). The Seafood Industry in Vietnam – Aquaculture, Five Year Plans, and the TPP. Retrieved on 13 November 2022 from: <https://www.vietnambriefing.com/news/seafood-industry-vietnam-aquaculture-year-plans-tpp.html/>.
- Freeman, M.C, Pringle, C.M, Jackson, C.R. (2007). Hydrologic Connectivity and the Contribution of Stream Headwaters to Ecological Integrity at Regional Scales. *Journal of the American Water Resources Association (JAWRA)*.
- Galappaththi, E.K,Ichien, S.T, Hyman, A.A, Aubrac, C.J, Ford, J.D. Climate change adaptation in aquaculture. *Rev. Aquac.*, 12 (2020), pp. 2160-2176.
- Kantoush, S., Binh, D.V, Sumi, T., Trung, L.V. (2017). Impact of Upstream hydropower dams and climate changes on hydrodynamics of Vietnamese Mekong Delta. *Journal of Japan Society of Civil Engineers*, 73, p. 109-114.
- Linden, J. (2022). Vietnam seeks investors in aquaculture. Retrieved on 14 November 2022 from <https://www.feedstrategy.com/aquaculture/vietnam-seeks-investors-in-aquaculture/>.

- Nadarajah, S & Eide, A. (2020). Are Asian fresh and brackish water aquaculture production vulnerable or resilient towards climate change impacts? *Aquac. Econ. Manag.*, 24, pp. 232-254.
- National Geographic. (2018). Monster Fish. Retrieved on 14 November 2022 from: <https://www.natgeotv.com/asia/monster-fish/about>.
- Ng'onga, M., Kalaba, M.F, Mwitwa, J., Nyimbiri, B. (2019). The interactive effects of rainfall, temperature and water level on fish yield in Lake Bangweulu fishery, Zambia, *Journal of Thermal Biology*, Volume 84, Pages 45-52.
- Nguyen, M. D. (2011). River Sand Mining and Management: a Case of Cau River in Bac Ninh Province, Vietnam. Singapore, EEPSEA Research Reports, 61 p.
- Park, E., Ho, H. L., Tran, D. D., Yang, X., Alcantara, E., Merino, E., & Son, V. H. (2020). Dramatic decrease of flood frequency in the Mekong Delta due to riverbed mining and dyke construction. *Science of the Total Environment*, 723.
- Pringle, C. (2003). What is hydrologic connectivity and why is it ecologically important? John Wiley & Sons. 17, p. 2685-2689.
- Siddiqui, S., Jeremy L. C., Scarpa, J., Sadovski, A. (2020). An analysis of U.S. wastewater treatment plant effluent dilution ratio: Implications for water quality and aquaculture, *Science of The Total Environment*, Volume 721.
- Schandl, H., Fischer-Kowalski, M., West, J., Giljum, S., Dittrich, M., Eisenmenger, N.,...Fishman, T. (2016). Global Material Flows and Resource Productivity. Assessment Report for the UNEP.
- Smajgl, A., Toan. T.Q, Nhan. D.K, Ward. J, Trung, N.H., Tri, L.Q., Tri, V.P.D., Vu, P.T. (2015). Responding to rising sea levels in the Mekong Delta. *Nat. Clim. Change*, 1–8.
- Stevens, J.R., Newton, R.W., Tlustý, M., Little, D.C. (2018). The rise of aquaculture by products: Increasing food production, value, and sustainability through strategic utilisation. *Elsevier*, 90, 115-124.
- Tamajit, M. & Sayondeep, C. & Ayush, N. (2020). Transportation of water through capillary action to a certain height without electricity and comparison of the model with a tree.
- United Nation Environment Programme (UNEP). (2019). Sand and Sustainability: Finding new solutions for environmental governance of global sand resources. GRID Geneva, United Nations Environment Programme, Geneva, Switzerland.
- World Wildlife Fund (WWF). (2010). River of Giants. Giant fish of Mekong. WWF International.
- World Wildlife Fund (WWF). (2018). Living planet report (2018) risk and resilience in a new era. Gland, Switzerland: WWF International.
- Yoshida, Y., Lee, H. S., Trung, B. H., Tran, H.D., Lall, M. K., Kakar, K., & Xuan, T. D. (2020). Impacts of Mainstream Hydropower Dams on Fisheries and Agriculture in Lower Mekong Basin. *Sustainability*, 12(6), 2408.
- Zhang, P., Li, L., Wang, Y., Shi, C., & Fan, C. (2021). Influence of Riverbed Incision and Hydrological Evolution on Water Quality and Water Age Based on Numerical Simulation: A Case Study of the Minjiang Estuary. *International journal of environmental research and public health*, 18(11), 6138.

Evaluation of the Influence of Crack Geometry in High-Performance Concrete Members Using Non-Destructive Testing for Structural Safety Management

Nhan PhamThi^{*}, Phi DangVan

Hanoi University of Mining and Geology, 18 Vien street, Dong Ngac commune, Hanoi, Vietnam

^{*}Email: phamthinhan@humg.edu.vn

Abstract: The ultrasonic pulse method is one of the non-destructive testing methods. This method is highly effective in determining material conditions and detecting internal flaws in concrete or high-performance concrete. Widely utilized in modern infrastructure, the detection and evaluation of crack characteristics are essential to ensuring structural integrity and service life. This study applies the ultrasonic pulse technique to investigate the effects of crack geometry and crack density on wave propagation in high-performance concrete members. Key parameters examined include crack width, orientation (vertical or inclined), and the number of cracks, with their influence on signal travel time systematically analyzed. The outcomes of this research provide a scientific basis for the calibration and interpretation of Non-destructive testing (NDT) data in engineering practice, thereby improving the diagnostic accuracy and reliability of concrete structural assessments. In the context of structural safety management and sustainable infrastructure, understanding the effects of crack geometry in high-performance concrete is crucial for ensuring long-term durability. This study contributes to the proactive monitoring and maintenance of concrete structures, optimizing safety management practices while supporting the transition to environmentally responsible construction techniques. By improving the resilience and longevity of concrete, the findings help reduce material waste, energy consumption, thus aligning with the goals of green growth and sustainable development.

Keywords: High-performance concrete (HPC), Non-destructive testing (NDT), Crack, Compress strength, Matrix.

INTRODUCTION

In modern construction, the assessment of high-performance concrete (HPC) structures is crucial for ensuring their durability and safety. Destructive testing methods including compressive strength tests, bending tests, and tensile tests, were once commonly employed for assessing the mechanical properties of concrete, [8]. The primary disadvantage of destructive testing methods is their inherently invasive nature, as they require specimen destruction, thereby preventing further reuse or further investigation of the material after testing, [6]. This limitation can reduce the number of tests that can be conducted, particularly when sample materials are scarce or costly. Furthermore, the considerable costs and complexities associated with these tests, including the need for specialized equipment and controlled environments, restrict their broader application, particularly in large-scale projects. In contrast, non-destructive testing (NDT) techniques, particularly those based on ultrasonic methods, have gained significant attention for their ability to evaluate the condition of concrete without causing damage. Among these techniques, the Time-of-Flight Diffraction (TOFD) method stands out for its precision in detecting internal defects, especially cracks, which are a common form of degradation in concrete structures [2],[4]. Cracks in concrete can arise due to various

factors, such as thermal cycling, loading, or environmental influences, potentially leading to reduced structural integrity and safety risks [2], [14]. Therefore, accurately measuring the geometry of these cracks is vital for assessing the overall health of the structure [15].

A variety of research has explored the transmission of ultrasonic waves in both conventional and fiber-reinforced concrete, with an emphasis on factors such as material composition, curing conditions, and fiber content [1], [3], [10], [12].

This paper investigates the influence of crack geometry, including crack width, orientation, and density on ultrasonic wave propagation in HPC members, utilizing the TOFD technique. By systematically analyzing how different crack characteristics affect signal travel times, the study aims to enhance the understanding of crack behavior and improve the diagnostic reliability of ultrasonic methods. Specifically, the relationship between compressive strength degradation and ultrasonic wave transit time is explored, providing a basis for more accurate calibration of NDT methods in structural assessments [4], [14]. Through this research, we aim to refine the application of TOFD for non-destructive crack evaluation, contributing to better maintenance practices and longer service lives for concrete infrastructure [7], [15].

EXPERIMENTS

Materials and specimen preparation

Table 1 summarizes the composition of the high-performance fiber-reinforced concrete

(HPFRCC) matrix based on the cement mass ratio. The HPFRCC mixture in this study includes cement, silica fume, river sand, water, and superplasticizer, designed according to the cement weight ratio.

Table 1. Composition Ratios of HPFRCC Materials by Cement Mass

Notation	Cement	Silica fume	River sand	W/C	SP	Crack
FoCo	1	0.25	1.25	0.2	0.035	0
FiCo	1	0.25	1.25	0.2	0.035	0
FiC1	1	0.25	1.25	0.2	0.035	1
FiC2	1	0.25	1.25	0.2	0.035	2
FiC1l	1	0.25	1.25	0.2	0.035	1

The mix design used in this study was derived from earlier works by the authors and our research group [13]. The notations SF₀ and SF₁ represent steel fiber volume contents of 0% and 1.0 vol% in HPFRCC, respectively. To investigate the impact of cracks on ultrasonic pulse transmission, vertical and slanted notches were preformed in the test specimens. In the notation system, C represents notches in the samples, and the number following the letter C indicates the number of notches in the samples (Table 1). Meanwhile, I refers to the inclination of the notch. W/C represents the water-to-cement ratio, and SP refers to the Superplasticizer component.

Fig. 1 presents images of the key materials used in this study. Ordinary Portland cement was selected in accordance with the ASTM C150 Type 1 specifications for hydraulic cement. Additionally, silica fume, comprising 90% SiO₂ with an average particle size of 10 µm, was incorporated as a binder in the matrix.



a) Cement



b) Silica fume



c) River sand

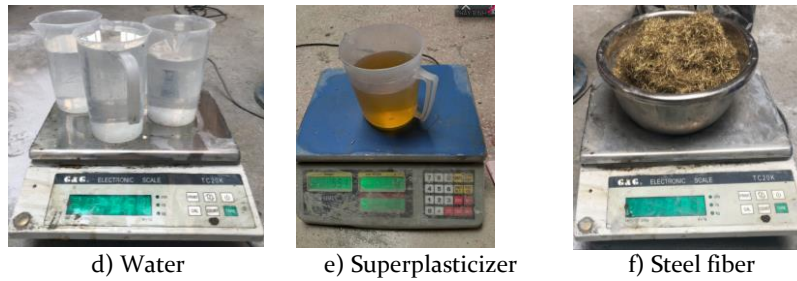


Figure 1. Images of the main materials used in the study

The river sand used in the mix had an average particle size of 1.25 mm. The water-to-cement ratio (W/C) was set at 0.2 with a polycarboxylate-based superplasticizer incorporated at a cement ratio of 0.035. Table 2 outlines the specifications of the steel fibers, which have a diameter of 0.2 mm, a length of 13 mm, and an elastic modulus of 200 GPa. A 30-liter mixer was employed to ensure proper blending of the materials. The mixing procedure commenced with the incorporation of dry ingredients, such as silica fume and cement, and was mixed for approximately 3 minutes. Following this, river sand was added and blended for an additional 5 minutes. Water was then introduced gradually, and the mixture was mixed for 2 minutes to achieve a uniform consistency. Afterward, the superplasticizer was added and mixed for another 2 minutes.

Finally, steel fibers were manually introduced and mixed for an additional 2 minutes.

Table 2. Characteristics of steel fiber

Type	Diameter (mm)	Length (mm)	Elastic modulus (Gpa)	Tensile strength (Mpa)
Smooth straight	1	0.25	1.25	0.2

Bending tests were performed on specimen sizes of 150×150×600 mm³ using a three-point bending setup in three dimensions, as shown in Fig. 2. The specimens used for compression testing had dimensions of 50×50×50 mm³. To maintain a constant laboratory temperature of 25 ± 2 °C, all specimens were covered with a plastic sheet. After 48 hours, they were taken out of the molds and placed in a hot water bath maintained at 80 ± 5 °C for 72 hours.

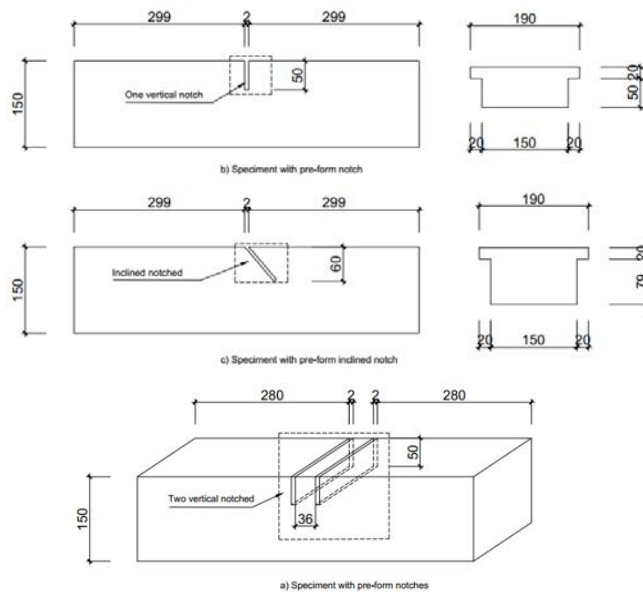


Figure 2. Flexural specimens

Test setup

Fig.3 a and 3b depict the specimen geometries used to investigate the effects of cracking on UPPT (Ultrasonic pulse propagation time) in HPFRC through direct measurement method (DMM), as shown in Fig. 3 a,b . In SF₁C₁, SF₁C₁I and SF₁C₂ specimens,

vertical notches with a width of 2 mm and depths of 50 mm and 60 mm were placed in the middle of specimens, as shown in Fig. 2a. In addition, Figure 3c, 3d and 3e depicts the measurement locations used to evaluate the effects of cracks on UPPT in HPFRC through the indirect measurement method (IMM).

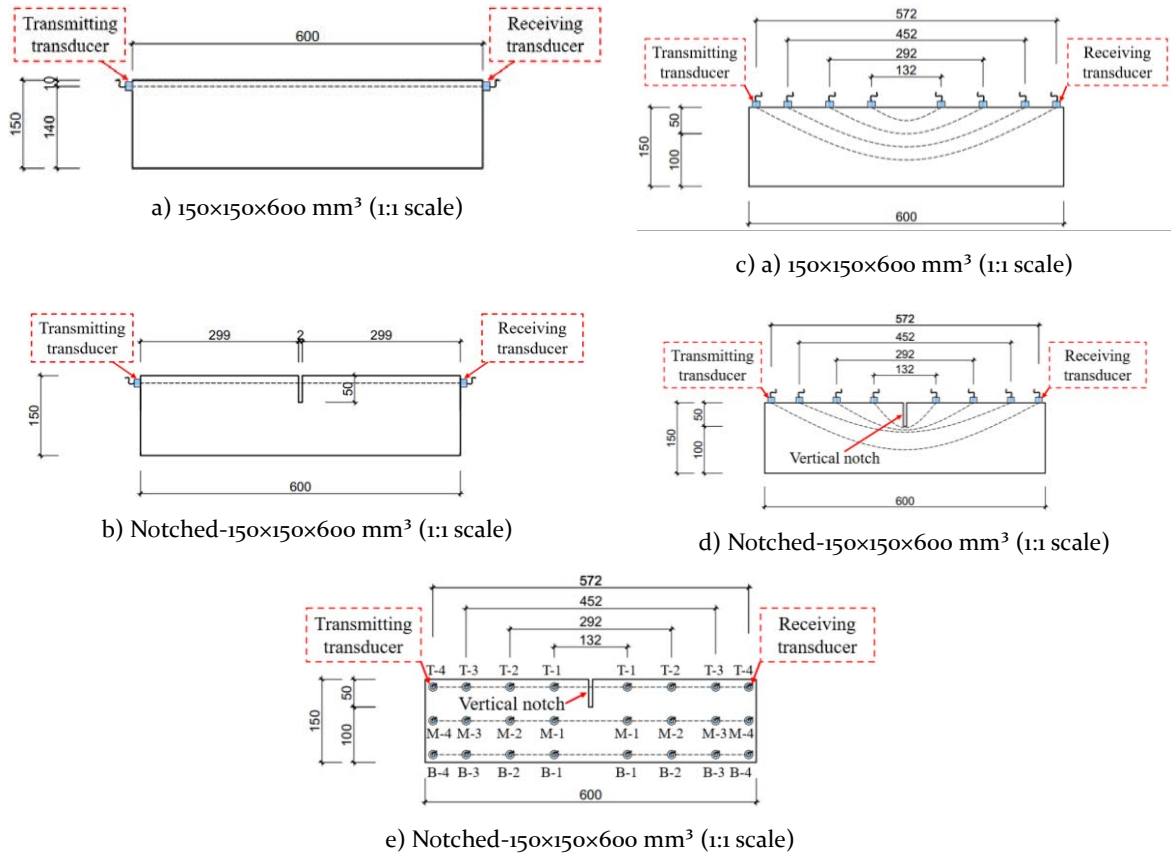


Figure 3. Specimen geometries characterized using DMM and IMM

The three-point bending test was conducted using an ADVANTEST 9 machine with a capacity of 3000 kN. The applied loading rate for specimens measuring 150×150×600 mm³ was 0.05 MPa/s as shown in Fig.4. Meanwhile, compressive strength tests were also performed on the same testing system. The ultrasonic pulse propagation time (UPPT) of

the matrices was measured with the PULSONIC 58-E4900 equipment. Before conducting the experiment, the ultrasonic pulse velocity on the reference bar was calibrated multiple times to ensure that the pulse travel time on the reference bar was 55.9 μs.

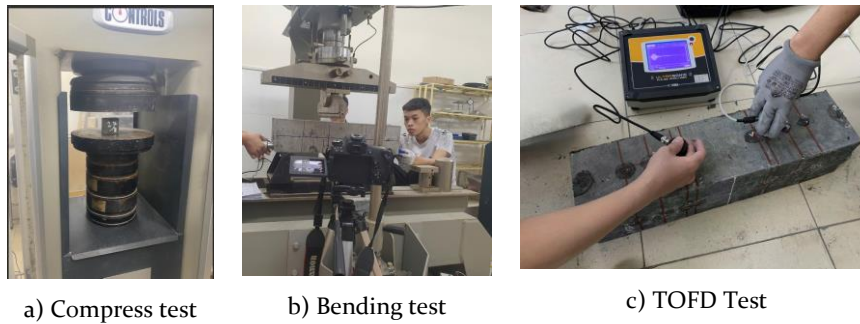


Figure 4. Testing systems

ANALYSIS AND INTERPRETATION OF RESULTS

Mechanical properties of HPFRC

Compressive strength measurements for the F1Co and FoCo samples indicate that the addition of fibers substantially enhances the material's strength, with both exceeding 60 MPa. This demonstrates that the mix proportions used in the experimental program fully meet the requirements for high-strength concrete production. The data presented in Table 3 compare the flexural strength of HPFRC matrices with varying steel fiber volume contents and notch configurations. The data show a noticeable increase in flexural strength when the steel fiber volume content increases from 0% (FoCo) to 1.0% (F1Co) as seen in the flexural strength rising from 7.74 MPa (FoCo) to 10.12 MPa (F1Co). In addition, the bending test results for the 40x40x160 mm³ samples also show a similar trend. With the presence of steel fibers, the bending strength increased by 60%.

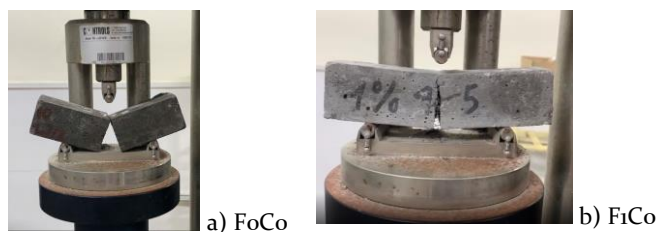
The matrices with notches (F1C1, F1C2, F1C1I) show a reduction in flexural strength

compared to the un-notched matrices. The F1C1 matrix, with a single vertical notch, has a flexural strength of 8.24 MPa, which is a decline from the F1Co matrix's 10.12 MPa. The F1C2 matrix, with two notches, shows a more substantial drop in flexural strength to 4.34 MPa, indicating the increasing effect of multiple notches on the material's structural integrity.

Table 3. Composition Ratios of HPFRCC Materials

Matrix	Compress Strength (MPa)	Flexural strength (MPa)	
		150x150x600 (mm ³)	40x40x160 (mm ³)
FoCo	63.95	7.74	10.82
F1Co	90.42	10.12	17.41
F1C1	-	8.24	-
F1C2	-	4.34	-
F1C1I	-	6.42	-

The F1C1I matrix, which includes a single inclined notch, has a flexural strength of 6.42 MPa, which suggests that the orientation of the notch (vertical versus inclined) influences the flexural strength, but the effect is less pronounced than with multiple notches.



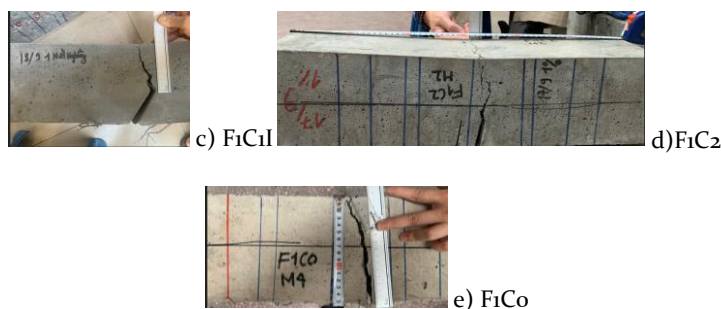


Figure 5. Crack images of HPFRC specimen at the peak flexural stress.

The improvement in flexural strength observed with steel fibers is due to the superior bridging effect provided by the fibers (Fig. 5 a, b), which enhances the material's resistance to micro-cracks, and facilitates the redistribution of stresses throughout the matrix, [16],[17]. The data demonstrate that an increase in steel fiber content generally enhances the flexural strength of HPFRC. Figure 6 demonstrates a uniform distribution of steel fibers within the concrete specimen structure. This suggests that the sample fabrication process effectively mitigates issues related to uneven fiber distribution and fiber clumping. Therefore, the fabrication method used in this study is designed to prevent any negative impact on the durability of the concrete samples due to the uneven distribution of steel fibers.



Figure 6. Fiber distribution of the cross-section of the specimen

However, the presence of notches, particularly multiple notches and inclined notches, leads to a marked decrease in flexural strength. This reduction could be attributed to the initiation and propagation of cracks along the notch path, which compromises the

material's load-bearing capacity. Therefore, it can be inferred that while fiber content contributes positively to flexural performance, the presence and configuration of notches play a significant role in weakening the material's performance under bending stresses.

Effect of some characteristics of the cracks on UPPT behavior in HPFRC

Upon examining Table 4, the UPPT values obtained through both direct (DMM) and indirect (IMM) methods indicate that the presence of 1 % fiber content reduces the UPPT values. This effect is further demonstrated in the experimental samples once the peak stress value is reached. When no steel fibers are present, the sample fractures into two parts (Fig. 5a); however, with fibers, the samples maintain their integrity due to the connections made by the fibers (Fig. 5b). From Figures 5c and 5d, it can be observed that the presence of cracks not only causes wave scattering, increasing the UPPT, but also affects the sample's strength. As the number of cracks increases, the bending strength of the sample decreases, and the number of secondary cracks increases (Figure 5d). In contrast, for the FiC1l and FiCo samples, secondary cracks hardly appear.

Table 4. UPPT values of samples

Matrix	DMM (μ s)	IMM (μ s)			Crack width (mm)
		132 mm	292 mm	572 mm	
FoCo	149.5	84.5	132.4	244.2	-
FiCo	141	65-84	111.4	208.4	12
FiC1	166.8	81	117	196.8	14
FiC2	153.2	85.5	125.9	211.8	30
FiC1l	254	117.6	134.9	224.7	32

For samples with 1% fiber content, the introduction of cracks significantly alters the UPPT value. As the number of cracks increases, the propagation time decreases in the Direct Measurement Method (DMM), while it remains relatively constant in the Indirect Measurement Method (IMM), resulting in a longer wave propagation time. This observation suggests that as the number of cracks increases, the trend in UPPT changes become more complex and less predictable, especially when other factors such as crack orientation, crack length, sensor placement, and measurement distance are held constant. The presence of steel fibers plays a crucial role in mitigating the effect of cracks on wave propagation. Steel fibers act as bridging agents, helping to redistribute stresses and prevent the further extension of cracks. This leads to enhanced structural integrity and a more stable wave propagation time despite the presence of cracks. Therefore, even with an increasing number of cracks, the overall effect on the UPPT is less severe compared to non-fiber-reinforced samples, showcasing the beneficial impact of fibers in improving the durability and resistance of high-performance concrete (HPC) under stress.

Conversely, the UPPT value for the F1C1 sample is the highest among all the samples, reaching 254 μ s. When compared to the FoCo sample, the value increases by 69.89% using the DMM method. This highlights the importance of considering the effect of crack orientation on the direction of ultrasonic wave propagation. The UPPT results for the F1C1 sample using the IMM method show the largest increase at distances of 100mm and 132mm, but a decrease at a measurement distance of 292mm.

The UPPT values obtained for all samples using the IMM method reveal a clear pattern for measurement distances ranging from 132mm to 292mm, regarding the impact of fiber content, crack presence, number of cracks, and crack angles. However, when the measurement distance is increased to 572mm, the effect of the number of cracks and crack angles becomes

less pronounced and more difficult to ascertain. This observation suggests that the optimal distance between the transducer heads should range from 132mm to 292mm, which aligns with current industry standards. Table 5 presents a summary of the UPPT values for the notched specimens at various measurement distances from the vertical notch, as illustrated in Fig. 3e. The IMM was applied before the bending test with measurement distances of 132 mm, 292 mm, 452 mm, and 572 mm. The symbols T (Top), M (Middle), and B (Bottom) indicate different positions on the surface of the F1C1 specimen, facilitating the analysis of the relative positioning between the transducers and the notch. The observed differences in UPPT at various locations on the specimen suggest that the effect of the vertical notch on wave transmission is location-dependent. The top location, closest to the notch, demonstrates the highest pulse propagation times, likely due to increased wave dispersion and attenuation from the crack. The middle location also experiences a reduction in pulse velocity, though the change is smaller. The bottom location records the lowest UPPT values, which could be due to minimal crack interaction, resulting in less wave dispersion. At a measurement distance of 132 mm, the UPPT at the top is 86.6 μ s, while at the middle and the bottom, it is 77.0 μ s and 48.6 μ s, respectively (Table 5).

Table 5. The UPPT values at various positions on F1C1 sample

Location	UPPT(μ s)			
	132 mm	292mm	452mm	572mm
Top	86.6	150.4	171.3	214.6
Middle	77.0	140.1	165.2	206.4
Bottom	48.6	125.1	134.1	173.7

This trend continues as the measurement distances increase, with pulse propagation time gradually rising at each location. Specifically, at 572 mm, the UPPT at the top reaches 214.6 μ s, at the middle 206.4 μ s, and at the bottom 173.7 μ s (Table 5). This finding is consistent with previous studies that highlight the substantial effect of notch location on pulse propagation [5], [7], [9], [11]. The presence of cracks and

their orientation in relation to the transducer has a significant effect on wave velocity and propagation time, with reduced transducer-to-crack distances resulting in increased sensitivity for detecting cracks [5],[9].

CONCLUSION

This study has highlighted key factors affecting the durability and integrity of high-performance fiber-reinforced concrete (HPFRC) through non-destructive testing (UPV). The results indicate that an increase in the steel fiber content of concrete positively impacts flexural strength, enhancing crack resistance and stress distribution within the concrete structure. The presence of cracks alters the ultrasonic pulse transmission time (UPPT), with a distinct difference between cracked and non-cracked samples. Notably, inclined cracks were found to significantly influence crack width and UPPT, with UPPT values increasing substantially compared to the control sample with vertical cracks.

With the presence of multiple cracks, the UPPT values show an unclear trend, which could be due to the reduced material density around the cracks, creating unfavorable conditions for ultrasonic wave propagation. The effect of the number of cracks, particularly those with similar characteristics in depth, shape, and orientation, requires further investigation. Additionally, the positioning of the transducer with respect to the crack also affects the UPPT values, which should be taken into consideration during real-world structural assessments. In the context of structural safety management, understanding the effects of crack geometry is crucial for ensuring the long-term durability of concrete structures. The study's outcomes contribute to the refinement of non-destructive testing methods for more reliable monitoring and maintenance of concrete infrastructure, ultimately supporting sustainable construction practices by extending the service life of high-performance concrete structures.

REFERENCES

- [1]. AL-Ridha, A.S.D., Atshan, A.F., Abbood, A.A., Dheyab, L.S. (2017). Effect of Steel Fiber on Ultrasonic Pulse Velocity and Mechanical Properties of Self-Compact Concrete. <https://doi.org/DOI:10.15680/IJIRSET.2016.0608223>.
- [2]. Chaix, J.-F., Garnier, V., Corneloup, G. (2006). Ultrasonic wave propagation in heterogeneous solid media: Theoretical analysis and experimental validation. *Ultrasonics*, 44(200-210).
- [3]. Ersoy, H., Karahan, M., Babacan, A.E., Sünnetci, M.O. (2019). A new approach to the effect of sample dimensions and measurement techniques on ultrasonic wave velocity. *Eng. Geol.* 251, 63–70. <https://doi.org/10.1016/j.enggeo.2019.02.011>.
- [4]. Hasbullah, M.A., Yusof, R., Yusoff, M.N. (2017). Assessing the performance of concrete structure based on the width of the crack using UPV. *Journal of Engineering Science and Technology Special Issue on ISSC'2016*.
- [5]. Ivo, J., Roberto, C.A., Patrícia, B. (2010). Use of ultrasound to estimate depth of surface opening cracks in concrete structures. *E-Journal Nondestruct. Test. Ultrason.*
- [6]. Jedidi, M. (2018). Evaluation of the concrete quality using destructive and non-destructive tests. *MOJ Civ. Eng.* 4, 219–223. <https://doi.org/10.15406/mojce.2018.04.00122>.
- [7]. Kalyan, T.S., Kishen, J.M.C. (2013). Experimental Evaluation of Cracks in Concrete by Ultrasonic Pulse Velocity. *Proc. APCNDT*. www.ndt.net/?id=15207.
- [8]. Malek, J., Kaouter, M. (2014). Destructive and non-destructive testing of concrete structures. *Jordan J. Civ. Eng.* 8, 432–441.
- [9]. Ndagi, A., Umar, A.A., Hejazi, F., Jaafar, M.S. (2019). Non-destructive assessment of concrete deterioration by ultrasonic pulse velocity: A review. *IOP Conf. Ser. Earth Environ. Sci.* 357, 012015. <https://doi.org/10.1088/1755-1315/357/1/012015>.
- [10]. Pahlavan, L., Zhang, F., Blacquièrre, G., Yang, Y., Hordijk, D. (2018). Interaction of ultrasonic waves with partially-closed cracks in concrete structures. *Constr. Build. Mater.* 167, 899–906. <https://doi.org/10.1016/j.conbuildmat.2018.02.098>.
- [11]. Parihar, H.S., Shanker, R., Singh, V. (2022). Effect of variation of steel reinforcement on ultrasonic pulse velocity prediction in concrete beam. *Mater. Today Proc.* 65, 1486–1490. <https://doi.org/10.1016/j.matpr.2022.04.468>.

- [12]. Petro, J.T., Kim, J. (2012). Detection of delamination in concrete using ultrasonic pulse velocity test. *Constr. Build. Mater.* 26, 574–582. <https://doi.org/10.1016/j.conbuildmat.2011.06.060>.
- [13]. Pham Thi, N., Nguyen Sy, D., Dang Van, P., Dang Van, K., Nghia Nguyen, V., Do Anh, T., Liem Nguyen, D., Le Huy, V. (2021). Mechanical and damage sensing properties of smart high-performance fibre-reinforced concrete beams under bending. *Nondestructive Testing and Evaluation*. ISSN: 1058-9759 (Print) 1477-2671 (Online). Journal homepage: www.tandfonline.com/journals/gnte20.
- [14]. Pinto, R.C.A., Medeiros, A., Padaratz, I.J., Andrade, P.B. (2005). Use of ultrasound to estimate depth of surface opening cracks in concrete structures. *NDT.net*.
- [15]. Ryzy, M., Grabec, T., Sedlák, P., Veres, I.A. (2018). Influence of grain morphology on ultrasonic wave attenuation in polycrystalline media with statistically equiaxed grains. *The Journal of the Acoustical Society of America*, 143, 219-229.
- [16]. Wu, Z., Shi, C., He, W., Wu, L. (2016). Effects of steel fiber content and shape on mechanical properties of ultra high performance concrete. *Constr. Build. Mater.* 103, 8–14. <https://doi.org/10.1016/j.conbuildmat.2015.11.028>.
- [17]. Yoo, D.Y., Lee, J.H., Yoon, Y.S. (2013). Effect of fiber content on mechanical and fracture properties of ultra high performance fiber reinforced cementitious composites. *Compos. Struct.* 106, 742–753. <https://doi.org/10.1016/j.compstruct.2013.07.033>.

Assessment of interfacial bonding of recycled polymer fibers from waste fishing nets in concrete

Dang Van Phi^{1,2}

¹Department of Civil Engineering, Hanoi University of Mining and Geology, Hanoi, Viet Nam

²GECS Research Group, Hanoi University of Mining and Geology, Hanoi, Viet Nam

E-mail: dangvanphi@humg.edu.vn

Abstract: This study investigates the interfacial bonding behavior of recycled polymer fibers derived from discarded fishing nets when embedded in concrete. Utilizing waste fishing nets as reinforcement not only provides a sustainable alternative to conventional synthetic fibers but also contributes to environmental protection and resource efficiency. To assess bond performance, single-fiber pullout tests were conducted on recycled fibers with different geometries. The results demonstrated that fiber geometry, particularly diameter, plays a critical role in fiber-matrix interaction. Larger fibers (1.50 mm) exhibited approximately 46% higher bond strength and nearly seven times greater pull-out energy than finer fibers (0.30 mm), due to their increased contact perimeter, higher stiffness, and more effective stress transfer. These findings indicate that recycled fishing net fibers with moderate to large diameters can significantly enhance bond strength, energy absorption, and post-cracking toughness in cementitious composites. However, potential workability issues associated with larger fibers highlight the need for optimized mixing procedures. Further research employing advanced microstructural techniques is recommended to elucidate the role of fiber surface morphology and to develop surface modification strategies for improving the efficiency of finer fibers. Overall, this research advances the understanding of fiber-matrix interfacial behavior while presenting a viable pathway for recycling marine plastic waste into high-value construction materials.

Keywords: Interfacial bonding; recycled polymer fibers; concrete.

INTRODUCTION

The construction industry has long stood as a foundation of global progress, playing a pivotal role in driving infrastructure development, accelerating urbanization, and fostering socioeconomic growth (Ajayi et al., 2017). However, alongside these achievements, the sector is also associated with significant environmental challenges. The intensive extraction of mineral resources and fossil fuels, coupled with the generation of large quantities of construction and demolition waste, has contributed to severe environmental degradation, including greenhouse gas emissions, resource depletion, and ecosystem disruption (Zhang et al., 2019). Besides, global ecosystems face increasing threats from marine debris, which predominantly consists of plastic-based materials that are either slowly biodegradable or entirely non-biodegradable. Among these, abandoned, lost, or discarded fishing nets represent one of the most hazardous forms of marine litter (Spirkovski et al., 2019). These nets not only endanger marine biodiversity through entanglement and ingestion by aquatic organisms but also pose risks to human activities, such as maritime navigation, by becoming entangled in ship propellers (Richardson et al., 2019). The persistence of such waste materials in marine environments has raised concerns about long-term ecological impacts and potential risks to food security through microplastic contamination in seafood (Wang et al., 2016).

Several studies have explored the recycling of waste fishing nets (WFNs) in construction applications, mainly through their incorporation into soil- or cement-based materials, with the aim of enhancing mechanical strength and ductility as a potential alternative to conventional synthetic polymeric fibers (Orasutthikul et al., 2017) (Kim et al., 2008)(Spadea et al., 2015). Research on the mechanical properties of fishing nets recovered from the seafloor revealed that macro WFNs fibers exhibited approximately 20% lower tensile strength than new (unused) fishing nets that had not been exposed to seawater, while their elongation at break and Young's modulus remained comparable (Bertelsen et al., 2016). The effectiveness of recycled nylon fibers obtained from WFNs as reinforcement was investigated by applying tensile loads to cement mortar specimens (Spadea et al., 2015).

The recycling of WFNs has emerged as a sustainable approach to reduce marine plastic pollution while providing an alternative source of fiber reinforcement for cementitious composites. Although previous studies demonstrated that recycled WFN fibers retain acceptable mechanical properties with only a moderate loss in tensile strength, their reinforcing efficiency in concrete remains insufficiently understood. Therefore, this study examines: (1) the influence of fiber type on bond strength and (2) the effect of fiber type on pull-out energy in concrete.

MATERIALS AND EXPERIMENTAL PROCEDURE

Materials

Table 1 provides the mix proportions of the materials employed in this study, expressed as mass ratios of each constituent to cement (C) (Park et al., 2021). A matrix proportioned with a cement-to-sand ratio (C/S) of 1.0:1.5, incorporating 0.0009 superplasticizer and a water-to-cement ratio (W/C) of 0.45. A superplasticizer (SP) containing 25% polycarboxylate ether was employed to enhance the workability of the concrete mixture. Table 2 presents the physical

characteristics of the recycled polymer fibers, where Type 1 fiber (F1) exhibits a smaller diameter (0.3 mm) and lower specific gravity (0.95 g/cm³), while Type 2 fiber (F2) shows a larger diameter (1.5 mm) and higher density (1.20 g/cm³), with both types having the same fiber length of 40 mm. The characterization of WFNs fiber properties and its preparation for incorporation into cementitious composites were conducted in accordance with the procedures outlined in reference (Park et al., 2021).

Table 1. Matrix composition by weight ratio.

C	C/S	SP	W/C	Compressive strength (MPa)	Slump flow (mm)
1.0	1.5	0.0009	0.45	72.86	260

Table 2. Properties of recycled polymer fibers.

Fiber type	Diameter (mm)	Length (mm)	Specific Gravity (g/cm ³)
F1	0.3	40	0.95
F2	1.5	40	1.20

Experimental Procedure

The principal stages of the specimen preparation are described as follows (Park et al., 2021): Cement and silica sand were blended for 2 min before adding water and a polycarboxylate-based superplasticizer, followed by 3 min of mixing. Prior to casting, fibers were positioned in molds with a 10 mm embedment length, and the fresh mortar was slightly vibrated. Samples were then covered with plastic sheets and kept at room temperature for 24 h, demolded, and subsequently cured in water at 20 ± 2 °C for 28 d. Mechanical testing was carried out under dry conditions at 28 d. Figure 1 presents two groups of specimens prepared using fiber types F1 and F2, which are designated as MF1 and MF2, respectively.

The evaluation of concrete workability was conducted in accordance with ASTM C1437. The experimental device consisted of a truncated cone, 60 mm in height, with a base diameter of 100 mm and a top diameter of 70 mm. The matrix without any incorporated

fibers exhibited a slump flow of 260 mm, as summarized in Table 1. Besides, compressive strength testing was performed following ASTM C109/C109M. The specimens were subjected to a loading rate corresponding to a crosshead displacement of 1.0 mm/min, equivalent to a force application rate of 1000 N/s. The pullout response was determined using bell-shaped pullout specimens, following the methodology and procedures reported by Park et al. (Park et al., 2019). For each matrix, three specimens were subjected to pull-out testing, and the average bond strength was subsequently calculated (Park et al., 2021).

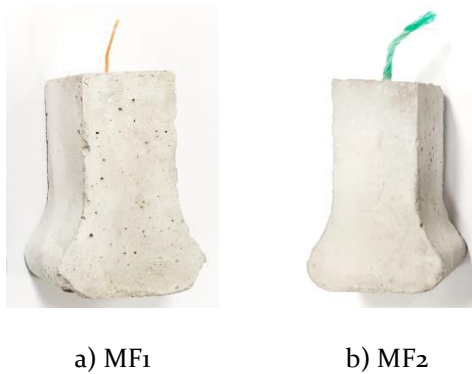


Figure 1. Sample of matrices

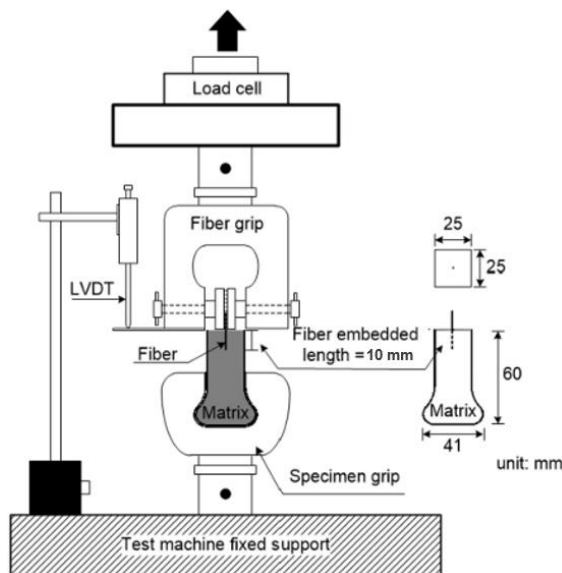


Figure 2 Experimental setup of the pullout test under static loading rate (Park et al., 2019).

A displacement rate of 0.0167 mm/s was adopted for the pull-out test to maintain stable testing conditions and reliably characterize the mechanical behavior of the fiber–concrete interaction (Park et al., 2019). The pull-out force was obtained through a load cell attached to the loading frame, whereas the fiber displacement during testing was monitored using a displacement measuring device (Fig. 2).

Figure 3 shows the pull-out behavior of straight fibers embedded in cement mortar. In this initial stage, the fiber-matrix system behaves elastically. The pullout load increases almost linearly with slip until reaching the critical load (P_{crit}) at displacement Δ_{crit} , where interfacial debonding starts to occur. As slip continues to increase, the pullout load rises further until it reaches the peak load (P_{peak}) at Δ_{peak} . This represents the maximum bond resistance of the interface, after which progressive debonding dominates. Beyond Δ_o , the interface is fully debonded, and the pullout resistance decreases gradually. The descending branch is governed mainly by frictional sliding and possible mechanical anchorage, while the shaded area under the curve represents the total pullout energy absorbed during the process.

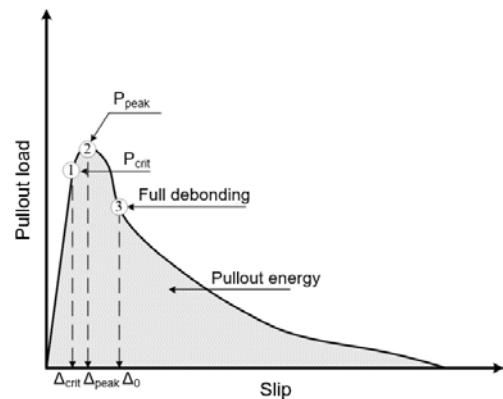


Figure 3. Force–displacement curve of a fiber during the pullout process (Park et al., 2019).

The resistance offered during fiber extraction is governed by the quality of the interfacial bond between the fibers and the mortar matrix. This bond can be categorized into three primary components: chemical,

frictional, and mechanical. The chemical component arises from adhesion between the fibers and the cementitious matrix formed during hydration. The frictional bond originates from the surface roughness at the interface between the fiber and the mortar, while the mechanical bond is attributed to deformation of the fiber geometry during extraction (Park et al., 2020).

The interfacial bond strength of steel fibers was evaluated using Equations (1) and (2). In these equations, τ_{eq} denotes the equivalent bond strength, calculated from the work performed during the fiber pull-out process, whereas τ_{peak} corresponds to the bond strength determined from the maximum pull-out load (P_{peak}). The exposed perimeter ($p_{exposed}$) is defined as the effective perimeter of fiber bundles that is directly in contact with the matrix, reflecting the actual surface curvature of the bundled fibers, as expressed in Equation (3). The parameter E_p was derived under the assumption that the bond strength remains constant along the entire embedment length (L_{em}) (Park et al., 2020).

$$\tau_{eq} = \frac{2E_p}{p_{exposed}L_{em}^2} \quad (1)$$

$$\tau_{peak} = \frac{P_{peak}}{p_{exposed}L_{em}}; \quad (2)$$

$$p_{exposed} = 2\pi R \frac{0.5\pi d_f}{d_f} = \pi^2 R. \quad (3)$$

where: R denotes the estimated radius of the fiber bundle, whereas d_f specifies the diameter of the constituent individual fibers forming the bundle.

RESULTS AND DISCUSSIONS

Influence of fiber type on the bond strength of concrete

Table 3 summarizes the properties of the recycled polymer fibers, showing a marked difference in diameter between F1 (0.30 mm)

and F2 (1.50 mm) while maintaining similar embedded lengths (10 mm).

Table 3. Mechanical properties of matrices in pullout test

Matrix	Peak bond strength (MPa)	Equivalent bond strength (MPa)	Pullout energy (N.mm)
MF1	1.71	1.67	99.19
MF2	2.50	2.44	691.25

The experimental results indicate a clear influence of fiber type on the interfacial bond strength between recycled polymer fibers and the cementitious matrix. Specifically, the peak bond strength (τ_{peak}) for MF2 was 2.50 MPa, which is approximately 46% higher than that of MF1 (1.71 MPa), as shown in Figure 4. Similarly, the equivalent bond strength (τ_{eq}) for MF2 reached 2.44 MPa, compared to 1.67 MPa for MF1 (Fig. 4). These findings confirm that variations in fiber geometry, particularly fiber diameter, play a decisive role in governing bond performance. Larger fiber dimensions lead to an increased maximum pullout load, a trend consistent with previously reported findings (Qi et al., 2019).

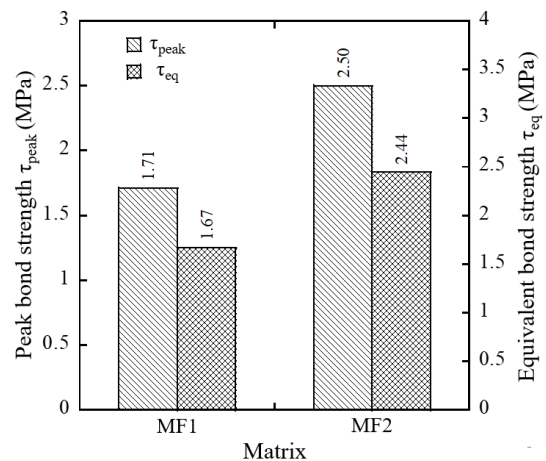


Figure 4. Comparison of bond strength between MF1 and MF2

Slender fibers are often considered beneficial due to their relatively high surface-to-volume ratio, which theoretically enhances interfacial adhesion and mechanical interlock (Wiemer et al., 2020). However, when the fiber

cross-section becomes excessively small, this advantage is offset by a reduced absolute contact perimeter with the surrounding matrix. In the case of MF1, the F1 fibers exhibited a high aspect ratio ($L/d \approx 133.33$), yet their fine diameter (0.30 mm) limited the effective area available for stress transfer. As a result, once interfacial debonding was initiated, the stress level dropped abruptly, leading to reduced pull-out resistance and lower energy absorption capacity (Park et al., 2020). In contrast, the thicker F2 fibers (diameter = 1.50 mm, $L/d \approx 26.67$) offered a substantially larger perimeter and higher stiffness, which facilitated a more uniform stress distribution along the embedded length. This enhanced contact area improved frictional resistance during pull-out and enabled the fibers to sustain higher bond stresses before failure.

Effect of fiber type on pull-out energy of concrete

The pull-out energy exhibited a consistent trend with bond strength. For MF2, the pull-out energy was 691.25 N-mm, compared with only 99.19 N-mm for MF1 (Fig. 5). These results indicate that fiber diameter plays a critical role in energy absorption capacity. In particular, F2 fibers exhibited nearly seven times greater pull-out energy than F1 fibers, reflecting their ability to mobilize higher peak shear resistance and sustain prolonged frictional sliding after debonding. The superior performance of F2 can also be attributed to the surface morphology of recycled polymer fibers. In the case of fibers with larger diameters, the interaction with the cementitious paste becomes more effective, thereby improving micro-mechanical interlock and resistance to sliding. This mechanism is likely responsible for the markedly higher pull-out energy recorded in MF2 (Sigrüner et al., 2023).

This study suggests that recycled polymer fibers with moderate to large diameters (≈ 1.5 mm) are more suitable for enhancing bond strength and energy absorption, which in turn contributes to improved post-cracking toughness of cement-based composites. However, the influence of fiber size must be balanced against workability concerns, as the

use of larger fibers may necessitate refined mixing approaches to minimize agglomeration. In addition, further research utilizing advanced characterization methods, such as scanning electron microscopy (SEM), X-ray diffraction (XRD), and mercury intrusion porosimetry (MIP), is essential to clarify how fiber surface features influence the bonding process and to design surface modification techniques that can improve the efficiency of recycled polymer fibers.

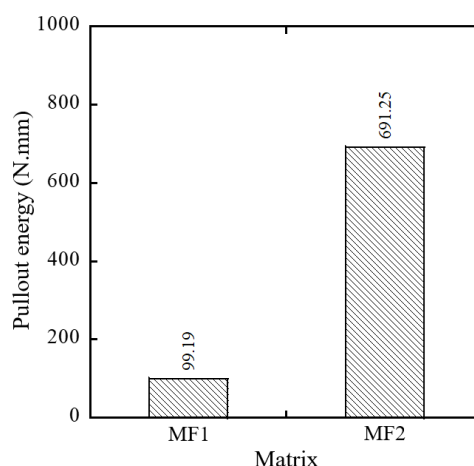


Figure 5. Comparison of pullout energy between MF1 and MF2 matrix

CONCLUSIONS

This study examined the bond performance of recycled polymer fibers derived from waste fishing nets (WFNs) in cementitious composites, with particular attention to the influence of fiber type on interfacial bond strength and pull-out energy. Two fiber types were tested: F1 (0.30 mm) and F2 (1.50 mm), both with the same embedded length (10 mm). Based on the experimental results, the following conclusions can be drawn:

- Fiber geometry, particularly diameter, plays a key role in bond behavior. Larger F2 fibers (1.50 mm) achieved approximately 46% higher bond strength than finer F1 fibers (0.30 mm).
- Pull-out performance was strongly dependent on fiber size, with F2 fibers

exhibiting nearly seven times greater pull-out energy than F1 fibers, attributed to increased contact perimeter, higher stiffness, and improved stress transfer.

- Recycled polymer fibers with moderate to large diameters are more effective in enhancing post-cracking toughness of cementitious composites, though workability concerns must be addressed. Further studies using advanced microstructural techniques are recommended to optimize fiber surface properties, particularly for finer fibers.

This study investigated the effects of various recycled polymer fibers on the bond strength and pullout behavior of concrete. Environmental factors, including humidity and temperature, which may influence fiber-matrix interactions, were not considered. Besides, the tensile strength and flexural strength of concrete containing recycled polymer fibers were not evaluated. Therefore, future research should examine these variables to achieve a more comprehensive understanding.

REFERENCES

- Ajayi, S.O., Oyedele, L.O., Bilal, M., Akinade, O.O., Alaka, H.A., Owolabi, H.A., 2017. Critical management practices influencing on-site waste minimization in construction projects. *Waste Manag.* 59, 330–339.
- Bertelsen, L., Svendsen, J.H., Køber, L., Haugan, K., Højberg, S., Thomsen, C., Vejstrup, N., 2016. Flow measurement at the aortic root - Impact of location of through-plane phase contrast velocity mapping. *J. Cardiovasc. Magn. Reson.* 18, 1–8.
- Kim, Y.T., Kim, H.J., Lee, G.H., 2008. Mechanical behavior of lightweight soil reinforced with waste fishing net. *Geotext. Geomembranes* 26, 512–518.
- Orasutthikul, S., Unno, D., Yokota, H., 2017. Effectiveness of recycled nylon fiber from waste fishing net with respect to fiber reinforced mortar. *Constr. Build. Mater.* 146, 594–602.
- Park, J.K., Kim, D.J., Kim, M.O., 2021. Mechanical behavior of waste fishing net fiber-reinforced cementitious composites subjected to direct tension. *J. Build. Eng.* 33, 101622.
- Park, J.K., Kim, M.O., Kim, D.J., 2020. Pullout behavior of recycled waste fishing net fibers embedded in cement mortar. *Materials (Basel)*. 13.
- Park, J.K., Ngo, T.T., Kim, D.J., 2019. Interfacial bond characteristics of steel fibers embedded in cementitious composites at high rates. *Cem. Concr. Res.* 123, 105802.
- Qi, J., Yao, Y., Wang, J., Han, F., Lv, J., 2019. Effect of sand grain size and fibre size on macro-micro interfacial bond behaviour of steel fibres and UHPC mortars.
- Richardson, K., Asmutis-Silvia, R., Drinkwin, J., Gilardi, K.V.K., Giskes, I., Jones, G., O'Brien, K., Pragnell-Raasch, H., Ludwig, L., Antonelis, K., Barco, S., Henry, A., Knowlton, A., Landry, S., Mattila, D., MacDonald, K., Moore, M., Morgan, J., Robbins, J., van der Hoop, J., Hogan, E., 2019. Building evidence around ghost gear: Global trends and analysis for sustainable solutions at scale. *Mar. Pollut. Bull.* 138, 222–229.
- Sigrüner, M., Hüsken, G., Pirsawetz, S., Herz, J., Muscat, D., Strübbe, N., 2023. Pull-out behavior of polymer fibers in concrete. *J. Polym. Sci.* 61, 2708–2720.
- Spadea, S., Farina, I., Carrafiello, A., Fraternali, F., 2015. Recycled nylon fibers as cement mortar reinforcement. *Constr. Build. Mater.* 80, 200–209.
- Spirkovski, Z., Ilik-Boeva, D., Ritterbusch, D., Peveling, R., Pietrock, M., 2019. Ghost net removal in ancient Lake Ohrid: A pilot study. *Fish. Res.* 211, 46–50.
- Wang, J., Tan, Z., Peng, J., Qiu, Q., Li, M., 2016. The behaviors of microplastics in the marine environment. *Mar. Environ. Res.* 113, 7–17.
- Wiemer, N., Wetzel, A., Schleiting, M., Krooß, P., Vollmer, M., Niendorf, T., Böhm, S., Middendorf, B., 2020. Effect of fibre material and fibre roughness on the pullout behaviour of metallic micro fibres embedded in UHPC. *Materials (Basel)*. 13, 1–21.
- Zhang, Y., Luo, W., Wang, J., Wang, Y., Xu, Y., Xiao, J., 2019. A review of life cycle assessment of recycled aggregate concrete. *Constr. Build. Mater.* 209, 115–125.

Proposing a solution to build pedestrian tunnels combined with commercial spaces in big cities in Viet Nam

Dang Van Kien^{1,2*}, Trivié Jeremy³, Daniel Dias^{2,3}, Do Ngoc Anh^{1,2}, Vo Trong Hung¹, Tran Tuan Diep⁴, Nguyen Khoa Linh¹

¹Hanoi University of Mining and Geology, Ha Noi, Viet Nam

²Tunnelling and Underground Space (TUS), Ha Noi, Viet Nam

³Polytech Grenoble, 14 place du Conseil Nationale de la Résistance, 38400 Saint-Martin-d'Hères, Grenoble, France

⁴Institute of Applied Mechanics and Informatics, Ho Chi Minh, Viet Nam

*Email: dangvankien@humg.edu.vn

Abstract: In Vietnam, pedestrian tunnels have been built quite extensively in some major cities such as the capital Hanoi and Ho Chi Minh City, Vung Tau... over the past 10 years. However, due to factors such as construction techniques, technology, and the habits of the people, the number of users of pedestrian tunnels is low. This research proposes to enhance the functionality of pedestrian tunnels by constructing commercial spaces such as souvenir and fast food stalls to attract more people to use the tunnels. This paper also develops a calculation model based on adjusting the size of the pedestrian tunnels to increase their functionality. To estimate stress and displacements of surrounding rock/soil and rock support by FEM analysis during build pedestrian tunnels in big cities in Viet Nam combined with commercial spaces. The pattern of deformation, stress state, and distribution of plastic areas are analyzed by Plaxis 2D or 3D software. The project was developed using Plaxis 3D based on detailed geotechnical data. The study includes safety factor analysis and ground displacement monitoring at Thuy Van pedestrian tunnels in Vung Tau city, Viet Nam. An optimized tunnel design was proposed. The study result provides a reliable way to analyze the stability of a pedestrian tunnel combined with commercial spaces and also will help to design or optimize the subsequent support.

Keywords Pedestrian tunnels, commercial spaces, Vung Tau, Hanoi, FEM analysis.

INTRODUCTION

Vietnamese citizens suggest that pedestrian tunnels should offer more functions and services such as better lighting, security, accessibility for disabled people, and even small shops or services to encourage their use. We can add that the locations of the pedestrian tunnels are designed inappropriately and have become a waste. For example, the pedestrian tunnels on Hoang Sa and Truong Sa streets with significant investment, were started in 2005 and inaugurated in 2015, but the current state of these pedestrian tunnels in the area has serious maintenance and cleanliness issues [1-2].

The pedestrian tunnel on Pham Hung Street in Ha Noi is another example, it has deteriorating infrastructure with cracks and damage. The issue of improving sanitation is quite urgent due to waste and stagnant groundwater. The tunnel lacks cameras to ensure the safety of pedestrians. The absence of signage inside the tunnel makes it difficult for residents [1-3].

Even the current situation of the pedestrian tunnel at Nga Tu So, Ha Noi remains quite deserted, with most residents using it for exercise. However, the tunnel is nearly 500 meters long and includes 12 entrances. The tunnel is designed for both pedestrians and cyclists, with lighting available 24/7. The security system includes cameras and patrols, making the tunnel relatively safe.

There are some images illustrating the reasons why pedestrian tunnels and exhibition are as should be combined. The reason is that pedestrian tunnels are built extensively in Hanoi and Ho Chi Minh City, but they are not used by the public. People still cross the busy streets, which is very dangerous (Figure 1)[1-2].



Figure 1. The pedestrian tunnel in Nguyen Xien, Ha noi

The tunnel project in Norway, where the longest cycling and pedestrian tunnel in Europe was opened in Bergen in 2023. This tunnel was not only built for mobility but also designed as a pleasant space to walk through with lights, art, and a safe environment (Figure 2). It became a strong symbol of sustainable mobility and urban innovation (Euronews Green, 2023) [4].



Figure 2. Artwork and installations line the tunnel in Bergen, taken from the Euronews website [4]

In modern urban areas around the world, the integration of pedestrian tunnels with commercial spaces has become popular. The large number of pedestrians crossing major intersections leads to congestion and accidents at four-way and five-way junctions. It is necessary to incorporate additional commercial and entertainment services to enhance infrastructure and increase public usage. However, the combination of pedestrian tunnels with commercial spaces has never been seen in Vietnam. For example, In South Korea, pedestrian tunnels are designed in conjunction with shopping centers, and these tunnels include business services, shopping stalls, and supermarkets as in the Figure 3.



Figure 3. Example of one pedestrian tunnels in South Korea

All around the world, pedestrian tunnels are developing, we can mention Canada with the Underground City in Montreal. A 32 km long network of tunnels with ceilings adorned with colorful LED lights, granite floors, and modern shopping centers. It is particularly connected to 10 subway stations, 2,000 shops, and office buildings (Figure 3). There is also the Inato Mirai Tunnel in Yokohama in Japan. It is a clean tunnel with shiny stone floors, featuring signage in both Japanese and English. It notably connects the port area to the train station, equipped with elevators and escalators (Figure 4).

Pedestrian tunnels around the world are not only a transportation solution but also a symbol of urban creativity, combining functionality and aesthetics. Major cities worldwide are heavily investing in this type of

infrastructure to move towards an environmentally friendly "walkable city" model.



Figure 4. A pedestrian tunnel in Canada [4]



Figure 5. A pedestrian tunnel in Japan [2]

All of this gave the idea to design a new type of pedestrian tunnel in the Vietnamese context, one that is larger, more welcoming, and includes small commercial spaces (like cafés, shops, or services). These additions could transform the tunnel into a useful and attractive urban space, not just a crossing point. The goal is to encourage real use by making the tunnel part of city life, rather than just an underground passage.

Case Study in Pedestrian Tunnel in Vung Tau

The study carried out on a real project site located in Vung Tau, a coastal city in southern Vietnam. It is situated near the Back Beach (Bãi Sau), which is a very popular area for both tourists and residents. As shown in the Figure 6, the proposed tunnel is designed to pass under Thùy Vân Street, a very wide and busy road. It has six traffic lanes, and it separates the beach from hotels, restaurants, and residential areas. Because of the heavy traffic, it is difficult and sometimes dangerous for pedestrians to cross the road, especially during weekends or holidays.



Figure 6. Location map of the tunnel [9]

The idea of building a pedestrian tunnel here is to improve safety and comfort for people going from the hotel zone to the beach. To make it more attractive and used by the public, the tunnel could include small commercial spaces, such as kiosks selling drinks, snacks, beach gear, or local products. This real location and its urban context were used as the base for my modelling work with Plaxis 3D in the following sections.

For the analysis of the tunnel stability, The study used the Strength Reduction Method in Plaxis 3D, which is based on calculating safety factors (F_s). This method is commonly used in geotechnical engineering and follows the principles of the Eurocode 7, which is the European standard for geotechnical design. Although The study used other tools and approaches during the project, this report focuses only on the Strength Reduction Method to give a clear overview of the overall study [10-11].

Plaxis calculates the safety factor by gradually reducing the soil strength parameters, cohesion (c) and friction angle (ϕ), until the model becomes unstable. This process simulates what happens if the soil is weaker than expected.

The software applies a reduction factor (strength reduction factor, SRF) to these parameters [5]:

$$C_{reduced} = \frac{c}{SRF}; \tan(\phi_{reduced}) = \frac{\tan(\phi)}{SRF};$$

It increases the SRF step by step until the model no longer reaches equilibrium. The last stable SRF value before failure is the global safety factor. According to Eurocode 7, two main safety factors are typically used [5]:

- 1.5 for long-term (permanent) conditions, which ensures long-term stability (e.g., when the tunnel is completed and in service),

- 1.3 for short-term conditions, such as during construction stages, when soil has not yet fully consolidated or drained.

These values mean that in the long term, the soil should be 50% stronger than the minimum required to resist failure. In the short term, a 30% margin is considered acceptable.

This method is useful because it does not require manually applying partial factors to each load or material, it gives a clear and global measure of stability, which is easy to compare across designs. Also, it can be used in complex 3D models where many interacting elements exist. In this case, this method helped me assess the tunnel's stability at different phases and identify potential weaknesses in the design.

Numerical modelling by Plaxis 3D Software and the Strength Reduction Method

The geometry of the tunnel was designed to meet both functional and safety requirements for pedestrian use in an urban environment. As shown in the Figure 8, the structure consists of a central underground passage going beneath the road, and four entrance and exit ramps connecting the tunnel to the surface.

This configuration allows easy access from both sides of the road and supports a good flow of pedestrians. The surface connections are placed strategically to reach sidewalks and nearby points of interest such as the beach and surrounding hotels.

This structure not only makes it safer to cross a wide avenue, but also offers space for small shops, making the tunnel more attractive

and useful for daily use. Figure 7 shows a cross-sectional plan of the base tunnel [7].

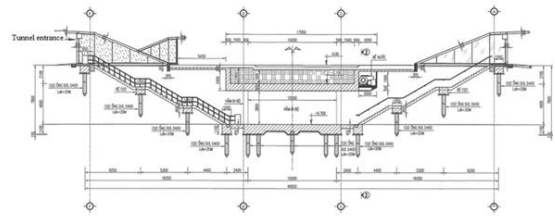


Figure 7: The cross-sectional plan of the base tunnel [7]

The pedestrian tunnel has a total width of 10 meters and a uniform height of 3 meters. It consists of a central walkway that is 6 meters wide, and a 4-meter-wide area on one side designed for kiosks. The total length of the tunnel body is 53.4 meters. Inside, the kiosks are separated by brick walls, which can either be decorated or left open, depending on how the space is intended to be used.

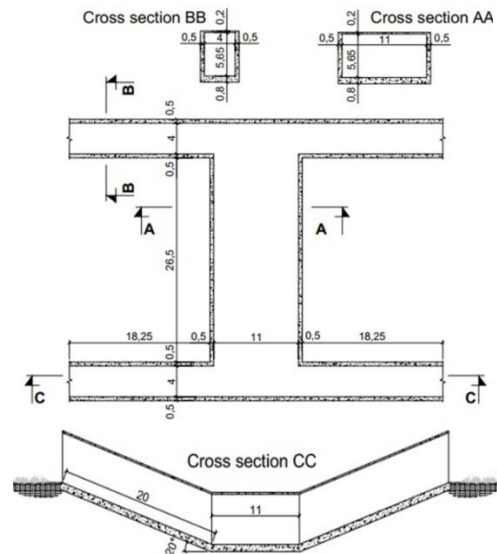


Figure 8. Plan and cross-sections of the pedestrian tunnel [7]

Figure 9 and Figure 10 illustrate the tunnel's cross-section dimensions and a general plan of the pedestrian tunnel. These drawings clearly show the areas dedicated to kiosks and small shops along the tunnel. These commercial spaces are designed to make the tunnel more attractive and inviting for pedestrians. The idea

is to encourage people to use this underground passage not only as a transit route, but also as a place for daily stops, promoting a livelier and more functional urban space.

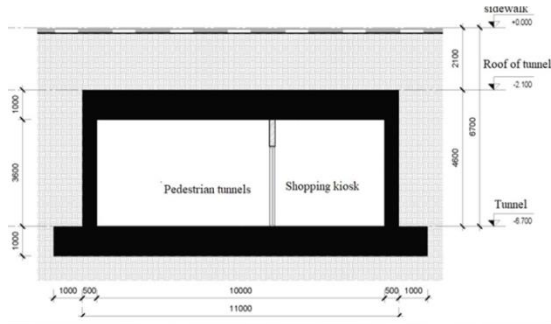


Figure 9. Tunnel's cross-section dimensions

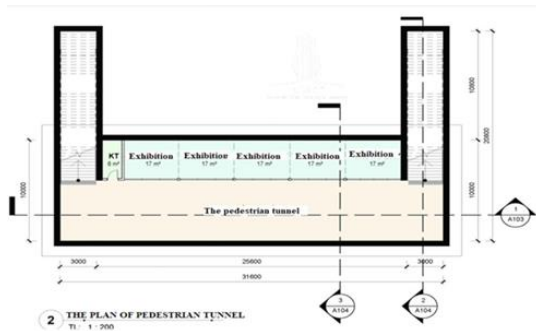


Figure 10: The general plan of the pedestrian tunnel

Approximately 40% of the tunnel's width is allocated to kiosks, while the remaining 60% is reserved for pedestrian circulation. This layout ensures that pedestrians can move freely in both directions without feeling confined or crowded. As shown in the plan, five individual commercial spaces of around 17 m² each can be created along the tunnel. These small shops will bring activity and life to the space, encouraging people to use the underpass and transforming it into a dynamic, multifunctional urban corridor.

Soil Characteristics

To run the 3D numerical simulation in Plaxis, the study used a detailed geotechnical soil model provided by my local supervisor. The data comes from a site in Thùỵ Vn, in Vung Tau, Viet Nam. Even though this is not the exact location of the tunnel, the geological conditions in the region are similar and the model is very complete. It provides values for 10 soil layers, including both sand and clay, with different mechanical behaviours. The Table 1 below shows the main geotechnical parameters used in the simulation.

Table 1. Presentation of the soil layer characteristics [7]

Soil layer	SL - Backfill	Layer 1.1 - Sand	Layer 1.2 - Clay	Layer 2.1 - Clay	Layer 2.2 - Clay	Layer 3 - Sand mix	Layer 4 - Fine sand	Layer 5 - Clay	Layer 6 - Clay loam	Layer 7 - Sand mix
Method	HS – DR	HS - UDR	HS - UDR	HS - UDR	HS - UDR	HS - DR	HS - DR	HS - UDR	HS - UDR	HS - UDR
γ_{unsat} (KN/m ³)	18	14,7	14,7	18,7	18,7	20	0,7	20,5	20	20,5
γ_{sat} (KN/m ³)	18,5	15,3	15,3	18,9	18,9	20,5	21,1	20,9	20,4	20,9
E_{50}^{ref} (KN/m ³)	10000	5243	5797	12319	8847	36555	28606	20373	16028	36941
E_{eo}^{ref} (KN/m ³)	10000	3985	4406	11211	8051	36555	28606	20373	16028	36941
E_{ur}^{ref} (KN/m ³)	30000	27265	30144	64061	46004	1E+05	85817	61119	48084	110823
m	0,5	0,9	0,9	0,85	0,85	0,5	0,5	0,8	0,8	0,5
v	0,25	0,35	0,35	0,3	0,3	0,3	0,3	0,3	0,3	0,3
c (KN/m ²)	5	11,7	13,8	35,2	27,9	8,2	0	68,4	46,6	14,2
φ (°)	25	12	13	15,1	13,2	28,5	33,5	19,5	25,6	27,9

R_{inter}	0,5	0,55	0,55	0,7	0,7	0,75	0,8	0,8	0,8	0,8
Base elevation of layer	-2,3	-11	-17,3	-26	-35,9	-39,2	-44,7	-54,8	-58,7	-65,1

Each soil layer is defined by several physical and mechanical parameters:

Soil layer: Name and number of the layer, ordered from top to bottom.

- Method: The soil behaviour model used in Plaxis. In this case, all layers use the Hardening Soil model (HS), which is more advanced than the Mohr-Coulomb model. It allows better simulation of real soil behaviour under loading.

The addition of DR (Drained) or UDR (Undrained) indicates whether the simulation allows water to flow through the soil.

- Drained conditions (DR) are used for coarse soils like sand, where water can move easily.

- Undrained conditions (UDR) are used for fine soils like clay, where water cannot escape quickly during construction phases.

- $\gamma_{unsat}/\gamma_{sat}$: Unsaturated and saturated unit weights of the soil. These represent the weight of the soil when it is dry (unsaturated) and when it is fully filled with water (saturated).

- $E_{50}^{ref}/E_{eod}^{ref}/E_{ur}^{ref}$: These are the main stiffness parameters used in the Hardening Soil model;

- E_{50}^{ref} : Secant stiffness in a standard drained triaxial test;

- E_{eod}^{ref} : Tangent stiffness for primary oedometer loading (used in 1 D compression);

- E_{ur}^{ref} : Unloading and reloading stiffness (elastic behavior);

- m: Power for stress dependency of stiffness moduli. A higher value means that stiffness changes more with pressure.

- ν : Poisson's ratio, which describes how the soil deforms laterally when compressed;

- c: Cohesion of the soil, which is the shear strength without friction;

- ϕ : Internal friction angle. It defines how well the soil particles resist sliding over each other;

- R_{inter} : Interface strength reduction factor between soil and structure (important for soil-structure interaction);

- Base elevation of layer: The depth at the bottom of each soil layer, used to define the vertical position in the model.

Before starting the numerical modelling in Plaxis 3D, it is essential to follow a clear sequence of steps to ensure a consistent and reliable simulation. The Figure 11 presents a flow chart outlining the main steps followed when using Plaxis 3D to simulate the excavation process and analyse the structural behaviour of the tunnel. It summarizes the different phases of modelling, including geometry definition, soil layering, boundary conditions, construction stages, and safety analysis. The diagram Figure 11 provides a clear overview of the overall methodology used throughout the project.

The numerical modelling of the pedestrian tunnel is presented based on a realistic construction sequence. Each step of the project is simulated in Plaxis 3D, considering soil-structure interaction and the local geotechnical conditions. At every stage, a stability analysis is performed using the Strength Reduction Method to ensure the safety and consistency of the design.

The modelling begins with the excavation of the central area of the tunnel, which runs under the main road. Once the excavation is complete, the central tunnel section is installed. The next steps involve the excavation of the four lateral ramps, which will provide pedestrian access from the surface. After this,

the temporary walls separating the central zone from the side ramps are removed, allowing full connection throughout the tunnel. The side sections of the tunnel are then installed. Finally, the entire structure is backfilled, completing the construction process.

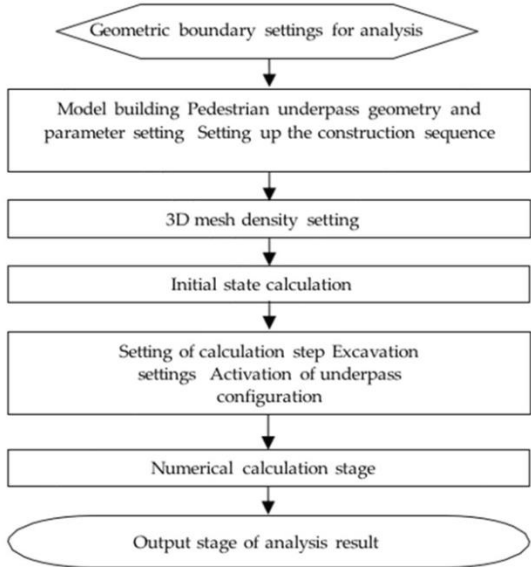


Figure 11. The flow chart outlining the main steps followed when using Plaxis 3D [3]

This progressive phasing helps to evaluate soil deformation and the global stability of the structure during each critical stage of the construction.

Regarding the mesh and computation settings, it could not refine the mesh too much because it made the calculations too heavy and very long on my computer. Despite this limitation, the study managed to reach around 100,000 nodes, which is already quite detailed for a student project and allows for good quality results. The study tried to keep a balance between accuracy and reasonable computation time.

RESULTS OF NUMERIAL MODEL

Excavation of the central area of the tunnel

The first phase of the project focuses on the excavation of the central underground zone, which corresponds to the main part of the tunnel that passes beneath the road. To

support the soil during the excavation, diaphragm walls were installed on both sides. These walls are 9 meters deep and 1 meter thick. The Figure 12, Figure 13 show the before and after of this step.

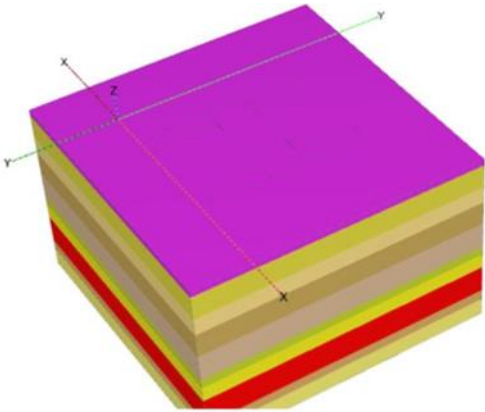


Figure 12. Plaxis 3D model before excavation

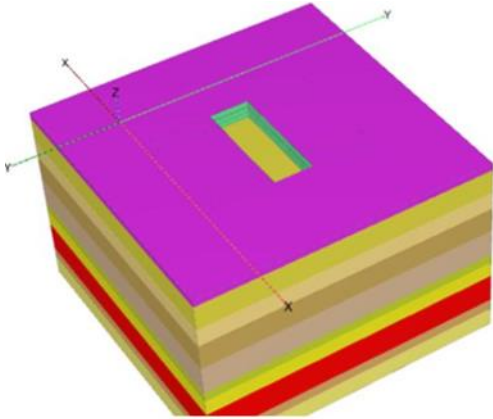


Figure 13: Plaxis 3D model after central excavation

The excavation was then carried out in six successive stages, allowing for gradual digging and better control of deformations. The model has analysed using the Strength Reduction Method to check the safety factors at the final stage (the most critical one). The horizontal displacement results obtained during the six excavation stages. The displacement results are presented in the Table 2.

The study carried out a small parametric study to optimize the thickness of the diaphragm walls. Several values tested: 1.0 m, 0.8 m, 0.7 m, 0.6 m, and 0.5 m, and observed the variations

in safety factors during the final excavation stage. The results are presented in the Table 3:

Table 2. Displacement results with a 1 meter thick diaphragm wall

Phase number	Excavation depth [m]	Horizontal displacement U_x [mm]	Horizontal displacement U_y [mm]
Phase 1	0	-	-
Phase 2	2	2.287	6.196
Phase 3	2.3	2.402	7.579
Phase 4	4	3.470	16.080
Phase 5	6	5.865	32.950
Phase 6	7.75	11.070	54.150

Table 3. Results of safety factors for different diaphragm wall thicknesses

Wall Thickness [m]	Safety Factor
1	4.370
0.8	3.835
0.7	3.857
0.6	3.816
0.5	3.625

However, the safety factor alone is not sufficient to determine the optimal wall thickness. The study therefore decided to analyse the horizontal ground displacements during each excavation phase for each tested thickness. The graph below shows the horizontal displacement U_x for each wall thickness (Figure 14).

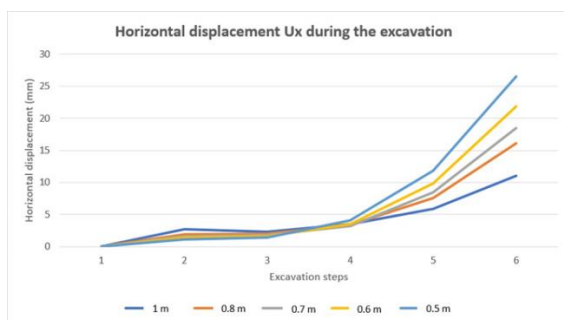


Figure 14. Graph showing horizontal displacement (U_x) for different wall thicknesses during excavation

The graph below shows the horizontal displacement U_y for each wall thickness (Figure 15).

The analysis of horizontal displacements revealed that for diaphragm wall thicknesses

down to 0.7 m, lateral movements remain below 20 mm along the x-axis and under 100 mm along the y-axis, even during the most critical excavation stages. Compared to thinner wall configurations, the 0.7 m thickness shows significantly better control of ground displacements, both along the x- and y-axes. This suggests improved performance in limiting deformations, which is essential in urban tunnelling projects.

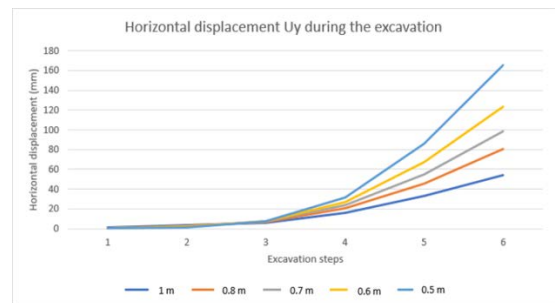


Figure 15: Graph showing horizontal displacement (U_y) for different wall thicknesses during excavation

Based on these findings, a wall thickness of 0.7 m appears to be a well-balanced solution, offering improved material efficiency and reduced construction costs compared to the initial 1.0 m design, while still maintaining satisfactory safety margins and deformation control.

Installation of the central part of the tunnel

To make the model as realistic as possible, the central part of the tunnel using three adjacent tunnel elements is represented. The main section is located in the center, while two smaller side sections were added in the opposite direction to align the tunnel openings with the future access ramps. This configuration was chosen to best match the real geometry of the tunnel entrances.

Although this is not a perfect solution, since it introduces two internal walls at the center of the tunnel that should not exist, it remains the closest approach I could implement within the limits of the software. A visual of the tunnel model is presented in the Figure 16.

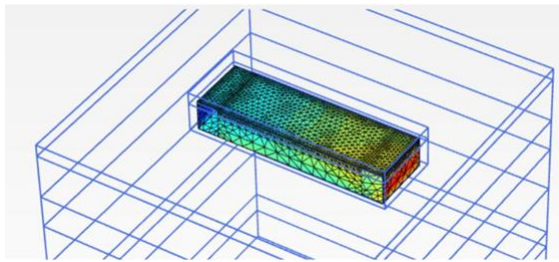


Figure 16. Plaxis 3D modelling of the central tunnel

Regarding results, the maximum horizontal displacement observed after this stage is 22.78 mm, as shown in the image below. The safety factor computed using the Strength Reduction Method is 1.869, indicating a stable configuration at this point of the construction (Figure 17).

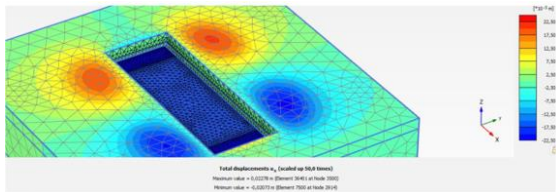


Figure 17: Displacement results of the installation of the central part of the tunnel

These results indicate a very stable structural behaviour at this stage of construction. The safety factor of 1.869 is well above the commonly accepted threshold of 1.5 for long-term conditions, suggesting that the system has a good margin of safety. Additionally, the maximum horizontal displacement of 22.78 mm remains relatively low, which is a positive outcome. Overall, this confirms that the design of the central tunnel section is both safe and effective.

Excavation of the four side sections

At this stage of the project, the excavation of the four side sections of the tunnel was carried out. These areas correspond to the future access ramps that will connect pedestrians from street level to the underground passage.

Before proceeding with the excavation, new diaphragm walls were installed around

each of these zones. These walls were modelled with the same optimized thickness of 0.7 meters as those used in the central section. Their role is to ensure soil retention and stability during the excavation phases of the access ramps.

The analysis focused on horizontal displacements (along the x and y axes) during three key stages of excavation: an initial phase, an intermediate phase, and a final phase. Figure 19 shows these three excavation stages in Plaxis 3D (Figure 18).

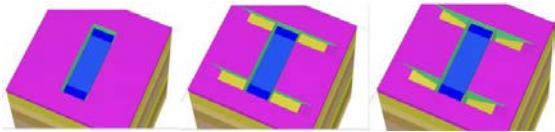


Figure 18. Plaxis 3D modelling of the three excavation stages

The Table 4 shows that the maximum displacements remain quite stable and low throughout the process, which confirms the good performance of the structure. These values are consistent with those observed during the previous stages. In parallel, the safety factors were recalculated after this excavation step. A slight decrease is observed, from 1.869 to 1.835. However, this variation is minimal and remains well above the critical thresholds, indicating that the overall stability of the model is not affected by this additional phase of excavation.

Table 4. Results of the three excavation stages

Stage 0		Stage 1		Stage 2		
Ux [mm]	Uy [mm]	Ux [mm]	Uy [mm]	Ux [mm]	Uy [mm]	
22.89	113.4	22.89	112	22.88	110.4	
1.869		1.861		1.835		Safety factors

CONCLUSION

In this study, a numerical analysis using finite element software has been conducted to investigate on the build pedestrian tunnels combined with commercial spaces in big cities in Viet Nam. Some interesting conclusions arising from numerical simulations are given: Throughout the different modelling phases,

excavation, structure installation, the results demonstrate a globally stable behaviour of the tunnel, with moderate displacements and satisfactory safety factors. The optimizations made, especially regarding the diaphragm wall thickness, helped achieve a good balance between structural stability and material efficiency. The final model meets safety requirements while displaying consistent and effective mechanical performance. A technically and economically viable solution, checked its compatibility with the ground conditions by analysing displacements, global stability, and structural deformability. Safety was also a major consideration, particularly through the calculation of safety factors at critical construction stages.

REFERENCES

- [1] An Sinh Xã Hội newspaper. (n.d.). Social Welfare and Mobility Initiatives. <https://ansinhxahoi.vn>
- [2] Dân Trí. (2023, September 23). *Nên bổ sung thêm công năng cho hầm đi bộ để khuyến khích người dân*. <https://dantri.com.vn/ban-doc/nen-bo-sung-them-cong-nang-cho-ham-di-bo-de-khuyen-khich-nguoi-dan-20230923142837450.htm>
- [3] Dang Van Kien, Lagrange, A., Tran Thu-Hang, Dias, D., & Do Ngoc Anh. (2024). *Research on displacement and deformation of diaphragm wall and adjacent structures during underground parking at Tran Hung Dao Station* [Unpublished student research project].
- [4] Euronews Green. (2023, May 3). *Car-free future: Europe's longest cycle tunnel aims to cut traffic in this Norwegian city*. <https://www.euronews.com/green/2023/05/03/car-free-future-europes-longest-cycle-tunnel-aims-to-cut-traffic-in-this-norwegian-city>
- [5] EN 1997-1 is Eurocode 7, a European standard for geotechnical design, specifically Part 1.
- [6]. City-level Research Project: Study on the Design of Public Underground Parking Systems in Hanoi. Code number 01C-04/06-2008-2.
- [7] Joint venture of BR Design Consulting Co., Ltd. and LMP Trading Investment Joint Stock Company BR-LMP. Design documents. Proposed technology solution for constructing the road tunnel under Thuy Van street at the intersection of Pho Duc Chinh street and Thuy Van street, Vung tau city. Vung Tau. 2024.
- [8] Doan The Tuong: Types of Foundations in Hanoi and Ho Chi Minh City and Their Evaluation for Underground Construction. APAVE. Expert Article - Underground Construction. 2008.
- [9] VOV Traffic newspaper. (n.d.). Traffic News and Public Transport Updates. <https://vovgiaothong.vn>
- [10] Zhang, D., Liu, B., & Qin, Y. (2016). Construction of a large section long pedestrian underpass using pipe jacking in muddy silty clay: A case study. *Tunnelling and Underground Space Technology*, 59, 200–210. <https://doi.org/10.1016/j.tust.2016.07.005>
- [11] Roger Frank, Fahd Cuira, Sébastien Burlon. Design of Shallow and Deep Foundations. CRC Press is an imprint of Taylor & Francis Group, LLC, 2022.

Research on the effect of thermodynamics in the LPG storage cavern of Cai Mep

Vu Tien Dung¹, Dang Van Kien^{1,*}, Nicolas GITZINGER², Ngo Minh Hoang¹, Le Sy Ha³

¹Ph.D student of Hanoi University of Mining and Geology, Ha Noi, Viet Nam

²Polytech Grenoble, 14 place du Conseil Nationale de la Résistance, 38400 Saint-Martin-d'Hères, Grenoble, France

³Military Engineering College, Thu Dau Mot, Ho Chi Minh, Viet Nam

*Email: dangvankien@humg.edu.vn

Abstract: The underground storage of GPL in a salt rock cavern must take the effects of temperature variations into account to model the different stress applied on the walls. The variations in temperature are caused either by the filling/emptying of the cavern but also because of the natural temperature of the rock around the cavern. The objective of this study is to understand and model the thermal and mechanical effects occurring within a salt cavern during LPG injection and withdrawal cycles. These processes are highly interdependent and governed by a set of coupled physical equations describing heat transfer, rock deformation, gas compression, and volume changes due to creep. The paper estimates stress and displacements of surrounding rock and rock support of the (LPG) storage cavern by FEM analysis. The pattern of deformation, stress state, and distribution of plastic areas are analyzed by RocScience – RS2 software. The stress concentrations, plasticity development, and displacements are all consistent with theoretical predictions and acceptable performance limits. This integrated approach strengthens the reliability of the design and supports the long-term use of salt caverns for LPG storage, with the condition that long-term surveillance and adaptive operational control are strictly followed. The study result provides a reliable way to analyze the effect of thermodynamics in the (LPG) storage cavern and also will help to design or optimize the subsequent support.

Keywords Thermodynamics, storage cavern, LPG, Cai Mep, FEM analysis.

INTRODUCTION

The Cai Mep LPG Cavern project is the largest underground storage facility in Southeast Asia, with a capacity of 240,000 tons of liquefied petroleum gas. This project is allowing the country to secure its energy needs by providing a consequent reserve of LPG, reducing the risks associated with importation or local production disruptions. This project is contributing to Vietnam's economy by decreasing gas prices and strengthening the country's strategic position in the regional energy sector. As shown in Figure 1, the Cai Mep LPG storage cavern was constructed near Vietnam's largest commercial port (Cai Mep's Port) to maximize logistical and economic efficiency. Situated just 10 km from the port, the cavern has direct access to the maritime transport infrastructure, facilitating the importation and the exportation of liquefied petroleum gas. This proximity decreases transportation costs and delivery costs. Near one of Vietnam's largest cities, Ho Chi Min city, it can provide a competitive storage and a good distribution in all the city.

Temperature variations cause thermal expansion and contraction in surrounding rock and soil, which leads to significant changes in stress and displacement. This can result in an increase in stress and deformation, affecting the overall stability of the storage cavern. Higher temperatures can increase deformation

rates and the risk of damage, especially near the cavern walls, while cyclic temperature and pressure changes can cause fatigue and creep deformation over time. It makes the increased stress and deformation: Temperature variations induce thermal stresses, which, combined with existing stress from the surrounding rock mass, can cause significant stress changes and lead to deformation. Greater deformation: Higher temperatures lead to greater deformation, with the maximum vertical and horizontal displacement often occurring in the vault (roof) and sidewalls of the cavern. Stress concentration: The range and concentration of principal stress increase with temperature, potentially leading to a greater plastic zone around the cavern. Cyclic loading effects: Repeated cycles of temperature and pressure changes, such as during gas injection and withdrawal, can lead to creep deformation and affect the long-term stability of the cavern. Research on the effect of thermodynamics in the LPG storage cavern is often carried out through analytical methods, experimental methods, and numerical modeling methods. However, the numerical modeling method is used more because it takes into account many influencing factors such as geological conditions, geomechanics, groundwater... In addition, numerical method takes into account heterogeneity, containing cracks in the rock mass [2-12]. The LPG storage cavern analysis has made remarkable growth for past several years due to development of numerical analysis method and computer development, given the situation that it was difficult to solve formula of elasticity, viscoelasticity and plasticity for dynamic feature of the ground when the constituent laws, yielding conditions of ground materials, geometrical shape and boundary conditions of structure were simulated in the past. That is, numerical analysis method has been introduced to geotechnical engineering and has contributed to analysis of creep feature, plastic (yielding) conditions and non-linearity of stress strain relations of the ground. The study selects the numerical method using Phase 2 software to simple analysis and more

reasonable design and construction management materials have been obtained.

GEOLOGICAL CONTEXT

This underground storage cavern was constructed at a depth of approximately 150 meters in hard rock. Geological analyses of the site were conducted by the Korean company HYOSUNG, which was also responsible for the construction. An additional soil layer lies above the rock mass. This layer is 54.6 meters thick and has an average unit weight of 18 kN/m^3 .

The site where the construction was carried out consists in different rock quality, present in various conditions, evaluated using the RMR scale from Grade 1 (VERY GOOD condition) to Grade 5 (POOR condition). Figure 1 below shows the distribution of rock mass quality around the different parts of the storage cavern [1].

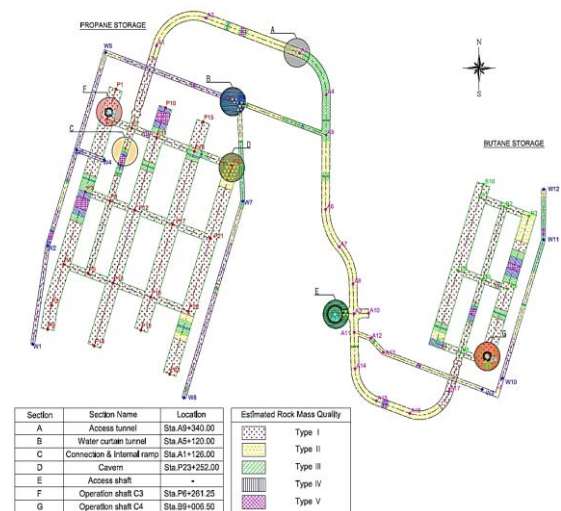


Figure 1. Storage cave plan with Rock Mass Quality rating

The entire storage cavern has been divided into different sections based on their use. For each section, an analysis of the distribution of rock classes was conducted. The predominant RMR (Rock Mass Rating) classes for each section of the tunnel, from section A (Access Tunnel) to section G (Operation Shaft) (Figure 2), are available in Table 1 below.

Table 1. Predominant RMQ classes for each section of the project [1]

Section	Section Name	Most Prevalent Rock Class
A	Access Tunnel	II
B	Water Curtain Tunnel	I
C	Connection and Internal Ramp	I

D	Cavern	I
E	Access Shaft	II
F	Operation and Shaft C ₃	I
G	Operation and Shaft C ₄	I

An estimation of the rock mass properties was then carried out on-site. Table 2 below summarizes the properties of the rocks sorted by RMR class (from Grade I to Grade V).

Table 2. Mechanical characteristics of the rock according to the RMR class [1]

Type	Unit Weight (kN/m ³)	Cohesion (kPa)	Internal Friction Angle (°)	Deformation Modulus (MPa)	Poisson's Ratio
GradeI	26.6	9000	54.8	41000	0.25
GradeII	26.5	7100	52.6	31300	0.25
GradeIII	26.4	5100	49.4	16100	0.25
GradeIV	26.1	3700	44.5	8300	0.25
Grade V	25.6	2500	40.6	4400	0.26

It is noticeable that the condition of the rocks surrounding the project is not homogeneous.

PROJECT GEOMETRY

In this study, this study will be focused on the section labeled S (in black dashed lines) in Figure 2. To simplify conversions and calculations, this section S will have a thickness of 1 meter for the subsequent modeling. The dimensions of this section, which represent the geometry of the model presented later, are shown below in Figure 3.

In this model, only the sections labeled B (water curtain), C (connection and internal ramp), and D (main cavern) will be included, as shown in Figure 2. A set of shotcrete liners and a rock bolt pattern were used to improve the mechanical stability of the gallery. Mechanical characteristics of support (by section) in the appendix. The elements were sized according to each type of gallery (different characteristics for sections B, C, and D of the model) [1].

THERMAL MODELING OF THE CAVERN

This equation models how temperature changes in the rock mass over time due to heat diffusion from or toward the cavern. It accounts for the 2D axisymmetric geometry of the cavern and is essential to capture the

thermal behavior of the surrounding salt (Figure 3) [4].

$$\frac{\partial T}{\partial t} = \alpha \left(\frac{1}{r} \frac{\partial}{\partial r} \left(r \frac{\partial T}{\partial r} \right) + \frac{\partial^2 T}{\partial z^2} \right)$$

In our case:

$k = 5 \text{ W/(m}^*\text{K)}$ the Thermal conductivity;

$\rho = 2650 \text{ kg/m}^3$ the density of the rock;

$C_p = 900 \text{ J/(kg}^*\text{K)}$ the heat capacity of the rock [4].

$$\alpha = \frac{k}{\rho x C_p} = \frac{5}{2650 \times 900} = 2,1 \times 10^{-6} \text{ m}^2/\text{s}$$

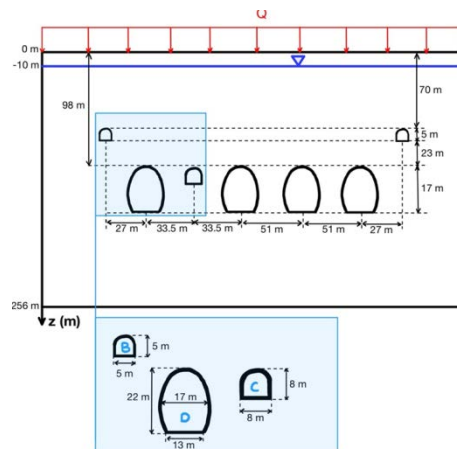


Figure 2: Model geometry

This diffusion controls how fast the rock heats

or cools. If it's low, heat stays trapped in the rock, delaying equilibrium with the gas. This influences cavern wall temperatures and resulting thermal stresses. Another equation can describe the rate at which heat is transferred through the rock to or from the gas [4]:

With: $q_{cond} = -k_{salt} \chi \frac{\delta T}{\delta r}$; $k_{salt} = 5 \text{ W/(m}^2\text{K)}$

$T_{rock} = 25 + 0.03 \times 161 = 30^\circ\text{C}$ the temperature of the rock at 161m deep (half of the cavern $T_{gas} = 15^\circ\text{C}$ as we can see on Figure 3 below; $e = 25\text{m}$, the distance from the cavern where the rock is affected by the gas temperature from Figure 3 below.

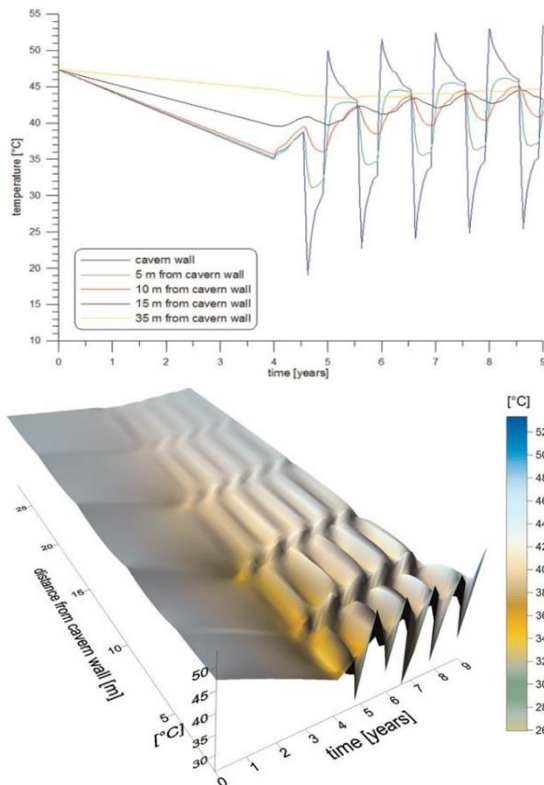


Figure 3. The temperature over time in underground cavern

With this result we can quantify how quickly the gas will equilibrate thermally, if this value is too high, it can affect the rapidity of the variation in stresses and so weaken the rock. The injection of GPL in the cavern can make variations in the gas temperature and convection can append in this situation. We can calculate it by using the equation [4]:

$$q_{conv} = hx(T_{salt} - T_{gas})$$

with:

$H = 17\text{m}$, the height of the cavern;

$T_{salt} = 30^\circ\text{C}$ and $T_{gas} = 15^\circ\text{C}$ as before

$$q_{conv} = h \times (T_{salt} - T_{gas}) = 17 \times (30 - 15) = -255 \text{ W/m}^2.$$

This equation allows to estimate the heat exchange between the rock and gas that can affect the pressure of the gas and the stress in the cavern. After calculating the thermal exchanges between the rock and the gas, we can estimate the stresses in the rock salt.

Firstly, with the thermal strain, that can be used to know if the salt will expand or contract and can prevent the potential cracks if the tension is too high.

$$\varepsilon_{th} = \alpha_T \times \Delta T = 4 \times 10^{-5} \times -15 = -6 \times 10^{-4}$$

With $\alpha_T = 4 \times 10^{-5}^\circ\text{C}^{-1}$, the coefficient of thermal expansion of the rock.

The thermal stress is the next calculation. It helps to find the stress caused by the change in temperature in the rock [4].

$$\sigma_{th} = E \times \alpha_T \times \Delta T$$

With, $E = 25000 \text{ MPa}$, the Young modulus of the salt rock

$$\sigma_{th} = E \times \alpha_T \times \Delta T = 25000 \times 4 \times 10^{-5} \times -15 = -15 \text{ MPa}$$

This tensile traction simulates the effect of thermal contraction due to the LPG cooling the cavern wall, but since salt is in a confined state, it cannot expand freely and then is subject to internal stress changes.

This stress needs to be inferior to the tensile strength of the salt which is around 1,5 MPa or it can cause fracturing and increase the permeability of the rock.

Then, effective stress is used to evaluate the combination of gas pressure and in-situ stresses, to verify the condition of the rock [4].

$$\sigma_{eff} = \sigma_{min} - P_{cavern}$$

With: $\sigma_{min} = 2650 \times 9.81 \times 161 = 4 \times 10^6 \text{ Pa}$ the

minimum stress on the cavern walls; $P_{cavern} = 0.8 \text{ MPa}$, the pressure of the LPG in the cavern.

$$\sigma_{eff} = \sigma_{min} - P_{cavern} = 4 - 0.8 = 3.2 \text{ MPa}$$

NUMERICAL MODEL OF THERMAL CAVERN

To make the model of the cavern, the study used the software Phase2, used for all types of models. It is particularly useful for analyzing slope stability, designing underground and surface excavations, and assessing support systems in rock and soil. It's also used for groundwater analysis, dynamic analysis, and even the design of foundations and embankments (see Figure 4).

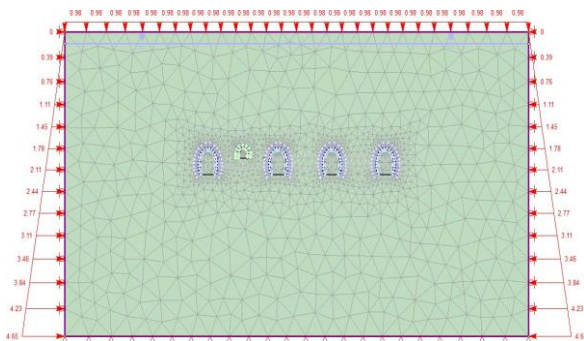


Figure 4. Numerical model with the thermodynamics boundary conditions

To create the model, the study need to start by adding the geometry of the project, with the excavations the study will do later. The model only represents the rock part, there is a layer of 54,6m of soil of 18 kN/m³, above, defined by the added the studyight of 18x54,6=984 kPa ≈0,98 MPa.

The boundaries added are, on the bottom, fixed in x and y axis, to stabilize the model and represent the fact that there is rock under and on the sides of the model, so the rock can't move. On the sides, the x axis is fixed to represent the rocks on the sides outside of the model.

To estimate the value of the stress added by the increase of temperature depending on the depth on the sides of the model, the study need to know the temperature at the bottom of the model. The study know that the dept is

310m so by estimating an added temperature of 0.03°C/m, the study can find:

$$\Delta T_{310m} = 310 \times 0.03 = 9,3 \text{ }^{\circ}\text{C}$$

By using the equation

$$\sigma_{therm} = E \times \alpha \times \Delta T$$

The study can find added stress due to the temperature of the rock, With, $E = 25000 \text{ MPa}$, the young modulus of the salt rock, $\alpha = 4 \times 10^{-5} \text{ }^{\circ}\text{C}^{-1}$, the coefficient of thermal expansion of the rock; $\Delta T = 15^{\circ}\text{C}$,

$$\sigma_{therm} = E \times \alpha \times \Delta T = 25000 \times 4 \times 10^{-5} \times 9,3 = 9,3 \text{ MPa}$$

The added stress due to the increase in temperature in the model is 9,3 MPa, that we can add on the vertical sides of the model by using a triangular force because the stress increase with the depth (see Figure 5).

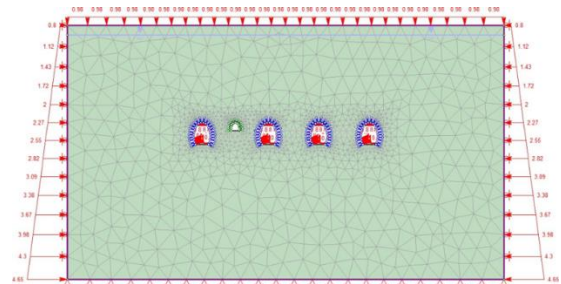


Figure 5. Model geometry

In the present simulation, thermal stresses induced by gas injection were modeled. The injected LPG enters the cavern at a temperature of approximately 15°C, while the surrounding rock mass at a depth of 160 meters maintains a natural geothermal temperature of around 30°C. This results in a negative thermal gradient between the cavern wall and the gas.

Due to this temperature drop, the surrounding rock tends to contract. However, because this contraction is limited by the surrounding formation, it generates tensile thermal stresses that act radially toward the cavern center. To simulate this mechanical behavior, an equivalent thermal traction load of 15 MPa was applied inward on the cavern wall in the model.

The magnitude of this thermal stress is estimated using the classical linear thermoelastic formula:

$$\sigma_{therm} = E \times \alpha \times \Delta T = 25000 \times 4 \times 10^{-5} \times -15 = -15 \text{ MPa}$$

Where:

$E = 25 \text{ GPa}$ is the Young's modulus of salt rock;

$\alpha = 4 \times 10^{-5} \text{ } ^\circ\text{C}^{-1}$ is the thermal expansion coefficient;

$\Delta T = -15 \text{ } ^\circ\text{C}$ is the temperature difference between the rock and the gas.

This gives a resulting tensile stress of -15 MPa , consistent with the value used in the model. The direction and magnitude of the load were validated and applied in the numerical simulation, ensuring realistic representation of thermal contraction effects. This consideration is essential to assess potential fracturing or dilatancy risks due to cooling of the cavern wall (See Figure 6).

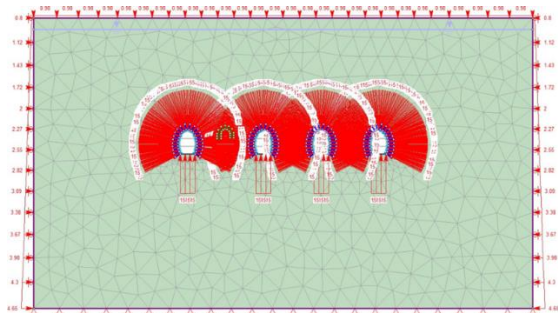


Figure 6. Model geometry

RESULTS OF NUMERIAL MODEL

Stress distribution

The simulation results show a redistribution of the mechanical stress field around the cavern due to the presence of excavations and the application of internal pressure and thermal contraction. As expected, stress concentrations appear around the cavern roof, floor, and side walls, particularly at points where the geometry is a curve or has discontinuities. This is consistent with theoretical predictions from elastic cavity

mechanics, where local curves increase stress magnitude (See Figure 7).

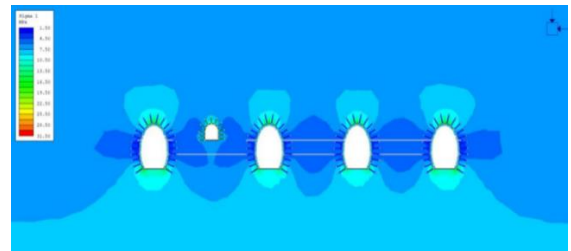


Figure 7: Stress distribution around the cavern

The peak vertical stress reaches values around 22 MPa in the top and floor of the cavern. This remains below the compressive strength of salt, which generally lies between 25 and 30 MPa in confined conditions. The horizontal stresses also show better values in the inter-pillar zones between neighboring caverns, with the geometry increasing the stress intensity locally.

Importantly, the presence of thermal stress slightly reduces confinement near the cavern wall. However, it does not cause the vertical or horizontal principal stress to become tensile anywhere in the model. The minimum principal stress remains negative, indicating that tensile failure does not occur even under the applied cooling condition.

This stress state is critical for safety. Theoretical framework, salt's tensile strength is very low ($1\text{--}3 \text{ MPa}$ unconfined), and tensile fracturing is a major risk during rapid cooling. In this model, thermal loading has been applied as a static traction, ensuring that this aspect of the design remains within safe boundaries

Plastic Zones

The next critical result from the simulation involves identifying the development of plastic zones around the cavern boundary. Phase2 identifies zones where the stress state meets or exceeds this limit, marking them as "yielded."

In the current simulation, yielded zones are most prominent in the roof and shoulder regions of the cavern, where geometric curves

intensify stress. This aligns with expected theoretical behavior: the transition from wall to roof typically concentrates both shear and tensile components of stress. These areas are often the most critical in underground excavation design.

The yielded zones remain shallow and do not extend beyond 4 meters from the cavern wall. Furthermore, yielded zones remain disconnected and localized, avoiding formation of continuous failure surfaces and no plasticization occurs in the vertical bolts separating adjacent caverns, ensuring that the mechanical separation is preserved Figure 7 .

Yielded zones in salt are not necessarily indicative of failure because of salt's ductile nature means that some localized yielding is expected and even beneficial, as it allows stress redistribution without catastrophic rupture. However, if yielding becomes continuous or progresses to large zones, the risk of progressive damage increases, especially under cyclic loading or long-term creep.

During the use of the storage cavern, these plastic regions are likely to accelerate local creep, meaning displacements may concentrate in these zones over time. Also, because the yield penetration remains limited, there is no indication of global instability in the cavern system under current loading. Vietnam's tropical monsoon climate, with three-quarters of its territory being mountainous and a coastline of over 3,260 km, provides significant renewable resource potential. The country possesses abundant biomass, solar, hydropower, and wind resources.

Displacement Field

Mechanical convergence and vertical displacement are natural responses of salt under pressure. In Phase2, displacements are calculated using the elastic and plastic properties of the material and boundary conditions. These results provide information about cavern closure behavior, surface settlement risk, and long-term deformation trends.

The simulation shows that radial convergence of the cavern walls reaches a maximum of 6 mm at the center of the walls, this displacement is symmetric around the cavern, indicating stable boundary conditions and a well-centered cavity.

Convergence of this order is expected in salt storage caverns, especially during early operational phases. It reflects a combination of, internal gas pressure, thermal stress and elastic-plastic material response.

In practice, such displacements would be compensated by pressure adjustments to maintain volume integrity. The magnitude and symmetry of this result confirm that the model behaves consistently with real-life salt cavern operations.

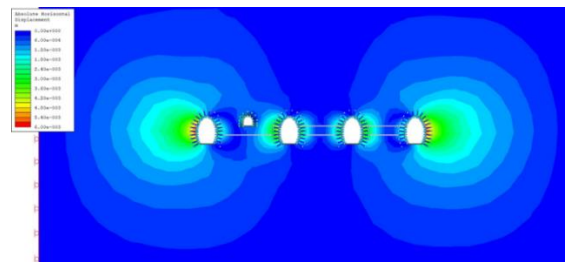


Figure 7. Plastic zones around the cavern

Vertical movements were also recorded, with the roof settlement that is observed at around 2,5 cm, concentrated above the cavern and surface settlement at the top of the domain remains minimal, at less than 4 mm.

These values are considered safe because the vertical displacements are moderate and do not threaten the integrity of the cavern roof and surface settlements remain well below thresholds of concern for infrastructure.

These observations are consistent with the typical behavior of salt formations, in which stress redistributes laterally, limiting vertical deformation propagation. This further supports the validity of the model geometry and boundary conditions.

THERMAL Effects

The interaction between thermal loading and mechanical response is a central concern

in the design and operation of LPG storage caverns. The injection of cooler LPG into warmer rock salt leads to a temperature gradient that induces stress through thermoelastic contraction.

This stress is tensile and radial, acting inwardly on the cavern wall. In the simulation, this is implemented as a boundary load of -15 MPa. The value is significant because the tensile strength of salt is low (1-3 MPa unconfined), but under confined in-situ conditions, salt can accommodate higher tensile stresses due to lateral support from the surrounding material.

The simulation shows that this thermal stress can reduce the confinement at the cavern boundary, increases the potential for yielding, particularly near curved zones and has a controlled and symmetric effect.

If LPG were injected at 0 °C instead of 15 °C, the thermal gradient would increase to -30 °C:

$$\sigma_{th} = E \times \alpha_T \times \Delta T = 25000 \times 4 \times 10^{-5} \times -30 = -30 \text{ MPa}$$

This level of thermal stress would approach or exceed the confined tensile strength of the salt, so most likely cause fracturing, particularly in already yielded or curved areas

This shows the importance of thermal management to avoid rapid temperature changes, control injection temperature to prevent excessive contraction and monitor thermal fronts through sensors embedded in the salt body.

The low thermal diffusivity of salt means that temperature changes propagate slowly. This supports the simulation's decision to apply a uniform thermal stress over the cavern wall, representative of a long-duration thermal equilibrium.

One limitation of the current model is its inability to explicitly simulate fracture initiation. Phase2 models plasticity and stress states, but not discrete cracking unless additional fracture mechanics modules are

used. However, based on the theoretical tensile stress thresholds and the observed stress fields, it is clear that the current 15°C thermal gradient is safe, but a greater thermal gradient (>30°C) could initiate fracture. Also, repeated thermal cycling could degrade integrity over time through fatigue.

To mitigate such risks, the design must limit thermal gradients to below 20-25°C during rapid injections and possibly preheat caverns or slow down injection rates. Moreover, there is a need to consider integrating a fracture model in future simulations to be sure about the stability of the cavern.

In reality, heat exchange between the LPG and surrounding rock is not instantaneous. Instead, a thermal front develops around the cavern, that causes stress to build up progressively as this front move,

The thermal diffusivity α is around $2.1 \times 10^{-6} \text{ m}^2/\text{s}$, as found before. This low value justifies the assumption of near stable conditions in the simulation and supports the use of uniform radial thermal stress instead of transient thermal-mechanical coupling.

However, for more precise simulations, we should use a transient thermal field that could be computed using time-stepping (not possible on this version of Phase2). This would yield time- varying thermal stress, allowing the evaluation of fracture timing. It would also better capture thermal fatigue over multiple injection cycles.

CONCLUSION

In this study, a numerical analysis using finite element software has been conducted to investigate on the effect of the thermodynamics in the LPG storage cavern of Cai Mep. Some interesting conclusions arising from numerical simulations are given: the modeled LPG storage cavern, located at 160 meters depth in a salt formation, is mechanically stable and operationally safe under the modeled conditions. The stress concentrations, plasticity development, and

displacements are all consistent with theoretical predictions and acceptable performance limits.

This integrated approach strengthens the reliability of the design and supports the long-term use of salt caverns for LPG storage, with the condition that long-term surveillance and adaptive operational control are strictly followed.

REFERENCES

- [1] Hyosung VINA Chemicals Co., Ltd. (2019). Report on technical design of underground storage Cai Mep-LPG-CV-GR-U-0002. Vung Tau.
- [2] Dang Van Kien, Do Ngoc Anh, Do Ngoc Thai (2022). Numerical Simulation of the Stability of Rock Mass around Large Underground Cavern. *Civil Engineering Journal*, 8, 1, pp. 81-91.
- [3] Hung Trong Vo, Kien Van Dang, Anh Ngoc Do và Thai Ngoc Do (2022). Study on the stability of rock mass around large underground cavern based on numerical analysis: A case study in the Cai Mep project. *Journal of Mining and Earth Sciences* Vol. 63, Issue 3a (2022), pp.50 – 58.
- [4] Chao Zhang, Pinjia Duan, Yuke Cheng, Na Chen, Huan Huang, Feng Xiong, Shaoqun Don. A 2D stability analysis of the rock surrounding underground liquified natural gas storage cavern based on COMSOL Multiphysics. *Environmental Earth Sciences* (2022) 81:172. *Energy Geoscience*. Volume 5, Issue 3, July 2024, 100301
- [5] Åberg, B. (1978). Prevention of gas leakage from unlined reservoirs in rock. *Storage in Excavated Rock Caverns: Rockstore* 77, 399–413. doi:10.1016/b978-1-4832-8406-4.50074-9
- [6] Bjorn Nilsen, 2021, Norwegian oil and gas storage in rock caverns e Technology based on experience from hydropower development
- [7] NAN ZHANG and all., 2019, Tightness Analysis of Underground Natural Gas and Oil Storage Caverns With Limit Pillar Widths in Bedded Rock Salt
- [8] Zhechao Wang and all., 2015, Design and test aspects of a water curtain system for underground oil storage caverns in China
- [9] Zhongkui Li and all., 2016, Design and operation problems related to water curtain system for underground water-sealed oil storage caverns
- [10] Qi-Hua Zhang and all., 2021, Hydraulic Conductivity of Rock Masses Surrounding Water Curtain Boreholes for Underground Oil Storage Caverns
- [11] Hiroki KUROSE and all., 2014, Construction of Namikata underground LPG storage cavern in Japan
- [12] Altaf Usmani and G. Kannan, 2010, Analysis of Ground water flow in Underground storage caverns. International conference on Environmental GeotechnologyAt: New DelhiVolume: Proceedings of ICEG, 210 New Delhi.

DOI: 10.15625/vap.2025.0255

Mitigation Measures Against Salinity Intrusion in Civil Engineering Works: A Brief Review

Nguyen Trong Van, Nguyen Ngoc Truc*, Nguyen Thao Ly

VNU-School of Interdisciplinary Sciences and Arts, Vietnam National University, Hanoi. No.144 Xuan Thuy str., Cau Giay ward., Hanoi, Vietnam

*Email: trucnn@vnu.edu.vn

Abstract: Saltwater intrusion is an increasingly critical issue affecting the durability and sustainability of civil structures, especially in coastal and deltaic regions. This paper provides a brief review of anti-salinization solutions for civil engineering structures and coastal infrastructure systems. The study synthesizes anti-corrosion techniques for reinforced concrete, waterproofing methods for subsurface structures, and retroactive sealing measures for existing constructions. The limitations of anti-salinization solutions were discussed. The findings highlight that integrating material innovation, multilayer protection systems, and moisture control technologies can significantly enhance the longevity of structures exposed to saline environments. This review serves as a reference for designing resilient infrastructures in regions vulnerable to saltwater intrusion.

Keywords: saltwater intrusion, corrosion protection, waterproofing, rising damp, electro-osmosis, sustainable construction.

INTRODUCTION

Saltwater intrusion has severe and far-reaching consequences across multiple sectors, including socio-economic systems and the environment, including increased economic costs associated with desalination, infrastructure repair (Alameddine et al., 2018). Another significant aspect of saltwater intrusion lies in its detrimental effects on civil engineering structures and infrastructure systems. Saline environments decrease the durability, service life, and safety of buildings and infrastructure, especially in coastal and

deltaic areas (Gao & Wang, 2017; Tansel & Zhang, 2022). The major impacts on civil structures include material corrosion, loss of concrete strength, foundation settlement and deformation, degradation of locally sourced construction materials, corrosion of technical equipment and utilities, and increased maintenance and repair costs for corrosion control (Schmitt et al., 2009; Abdelhafez et al., 2022).

Globally, numerous studies have focused on the technical challenges posed by salinity intrusion and have proposed increasingly sophisticated and effective engineering mitigation measures.

REINFORCED CONCRETE CORROSION PROTECTION APPROACHES

Corrosion of reinforced concrete is one of the primary causes of deterioration, reduced durability, and compromised structural safety in saline or marine environments. Studies have demonstrated that the presence of chloride (Cl^-) and sulfate (SO_4^{2-}) ions in seawater, saline vapors, or brackish groundwater disrupts the passive protective film on the surface of reinforcing steel, thereby initiating electrochemical corrosion processes (Alonso et al., 2000; Angst et al., 2009). To mitigate these effects, various anti-corrosion strategies have been developed, which can be broadly categorized into three main approaches: (1) enhancement of steel rebar corrosion resistance, (2) improvement of concrete properties, and (3) application of surface coatings and protective admixtures.

Improvement of steel rebar properties

Alloyed steel has been one of the earliest research directions in corrosion control. Since the studies of Stodart and Faraday (1820), it has been demonstrated that the incorporation of nickel or chromium in steel significantly enhances its corrosion resistance. Stainless steels containing 11-30% chromium are now considered optimal materials for use in saline and aggressive environments (Adams, 1983; Cobb, 2010; Liu et al., 2016).

In addition, heat treatment methods such as cooling by oil-water mixture help control the microstructure of the oxide layer on the steel surface, thereby improving corrosion resistance compared with conventional water cooling methods (Chen et al., 2017). Recent studies (Shang et al., 2021) have proposed graphene-epoxy composite coatings on steel surfaces, which improve bond strength with concrete and reduce corrosion current density by up to 60%. In Japan, the use of galvanized steel combined with high-strength concrete in the coastal bridge projects has been shown to extend the service life of structures by 25-30 years (Goyal et al., 2018).

Surface treatment of steel rebar reinforcement

Protective coatings are a widely adopted measure to prevent direct exposure of steel to corrosive environments. These can be broadly divided into two categories: (1) physical barrier coatings and (2) electrochemical coatings. Physical barrier coatings such as epoxy, polyurethane resins, and polymer films provide isolation between steel and the surrounding medium. Metallic coatings (Zn, Ni, Cr, Al, etc.) are also commonly applied to improve resistance to saline environments. Among them, zinc coating has proven to be the most effective, reducing corrosion rates by 10-100 times depending on exposure conditions (Panossian et al., 2005; Dudek et al., 2018). Epoxy coatings have also shown high durability and adhesion, effectively minimizing the penetration of water and salts (Manning, 1996; Nguyen & Nguyen, 2018). The sacrificial coating method, based on electrochemical principles, employs active metals such as zinc, aluminum, or magnesium

to act as sacrificial anodes, thereby protecting the underlying steel (Schmidt et al., 2006; Al-Nafai, 2022). These systems not only provide a physical barrier but also maintain active cathodic protection, offering excellent performance in marine environments (Bates & Arnell, 1997; Morton et al., 2021).

Improvement of concrete properties

Concrete serves as the primary physical barrier preventing the ingress of aggressive ions. Reducing porosity and permeability significantly enhances the durability and service life of structures. According to Fajrin and Pratama (2016), increasing the cement-to-sand ratio from 20:80 to 30:70 reduces concrete water absorption by up to 65%. Studies have also confirmed that the permeability coefficient increases proportionally with the water-to-cement ratio (Shamsai et al., 2012). Besides mixture proportion optimization, the incorporation of mineral admixtures such as fly ash, silica fume, or marble dust effectively fills capillary pores, reducing chloride ion penetration. Bargaheiser and Butalia (2007) reported a 30-40% decrease in permeability when 30-50% fly ash was added. Similarly, Anwar and Roushdi (2013) found that concrete containing 10% silica fume and 25% fly ash absorbed 60% fewer chloride ions compared to ordinary concrete. In addition, Ghorbani et al. (2018) demonstrated that replacing 20% of cement with marble-granite dust effectively inhibited corrosion in a 3.5% NaCl solution after 92 days of exposure.

Surface treatment of concrete

Surface treatment of concrete is a cost-effective solution to prevent the ingress of aggressive agents. According to EN 1504-2:2004, three main categories of surface protection methods include (1) surface coatings, (2) hydrophobic impregnation, and (3) impregnation. Polymer-based coatings (e.g., epoxy, acrylic, polyurethane) or polymer nanocomposites have been shown to enhance durability, elasticity, and abrasion resistance (Pour-Ali et al., 2015; Sakr & Bassuoni, 2021). Moreover, polymer-cement mortars incorporating acrylate or epoxy binders have

demonstrated excellent chemical resistance and waterproofing performance (Diamanti et al., 2013). The hydrophobic impregnation technique, using silane or siloxane compounds, creates a water-repellent surface layer that limits the penetration of water and saline ions without altering the appearance of concrete (de Vries & Polder, 1997). Meanwhile, impregnation with silicate-based solutions (Li et al., 2024) seals internal capillary pores, improving concrete density and reducing permeability.

Table 1. Summary of main solutions for reinforced concrete corrosion protection

Category	Technical Objective
Improvement of steel rebar properties	Enhance corrosion resistance and minimize electrochemical reactions (Adams, 1983; Liu et al., 2016).
Surface treatment of steel rebar	Create anti-corrosive coatings using epoxy, polyurethane, or galvanization (Panossian et al., 2005).
Improvement of concrete properties	Reduce porosity, increase density, and enhance resistance to saline ion ingress (Fajrin & Pratama, 2016).
Surface treatment of concrete	Apply polymer coatings, hydrophobic impregnation, or silicate-based sealers (Li et al., 2024).

In summary, corrosion protection measures focus on improving material performance, applying protective coatings, and enhancing concrete compactness to restrict the ingress of chloride (Cl^-) and sulfate (SO_4^{2-}) ions. The main groups of anti-corrosion strategies are summarized in Table 1.

WATERPROOFING FOR SUBSURFACE INFRASTRUCTURES

In civil engineering projects located in areas with high groundwater tables or exposure to saline water, capillary rise and upward moisture intrusion from the subsoil are major factors causing material degradation, reinforcement corrosion, and a consequent reduction in the service life of structures. Therefore, the design and implementation of

waterproofing systems for underground and below-grade structures are essential requirements in modern construction, particularly in coastal and low-lying deltaic regions.

Installation of physical waterproofing layers

Physical waterproofing layers represent the most fundamental and widely adopted approach to prevent the ingress of moisture and groundwater through the capillary pores of walls and floors (Henshell, 2016). The mechanism relies on the formation of a continuous impermeable membrane that completely isolates the structure from damp soil and external moisture sources. Historically, waterproofing materials have evolved from slate and lead sheets used in the 19th century to modern materials such as bituminous membranes, polyethylene (PE) films, bitumen felt, plastic-coated metal sheets, and silicone-based creams (BSI, 2022; Kubal, 2008). According to the British Standard BS 8102:2022, waterproofing membranes may be applied on the external face, internal face, or sandwiched between wall and floor layers to block water ingress from the surrounding environment. Modern waterproofing systems employ a wide variety of materials, including bituminous felt sheets, polyethylene membranes, silicone creams or injectable wall sealants, and thick bitumen coatings (ABCB, 2022). The Australian Building Code (ABCB, 2022) and the New South Wales Residential Construction Standard specify minimum material thicknesses: 0.5 mm for embossed polyethylene membranes and 2.5 mm for bitumen-impregnated materials. Waterproofing layers must be continuous and carefully detailed at critical points such as wall-floor junctions, base slabs, door thresholds, roofs, and pillars. Additionally, damp-proof membranes should extend at least 150 mm above ground level to ensure adequate protection against rising damp and surface water splash.

Masonry drainage system

For structures exposed to a high risk of groundwater infiltration, the installation of an internal drainage system provides an effective

supplementary measure to the external waterproofing layer. The principle of this system is to allow a limited amount of water to penetrate through dense concrete, which is then collected and discharged via channels or sump pits (Chudley & Greeno, 2014). According to the BS 8102:2022 classification, this method corresponds to a Type C waterproofing system, which employs an internal cavity behind the wall to create a drainage zone. This is combined with a sloped concrete floor directing water toward a collection sump and an automatic pumping system. The approach is particularly advantageous for the retrofitting of basements or existing structures, where installing external membranes is difficult or impractical (BSI, 2022).

Physical barrier and drainage system combination

Studies have shown that the integration of both waterproofing membranes and internal drainage systems achieves more durable and reliable waterproofing performance than either method used independently (Chudley & Greeno, 2014). In such hybrid systems, the inner wall surface is replaced by a cavity drainage membrane, typically a thick polymer sheet with studded dimples that allow free water flow toward the drainage collection system. This configuration not only prevents seepage but also maintains a dry, maintainable interior environment with minimal aesthetic impact.

Sub-soil drainage system

One of the traditional waterproofing techniques, dating back to ancient Roman engineering, involves constructing sub-soil drains along the exterior of foundation walls to relieve hydrostatic pressure and prevent lateral seepage (Franzoni, 2014). These drains are often filled with coarse-grained, permeable materials such as gravel or left as open cavities to promote evaporation and help maintain wall dryness. However, as Franzoni (2018) noted, empirical data on the quantitative performance of such systems remain limited, and design

practices largely rely on local experience and site-specific geotechnical conditions.

RISING DAMP TREATMENT APPROACHES FOR EXISTING BUILDINGS

Rising damp is among the primary factors contributing to the deterioration and loss of durability in civil structures, especially in regions with high groundwater tables or saline intrusion. When water and dissolved salts migrate upward through the capillary pores of walls, floors, or foundations, they not only induce moisture accumulation but also promote salt crystallization, leading to cracking, spalling, and structural degradation (Franzoni, 2014; Delgado et al., 2016). Remediation of rising damp in existing buildings is often complex due to limitations in structural intervention. Recent studies classify remedial measures into two main categories: (1) passive solutions, which aim to control environmental conditions, reduce moisture, and limit salt transport; and (2) active solutions, which actively extract or redirect moisture and salts from building materials (Delgado et al., 2016).

Physical damp proof course (DPC)

The traditional and most effective method to prevent capillary rise is the installation of a physical damp-proof barrier between the wall and the foundation. This approach involves horizontally cutting the wall at 150-200 mm above ground level and inserting an impermeable layer such as polyethylene sheeting, rubber membranes, or bituminous plastic materials (Camuffo, 2019). The inserted DPC layer blocks upward moisture and salt migration from the soil into the wall, significantly reducing the moisture content above it. However, the section of the wall below the barrier remains exposed to salt accumulation and may continue to deteriorate over time. Therefore, physical DPC installation is more suitable for new constructions or cases where structural cutting can be safely executed.

Chemical damp proof course (CDPC)

For structures where wall cutting is not feasible, the chemical damp-proof course provides a viable alternative. This technique involves drilling a horizontal series of holes along the base of the wall and injecting waterproofing solutions (Franzoni, 2014). Commonly used agents include sodium or potassium silicates (Na_2SiO_3 , K_2SiO_3), melted paraffin, aluminum stearate, or silicon-based compounds such as silanes and siloxanes, which either block capillary pores or form a hydrophobic lining (I'Anson & Hoff, 1988; Alfano et al., 2006). In some cases, silicate solutions react chemically with calcium hydroxide ($\text{Ca}(\text{OH})_2$) in the substrate to form calcium silicate hydrate gels (C-S-H), which reduce porosity and enhance waterproofing performance (Sharpe, 1977). Although the effectiveness of CDPC depends strongly on the salinity level and porosity of the substrate, it remains one of the least invasive and most practical methods for existing structures.

Moisture evaporation enhancement techniques

Another approach focuses on enhancing internal evaporation to balance capillary moisture movement. As early as the 20th century, the Knapen siphon system was introduced, where perforated ceramic or metal tubes were installed diagonally into walls to allow moist air to escape while enabling dry air ingress (Heiman et al., 1973). Although this method is energy-free and mechanically simple, subsequent studies revealed that salt crystallization within the tubes can lead to blockage and performance reduction after a few years (Heiman, 1982). Modern systems employ automated base-wall ventilation, with adjustable airflow rates responsive to ambient temperature and humidity conditions (Torres & Peixoto de Freitas, 2007), helping maintain stable dryness and significantly reduce rising damp effects.

Electrokinetic moisture control systems

Recent developments in electrokinetic technologies (electro-osmotic drying) provide innovative means to control moisture flow in

capillary-active materials through the application of an electric field. In the active electro-osmosis method, electrodes are embedded into the wall and the surrounding soil. When a direct current is applied, water molecules migrate toward the cathode, thereby reducing the moisture content within the wall (Franzoni, 2014). Experimental studies have reported moisture reductions of up to 60-70% after several weeks of operation. Conversely, passive electro-osmosis operates without external power, relying on the natural potential difference between damp walls and the surrounding ground to maintain long-term equilibrium (Camuffo, 2019). Although installation and operational costs are relatively high, electrokinetic systems are regarded as advanced, non-invasive technologies, suitable for heritage buildings and massive masonry walls where traditional mechanical interventions are impractical.

Table 2 summarizes the main remedial and mitigation approaches for rising damp treatment in existing buildings.

Table 2. Summary of main approaches for rising damp treatment in historical buildings

Method	Working Principle
Physical damp-proof course	Insertion of a polyethylene or bitumen moisture barrier at 15-20 cm above ground level (Camuffo, 2019)
Chemical dam proof course	Injection of silicate, paraffin, or siloxane solutions to seal capillary pores (Alfano et al., 2006; Sharpe, 1977)
Base-wall Ventilation	Inducing airflow at the wall base to promote drying and reduce internal moisture (Vogeley, 1985)
Active Electro-osmosis	Application of a DC electric field to drive water migration away from the wall (Landivar Macias & Rotta Loria, 2020)

DISCUSSION

From the synthesis above, it can be seen that solutions for mitigating steel reinforced concrete corrosion are now relatively diverse, ranging from enhancing steel quality and

applying protective coatings to improving concrete properties and employing surface treatments. However, each method has inherent limitations. For example, the effectiveness of protective coatings applied to steel reinforcement is highly dependent on coating thickness (Morcillo, 1984). These coatings may also be damaged during transportation or installation, resulting in localized corrosion (Kumar, 1998). Several studies have further indicated that such coatings may impair the bond between steel and concrete, thereby facilitating corrosion (Shang et al., 2021). Similarly, concrete surface protection systems are only effective when cracking does not occur before the application of waterproofing agents (Dai et al., 2010). Concrete may crack due to transportation, during construction processes, compromising the effectiveness of protective layers. Waterproofing agents themselves deteriorate when exposed to the fluctuations in temperature, humidity, and solar radiation (Kozak, 2015). Moreover, their performance depends on the penetration depth of the treatment into the pore system, which in turn is influenced by the concrete moisture content at the time of application (Basheer et al., 1998). This necessitates careful assessment of concrete moisture and meticulous selection of coating materials. Despite these challenges, advancements in science and technology, together with integrated protective measures, have led to substantial progress in reinforced concrete durability, extending service life and delaying the corrosion initiation process.

In contrast, protective measures specifically aimed at preventing salt ingress into building materials have received much less attention. Some existing methods originated from concepts intended solely for waterproofing subgrade components and thus do not account for salt-induced structural deterioration. For example, installing internal wall drainage systems only mitigates moisture on the interior side, while salts continue to attack the exterior masonry, ultimately degrading construction materials. Physical barrier systems are considered among the most

effective solutions for both waterproofing and blocking salt migration into building envelopes. However, these systems also present considerable limitations. The waterproofing performance of membrane installations depends primarily on the integrity of the barrier layers. Any defects or discontinuities allow water and salts to infiltrate the structural system. Physical membranes may fail due to chemical attack, differential settlement-induced cracking, or incorrect installation, which may create a direct pathway linking the saline environment below and the structure above (Young, 2008). A solution considered as simple in principle and straightforward to implement is the construction of subsurface drainage trenches beneath walls. Although this method has been proposed for a long time, its effectiveness and the corresponding systematic evaluations have not been thoroughly documented in the literature. Consequently, its actual moisture prevention performance, selection of construction materials, and optimal design thickness remain challenging. Meanwhile, many technical measures proposed for mitigating rising damp in existing buildings are inherently passive. They merely reduce the height of capillary rise rather than completely preventing the process. Therefore, to ensure the effectiveness when applied to newly constructed buildings, further research is required to refine, revise, and enhance these existing solutions.

CONCLUSION

Saltwater intrusion poses serious threats to the durability and service life of civil and coastal infrastructures. This review highlights that the most effective mitigation strategy lies in the integrated application of corrosion protection, waterproofing, and moisture control technologies. For reinforced concrete, the combination of dense concrete mixes, corrosion-resistant steel, and protective coatings significantly improves performance in saline environments. The retrofitting techniques, such as chemical damp-proofing, ventilation systems, and electrokinetic drying provide significant protection for existing

structures. Subgrade waterproofing approaches require more in-depth and systematic studies. Providing guidelines on the applicability conditions of anti-salinity solutions is one of the research interests. In addition, future research should focus on the development of self-healing materials, real-time corrosion monitoring systems, and predictive modeling of structural degradation under salinization. The synergy between materials innovation, advanced monitoring, and sustainable design practices will be crucial for ensuring the long-term resilience of construction in salt-affected regions.

ACKNOWLEDGEMENTS

This research was funded by Vietnam National University, Hanoi, under grant number QG.23.69, "Research and development of anti-salinity technology for civil construction with shallow foundation in coastal areas".

REFERENCES

- ABC. (2022). Housing provisions standard. Australian Building Codes Board.
- Abdelhafez MA, Ellingwood B, Mahmoud H. Hidden costs to building foundations due to sea level rise in a changing climate. *Sci Rep.* 2022 Aug 18;12(1):14020. doi: 10.1038/s41598-022-18467-3. PMID: 35982136; PMCID: PMC9388630.
- Adams, R. O. (1983). A review of the stainless steel surface. *Journal of Vacuum Science & Technology A: Vacuum, Surfaces, and Films*, 1(1), 12-18. <https://doi.org/10.1116/1.572301>.
- Alameddine, I., Tarhini, R., & El-Fadel, M. (2018). Household economic burden from seawater intrusion in coastal urban areas. *Water International*, 43(2), 217-236. <https://doi.org/10.1080/02508060.2017.1416441>.
- Alfano, G., Chianarella, C., Cirillo, E., Fato, I., & Martellotta, F. (2006). Long-term performance of chemical damp-proof courses: Twelve years of laboratory testing. *Building and Environment*, 41(8), 1060-1069. <https://doi.org/10.1016/j.buildenv.2005.04.020>.
- Al-Nafai, I. (2022). Novel zinc-rich organic coatings for offshore and infrastructure applications [Doctoral dissertation, The University of Manchester]. <https://research.manchester.ac.uk/en/studentTheses/novel-zinc-rich-organic-coatings-for-offshore-and-infrastructure->.
- Alonso, C., Andrade, C., Castellote, M., & Castro, P. (2000). Chloride threshold values to depassivate reinforcing bars embedded in a standardized OPC mortar. *Cement and Concrete Research*, 30(7), 1047-1055. [https://doi.org/10.1016/S0008-8846\(00\)00265-9](https://doi.org/10.1016/S0008-8846(00)00265-9).
- Angst, U., Elsener, B., Larsen, C. K., & Vennesland, Ø. (2009). Critical chloride content in reinforced concrete—A review. *Cement and Concrete Research*, 39(12), 1122-1138. <https://doi.org/10.1016/j.cemconres.2009.08.006>.
- Anwar, M., & Roushdi, M. (2013). Improved concrete properties to resist saline water using environmental by-products. *Water Science*, 27(54), 30-38. <https://doi.org/10.1016/j.wsj.2013.12.003>.
- Bargaheiser, K., & Butalia, T. S. (2007). Prevention of corrosion in concrete using fly ash concrete mixes. *Concrete Technology Forum*, 1-16. <https://citeseerx.ist.psu.edu/document?repid=rep1&type=pdf&doi=0f77cc5f37e4317efd3085497f85546af71c04d2>.
- Basheer, L., Cleland, D. J., & Long, A. E. (1998). Protection provided by surface treatments against chloride induced corrosion. *Materials and Structures*, 31(7), 459-464. <https://doi.org/10.1007/BF02480469>.
- Bates, R. I., & Arnell, R. D. (1997). Microstructure of novel corrosion-resistant coatings for steel components by unbalanced magnetron sputtering. *Surface and Coatings Technology*, 89(3), 204-212. [https://doi.org/10.1016/S0257-8972\(96\)02890-3](https://doi.org/10.1016/S0257-8972(96)02890-3).
- BSI. (2022). Protection of below ground structures against water ingress: Code of practice. British Standards Institution.
- Camuffo, D. (2019). Rising damp treatment and prevention. In *Microclimate for cultural heritage* (pp. 153-166). Elsevier. <https://doi.org/10.1016/B978-0-444-64106-1.00009-0>.
- Chen, Q. A., Liu, L. Z., Liu, X., & Liu, X. H. (2017). Improvement to anti-rust property of hot rolled rebar by compact oxide scale. *Journal of Central South University*, 24(12), 2813-2818. <https://doi.org/10.1007/s11771-017-3696-1>.
- Chudley, R., & Greeno, R. (2014). *Building construction handbook* (10th ed.). Routledge.

- de Vries, I. J., & Polder, R. B. (1997). Hydrophobic treatment of concrete. *Construction and Building Materials*, 11(4), 259–265. [https://doi.org/10.1016/S0950-0618\(97\)00046-9](https://doi.org/10.1016/S0950-0618(97)00046-9).
- Delgado, J. M. P. Q., Guimarães, A. S., de Freitas, V. P., Antepara, I., Kočí, V., & Černý, R. (2016). Salt damage and rising damp treatment in building structures. *Advances in Materials Science and Engineering*, 2016, 1–13. <https://doi.org/10.1155/2016/2456384>.
- Dai, J.-G., Akira, Y., Wittmann, F. H., Yokota, H., & Zhang, P. (2010). Water repellent surface impregnation for extension of service life of reinforced concrete structures in marine environments: The role of cracks. *Cement and Concrete Composites*, 32(2), 101–109. <https://doi.org/10.1016/j.cemconcomp.2009.11.001>.
- Diamanti, M. V., Brenna, A., Bolzoni, F., Berra, M., Pastore, T., & Ormellese, M. (2013). Effect of polymer modified cementitious coatings on water and chloride permeability in concrete. *Construction and Building Materials*, 49, 720–728. <https://doi.org/10.1016/j.conbuildmat.2013.08.050>.
- Dudek, A., Strzelczak, K., & Lisiecka, B. (2018). Surface properties in S500MC steel with zinc coating. *MATEC Web of Conferences*, 183, 02006. <https://doi.org/10.1051/mateconf/201818302006>.
- EN 1504-2:2004. (2004). Products and systems for the protection and repair of concrete structures-Part 2: Surface protection systems for concrete. European Committee for Standardization.
- Fajrin, J., & Pratama, L. G. (2016). Improving mortar properties in saline environment. In *Proceedings of the Sriwijaya International Conference on Engineering, Science and Technology (SICEST)* (pp. 35–38). <http://eprints.unram.ac.id/17653/>.
- Franzoni, E. (2014). Rising damp removal from historical masonries: A still open challenge. *Construction and Building Materials*, 54, 123–136. <https://doi.org/10.1016/j.conbuildmat.2013.12.021>.
- Franzoni, E. (2018). State-of-the-art on methods for reducing rising damp in masonry. *Journal of Cultural Heritage*, 31, S3–S9. <https://doi.org/10.1016/j.culher.2017.12.005>.
- Gao, X. J., & Wang, X. Y. (2017). Impacts of global warming and sea level rise on service life of chloride-exposed concrete structures. *Sustainability (Switzerland)*, 9(3). <https://doi.org/10.3390/su9030460>.
- Ghorbani, S., Taji, I., Tavakkolizadeh, M., Davodi, A., & de Brito, J. (2018). Improving corrosion resistance of steel rebars in concrete with marble and granite waste dust as partial cement replacement. *Construction and Building Materials*, 185, 110–119. <https://doi.org/10.1016/j.conbuildmat.2018.07.066>.
- Goyal, A., Pouya, H. S., Ganjian, E., & Claisse, P. (2018). A review of corrosion and protection of steel in concrete. *Arabian Journal for Science and Engineering*, 43(10), 5035–5055. <https://doi.org/10.1007/s13369-018-3303-2>.
- Heiman, J., Waters, E. H., & McTaggart, R. C. (1973). The treatment of rising damp. *Architectural Science Review*, 16(4), 170–177. <https://doi.org/10.1080/00038628.1973.9696843>.
- Henshell, J. (2016). *The manual of below-grade waterproofing* (2nd ed.). Routledge.
- l'Anson, S. J., & Hoff, W. D. (1988). Chemical injection remedial treatments for rising damp—I. The interaction of damp-proofing fluids with porous building materials. *Building and Environment*, 23(3), 171–178. [https://doi.org/10.1016/0360-1323\(88\)90027-3](https://doi.org/10.1016/0360-1323(88)90027-3).
- Kozak, A. (2015a). Multi-criteria assessment of an acrylic coating exposed to natural and artificial weathering. *Procedia Engineering*, 108, 664–672. <https://doi.org/10.1016/j.proeng.2015.06.197>.
- Kubal, M. T. (2008). *Construction waterproofing handbook* (2nd ed.). McGraw-Hill.
- Kumar, V. (1998a). Protection of Steel Reinforcement for Concrete- A Review. *Corrosion Reviews*, 16(4), 317–358. <https://doi.org/10.1515/CORRREV.1998.16.4.317>.
- Landivar Macias, A., & Rotta Loria, A. F. (2020). Electrokinetic treatments of soils: potential for geoenery applications. *E3S Web of Conferences*, 205, 09002. <https://doi.org/10.1051/e3sconf/202020509002>.
- Li, J., Song, J., Zhang, S., Liu, W., Cui, Z., & Li, W. (2024). The effects of various silicate coatings on the durability of concrete: Mechanisms and implications. *Buildings*, 14(2), 381. <https://doi.org/10.3390/buildings14020381>.
- Liu, M., Cheng, X., Li, X., Yue, P., & Li, J. (2016). Corrosion behavior and durability of low-alloy steel rebars in marine environment. *Journal of Materials Engineering and Performance*, 25(11), 4967–4979. <https://doi.org/10.1007/s11665-016-2342-7>.

- Manning, D. G. (1996). Corrosion performance of epoxy-coated reinforcing steel: North American experience. *Construction and Building Materials*, 10(5), 349-365. [https://doi.org/10.1016/0950-0618\(95\)00028-3](https://doi.org/10.1016/0950-0618(95)00028-3).
- Morcillo, M. (1984). Minimum Film Thickness for Protection of Hot-Rolled Steel: Results after 23 Years of Exposure at Kure Beach, North Carolina. In *New Concepts for Coating Protection of Steel Structures* (pp. 95–112). ASTM International 100 Barr Harbor Drive, PO Box C700, West Conshohocken, PA 19428-2959. <https://doi.org/10.1520/STP29530S>.
- Morton, D., Prieto, A., Alhambra, T., Morales, R., & Juni, C. (2021). The importance of surface preparation method on the corrosion resistance and mechanical properties of zinc-rich primers. *CORROSION* 2021, 1–15. <https://doi.org/10.5006/C2021-16642>.
- Nguyen, T. H., & Nguyen, T. A. (2018). Protection of steel rebar in salt-contaminated cement mortar using epoxy nanocomposite coatings. *International Journal of Electrochemistry*, 2018, 8386426. <https://doi.org/10.1155/2018/8386426>.
- Panossian, Z., Mariaca, L., Morcillo, M., Flores, S., Rocha, J., Peña, J. J., Herrera, F., Corvo, F., Sanchez, M., Rincon, O. T., Priddybailo, G., & Simancas, J. (2005). Steel cathodic protection afforded by zinc, aluminium and zinc/aluminium alloy coatings in the atmosphere. *Surface and Coatings Technology*, 190(2-3), 244-248. <https://doi.org/10.1016/j.surfcoat.2004.04.023>.
- Pour-Ali, S., Dehghanian, C., & Kosari, A. (2015). Corrosion protection of reinforcing steels in chloride-laden concrete environment through epoxy/polyaniline–camphorsulfonate nanocomposite coating. *Corrosion Science*, 90, 239-247. <https://doi.org/10.1016/j.corsci.2014.10.015>.
- Sakr, M. R., & Bassuoni, M. T. (2021). Silane and methyl-methacrylate based nanocomposites as coatings for concrete exposed to salt solutions and cyclic environments. *Cement and Concrete Composites*, 115, 103841. <https://doi.org/10.1016/j.cemconcomp.2020.103841>.
- Schmidt, D. P., Shaw, B. A., Sikora, E., Shaw, W. W., & Laliberte, L. H. (2006). Corrosion protection assessment of sacrificial coating systems as a function of exposure time in a marine environment. *Progress in Organic Coatings*, 57(4), 352-364. <https://doi.org/10.1016/j.porgcoat.2006.09.021>.
- Schmitt, G. a., Schütze, M., Hays, G. F., Burns, W., Han, E., Pourbaix, A., & Jacobson, G. (2009). Global Needs for Knowledge Development in Materials Deterioration and Corrosion Control in cooperation with. Federal Highway Administration, FHWA-RD-01(May), 1–44.
- Shamsai, A., Peroti, S., Rahmani, K., & Rahemi, L. (2012). Effect of water-cement ratio on abrasive strength, porosity and permeability of nano-silica concrete. *World Applied Sciences Journal*, 17(8), 929-933.
- Shang, H., Shao, S., & Wang, W. (2021). Bond behavior between graphene modified epoxy coated steel bars and concrete. *Journal of Building Engineering*, 42, 102481. <https://doi.org/10.1016/j.jobbe.2021.102481>.
- Sharpe, R. W. (1977). Injection systems for damp-proofing. *Building and Environment*, 12(3), 191–197. [https://doi.org/10.1016/0360-1323\(77\)90017-8](https://doi.org/10.1016/0360-1323(77)90017-8).
- Tansel, B., & Zhang, K. (2022). Effects of saltwater intrusion and sea level rise on aging and corrosion rates of iron pipes in water distribution and wastewater collection systems in coastal areas. *Journal of Environmental Management*, 315, 115153. <https://doi.org/https://doi.org/10.1016/j.jenvman.2022.115153>.
- Torres, M. I., & Peixoto de Freitas, V. (2007). Treatment of rising damp in historical buildings: Walls with ventilated baseboards. *Construction and Building Materials*, 21(3), 505-514. <https://doi.org/10.1016/j.conbuildmat.2005.08.014>.
- Vogele, J. (1985). Protection against rising damp in masonry: the baroque palace in Ludwigsburg, a case study. *Proceedings of the International Conference on Building Appraisal, Maintenance and Preservation*, 113–123.
- Young, D. (2008). Salt attack and rising damp: a guide to salt damp in historic and older buildings. <https://www.environment.nsw.gov.au/publications/salt-attack-and-rising-damp-guide-salt-damp-historic-and-older-buildings>.

ISBN: 978-604-357-453-1



NOT FOR SALE